FACULTY OF SCIENCE
UNIVERSITY OF COPENHAGEN

PhD Thesis

Diana Juncher

Modeling the Cloudy Atmospheres of Cool Stars, Brown Dwarfs and Hot Exoplanets

Supervisor:
Uffe Gråe Jørgensen

Co-supervisors:
Lars Astrup Buchhave
Christiane Helling

January 11, 2016

Modeling the Cloudy Atmospheres of Cool Stars, Brown Dwarfs and Hot Exoplanets

Diana Juncher
Niels Bohr Institute & Starplan
University of Copenhagen

This thesis has been submitted to the

PhD School of The Faculty of Science, University of Copenhagen

for the degree of

Philosophiæ Doctor

January 11, 2016

Abstract

The search for exoplanets is one of the most exciting fields in astronomy and since the discovery of the first exoplanet orbiting a main sequence star in 1995, we have found thousands of new worlds beyond our own. The various techniques we use for the detection and characterization of exoplanets are based on very different principles, but they all have one important thing in common: The properties of an exoplanet cannot be determined without knowing the properties of its host star. It is therefore crucial that the stellar models linking the observations of a star to its properties are as precise as possible.

M-dwarfs are very attractive targets when searching for new exoplanets. Unfortunately, they are also very difficult to model since their temperatures are low enough for dust clouds to form in their atmospheres. The primary goal of this project is therefore to merge the model atmosphere code `MARCS` with the dust model code `DRIFT`, thus facilitating the computation of self-consistent cloudy atmosphere models that can be used to properly determine the stellar parameters of cool stars.

With this enhanced model atmosphere code we have created a small grid of cool, dusty atmosphere models ranging in effective temperatures from $T_{\text{eff}} = 2000 - 3000$ K. We have found that dust formation appears in models with $T_{\text{eff}} < 2700$ K and can have a significant effect on the structure and the spectrum of the atmosphere. We have compared the synthetic spectra of our models with observed spectra and found that they fit the spectra of mid to late type M-dwarfs and early type L-dwarfs well. We have also illustrated how these models - with additional development into the regime of exoplanet atmospheres - can be compared with spectrum observations to characterize the atmospheres of exoplanets.

Dansk referat

Jagten på exoplaneter er et af de mest spændende områder inden for astronomien, og siden opdagelsen af den første i 1995 har vi fundet tusinder af nye verdener uden for vores Solsystem. De metoder vi bruger til at finde og karakterisere exoplaneter er meget forskellige, men de har alle en vigtig ting tilfælles: Det er ikke muligt at bestemme en exoplanets egenskaber uden at kende dens værtsstjernes egenskaber. Det er derfor nødvendigt at de stjernemodeller, der forbinder observationerne af en stjerne med dens egenskaber, er så præcise som muligt.

Når vi leder efter nye exoplaneter er M-dværge et attraktivt sted at kigge, da det på grund af deres relativt små dimensioner er nemmere at finde exoplaneter omkring dem. Desværre er det meget vanskeligt at lave modeller af deres atmosfærer, idet deres temperaturer er tilstrækkeligt lave til at der kan dannes støvskyer øverst i deres atmosfærer. Formålet med dette projekt er derfor at kombinere `MARCS`, et program der modellerer stjerneatmosfærer, med `DRIFT`, et program der modellerer støvdannelse, for dermed at kunne lave bedre modeller af kølige stjerneatmosfærer med støv, som kan bruges til mere præcist at kunne bestemme parametrene for M-dværge.

Med dette udvidede program har vi lavet en række kølige atmosfærer med støv med effektive temperaturer mellem $T_{\rm eff} = 2000 - 3000$ K. Vi har vist, at støvdannelse forekommer i kølige atmosfærer med $T_{\rm eff} < 2700$ K og kan have en stor indflydelse på atmosfærens struktur og spektrum. Vi har sammenlignet syntetiske spektra baseret på vores modeller med observerede spektra og konkluderet, at de er sammenlignelige med de koldeste M-dværge og de varmeste L-dværge. Vi har vist, hvordan disse modeller - efter yderlige udvikling med fokus på exoplaneters atmosfærer - kan anvendes til at bestemme indholdet af en exoplanets atmosfære ud fra observationer af dens spektrum.

Acknowledgements

I would like to thank everybody I have worked with, and everyone that has inspired and supported me during my three years as a PhD student.

First of all, I would like to thank my supervisor Uffe Gråe Jørgensen for giving me this opportunity and for his continued guidance and support - even on the weekends. I would also like to thank him for involving me in observations with the Danish 1.54m telescope at La Silla which has added a different and exciting dimension to my project.

A big thank you also to my co-supervisor Lars Buchhave who came up with the idea of my project in the first place. I am very grateful for his advice and to have been involved in various of his exoplanet follow-up observation projects.

My thanks also goes to my second co-supervisor Christiane Helling for inviting me to join her group in St Andrews for half a year and for all of her help. Our discussions about dust and dust formation have been a vital part of my work.

I would also like to thank the Niels Bohr Institute, Starplan, University of St Andrews, IDA and the Wieth Knudsen foundation for the financial support of my PhD.

Thank you to the people of Starplan and the astronomy group of NBI for good company and for providing a creative and stimulating working environment. A special thank you to Andrius Popovas for numerous discussions about `MARCS`.

Thank you to the people at Room 321 at St Andrews for being my colleagues and friends and for making me feel at home in a foreign country.

Finally, I would like to thank my family and friends for all their love and support.

Contents

1

Introduction

The search for exoplanets is one of the most exciting fields in astronomy. It seeks to answer questions that have been teasing our curiosity and imagination for centuries: Is the Earth unique? Are there other habitable planets out there? What are they like? Can they host life? Are we alone?

Since the discovery of the first exoplanet orbiting a main sequence star in 1995 (Mayor and Queloz, 1995), we have found thousands of new worlds outside our Solar system, and we now know that planets are more common than stars in the Milky Way. Over the years we have developed and refined several techniques for detecting exoplanets, and although they are based on very different principles with each their strengths and weaknesses, they all have one important thing in common: The properties of an exoplanet cannot be determined without knowing the properties of its host star. It is therefore crucial that the stellar models linking the observations of a star to its properties are as precise as possible.

M-dwarf stars are small and relatively cool stars located in the lower end of the main sequence of the Hertzsprung-Russell diagram. They are particularly interesting when it comes to searching for new exoplanets as their smaller dimensions makes it easier to detect if they have any planets. For example, a planet orbiting an M-dwarf will generate a larger radial velocity signal and a greater transit depth than if the same planet was orbiting a Sun-like star. Furthermore, recent results indicate that 40% of the M-dwarfs in our galaxy have a super-Earth class planet orbiting in the habitable zone (Bonfils et al., 2013). Because of the sheer number of M-dwarfs in our galaxy - more than 80% of the total number of stars - this makes them very attractive targets.

Despite the fact that most of the stars in our Solar neighborhood are M-dwarfs, none of them are visible to the naked eye. Even the brightest known M-dwarf and our nearest neighbor, Proxima Centauri, is about five magnitudes fainter than the limit of the naked eye. The reason is that with a typical luminosity of $0.01 - 1\%$ of the Sun, M-dwarfs are very faint and therefore relatively difficult to observe. On top of that, the stellar atmospheres of late M-dwarfs are also among the most difficult to model since their temperatures are low enough for dust clouds to form in their atmospheres (Tsuji et al., 1996).

The primary goal of this project is to merge the model atmosphere code `MARCS` (Gustafsson et al., 1975) with the dust model code `DRIFT` (Helling et al., 2008c) to compute self-consistent cloudy atmosphere models that can be used to properly determine the stellar parameters of cool stars. This is becoming of critical importance as more and more focus is being directed towards the discovery of small exoplanets orbiting M-dwarfs in the habitable zone. In 2017 NASA will launch the space telescope Transiting Exoplanet Survey Satellite (TESS), the objective of which is to monitor the brightest stars in the sky, including the 1,000 closest M-dwarfs.

In addition, these enhanced models could also be adapted to probe the atmospheres of brown dwarfs and hot exoplanets. Brown dwarfs are substellar objects that are not massive enough to sustain sufficient hydrogen fusion in their cores to stop the gravitational contraction as in stars, and they occupy the mass range between the heaviest gas giants and the lightest stars. Modeling their atmospheres is therefore a natural step towards modeling the atmospheres of exoplanets. Such models would soon be able to be confronted with observations of the atmospheres of hot Jupiters and mini-Neptunes orbiting bright stars discovered by e.g. TESS. Several initiatives to allow the observation of exoplanet atmospheres are currently underway, including the James Web Space Telescope (JWST) and Earth-based extremely large telescopes such as the Giant Magellan Telescope (GMT) and the European Extremely Large Telescope (E-ELT).

The outline of this thesis is as follows: In Chapter 2 I describe the physical and spectral characteristics of cool dwarf stars and brown dwarfs and review the approaches and results of current cloudy atmosphere models. In Chapters 3 and 4 I go through the basic concepts and equations of stellar atmospheres and cloud formation and describe how they are modeled by `MARCS` and `DRIFT`. This is followed by a presentation of the code I have developed, how I have implemented it and what input data I have used in Chapter 5. In Chapters 6-7 I present a detailed analysis of my cloudy atmosphere models and examine how they compare with observations. In Chapter 8 exoplanets are in focus, and I will describe some of the most successful detection methods and their results. I will also present the exoplanet observation projects I have been a part of and illustrate how my cloudy atmosphere models will be able to contribute to the characterization of exoplanet atmospheres in the future. In Chapter 9 I offer my conclusions and discuss the next steps in the continued development of the `DRIFT-MARCS` code.

2

Review: Ultra cool dwarf atmospheres

2.1 Stars, brown dwarfs and giant planets

Stars are born within the vast interstellar clouds that span the universe. Fluctuations in density can cause the gas and dust to collapse under their own gravity, breaking into smaller and smaller fragments until they eventually reach stellar masses. At some point, the release of gravitational potential energy has heated the dense cores of these fragments enough for nuclear fusion to begin, and the bright light of a new star is ready to join its billions of siblings (Jeans, 1902).

Stars spend the majority of their lives fusing hydrogen to helium deep in their cores. The outflow of energy from this process provides the pressure necessary to keep the stars from collapsing as well as the energy by which they shine. Stars in this first phase of their life are known as main sequence stars and they occupy a distinct broad band in the Hertzsprung-Russel diagram, stretching from the bright and hot high mass stars to the dim and cool low mass stars. It is in the latter end of the diagram that we find the ultra cool dwarfs.

M dwarfs are the coolest stars on the main sequence. The smallest and coolest of these, the late type M dwarfs with spectral types between M6V-M9V, have masses of about 10% of the Solar mass, luminosities between 0.01-0.1% of the Solar luminosity, and effective temperatures less than 2800 K reaching down below 2000 K depending on their age and metallicity, which, as we shall see, allows for dust formation in the upper part of their atmospheres (Kaltenegger

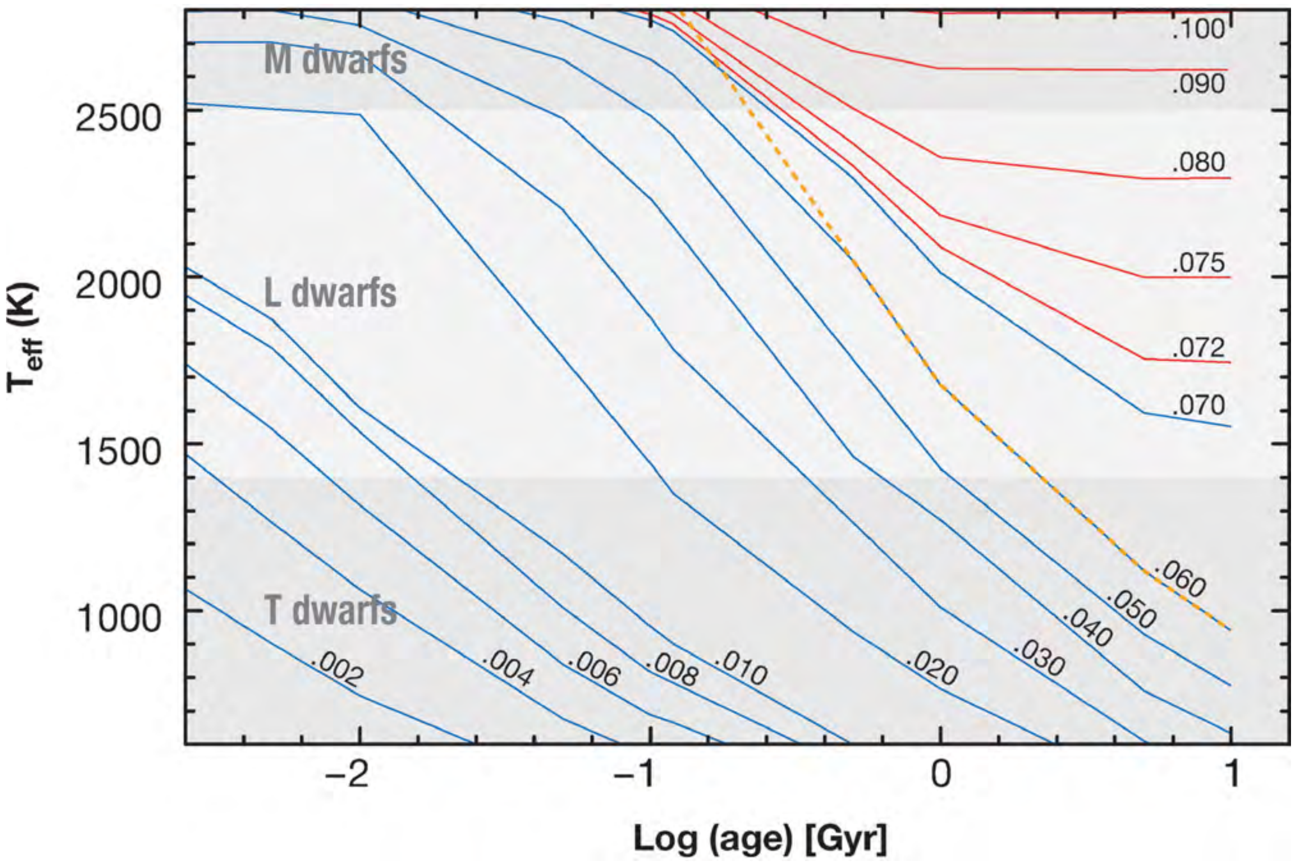

Figure 2.1.1: Theoretical tracks showing the evolution of effective temperature with age for low-mass stars (red) and brown dwarfs (blue) of solar composition. Grey areas indicate the approximate temperature ranges. The tracks warmer than 1500 K come from Chabrier et al. (2000) (using the `AMES-dusty` models of Allard et al. (2001)) and the tracks cooler than 1500 K come from Baraffe et al. (2003) (using the `AMES-cond` models of Allard et al. (2001)). The orange dotted line marks the boundary for lithium fusion, objects to the left of this line will not have burned their lithium. Source: Kirkpatrick (2005).

and Traub, 2009).

The lower-mass limit of the main sequence lies at the minimum mass for stable hydrogen burning ($M \approx 0.07M_{\odot}$) for objects with solar composition (Chabrier and Baraffe, 1997). Below this mass we find the brown dwarfs: substellar objects that are too small to ever develop strong enough hydrogen fusion to stop them from contracting. Brown dwarfs are brightest when they are born, and the highest mass brown dwarfs might even experience some hydrogen fusion in their early life. Furthermore, brown dwarfs with masses above $M > 0.012M_{\odot}$ will be able to fuse deuterium, while brown dwarfs with masses above $M > 0.06M_{\odot}$ will also be able to fuse lithium (Saumon et al., 1996). Still, the energy released from this is not enough to counterbalance the gravitational collapse, and brown dwarfs will continue to contract until their cores become electron-degenerate, growing ever fainter and cooler over time (Basri, 2000). The coolest observed brown dwarfs have temperatures of only a few hundred kelvin (Wright et al., 2014).

The distinction between brown dwarfs and giant planets is a topic of some debate. Different suggestions for the dividing line between the two include the minimum mass for deuterium burning, the opacity limited minimum mass for fragmentation and formation history. It is not enough to consider mass alone, for example Béjar et al. (2001) have observed brown dwarfs of only a few Jupiter masses which is smaller than the masses of some observed exoplanets. Chabrier et al. (2005) suggests that brown dwarfs should be defined as objects that are formed from the collapse of a cloud and have masses smaller than the minimum mass for hydrogen burning, while planets should be defined as objects formed in a protoplanetary disk around a parent star, with a high mass ratio, and with an enhanced average abundance of heavy elements.

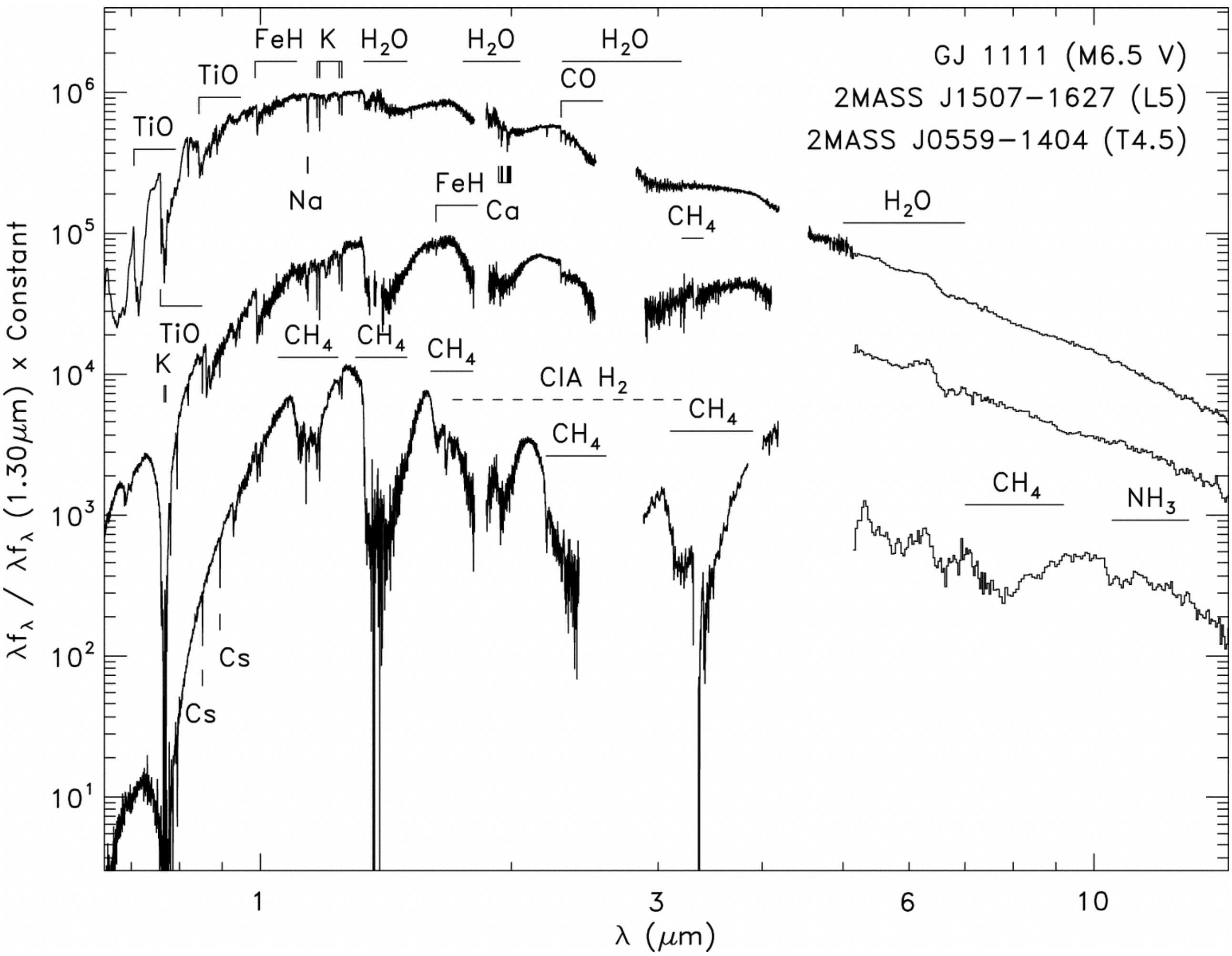

Figure 2.1.2: Observed spectra of representative M-type, L-type and T-type dwarfs. The red-optical spectra are from Kirkpatrick et al. (1991), Reid et al. (2000), and Burgasser et al. (2003), and the near-infrared spectra are from Cushing et al. (2005) and Rayner et al. (2006). Source: Cushing et al. (2006).

2.2 Spectral characteristics

The effective temperatures of M dwarfs are low enough for the atoms in the atmosphere to form numerous molecules. In particular, metal oxides and hydrides like TiO, VO, FeH, CrH, CaH and MgH are major absorbers in the optical, while CO and H_2O dominate the infrared part of the spectrum. The bands of these molecules grows increasingly stronger as we move through the spectral subclasses and the effective temperature decreases (Chabrier et al., 2005; Lodders and Fegley, 2006). Additionally, atomic lines of Al, Fe, Mg, Ca, Ti, Na, and K are also visible (Cushing et al., 2005). In the coolest type M dwarfs, the temperature in the atmosphere is low enough for some of the metals and silicates to condense into dust grains, but they bind only a small fraction of the affected molecules and the effect on the observed spectrum is small (Tsuji et al., 1996).

Below effective temperatures of about $T_{\text{eff}} \approx 2200$ K (depending on the age and metallicity, see Figure 2.1.1) we enter the regime of brown dwarfs. Unlike stars, their spectral appearance varies with time as they cool, moving through the M, L and T spectral classes. The L dwarfs are characterized by the growing strength of the H_2O and metal hydride bands, and the gradual disappearance of the TiO and VO bands. The absorption lines of Ca, Al, Ti, and Fe may also weaken and eventually disappear, as an increasing fraction of the elements are bound in dust grains (Lodders and Fegley, 2006). This increase in dust grains gives rise to highly reddened spectral energy distributions and absorption features (Cushing et al., 2006). T dwarfs are the coldest known class of brown dwarfs, and they are characterized by even stronger H_2O bands as well as the appearance of CH_4, as this is the dominant form of carbon for temperatures below $T \approx 1300 - 1500$K (Fegley and Lodders, 1996). The spectra of the latest type T dwarfs also contain absorption bands of NH_3 (Lodders and Fegley, 2006).

2.3 Atmosphere models

Modeling dust formation is a complex problem involving many and different coupled processes that depend on a wide range of physical and chemical parameters. Rossow (1978), Lewis (1969) and Carlson et al. (1988) were among the first to develop cloud models for the atmospheres of the giant gas planets in our Solar System, while Lunine et al. (1986) and Burrows et al. (1989) were among the first to introduce cloud formation into their atmospheres models of brown dwarfs. Later, Tsuji et al. (1996) suggested that cloud formation should be considered for all objects with $T_{\text{eff}} < 2800$ K and should therefore also be included in models of late type M dwarf atmospheres as well. Some of these older models are discussed in Ackerman and Marley (2001).

Many of the early models of cloudy atmospheres were able to reproduce basic features of ultra cool dwarfs by simply turning on or off the opacity of dust in the atmosphere at its chemical equilibrium temperature-pressure location. Over the years the models have grown more detailed and more realistic, and today several independent groups are working on complex models of cloud formation using different strategies. Some are based on practical considerations (Tsuji, 2001; Barman et al., 2011; Burrows et al., 2006), while others are inspired by measurements of the atmospheres of the planets in our Solar system (Allard et al., 2001; Cooper et al., 2003), terrestrial cloud formation (Ackerman and Marley, 2001) or asymptotic giant branch stars (Helling et al., 2001; Woitke and Helling, 2003, 2004).

Below we briefly review six different cloud models that are currently used to model the atmospheres of ultra cool dwarfs. They are all 1D models assuming local thermodynamic equilibrium, that the dust and gas have the same temperature, that the gas-phase abundances determine the kind and the amount of dust condensing. Furthermore, they all use equilibrium constants Kp in their gas-phase treatments.

2.3.1 Current models

1) The Tsuji model

In the `Unified Cloudy Model` by Tsuji and collaborators (Tsuji, 2001, 2002; Tsuji et al., 2004; Tsuji, 2005) it is assumed that the gas and condensates are in phase equilibrium, and that dust forms as soon as the thermodynamical condition for condensations is satisfied, i.e. when the supersaturation ratio is $S = 1$. The resulting dust cloud has strict lower and upper boundaries defined by the condensation temperature $T_{\rm cond}$ and the slightly cooler critical temperature $T_{\rm cr}$. For temperatures $T > T_{\rm cond}$ the photosphere is too hot for dust to form, for temperatures $T_{\rm cond} > T > T_{\rm cr}$ small dust grains remain suspended in the photosphere, and for temperatures $T < T_{\rm cr}$ dust grains are assumed to instantly grow large and precipitate into the optically thick parts of the photosphere. The formation of dust grains thereby leads to an element depleted gas phase for $T < T_{\rm cond}$, but only the small grains at $T_{\rm cond} > T > T_{\rm cr}$ contribute as an opacity source.

For the opacity treatment, a small representative set of three condensates are included: Al_2O_3, Fe and $MgSiO_3$. It is assumed that the dust grains are spherical and homogeneous. Because the dust grains that make up the clouds are small, the opacity depends only little on their size distribution and all dust grains are therefore given a constant size of $a = 0.01$ μm.

Yamamura et al. (2010); Tsuji et al. (2011); Sorahana and Yamamura (2012, 2014) have applied the `Unified Cloudy Model` to derive the effective temperature, critical temperature and surface gravity of a selection of brown dwarfs, to investigate how the effective temperature correlates with the spectral type, and to examine the appearance and strength of specific molecular absorptions bands and how they correlate with element abundances. Sorahana et al. (2014) has also used the models to show how some molecular absorption bands can be good tracers of chromospheric activity in brown dwarfs.

2) The Allard & Homeier model

Allard and collaborators have included dust formation in the `PHOENIX` stellar atmosphere model code (Allard et al., 2001), most recently creating the `Settl` model, which takes into account a number of microphysical processes as well as gravitational settling and convective mixing (Allard et al., 2003, 2012; Allard, 2014). Dust is assumed to form when the supersaturation ratio $S > 1.001$. For each layer in the photosphere, the dust grain mean sizes and number densities are calculated by comparing the timescales for condensation, coagulation, gravitational settling (based on a planetary cloud microphysical study by Rossow (1978)) with the time scale for mixing due to convective overshooting (based on 3D radiative hydrodynamical convection simulation results for M dwarfs by Ludwig et al. (2002)). The resulting dust cloud have a lower boundary defined by the condensation temperature $T_{\rm cond}$ and an upper boundary that is a few pressure scale heights from the top of the convection zone. Above the clouds the gravitational settling is more efficient than the element mixing, leaving an element depleted dust free photosphere.

For the opacity treatment, 55 condensate are included, the most important being ZrO_2, Al_2O_3, $CaTiO_3$, $Ca_2Al_2SiO_7$, $MgAl_2O_4$, Ti_2O_3, Ti_4O_7, $Ca_2MgSi_2O_7$, $CaMgSi_2O_6$, $CaSiO_3$, Fe, Mg_2SiO_4, $MgSiO_3$, Ca_2SiO_4, $MgTiO_3$, $MgTi_2O_5$, $Al_2Si_2O_{13}$, VO, V_2O_3, and Ni (Allard et al., 2014). It is assumed that the dust grains are spherical and homogeneous and distributed according to a log-normal distribution.

Crossfield et al. (2014) has used the `Settl` model to identify patchy clouds and to evaluate the characteristic timescale for the evolution of global weather patterns on the brown dwarf Luhman 16.

3) The Barman model

Barman et al. (2011) have included their own dust model in the `PHOENIX` stellar atmosphere model code (Hauschildt, 1992). They assume phase-equilibrium and that dust forms when the supersaturation ratio $S = 1$ which gives a well defined cloud base. Above the cloud base the cloud height and density is determined by a single free parameter $P_{\rm min}$. For $P_{\rm g} \geq P_{\rm min}$ the equilibrium dust concentration is assumed, for $P_{\rm g} < P_{\rm min}$ the equilibrium dust concentration is multiplied by an exponentially decaying function. The dust grain sizes are distributed according to a log-normal distribution with a prescribed modal size of $a_0 = 1-100\ \mu$m that is independent of height.

For the opacity treatment, the 31 condensates listed in Ferguson et al. (2005) are included. It is assumed that the dust grains are spherical and heterogeneous.

Barman et al. (2011) have applied their model to the observed spectra of the young exoplanet HR8799b, demonstrating the presence of thick dust clouds and a hydrogen-rich atmosphere.

4) The Cooper model and the Burrows model

The models by Cooper et al. (2003) and Burrows et al. (2006, 2011) share some similarities. They both assume that dust forms when the supersaturation ratio $S > 1 + S_{\rm max}$, where the free parameter $S_{\rm max}$ is independent of height.

In the Cooper model it is assumed that the abundance of condensation nuclei is sufficient for nucleation to begin at $S_{\rm max} \approx 0.01$ for all dust species. The mean dust grain size a_0 is determined by the comparison of the timescales of nucleation, coagulation, coalescence and gravitational settling from Rossow (1978) with the timescale of convective mixing.

In the Burrows model $S_{\rm max}$ depends on the type of dust grain in question. For example, $S_{\rm max} = 0.01$ for Fe, while $S_{\rm max} = 1.0$ for the silicates such as Mg_2SiO_4. The height and density of the cloud is determined by scaling the equilibrium dust concentration with the cloud shape function $f(P_{\rm g})$ that causes an exponential fall-off above the cloud deck and below the cloud base. The mean dust grain size is set to $a_0 = 30\ \mu$m. The model includes 16 dust grain species.

For the opacity treatment, a small representative set of four condensates are included: Fe, Mg_2SiO_4, $Ca_2Al_2SiO_7$, H_2O. Both models assume that the dust grains are spherical and homogeneous and that their size distribution is an exponentially decaying power law consistent with measurements of particle size distributions in the water clouds of Earth (Sudarsky et al., 2000).

Apai et al. (2013) have used the Burrows model to show that two L/T transition brown dwarfs have patchy cloud covers with large structures, and to explain how their observed atmospheric variability is a result of the presence of two different cloud layers - an upper, cool thick layer and a lower, warm thin layer.

5) The Marley, Ackerman & Lodders model

In the cloud model by Ackerman and Marley (2001); Marley et al. (2002) it is assumed that dust forms when the supersaturation ratio $S > 1$. The chemical equilibrium calculations are performed with the `CONDOR` code (Lodders and Fegley, 1993; Fegley and Lodders, 1994), which removes the primary condensates from the gas into cloud layers thereby preventing the creating of secondary condensate (Lodders, 2004; Lodders and Fegley, 2006). The vertical extension of the cloud is governed by a balance between the upward turbulent mixing of gas and dust, and the downward transport of dust by gravitational settling. The free parameter $f_{\rm rain}$ describes the efficiency of the gravitational settling and constrains the size of the dust grains. High values of $_{\rm rain}$ describe rapid dust grain growth and efficient gravitational settling, which leads to geometrically and optically thin clouds. Conversely, small values of $f_{\rm rain}$ describe slow dust grain growth and inefficient gravitational settling, which leads to geometrically and optically thick clouds.

For the opacity treatment, a small representative set of four condensates are included: Fe, $MgSiO_3$, and H_2O. It is assumed that the dust grains are spherical and homogeneous and that they are distributed according to a log-normal distribution.

Fortney et al. (2008) have applied the Marley, Ackerman & Lodders model to the spectra of highly irradiated close-in giant planets to suggest the existence of two classes of irradiated planets. Morley et al. (2012) have applied the Marley, Ackerman & Lodders model to the spectra of two T dwarfs to suggest the existence of sulfide clouds in their cool atmospheres.

6) The Woitke & Helling + Dehn & Hauschildt model

The DRIFT model developed by Woitke & Helling (Helling et al., 2001; Woitke and Helling, 2003, 2004; Helling and Woitke, 2006; Helling et al., 2008a) is described in detail in Chapter 4 but for the sake of comparison we will briefly go through it here as well.

The model describes cloud particle formation by modeling seed formation and growth and evaporation coupled to gravitationally settling, convective mixing and element depletion. The model assumes that seed formation can only take place when the supersaturation ratio $S \gg 1$, while subsequent reactions on an existing grain surface only requires $S > 1$. Grain sizes, grain material composition, total grain volume, and remaining gas-phase element abundances are estimated by solving conservation equations of dust moments and element conservation. Element replenishment is controlled by a parametrized mixing time-scale $\tau_{\rm mix}(z)$.

For the opacity treatment, 12 condensates are included: TiO_2, SiO, SiO_2,Fe, FeO, Fe_2O_3, FeS, MgO, $MgSiO_3$, Mg_2SiO_4, Al_2O_3, and $CaTiO_3$. It is assumed that the dust grains are spherical and heterogeneous and that they are distributed according to a double delta-peaked size distribution function.

The DRIFT model code has been adopted as a module in the PHOENIX model atmosphere code, creating the combined DRIFT-PHOENIX model code (Dehn, 2007; Helling et al., 2008b). Witte et al. (2009) have applied the DRIFT-PHOENIX model to study metal deficient brown dwarfs. Helling et al. (2011b,a, 2013); Rimmer and Helling (2013); Stark et al. (2013) have applied the DRIFT-PHOENIX model to study ionization and discharge processes in ultra-cool, cloudy atmospheres.

2.3.2 Comparison of models

Models 1-5 consider observed timescales of dust formation in the atmosphere of Jupiter and/or parametrize the vertical extension of the dust clouds, while model 6 models seed formation, grain growth and evaporation, gravitational settling, element depletion and their interactions from first principles. Helling et al. (2008a) have performed an extensive comparison of the chemistry and dust cloud formation of the Tsuji model, Allard & Homeier model, Marley, Ackerman & Lodders model, and the Woitke & Helling + Dehn model. They found that the models generally predicted comparable cloud structures despite their different approaches. Most of the models agreed that small grains composed mainly of silicates populate the upper clouds layers, while iron is a major component of the large grains at the cloud base. In detail, however, they differed substantially, with varying grain sizes, amount of dust, and dust- and gas-phase composition. Considering their spectral appearance, the results of the models appear

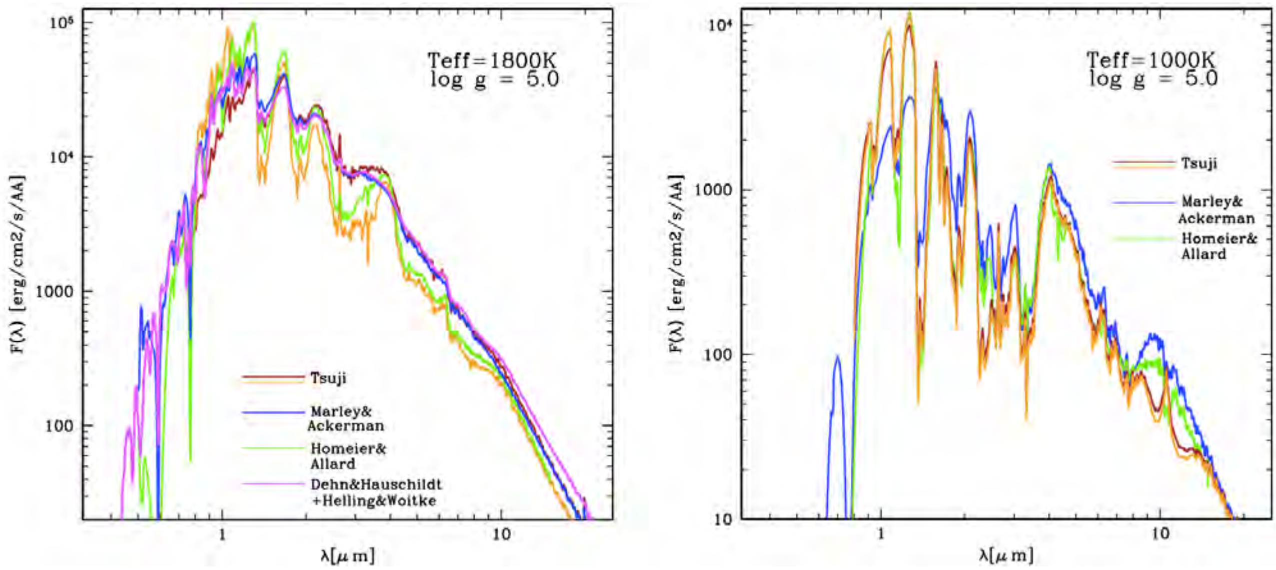

Figure 2.3.1: Synthetic spectra for $T_{\rm eff}$ = 1800 K (left) and $T_{\rm eff}$ (right) with $\log(g) = 5.0$ and solar element composition. Two spectra are plotted for the Tsuji dust model: $T_{\rm cr}$ = 1700 K (brown) and $T_{\rm cr}$ = 1900K (orange). Source: Helling et al. (2008a)

.

to fall into two categories: 1) The high-altitude cloud models (Tsuji ($T_{\rm cr}$ = 1700 K); Marley, Ackerman & Lodders; Woitke & Helling + Dehn & Hauschildt) where the dust-to-gas ratio peaks at high altitudes, and small dust grains are present well above this peak, 2) The low-altitude cloud models (Tsuji ($T_{\rm cr}$ = 1900 K); Allard & Homeier) where the dust-to-gas ratio peaks further inside the atmosphere and no dust grains are present above the peak.

3

Theory: Stellar atmospheres

In astronomy we study the distant celestial objects whose existence has had us gazing at the night sky in wonder for thousands of years. They capture our minds and souls with their enormous dimensions, fascinating beauty, and slow majestic evolution that spans billions of years. The study of these objects comes with a catch, though: We cannot actually touch most of the objects we study, be it stars, nebulae or galaxies. Our main source of information about them comes from the light they emit. It is impressive to think that the faint, twinkling light from a star in the night sky can tell us the distance of the star along with its mass, age and chemical composition, and even whether or not it has any planets and when and how its life will end. We interpret our observations with the help of theoretical models, they are the link between the light we observe and the star itself.

Stars are powered by the thermonuclear fusion of elements deep in the cores of their interiors. The energy released travels through the star, being repeatedly absorbed and emitted by the surrounding stellar matter, until it eventually reaches the thinner outer layers known as the stellar atmosphere. Here the opacity is low enough for most of the light to escape and - some hundreds or thousands of years later - arrive at our telescopes. As the light passes through the atmosphere it is affected by the presence of different atoms, ions and molecules, the gravitational pull of the star, the temperature of its surroundings, and turbulence on both microscopic and macroscopic scales, magnetic fields and so on. It is by studying these effects through the comparison of observations with models that we can learn about the properties of the star.

The first modern computer models of stellar atmospheres began to appear in the late 1960s and early 1970s, and since then they have greatly evolved, their complexity growing in step with the advancement of computer power and available physical data. Now a vital tool for constructing atmosphere models, their purpose is easily defined - to create the simplest possible model of a stellar atmosphere that can account for all observations - but far more difficult to achieve. Nevertheless, today we have programs that can model the atmospheres of early to late type stars of different metallicities, Wolf-Rayet stars, supernovae and substellar objects such as brown dwarfs. Some of the more famous stellar atmosphere models that are still in development today are `ATLAS` by Kurucz (1970), `MARCS` by Gustafsson et al. (1975) and `PHOENIX` by Hauschildt (1992).

3.1 The stellar atmosphere

The atmosphere of a star can be described as the transition region from the stellar interior to the interstellar medium, and it is normally divided into three distinct regions named - from bottom to top - the photosphere, the chromosphere and the corona.

As an example, we consider the atmosphere of the Sun. The photosphere is about 300 km thick, so it is quite thin compared to the full $700,000$ km radius of the Sun. It has a very low density of about 10^{-8} g/cm^3, and its temperature decreases from about $6,000$ K at the bottom to about $4,500$ K at the top. Most importantly, the photosphere is where the majority of the emergent visible spectrum originates. The chromosphere lies above the photosphere, is about $2,000$ km thick and about four magnitudes less dense than the photosphere. Paradoxically, the temperature of the chromosphere increases with height, reaching up to about $25,000$ K at its top. The reason for this is related to the evolving magnetic fields of the Sun. The low density of the chromosphere makes it virtually transparent to most of the radiation emerging from the photosphere, and it therefore contributes very little to the solar spectrum and only at very short wavelengths. The corona is an aura of very hot plasma that extends thousands of kilometers into space and has a temperature in the order of 10^6 K. Like the chromosphere, the corona is transparent to visible light, but it shines very brightly in the x-ray part of the spectrum because of its high temperature (Emerson, 1996).

In general, the atmosphere of a main sequence star resembles that of the Sun although the specific characteristics of its photosphere, chromosphere and corona will depend on the spectral type of the star, as cooler stars will have cooler atmospheres. The chromosphere and the corona cannot be described by standard stellar atmosphere model techniques since they are affected by non-radiative energy input from acoustic and/or magnetic sources, but since they have very low densities and are essentially transparent to the majority of the radiation leaving the star, they do not need to be included for most purposes. Stellar atmosphere models therefore model only the photosphere.

3.2 Common simplifications

The computation of a stellar atmosphere model can easily become an exhaustingly complex and computationally expensive endeavor. A complete treatment of every possible mechanical, thermal, radiative, and chemical process that takes place in the atmosphere of a three-dimensional evolving star is as good as impossible. It is therefore necessary to employ a selection of simplifying assumptions and compromises. In the following we will review some of the most common simplifications along with their advantages and limits.

3.2.1 Geometry

Consider the spatial geometry of a star. Assuming that it is spherically symmetric, any physical parameter such as temperature or gas pressure will only depend on the distance to its center. Reducing the model from 3D to 1D allows us to trim down the number and the complexity of the equations needed thereby freeing up computer time and space that can be used to implement additional physical processes. Of course, real stars are not perfectly symmetrical spheres and by using this simplification, we inherently assume that all non-radial structures such as granulation, starspots, and magnetic fields only have a negligible effect.

During the past decade, the ever advancing power of computers has prompted the development of several 3D magneto-hydrodynamic codes for the modeling of stellar atmospheres. These include `STAGGER` (Nordlund and Stein, 1995), `CO`^{5}`BOLT` (Freytag et al., 2012), `MURaM` (Vögler et al., 2005) and `ANTARES` (Muthsam et al., 2010). Magic et al. (2013) have shown that the differences between 1D and 3D models can be rather significant, especially for metal-poor stars, potentially leading to large systematic errors in spectroscopic abundance determination.

If the geometrical thickness of a stellar photosphere is sufficiently small compared to the radius of the star, we can simplify the model geometry even more by assuming that the photosphere is plane-parallel. For example, the ratio between the two is less than 0.1% for the Sun, and we can therefore safely use the plane-parallel approximation to model its photosphere. In fact, we can use plane-parallel models for most main sequence and giant stars, while spherical models are needed for supergiants as they usually have greatly extended photospheres comparable in size to the radius of the star (Gray, 2005).

3.2.2 Stability

Stars have impressive births and sometimes even more spectacular deaths, but they spend the majority of their lives evolving slowly over millions or billions of years as they fuse their vast reserves of hydrogen to helium. The Sun itself is 4.5 billion years old, yet only half way through its main sequence state, its brightness currently increasing with only 1% every 100 million years (Bahcall et al., 2001). This is possible because the Sun and other main sequence stars are in a state of nearly perfect hydrostatic equilibrium, the inward force of gravity balancing the outward forces of pressure, and are able to regulate themselves to stay this way. If for example the fusion rate increases slightly, then the temperature will also increase and with it the pressure, which will cause the core to expand. This expansion will decrease the density and temperature, forcing the fusion rate to decrease again. As long as any fluctuations or changes are small enough or take place on timescales much longer than those of the hydrodynamic and radiative processes in the star, the star will be able to adapt and remain stable. We can therefore assume that a main sequence star is in hydrostatic equilibrium at any given time. Examples of stars that are not in hydrostatic equilibrium include supernovae or pulsating stars, where large-scale gas motions expand or contract the star, or close binaries, where the star is rapidly gaining or loosing a significant amount of mass from its companion.

3.2.3 Local thermodynamic equilibrium

A thermodynamic system that is simultaneously in thermal, mechanical, chemical, and radiative equilibrium is said to be in thermodynamic equilibrium. It is impossible for a star as a whole to be in thermodynamic equilibrium; the mere fact that we can observe stars implies that energy is escaping them. But since thermodynamic equilibrium offers some great simplifications of the equations that describe how gas behaves, models of stellar atmospheres often implement what is known as *local* thermodynamic equilibrium (LTE) in order to avoid having to do full non-equilibrium calculations, which - depending on the complexity of the atmosphere - can be very computationally demanding.

In the LTE approximation we assume that thermodynamic equilibrium holds within any local computational volume. This compromise allows the properties of the stellar atmosphere to vary in space and time as long as they vary sufficiently slowly. For example, the temperature difference between the lower and upper part of a stellar atmosphere can vary with several thousand kelvin, its gradient necessary for driving the outward flow of energy, but for a small neighborhood around any single point in the atmosphere, we can assume it constant.

At the bottom of the stellar atmosphere LTE is a good approximation, since the high densities ensure that the mean free path of both particles and photons is much smaller than the size of the neighborhood they are equilibrated to. Moving up through the atmosphere, we would expect it to deviate more and more from LTE as the opacity decreases and the mean free path of the photons increases. Near the surface the density can still be high enough for the particles to be in LTE with each other, but photons can escape to such a degree that their energy distribution departs from that of a thermodynamic equilibrium, potential creating non-LTE effects in the spectrum of the star.

3.3 Molecules in cool stars

Molecules do not stand a chance in the hot atmospheres of early type stars where the temperatures are so high that most of the atoms are partially or completely ionized. As we move through the spectral classes toward the late type stars, the formation of molecules becomes increasingly important in the successively cooler stars. Even though our Sun has a relatively high effective temperature of $T_{\rm eff} = 5,777$ K, many molecules have been detected in its atmosphere, and it is estimated that about 20% of the spectral lines in the visible regions of the Solar spectrum are due to molecules, although most of these are probably confined to the cooler sunspots, which have spectral properties comparable to those of a K dwarf (Jørgensen, 1996). The spectra of cool stars with effective temperatures less than about $T_{\rm eff} = 4,000$ K are completely flooded with molecular absorption lines.

The molecules we observe in stellar atmospheres are not very complex but they are unique in their ability to survive in the high temperatures of stars. Once the temperature is low enough for atoms to combine and form molecules, almost all the carbon and oxygen atoms free to react with each other will pair up to form the strongly bound CO molecule, which has the largest dissociation energy of any of the molecules found in stellar atmospheres. In oxygen-rich stars like the Sun, where the abundance of oxygen is greater than that of carbon, this pairing of oxygen and carbon will leave an excess of oxygen atoms that are then free to make other less stable oxides such as TiO, SiO and OH. Conversely, in carbon-rich stars, the excess carbon can make carbides like C_2, CN and CH. In cooler stars, fragile molecules become more abundant and most of the hydrogen is in the form of H_2, which has a very modest dissociation energy, with considerable amounts in other hydrides and H_2O.

The presence of molecules can have a big influence on the structure of a stellar atmosphere. Molecular absorption in general causes a back-warming of the deeper layers, potentially increasing their temperature by several hundred kelvin. This can be explained as a consequence of flux conservation (see Section 3.4.1); to compensate for the blocked flux, a hotter continuum is needed to keep the total flux constant. Near the surface of the atmosphere, molecular absorption can both cause a cooling and a heating of the layers depending on the type of molecule and the local temperature, and the final temperature is determined by the balance of the heating and the cooling. It should also be mentioned that the increased heating from molecule formation causes the atmosphere to expand and, consequently, its pressure to decrease (Tsuji, 1986).

In cool oxygen-rich stars, water vapor is one of the most important opacity sources in the infrared, and the H_2O molecules contribute to a heavy blocking of the flux and thus creates a considerable back-warming. Near the surface, CO and SiO molecules cool the layers but their effect is significantly dampened by the heating from TiO molecules. OH also contributes to both the back-warming and surface heating. The spectrum of these stars are dominated by the absorption lines of SiO, CO, TiO, and H_2O.

3.3.1 Molecular absorption lines

Much like atoms and ions, molecules can absorb and emit energy by electronic transitions. In addition, the nuclei of a molecule can also vibrate about the mean internuclear separation and rotate. The total inner energy of a molecule is therefore the sum of the energy of its electronic state, vibrational state and rotational state:

$$E(n, v, J) = E^{\mathrm{el}}(n) + E^{\mathrm{vib}}_{\mathrm{n}}(v) + E^{\mathrm{rot}}_{\mathrm{n,v}}(J), \tag{3.3.1}$$

where n, v and J are the electronic, vibrational and rotational quantum numbers of the particular state. Because asymmetric molecules have a permanent dipole moment, they can interact with electromagnetic radiation and thus undergo vibrational and rotational transitions by emitting or absorbing light.

The electronic energies of a molecule are much greater than the vibrational energies, which in turn are much greater than the rotational energies. Electronic transitions are usually found in the visual and ultraviolet part of the spectrum, pure vibrational transitions in the infrared, and pure rotational transitions in the microwave. Furthermore, each electronic transition is associated with a cascade of vibrational and rotational transitions, so an electronic transition in a molecule does not show up as a single spectral line as it does for atoms, but as a whole system of vibrational-rotational bands centered around the energy of the electronic transition. Consequently, the presence of a single species of molecule can be the cause of millions or even billions of spectral lines. This is why molecular lines crowd the spectrum of cool stars, overlapping each other, obscuring the weaker atomic lines and even the continuum, making the lives of astronomers very difficult.

3.3.2 Molecular opacity data

Molecular data is essential for the evaluation of molecular opacities in stellar model atmospheres and for the interpretation and analysis of molecular lines in stellar spectra, and there is a constant need for new and updated data. For each molecule, all the line positions and intensities of the spectral lines originating from every relevant transition are needed. Usually the computation of synthetic spectra requires higher precision than the computation of model atmospheres, where it is much more important to have completeness in the number of included lines (Jørgensen, 1996).

Since most of the molecular constants determined from laboratory analysis are based on low-temperature sources, they do not have the required accuracy for transitions that are important in the high temperatures of stellar atmospheres. It has therefore become standard to use theoretical quantum-mechanical ab initio calculations to generate large lists of molecular transitions (Tennyson, 2012). Initial databases of molecular data relevant for high temperatures began to appear not long after the importance of molecules in stellar atmospheres was recognized. The molecular data available today is very extensive and much more complete and accurate than a decade ago, but its is still far from complete. Several groups are working on updating and expanding online data bases with high temperature molecular opacity data, including Kurucz (Kurucz, 2001), SCAN (Jørgensen, 2001), HITEMP (Rothman et al., 2005), UGAMOP (Stancil et al., 2002) and ExoMoL (Tennyson et al., 2011).

3.3.3 Opacity sampling

Once the required molecular opacity data has been acquired, the next problem is how to implement it into the computation of the stellar atmosphere model. Ideally, line absorption coefficients should be computed at several points across each spectral line, but with millions of spectral lines this would quickly become very time demanding.

Over the years several opacity sampling methods have been developed, the two most widely used are the Opacity Sampling (OS, used in MARCS (Gustafsson et al., 2008) and PHOENIX (Hauschildt, 1992) models) method and the Opacity Distribution Function (ODF, used in ATLAS (Kurucz, 2005) models) method. In short, the OS method evaluates the opacity at a number of wavelengths spread across the interesting parts of the spectrum, using as few as possible while still producing a realistic model, while the ODF method divides the spectrum into subsections within which the absorption probabilities are simplified to one smooth function. The ODF method works well for stellar atmosphere models but is usually not detailed enough for the calculation of synthetic spectra. In cool stars where millions of molecular lines dominate, the OS method is more flexible and can also be used to calculate moderate resolution spectra.

In the end, the two methods produce stellar atmosphere models with the same level of accuracy.

3.4 Fundamental equations

Different stellar atmosphere codes implement different variations of theories, assumptions and data, but no matter how different they are, most of them are based on the same set of fundamental equations described in this section.

3.4.1 Conservation of energy

Conservation of energy is a natural extension of the assumption that a star can be considered stable. All the energy production takes place by fusion in the stellar interior, and since there are no energy sources or sinks in the atmosphere the energy flux must be conserved at any given radius, and the total flux passing through successive layers will therefore be constant (although the distribution of the radiation flux as a function of wavelength can and will change). For a plane-parallel atmosphere, where the total flux passing through the layers is the sum of the fluxes from radiation and convection, we have that

$$\frac{\mathrm{d}}{\mathrm{d}z}(F_{\mathrm{rad}} + F_{\mathrm{conv}}) = 0, \tag{3.4.1}$$

where z is the altitude. The total emergent flux is related to the effective temperature T_{eff} of the star via Stefan-Boltzmann's law:

$$F_{\mathrm{tot}} = F_{\mathrm{rad}} + F_{\mathrm{conv}} = \sigma T_{\mathrm{eff}}^4, \tag{3.4.2}$$

where σ is the Stefan-Boltzmann constant (Gray, 2005). For the Sun, the effective temperature is $T_{\mathrm{eff}} = 5,777$ K and the total emergent flux is $F_\odot = 6.3 \times 10^{10}$ erg/(s cm^2). For an M dwarf with $T_{\mathrm{eff}} = 2,200$ K it is $F_{\mathrm{M}} = 1.3 \times 10^9$ erg/(s cm^2) $= 0.02 F_\odot$.

3.4.2 Hydrostatic equilibrium

If the star is in hydrodynamic equilibrium, any small volume element in its atmosphere will be held in place by the balance between the inwards pull of gravity and the outwards push of pressure:

$$\frac{\mathrm{d}P_{\mathrm{tot}}}{\mathrm{d}z} = -g\rho_g,$$

where g is the gravitational acceleration, ρ_g is the gas density, and P_{tot} is the total pressure supporting the small volume element. In most stars P_{tot} is dominated by the gas pressure, which is the sum of the partial pressures of each of the components - atoms, ions, electrons and molecules - that make up the gas:

$$P_g = \sum_i P_i. \tag{3.4.3}$$

There can also be contributions from e.g. radiation pressure, magnetic pressure and turbulence pressure. The radiation pressure is proportional to the fourth power of the local temperature,

$$P_r = \frac{1}{3} a T^4, \tag{3.4.4}$$

where a is the radiation constant. It follows that the hotter the star is, the more important it is to consider the radiation pressure (Emerson, 1996).

The equation of state for atmospheres of main sequence stars is well approximated by the ideal gas law,

$$P_g = \frac{k_B}{\mu m_u} \rho_g T, \tag{3.4.5}$$

where P_g is the pressure of the volume V of gas at temperature T, k_B is the Boltzmann constant, μ is the average particle mass, and m_u is the atomic mass constant. In cool stars $P_{\text{tot}} \approx P_g$ and the equation of hydrostatic equilibrium becomes

$$\frac{dP_{\text{tot}}}{dz} = -\frac{g\mu m_u}{k_B} \frac{P_g}{T}. \tag{3.4.6}$$

3.4.3 Chemical equilibria of gases

Regardless of whether the gas in a stellar atmosphere is in chemical equilibrium or not, the conservation of matter dictates that since no chemical process can produce new kinds of elements, the total quantity of a specific element present in the atmosphere - either in the form of an atom, an ion or as part of a molecule - is constant. This is expressed by the set of mass balance equations,

$$N_i = \sum_j \gamma_{ij} N_j, \tag{3.4.7}$$

where N_i is the total number of element i in any form, γ_{ij} is the number of element i in particle j, and N_j is the number of particle j. For example, for hydrogen in water we have that $i =$ H, $j = H_2O$ and $\gamma_{ij} = 2$. There is one equation for each element, but since most elements are part of several types of particles (the neutral atom, the one time ionized atom, several different molecules and so on) the mass balance equations by themselves are not enough to deduce the abundance of each of the different particles. The balance of their abundances can be very complicated as it depends on complex dynamical processes in the gas, but if the time scales of these dynamic processes are much longer than the time scales of the chemical reactions between the particles, we can assume that the gas is in chemical equilibrium.

For a closed system of volume V, pressure P_g, temperature T, entropy S and internal energy E, the Gibbs free energy G is defined by the equation

$$G = E + P_g V - TS. \tag{3.4.8}$$

An infinitesimally small change in G is given by

$$\begin{aligned} \mathrm{d}G &= \mathrm{d}E + \mathrm{d}(P_g V) - \mathrm{d}(TS) \\ &= (T\mathrm{d}S - P_g \mathrm{d}V) + (P_g \mathrm{d}V + V\mathrm{d}P_g) - (T\mathrm{d}S + S\mathrm{d}T) \\ &= V\mathrm{d}P_g - S\mathrm{d}T, \end{aligned} \tag{3.4.9}$$

where we have assumed the system is in thermal equilibrium and used the fundamental thermodynamic relation $\mathrm{d}E = T\mathrm{d}S - P_g\mathrm{d}V$. If the system changes from one state (1) to another (2) by undergoing a reversible process, the total change in G is then

$$\Delta G = \int_{G_1}^{G_2} dG = \int_{P_1}^{P_2} V(P_g)\mathrm{d}P_g - \int_{T_1}^{T_2} S(T)\mathrm{d}T. \tag{3.4.10}$$

For an ideal gas, an isothermal ($dT = 0$) change of the pressure from P_1 to P_2 causes G to change by

$$\begin{aligned} \Delta G &= \int_{P_1}^{P_2} V(P_g)\mathrm{d}P_g \\ &= \int_{P_1}^{P_2} \frac{nRT}{P_g}\mathrm{d}P_g \\ &= nRT\ln(P_2/P_1). \end{aligned} \tag{3.4.11}$$

Because we can only measure the differences in the Gibbs free energy but not its absolute value, it is normal to express G relative to the so-called standard Gibbs free energy G^0. If we set P_1 equal to the standard-state pressure of 1 bar then $G_1 = G^0$, and we can write

$$G = G^0 + nRT\ln(P_g). \tag{3.4.12}$$

This equation gives G of a pure, ideal gas at pressure P_g and temperature T relative to the standard-state pressure and temperature (Fegley, 2012).

For a gas mixture of ideal gases the total Gibbs free energy G is the sum of the Gibbs free energy G_i of each gas species i:

$$G = \sum G_i = \sum n_i \overline{G}_i, \tag{3.4.13}$$

where n_i is the number of moles of gas species i, and $\overline{G}_i = G_i/n_i$ is the partial molar Gibbs free energy of species i. A chemical reaction between some of the gas species will change G by

$$\Delta G = \sum G_{i,\mathrm{products}} - \sum G_{i,\mathrm{reactants}}. \tag{3.4.14}$$

The sign of ΔG determines whether or not the reaction is favorable; a reaction with $\Delta G < 0$ is favorable, but the reverse reaction is favorable if $\Delta G > 0$. If $\Delta G = 0$, the gas mixture is in equilibrium, and both the reaction and its reverse are equally favorable. An important point is that even though the gas mixture is in equilibrium, the reaction and its reverse still take place but at the same rate, such that the amount of each type of gas species is constant (Fegley, 2012).

As an example we consider the reaction of A and B to form C and D. We can write this as

$$\nu_A A + \nu_B B \rightarrow \nu_C C + \nu_D D, \tag{3.4.15}$$

where ν_i is the stoichiometric coefficients of the gas species i, or the number of moles needed of each gas species to balance the reaction, keeping the total number of elements constant before and after the reaction. The species i can be an element, electron, ion or molecule. According to Equation 3.4.14 and Equation 3.4.12 we have that

$$\begin{aligned}
\Delta G &= \nu_C \overline{G}_C + \nu_D \overline{G}_D - (\nu_A \overline{G}_A + \nu_B \overline{G}_B) \\
&= \nu_C(\overline{G}_C^0 + RT\ln(P_C)) + \nu_D(\overline{G}_D^0 + RT\ln(P_D)) - \nu_A(\overline{G}_A^0 + RT\ln(P_A)) - \nu_B(\overline{B}_B^0 + RT\ln(P_B)) \\
&= (G_C^0 + G_D^0 - G_A^0 - G_B^0) + RT(\nu_C \ln P_C + \nu_D \ln P_D - \nu_A \ln P_A - \nu_B \ln P_B) \\
&= \Delta G^0 + RT\ln\left(\frac{P_C^{\nu_C} P_D^{\nu_D}}{P_A^{\nu_A} P_B^{\nu_B}}\right)
\end{aligned} \tag{3.4.16}$$

While ΔG^0 is a constant, the partial pressures of the gas species may vary as A and B are consumed to form C and D (or vice versa). For $\Delta G = 0$ the reaction is in equilibrium and we can write

$$\Delta G^0 = -RT\ln\left(\frac{P_C^{\nu_C} P_D^{\nu_D}}{P_A^{\nu_A} P_D^{\nu_D}}\right)_{eq} = -RT\ln K_p, \tag{3.4.17}$$

where K_p is known as the equilibrium constant of the reaction. It is not really a constant but rather a function of temperature given by

$$K_p = \exp\left(-\frac{\Delta G^0}{RT}\right). \tag{3.4.18}$$

Suppose we make a gas mixture of A and B, keeping the temperature T and total pressure P_g constant. If we known the initial conditions of the system (P_A, P_B, T, P_g), the stoichiometric coefficients of the reaction, and $K_p(T)$, we have enough information to calculate the equilibrium partial pressures of each of the gas species A, B, C, and D.

For a specific reaction we can calculate the value of K_p as a function of T and $G^0 = \sum G_i^0$. As we cannot measure the absolute value of the Gibbs energy, G^0 is always expressed relative to another Gibbs energy, namely the standard Gibbs free energy of formation of the constituent elements in their reference states (Fegley, 2012). The latter is per definition zero at all temperatures, and so

$$G_i^0 = \Delta_f G_i^0. \tag{3.4.19}$$

We can look up the value of $\Delta_f \overline{G}_i^0$ in various thermodynamic compilations such as The CRC Handbook of Chemistry and Physics (Haynes, 2015) or the NIST-JANAF Thermochemical Tables (Chase et al., 1985).

Alternatively, the value of K_p at chemical equilibrium can also be expressed as the ratio of the total partition function of the products to the total partition function of the reactants. For the reaction in Equation 3.4.15 we have that

$$K_p = \frac{q_C^{\nu_C} q_D^{\nu_D}}{q_A^{\nu_A} q_B^{\nu_B}} \left(\frac{k_B T}{V}\right)^{\Delta n} \exp\left(\frac{\nu_C D_0^C + \nu_D D_0^D - \nu_A D_0^A - \nu_B D_0^B}{k_B T}\right), \tag{3.4.20}$$

where q_i is the total partition function of gas species i (defined as the weighted Boltzmann factors summed over all electronic, vibrational, rotational and translational energy evels), $\Delta n = \nu_C + \nu_D - \nu_A - \nu_B$ is the change in the number of moles during the reaction, and D_0^i is the dissociation energy of i (defined as the energy required to dissociate a molecule from the lowest rovibrational level of its ground state to two atoms each in their lowest level). If i is not a molecule, then $D_0^i = 0$ (Tatum, 1966). We can thus also calculate the value of K_p at chemical equilibrium if we know the total partition function and dissociation energy of each gas species.

In the atmospheres of ultra cool dwarfs there are hundreds of gas species to consider and even more reactions between them. Since a single gas species usually takes part in several different reactions, the stellar atmosphere model code has to solve all equilibrium equations for all reactions simultaneously.

3.4.4 Radiation transfer

The equation of radiative transfer is the backbone of any stellar atmosphere model program. It describes how the radiation propagates out through the layers of the atmosphere, its intensity both affecting and being affected by the atmosphere itself.

Any process that removes photons from the beam of light is called absorption. This includes scattering of photons (e.g. Compton scattering) as well as true absorption (upward atomic and molecular energy-level transitions). The corresponding change in intensity is described by the

Beer-Lambert law:

$$\mathrm{d}I_\lambda = -\kappa_\lambda \rho_g I_\lambda \mathrm{d}z, \tag{3.4.21}$$

where κ_λ is the mass absorption coefficient. In the same way, any process that contributes photons to the beam of light is called (stimulated) emission and changes the intensity by

$$\mathrm{d}I_\lambda = j_\lambda \rho_g \mathrm{d}z, \tag{3.4.22}$$

where j_λ is the emission coefficient. The total change in the intensity as the light passes through a layer of atmosphere of thickness dz is then:

$$\mathrm{d}I_\lambda = j_\lambda \rho_g \mathrm{d}z - \kappa_\lambda \rho_g I_\lambda \mathrm{d}z. \tag{3.4.23}$$

If we define the optical depth

$$\tau_\lambda = \kappa_\lambda \rho_g \mathrm{d}z, \tag{3.4.24}$$

we can write the equation of radiative transfer in it final form:

$$\frac{\mathrm{d}I_\lambda}{\mathrm{d}\tau_\lambda} = I_\lambda - S_\lambda, \tag{3.4.25}$$

where

$$S_\lambda = \frac{j_\lambda}{\kappa_\lambda}. \tag{3.4.26}$$

S_λ is known as the source function, and it can be thought of as the intensity originating from a single layer of gas. The flux we observe emerging from the surface of a star is a superposition of the source functions of all the different layers of the atmosphere (Gray, 2005).

For a volume of gas in thermodynamic equilibrium, the source function is given by the Planck function:

$$S_\lambda = B_\lambda(T) = \frac{2hc^2}{\lambda^5} \frac{1}{e^{\frac{hc}{\lambda k_B T}} - 1}, \tag{3.4.27}$$

where h is the Planck constant and c is the speed of light. This is known as Kirchhoff's law of thermal radiation.

3.4.5 Convection

In addition to radiation, convection is another important way to transport energy out through the star. It occurs when a volume of gas - also called a convection cell - warmer (or cooler) than the surrounding gas rises (or falls), carrying with it an excess (or deficit) of heat. The flux carried by convection is given by

$$F_{\mathrm{conv}} = \rho C_p v_z \Delta T, \tag{3.4.28}$$

where ΔT is the temperature difference between the cell and its surroundings, C_p is the specific heat at constant pressure, ρ is the density of the cell and v is the upwards velocity of the cell. If we assume that a convective cell cannot exchange energy with its surroundings, it will behave adiabatically. We can then use the Schwartzschild criterion to test whether or not a layer in the atmosphere is stable against convection. The criterion states that if the radiative temperature gradient is larger than the adiabatic temperature gradient:

$$\left(\frac{\mathrm{d}\ln T}{\mathrm{d}\ln P_g}\right)_R > \left(\frac{\mathrm{d}\ln T}{\mathrm{d}\ln P_g}\right)_A, \tag{3.4.29}$$

then the layer is not stable against convection, and an upwards (or downwards) displaced gas cell will continue to rise (or sink) to the upper (lower) layer. This can for example happen if the opacity is high, as this will give rise to a large radiative temperature gradient (Gray, 2005).

The interior of most low mass stars can be divided into three regions; the core where the energy is generated by nuclear fusion, the radiative zone where energy is transported primarily by radiation and the convection zone where energy is transported primarily by convection. The surface of the convection zone is the bottom of the photosphere, and the rising and sinking convective cells are visible on the surface as granulation. The depths of the core, radiation zone and convection zone in the Sun are about 25%, 50% and 25% of the Solar radius. In cooler stars the convection zone grows larger on the expense of the radiation zone as opacity in general increases with decreasing temperature, and because the formation of more and more molecules also adds significantly to the opacity of the outer layers. The coolest stars, the late type M-dwarfs, can be fully convective, their convection zones reaching all the way to the center of the star.

The granulation pattern visible on the surface of the Sun is the top of the convection cells. This region is at the bottom of the photosphere, where $\rho \approx 10^{-7}$ g/cm^2. The temperature difference between the convection cells and their surroundings is about $\Delta T \approx 100$K, and their characteristic upwards velocities are about $v_z \approx 1-2$ km/s. Since hydrogen is the dominant gas, we can approximate the specific heat as that of an ideal mono-atomic gas, $C_p \approx \frac{5}{2}R = 8 \times 10^7$ erg/(g K). From Equation 3.4.28 we then have that the convective flux is $F_{\mathrm{conv}} \approx 2 \times 10^8$ erg/(s cm^2), which is only about 0.1% of the total emergent flux of $F_\odot = 6.3 \times 10$ erg/(s cm^2) (Gray, 2005). Even so, convection is still the primary method of energy transport, since convection conveys energy faster than radiative diffusion. The mean free path of a diffusing photon is in the order of 10^{-1} cm in the Sun, and the time it takes for a photon to travel from the center of the core to the outer edge of the radiative zone is on average about 1.7×10^5 years (Mitalas and Sills, 1992). In comparison, energy can travel through the convective zone in about 3 weeks.

Convection is an efficient mixing mechanism, as material is transported with the moving convection cells. In the core regions of main sequence stars with masses larger than about $2M_\odot$, the convection zone lies below the radiation zone, and it acts to stir up the newly formed helium, mixing it with the hydrogen, thereby ensuring that the fuel needed for fusion is available.

In low mass stars, vigorous convection can produce chemical homogeneity in the photosphere (Gray, 2005).

Since convection is a highly turbulent, three-dimensional and non-local process it can not arise "naturally" in our simple plane-parallel 1D atmosphere models, and we will therefore have to include it manually, using some correspondingly simple approximation. One of the most widely used solutions is to use mixing length theory, which was first introduced by Prandtl (1925). Mixing length theory has one free parameter, the mixing length l, which is the mean distance a convective cell travels before it is dissolved, either releasing thermal energy to or absorbing thermal energy from its surroundings. If we assume pressure equilibrium and constancy of the mean molecular weight, the convective flux becomes

$$F_{\mathrm{conv}} = \rho C_p \left(\frac{gl}{T}\right)^{1/2} \Delta T^{3/2}. \tag{3.4.30}$$

The value used for the mixing length is based on empirical calibrations of stellar interior models and is thus not theoretically derived. It is often expressed as a product of the mixing-length parameter α_{MLT} and the scale height:

$$l = \alpha_{\mathrm{MLT}} H = \alpha_{\mathrm{MLT}} \frac{k_B T}{\mu m_u g}. \tag{3.4.31}$$

For the Sun the mixing-length parameter is about $\alpha_{\mathrm{MLT}} \approx 1.5$ (Gray, 2005), for cool stars and brown dwarfs it is about $\alpha_{\mathrm{MLT}} \approx 2.0$ (Ludwig et al., 2002).

3.5 The iterative method of computing a stellar atmosphere model

The computation of a stellar atmosphere model centers around finding a self-consistent solution to the equation of radiative transfer:

$$\frac{\mathrm{d}I_\lambda}{\mathrm{d}\tau_\lambda} = I_\lambda - S_\lambda. \tag{3.5.1}$$

Unfortunately, it is not possible to construct a straightforward analytical solution since the source function usually depends on the intensity. We therefore have to approach the problem numerically and iterate through the equation again and again until our model converges.

For a chosen effective temperature, surface gravity and metallicity the first iteration proceeds as follows:

1. Make an educated guess of a temperature and pressure structure that satisfies the Equation of Hydrostatic Equilibrium.

2. Use the Chemical Equilibrium equations to calculate the partial pressures of all atoms, ions, electrons and molecules in each layer.

3. Calculate the absorption of each species from their partial pressures.

4. Calculate the emission by assuming that the intensity is given by the Planck function.

5. Calculate the source function from the absorption and emission.

6. Calculate the intensity by solving the equation of radiative transfer for the source function.

7. Adjust the temperature and pressure structure.

All the subsequent iterations begin at Step 2 and use the calculated intensity in Step 4 but otherwise follow the same procedure. Eventually the adjustment between one iteration and the next is small enough to consider the model converged.

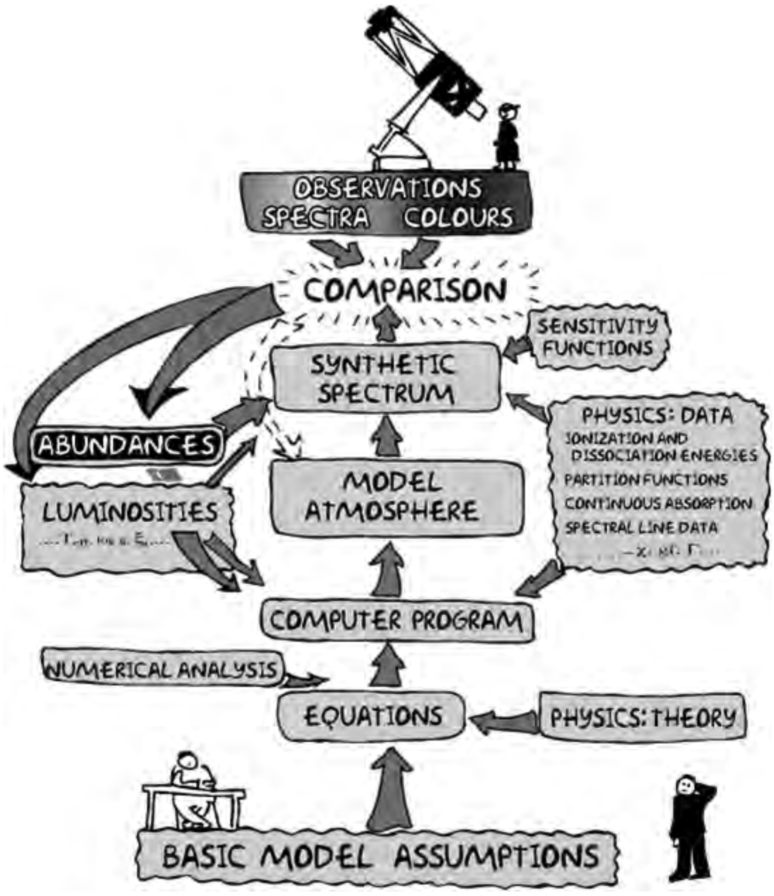

Figure 3.5.1: The iterative process of computing a stellar model atmosphere. Credit: Bengt Gustafsson.

Once we have succeeded in creating a converged model a new and much larger iterative process begins as illustrated in Figure 3.5.1. We are constantly working on reducing the discrepancies between our models and observations in order to better understand the stars we are studying. We modify our theories and equations correspondingly, reducing the number of simplifying assumptions as our computer power increases, and we are always hungry for newer and more complete physical data. It is a process that spans decades, but with every new iteration our understanding of the stars grow.

3.6 The MARCS model

The MARCS code was introduced in the early 1970s by Gustafsson et al. (1975). In the beginning, it was used to model the atmospheres of low-metallicity G and K giants (Bell et al., 1976) as well as carbon stars (Olander, 1981). The calculated spectra were generally in good agreement with observations and the models were applied in several studies, for example in determining the abundances in globular cluster stars (Dickens et al., 1979; Smith et al., 1989). The original version of MARCS used the ODF method to sample line opacities, but due to its inflexibility concerning changing chemical compositions, the OS method was later implemented by Lambert et al. (1986), who also increased the number of frequency points for sampling by up to two magnitudes for better precision. During the following years, this updated version of MARCS was used to calculate grids of models for different types of stars such as carbon stars (Lambert et al., 1986), M-giants (Plez, 1992), M-dwarfs (Brett and Plez, 1993), and even hydrogen-poor carbon stars (Asplund et al., 1997). The most recent grid of MARCS models was published by Gustafsson et al. (2008) and contains about 10,000 atmosphere models extending from late A-type to early M-type stars, both dwarfs and supergiants, for varying metallicities and C/O-ratios.

The starting point of our work is one the most recent versions of the MARCS code, and details of the implementation of the equations of hydrostatic equilibrium, radiative transfer, convection and mixing lengths can be found in Gustafsson et al. (2008). For the equilibrium calculations we use a version of Tsuji's program (1964) implemented by Helling et al. (1996).

4

Theory: Cloud formation

The clouds here on Earth are collections of droplets of liquid water or ice crystals that form when humid air cools down enough for the water vapor to condense. Normally, unless the temperatures are very low, water vapor requires a non-gaseous surface to make the transition from vapor to liquid, and in the atmosphere this surface presents itself as tiny solid or liquid particles called cloud condensation seeds. They come in many different types and sizes, a few examples include sea salt from ocean wave spray, sulphate from volcanic activity, and sand from desert storms.

The clouds in the atmospheres of cool stars, brown dwarfs and hot exoplanets are in some ways much like the ones we know from Earth and in other ways very different. They too consist of droplets or crystals that have condensed from the atmosphere, but because of the high temperatures they are composed not of water, but of minerals such as rutile (TiO_2), forsterite (Mg_2SiO_4) and corundum (Al_2O_3). Their presence can have a big influence on the atmosphere structure and spectra in several different ways. First of all, cloud formation depletes the atmosphere of elements from the gas phase as they are bound in dust grains, thereby preventing them from absorbing or scattering the light as atoms or molecules. Secondly, the presence of an optically thick cloud layer causes a back-warming effect that results in a heating of the atmosphere. And thirdly, the strong opacity of the clouds tends to smooth out the visible and infrared part of the spectrum, obscuring prominent spectral features. For these reasons cloud formation is an essential part of modeling the atmospheres of cool stars, brown dwarfs and hot exoplanets.

4.1 The formation of clouds

In general, clouds can form in an atmosphere when the gas becomes dense and cool enough for one or more species of atoms or molecules to condense into solids. The chemical composition of the atmosphere determines what kind species are available for cloud formation and thus what kind of clouds can form. We can use the concept of phase equilibrium to examine which elements might condense in the conditions of an ultra cool dwarf atmosphere.

A solid s is said to be in phase equilibrium with its gaseous form x if the condensation rate is equal to the evaporation rate. The pressure of x needed to maintain this equilibrium is called the saturation gas pressure $p_{\mathrm{sat,s}}$, and we define the saturation ratio of the solid s as

$$S_s = \frac{p_{\mathrm{x}}(T_{\mathrm{gas}}, p_{\mathrm{gas}})}{p_{\mathrm{sat,s}}(T_s)}, \tag{4.1.1}$$

where p_{x} is the partial pressure of the gas species x. For $S_s > 1$, $S = 1$, and $S_s < 1$ we say that the gas is supersaturated, saturated and unsaturated, respectively.

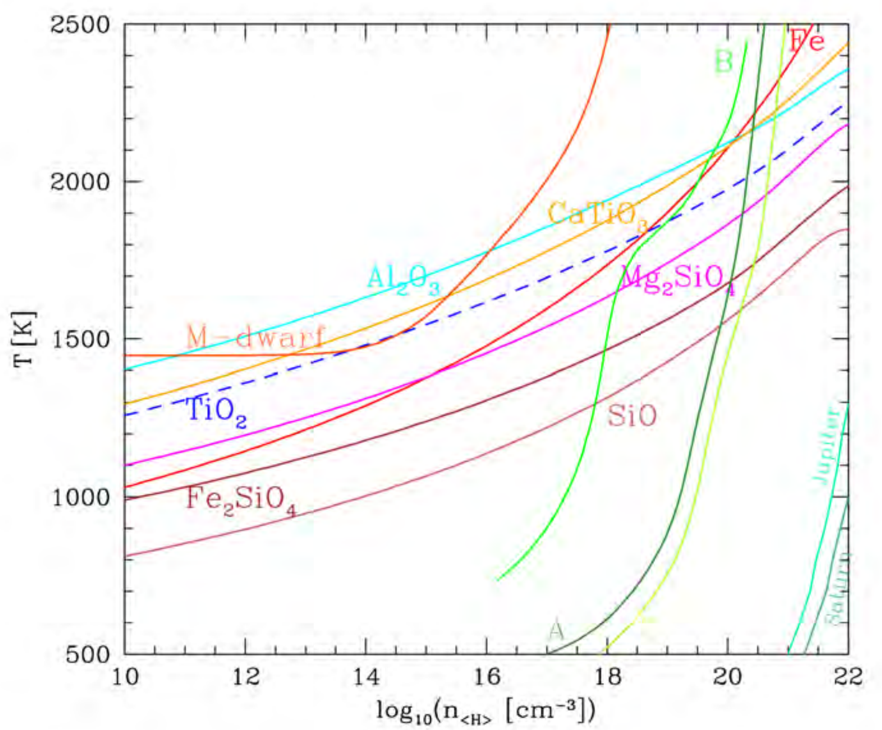

Figure 4.1.1: Condensation curves for various species in a gas of solar composition. The $T_{\mathrm{gas}} - n$ profiles for an M dwarf, different brown dwarfs (A: dust free, B: dust included as element sink and opacity source, C: dust included only as element sink) and Jupiter and Saturn are also included. Source: Helling et al. (2001).

In Figure 4.1.1 we compare the condensation curves for various atomic and molecular species present in ultra cool dwarfs of solar composition. Each curve shows where $S_s(T_{\rm gas}, n_{<H>}) = 1$ for a specific species, thereby defining a line above which that species will evaporate. For comparison, we have also included the temperature-density profile of an M dwarf, different brown dwarfs and Jupiter and Saturn. The condensation curves can be thought of as describing a stability sequence for decreasing temperature. Starting at the top we find the most refractory condensates, Fe (for high densities), Al-oxides, Ca-Ti-oxides and Ti-oxides, the specific composition of the initial compensate depending on the total gas pressure (Lodders, 2002). These are followed by the more volatile Mg-silicates, Fe-silicates, and Si-oxides. Although H_2, N_2 and CO are some of the most abundant molecules in ultra cool dwarfs they condense at much lower temperatures ($T < 500$ K) and are therefore not included in the figure.

Based on Figure 4.1.1 we would expect the clouds of an M-dwarf to consist of condensates containing Al, Ca, and Ti. In L dwarfs and early T dwarfs the temperatures are low enough for Mg-silicates, Fe-silicates and Fe to condense as well. The condensation of Ti in M dwarfs explains the gradual disappearance of TiO bands from the spectra of early L dwarfs. When a condensate is formed, its component elements are removed from the gas phase, affecting all gases containing those elements. When Ti condenses, the amount of gaseous Ti, TiO, TiO_2 etc. is thus reduced, causing the TiO absorption bands to weaken (Lodders and Fegley, 2006).

4.1.1 Chemical equilibria between gases and condensates

The chemical equilibria equations derived in Section 3.4.3 are only concerned with reactions where both the reactants and products are in the gas phase. In order to model cloud formation, we will need to extend them to include reactions where the reactants and products can be in the condensed phase as well. The change in the Gibbs free energy for a reaction is still given by the equation

$$\Delta G = \sum G_{i,\rm products} - \sum G_{i,\rm reactants}, \tag{4.1.2}$$

but the way we calculated G depends on the phase of the material. The closer a gas gets to its condensation point, the less it behaves like an ideal gas. We therefore introduce the fugacity f which can be thought of as the pressure a real gas would have if it behaved ideally. The ratio of the fugacity to the real pressure is given by the fugacity coefficient γ:

$$\gamma = \frac{f}{P_g}. \tag{4.1.3}$$

Fugacity is partially defined by the equation

$$G = G^0 + nRT \ln(f/f^*), \tag{4.1.4}$$

where f^* is the fugacity of the gas in a standard state. For an ideal gas $\gamma = 1$ and Equation 4.1.4 reduces to Equation 3.4.12. The ratio f/f^* is also called the activity a, and it is defined as the ratio between the vapor pressure p_i of a material i at some pressure, temperature and concentration relative to the saturation vapor pressure of the pure material at the same temperature:

$$a_i = \frac{f}{f^*} = \frac{p_i}{p_{\mathrm{sat,i}}}. \tag{4.1.5}$$

As an example we consider the reaction of A (gas) with B (gas) to form C (solid):

$$\nu_A A + \nu_B B \rightarrow \nu_C C, \tag{4.1.6}$$

where $\nu_C = 1$. The change in G is then given by

$$\begin{aligned} \Delta G &= \overline{G}^0_C + RT\ln(a_C) - \nu_A(\overline{G}^0_A + RT\ln(P_A)) - \nu_B(\overline{B}^0_B + RT\ln(P_B)) \\ &= \Delta G^0 + RT\ln\left(\frac{a_C}{P_A^{\nu_A} P_B^{\nu_B}}\right), \end{aligned} \tag{4.1.7}$$

where $\Delta G^0 = G^0_C - G^0_A - B^0_B$. For $\Delta G = 0$ the reaction is in equilibrium and we can write

$$\Delta G^0 = -RT\ln\left(\frac{a_C}{P_A^{\nu_A} P_B^{\nu_B}}\right). \tag{4.1.8}$$

Using $a_C = p_C/p_{\mathrm{sat},C}$ we can express the saturation vapor pressure of C as

$$p_{\mathrm{sat},C} = \frac{P_C}{P_A^{\nu_A} P_B^{\nu_B}} \exp\left(\frac{\Delta_f G^0_C - \Delta_f G^0_A - \Delta_f G^0_B}{RT}\right), \tag{4.1.9}$$

and the saturation ratio of C as

$$S_C = \frac{P_C}{p_{\mathrm{sat},C}} = P_A^{\nu_A} P_B^{\nu_B} \exp\left(-\frac{\Delta_f G^0_C - \Delta_f G^0_A - \Delta_f G^0_B}{RT}\right). \tag{4.1.10}$$

We can look up the values of $\Delta_f \overline{G_i}^0$ for both gases and solids in various thermodynamic compilations.

4.2 The DRIFT model

The DRIFT model describes cloud particle formation by modeling seed formation and growth and evaporation coupled to gravitationally settling, convective mixing and element depletion. For a given atmosphere structure it calculates a stationary cloud system, providing details about the dust grain composition, the mean grain sizes, and the size distributions as a function of atmospheric height.

Figure 4.2.1 illustrates the different stages in the life cycle of a dust grain that are considered by the DRIFT model. The formation of dust grains begins in the high layers of the atmosphere where the temperature is low enough for certain gas molecules to form large, stable clusters that condense into small seed particles. More complicated solids can form on top of these seeds, creating dirty dust grains that grow as each new atom or molecule condenses on its surface. When the density of the dust grains becomes higher than that of the surrounding gas they will precipitate down through the atmosphere, where the increased density makes the dust grains grow even faster. Eventually, the falling dust grains will reach deeper layers which are hot enough to cause them to evaporate. The released material is thereby returned to the gas phase and mixed back into the higher layers by convection and overshooting where it can form new seed particles, thus completing the cycle. In this section I will describe each of these processes in more detail, presenting the approaches and results of Gail and Sedlmayr (1988), Woitke and Helling (2003, 2004), Helling and Woitke (2006), and Helling et al. (2008c).

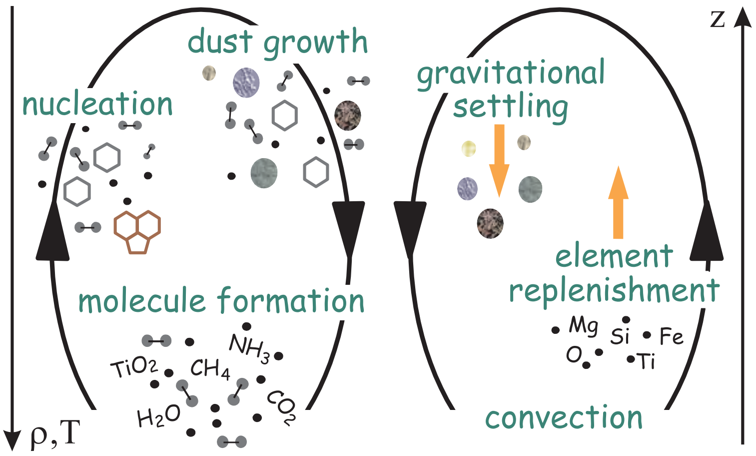

Figure 4.2.1: The life cycle of dust grains from atoms to molecules to seed particles to mixed grains and back to atoms again. Convection ensures that the elements in the upper layers are replenished (Woitke and Helling, 2004).

4.2.1 Formation of seed particles

In the definition of the saturation gas pressure p_{sat} there is an implicit assumption that it is acting on a flat solid surface. However, a sharply-curved solid surface - such as the surface of a small droplet - requires a higher pressure than a flat solid surface to maintain equilibrium (Seinfeld and Pandis, 1998). Therefore, a saturation ratio of $S > 1$ is necessary but not always sufficient for clouds to form, depending on whether condensation seeds are present in the atmosphere or not. As mentioned, the atmosphere on Earth is full of condensation seeds that provide more than enough flat solid surfaces for saturated water vapor to condense on, and the saturation ratio is rarely more than a few percent. In contrast, condensation seeds are not readily available in the atmospheres of ultra cool dwarfs. They have to form from the gas itself to initiate cloud formation, and this can require high supersaturation ratios of several hundred percent.

Homogeneous classic nucleation theory describes how seed particles can form by a process known as homogeneous nucleation (Gail and Sedlmayr, 1988), where some species of atoms or molecules bind chemically to each other to form large, stable clusters that eventually will condense. This process can be described by

$$A_1 \leftrightarrows A_2 \leftrightarrows ... \leftrightarrows A_{N_*} \leftrightarrows ... \leftrightarrows A_N, \tag{4.2.1}$$

where the polymer A_i consisting of i monomers can grow or evaporate by gaining or loosing monomers. If a cluster is in equilibrium with its surroundings the reaction rates for growth and evaporation are roughly the same, but if a cluster reaches a critical size A_{N_*}, the growth rates become smaller than the evaporation rates, and it will continue to grow until it condenses into a seed particle. A_1 is called the nominal atom or molecule of the condensate A_N. The nucleation rate describes how many seed particles are formed per volume per second and can be approximated as

$$J_* \approx \frac{\dot{f}(N_*)}{\tau_{N_*}^{\text{growth}}}, \tag{4.2.2}$$

where $f(N)$ is the distribution of clusters of size N, and $\tau_{N_*}^{\text{growth}}$ is the time scale of the growth reaction $A_{N_*-1} \rightarrow A_{N_*}$. Once the seeds of one kind of species begin to form, all other supersaturated gas species will condense on their surfaces, preventing them from forming seeds themselves. We will therefore need to identify and model only one seed-forming species, namely the one with the highest nucleation rate. Based on arguments of phase stability, some of the most promising candidates for seed formation are the high temperature condensates Fe, Al_2O_3, $CaTiO_3$, TiO_2 and SiO. In addition, we should also consider the stability of clusters that have not yet reached the critical size as well as the abundance of the nominal species.

Jeong et al. (2003) have studied the nucleation rates of several high temperature condensates in the atmospheres of AGB stars, including Fe, Al_2O_3, TiO_2 and SiO. Their nucleation rates are presented Figure 4.2.2. Fe is one of most abundant elements having a stable condensate, but small clusters such as $(Fe)_2$ and $(Fe)_3$ are too unstable to be abundant above $T > 1000$ K, and the nucleation rate of Fe is therefore very low in temperature-density range we are interested in (John, 1995). Chemical equilibrium calculations by Patzer et al. (1999) show that the abundance of Al_2O_3 is almost negligible because of the low stability of the molecule, resulting in a very low nucleation rate as well. SiO is both very stable and highly abundant, but its nucleation is very inefficient because Si and O are part of many silicate materials that grow efficiently as soon as the first seed particles are formed, limiting the seed formation itself (Lee et al., 2015). Even though the element Ti is considerable less abundant than Fe, Al and Ca, the high stability of TiO_2 clusters even at high temperatures result in the highest nucleation rate of them all.

Helling et al. (2001) eliminates $CaTiO_3$ as the most efficient seed-forming species on the account that it is usually only present in negligible amounts and therefore has a very low nucleation rate. TiO_2 is therefore used as the primary condensate in DRIFT. However, it should be noted that a more recent study by Plane (2013) that also examined the nucleation rates of high temperature condensates in the atmospheres of AGB stars concluded that the nucleation of $CaTiO_3$ takes place at much higher rates than the nucleation of TiO_2.

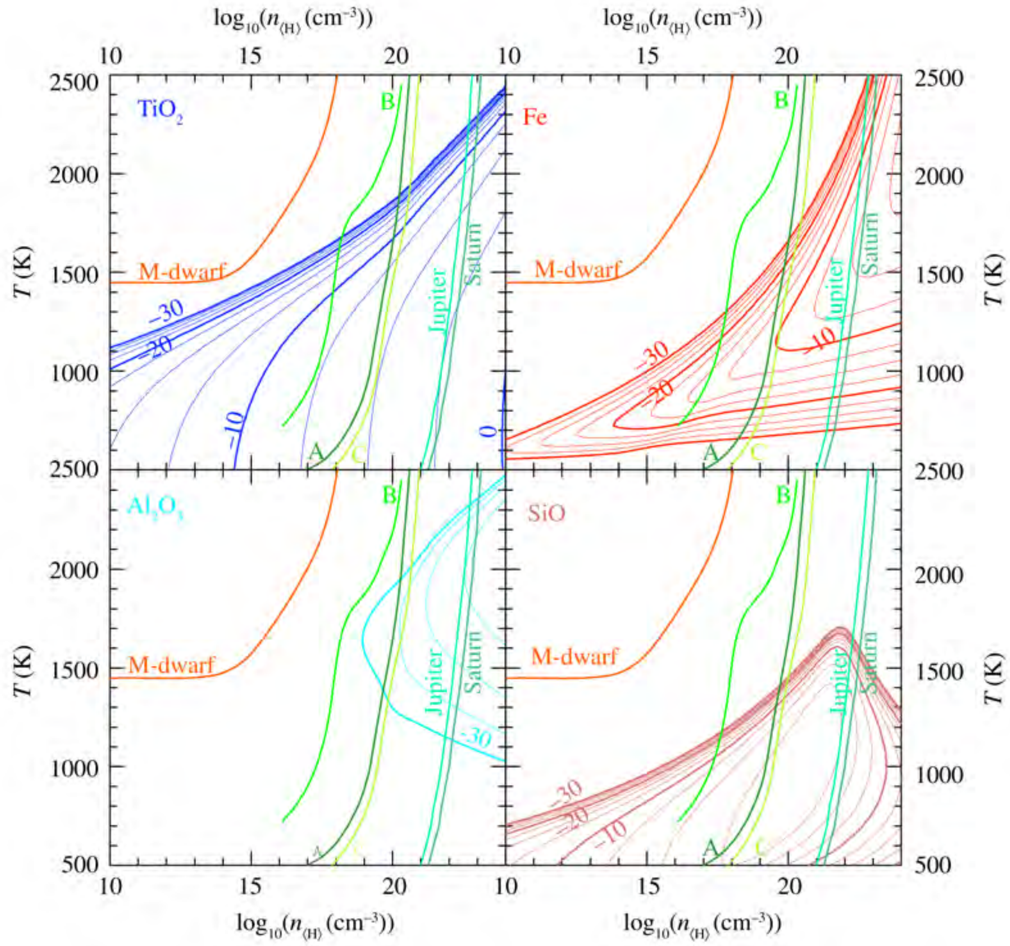

Figure 4.2.2: Contour lines of $\log(J_*/n_{\langle H\rangle})$ in steps of 2.5 for TiO_2, Al_2O_3, SiO and Fe from Jeong et al. (2003). The temperature-density profiles for an M dwarf, different brown dwarfs (A: dust free, B: dust included as element sink and opacity source, C: dust included only as element sink) and Jupiter and Saturn are included. Source: Helling and Fomins (2013).

According to the modified classical nucleation theory of Gail et al. (1984), the nucleation rate for homogeneous $(TiO_2)_N$-clusters is given by

$$J_* = \frac{n_{\mathrm{TiO_2}}}{\tau} Z \exp\left[(N_* - 1)\ln(S) - \left(\frac{T_\Theta}{T}\right)\frac{(N_* - 1)}{(N_* - 1)^{1/3}}\right]. \tag{4.2.3}$$

Here we have defined $T_\Theta = 4\pi a_0^2 \sigma_{\mathrm{TiO_2}}/k_B$, where $\sigma_{\mathrm{TiO_2}} = 620$ erg/cm^2 is the surface tension of TiO (Jeong, 2000) and a_0 is the hypothetical monomer radius. The seed growth time scale for a TiO_2 particle with surface area A_0 moving with relative velocity v_{ref} is $\tau^{-1} = n_{\mathrm{TiO_2}} v_{\mathrm{rel}} N_*^{2/3} A_0$, where $N_* = \left(\frac{2}{3}\frac{T_\Theta}{T}\frac{1}{\ln S}\right)^3$ is the critical cluster size. Z is the Zeldovich factor. The nucleation rate of TiO_2 is thus essentially a function of the number density of gaseous TiO_2 and the temperature of the gas.

4.2.2 Growth and evaporation

Once the seed particles begin to form, all the other supersaturated materials will be able to condense on their surface, creating a mixed dust grain particle that can grow to macroscopic sizes. The two key processes are the growth of dust particles by accretion of molecules and the corresponding reverse process of thermal evaporation. In a subsonic gas molecules of all kinds are freely impinging onto the surface of a dust grain, and some of these dust-molecule collisions can initiate a surface reaction which causes either a growth step or an evaporation step of the dust particle. The effective growth rate can be expressed as a sum over each type of solid s and each type of reaction r:

$$\chi_{\mathrm{net}} = \sqrt[3]{36\pi} \sum_s \sum_r \frac{\Delta V_r n_r v_r^{\mathrm{rel}} \alpha_r}{\nu_r^{\mathrm{key}}} \left(1 - \frac{1}{S_r}\frac{1}{b_s^{\mathrm{surf}}}\right), \tag{4.2.4}$$

where ΔV_r is the change of the dust species volume caused by the reaction r, n_r is the particle density of the key gas species of which the collision rate limits the rate of the surface reaction r, v_r^{rel} is the thermal relative velocity, α_r is a sticking coefficient (usually set to $\alpha_r = 1$ due to lack of data), $b_s^{\mathrm{surf}} = V_{\mathrm{tot}}/V_{\mathrm{s}}$ is the relative surface area of the dust species, and S_r is the supersaturation ratio of the surface reaction r (Helling and Woitke, 2006). It is the product of S_r and b_s^{surf} that determines the sign of χ_{net}.

Equation 4.2.4 allows for the treatment of heterogeneous growth where different types of solids can grow simultaneously on the same surface creating dirty grains. A maximum dust grain size a_{max} is reached when the growth time-scale exceeds the time-scale for gravitational settling, that is, when the dust grain is already removed from the atmosphere before it can be formed (Woitke and Helling, 2003).

Each of these surface reactions will heat or cool the dust grain. In typical ultra cool dwarf atmospheres the effect is very small, and the temperature change is $\Delta \lesssim 3.5$ K (Woitke and

Helling, 2003). We will therefore ignore the effect and assume that the temperature of the gas is equal to the temperature of the dust grains.

4.2.3 Gravitational settling

Newly formed dust grains are so small and light that they follow along with the flow of the gas, moving like the molecules and atoms do. As they grow larger they will gradually decouple from the gas and be subject to a frictional force $\mathbf{F}_{\mathrm{fric}}$ arising from collisions with the gas particles. This force depends on the size of the dust grains and their relative velocity to the gas. Furthermore, the larger dust grains also have a much higher density than the surrounding gas, and the downwards gravitational force $\mathbf{F}_{\mathrm{rad}}$ will therefore cause them to sink down through the atmosphere. A strong radiative field can also exert a significant force on the dust grains, but in cool stars and brown dwarfs the force of radiation is typically much weaker than the gravitational force and can therefore be neglected (Woitke and Helling, 2003).

The equation of motion for a spherical dust particle of radius a and mass m_{d} moving through an atmosphere is determined by Newton's law,

$$m_{\mathrm{d}}\ddot{\mathbf{x}} = \mathbf{F}_{\mathrm{grav}}(\mathbf{x}, a) + \mathbf{F}_{\mathrm{fric}}(\mathbf{x}, a, \mathbf{v}_{\mathrm{drift}}), \tag{4.2.5}$$

where $\mathbf{v}_{\mathrm{drift}}$ is the relative velocity, the drift velocity, between the dust grain and the gas.

The gravitational force on the dust grain is given by

$$\mathbf{F}_{\mathrm{grav}}(\mathbf{x}, a) = m_{\mathrm{d}}\mathbf{g}(\mathbf{x}), \tag{4.2.6}$$

where $\mathbf{g}(\mathbf{x})$ is the gravitational acceleration. Because the extension of the atmospheres of cool dwarfs stars and brown dwarfs is very small compared to the radius, $\mathbf{g}$ can to a good approximation be considered a constant.

The frictional force on the dust grain is a bit more complicated to define since it depends on the behavior of the gas flow, the size of the dust grain, the drift velocity, and the possibly changing thermodynamic state of the gas. The low gas densities ($\rho_g \lesssim 10^{-7}$ g/cm^3) and small grain sizes ($a \lesssim 100\mu$m) in the atmospheres of cool stars and brown dwarfs allow us to assume the particles follow a subsonic free molecular flow (Woitke and Helling, 2003). This allow us to write the frictional force as

$$\mathbf{F}_{\mathrm{fric}}(a, \rho_g, T, v_{\mathrm{drift}}) = \frac{8\sqrt{\pi}}{3} a^2 \rho_g v_{\mathrm{s}} \mathbf{v}_{\mathrm{drift}}, \tag{4.2.7}$$

where v_s is the sound velocity. A dust grain floating in a gas will be accelerated by the gravitational and frictional forces until equilibrium is reached, after which the dust grain will retain a constant velocity as the gravitational acceleration is balanced by the frictional deceleration.

Solving equation Equation 4.2.5 for $m_\mathrm{d}\ddot{\mathbf{x}} = 0$, we can then express the drift velocity as

$$\mathbf{v}_\mathrm{drift} = \frac{\sqrt{\pi}}{2}\frac{\rho_\mathrm{d}\mathbf{g}}{\rho v_\mathrm{s}}a. \tag{4.2.8}$$

Note that the drift velocity is always directed towards the center of gravity. The total velocity of the dust grain is the sum of the drift velocity and the gas velocity:

$$\mathbf{v}_\mathrm{d} = \mathbf{v}_\mathrm{drift} + \mathbf{v}_\mathrm{gas} \tag{4.2.9}$$

4.2.4 Element depletion and convective mixing

The formation and growth of dust grains consumes elements which results in an element depletion of the surrounding gas. If there was no mechanism for returning the elements to gas, all the dust particles would simply settle gravitationally and leave behind a strongly metal-deficient dust-free atmosphere above the cloud base. Fortunately, cool stars and brown dwarfs can be fully convective, which allows non-depleted gas from the interior of the star to be transported upwards by rising convective cells. This convective mixing is extended into the upper, radiative atmosphere via overshooting, leading to a replenishment of the depleted gas above the cloud base, thereby maintaining the dust cycle (Woitke and Helling, 2004).

The element conservation equations are given by

$$\frac{n_{\langle H\rangle}(\epsilon_i^0 - \epsilon_i)}{\tau_\mathrm{mix}} = \nu_{i,0}N_l J_* + \sqrt[3]{36\pi}\rho_g L_2 \times \sum_r \frac{\nu_{i,s} n_r^\mathrm{key} v_r^\mathrm{rel}\alpha_r}{\nu_r^\mathrm{key}}\left(1 - \frac{1}{S_r}\frac{1}{b_s^\mathrm{surf}}\right), \tag{4.2.10}$$

where $n_{\langle H\rangle}$ is the total hydrogen nuclei density and ϵ_i^0 and ϵ_i are the initial and depleted element abundances of element i (Helling et al., 2008c). The term on the left hand side describes the element replenishment by convective overshooting, while the two terms on the right hand side describes element depletion by nucleation and growth/evaporation, respectively. The moment L_2 will be defined in the following section.

4.2.5 Solution method

The physical and chemical processes described all occur at the same time in the atmosphere and can be strongly coupled. Gail and Sedlmayr (1988), Dominik et al. (1993), Woitke and Helling (2003) and Helling and Woitke (2006) have developed a system of partial differential equations that describe the evolution of the dust grains by means of the moments of their size distribution function. Considering a distribution of dust grains $f(V)$, the master equation for dust grains in the volume interval $[V, V + \mathrm{d}V]$ is given by

$$\frac{\mathrm{d}}{\mathrm{d}t}(f(V)dV) + \nabla\left(\mathbf{v}_\mathrm{d} f(V)\mathrm{d}V\right) = \left(R_\uparrow - R^\uparrow + R_\downarrow - R^\downarrow\right)\mathrm{d}V, \tag{4.2.11}$$

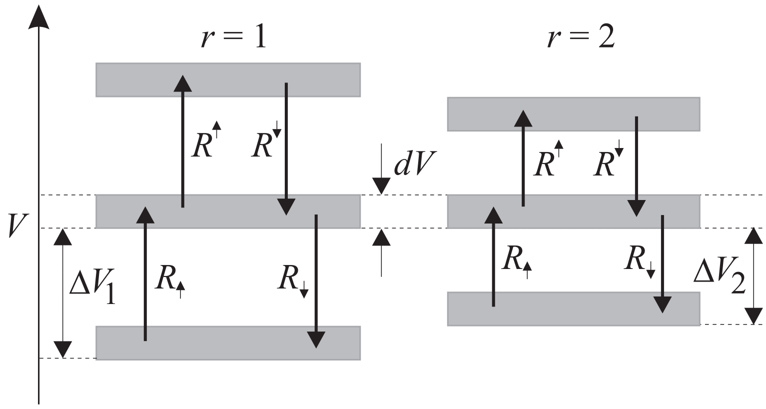

Figure 4.2.3: Two different surface reactions ($r = 1$ and $r = 2$) populating or depopulating the same infinitesimal dust grain volume interval $[V, V + \mathrm{d}V]$. (Woitke and Helling, 2003).

where the right hand side expresses the rate of the population and depopulation of the volume interval due to accretion or evaporation of molecules. This is illustrated in Figure 4.2.3.
To reduce the number of equations, we define the dust moments $L_j(\mathbf{x}, t)$:

$$\rho L_j(\mathbf{x}, t) = \int_{V_l}^{\infty} f(V, \mathbf{x}, t) V^{j/3} \mathrm{d}V, \tag{4.2.12}$$

where $j \in \mathbb{N}$ and V_l is the minimum volume of a larger molecule cluster to be counted as a dust grain (assumed to be 1000 times the volume of a TiO_2 monomer (Woitke and Helling, 2003)). The dust moments are directly related to the physical mean properties of the gas (Gail and Sedlmayr, 1988) by

$$\begin{aligned} \rho L_0 &= n_\mathrm{d} && \text{total number of grains per cm}^3 \\ \sqrt[3]{3/4\pi} L_1/L_0 &= \langle a \rangle && \text{mean particle radius in cm} \\ \sqrt[3]{36\pi} L_2/L_0 &= \langle A \rangle && \text{mean dust surface cm}^2 \\ L_3/L_0 &= \langle V \rangle && \text{mean dust volume cm}^3 \end{aligned}$$

With the definition of the dust moments we can transform the master equation to the much more simple moment equations:

$$-\frac{\mathrm{d}}{\mathrm{d}z}\left(\frac{L_{j+1}}{c_T}\right) = \frac{1}{\xi}\left(-\frac{\rho_g L_j}{\tau_\mathrm{mix}} + V_l^{l/3} J_* + \frac{j}{3}\chi_\mathrm{net}\rho_g L_{j-1}\right) \tag{4.2.13}$$

where ξ is the characteristic gravitational force density, c_T is the mean thermal gas particle velocity and we have assumed a plane parallel atmosphere. A detailed derivation is described by Woitke and Helling (2004).

Equation 4.2.13 is not a closed differential equation since there will always be one more dust moment than there are equations. We therefore include a closure condition $L_0(L_1, L_2, L_3, L_4)$ in the form of a double delta-peaked grain size distribution as discussed in Helling et al. (2008c).

4.3 Dust opacity

`DRIFT` computes the distribution of the dust clouds and the size and composition of their dust grains but to assess how the opacity of the dust clouds affect the structure and spectrum of an atmosphere, we also need to calculate the absorption and scattering of the dust grains. In the following we describe how this is done using Effective Medium Theory and Mie Theory under the assumption that the dust grains are spherical, compact and made of randomly mixed solids.

4.3.1 Complex index of refraction

When light passes through solid matter, some of it is transmitted straight through, some of it is scattered in other directions and some of it is absorbed. The details of what happens to the light depend on the wavelength of the light itself as well as on the type of matter it passes through.

For a given type of solid matter the complex index of refraction describes its optical properties:

$$m(\lambda) = n(\lambda) + ik(\lambda). \tag{4.3.1}$$

The real part n is called the refractive index and describes how much of the light is scattered, and the imaginary part k is called the extinction coefficient and describes how much of the light is absorbed. Together they are known as the optical constants although they are not constant but depend on the wavelength of the light. They cannot be measured directly but they can be deduced from measurable quantities that depend on them such as reflectance and transmittance.

4.3.2 Effective medium theory

The optical properties of composite materials depend on the optical properties of each of the included materials and how they are mixed. We therefore use an analytical approach known as Effective Medium Theory (EMT) to estimate the *effective* index of refraction for various composite materials. Different mathematical expressions are used to describe different types of composite materials: The Lorentz-Lorenz equation describes point polarizable particles embedded in a vacuum, the Maxel-Garnett equation (Maxwell Garnett, 1904) describes inclusions embedded in a host medium other than vacuum, and the Bruggeman equation (Bruggeman, 1935) describes inclusions in a host medium that is identified as the effective medium itself. In other words, the Bruggeman equation describes compact, randomly mixed particles, which is exactly how we want to model our dust particles. The Bruggeman equation for a composite materials consisting of N spherical inclusions is given by

$$\sum_{i=1}^{N} \frac{V_i}{V_{\text{tot}}} \frac{m_i^2 - \overline{m}}{m_i + 2\overline{m}} = 0, \tag{4.3.2}$$

where $\overline{m}$ is the effective complex index of fraction of the composite material and m_i and V_i/V_{tot} are the complex index of refraction and the volume fraction of inclusion i (Bosch et al., 2000). Knowing the index of refraction and volume fraction of every inclusion in a composite material, we can thus solve Equation 4.3.2 iteratively to find the effective index of refraction of the composite material. We use the Newton-Raphson method with complex arguments to solve the equation (Press et al., 1992).

4.3.3 Mie theory

The sizes a of the dust particles in cool stellar atmospheres are of the same order as the wavelength λ of the starlight, so we can not use the Rayleigh ($a \ll \lambda$) or the geometrical ($a \gg \lambda$) approximations to describe how they interact with the light. Instead we have to use the full Mie theory, which is a complete solution to Maxwell's equations that describe how electromagnetic plane waves are scattered by homogeneous spherical particles (Bohren and Huffman, 1983; Mie, 1908).

For light with wavelength λ that is incident on a particle of size a, Mie theory states that the extinction, scattering and absorption efficiency factors for their interaction are given by

$$Q_{\text{ext}}(\lambda, a) = \frac{2}{x^2} \sum_{n=1}^{\infty} (2n+1)\text{Re}\{a_n + b_n\}, \tag{4.3.3}$$

$$Q_{\text{sca}}(\lambda, a) = \frac{2}{x^2} \sum_{n=1}^{\infty} (2n+1)(|a_n|^2 + |b_n|^2), \tag{4.3.4}$$

$$Q_{\text{abs}}(\lambda, a) = Q_{\text{ext}} - Q_{\text{sca}}, \tag{4.3.5}$$

where $x = 2\pi a/\lambda$ is the size parameter and

$$a_n = \frac{mS_n(mx)S_n'(x) - S_n(x)S_n'(mx)}{mS_n(mx)\xi_n'(x) - \xi_n(x)S_n'(mx)} \tag{4.3.6}$$

$$b_n = \frac{S_n(mx)S_n'(x) - mS_n(x)S_n'(mx)}{S_n(mx)\xi_n'(x) - m\xi_n(x)S_n'(mx)} \tag{4.3.7}$$

are the scattering coefficients. Here, m is the complex index of refraction of the particle and S_n and ξ_n are Riccatti-Bessel functions defined by

$$S_n(x) = xJ_n(x), \tag{4.3.8}$$

$$\xi_n(x) = xJ_n(x) + ixY_n(x), \tag{4.3.9}$$

where $J_n(x)$ and $Y_n(x)$ are spherical Bessel functions of the 1st and 2nd kind.

Finally, we can now find the scattering and absorption coefficients by multiplying the efficiency factors with the number density of the particles:

$$\kappa_{\rm sca}(\lambda, a) = n_{\rm d} C_{\rm sca}(\lambda, a) = n_{\rm d} \pi a^2 Q_{\rm sca}(\lambda, a) \quad (4.3.10)$$

$$\kappa_{\rm abs}(\lambda, a) = n_{\rm d} C_{\rm abs}(\lambda, a) = n_{\rm d} \pi a^2 Q_{\rm abs}(\lambda, a) \quad (4.3.11)$$

If the particle is not homogeneous as is the case with our dust particles, we simply replace m with $\overline{m}$ when we calculate the scattering coefficients. This form of the opacities are used in `MARCS` when it is coupled with `DRIFT` and in our synthetic spectrum calculations.

5

Approach

The physical data that is used in the computation of an atmosphere model is just as important as the equations behind the model. Without it, we would not be able to relate our models to the real world. I therefore start this chapter off by describing the acquisition, implementation and improvement of the physical data used by the `MARCS` and `DRIFT` codes. I will then describe how I merged the `MARCS` code with the `DRIFT` code to create an enhanced model code for the computation of dusty atmospheres.

5.1 Physical Data

5.1.1 Equilibrium constants

The equilibrium calculations are based on the 38 atoms and 210 molecules presented in Section A.1. We have adopted the chemical composition of the Sun as reported by Grevesse et al. (2007) for all our models.

For the atoms and ions, `MARCS` uses Equation 3.4.20 to calculate the equilibrium constants. We use the data from Irwin (1981), who approximates the internal partition function as a polynomial of the form

$$\ln Q = \sum_{i=0}^{5} a_i \left(\ln T\right)^i . \tag{5.1.1}$$

Below is shown the first few lines of the input file based on the data table from Irwin (1981). They give the coefficients $a_0 - a_5$ for the species H (1.00), H^+ (1.01), He (2.00) and He^+ (2.01).

Species	a0	a1	a2	a3	a4	a5
1.00	−2.61655891D+02	1.63428326D+02	−4.06133526D+01	5.03282928D+00	−3.10998364D−01	7.66654594D−03
1.01	0.00000000D+00	0.00000000D+00	0.00000000D+00	0.00000000D+00	0.00000000D+00	0.00000000D+00
2.00	−3.76575219D−01	2.33951687D−01	−5.79755525D−02	7.16333160D−03	−4.41302573D−04	1.08442997D−05
2.01	6.93147179D−01	9.29636701D−10	−2.30049742D−10	2.83829746D−11	−1.74590774D−12	4.28355287D−14

The `MARCS` code reads in the coefficients and calculates first the internal partition function Q, then the total partition function q, and finally the equilibrium constant K_p for each atom and ion.

The data from Irwin (1981) covers the temperature range from 1,000 to 16,000 K. For lower temperatures `MARCS` keeps the partition functions constant. This is not a durable solution as the upper atmospheric layers of the coolest brown dwarfs and hot exoplanets have temperatures of only a few hundred kelvin, and the data will have to be updated at some point. For this project, however, it should be an acceptable approximation since only our coolest models reach temperatures below 1000 K and then only in the outermost layers and never below 900 K.

For the molecules, `MARC` uses Equation 3.4.18 to calculate the equilibrium constant. It uses an polynomial approximation of the molar standard Gibbs free energy of formation given by

$$\Delta_f \overline{G}^0 = \sum_{i=0}^{4} c_i \left(\frac{T}{1000 \text{ K}} \right)^i , \tag{5.1.2}$$

in units of J/mol. The original version of `MARCS` used the data from Tsuji (1973), and we have updated to more recent data from Burrows and Sharp (1999) when possible. For TiH only we used the data from Burrows et al. (2005). Burrows and Sharp (1999) uses a slightly different polynomial approximation for the molar standard Gibbs free energy of formation given by

$$\Delta_f \overline{G}^0 = \frac{a}{T} + b + cT + dT^2 + eT^3, \tag{5.1.3}$$

in units of cal/mol. We therefore had to convert the coefficients $a - e$ to the coefficients $c_0 - c_4$, this was done with the `IDL` program shown in Section B.1. Below is shown the first few lines of the resulting input file.

Species	c_0	c_1	c_2	c_3	c_4
H–	−0.79015E+02	0.22776E+02	0.17031E+02	−0.24351E+01	0.14863E+00
H2	−0.43531E+03	0.94254E+02	0.11833E+02	−0.21235E+01	0.14000E+00
H2O	−0.92710E+03	0.19682E+03	0.22617E+02	−0.42069E+01	0.28512E+00
OH	−0.42686E+03	0.87031E+02	0.12051E+02	−0.21797E+01	0.14644E+00

Even though more than 80% of the equilibrium constants were updated the resulting change in the atmosphere models was less than 10 K and it only affected the inner layers.

5.1.2 Continuum absorption

We included the continuum absorption from about a dozen ions as well as electron scattering and Rayleigh scattering by HI. The sources are listed in Table 5.1.1.

Ion	Process	Reference
H^-	b-f, f-f	Doughty et al. (1966); Doughty and Fraser (1966)
HI	b-f, f-f	Karzas and Latter (1961)
HI+HI	CIA	Doyle (1968)
H_2^-	f-f	Somerville (1964)
H_2^+	f-f	Mihalas (1965)
He^-	f-f	Somerville (1965); John (1967)
HeI, CI, MgI, AlI, SiI	f-f	Peach (1970)
e^-	scattering	Mihalas (1978)
HI	scattering	Dalgarno, quoted by Kurucz (1970)

Table 5.1.1: Sources of data for continuum opacities. "b-f" and "f-f" denote bound-free and free-free processes, respectively. CIA stands for collision induced absorption.

5.1.3 Line absorption

The line opacities for atoms and ions were recently updated by Popovas (2014) with atomic line data from VALD-3 (Kupka et al., 2011). Atomic line profiles are both temperature and pressure dependent, so the opacity was sampled for models of varying effective temperatures and surface gravities using the OS method with a resolution of 20,000 $\Delta\nu/\nu$ in the wavelength range 1,250−250,000 Å.

We included and added the line absorption of the 22 molecules listed in Table 5.1.2. We used the program `OSMOL` developed by U. G. Jørgensen to sample the opacity of each molecule for varying temperatures using the OS method with a resolution of 20,000 $\Delta\nu/\nu$ in the wavelength range 1,250−250,000 Å. We only made a few modifications to the program to include the new molecules. For every molecule, `OSMOL` needs information about the mean molecular weight, the internal partition function and the position and strength of each absorption line. We calculated the mean molecular weight using the program `isomol`, a part of it is shown in Section B.2.1. We obtained the internal partition functions and line data from many different sources, as indicated in Table 5.1.2. Each source usually present their data in their own way, so we had to write a separate program for each molecule, to convert the internal partition function and line data to the input format of `OSMOL`. An example is shown for FeH in Section B.2.2.

The molecules TiH, CaH, FeH, and CrH were not initially a part of the equilibrium routines of `MARCS` and had to be added. We did this by adding their names, composition and equilibrium constants to the input data files, extending the arrays containing this information for all molecules, and including a few extra lines in some of the subroutines.

Molecule	Transitions	# of lines	Reference
Hydrides			
LiH	vib-rot	19,000	Coppola et al. (2011)
MgH	vib-rot	20,000	Yadin et al. (2012)
	A-X, B′-X	31,000	GharibNezhad et al. (2013)
SiH	A-X	78,000	Kurucz (2011)
CaH	vib-rot	27,000	Yadin et al. (2012)
	A-X, B-X, C-X, D-X, E-X	116,000	Weck et al. (2003)
TiH	A-X, B-X	171,000	Burrows et al. (2005)
CrH	A-X	14,000	Burrows et al. (2002)
FeH	F-X	111,000	Wende et al. (2010)
CH	vib-rot, A-X, B-X, C-X	104,000	Masseron et al. (2014)
NH	vib-rot	10,000	Brooke et al. (2014a)
	A-X, A-C	36,000	Kurucz (2011)
OH	vib-rot, A-X	82,000	Kurucz (2011)
Oxides			
SiO	vib-rot	1,784,000	Barton et al. (2013)
	A-X, E-X	1,827,000	Kurucz (2011)
TiO	A-X, B-X, C-X, E-X, c-a, b-a, b-d, f-a	37,744,000	Schwenke (1998)
VO	A-X, B-X, C-X	4,500,000	Kurucz (2011)
ZrO	B-A, B-X, C-X, E-A, b-a,d-a,e-a,f-a	16,391,000	Plez et al. (2003)
CO	vib-rot, A-X	555,000	Kurucz (2011)
NO	vib-rot	114,000	Rothman et al. (2010)
H_2O	vib-rot	101,477,000	Jørgensen et al. (2001)
Other			
H_2, HD	vib-rot, quad, B-X, C-X	45,000	Kurucz (2011)
C_2	A-X, b-a, E-A	2,650,000	Kurucz (2011)
	d-a	155,000	Brooke et al. (2013)
CN	vib-rot, A-X, B-X	413,000	Brooke et al. (2014b)
CO_2	vib-rot	10,814,000	Rothman et al. (2010)
HCN	vib-rot	68,592,000	Harris et al. (2006) Harris et al. (2008)

Table 5.1.2: Molecular line transitions and their sources. Some were used in the most recent published grid of `MARCS` models by Gustafsson et al. (2008) (black), some have been updated (blue) and some are completely new (green).

5.1.4 Dust species

The most current version of `DRIFT` includes the condensation of 12 different species (Helling et al., 2008c). We decided to start with only the 7 species that were used in the first versions of `DRIFT` to make the implementation as simple as possible to begin with. It is our intention to add the remaining 5 species later. The 7 species used are: TiO_2[s], $MgSiO_4$[s], SiO_2[s], Fe[s], Al_2O_3[s], MgO[s] and $MgSiO_3$[s]. They were chosen partly for their stability at high temperatures (see Figure 4.1.1), and partly for possessing stoichiometric ratios that ensure they can easily be build up from the gas phase. Table A.2.1 in Appendix A lists the included 32 chemical surface reactions that lead to their formation. The data sources for the supersaturation ratios of the difference dust species are Helling and Woitke (2006), Nuth and Ferguson (2006) and Sharp and Huebner (1990).

Solid species	$\lambda_{\min}[\mu m]$	$\lambda_{\min}[\mu m]$	Reference
TiO_2[s]	0.1	1000	Ribarsky in Palik (1985)
Mg_2SiO_4[s]	0.1	1000	Jäger et al. (2003)
SiO_2[s]	0.1	1000	Posch et al. (2003)
Fe[s]	0.1	1000	Posch et al. (2003)
Al_2O_3[s]	6.7	10,000	Zeidler et al. (2013)
MgO[s]	0.002	625	Roessler & Huffman in Palik (1985)
$MgSiO_3$[s]	0.22	500	Dorschner et al. (1995)

Table 5.1.3: References for the n and k optical constants of the 7 different solids.

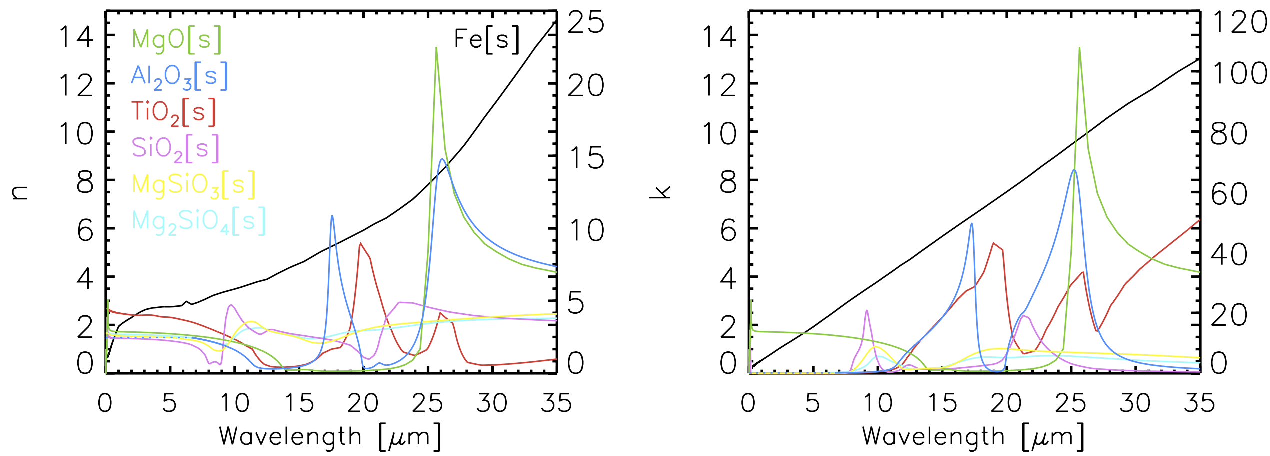

Figure 5.1.1: The n and k optical constants as a function of temperature. Dotted lines represent extrapolated data. Note that the scale of Fe[s] is on the right hand side y-axis.

5.1.5 Saturation vapor pressures

The saturation vapor pressures of the included condensates are calculated using Equation 4.1.9. For TiO_2[s] we use the data from Woitke and Helling (2003) which is listed as fitting coefficients for the function

$$\ln(p_{\rm sat}) = c_1 - c_2 T. \tag{5.1.4}$$

For the rest of the condensates we use the data from Sharp and Huebner (1990) which is listed as the fitting coefficients from the function

$$\Delta_f \overline{G}^0 = \sum_{i=1}^{i=5} c_i T^{i-1}. \tag{5.1.5}$$

The coefficients are listed in Table 5.1.4.

Solid species	c_1	c_2	c_3	c_4	c_5	Reference
TiO_2[s]	35.8027	-7.47347e4	0.0	0.0	0.0	(*)
SiO_2[s]	0.0	-4.44364e5	1.08531e2	-6.59213e-4	0.0	(**)
Fe[s]	7.37828e5	-4.22183e5	1.71919e2	-1.76037e-2	2.31459e-6	(**)
Mg_2SiO_4[s]	7.52334e4	-9.38369e5	2.47581e2	-3.14980e-3	0.0	(**)
Al_2O_3[s]	0.0	-7.32976e5	1.84782e2	-2.57313e-3	0.0	(**)
$MgSiO_3$[s]	8.74400e3	-6.92565e5	1.77877e2	-1.41412e-3	0.0	(**)
MgO[s]	4.38728e3	-2.38741e5	6.86582e1	-1.19852e-3	5.72304e-8	(**)

Table 5.1.4: Fit coefficients c_i for the calculation of the saturation vapor pressures and difference Gibbs free energies of the condensates. (*): Woitke and Helling (2003). (**): Sharp and Huebner (1990).

5.1.6 Optical constants

The sources of the optical constants used to calculate the effective index of refraction of the mixed dust grains are given in Table 5.1.3. Most of the data covers the wavelength range 1,250−250,000 Å, only the data for Al_2O_3[s] and $MgSiO_3$[s] had to be extrapolated down to λ =1,250 Å. We did this by freezing n and k from the first known wavelength point.

Figure 5.1.1 shows how n and k for the different solids changes as a function of wavelength. The wavelike features originate from resonances in the different lattices. For example, the wide dip in n for Al_2O_3 at $\lambda \approx 15\mu$m is caused by vibrations of the Al-O bond.

5.2 Merging `MARCS` with `DRIFT`

The `DRIFT` code was originally designed as an independent set of subroutines and it can therefore relatively easily be integrated into a model atmosphere code such as `MARCS` as an extra module.

Before we can merge the two a few preparations are necessary. First of all, we have to create an interface between them, allowing them to exchange data. Secondly, at few changes has to be made to the MARCS code for it to be able to handle the presence of clouds in its opacity routines.

5.2.1 Data exchange

In order to calculate the details of the cloud layers in an atmosphere, DRIFT needs information about the structure, chemical composition and convection of the atmosphere. Similarly, MARCS needs information about the size and composition of the dust grains as well as the depletion of elements to calculate the effects of clouds in the atmosphere. The data exchange between MARCS and DRIFT is managed through input and output files containing the information listed in Table 5.2.1.

MARCS to DRIFT			DRIFT to MARCS
layer height	z	$a(z)$	average grain size
gas temperature	$T(z)$	$V_i(z)$	average grain volume fractions
gas pressure	$P_g(z)$	$\epsilon_i(z)$	depleted element abundances
gas density	$\rho_g(z)$		
gravitational acceleration	$g(z)$		
convection velocity	$v_c(z)$		
mixing length parameter	l		
initial element abundances	ϵ_i^0		
mean molecular mass	$\mu(z)$		

Table 5.2.1: The information exchanged between MARCS and DRIFT.

5.2.2 Changes to the MARCS code

In the initial version of the MARCS code the element abundances were considered constant throughout the atmosphere. Since diffusion of atoms is a very slow process that only becomes dominant in stars hotter than $T_{\text{eff}} \approx$ 11,500 K (Hui-Bon-Hoa et al., 2000), this is usually an excellent approximation and especially so for late type stars, where the deep convective envelopes will keep the gas well mixed. However, if we include dust formation, there will be a depletion of elements in the top layers where the dust grains form, and a corresponding augmentation of elements in the layers where the dust grains evaporates. We therefore expanded the initial one-dimensional array containing element abundances with an extra dimension to account for their depth dependence.

We then added a group of subroutines that handles the effect of clouds formation and communication with DRIFT. They subroutines are presented in Section B.3. In the initialization phase of MARCS the following subroutines are called:

drift2marcs Reads in the dust data from the DRIFT output file. Then calls optical_data, NR and mie to calculate a general table containing the absorption and scattering of the dust grains.

optical_data Reads in the optical data for the condensates and interpolates/extrapolates if necessary.

NR Minimizes Equation 4.3.2 to calculate the effective index of refraction using the Newton-Raphson method. This part of the code is based on Peter Woitke's program (2011).

mie Calculates the efficiency factors for absorption and scattering. Is based on the Bohren-Huffman Mie subroutine (Bohren and Huffman, 1983).

At the beginning of each iteration the following subroutines are called:

dust_opac Interpolates the table created by drift2marcs to calculate the absorption and scattering in each layer for the wavelength range used by MARCS.

dust_eps Updates the depleted element abundances of Mg, Si, Ti, O, Fe and Al.

Finally, after the last iteration, the following subroutine is called:

marcs2drift Writes out the atmospheric structure as an input file for DRIFT.

5.2.3 Changes to the DRIFT code

The changes to the DRIFT code were minimal. We added one routine and a few lines in two other routines to handle the communication with MARCS. The new subroutine is called init_marcs and is presented in Section B.4.

5.2.4 Running DRIFT-MARCS

While MARCS needs to know the element depletion and dust opacity before it can solve the radiative transfer equation, DRIFT needs to know the convection speed which is calculated by MARCS as it solves the equation of radiation. At a first glance it seems like we are in a deadlock, but the solution to this conundrum is actually quite simple. If we start with a dust free model of $T_{\rm eff} \approx 3000$ K and then proceed to gradually lower the effective temperature, iterating through MARCS and DRIFT for each step, the data exchange files will be updated in sync with the increasing dust formation. For this to work the change in the effective temperature between each step should be relatively small, about $\Delta T_{\text{eff}} = 10 - 50$ K depending on the impact of the dust formation.

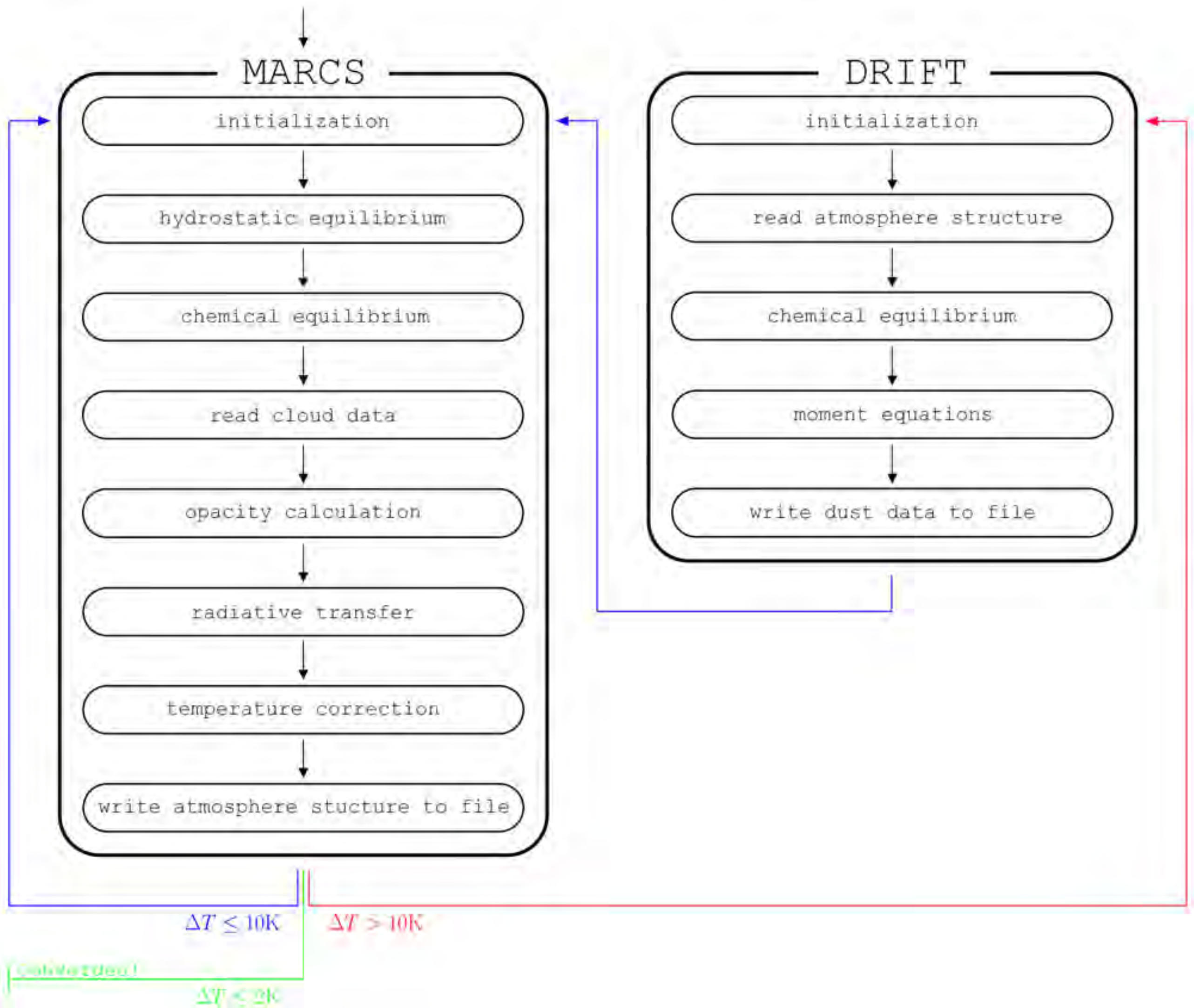

Figure 5.2.1: Flowchart for the merged `DRIFT-MARCS` code.

The dust free version of `MARCS` will keep iterating over a model until the temperature correction is below a given value, usually $\Delta T \leq 2$ K. However, if we allow `MARCS` to fulfill this convergence criterion every time we run `DRIFT`, we can easily end up in a endless loop with no convergence in sight. When `DRIFT` adds a layer of dust to the atmosphere, `MARCS` will heat the layers as a reaction to the increased opacity. In response, `DRIFT` will then reduce the amount of dust as the higher temperatures impede the dust formation. `MARCS` will of course react to the decreased opacity by cooling the layers again, and we are thus back where we started - or even further away! To avoid this, we only let `MARCS` iterate once, and we limit the temperature correction to half of what the code suggests. This way we stop the overheating of the atmosphere and allow the dust formation to react to the temperature change before it becomes too large. When the temperature correction is below $\Delta T \leq 10$ K we consider the cloud layer stable and let `MARCS` converge fully without calling `DRIFT` again. A rough flow chart of this process is shown in Figure 5.2.1. The source code for the program that call `MARCS` and DRIFT and checks the convergence is presented in Section B.5.

6
Cloudy atmosphere models

We have created a small grid of models for late type M-dwarfs and early L-type brown dwarfs with effective temperatures of $T_{\text{eff}} = 2000 - 3000$ K in steps of $\Delta T = 100$ K. They all have solar initial abundances and a surface gravity of $\log(g) = 4.5$.

6.1 Overview

In Figure 6.1.1 we present the temperature-pressure profiles for our models. The bottom left part of the figure represents the outer layers of the atmosphere, and the top right part represents the inner layers of the atmosphere. Convection sets in at around $P_g > 10^4$ dyn/cm^{-1} and is the predominant mode of energy transport in the bottom of the atmosphere. In the outer layers of the atmosphere, the opacity is almost constant and close to zero and the temperature is therefore almost constant as well.

When $T_{\text{eff}} < 2700$K, the temperature in the outer layers of the atmosphere is low enough for dust formation to set in, but the effect is so small in the beginning that it barely affects the structure of the model. At $T_{\text{eff}} = 2600$ K the amount of dust formation has increased enough

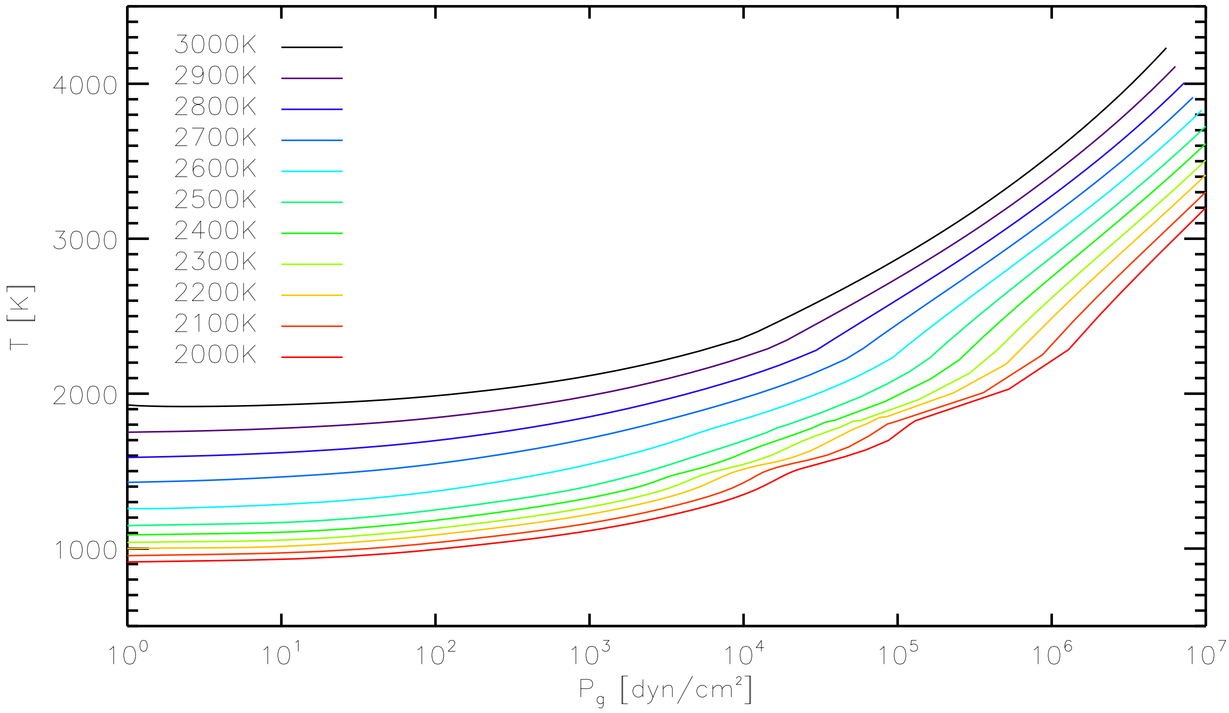

Figure 6.1.1: The T-P_g profiles for our grid of models with varying effective temperatures, $\log(g) = 4.5$ and solar initial abundances.

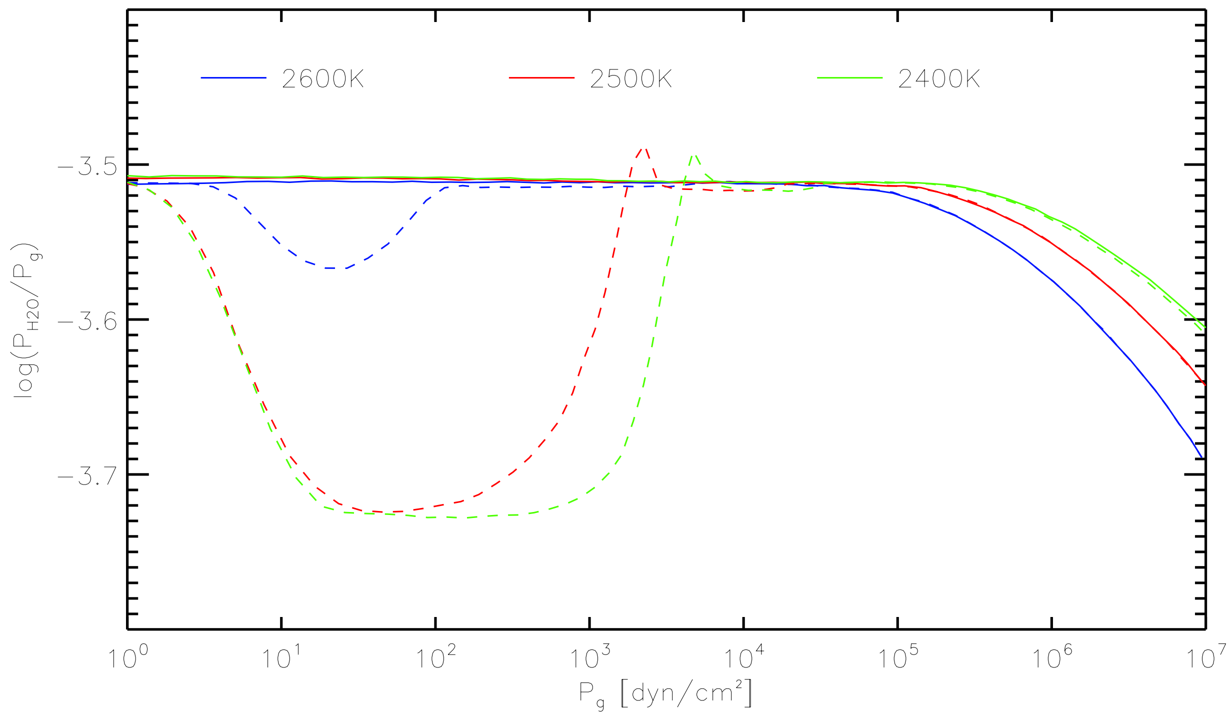

Figure 6.1.2: The relative partial pressure of H_2O as a function of the total gas pressure for three models of decreasing effective temperature for which dust formation becomes increasingly important.

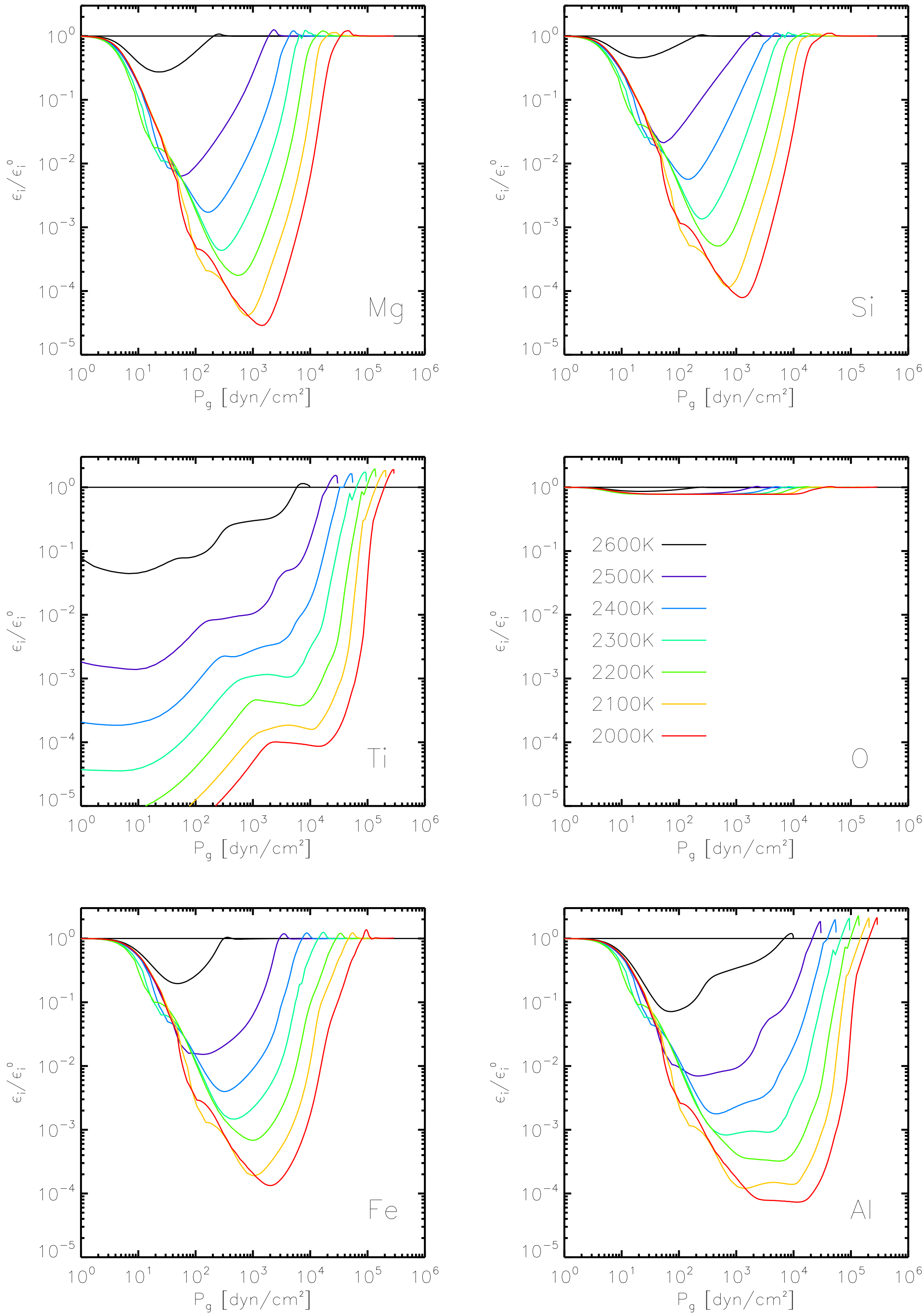

Figure 6.1.3: Element depletion as a function of depth for different effective temperatures.

to cause a cooling effect in the outer layers. This happens because the element depletion reduces the amount of molecules and therefore also their opacity, this is illustrated for H_2O in Figure 6.1.2. As long as the dust clouds are not substantial enough for their own opacity to compensate, the affected layers will cool a little. At $T_{\rm eff} = 2600$ K the outer layers cool about $10 - 20$ K, at $T_{\rm eff} = 2500$ K the dust opacity is starting to catch up, and at $T_{\rm eff} \leq 2400$ K there is a clear heating of the outer layers from dust formation. As we move to cooler effective temperatures this heating increases.

For the coolest models we also see fluctuations in the temperatures of the middle layers of the model caused by back-warming. There is a tendency for the temperature fluctuations to shift inwards for decreasing effective temperatures. This can be explained by the withdrawal of the convection zone and the lower velocities of the convective cells, which makes the element replenishment less effective and causes the clouds to sink down a little into the atmosphere.

The dust grains are formed from the elements Mg, Si, Ti, O, Fe and Al. In Figure 6.1.3 we show how their abundance changes as a function of depth for the different models as they are bound in dust grains. In general, the more rare elements are usually stronger depleted. While the large abundance of O is barely affected by the dust formation, the other elements are clearly depleted in the dust forming regions. Since we use TiO_2[s] to create seed particles, the relatively small abundance of Ti is strongly depleted in the outer layers. The element depletion of the remaining elements sets in a little later when there is available seed particles for them to condense on. The depletion is largest when the nucleation peaks (see Figure 6.3.1) and then decreases as the dust grains reach the lower warmer layers and start to evaporate. Because the elements rain out with the dust grains, we see an overabundance of elements right below the cloud base.

6.2 Molecular and atomic opacities

We will now take a look at how the opacities of atoms and especially molecules affect the spectrum of cool stars. Figure 6.2.1 illustrates the impact of atomic (blue) and molecular (red) line absorption on the spectrum of a dust free model with $T_{\rm eff} = 2500$K, $\log(g) = 4.5$ and [Fe/M] $= 0$. At these low temperatures the absorption of atoms does not really affect the structure of the model, but they do create a few strong absorption lines in the ultraviolet and visible part of the spectrum. The most prominent are the two Ca II lines at 3968/3934 Å, the Ca I line at 4227 Å, the Mg I triplet at 5167/5173/5184 Å, the Na I doublet at 5890/5895 Å, and the K I doublet at 7665/7699 Å (Walker, 2014). Still, it is the molecules that dominate the spectrum, completely obscuring most of the atomic lines except in the ultraviolet region.

A more detailed look at the individual absorption of the molecules is presented in Figures

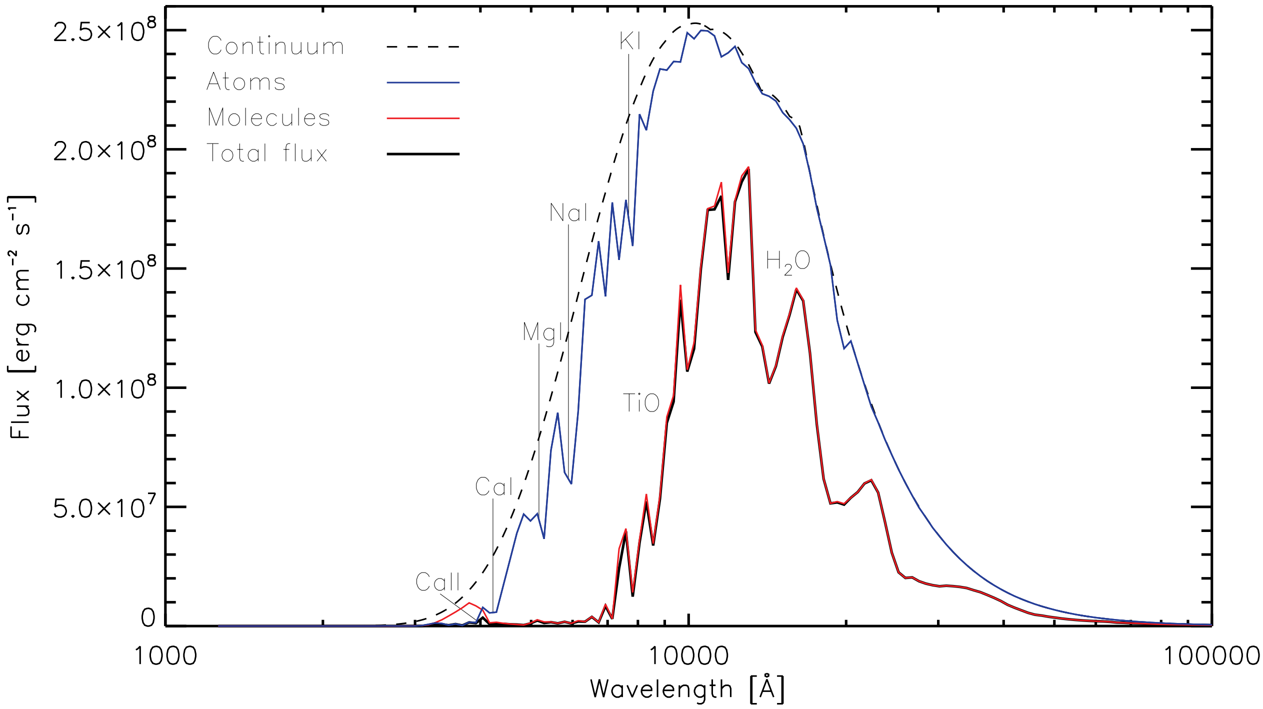

Figure 6.2.1: Spectrum of a dust free stellar model atmosphere with $T_{\rm eff}$ = 2500K. The dashed line is the continuum level, the blue and red lines are the atomic and molecular absorption, and the black line almost entirely obscured by the red line is the total flux.

6.2.2, 6.2.3 and 6.2.4. At the shortest wavelengths, SiO, H_2, and CO are all very strong absorbers, with SiO being the most influential from 1,800-3,000 Å. OH also has a fairly strong absorption from 2,600-3,200 Å, but it is obscured by the SiO absorption. NH makes a short appearance around 3,400 Å. TiO absorption starts to grow from 4,000 Å and completely dominates the spectrum from 4,400-9,000 Å with a few exceptions; at 7,500 Å and 8,800 Å the absorption of TiO weakens but is compensated for by the absorption of VO and CrH, respectively. In fact, if there had been no TiO in the atmosphere, the metallic hydrides would have provided most of the absorption from 4,000-11,000 Å with CaH peaking at 6,800 Å, CrH at 8,800 Å and 10,000 Å, FeH at 10,000 Å, MgH at 5,100 Å, SiH at 4,200 Å and TiH at 5,300 Å. ZrO also shows its strongest absorption in this region. Finally, H_2O absorption shows up at 11,000 Å and completely dominates the spectrum in the infrared and beyond.

LiH and NO absorption both have a negligible effect on the spectrum because of their very low partial pressures. Even though the absorption coefficient of CO_2 is larger than that of CO in the optical, the partial pressure of CO_2 at these high temperatures is less than a thousandth of the partial pressure of CO, and its spectroscopic features are therefore almost imperceptible. CH, C_2, CN and HCN are barely present in oxygen-rich atmospheres at these temperatures, and their contribution to the absorption is consequently negligible.

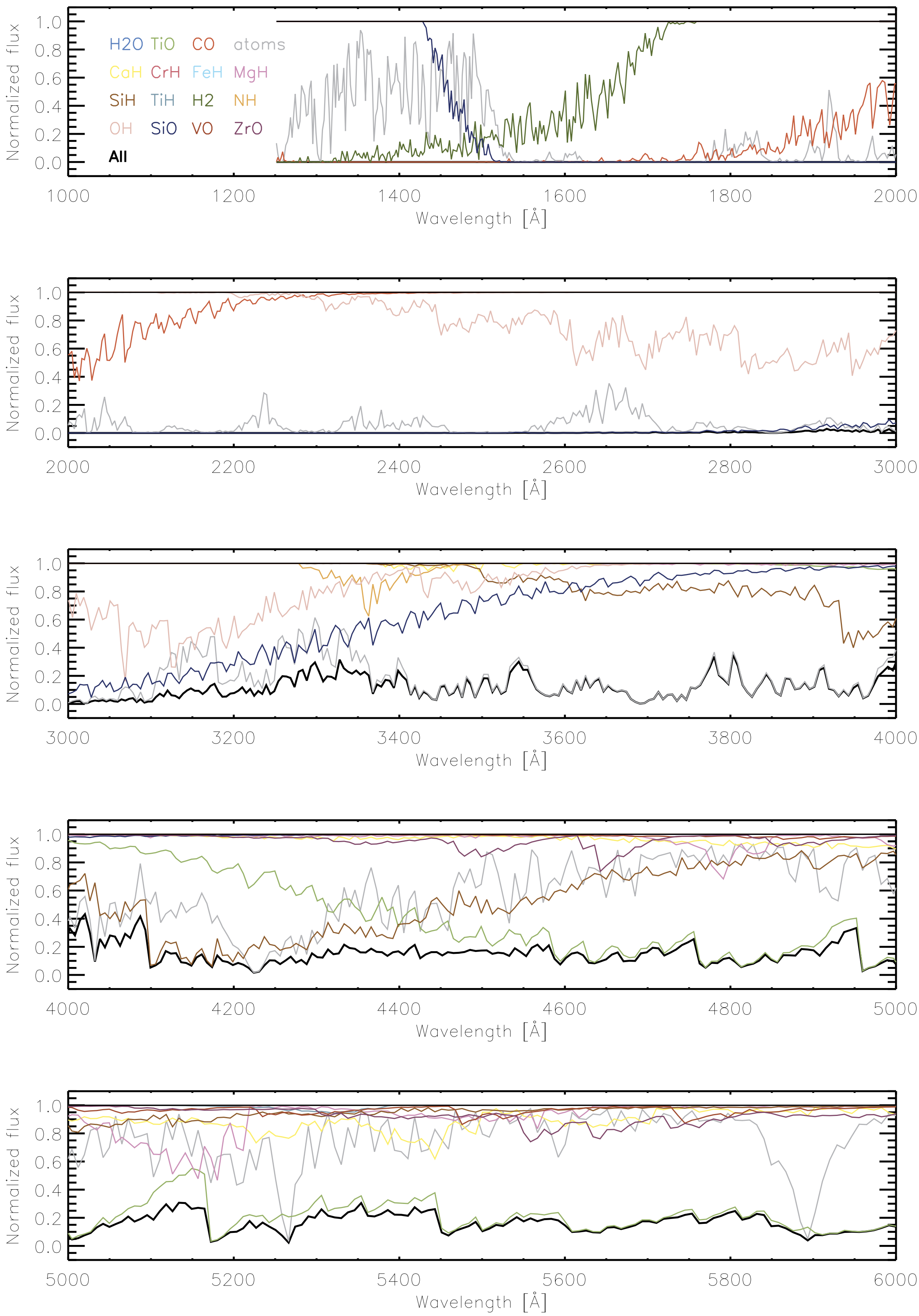

Figure 6.2.2: The atomic and molecular absorption in a model with $T_{\mathrm{eff}} = 3000\mathrm{K}$, $\log(g) = 4.5$ and $[\mathrm{Fe/M}] = 0$.

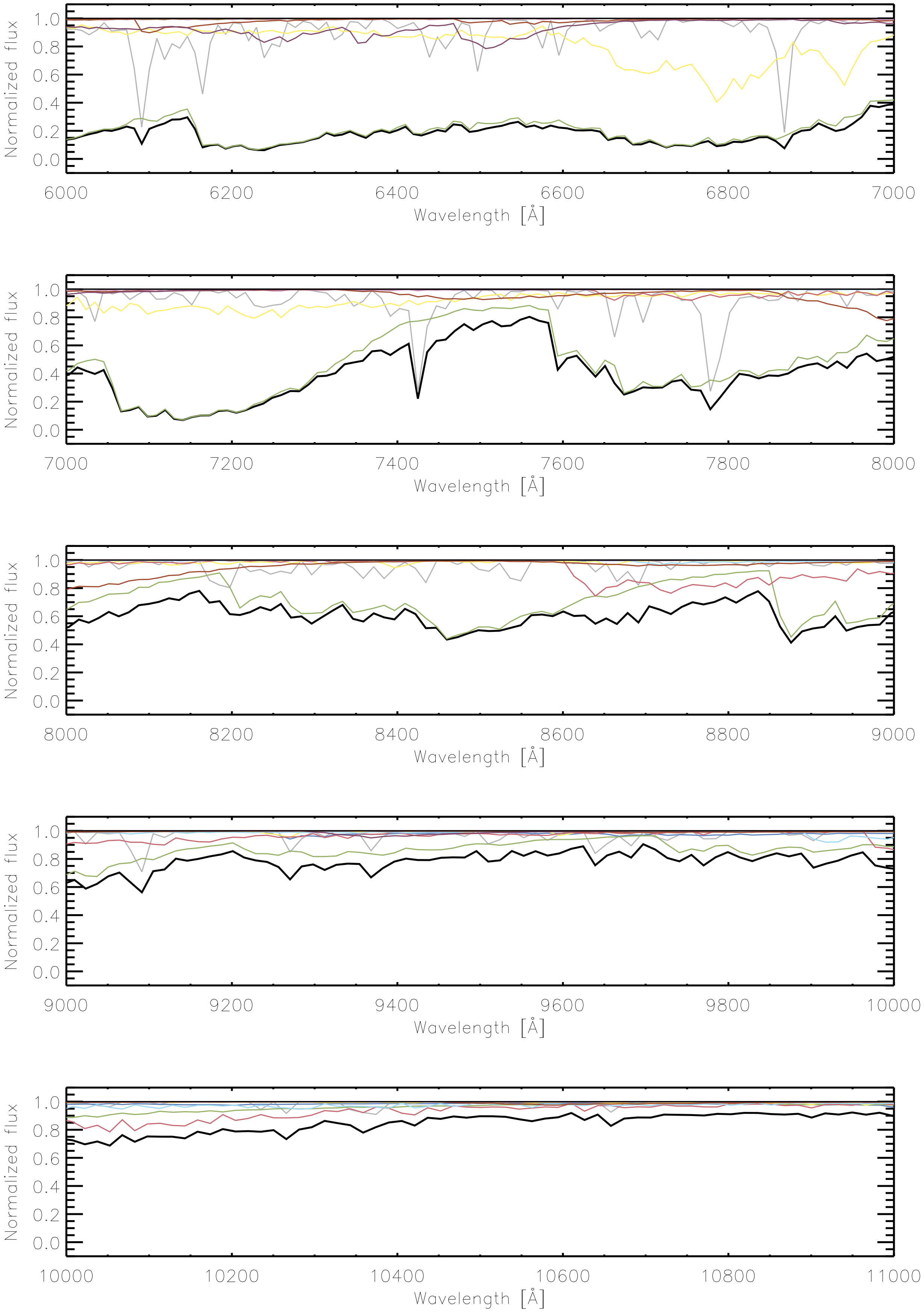

Figure 6.2.3: The atomic and molecular absorption in a model with $T_{\mathrm{eff}} = 3000$K, $\log(g) = 4.5$ and $[\mathrm{Fe/M}] = 0$.

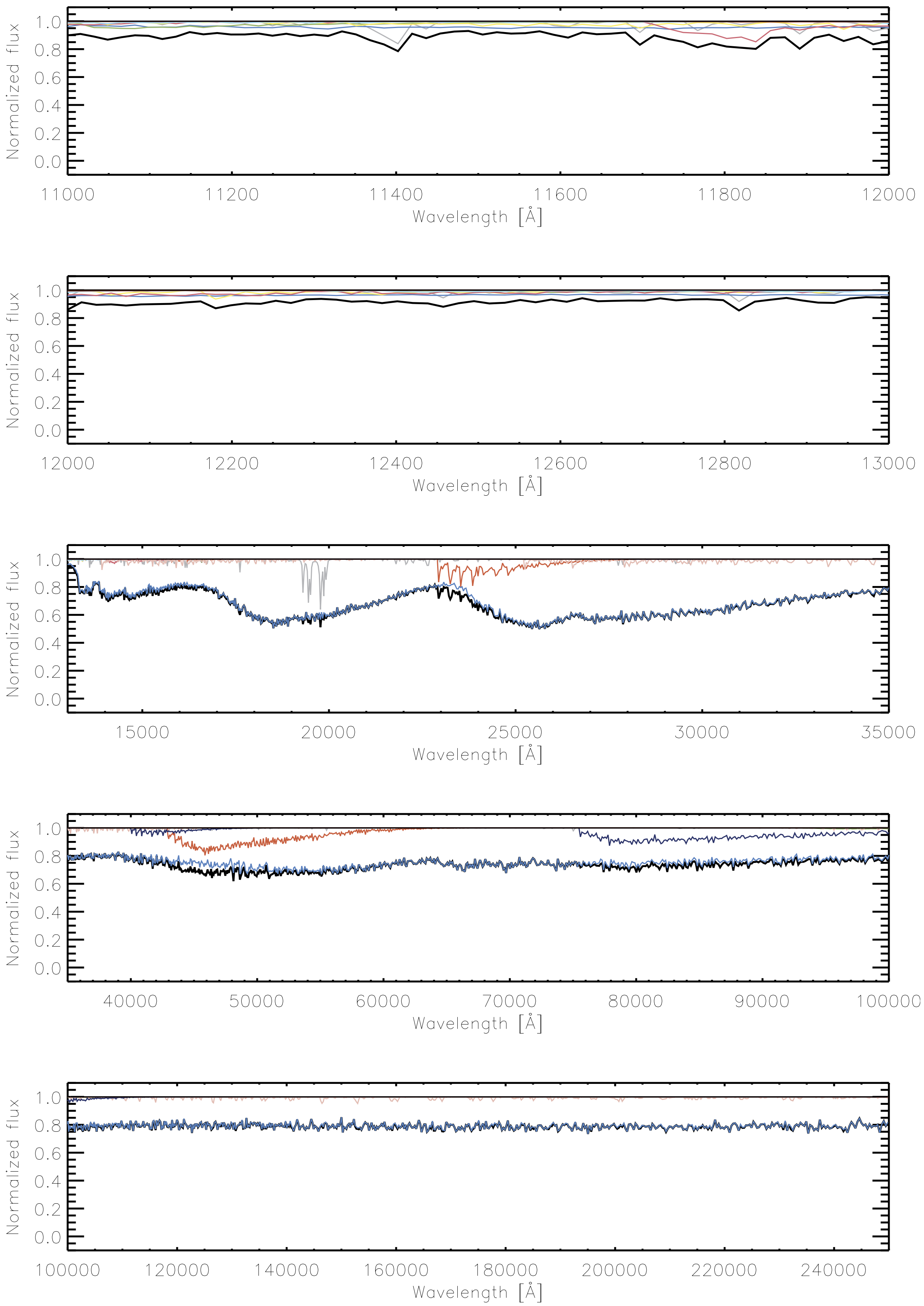

Figure 6.2.4: The atomic and molecular absorption in a model with $T_{\mathrm{eff}} = 3000\mathrm{K}$, $\log(g) = 4.5$ and $[\mathrm{Fe/M}] = 0$.

6.3 Dust cloud details

In Figure 6.3.1 we have plotted some of the expressions that enter or is the result of the moment equations to get an idea of how the dust behaves and why.

Starting in the top of the atmosphere and moving down, the nucleation rate J_* rises quickly as the density increases. When a distinct local temperature $T_\Theta \approx 1300$ K is exceeded (see Equation 4.2.3), the nucleation rate drops to zero very fast. Consequently, the peak of the nucleation rate reaches deeper into the atmosphere the cooler the effective temperature of the model is.

The nucleation rate causes a rise in the number density of dust grains n_d, and the peak coincides with the first rapid increase in the number of dust particles. After the nucleation rate peaks the numbers density flattens out until it sharply increases again at the bottom of the cloud layers. In the middle of the cloud layer, the mass density ρ_d keeps increasing while the number density does not, showing that while the nucleation of new dust grain particles have stopped, the already existing ones are still growing larger. At the bottom of the cloud layers the dust grains evaporate at the high temperatures, causing a rapid decrease in their mass density and a just as rapid increase in their number density, as the larger dust grains break into smaller grains before they completely disappear.

The net growth rate is $\chi_\mathrm{net} > 0$ when the grains are growing and $\chi_\mathrm{net} < 0$ when the grains are evaporating. The first growth period begins when we are far enough down in the atmosphere for the solids to effectively condense on the the nucleation particles. It peaks before the nucleation rate indicating that it depends more on the amount of available surface area than on the formation of new small particles. The mean grain size $<a>$ is closely linked to the net growth rate, and the first and second increase in the mean grain size happens in sync with the first and second period of growth. Near the bottom of the cloud layers the net growth rate and mean grain size rapidly drops as the dust grains completely evaporate. The fluctuations in the net growth rate is due to the different solid species evaporating at different temperatures.

The drift velocity is initially decreasing as the gas density - and therefore the friction - increases. The decreasing ends when the second period of growth sets in, as the larger dust particles can more easily overcome the friction.

6.3.1 Cloud structure regions

Based on the analysis in the previous section it is possible to identify different regions within the dust clouds that each have their own characteristics. This was described for a pure TiO_2 model by Woitke and Helling (2004) and for a similar model with the same 7 dust species by Witte (2011). With respect to the grain size distribution, we can divide the dust clouds into

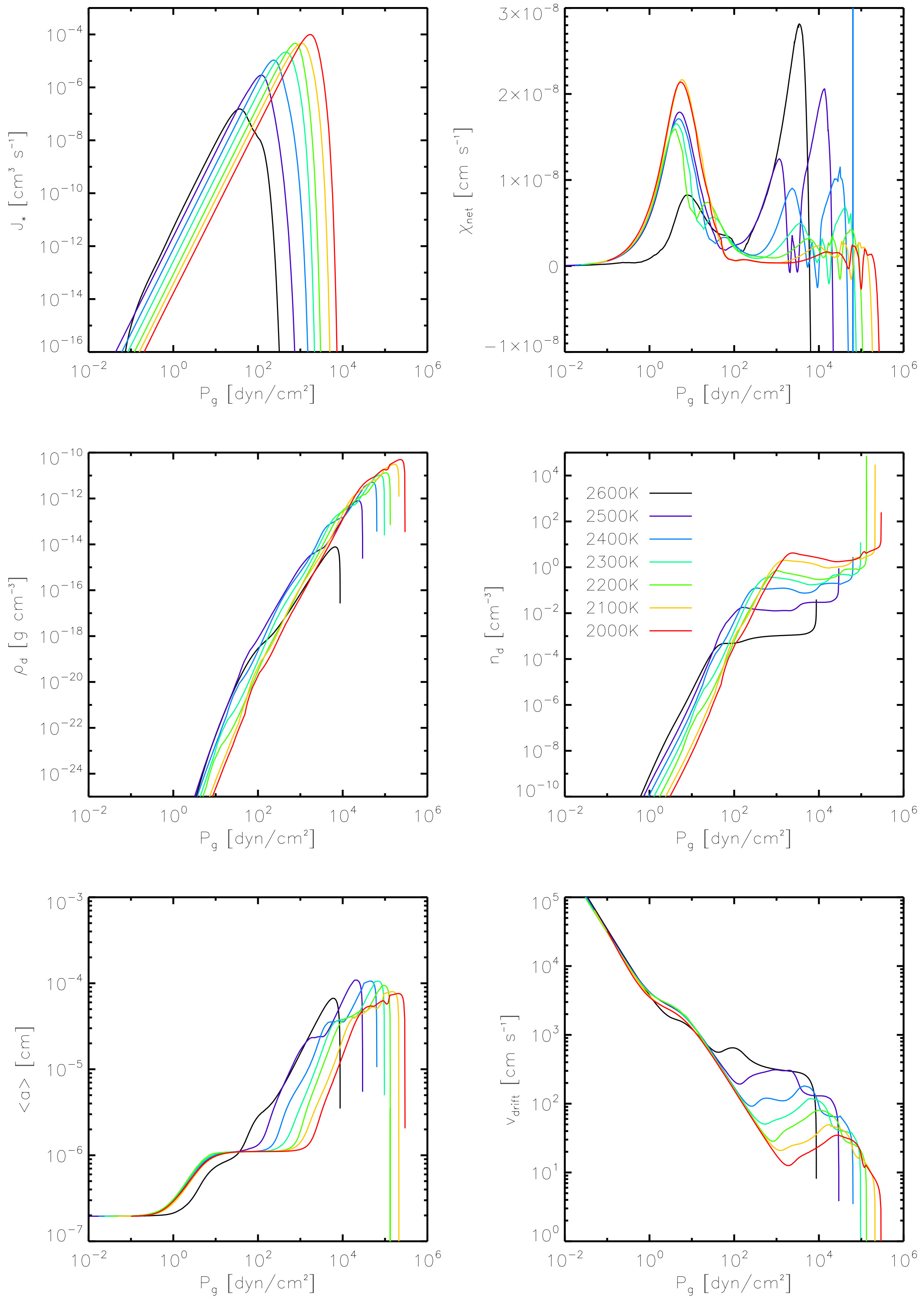

Figure 6.3.1: The nucleation rate J_*, net growth rate $\chi_{\rm net}$, mass density $\rho_{\rm d}$ and number density $n_{\rm d}$ of the dust grains, the mean grain size $<a>$ and the drift velocity $v_{\rm d}$ as a function of gas pressure.

five distinct zones based on the how the mean size of a dust grain changes as we move from the top to the base of the clouds. The five regions are illustrated for a model with $T_{\rm eff} = 2000$ K, $\log(g) = 4.5$ and [M/H] = 0.0 in Figure 6.3.2.

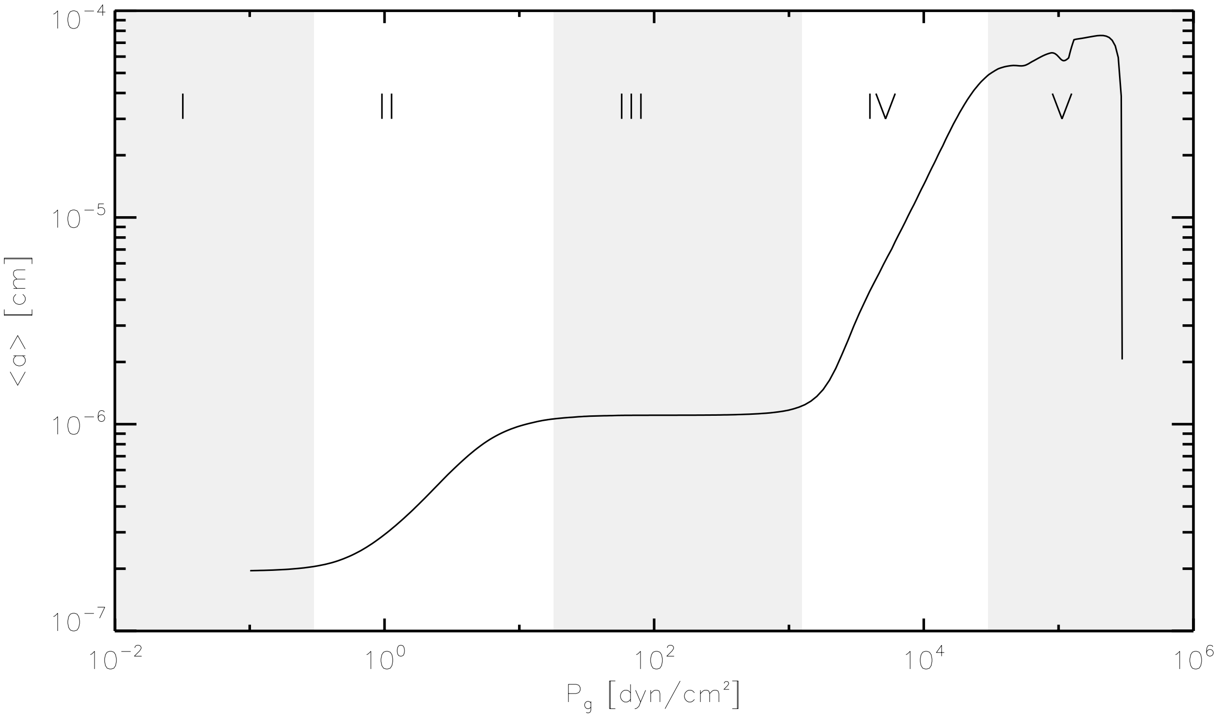

Figure 6.3.2: The five regions of the dust cloud: I nucleation, II first growth, III drift, IV second growth, V evaporation.

The five regions are characterized as follows:

I Nucleation

In the top of the cloud layers the nucleation of gas molecules is the dominant process, and the gas phase is highly depleted in Ti. We are too high above the convection zone for efficient element replenishment, so the dust grains stay small and sparse.

II First growth

As the dust grains fall down through the dust layers, the increasing density and element replenishment allow for a growing number of possible surface reactions on the seed particles, and the dust grains increase considerably in size. As a result, the gas becomes more and more depleted in the elements that make up the dust grains. The rate of newly forming seed particles still increases in this region, but it is the growth that has the most effect on the dust grain sizes.

III Drift

The increasing density of the gas causes the decent of the dust grains to slow, which reduces the collision rate between the dust grains and the gas molecules. This will decrease the growth rate. In the same region the nucleation rate peaks and the average dust grain size remains constant, as the impeded growth of the large dust grains is compensated for by the rapid formation of new small grains.

IV Second growth

When the nucleation rate suddenly drops, the mean grain size is no longer kept in check by the formation of small dust grains and increases rapidly again. This ends the decrease of the drift velocity which remains more or less constant until the grains start evaporating. This and the still increasing density allow for an increase in the net growth rate.

V Evaporation

In the lowest layers of the dust clouds the dust grains start to evaporate as the temperature reaches the atomization energies of the different solids, and the mean grain size decreases, dropping very fast as the last dust grains evaporate at the cloud base.

6.3.2 Dust grain composition

In Figure 6.3.3 we have plotted the volume fraction of each of the dust species as a function of gas pressure. This gives us an idea of how the composition of a dust grain varies as it forms, grows, drifts and eventually evaporates. In the high layers of the clouds, the dust grains are made purely of TiO_2[s] as this is the species used for seed formation. As the growth rate becomes significant and the other dust species begin to condense on to the surface of the seed particles, the relative volume of TiO_2[s] quickly drops. The silicates Mg_2SiO_4[s], $MgSiO_3$[s] and SiO_2[s] are the first dust species that start to condense on the seed particles, quickly followed by MgO[s] and Fe[s] and then finally Al_2O_3[s]. The silicates dominate a wide part of the clouds, but in the deeper parts where the temperatures are high, they are also the first to evaporate. In the end, only Fe[s] and Al_2O_3[s] remain and are the two major constituents of a dust grain before it completely evaporates. For the coolest models, the peak in the relative volumes of Fe[s] and Al_2O_3[s] are reflected in the net growth rate and the mean dust grain size in Figure 6.3.1.

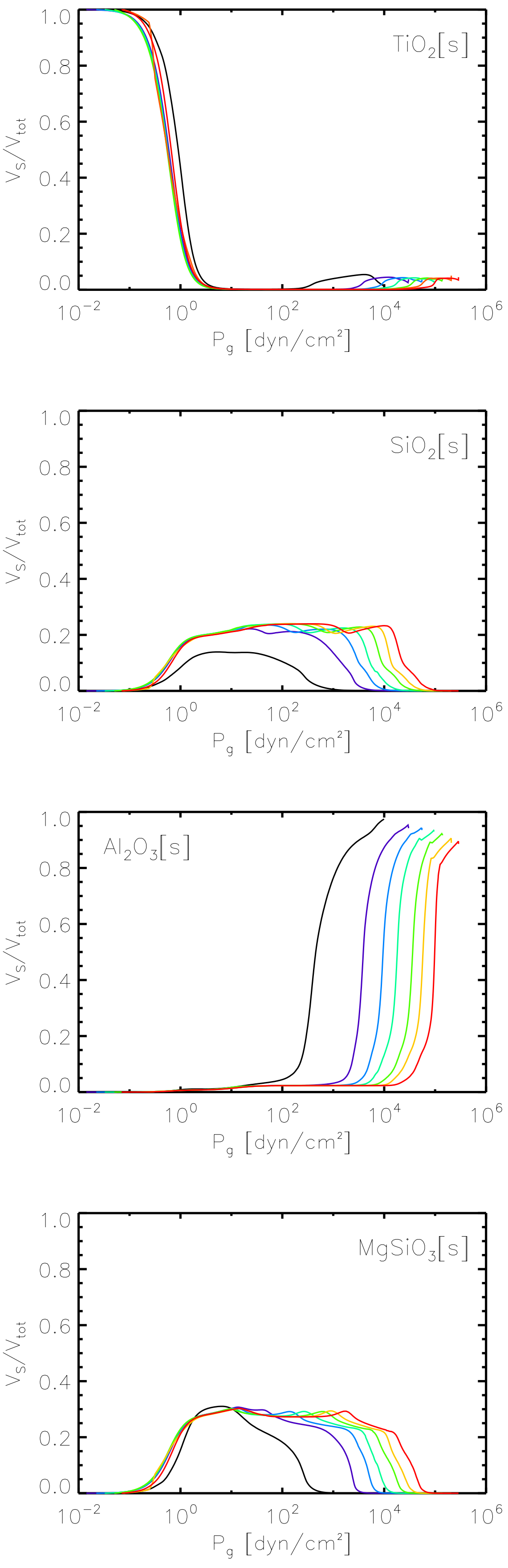

Figure 6.3.3: The volume fraction of each of the seven dust species in a dust grain as a function of gas pressure. All fractions sum up to unity. The color coding is the same as in Figure 6.3.3.

6.4 Dust grain porosity

The DRIFT code models dust grains as compact, randomly mixed particles composed of many small islands of different solid condensates, but the fact is that we do not know if the real dust grains in M-dwarfs are porous or not and to what extent. It is certainly a possibility.

In Figure 6.4.1 we show that the porosity of the dust grains can have a great effect on the opacity. We compare the integrated opacity for our model with $T_{\rm eff} = 2000$ K, $\log(g) = 4.5$ and [M/H]=0.0 for three types of dust grains: one is the original compact type, one contains 10% vacuum and one contains 50% vacuum. We did this simply by adding the vacuum as an eighth solid condensate in our dust opacity routines. The model has not been iterated with the new dust opacity, we have just re-calculated the opacity of the dust layer in the already converged model to illustrate that there is an effect. Interestingly, we see that by increasing the porosity slightly the dust grains become more opaque. If the porosity is too high the opacity drops again since the light can pass unhindered through a large part of the dust grains.

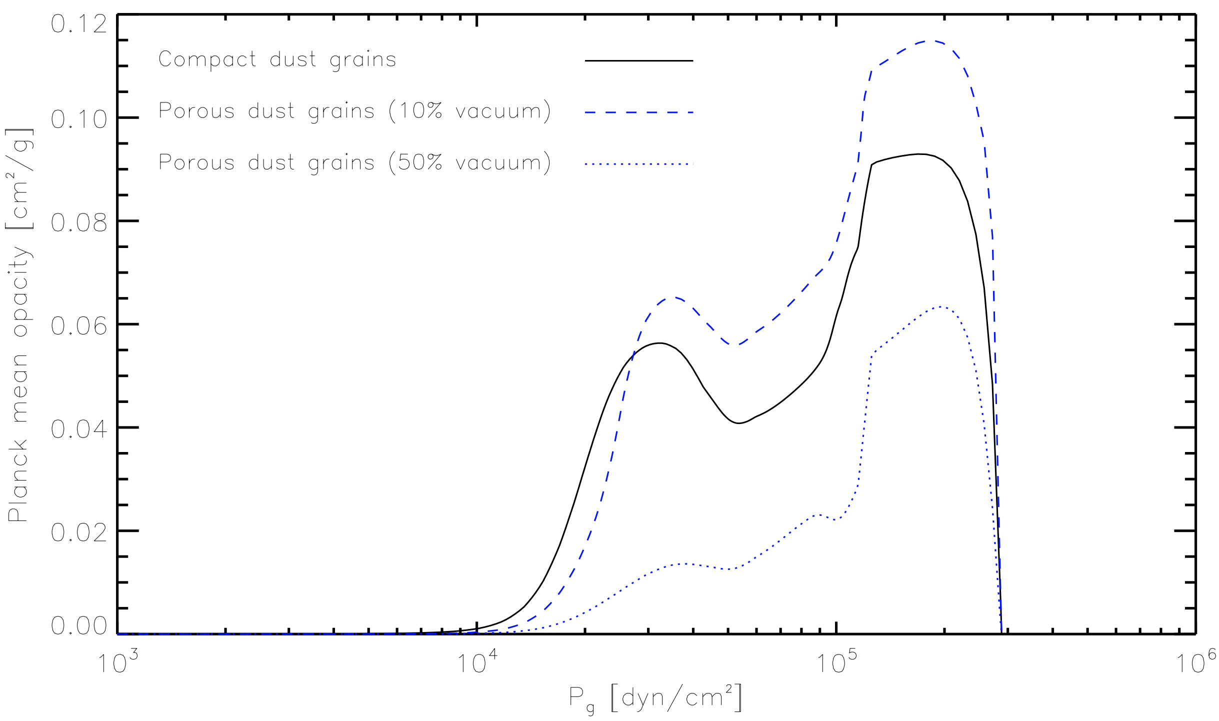

Figure 6.4.1: Comparison of the integrated opacity of three different types of dust grain porosity for a model with $T_{\rm eff} = 2000$ K, $\log(g) = 4.5$ and [M/H]=0.0.

6.5 Synthetic spectra

The synthetic spectra that we calculate based on the model atmospheres allow us to compare our models with observations. We will therefore briefly take a look at how much and in what way the formation of dust affects the spectrum.

In Figure 6.5.1 we plot the effect of dust extinction as a function of wavelength for models of decreasing effective temperatures. The whole wavelength range of `MARCS` is considered. The dust extinction clearly increases with decreasing effective temperatures as expected. The dust extinction increases in a broad band that covers the optical and near-infrared wavelength regions and peaks at around $1 - 10$ μm. At short wavelengths there are two noticeable sharp peaks. If we look at the dust absorption and scattering separately we find that although the peaks are present in both dust absorption and scattering, the absorption peaks are about 8 times larger than the scattering peaks. We are not sure what produces these peaks. It is possible that they are a product of some of our approximations such as the calculation of the dust opacity based on the mean grain size. In any case, they occur in the ultraviolet part of the spectrum where the opacity is heavily dominated by atomic absorption and therefore does not have an effect on at least the spectrum.

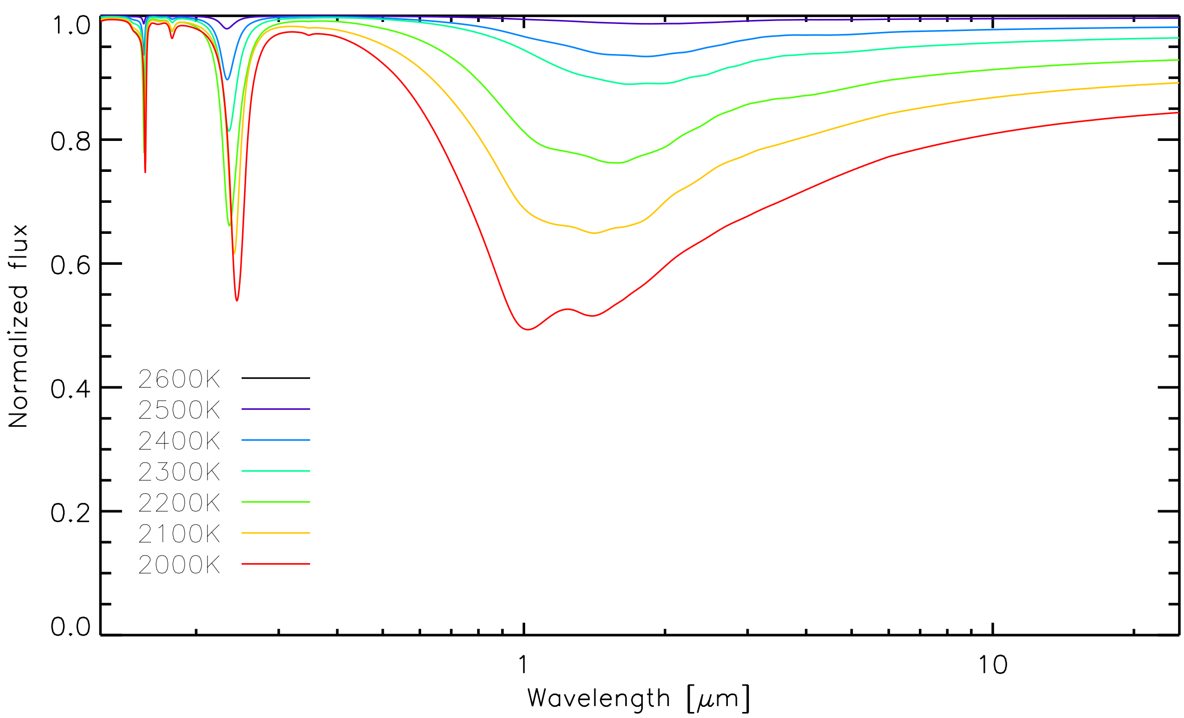

Figure 6.5.1: Dust absorption and scattering for models of decreasing effective temperature.

In Figure 6.5.2 we compare the extinction of dust with the extinction of atoms and molecules in a model with $T_{\rm eff} = 2000$ K, $\log(g) = 4.5$ and $[{\rm M/H}] = 0.0$. For $\lambda > 10$ μm the dust extinction has a clear dampening effect on the molecular absorption bands, which would otherwise have defined the spectrum. In one region the dust extinction is actually greater than the molecular absorption, clearly showing the importance of including dust formation when modeling the atmospheres of cool stars and brown dwarfs.

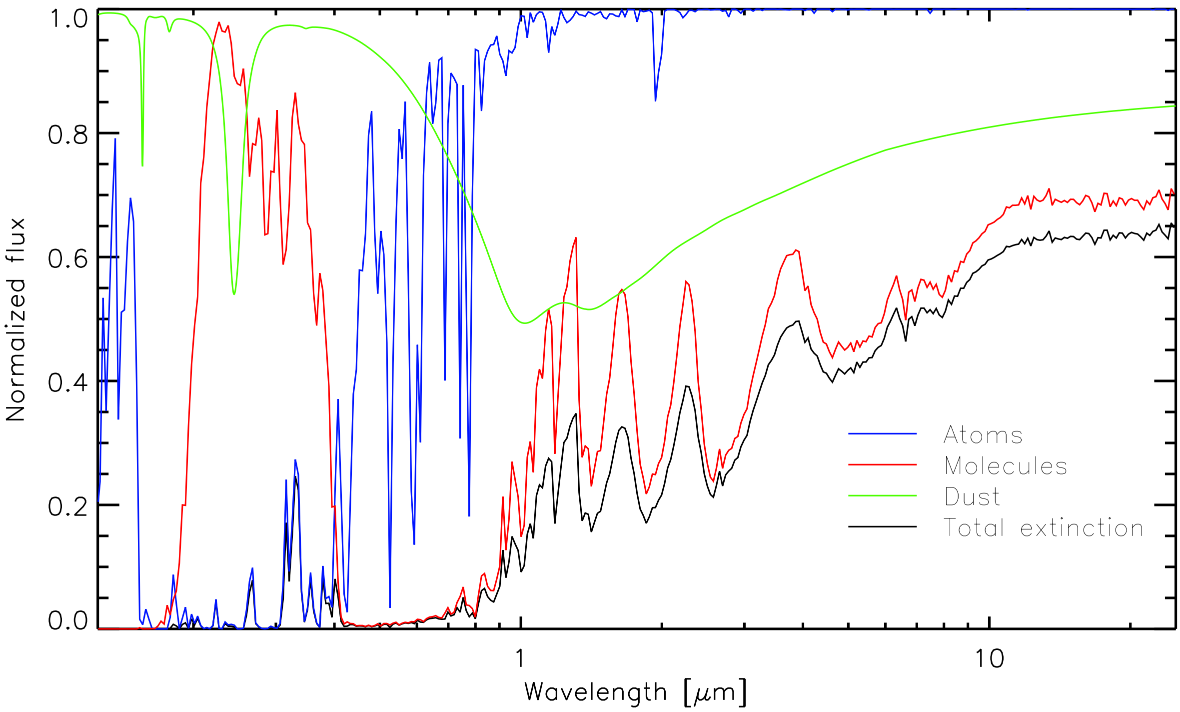

Figure 6.5.2: Dust absorption compared with absorption of atoms and molecules in a model with $T_{\rm eff} = 2000$ K, $\log(g) = 4.5$ and $[\rm M/H] = 0.0$.

6.6 Optical depth

The opacity of the atmosphere changes with wavelength and therefore so does the optical depth $\tau(\lambda)$. In Figure 6.6.1 we compare the normalized flux with the depth at which $\tau(\lambda) = 1$ in a model with $T_{\rm eff} = 2000$ K, $\log(g) = 4.5$ and $[\rm M/H] = 0.0$. This gives us an estimate of how far down into the atmosphere we can see at a specific wavelength. When the opacity is high, the flux is low and we cannot see as far into the atmosphere as when the opacity is low and the flux is high.

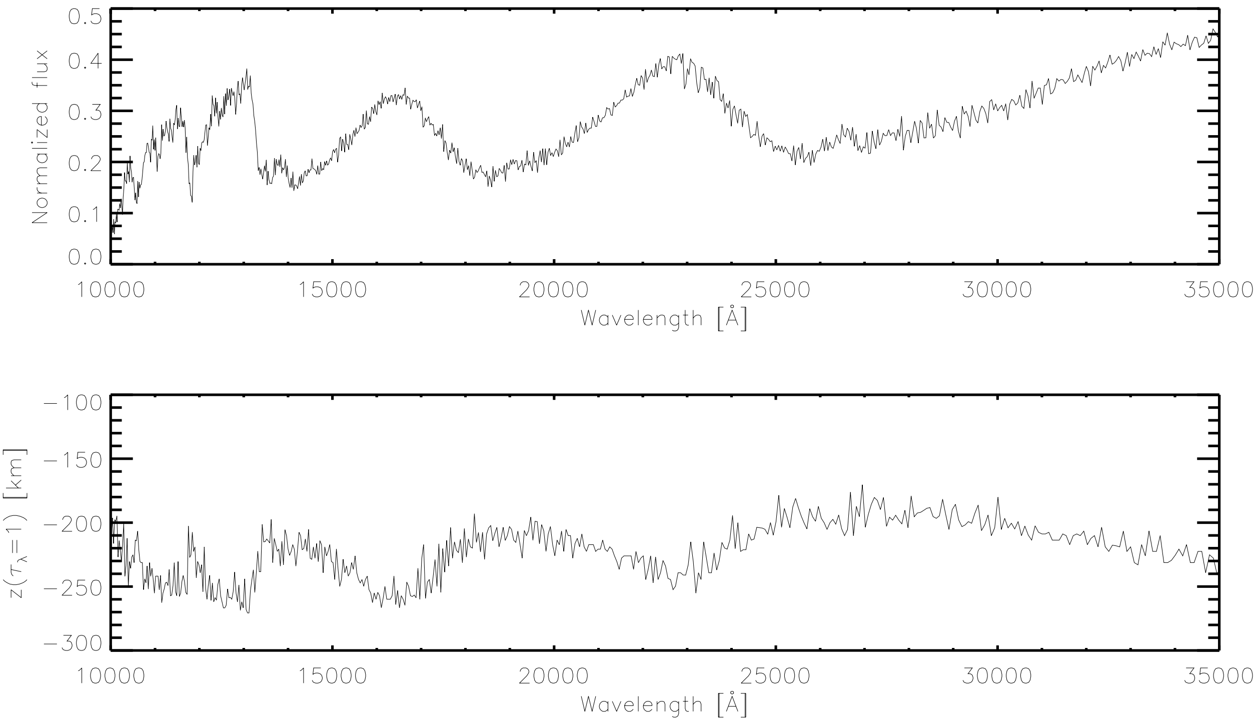

Figure 6.6.1: The synthetic spectrum and optical depth of a model with $T_{\rm eff}$ = 2000 K, $\log(g)$ = 4.5 and [M/H] = 0.0. The surface of the atmosphere is at $z = 0$, the bottom of the atmosphere is at $z = 333$ km.

7

Comparison with observations

Now that we have analyzed our grid of converged models it is time to compare them with real observed data. If our synthetic spectra matches observed spectra of cool stars and brown dwarfs well, it is certainly a mark of validation for our models and thus our understanding of the physics of such objects. In the following we will present our obtained observational data, describe the fitting process and discuss the results of the best fits. We will also take a closer look at the H_2O absorption in the infrared part of the spectrum and how it depends on the line list data we use.

7.1 Data and fitting process

M-dwarfs and brown dwarfs emit the majority of their radiation flux at near-infrared (NIR) wavelengths and so their discovery and classification is carried out by NIR spectroscopic instruments. One of these is the SpeX spectrograph mounted on the 3m NASA Infrared Telescope Facility, which provides moderate and low resolution broad-band NIR spectra (Rayner et al., 2003). SpeX spectra has proved ideal for NIR classification, characterization of atmospheric and physical properties as well as testing atmosphere models (Burgasser, 2014). We have therefore selected a few hundred SpeX spectra of M-dwarfs (159) and L-dwarfs (261) from the online SpeX Prism Spectral Libraries (maintained by Burgasser (2008)) to compare with the synthetic spectra of our models.

The SpeX spectra all have a resolution of $\Delta\nu/\nu \approx 120$ and span roughly $\lambda \approx 0.65 - 2.55$ μm. When fitting a single spectrum, we re-sampled our synthetic spectrum to match the resolution and range of the observed spectra and used a non-linear least squares curve fitting routine to scale the synthetic spectrum to fit the observed spectrum as well as possible. The best fitting synthetic spectrum for each observed spectrum was identified as the one with the lowest value of χ^2. Most of the χ^2 values were in the range $\chi^2 \approx 1.5 - 15$ with a few very large exceptions. Since our grid is very small and does not include variation in surface gravity or metallicity, we expect that a good deal of the comparisons can be improved, and we therefore only consider the best fit of a few selected spectral subclasses, where $\chi^2 < 2.5$ is low enough to assume we matched the observed data with the correct model. The selected data and their best fit models are presented in Table 7.1.1.

Object			**Best fit model**	
Name	SpT	data reference	$T_{\rm eff}$	χ^2
2MASS J12471472-0525130	M4.5	Kirkpatrick et al. (2010)	3000 K	1.41
Gliese 866AB	M5.6	Burgasser et al. (2008)	2900 K	1.60
2MASS J11150577+2520467	M6.5	Burgasser et al. (2004)	2800 K	2.02
VB 8	M7	Burgasser et al. (2008)	2800 K	1.77
2MASS J17364839+0220426	M8	Burgasser et al. (2004)	2700 K	2.05
2MASS J11240487+380854	M8.5	Burgasser et al. (2004)	2600 K	2.49
2MASSW J0320284-044636	M8/L0.5	Burgasser et al. (2008)	2500 K	2.22
2MASS J15500845+1455180	L2	Burgasser et al. (2009)	2000 K	2.33
2MASSW J0036159+182110	L3.5	Burgasser et al. (2008)	2100 K	2.09
2MASS J1104012+195921	L4	Burgasser et al. (2004)	2000 K	2.08
SDSS J154849.02+172235.4	L5	Chiu et al. (2006)	2000 K	1.91
2MASS J14162409+1348267	L6	Schmidt et al. (2010)	2300 K	2.20

Table 7.1.1: The name, spectral type and data reference for the best fitted spectra together with the parameters of the best fit model. All models have $\log(g) = 4.5$ and [M/H]=0.

7.2 Mid to late type M-dwarfs

In Figure 7.2.1 we present the comparison between 6 M-dwarf spectra and our best fit models. The earliest subtype that can be fitted by our models is M4.5. With an effective temperature of $T_{\rm eff} = 3000$ K it is dust free and generally well modeled by our synthetic spectrum. The famous TiO bands of M-dwarfs dominate the total absorption from $0.7 - 1.0$ μm, only disturbed

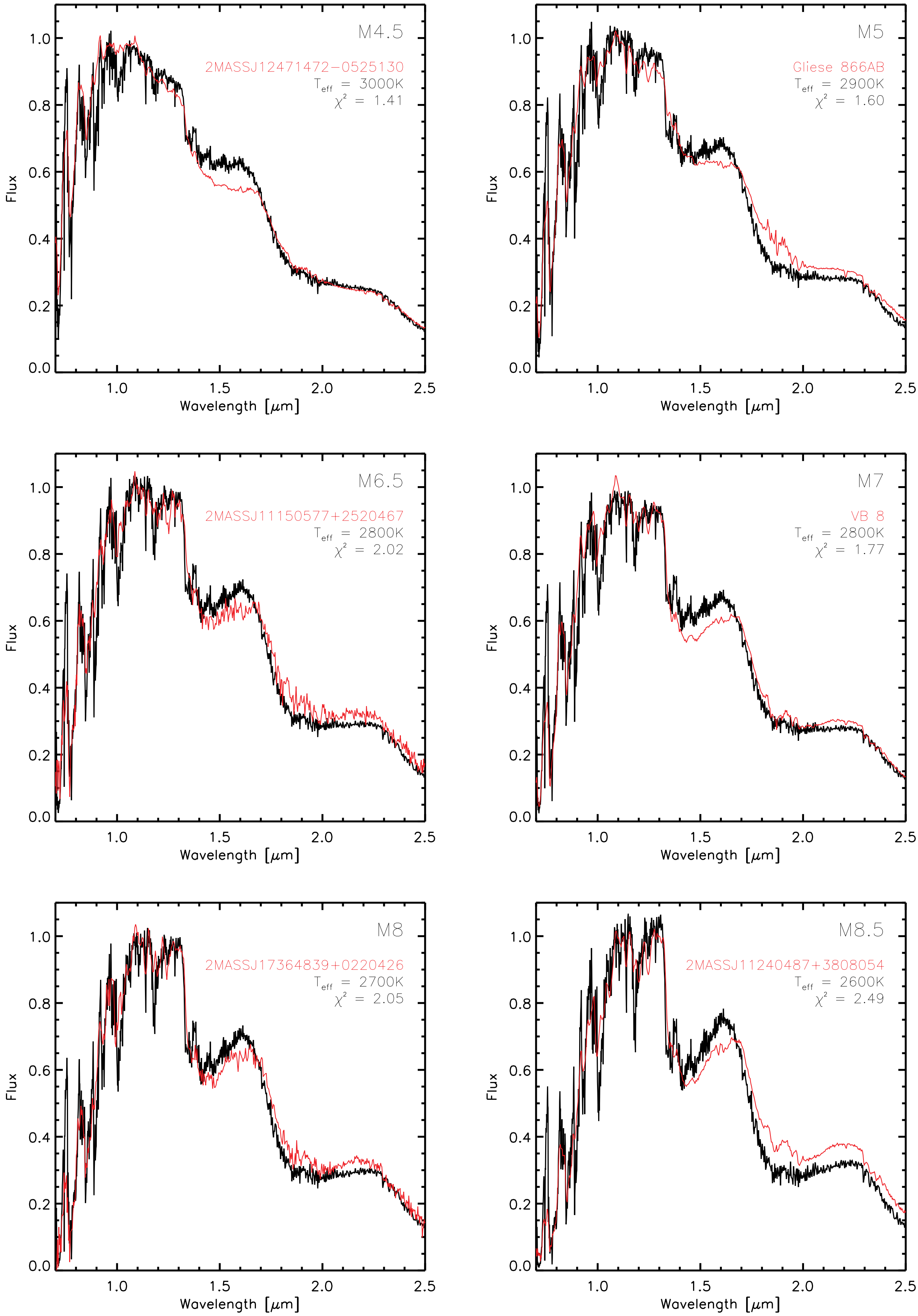

Figure 7.2.1: Comparison of synthetic (black) and observed (red) spectra of mid to late type M-dwarfs.

slightly by VO at 0.8 μm and CrH at $0.85 - 0.9$ μm. The absorption band in the model at $\lambda = 1.0$ μm is a mix of CrH, TiO and FeH in order of influence, but it is not observed in the data for this star. From $\lambda = 1.3$ μm the broad absorption bands of H_2O become the main absorption features and they stay almost undisturbed by other molecules and atoms except at $\lambda = 2.3 - 2.4$ μm where CO absorption causes the small fluctuations. The H_2O absorption is notably underestimated at $\lambda = 1.4 - 1.7$ μm and slightly overestimated at $\lambda = 1.8 - 2.3$ μm, a pattern that repeats itself for most of the other M-dwarfs and L-dwarfs. We will discuss this in detail in Section 7.4.

Dust continues to play no significant role in the spectrum of the cooler M-dwarfs. As we move towards lower effective temperatures the peak of the spectrum shifts toward longer wavelengths. The intensity of the TiO bands grows larger and are blended with the increasing absorption of VO and CrH. The absorption of CaH also increases at $\lambda = 0.7 - 0.75$ but has a very small effect on the spectrum. The absorption of CrH, VO and FeH at $\lambda = 1.0$ μm increases and is well matched by the models. Finally, the absorption of H_2O in the infrared increases significantly as well, each band growing deeper with decreasing effective temperature. With the massive gaps in the continuum due to the absorption of molecules, the coolest M-dwarfs are clearly far away from being ideal black body radiators.

7.3 Early to mid type L-dwarfs

In Figure 7.3.1 we present the comparison between 6 L-dwarf spectra and our best fit models. The latest subtype that can be fitted by our models is L6, for later subtypes χ^2 becomes too large as the effective temperature goes below $T_{\text{eff}} < 2000$ K. As we move through the sequence of decrease effective temperature, we find that the absorption from $0.7 - 1.0$ μm gradually becomes characterized by equally strong TiO and VO bands. The absorption of CaH and CrH also becomes stronger in that region, but since their bands tend to coincide with the stronger TiO and VO bands, they do not affect the spectrum that much. The absorption feature at $\lambda = 1.0$ μm is the result of a peak in CrH absorption as well as absorption from TiO and FeH. The other absorption feature at $\lambda = 1.2$ μm is caused by the superposition of the absorption peaks of CrH, H_2O, VO and CaH and FeH. In the infrared, where the absorption of dust becomes more and more significant, all the observed L-dwarf spectra have an growing bump at $\lambda = 1.9$ μ that our models can not reproduce. Since it is located right where the dust extinction peaks the explanation could be that our models produce a little to much dust. In general we see the TiO and VO absorption bands dominate in the optical, strong metal hydride bands (CrH, FeH and CaH) at $\lambda < 1.3$ μm, and the broad, dust dampened H_2O absorption bands in the infrared.

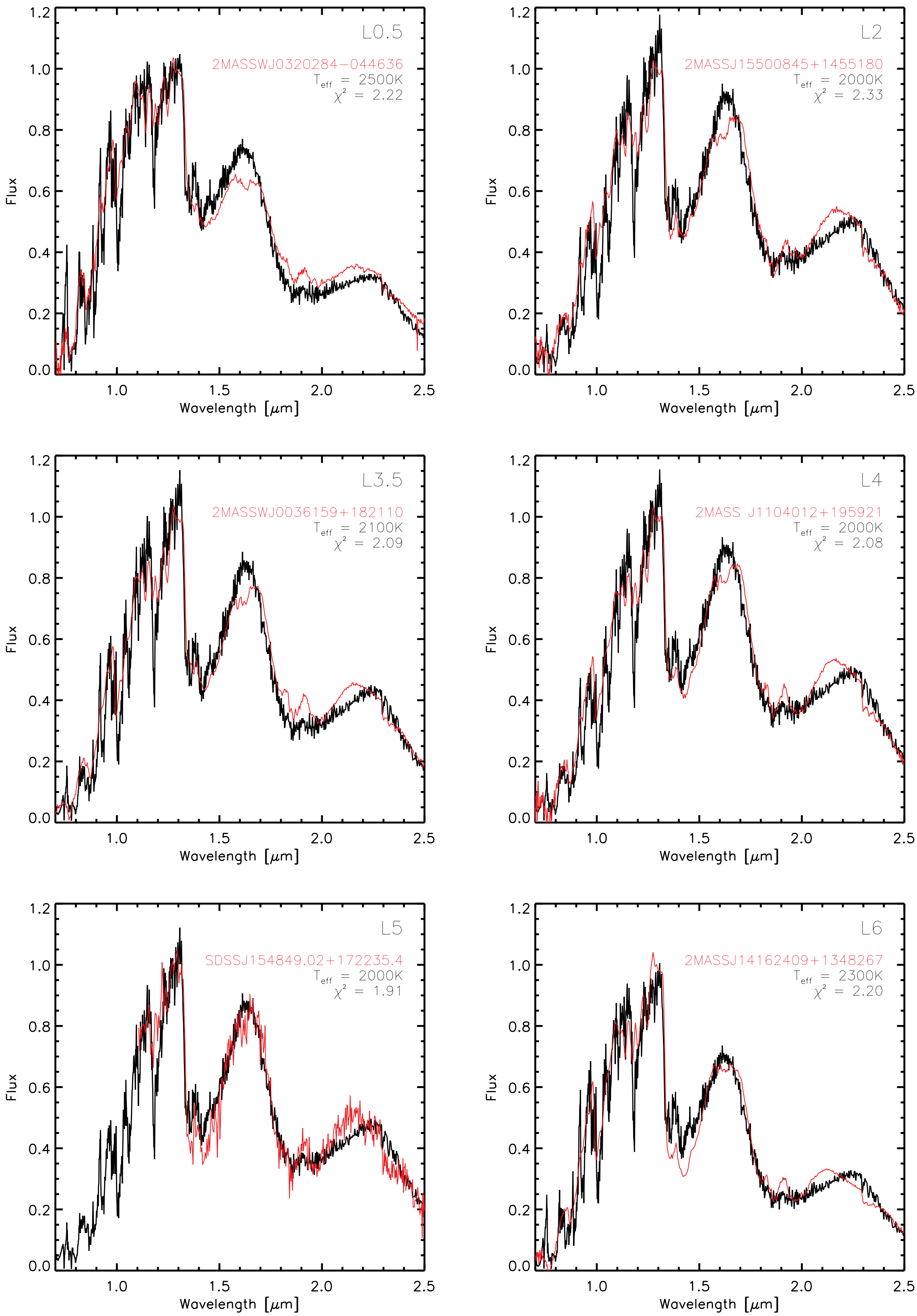

Figure 7.3.1: Comparison of synthetic (black) and observed (red) spectra of early type L-dwarfs.

7.4 H_2O absorption

In Section 7.2 we noted how the models tend to underestimate the absorption at $\lambda = 1.5 - 1.6$ μm and overestimate the absorption at $\lambda > 1.8$ μm. These regions are dominated by H_2O absorption, so the discrepancies lead our attention towards the line list from which the absorption is calculated. We use the SCAN list by Jørgensen et al. (2001), but there are other alternatives such as the line list by Partridge and Schwenke (1997) and the HITEMP line list by Rothman et al. (2010). All three line lists consider the ro-vibrational transitions of $H_2^{16}O$ and contain about 70-110 million lines. The two latter also considers additional isotopes, but since the main isotope has a relative abundance of 99.95% this should not make much of a difference.

We have computed three dust free models with $T_{\rm reff} = 2900$K, $\log(g) = 4.5$ and [M/H] = 0.0, each computed using a different H_2O line list. In Figure 7.4.1 (top) we compare their synthetic spectra. SCAN and HITEMP compare nicely in the first H_2O band centered around $\lambda = 1.5$, but at longer wavelengths the SCAN line list yields a stronger absorption. The absorption based on the line list by Partridge & Scwhenke persistently underestimates the H_2O absorption compared to both SCAN and HITEMP. All three line lists are based on ab initio calculations, but the details in the different approaches are quite strongly reflected in the computed spectra.

To identify the most suitable line list for our models, we compare each of the different model spectra with the observed spectrum of an M6-dwarf in Figure 7.4.1. Again, we see how the spectrum based on the line list from SCAN generally fits the observed spectrum nicely, yet still underestimates the absorption band at $\lambda = 1.5$ μm and slightly overestimates the absorption at $\lambda = 1.8$ μm. The HITEMP spectrum, it seems, has a choice between fitting the observed spectrum in the inner part or in the outer part.

Rothman et al. (2010) compared synthetic spectra based on the H_2O line lists from HITEMP and SCAN with observations and found that the line list from HITEMP produced the best fit. However, they only focused on the infrared part of the spectrum and did not include the optical part like we do. If we only consider the outer part ($\lambda > 1.4$ μm), the HITEMP spectrum does seem to produce a better fit than the SCAN, but since we are working with a much larger wavelength range, we still favor the SCAN line list over the HITEMP line list. As previously noted, the Patridge & Schwenke line list greatly underestimates the H_2O absorption, leading to the worst fit of the three.

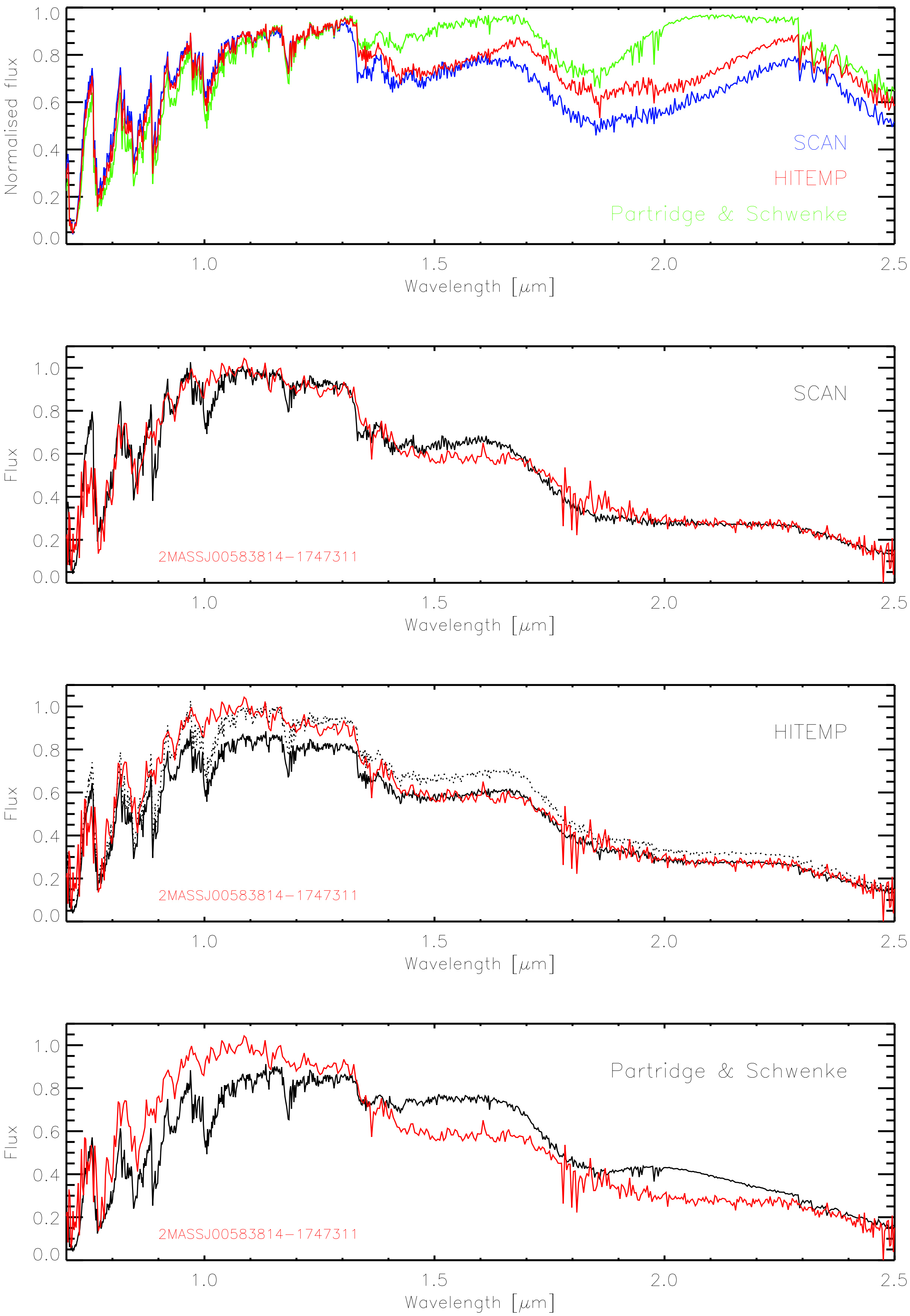

Figure 7.4.1: Comparison of observational spectra with synthetic spectra based on the H_2O line lists from SCAN by Jørgensen et al. (2001), HITEMP by Rothman et al. (2010) and Partridge and Schwenke (1997).

8

Exoplanets

The search for exoplanets is a young and exciting field and it is growing almost explosively. The first exoplanet orbiting a Sun-like star was discovered just 20 years ago and today we know of more than 2000 confirmed worlds beyond our Solar System. Our detection methods are constantly evolving and improving, and new discoveries and milestones are announced with increasing frequency. The Milky Way is teeming with an almost unimaginable diversity of exoplanets that still manages to surprise us, and by now we are past the point where just the detection of a new planet is enough. Now we are exploring the physical properties of the exoplanets in our galaxy, probing their composition, atmospheres and the possibility of them hosting life.

In this chapter I will discuss some of the most successful methods of detecting exoplanets. I will also describe some of the observation projects I have been a part of and show how my models with time will be able to contribute to the characterization of exoplanet atmospheres.

8.1 History of discovery

Scientists and philosophers alike have speculated about the existence of other worlds beyond our own for thousands of years, but the research field itself is quite young. In 1952, the astronomer Otto Struve proposed that Doppler spectroscopy and differential temporal photometry could be used to detect giant planets in close orbits (Struve, 1952), but the instruments of the time were not sensitive enough for such feats, and almost 40 years had to pass before the first exoplanet was discovered.

In 1989 David Latham and his colleagues discovered a low-mass object orbiting a main sequence star using the radial velocity method first suggested by Otto Struve (Latham et al., 1989). They carefully suggested that "the companion is probably a brown dwarf, and may even be a giant planet". Its existence was confirmed a few years later by Cochran et al. (1991) but the discovery received very little attention, most likely because only the lower mass limit of the object could be determined. Had it been discovered today, it would have been announced as an exoplanet. In 1992 radio astronomers Aleksander Wolszczan and Dale Frail discovered two exoplanets orbiting a pulsar, a rapidly rotating neutron star, using a method known as pulsar timing (Wolszczan and Frail, 1992). A few years later Michel Mayor and Didier Queloz discovered an exoplanet orbiting a Sun-like star (Mayor and Queloz, 1995). These discoveries marked the beginning of the modern era of exoplanet research and an avalanche of new discoveries that changed the way we view our galaxy were soon to follow.

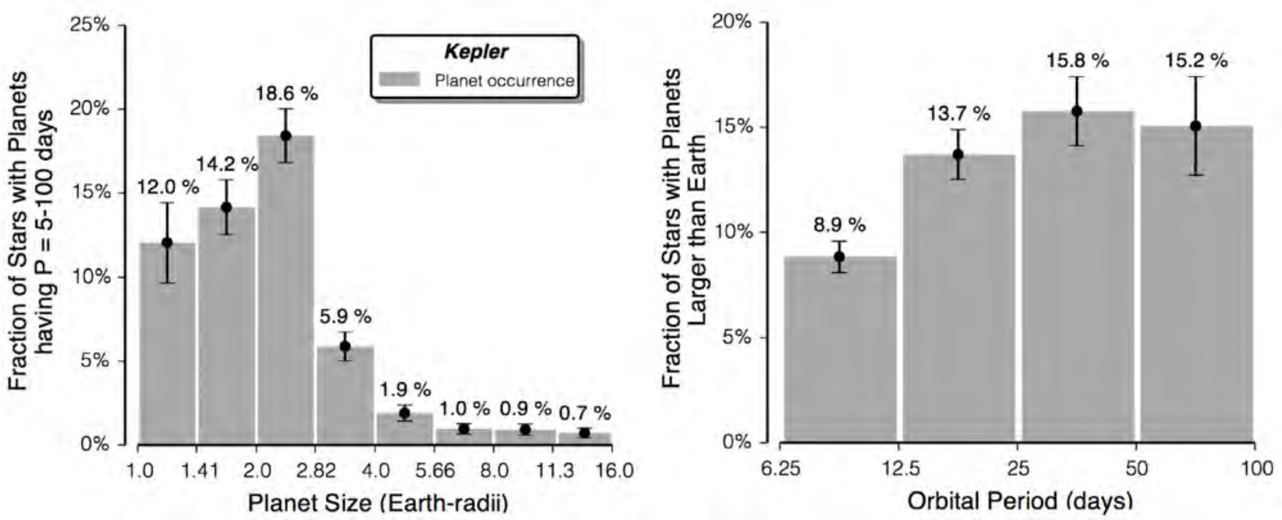

Figure 8.1.1: Left: The size distribution of planets around Sun-like stars. Only planets with orbit periods of 5−100 days (0.05−0.42 AU) are included. The two lowest bins show that 26% of Sun-like stars have planets of $1{-}2R_\oplus$ orbiting within ~0.4 AU. Right: The fraction of Sun-like stars having planets larger than the Earth. The occurrence of planets appear to remain constant for longer orbital periods out to at least 100 days. Source: Petigura et al. (2013).

The exoplanet discovered in 1995 was a giant gas planet that orbited very close to its parent star, a so-called hot Jupiter. In the beginning, most of the discovered exoplanets were of this type simply because they were the easiest to find. Today we know that the more than 2000 known exoplanets in our galaxy come in a great variety of sizes, orbital distances and compositions as well as in great number; on average every star is host to 1.6 planets with a mass larger than $5M_\oplus$ (Cassan et al., 2012), and even more are likely to exist with masses below

$5M_\oplus$ (Howard et al., 2012). As it turns out, small planets are incredibly common. On top of that, observations have revealed that about 1 in 5 Sun-like stars have an Earth-sized planet in the habitable zone (Petigura et al., 2013). It is amazing how far we have come in just two decades, and it certainly seems like the discovery of Earth's twin is just around the corner.

8.2 Detection methods

Planets are extremely faint compared to stars. At visible wavelengths the brightness of a planet is usually less than a millionth of a star. It is very difficult to detect such a faint light source next to a star as it will be almost completely washed out. Consequently, very few exoplanets have been directly imaged and most exoplanets are discovered using indirect methods of observation. The most successful of these are the radial velocity method, the transit method and the microlensing method. The three methods complement each other very well. While the radial velocity and the transit method are most sensitive to planets with large masses in close orbits, the microlensing method is most sensitive to planets in wider orbits. In this section I will describe the theory behind each of these methods as well as discuss their involvement in some of the current and future exoplanet search missions.

8.2.1 The radial velocity method

When a planet orbits a star, the star itself will also move in its own small orbit around their common center of mass, and their movements can be treated as a gravitational two-body problem. As the star moves around its orbit, its light will appear blue or red-shifted as it moves towards and away from an observer. This is known as the Doppler effect, and the relation between the emitted wavelength λ_0, the observed wavelength λ and the radial velocity of the star V_r is given by

$$\lambda = \lambda_0 \frac{1 + V_r/c}{\sqrt{1 - \frac{V_r^2}{c^2}}}, \tag{8.2.1}$$

where c is the speed of light in vacuum (Einstein, 1905). With spectroscopic observations of the star we can measure the shift in the star's spectral lines and derive the corresponding radial velocity of the star. Once we known the radial velocities of a star during different phases of its orbit, we can fit a model to the data to determine the period and eccentricity of the orbit as well as the minimum mass of the planet. How close this minimum mass is to the true mass depends on the inclination of the system. If the planet is also a transiting planet, we can determine the planet's true mass.

The relation between the radial velocity of a star and its position in its orbit is given by

$$V_r(t) = K \cdot (\cos(\omega + f(t)) + e\cos(\omega)) + V_r^0, \tag{8.2.2}$$

where K is the absolute value of the maximum radial velocity, e is the eccentricity of the orbit, ω is the angle between the periastron and the line-of-sight toward the observer, and $f(t)$ is the periastron angular distance (Lovis and Fischer, 2010). For a circular orbit the time derivative of $f(t)$ is constant, but for an eccentric orbit it will vary with time as the star moves faster when the planet is close and slower when the planet is far away. The maximum radial velocity

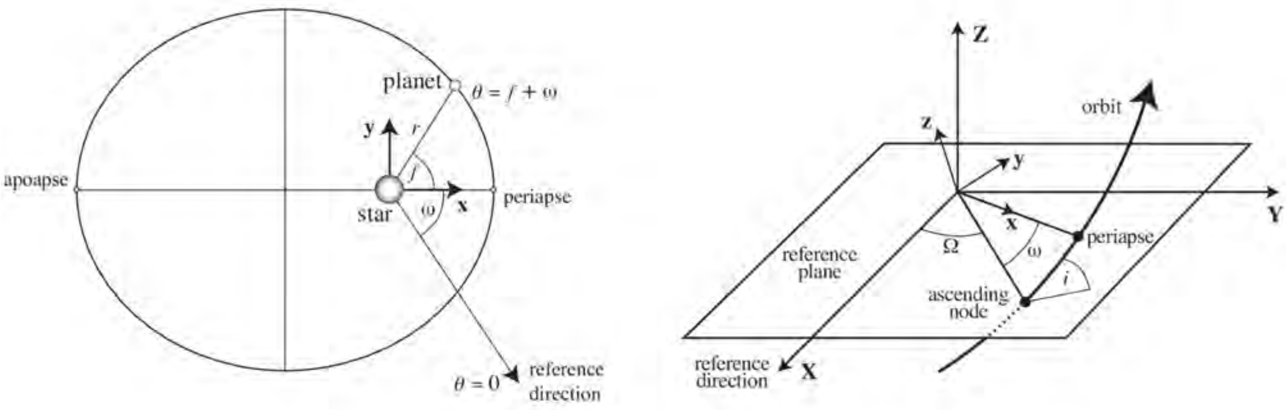

Figure 8.2.1: Left: The geometry of a star and a planet orbiting their common center of mass. Right: The relationship between the inclination of the system and the reference direction. Source: Murray and Correia (2010).

depends on the mass of the star M_*, the mass of the planet M_p, and the period P, eccentricity e, and inclination i of the orbit:

$$K = \frac{28.43 \text{ ms}^{-1}}{\sqrt{1-e^2}} \frac{M_p \sin i}{M_J} \left(\frac{M_* + M_p}{M_\odot}\right)^{-2/3} \left(\frac{P}{1 \text{ yr}}\right)^{-1/3}. \tag{8.2.3}$$

Assuming that $M_* + M_p \approx M_*$, we can write the minimum mass of the planet in units of Jupiter masses as:

$$M_p \sin i = \frac{K}{28.43 \text{ ms}^{-1}} \sqrt{1-e^2} \left(\frac{M_*}{M_\odot}\right)^{2/3} \left(\frac{P}{1 \text{ yr}}\right)^{1/3}. \tag{8.2.4}$$

If we know the values of K, P and e from radial velocity observations and the value of M_* from spectral classification of the star, we can then determine the minimum mass of the planet. Note that if we do not known the inclination i of the system, we cannot determine the true mass of the planet. Exoplanets presumably have randomly oriented orbits, and 87% of observed exoplanets will therefore have a true mass between 1 and 2 times $M_p \sin i$. On average, the true mass is 1.27 times larger than the minimum mass, so statistically the true mass will most often be close to the measured value of the minimum mass. Still, from radial velocity observations of the star alone, we will never be able to exclude the possibility that the system has a high inclination and harbors a brown dwarf instead of a planet (Jørgensen, 2015).

The radial velocity method has been used to discover more than 500 exoplanets and among them the very first exoplanet found orbiting a Sun-like star (Mayor and Queloz, 1995). Up until a few years ago it was by far the most successful method in terms of the number of detected exoplanets, accounting for the discovery of about 70% of the known exoplanets by the end of 2010 (NASA Exoplanet Archive). The radial velocity method is most sensitive to giant planets in small orbits, as they give rise to the largest variations in the stellar radial velocity over the shortest length of time.

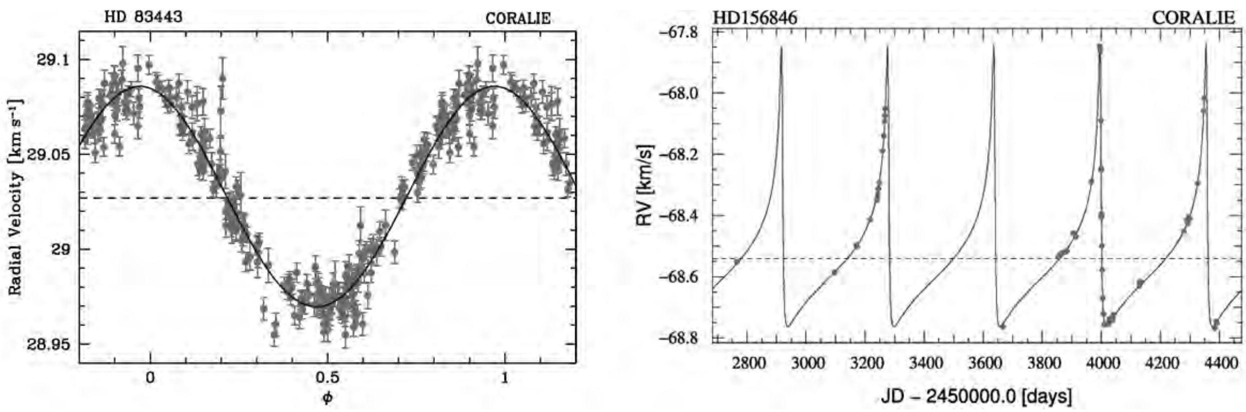

Figure 8.2.2: Left: Phase-folded radial velocity measurements of HD 83443, a hot Jupiter orbiting a K type main sequence star at a distance of 0.039 AU. The orbit is very close to being circular. Source: Mayor et al. (2004). Right: Radial velocity measurements of HD 156846, a Super-Jupiter orbiting a G type main sequence star at a distance of 0.99 AU. The orbit has a very high eccentricity of $e = 0.847$. Source: Tamuz et al. (2008).

When Otto Struve proposed radial velocity measurements as a method for detecting exoplanets back in 1952, the accuracy of the spectrographs were typically of a few hundred meters per second. In comparison, the gravitational pull from Earth or Jupiter makes the Sun orbit their common center of mass with a velocity of about 0.1 m/s or 12.5 m/s, respectively. Even for the hot Jupiter discovered in 1995, the maximum radial velocity of the star is little more than 60 m/s. Evidently, the accuracy of the spectrographs of the 50s was too poor for reliable planet detections. Today, the best spectrographs can reach a precision of less than 1 m/s (Mayor et al., 2003; Latham and HARPS-N Collaboration, 2013), and setting $K = 1$ m/s, $M_* = M_\odot$, and $P =$ 1 yr in Equation 8.2.4 we see that this corresponds to a planet of about 11 Earth masses orbiting a Sun-like star at a distance of 1 AU. In 2016, the highly anticipated `ESPRESSO` spectrograph will see first light, and it will in principle be able to achieve precisions of 10 cm/s (Pepe et al., 2010), making it capable of detecting an Earth-size planet in an Earth-like orbit around a Sun-like star.

8.2.2 The transit method

When a planet passes in front of its host star as seen from Earth it will block a small part of the star light. This is called a planetary transit, and we can use photometric observations to measure the resulting dimming of the brightness of the star. Sometimes we can even measure the tiny dimming of the combined light from the star and the planet as the planet half an orbit later moves behind the star, a phenomenon known as an occultation or secondary transit.

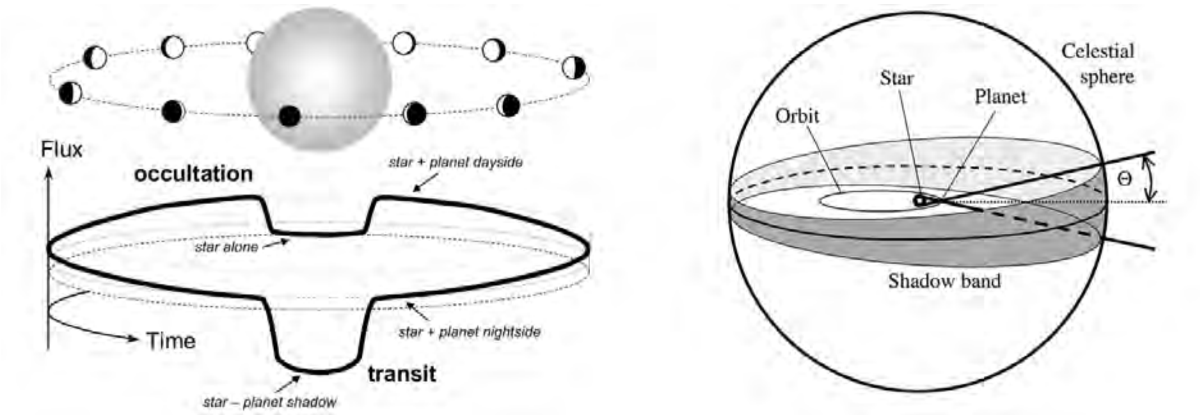

Figure 8.2.3: Left: Illustration of transit and occultation. The upper panel shows the geometry, and the lower panel shows the total flux of the planet and star during one orbit (thick) and the stellar flux alone (dotted). Right: Transits are visible by observers within the shadow of the planet, a cone with opening angle Θ with $\sin\Theta = (R_* + R_p)/r$, where r is the distance between the planet and the star. Source: Winn (2010).

The combined flux of a star and its transiting planet is plotted in the left panel of Figure 8.2.3. From an observer's point of view, the flux will drop during a transit, rise as the planet's day side comes into view, and then drop again when the planet is occulted by the star. The observed flux can be described as

$$F(t) = F_* + F_p - \begin{cases} \left(\frac{R_p}{R_*}\right)^2 \alpha_{\text{tra}}(t) F_* & \text{transits} \\ 0 & \text{outside eclipses} \\ \alpha_{\text{occ}}(t) F_p & \text{occultations} \end{cases} \tag{8.2.5}$$

where F_* and R_* are the flux and radius of the star, and F_p and R_p are the flux and radius of the planet (Winn, 2010). The functions α_{tra} and α_{occ} are time dependent and describe the overlap area between the stellar and planetary disks, taking into account ingress and egress events as well as the impact parameter (see e.g. Mandel and Agol (2002)). In general, both the stellar flux and the planetary flux are not constants neither in time nor in space. The changing illuminated fraction of the planetary disk causes F_p to vary over time, while flares, the rotation of star spots and plages, and the rotation of the tidal bulge raised by the planet will all cause F_* to vary over time. Furthermore, limb darkening will cause F_* to be brighter in the middle of the stellar disk and fainter at the edge, so the details of a transit light curve can thus also reveal information about the structure of the star, such as the $T - p_{\text{gas}}$-structure that causes the inferred limb darkening.

We can determine R_p/R_* by fitting our model for $F(t)$ to a transit light curve. If we also know the value of R_* from spectral classification of the star, we can calculate the radius of the planet. Suppose we also have radial velocity observations of the same planet system, then we will be able to determine the true mass of the planet (since $i \approx 90°$) and thereby also the mean density of the planet. The mean density of a planet offers us insight into its interior composition, and although there is an inherent degeneracy arising from the fact that planets of different compositions can have identical masses and radii, this information allows us to map the diversity and distribution of exoplanets and even put constraints on models of planetary structure and formation theories.

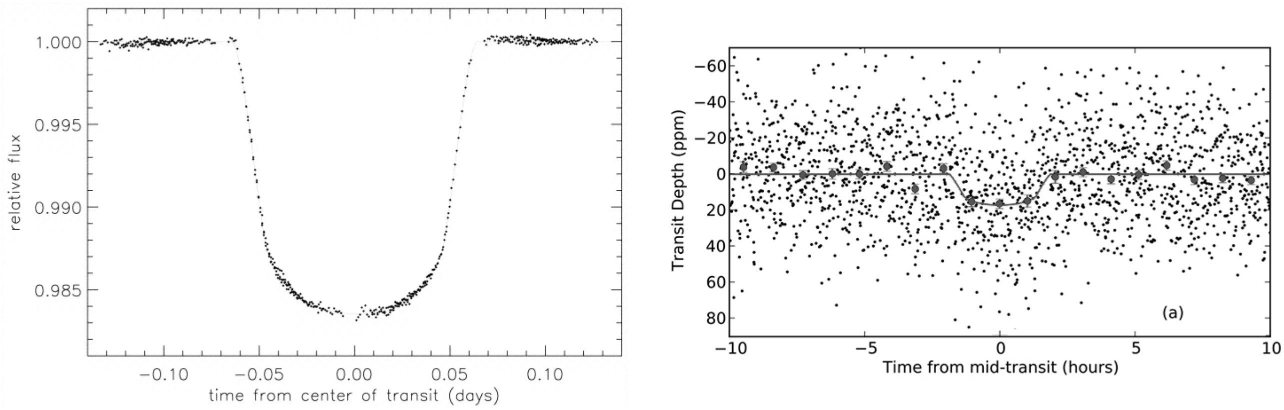

Figure 8.2.4: Left: Phased light curve for transits of HD 209458b obtained with the Hubble Space Telescope. This was the first exoplanet to be observed transiting its parent star. It has a radius of $1.35R_J$ and orbits a G type main sequence star, and its transit signal is therefore relatively strong. Source: Brown et al. (2001). Phased light curve for transits of Kepler-37b obtained with Kepler. The planet is only slightly larger than the Moon, making it one of the smallest known exoplanets. It orbits a G type main sequence star, and its weak transit signal is pushing at the limits of Kepler. Source: Barclay et al. (2013).

To a first approximation we can express the relative dimming at mid-transit as

$$\delta = \frac{F_* - F(t_0)}{F_*} \approx \left(\frac{R_p}{R_*}\right)^2. \tag{8.2.6}$$

From this equation we estimate that a hot Jupiter transiting a Sun-sized star will cause a dimming of the star's light by about $\delta = 0.01$ or 10 milimag. The first ever observed exoplanet transit was that of the hot Jupiter HD 209458b (Charbonneau et al., 2000), and the observations were obtained with the 0.99 cm STARE telescope. This telescope is designed to search for planetary transits in large samples of stars and has a precision of about 2 milimag (Brown and Charbonneau, 2000), which was more than enough to detect the 16 milimag dimming caused by the transit of HD 209458b. However, the Earth - being both smaller and farther away from the Sun - will cause a dimming of only 84 micromag during a transit, its signal about 1/200 weaker than the signal of a hot Jupiter and completely impossible for wide field telescopes like STARE to observe. Even the largest ground-based telescopes can only achieve precisions of a few hundred micromag as they are limited by the effect the atmosphere has on the starlight as it passes through. Space-based telescopes do not have this problem and can perform extremely precise photometry, limited only by the size of the telescope and the quality of the detector. For example, the 2.4 m Hubble Space Telescope has a precision of about 100 micromag. The even smaller 1 m Kepler space telescope has an impressive precision of 20 micromag, which is exactly the kind of precision needed to detect Earth-sized planets orbiting Sun-sized stars.

Until now, we have been assuming that the shadow of the planet has a well defined edge, but if the planet has an atmosphere it will be more or less blurry. During a transit, a small fraction of the starlight will be filtered through the upper atmosphere of the planet, being only partially absorbed. Since the absorption is wavelength dependent, the atmosphere will be more opaque at wavelengths of strong atomic or molecular absorption, which causes the planet to appear larger. We can use this phenomenon to our advantage. By observing a transit at multiple wavelengths and then fitting each light curve with a limb-darkened model, we can create a so-called transmission spectrum of the planet's upper atmosphere, allowing us to explore the nature of its composition.

A model for the transmission spectrum must describe the radiative transfer of the incident starlight along a grazing path through the planet's atmosphere, and the calculations can be rather complicated. To estimate how much the dimming of the star varies with wavelength, we consider the scale height of the atmosphere of the transiting planet given by

$$H = \frac{k_B T}{\mu m_u g}. \tag{8.2.7}$$

For a strong absorption line the effective size of the planet can grow by a few H. If we define R_p as the radius within which the planet is optically thick at all wavelengths, then the extra wavelength dependent absorption from the optically thinner part of the atmosphere will cause the transit depth to increase by

$$\Delta\delta = \frac{\pi(R_p + N_H H)^2}{\pi R_*^2} - \frac{\pi R_p^2}{\pi R_*^2} \approx 2N_H \delta \frac{H}{R_p}, \tag{8.2.8}$$

where N_H is the number of scale heights (Winn, 2010). The increase is largest for planets with large H, i.e. with low surface gravity, low mean molecular mass, and high temperature. For a hot Jupiter orbiting a Sun-like star ($\delta \approx 0.01$, $T \approx 1300$ K, $g \approx 25$ m/s^2, $\mu_m = 2$ amu) the signal is $\Delta\delta \sim 10^{-4}$, just enough to be observable with our best telescopes. For an Earth-like planet orbiting a Sun-like star ($\delta = 0.0001$, $T \approx 273$ K, $g \approx 25$ m/s^2, $\mu_m = 28$ amu) the signal is only $\Delta\delta \sim 10^{-6}$, so we will have to wait for the next generation of telescopes before we can examine such atmospheres.

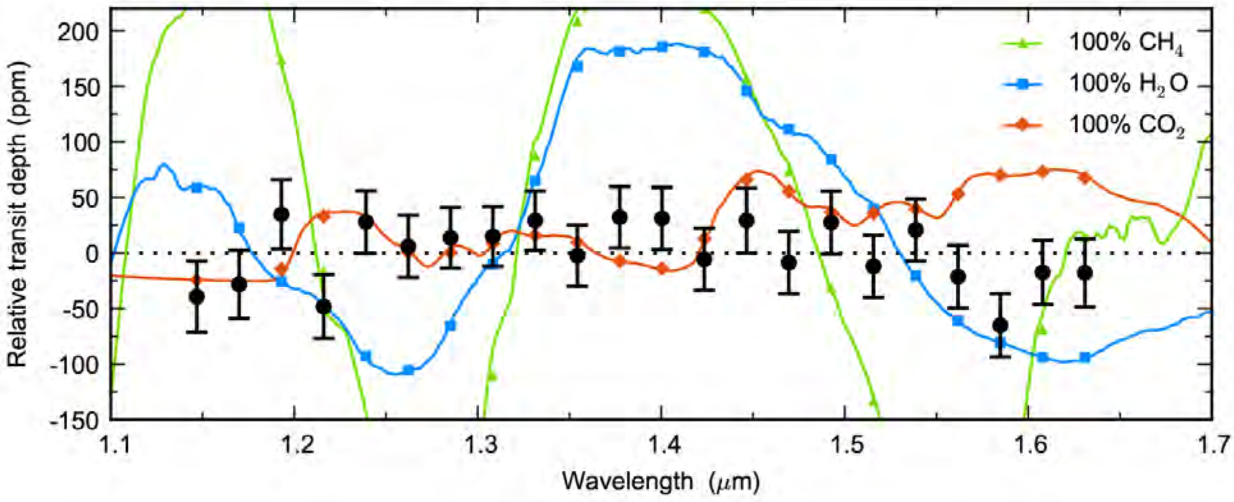

Figure 8.2.5: The transmission spectrum (black dots) of GJ 1214b, a super-Earth in a close orbit around an M dwarf. 15 transits were observed with the Hubble Space Telescope, making it one of the longest exposure spectra ever taken with the telescope. The blue, green and brown lines represent models of what the measurements would have looked like if the atmosphere of the planet was made of 100% methane, water or carbondioxide, respectively. From the flatness of the observed spectrum it was concluded that the the upper part of the atmosphere was covered in a thick layer of clouds. Source: Kreidberg et al. (2014).

Transits can only be seen if the observer is lucky enough to view the planet's orbit nearly edge-on. As the planet moves in front of the star, its shadow describes a cone that sweeps out a band on the celestial sphere (see Figure 8.2.3 (right)), and all observers within this shadow will be able to see the transit. Assuming that exoplanets have randomly oriented orbits, the probability of being able to detect a transit can be calculated as the shadowed fraction of the line of longitude and is given by

$$P_{\text{tra}}(\omega) = \left(\frac{R_* + R_p}{a}\right)\left(\frac{1 + e\sin\omega}{1 - e^2}\right), \tag{8.2.9}$$

where a and ω are the semimajor axis and orientation of the orbital ellipse, respectively (Winn, 2010). We can then estimate the expected number of transiting planets to be found in a survey by averaging equation 8.2.9 over ω, giving

$$P_{\text{tra}} = \left(\frac{R_* + R_p}{a}\right)\left(\frac{1}{1 - e^2}\right). \tag{8.2.10}$$

For $R_p \ll R_*$ and $e = 0$ this reduces to

$$P_{\text{tra}} = \frac{R_*}{a} \approx 0.005\left(\frac{R_*}{R_\odot}\right)\left(\frac{a}{1\ \text{AU}}\right)^{-1}. \tag{8.2.11}$$

From the above equations we can see that the transit method is biased towards finding planets in small orbits, as they have the largest probability of detection. The probability that a planet orbiting a Sun-like star at a distance of 1 AU transits the star from our point of view is only about 0.5%, while the probability for a planet orbiting the same star at 0.05 AU is about 10%. Of course, many other factors affect the possibility of detection in practice, the most important being the precision of the measurements.

The transit method has been used to discover more than 1,200 exoplanets and it is currently the most effective and sensitive method we have in the sense that is has both discovered the majority as well as the smallest of all known exoplanets. Several missions, both ground-based and space-based, are currently searching for new exoplanets with the transit method. The most famous of these is the NASA Kepler mission, a 1 m space telescope that was pointed at a fixed part of the sky, monitoring the light of about 160,000 stars. It was launched in 2009 with the purpose of searching for the transits of Earth-sized and smaller planets in the habitable zone of other stars. The mission has been very successful as it has so far discovered more than 1,000 confirmed and 4,000 candidate exoplanets, among them almost all the confirmed sub-Earth mass exoplanets of which a handful is within or close to the habitable zone (Jørgensen, 2015).

The Kepler mission has greatly advanced the field of exoplanet research, revealing to us that our galaxy is simply teeming with planets. Today, the announcement of the discovery of a new exoplanet is not the sensation it used to be. We are preparing for the next chapter in exoplanet research, the characterization of exoplanet compositions and atmospheres, and the next generation missions are just a few years ahead. Kepler's successor, the NASA TESS mission, will launch in 2017. It will search for the transit of Earth-like planets around nearby, bright stars, making detailed follow-up observations possible. These will include observations by the James Webb space telescope, the Hubble's successor which will launch in 2018, and the E-ELT ground-based telescope which is currently under construction and will see first light in 2024. Both of these will be able to probe the atmospheres of Earth-sized planets, possibly revealing whether or not they are influenced by biological activities (Jørgensen, 2015).

8.2.3 The microlensing method

The microlensing method is based on Einstein's theory of general relativity. Gravitational microlensing happens when a foreground star passes very close to our line of sight to a more distant background star. The gravitational field of the foreground star will then act like a lens and distort and magnify the light of the background star. This is known as a microlensing event. If the lensing star is host to a planet, then the planet can also act like a lens and further perturb the light from the source star, creating a unique signature that allow us to observe and characterize it.

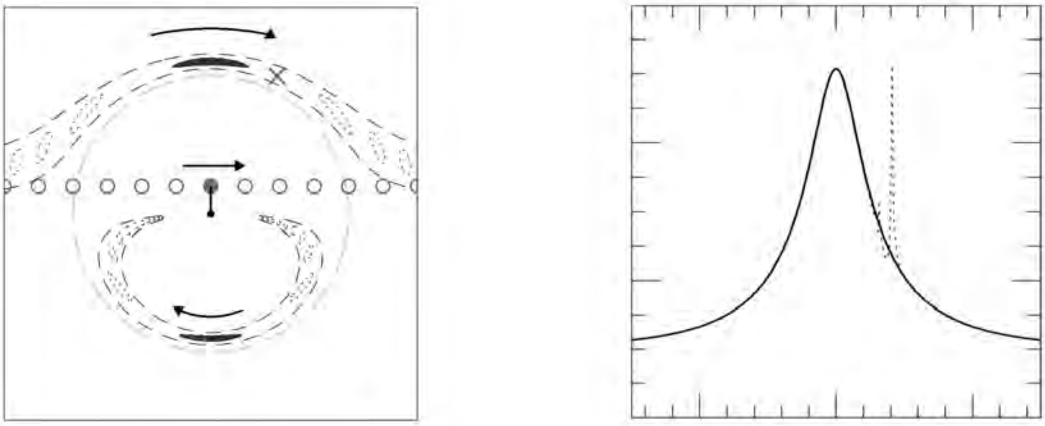

Figure 8.2.6: Left: The perturbed light (dotted ovals) for several different positions of the background star (solid circles), the foreground star (dot) and the Einstein ring (long dashed circle). If the foreground star has a planet within the short-dashed lines, then the planet will also perturb the light from the background star. Right: The magnification of the background star as a function of time for a foreground star (solid line) and a planet (dotted line) located at the position marked X in the left panel. Source: Gaudi (2010).

The left panel in Figure 8.2.7 illustrates the basic geometry of microlensing. According to general relativity, light from the source star at distance D_s from the observer O is deflected by an angle $\hat{\alpha}_d$ by the lens star at distance D_l. Assuming the lens star is a point mass, we have

$$\hat{\alpha}_d = \frac{4GM_l}{c^2 D_l \theta}, \tag{8.2.12}$$

where M_l is the mass of the lens star, θ is the angle between the lens star and the apparent position of the source star, and we have assumed that θ is small enough for $\tan\theta \approx \theta$ to hold. The relation between θ and the angle β between the lens star and the true position of the source star is

$$\begin{aligned}
\beta &= \theta - \alpha_d \\
&= \theta - \hat{\alpha}_d \frac{D_s - D_l}{D_s} \\
&= \theta - \frac{4GM_l}{c^2\theta} \frac{D_s - D_l}{D_s D_l},
\end{aligned} \tag{8.2.13}$$

where we have used that $\hat{\alpha}_d(D_s - D_l) = \alpha_d D_s$ under the small-angle approximation (Gaudi, 2010). This is known as the lens equation and by solving it for θ we can find the positions of the two images of the source star:

$$\theta_\pm = \frac{\beta}{2} \pm \sqrt{\left(\frac{\beta}{2}\right)^2 + \frac{4GM_l}{c^2} \frac{D_s - D_l}{D_s D_l}}. \tag{8.2.14}$$

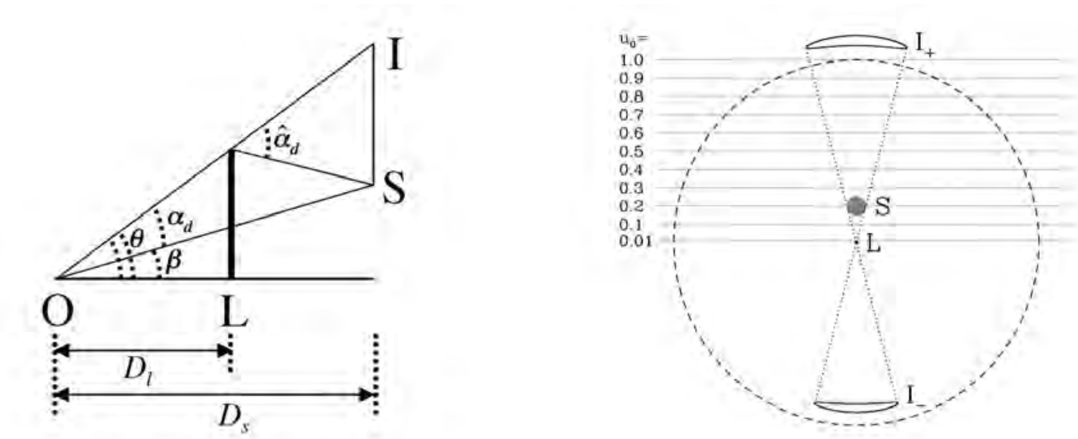

Figure 8.2.7: Left: The lens (L) at distance D_l from the observer (O) deflects light from the source (S) at distance D_s by the angle $\hat{\alpha}_d$. Right: All angles are normalized by the angular Einstein ring radius θ_E, shown as a dashed circle. The angle between the source (S) and the lens (L) is $u = 0.2$. The two images of the source star have a surface brightness of I_+ and I_-. Source: Gaudi (2010).

If the lens star is perfectly aligned with the source star ($\beta = 0$), it bends the light from the source star into a so-called Einstein ring with a radius of

$$\theta_E = \sqrt{\frac{4GM_l}{c^2}\frac{D_s - D_l}{D_s D_l}}. \tag{8.2.15}$$

Normalizing β and θ by θ_E, we define $u = \beta/\theta_E$ and $y = \theta/\theta_E$, and the equation for the position of the two images then becomes

$$y_\pm = \frac{u}{2} \pm \sqrt{\left(\frac{u}{2}\right)^2 + 1}. \tag{8.2.16}$$

Since $\sqrt{(u/2)^2 + 1} \geq u/2$, the positive image will always lie on or outside the Einstein ring. From a similar argument, the negative image will always lie on or inside the Einstein ring. Furthermore, the separation angle between the two images is always larger than or equal to $2\theta_E$. This is illustrated in the left panel in Figure 8.2.6 and the right panel in Figure 8.2.7. At the time of closest alignment, the angle between the two images will be close to $2\theta_E$ for $u < 1$, and converge to precisely $2\theta_E$ if the source star passes directly behind the lens star. For typical lens masses of $0.1-1M_\odot$ and lens and source distances $1-10$ kpc, the radius of the Einstein ring is in the order of $0''.001$ or less. A typical ground-based observation can obtain resolutions of about $1''$, and the images of a microlensing event can therefore not be resolved. However, one of the central results of general relativity is that the surface brightness of the source star is unchanged, while the area of the image is magnified. The magnification is therefore just the area of the distorted images relative to the unmagnified area of the source star image.

Assuming that the source star is a point mass, we can express the magnification of each of its images is

$$A_\pm = \frac{1}{2}\left(\frac{u^2+2}{u\sqrt{u^2+4}\pm 1}\right), \tag{8.2.17}$$

and the total magnification as

$$A = A_+ + A_- = \frac{u^2+2}{u\sqrt{u^2+4}}. \tag{8.2.18}$$

Since the source star is moving relative to the lens star, u is a function of time, and so is the magnification. For uniform motion in a straight line we have that

$$u(t) = \left[u_0^2 + \left(\frac{t-t_0}{t_E}\right)^2\right]^{1/2}, \tag{8.2.19}$$

where t_0 is the time of the closest alignment u_0, and $t_E = \theta_E/\mu_{\rm rel}$ is the time it takes the source star to cross the Einstein ring as it moves with angular velocity $\mu_{\rm rel}$ (Gaudi, 2010). The value of t_E can range from less than a day to years but is typically of the order of a month. The magnification is $A > 1.34$ for $u \leq 1$, so the signal can be very strong. A big advantage of the microlensing method is that the strength of the signal depends much more on u than on the lens mass. Instead of being weaker, the signal of a low-mass lens (such as a planet) will have a shorter duration and thereby a lower detection probability than that of a high-mass lens (Bennett and Rhie, 2002).

From Equation 8.2.18 we see that $A \to \infty$ for $u \to 0$, i.e. that the light from the source star becomes infinitely magnified if it aligns perfectly with the lens star, and $u = 0$ is therefore called a caustic point. This obviously unphysical magnification is a consequence of our point mass source star approximation, but also in reality the brightness will increase significantly for small values of u. When a lens star passes very close to the source star, the two perturbed images will become highly elongated, almost covering the entire Einstein ring, and very sensitive to all planets with separations near θ_E. Such a planet would cause the already magnified brightness to increase even more, thereby revealing its existence to us. The physical stellar Einstein ring radius at the distance of the lens star is

$$r_E = \theta_E D_l \approx 4.0 \text{ AU}\left(\frac{M}{M_\odot}\right)^{1/2}\left(\frac{D_s}{8 \text{ kpc}}\right)^{1/2}\left(\frac{D_l/D_s(1-D_l/D_s)}{0.25}\right)^{1/2}. \tag{8.2.20}$$

We see that for a typical lens star distance of 4 kpc and a typical source star distance of 8 kpc, the planet of a Sun-like star will produce the strongest microlensing signal if it orbits at a distance of about 4 AU. For an M dwarf it will be 1-2 AU. Unlike the radial velocity and transit methods, the microlensing method is therefore most sensitive to planets in wider orbits.

For a lens system consisting of multiple lenses, the deflection angle and thus the lens equation become a sum involving the individual masses and angular positions of each lens. The light from the source star will be split into more than two images, each image either larger or smaller than the unmagnified source star image. Expressing the now two-dimensional positions of the source and its images in complex form as $\zeta = u_1 + iu_2$ and $z = y_1 + iy_2$ respectively, the lens equation becomes

$$\zeta = z - \sum_i^N \frac{\epsilon_i}{\bar{z} - \bar{z}_i}, \tag{8.2.21}$$

where z_i is the positions of lens i with relative mass $\epsilon_i = m_i/M$ (Gaudi, 2010). The Einstein ring will no longer be a ring but rather are more general critical curve. Furthermore, there is now one or more caustic curves rather than a single caustic point, marking the regions a point-like source star has to cross in order to be magnified "infinitely". These curves are plotted in

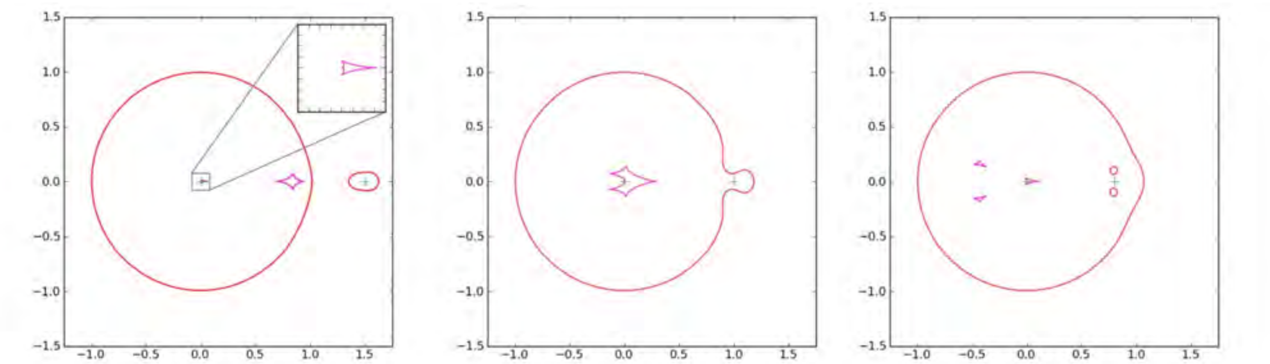

Figure 8.2.8: The critical curves (red) and caustic regions (purple) for three different configurations of a star-planet lens system (green pluses) with mass ratio $q = 10^{-3}$. In the left panel the planet is far from the star, in the middle panel the planet is at the stellar Einstein ring, and at the right panel the planet is inside the stellar Einstein ring. Source: Jørgensen (2015).

Figure 8.2.8 for a star-planet lens system where the planet is outside, close to and inside the stellar Einstein ring, respectively. For a binary lens system such as this, there will be either one, two, or three closed and disjoint caustic curves depending on the angular separation of the star and the planet $d = |z_1 - z_2|$, and on the ratio of their masses $q = M_p/M_*$.

When we observe a microlensing event, we observe the flux of the unresolved event as a function of time, which is given by

$$F(t) = F_s A(t) + F_b, \tag{8.2.22}$$

where F_s is the flux of the source star and F_b is the flux of any blended light that is not being lensed (Gaudi, 2010). This light could e.g. come from a companion to the source star, from nearby unrelated stars, or from the lens itself. By fitting the observed time-dependent flux with a rather complex model, we can glean information about the geometry and components of the source star and lens system. For a star-planet lens system, the model has at least 8 parameters: t_0, $u(t_0)$, t_E, F_s, F_b, d, q and α, where α is the angle of the source star trajectory relative to the star-planet lens axis. To make matters even more complicated, many of these parameters are highly degenerate. Usually, the analysis of the observed light curve is done by running simulations of thousands of different configurations and estimating which one yields a model light curve that resembles the observed one the most. Some of the parameters can be further constrained by high-resolution follow-up observations of the lens star if possible.

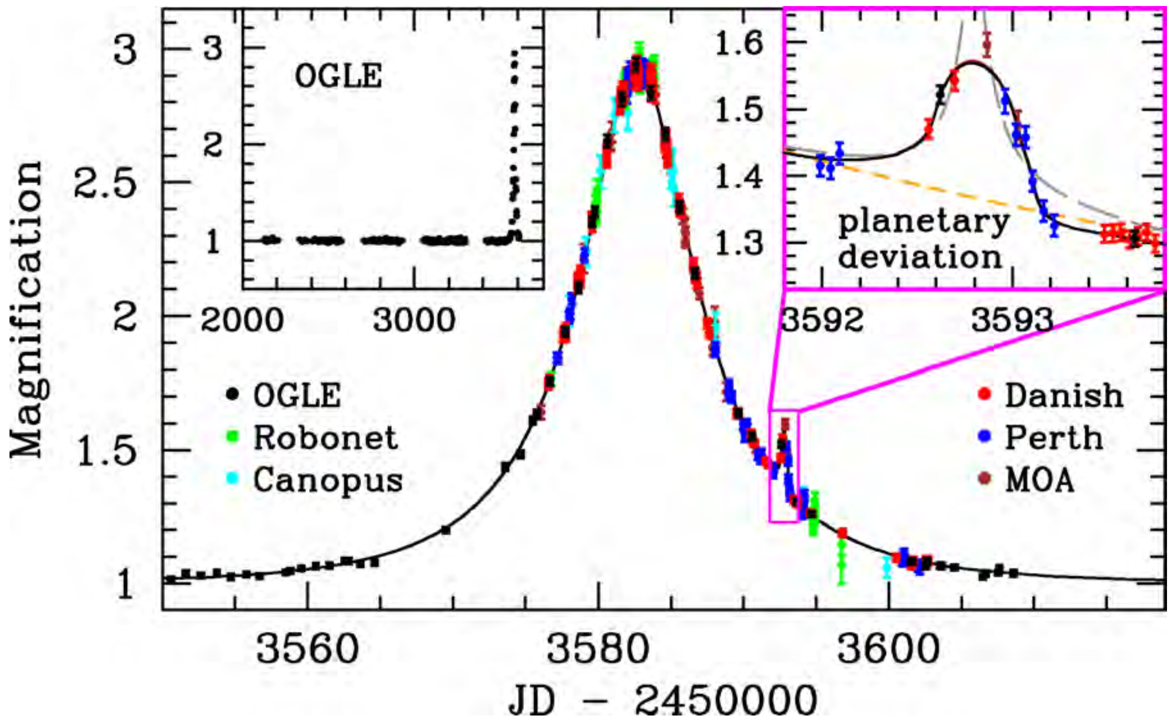

Figure 8.2.9: Data for the microlensing event OGLE 2005-BLG-390 observed by a network of telescopes in Chile, Australia, Tasmania, Hawaii and New Zealand. Also shown is the planetary model for the event (black curve), as well as the model light curve for a single lens star (orange, short-dashed) and a binary source star (gray, long-dashed) - the two latter clearly failing to match the data. Source: Beaulieu et al. (2006).

The sensitivity of the microlensing method depends on the angular size of the source star θ_*. As long as θ_* is smaller than the "zone of influence" of the planet, which is about the angular size of the planet's Einstein ring $\theta_{E,p}$, the magnification caused by the planet is almost independent of the planet mass, and we can use the point mass source star approximation. But when $\theta_* \gtrsim \theta_{E,p}$, different points of the source star will reach maximum magnification at different times as it crosses the caustic regions, causing a smoothing out of the final magnification. This is known as the finite size effect and the larger it is the more the magnification is smoothed out, and the harder it becomes to detect the planetary signal. For a typical microlensing event in the direction of the Galactic bulge we have that $\theta_* \sim \frac{R_*}{R_\odot}$ and $\theta_{E,p} \sim \sqrt{\frac{M_p}{M_\oplus}}$ in units of micro-arc-seconds. For giant source stars with $R_* \sim 10R_\odot$ the sensitivity limit is $\lesssim 5M_\oplus$, but for main-sequence sources with $R \sim R_{\odot}$ it is possible to detect planets with masses down to $\sim 0.02M_{\oplus}$. For sufficiently small source sizes, the microlensing method can thus detect Mars-mass planets and even planets a few times the mass of the Moon (Gaudi, 2010).

The duration of a typical primary lensing event in the direction of the Galactic bulge is about 10-100 days, but a planetary high-magnification event only lasts a few hours for an Earth-mass planet and a few days for a Jupiter-mass planet. Therefore microlensing planet searches use a two-step strategy. Wide field microlensing surveys such as OGLE (Udalski, 2003) and MOA (Sako et al., 2008) constantly monitor a few hundred million stars toward the Galactic bulge, reducing their data right away so that they can detect microlensing events in progress. A selection of these are then closely followed by several different follow-up collaborations such as RoboNet (Tsapras et al., 2009) and MiNDSTEp (Dominik et al., 2008) that work together to obtain the number of observations and photometric accuracy needed to detect a planetary signal.

Microlensing events are very rare, and even in the high density field of the Galactic bulge, only about 3 in 1 million stars are microlensed at any given time (Alcock et al., 2000). Furthermore, the probability of detecting an Earth-mass planet within $2r_E$ is only a few percent, if we require A > 0.05. For a Jupiter-mass planet the detection probability is about 20% (Bennett and Rhie, 1996). Microlensing planet searches therefore make relatively few discoveries despite being observationally intensive. During the past decade we have detected thousands of stellar microlensing events which has led to the discovery of about 40 exoplanets. Still, since the method covers a parameter space that is not easily accessed by any other, microlensing observations are definitely worth the effort. One of the first exoplanets discovered with the microlensing method was OGLE-2005-BLG-390Lb, the first known low-mass exoplanet in a wide orbit, and the most Earth-like exoplanet at the time (Beaulieu et al., 2006).

8.3 Projects

8.3.1 HATNet

HATNet is a ground-based wide-field survey that searches for transiting exoplanets around stars brighter than ∼13 magnitudes. It consists of six small fully automated wide-field telescopes of which four are located at the Fred Lawrence Whipple Observatory (FLWO) in Arizona and two are located at the Mauna Kea Observatory in Hawaii (Bakos et al., 2004). For the brightest stars, the HATNet telescopes can achieve a precision of about 2 milimag, making them perfect for detecting gas giants in close orbits. Since HATNet saw first light in 2003 it has discovered 57 exoplanets of which more than 80% are hot Jupiters.

The HATNet cameras continuously monitors millions of stars and when a sufficient amount of observations has been made, the large time-series data sets are run through sophisticated algorithms that are designed to find planetary transit signals. However, there exists many other phenomenona than planet transits that can cause a periodic dimming of the brightness of a star, so when a planet candidate has been found further observations are needed to confirm whether the signal is from a planet or not. These follow-up observations usually include additional photometric observations with a larger telescope as well as radial velocity observations.

I have participated in several follow-up radial velocity observations of HATNet planet candidates with the FIES spectrograph mounted on the 2.6 m Nordic Optical Telescope (Djupvik and Andersen, 2010), which with a precision of about 15 m/s is well suited for follow-up observations of HATNet candidates. I am also the first-author of the paper that announced the discovery of HAT-P-55b, a hot Jupiter with a mass of $0.58M_J$ orbiting a Sun-like star at a distance of 0.05 AU (Juncher et al., 2015).

8.3.2 SuperWASP

SuperWASP is another ground-based wide-field survey that searches for transiting exoplanets around bright stars. It consists of two robotic observatories that each have an array of eight wide-field telescopes. One of them is located at Roque de los Muchachos Observatory on the island of La Palma and the other is located at the South African Astronomical Observatory in South Africa. Being very similar to the HATNet telescopes, the SuperWASP telescopes also have a precision of a few milimag and specializes in finding gas giants in close orbits. SuperWASP has since 2006 discovered 117 exoplanets of which about 80% are hot Jupiters.

During my stay in St. Andrews, Scotland, I participated in several research projects at the 2.5 m James Gregory Telescope. One of them involved performing follow-up photometric observations to confirm or reject SuperWASP exoplanet candidates.

I have also participated in observations of already confirmed SuperWASP exoplanets with the Danish 1.54 m telescope at La Silla, Chile. The purpose of these additional observations was to measure the physical and orbital properties of the planet systems to high precision. The observations were performed with relatively long exposure times (of several minutes) and with the telescope heavily defocused, causing the images of the stars to appear donut-shaped. This was done to reduce the influence of individual potentially bad pixels in the CCD detector, and to counteract as many as possible of the effects of atmospheric scintillation, changes in the atmosphere during the observation, telescope tracking errors, and problems with saturation and flat-fielding of the detector. By dispersing a large number of photons over many pixels, the flat-fielding noise goes down by orders of magnitude compared to focused observations, changes in the seeing have only a negligible effect on the photometry, and the tracking errors are reduced a little. Furthermore, the long exposure times mean a low Poisson noise and low scintillation noise per exposure. Of course, the longer exposure times and larger point spread functions will cause a much higher sky background level, but signal-to-noise calculations have shown that this is unimportant in many cases (Southworth et al., 2009). I am a co-author of 7 papers that treat the observations of WASP-80 (Mancini et al., 2014b), WASP-67 (Mancini et al., 2014a), WASP-24, 25 and 26 (Southworth et al., 2014) WASP-103 (Southworth et al., 2015a), WASP-45 and 46 (Ciceri et al., 2015), WASP-57 (Southworth et al., 2015b), and WASP-22, 41, 42 and 55 (Southworth et al., 2015c).

8.3.3 MiNDSTEp

The MiNDSTEp consortium is a network of ground-based telescopes that studies the population of planets in the Milky Way using the microlensing method. The network consists of the Danish 1.54 m telescope at La Silla in Chile (operated for the exoplanet project since 2003), the 0.7 m Salerno University telescope in Salerno, Italy (in operation since 2015), the 1.2 m MONET telescope at the South African Astronomical Observatory in South Africa (expected in operation from 2016), and the 1 m SONG telescope at the island of Tenerife in Spain (expected in operation from 2016). They rely heavily on microlensing surveys such as OGLE or MOA to identify microlensing events involving stars with potential exoplanets. When such an event has been detected the network of telescopes spread across the globe monitors it continuously for any signs of anomalies that could be caused by the presence of an exoplanet. As a part of this, MiNDSTEp has also developed a software system, `ARTEMIS`, which based on the stellar lensing event predicts the probability of detecting potential planets, thereby guiding the telescopes to an optimal observing strategy. `ARTEMIS` also collects the observations from all follow-up collaborations (MiNDSTEp, RoboNet etc.) to produce light curves and related models which are publicly available online (http://www.artemis-uk.org/CurrentEvents). This strategy is described in Dominik et al. (2010).

Normally, only space-based telescopes can achieve the angular resolution of less than $1''$ that is needed to resolve the source star of a microlensing event in the high density fields of the Galactic bulge. Ground-based telescopes using normal CCD detectors (without adaptive optics) are limited to a resolution of about $1''$. However, it is possible for the Danish 1.54 m telescope to achieve spacial resolutions less than $0''.5$ by using an EMCCD detector and the Lucky Imaging technique. The negligible readout noise of this type of detector enables the possibility of high frame-rate imaging. At very short exposure times (about 100 ms) it is possible to take stationary snapshots of the wavefront of the starlight. In a few percent of these snapshots the wavefront will have made it through the atmosphere almost unperturbed, and by stacking them it is possible to achieve very high spatial resolutions. This is what is known as Lucky Imaging.

I have participated in the Lucky Imaging observations of microlensing events with the Danish 1.54 m telescope and co-authored 3 associated papers: the discovery of a gas giant orbiting an M-dwarf at more than 3 AU (Tsapras et al., 2014), an estimate of the distribution of planets in the Milky Way based on data for 21 (apparently) isolated lenses (Calchi Novati et al., 2015), and an investigation of how systematic errors might have lead to a false-positive detection (Bachelet et al., 2015).

To exploit the full length of the night, the Danish 1.54 m telescope is also involved in several side projects. These additional observations are usually carried out before or after the microlensing observations (depending on the season) when the Galactic bulge is below the horizon. One of these projects is concerned with the detection and characterization of variable stars in the cores of a number of globular clusters. The observations are performed with the EMCCD detector, the high frame-rate imaging making it possible to observe dim stars very close to bright stars without saturating the CCD. Lucky Imaging is also used to resolve the stars in the crowded cores. While this is an interesting project in itself, it also contributes to the more general development of the reduction and analysis software for the EMCCD, which in the end will improve the microlensing observations.

I have participated in the observations of globular clusters with the Danish 1.54 m telescope and co-authored 6 associated papers: the discovery of two new variables in M72 (Skottfelt et al., 2013), a refined estimation of the parameters of M30 (Kains et al., 2013), a survey of the variable stars in M9 (Arellano Ferro et al., 2013), a survey of the variable stars in cores of five different globular clusters (Skottfelt et al., 2015), and a survey of the variables in M68 (Kains et al., 2015).

8.3.4 Exoplanet populations

If we have both transit and radial velocity observations of a host star, we can determine the mean density of its planet. This allows us to estimate the composition of the planet and once we know that for enough planets, we can better map the diversity and distribution of the exoplanets as well as put constraints on our models of planetary structure and formation theories.

By analyzing the metallicities of more than 400 stars hosting 600 exoplanet candidates, Buchhave et al. (2014) found that the exoplanets could be categorized into three populations defined by statistically distinct metallicity regions: terrestrial-like planets (radii less than 1.7 Earth radii), gas dwarf planets with rocky cores and hydrogen-helium envelopes (radii between 1.7 and 3.9 Earth radii) and ice or gas giant planets (radii greater than 3.9 Earth radii). This implies that the metallicity of a host star plays a key role in the formation of its planets.

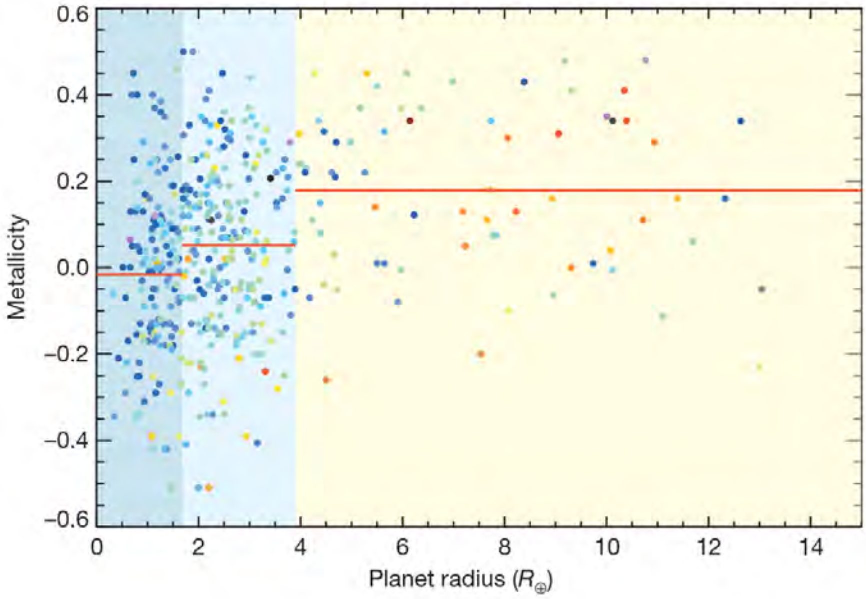

Figure 8.3.1: Host star metallicities and three types of exoplanets with different composition. Point color represents the logarithm of the period of the planets (blue, shortest period; red, longest period). The solid red lines are the average metallicities in the three regions. Source: Buchhave et al. (2014).

I participated in this work by performing spectroscopic observations that were used for the classification of the stellar parameters with the FIES spectrograph at the 2.6 m Nordic Optical Telescope and am a co-author of the paper.

8.3.5 The effect of stellar activity

With the constantly improving sensitivity of our instruments we are able to detect increasingly smaller planets in increasingly larger orbits. Unfortunately, the improved precision has introduced us to a new problem: The possibility of misidentifying planets due to stellar activity. The presence of star spots or changing granulation patterns can create time-variable photometric and spectroscopic signatures that can be confused with that of an exoplanet, while the sudden brightening caused by a stellar flare can mimic a microlensing event with a planet sized lens. Since many mid-F to M type stars show significant levels of activity, and since these are the stars most exoplanet searches target, it is important to understand how stellar activity affects the detection and characterization of exoplanets.

Korhonen et al. (2015) have conducted a statistical investigation of how cool star spots can effect radial velocity observations of Sun-like stars and M dwarfs. They developed a method that uses radiative transfer models to calculate the spectral line profiles of spotted stellar surfaces, allowing for the creation of many different spot filling factors and configurations. For varying patterns of solar-like activity, the maximum radial velocity jitter caused by star spots was found to be between 1-9 m/s, depending on the concentration of the spots. It was concluded that a Neptune-mass planet in a one year orbit can be detected with high significance, while the detection of an Earth-mass planet in a similar orbit is very difficult. Furthermore, the investigation showed that in addition to creating noise, star spots can affect the shape of the radial velocity curve in such a way that it changes the inferred orbital parameters. Today most radial velocities are biased by a necessary selection of magnetically quite stars in order to avoid these problems. In order to study an unbiased representative sample of stars, we need to be able to distinguish the activity noise from planet signals. I am a co-author of the paper and my contribution included computing a grid of synthetic spectra of early to mid-type M dwarf models that covered a wavelength range of $3000 - 9200$ Å.

8.3.6 A 2D cloud map of a hot Jupiter

The bright host star and large planet-to-star radius of the exoplanet system HD 189733 makes it a very attractive target for the study of hot Jupiter atmospheres. Several studies of the combined observations performed with the Hubble and Spitzer space telescopes show that the transmission spectrum of the atmosphere of HD 189733b is dominated by Rayleigh scattering over the whole visible range, indicating the presence of clouds. To examine the properties of these clouds, Lee et al. (2015) have computed a 2D cloud model for HD 189733b. This was done by applying the `DRIFT` model to the results from a 3D radiative hydrodynamical simulation of the atmosphere, selecting 1D atmosphere trajectories as input. They found that HD 189733b has a significant cloud component in the atmosphere that changes from dayside to nightside and from equator to mid latitudes, varying in grain size, number density and wavelength dependent opacity. These differences will affect how observations of HD 189733b are interpreted, depending on what region and depth of the planet is probed. I am a co-author of the paper and my contribution included writing the program that calculated the optical properties of the clouds.

8.3.7 A nearby brown dwarf binary

Luhman-16 is a recently discovered brown dwarf binary located at a distance of only 2.0 pc, making it the third closest system to the Sun. The primary is of spectral type L7.5, and the secondary is of spectral type T0.5. They orbit each other at a distance of about 3 AU with an orbital period of 25 years (Luhman, 2013). They exhibit a high degree of photometric variability of about 0.1 mag, which is thought to be related to the evolution of clouds in their atmospheres. The proximity of the system and the fact that both components are close to the L/T transition regime makes Luhman-16 a very interesting test case for models of brown dwarf atmospheres.

Street et al. (2015) have performed long-time photometric observations of Luhman-16 with a small network of 1 m telescopes. The obtained spacial resolution made it difficult to separate the components, so Luhman-16 was treated as a single object during data reduction. Differential photometry was used to identify and study the photometric variability of the object and thereby probe the patchiness of the clouds. The rotational period was found to be close to 5.28 hours, though varying significantly over longer periods of time due to intrinsic variability. The amplitude was typically around 0.05 mag and could change rapidly by up to a factor of 2 over the course of one rotational cycle. This could be explained by the existence of an inhomogeneous cloud layer in the upper atmosphere as it would periodically expose deeper layers as the objects rotated, causing variability in flux. To examine the opacity of these clouds they computed a `DRIFT-PHOENIX` model atmosphere for an object with $T_{\rm eff} = 1300$ K and $\log g = 5.0$. They found that the upper cloud layers were largely transparent for observations at the central wavelengths of the used filters. I am a co-author of the paper and my contribution included calculating the optical properties of the clouds in the `DRIFT-PHOENIX` model atmosphere.

Mancini et al. (2015) have monitored Luhman-16 over a period of two years with the Danish 1.54 m telescope. The observations were performed using the Lucky Imaging technique which made it possible to clearly resolve the two brown dwarfs. By studying the photometric variability of each component, they found that the rotational periods of Luhman-16A and Luhman-16B are about 8 and 5 hours, respectively. This implies that their rotation axes are well aligned, possible because the two objects were part of the same accretion process. In addition, a detailed astrometric analysis did not indicate the presence of an additional small companion, however more data is needed make a solid conclusion. I have participated in the observations of Luhman-16 with the Danish 1.54 m telescope and am a co-author of the paper.

8.4 Exoplanet atmospheres

In Section 6.6 we saw how the opacity of the atmosphere of a star or a brown dwarf determines at what atmosphere depth we reach a certain value of the optical depth (e.g. $\tau_\lambda = 1$). This is of course also true for exoplanet atmospheres. To relate this wavelength dependent property to what we can observe, we can express it as a change in the apparent magnitude defined by

$$\Delta\mathrm{mag} = -2.5\log\left(\frac{(R_{\rm p} + R_{\rm atm})^2}{R_{\rm p}^2}\right), \tag{8.4.1}$$

where R_p is the radius of the planet and R_atm is the perceived size of the atmosphere. This is only a first approximation, for a more precise analysis we would have to take in to account that the light from the star does not pass vertically through the atmosphere of the planet but rather approaches it from the side. The light will therefore have to travel through a larger and denser amount of atmosphere if it passes close the to surface of the planet, and through a smaller and thinner amount of atmosphere if it passes near the outer edge of the atmosphere.

In Figure 8.4.1 we plot the normalized flux and the variation in the apparent magnitude as a function of wavelength for a model with $T_\mathrm{eff} = 2000$ K, $\log(g) = 4.5$ and [M/H] = 0.0. Even though our model is of a brown dwarf and not a planet, its surface area is comparable to that of a giant gas planet since $R = \sqrt{GM/g} \approx 3R_\mathrm{J}$, and it gives us an idea of how the magnitude changes with wavelength.

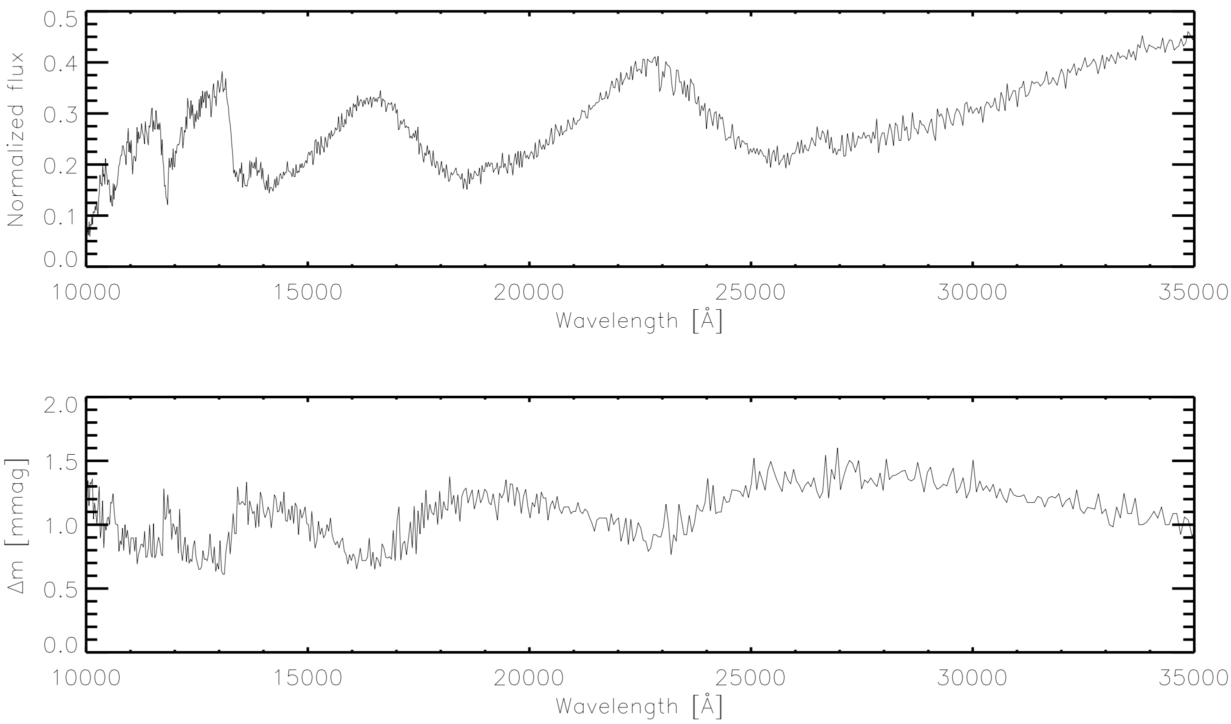

Figure 8.4.1: The normalized flux and the variation of the apparent magnitude as a function of wavelength for a model with $T_\mathrm{eff} = 2000$ K, $\log(g) = 4.5$ and [M/H] = 0.0.

We can also reverse this procedure to probe the atmosphere of an observed exoplanet. By comparing its transmission spectrum to our models of how the observed magnitude should change, we can begin to characterize the composition and structure of the exoplanet's atmosphere.

8.4.1 WASP-19b

Hot Jupiters have deep hydrogen-helium atmospheres with element abundances comparable to those of a star. Some of them orbit so close to their parent stars that they have surface temperatures larger than $T > 2000$ K. It is tempting to try and model the atmosphere of such a hot Jupiter with one of our ultra cool dwarf atmospheres. In fact, that is what we will do in the following.

The atmosphere of WASP-19b was modeled by Anderson et al. (2013) using the methods developed in Madhusudhan and Seager (2009, 2010, 2011). We will try to do the same with our models, using the information about the planet from their publication.

Wavelength	$F_p/F_\star$	Reference
1.6 μm	0.00276 ± 0.00044	Anderson et al. (2010)
2.09 μm	0.00366 ± 0.00067	Gibson et al. (2010)
3.6 μm	0.00483 ± 0.00025	Anderson et al. (2013)
4.5 μm	0.00572 ± 0.00030	Anderson et al. (2013)
5.8 μm	0.0065 ± 0.0011	Anderson et al. (2013)
8.0 μm	0.0073 ± 0.0012	Anderson et al. (2013)

Table 8.4.1: The relative flux of the exoplanet WASP-19b with respect to its star at different wavelengths.

WASP-19b is a transiting exoplanet with a mass of $M_p = 1.165 M_J$ and a radius of $R_p = 1.383 R_J$ in a close orbit around its parent star with a period of only $P = 0.789$ days. It can therefore be classified as a hot Jupiter. The day-side flux of WASP-19b has been measure by observing the occultation of the planet by its parent star with the Spitzer Space Telescope. The relative flux of the planet with respect to its star is presented in Table 8.4.1 (Table 4, Anderson et al. 2013).

A few words of warning must be said before we begin: Our models are of stars and brown dwarfs with masses larger than even the largest known gas giant. More importantly, the atmosphere of a planet - especially one so close to its parent star as a hot Jupiter - is significantly irradiated by the light from its parent star, and this can have a huge effect on the structure of the planet's atmosphere. As `MARCS` was originally designed to model stars, irradiation has not been included yet.

The parent star of WASP-19b is a G8V type star with $T_{\rm eff} = 5475$ K, $\log(g) = 4.43$ and $[{\rm Fe/H}] = 0.02$. We used our model code to create a synthetic spectrum of a star with these parameters and then computed the relative flux of each of our dusty models with respect to the flux of the star model. We then fitted the relative flux of the models to the data and found that our best fit model was $T_{\rm eff} = 2200$ K, $\log(g) = 4.5$ and $[{\rm Fe/H}] = 0$. The result is plotted in Figure 8.4.2. Despite the limitations of our code it fits the data remarkably well. Perhaps

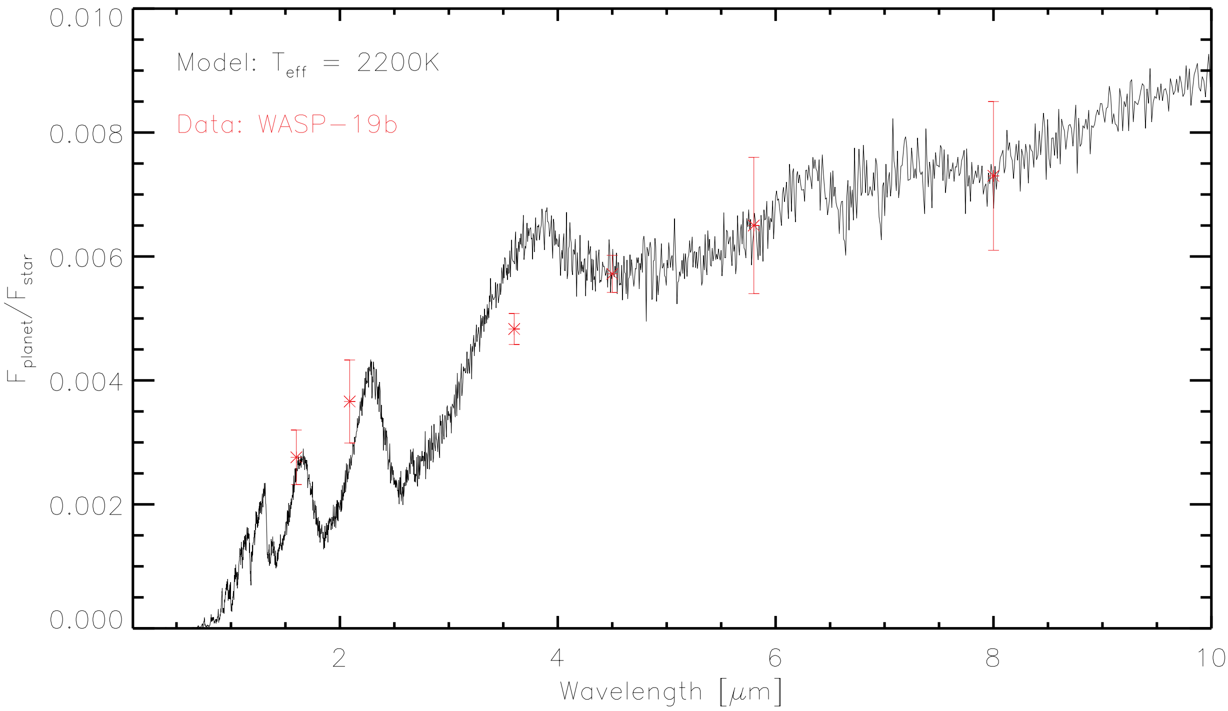

Figure 8.4.2: The relative flux of the hot Jupiter WASP-19b to its star compared to the best fit model with $T_{\rm eff} = 2200$ K, $\log(g) = 4.5$.

part of the explanation is that WASP-19 is a very active star, and that temperature inversion is suppressed in hot Jupiters orbiting active stars (Knutson et al., 2010). Perhaps we have just been lucky. Either way, the comparison in Figure 8.4.2 is just an illustration of the kind of results that can be achieved with the right modifications to our model code.

9
Conclusions

I have successfully merged the stellar model atmosphere code `MARCS` with the dust model code `DRIFT` and computed a grid of self-consistent cloudy atmosphere models.

- I have found that dust formation appears in model atmospheres with $T_{\rm eff} < 2700$ K. For $T_{\rm eff} < 2400$ K it has a significant effect on the structure and the spectrum of the atmosphere. The strong opaqueness of the dust grains causes a heating of the outer layers and middle layers of the atmosphere as well as a depletion of the elements in the gas phase that become bound in dust grains. Furthermore, the dust opacity also dampens the molecular absorption bands of H_2O in the infrared region of the spectrum.

- I have described the properties of dust formation and have found that the dust clouds forming in the atmospheres of ultra cool dwarfs can be divided into five distinct regions based on how the mean size of the dust grains changes with altitude.

- I have shown that the amount of dust in an atmosphere increases as the effective temperature decreases. As a result, dust absorption has a significant effect on the spectrum of our coolest models and partly determines the optical depth of the atmosphere.

- I have compared the synthetic spectra of our models with observed spectra and found that they fit the spectra of mid to late type M-dwarfs and early type L-dwarfs well. Many of the common absorption features are matched, including the absorption of TiO and H_2O in M-dwarfs and of metallic hydrides, H_2O and dust in L-dwarfs.

- I have compared the H_2O line lists of different sources and confirmed that the one we used is the most appropriate for our purposes.
- I have described the exoplanet observation projects I have been a part of during my time as a PhD student. I have also attempted to fit the observed flux from a hot Jupiter with synthetic spectra of my coolest brown dwarf models. The purpose of this was to illustrate how my cloudy atmosphere models will be able to contribute to the characterization of exoplanet atmospheres once they have been further developed.

I am currently working on two papers that describe the results of Chapter 6 and Chapters 7, respectively (Juncher et al. 2016a, Juncher et al. 2016b).

The next few steps in the continued development of the `DRIFT-MARCS` code will be to include all 12 condensation species that are currently a part of the most recent version of `DRIFT` and to update the data for the chemical equilibrium routines - and the routines themselves - such that the models can advance towards even cooler effective temperatures. This might also require a few changes to parts of the radiative transfer routines in `MARCS`. Following this, the grid of models should be expanded to include a broader range of effective temperatures, surface gravities and metallicities for a more complete modeling of observed spectra. For the study of hot exoplanets, an irradiation routine should be added as well.

One day models like the ones that have been initiated in this work and elsewhere may contribute to the decryption of the information that lies hidden in yet unobserved spectra of remote Earth-like exoplanets. Perhaps, in a not too distant future, they may even reveal to us the chemical imbalance in an atmosphere of such a planet; a sign of the mysterious process we call life.

A

Appendix: Model data

A.1 Included atoms and molecules

We have adopted the chemical composition of the Sun as reported by Grevesse et al. (2007). The abundances for each of the 38 atoms used in the equilibrium calculations are listed in Table A.1.1.

Atomic number	Name	Abundance	Atomic number	Name	Abundance
1	H	12.00	22	Ti	4.90
2	He	10.93	23	V	4.00
3	Li	1.05	24	Cr	5.64
4	Be	1.38	25	Mn	5.39
5	B	2.70	26	Fe	7.45
6	C	8.39	28	Ni	6.23
7	N	7.78	29	Cu	4.21
8	O	8.66	31	Ge	3.58
9	F	4.56	34	Br	2.56*
11	Na	6.17	37	Rb	2.60
12	Mg	7.53	38	Sr	2.92
13	Al	6.37	39	Y	2.21
14	Si	7.51	40	Zr	2.58
15	P	5.36	41	Nb	1.42
16	S	7.14	53	I	1.51*
17	Cl	5.50	56	Ba	2.17
19	K	5.08	57	La	1.13
20	Ca	6.31	58	Ce	1.70
21	Sc	3.17	60	Nd	1.45

Table A.1.1: The solar abundances of the 38 atoms used in `MARCS` (Grevesse et al., 2007). Element abundances marked with * are determined from meteorites.

The equilibrium calculations also included the following 210 molecules:

H^-, H_2, H_2O, OH, CH, CO, CN, C_2, N_2, O_2, NO, NH, C_2H_2, HCN, C_2H, HS, SiH, C_3, CS, SiC, SiC_2, NS, SiN, SiO, SO, S_2, SiS, TiO, VO, ZrO, MgH, HF, HCl, CH_4, CH_2, CH_3, NH_2, NH_3, C_2N_2, C_2N, CO_2, F^-, AlF, CaF, CaF_2, MgOH, Al_2O, AlOH, AlOF, AlOCl, NaOH, Si_2C, SiO_2, H_2S, CS_2, AlCl, NaCl, KCl, KOH, CaCl, $CaCl_2$, CaOH, TiO_2, VO_2, LiH, LiO, LiF, LiCl, BeH_2, BeO, BeF, BeCl, $BeCl_2$, BeOH, BH, BH_2, BO, B_2O, BS, BF, BCl, HBO, HBO_2, C^-, C_2^-, C_2H_4, NO_2^-, N_2H_2, N_2H_4, CN_2, C_4N_2, NO_2, NO_3, N_2O, N_2O_4, HNO, HNO_2, HNO_3, HCNO,

O^-, O_2^-, OH^-, CO_2^-, C_2O, HCO, H_2CO, F_2, FO, NaH, NaO, NaF, MgO, MgS, MgF, MgF_2, MgCl, $MgCl_2$, AlH, AlO, AlO_2, AlS, AlF_2, $AlCl_2$, SI^-, SiH_4, SiF, SiF_2, SiCl, $SiCl_2$, PH, PH_2, PH_3, CP, NP, PO, PO_2, PS, PF, PF_2, PCL, COS, SO_2, S_2O, SO_3, Cl^-, Cl_2, CCl, CCl_2, CCl_3, CCl_4, ClO, ClO_2, Cl_2O, SCl, SCl_2, HClO, CClO, KH, KO, KF, CaO, CaS, TiF, TiF_2, TiCl, $TiCl_2$, VN, CrN, CrO, CrO_2, FeO, FeS, FeF, FeF_2, FeCl, $FeCl_2$, NiCl, CuO, CuF, CuCl, SrO, SrS, SrF, SrF_2, SrCl, $SrCl_2$, SrOH, ZrH, ZrN, ZrO_2, ZrF, ZrF_2, ZrCl, $ZrCl_2$, HI, BaO, BaS, BaF, BaF_2, BaCl, $BaCl_2$, BaOH, NBO, C_4, C_5, TiH, CaH, FeH, CrH.

A.2 Dust growth reactions

Table A.2.1: The chemical surface reactions r that form the 7 dust species in our model.

Index r	Solid s	Surface reaction		
1	TiO_2[s]	TiO_2	$\longleftrightarrow$	TiO_2[s]
2	TiO_2[s]	$Ti + 2H_2O$	$\longleftrightarrow$	TiO_2[s] + $2H_2$
3	TiO_2[s]	$TiO + H_2O$	$\longleftrightarrow$	TiO_2[s] + H_2
4	TiO_2[s]	$TiS + 2H_2O$	$\longleftrightarrow$	TiO_2[s] + $H_2S + H_2$
5	Mg_2SiO_4[s]	$2Mg + SiO + 3H_2O$	$\longleftrightarrow$	Mg_2SiO_4[s] + $3H_2$
6	Mg_2SiO_4[s]	$2MgOH + SiO + H_2O$	$\longleftrightarrow$	Mg_2SiO_4[s] + $2H_2$
7	Mg_2SiO_4[s]	$2Mg(OH)_2 + SiO$	$\longleftrightarrow$	Mg_2SiO_4[s] + $H_2O + H_2$
8	Mg_2SiO_4[s]	$2Mg + SiS + 4H_2O$	$\longleftrightarrow$	Mg_2SiO_4[s] + $H_2S + 3H_2$
9	Mg_2SiO_4[s]	$2MgOH + SiS + 2H_2O$	$\longleftrightarrow$	Mg_2SiO_4[s] + $H_2S + 2H_2$
10	Mg_2SiO_4[s]	$2Mg(OH)_2 + SiS$	$\longleftrightarrow$	Mg_2SiO_4[s] + $H_2 + H_2S$
11	SiO_2[s]	SiO_2	$\longleftrightarrow$	SiO_2[s]
12	SiO_2[s]	$SiO + H_2O$	$\longleftrightarrow$	SiO_2[s] + H_2
13	SiO_2[s]	$SiS + 2H_2O$	$\longleftrightarrow$	SiO_2[s] + $H_2 + H_2S$
14	Fe[s]	Fe	$\longleftrightarrow$	Fe[s]
15	Fe[s]	$FeO + H_2$	$\longleftrightarrow$	Fe[s] + H_2O
16	Fe[s]	$FeS + H_2$	$\longleftrightarrow$	Fe[s] + H_2S
17	Fe[s]	$Fe(OH)_2 + H_2$	$\longleftrightarrow$	Fe[s] + $2H_2O$
18	Al_2O_3[s]	$2AlOH + H_2O$	$\longleftrightarrow$	Al_2O_3[s] + $2H_2$
19	Al_2O_3[s]	$2AlH + 3H_2O$	$\longleftrightarrow$	Al_2O_3[s] + $4H_2$
20	Al_2O_3[s]	$Al_2O + 2H_2O$	$\longleftrightarrow$	Al_2O_3[s] + $2H_2$
21	Al_2O_3[s]	$2AlS + 3H_2O$	$\longleftrightarrow$	Al_2O_3[s] + $2H_2S + H_2$
22	Al_2O_3[s]	$2AlO_2H$	$\longleftrightarrow$	Al_2O_3[s] + H_2O
23	MgO[s]	MgO	$\longleftrightarrow$	MgO[s]
24	MgO[s]	$Mg + H_2O$	$\longleftrightarrow$	MgO[s] + H_2
25	MgO[s]	2MgOH	$\longleftrightarrow$	2MgO[s] + H_2
26	MgO[s]	$Mg(OH)_2$	$\longleftrightarrow$	MgO[s] + H_2O
27	$MgSiO_3$[s]	$Mg + SiO + 2H_2O$	$\longleftrightarrow$	$MgSiO_3$[s] + $2H_2$
28	$MgSiO_3$[s]	$Mg + SiS + 3H_2O$	$\longleftrightarrow$	$MgSiO_3$[s] + $H_2S + 2H_2$
29	$MgSiO_3$[s]	$2MgOH + 2SiO + 2H_2O$	$\longleftrightarrow$	$2MgSiO_3$[s] + $3H_2$
30	$MgSiO_3$[s]	$2MgOH + 2SiS + 4H_2O$	$\longleftrightarrow$	$2MgSiO_3$[s] + $2H_2S + 3H_2$
31	$MgSiO_3$[s]	$Mg(OH)_2 + SiO$	$\longleftrightarrow$	$MgSiO_3$[s] + H_2
32	$MgSiO_3$[s]	$Mg(OH)_2 + SiS + H_2O$	$\longleftrightarrow$	$MgSiO_3$[s] + $H_2S + H_2$

B
Appendix: Source code

B.1 Equilibrium constants

```
PRO fit

name = 'name'
openr,lun,'Burrows_coeff.txt',/get_lun
skip_lun,lun,7,/lines

openw,lun2,'MARCS_coeff.txt',/get_lun

for i=1,1629 do begin
        readf,lun,name,a,b,c,d,e,tmin,tmax,format='(a16,5e12.5,2f5.0)'
                npoints = (fix(tmax-tmin)/100)+1
                if(tmin eq tmax) then continue
                if(tmin eq 0) then begin
                        npoints = npoints-1
                        tmin = 100
                endif
                T = fltarr(npoints)
                dG = fltarr(npoints)
                err = fltarr(npoints)

                for j=0,npoints-1 do begin
                  T(j) = tmin + 100.*j
                  dG(j) = (a/T(j)+b+c*T(j)+d*T(j)^2+e*T(j)^3)*4.184/1000.
        endfor

        x = reform(T,npoints)
        y = reform(dG,npoints)
        err = 0.001

        functargs = {x:x, y:y, err:err}
                start_params = [-1075.09d,117.521d,10.6976d,-1.97961d,0.137773d]

                k_fit = mpfit('fitfunc',start_params,functargs=functargs,perror=perror,/quiet)
        c1 = k_fit[0]
        c2 = k_fit[1]
        c3 = k_fit[2]
        c4 = k_fit[3]
        c5 = k_fit[4]

        printf, lun2,name, c1,c2,c3,c4,c5,format='(a13,5e15.5)'
endfor

close,/all

end

function fitfunc, param, x=x, y=y, err=err
        model = (((param[4]*(x/1000.) + param[3])*(x/1000.) + param[2])*(x/1000.) + param[1])*(x/1000.) + par
        return, (y-model)
end
```

B.2 Molecular line opacities

B.2.1 Mean molecular weight

```
!------------------------------------------------------------------------
! Calculates the mean molecular weight of H2, CO and TiO2
!------------------------------------------------------------------------
program isomol

implicit none
integer :: i, j, k, nH, nC, nO, nTi, nH2, nCO, nTiO,
real*8  :: scalefactor
real*8  :: wgt_H(2), wgt_C(2), wgt_O(3), wgt_Ti(5)
real*8  :: rel_H(2), rel_C(2), rel_O(3) rel_Ti(5)
real*8  :: wgt_H2, wgt_CO, wgt_TiO


! Atomic weights and abundances, arrays sorted by abundance
wgt_H = (/ 1.0078, 2.0141 /)
rel_H = (/ 0.9999, 0.0001 /)

wgt_C = (/ 12.000, 13.003 /)
rel_C = (/ 0.9893, 0.0107 /)

wgt_O = (/ 15.995, 17.999, 16.999 /)
rel_O = (/ 0.9976, 0.0021, 0.0004 /)

wgt_Ti = (/ 47.948, 45.953, 46.952, 48.948, 49.945 /)
rel_Ti = (/ 0.7372, 0.0825, 0.0744, 0.0541, 0.0518 /)


! H2: 1H-1H, 1H-D
nH = 2
nH2 = 2

rel_H2(1) = rel_H(1)*rel_H(1)
rel_H2(2) = rel_H(1)*rel_H(2)
scalefactor = 1./sum(rel_H2(1:2))
rel_H2(1:2) = scalefactor*rel_H2(1:2)

wgt_H2 = (wgt_H(1)+wgt_H(1))*rel_H2(1) + (wgt_H(1)+wgt_H(2))*rel_H2(2)

write(6,*)
write(6,'(a3)'), 'H2:'
write(6,'(a23,f8.4)'), 'Mean molecular weight: ', wgt_H2
write(6,'(a33,f7.5,a1)'), 'Isotopic abundances:     1H-1H  (', rel_H2(1), ')'
write(6,'(a33,f7.5,a1)'), '                         1H-D   (', rel_H2(2), ')'


! CO: 12C-16O, 13C-16O, 12C-18O, 12C-17O
nC = 2
nO = 3
nCO = 4

```

```
rel_CO(1) = rel_C(1)*rel_O(1)
rel_CO(2) = rel_C(2)*rel_O(1)
rel_CO(3) = rel_C(1)*rel_O(2)
rel_CO(4) = rel_C(1)*rel_O(3)
scalefactor = 1./sum(rel_CO(:))
rel_CO(:) = scalefactor*rel_CO(:)

wgt_CO = (wgt_C(1)+wgt_O(1))*rel_CO(1) + (wgt_C(2)+wgt_O(1))*rel_CO(2) + (wgt_C(1)+wgt_O(2))*rel_CO(3) +&
                                  (wgt_C(1)+wgt_O(3))*rel_CO(4)

write(6,*)
write(6,'(a4)'), 'CO:'
write(6,'(a23,f8.4)'), 'Mean molecular weight: ', wgt_CO
write(6,'(a33,f7.5,a1)'), 'Isotopic abundances:    12C-16O (', rel_CO(1), ')'
write(6,'(a33,f7.5,a1)'), '                        13C-16O (', rel_CO(2), ')'
write(6,'(a33,f7.5,a1)'), '                        12C-18O (', rel_CO(3), ')'
write(6,'(a33,f7.5,a1)'), '                        12C-17O (', rel_CO(4), ')'


! TiO: 48Ti-16O, 46Ti-16O, 47Ti-16O, 49Ti-16O, 50Ti-16O
nTi = 5
nO = 1
nTiO = 5

rel_TiO(:) = rel_Ti(:)

wgt_TiO = (wgt_Ti(1)+wgt_O(1))*rel_TiO(1)+(wgt_Ti(2)+wgt_O(1))*rel_TiO(2)+(wgt_Ti(3)+wgt_O(1))*rel_TiO(3)+ &
                                  (wgt_Ti(4)+wgt_O(1))*rel_TiO(4)+(wgt_Ti(5)+wgt_O(1))*rel_TiO(5)

write(6,*)
write(6,'(a3)'), 'TiO:'
write(6,'(a23,f8.4)'), 'Mean molecular weight: ', wgt_TiO
write(6,'(a33,f7.5,a1)'), 'Isotopic abundances: 48Ti-16O  (', rel_TiO(1), ')'
write(6,'(a33,f7.5,a1)'), '                     46Ti-16O  (', rel_TiO(2), ')'
write(6,'(a33,f7.5,a1)'), '                     47Ti-16O  (', rel_TiO(3), ')'
write(6,'(a33,f7.5,a1)'), '                     49Ti-16O  (', rel_TiO(4), ')'
write(6,'(a33,f7.5,a1)'), '                     50Ti-16O  (', rel_TiO(5), ')'
write(6,'(a33,f7.5,a1)'), '                         Sum   (', sum(rel_TiO(:)), ')'

end program isomol
```

B.2.2 FeH linelist

```
!--------------------------------------------------------------------------
! Reads in data for states and transitions and computes the linelist
! for FeH
!--------------------------------------------------------------------------
program FeH_linelist

implicit none
integer            :: i, j, k, nlines, nstates, ntrans, V1, V2, id1, id2
real*8             :: wn, a, E1, E2, J1, J2, loggf, wl_vac, wl_air
real,parameter     :: pi = 3.14159265
character          :: ef1*1, ef2*1, sym1*1, sym2*1
real*8,dimension(:,:),allocatable  :: linelist, energy
```

```
character,dimension(:),allocatable :: label1*5, label2*5

nstates = 3563
ntrans  = 93040
nlines = 88479

allocate(linelist(nlines,10))
allocate(label1(ntrans))
allocate(label2(ntrans))
allocate(energy(nstates,6))

open(1, file='data/FeH_states.txt')
do i=1,nstates
  read(1,'(i12,f13.6,7x,f8.1,i5,5x,4x,a1,4x,a1)') id1, E1, J1, &
    V1, ef1,sym1
  energy(i,1) = real(id1)
  energy(i,2) = real(V1)
  energy(i,3) = J1
  energy(i,4) = E1
  if(ef1 .eq. 'e')  energy(i,5) = 1.
  if(ef1 .eq. 'f')  energy(i,5) = 2.
  if(sym1 .eq. 'X') energy(i,6) = 1.
  if(sym1 .eq. 'F') energy(i,6) = 2.
end do
close(1)

k = 1
open(2, file='data/FeH_trans.txt')
do i=1,ntrans
  read(2,'(i12,i13,e11.4)') id2, id1, a
  if(a .eq. 0.) cycle
  do j=1,nstates
    if(id1 .eq. int(energy(j,1))) then
      V1 = int(energy(j,2))
      J1 = energy(j,3)
      E1 = energy(j,4)
      if(energy(j,5) .eq. 1.) ef1 = 'e'
      if(energy(j,5) .eq. 2.) ef1 = 'f'
      if(energy(j,6) .eq. 1.) sym1 = 'X'
      if(energy(j,6) .eq. 2.) sym1 = 'F'
    end if
    if(id2 .eq. int(energy(j,1))) then
      V2 = int(energy(j,2))
      J2 = int(energy(j,3))
      E2 = energy(j,4)
      if(energy(j,5) .eq. 1.) ef2 = 'e'
      if(energy(j,5) .eq. 2.) ef2 = 'f'
      if(energy(j,6) .eq. 1.) sym2 = 'X'
      if(energy(j,6) .eq. 2.) sym2 = 'F'
    end if
  end do

  wn = abs(E2-E1)
  wl_vac = 1e7/wn
  wl_air = wl_vac/(1.000064328+2949810./(1.46E10-wn**2)+25540./ &
```

```
     (4.1E9-wn**2))

   linelist(k,1) = wl_air
   linelist(k,2) = log10(18.839*(1/wn**2)*a*(2*J2+1)/(4*pi))
   linelist(k,3) = J1
   linelist(k,4) = abs(E1)
   linelist(k,5) = J2
   linelist(k,6) = abs(E2)
   linelist(k,7) = 24
   linelist(k,8) = k
   linelist(k,9) = 1

   label1(k)(1:5) = sym1 // '4Del'
   label2(k)(1:5) = sym2 // '4Del'
   k = k + 1
end do
close(2)

call sort(nlines,10,1,linelist)

open(unit=3, file='FeH.asc')
do i=1,nlines
   j = linelist(i,8)
   if(linelist(i,1) .lt. 1e6 .and. linelist(i,3) .ge. 0. .and. &
     linelist(i,5) .ge. 0.) then
     write(3,'(f12.4,f8.3,f5.1,f11.3,f5.1,f11.3,i4,1x,a5,1x,a5,1x, &
       i2,1x,a10)') &
       linelist(i,1:6), int(linelist(i,7)), label1(j)(1:5), &
       label2(j)(1:5), int(linelist(i,9)), '      Wende'
   end if
end do
close(3)

end program FeH_linelist
```

B.3 MARCS subroutines

```
!------------------------------------------------------------------------
! Reads in the dust data from the DRIFT output file and makes a table
! of dust opacities
!------------------------------------------------------------------------
      subroutine drift2marcs

      implicit real*8 (a-h,o-z)
      include 'parameter.inc'
      real*8     :: L0(max_lay), L1(max_lay), object
      real*8, parameter :: pi = 3.14159265
      complex*8  :: M_inc(max_inc,nwl),M_eff0,M_eff(nwl,max_lay)
      logical    :: first
      dimension  :: elnr(max_eps), rho(max_lay),V_inc(max_inc,max_lay),
     *              a(max_lay)
      dimension  :: wn(2000),p(2),step(2),var(2)
      common/cos/wnos(nwl),conos(ndp,nwl),wlos(nwl),wlstep(nwl),
     *     kos_step,nwtot
```

```
      common /cdustdata/ dabstable(max_lay,nwl),dscatable(max_lay,nwl),
     *     eps(max_eps,max_lay),temp(max_lay),pgas(max_lay),n_lay,idust

! Read in dust data from DRIFT
      open(110,file='drift2marcs.dat',status='old',readonly)
      do i=1,24
        read(110,*)
      end do
      read(110,'(i4)') n_inc
      if(n_inc .gt. max_inc) then
        print *, 'Error: increase max_inc.'
        stop
      end if
      do i=1,n_inc
        read(110,*)
      end do
      read(110,'(i4)') n_eps
      if(n_eps .gt. max_eps) then
        print *, 'Error: increase max_eps.'
        stop
      end if
      do i=1,n_eps
        read(110,*) elnr(i)
      end do
      read(110,*)
      read(110,*)
      i = 1
      do
        read(110,'(20x,5e20.12,40x,99e20.12)',iostat=io)
     *     temp(i),rho(i),pgas(i),L0(i),L1(i),V_inc(1:n_inc,i),
     *     eps(1:n_eps,i)
        if(io .lt. 0) exit
        if(L0(i) .le. 0.) then
          a(i) = 0.
        else
          a(i) = (3./4./pi)**(1./3.)*L1(i)/L0(i)
        end if
        i = i + 1
      end do
      close(110)
      n_lay = i-1
      if(n_lay .gt. max_lay) then
        print *, 'Warning: only used the first 1000 layers from DRIFT.'
      end if

! Read in optical constants
      call optical_data(n_inc,M_inc)

! Make opacity table
      do i=1,nwtot
        do j=1,n_lay
          if(i .eq. 1) then
            M_eff0 = (0.0,0.0)

            do k=1,n_inc
```

```
                M_eff0 = M_eff0 + V_inc(k,j)*M_inc(k,i)
              end do
            else
              M_eff0 = M_eff(i-1,j)
            end if

            call NR(M_inc(:,i),V_inc(:,j),M_eff0,M_eff(i,j),n_inc)

            x = 2.*3.141593*a(j)*1e8/wlos(i)       ! a: cm -> AA
            if(x .eq. 0.) then
              q_abs = 0.
              q_sca = 0.
            else
              call mie(M_eff(i,j),x,q_abs,q_sca)
            end if
            dabstable(j,i) = L0(j)*pi*a(j)**2*q_abs
            dscatable(j,i) = L0(j)*pi*a(j)**2*q_sca

          end do
        end do

        return
        end


!------------------------------------------------------------------------
! Reads in optical data for solids
!------------------------------------------------------------------------
        subroutine optical_data(n_inc,M_inc)

        implicit real*8 (a-h,o-z)
        include 'parameter.inc'
        integer :: i, j, k, io, nlines, counter, n_inc
        real*8  :: a, b, nkdata(3,3000)
        real*8  :: ndata(max_inc,nwl), kdata(max_inc,nwl)
        complex*8 :: M_inc(max_inc,nwl)
        character :: filename(12)*50
        common/cos/wnos(nwl),conos(ndp,nwl),wlos(nwl),wlstep(nwl),
     *     kos_step,nwtot

        filename(1) = 'data/DRIFT/nk_TiO2.txt'             ! TiO2
        filename(2) = 'data/DRIFT/nk_Mg2SiO4.txt'     ! Mg2SiO4
        filename(3) = 'data/DRIFT/nk_SiO2.txt'             ! SiO2
        filename(4) = 'data/DRIFT/nk_Fe.txt'                          ! Fe
        filename(5) = 'data/DRIFT/nk_Al2O3.txt'            ! Al2O3
        filename(6) = 'data/DRIFT/nk_MgO.txt'                         ! MgO
        filename(7) = 'data/DRIFT/nk_MgSiO3.txt'      ! MgSiO3

        do i=1,n_inc
! n values
          open(unit=1,file=filename(i))
          read(1,*) nlines
          counter = 1
          do j=1,nlines
            read(1,*) nkdata(1:3,counter)
```

```fortran
          if(nkdata(2,counter) .gt. 0.) then
            counter = counter + 1
          end if
        end do
        close(1)
        nlines = counter - 1
        nkdata(1,:) = 10000.*nkdata(1,:)      ! micron > AA

        do j=1,nwtot
          if(wlos(j) .lt. nkdata(1,1)) then
            ndata(i,j) = nkdata(2,1)
            cycle
          end if
          if(wlos(j) .gt. nkdata(1,nlines)) then
            if(i .le. 5) then
              print *, 'Missing n-data for inclusion #', i
              stop
            else
              ndata(i,j) = nkdata(2,nlines)
            end if
            cycle
          end if
          do k=1,nlines-1
            if(wlos(j).ge.nkdata(1,k).and.wlos(j).le.nkdata(1,k+1))then
              a=(nkdata(2,k+1)-nkdata(2,k))/(nkdata(1,k+1)-nkdata(1,k))
              b=nkdata(2,k) - a*nkdata(1,k)
              ndata(i,j) = a*wlos(j)+b
              exit
            end if
          end do
        end do

! k values
        open(unit=1,file=filename(i))
        read(1,*) nlines
        counter = 1
        do j=1,nlines
          read(1,*) nkdata(1:3,counter)
          if(nkdata(3,counter) .gt. 0.) then
            counter = counter + 1
          end if
        end do
        close(1)
        nlines = counter - 1
        nkdata(1,:) = 10000.*nkdata(1,:)      ! micron > AA
        do j=1,nwtot
          if(wlos(j) .lt. nkdata(1,1)) then
            kdata(i,j) = nkdata(3,1)
            cycle
          end if
          if(wlos(j) .gt. nkdata(1,nlines)) then
            if(i .le. 5) then
              print *, 'Missing k-data for inclusion #', n_inc
            else
              kdata(i,j) = nkdata(3,nlines)*wlos(i)/nkdata(1,nlines)
```

```
          end if
          cycle
        end if
        do k=1,nlines-1
          if(wlos(j).ge.nkdata(1,k).and.wlos(j).le.nkdata(1,k+1))then
            a=(nkdata(3,k+1)-nkdata(3,k))/(nkdata(1,k+1)-nkdata(1,k))
            b=nkdata(3,k) - a*nkdata(1,k)
            kdata(i,j) = a*wlos(j)+b
            exit
          end if
        end do
      end do
    end do

    do i=1,nwtot
      M_inc(1:n_inc,i) = dcmplx(ndata(1:n_inc,i),kdata(1:n_inc,i))
    end do

    end


!--------------------------------------------------------------------------
! Minimizes a multidimensional function using the Newton-Raphson method
!--------------------------------------------------------------------------
    subroutine NR(M_inc,V_inc,M_eff0,M_eff,n_inc)

    implicit real*8 (a-h,o-z)
    include 'parameter.inc'
    integer,parameter :: itmax = 30
    complex*8 :: M_inc(n_inc), M_eff0, M_eff
    real*8 :: V_inc(n_inc),F(2),F1(2),F2(2),J(2,2)
    real*8 :: corr(2),xold(2),xnew(2)

    do i=1,itmax
      call bruggeman(M_eff0,M_inc,V_inc,n_inc,F)

      if(F(1)**2+F(2)**2 .lt. 1e-13) exit
      call jacobian(M_eff0,M_inc,V_inc,J,n_inc)
      call gauss(2,J,corr,F)
      corr = -corr

      xold(1) = real(M_eff0)
      xold(2) = imag(M_eff0)
      xnew = xold + corr

      if(xnew(1).gt.0 .and. xnew(2).gt.0) then
        M_eff0 = cmplx(xnew(1),xnew(2))
      else
        print *, 'xnew is unphysical: ', xnew(1),xnew(2)
        stop
      end if

      if(i .eq. itmax) then
        print *, 'Reached max number of iterations.'
        print *, '|F| = ', F(1)**2+F(2)**2
```

```
          end if

        end do

        M_eff = M_eff0

        return
        end


!---------------------------------------------------------------------------
! Finds the Jacobian of F(M_eff0)
!---------------------------------------------------------------------------
        subroutine jacobian(M_eff0,M_inc,V_inc,J,n_inc)

        implicit none
        integer :: n_inc
        real*8 :: dx, dy, V_inc(n_inc), J(2,2), F1(2), F2(2)
        complex*8 :: M_eff0, M_inc(n_inc)

        dx = 1.e-5*real(M_eff0)
        call bruggeman(M_eff0+cmplx(dx,0.0),M_inc,V_inc,n_inc,F1)
        call bruggeman(M_eff0-cmplx(dx,0.0),M_inc,V_inc,n_inc,F2)
        J(1,1) = (F1(1)-F2(1))/(2.0*dx)
        J(2,1) = (F1(2)-F2(2))/(2.0*dx)

        dy = 1.e-5*imag(M_eff0)
        call bruggeman(M_eff0+cmplx(0.,dy),M_inc,V_inc,n_inc,F1)
        call bruggeman(M_eff0-cmplx(0.,dy),M_inc,V_inc,n_inc,F2)
        J(1,2) = (F1(1)-F2(1))/(2.0*dy)
        J(2,2) = (F1(2)-F2(2))/(2.0*dy)

        return
        end


!---------------------------------------------------------------------------
! Bruggeman's equation for F
!---------------------------------------------------------------------------
        subroutine bruggeman(M_eff0,M_inc,V_inc,n_inc,F)

        implicit none
        integer :: i, n_inc
        real*8  :: V_inc(n_inc), F(2)
        complex*8 :: M_eff0, M_inc(n_inc), Fcmplx

        Fcmplx = cmplx(0.0,0.0)
        do i=1,n_inc
          Fcmplx = Fcmplx + V_inc(i)*(M_inc(i)**2-M_eff0**2)/
     *                     (M_inc(i)**2+2.*M_eff0**2)
        end do

        F(1) = real(Fcmplx)
        F(2) = imag(Fcmplx)

```

```
      return
      end


!-----------------------------------------------------------------------
! Solves a matrix equation of the form: A*x = b using Gaussian
! elimination and back-substitution
!-----------------------------------------------------------------------
      subroutine gauss(N,a,x,b)

      implicit none
      integer :: N,i,j,k,kmax,piv(N),istat
      real*8  :: a(N,N),x(N),b(N),c,amax

      do i=1,N-1
        kmax = i
        amax = ABS(a(i,i))
        do k=i+1,N
          if(ABS(a(k,i)) .gt. amax) then
            kmax = k
            amax = ABS(a(k,i))
          endif
        end do

        if(kmax.ne.i) then
          do j=1,N
            c         = a(i,j)
            a(i,j)    = a(kmax,j)
            a(kmax,j) = c
          end do
          c       = b(i)
          b(i)    = b(kmax)
          b(kmax) = c
        endif

        do k=i+1,N
          c = a(k,i) / a(i,i)
          a(k,i) = 0.e0
          do j=i+1,N
            a(k,j) = a(k,j) - c * a(i,j)
          end do
          b(k) = b(k) - c * b(i)
        end do
      end do

      do i=N,1,-1
        c = 0.e0
        if (i.lt.N) then
          do j=i+1,N
            c = c + a(i,j) * x(j)
          end do
        end if
        x(i) = (b(i) - c) / a(i,i)
      end do

```

```fortran
      return
      end


!------------------------------------------------------------------------------
! Calculates the calculates efficiency factors for absorption and
! scattering (based on the Bohren-Huffman Mie subroutine)
!------------------------------------------------------------------------------
      subroutine mie(M_eff,x,q_abs,q_sca)

      implicit real*8 (a-h,o-z)
      complex*8 refrel,M_eff,d(2000000),xi,xi1,an,bn

      refrel = M_eff/1.    ! ref. index of sphere / ref. index of medium
      q_sca = 0.
      q_ext = 0.
      q_sca1 = -1.
      q_ext1 = -1.

      npoints = max(x+4.*x**(1./3.)+2.,abs(x*refrel))
      if(npoints .gt. 2000000) then
        print *, 'increase max dimension of d'
        stop
      end if
      d(npoints+15) = (0.,0.)
      do i=npoints+14,1,-1
        d(i) = (i+1)/(x*refrel) - 1./(d(i+1)+(i+1)/(x*refrel))
      end do

      psi0 = cos(x)
      psi1 = sin(x)
      chi0 = -sin(x)
      chi1 = cos(x)
      xi1 = dcmplx(psi1,-chi1)

      do i=1,npoints
        psi = (2.0*i-1.)*psi1/x-psi0
        chi = (2.0*i-1.)*chi1/x-chi0
        xi = dcmplx(psi,-chi)

        an = ((d(i)/refrel+i/x)*psi-psi1)/((d(i)/refrel+i/x)*xi-xi1)
        bn = ((d(i)*refrel+i/x)*psi-psi1)/((d(i)*refrel+i/x)*xi-xi1)

        q_sca = q_sca + (2.*i+1)*(abs(an)**2+abs(bn)**2)
        q_ext = q_ext + (2.*i+1)*real(an+bn)

        if(abs(q_sca-q_sca1).lt.1e-8.and.abs(q_ext-q_ext1).lt.1e-8) then
          exit
        end if

        psi0 = psi1
        psi1 = psi
        chi0 = chi1
        chi1 = chi
        xi1  = dcmplx(psi1,-chi1)
```

```
          q_sca1 = q_sca
          q_ext1 = q_ext
        end do

        q_sca = (2./x**2)*q_sca
        q_ext = (2./x**2)*q_ext
        if(imag(refrel) .eq. 0.) then
          q_abs = 0.
        else
          q_abs = q_ext - q_sca
        end if

        return
        end


!-----------------------------------------------------------------------
! Calculates the dust opacity for each wavelength at each depth layer
! by interpolating the dust opacity table.
!-----------------------------------------------------------------------
        subroutine dust_opac

        implicit real*8 (a-h,o-z)
        include 'parameter.inc'

        common /statec/ppr(ndp),ppt(ndp),pp(ndp),gg(ndp),zz(ndp),dd(ndp),
     *  vv(ndp),ffc(ndp),ppe(ndp),tt(ndp),tauln(ndp),ro(ndp),ntau,iter
        common/ci1/fl2(5),parco(45),parq(180),shxij(5),tparf(4),
     *   xiong(16,5),eev,enamn(ndp),sumh(ndp),xkbol,nj(16),iel(16),
     *   summ(ndp),nel
        common /cdustdata/ dabstable(max_lay,nwl),dscatable(max_lay,nwl),
     *      eps(max_eps,max_lay),temp(max_lay),pgas(max_lay),n_lay,idust
        common /cdustopac/ dust_abs(ndp,nwl), dust_sca(ndp,nwl)
        common/cos/wnos(nwl),conos(ndp,nwl),wlos(nwl),wlstep(nwl),
     *      kos_step,nwtot
        dimension pg(ndp),diff(ndp,max_lay),imin(ndp),itemp(12)
        common /cmolrat/ fold(ndp,8),molold,kl

        dust_abs(1:ntau,1:nwtot) = 0.
        dust_sca(1:ntau,1:nwtot) = 0.

        do i=1,ntau
          kl = i
          call jon(tt(i),ppe(i),1,pgx,rox,dumx,0)
          pg(i) = pgx
        end do

        do i=1,ntau
          do j=1,n_lay
            diff(i,j) = abs((tt(i)-temp(j))/tt(i)) +
     *                  abs((pg(i)-pgas(j))/pg(i))
          end do
          imin(i) = minloc(diff(i,1:n_lay),1)

```

```
          if(tt(i) .le. temp(n_lay)) then
            dust_abs(i,1:nwtot) = dabstable(imin(i),1:nwtot)
            dust_sca(i,1:nwtot) = dscatable(imin(i),1:nwtot)
          end if
        end do

        return
        end

!---------------------------------------------------------------------------
! Updates the initial element abundances (read from elabund.dat) with
! the dust depleted abundances
! From DRIFT: Mg Si Ti O Fe Al
! 17 MARCS: H HE C N O NE NA MG AL SI S K CA CR FE NI Ti
!---------------------------------------------------------------------------
        subroutine dust_eps

        implicit real*8 (a-h,o-z)
        include 'parameter.inc'

        common/statec/ppr(ndp),ppt(ndp),pp(ndp),gg(ndp),zz(ndp),dd(ndp),
     *  vv(ndp),ffc(ndp),ppe(ndp),tt(ndp),tauln(ndp),ro(ndp),ntau,iter
        common /cdustdata/ dabstable(max_lay,nwl),dscatable(max_lay,nwl),
     *      eps(max_eps,max_lay),temp(max_lay),pgas(max_lay),n_lay,idust
        common/ci5/abmarcs(17,ndp),anjon(17,5),h(5),part(17,5),dxi,
     *           f1,f2,f3,f4,f5,xkhm,xmh,xmy(ndp)
        common/ci1/fl2(5),parco(45),parq(180),shxij(5),tparf(4),
     *   xiong(16,5),eev,enamn(ndp),sumh(ndp),xkbol,nj(16),iel(16),
     *   summ(ndp),nel
        common/ci9/ai(16)
        common /tsuji/ nattsuji,nmotsuji,parptsuji(500),abtsuji(17,ndp)
        dimension pg(ndp),diff(ndp,max_lay),imin(ndp),sum(ndp)
        common /cmolrat/ fold(ndp,8),molold,kl
        data eev/1.602095e-12/,xmh/1.67339e-24/

        do i=1,ntau
          do j=1,n_lay-1
            if(tt(i).lt.temp(1)) then
              abmarcs(8,i)  = log10(eps(1,1))+12.       ! 12 Mg
              abmarcs(10,i) = log10(eps(2,1))+12.       ! 14 Si
              abmarcs(17,i) = log10(eps(3,1))+12.       ! 22 Ti
              abmarcs(5,i)  = log10(eps(4,1))+12.       !  8  O
              abmarcs(15,i) = log10(eps(5,1))+12.       ! 26 Fe
              abmarcs(9,i)  = log10(eps(6,1))+12.       ! 13 Al
              exit
            end if

            if(tt(i).ge.temp(j) .and. tt(i).le.temp(j+1)) then
              abmarcs(8,i)  = log10(eps(1,j))+12.       ! 12 Mg
              abmarcs(10,i) = log10(eps(2,j))+12.       ! 14 Si
              abmarcs(17,i) = log10(eps(3,j))+12.       ! 22 Ti
              abmarcs(5,i)  = log10(eps(4,j))+12.       !  8  O
              abmarcs(15,i) = log10(eps(5,j))+12.       ! 26 Fe
              abmarcs(9,i)  = log10(eps(6,j))+12.       ! 13 Al
              exit
```

```
          end if
        end do
      end do

      abtsuji = abmarcs

      write(6,'(a25)') 'Dust depleted abundances:'
      write(6,'(7a6)') 'k', 'Mg','Si','Ti','O','Fe','Al'
      do i=1,ntau,10
        write(6,'(i6,6f6.2)') i, abmarcs(8,i),abmarcs(10,i),
     *     abmarcs(17,i),abmarcs(5,i),abmarcs(15,i),abmarcs(9,i)
      end do

      sum(1:ntau) = 0.
      xmy(1:ntau) = 0.

      do i=1,nel
        abmarcs(i,1:ntau)=10.**abmarcs(i,1:ntau)
        sum(1:ntau)=SUM(1:ntau)+abmarcs(I,1:ntau)
      end do
      abmarcs(17,1:ntau)=10.**abmarcs(17,1:ntau)

      xmy(1:ntau)=0.
      aha=abmarcs(1,1)
      do i=1,nel
        abmarcs(i,1:ntau)=abmarcs(i,1:ntau)/aha
        summ(1:ntau)=summ(1:ntau)+abmarcs(i,1:ntau)
        xmy(1:ntau)=xmy(1:ntau)+abmarcs(i,1:ntau)*ai(i)
      end do
      abmarcs(17,1:ntau)=abmarcs(17,1:ntau)/aha
      xmy(1:ntau)=xmy(1:ntau)/ai(1)
      sumh(1:ntau)=sum(1:ntau)/aha-1.
      summ(1:ntau)=summ(1:ntau)-abmarcs(1,1:ntau)-abmarcs(3,1:ntau)-
     *  abmarcs(4,1:ntau)-abmarcs(5,1:ntau)

      enamn(1:ntau) = eev/(xmh*xmy(1:ntau))

      return
      end


!-----------------------------------------------------------------------
! Writes a MARCS output file to be read by DRIFT
!-----------------------------------------------------------------------
      subroutine marcs2drift

      implicit real*8 (a-h,o-z)
      include 'parameter.inc'
      character flag(ndp)
      dimension pg(ndp),surfgrav(ndp),v(ndp),emu(ndp),rad(ndp)
      dimension flip_rad(ndp), abundances(ndp,100), pg2(ndp)
      common /tauc/tau(ndp),dtauln(ndp),jtau
      common /cg/grav,konsg /cteff/teff,flux
      common /masse/relm
      common /mixc/palfa,pbeta,pny,py /cvfix/vfix
```

```
      common /statec/ppr(ndp),ppt(ndp),pp(ndp),gg(ndp),zz(ndp),dd(ndp),
     & vv(ndp),ffc(ndp),ppe(ndp),tt(ndp),tauln(ndp),ro(ndp),ntau,iter
      common /cstyr/mihal,noconv
      common /rossc/xkapr(ndp),cross(ndp)
      common /cabinit/abinit(natms),kelem(natms),nelem
      common /tsuji/ nattsuji,nmotsuji,parptsuji(500),abtsuji(17,ndp)
      common /cdustdata/ dabstable(max_lay,nwl),dscatable(max_lay,nwl),
     *     eps(max_eps,max_lay),temp(max_lay),pgas(max_lay),n_lay,idust
      common /cmolrat/ fold(ndp,8),molold,kl

      sun_rad = 6.96342e10    ! cm

! Radius
      relr = sqrt(relm/grav*10**(4.44))

      flip_rad(1:ntau) = 0.
      do k=1,ntau
        kl = k
        furem = fure
        call termo(tt(k),ppe(k),ppr(k),ptot,rro,cp,cv,agrad,q,u2)
        fure = 1./(xkapr(k)*rro)
        if(k .eq. 1) cycle
        flip_rad(k) = flip_rad(k-1) + (tau(k)-tau(k-1))*(fure+furem)*0.5
      end do
      rad(1:ntau) = 0.
      do k=1,ntau
        rad(k) = flip_rad(ntau-k+1)+relr*sun_rad
      end do

! Gas pressure
      do k=1,ntau
        kl = k
        call jon(tt(k),ppe(k),1,pgx,rox,dumx,0)
        pg(k) = PGx
      end do

! Surface gravity
      do k=1,ntau
        surfgrav(k) = (relr*sun_rad/rad(k))*grav
      end do

! Convective velocity
      do k=1,ntau
        if(k .gt. 1) go to 13
        v(k) = 0.
        go to 15

13      if(k .eq. ntau) go to 14
        ya=(tau(k)-tau(k-1))/(tau(k+1)-tau(k-1))
        yb=1.-ya
        v(k)=ya*vv(k+1)+yb*vv(k)
        if(vv(k).gt.0..and.vv(k+1).gt.0.) v(k)=
     *     exp(ya*log(vv(k+1))+yb*log(vv(k)))
        go to 15

```

```
14        continue
          ya=(2.*tau(k)-tau(k-1)-tau(k-2))/(tau(k)-tau(k-2))
          yb=1.-ya
          v(k)=ya*vv(k)+yb*vv(k-1)
15        continue
        end do

! Convection flag
        do k=1,ntau
          if(v(k) .eq. 0.) then
            flag(k) = 'F'
          else
            flag(k) = 'T'
          end if
        end do

! Mean molecular mass
        do k=1,ntau
          kl = k
          call termo(tt(k),ppe(k),ppr(k),ptot,rro,cp,cv,agrad,q,u2)
          emu(k) = (1.38*rro*tt(k))/(1.67e-8*pg(k))
        end do

! Save to file
        open(unit=33,file='marcs2drift.dat')
        write(33,'(a2)') ' !'
        write(33,'(a43)')' ! MARCS output file to be read in by DRIFT'
        if(idust .eq. 0) then
          write(33,'(a2)') ' ! Dust not included'
        else
          write(33,'(a2)') ' ! Dust included'
        end if
        write(33,'(a2)') ' !'
        write(33,'(a32,a19)') ' ! Model parameters: Teff, logg,',
     *  ' mixing, overshoot:'
        write(33,'(f12.3,f13.3,f13.3,f13.3)') teff, log10(grav),
     *  palfa, 2.200
        write(33,'(a2)') ' !'
        write(33,'(a31)') ' ! Number of atmosphere layers:'
        write(33,'(i5)') ntau
        write(33,'(a2)') ' !'
        write(33,'(a42)') ' ! Number of elements in abundances table:'
        write(33,'(i5)') nelem
        write(33,'(a2)') ' !'
        write(33,'(a32)') ' ! Z of the considered elements:'
        do i=1,nelem,8
          if(i .gt. nelem-8) then
            write(33,'(8(i5.2,1x))') (kelem(j), j=i,nelem)
          else
            write(33,'(8(i5,1x))') (kelem(j), j=i,i+7)
          end if
        end do
        write(33,'(a2)') ' !'
        write(33,'(a5,6a16,a6,a16)') ' !  #', 'Rad [cm]',
     *  'Temp [K]', 'Pgas [dyn cm-2]', 'Ro [g cm-3]', 'g [cm s-2]',
```

```
     *  'v_conv [cm s-1]', 'Flag', 'mu [amu]'
      do k=1,ntau
        write(33,'(i5,6e16.8,a6,e16.8)') k, rad(k), tt(k), pg(k),
     *  ro(k), surfgrav(k), v(k), flag(k), emu(k)
      end do
      write(33,'(a2)') ' !'
      write(33,'(a41)') ' ! Initial Element abundances for each Z:'
      do i=1,nelem-1,8
        if(i .gt. nelem-9) then
          write(33,'(8f6.2)') (abinit(j), j=i,nelem-1)
        else
          write(33,'(8f6.2)') (abinit(j), j=i,i+7)
        end if
      end do
      close(33)

      return
      end
```

B.4 DRIFT subroutines

```
!-------------------------------------------------------------------------
! Reads in model data from MARCS output file
!-------------------------------------------------------------------------
      subroutine init_marcs(beta)

      use drift_data,ONLY: NELEM,maxElementCount,maxLayers,
     *                     bk,amu,bar,Nl,abschluss,sizedist,
     *                     eps0,logg,Teff,mixLength,Rnull,
     *                     Rlay,Tlay,play,rholay,glay,mulay,
     *                     wmixlay,zlay,pconv,Nlayers
      implicit none
      real*8,intent(IN) :: beta
      real*8  epsMarcs(maxElementCount), vconvlay(maxLayers)
      integer Z(maxElementCount)
      integer elementCount,i,j
      real*8  dum,rr,p,T,nH,rho,g,mu,wmix,err,pnorm,Tnorm
      real*8  epsH,Hp,grad
      logical flag_conv(maxLayers),conv
      integer H,He,C,N,O,Ne,Na,Mg,Al,Si,S,K,Ca,Cr,Mn,Fe,Ni,Ti

      data H/1/, He/2/, C/6/, N/7/, O/8/, Ne/10/, Na/11/, Mg/12/
      data Al/13/, Si/14/, S/16/, K/19/, Ca/20/, Cr/24/, Mn/25/
      data Fe/26/, Ni/28/, Ti/22/

      write(*,*)
      write(*,*) "Reading MARCS structure ..."
      write(*,*) "=============================="

      open(42, file='marcs2drift.dat', status='old')
      do i=1,5
         read(42,*)
      enddo
      read(42,'(3(f12.3, 1x))') Teff, logg, mixLength
```

```fortran
      write(*,1000) Teff, logg, mixLength
      read(42,*)
      read(42,*)
      read(42,'(i5)') Nlayers
      write(*,*) "Nlayers", Nlayers
      read(42,*)
      read(42,*)
      read(42,'(i5)') elementCount
      read(42,*)
      read(42,*)
      read(42,'(8(i5, 1x))') (Z(i), i=1, elementCount)
      read(42,*)
      read(42,*)
      do i=1,Nlayers
        read(42,'(5x,6e16.8,a6,e16.8)') Rlay(i),Tlay(i),play(i),
     *       rholay(i),glay(i),vconvlay(i),flag_conv(i),mulay(i)
      end do
      read(42,*)
      read(42,*)
      read(42,'(8f6.2)') (epsMarcs(i), i=1,elementCount)
      close(42)

      eps0(:)   = 1.d-99
      eps0(H)   = 10.d0**(epsMarcs(1)-12.0)
      eps0(He)  = 10.d0**(epsMarcs(2)-12.0)
      eps0(C)   = 10.d0**(epsMarcs(6)-12.0)
      eps0(N)   = 10.d0**(epsMarcs(7)-12.0)
      eps0(O)   = 10.d0**(epsMarcs(8)-12.0)
      eps0(Na)  = 10.d0**(epsMarcs(11)-12.0)
      eps0(Mg)  = 10.d0**(epsMarcs(12)-12.0)
      eps0(Al)  = 10.d0**(epsMarcs(13)-12.0)
      eps0(Si)  = 10.d0**(epsMarcs(14)-12.0)
      eps0(S)   = 10.d0**(epsMarcs(16)-12.0)
      eps0(K)   = 10.d0**(epsMarcs(19)-12.0)
      eps0(Ca)  = 10.d0**(epsMarcs(20)-12.0)
      eps0(Ti)  = 10.d0**(epsMarcs(21)-12.0)
      eps0(Fe)  = 10.d0**(epsMarcs(25)-12.0)

 1000 format(' Teff=',0pF8.3,' logg=',0pF5.2,' mixLengthPara=',0pF5.2)

      end
```

B.5 Master program

```fortran
!-------------------------------------------------------------------------
! Calls MARCS and DRIFT in turn and checks convergence.
!-------------------------------------------------------------------------
program dmarcs

integer :: idriftok, io
character :: line*27
real*8   :: Tcormx

do
```

```
    print *, 'Calling MARCS.'
    call system('./marcs_dj_2b')
    call system('rm fort*')

    print *, 'Checking convergence.'
    open(unit=1,file='Tcorr.txt',status='old')
    read(1,'(f10.1)') Tcormx
    if(Tcormx .le. 10.) exit
    close(1)

    print *, 'Calling DRIFT.'
    call system('cp drift2marcs.dat d2m.save')
    call system('./static_weather8 > drift.out')

    print *, 'Checking output.'
    open(unit=2,file='drift.out',readonly)
    idriftok = 0
    do
      read(2,'(a27)',iostat=io) line(1:27)
      if(io .lt. 0) exit
      if(index(line,' regular end of integration')) then
        idriftok = 1
        exit
      end if
    end do
    close(2)

    if(idriftok .ne. 1) then
      print *, 'DRIFT did not converge, using old DRIFT file'
      call system('cp d2m.save drift2marcs.dat')
    end if

    call system('rm restart.dat')
    call system('cp arcivaab.dat arcivaaa.dat')
  end do

  print *, 'DRIFT-MARCS converged successfully! :)'

  end
```

C

Appendix: Publications

Papers in preparation

- D. Juncher, U. G. Jørgensen, and C. Helling. Modeling the Cloudy Atmospheres of Ultra Cool Dwarfs II: Comparison of synthetic and observed spectra. Manuscript in preparation.

- D. Juncher, U. G. Jørgensen, and C. Helling. Modeling the Cloudy Atmospheres of Ultra Cool Dwarfs I: Creating a cloudy model atmosphere. Manuscript in preparation.

- J. Southworth, J. Tregloan-Reed, M. I. Andersen, et al. High-precision photometry by telescope defocussing. VIII. WASP-22, WASP-41, WASP-42 and WASP-55. *Monthly Notices of the RAS*, 2015, submitted.

- R. Figuera Jaimes, D. M. Bramich, J. Skottfelt, et al. Exploring the crowded central region of 10 Galactic globular clusters using EMCCDs. *The Astrophysical Journal*, 2015, accepted.

- S. Ciceri, L. Mancini, J. Southworth, et al. Physical properties of the planetary systems WASP-45 and WASP-46 from simultaneous multi-band photometry. *Monthly Notices of the RAS*, 2015, accepted.

Papers in peer-refereed scientific journals

- J. Southworth, L. Mancini, J. Tregloan-Reed, et al. Larger and faster: revised properties and a shorter orbital period for the WASP-57 planetary system from a pro-am collaboration. *Monthly Notices of the RAS*, 454:3094-3107, 2015.

- L. Mancini, P. Giacobbe, S. P. Littlefair, et al. Rotation periods and astrometric motions of the Luhman 16AB brown dwarfs by high-resolution lucky-imaging monitoring. *Astronomy & Astrophysics*, , 584:A104, 2015.

- R. A. Street, B. J. Fulton, A. Scholz, et al. Extended Baseline Photometry of Rapidly Changing Weather Patterns on the Brown Dwarf Binary Luhman-16. *The Astrophysical Journal*, 812:21, 2015.

- D. Juncher, L. A. Buchhave, J. D. Hartman, et al. HAT-P-55b: A Hot Jupiter Transiting a Sun-like Star. *Publications of the Astronomical Society of the Pacific*, 127:851-856, 2015.

- E. Bachelet, D. M. Bramich, C. Han, et al. Red Noise Versus Planetary Interpretations in the Microlensing Event Ogle-2013-BLG-446. *The Astrophysical Journal*, 812:136, 2015.

- G. Lee, C. Helling, I. Dobbs-Dixon, and D. Juncher. Modeling the local and global cloud formation on HD 189733b. *Astronomy & Astrophysics*, 580:A12, 2015.

- N. Kains, A. Arellano Ferro, R. Figuera Jaimes, et al. A census of variability in globular cluster M 68 (NGC 4590). *Astronomy & Astrophysics*, 578:A128, 2015.

- S. Calchi Novati, A. Gould, A. Udalski, et al. Pathway to the Galactic Distribution of Planets: Combined Spitzer and Ground-Based Microlens Parallax Measurements of 21 Single-Lens Events. *The Astrophysical Journal*, 804:20, 2015.

- H. Korhonen, J. M. Andersen, N. Piskunov, et al. Stellar activity as noise in exoplanet detection - I. Methods and application to solar-like stars and activity cycles. *Monthly Notices of the RAS*, 448:3038-3052, 2015.

- J. Southworth, L. Mancini, S. Ciceri, et al. High-precision photometry by telescope defocusing - VII. The ultrashort period planet WASP-103. *Monthly Notices of the RAS*, 447:711-721, 2015.

- J. Skottfelt, D. M. Bramich, R. Figuera Jaimes, et al. Searching for variable stars in the cores of five metal-rich globular clusters using EMCCD observations. *Astronomy & Astrophysics*, 573:A103, 2015.

- J. Southworth, T. C. Hinse, M. Burgdorf, et al. High-precision photometry by telescope defocussing - VI. WASP-24, WASP-25 and WASP-26. *Monthly Notices of the RAS*, 444:776-789, 2014.

- L. Mancini, J. Southworth, S. Ciceri, et al. Physical properties of the WASP-67 planetary system from multi-colour photometry. *Astronomy & Astrophysics*, 568:A127, 2014.

- L. A. Buchhave, M. Bizzarro, D. W. Latham, et al. Three regimes of extrasolar planet radius inferred from host star metallicities. *Nature*, 509:593-595, 2014.

- Y. Tsapras, J.-Y. Choi, R. A. Street, et al. A Super-Jupiter Orbiting a Late-type Star: A Refined Analysis of Microlensing Event OGLE-2012-BLG-0406. *The Astrophysical Journal*, 782:48, 2014.

- L. Mancini, J. Southworth, S. Ciceri, et al. Physical properties and transmission spectrum of the WASP-80 planetary system from multi-colour photometry. *Astronomy & Astrophysics*, 562:A126, 2014.

- A. Arellano Ferro, D. M. Bramich, R. Figuera Jaimes, et al. A detailed census of variable stars in the globular cluster NGC 6333 (M9) from CCD differential photometry. *Monthly Notices of the RAS*, 434:1220-1238, 2013.

- N. Kains, D. M. Bramich, A. Arellano Ferro, et al. Estimating the parameters of globular cluster M 30 (NGC 7099) from time-series photometry. *Astronomy & Astrophysics*, 555:A36, 2013.

- J. Skottfelt, D. M. Bramich, R. Figuera Jaimes, et al. EMCCD photometry reveals two new variable stars in the crowded central region of the globular cluster NGC 6981. *Astronomy & Astrophysics*, 553:A111, 2013.

Posters at international conferences

- D. Juncher, A. Popovas, C. Helling, and U. G. Jørgensen: Modelling the Cloudy Atmospheres of Cool Stars. Presented at:
  - *LEAP conference: Electrification in dusty atmospheres inside and outside the solar system*. Pitlochry, Scotland. 2014.
  - *Exoplanet UK Community Meeting*. Cambridge, England. 2014.

- A. Popovas, D. Juncher, U. G. Jørgensen: Modelling the atmospheric structure of the coolest dwarf stars and of exoplanetary atmospheres. Presented at:

    - *Danish National Astronomy Meeting*. Odense, Denmark. 2014.
    - *Joint Meeting of the Nordic Network of Astrobiology and the Centre of Geobiology: Biosignatures across space and time*. Bergen, Norway, 2014.

- D. Juncher, C. Helling and U. G. Jørgensen: Modelling cloudy atmospheres with MARCS. Presented at:

    - *RAS specialist discussion meeting: Ionising processes in atmospheric environments of planets, brown dwarfs and M dwarfs*. London, England. 2014.

Monthly Notices of the Royal Astronomical Society
MNRAS **454**, 3094–3107 (2015) doi:10.1093/mnras/stv2183

Larger and faster: revised properties and a shorter orbital period for the WASP-57 planetary system from a pro-am collaboration

John Southworth,[1★] L. Mancini,[2] J. Tregloan-Reed,[3] S. Calchi Novati,[4,5,6] S. Ciceri,[2] G. D'Ago,[6,5,7] L. Delrez,[8] M. Dominik,[9] D. F. Evans,[1] M. Gillon,[8] E. Jehin,[8] U. G. Jørgensen,[10] T. Haugbølle,[10] M. Lendl,[8,11] C. Arena,[12,13] L. Barbieri,[12,14] M. Barbieri,[15] G. Corfini,[12] C. Lopresti,[12,16] A. Marchini,[12,17] G. Marino,[12,18] K. A. Alsubai,[19] V. Bozza,[5,7] D. M. Bramich,[19] R. Figuera Jaimes,[9,20] T. C. Hinse,[21] Th. Henning,[2] M. Hundertmark,[10] D. Juncher,[10] H. Korhonen,[10,22] A. Popovas,[10] M. Rabus,[2,23] S. Rahvar,[24] R. W. Schmidt,[25] J. Skottfelt,[10,26] C. Snodgrass,[27] D. Starkey,[9] J. Surdej[8] and O. Wertz[8]

Affiliations are listed at the end of the paper

Accepted 2015 September 18. Received 2015 September 16; in original form 2015 July 21

ABSTRACT

Transits in the WASP-57 planetary system have been found to occur half an hour earlier than expected. We present 10 transit light curves from amateur telescopes, on which this discovery was based, 13 transit light curves from professional facilities which confirm and refine this finding, and high-resolution imaging which show no evidence for nearby companions. We use these data to determine a new and precise orbital ephemeris, and measure the physical properties of the system. Our revised orbital period is 4.5 s shorter than found from the discovery data alone, which explains the early occurrence of the transits. We also find both the star and planet to be larger and less massive than previously thought. The measured mass and radius of the planet are now consistent with theoretical models of gas giants containing no heavy-element core, as expected for the subsolar metallicity of the host star. Two transits were observed simultaneously in four passbands. We use the resulting light curves to measure the planet's radius as a function of wavelength, finding that our data are sufficient in principle but not in practise to constrain its atmospheric properties. We conclude with a discussion of the current and future status of transmission photometry studies for probing the atmospheres of gas-giant transiting planets.

Key words: stars: fundamental parameters – stars: individual: WASP-57 – planetary systems.

1 INTRODUCTION

Although the first transiting extrasolar planet (TEP) was only discovered in late 1999 (Charbonneau et al. 2000; Henry et al. 2000), and the second as recently as 2003 (Konacki et al. 2003), the number currently known has already exceeded 1200.[1] The great majority of those are small objects observed using the NASA *Kepler* satellite: validation of the planetary nature of these bodies has been greatly helped by their occurrence in systems of multiple planets (see Rowe et al. 2014) but detailed studies are difficult due to their small size and long orbital periods ($P_{\rm orb}$s).

A significant number (231 as of 2015/07/21) of the known TEPs are hot Jupiters, adopting a definition of mass $M_{\rm b} > 0.3\,M_{\rm Jup}$ and $P_{\rm orb} < 10$ d. These are much better suited to characterization with existing facilities, as their relatively large masses and radii, short orbital periods, and bright host stars make photometric and spectroscopic observations easier and more productive. Perhaps the single most important observable property of a planet is its orbital period: the period distributions of exoplanets provide an insight into the mechanisms governing their formation and evolution (e.g. Mordasini, Alibert & Benz 2009a; Mordasini et al. 2009b; Benítez-Llambay, Masset & Beaugé 2011; Hellier et al. 2012), and a precise value is mandatory for performing follow-up observations.

★ E-mail: astro.js@keele.ac.uk

[1] See TEPCat (Transiting Extrasolar Planet Catalogue; Southworth 2011) at: http://www.astro.keele.ac.uk/jkt/tepcat/

In this work, we study the WASP-57 system, whose planetary nature was discovered by the SuperWASP consortium (Faedi et al. 2013, hereafter F13). WASP-57 contains a star slightly cooler and less massive than the Sun ($T_{\rm eff}$ = 5600 ± 100 K, $M_{\rm A}$ = 0.89 ± 0.07 M$_\odot$) orbited by a planet which is the same size but less massive than Jupiter ($M_{\rm b}$ = 0.64 ± 0.06 $M_{\rm Jup}$, $R_{\rm b}$ = 1.05 ± 0.05 $R_{\rm Jup}$). The moderately different properties found by F13 placed the planet at the lower edge of the distribution of gas giant TEPs in the mass–radius diagram, making it a good candidate for hosting a heavy-element core despite the subsolar metallicity of the host star ([Fe/H] = −0.25 ± 0.10). The analysis by F13 was based on SuperWASP photometry (Pollacco et al. 2006), radial velocities from CORALIE spectra, plus two complete and one partial transit light curves from the Euler and TRAPPIST telescopes at ESO La Silla, Chile. No further work on this system has been published.

Early in the 2014 observing season a group of amateur astronomers noticed that the transits of WASP-57 were occurring half an hour earlier than expected, which is a significant fraction of the 2.3 h total transit duration. This was immediately confirmed using a transit of WASP-57 which had been serendipitously observed on 2014/05/18 using the Danish 1.5 m telescope, at La Silla. A second transit observation was scheduled on 2014/06/24 with the Danish telescope, the ESO 2.2 m telescope and GROND imager, and the immediately following transit with the amateur observers in Europe, allowing its early arrival to be reconfirmed. We also possess high-precision light curves of WASP-57 obtained in the 2012 season, before the imprecision of the original orbital ephemeris became apparent. In this work, we present all the data we have obtained for WASP-57, produce a revised ephemeris which can be used for follow-up observations in future, measure the physical properties of the system to high precision, and search for variations of the measured planetary radius with wavelength.

2 OBSERVATIONS AND DATA REDUCTION

A total of 10 transit light curves were obtained by LB, GC, CL, AM and GM using telescopes of apertures between 180 and 300 mm, sited in Italy. Further details of the observational setup and numbers of data points are given in Table 1.

Two complete transits of WASP-57 were observed using the 1.54 m Danish Telescope and DFOSC instrument at ESO La Silla, Chile (see Dominik et al. 2010), on the dates 2014/05/18 and 2014/06/24. DFOSC has a plate scale of 0.39 arcsec pixel^{-1} and a 2048^2 pixel CCD, giving a field of view of 13.7 arcmin × 13.7 arcmin. We windowed the CCD down to 1100 × 900 and 1045 × 920 pixels to shorten the dead time between exposures, resulting in images containing WASP-57 and six decent comparison stars. Both transits were obtained through a Bessell *R* filter. The instrument was defocussed in order to improve the efficiency of the observations, and to combat time-correlated noise (see Southworth et al. 2009). The telescope was autoguided to limit pointing drifts to less than five pixels over each observing sequence. An observing log is given in Table 2 and the light curves are plotted individually in Fig. 1.

The transit on 2014/06/24 observed with DFOSC was also monitored using GROND (Greiner et al. 2008) mounted on the MPG 2.2 m telescope at La Silla, Chile. GROND was used to obtain light curves simultaneously in four passbands, which approximate the SDSS *g*, *r*, *i* and *z* bands. The small field of view of this instrument (5.4 arcmin × 5.4 arcmin at a plate scale of 0.158 arcsec pixel^{-1}) meant that fewer comparison stars were available. The instrument was defocussed and the telescope was autoguided throughout the observing sequence. Poor weather conditions (high wind) forced closure of the telescope before the transit finished, so the light curves have only partial coverage of the transit (see Table 2 and Fig. 1).

We now turn to observations obtained prior to the conception of the current work. We observed WASP-57 on the night of 2012/05/10 using the BUSCA instrument on the 2.2 m telescope at Calar Alto Astronomical Observatory. BUSCA is capable of observing simultaneously in four passbands, for which we chose Gunn *u*, *g*, *r* and *z*. The motivation for these choices, and a detailed discussion on the use of BUSCA for planetary transit observations, can be found in Southworth et al. (2012). All four CCDs on BUSCA have a plate scale of 0.176 arcsec pixel^{-1}, but were operated with 2 × 2 binning. Whilst the full field of view of 12 × 12 arcmin was accessible in the *u* band, the available field in the *g*, *r* and *z* bands was vignetted into a circle of diameter of approximately 6 arcmin. The instrument was defocussed and the telescope was autoguided throughout the observations (Table 2). The *u*-band data are of insufficient quality for full modelling but can be used to obtain a time of minimum and to check for a possible variation of measured planetary radius with wavelength.

One transit of WASP-57 was observed on 2012/04/01 with EulerCam, using the same methods as for the EulerCam transit in F13. EulerCam is a CCD imager mounted on the 1.2 m Euler-Swiss telescope, La Silla, with a field of view of 14.7 arcmin × 14.7 arcmin at 0.23 arcsec pixel^{-1}. We obtained 212 images through a Gunn *r* filter, without applying a defocus to the instrument. Further details on EulerCam and the data reduction procedure can be found in Lendl et al. (2012).

Two transits of WASP-57 were observed on 2012/03/15 and 2012/04/01 using the 0.6 m TRAPPIST robotic telescope located at La Silla (Gillon et al. 2011; Jehin et al. 2011). The 2k × 2k CCD was thermoelectrically cooled and yielded a field of view of 22 arcmin × 22 arcmin at 0.65 arcsec pixel^{-1}. Images were obtained with a slight defocus and through a blue-blocking filter[2] that has a transmittance greater than 90 per cent from 500 nm to beyond 1000 nm.

2.1 Data reduction

The data from the amateur telescopes were all reduced using MaxIm DL.[3] In each case, the science images were calibrated using dark and flat-field frames.

The data from DFOSC, GROND and BUSCA were reduced using aperture photometry as implemented in the DEFOT code (Southworth et al. 2009, 2014), which relies on the IDL[4]/ASTROLIB[5] implementation of DAOPHOT (Stetson 1987). Master bias and flat-field images were constructed but generally found to have an insignificant effect on the quality of the photometry. Image motion was tracked by cross-correlating individual images with a reference image.

We obtained photometry on the instrumental system using software apertures of a range of sizes, and retained those which gave light curves with the smallest scatter (Table 2). We found that the choice of aperture size affects the scatter but not the shape of the

[2] http://www.astrodon.com/products/filters/exoplanet/
[3] http://www.cyanogen.com/maxim_main.php
[4] The acronym IDL stands for Interactive Data Language and is a trademark of ITT Visual Information Solutions. For further details see: http://www.exelisvis.com/ProductsServices/IDL.aspx.
[5] The ASTROLIB subroutine library is distributed by NASA. For further details see: http://idlastro.gsfc.nasa.gov/.

Table 1. Instrumental setup for the amateur observations. $N_{\rm obs}$ is the number of observations.

Date	Observer	Telescope	CCD	Filter	$N_{\rm obs}$
2014/05/24	C. Lopresti	180 mm Maksutov–Newton	SBIG ST10XME	Red	39
2014/06/10	G. Corfini	200 mm aperture, 800 mm focal length	SBIG STT-1603	Clear	87
2014/06/10	C. Lopresti	300 mm aperture, 1500 mm focal length	SBIG ST10XME	Red	42
2014/06/10	A. Marchini	300 mm Zen Maksutov–Cassegrain	STL-6303	Cousins *R*	58
2014/06/27	L. Barbieri	300 mm aperture, 3000 mm focal length	SBIG ST9	Clear	40
2014/06/27	G. Corfini	200 mm aperture, 800 mm focal length	SBIG STT-1603	Clear	34
2014/06/27	C. Lopresti	180 mm Maksutov–Newton	SBIG ST10XME	Red	16
2014/06/27	C. Lopresti	300 mm aperture, 1500 mm focal length	SBIG ST10XME	Red	58
2014/06/27	G. Marino	250 mm aperture, 1200 mm focal length	SBIG ST7-XME	Clear	64
2015/05/28	C. Lopresti	180 mm Maksutov–Newton	SBIG ST10XME	Red	30

Table 2. Log of the observations obtained from professional telescopes. $N_{\rm obs}$ is the number of observations, $T_{\rm exp}$ is the exposure time, $T_{\rm dead}$ is the dead time between exposures, 'Moon illum.' is the fractional illumination of the Moon at the mid-point of the transit, and $N_{\rm poly}$ is the order of the polynomial fitted to the out-of-transit data. The aperture radii are target aperture, inner sky and outer sky, respectively. The 'bb' filter is a blue-blocking filter.

Instrument	Date of first obs	Start time (UT)	End time (UT)	$N_{\rm obs}$	$T_{\rm exp}$ (s)	$T_{\rm dead}$ (s)	Filter	Airmass	Moon illum.	Aperture radii (pixels)			$N_{\rm poly}$	Scatter (mmag)
TRAPPIST	2012/03/15	04:34	08:20	367	20	10	bb	1.83 → 1.12 → 1.13	0.463	11.3	22.7	36.3	1	2.25
TRAPPIST	2012/04/01	04:40	09:36	701	15	7	bb	1.36 → 1.12 → 1.45	0.649	13.5	19.3	30.9	1	3.49
Euler	2012/04/01	05:20	09:35	212	50–180	16	*r*	1.23 → 1.12 → 1.44	0.649	24			0	0.98
BUSCA	2012/05/10	23:16	02:49	82	120	35	*u*	1.31 → 1.29 → 1.86	0.665	15	25	45	1	3.46
BUSCA	2012/05/10	23:16	03:37	100	120	35	*g*	1.31 → 1.29 → 2.46	0.665	17	27	50	1	1.26
BUSCA	2012/05/10	23:16	03:34	99	120	35	*r*	1.31 → 1.29 → 2.44	0.665	18	28	50	1	0.82
BUSCA	2012/05/10	23:16	03:37	98	120	35	*z*	1.31 → 1.29 → 2.46	0.665	18	28	50	1	1.58
DFOSC	2014/05/18	01:58	06:51	162	100	9	*R*	1.32 → 1.12 → 1.70	0.761	12	20	40	1	0.74
DFOSC	2014/06/24	23:33	04:15	155	100	8	*R*	1.27 → 1.12 → 1.53	0.050	16	26	45	1	0.71
GROND	2014/06/24	23:38	02:34	53	90–110	54	*g*	1.25 → 1.12 → 1.17	0.050	40	60	90	1	0.89
GROND	2014/06/24	23:38	02:34	53	90–110	54	*r*	1.25 → 1.12 → 1.17	0.050	40	60	90	1	0.58
GROND	2014/06/24	23:38	02:34	53	90–110	54	*i*	1.25 → 1.12 → 1.17	0.050	32	55	75	1	0.58
GROND	2014/06/24	23:38	02:34	53	90–110	54	*z*	1.25 → 1.12 → 1.17	0.050	30	50	80	1	1.02

transit in the final light curve. The instrumental magnitudes were then transformed to differential-magnitude light curves, normalized to zero magnitude outside transit using first-order polynomials (Table 2) fitted to the out-of-transit data. The differential magnitudes are relative to a weighted ensemble of typically five (DFOSC) or two to four (GROND) comparison stars. The comparison star weights and polynomial coefficients were simultaneously optimized to minimize the scatter in the out-of-transit data.

Finally, the timestamps for the data points were converted to the BJD(TDB) time-scale (Eastman, Siverd & Gaudi 2010). We performed manual time checks for several images obtained with DFOSC and verified that the FITS file timestamps are on the UTC system to within a few seconds. In recent work on the WASP-103 system, we found that the timestamps from DFOSC and GROND agree to within a few seconds, supporting the reliability of both (Southworth et al. 2015). The reduced data are given in Table 3 and will be lodged with the CDS.[6]

The data from EulerCam were reduced using aperture photometry following the methods given by Lendl et al. (2012). Differential aperture photometry was also used on the TRAPPIST data, using carefully selected extraction apertures and reference stars. For more details on the TRAPPIST data reduction procedures, see e.g. Gillon et al. (2013). The transit on 2012/04/01 was obtained in two sequences separated by a meridian flip, and the two sets of data were reduced independently.

2.2 High-resolution imaging

We obtained several images of WASP-57 with DFOSC in sharp focus, allowing us to check for the presence of faint nearby stars whose light might act to decrease the observed transit depth (Daemgen et al. 2009). The closest stars we found on any image are much fainter than WASP-57, and are over 45 arcsec distant, so are too far away to affect our photometry.

We also obtained a high-resolution image of WASP-57 using the Lucky Imager (LI) mounted on the Danish telescope (see Skottfelt et al. 2013, 2015). The LI uses an Andor 512 × 512 pixel electron-multiplying CCD, with a pixel scale of 0.09 arcsec pixel^{-1} giving a field of view of 45 arcsec × 45 arcsec. The data were reduced using a dedicated pipeline and the 2 per cent of images with the smallest point spread function (PSF) were shifted and added to yield a combined image whose PSF is smaller than the seeing limit. A long-pass dichroic was used, resulting in a response function which approximates that of SDSS *i*+*z*. An overall exposure time of 600 s corresponds to an effective exposure time of 12 s for the best 2 per cent of the images (Fig. 2). The full width at half-maximum (FWHM) of the PSF is 4.0 × 4.2 pixels (0.36 arcsec × 0.38 arcsec).

Two faint stars were detected on the LI image, at angular distances of 10.99 ± 0.05 arcsec and 21.56 ± 0.07 arcsec from WASP-57, and fainter by 8.7 ± 0.7 and 8.2 ± 0.4 mag. Neither of these stars is sufficiently bright and close to WASP-57 to affect the analysis presented in the current work. We assessed the limiting magnitude of the LI image by placing a box with sides equal to the FWHM of the star on each pixel on the image. The standard deviation of the counts within each box was calculated, and a 3σ detection threshold

[6] http://vizier.u-strasbg.fr/

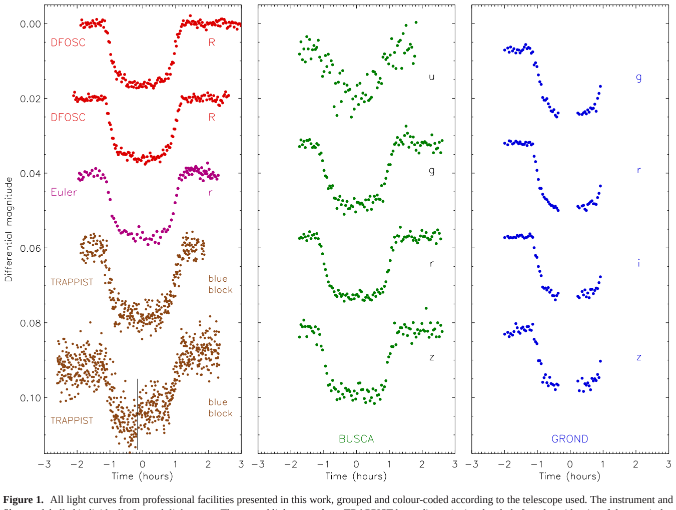

Figure 1. All light curves from professional facilities presented in this work, grouped and colour-coded according to the telescope used. The instrument and filter are labelled individually for each light curve. The second light curve from TRAPPIST has a discontinuity shortly before the mid-point of the transit due to a meridian-flip. This is indicated using a vertical black line.

was generated. The mean detection threshold at a given radius from the target star was then converted to a relative magnitude. Further details of the detection and reduction methods are given in Evans et al. (in preparation). The contrast curve is shown in Fig. 3.

3 TRANSIT TIMING ANALYSIS

The issue which brought WASP-57 to our attention was the offset between the predicted and actual times of transit. We have therefore obtained as many measured times of mid-transit as possible. We first modelled the two DFOSC transits individually using the JKTEBOP code (see below), as these are the two light curves which have full coverage of a transit with a low scatter in the data. We scaled the error bars for each light curve to yield a reduced χ^2 of $\chi^2_\nu = 1.0$ versus the fitted model. This step is necessary because the uncertainties from the APER algorithm tend to be moderately too small.

We then modelled the light curves from the amateur telescopes with JKTEBOP but fitting for only the time of mid-transit and the out-of-transit brightness of the system. The other photometric parameters were fixed to the best-fitting values from the two DFOSC light curves. The uncertainties in the transit times were multiplied by $\sqrt{\chi^2_\nu}$ to account for the underestimated observational errors in most of the data sets. We performed the same process on the GROND data, except this time we fitted the out-of-transit brightness as a linear function of time rather than just a constant offset from zero differential magnitude.

We then turned to published data. The discovery paper of WASP-57 (F13) contains two light curves observed with TRAPPIST and one with the Euler telescope. We fitted these as above, with the photometric parameters fitted for the two light curves with complete transit coverage and fixed for the TRAPPIST light curve which only contains the second half of a transit. We also included one transit time obtained by U. Dittler and lodged on the Exoplanet Transit Database[7] (Poddaný, Brát & Pejcha 2010).

The SuperWASP data which triggered the discovery of the planetary nature comprise approximately 30 000 data points obtained during the 2008, 2009 and 2010 observing seasons. These data were obtained and separated into individual seasons, then fitted with JKTEBOP in the same way as for the data obtained using amateur telescopes. The resulting season-averaged times of minimum are consistent with the linear ephemeris found below, but are of low precision. WASP-57 A, at V = 13.04, is comparatively faint for the SuperWASP telescopes so suffers from a large scatter in its light curve. We included these times of minimum light in the following

[7] The Exoplanet Transit Database (ETD) can be found at: http://var2.astro.cz/ETD/credit.php; see also TRESCA at: http://var2.astro.cz/EN/tresca/index.php.

Table 3. Sample of the data presented in this work (the first and last data points of each light curve). The full data set will be made available at the CDS.

Instrument	Filter	BJD(TDB)	Diff. mag.	Uncertainty
TRAPPIST	bb	2456001.690740	0.001 4100	0.003 3979
TRAPPIST	bb	2456001.847510	0.001 8100	0.001 9776
TRAPPIST	bb	2456018.694550	0.006 2000	0.004 1227
TRAPPIST	bb	2456018.900580	– 0.004 2000	0.004 1094
Euler	r	2456018.722460	0.001 5300	0.001 4096
Euler	r	2456018.899430	0.000 6000	0.001 0572
BUSCA	u	2456058.476778	0.001 1721	0.002 7719
BUSCA	u	2456058.624676	– 0.007 3014	0.005 0536
BUSCA	g	2456058.476778	0.000 8973	0.001 0736
BUSCA	g	2456058.657776	– 0.000 6933	0.001 5483
BUSCA	r	2456058.476778	0.000 4552	0.000 7219
BUSCA	r	2456058.655976	0.000 5960	0.000 9239
BUSCA	z	2456058.476778	0.001 8345	0.001 5082
BUSCA	z	2456058.657776	0.000 3519	0.001 7916
DFOSC	R	2456796.588810	0.000 4779	0.000 6752
DFOSC	R	2456796.792254	0.000 6067	0.000 8685
DFOSC	R	2456833.486396	– 0.000 6900	0.000 7120
DFOSC	R	2456833.683083	– 0.000 7523	0.000 7212
GROND	g	2456833.490392	0.000 0938	0.000 8559
GROND	g	2456833.611846	0.009 7990	0.000 9372
GROND	r	2456833.490392	0.000 0128	0.000 5593
GROND	r	2456833.611846	0.011 4375	0.000 6182
GROND	i	2456833.490392	0.000 2314	0.000 5610
GROND	i	2456833.611846	0.010 7411	0.000 9272
GROND	z	2456833.490392	0.001 0646	0.001 0125
GROND	z	2456833.611846	0.008 2877	0.001 0501

analysis, but note that they do not have a significant effect on the results.

All times of mid-transit were then fitted with a straight line versus cycle number to determine a new linear orbital ephemeris. Table 4 gives all transit times plus their residual versus the fitted ephemeris. We chose the reference epoch to be that for our BUSCA observations, in order to limit the covariance between the reference time of minimum and the orbital period. The resulting ephemeris is

$$T_0 = \mathrm{BJD(TDB)}\ 2\,456\,058.549\,10(16) + 2.838\,918\,56(81) \times E,$$

where E gives the cycle count versus the reference epoch and the bracketed quantities indicate the uncertainty in the final digit of the preceding number. This orbital period is 4.5 s (24σ) smaller than the value of 2.838 971 (2) d found by F13, explaining why we found the transits of WASP-57 to occur earlier than predicted. There are several plausible reasons for such a discrepancy to occur, but we are not in a position to choose between them.

The χ^2_ν of the fit is 1.99, and we interpret this as an indication that the uncertainty estimates for the timings are too small. Fig. 4 shows the residuals of the times of mid-transit versus the ephemeris given above. There is no sign of long-term transit timing variations.

4 LIGHT-CURVE ANALYSIS

Eight of our light curves cover a full transit at high photometric precision. The Euler and one of the two TRAPPIST light curves from F13 also satisfy this criterion. Each of these 10 data sets was modelled separately using the JKTEBOP[8] code (Southworth, Maxted & Smalley 2004) and the *Homogeneous Studies* methodology (Southworth 2012, and references therein). We did not subject those light curves with only partial coverage of a transit to this analysis, because the parameters derived from partial light curves are highly uncertain – so have little effect on the final results – and are often unreliable (e.g. Gibson et al. 2009).

The JKTEBOP model is based on the fractional radii of the star and the planet (r_A and r_b), which are the ratios between the true radii and the semimajor axis ($r_{A,b} = \frac{R_{A,b}}{a}$). The parameters of the fit to each light curve were the sum and ratio of the fractional radii ($r_A + r_b$ and $k = \frac{r_b}{r_A}$), the orbital inclination (i), limb darkening (LD) coefficients, and the time of mid-transit. We assumed an orbital eccentricity of zero, based on the finding by F13 that the Lucy & Sweeney (1971) test yielded a 100 per cent probability that the orbit was circular. We fixed the orbital period to the value found in Section 3. We also fitted for the coefficients of a first-order polynomial relating differential magnitude and time (Southworth et al. 2014), in order to allow for any errors in flux normalization which change with time or airmass. The TRAPPIST light curve obtained on the night of 2012/04/01 was split into two sequences by a meridian flip. This was accounted for by modelling both sequences together but specifying a separate polynomial (of order 1) for each sequence.

LD was incorporated using each of five laws (see Southworth 2008), with the linear coefficients either fixed at theoretically predicted values[9] or included as fitted parameters. We did not calculate fits for both LD coefficients in the four two-coefficient laws as they are very strongly correlated (Carter et al. 2008). The non-linear coefficients were instead perturbed by ± 0.1 on a flat distribution

[8] JKTEBOP is written in FORTRAN77 and the source code is available at http://www.astro.keele.ac.uk/jkt/codes/jktebop.html

[9] Theoretical LD coefficients were obtained by bilinear interpolation in $T_{\rm eff}$ and $\log g$ using the JKTLD code available from: http://www.astro.keele.ac.uk/jkt/codes/jktld.html

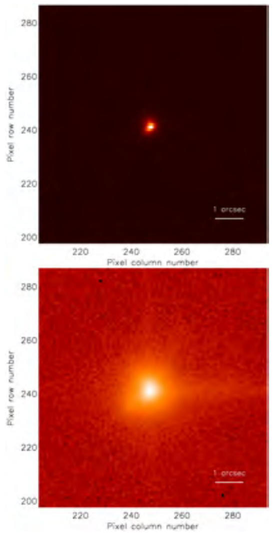

Figure 2. High-resolution Lucky Image of the field around WASP-57. The upper panel has a linear flux scale for context and the lower panel has a logarithmic flux scale to enhance the visibility of any faint stars. Each image covers 8 arcsec × 8 arcsec centred on WASP-57. A bar of length 1 arcsec is superimposed in the bottom-right of each image. The image is a sum of the best 2 per cent of the original images.

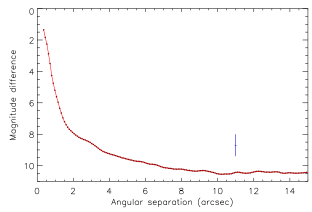

Figure 3. Contrast curve giving the limiting magnitude of the LI observation as a function of angular distance from WASP-57 (dark red circles connected by a red line). The closest detected star is shown as a blue data point.

during the error analysis simulations, to account for the uncertainty in theoretical LD coefficients.

Error estimates for the fitted parameters were obtained in four steps. Steps 1 and 2 were residual-permutation and Monte Carlo simulations (Southworth 2008), and the larger of the two alternatives was retained for each fitted parameter. For step 3, we ran solutions using the five different LD laws, and increased the error bar for each parameter to account for any disagreement between these five solutions. For step 4, we calculated the weighted mean of each photometric parameter using the values found separately from each light curve. This final step is a powerful external check on the reliability and mutual agreement between different data sets, as any discrepancies are obvious and quantifiable.

For all 10 light curves, we found that it was possible to fit for one of the two LD coefficients: reasonable values for the coefficients were obtained as well as a slightly smaller χ^2_ν compared to fits with both LD coefficients fixed. We therefore adopt these results, which are summarized in Table 5. Detailed tables of results for each light curve are available in the online-only appendix. The best fits are plotted in Fig. 5.

We find that the results from the different light curves are not in perfect agreement, with a χ^2_ν of 2.0 for $r_A + r_b$ and r_A, 2.8 for r_b and 3.7 for k versus the weighted mean of their values. This is due primarily to the TRAPPIST light curve from F13, which has a very small r_A and high i compared to the other data sets (Table 5). A degeneracy between these parameters is common (e.g. Carter et al. 2008; Southworth 2008) and arises because these two values together specify the observed transit duration, a quantity which is well determined by high-quality light curves. If we adopt instead the results from fitting this light curve with both LD coefficients fixed, the agreement becomes much better: k has $\chi^2_\nu = 2.5$, the other four parameters in Table 5 all have $\chi^2_\nu < 0.9$, and all photometric parameters change by less than their 1σ error bars. We have, however, chosen not to take this step for two reasons. First, theoretical LD coefficients are not perfect – if they were then different sources would give exactly the same values – and none are available calculated specifically for the TRAPPIST I+z filter. Secondly, taking an alternative approach for a discrepant data set raises the possibility of causing an underestimate of the true uncertainties in the measured quantities. We have therefore retained the discrepant values when calculating the weighted means of the photometric parameters, and have inflated the error bars on the weighted means by $\sqrt{\chi^2_\nu}$ in order to account for the discrepancy.

The photometric parameters found by F13 differ significantly from our results, by 4.7σ for r_A and 3.8σ for r_b (using our error bars to calculate the σ values as error estimates were not provided by F13 for these two quantities). This is due to the dependence of the F13 solution on only three transit light curves (two complete and one only partially covering a transit), all modelled simultaneously, of which one was the TRAPPIST data set we find to be discrepant. The value of k found by F13 (0.1127 ± 0.0006) is 3.8σ smaller than ours, and is evidence that the error estimates quoted by F13 are too small (see Southworth 2012 and references therein for other examples). An alternative explanation is the presence of star-spots, which is plausible for a star of this temperature. However, no traces of spot occultations are seen in our light curves and no rotational modulation is seen in the long-term WASP light curves.

5 PHYSICAL PROPERTIES

We measured the physical properties of the WASP-57 system using the results from Section 4, five grids of predictions from

Downloaded from http://mnras.oxfordjournals.org/ at Royal Library/Copenhagen University Library on December 20, 2015

Table 4. Times of minimum light and their residuals versus the ephemeris derived in this work. All but one of the timings were derived in the current work, from the source data given in the final column.

Time of min. (BJD/TDB)	Error (d)	Cycle no.	Residual (d)	Source
2454602.18313	0.003 17	– 513.0	– 0.000 75	This work (WASP 2008)
2454900.26529	0.003 06	– 408.0	– 0.005 04	This work (WASP 2009)
2455351.65767	0.002 55	– 249.0	– 0.000 71	This work (WASP 2010)
2455686.65086	0.000 55	– 131.0	0.000 09	This work (TRAPPIST)
2455723.55722	0.000 25	– 118.0	0.000 51	This work (Euler)
2455723.55606	0.000 28	– 118.0	– 0.000 65	This work (TRAPPIST)
2456001.76950	0.000 35	– 20.0	– 0.001 23	This work (TRAPPIST)
2456018.80454	0.000 17	– 14.0	0.000 30	This work (Euler)
2456018.80315	0.000 42	– 14.0	– 0.001 09	This work (TRAPPIST)
2456058.54852	0.001 43	0.0	– 0.000 58	This work (BUSCA u)
2456058.54891	0.000 39	0.0	– 0.000 19	This work (BUSCA g)
2456058.54959	0.000 23	0.0	0.000 49	This work (BUSCA r)
2456058.54913	0.000 42	0.0	0.000 03	This work (BUSCA z)
2456728.54099	0.001 71	236.0	0.007 11	Dittler (TRESCA)
2456796.66754	0.000 19	260.0	– 0.000 38	This work (DFOSC)
2456802.35000	0.007 10	262.0	0.004 24	This work (Lopresti)
2456819.38110	0.001 00	268.0	0.001 83	This work (Corfini)
2456819.36760	0.005 10	268.0	– 0.011 67	This work (Marchini)
2456833.57422	0.000 17	273.0	0.000 36	This work (DFOSC)
2456833.57442	0.000 34	273.0	0.000 56	This work (GROND g)
2456833.57296	0.000 21	273.0	– 0.000 90	This work (GROND r)
2456833.57389	0.000 22	273.0	0.000 03	This work (GROND i)
2456833.57460	0.000 39	273.0	0.000 74	This work (GROND z)
2456836.41480	0.002 90	274.0	0.002 02	This work (LBarbieri)
2456836.41880	0.002 50	274.0	0.006 02	This work (Corfini)
2456836.41490	0.001 90	274.0	0.002 12	This work (Lopresti)
2456836.41960	0.003 10	274.0	0.006 82	This work (Lopresti)
2456836.41840	0.002 90	274.0	0.005 62	This work (Marino)
2457171.40240	0.003 50	392.0	– 0.002 77	This work (Lopresti)

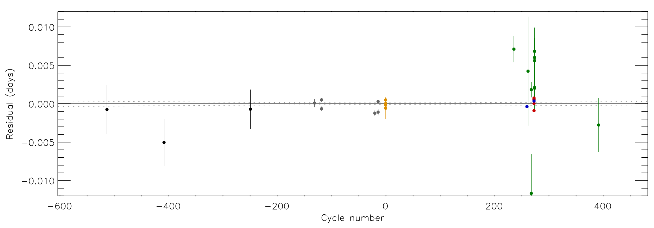

Figure 4. Plot of the residuals of the timings of mid-transit for WASP-57 versus a linear ephemeris (see Table 4). The points are colour-coded according to their source: black for the WASP data, green for the amateur timings in the current work, blue for DFOSC, red for GROND, off-yellow for BUSCA, and grey for the TRAPPIST and Euler telescopes. The dotted lines show the 1σ uncertainty in the ephemeris as a function of cycle number.

theoretical models of stellar evolution (Claret 2004; Demarque et al. 2004; Pietrinferni et al. 2004; VandenBerg, Bergbusch & Dowler 2006; Dotter et al. 2008), and the host-star spectroscopic properties. Theoretical models provide an additional constraint on the stellar properties, needed because the system properties cannot be obtained from only measured quantities. The spectroscopic properties were obtained by F13 and comprise effective temperature ($T_{\rm eff} = 5600 \pm 100$ K), metallicity ($[{\rm Fe/H}] = -0.25 \pm 0.10$) and velocity amplitude ($K_A = 100 \pm 7$ m s^{-1}). We used the physical constants tabulated by Southworth (2011).

We first estimated the velocity amplitude of the *planet*, K_b, which was used along with the measured r_A, r_b, i and K_A to determine the physical properties of the system (Southworth 2009). The estimate of K_b was then iterated to find the best match between the measured r_A and the calculated $\frac{R_A}{a}$, and the observed $T_{\rm eff}$ and that predicted by a theoretical model for the obtained stellar mass, radius and

Downloaded from http://mnras.oxfordjournals.org/ at Royal Library/Copenhagen University Library on December 20, 2015

Table 5. Parameters of the fit to the light curves of WASP-57 from the JKTEBOP analysis (top). The final parameters are given in bold and the parameters found by F13 are given below this. Quantities without quoted uncertainties were not given by F13 but have been calculated from other parameters which were.

Source	$r_A + r_b$	k	i (°)	r_A	r_b
Euler (2011/06/10)	0.1198 ± 0.0084	0.1139 ± 0.0027	87.04 ± 1.10	0.1075 ± 0.0073	0.01225 ± 0.001 09
TRAPPIST (2011/06/10)	0.1065 ± 0.0065	0.1087 ± 0.0027	89.94 ± 1.36	0.0961 ± 0.0055	0.01044 ± 0.000 73
Euler (2012/04/01)	0.1256 ± 0.0066	0.1190 ± 0.0029	86.56 ± 0.73	0.1123 ± 0.0057	0.01335 ± 0.000 99
TRAPPIST (2012/03/15)	0.1436 ± 0.0095	0.1263 ± 0.0026	85.28 ± 0.84	0.1275 ± 0.0082	0.01610 ± 0.001 36
TRAPPIST (2012/04/01)	0.1405 ± 0.0153	0.1179 ± 0.0042	85.16 ± 1.20	0.1257 ± 0.0140	0.01482 ± 0.001 94
BUSCA g (2012/05/10)	0.1370 ± 0.0131	0.1188 ± 0.0056	85.53 ± 1.12	0.1224 ± 0.0113	0.01455 ± 0.001 70
BUSCA r (2012/05/10)	0.1340 ± 0.0057	0.1186 ± 0.0015	85.70 ± 0.52	0.1198 ± 0.0050	0.01421 ± 0.000 74
BUSCA z (2012/05/10)	0.1328 ± 0.0098	0.1230 ± 0.0018	85.69 ± 0.84	0.1182 ± 0.0086	0.01454 ± 0.001 16
DFOSC (2014/05/18)	0.1309 ± 0.0057	0.1173 ± 0.0018	86.04 ± 0.52	0.1171 ± 0.0049	0.01374 ± 0.000 77
DFOSC (2014/06/24)	0.1306 ± 0.0066	0.1166 ± 0.0017	86.05 ± 0.63	0.1170 ± 0.0057	0.01364 ± 0.000 86
Final results	**0.1278 ± 0.0033**	**0.1182 ± 0.0013**	**86.05 ± 0.28**	**0.1143 ± 0.0029**	**0.01331 ± 0.000 51**
F13	0.1122	0.1127 ± 0.0006	$88.0^{+0.1}_{-0.2}$	0.1008	0.011 35

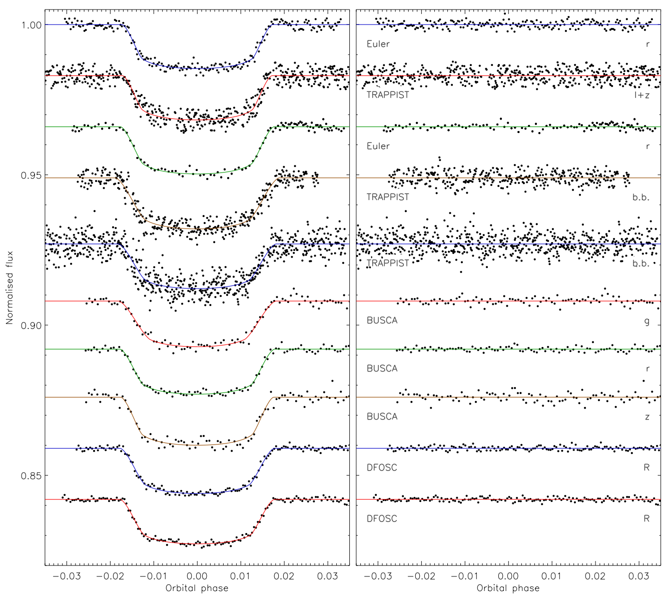

Figure 5. Phased light curves of WASP-57 compared to the JKTEBOP best fits (left) and the residuals of the fits (right). Labels give the source and passband for each data set. The polynomial baseline functions have been removed from the data before plotting. Only light curves with full coverage of a transit were included in this analysis.

Downloaded from http://mnras.oxfordjournals.org/ at Royal Library/Copenhagen University Library on December 20, 2015

Table 6. Derived physical properties of WASP-57. The values found by F13 are given for comparison.

Quantity	Symbol	Unit	This work	F13
Stellar mass	$M_{\rm A}$	$M_{\odot}$	$0.886 \pm 0.061 \pm 0.028$	0.954 ± 0.028
Stellar radius	$R_{\rm A}$	$R_{\odot}$	$0.927 \pm 0.031 \pm 0.010$	$0.836^{+0.07}_{-0.16}$
Stellar surface gravity	$\log g_{\rm A}$	cgs	$4.452 \pm 0.024 \pm 0.005$	$4.574^{+0.009}_{-0.012}$
Stellar density	$\rho_{\rm A}$	$\rho_{\odot}$	1.113 ± 0.085	$1.638^{+0.044}_{-0.063}$
Planet mass	$M_{\rm b}$	$M_{\rm Jup}$	$0.644 \pm 0.060 \pm 0.014$	$0.672^{+0.049}_{-0.046}$
Planet radius	$R_{\rm b}$	$R_{\rm Jup}$	$1.050 \pm 0.052 \pm 0.011$	$0.916^{+0.017}_{-0.014}$
Planet surface gravity	$g_{\rm b}$	m s^{-2}	14.5 ± 1.5	$18.3^{+2.9}_{-1.3}$
Planet density	$\rho_{\rm b}$	$\rho_{\rm Jup}$	$0.521 \pm 0.072 \pm 0.006$	$0.873^{+0.076}_{-0.071}$
Equilibrium temperature	$T'_{\rm eq}$	K	1338 ± 29	1251^{+21}_{-22}
Safronov number	Θ		$0.0522 \pm 0.0045 \pm 0.0006$	
Orbital semimajor axis	a	au	$0.037\,69 \pm 0.000\,88 \pm 0.000\,40$	0.0386 ± 0.0004

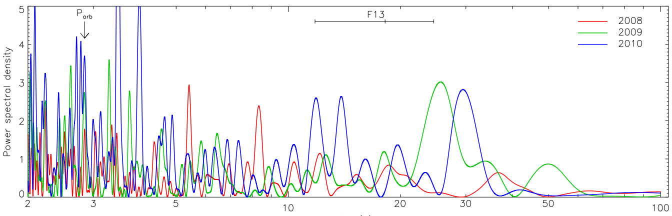

Figure 6. Scargle periodograms of the SuperWASP data from the 2008, 2009 and 2010 seasons. The orbital period of the system is shown with a downward-pointing arrow. The stellar rotational period inferred by F13 from its projected rotational velocity is shown by the horizontal error bar.

[Fe/H]. This was done for a grid of ages from the zero-age main sequence to beyond the terminal-age main sequence for the star, in 0.01 Gyr increments, and the overall best $K_{\rm b}$ was adopted. The statistical errors in the input quantities were propagated to the output quantities by a perturbation approach.

We ran the above analysis for each of the five sets of theoretical model predictions, yielding five different estimates of each output quantity. These were transformed into a single final result for each parameter by taking the unweighted mean of the five estimates and their statistical errors, plus an accompanying systematic error which gives the largest difference between the mean and individual values. The final results of this process are a set of physical properties for the WASP-57 system, each with a statistical error and a systematic error. The stellar density, planetary surface gravity and planetary equilibrium temperatures can be calculated without resorting to theoretical predictions (Seager & Mallén-Ornelas 2003; Southworth, Wheatley & Sams 2007; Southworth 2010), so do not have an associated systematic error.

Table 6 contains our measurements of the physical properties of the WASP-57 system. Compared to F13, we find a less massive but larger star. As planetary properties are measured relative to those of their parent star, the planet is similarly affected. The measured planetary density is 3.5σ lower, at $0.521 \pm 0.072\,\rho_{\rm Jup}$ compared to the value of $0.873^{+0.076}_{-0.071}\,\rho_{\rm Jup}$ found by F13. Our results are based on a much more extensive set of photometric data so are to be preferred to previous measurements, even though the error bars have not changed by much. A significant advance in our understanding of the WASP-57 system could be achieved by obtaining further spectroscopy of the host star, from which more precise values for $T_{\rm eff}$, [Fe/H] and $K_{\rm A}$ could be measured. This is of particular interest because of its metal-poor nature, whose effect on the incidence of different types of planets is currently under discussion (Buchhave et al. 2014; Wang & Fischer 2015).

The age of the system is unconstrained in our analysis above, as often occurs when the host star is significantly less massive than 1 M$_{\odot}$. F13 inferred age estimates of $\gtrsim$2 Gyr for WASP-57 A from its photospheric lithium abundance, and $\sim 1.9^{+2.4}_{-1.2}$ Gyr from gyrochronological arguments and its rotation period derived from its radius and projected rotational velocity. The $T_{\rm eff}$ of the star is within the regime where star-spots are common so we have checked if it is possible to precisely determine its rotation period from spot-induced modulation. A Lomb–Scargle periodogram was calculated for each of the three seasons of SuperWASP data and can be seen in Fig. 6. There are no strong peaks in the period interval of interest (5–30 d), and no moderately strong peaks present at the same period in all three seasons. We conclude that the rotational modulation of the star is below the level of detection with the current data.

5.1 Comparison with theoretical models of giant planets

F13 found that the measured mass and density of WASP-57 b implied the presence of a heavy-element core of mass roughly 50 M$_{\oplus}$, via a comparison to the theoretical predictions of Fortney, Marley & Barnes (2007). This rather large core mass is surprising given the significantly subsolar metal abundance of the host star ([Fe/H] $= -0.25 \pm 0.10$). As we have found a significantly lower density for the planet (smaller by 40 per cent or 3.5σ), it is germane to reconsider this conclusion. We have therefore compared our new mass and radius measurements with predictions based on three batches of theoretical models.

Bodenheimer, Laughlin & Lin (2003, their tables 1 and 2) provided predicted radii for planets of mass 0.69 $M_{\rm Jup}$ and $T'_{\rm eq} = 1000$ and 1500 K. Their radii are 1.01–1.10 $R_{\rm Jup}$ with, and 1.03–1.13 $R_{\rm Jup}$ without, a core or additional kinetic heating of the planetary interior. Both are in very good agreement with the radius of $1.05 \pm 0.05\,R_{\rm Jup}$ we find for WASP-57 b.

Baraffe, Chabrier & Barman (2008, their table 4) find planetary radii of 0.97–1.06 $R_{\rm Jup}$ for planets of mass 0.5–1.0 $M_{\rm Jup}$ and age 0.5–5 Gyr, again in accord with our results. These values are for a heavy-element fraction of $Z = 0.02$, and larger fractions result in progressively smaller radii and thus poorer agreement with our radius measurement.

Finally, the properties of WASP-57 b match the predictions of Fortney et al. (2007, their fig. 6) for a 25 M$_{\oplus}$ heavy-element core. The difference in radius between models with and without this core are only 0.05 $R_{\rm Jup}$ for a 1 $M_{\rm Jup}$ planet and 0.18 $R_{\rm Jup}$ for a 0.3 $M_{\rm Jup}$ planet, so are of a comparable size to the uncertainty in the radius of WASP-57 b. Our measured properties for this planet therefore do not provide significant support for a high metallicity or the presence of a heavy-element core.

6 VARIATION OF RADIUS WITH WAVELENGTH

Two of our data sets include observations in four passbands simultaneously ($ugrz$ for BUSCA and $griz$ for GROND), whereas we have r- or R-band photometry from four different sources (DFOSC, EulerCam, BUSCA and GROND), so it is relevant to search for possible changes in the measured radius of the planet as a function of wavelength. Such analyses are the photometric equivalent of transmission spectroscopy (Seager & Sasselov 2000) and have been pioneered at optical wavelengths by Sing et al. (2011b), de Mooij et al. (2012) and Southworth et al. (2012).

Changes in the radius measured from planetary transits, as a function of wavelength, are predicted to occur due to opacity variations which affect the height at which the atmosphere transmits light coming from the parent star in the direction of the observer. At blue wavelengths, a greater atmospheric opacity due to Rayleigh and Mie scattering leads to a higher maximum depth at which starlight is transmitted, causing an increase in the measured radius of the planet (e.g. Pont et al. 2008; Nikolov et al. 2015). Enhanced opacity also leads to signatures of sodium and potassium at optical wavelengths (Fortney et al. 2008), although only narrow absorption cores have been detected so far (Nikolov et al. 2015).

The fundamental observable in this work is the transit depth, represented in our notation by the ratio of the radii k or the fractional planetary radius $r_{\rm b}$. The parameter directly comparable to theoretical predictions is the true planetary radius, $R_{\rm b}$. The parameter $r_{\rm b}$ is correlated with other photometric parameters (see e.g. Southworth 2008), and its transformation into $R_{\rm b}$ requires other parameters which have uncertainty but are common to all photometric passbands (the error budgets calculated in the previous section show that these are $r_{\rm A}$, $T_{\rm eff}$ and [Fe/H]).

We removed these two effects in order to determine $R_{\rm b}$ values with relative error bars. We did this by refitting the light curves

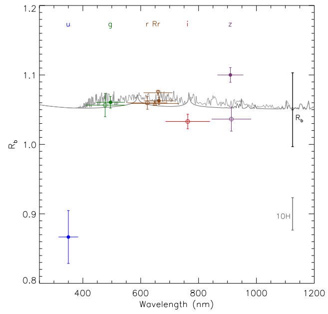

Figure 7. Measured planetary radius ($R_{\rm b}$) as a function of the central wavelength of the passbands used for the different light curves. The data points show the $R_{\rm b}$ measured from each light curve. The vertical error bars show the relative uncertainty in $R_{\rm b}$ (i.e. neglecting the common sources of error) and the horizontal error bars indicate the FWHM of the passband. The data points are colour-coded according to passband, and the passbands are labelled at the top of the figure. The symbol types are filled circles (BUSCA), open circles (GROND), upward-pointing arrow (DFOSC) and downward-pointing arrow (Euler). On the right of the plot, we show the value of $R_{\rm b}$ measured in Section 4 and the size of 10 atmospheric pressure scaleheights (10 H). The grey lines through the empirical data points show theoretical predictions for a transmission spectrum of a gas-giant planet of solar chemical composition from Madhusudhan (priv. comm.). The darker-grey line includes features due to Na and K whereas the lighter grey line also includes TiO opacity.

with all parameters fixed except k, T_0, the linear LD coefficient for the quadratic LD law, and the coefficients of the polynomials between differential magnitude and time. We then transformed the resulting $r_{\rm b}$ values into $R_{\rm b}$ using a fixed orbital semimajor axis, a. This yielded a set of $R_{\rm b}$ values and error bars which are directly comparable to each other. The uncertainties in $r_{\rm b}$ were measured using 1000 Monte Carlo simulations each.

The data included in this analysis were the two Euler light curves (modelled simultaneously), the two DFOSC light curves (modelled simultaneously), the BUSCA $ugrz$ and the GROND $griz$ data. We did not include the TRAPPIST light curves because the very wide passbands ($I+z$ or blue-blocking filters) yield minimal spectral resolution. Although the GROND data only partially cover a transit, which precluded their use in Section 4, they give reliable results here because $r_{\rm A}$ and i were fixed during the fitting process.

Fig. 7 shows the resulting values of $R_{\rm b}$ as a function of the central wavelength of the passbands used. The FWHMs of the passbands are shown for reference using horizontal lines. The originating $r_{\rm b}$ values and passband characteristics are collected in Table 7. Two conclusions are immediately apparent from this figure. First, the planetary radius in the u-band is very small and very uncertain. Secondly, the $grRiz$ results are consistent with no variation of $R_{\rm B}$ with wavelength.

The u-band light curve shows a small transit depth and a high scatter (see Fig. 7), which causes the anomalous $r_{\rm b}$ measurement in

Table 7. Values of $r_{\rm b}$ and $R_{\rm b}$ for each of the light curves. The error bars exclude all common sources of uncertainty in $r_{\rm b}$ and $R_{\rm b}$ so should only be used to compare different values of $r_{\rm b}(\lambda)$. The final column gives the size of the error bar on $R_{\rm b}$ in atmospheric scaleheights.

Instrument	Passband	$\lambda_{\rm cen}$ (nm)	FWHM (nm)	$r_{\rm b}$	$R_{\rm b}$ ($R_{\rm Jup}$)	σ (H)
Euler	Gunn r	660.0	100.0	$0.013\,62 \pm 0.000\,04$	0.867 ± 0.038	8.2
BUSCA	Gunn u	350.0	68.0	$0.010\,99 \pm 0.000\,48$	1.061 ± 0.008	1.8
BUSCA	Gunn g	495.5	99.5	$0.013\,45 \pm 0.000\,11$	1.063 ± 0.005	1.2
BUSCA	Gunn r	663.0	105.0	$0.013\,48 \pm 0.000\,07$	1.100 ± 0.011	2.3
BUSCA	Gunn z	910.0	90.0	$0.013\,95 \pm 0.000\,13$	1.057 ± 0.017	3.6
DFOSC	Bessell R	648.9	164.7	$0.013\,43 \pm 0.000\,03$	1.060 ± 0.009	2.0
GROND	Gunn g	477.0	137.9	$0.013\,40 \pm 0.000\,21$	1.033 ± 0.010	2.2
GROND	Gunn r	623.1	138.2	$0.013\,44 \pm 0.000\,11$	1.036 ± 0.017	3.7
GROND	Gunn i	762.5	153.5	$0.013\,10 \pm 0.000\,13$	1.059 ± 0.003	0.6
GROND	Gunn z	913.4	137.0	$0.013\,14 \pm 0.000\,22$	1.074 ± 0.004	0.8

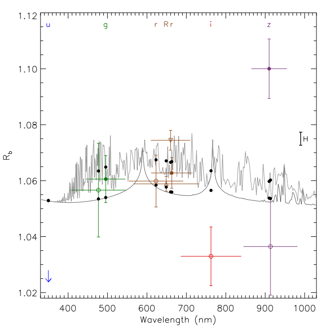

Figure 8. Close-up of the main part of Fig. 7 showing the $R_{\rm b}$ measurements and theoretical transmission spectra. The u-band result is off the plot. Its central wavelength is indicated with a downward-pointing arrow. The size of one atmospheric scaleheight is indicated to the right of the plot. The black circles are the values of passband averages of the two transmission spectra, and are shown at the central wavelengths of the relevant passbands.

this band. The discrepancy relative to the overall $r_{\rm b}$ value obtained in Section 4 is highly significant at 4.8σ, and corresponds to approximately 39H. H is the pressure scaleheight, and in the case of WASP-57 b is 334 ± 35 km ($0.0047 \pm 0.0005\,R_{\rm Jup}$). A variation in $R_{\rm b}$ of the size of 39H is difficult to explain, and is not believable unless confirmed by additional data of much higher quality. The two z-band light curves also show a clear disagreement of size 3.2σ.

Fig. 7 also shows two theoretical transmission spectra calculated under different assumptions by Madhusudhan (priv. comm.) using the atmosphere code of Madhusudhan & Seager (2009). These predictions are for a gas-giant planet of radius 1.25 $R_{\rm Jup}$ and surface gravity 25 m s^{-2} so have been scaled to match the smaller radius and lower gravity of WASP-57 b. Our finding of a small u-band $r_{\rm b}$ is not consistent with these theoretical predictions.

A close-up of the main part of Fig. 7 is shown in Fig. 8. Passband-averaged values for the transmission spectra are shown with black filled circles, and differ by up to 2H. The Rayleigh scattering slope could be significantly greater than this: Sing et al. (2011a) found that Rayleigh scattering caused the measured radius of HD 189733 b to be larger by 5H at 400 nm than at 900 nm.

The relative uncertainties in our measured radii for WASP-57 b are below 1H for two, and below 2H for five, of the 10 light curves (see Table 7). We are therefore sensitive to radius variations at the level of 1H, which is smaller than both the difference between the two theoretical transmission spectra and the size of the Rayleigh scattering slope detected for HD 189733 b. Our data are therefore sensitive, in principle, to the atmospheric properties of WASP-57 b. However, in practise, our measurements are insufficient for studying the atmosphere of this planet due to the anomalous result for the u band and the scatter of the radius measurements in the i and z bands. The situation could be improved by obtaining data in narrower passbands (i.e. higher spectral resolution), and with repeated observations over the full optical wavelength range. Particular attention should be paid to the u band, which is an important discriminant between the two transmission spectra and also enhances sensitivity to the Rayleigh scattering slope.

7 SUMMARY AND CONCLUSIONS

WASP-57 b is a relatively low-mass hot Jupiter orbiting a cool star. Amateur astronomers first noticed that its transits were occurring earlier than predicted, a finding subsequently confirmed by observations from professional facilities. We have presented 10 transit light curves from amateur astronomers, plus 13 obtained using professional telescopes of which seven predate the discovery of inaccuracy in the orbital ephemeris of the system. We have determined a revised orbital ephemeris which differs by 24σ from the orbital period in the discovery paper, and can be used to predict transits to a precision of less than 1 min until the year 2170. We also obtained high-resolution Lucky Imaging observations, which show no evidence for nearby companions whose flux might have contaminated our light curves.

We have used these and previously published data to redetermine the physical properties of the WASP-57 system, finding that both the planet and its host star are larger and less massive than previously thought. A comparison of our new results for WASP-57 b to theoretical predictions for the properties of gaseous planets reveals a good agreement with models lacking a core or additional heat sources. This disagrees with the core mass of 50 M$_{\oplus}$ postulated by F13, but is in accord with expectations for a planet which formed around a star of significantly subsolar metal abundance.

We observed two of the transits of WASP-57 using two 2.2 m telescopes equipped with simultaneous multiband imaging instruments: GROND ($griz$ passbands) and BUSCA ($ugrz$ passbands). These data are well suited to investigating the possible wavelength-dependence of the planet's measured radius due to effects such as Rayleigh and Mie scattering, and atomic and molecular absorption. Whilst the radii in the g and r/R bands are in generally good agreement, the i-band measurement is slightly smaller than expected and the two z-band measurements are discrepant by 3σ. The u-band radius is crucial for measuring the Rayleigh scattering slope, as well as separating the pM and pL classes proposed by Fortney et al. (2008). Our measurement is 5σ below theoretical predictions, and the size of the discrepancy is inexplicable using current theoretical transmission spectra. This result is almost certainly spurious, and can plausibly be blamed on the strong absorption by Earth's atmosphere at blue-optical wavelengths plus the faintness of the host star in this passband.

7.1 Future opportunities for transmission photometry

Successful detections of radius variations in optical transmission photometry have recently been announced for the TEPs GJ 3470 b (Nascimbeni et al. 2013; Biddle et al. 2014), Qatar-2 b (Mancini et al. 2014) and WASP-103 b (Southworth et al. 2015). Only one of these studies presented data obtained shortward of the Balmer jump, which is an important but observationally difficult wavelength interval (see Fig. 8).

Transit light curves in the u and U bands have previously been presented for several TEPs, and have shown planetary radii either consistent with other optical passbands (WASP-12, Copperwheat et al. 2013; TrES-3, Turner et al. 2013; WASP-17, Bento et al. 2014; WASP-39 and WASP-43, Ricci et al. 2015; XO-2, Zellem et al. 2015) or somewhat larger than other optical passbands (HAT-P-5, Southworth et al. 2012; Dittman 2012, priv. comm.; GJ 3470, Nascimbeni et al. 2013). A universal feature of these studies is the reliance on either a single u-band transit light curve, which yields large uncertainties on the measured planetary radius, or the use of data not obtained simultaneously in multiple passbands, so the results are hostage to temporal changes such as induced by magnetic activity in the host stars. Most transmission photometry studies also suffer from the use of wide passbands, which are insensitive to spectral features other than broad continuum slopes (see Nikolov et al. 2013).

Whilst suffering from a lower spectral resolution, transmission photometry has several advantages over transmission spectroscopy. These include being able to observe over a wide wavelength interval without being subject to second-order contamination, the ability to use comparison stars more distant from the planet host star, and the option to use telescope defocusing techniques to avoid systematic noise (but see Burton et al. 2015, for a counter-example). Smaller telescopes can be used, making it easier in particular to observe multiple transits and thus demonstrate the repeatability of the experiment (Bean et al. 2013; Gibson 2014).

We therefore advocate studies based on observations of multiple transits, obtained simultaneously through many intermediate or narrow passbands. These passbands should be well defined by interference filters, thus avoiding compromises such as the variable red edge of the z filter due to its reliance on the quantum efficiency curve of the CCD used (e.g. Fukugita et al. 1996) or the red leak in some u and U filters which is capable of causing spurious results for optically blue objects (e.g. Guhathakurta et al. 1998). With a sufficient number of passbands, it should be possible to achieve low-resolution spectroscopy of the atmospheres of extra-solar planets through the full optical wavelength range using the transmission-photometry approach.

ACKNOWLEDGEMENTS

Giorgio Corfini suddenly passed away at the end of 2014. He had been for many years an active observer and member of the 'Unione Astrofili Italiani' (UAI). The UAI and the working groups of the sections 'Extrasolar Planets' and 'Variable Stars' acknowledge his important contribution and would like to dedicate this paper to his memory.

The operation of the Danish 1.54 m telescope is financed by a grant to UGJ from the Danish Natural Science Research Council (FNU). This paper incorporates observations collected using the Gamma Ray Burst Optical and Near-Infrared Detector (GROND) instrument at the MPG 2.2 m telescope located at ESO La Silla, Chile, program 093.A-9007(A). GROND was built by the high-energy group of MPE in collaboration with the LSW Tautenburg and ESO, and is operated as a PI-instrument at the MPG 2.2 m telescope. This paper incorporates observations collected at the Centro Astronómico Hispano Alemán (CAHA) at Calar Alto, Spain, operated jointly by the Max-Planck Institut für Astronomie and the Instituto de Astrofísica de Andalucía (CSIC). TRAPPIST is funded by the Belgian Fund for Scientific Research (Fond National de la Recherche Scientifique, FNRS) under the grant FRFC 2.5.594.09.F, with the participation of the Swiss National Science Fundation (SNF). MG and EJ are FNRS Research Associates. LD is a FNRS/FRIA Doctoral Fellow. We thank the anonymous referee for a helpful report and Dr Francesca Faedi for discussions. The reduced light curves presented in this work will be made available at the CDS (http://vizier.u-strasbg.fr/) and at http://www.astro.keele.ac.uk/∼jkt/. J Southworth acknowledges financial support from STFC in the form of an Advanced Fellowship. This publication was partially supported by grant NPRP X-019-1-006 from Qatar National Research Fund (a member of Qatar Foundation). TCH is supported by the Korea Astronomy & Space Science Institute travel grant #2014-1-400-06. TCH acknowledges support from the Korea Astronomy and Space Science Institute (KASI) grant 2014-1-400-06. OW (FNRS research fellow) and J Surdej acknowledge support from the Communauté française de Belgique – Actions de recherche concertées – Académie Wallonie-Europe. The following internet-based resources were used in research for this paper: the ESO Digitized Sky Survey; the NASA Astrophysics Data System; the SIMBAD data base and VizieR catalogue access tool operated at CDS, Strasbourg, France; and the arχiv scientific paper preprint service operated by Cornell University. Based on data collected by MiNDSTEp with the Danish 1.54 m telescope, and data collected with GROND on the MPG 2.2 m telescope, both located at ESO La Silla.

REFERENCES

Baraffe I., Chabrier G., Barman T., 2008, A&A, 482, 315
Bean J. L., Désert J.-M., Seifahrt A., Madhusudhan N., Chilingarian I., Homeier D., Szentgyorgyi A., 2013, ApJ, 771, 108
Benítez-Llambay P., Masset F., Beaugé C., 2011, A&A, 528, A2
Bento J. et al., 2014, MNRAS, 437, 1511
Biddle L. I. et al., 2014, MNRAS, 443, 1810
Bodenheimer P., Laughlin G., Lin D. N. C., 2003, ApJ, 592, 555
Buchhave L. A. et al., 2014, Nature, 509, 593
Burton J. R., Watson C. A., Rodríguez-Gil P., Skillen I., Littlefair S. P., Dhillon S., Pollacco D., 2015, MNRAS, 446, 1071

Carter J. A., Yee J. C., Eastman J., Gaudi B. S., Winn J. N., 2008, ApJ, 689, 499
Charbonneau D., Brown T. M., Latham D. W., Mayor M., 2000, ApJ, 529, L45
Claret A., 2004, A&A, 424, 919
Copperwheat C. M. et al., 2013, MNRAS, 434, 661
Daemgen S., Hormuth F., Brandner W., Bergfors C., Janson M., Hippler S., Henning T., 2009, A&A, 498, 567
de Mooij E. J. W. et al., 2012, A&A, 538, A46
Demarque P., Woo J.-H., Kim Y.-C., Yi S. K., 2004, ApJS, 155, 667
Dominik M. et al., 2010, Astron. Nachr., 331, 671
Dotter A., Chaboyer B., Jevremović D., Kostov V., Baron E., Ferguson J. W., 2008, ApJS, 178, 89
Eastman J., Siverd R., Gaudi B. S., 2010, PASP, 122, 935
Faedi F. et al., 2013, A&A, 551, A73
Fortney J. J., Marley M. S., Barnes J. W., 2007, ApJ, 659, 1661
Fortney J. J., Lodders K., Marley M. S., Freedman R. S., 2008, ApJ, 678, 1419
Fukugita M., Ichikawa T., Gunn J. E., Doi M., Shimasaku K., Schneider D. P., 1996, AJ, 111, 1748
Gibson N. P., 2014, MNRAS, 445, 3401
Gibson N. P. et al., 2009, ApJ, 700, 1078
Gillon M., Jehin E., Magain P., Chantry V., Hutsemékers D., Manfroid J., Queloz D., Udry S., 2011, in Bouchy F., Díaz R., Moutou C., eds, European Physical Journal Web of Conferences, Vol. 11, Detection and Dynamics of Transiting Exoplanets. EPJ Web Conf., p. 6002
Gillon M. et al., 2013, A&A, 552, A82
Greiner J. et al., 2008, PASP, 120, 405
Guhathakurta P., Webster Z. T., Yanny B., Schneider D. P., Bahcall J. N., 1998, AJ, 116, 1757
Hellier C. et al., 2012, MNRAS, 426, 739
Henry G. W., Marcy G. W., Butler R. P., Vogt S. S., 2000, ApJ, 529, L41
Jehin E. et al., 2011, The Messenger, 145, 2
Konacki M., Torres G., Jha S., Sasselov D. D., 2003, Nature, 421, 507
Lendl M. et al., 2012, A&A, 544, A72
Lucy L. B., Sweeney M. A., 1971, AJ, 76, 544
Madhusudhan N., Seager S., 2009, ApJ, 707, 24
Mancini L. et al., 2014, MNRAS, 443, 2391
Mordasini C., Alibert Y., Benz W., 2009a, A&A, 501, 1139
Mordasini C., Alibert Y., Benz W., Naef D., 2009b, A&A, 501, 1161
Nascimbeni V., Piotto G., Pagano I., Scandariato G., Sani E., Fumana M., 2013, A&A, 559, A32
Nikolov N., Chen G., Fortney J., Mancini L., Southworth J., van Boekel R., Henning T., 2013, A&A, 553, A26
Nikolov N. et al., 2015, MNRAS, 447, 463
Pietrinferni A., Cassisi S., Salaris M., Castelli F., 2004, ApJ, 612, 168
Poddaný S., Brát L., Pejcha O., 2010, New Astron., 15, 297
Pollacco D. L. et al., 2006, PASP, 118, 1407
Pont F., Knutson H., Gilliland R. L., Moutou C., Charbonneau D., 2008, MNRAS, 385, 109
Ricci D. et al., 2015, PASP, 127, 143
Rowe J. F. et al., 2014, ApJ, 784, 45
Seager S., Mallén-Ornelas G., 2003, ApJ, 585, 1038
Seager S., Sasselov D. D., 2000, ApJ, 537, 916
Sing D. K. et al., 2011a, MNRAS, 416, 1443
Sing D. K. et al., 2011b, A&A, 527, A73
Skottfelt J. et al., 2013, A&A, 553, A111
Skottfelt J. et al., 2015, A&A, 574, A54
Southworth J., 2008, MNRAS, 386, 1644
Southworth J., 2009, MNRAS, 394, 272
Southworth J., 2010, MNRAS, 408, 1689
Southworth J., 2011, MNRAS, 417, 2166
Southworth J., 2012, MNRAS, 426, 1291
Southworth J., Maxted P. F. L., Smalley B., 2004, MNRAS, 349, 547
Southworth J., Wheatley P. J., Sams G., 2007, MNRAS, 379, L11
Southworth J. et al., 2009, MNRAS, 396, 1023
Southworth J., Mancini L., Maxted P. F. L., Bruni I., Tregloan-Reed J., Barbieri M., Ruocco N., Wheatley P. J., 2012, MNRAS, 422, 3099
Southworth J. et al., 2014, MNRAS, 444, 776
Southworth J. et al., 2015, MNRAS, 447, 711
Stetson P. B., 1987, PASP, 99, 191
Turner J. D. et al., 2013, MNRAS, 428, 678
VandenBerg D. A., Bergbusch P. A., Dowler P. D., 2006, ApJS, 162, 375
Wang J., Fischer D. A., 2015, AJ, 149, 14
Zellem R. T. et al., 2015, ApJ, 810, 11

SUPPORTING INFORMATION

Additional Supporting Information may be found in the online version of this article: (http://mnras.oxfordjournals.org/lookup/suppl/doi:10.1093/mnras/stv2183/-/DC1)

Table 1. Instrumental setup for the amateur observations.
Table 2. Log of the observations obtained from professional telescopes.
Table 3. Sample of the data presented in this work (the first and last data points of each light curve).
Table 4. Times of minimum light and their residuals versus the ephemeris derived in this work.
Table 5. Parameters of the fit to the light curves of WASP-57 from the JKTEBOP analysis (top).
Table 6. Derived physical properties of WASP-57.
Table 7. Values of $r_{\rm b}$ and $R_{\rm b}$ for each of the light curves.

Please note: Oxford University Press are not responsible for the content or functionality of any supporting materials supplied by the authors. Any queries (other than missing material) should be directed to the corresponding author for the article.

[1] *Astrophysics Group, Keele University, Staffordshire ST5 5BG, UK*
[2] *Max Planck Institute for Astronomy, Königstuhl 17, D-69117 Heidelberg, Germany*
[3] *NASA Ames Research Center, Moffett Field, CA 94035, USA*
[4] *NASA Exoplanet Science Institute, MS 100-22, California Institute of Technology, Pasadena, CA 91125, USA*
[5] *Dipartimento di Fisica 'E.R. Caianiello', Università di Salerno, Via Giovanni Paolo II 132, I-84084 Fisciano (SA), Italy*
[6] *Istituto Internazionale per gli Alti Studi Scientifici (IIASS), I-84019 Vietri Sul Mare (SA), Italy*
[7] *Istituto Nazionale di Fisica Nucleare, Sezione di Napoli, I-80126 Napoli, Italy*
[8] *Institut d'Astrophysique et de Géophysique, Université de Liège, B-4000 Liège, Belgium*
[9] *SUPA, University of St Andrews, School of Physics & Astronomy, North Haugh, St Andrews KY16 9SS, UK*
[10] *Niels Bohr Institute & Centre for Star and Planet Formation, University of Copenhagen, Øster Voldgade 5, DK-1350 Copenhagen, Denmark*
[11] *Observatoire de Genève, Université de Genève, Chemin des maillettes 51, CH-1290 Sauverny, Switzerland*
[12] *Sezione Pianeti Extrasolari – Unione Astrofili Italiani (UAI)*
[13] *Gruppo Astrofili Catanesi – Catania, Italy*
[14] *AAB Associazione Astrofili Bolognesi, Bologna, Italy*
[15] *Department of Physics, University of Atacama, Copayapu 485, Copiapo, Chile*
[16] *Istituto Spezzino Ricerche Astronomiche – I.R.A.S., La Spezia, Italy*
[17] *DSFTA – Astronomical Observatory, University of Siena, Via Roma 56, I-53100 Siena, Italy*
[18] *Gruppo Astrofili Catanesi (GAC) – Catania, Italy*
[19] *Qatar Environment and Energy Research Institute, Qatar Foundation, Tornado Tower, Floor 19, 5825 Doha, Qatar*
[20] *European Southern Observatory, Karl-Schwarzschild-Straße 2, D-85748 Garching bei München, Germany*
[21] *Korea Astronomy and Space Science Institute, Daejeon 305-348, Republic of Korea*

[22] *Finnish Centre for Astronomy with ESO (FINCA), University of Turku, Väisäläntie 20, FI-21500 Piikkiö, Finland*
[23] *Instituto de Astrofisica, Facultad de Fısica, Pontificia Universidad Católica de Chile, Av. Vicuña Mackenna 4860, 7820436 Macul, Santiago, Chile*
[24] *Department of Physics, Sharif University of Technology, 11155-9161 Tehran, Iran*
[25] *Astronomisches Rechen-Institut, Zentrum für Astronomie, Universität Heidelberg, Mönchhofstraße 12-14, D-69120 Heidelberg, Germany*
[26] *Centre of Electronic Imaging, Department of Physical Sciences, The Open University, Milton Keynes MK7 6AA, UK*
[27] *Planetary and Space Sciences, Department of Physical Sciences, The Open University, Milton Keynes MK7 6AA, UK*

This paper has been typeset from a TEX/LATEX file prepared by the author.

A&A 584, A104 (2015)
DOI: 10.1051/0004-6361/201526899

Astronomy & Astrophysics

Rotation periods and astrometric motions of the Luhman 16AB brown dwarfs by high-resolution lucky-imaging monitoring[⋆,⋆⋆]

L. Mancini[1,2], P. Giacobbe[2], S. P. Littlefair[3], J. Southworth[4], V. Bozza[5,6], M. Damasso[2], M. Dominik[7], M. Hundertmark[7], U. G. Jørgensen[8], D. Juncher[8], A. Popovas[8], M. Rabus[9,1], S. Rahvar[10], R. W. Schmidt[11], J. Skottfelt[12,8], C. Snodgrass[13], A. Sozzetti[2], K. Alsubai[14], D. M. Bramich[14], S. Calchi Novati[15,5,16], S. Ciceri[1], G. D'Ago[16,5,6], R. Figuera Jaimes[7,17], P. Galianni[7], S.-H. Gu[18,19], K. Harpsøe[8], T. Haugbølle[8], Th. Henning[1], T. C. Hinse[20], N. Kains[21], H. Korhonen[22,8], G. Scarpetta[5,6,16], D. Starkey[7], J. Surdej[23], X.-B. Wang[18,19], and O. Wertz[23]

1 Max-Planck Institute for Astronomy, Königstuhl 17, 69117 Heidelberg, Germany
e-mail: mancini@mpia.de
2 INAF–Osservatorio Astrofisico di Torino, via Osservatorio 20, 10025 Pino Torinese, Italy
3 Department of Physics and Astronomy, University of Sheffield, Sheffield S3 7RH, UK
4 Astrophysics Group, Keele University, Keele ST5 5BG, UK
5 Department of Physics, University of Salerno, Via Giovanni Paolo II 132, 84084 Fisciano (SA), Italy
6 Istituto Nazionale di Fisica Nucleare, Sezione di Napoli, 80126 Napoli, Italy
7 SUPA, University of St Andrews, School of Physics & Astronomy, North Haugh, St Andrews, Fife KY16 9SS, UK
8 Niels Bohr Institute & Centre for Star and Planet Formation, University of Copenhagen, Østervoldgade 5, 1350 Copenhagen K, Denmark
9 Instituto de Astrofísica, Pontificia Universidad Católica de Chile, Av. Vicuña Mackenna 4860, 7820436 Macul, Santiago, Chile
10 Department of Physics, Sharif University of Technology, PO Box 11155-9161, Tehran, Iran
11 Astronomisches Rechen-Institut, Zentrum für Astronomie, Universität Heidelberg, Mönchhofstrasse 12-14, 69120 Heidelberg, Germany
12 Centre for Electronic Imaging, Dept. of Physical Sciences, The Open University, Milton Keynes MK7 6AA, UK
13 Planetary and Space Sciences, Dept. of Physical Sciences, The Open University, Milton Keynes MK7 6AA, UK
14 Qatar Environment and Energy Research Institute, Qatar Foundation, Tornado Tower, Floor 19, PO Box 5825, Doha, Qatar
15 NASA Exoplanet Science Institute, MS 100-22, California Institute of Technology, Pasadena, CA 91125, USA
16 Istituto Internazionale per gli Alti Studi Scientifici (IIASS), 84019 Vietri Sul Mare (SA), Italy
17 European Southern Observatory, Karl-Schwarzschild-Strasse 2, 85748 Garching bei München, Germany
18 Yunnan Observatories, Chinese Academy of Sciences, 650011 Kunming, PR China
19 Key Laboratory for the Structure and Evolution of Celestial Objects, Chinese Academy of Sciences, 650011 Kunming, PR China
20 Korea Astronomy and Space Science Institute, 305-348 Daejeon, Republic of Korea
21 Space Telescope Science Institute, 3700 San Martin Drive, Baltimore, MD 21218, USA
22 Finnish Centre for Astronomy with ESO (FINCA), University of Turku, Väisäläntie 20, 21500 Piikkiö, Finland
23 Institut d'Astrophysique et de Géophysique, Université de Liège, 4000 Liège, Belgium

Received 5 July 2015 / Accepted 25 October 2015

ABSTRACT

Context. Photometric monitoring of the variability of brown dwarfs can provide useful information about the structure of clouds in their cold atmospheres.The brown-dwarf binary system Luhman 16AB is an interesting target for such a study, because its components stand at the L/T transition and show high levels of variability. Luhman 16AB is also the third closest system to the solar system, which allows precise astrometric investigations with ground-based facilities.

Aims. The aim of the work is to estimate the rotation period and study the astrometric motion of both components.

Methods. We have monitored Luhman 16AB over a period of two years with the lucky-imaging camera mounted on the Danish 1.54 m telescope at La Silla, through a special $i + z$ long-pass filter, which allowed us to clearly resolve the two brown dwarfs into single objects. An intense monitoring of the target was also performed over 16 nights, in which we observed a peak-to-peak variability of 0.20 ± 0.02 mag and 0.34 ± 0.02 mag for Luhman 16A and 16B, respectively.

Results. We used the 16-night time-series data to estimate the rotation period of the two components. We found that Luhman 16B rotates with a period of 5.1 ± 0.1 h, in very good agreement with previous measurements. For Luhman 16A, we report that it rotates more slowly than its companion, and even though we were not able to get a robust determination, our data indicate a rotation period of roughly 8 h. This implies that the rotation axes of the two components are well aligned and suggests a scenario in which the two objects underwent the same accretion process. The 2-year complete data set was used to study the astrometric motion of Luhman 16AB. We predict a motion of the system that is not consistent with a previous estimate based on two months of monitoring, but cannot confirm or refute the presence of additional planetary-mass bodies in the system.

Key words. binaries: visual – brown dwarfs – stars: variables: general – techniques: photometric – techniques: image processing

⋆ Based on data collected by MiNDSTEp with the Danish 1.54 m telescope at the ESO La Silla Observatory.
⋆⋆ The photometry is only available at the CDS via anonymous ftp to cdsarc.u-strasbg.fr (130.79.128.5) or via http://cdsarc.u-strasbg.fr/viz-bin/qcat?J/A+A/584/A104

1. Introduction

Brown dwarfs are very intriguing astrophysical objects owing to their mass range between the gas planets and the lightest M-type stars. They are classified into M→L→T→Y classes based on their spectral characteristics. Since brown dwarfs are not massive enough to trigger sufficient nuclear fusion reaction rates in their cores to sustain hydrostatic equilibrium, they are destined to gradually cool, and this classification also represents an evolutionary sequence (e.g. Kirkpatrick et al. 1999, 2012; Burgasser et al. 2006; Cushing et al. 2011). As a brown dwarf cools, the temperature and gas pressure of its photosphere become such that it starts to be progressively dominated by molecular gas. When an L-type brown dwarf cools down to hot-Jupiter temperatures, the molecular gas can condense into thin or thick clouds or a mixture of them. Aerosols can form in its atmosphere through the condensation of very refractory species, such as metallic oxides, silicates, and iron (Lodders 1999; Marley et al. 2002; Woitke & Helling 2003, 2004; Burrows et al. 2006; Helling et al. 2008). At the L-to-T class transition ($T_{\rm eff} \approx 1200-1300$ K), these clouds could break up and unveil the naked photosphere, causing a brown dwarf to be very variable over short timescales (∼h), depending on the inclination angle of the rotation axis (Ackerman & Marley 2001; Burgasser et al. 2002; Marley et al. 2010). It is also possible that the clouds can become thinner and thinner and eventually disappear because of the increasing size of their particles and subsequent rain-out (Tsuji & Nakajima 2003; Knapp et al. 2004). Photometric time-variability monitoring of brown dwarfs is therefore a useful diagnostic tool for investigating the properties of clouds in their atmospheres, and periodic or quasi-periodic rapid variability has been found in several cases both at optical and near-infrared (NIR) wavelengths (e.g. Artigau et al. 2009; Radigan et al. 2012, 2014; Buenzli et al. 2012, 2014; Heinze et al. 2013; Biller et al. 2013).

In this context, the binary system Luhman 16AB (aka WISE J104915.57−531906.1; Luhman 2013), being composed of L7.5 (A component) and T0.5 (B component) brown dwarfs (Kniazev et al. 2013; Burgasser et al. 2013), represents an emblematic case for studying the L/T transition states of brown dwarfs and investigating the disappearance of clouds.

A first 12-day-long monitoring of this system was performed by Gillon et al. (2013) with the TRAPPIST 60 cm telescope through a $i + z$ filter. Even though they were not able to resolve the two components of the system, they found a large variability (∼10%) and, attributing this variability to the cooler component, estimated a rotation period of 4.87 ± 0.01 h for Luhman 16B.

Using the GROND instrument (Greiner et al. 2008) mounted on the MPG 2.2 m telescope, the two components were resolved and monitored for 4 h in four optical and three NIR passbands simultaneously by Biller et al. (2013). They found that the B component also shows variability in the NIR bands and reported a low-amplitude intrinsic variability in the i and z-bands for the A component. A subsequent, additional seven-day monitoring with the TRAPPIST telescope led to finding a rotation period of 5.05 ± 0.10 h for Luhman 16B (Burgasser et al. 2014), which is consistent with the previous measurement.

A fascinating surface map of Luhman 16B was deduced by Crossfield et al. (2014) by using the Doppler-imaging technique on high-resolution spectra taken with the CRIRES spectrograph (Käufl et al. 2004) at the ESO Very Large Telescope (VLT). The surface of Luhman 16B appears to be structured into large bright and dark regions, reasonably recognised as patchy clouds. Monitoring of these clouds for several hours allowed to confirm the rotation period of ∼5 h for Luhman 16B. Other useful information was extracted from the CRIRES data, which show that CO and H_2O absorption features dominate the spectra of both the components. The projected rotational velocities were estimated to be 17.66 ± 0.1 km s^{-1} and 26.16 ± 0.2 km s^{-1} for Luhman 16A and 16B, respectively. This implies that component B should have a rotational axis inclined by less than ∼30° to the plane of the sky, assuming that its radius is roughly 1 $R_{\rm Jup}$ (Crossfield et al. 2014).

Another peculiarity of Luhman 16 is that, after Alpha Centari AB, it is the nearest known binary system to the solar system at ∼2 pc. This occurrence allows astrometric studies to be performed for the two components of the system, in order to detect their orbital motion and measure their parallax. This was done by Boffin et al. (2014), who monitored Luhman 16AB for a period of two months with the FORS2 instrument at the ESO-VLT, measuring a distance of 2.020 ± 0.019 pc and a proper motion of about 2.8″/year. Moreover, they found that the relative orbital motion of the two objects is perturbed, suggesting the presence of a substellar companion around one of the two components. However, the existence of a substellar object in the system was not confirmed by Melso et al. (2015), who based on multi-epoch images from the *Spitzer* Space Telescope and adaptive optics images from the VLT, did not detect any new companion.

In this work we present new long-term, high-resolution, photometric monitoring of the Luhman 16 system over two years, performed through an optical broad-band filter (700−950 nm) with a lucky-imaging camera. The new data have been used to study the variability in red-optical light (Sect. 2) and revise the astrometric motion of the two brown dwarfs (Sect. 3). Section 4 summarises our results.

2. Photometry

2.1. Observations and data reduction

We monitored the brown-dwarf binary system Luhman 16AB in lucky-imaging mode with the EMCCD (electron-multiplying charge-couple device) instrument (Skottfelt et al. 2015b) mounted on the Danish 1.54 m Telescope, located at the ESO Observatory in La Silla. This device consists of an Andor Technology iXon+ model 897, 512 × 512 pixel EMCCD Lucky-Imaging (LI) Camera. Its pixel scale is 0.09 arcsec pixel^{-1}, resulting in a field of view of 45 × 45 arcsec^2. The LI camera is mounted behind a dichroic mirror, which acts as a long-pass filter roughly corresponding to a combination of the SDSS i and z filters (Skottfelt et al. 2013, 2015a).

The Luhman 16AB system was monitored during two seasons. The first season started on May 2, 2013 and finished on May 16, 2013. Three hundred fifty-two images were collected during 14 nights, with an exposure time of 3 min. The second season started on April 19, 2014 and finished on July 16, 2014, and comprises 728 images with an exposure time of 5 min. In particular, a dense monitoring of the target was performed between April 19 and May 5, 2014, in which we obtained 708 images spread over 16 nights, with 14 of them consecutive; after that, the target was observed a few times at intervals of several nights. In total, considering both the seasons, we observed the target for 42 nights. However, the quality of the data is not the same for all the nights. In particular, the two components were not resolved well in the images observed with a seeing ≳1 arcsec, and such data turned out to be of no use to our analysis.

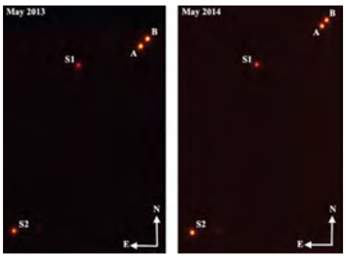

Fig. 1. Two images of the brown-dwarf binary system Luhman 16AB, obtained with the LI camera mounted on the Danish 1.54 m Telescope. The images were taken one year apart. The same two comparison stars are also present in the FOV.

Table 1. Summary of the data collected with the LI camera mounted on the Danish 1.54 m telescope.

Date	$N_{\rm obs}$	Rotation period	Astrometry
2013:			
2013.05.02	3	No	No
2013.05.04	9	No	Yes
2013.05.05	20	No	Yes
2013.05.06	33	No	Yes
2013.05.07	38	No	Yes
2013.05.08	36	No	No
2013.05.09	26	No	Yes
2013.05.10	38	No	No
2013.05.11	37	No	No
2013.05.12	28	No	No
2013.05.13	10	No	Yes
2013.05.14	31	No	Yes
2013.05.15	19	No	Yes
2013.05.16	24	No	No
2014:			
2014.04.19	3	Yes	Yes
2014.04.20	26	Yes	No
2014.04.21	2	Yes	Yes
2014.04.22	42	Yes	Yes
2014.04.23	53	Yes	Yes
2014.04.24	66	Yes	Yes
2014.04.25	64	Yes	Yes
2014.04.26	39	Yes	No
2014.04.27	40	Yes	Yes
2014.04.28	54	Yes	Yes
2014.04.29	66	Yes	No
2014.04.30	15	Yes	Yes
2014.05.01	56	Yes	Yes
2014.05.02	52	Yes	No
2014.05.04	65	Yes	Yes
2014.05.05	65	Yes	No
2014.05.09	3	No	Yes
2014.05.17	3	No	Yes
2014.05.27	2	No	No
2014.05.31	1	No	No
2014.06.07	2	No	No
2014.06.14	2	No	No
2014.06.17	1	No	No
2014.06.20	2	No	No
2014.06.21	1	No	No
2014.06.23	1	No	No
2014.07.04	1	No	No
2014.07.16	1	No	No

Notes. $N_{\rm obs}$ is the number of observations for each single night. Column 3 indicates if the data were used for estimating the rotation periods of the components of Luhman 16. Column 4 indicates if the data were used for the astrometric study of the components of Luhman 16.

Table 1 summarises the data collection. Bias and dome flat-field frames were taken every night and used to calibrate the science images. A comparison between the 2013 and 2014 positions of the brown dwarfs with respect to two comparison stars is illustrated in Fig. 1. It also clearly shows that our observations consistently resolved the two components of the brown-dwarf binary.

Each observation consists of a data cube containing 1800 (2013 season) or 3000 (2014 season) single exposures of exposure time 0.1 s. They were calibrated using algorithms described in Harpsøe et al. (2012), and the output of the reduction of a single observation was a ten-layer image cube-fits file. The flux from each of the brown dwarfs was extracted through point spread function (PSF) photometry using a modified version of the pipeline, written in IDL[1] (Southworth et al. 2014 and reference therein). An ensemble of comparison stars in the field of view (FOV) were used for this purpose. All the data will be made available at the CDS. The resulting light curves of both the components, corresponding to the 16-night dense monitoring, are shown in Fig. 2, together with that of a comparison star. The peak-to-peak variability is 0.20 ± 0.02 mag for Luhman16 A and 0.34 ± 0.02 mag for Luhman16 B. The two data sets were assembled in tables, which are available at the CDS, each containing the timestamps, differential magnitudes and corresponding uncertainties.

2.2. Time-series analysis

We analysed the 16-night photometric time series taken in 2014 (Fig. 2), to investigate whether their variability is periodic and thus ascribable to the rotation of the brown dwarfs and caused by possible inhomogeneities (clouds) in their atmospheres. The monitoring performed in all other nights (see Table 1) is too sparsely sampled to yield robust results.

We attempted to measure the rotation periods of Luhman 16AB by fitting the photometric data for each component individually with a Gaussian process model. The data points in the light curves were modelled as being drawn from a multivariate Gaussian distribution; time correlations between data points were reflected in non-zero values for the off-diagonal elements of the covariance matrix. Following Vanderburg et al. (2015), we parameterised the covariance matrix with a quasi-periodic kernel function. In principle this is an improvement on a periodogram analysis since the evolving cloud features on Luhman 16AB produce variability that is neither sinusoidal nor strictly periodic. The kernel function adopted is given by

$$k_{ij} = A^2 \exp\left[\frac{-(x_i - x_j)^2}{2l^2}\right] \exp\left[\frac{-\sin^2\left(\frac{\pi(x_i - x_j)}{P}\right)}{g_{\rm q}^2}\right] + s^2\delta_{ij},$$

1 The acronym IDL stands for Interactive Data Language and is a trademark of ITT Visual Information Solutions.

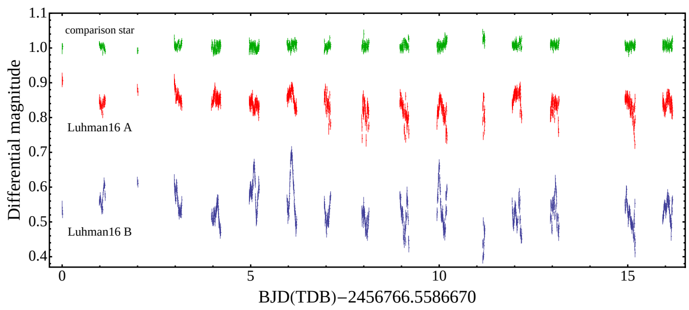

Fig. 2. Globally normalised unbinned PSF photometry for the two components of Luhman 16 and for one of the comparison stars used in the reduction (shifted along the y axis), based on 16 nights of photometric monitoring with the LI camera. Red points refer to Luhman 16A, blue to Luhman 16B, and green to a comparison star.

where A is the amplitude of the correlation, l the timescale of the exponential decay term, P the rotation period, $g_{\rm q}$ a scaling factor for the exponentiated sinusoidal term, and s a white-noise hyper-parameter. Here, $g_{\rm q}$ and l are hyper-parameters related to the time-evolving features (clouds) in the atmospheres of the brown dwarfs: the first is a scale factor that takes the changes in sizes of the features into account, and the second is related to their lifetimes. Essentially, the scaling factor $g_{\rm q}$ affects the regularity of the resulting light curve, with lower values producing models that are increasingly sinusoidal.

Our analysis made use of (Foreman-Mackey et al. 2014), a Gaussian-process library that uses a fast matrix inversion method (Ambikasaran et al. 2014), to implement our Gaussian process. We explored the posterior distributions of the hyper-parameters using a Markov-chain Monte-Carlo analysis with the affine invariant ensemble sampler within *emcee* (Foreman-Mackey et al. 2013).

For Luhman 16A, the posterior distribution for the rotation period P is not well defined (Fig. 3). A period of around eight hours is preferred, but a wide range of rotation periods is compatible with the data. This is essentially caused by the fact that Luhman 16A is rotating more slowly than its companion and that the evolutionary timescale of the global weather on Luhman 16A is roughly one day, while the monitoring with the Danish Telescope lasted 4−5 h per night. Nevertheless, it is interesting to notice that, based on comparison with $v \sin i$ data (Crossfield et al. 2014), a rotation period of ∼8 h is exactly what is expected when assuming that the rotational axes of the two components are aligned, and it very likely implies that they experienced the same accretion process (Wheelwright et al. 2011). Such spin-orbit alignment has already been observed in the very low-mass dwarf-binary regime (Harding et al. 2013) and can be explained by different formation theories (see discussion in Harding et al. 2013).

For Luhman 16B, the posterior distribution for the period is sharply peaked around five hours, with a "background" of low probability covering a wide range of periods (Fig. 4). We modelled the samples from the posterior distribution with a Gaussian mixture model with two components. The sharp spike is modelled well by a Gaussian distribution, yielding an estimate of the rotation period for Luhman 16B of 5.1 ± 0.1 h, which is fully consistent with the value of 5.05 ± 0.10 h estimated by Burgasser et al. (2014). In Figs. 5 and 6 we show the light curves for Luhman 16A and Luhman 16B, respectively, together with a representation of the best fit implied by the Gaussian process model.

3. Astrometry

3.1. Astrometic reduction

For each image, we extracted the x, y (plate) coordinates via PSF fitting (using SExtractor and PSFExtractor; Bertin et al. 2011). A reference image was adopted, and the roto-translation between the reference image and the ith image was derived using all sources in the field (except the two components of Luhman 16). The sample of images was limited to those where the two components of Luhman 16AB were perfectly resolved and measured. Table 1 indicates the data that were used for the astrometric analysis. The individual images of a single night were stacked together by minimising the scatter in x and y for every source. The resulting uncertainty on the positions – between 6 mas and 96 mas for the first season and between 16 mas and 111 mas for the second season – was computed as the standard deviation after a 2σ clipping filter. The ICRS (α and δ, i.e. the right ascension and the declination, respectively) coordinates were finally restored by measuring the positions of four stars in the first image of each season and deriving a tangent-plane astrometric plate solution. The α and δ of the four reference stars were extracted from the PPMXL catalogue. The accuracy of such a roto-translation and stacking procedure relies heavily upon a key assumption: no other point source on the field of view is moving over the duration of the observations. Point source here means a single star with a noticeable parallax and/or proper motion or a binary (unresolved or with only one component visible) with a significant orbital motion. At the 10 mas level, no

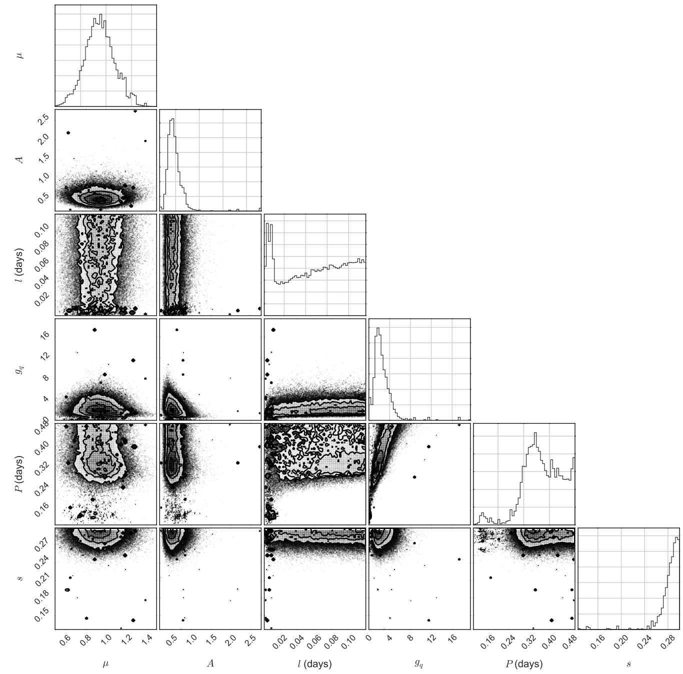

Fig. 3. Samples from the posterior probability distributions of the correlations for the six fitted parameters (see text) of Luhman 16A. μ is the mean level of the light curve. The full file of samples from the posterior distributions is available on request by sending an email to the first author.

disturbing point source is present in the field of view, thus making the stacked image robust.

3.2. Astrometric models

Our observational campaign was unfortunately too short to independently derive either the parallax, the proper motion, or the orbital motion of the two brown dwarfs in the binary system. We can nevertheless compare our data with the older data in the literature, in particular those from Boffin et al. (2014), to verify some predictions of the fundamental astrometric parameters and of the relative motion of the two components. The motion of a resolved binary is described by the motion of its barycentre (position, parallax, and proper motion) and the orbital motion of each component around it (Binnendijk 1960). The two orbits only differ by their size (i.e. the scale factor ρ in the model equation) and the arguments of periastron, which are 180° apart.

Furthermore, taking two different stacks of reference stars into account (one per season), we add to the model two linear parameters ($\xi_{\rm off}$ and $\eta_{\rm off}$) to cope with some misalignment between the first and the second season data sets. Thirteen parameters are thus required (seven parameters to describe the relative motion of the binary star and five to describe the motion of the barycentre).

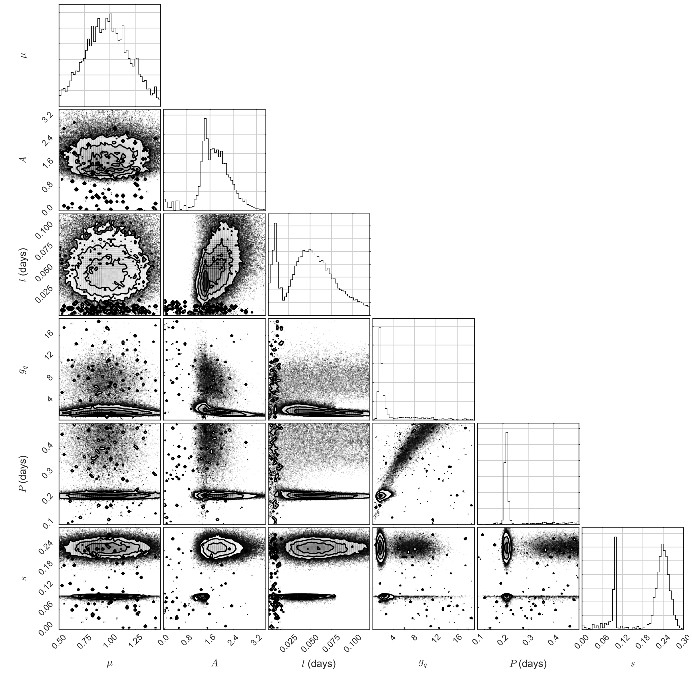

Fig. 4. Samples from the posterior probability distributions of correlations for the six fitted parameters (see text) of Luhman 16B. μ is the mean level of the light curve. The full file of samples from the posterior distributions is available on request by sending an email to the first author.

The resulting model is therefore given by

$$\xi' = \xi'_0 + \xi_{\rm off} + f_{\rm a}\,\pi + \mu_\xi(t - 2000.0) + BX(t) + GY(t)$$
$$\eta' = \eta'_0 + \eta_{\rm off} + f_{\rm d}\,\pi + \mu_\eta(t - 2000.0) + AX(t) + FY(t)$$

for the primary,

$$\xi'' = \xi''_0 + \xi_{\rm off} + f_{\rm a}\,\pi + \mu_\xi(t - 2000.0) + B\rho X(t) + G\rho Y(t)$$
$$\eta'' = \eta''_0 + \eta_{\rm off} + f_{\rm d}\,\pi + \mu_\eta(t - 2000.0) + A\rho X(t) + F\rho Y(t)$$

for the secondary, and

$$\xi = \xi_0 + \xi_{\rm off} + f_{\rm a}\,\pi + \mu_\xi(t - 2000.0)$$
$$\eta = \eta_0 + \eta_{\rm off} + f_{\rm d}\,\pi + \mu_\eta(t - 2000.0)$$

for the barycentre. Here, ξ and η are the standard coordinates[2]; t denotes the time; $f_{\rm a}$ and $f_{\rm d}$ denote the "*parallax factors*" (Kovalevsky & Seidelmann 2004); π is the parallax; μ_ξ and μ_η are the proper motions in ξ and η; A, B, F, G are the Thiele-Innes parameters (Wright & Howard 2009); ρ is the scaling factor of the orbit; and X and Y are the so-called elliptical rectangular coordinates (from the solutions of the Kepler motion).

To compare our findings with the others in the literature, we fit the relative motion over a grid of parameters, because the relative motion is not sufficiently well sampled for performing a

[2] http://www2.astro.psu.edu/users/rbc/a501/Girard_coordinates.pdf

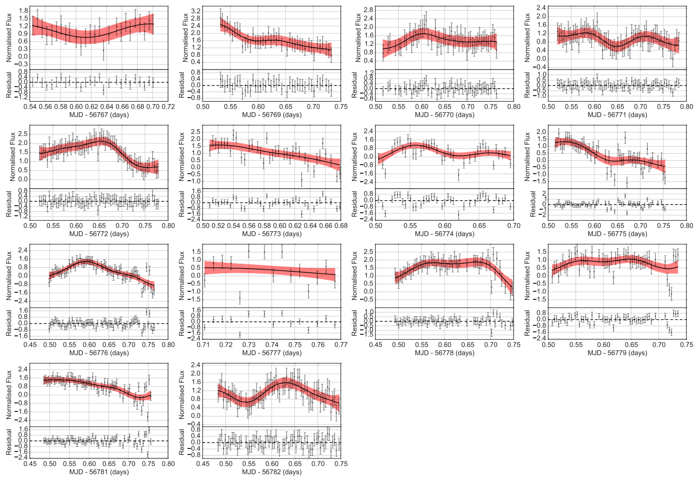

Fig. 5. Single-night light curves for Luhman 16A, together with a representation of the best fit implied by the Gaussian process model. The solid black line represents the mean of 300 samples drawn from the Gaussian process model conditioned on the full data set. The red-shaded region represents the 2σ confidence interval, as estimated from these samples.

real fit in a least squares sense. We discuss the validity of such a simplification in the next section. To focus our analysis on the relative (orbital) motion of the two stars of the binary system, we consider the two quantities $\Delta\xi$ and $\Delta\eta$, defined as the differences between the coordinates of the two stars.

To compare our findings with others in the literature we modelled $\Delta\xi$ and $\Delta\eta$ with an arc of parabola instead of the true Keplerian orbital model. This assumption works in the limit of a short timespan of the observations with respect to the orbital period. We discuss the validity of such a simplification for our data and for data in literature in the next section.

3.3. Results and discussion

The results of the least-squares fit of the absolute positions of the components A and B (i.e. the model from Sect. 3.2) are plotted in the left-hand panel of Fig. 7. In the least-squares fit, we kept the proper motion and parallax values fixed to those of Boffin et al. (2014), so we really "adjust" the constants, the offsets, and the orbital solution (over a grid of parameters). We fit simultaneously the coordinates of the two stars. The accuracy of such a fitting procedure relies upon an assumption: if any systematics are present in our data, they affect the two components evenly. This is reasonable when taking the short distance (~1 arcsec) of the two components into account.

The consequence of such an assumption is a symmetry in the χ^2 calculated, using the simultaneous best-fit model, over the data set of each component (left panel of Fig. 7). This symmetry seems to be violated. The contribution of the primary to the χ^2 is ~18% larger than that owing to the secondary. Under our hypothesis of no-graded systematic effects, we suggest three possible scenarios:

- the orbital solution of the binary system is not accurate;
- the proper motion estimate is not accurate;
- a companion might be present around component A, making it oscillate.

We compared the parabolic least-squares fit of the relative positions with the results of Boffin et al. (2014). Both $\Delta\alpha$ and $\Delta\delta$ are fitted with distinct parabolae (solid lines in the middle panel of Fig. 7). It appears clear that the curvature predicted by the parabolic fit over the two months of data (dashed lines) by Boffin et al. (2014) is not supported by our findings after one year. This is not unexpected because Boffin et al. (2014) estimates the probability of rejecting the parabola by accident to be 12.95%. As shown by Boffin et al. (2014), the residuals of the parabolic fit are highly correlated (right panel of Fig. 7). This correlation in our data does not have the same amplitude as the one presented in Boffin et al. (2014), and it seems to be correlated with the amplitude of the errors. This suggests that we need to interpret the correlation as a systematic effect because of the roto-translation

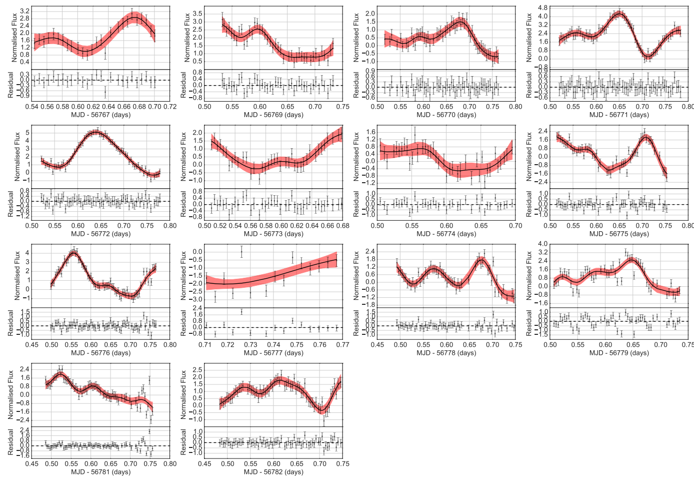

Fig. 6. Single-night light curves for Luhman 16B, together with a representation of the best fit implied by the Gaussian process model.

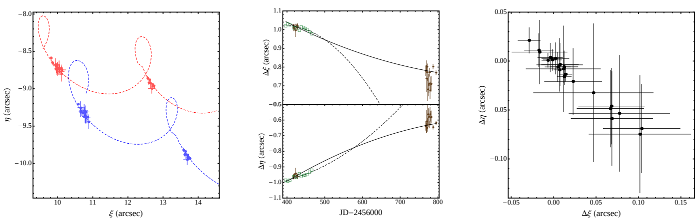

Fig. 7. *Left panel*: absolute positions, $\{\xi, \eta\}$, of the components A and B of the binary system Luhman 16, estimated from the data taken with the LI camera mounted on the Danish 1.54 m Telescope over two seasons. Points marked in red (blue) are from Luhman 16A (16B). Dashed lines represent the best model fits to the data with the models (for the primary and for the secondary) as described in Sect. 3.2. *Middle panel*: relative positions of the A component with respect to the B component of the binary system Luhman 16 as a function of time. Brown points are those estimated with the Danish Telescope over two seasons, while the open boxes refer to the measurements of Boffin et al. (2014; the size of their error bars is lower than the size of the boxes, and they were suppressed for clarity). Solid lines represent the best parabolic fits of both the data sets, while the dashed lines are the fits based on the prediction from Boffin et al. (2014). *Right panel*: residuals of the LI camera data based on the parabolic fit.

procedures. Actually, our precision does not allow us to confirm or reject the presence of a planetary signature, but our findings highlight the need for an improved determination of the orbit of the binary system.

4. Summary

We have photometrically monitored the brown-dwarf binary system Luhman 16AB over two seasons, 2013 and 2014, for a total of 38 nights. For this task, we utilised the EMCCD LI camera on the Danish 1.54 m Telescope, and the target was observed in a wavelength range corresponding to a combination of the SDSS i and z filters. Thanks to this instrumentation, we were able to collect 1132 high-resolution images in which the two components of the binary system are consistently well-resolved.

Between April and May 2014, we obtained an optimum time coverage during sixteen nights, fourteen of them continuous. The data from the 16-night time series were used to analyse the variability of the two brown dwarfs, which is likely to be caused by the circulation of clouds in their atmospheres, and to estimate their rotational velocity. For this purpose, we fitted the photometric data for each component with a Gaussian process model. In the case of Luhman 16A, the hotter component, we estimated that the most probable rotation period is $\sim$8 h, suggesting that it rotates more slowly than its companion, and their rotational axes are therefore well aligned. For the colder component, Luhman 16B, we estimated 5.1 ± 0.1 h for its rotation period, which is in very good agreement with previous estimates (Gillon et al. 2013; Burgasser et al. 2014).

Data from both 2013 and 2014 were used for a detailed astrometric analysis and for investigating the possible presence of an additional small companion in the system, as proposed by Boffin et al. (2014). Our two-season monitoring is not consistent with the predicted motion of Luhman 16AB by Boffin et al. (2014), which was only based on a two-month data set. However, our data do not have enough phase coverage and precision to perform a conclusive analysis of the parallax, proper motion, and relative motion of the binary system. Ultimately, we cannot confirm or reject the presence of any astrometric signal induced by a massive planet or low-mass brown dwarf, as hinted by Boffin et al. (2014). Further high-cadence astrometric monitoring of the Luhman 16AB system is thus highly encouraged, particularly to provide a set of measurements coincident with those that are being collected by *Gaia*, which is expected to deliver astrometry for the system at the milli-arcsecond level (e.g. Sozzetti 2014).

Acknowledgements. The operation of the Danish 1.54 m telescope is financed by a grant to UGJ from the Danish Natural Science Research Council (FNU). The reduced light curves presented in this work will be made available at the CDS. J. Southworth acknowledges financial support from the STFC in the form of an Advanced Fellowship. O.W. and J. Surdej acknowledge support from the Communauté française de Belgique – Actions de recherche concertées – Académie Wallonie-Europe. S.H.G. and X.B.W. would like to acknowledge the financial support from the National Natural Science Foundation of China through grants Nos. 10873031 and 11473066. M.H. acknowledges support from the Villum Foundation. We acknowledge the use of the following internet-based resources: the ESO Digitized Sky Survey; the TEPCat catalogue; the SIMBAD data base operated at the CDS, Strasbourg, France; and the arXiv scientific paper preprint service operated by Cornell University.

References

Ackerman, A. S., & Marley, M. S. 2001, ApJ, 556, 872
Ambikasaran, S., Foreman-Mackey, D., Greengard, L., et al. 2014, ArXiv eprints [arXiv:1403.6015]
Artigau, É., Bouchard, S., Doyon, R., & Lafrenière, D. 2009, ApJ, 701, 1534
Bertin, E. 2011, ASP Conf. Proc., 442, 435
Biller, B. A., Crossfield, I. J. M., Mancini, L., et al. 2013, ApJ, 778, L10
Boffin, H. M. J., Pourbaix, D., Mužić, K., et al. 2014, A&A, 561, L4
Buenzli, E., Apai, D., Morley, C. V., et al. 2012, ApJ, 760, L31
Buenzli, E., Apai, D., Radigan, J., et al. 2014, ApJ, 782, 77
Burgasser, A. J., Marley, M. S., Ackerman, A. S., et al. 2002, ApJ, 571, L151
Burgasser, A. J., Geballe, T. R., Leggett, S. K., et al. 2006, ApJ, 637, 1067
Burgasser, A. J., Sheppard, S. S., & Luhman, K. L. 2013, ApJ, 772, 129
Burgasser, A. J., Gillon, M., Faherty, J. K., et al. 2014, ApJ, 785, 48
Burrows, A., Sudarsky, D., & Hubeny, I. 2006, ApJ, 640, 1063
Crossfield, I. J. M., Biller, B., Schlieder, J. E., et al. 2014, Nature, 505, 654
Cushing, M. C., Kirkpatrick, J. D., Gelino, C. R., et al. 2011, ApJ, 743, 50
Foreman-Mackey, D., Hogg, D. W., Lang, D., & Goodman, J. 2013, PASP, 125, 306
Foreman-Mackey, D., Hogg, D. W., & Morton, T. D. 2014, ApJ, 795, 64
Gillon, M., Triaud, A. H. M. J., Jehin, E., et al. 2013, A&A, 555, L5
Greiner, J., Bornemann, W., Clemens, C., et al. 2008, PASP, 120, 405
Harding, L. K., Hallinan, G., Konopacky, Q. M., et al. 2013, A&A, 554, A113
Harpsøe, K. B. W., Jørgensen, U. G., Andersen, M. I., & Grundahl, F. 2012, A&A, 542, A23
Helling, Ch., Ackerman, A., Allard, F., et al. 2008, MNRAS, 391, 1854
Heinze, A. N., Metchev, S., Apai, D., et al. 2013, ApJ, 767, 173
Käufl, H. U., Ballestera, P., Biereichel, P., et al. 2004, Proc. SPIE 5492, 1218
Knapp, G. R., Leggett, S. K., Fan, X., et al. 2004, AJ, 127, 3553,
Kirkpatrick, J. D., Reid, I. N., Liebert, J., et al. 1999, ApJ, 519, 802,
Kirkpatrick, J. D., Gelino, C. R., Cushing, M. C., et al. 2012, ApJ, 753, 156
Kniazev, A. Y., Vaisanen, P., Mužić, K., et al. 2013, ApJ, 770, 124
Lodders, K. 1999, ApJ, 519, 793
Luhman, K. L. 2013, ApJ, 767, L1
Marley, M. S., Seager, S., Saumon, D., et al. 2002, ApJ, 568, 335
Marley, M. S., Saumon, D., & Goldblatt, C. 2010, ApJ, 723, L117
Melso, N. D., Kaldon, K. M., & Luhman, K. L. 2015, AJ, 150, 62
Radigan, J., Jayawardhana, R., Lafrenière, D., et al. 2012, ApJ, 750, 105
Radigan, J., Lafrenière, D., Jayawardhana, R., & Artau, E. 2014, ApJ, 793, 29
Skottfelt, J., Bramich, D. M., Figuera Jaimes, R., et al. 2013, A&A, 553, A111
Skottfelt, J., Bramich, D. M., Figuera Jaimes, R., et al. 2015a, A&A, 573, A103
Skottfelt, J., Bramich, D. M., Hundertmark, M., et al. 2015b, A&A, 574, A54
Southworth, J., Hinse, T. C., Burgdorf, M., et al. 2014, MNRAS, 444, 776
Sozzetti, A. 2014, Mem. Soc. Astron. It., 85, 643
Tsuji, T., & Nakajima, T. 2003, ApJ, 585, L151
Vanderburg, A., Montet, B. T., Johnson, J. A., et al. 2015, ApJ, 800, 59
Wheelwright, H. E., Vink, J. S., Oudmaijer, R. D., & Drew, J. E. 2011, A&A, 532, A28
Woitke, P., & Helling, Ch. 2003, A&A, 399, 297
Woitke, P., & Helling, Ch. 2004, A&A, 414, 335
Wright, J. T., & Howard, A. W. 2009, ApJS, 182, 205

THE ASTROPHYSICAL JOURNAL, 812:161 (21pp), 2015 October 20 doi:10.1088/0004-637X/812/2/161

EXTENDED BASELINE PHOTOMETRY OF RAPIDLY CHANGING WEATHER PATTERNS ON THE BROWN DWARF BINARY LUHMAN-16

R. A. STREET[1], B. J. FULTON[1,2], A. SCHOLZ[3], KEITH HORNE[3], C. HELLING[3], D. JUNCHER[3], G. LEE[3], AND S. VALENTI[1]
[1] LCOGT, 6740 Cortona Drive, Suite 102, Goleta, CA 93117, USA; rstreet@lcogt.net
[2] Institute for Astronomy, University of Hawaii, 2680 Woodlawn Drive, Honolulu, HI 96822-1839, USA
[3] School of Physics and Astronomy, University of St Andrews, St Andrews, Fife, KY16 9SS, UK
Received 2014 April 15; accepted 2015 September 10; published 2015 October 20

ABSTRACT

Luhman-16 (WISE J1049-5319) was recently discovered to be a nearby (∼2 pc) brown dwarf binary that exhibits a high degree of photometric variability ($\Delta m \sim 0.1$ mag). This is thought to be due to the evolution of "cloud" features on the photosphere, but Luhman-16 has been found to show unusually rapid changes, possibly resulting from fast-evolving "weather." This target is of particular interest because it consists of a co-evolutionary pair of brown dwarfs spanning the transition between L and T spectral types (L7.5 and T0.5), which are expected to be associated with changes in cloud surface coverage. Being comparatively bright ($I \sim 15.5$ mag), the target is well suited for observation with the new Las Cumbres Observatory Global Telescope Network (LCOGT) of 1 m telescopes. We present long-time baseline photometric observations from two of LCOGT's southern hemisphere sites, which were used in tandem to monitor Luhman-16 for up to 13.25 hr at a time (more than twice the rotation period), for a total of 41.2 days in the SDSS-i′ and Pan-STARRS-Z filters. We use this data set to characterize the changing rotational modulation, which may be explained by the evolution of cloud features at varying latitudes on the surfaces of the two brown dwarfs.

Key words: brown dwarfs – stars: general – stars: individual (Luhman-16, WISE-J1049-0053) – stars: low-mass

1. INTRODUCTION

Luhman (2013) recently discovered the brown dwarf binary WISE J104915.57-531906.1 at a distance of 2.0 pc, making it the third closest system to the Sun. The object was found through multi-epoch photometry in the *WISE* database (Wright et al. 2010) and was also detected in the catalogs from 2MASS (Skrutskie et al. 2006), DENIS (Epchtein et al. 1999), DSS (Luhman 2013), *IRAS*, AKARI (Ishihara et al. 2010), and GSC (Mamajek 2013). The two components of the binary have a projected separation of 3.1 AU and spectral types of L7.5 and T0.5 (Burgasser et al. 2013; Kniazev et al. 2013), with $T_{\rm eff} = 1310 \pm 30$ and 1280 ± 75 K, respectively (Faherty et al. 2014). This pair, with the short-hand name "Luhman-16," is one of a series of discoveries of very nearby brown dwarfs, following the publication of objects between 3 and 6 pc (McCaughrean et al. 2004; Artigau et al. 2006; Lucas et al. 2010; Scholz et al. 2011).

This very short distance, combined with the fact that both components are close to the L/T transition regime in terms of their spectral type, makes Luhman-16 an intriguing test case for models of brown dwarf atmospheres. The cool atmospheres of brown dwarfs allow the condensation of metal-rich dust grains, which form clouds and provide an additional source of opacity (Tsuji et al. 1996). Below effective temperatures of 2000 K, dust clouds significantly alter the temperature and pressure structure in the atmosphere and as a result, the colors and spectra of the objects (Witte et al. 2009).

While clouds in brown dwarfs may seem like a nuisance for those who aim to determine the fundamental parameters of these objects with great accuracy, for others they are an interesting environment for investigating physical mechanisms that may also affect the atmospheres of giant extrasolar planets (Helling et al. 2008b). There is already evidence that the spectra of planetary-mass companions around nearby stars and brown dwarfs can only be explained with the help of sophisticated cloud models (Barman et al. 2011a, 2011b; Skemer et al. 2011; Oppenheimer et al. 2013).

Over the past decade several independent groups have developed models of dust formation in brown dwarf atmospheres with varying simplifications, parameterizations, and assumptions (Ackerman & Marley 2001; Allard et al. 2003; Woitke & Helling 2003; Burrows et al. 2006, e.g.,). For a more detailed discussion of these cloud models, we refer to Helling et al. (2008a). Compared with the observations, several existing models agree reasonably well with the colors and spectra of L dwarfs, down to temperatures around 1600 K (Witte et al. 2011, e.g.,). The next challenge is to interpret the phenomena observed at even cooler temperatures, in particular at the L/T transition.

At this boundary, the observations indicate that the cloud properties undergo a fundamental change. This is evident from two empirically established findings.

(1) The $J - K$ near-infrared colors of brown dwarfs show a clear discontinuity around the L/T transition and turn sharply toward the blue. This is related to the so-called "J-band bump" (Tinney et al. 2003), a brightening in the J-band toward cooler temperatures. Luhman-16 shows this behavior exactly, with the cooler component being brighter in the *J*-band by 0.3 mag and bluer in $J - K$ by 0.6 mag (Burgasser et al. 2013). While this behavior can partly be attributed to a global change of the cloud layer (for example, clouds sinking below the photosphere or a more efficient rain-out of the clouds), Burgasser et al. (2002) and others suggested that the sharpness of the transition requires a break-up of the cloud coverage.

(2) Several objects around the L/T transition show pronounced quasi-periodic variability (Artigau et al. 2009; Radigan et al. 2012, 2013; Girardin et al. 2013; Heinze et al. 2013, 2015; Buenzli et al. 2014), whereas most L dwarfs are somewhat less variable (Bailer-Jones & Mundt 2001; Gelino et al. 2002; Koen 2013, e.g.,). Observations to date have

supported model where patchy or inhomogeneous cloud, carried in and out of view by the object's rotation, is the cause of this variability (Burgasser et al. 2002; Marley et al. 2010).

Radigan et al. (2012) used linear combinations of one-dimensional (1D) atmospheric models matched to the NIR spectrum and time series photometry of 2MASS J21392676+0220226 (2M2139) and concluded that the atmosphere contained either a thick, cooler cloud overlaying a thinner cloud deck or regions of high condensate opacity interspersed with warmer ($\Delta\, T_{\rm eff} \sim 175$–425 K) regions of lower opacity. This was supported by a study of times series spectra of 2M2139 and SIMP0136 (2MASS J0136565+093347) by Apai et al. (2013), who found a model with two spectral components with different cloud properties and effective temperatures were required to fit the observations. Both authors ruled out a model where holes in the cloud were cleared entirely, favoring instead a thin/thick cloud scenario (see Apai et al. 2013, Figure 6). These variations are often interpreted as "weather" on brown dwarfs, although we note that this is an observational bias in the following sense: L dwarfs have so much dust that we might not see any variability, whereas in T dwarfs the dust may form so deep inside the atmosphere that the gas alone is optically thick enough to prevent observation of intrinsic cloud variability.

In summary, the L/T transition is expected to be associated with cloud patchiness, which can be probed by studying the photometric variability, and the proximity of the Luhman-16 binary, with co-evolutionary components spanning this transition make it an excellent target for observation.

Earlier photometric monitoring campaigns for Luhman-16 have indeed shown that the object is strongly variable. Gillon et al. (2013) and Biller et al. (2013) demonstrated that while both components are variable to some degree, the T0.5 dwarf displays the greatest amplitude. Buenzli et al. (2014) obtained a time series of spatially resolved NIR spectra on both binary components with the *Hubble Space Telescope* (*HST*)/WFC3 which supported a two-layer cloud model of warm ($T_{\rm eff} = 1300$ K), thinner cloud and a cooler ($T_{\rm eff} =$ 1000–1100 K), thicker cloud, with out-of-equilibrium atmospheric chemistry. They were also able to compare models for Luhman-16A (which was consistent with a single cloud layer model) with Luhman-16B, finding different effective temperatures and sedimentation efficiencies across the L/T transition. Crossfield et al. (2014) graphically reinforced this model by mapping the surface of Luhman-16B by means of Doppler Imaging analysis. They obtaining a time series of Very Large Telescope (VLT)/CRIRES spectra over the course of ∼1 rotation cycle and observed bright and dark regions rotating in and out of view, which they interpreted as a snapshot of the clouds during that rotation cycle. Osten et al. (2015) looked for radio and X-ray emission from Luhman-16 without success from the Australia Telescope Compact Array and *Chandra* facilities, respectively. They inferred upper limits on the maximum size of any coherent radio emitting region to <0.2% of the brown dwarf's radius or <20% of the radius for incoherent radio emission.

While the light curves presented by Gillon et al. (2013) and Buenzli et al. (2014) clearly show a periodicity of close to 5 hr, presumably corresponding to the rotation period, they also show rapid evolution on timescales of days or less, possibly indicating fast-evolving weather patterns. To characterize the atmosphere of this benchmark object and its evolution, continuous monitoring over many consecutive rotational cycles is needed. In this paper, we present monitoring of Luhman-16 using the Las Cumbres Observatory Global Telescope Network (hereafter LCOGT). Our focus is to characterize the evolving light curve of this extraordinary object in two optical bands. These observations were coordinated with Burgasser et al. (2014), and overlap their intensive, multi-instrument monitoring campaign. They obtained contemporaneous measurements on 2013 April 26 UTC consisting of a 45 minute time series of NIR spectra from IRTF/SpeX and photometry (spanning 7.5 hr) from ESO/TRAPPIST using a broadband I+z filter. Both data sets exhibit clear variability from the B-component of the binary. That study measured the colder spots of the atmosphere to cover ∼30%–50% of the surface, varying by 15%–30% over the rotation period.

Burgasser et al. (2014) related the variation in spot coverage to the maximum fractional feature size predicted by the Rhines scaling relation (Rhines 1970), which was derived from jet features in solar system giant planets. Assuming the same relation holds for the atmospheres of brown dwarfs, they inferred wind speeds on Luhman-16B between 1.6 and 3.4 $\rm Km^{-1}$ for "hot regions" of $1700\,{\rm K} < T_{\rm hot} < 1900$ K. This implies advection timescales of $\tau_{\rm adv} \sim (2\text{–}5) \times 10^4\,{\rm s} \sim$ 1–3 rotation cycles, consistent with the timescales of the variation seen in the light curve.

This work explores the evolution of the variability of this fascinating object over timescales much longer than the rotation period. We describe our observations and data reduction in Sections 2 and 3 and present an analysis of the variability over different timescales in Section 4. In Section 5 we discuss our findings in context of the causes of the variability.

2. OBSERVATIONS

LCOGT operates a network of 1 and 2 m telescopes distributed across the globe in both hemispheres (for a complete description, see Brown et al. 2013). The 1 m telescopes in the southern hemisphere are organized in clusters, and this program made use of the three telescopes at the Cerro-Tololo Interamerican Observatory (CTIO, Chile), and the three at the South African Astronomical Observatory (SAAO, South Africa). Two telescopes have also been installed alongside LCOGT's 2 m telescope (Faulkes Telescope South, FTS) at the Siding Spring Observatory in Australia, but were not available at the time of these observations, while FTS was offline for an extended period due to mirror realuminizing. All of the telescopes are robotically operated, and at the time of the observations (during the network's 2013 commissioning period), all of the 1 m telescopes hosted SBIG STX-16803 cameras with Kodak KAF-16803 front-illuminated 4096 × 4096 pix CCDs, used in bin 2 × 2 mode. The 1 m telescopes are designed to be as identical as possible to facilitate networked observations, and all feature the same complement of filters. These observations were made in both SDSS-i′ and Pan-STARRS-Z due to the very red nature of the target.

The availability of telescopes at multiple sites, and multiple identical telescopes at each site make the LCOGT network an extremely powerful tool for time domain astronomy. For the purposes of this project we exploited two distinct observing modes.

To capture the short-term (hours–days) evolution of the target's light curve, we scheduled continuous, simultaneous

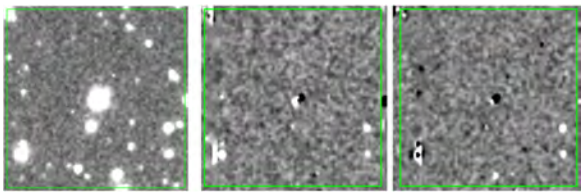

Figure 1. (Left): Reference image in the Pan-STARRS-Z band, centered on Luhman-16 with a 1 arcmin square field of view. (Right): Difference images, also in the Pan-STARRS-Z band and centered on Luhman-16, from the LCOGT-Chile, Dome C data set. The green box indicates a 1 arcmin square field and all images are oriented with north up and east to the left. These images show the subtracted frames for some of the best seeing images obtained: 1.17 arcsec on 2013 April 09 (left) and 1.27 arcsec on 2013 April 16 (right). The changing PSF of Luhman-16 is due to the varying light contributed by both components.

imaging on two parallel telescopes at each site, one in each filter, for as long as the object was visible from that site. At SAAO we observed between 17:00-00:30 UTC and at CTIO between 23:00-06:15 UTC each night for multiple nights back-to-back (2013 April 18–21, April 23–26 UTC), resulting in a light curve with continuous (imaging every ∼2 minute) segments of up to 13.25 hr.

In order to explore periodicities and variability on timescales of days-weeks, we also performed "monitoring" observations where a single telescope would take sets of exposures in alternating filters. These observation groups were then slotted into gaps in the telescope schedule between other programs wherever possible. Though at lower and irregular cadence, these observations have a much lower impact on other programs and can therefore continue for much longer. We gathered data in this mode between 2013 April 11–May 20 UTC.

3. DATA REDUCTION

Preprocessing (bias, dark, and flat-field correction) was performed by LCOGT's Standard Pipeline, which is based around ORAC-DR recipes (Cavanagh et al. 2008).

The 1.5 arcsec angular separation of the Luhman-16 component stars is close to the median full width at half maximum (FWHM) of the point-spread function (PSF) in most of these data sets, making it difficult to separate the independent variability of the stars. Since the seeing at LCOGT's Chilean site is often better than at other sites (∼1.1–1.2 arcsec), we attempted to derive photometry for two of the best data sets using the DanDIA (Bramich 2008) package to apply Difference Image Analysis techniques. The reference image selected is shown in Figure 1, and difference images from some of the best seeing frames are also shown. Upon extracting the light curves of both component stars in Pan-STARRS-Z and SDSS-i′, it became clear that the variability observed in both was highly correlated.

This happens in DIA analysis when the PSFs of two variables overlap and the PSF fitting performed on the difference images only fits one star at a time, which is the case with DanDIA (see V52 and V53 in Arellano Ferro et al. 2012). In the case of Luhman-16, there is the added complication that the binary has a high proper motion and parallax (0.496 ± 0.037 arcsec, Luhman 2013), and will have moved ∼0.2 arcsec over the course of our observations. Hence, the PSF model to fit to the difference images requires a simultaneous PSF fit at two positions that also change over the course of the observations. For our data sets with poorer seeing, these problems are further exacerbated. We therefore chose to pursue aperture photometry to reduce these data, effectively taking the Luhman-16 binary as a single object. However, from visual inspection of the difference frames, we note that the highest degree of variability appears to come from the southeastern star during this period.

The data were then reduced with two independent aperture photometric pipelines to provide a consistency check, both employing implementations of DAOphot to derive aperture photometry (Stetson 1987). Although LCOGT's cameras are designed to be as homogeneous as possible, the images from each telescope/camera combination were reduced separately to ensure the correct gain and read noise properties were applied for each camera. We selected an initial set of reference stars by manual inspection and derived differential light curves of Luhman-16 for each of the six cameras.

Differential photometry did a reasonable job of removing the signature of changing atmospheric extinction over the course of an individual data set. However, when the light curves in each filter were plotted together, magnitude offsets of the order of $\Delta m \sim 0.1$ mag were evident between them.

A number of authors have discussed techniques for obtaining high-precision differential photometry, notably transiting planet search teams. The most common case is light curves from a single observatory (e.g., WASP, *Kepler*, TRAPPIST) that can span days to many months. Data from LCOGT's network differs from these cases due to two factors: (1) the field of view is small when compared with a survey such as WASP, and it cannot be safely assumed that a significant number of non-variable stars with cataloged brightness and color data will be present in every field and (2) LCOGT can have multiple cameras at longitudinally distributed sites observing the same target through different airmasses. These data sets may or may not include data taken simultaneously.

We explored a number of avenues for combining data from different telescopes, including the SYSREM (Tamuz et al. 2005) and TFA (Kovács et al. 2005) algorithms, and the PDC-MAP technique used by the *Kepler* team (Smith et al. 2012). The essential approach is to recognize that the raw (non-differential) light curves of all stars within the field of view are dominated

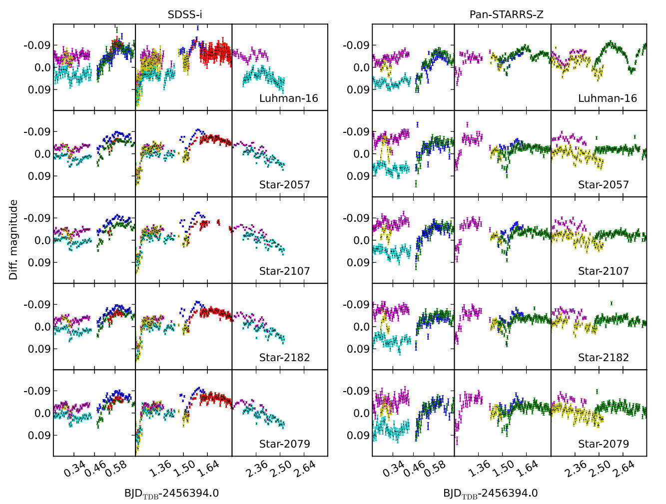

Figure 2. Representative 3-day section of the raw light curves of the target and comparison stars, including data from multiple instruments distinguished by different colors.

by trends due to a number of atmospheric and instrumental effects, giving even constant stars the same apparent variability. Each algorithm aims to select a set of stars that are not intrinsically variable to the precision of the data and use these stars to empirically determine the time-dependent trends in the data. Once identified, these trends can then be removed from all light curves in the data set, but care must be taken to avoid mistaking genuine variability for an instrumental artifact.

Our approach was not to distinguish the instrumental effects due to different nights on the same camera from those due to observations taken with different cameras. Instead we simply attempt to identify common systematic trends. Therefore, for each star, we concatenated all data sets in a given filter to produce a set of combined raw light curves.

The mean magnitude and rms scatter was first computed for all combined raw light curves, weighted by the inverse variance of each data point's measurement error. Of the 2466 stars measured, we restricted our choice of comparison stars to those that had at least the same number of valid measurements as the target, and had instrumental mean magnitudes within ∼4 mag of that of the target. At this stage, all light curves were dominated by instrumental trends and the rms of the stars was fairly constant with magnitude, so we used a 3σ cut on rms to reject any stars showing obvious variability over and above that. This produced a preliminary list of 13 comparison stars.

After subtracting the mean flux from each comparison star light curve, we calculated the mean of the comparison star residual fluxes for each image. The resulting time series represents the combined trends common to all light curves. The light curves of both target and comparison stars were divided by this supercomparison, and normalized by their mean flux, computed by weighting each data point by its photometric errors. The differential light curves of the comparison stars were then inspected to weed out any showing signs of variability. After each rejection, the differential photometry was re-computed and the process was iterated until a satisfactory set of four stars was reached. This procedure was carried out using the Pan-STARRS-Z data and then the same set of stars was then used to derive differential photometry from the SDSS-i′ light curves. Figures 2 and 3 compare a representative section of the raw light curves for our target and comparison stars with the same data section, post-differential photometry. Table 1 provides the details of all comparison stars, and their distribution within the reference image is shown in Figure 4.

To test how well data from different telescopes were combined, we plotted the resulting light curves for the target

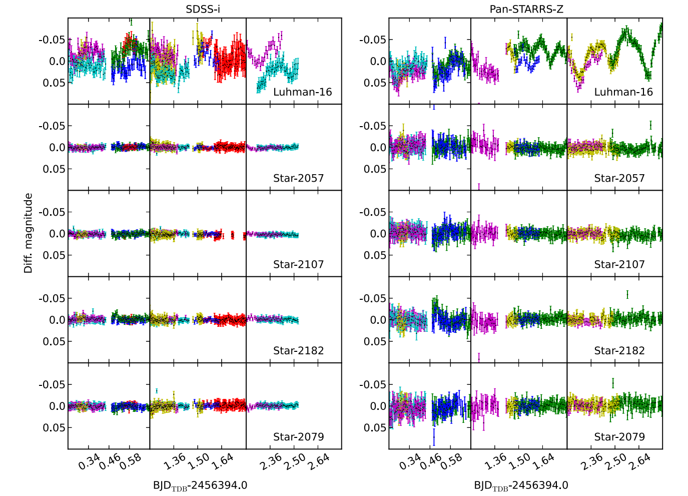

Figure 3. Same 3-day section of data as in Figure 2 of the differential photometry for the target and comparison stars, including data from multiple instruments distinguished by different colors. The residual bulk offsets described in the text can be seen in the light curves.

Table 1
Details of the Target and Comparison Stars

Star ID	R.A. (J2000.0)	Decl. (J2000.0)	J (mag)	H (mag)	K_S (mag)
Luhman-16	10:49:18.915	−53:19:10.08	10.733 ± 0.026	9.563 ± 0.029	8.841 ± 0.021
Comparison Stars in Final Cut					
2057	10:49:05.365	−53:21:23.64	13.606 ± 0.026	13.263 ± 0.029	13.190 ± 0.030
2079	10:49:15.748	−53:20:54.32	13.795 ± 0.027	13.383 ± 0.027	13.290 ± 0.037
2107	10:49:03.233	−53:20:38.82	13.480 ± 0.026	13.150 ± 0.030	13.112 ± 0.030
2182	10:49:06.242	−53:20:21.01	12.985 ± 0.024	12.185 ± 0.029	11.966 ± 0.023
Additional Comparison Stars in Preliminary Cut					
649	10:49:52.972	−53:15:13.53	12.562 ± 0.024	12.042 ± 0.027	11.958 ± 0.026
789	10:48:39.473	−53:16:09.76	12.726 ± 0.026	12.361 ± 0.022	12.328 ± 0.024
1054	10:49:08.909	−53:18:05.81	11.694 ± 0.024	11.025 ± 0.027	10.862 ± 0.023
1058	10:49:30.163	−53:17:55.95	12.234 ± 0.024	11.657 ± 0.024	11.466 ± 0.023
1126	10:49:47.365	−53:18:41.04	9.945 ± 0.023	8.902 ± 0.031	8.486 ± 0.017
1143	10:49:51.250	−53:18:29.70	12.656 ± 0.024	12.509 ± 0.023	12.422 ± 0.023
1367	10:48:33.726	−53:25:44.14	12.546 ± 0.026	12.322 ± 0.025	12.257 ± 0.026
1541	10:48:30.440	−53:24:19.78	12.703 ± 0.026	12.314 ± 0.022	12.216 ± 0.024
1750	10:49:10.230	−53:23:13.98	12.755 ± 0.024	12.456 ± 0.027	12.384 ± 0.026
1758	10:49:30.540	−53:22:47.08	12.432 ± 0.023	11.887 ± 0.024	11.703 ± 0.019
1763	10:49:23.635	−53:23:11.08	11.309 ± 0.023	10.439 ± 0.026	10.068 ± 0.019
2081	10:49:34.852	−53:20:56.07	12.613 ± 0.029	12.299 ± 0.027	12.233 ± 0.027
2194	10:49:36.609	−53:19:58.29	12.515 ± 0.033	12.318 ± 0.039	12.231 ± 0.032

Note. The coordinates and magnitudes are derived from the 2MASS point source catalog (Skrutskie et al. 2006).

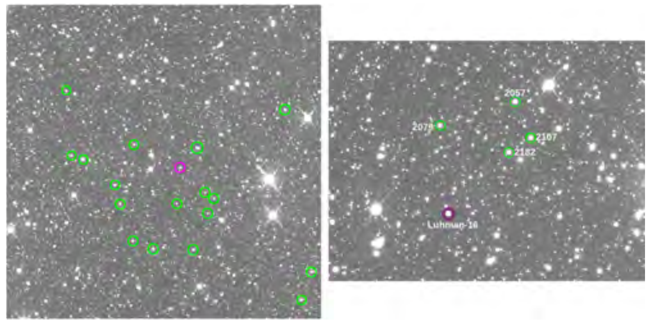

Figure 4. Distribution of the comparison stars in the Pan-STARRS-Z reference image. (Left): The preliminary selection of stars. (Right): The final selection. Luhman-16 is in the center in the left image and is indicated with a different color ring in both images.

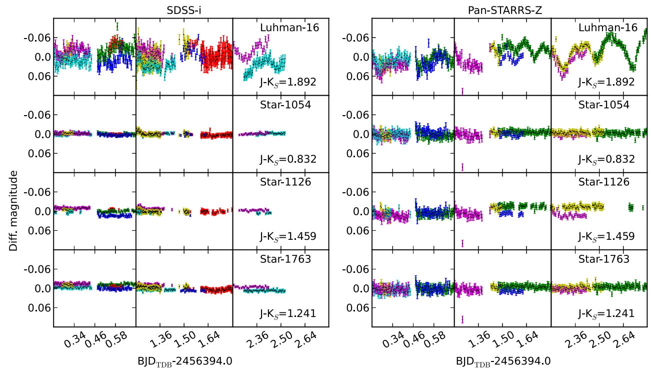

Figure 5. Same 3-day section of data as in Figure 2 of the differential photometry for the target and a selection of field stars of different $J - K_S$, showing the residual offsets between data from multiple instruments (distinguished by different colors).

and a selection of field stars of different $J - K_S$, distinguishing the data from different instruments, in Figure 5. This revealed small (<0.02 mag) residual offsets between simultaneous data in the same filter from different telescopes, including data from telescopes at the same site.

Differential photometry generally corrects for photometric trends due to atmospheric absorption to first-order, accounting for the decrease in apparent magnitude with increasing airmass, but since the absorption is a function of wavelength, there is a second-order term dependent on star color. For a star as red as Luhman-16 we would expect this term to be significant. However, simultaneous data sets in the same filter from telescopes at the same site are taken with effectively the same airmass, so this alone does not explain the offsets. Other possible causes of the residual offsets include the different instrumental (flat-field) signatures of the different

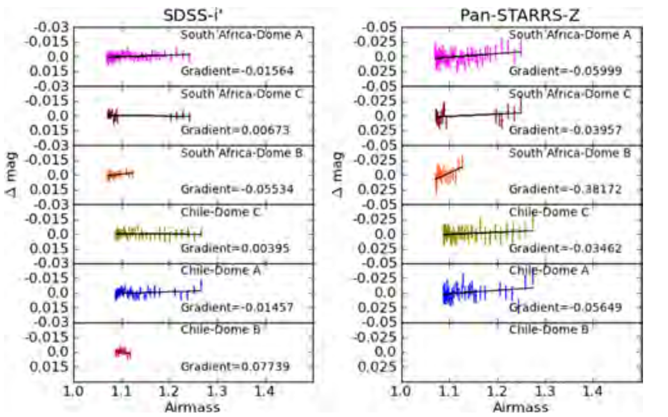

Figure 6. Differential photometry for field star 1126 from the different telescopes, normalized with their respective means, plotted against the airmass of each measurement.

cameras, and the variation in pixel position of each star in each frame.

Looking for the cause of these offsets, we searched for correlations between these factors and the residuals of differential light curves (the light curves normalized by their own means) for a set of field stars distributed across the CCD frame and in $J - K_S$ color. We used the "preliminary comparison star" set (excluding the final comparison stars) given in Table 1 for this analysis, concentrating on the 1–3 day sections of high cadence data taken in consistently good conditions with multiple telescopes. This provides data spread over a range of airmass and telescope pointing while excluding periods of poor weather.

Figure 6 shows the differential residuals as a function of airmass for the different telescopes for the field star closest to Luhman-16 in color. We fitted a linear function of airmass to the data to each data section. In general we find very small overall gradients in SDSS-i′ but consistently higher gradients in Pan-STARRS-Z, a symptom of second-order atmospheric extinction. Similar plots were produced for bluer field stars, which showed lower gradients. This is reinforced by Figure 7, which shows an increase in the standard deviation of the differential residuals for redder stars. This is not unexpected, since the comparison stars are necessarily bluer than the target. We note that the amplitude of this residual is still lower than the amplitude of the variability of the target by a factor ~2.5, but since no non-variable star of similar color to Luhman-16 was available for direct comparison, we performed additional tests to look for signs of correlations between the photometric residuals and observational and instrumental parameters.

We searched for correlations between the photometric residuals, airmass, and CCD pixel position. We found strong correlations between the pixel positions with airmass, implying that the movement of the telescopes toward higher airmass causes the pointing to change somewhat. This may be the result of slight imbalances in the weight distribution of the telescopes. The stars typically move up to ~40 pix over the CCD during the nights but additionally shift ±25 pix between one night's data and the next. Since different regions of the CCD have different sensitivities at different wavelengths, this introduces a source of color-dependent photometric variation. More sophisticated pointing and guiding algorithms are under development by LCOGT's software team to help eliminate this source of red noise.

LCOGT's normal procedure is to flat-field each frame with the master flat-field closest to it in date. Frequently this means that the image data for a night are flat-fielded with the same master flat-field, but of course different master flats for each camera. This could also contribute to night-to-night offsets between data taken with different cameras.

Nevertheless, a star may be assumed to show the same behavior at any given time in data taken with the same filter, meaning that the simultaneous single-color light curve segments should overlap in a differential light curve whose mean is normalized to zero.

We therefore developed a second-stage algorithm that took each single-filter differential light curve from the first stage and separated the data from different cameras. As simultaneous light curve segments do not consist of frames taken at precisely the same instant, the per-camera light curves were binned such that they were sampled at the same time intervals with a

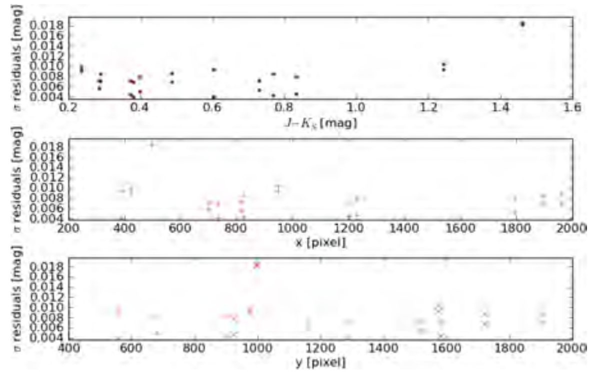

Figure 7. Standard deviation, σ, of differential light curves for a set of field stars distributed across the image and in $J - K_S$ color.

30 minute cadence. The code then calculates the mean bulk offset per segment between all data points in contiguous, overlapping sections of data (typically several hours long), applying the correction to the light curve segment furthest from the overall differential mean of zero.

Following this step, it is advisable to verify the data reduction strategy and to quantify the residual noise in the light curves. This is usually described as a combination of "white" (uncorrelated) and "red" (correlated) noise. The latter term is particularly important as it results from noise sources that cause apparent trends in the light curves that could potentially mimic a true signal or produce misleading parameters when superimposed on intrinsic variability.

In Figures 8–10, we plot the target's final differential light curve as functions of airmass, pixel position, and the average FWHM of stars in each frame as a proxy for the seeing. That the target's light curve variation is intrinsic and not a symptom of systematic trends is supported by the lack of correlation between these parameters and the photometric residuals.

Our aim is to measure the intrinsic periodicity(ies) of Luhman-16, if any. The most natural approach is to produce a power spectrum (squared variability amplitude) from the light curve, provided the intrinsic signal can be distinguished from the noise. Vaughan (2012) presents a good review of a range of techniques for time series analysis as applied in many different fields of astronomy, and discusses the recovery of reliable noise power spectra from sparsely sampled time series.

The analysis of Luhman-16 is particularly challenging because the variability is both quasi-periodic *and* changes on timescales that are short relative to the periodicity itself. This rules out the application of many commonly used techniques such as, for example, the Bartlett method Bartlett (1948), which relies on computing a series of periodograms at intervals along the light curve and taking the average. As we show in Section 4, Luhman-16 is non-stationary (the periodicities vary) on the shortest timescales for which we are able to estimate power spectra.

A great deal of work in the analysis of red noise in light curves has been derived from exoplanet transit work, following from Pont et al. (2006). Their technique depends on excluding data taken during transits from the target light curve, then analyzing the noise in the remaining photometry, under the assumption that the rest of the light curve should maintain constant brightness out of transit. This is problematic to apply directly to Luhman-16 because the photometric variations are continuous and unpredictable, making it difficult to distinguish systematic noise sources from intrinsic variability. However, our differential photometry depends on the assumption that our reference stars are constant throughout the observations. The data on these stars, which span a range of colors, were subjected to the same observation conditions, instrumentation, and data reduction process, and therefore should reflect similar systematics.

To quantify the red noise in our data, we followed a similar procedure to Pont et al. (2006) for the light curves of each of our reference stars. They relate the uncertainty on the signal amplitude, σ_d, as $\sigma_d = \nu^{1/2}(n)$, where

$$\nu(n) \equiv \frac{1}{n^2}\sum C_{ij}, \tag{1}$$

and C_{ij} are the covariance coefficients between the ith and jth measurements. $\nu(n)$ is estimated from the variance of the average of n data points within time interval l, which is free from any known signal.

1. We calculated the mean flux (F_j) within sliding intervals ($j = 1 ... N_l$) of duration l, which progress through each light curve in steps smaller than the time-sampling

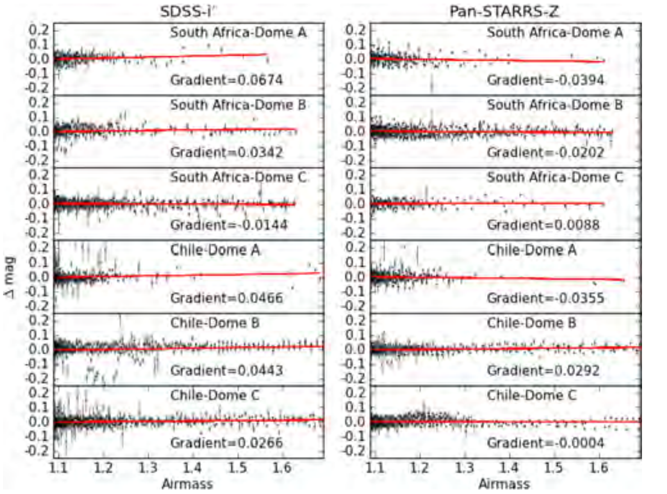

Figure 8. Differential photometry for Luhman-16 from the different telescopes, normalized with their respective means, plotted against the airmass of each measurement. The gradient of the fitted straight line is indicated for each data set.

interval. The number of data points lying in each interval is recorded.

2. F_j was then sorted into bins according to n_j.
3. The variance of F_j within each bin was then calculated as an estimate of the $\nu(n)$ function.

Figure 11 presents $\nu^{1/2}(n)$ for our reference stars and compares our data to the $n^{-1/2}$ relation expected for pure white noise and the function $\nu(n) = \sigma_w^2/n + \sigma_r^2$, combining red and white noise sources. We estimate the amplitude of white noise by calculating the standard deviation of the whole light curve and that of the red noise for each star by fitting the above relation to the data. σ_r was found to be between 0.001 and 0.007 mag in Pan-STARRS-Z but more consistently between 0.0025 and 0.0030 mag in SDSS-i′. We also note that $\nu(1)$ is always higher than σ_w. This value is computed for lone data points within duration l, implying that no other valid measurements were obtained around that time. This often occurs due to a local dawn at a given site or the onset of poor conditions, so we would expect higher scatter.

4. TIME SERIES ANALYSIS

Figures 12–14 show the data collected. The lower light curve on each plot represents the difference between the SDSS-i′ and Pan-STARRS-Z light curves, computed from time-averaged bins that are 30 minutes wide, designed to make apparent any distinction in phase or amplitude of variation. It confirms that the periodic, quasi-sinusoidal variability observed by other authors occurs in our data with a similar amplitude ($\Delta m \sim 0.1$ mag) in both bandpasses. In general the variability occurs in both passbands, but interestingly not always with exactly the same morphology or amplitude. It should be noted that the variability is better defined in the Pan-STARRS-Z light curve in part because the target is markedly brighter in that filter.

We initially used an implementation of the Schwarzenberg-Czerny algorithm to search for periods between 0.04 and 20.6 d in both time series, as it is optimized for the analysis of non-continuously sampled data sets (Schwarzenberg-Czerny 1999). The range of periods searched was set by the average sampling cadence at the short end and by half the length of the data set at the long end in order to include at least two full cycles to confirm the period. The periodograms resulting from the whole light curves are shown in Figure 15. The strongest peaks in both cases are dominated by the window function of the data sets, particularly between frequencies, f = 0–1d^{-1}. However, visual inspection of the light curve clearly shows periodic signals on timescales of hours, which manifest as frequency peaks around $f \sim 4.4$–5.1 d^{-1}, with aliases around $f \sim 2.297$ d$^{-1} \cong 10.45$ hr. These groups of peaks with similar power indicate that there is no one single clear period occurring

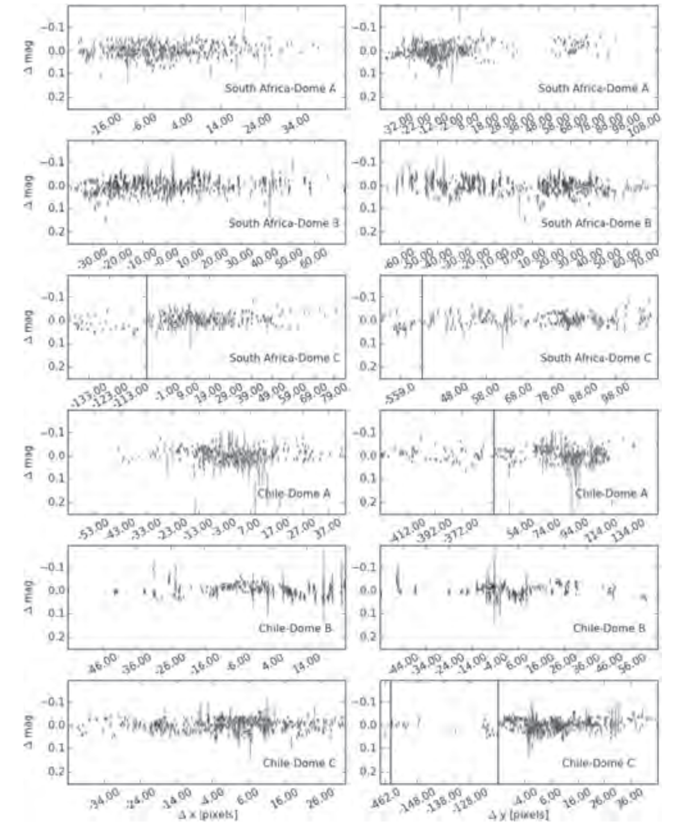

Figure 9. Magnitude residuals (Pan-STARRS-Z) for the target photometry plotted as a function of its relative CCD pixel position, separated into the different cameras. In some data sets, the pointing was substantially offset in position for some frames. These data have been included, but the white space has been eliminated for clarity.

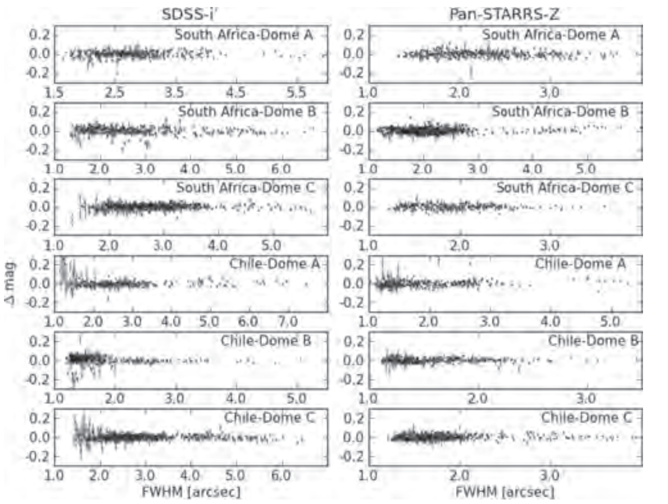

Figure 10. Differential photometry for Luhman-16 from the different telescopes, normalized with their respective means, plotted against the average FWHM of stars in the corresponding image.

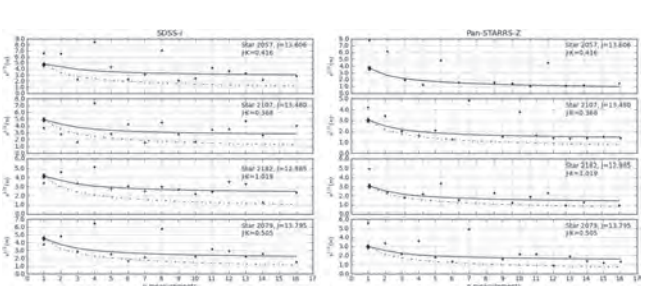

Figure 11. Plots of the $\nu(n)$ function for constant reference stars. Overplotted are functions representing pure white noise (dotted–dashed line) and a combination of red+white noise (solid line). In both cases, the white noise term is estimated from the standard deviation of the whole light curve, indicated by a diamond, while the degree of red noise was estimated by fitting this relation to the data.

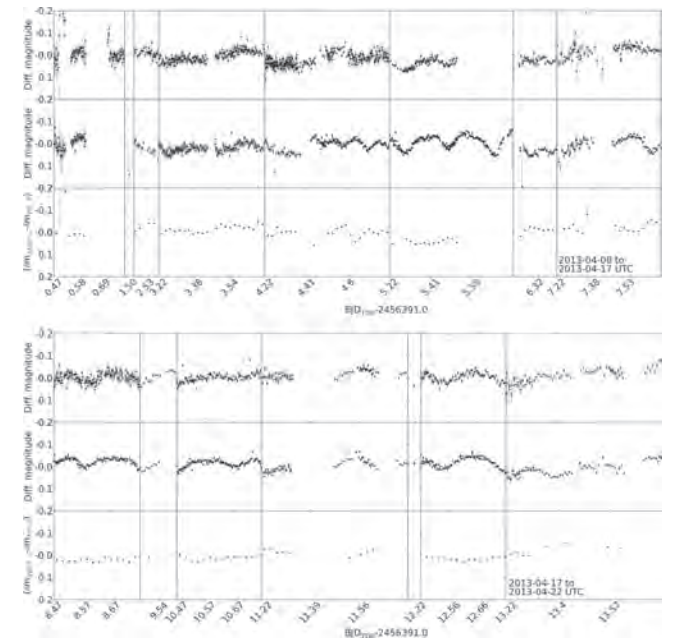

Figure 12. First two sections of the light curve of Luhman-16 in SDSS-i′ (top curve) and Pan-STARRS-Z (middle). The color index ($Z - i$) curve is indicated in the bottom plot, binned in time with a 30-minute cadence.

consistently across the whole data set. We measured each of the peaks around these frequency bands, estimating the error on the measurements from the width of the peak, and verified each one by folding the light curve on that period and its integer multiples to identify aliases. When folded on a period of ~10.45 hr, the light curves showed two minima in light, suggesting that the true period is actually half of this. We measure this period to be 5.28 ± 0.01 hr in both colors. However, when the whole light curves were folded on this period, there remained a fairly high degree of scatter. Some data folded cleanly on this period, but data from other nights showed quasi-sinusoidal trends offset in phase. This suggested that the ephemeris was not constant for the duration of the observations.

To investigate this, we performed a periodicity analysis of the four extended sections of the light curve that have the densest coverage spanning two sites: 2013 April 11–14, April 18–21, April 24–26, and May 10–13 UTC (see Figure 16). We measured periods independently from both the SDSS-i′ and Pan-STARRS-Z light curves, and the results are compared in Table 2. While most often similar, the period measured in Pan-STARRS-Z is sometimes smaller.

To test the veracity of these periods, we folded the light curves on each one in turn. The most clearly defined epoch of minimum light occurred at BJD_{TDB}[4] = 2456403.54 ± 0.04 d. However, we note a high degree of asymmetry when the light

[4] Barycentric Julian Date (Barycentric Dynamical Time).

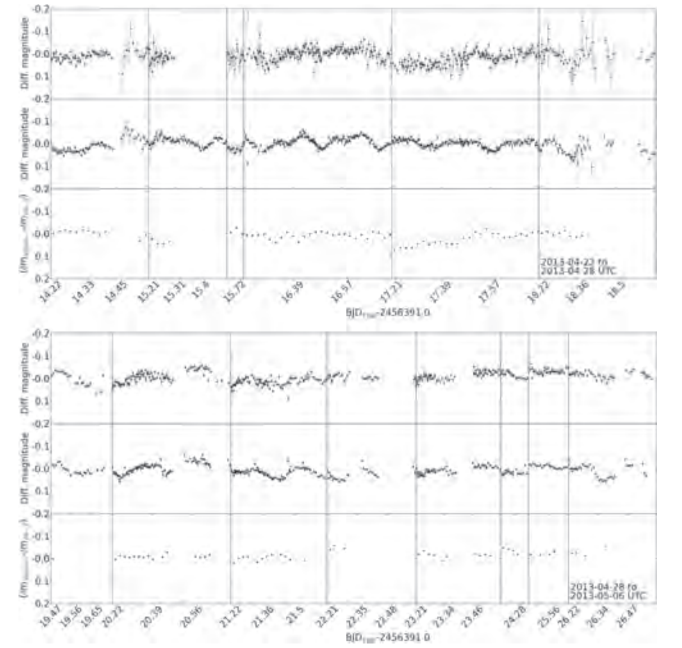

Figure 13. Middle two sections of the light curve of Luhman-16 in SDSS-i′ (top curve) and Pan-STARRS-Z (middle). The color index $(Z - i)$ curve is indicated in the bottom plot, binned in time with a 30-minute cadence.

curves are folded on these periods, even when data from a single night are used, so for clarity we adopted the most recent minimum-light epoch in each section during this analysis. Figures 17 and 18 show the most extended sections of the light curves in detail. Each section spans ∼13 hr, and >2× the 4.87 ± 0.01 hr-period measured by Gillon et al. (2013), and it can be seen that the morphology of the light curves changed markedly within this timeframe.

To further test the periodicities identified, and also to explore the possibility of multiple periods, we also employed the period04 software package to analyze the Pan-STARRS-Z time series. This package, including its handling of photometric and period uncertainties, is described in Lenz & Breger (2005). This analysis considered both the whole light curve and the sections described above, for comparison. Once the software identified each period in the data via a Fourier transform, it is removed from the time series and the residuals are searched for secondary frequencies. This procedure found evidence of multiple periods only in those light curve sections longer than 1 day (presented for comparison in Table 3). The two single-night time series of Section 3 manifested single periods of 5.07 and 5.37 hr. We therefore interpret the apparent multi-periodicity in longer data sections to be a result of variations in the quasi-periodic photometric modulation over time rather than simultaneous frequencies. That is, the light curves consistently exhibit modulation on a period close to 5.28 hr, but which fluctuates in phase and/or cycle period.

In order to quantify the rate of change in the measured periodicities, we focused on the Pan-STARRS-Z data in light curve Section 3 (2013 April 24–26) and attempted to

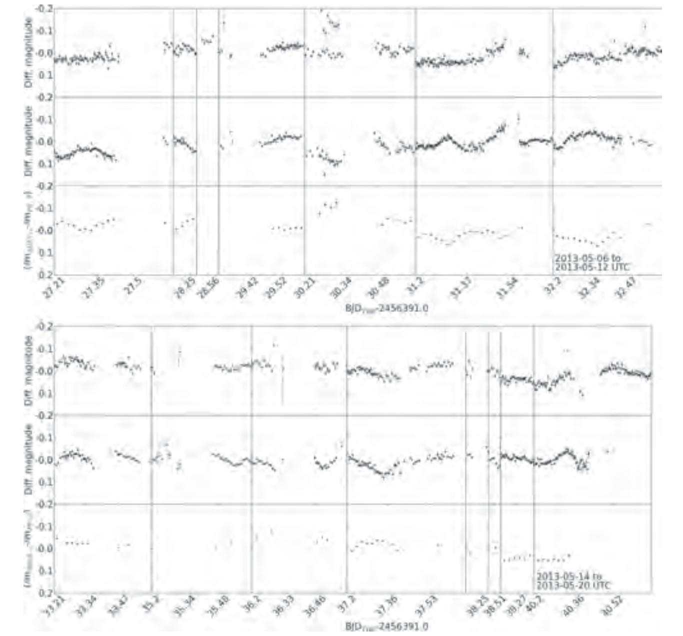

Figure 14. Final two sections of the light curve of Luhman-16 in SDSS-i′ (top curve) and Pan-STARRS-Z (middle). The color index $(Z - i)$ curve is indicated in the bottom plot, binned in time with a 30-minute cadence.

independently measure the period from subsequent nights of data. The corresponding periodograms are compared in Figure 19 and Table 3. Data from the 24th to 25th shows a distinct rotational cycle on a frequency of $f = 4.738\ \mathrm{d}^{-1}$, period $P = 5.066$ hr. The frequency peak is less well-defined for the data from the 25 to the 26th due to marked changes in amplitude and modulation within the same night, but is clearly offset from the earlier periodicity. The estimated frequency was $f = 4.464\ \mathrm{d}^{-1}$, $P = 5.37$ hr.

We note that the presence of red noise in the photometry could in principle produce spurious periodic signatures, particularly in shorter sections of data. To test our confidence that the periods measured in the target light curve are due to intrinsic variability, we used period04 to produce periodograms for the comparison star light curves. If the periodicities detected were due to red noise, the comparison star periodograms should show a signal at the same frequency. If little or no signal is evident, we may have greater confidence that the period is intrinsic to the target. We compare the periodograms of the comparison stars with that of the target in Figure 19. By averaging together the former, we computed the amplitude of the periodogram of constant stars (a_{target} (f)) at the frequencies of the periods detected in the target light curve. These are compared with the amplitude of the target's periodogram (a_{target} (f)) as an amplitude ratio = a_{target} $(f)/a_{\mathrm{target}}$ (f) in Table 3. The periodicities detected in all sections of the Luhman-16 light curve are stronger by several factors than any quasi-periodic signatures due to residual red noise.

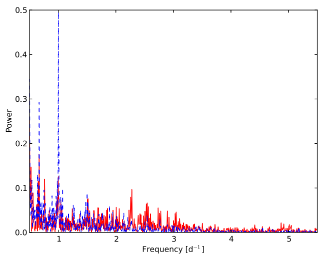

Figure 15. Periodogram analysis of the complete SDSS-i′ (blue, dashed) and Pan-STARRS-Z (red, solid) light curves of Luhman-16. No significant structure is seen at $f > 5.5\ \mathrm{d}^{-1}$.

Finally, we examined all sections of the light curves where simultaneous SDSS-i′ and Pan-STARRS-Z data were available, looking for evidence of phase shifts between the variability in the two colors. Most commonly, the same broad trends were observed with no discernible time-lag but sometimes with a slightly lower amplitude in SDSS-i′ (e.g., 2013 April 20–21, $\mathrm{BJD_{TDB}} = 2456403$-4, Section 2). But there were also occasions when the variability was not echoed in both light curves: 2013 May 10–11, $\mathrm{BJD_{TDB}} = 2456422$-3 (Section 4) is a good example of this.

While there was some variation in the morphology of the simultaneous light curves, in general the amplitude of modulation was found to be similar in both bands: ∼0.05 mag in SDSS-i′ and ∼0.06 mag in Pan-STARRS-Z, occasionally with more dramatic features, with amplitudes up to 0.1 mag. Figures 17 and 18 highlight how quickly the amplitude can change. For example, on 2013 May 10–11, the amplitude in Pan-STARRS-Z increased from 0.043 to 0.09 mag in 4.8 hr.

5. DISCUSSION

From our analysis the following main characteristics of the light curve of Luhman-16 emerge.

1. The period as measured from the photometric modulation was consistently close to 5.28 hr in both filters. However, it was observed to vary markedly, even over the course of 24 hr, and may be different in different filters. We measured *apparent* periods ranging between 4.464 and 5.844 d in Pan-STARRS-Z and 4.493–5.37 d in SDSS-i′ from different data sections between 1 and 3 d in length. We interpret this as quasi-periodic modulation rather than as multiple periodicities.
2. The amplitude in the i′- and Z-bands was generally similar, though that in the Z-band was sometimes slightly larger (∼20%). Both are typically ∼0.05 mag, though modulations of up to 0.1 mag were observed.
3. The amplitude changes rapidly, by up to a factor of ∼2 over the course of one rotational cycle.
4. Generally the variability appears in both filters at the same time and we find no clear evidence for phase shifts between passbands, but note some occasions when the object is variable in Pan-STARRS-Z but not in SDSS-i′.

Gillon et al. (2013) were able to separate the components during a part of their monitoring campaign and show that the variations at that time are caused by the T component. Biller et al. (2013) confirmed that the majority of the variation is due to the T-dwarf, though they found evidence of low-amplitude variability in the L-component as well. This fits well with the other known cases of pronounced, periodic variability in the L/T regime that are also found for objects with early T spectral types (T0.5, T1.5, T2.5, Artigau et al. 2011; Radigan et al. 2012; Girardin et al. 2013), with periods ranging between 2 and 20 hr (Herbst et al. 2007, pp. 297–311; Reiners & Basri 2008). It should be borne in mind that the spatially resolved monitoring has only been possible for relatively short periods of time and it is clear that the modulating surface features can change quite markedly. It remains possible that the L-component is not generally "quieter" but was simply quiescent at the time the data were obtained. However, it seems likely that the L-component undergoes lower-amplitude variations (at least in optical passbands) and therefore the following discussion assumes that our data represent variability in the cooler binary component. Significantly, Luhman-16 shows clear changes in the photometric modulation on timescales shorter than it's own average period and even more so within one (Earth) day. We observe changes in amplitude by up to a factor of two over the course of ∼5 hr, a behavior that is unprecedented for this type of object.

Biller et al. (2013) report an anticorrelation in variation between their (spatially resolved) r', i', and z' H light curves. We did not observe this phenomenon but suggest that this may be a result of the different bandpasses of "z" filter used. The Pan-STARRS-Z filter used by the LCOGT 1 m network has a central wavelength of 869.3 nm and a relatively narrow 818.0–920.5 nm bandpass compared with the 120 nm-wide SDSS-z' filter centered at 910 nm. The data presented in this work sample the optical rather than NIR behavior of this object.

We next consider a number of possible causes of this variability.

5.1. Magnetic Activity

A large fraction of late-type M dwarfs show periodic variations due to magnetically induced star spots, analogous to the solar spots (see the discussion in Scholz & Eislöffel 2004, 2005). However, several arguments can be used to exclude this option for early T dwarfs. First, such star spots are typically stable over several weeks and many rotational cycles, over a wide range of stellar masses (Hussain et al. 2001; Scholz & Eislöffel 2004). Second, toward late M dwarfs the photometric amplitudes produced by such spots drop considerably (Scholz et al. 2009). Other indicators of magnetic activity tend to disappear in the same spectral regime (continuous X-ray- and Hα emission, Mohanty et al. 2002; Stelzer et al. 2006). For L dwarfs stable periodic variations are rare (Bailer-Jones & Mundt 2001; Gelino et al. 2002), and apart from radio emission and transient events, signs of magnetic activity are also rarely observed (Schmidt et al. 2007; Berger et al. 2010, e.g.,), and stringent upper limits have already been placed for Luhman-16 by Osten et al. (2015). A re-appearance

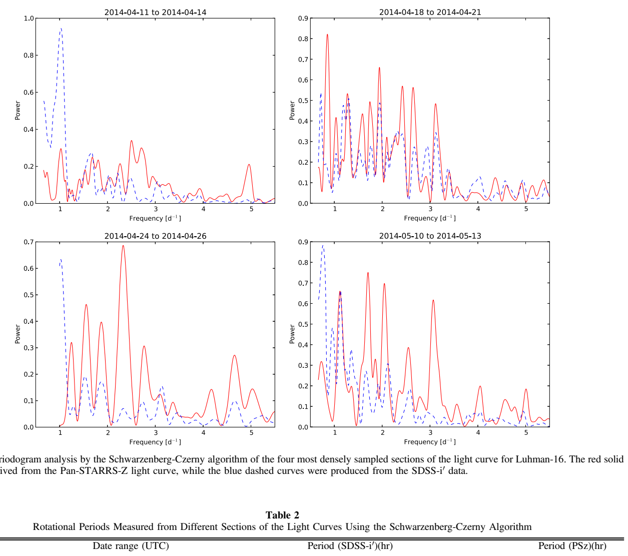

Figure 16. Periodogram analysis by the Schwarzenberg-Czerny algorithm of the four most densely sampled sections of the light curve for Luhman-16. The red solid curves are derived from the Pan-STARRS-Z light curve, while the blue dashed curves were produced from the SDSS-i′ data.

Table 2
Rotational Periods Measured from Different Sections of the Light Curves Using the Schwarzenberg-Czerny Algorithm

Section	Date range (UTC)	Period (SDSS-i′)(hr)	Period (PSz)(hr)
1	2013 Apr 11–14	4.84 ± 0.58	4.84 ± 0.12
2	2013 Apr 18–21	4.86 ± 0.11	4.53 ± 0.37
3	2013 Apr 24–26	5.15 ± 0.22	5.15 ± 0.91
4	2013 May 10–13	4.85 ± 0.09	4.79 ± 0.10
Whole	2013 Apr 11—May 20	5.277 ± 0.011	5.280 ± 0.010

of the star-like magnetically induced cool spots in the T dwarfs regime seems unlikely and is not further considered here. This does not preclude the presence of other surface features related to the interaction of the magnetic field (which still exist, as evidenced by the radio emission) and the atmospheric layers (e.g., charged clouds, see Helling et al. 2013).

5.2. Patchy Cloud in the Atmosphere of a Rotating Brown Dwarf

An inhomogeneous cloud level in the upper atmosphere would periodically expose deeper layers as the object rotated, causing variability in flux (Marley et al. 2010). This scenario would explain the changing amplitude as the evolution of the cloud layers over time and may also explain the apparent changes in period as clouds occurring at different latitudes. This interpretation has been supported by spectral and photometric studies of a number of early T dwarfs including Luhman-16 (e.g., Radigan et al. 2012; Apai et al. 2013; Buenzli et al. 2014), where models of time series spectra have ruled out the existence of cleared atmospheric "holes" in favor of regions of warmer, thinner clouds versus thicker, cooler clouds. Interesting, periodic variations have also been reported for objects of later spectral type, including the T6.5 dwarf 2MASS J22282889-4310262 (2M2228). Buenzli et al. (2012) identified significant phase shifts as a function of wavelength from NIR *HST/WFC3* spectroscopy and *Spitzer* photometry of this object, which they interpreted as probing different pressure levels within the object's atmosphere and discuss a number of plausible models of heterogeneous cloud scenarios.

A critical question is then "what level of the atmosphere do our observations probe?" To answer this, we used a Drift-

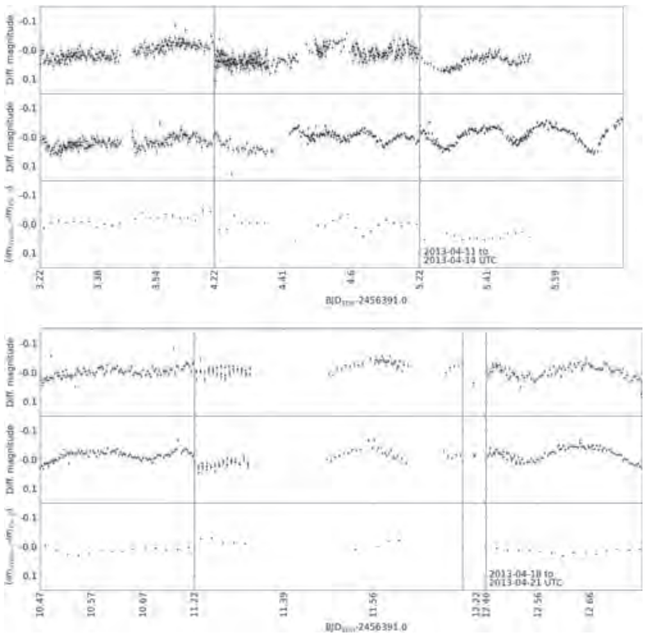

Figure 17. Close-up sections of the most densely sampled sections of the light curves, taken between 2013 April 11–14 (Section 1, top), April 18–21 (Section 2). The SDSS-i′ data are shown in the upper curve and the Pan-STARRS-Z data are in the middle curve. The difference between the time-binned light curves is indicated in the bottom plot.

Table 3
Periodicities Measured from Different Sections of the Pan-STARRS-Z Light Curve Using PERIOD04

Section	Date range (UTC)	Period (PSz)(hr)	Frequency (d^{-1})	Amplitude Ratio
1	2013 Apr 11–14	4.773 ± 0.032	5.029 ± 0.033	14.680
		4.493 ± 0.028	5.341 ± 0.034	14.985
2	2013 Apr 18–21	4.500 ± 0.017	5.333 ± 0.020	9.621
		5.061 ± 0.044	4.742 ± 0.041	8.908
3	2013 Apr 24–26	5.112 ± 0.016	4.695 ± 0.015	14.408
3a	2013 Apr 24–25	5.066 ± 0.085	4.738 ± 0.079	6.385
3b	2013 Apr 25–26	5.37 ± 0.089	4.464 ± 0.074	6.577
4	2013 May 10–13	4.716 ± 0.011	5.089 ± 0.011	22.259
Whole l/c		5.326 ± 0.001	4.507 ± 0.001	6.597
		5.271 ± 0.001	4.5528 ± 0.0009	12.0658
		4.744 ± 0.0008	5.0595 ± 0.0008	10.2985
		4.613 ± 0.001	5.203 ± 0.001	11.170
		4.107 ± 0.001	5.844 ± 0.002	7.206

Note. The amplitude ratio compares the amplitude of the target's periodogram with that of the combined periodograms of the comparison stars at each frequency.

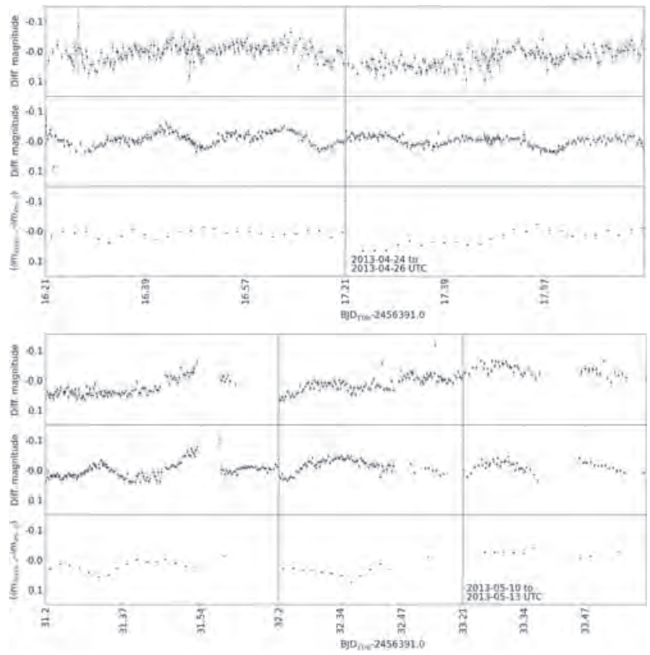

Figure 18. Close-up sections of the most densely sampled sections of the light curves, taken between April 24–26 (Section 3, top) and May 10–13 (Section 4). The SDSS-i′ data are shown in the upper curve and the Pan-STARRS-Z data are in the middle curve. The difference between the time-binned light curves is indicated in the bottom plot.

Phoenix model atmosphere (Helling et al. 2008c; Witte et al. 2011) to explore the cloud opacity and the extinction as a function of wavelength for an object with $T_{\rm eff} = 1300$ K and $\log g = 5.0$. The model atmosphere included a detailed simulation of cloud formation based on a kinetic description of the microphysical processes involved (Helling & Fomins 2013).

Figure 20 (left) demonstrates that the upper cloud levels are largely transparent for observations at the central wavelength of the filters we used. Gas opacity becomes significant at temperatures between ~1200 and 1600 K. The cloud layers at $T_{\rm gas} = 1500$–1800 K have similar mean grain sizes but differ in composition (silicate versus iron), while for layers between $T_{\rm gas} = 1200$–1500 K the opposite is true (Figure 20, right). This is consistent with Buenzli et al. (2012) in that comparing different IR band (or IR with optical filter) observations would probe different levels of the atmosphere. However, we would not expect to see phase offsets between our optical light curves in this model, given the similarity of the extinction profiles in Figure 20.

We also examined the timescales needed for convective mixing, advection, and gravitational settling, applying the same model atmosphere structure as in Figure 20 (Figure 21). We found that convective mixing with overshooting is too slow ($\tau_{\rm mix} > 100$ d) to explain our observations. The advection timescale is very small if the velocities recommended in

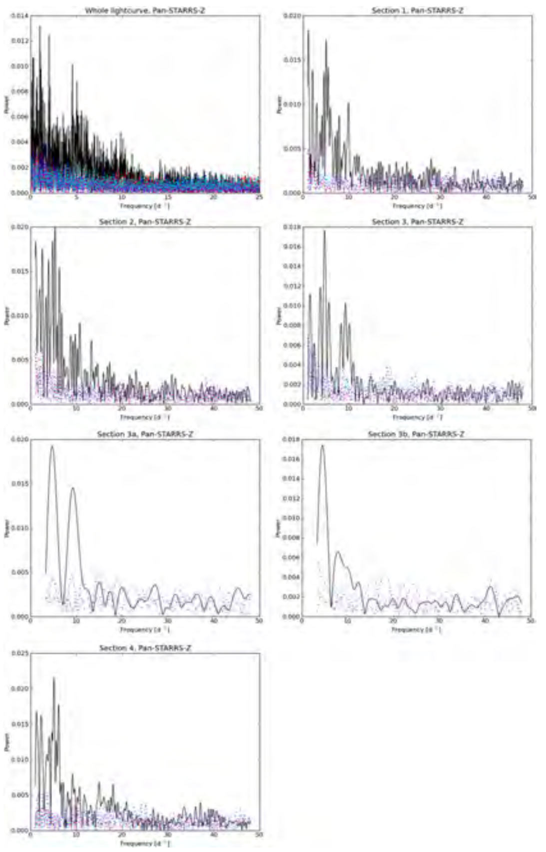

Figure 19. PERIOD04 periodogram of the Pan-STARRS-Z light curve for Luhman-16 compared with the periodograms of the comparison star light curves for the same data section: (top to bottom) whole light curve, 2013 April 11–14 (Section 1), April 18–21 (Section 2), April 24–26 (Section 3), April 24–25 (Section 3a), April 25–26 (Section 3b), and May 10–13 (Section 4).

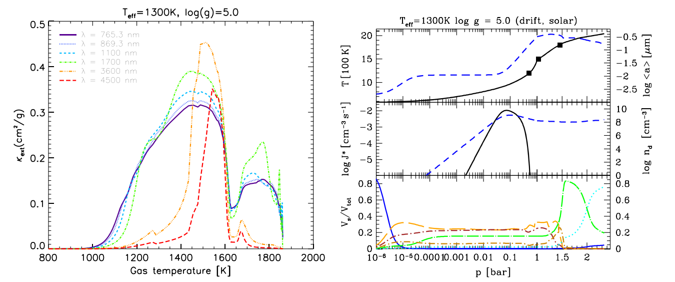

Figure 20. Drift-Phoenix model atmosphere results for $T_{\rm eff} = 1300$ K and $\log g = 5.0$. (Left): The total opacity, $\kappa_{\rm ext}$, including absorption and scattering, due to gas in clouds as a function of pressure for observations in the optical bandpasses used in this work (SDSS-i′ $\lambda_c = 765.3$ nm, Pan-STARRS-Z $\lambda_c = 869.3$ nm), with NIR filters used in other studies plotted for comparison. (Right): The cloud structure with atmospheric pressure in terms of temperature (top)/mean grain size $\langle a \rangle$, rate of formation per second and per cm^3 atmospheric gas/density of dust particles (middle) and composition (bottom), where $V_S/V_{\rm tot}$ indicates the amounts of the following materials as a fraction of the total: dark blue—TiO_2[s], green—Fe[s], light blue—[Al_2O_3], orange—Mg_2SiO_4[s], brown—SiO[s], brown-orange—MgO.

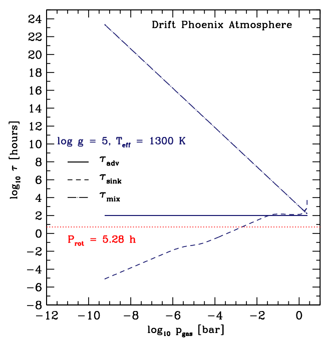

Figure 21. Advective ($\tau_{\rm adv}$), convective mixing ($\tau_{\rm mix}$), and gravitational settling ($\tau_{\rm sink}$) timescales evaluated for an example Drift-Phoenix model atmosphere with $T_{\rm eff} = 1300$ K and $\log g = 5.0$.

Showman & Kaspi (2013) are adopted, although the correct length scale to use for the process is unclear. The timescale for gravitational settling depends strongly on height and grain sizes, leveling out at lower altitudes due to increasing gas density. The grain size is, however, not a parameter but the result of a kinetic dust formation model in the Drift-Phoenix model atmosphere simulations that were used here.

Our opacity calculations suggest that with some degree of mixing/rotational sheering, the lower and darker cloud layers would become visible and could be advected with the rotationally driven flow. Our simple timescale analysis further suggests that the observed variability is also connected with the cloud formation process, which is influenced by the gravitational settling. We also note that external processes can affect cloud formation: Rimmer & Helling (2013) found that cosmic rays can impact upper cloud layers, causing a higher rate of nucleation and number of grains, and a corresponding drop in the grain size. This in turn can influence gas opacity. The cosmic ray flux will vary in space and time due to the object's magnetic field structure, as well as external conditions in the interstellar medium and the origin of the cosmic rays. Whether this is a factor in the atmosphere of Luhman-16 remains an open question; it would be very interesting to measure a magnetic field on this object. Further work is necessary to incorporate cosmic ray processes into present cloud models.

This research has made use of the LCOGT Telescope Network, and the LCOGT Archive, which is operated by the California Institute of Technology, under contract with the Las Cumbres Observatory. K.H. is supported by a Royal Leverhulme Trust Senior Research Fellowship and by the UK Science and Technology Facilities Council (STFC) grant ST/J001651/1. C.H. and G.L. highlight the financial support of the European Community under the FP7 by the ERC starting grant 257431. This research has made use of NASA's Astrophysics Data System Bibliographic Services.

Facility: LCOGT.

REFERENCES

Ackerman, A. S., & Marley, M. S. 2001, ApJ, 556, 872
Allard, N. F., Allard, F., Hauschildt, P. H., Kielkopf, J. F., & Machin, L. 2003, A&A, 411, 473
Apai, D., Radigan, J., Buenzli, E., et al. 2013, ApJ, 768, id.121
Arellano Ferro, A., Bramich, D. M., Figuera Jaimes, R., Giridhar, S., & Kuppuswamy, K. 2012, MNRAS, 420, 1333
Artigau, É., Doyon, R., Lafreniére, D., et al. 2006, ApJL, 651, L57
Artigau, É., Bouchard, S., Doyon, R., & Lafrenié, D 2009, ApJ, 701, 1534

Artigau, É, Lafreniére, D., Doyon, R., et al. 2011, ApJ, 739, id.48
Bailer-Jones, C. A. L., & Mundt, R. 2001, A&A, 367, 218
Barman, T. S., Macintosh, B., Konopacky, Q. M., & Marois, C. 2011a, ApJ, 735, id.L39
Barman, T. S., Macintosh, B., Konopacky, Q. M., Marois, C., et al. 2011b, ApJ, 733, id.65
Bartlett, M. S. 1948, Natur, 161, 686
Berger, E., Basri, G., Fleming, T. A., et al. 2010, ApJ, 709, 332
Biller, B. A., Crossfield, I. J. M., Mancini, L., et al. 2013, ApJ, 778, 10
Bramich, D. 2008, MNRAS, 386, L77
Brown, T., Baliber, N., Bianco, F. B., et al. 2013, PASP, 125, 1031
Buenzli, E., Apai, D., Morley, C. V., et al. 2012, ApJL, 760, L31
Buenzli, E., Apai, D., Radigan, J., Reid, I. N., & Flateau, D. 2014, ApJ, 782, 77
Burgasser, A., Marley, M. S., Ackerman, A. S., et al. 2002, ApJL, 571, L151
Burgasser, A. J., Sheppard, S. S., & Luhman, K. L. 2013, arXiv:1303.7283
Burgasser, A. J., Gillon, M., Faherty, J. K., et al. 2014, ApJ, 785, 48
Burrows, A., Sudarsky, D., & Hubeny, I. 2006, ApJ, 640, 1063
Cavanagh, B., Jenness, T., Economou, F., & Currie, M. J. 2008, AN, 329, 295
Crossfield, I. J. M., Biller, B., Schlieder, J. E., et al. 2014, Natur, 505, 654
Epchtein, N., Deul, E., Derriere, S., et al. 1999, A&A, 349, 236
Faherty, Jk., Tinney, C. G., Skemer, A., et al. 2014, ApJ, 790, 90
Gelino, C. R., Marley, M. S., Holtzman, J. A., Ackerman, A. S., & Lodders, K. 2002, ApJ, 577, 433
Gillon, M., Triaud, A. H. M. J., Jehin, E., et al. 2013, A&A, 555, 5
Girardin, F., Artigau, É, & Doyon, R. 2013, ApJ, 767, id.61
Heinze, A., Metchev, S., Apai, D., et al. 2013, ApJ, 767, 173
Heinze, A., Metchev, S., Kellogg, K., et al. 2015, ApJ, 801, 104
Helling, C., & Fomins, A. 2013, RSPTA, 371, 20110581
Helling, Ch., Ackerman, A., Allard, F., et al. 2008a, MNRAS, 391, 1854
Helling, Ch., Woitke, P., Thi, W.-F., et al. 2008b, A&A, 485, 547
Helling, Ch., Dehn, M., Woitke, P., & Hauschildt, P. H. 2008c, ApJL, 675, L105
Helling, Ch., Jardine, M., Stark, C., & Diver, D. 2013, ApJ, 767, 136
Herbst, W., Eislöffel, J., Mundt, R., & Scholz, A. 2007, in Protostars and Planets V, Vol. 951, ed. B. Reipurth, D. Jewitt, & K. Keil (Tucson, AZ: Univ. Arizona Press), 297
Hussain, G. A. J., Jardine, M., & Collier Cameron, A. 2001, MNRAS, 322, 681
Ishihara, D., Onaka, T., Kataza, H., et al. 2010, A&A, 514, A1
Kniazev, A. Y., Vaisanen, P., Muzić, K., et al. 2013, ApJ, 770, id.124
Koen, C. 2013, MNRAS, 429, 652
Kovács, G., Bakos, G., & Noyes, R. W. 2005, MNRAS, 356, 557
Lenz, P., & Breger, M. 2005, CoAst, 146, 53
Lucas, P. W., Tinney, C. G., Burningham, B., et al. 2010, MNRAS, 408, L56
Luhman, K. L. 2013, arXiv:1303.2401
Mamajek, E. E. 2013, arXiv:1303.5345
Marley, M. S., Saumon, D., & Goldblatt, C. 2010, ApJL, 723, L117
McCaughrean, M. J., Close, L. M., Scholz, R.-D., et al. 2004, A&A, 413, 1029
Mohanty, S., Basri, G., Shu, F., Allard, F., & Chabrier, G. 2002, ApJ, 571, 469
Oppenheimer, B. R., Baranec, C., Beichman, C., et al. 2013, ApJ, 768, 24
Osten, R. A., Melis, C., Stelzer, B., et al. 2015, ApJ, 805, 3
Pont, F., Zucker, S., & Queloz, D. 2006, MNRAS, 373, 231
Radigan, J., Jayawardhana, R., Lafreniére, D., et al. 2012, ApJ, 750, 105
Radigan, J., Jayawardhana, R., Lafreniére, D., et al. 2013, ApJ, 778, 36
Reiners, A., & Basri, G. 2008, ApJ, 684, 1390
Rhines, P. 1970, GApFD, 1, 273
Rimmer, P. B., & Helling, C. 2013, ApJ, 774, 108
Schmidt, S. J., Cruz, K. L., Bongiorno, B. J., Liebert, J., & Reid, I. N. 2007, AJ, 133, 2258
Scholz, A., & Eislöffel, J. 2004, A&A, 419, 249
Scholz, A., & Eislöffel, J. 2005, A&A, 429, 1007
Scholz, A., Eislöffel, J., & Mundt, R. 2009, MNRAS, 400, 1548
Scholz, A., et al. 2011, in Proc. of Stellar Clusters & Associations: A RIA Workshop on Gaia, ed. E. J. Alfaro Navarro, A. T. Gallego Calvente & M. R. Zapatero Osorio (Granada: IAA-CSIC), 250
Schwarzenberg-Czerny, A. 1999, ApJ, 516, 315
Showman, A. P., & Kaspi, Y. 2013, ApJ, 776, 85
Skemer, A. J., Close, L. M., Szücs, L., et al. 2011, ApJ, 732, 107
Skrutskie, M., Cutri, R. M., Stiening, R., et al. 2006, AJ, 131, 1163
Smith, J. C., Stumpe, M. C., Van Cleve, J. E., et al. 2012, PASP, 124, 1000
Stelzer, B., Schmitt, J. H. M. M., Micela, G., & Liefke, C. 2006, A&A, 460, L35
Stetson, P. B. 1987, PASP, 99, 191
Tamuz, O., Mazeh, T., & Zucker, S. 2005, MNRAS, 356, 1466
Tinney, C. G., Burgasser, A. J., & Kirkpatrick, J. D. 2003, AJ, 126, 975
Tsuji, T., Ohnaka, K., Aoki, W., & Nakajima, T. 1996, A&A, 308, 29
Vaughan, S. 2012, RSPTA, 371, 20110549
Witte, S., Helling, C., & Hauschildt, P. H. 2009, A&A, 506, 1367
Witte, S., Helling, Ch., Barman, T., Heidrich, N., & Hauschildt, P. H. 2011, A&A, 529, A44
Woitke, P., & Helling, C. 2003, A&A, 339, 297
Wright, E. L., Eisenhardt, P. R. M., Mainzer, A. K., et al. 2010, AJ, 140, 1868

PUBLICATIONS OF THE ASTRONOMICAL SOCIETY OF THE PACIFIC, 127:851–856, 2015 September

HAT-P-55b: A Hot Jupiter Transiting a Sun-Like Star[1]

D. JUNCHER,[2,3] L. A. BUCHHAVE,[3,4] J. D. HARTMAN,[5] G. Á. BAKOS,[5] A. BIERYLA,[4] T. KOVÁCS,[5,6,9] I. BOISSE,[7]
D. W. LATHAM,[4] G. KOVÁCS,[6] W. BHATTI,[5] Z. CSUBRY,[5] K. PENEV,[5] M. DE VAL-BORRO,[5] E. FALCO,[4]
G. TORRES,[4] R. W. NOYES,[4] J. LÁZÁR,[8] I. PAPP,[8] AND P. SÁRI[8]

Received 2015 March 30; accepted 2015 June 11; published 2015 August 17

ABSTRACT. We report the discovery of a new transiting extrasolar planet, HAT-P-55b . The planet orbits a $V = 13.207 \pm 0.039$ sun-like star with a mass of $1.013 \pm 0.037\ M_\odot$, a radius of $1.011 \pm 0.036\ R_\odot$, and a metallicity of -0.03 ± 0.08. The planet itself is a typical hot Jupiter with a period of 3.5852467 ± 0.0000064 days, a mass of $0.582 \pm 0.056\ M_J$ and a radius of $1.182 \pm 0.055\ R_J$. This discovery adds to the increasing sample of transiting planets with measured bulk densities, which is needed to put constraints on models of planetary structure and formation theories.

Online material: machine-readable table

1. INTRODUCTION

Today we know of almost 1800 validated exoplanets and more than 4000 exoplanet candidates. Among these, the transiting exoplanets (TEPs) are essential in our exploration and understanding of the physical properties of exoplanets. While radial velocity observations alone only allow us to estimate the minimum mass of a planet, we can combine them with transit observations for a more comprehensive study of the physical properties of the planet. When a planet transits, we can determine the inclination of the orbit and the radius of the planet, allowing us to break the mass degeneracy and, along with the mass, determine the mean density of the planet. The mean density of a planet offers us insight into its interior composition, and although there is an inherent degeneracy arising from the fact that planets of different compositions can have identical masses and radii, this information allows us to map the diversity and distribution of exoplanets and even put constraints on models of planetary structure and formation theories.

The occurrence rate of hot Jupiters in the Solar neighborhood is around 1% (Udry & Santos 2007; Wright et al. 2012). With a transit probability of about ~10%, roughly one thousand stars need to be monitored in photometry to find just a single hot Jupiter. Therefore, the majority of the known transiting hot Jupiters have been discovered by photometric wide field surveys targeting tens of thousands of stars per night.

In this paper, we present the discovery of HAT-P-55b by the Hungarian-made Automated Telescope Network (HATNet; see Bakos et al. [2004]), a network of six small fully automated wide field telescopes of which four are located at the Fred Lawrence Whipple Observatory in Arizona, and two are located at the Mauna Kea Observatory in Hawaii. Since HATNet saw first light in 2003, it has searched for TEPs around bright stars ($V \lesssim 13$) covering about 37% of the Northern sky, and discovered approximately 25% of the known transiting hot Jupiters.

The layout of the paper is as follows. In § 2, we present the different photometric and spectroscopic observations that lead to the detection and characterization of HAT-P-55b. In § 3, we derive the stellar and planetary parameters. Finally, we discuss the characteristics of HAT-P-55b in § 4.

2. OBSERVATIONS

The general observational procedure used by HATNet to discover TEPs has been described in detail in previous papers (e.g., Bakos et al. 2010; Latham et al. 2009). In this section, we

[1] Based on observations obtained with the Hungarian-made Automated Telescope Network. Based in part on radial velocities obtained with the SOPHIE spectrograph mounted on the 1.93-m telescope at Observatoire de Haute-Provence, France. Based in part on observations made with the Nordic Optical Telescope, operated on the island of La Palma jointly by Denmark, Finland, Iceland, Norway, and Sweden, in the Spanish Observatorio del Roque de los Muchachos of the Instituto de Astrofísica de Canarias. Based in part on observations obtained with the Tillinghast Reflector 1.5-m telescope and the 1.2-m telescope, both operated by the Smithsonian Astrophysical Observatory at the Fred Lawrence Whipple Observatory in Arizona.

[2] Niels Bohr Institute, University of Copenhagen, Copenhagen DK-2100, Denmark.
[3] Centre for Star and Planet Formation, Natural History Museum of Denmark, University of Copenhagen, DK-1350 Copenhagen, Denmark.
[4] Harvard-Smithsonian Center for Astrophysics, Cambridge, MA 02138.
[5] Department of Astrophysical Sciences, Princeton University, Princeton, NJ 08544.
[6] Konkoly Observatory, Budapest 1121, Hungary.
[9] Fulbright Fellow.
[7] Aix Marseille Université, CNRS, LAM (Laboratoire d'Astrophysique de Marseille) UMR 7326, 13388 Marseille, France.
[8] Hungarian Astronomical Association (HAA), Budapest, Hungary.

present the specific details for the discovery and follow-up observations of HAT-P-55b.

2.1. Photometry

2.1.1. Photometric Detection

HAT-P-55b was initially identified as a candidate transiting exoplanet based on photometric observations made by the HATNet survey (Bakos et al. 2004) in 2011. The observations of HAT-P-55 were made on nights between February and August with the HAT-5 telescope at the Fred Lawrence Whipple Observatory (FLWO) in Arizona, and on nights between May and August with the HAT-8 telescope at Mauna Kea Observatory in Hawaii. Both telescopes used a Sloan r-band filter. HAT-5 provided a total of 10,574 images with a median cadence of 218 s, and HAT-8 provided a total of 6428 images with a median cadence of 216 s.

The results were processed and reduced to trend-filtered light curves using the External Parameter Decorrelation method (EPD; see Bakos et al. 2010) and the Trend Filtering Algorithm (TFA; see Kovács et al. 2005). The light curves were searched for periodic transit signals using the Box Least-Squares method (BLS; see Kovács et al. 2002). The individual photometric measurements for HAT-P-55 are listed in Table 1, and the folded light curves together with the best-fit transit light curve model are presented in Figure 1.

TABLE 1
DIFFERENTIAL PHOTOMETRY OF HAT-P-55

BJD[a] (2,400,000+)	Mag[b]	σ_{Mag}	Mag (orig)[c]	Filter	Instrument
55667.80829	−0.01089	0.02455	…	r	HATNet
55649.88231	0.00947	0.01537	…	r	HATNet
55778.95165	0.02246	0.01538	…	r	HATNet
55692.90580	−0.00422	0.01713	…	r	HATNet
55735.92912	0.00602	0.02207	…	r	HATNet
55771.78174	−0.01054	0.01241	…	r	HATNet
55710.83270	−0.01741	0.01609	…	r	HATNet
55674.98046	0.01418	0.01771	…	r	HATNet
55728.75933	0.04136	0.03816	…	r	HATNet
55710.83315	0.00822	0.01348	…	r	HATNet

NOTE—Table 1 is published in its entirety in the electronic edition of the *PASP*. A portion is shown here for guidance regarding its form and content.
[a] Barycentric Julian Date calculated directly from UTC, *without* correction for leap seconds.
[b] The out-of-transit level has been subtracted. These magnitudes have been subjected to the EPD and TFA procedures, carried out simultaneously with the transit fit for the follow-up data. For HATNet, this filtering was applied *before* fitting for the transit.
[c] Raw magnitude values after correction using comparison stars, but without application of the EPD and TFA procedures. This is only reported for the follow-up light curves.

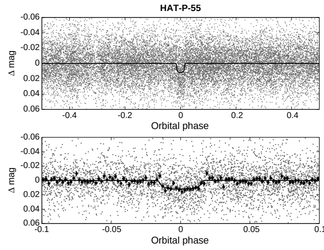

FIG. 1.—HATNet light curve of HAT-P-55 phase folded with the transit period. The *top panel* shows the unbinned light curve, while the *bottom panel* shows the region zoomed-in on the transit, with *dark filled circles* for the light curve binned in phase with a bin size of 0.002. The *solid line* represents the best-fit light curve model.

2.1.2. Photometric Follow-Up

We performed photometric follow-up observations of HAT-P-55 using the KeplerCam CCD camera on the 1.2-m telescope at the FLWO, observing a transit ingress on the night of 2013 May 23, and a full transit on the night of 2014 April 7. Both transits were observed using a Sloan i-band filter. For the first event we obtained 230 images with a median cadence of 64 s, and for the second event we obtained 258 images with a median cadence of 67 s.

The results were reduced to light curves following the procedure of Bakos et al. (2010), and EPD and TFA were performed to remove trends simultaneously with the light curve modeling. The individual photometric follow-up measurements for HAT-P-55 are listed in Table 1, and the folded light curves together with our best-fit transit light curve model are presented in Figure 2.

Subtracting the transit signal from the HATNet light curve, we used the BLS method to search for additional transit signals and found none. A Discrete Fourier Transform also revealed no other periodic signals in the data.

2.2. Spectroscopy

We performed spectroscopic follow-up observations of HAT-P-55 to rule out false positives and to determine the RV variations and stellar parameters. Initial reconnaissance observations were carried out with the Tillinghast Reflector Echelle Spectrograph (TRES; Fűrész 2008) at the FLWO. We obtained two spectra near opposite quadratures on the nights of October 4 and 31, 2012. Using the Stellar Parameters Classification method (SPC; see Buchhave et al. [2012]), we determined

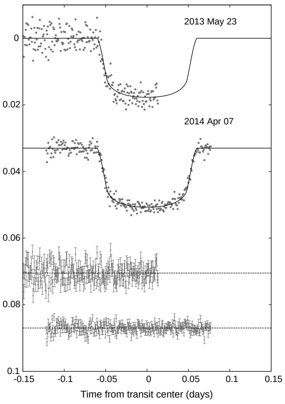

FIG. 2.—Unbinned transit light curves for HAT-P-55, acquired with KeplerCam at the FLWO 1.2-m telescope. The light curves have been EPD- and TFA-processed, as described in Bakos et al. (2010). The *solid lines* represents the best-fit from the global modeling described in § 3 . Residuals from the fit are displayed below at the bottom of the figure. The error bars represent the photon and background shot noise, plus the readout noise.

the initial RV measurements and stellar parameters. We found a mean absolute RV of $-9.42\ \mathrm{km\,s^{-1}}$ with an rms of $48\ \mathrm{ms^{-1}}$, which is consistent with no detectable RV variation. The stellar parameters, including the effective temperature $T_{\mathrm{eff}\star} = 5800 \pm 50$ K, surface gravity $\log g_\star = 4.5 \pm 0.1$ (log cgs), and projected rotational velocity $v \sin i = 5.0 \pm 0.4\ \mathrm{km\,s^{-1}}$, correspond to those of a G2 dwarf.

High-resolution spectroscopic observations were then carried out with the SOPHIE spectrograph mounted on the 1.93-m telescope at Observatoire de Haute-Provence (OHP) (Perruchot et al. 2011; Bouchy et al. 2013), and with the FIES spectrograph mounted on the 2.6-m Nordic Optical Telescope (Djupvik & Andersen 2010). We obtained six SOPHIE spectra on nights between 2013 June 3 and 12, and ten FIES spectra on nights between May 15, 2013 and August 26, 2013.

We reduced and extracted the spectra and derived radial velocities and spectral line bisector span (BS) measurements following the method of Boisse et al. (2013) for the SOPHIE data and the method of Buchhave et al. (2010) for the FIES data. The final RV data and their errors are listed for both instruments in Table 2, and the folded RV data together with our best-fit orbit

TABLE 2
RELATIVE RADIAL VELOCITIES, AND BISECTOR SPAN MEASUREMENTS OF HAT-P-55

BJD[a] (2,456,000+)	RV[b] ($\mathrm{ms^{-1}}$)	σ_{RV}[c] ($\mathrm{ms^{-1}}$)	BS ($\mathrm{ms^{-1}}$)	σ_{BS} ($\mathrm{ms^{-1}}$)	Phase	Instrument
427.61363	−50.8	19.0	20.0	38.0	0.425	FIES
428.54873	90.9	16.0	−5.0	32.0	0.686	FIES
446.59498	102.0	15.1	−15.9	30.2	0.720	OHP
448.51197	−39.8	13.1	7.5	26.2	0.254	OHP
450.47096	61.0	9.1	−8.2	18.2	0.801	OHP
454.49007	9.8	9.1	−2.2	18.2	0.922	OHP
455.52529	−86.4	10.9	3.4	21.8	0.211	OHP
456.44155	−48.4	6.8	2.2	13.6	0.466	OHP
528.43752	43.8	17.7	−50.0	35.4	0.547	FIES
528.48816	18.5	15.6	−31.0	31.2	0.561	FIES
529.50540	54.6	14.7	0.0	29.4	0.845	FIES
529.55576	38.8	23.8	−27.0	47.6	0.859	FIES
530.41408	−26.2	13.0	22.0	26.0	0.099	FIES
530.46398	−51.0	15.6	18.0	31.2	0.112	FIES
531.47003	−51.4	14.4	24.0	28.8	0.393	FIES
531.52009	−57.7	13.0	27.0	26.0	0.407	FIES

[a] Barycentric Julian Date calculated directly from UTC, *without* correction for leap seconds.
[b] The zero-point of these velocities is arbitrary. An overall offset γ_{rel} fitted to these velocities in § 3 has *not* been subtracted.
[c] Internal errors excluding the component of astrophysical jitter considered in § 3.

and corresponding residuals and bisectors are presented in Figure 3. To avoid underestimating the BS uncertainties we base them directly on the RV uncertainties, setting them equal to twice the RV uncertainties. At a first glance, there does seem to be a slight hint of variation of the BSs in phase with the RVs suggesting there might be a blend. This is not the case, however, as we will show in our detailed blend analysis in § 3.

We applied the SPC method to the FIES spectra to determine the final spectroscopic parameters of HAT-P-55. The values were calculated using a weighted mean, taking into account the cross correlation function (CCF) peak height. The results are shown in Table 3.

3. ANALYSIS

In order to rule out the possibility that HAT-P-55 is a blended stellar eclipsing binary system, and not a transiting planet system, we carried out a blend analysis following Hartman et al. (2012). We find that a single star with a transiting planet fits the light curves and catalog photometry better than models involving a stellar eclipsing binary blended with light from a third star. While it is possible to marginally fit the photometry using a G star eclipsed by a late M dwarf that is blended with another bright G star, simulated spectra for this scenario are obviously composite and show large (multiple km $\mathrm{s^{-1}}$) bisector span and RV variations that are inconsistent with the observations. Based on this analysis we conclude that HAT-P-55 is not a blended stellar eclipsing binary system, and is instead best explained

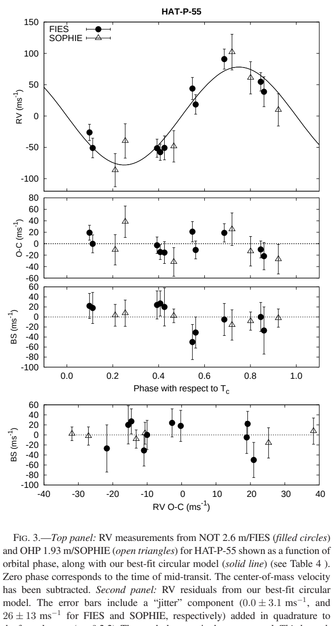

FIG. 3.—*Top panel:* RV measurements from NOT 2.6 m/FIES (*filled circles*) and OHP 1.93 m/SOPHIE (*open triangles*) for HAT-P-55 shown as a function of orbital phase, along with our best-fit circular model (*solid line*) (see Table 4). Zero phase corresponds to the time of mid-transit. The center-of-mass velocity has been subtracted. *Second panel:* RV residuals from our best-fit circular model. The error bars include a "jitter" component ($0.0 \pm 3.1\ \mathrm{ms^{-1}}$, and $26 \pm 13\ \mathrm{ms^{-1}}$ for FIES and SOPHIE, respectively) added in quadrature to the formal errors (see § 2.2). The symbols are as in the upper panel. *Third panel:* Bisector spans (BS), adjusted to have a median of 0. *Bottom panel:* RV residuals from our best-fit circular model vs. BS. There is no sign of correlation. Note the different vertical scales of the panels.

as a transiting planet system. We also consider the possibility that HAT-P-55 is a planetary system with a low-mass stellar companion that has not been spatially resolved. The constraint on this scenario comes from the catalog photometric measurements, based on which we can exclude a physical companion star with a mass greater than $0.7\ M_\odot$. Any companion would dilute both the photometric transit and radial velocity orbit. The maximum dilution allowed by the photometry would increase the planetary radius by ~15%.

TABLE 3
STELLAR PARAMETERS FOR HAT-P-55

Parameter	Value	Source
Identifying information		
R.A. (h:m:s)	$17^h37^m05.52$ s	2MASS
Dec. (d:m:s)	+254352.3	2MASS
GSC ID	GSC 2080-00517	GSC
2MASS ID	2MASS 17370562+2543522	2MASS
HTR ID	HTR 287-004	HATNet
Spectroscopic properties		
$T_{\mathrm{eff}\star}$ (K)	5808 ± 50	SPC[a]
[Fe/H]	−0.030 ± 0.080	SPC
$v \sin i$ (km $\mathrm{s^{-1}}$)	1.80 ± 0.50	SPC
γ_{RV} (km $\mathrm{s^{-1}}$)	−9.42 ± 0.05	TRES
Photometric properties		
B (mag)	13.871 ± 0.039	APASS
V (mag)	13.207 ± 0.039	APASS
I (mag)	12.67 ± 0.14	TASS
g (mag)	13.50 ± 0.04	APASS
r (mag)	13.06 ± 0.02	APASS
i (mag)	12.88 ± 0.04	APASS
J (mag)	12.020 ± 0.022	2MASS
H (mag)	11.714 ± 0.026	2MASS
K_s (mag)	11.627 ± 0.025	2MASS
Derived properties		
$M_\star (M_\odot)$	1.013 ± 0.037	Isochrones+$\rho_\star$+SPC[b]
$R_\star (R_\odot)$	1.011 ± 0.036	Isochrones+$\rho_\star$+SPC
$\log g_\star$ (cgs)	4.434 ± 0.032	Isochrones+$\rho_\star$+SPC
$L_\star (L_\odot)$	1.042 ± 0.089	Isochrones+$\rho_\star$+SPC
M_V (mag)	4.785 ± 0.097	Isochrones+$\rho_\star$+SPC
M_K (mag, ESO)	3.266 ± 0.081	Isochrones+$\rho_\star$+SPC
Age (Gyr)	4.2 ± 1.7	Isochrones+$\rho_\star$+SPC
A_V (mag)[c]	$0.020^{+0.060}_{-0.020}$	Isochrones+$\rho_\star$+SPC
Distance (pc)	480 ± 19	Isochrones+$\rho_\star$+SPC
$\log R'_{HK}$	−5.0 ± 0.1	Boisse et al 2010

[a] SPC = Stellar Parameter Classification; method based on cross-correlating high-resolution spectra against synthetic templates (Buchhave et al. 2012). These parameters rely primarily on SPC, but also have a small dependence on the iterative analysis incorporating the isochrone search and global modeling of the data, as described in the text.
[b] Isochrones+$\rho_\star$+SPC = Based on the Y^2 isochrones (Yi et al. 2001), the stellar density used as a luminosity indicator, and the SPC results.
[c] Total V band extinction to the star determined by comparing the catalog broad-band photometry listed in the table to the expected magnitudes from the Isochrones+$\rho_\star$+SPC model for the star. We use the Cardelli et al. (1989) extinction law.

We analyzed the system following the procedure of Bakos et al. (2010) with modifications described in Hartman et al. (2012). In short, we (1) determined the stellar atmospheric parameters of the host star HAT-P-55 by applying the SPC method to the FIES spectra; (2) used a Differential Evolution Markov-Chain Monte Carlo procedure to simultaneously model the RVs and the light curves, keeping the limb-darkening coefficients fixed to those of the Claret (2004) tabulations; and (3) used the spectroscopically inferred effective temperatures and metallicities of the star, the stellar densities determined from the light curve modeling, and the Yonsei-Yale theoretical stellar

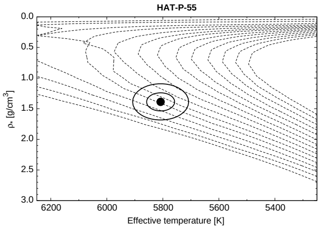

FIG. 4.—Comparison between the measured values of $T_{\mathrm{eff}\star}$ and $\rho_\star$ (from SPC applied to the FIES spectra, and from our modeling of the light curves and RV data, respectively), and the Y^2 model isochrones from Yi et al. (2001). The best-fit values, and approximate 1σ and 2σ confidence ellipsoids, are shown. The Y^2 isochrones are shown for ages of 0.2 Gyr, and 1.0–14.0 Gyr in 1 Gyr increments.

evolution models (Yi et al. 2001) to determine the stellar mass, radius, and age, as well as the planetary parameters (e.g., mass and radius) which depend on the stellar values (Fig. 4).

We conducted the analysis inflating the SOPHIE and FIES RV uncertainties by adding a "jitter" term in quadrature to the formal uncertainties. This was done to accommodate the larger-than-expected scattering of the RV observations around the best-fit model. Independent jitters were used for each instrument, as it is not clear whether the jitter is instrumental or astrophysical in origin. The jitter term was allowed to vary in the fit, yielding a χ^2 per degree of freedom of unity for the RVs in the best-fit model. The median values for the jitter are 26 ± 13 ms^{-1} for the SOPHIE observations and 0.0 ± 3.1 ms^{-1} for the FIES observations. This suggests that either the formal uncertainties of the FIES instrument were overestimated, or that the jitter from the SOPHIE instrument is not from the star but from the instrument itself.

The analysis was done twice: fixing the eccentricity to zero, and allowing it to vary. Computing the Bayesian evidence for each model, we found that the fixed circular model is preferred by a factor of ~500. Therefore the circular orbit model was adopted. The 95% confidence upper limit on the eccentricity is $e < 0.139$.

The best-fit models are presented in Figures 1, 2 and 3, and the resulting derived stellar and planetary parameters are listed in Tables 3 and 4, respectively. We find that the star HAT-P-55 has a mass of 1.013 ± 0.037 $M_\odot$ and a radius of 1.011 ± 0.036 $R_\odot$, and that its planet HAT-P-55b has a period of 3.5852467 ± 0.0000064 days, a mass of 0.582 ± 0.056 M_J, and a radius of 1.182 ± 0.055 R_J.

TABLE 4
PARAMETERS FOR THE TRANSITING PLANET HAT-P-55B

Parameter	Value[a]
Light curve parameters	
P (days)	3.5852467 ± 0.0000064
T_c (BJD) [b]	2456730.83468 ± 0.00027
T_{14} (days) [b]	0.1223 ± 0.0013
$T_{12} = T_{34}$ (days) [b]	0.0152 ± 0.0013
$a/R_\star$	9.79 ± 0.34
$\zeta/R_\star$ [c]	18.64 ± 0.10
$R_p/R_\star$	0.1202 ± 0.0019
b^2	$0.153^{+0.062}_{-0.060}$
$b \equiv a\cos i/R_\star$	$0.392^{+0.073}_{-0.086}$
i (deg)	87.70 ± 0.56
Limb-darkening coefficients [d]	
c_1, i (linear term)	0.2619
c_2, i (quadratic term)	0.3313
c_1, r	0.3466
c_2, r	0.3306
RV parameters	
K (ms^{-1})	76.7 ± 7.1
e [e]	<0.139
RV jitter NOT 2.6 m/FIES (ms^{-1}) [f]	0.0 ± 3.1
RV jitter OHP 1.93 m/SOPHIE (ms^{-1})	26 ± 13
Planetary parameters	
$M_p(M_\mathrm{J})$	0.582 ± 0.056
$R_p(R_\mathrm{J})$	1.182 ± 0.055
$C(M_p, R_p)$ [g]	−0.01
ρ_p (g cm^{-3})	0.435 ± 0.077
$\log g_p$ (cgs)	3.012 ± 0.060
a (AU)	0.04604 ± 0.00056
T_{eq} (K) [h]	1313 ± 26
Θ [i]	0.0446 ± 0.0048
$\langle F \rangle$ (10^9 erg s^{-1} cm^{-2}) [j]	6.71 ± 0.53

[a] The adopted parameters assume a circular orbit. Based on the Bayesian evidence ratio we find that this model is strongly preferred over a model in which the eccentricity is allowed to vary in the fit. For each parameter we give the median value and 68.3% (1σ) confidence intervals from the posterior distribution.

[b] Reported times are in Barycentric Julian Date calculated directly from UTC, *without* correction for leap seconds. T_c: reference epoch of mid transit that minimizes the correlation with the orbital period. T_{14}: total transit duration, time between first to last contact; $T_{12} = T_{34}$: ingress/egress time, time between first and second, or third and fourth contact.

[c] Reciprocal of the half duration of the transit used as a jump parameter in our MCMC analysis in place of $a/R_\star$. It is related to $a/R_\star$ by the expression $\zeta/R_\star = a/R_\star(2\pi(1 + e\sin\omega))/(P\sqrt{1-b^2}\sqrt{1-e^2})$ (Bakos et al. 2010).

[d] Values for a quadratic law, adopted from the tabulations by Claret (2004) according to the spectroscopic (SPC) parameters listed in Table 3.

[e] The 95% confidence upper-limit on the eccentricity from a model in which the eccentricity is allowed to vary in the fit.

[f] Error term, either astrophysical or instrumental in origin, added in quadrature to the formal RV errors for the listed instrument. This term is varied in the fit assuming a prior inversely proportional to the jitter.

[g] Correlation coefficient between the planetary mass M_p and radius R_p determined from the parameter posterior distribution via $C(M_p, R_p) = \langle (M_p - \langle M_p \rangle)(R_p - \langle R_p \rangle) \rangle / (\sigma_{M_p}\sigma_{R_p}) \rangle$, where $\langle \cdot \rangle$ is the expectation value operator, and σ_x is the standard deviation of parameter x.

[h] Planet equilibrium temperature averaged over the orbit, calculated assuming a Bond albedo of zero, and that flux is reradiated from the full planet surface.

[i] The Safronov number is given by $\Theta = \frac{1}{2}(V_{\mathrm{esc}}/V_{\mathrm{orb}})^2 = (a/R_p)(M_p/M_\star)$ (see Hansen & Barman 2007).

[j] Incoming flux per unit surface area, averaged over the orbit.

4. DISCUSSION

We have presented the discovery of a new transiting planet, HAT-P-55b , and provided a precise characterization of its properties. HAT-P-55b is a moderately inflated ~0.5 M_J planet, similar in mass, radius, and equilibrium temperature to HAT-P-1b (Bakos et al. 2007), WASP-34 (Smalley et al. 2011), and HAT-P-25b (Quinn et al. 2012).

With a visual magnitude of $V = 13.21$, HAT-P-55b is among the faintest transiting planet host stars discovered by a wide field ground-based transit survey (today, a total of 11 transiting planet host stars with $V > 13$ have been discovered by wide field ground-based transit surveys, the faintest one is HATS-6 with $V = 15.2$ [Hartman et al. 2014]). Of course, $V > 13$ is only faint by the standards of surveys like HATNet and WASP; most of the hundreds of transiting planets found by space-based surveys such as *OGLE*, *CoRoT*, and *Kepler* have host stars fainter than HAT-P-55 . It is worth noticing that despite the relative faintness of HAT-P-55, the mass and radius of HAT-P-55b has been measured to better than 10% precision (relative to the precision of the stellar parameters) using modest-aperture facilities. This achievement was possible because the relatively large size of the planet and its close proximity to its host star provided for a strong and therefore easy-to-measure signal. In comparison, only about 140 of all the 1175 known TEP's have masses and radii measured to better than 10% precision.

HATNet operations have been funded by NASA grants NNG04GN74G and NNX13AJ15G. Follow-up of HATNet targets has been partially supported through NSF grant AST-1108686. G. Á. B., Z. C., and K. P. acknowledge partial support from NASA grant NNX09AB29G. K. P. acknowledges support from NASA grant NNX13AQ62G. G. T. acknowledges partial support from NASA grant NNX14AB83G. D. W. L. acknowledges partial support from NASA's *Kepler* mission under Cooperative Agreement NNX11AB99A with the Smithsonian Astrophysical Observatory. D. J. acknowledges the Danish National Research Foundation (grant number DNRF97) for partial support.

Data presented in this paper are based on observations obtained at the HAT station at the Submillimeter Array of SAO, and the HAT station at the Fred Lawrence Whipple Observatory of SAO. Data are also based on observations with the Fred Lawrence Whipple Observatory 1.5-m and 1.2-m telescopes of SAO. This paper presents observations made with the Nordic Optical Telescope, operated on the island of La Palma jointly by Denmark, Finland, Iceland, Norway, and Sweden, in the Spanish Observatorio del Roque de los Muchachos of the Instituto de Astrofísica de Canarias. The authors thank all the staff of Haute-Provence Observatory for their contribution to the success of the ELODIE and SOPHIE projects and their support at the 1.93-m telescope. The research leading to these results has received funding from the European Community's Seventh Framework Programme (FP7/2007-2013) under grant agreement number RG226604 (OPTICON). The authors wish to recognize and acknowledge the very significant cultural role and reverence that the summit of Mauna Kea has always had within the indigenous Hawaiian community. We are most fortunate to have the opportunity to conduct observations from this mountain.

REFERENCES

Bakos, G., Noyes, R. W., Kovács, G., et al. 2004, PASP, 116, 266
Bakos, G. Á., Noyes, R. W., Kovács, G., et al. 2007, ApJ, 656, 552
Bakos, G. Á., Torres, G., Pál, A., et al. 2010, ApJ, 710, 1724
Boisse, I., Hartman, J. D., Bakos, G. Á., et al. 2013, A&A, 558, A86
Bouchy, F., Daz, R. F., Hébrard, G., et al. 2013, A&A, 549, A49
Buchhave, L. A., Bakos, G. Á., Hartman, J. D., et al. 2010, ApJ, 720, 1118
Buchhave, L. A., Latham, D. W., Johansen, A., et al. 2012, Nature, 486, 375
Cardelli, J. A., Clayton, G. C., & Mathis, J. S. 1989, ApJ, 345, 245
Claret, A. 2004, A&A, 428, 1001
Djupvik, A. A., & Andersen, J. 2010, in Highlights of Spanish Astrophysics V, eds. J. M. Diego, L. J. Goicoechea, J. I. González-Serrano, & J. Gorgas 211
Fürész, G. 2008, Ph.D. thesis, University of Szeged, Hungary
Hansen, B. M. S., & Barman, T. 2007, ApJ, 671, 861
Hartman, J. D., Bakos, G. Á., Béky, B., et al. 2012, AJ, 144, 139
Hartman, J. D., Bayliss, D., Brahm, R., Bakos, G. Á., Mancini, L., Jordán, A., Penev, K., Rabus, M., et al. 2015, AJ, 149, 166
Kovács, G., Bakos, G., & Noyes, R. W. 2005, MNRAS, 356, 557
Kovács, G., Zucker, S., & Mazeh, T. 2002, A&A, 391, 369
Latham, D. W., Bakos, G. Á., Torres, G., et al. 2009, ApJ, 704, 1107
Perruchot, S., Bouchy, F., Chazelas, B., et al. 2011, Proc. SPIE, 8151, 5
Quinn, S. N., Bakos, G. Á., Hartman, J.et al. 2012, ApJ, 745, 80
Smalley, B., Anderson, D. R., Collier Cameron, A., et al. 2011, A&A, 526, A130
Udry, S., & Santos, N. C. 2007, ARA&A, 45, 397
Wright, J. T., Marcy, G. W., Howard, A. W., et al. 2012, ApJ, 753, 160
Yi, S., Demarque, P., Kim, Y.-C., et al. 2001, ApJS, 136, 417

The Astrophysical Journal, 812:136 (11pp), 2015 October 20 doi:10.1088/0004-637X/812/2/136

RED NOISE VERSUS PLANETARY INTERPRETATIONS IN THE MICROLENSING EVENT OGLE-2013-BLG-446

E. Bachelet[1], D. M. Bramich[1], C. Han[2], J. Greenhill[3], R. A. Street[4], A. Gould[5], G. D'Ago[6,7], K. AlSubai[1], M. Dominik[8,60], R. Figuera Jaimes[8,9], K. Horne[8], M. Hundertmark[8], N. Kains[9], C. Snodgrass[10,11], I. A. Steele[12], Y. Tsapras[4,13]
(The RoboNet collaboration),
M. D. Albrow[14], V. Batista[5,15], J.-P. Beaulieu[15], D. P. Bennett[16], S. Brillant[17], J. A. R. Caldwell[18], A. Cassan[15], A. Cole[3], C. Coutures[15], S. Dieters[3], D. Dominis Prester[19], J. Donatowicz[20], P. Fouqué[21,22], K. Hill[3], J.-B. Marquette[15], J. Menzies[23], C. Pere[15], C. Ranc[15], J. Wambsganss[24], D. Warren[3]
(The PLANET collaboration),
L. Andrade de Almeida[25], J.-Y. Choi[2], D. L. DePoy[26], S. Dong[5,27], L.-W. Hung[5], K.-H. Hwang[2], F. Jablonski[25], Y. K. Jung[2], S. Kaspi[28], N. Klein[28], C.-U. Lee[29], D. Maoz[28], J. A. Muñoz[25], D. Nataf[5], H. Park[2], R. W. Pogge[5], D. Polishook[28], I.-G. Shin[2], A. Shporer[30,31], J. C. Yee[5]
(The μFUN collaboration),
F. Abe[32], A. Bhattacharya[33], I. A. Bond[34], C. S. Botzler[35], M. Freeman[35], A. Fukui[36], Y. Itow[32], N. Koshimoto[33], C. H. Ling[34], K. Masuda[32], Y. Matsubara[32], Y. Muraki[32], K. Ohnishi[37], L. C. Philpott[38], N. Rattenbury[38], To. Saito[39], D. J. Sullivan[40], T. Sumi[41], D. Suzuki[42], P. J. Tristram[39], A. Yonehara[40]
(The MOA collaboration),
and
V. Bozza[43,44], S. Calchi Novati[43,45,46], S. Ciceri[47], P. Galianni[8], S.-H. Gu[48,49], K. Harpsøe[50,51], T. C. Hinse[52], U. G. Jørgensen[50,51], D. Juncher[50,51], H. Korhonen[50,51,53], L. Mancini[47], C. Melchiorre[43,44], A. Popovas[50,51], A. Postiglione[54,55], M. Rabus[47,56], S. Rahvar[57], R. W. Schmidt[24], G. Scarpetta[43,44,46], J. Skottfelt[50,51], John Southworth[58], An. Stabile[43,44], J. Surdej[59], X.-B. Wang[48,49], and O. Wertz[59]
(The MiNDSTEp collaboration)
[1] Qatar Environment and Energy Research Institute, Qatar Foundation, P.O. Box 5825, Doha, Qatar
[2] Department of Physics, Chungbuk National University, Cheongju 361-763, Korea
[3] School of Mathematics and Physics, University of Tasmania, Private Bag 37, Hobart, TAS 7001, Australia
[4] Las Cumbres Observatory Global Telescope Network, 6740 Cortona Drive, Suite 102, Goleta, CA 93117, USA
[5] Department of Astronomy, Ohio State University, 140 W. 18th Ave., Columbus, OH 43210, USA
[6] Dipartimento di Fisica "E.R. Caianiello," Università di Salerno, Via Ponte Don Melillo, I-84084-Fisciano (SA), Italy
[7] Istituto Nazionale di Fisica Nucleare, Sezione di Napoli, Napoli, Italy
[8] SUPA, School of Physics & Astronomy, University of St Andrews, North Haugh, St Andrews KY16 9SS, UK
[9] European Southern Observatory, Karl-Schwarzschild-Str. 2, D-85748 Garching bei München, Germany
[10] Max Planck Institute for Solar System Research, Justus-von-Liebig-Weg 3, D-37077 Gttingen, Germany
[11] Planetary and Space Sciences, Department of Physical Sciences, The Open University, Milton Keynes, MK7 6AA, UK
[12] Astrophysics Research Institute, Liverpool John Moores University, Liverpool CH41 1LD, UK
[13] School of Physics and Astronomy, Queen Mary University of London, Mile End Road, London E1 4NS, UK
[14] Department of Physics and Astronomy, University of Canterbury, Private Bag 4800, Christchurch 8020, New Zealand
[15] UPMC-CNRS, UMR 7095, Institut dAstrophysique de Paris, 98bis boulevard Arago, F-75014 Paris, France
[16] Department of Physics, 225 Nieuwland Science Hall, University of Notre Dame, Notre Dame, IN 46556, USA
[17] European Southern Observatory, Casilla 19001, Vitacura 19, Santiago, Chile
[18] McDonald Observatory, 16120 St. Hwy Spur 78 #2, Fort Davis, TX 79734, USA
[19] Department of Physics, University of Rijeka, Omladinska 14, 51000 Rijeka, Croatia
[20] Technische Universitat Wien, Wieder Hauptst. 8-10, A-1040 Vienna, Austria
[21] IRAP, CNRS—Université de Toulouse, 14 av. E. Belin, F-31400 Toulouse, France
[22] CFHT Corporation 65-1238 Mamalahoa Hwy Kamuela, Hawaii 96743, USA
[23] South African Astronomical Observatory, P.O. Box 9, Observatory 7935, South Africa
[24] Astronomisches Rechen-Institut (ARI), Zentrum für Astronomie der Universität Heidelberg (ZAH), Mönchhofstr. 12-14, D-69120 Heidelberg, Germany
[25] Departamento de Astronomía y Astrofísica, Universidad de Valencia, E-46100 Burjassot, Valencia, Spain
[26] Department of Physics and Astronomy, Texas A&M University, College Station, TX 77843-4242, USA
[27] Institute for Advanced Study, Einstein Drive, Princeton, NJ 08540, USA
[28] School of Physics and Astronomy and Wise Observatory, Tel-Aviv University, Tel-Aviv 69978, Israel
[29] Korea Astronomy and Space Science Institute, 776 Daedukdae-ro, Yuseong-gu, Daejeon 305-348, Korea
[30] Las Cumbres Observatory Global Telescope Network, 6740B Cortona Dr, Goleta, CA 93117, USA
[31] Department of Physics, University of California, Santa Barbara, CA 93106, USA
[32] Department of Physics, University of Auckland, Private Bag 92019, Auckland, New Zealand; c.botzler@auckland.ac.nz, p.yock@auckland.ac.nz
[33] Department of Physics, University of Notre Dame, Notre Dame, IN 46556, USA; bennett@nd.edu
[34] Solar-Terrestrial Environment Laboratory, Nagoya University, Nagoya 464-8601, Japan; abe@stelab.nagoya-u.ac.jp, furusawa@stelab.nagoya-u.ac.jp, itow@stelab.nagoya-u.ac.jp, kmasuda@stelab.nagoya-u.ac.jp, ymatsu@stelab.nagoya-u.ac.jp
[35] Okayama Astrophysical Observatory, National Astronomical Observatory of Japan, 3037-5 Honjo, Kamogata, Asakuchi, Okayama 719-0232, Japan
[36] Nagano National College of Technology, Nagano 381-8550, Japan
[37] Tokyo Metropolitan College of Aeronautics, Tokyo 116-8523, Japan
[38] School of Chemical and Physical Sciences, Victoria University, Wellington, New Zealand
[39] Mt. John University Observatory, P.O. Box 56, Lake Tekapo 8770, New Zealand
[40] Department of Physics, Faculty of Science, Kyoto Sangyo University, 603-8555 Kyoto, Japan

[41] Department of Earth and Space Science, Graduate School of Science, Osaka University, Toyonaka, Osaka 560-0043, Japan; sumi@ess.sci.osaka-u.ac.jp
[42] Institute of Information and Mathematical Sciences, Massey University, Private Bag 102-904, North Shore Mail Centre, Auckland, New Zealand; i.a.bond@massey.ac.nz, c.h.ling@massey.ac.nz, w.sweatman@massey.ac.nz
[43] Dipartimento di Fisica "E.R. Caianiello," Università di Salerno, Via Giovanni Paolo II 132, I-84084, Fisciano (SA), Italy
[44] Istituto Nazionale di Fisica Nucleare, Sezione di Napoli, I-80126 Napoli, Italy
[45] NASA Exoplanet Science Institute, MS 100-22, California Institute of Technology, Pasadena, CA 91125, US
[46] Istituto Internazionale per gli Alti Studi Scientifici (IIASS), I-84019 Vietri Sul Mare (SA), Italy
[47] Max Planck Institute for Astronomy, Königstuhl 17, D-69117 Heidelberg, Germany
[48] Yunnan Observatories, Chinese Academy of Sciences, Kunming 650011, China
[49] Key Laboratory for the Structure and Evolution of Celestial Objects, Chinese Academy of Sciences, Kunming 650011, China
[50] Niels Bohr Institute, University of Copenhagen, Juliane Maries Vej 30, 2100 København Ø, Denmark
[51] Centre for Star and Planet Formation, Natural History Museum, University of Copenhagen, Østervoldgade 57, 1350 København K, Denmark
[52] Korea Astronomy and Space Science Institute, Daejeon 305-348, Korea
[53] Finnish Centre for Astronomy with ESO (FINCA), University of Turku, Väisäläntie 20, FI-21500 Piikkiö, Finland
[54] Dipartimento di Fisica "E. Amaldi," Università di Roma Tre, Via della Vasca Navale 84, I-00149 Roma, Italy
[55] Istituto Nazionale di Fisica Nucleare, Sezione di Roma Tre, Italy
[56] Instituto de Astrofisica, Facultad de Fisica, Pontificia Universidad Católica de Chile, Av. Vicuña Mackenna 4860, 7820436 Macul, Santiago, Chile
[57] Department of Physics, Sharif University of Technology, P. O. Box 11155-9161 Tehran, Iran
[58] Astrophysics Group, Keele University, Staffordshire, ST5 5BG, UK
[59] Institut d'Astrophysique et de Géophysique, Université de Liège, 4000 Liège, Belgium
Received 2015 April 15; accepted 2015 August 31; published 2015 October 16

ABSTRACT

For all exoplanet candidates, the reliability of a claimed detection needs to be assessed through a careful study of systematic errors in the data to minimize the false positives rate. We present a method to investigate such systematics in microlensing data sets using the microlensing event OGLE-2013-BLG-0446 as a case study. The event was observed from multiple sites around the world and its high magnification ($A_{\max} \sim 3000$) allowed us to investigate the effects of terrestrial and annual parallax. Real-time modeling of the event while it was still ongoing suggested the presence of an extremely low-mass companion ($\sim 3M_{\oplus}$) to the lensing star, leading to substantial follow-up coverage of the light curve. We test and compare different models for the light curve and conclude that the data do not favor the planetary interpretation when systematic errors are taken into account.

Key words: gravitational lensing: micro – planetary systems – techniques: photometric

1. INTRODUCTION

For the past 10 years, gravitational microlensing has been used to detect cool planets around G, K, and M-stars in the Milky Way, allowing access to a planetary regime difficult to observe with the transit or radial velocity methods (i.e., microlensing is sensitive to planets beyond the snowline). Due to the increased field of view of the OGLE-IV and MOA-II surveys, and the recently improved performance of follow-up teams, the number of planets detected by microlensing has gone up substantially (typically 10–20 planets detected per year and 33 published to date).

Another advantage of the microlensing method is that detection of planetary companions is possible over a larger mass range [$\sim 1M_{\oplus}$, $\sim 13M_J$], including brown dwarfs, if the projected orbital radius s is in the range 0.6–1.6 $R_{\rm E}$ (i.e., the classical "lensing zone"). Thanks to better photometric coverage of light curves, recent studies have advanced claims about the detection of small planets (Bennett et al. 2014). However, smaller mass ratios tend to produce smaller deviations from a single lens model most of the time. Failing to account for photometric systematics can potentially lead to false detections. The analysis of photometric systematics has been important in transit searches and has substantially improved the reliability of detections (Kovács et al. 2005; Smith et al. 2012). This point is too often neglected by the microlensing community.

In this work, we present an extensive study of photometric systematics for the case of OGLE-2013-BLG-0446 and we compare the significance when different microlensing models are considered. Section 2 presents a summary of the observations of microlensing event OGLE-2013-BLG-0446 from multiple sites around the world. We present our modeling process in Section 3 and conduct a study of systematics in the data in Section 4. We present our conclusions in Section 5.

[60] Royal Society University Research Fellow.

2. OBSERVATIONS

Microlensing event OGLE-2013-BLG-0446 ($\alpha = 18^{\rm h}06^{\rm m}56\overset{\rm s}{.}18$, $\delta = -31°39'27\overset{''}{.}2$ (J2000.0); $l = 0\overset{\circ}{.}049$, $b = -5\overset{\circ}{.}344$) was discovered on 2013 April 6 by the Optical Gravitational Lens Experiment (OGLE) Early Warning System (Udalski 2003b) and later alerted by the Microlensing Observations in Astrophysics (MOA) (Bond et al. 2001). Observations obtained on the rising part of the light curve indicated that this event could be highly magnified and might therefore be highly sensitive to planets (Griest & Safizadeh 1998; Gould et al. 2009; Yee et al. 2009). Follow-up teams, such as μFUN (Gould et al. 2006), PLANET (Beaulieu et al. 2006), RoboNet (Tsapras et al. 2009), and MiNDSTEp (Dominik et al. 2008), then began observations a few days before the peak of the event. The peak magnification was $\sim$3000 and the peak was densely sampled from different observatories.

The various teams used difference image analysis (DIA) to obtain photometry: μFUN used pySIS (Albrow et al. 2009), with the exception of the Auckland data, which were re-reduced using `DanDIA` (Bramich 2008; Bramich et al. 2013). `DanDIA` was also used to reduce the RoboNet and the Danish data sets. PLANET data were reduced online with the WISIS pipeline, and final data sets were

Table 1
Summary of Observations

Name	Collaboration	Location	Aperture(m)	Filter	Code	$N_{\rm data}$	Longitude(deg)	Latitude(deg)
OGLE_I	OGLE	Chile	1.3	I	Woźniak	463	289.307	−29.015
OGLE_V	OGLE	Chile	1.3	V	Woźniak	24	289.307	−29.015
Canopus_I	PLANET	Tasmania	1.0	I	pySIS	132	147.433	−42.848
Auckland_R	μFUN	New Zealand	0.4	R	`DanDIA`	107	147.777	−36.906
LSCB_i	RoboNet	Chile	1.0	SDSS-i	`DanDIA`	378	289.195	−30.167
LSCA_i	RoboNet	Chile	1.0	SDSS-i	`DanDIA`	385	289.195	−30.167
CPTA_i	RoboNet	South Africa	1.0	SDSS-i	`DanDIA`	22	20.810	−32.347
CTIO_I	μFUN	Chile	1.3	I	pySIS	112	289.196	−30.169
CTIO_V	μFUN	Chile	1.3	V	pySIS	13	289.196	−30.169
Danish_z	MiNDSTEp	Chile	1.5	$i+z$	`DanDIA`	452	289.261	−29.255
MOA_Red	MOA	New Zealand	1.8	Red	Bond	454	170.464	−43.987
Possum_N	μFUN	New Zealand	0.4	N	pySIS	244	177.856	−38.623
Salerno_I	MiNDSTEp	Italy	0.4	I	pySIS	20	14.799	40.772
Turitea_R	μFUN	New Zealand	0.4	R	pySIS	31	175.630	−40.353
Weizmann_I	μFUN	Israel	0.4	I	pySIS	60	34.811	31.908
SAAO_I	PLANET	South Africa	1.0	I	pySIS	58	20.789	−32.374

Note. N is unfiltered data set.

prepared using pySIS.[61] OGLE (Udalski & Szymański 2015) and MOA (Bond et al. 2001) used their own DIA code to reduce their frames. All other data sets were reduced using pySIS.

A total of 2955 data points from 16 telescopes were used for our analysis, after problematic data points were masked. A summary of each data set is available in Table 1.

3. MODELING

3.1. Source Properties

This event shows clear signs of finite-source effects and the limb darkening coefficients must be evaluated for each data set. We first consider a point-source point-lens model (PSPL) (Paczyński 1986). The PSPL model allows the estimation of the source and blended fluxes in the V and I passbands for the calibrated OGLE photometry, leading to a good approximation for the V and I magnitudes of the source, which in turn allows us to derive a rough color for the source. We found $(I, (V-I))_{\rm PSPL} = (19.07, 1.48)$. Using the Interstellar Extinction Calculator on the OGLE website[62] based on Nataf et al. (2013), we found that the Galactic Bulge true distance modulus for this line of sight is $\mu = 14.578 \pm 0.326$ mag ($d_{\rm Bulge} = 8.2 \pm 1.2$ kpc), the I band extinction is $A_I = 0.804$ mag, and the reddening is $E(V-I) = 0.683 \pm 0.036$ mag, leading to $R_I = A_I/E(V-I) = 1.177$, lower than the standard value of 1.5. This low extinction is known as the anomalous extinction law toward the Galactic Bulge; see Udalski (2003a). We derive the source properties as follows:

1. Assuming that the source suffers the same extinction as the Red Giant Clump (i.e., the source is at the same distance), we have $M_I = 19.07 - 0.804 - 14.578 = 3.7$ mag, so the source star is most likely a main sequence star. We adopt $\log g \sim 4.5$.
2. We derive its effective temperature using the dereddened color–magnitude relation for dwarfs and subgiants (relation (3) in Casagrande et al. 2010) with solar metallicity.
3. From Claret (2000) and using $\log g \sim 4.5$, we are able to find the linear limb-darkening coefficients u_λ (Milne 1921) for each filter. Following Albrow et al. (1999) and Yoo et al. (2004), we use the transformation:

$$\Gamma_\lambda = \frac{2u_\lambda}{3 - u_\lambda}. \quad (1)$$

These calculations form the starting point for an iterative fit of the finite source point lens (FSPL) model, together with error-bar rescaling as described in Section 3.3. Our best FSPL model converges to source magnitude and color $(I, (V-I)) = (19.00, 1.49)$. Correcting for extinction and reddening we have $(I_o, (V-I)_o) = (18.20, 0.81)$. The corresponding effective temperature of the source is $T_{\rm eff} \sim 5400\,K$, leading to $\Gamma_V = 0.63$ ($u_V = 0.72$), $\Gamma_R = 0.55$ ($u_R = 0.65$) and $\Gamma_I = 0.46$ ($u_I = 0.56$) for $\log g \sim 4.5$. Note that we also use $\Gamma_I = 0.46$ for the RoboNet telescopes (SDSS-i filter). Finally, given the dereddened magnitude and color of the source from our best FSPL model, we are able to estimate the angular source star radius θ_* using Kervella & Fouqué (2008):

$$\log_{10}(\theta_*) = 3.1982 + 0.4895(V-I)_o - 0.0657(V-I)_o^2 - 0.2I_o. \quad (2)$$

The uncertainty of this relation is 0.0238. The errors on our magnitude estimates are $(\Delta I, \Delta V) = (0.02, 0.02)$ mag. Assuming a conservative estimate of the error on A_I (0.1 mag) and using standard error propagation gives 9% precision: $\theta_* = 0.82 \pm 0.07\,\mu$as. With the adopted source distance (8.234 kpc), the source star radius is $R_* = 1.4 \pm 0.3\,R_\odot$. Therefore the source is a G6 or K0 star (Bessell & Brett 1988).

3.2. Single Lens Model

The PSPL model is described by the standard single-lens parameters: $t_{\rm E}$ the Einstein crossing time, u_o the minimum impact parameter, and t_o the time of this minimum. The

[61] Data from Tasmania were obtained at the Canopus 1 m observatory by John Greenhill. This was the last planetary candidate observed from Canopus before its decommissioning. These observations were also the last collected and reduced by John Greenhill (at the age 80). He has been our loyal collaborator and friend over the past 18 years and passed away on 2014 September 28.

[62] http://ogle.astrouw.edu.pl/

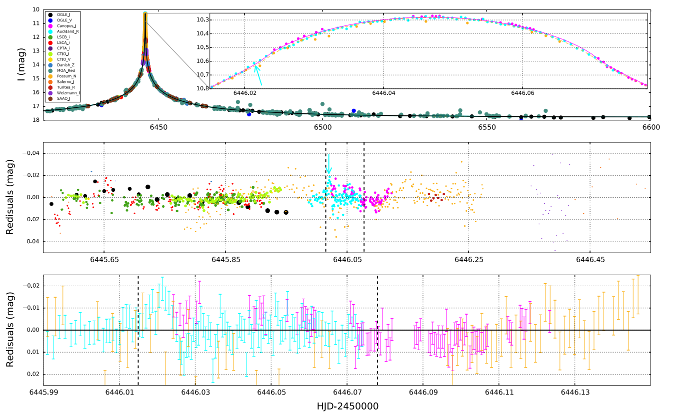

Figure 1. Light curve of OGLE-2013-BLG-0446 with our best FSPL model. The top panel shows the full 2013 light curve with a maximum magnification at HJD − 2450000 ∼ 6446.0 days. The insert on the right is a zoom of the peak. The pink model light curve is for $\Gamma_I = 0.46$ and the orange dashed model light curve is for $\Gamma_V = 0.63$. The cyan model for the R band is not shown for clarity. The cyan arrow indicates the position of the possible planetary anomaly. The middle panel shows residuals of the FSPL model close to the peak. The radius of each point is proportional to the inverse square of the error bar (bigger points have smaller error bars). The bottom panel is a closer view of the possible anomaly. For the bottom two panels, vertical dashed black lines indicate the time window corresponding to the insert in the top figure.

normalized angular source radius $\rho = \theta_*/\theta_{\rm E}$ (Gould 1994; Nemiroff & Wickramasinghe 1994; Witt & Mao 1994; Bennett & Rhie 1996; Vermaak 2000), where $\theta_{\rm E}$ is the angular Einstein ring radius, is included in the model along with the previous parameters to take into account finite-source effects close to the magnification peak. We used the method described in Yoo et al. (2004) to take into account the change in magnification due to the extended source. The FSPL model significantly improves the fit (see Table 3). The best FSPL model is shown in Figure 1.

Using the value of ρ from the FSPL model, we are able to estimate the angular radius of the Einstein ring $\theta_{\rm E} = \theta_*/\rho = 1.57 \pm 0.1$ mas and the lens-source proper motion $\mu = \theta_{\rm E}/t_{\rm E} = 7.4 \pm 0.7$ mas yr^{-1}.

3.3. Treatment of Photometric Uncertainties and Rejection of Outliers

Because of the diversity of observatories and reduction pipelines used in microlensing, photometric uncertainties need careful rescaling to accurately represent the real dispersion of each data set. This is an important preliminary step in modeling the event. Following Bachelet et al. (2012b), Miyake et al. (2012), and Yee et al. (2013), we rescale the uncertainties using:

$$e_i' = \sqrt{(fe_i)^2 + e_{\min}^2}, \quad (3)$$

where e_i are the original magnitude uncertainties, f is the rescaling parameter for low magnification levels, $e_{\min}$ is a minimal uncertainty to reproduce the practical limitations of photometry, and e_i' are the adjusted magnitude uncertainties. The classical rescaling method is to adjust f and $e_{\min}$ to force χ^2/degrees of freedom (dof) to be unity.

In this paper, we follow an alternative method of first adjusting f and $e_{\min}$ to force the residuals, normalized by e_i', to follow a Gaussian distribution around the model. If possible, we also aim to obtain a $\chi^2/{\rm dof} \sim 1$. Note that these two methods lead to the same results, except for the OGLE_I data set. For OGLE_I, the distribution without rescaling shows some data points with large residuals. This is not surprising because the OGLE_I data set covers the entire light curve with a large number of points, especially the faint baseline magnitude ($I \sim 17.8$), with a constant exposure time on the order of 100 s. Inspection of the OGLE_I light curve reveals that the uncertainties during high magnification are underestimated, so we adjust the $e_{\min}$ parameter. We tried to force $\chi^2/{\rm dof} \sim 1$ for this data set, but this generated large uncertainties for the low magnification part (i.e., the baseline), leading to a non-Gaussian distribution (lots of normalized residuals too close to the mean).

We finally checked isolated points far away from this Gaussian distribution, and reject as outliers ($>7\sigma$) two data points in the Auckland_R data set. The rescaling coefficients are presented in Table 2.

Table 2
Limg Darkening and Error Bar Rescaling Coefficients Used in this Paper

Name	N_{data}	Γ_λ	f	e_{min}
OGLE_I	463	0.46	1.0	0.002
OGLE_V	24	0.63	10.25	0.0
Canopus_I	132	0.46	3.0	0.005
Auckland_R	107	0.55	1.75	0.005
LSCB_i	378	0.46	1.4	0.003
LSCA_i	385	0.46	2.0	0.007
CPTA_i	22	0.46	1.19	0.0
CTIO_I	112	0.46	1.5	0.004
CTIO_V	13	0.63	1.0	0.0
Danish_z	452	0.46[a]	5.0	0.008
MOA_Red	454	0.51[b]	1.0	0.0
Possum_N	244	0.63[c]	1.5	0.008
Salerno_I	20	0.46	3.91	0.0
Turitea_R	31	0.55	1.0	0.005
Weizmann_I	60	0.46	3.2	0.01
SAAO_I	58	0.46	2.57	0.008

Notes.
[a] The transmission curve for this filter is close to a Johnson Cousin I; see Skottfelt et al. (2015).
[b] We select a bandpass between I and V.
[c] For this unfiltered data, we choose the filter closest to the CCD spectral response.

3.4. Annual and Terrestrial Parallaxes

We looked for second-order effects in the light curve. First, the relatively long Einstein-ring crossing time ($t_E \sim 80$ days) should allow the measurement of the displacement of the line of sight toward the target due to the Earth's rotation around the Sun. This annual parallax (Gould & Loeb 1992; Gould 2000, 2004; Smith et al. 2003; Skowron et al. 2011) is described by the vector $\pi_{E,a} = AU/\widetilde{r}_E = (\pi_{EN}, \pi_{EE})$, where $\widetilde{r}_E$ is the angular radius of the Einstein ring of the lens projected onto the observer plane and π_{EN} and π_{EE} are the components of this vector in the north and east directions respectively. In practice, the introduction of this parameter slightly changes the value of the impact parameter and $\tau = (t - t_o)/t_E$. Strong modifications of the light curve can be seen far from the peak of the event, i.e., in the wings of the light curve, with few changes around the peak; see, for example, Smith et al. (2003). To model this effect, the constant $t_{o,par}$ (Skowron et al. 2011) is added to give an invariant reference time for each model. We choose $t_{o,par} = 2456446.0$ HJD for our models.

Since this event is so highly magnified, it should also be possible to measure the terrestrial parallax. Hardy & Walker (1995) first introduced the idea that for an "Extreme Microlensing Event," the difference in locations of observatories should result in light curves where tiny changes in the line of sight toward the target become apparent, allowing a measurement of the Einstein ring (Holz & Wald 1996; Gould 1997; Dong et al. 2007). Again, this effect is described by the parallax vector $\pi_{E,t} = AU/r_\oplus(\Delta t_o/t_E, \Delta U_o)$, where $r_\oplus$ is the Earth radius. Gould & Yee (2013) estimated that the condition $\rho\widetilde{r}_E \leqslant 50 r_\oplus$ is required to expect a measurable difference in terms of magnification. This condition leads to $\pi_E > 0.24$ for this event by using an approximate value for the normalized source star radius $\rho \sim 5 \times 10^{-4}$. A summary of longitudes and latitudes of the observatories is in Table 1 and results are summarized in Table 3.

Note that we also compute the annual parallax model for a positive impact parameter ($u_0 > 0$) and found no significant difference with the model reported in the Table 3. This is the u_0 degeneracy described in the literature (Smith et al. 2003; Gould 2004; Skowron et al. 2011). For the terrestrial parallax, a positive impact parameter leads to a better fit ($\Delta\chi^2 \sim 60$) for equivalent π_{EN} and π_{EE} values , which is a similar result to Yee et al. (2009).

3.5. Binary Model

At the end of the 2013 observing season, several planetary models circulated (private communication) indicating the presence of the smallest microlensing planet ever detected ($q \sim 2 \times 10^{-5}$). In order to investigate these claims of the existence of a very low-mass ratio planetary companion to the primary lens, and to exclude the possibility of a false alarm, we used a finite-source binary lens model (FSBL) with three extra parameters: the projected separation (normalized by θ_E) between the two bodies s, the mass ratio q using the convention described in Bachelet et al. (2012a) (the most massive component on the left), and α the source trajectory angle measured from the line joining the two components (counter-clockwise angle). We first used a grid search and we finally explore minima with a full Markov-Chain Monte Carlo algorithm. Please see, for example, Dong et al. (2009) or Bachelet et al. (2012a) for more details. We find two local minima which correspond to the known theoretical degeneracy $s \Leftrightarrow s^{-1}$. We only explore the "wide" solution, which gives the best grid-search χ^2, for three reasons. First, as explained in the next section, the reliability of the planetary model is not clear. Second, we expect a strong degeneracy in terms of $s \Leftrightarrow s^{-1}$, so models should converge to solutions with similar shapes for the central caustic and therefore similar residuals. Finally, due to the really small value of ρ, modeling this event is very time consuming. We present our results in Table 3, our best caustic-crossing geometry in Figure 2, and redisuals to the FSPL model for data sets covering the magnification peak are plotted in Figure 3.

4. STUDY OF SYSTEMATIC TRENDS IN THE PHOTOMETRY

4.1. Generality and Method

Our best planetary model claims the detection of smooth deviations in the light curve away from the FSPL model at a peak-to-peak level of $\leqslant 1\%$, which is supposedly caused by the source passing over the central planetary caustic. It is well known to photometrists, however, that from ground-based telescopes the photometric precision at this level can be affected by systematic trends (or red noise) in the data.

In the early days of planet hunting using the transit method, researchers were confounded as to why they were not finding as many planets as predicted. The predictions were of course based on simulated light curves taking into account stochastic noise from the photons (sky and star) and the charge-coupled device (CCD), but ignoring the effects of sub-optimal data calibration/reduction that introduce correlated noise (e.g., Mallén-Ornelas et al. 2003 and Pepper & Gaudi 2005). It was soon realized that transit detection thresholds were severely affected by systematic trends in the light curves (Pont et al. 2006; Aigrain & Pont 2007) with the knock-on effect of reducing the predicted planetary yield of a transit survey, and at

Table 3
Model Parameters

Parameters	FSPL	FSPL+Annual Parallax	FSPL+Terrestrial Parallax	Wide Planetary (FSBL)
t_o(HJD)	$6446.04790 \pm 3\ 10^{-5}$	$6446.04678 \pm 3\ 10^{-5}$	$6446.04681 \pm 3\ 10^{-5}$	$6446.04659 \pm 3\ 10^{-5}$
$U_o(\theta_E)$	$-4.21\ 10^{-4} \pm 7\ 10^{-6}$	$-4.02\ 10^{-4} \pm 8\ 10^{-6}$	$-4.22\ 10^{-4} \pm 8\ 10^{-6}$	$-4.31\ 10^{-4} \pm 5\ 10^{-6}$
t_E(days)	76.9 ± 1.3	80.4 ± 1.5	76.5 ± 1.4	76.0 ± 0.7
$\rho(\theta_E)$	$5.22\ 10^{-4} \pm 9\ 10^{-6}$	$4.99\ 10^{-4} \pm 1\ 10^{-5}$	$5.24\ 10^{-4} \pm 9\ 10^{-6}$	$5.31\ 10^{-4} \pm 5\ 10^{-6}$
I_s(mag)	19.00 ± 0.02	19.05 ± 0.02	19.00 ± 0.02	18.99 ± 0.01
V_s(mag)	20.49 ± 0.02	20.54 ± 0.02	20.49 ± 0.02	20.48 ± 0.01
I_b(mag)	18.21 ± 0.01	18.18 ± 0.01	18.21 ± 0.01	18.22 ± 0.01
V_b(mag)	22.72 ± 0.11	22.35 ± 0.11	22.76 ± 0.13	22.85 ± 0.07
Π_{EN}	…	0.37 ± 0.15	0.07 ± 0.02	…
Π_{EE}	…	0.27 ± 0.005	0.01 ± 0.02	…
$s(\theta_E)$	…	…	…	1.68 ± 0.05
q	…	…	…	$3.1\ 10^{-5} \pm 2\ 10^{-6}$
α(rad)	…	…	…	-2.39 ± 0.02
χ^2	3900.781	3839.267	3877.241	3551.217

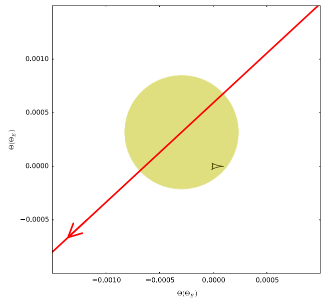

Figure 2. Lens geometry for our best fit planetary model. The yellow disk represents the source, the red line indicates the source trajectory, and the black closed curve represents the central caustic. The caustic signature in the light curve is highly "diluted" by the relatively large source star.

least partially explaining the unexpectedly low rate of transiting planet discoveries. The microlensing planet hunters face a similar problem for detecting low-amplitude ($\lesssim 1\%$) planetary deviations in microlensing light curves, especially when no "sharp" light curve features, caused by caustic crossing events, are predicted/observed. However, the microlensing community is now aiming for really low amplitude signal detection which requires extra care in the treatment of systematic errors (Yee et al. 2013).

Systematic trends in light curve data can be caused by an imperfect calibration of the raw data and sub-optimal extraction of the photometry. For instance, on the calibration side, flat fielding errors which vary as a function of detector coordinates can induce correlated errors in the photometry as the telescope pointing drifts slightly during a set of time-series exposures. On the software side, systematic errors in the photometry can be caused by errors in the point-spread function (PSF) model used during PSF fitting for example. Also the airmass and transparency variations in the data sets should be modeled in the DIA procedure by the photometric scale factor. However, there is no guarantee that the DIA modeling is perfect and this can create systematics trends in the data. As recently discussed by Bramich et al. (2015), an error ϵ_p in the estimate of the photometric scale factor leads directly to an error ϵ_p in the photometry. For example, the passage of clouds during data acquisition can create inhomogeneous atmospheric transparency in the frames and lead to a spatially varying photometric scale factor. The estimation of the photometric scale factor in DIA by using a "mean" value for the whole frame will produce different systematic trends for each star in the field of view. In practice, the expected error ϵ_p is of order of a few per cent, which is non-critical for the majority of microlensing deviations, but can easily imitate the smallest such as in OGLE-2013-BLG-0446.

Obtaining a photon-noise limited data calibration and photometric extraction is not always feasible. Therefore complementary techniques have been developed to perform a relative calibration of the ensemble photometry after the data reduction (i.e., a post-calibration). These techniques can be divided into two broad groups, namely, detrending methods that do not use any a priori knowledge about the data acquisition or instrumental set up (e.g., Tamuz et al. 2005), and photometric modeling methods that attempt to model the systematic trends based on the survey/instrumental properties (e.g., Honeycutt 1992; Padmanabhan et al. 2008; Regnault et al. 2009). Each data point is associated with a unique object and a unique image (epoch), and carries associated metadata such as magnitude uncertainty, airmass, (x, y) detector coordinates, PSF FWHM, etc. To investigate the systematic trends in the photometry, we first identified a set of object/image properties which we suspected of having influenced the quality of the data reduction. For each of these quantities, we defined a binning that covers the full range of values with an appropriate bin size. For each bin, we introduced an unknown magnitude offset to be determined, the purpose of which is to model the mean difference of the photometric measurements within the corresponding bin from the rest of the photometric measurements. We constructed our photometric model by adopting the unknown true instrumental magnitude of each object[63] and the magnitude offsets as parameters.

[63] Except for one object where we fixed the true instrumental magnitude to an arbitrary value to avoid degeneracy.

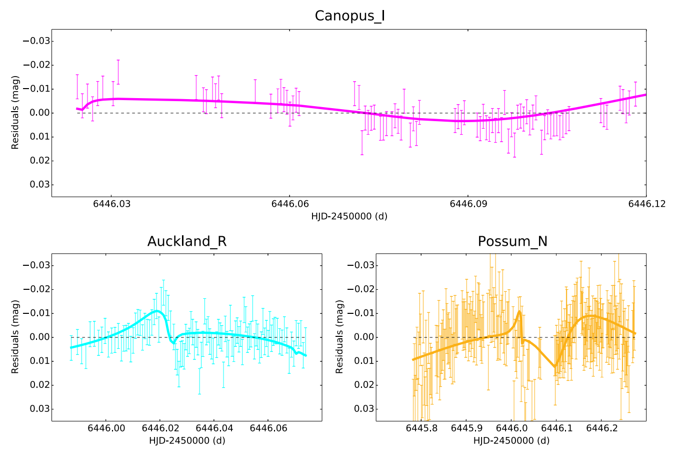

Figure 3. FSPL residuals close to the peak. The curves represent the best planetary model.

Since the model is linear, the best-fit parameter values corresponding to the minimum in χ^2 may be solved for directly (and in a single step using some matrix algebra—see Bramich & Freudling 2012). Iteration is of course mandatory to remove variable stars and strong outliers from the photometric data set. A valid criticism of this method is that the systematic trends are derived from the constant stars but then applied to all stars including the variable stars (the microlensing event in our case). The question arises as to whether this approach is consistent. To argue our case, we are limited to showing that the method works in practice and we direct the reader to Figure 1 of Kains et al. (2015) where RR Lyrae light curves in M68 are much improved by this self-calibration method. We used this method to analyze systematic trends in three data sets. They are listed below.

4.2. LSCA_i and LSCB_i : the Twins Paradox

We opted to employ the above methodology in order to investigate and understand the systematic trends in the LSCB_i and LSCA_i data sets using the algorithms described in Bramich & Freudling (2012).[64] These telescopes are twins: both are LCOGT 1 m telescope clones, both supporting Kodak SBIG STX-16803 CCDs at the time of these observations. SDSS-i prescription filters manufactured at the same time were use to observe OGLE-2013-BLG-0446 during the same period of observation, though not precisely synchronously.

We first chose to study LSCB_i because this telescope most strongly favors the planetary model ($\Delta\chi^2 \sim 128.3$; see Table 6). For LSCB_i, the `DanDIA` pipeline extracted 4272 light curves from the images in the LSCB_i data set, each with 378 data points (or epochs), which yields a total of 1,614,816 photometric data points. We investigated each object/image property in turn using the above method, and determined the peak-to-peak amplitude of the magnitude offsets in each case. The results are reported in Table 4. The trends in the photometry were found to be at the sub-mmag level for all correlating properties except for the epoch (2.0 mmag). The magnitude offsets determined for each epoch (or image) serve to correct for any errors in the fitted values of the photometric scale factors during DIA. The magnitude offsets as a function of detector coordinates (commonly referred to as an illumination correction—e.g., Coccato et al. 2014) were modeled using a two-dimensional cubic surface (as opposed to the binning previously described) so as to better capture the large-scale errors in the flat-fielding. The peak-to-peak amplitude of the cubic surface over the full detector area was found to be ∼60 mmag, but since the LSCB_i observations only drifted by ∼50 pixels in each coordinate, we found that the magnitude offsets applicable to the OGLE-2013-BLG-0446 light curve have a peak-to-peak amplitude of only ∼0.2 mmag. This can be seen in Figure 4. The overall level of systematic trends in the LSCB_i data set for OGLE-2013-BLG-446 is ∼2.0 mmag. To conclude, this analysis reveals that the illumination correction is not sufficient to explain the observed systematics.

[64] The code is a part of DanIDL, available at http://www.danidl.co.uk/.

Table 4
The Peak-to-Peak Amplitude of the Magnitude Offsets for Each Object/Image Property that We Investigated for Causing Systematic Trends in the Photometry for the LSCB_i, LSCA_i and Auckland_R Data Sets

Correlating Quantity	Possible Underlying Cause	Peak-To-Peak Amplitude(mmag)		
		LSCA_i	LSCB_i	Auckland_R
Exposure time	CCD non-linearities	20	0.3	60
Airmass	Varying extinction	22	0.8	40
PSF FWHM	Varying seeing disk	25	0.4	28
Photometric scale factor	Reduction quality at different transparencies	20	0.2	40
Epoch	Errors in photometric scale factor	60	2.0	120
Detector coordinates	Flat-field errors	10	0.2	*
Background	Reduction quality	27	0.5	45

Note. We also list a possible underlying cause for any systematic trends that are found as a function of the corresponding object/image property.

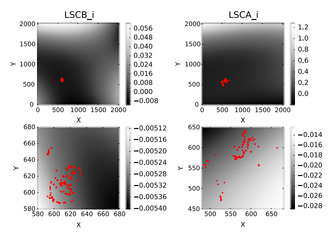

Figure 4. Illumination correction for LSCB_i and LSCA_i data sets. The bottom figures are zooms close to the pointing area.

We chose also to study the LSCA_i data set because this telescope observed the target at the same time but does not show any planetary significance ($\Delta\chi^2 \sim 20.7$). We conduct the same study and the results are summarized in Table 4 and Figure 4. The peak-to-peak amplitudes of the magnitude offsets are 10 times bigger than for the LSCB_i data set. It is surprising to see how two similar intruments can lead to such different data quality. A more careful check of the frames clearly shows a problem in the focus for the LSCA_i telescope. Because the Galactic Bulge fields are very crowded, this is a critical point for microlensing observations (e.g., increasing the blending). A plausible explanation for this difference between the twins is that during the time for observations, the telescopes were under commissioning, leading to non-optimal performance for LSCA_i.

4.3. Auckland_R

We conducted the same study for the Auckland_R data set because this telescope presents the clearest feature that mimics a planetary deviation, around HJD ∼ 6446.02, as can be seen in Figure 3. Results can be seen in Table 4. Because the pointing for this data set was extremely accurate (offset less than 2 pixels for the whole night of observation), the estimation of the illumination correction was not possible. There is not enough information in the matrix equations and they are degenerate. But this reflects the fact that the pointing did not induce systematic trends. However, a clear variation in the magnitude offset at each epoch is visible at the time of the deviation. Furthermore, we find that this offset is stronger for the brighter stars, as can be seen in Figure 5. There are strong similarities between the FSPL residuals and the magnitudes of the two brightest stars around the time of the anomaly HJD ∼ 6446.02, especially when the FSPL residuals get brighter at HJD ∼ 6446.03. Because the microlensing target is by far the brightest object in our field, we can expect that this systematics effect is probably even larger in our target. For this data set, we slightly modified our strategy by computing the offset at each epoch only for the brightest stars (mag < 18) and we rejected the microlensing target from the computation. Also, as can be seen in the bottom panel of Figure 5, the photometric scale factor shows variations during the night. This indicates the passage of clouds which can lead to systematics errors, as described previously. For example, the FSPL residuals in the interval 6446.01 ⩽ HJD ⩽ 6446.02 clearly share the pattern with the photometric scale factor.

4.4. Correction of Systematics

For the three studied data sets (LSCA_i, LSCB_i and Auckland_R), we corrected the systematics for the quantity that yielded the largest peak-to-peak amplitude in the magnitude offsets: namely the epoch. Moreover, this quantity is correlated with other quantities (airmass for example) and so the epoch correction should decrease the systematic trends measured for the other paramters listed in Table 4. We checked this and found that for the three data sets, the epoch correction leads to a significant improvement (order of a factor 10) for the systematics of the correlated quantities. This is a first order correction and we wanted to see the impact on the different models we analyzed. We repeated our modeling process with these new data sets using the previous models as starting points. The results are presented in Table 5. The new Auckland_R residuals can be seen in Figure 6. After correction, the amplitude of the "anomaly" is smaller but still exists. This is probably due to the fact that the amplitude of this feature in the light curves is brightness dependent, and the microlensing target is much brighter than all of the other stars, leading to an insufficient correcxtion fot the microlensing event.

As can be seen in Table 6, the correction of the systematics has a significant impact on the LSCA_i and Auckland_R data sets, which appear to suffer the most systematics. Note also that the planetary model is more significant after systematics correction, especially for these two telescopes. Even though the planetary model changes slightly before and after correction (the new s and q values are outside the error bars of the uncorrected data sets model), the caustic crossing is virtually

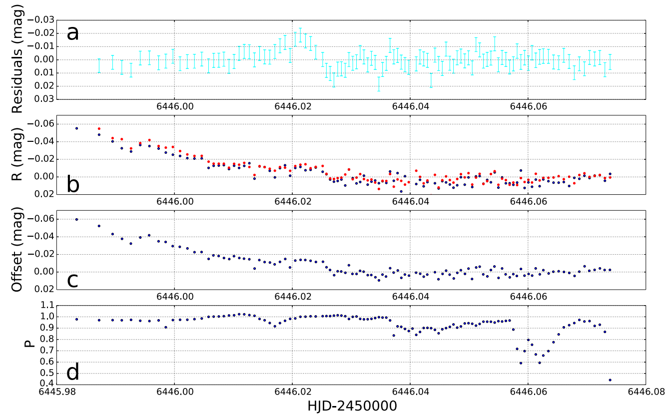

Figure 5. (a): Residuals of the FSPL model for the Auckland_R data set. (b): Light curves of the two other brightest stars in the field. (c): Systematics magnitude offsets as a function of the epoch computed for this data set; see text. (d): Photometric scale factor (normalized to a single exposure).

Table 5
Model Parameters after Correction of Systematics

Parameters	FSPL_c	FSPL_c+Annual Parallax	FSPL_c+Terrestrial Parallax	Wide Planetary (FSBL_c)
t_o(HJD)	$6446.04818 \pm 2\ 10^{-5}$	$6446.04681 \pm 3\ 10^{-5}$	$6446.04680 \pm 3\ 10^{-5}$	$6446.04665 \pm 3\ 10^{-5}$
$\boldsymbol{u_o}(\theta_E)$	$-4.21\ 10^{-4} \pm 1\ 10^{-6}$	$-4.01\ 10^{-4} \pm 8\ 10^{-6}$	$-4.19\ 10^{-4} \pm 7\ 10^{-6}$	$-4.34\ 10^{-4} \pm 5\ 10^{-6}$
t_E(days)	76.8 ± 0.1	80.6 ± 1.5	77.2 ± 1.3	74.9 ± 0.9
$\rho(\theta_E)$	$5.22\ 10^{-4} \pm 1\ 10^{-6}$	$4.97\ 10^{-4} \pm 4\ 10^{-5}$	$5.20\ 10^{-4} \pm 9\ 10^{-6}$	$5.40\ 10^{-4} \pm 7\ 10^{-6}$
I_s(mag)	19.00 ± 0.01	19.05 ± 0.02	19.01 ± 0.02	18.97 ± 0.01
V_s(mag)	20.49 ± 0.01	20.55 ± 0.02	20.50 ± 0.02	20.46 ± 0.01
I_b(mag)	18.21 ± 0.01	18.19 ± 0.01	18.21 ± 0.01	18.23 ± 0.01
V_b(mag)	22.72 ± 0.10	22.35 ± 0.10	22.70 ± 0.11	22.98 ± 0.11
Π_{EN}	⋯	0.34 ± 0.12	0.05 ± 0.01	⋯
Π_{EE}	⋯	0.28 ± 0.04	-0.00 ± 0.01	⋯
$s(\theta_E)$	⋯	⋯	⋯	1.50547 ± 0.04
q	⋯	⋯	⋯	$2.304\ 10^{-5} \pm 1.9\ 10^{-6}$
α(rad)	⋯	⋯	⋯	-2.39 ± 0.02
χ^2	3647.999	3571.000	3625.150	3258.842

unchanged (e.g., the central caustic is similar). However, the clearest signature of the planetary anomaly is still in the Auckland_R data set around HJD $\sim$ 6446.02.

4.5. Discussion

Due to strong finite source effects around a very small central caustic, the suspected planetary signature in OGLE-2013-BLG-0446 is very small. First of all, the low χ^2 improvement ($\Delta\chi^2 \sim 350$ and $\Delta\chi^2 \sim 389$ before and after the sysematics correction respectively) of the planetary model is far from the minimum value generally adopted in microlensing for a safe detection (Yee et al. 2013). Note also that even though the caustic crossing is similar, the two planetary models are not fully equivalent. As defined by Chung et al. (2005), the R_c parameter is the ratio of the vertical length and the horizontal length of a central caustic. This caustic parameter before and after correction is significantly different ($\sim$30%). Second, the highest $\Delta\chi^2$ contributor (LSCB_i) presents photometric systematics at the same level as the planetary deviations (2 versus 6 mmag). As can be seen in Figure 6, the systematics correction decreases the amplitude of the "anomaly" in the Auckland_R data set and it is therefore better fit by the planetary model. However, the increase in the FSPL residuals after HJD $\sim$ 6446.02 (from 1% to zero) is not

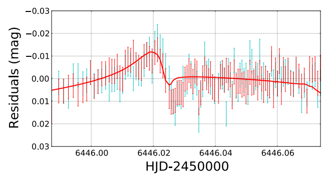

Figure 6. FSPL residuals of the Auckland_R before (cyan) and after (red) correction for systematics using the magnitude offsets as a function of epoch. The best planetary model after correction (FSBL_c) is shown in red.

explained by the planetary model, but similar behavior is seen in other bright stars. This clearly indicates that bright stars suffer from systematic effects in this data set which were not revealed by the different quantities we studied.

The planetary model is highly favored by the Canopus_I data set ($\Delta\chi^2 \sim 60$). However, a closer look at Figure 3 reveals that the planetary deviations are at a very low level ($\leqslant$0.5%). It cannot be excluded that the FSPL model correctly fits this data set and that this telescope also suffers from low level systematics errors. We however decided to not realize the same study of photometric systematic errors for the Canopus_I data set because there are no obvious deviations in the FSPL residuals and also because enough doubt has already been cast on the planetary model we found.

All these points reveal strong doubts about the reality of the planetary signature in OGLE-2013-BLG-0446. Even if we cannot firmly guarantee that the planet is not detected, we prefer to stay conservative and claim that we do not detect a planet in this event.

5. CONCLUSIONS

We presented the analysis of microlensing event OGLE-2013-BLG-0446. For this highly magnified event ($A \sim 3000$), several higher-order effects were investigated in the modeling process: annual and terrestrial parallax and planetary deviations. The study of photometric systematics for several data sets leads to various levels of confidence in the photometry. Moreover, a closer look at the data residuals and a precise study of photometric systematics reveals enough doubt to question any potential signals. Regarding the level of planetary signal ($\sim$1%) versus the various levels of systematics, we are not confident about the planetary signature in OGLE-2013-BLG-0446. Unfortunately, the clearest signature of the planetary signal was observed only in a single data set which presents some unexplained behavior for the brightest stars at the time of the anomaly. These doubts in addition to the relatively low improvement in χ^2 ($\Delta\chi^2 \leqslant 400$) encourage us to remain conservative and not to claim a planetary detection. This study stresses the importance of studying and quantifying the photometric systematic errors down to the level of 1% or lower for the detecion of the smallest microlensing planets.

The authors would like to thank the anonymous referee for the usefull comments. This publication was made possible by the NPRP grant # X-019-1-006 from the Qatar National Research Fund (a member of Qatar Foundation). The statements made herein are solely the responsibility of the authors. The authors thank the OGLE collaboration for the access of the optimized photometry. This work makes use of observations from the LCOGT network. This research has made use of the LCOGT Archive, which is operated by the California Institute of Technology, under contract with the Las Cumbres Observatory. This research has made much use of NASA's Astrophysics Data System. This research made use of the SIMBAD database, the VizieR catalog access tool, and the cross-match service provide d by CDS, Strasbourg, France. T.S. acknowledges the financial support from the

Table 6
χ^2 and rms of FSPL Residuals for Each Data Set Before and After Correction of Systematics

Telescope	rms		Raw Data		rms		Corrected	
	(mag)	χ^2_{FSPL}	χ^2_{Pla}	$\Delta\chi^2$	(mag)	χ^2_{FSPL}	χ^2_{Pla}	$\Delta\chi^2$
OGLE_I	0.029	770.308(459)	655.364(456)	114.944	0.029	765.677(459)	661.426(456)	104.251
OGLE_V	1.348	23.998(20)	24.005(17)	−0.007	1.348	23.998(20)	23.979(17)	0.019
Canopus_I	0.007	191.996(128)	132.410(125)	59.586	0.007	204.40(128)	137.769(125)	66.631
Auckland_R	**0.006**	**142.839(103)**	**128.294(100)**	**14.545**	**0.006**	**112.917(103)**	**72.331(100)**	**40.586**
LSCB_i	**0.007**	**446.170(374)**	**317.883(371)**	**128.287**	**0.007**	**442.338(374)**	**311.049(371)**	**131.189**
LSCA_i	**0.015**	**399.723(381)**	**379.065(378)**	**20.658**	**0.013**	**173.683(381)**	**133.422(378)**	**40.261**
CPTA_i	0.023	21.973(18)	21.926(15)	0.047	0.023	21.972(18)	21.925(15)	0.047
CTIO_I	0.006	159.174(108)	171.347(15)	−12.173	0.006	158.986(108)	167.376(105)	−8.48
CTIO_V	0.005	2.986(9)	5.385(6)	−2.399	0.005	3.036(9)	5.227(6)	−2.191
Danish_z	0.017	448.804(448)	470.960(445)	−22.156	0.017	450.589(448)	471.301(445)	−20.712
MOA_Red	0.785	727.979(450)	725.116(447)	2.863	0.783	727.760(450)	721.763(447)	5.997
Possum_N	0.012	355.767(240)	312.101(237)	43.666	0.012	354.002(240)	324.301(237)	29.701
Salerno_I	0.020	20.016(16)	18.911 (13)	1.105	0.020	19.990(16)	18.872(13)	1.118
Turitea_R	0.005	29.565(27)	29.341(24)	0.224	0.005	29.539(27)	28.965(24)	0.574
Weizmann_I	0.034	92.383(56)	92.667(53)	−0.284	0.034	92.389(56)	92.649(53)	−0.260
SAAO_I	0.014	67.100(54)	66.442(51)	0.658	0.014	67.085(54)	66 .487(51)	0.598
Total		3900.781	3551.217	349.564		3647.99	3258.842	389.157

Note. The three corrected data sets are rendered in bold. Numbers in parentheses are the degrees of freedom for each model/data set.

JSPS, JSPS23103002,JSPS24253004 and JSPS26247023. The M.O.A. project is supported by the grant JSPS25103508 and 23340064. D.P.B. acknowledges support from NSF grants AST-1009621 and AST-1211875, as well as NASA grants NNX12AF54G and NNX13AF64G. Work by I.A.B. and P.Y. was supported by the Marsden Fund of the Royal Society of New Zealand, contract no. MAU1104. The operation of the Danish 1.54 m telescope is financed by a grant to UGJ from the Danish Natural Science Research Council. We also acknowledge support from the Center of Excellence Centre for Star and Planet Formation (StarPlan) funded by The Danish National Research Foundation. The MiNDSTEp monitoring campaign is powered by ARTEMiS (Automated Terrestrial Exoplanet Microlensing Search; Dominik et al. 2008, AN 329, 248). K.A.A., M.D., K.H., M.H., C.S., R.A.S., and Y.T. are thankful to Qatar National Research Fund (QNRF), member of Qatar Foundation, for support by grant NPRP 09-476-1-078. C.S. has received funding from the European Union Seventh Framework Programme (FP7/2007–2013) under grant agreement No. 268421. Work by C.H. was supported by the Creative Research Initiative Program (2009-0081561) of National Research Foundation of Korea. S.H.G. and X.B.W. would like to thank the financial support from National Natural Science Foundation of China through grants Nos. 10873031 and 11473066. T.C.H. acknowledges support from the Korea Research Council of Fundamental Science & Technology (KRCF) via the KRCF Young Scientist Research Fellowship Programme and for financial support from KASI travel grant number 2013-9-400-00. H.K. acknowledges the support from the European Commission under the Marie Curie IEF Programme in FP7. M.R. acknowledges support from FONDECYT postdoctoral fellowship No. 3120097. O.W. (FNRS research fellow) and J. Surdej acknowledge support from the Communauté française de Belgique—Actions de recherche concertées—Académie Wallonie-Europe. The HPC (and/or scientific visualization) resources and services used in this work were provided by the IT Research Computing group in Texas A&M University at Qatar. IT Research Computing is funded by the Qatar Foundation for Education, Science and Community Development (http://www.qf.org.qa).

REFERENCES

Aigrain, S., & Pont, F. 2007, MNRAS, 378, 741
Albrow, M. D., Beaulieu, J.-P., Caldwell, J. A. R., et al. 1999, ApJ, 522, 1011
Albrow, M. D., Horne, K., Bramich, D. M., et al. 2009, MNRAS, 397, 2099
Bachelet, E., Fouqué, P., Han, C., et al. 2012a, A&A, 547, A55
Bachelet, E., Shin, I.-G., Han, C., et al. 2012b, ApJ, 754, 73
Beaulieu, J.-P., Bennett, D. P., Fouqué, P., et al. 2006, Natur, 439, 437
Bennett, D. P., Batista, V., Bond, I. A., et al. 2014, ApJ, 785, 155
Bennett, D. P., & Rhie, S. H. 1996, ApJ, 472, 660
Bessell, M. S., & Brett, J. M. 1988, PASP, 100, 1134
Bond, I. A., Abe, F., Dodd, R. J., et al. 2001, MNRAS, 327, 868
Bramich, D. M. 2008, MNRAS, 386, L77
Bramich, D. M., Bachelet, E., Alsubai, K. A., Mislis, D., & Parley, N. 2015, A&A, 577, 108
Bramich, D. M., & Freudling, W. 2012, MNRAS, 424, 1584
Bramich, D. M., Horne, K., Albrow, M. D., et al. 2013, MNRAS, 428, 2275
Casagrande, L., Ramírez, I., Meléndez, J., Bessell, M., & Asplund, M. 2010, A&A, 512, A54
Chung, S.-J., Han, C., Park, B.-G., et al. 2005, ApJ, 630, 535
Claret, A. 2000, A&A, 363, 1081
Coccato, L., Bramich, D. M., Freudling, W., & Moehler, S. 2014, MNRAS, 438, 1256
Dominik, M., Horne, K., Allan, A., et al. 2008, AN, 329, 248
Dong, S., Bond, I. A., Gould, A., et al. 2009, ApJ, 698, 1826
Dong, S., Udalski, A., Gould, A., et al. 2007, ApJ, 664, 862
Gould, A. 1994, ApJL, 421, L71
Gould, A. 1997, ApJ, 480, 188
Gould, A. 2000, ApJ, 542, 785
Gould, A. 2004, ApJ, 606, 319
Gould, A., Dong, S., Bennett, D. P., et al. 2009, arXiv:0910.1832
Gould, A., & Loeb, A. 1992, ApJ, 396, 104
Gould, A., Udalski, A., An, D., et al. 2006, ApJL, 644, L37
Gould, A., & Yee, J. C. 2013, ApJ, 764, 107
Griest, K., & Safizadeh, N. 1998, ApJ, 500, 37
Hardy, S. J., & Walker, M. A. 1995, MNRAS, 276, L79
Holz, D. E., & Wald, R. M. 1996, ApJ, 471, 64
Honeycutt, R. K. 1992, PASP, 104, 435
Kains, N., Arellano Ferrro, A., Figuera Jaimes, R., et al. 2015, A&A, 578, 128
Kervella, P., & Fouqué, P. 2008, A&A, 491, 855
Kovács, G., Bakos, G., & Noyes, R. W. 2005, MNRAS, 356, 557
Mallén-Ornelas, G., Seager, S., Yee, H. K. C., et al. 2003, ApJ, 582, 1123
Milne, E. A. 1921, MNRAS, 81, 361
Miyake, N., Udalski, A., Sumi, T., et al. 2012, ApJ, 752, 82
Nataf, D. M., Gould, A., Fouqué, P., et al. 2013, ApJ, 769, 88
Nemiroff, R. J., & Wickramasinghe, W. A. D. T. 1994, ApJL, 424, L21
Paczyński, B. 1986, ApJ, 304, 1
Padmanabhan, N., Schlegel, D. J., Finkbeiner, D. P., et al. 2008, ApJ, 674, 1217
Pepper, J., & Gaudi, B. S. 2005, ApJ, 631, 581
Pont, F., Zucker, S., & Queloz, D. 2006, MNRAS, 373, 231
Regnault, N., Conley, A., Guy, J., et al. 2009, A&A, 506, 999
Skottfelt, J., Bramich, D. M., Hundertmark, M., et al. 2015, A&A, 574, A54
Skowron, J., Udalski, A., Gould, A., et al. 2011, ApJ, 738, 87
Smith, J. C., Stumpe, M. C., Van Cleve, J. E., et al. 2012, PASP, 124, 1000
Smith, M. C., Mao, S., & Paczyński, B. 2003, MNRAS, 339, 925
Tamuz, O., Mazeh, T., & Zucker, S. 2005, MNRAS, 356, 1466
Tsapras, Y., Street, R., Horne, K., et al. 2009, AN, 330, 4
Udalski, A. 2003a, ApJ, 590, 284
Udalski, A. 2003b, AcA, 53, 291
Udalski, A., & Szymański, M. 2015, AcA, 65, 1
Vermaak, P. 2000, MNRAS, 319, 1011
Witt, H. J., & Mao, S. 1994, ApJ, 430, 505
Yee, J. C., Hung, L.-W., Bond, I. A., et al. 2013, ApJ, 769, 77
Yee, J. C., Udalski, A., Sumi, T., et al. 2009, ApJ, 703, 2082
Yoo, J., DePoy, D. L., Gal-Yam, A., et al. 2004, ApJ, 603, 139

A&A 580, A12 (2015)
DOI: 10.1051/0004-6361/201525982

Astronomy & Astrophysics

Modelling the local and global cloud formation on HD 189733b

G. Lee[1], Ch. Helling[1], I. Dobbs-Dixon[2], and D. Juncher[3]

[1] SUPA, School of Physics and Astronomy, University of St Andrews, North Haugh, St Andrews, Fife KY16 9SS, UK
e-mail: gl239@st-andrews.ac.uk
[2] NYU Abu Dhabi, PO Box 129188, Abu Dhabi, UAE
[3] Niels Bohr Institute & Centre for Star and Planet Formation, University of Copenhagen, 2100 Copenhagen, Denmark

Received 27 February 2015 / Accepted 21 May 2015

ABSTRACT

Context. Observations suggest that exoplanets such as HD 189733b form clouds in their atmospheres which have a strong feedback onto their thermodynamical and chemical structure, and overall appearance.
Aims. Inspired by mineral cloud modelling efforts for brown dwarf atmospheres, we present the first spatially varying kinetic cloud model structures for HD 189733b.
Methods. We apply a 2-model approach using results from a 3D global radiation-hydrodynamic simulation of the atmosphere as input for a detailed, kinetic cloud formation model. Sampling the 3D global atmosphere structure with 1D trajectories allows us to model the spatially varying cloud structure on HD 189733b. The resulting cloud properties enable the calculation of the scattering and absorption properties of the clouds.
Results. We present local and global cloud structure and property maps for HD 189733b. The calculated cloud properties show variations in composition, size and number density of cloud particles which are strongest between the dayside and nightside. Cloud particles are mainly composed of a mix of materials with silicates being the main component. Cloud properties, and hence the local gas composition, change dramatically where temperature inversions occur locally. The cloud opacity is dominated by absorption in the upper atmosphere and scattering at higher pressures in the model. The calculated 8 μm single scattering albedo of the cloud particles are consistent with *Spitzer* bright regions. The cloud particles scattering properties suggest that they would sparkle/reflect a midnight blue colour at optical wavelengths.

Key words. planets and satellites: individual: HD 189733b – planets and satellites: atmospheres – methods: numerical

1. Introduction

The atmospheres of exoplanets are beginning to be characterised in great detail. Spectroscopic measurements from primary and secondary transits of hot Jupiters have opened up the first examinations into the composition of their atmospheres. HD 189733b is one of the most studied hot Jupiters due to its bright parent star and large planet-to-star radius ratio. Observational data of this object has been collected by various groups from X-ray to radio wavelengths (Knutson et al. 2007; Tinetti et al. 2007; Charbonneau et al. 2008; Grillmair et al. 2008; Swain et al. 2008, 2009; Danielski et al. 2014). Transit spectra from the *Hubble* Space Telescope (Lecavelier Des Etangs et al. 2008; Sing et al. 2011; Gibson et al. 2012) between 0.3 μm and 1.6 μm show a featureless spectrum consistent with Rayleigh scattering from the atmosphere. These observations sample the outer limbs (dayside-nightside terminator regions) of the planet's atmosphere during primary eclipse. Lecavelier Des Etangs et al. (2008) suggests haze/clouds to be responsible for the Rayleigh slope and estimate cloud particle radii of $10^{-2}\ldots10^{-1}$ μm at $\sim10^{-6}\ldots10^{-3}$ bar local gas pressures. They suggest $MgSiO_3$[s] as the most likely cloud particle material due to its strong scattering properties. Pont et al. (2013) who reanalysed and combined the *Hubble* and *Spitzer* (Agol et al. 2010; Désert et al. 2011; Knutson et al. 2012) observations found that the spectrum was "Dominated by Rayleigh scattering over the whole visible and near-infrared range..." and also suggest cloud/haze layers as a likely scenario. Subsequent analysis by Wakeford & Sing (2015) showed that single composition cloud condensates could fit the Rayleigh scattering slope with grain sizes of 0.025 μm. Evans et al. (2013) measured the geometric albedo of HD 189733b over 0.29...0.57 μm and infer the planet is likely to be a deep blue colour at visible wavelengths, which they attribute to scattering mid-altitude clouds. These albedo observations sample the dayside face of the planet by comparing measurements before, during and after the secondary transit (occulation). Star spots (McCullough et al. 2014), low atmospheric metallicity (Huitson et al. 2012) and photo-chemical, upper atmosphere haze layers (Pont et al. 2013) have been proposed as alternative explanations to these observations.

Clouds present in optically thin atmospheric regions are thought to significantly impact the observed spectra of exoplanets by flattening the ultra-violet and visible spectrum through scattering by small cloud particles, by depletion of elements and by providing an additional opacity source (e.g. GJ 1214b; Kreidberg et al. 2014). The strong radiative cooling (or heating) resulting from the high opacity of the cloud particles also affect the local pressure which influences the local velocity field (Helling et al. 2004). These effects have been observed and modelled in brown dwarf atmospheres which are the inspiration for the current study. Clouds are also important for ionisation of the atmosphere by dust-dust collisions (Helling et al. 2011) and cosmic ray ionisation (Rimmer & Helling 2013). This leaves open the possibility of lightning discharge events in

exo-clouds (Bailey et al. 2014). Furthermore, Stark et al. (2014) suggest that charged dust grains could aid the synthesis of prebiotic molecules by enabling the required energies of formation on their surfaces. Multi-dimensional atmosphere simulations have been used to gain a first insight into the atmospheric dynamics of HD 189733b (e.g. Showman et al. 2009; Fortney et al. 2010; Knutson et al. 2012; Dobbs-Dixon & Agol 2013). Output from Showman et al. (2009) has been used for kinetic, non-equilibrium photo-chemical models of HD 189733b (Moses et al. 2011; Venot et al. 2012; Agúndez et al. 2014).

In this work, we present cloud structure calculations for HD 189733b based on 3D radiation-hydrodynamic (3D RHD) atmosphere results of Dobbs-Dixon & Agol (2013). With this 2-model approach, we investigate how the specific cloud properties vary locally and globally throughout HD 189733b's atmosphere. In Sect. 2 we outline our 2-model approach. We summarise our cloud formation model and discuss our approach to atmospheric mixing, cloud particle opacities and model limitations. In Sect. 3 the spatially varying cloud properties (particle sizes, number density, material composition, nucleation rate, growth rate and opacity) are presented. In Sect. 4 we use the results of the locally and spatially varying cloud properties to calculate the wavelength dependent opacity and contribution of the clouds to the reflected light and transit spectra for HD 189733b. Section 5 discusses our results with respect to observational findings for HD 189733b. Our conclusions are outlined in Sect. 6.

2. 2-model approach

We apply our kinetic dust cloud formation model to results from 3D RHD simulations of HD 189733b's atmosphere (Dobbs-Dixon & Agol 2013) and present a first study of spatially varying cloud formation on a hot Jupiter. We briefly summarise the main features of the kinetic cloud formation model (see: Woitke & Helling 2003, 2004; Helling et al. 2008b; Helling & Fomins 2013). This cloud model has been successfully combined with 1D atmosphere models (- ; Dehn et al. 2007; Helling et al. 2008a; Witte et al. 2009, 2011) to produce synthetic spectra of M dwarfs, brown dwarfs and *non-irradiated* hot Jupiter exoplanets. We then summarise the multi-dimensional radiative-hydrodynamical model from Dobbs-Dixon & Agol (2013) used as input for the kinetic cloud formation model. Finally, we outline our approach in calculating the absorption and scattering properties of multi-material, multi-disperse, mixed cloud particles.

2.1. Cloud formation modelling

Cloud formation proceeds via a sequence of processes that are described kinetically in our cloud formation model:

1. Formation of seed particles by homomolecular homogeneous nucleation (Jeong et al. 2003; Lee et al. 2015).
2. Growth of various solid materials by gas-grain chemical surface reactions on the existing seeds or grains (Gail & Sedlmayr 1986; Helling & Woitke 2006; Helling et al. 2008b).
3. Evaporation of grains when the materials that they are composed of become thermally unstable (Helling & Woitke 2006; Helling et al. 2008b).
4. Gravitational settling allowing a continuation of grain growth through transport of grains out of under-saturated regions (Woitke & Helling 2003, 2004).
5. Element depletion in regions of cloud formation which can stop new grains from forming (Helling & Woitke 2006).
6. Convective/turbulent mixing from deeper to higher atmospheric regions to provide element replenishment (Woitke & Helling 2003, 2004).

Without the nucleation step 1, grains do not form and a stationary atmosphere remains dust-free. We refer the reader to Helling & Fomins (2013) for a summary of the applied theoretical approach to model cloud formation in an oxygen-rich gas. The nucleation rate (formation of seed particles) J_* [cm^{-3} s^{-1}] for homomolecular homogeneous nucleation (Helling & Woitke 2006) is

$$J_*(t, \boldsymbol{r}) = \frac{f(1,t)}{\tau_{\rm gr}(1, N_*, t)} Z(N_*) \times \exp\left((N_* - 1) \ln S(T) - \frac{\Delta G(N_*)}{RT}\right), \quad (1)$$

where $f(1,t)$ is the number density of the seed forming gas species, $\tau_{\rm gr}$ the growth timescale of the critical cluster size N_*, $Z(N_*)$ the Zeldovich factor, $S(T)$ the supersaturation ratio and $\Delta G(N_*)$ the Gibbs energy of the critical cluster size. We consider the homogeneous nucleation of TiO_2 seed particles. A new value for the surface tension $\sigma_\infty = 480$ [erg cm^{-2}] is used based on updated TiO_2 cluster calculations from Lee et al. (2015).

The net growth/evaporation velocity $\chi^{\rm net}$ [cm s^{-1}] of a grain (after nucleation) due to chemical surface reactions (Helling & Woitke 2006) is

$$\chi^{\rm net}(\boldsymbol{r}) = \sqrt[3]{36\pi} \sum_s \sum_{r=1}^{R} \frac{\Delta V_r n_r v_r^{\rm rel} \alpha_r}{\nu_r^{\rm key}} \left(1 - \frac{1}{S_r} \frac{1}{b^s_{\rm surf}}\right), \quad (2)$$

where "r" is the index for the chemical surface reaction, ΔV_r the volume increment of the solid "s" by reaction r, n_r the particle density of the reactant in the gas phase, $v_r^{\rm rel}$ the relative thermal velocity of the gas species taking part in reaction r, α_r the sticking coefficient of reaction r and $\nu_r^{\rm key}$ the stoichiometric factor of the key reactant in reaction r (Helling & Woitke 2006). S_r is the reaction supersaturation ratio and $1/b^s_{\rm surf} = V_s/V_{\rm tot}$ the volume ratio of solid s. Our cloud formation method allows the formation of mixed heterogeneous grain mantles. We simultaneously consider 12 solid growth species (TiO_2[s], Al_2O_3[s], $CaTiO_3$[s], Fe_2O_3[s], FeS[s], FeO[s], Fe[s], SiO[s], SiO_2[s], MgO[s], $MgSiO_3$[s], Mg_2SiO_4[s]) with 60 surface chemical reactions (Helling et al. 2008b). The local dust number density $n_{\rm d}$ [cm^{-3}] and mean grain radius $\langle a \rangle$ [cm] are given by

$$n_{\rm d}(\boldsymbol{r}) = \rho_{\rm gas}(\boldsymbol{r}) L_0(\boldsymbol{r}), \quad (3)$$

$$\langle a \rangle(\boldsymbol{r}) = \sqrt[3]{\frac{3}{4\pi} \frac{L_1(\boldsymbol{r})}{L_0(\boldsymbol{r})}}, \quad (4)$$

respectively; where $\rho_{\rm gas}(\boldsymbol{r})$ [g cm^{-3}] is the local gas volume density and $L_0(\boldsymbol{r})$, $L_1(\boldsymbol{r})$ are derived by solving for $L_j(\boldsymbol{r})$ [$cm^j g^{-1}$] in the dust moment equations (Woitke & Helling 2003).

2.2. 3D radiative-hydrodynamical model

The 3D radiative-hydrodynamical [3D RHD] model solves the fully compressible Navier-Stokes equations coupled to a wavelength dependent two-stream radiative transfer scheme. The model assumes a tidally-locked planet with $\phi = 0°$, $\theta = 0°$ denoting the sub-stellar point (the closest point to the host star). There

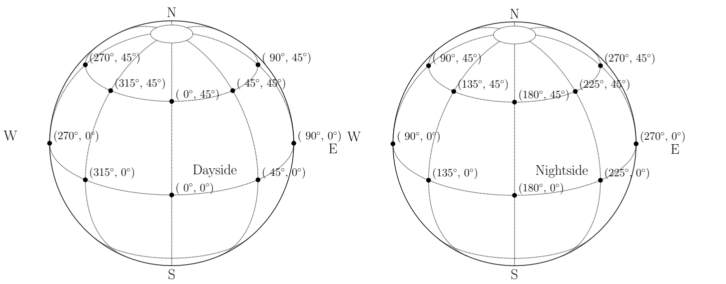

Fig. 1. Illustration of the sample trajectories (black points) taken from the 3D radiative-hydrodynamic model atmosphere of HD 189733b (Dobbs-Dixon & Agol 2013); longitudes $\phi = 0°\ldots315°$ in steps of $\Delta\phi = +45°$, latitudes $\theta = 0°, +45°$. The sub-stellar point is at $\phi = 0°$, $\theta = 0°$. We assume that the sample trajectories are latitudinal (north-south) symmetric.

are three components to the wavelength dependent opacities: molecular opacities consistent with solar composition gas, a gray component representing a strongly absorbing cloud deck, and a strong Rayleigh scattering component. Equations are solved on a spherical grid with pressures ranging from $\sim10^{-4.5}$ to $\sim10^3$ bar. Input parameters were chosen to represent the bulk observed properties of HD 189733b, but (with the exception of the opacity) were not tuned to match spectroscopic observations. The dominate dynamical feature is the formation of a super-rotating, circumplanetary jet (Tsai et al. 2014) that efficiently advects energy from day to night near the equatorial regions. This jet forms from the planetary rotation (Rossby waves) coupled with eddies which pump positive angular momentum towards the equator (Showman & Polvani 2011). A counter-rotating jet is present at higher latitudes. Significant vertical mixing, discussed later, is seen throughout the atmosphere. Calculated transit spectra, emission spectra, and light curves agree quite well with current observations from 0.3 μm to 8.0 μm. Further details can be found in Dobbs-Dixon & Agol (2013).

2.3. Model set-up and input quantities

We sampled vertical trajectories of the 3D RHD model at longitudes of $\phi = 0°\ldots315°$ in steps of $\Delta\phi = +45°$ and latitudes of $\theta = 0°, +45°$ (Fig. 1). The horizontal wind velocity moves in the positive ϕ direction. Figure 2 shows the ($T_{\rm gas}$, $p_{\rm gas}$) and vertical velocity profiles used to derive the cloud structure at the equator $\theta = 0°$ and latitude $\theta = 45°$. Local temperature inversions are present in the dayside ($T_{\rm gas}$, $p_{\rm gas}$) profiles which are exposed to the irradiation of the host star without the need for an additional opacity source. The local temperature maximum migrates eastward with increasing atmospheric depth. This is due to hydrodynamical flows funnelling gas towards the equator causing viscous, compressive and shock heating. The ($T_{\rm gas}$, $p_{\rm gas}$) profile at latitude $\theta = 45°$ has steeper temperature inversions on the dayside. Sample trajectories converge to equal temperatures at $p_{\rm gas} > 1$ bar for all longitudes and latitudes. We apply a 3-point boxcar smoothing to the vertical velocity profiles in order to reduce the effects of unresolved turbulence. Further required input quantities are a constant surface gravity of $\log g = 3.32$ and initial solar element abundances $\epsilon^0_{\rm x}/\epsilon_{\rm H}$ (element "x" to Hydrogen ratio) with C/O = 0.427 (Anders & Grevesse 1989) for all atmospheric layers. However, we note the element abundance of the gas phase will increase or decrease due to cloud formation or evaporation (Fig. 8). We assume local thermal equilibrium (LTE) for all gas-gas and dust-gas chemical reactions. The required input quantities for the kinetic cloud formation model are summarised in Table 1.

Table 1. Input quantities for the cloud formation model. Local $T_{\rm gas}$, $p_{\rm gas}$, $\rho_{\rm gas}$, v_z and z are taken from the 3D radiation-hydrodynamic model.

Input	Definition	Units
$T_{\rm gas}$ ($\boldsymbol{r}$)	local gas temperature	K
$p_{\rm gas}$ ($\boldsymbol{r}$)	local gas pressure	dyn cm^{-2}
$\rho_{\rm gas}$ ($\boldsymbol{r}$)	local gas density	g cm^{-3}
v_z ($\boldsymbol{r}$)	local vertical gas velocity	cm s^{-1}
z	vertical atmospheric height	cm
$\epsilon^0_{\rm x}/\epsilon_{\rm H(\boldsymbol{r})}$	element abundance	–
g ($\boldsymbol{r}$)	surface gravity	cm s^{-2}

2.4. Atmospheric vertical mixing

Vertical mixing is important to resupply the upper atmosphere with elements which have been depleted by cloud particle formation and their subsequent gravitational settling into deeper atmospheric layers (Woitke & Helling 2003). Without mixing, the cloud particles in the atmosphere would rain out and remove heavy elements from the upper atmosphere. This leaves a metal poor gas phase where no future cloud particles could form (Woitke & Helling 2004; Appendix A).

2.4.1. Previous brown dwarf approach

The main energy transport in the core of a brown dwarf is convection. The atmosphere is convectively unstable in the inner, hotter parts. This atmospheric convection causes substantial overshooting into even higher, and radiation dominated parts (e.g. Ludwig et al. 2002). Woitke & Helling (2003, 2004) define

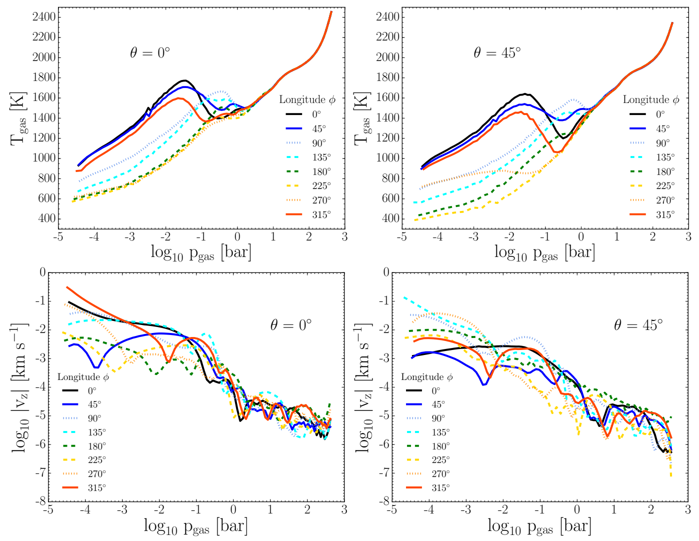

Fig. 2. 1D trajectory results from the 3D RHD HD 189733b atmosphere simulation used as input for the cloud formation model. *Top row*: ($T_{\rm gas}$, $p_{\rm gas}$) profiles in steps of longitude $\Delta\phi = +45°$ at equatorial, $\theta = 0°$ and latitude, $\theta = 45°$ profiles. *Bottom row*: smoothed vertical gas velocities $\boldsymbol{v}_z$ [km s^{-1}] in steps of longitude $\Delta\phi = +45°$ at equatorial, $\theta = 0°$ and latitude, $\theta = 45°$ profiles. Both latitudes show a temperature inversion on the dayside. The sub-stellar point is at $\phi = 0°$, $\theta = 0°$. Solid, dotted and dashed lines indicate dayside, day-night terminator and nightside profiles respectively.

the mixing timescale in low mass stellar atmospheres as the time for convective motions $v_{\rm conv}$ to travel a fraction of the pressure scale height, $H_{\rm p}(\boldsymbol{r})$

$$\tau_{\rm mix,conv}(\boldsymbol{r}) = {\rm const.} \cdot \frac{H_{\rm p}(\boldsymbol{r})}{v_{\rm conv}(\boldsymbol{r})}. \quad (5)$$

Helling et al. (2008b), Witte et al. (2009, 2011) represent values for $v_{\rm conv}(\boldsymbol{r})$, in their 1D - model atmospheres, above the convective zone (defined by the Schwarzschild criterion) from inertially driven *overshooting* of ascending gas bubbles.

2.4.2. Previous hot Jupiter approach

On hot Jupiters, in contrast to Earth, Jupiter and brown dwarf atmospheres, the intensity of stellar irradiation can suppress convective motions down to very large pressures (Barman et al. 2001). Therefore turbulent diffusion is likely the dominant vertical transport mechanism. The use of the 3D RHD model results allows us to apply the local vertical velocity component, $\boldsymbol{v}_z(\boldsymbol{r})$, in our cloud formation model. No additional assumptions are required. Hence, $v_z(\boldsymbol{r})$ is known for each atmospheric trajectory chosen, as visualised in Fig. 2.

Some chemical models of hot Jupiters (e.g. Moses et al. 2011) use an approximation of the vertical diffusion coefficient $\boldsymbol{K}_{zz}(\boldsymbol{r})$ [cm^2 s^{-1}] of the gaseous state.

$$\boldsymbol{K}_{zz}(\boldsymbol{r}) = H_{\rm p}(\boldsymbol{r}) \cdot v_z(\boldsymbol{r}). \quad (6)$$

The diffusion timescale is then

$$\tau_{\rm mix,diff}(\boldsymbol{r}) = {\rm const.} \cdot \frac{H^2_{\rm p}(\boldsymbol{r})}{K_{zz}(\boldsymbol{r})}. \quad (7)$$

Moses et al. (2011) apply the root-mean-square (rms) vertical velocities derived from global horizontal averages at each atmospheric layer to their chemical models. This results in a horizontally homogenous $K_{zz}(\boldsymbol{r})$ mixing parameter. Parmentier et al. (2013) derive a global mean value for $K_{zz}(\boldsymbol{r})$ as a function of local pressure using a passive tracer in their global circulation model (GCM) of HD 189733b resulting in $K_{zz}(\boldsymbol{r}) = 10^7$ $p^{-0.65}$ (p [bar]). Using a global mean smooths away all horizontally dependent vertical velocity variations. Any parameterisation of the vertical mixing will depend on the details of the underlying hydrodynamical structure. Parmentier et al. (2013) use a 3D primitive equation model where vertical hydrostatic equilibrium is assumed. The radiation hydrodynamic simulations performed by Dobbs-Dixon & Agol (2013), applied in this paper, solve the full Navier-Stokes equations and will produce larger vertical velocities compared to the primitive equations. In summary, vertical velocity may be substantially damped in models using the primitive equations. Both Eq. (6) and Parmentier et al. (2013) definitions for $K_{zz}(\boldsymbol{r})$ assume that the dominant mixing occurs in the vertical direction, possible mixing from horizontal flows are neglected. The time-scale comparison in Sect. 2.4.4 supports this assumption for cloud formation processes. It is worthwhile noting that the idea of diffusive mixing originates from shallow water approximations as applied in solar system research where a 2D velocity field produces shear which creates a turbulent velocity component. Hartogh et al. (2005) outline how local wind shear and the hydrostatic gas pressure are used to represent a vertical mixing.

Some arguments reinforce why vertical mixing is important:

- Regions with low vertical velocity can be replenished of elements by the horizontal winds from high vertical velocity regions in a 3D situation.
- Large Hadley cell circulation is present and here vertical velocities can be significant and element replenishment to the upper atmosphere may be more efficient.
- Vertical transport is a key mixing process on Earth which has been successfully applied to hot Jupiter chemical models (Moses et al. 2011; Venot et al. 2012; Agúndez et al. 2014).

We use Eq. (7) (const. = 1) as the 1D mixing timescale input for our kinetic dust formation model, with Eq. (6) as the definition of the diffusion coefficient. We adopt the local vertical velocities that result from the Dobbs-Dixon & Agol (2013) 3D RHD atmosphere simulations for HD 189733b as the values for $v_z(\boldsymbol{r})$ (Fig. 2). A 3-point boxcar smoothing was applied to these velocities to reduce the effects of unresolved turbulence. The longitude dependent K_{zz} (ϕ, r) for latitudes θ = 0°, 45° is shown in Fig. 3 (first row) and the resulting vertical mixing timescales (second row). We include the K_{zz} relation from Parmentier et al. (2013) in Fig. 3 (dash-dotted line) for comparison. Their linear fit is approximately one order of magnitude lower which is similar to the difference found in HD 189733b and HD 209458b chemical models (Agúndez et al. 2014) who compared the two $K_{zz}(\boldsymbol{r})$ expressions for Showman et al. (2009) GCM simulations. The current approach aims to capture the unique vertical mixing and thermodynamic conditions at each trajectory, while also accounting for practical modelling of atmospheric mixing.

2.4.3. Advective timescales

An important timescale to consider is the charcteristic advective timescale which is a representative timescale for heat to redistribute over the circumference of the globe. The advective timescale is given by

$$\tau_{\rm adv}(\boldsymbol{r}) = \frac{\pi r}{v_{\rm horiz}(\boldsymbol{r})}, \tag{8}$$

where $r(z)$ is the radial height of the planet and $v_{\rm horiz}(\boldsymbol{r})$ the local gas velocity in the horizontal direction (ϕ). This timescale gives an idea of how fast thermodynamic conditions can change in the longitudinal direction at a particular height z in the atmosphere. Figure 3 compares the advective timescale to the vertical diffusion timescale (Eq. (7)) and find that both time scales are of the same order of magnitude. This suggests that the convective/turbulent diffusion of upward gaseous material as described in Sect. 2.4.1 occurs approximately at the same timescales as gas advected across the globe. This suggests that, to a first approximation, the 1D ($T_{\rm gas}$, $p_{\rm gas}$) trajectories used as input for the cloud formation model do not fluctuate rapidly enough to substantially influence the cloud properties.

2.4.4. Cloud formation timescales

We compare the cloud particle settling, growth and nucleation timescales that result from our cloud model (Sect. 3) to the mixing and advection timescales that are derived from the hydrodynamic fluid field. The nucleation timescale $\tau_{\rm nuc}$ is defined as

$$\tau_{\rm nuc} = \frac{n_{\rm d}}{J_\star}, \tag{9}$$

the growth timescale $\tau_{\rm gr}$ by

$$\tau_{\rm gr} = \frac{\sqrt[3]{36\pi}\langle a\rangle}{3|\chi^{\rm net}|}, \tag{10}$$

and the cloud particle settling timescale $\tau_{\rm setl}$ by

$$\tau_{\rm setl} = \frac{H_{\rm p}}{|\langle v_{\rm dr}\rangle|}, \tag{11}$$

where $\langle v_{\rm dr}\rangle$ is the large Knudsen number frictional regime ($Kn \gg 1$) mean drift velocity (Woitke & Helling 2003, Eq. (63)). Figure 4 shows the timescales at the sub-stellar and anti-stellar points. Our results agree with earlier timescale analysis in Woitke & Helling (2003) who point out an hierarchical dominance of the cloud formation processes through the atmosphere. In the upper atmosphere nucleation is the most efficient process:

$$\tau_{\rm nuc} \lesssim \tau_{\rm gr} \ll \tau_{\rm mix} \sim \tau_{\rm adv} \ll \tau_{\rm setl}.$$

Deeper in the atmosphere nucleation eventually becomes inefficient and all timescales become comparable

$$\tau_{\rm gr} \lesssim \tau_{\rm mix} \sim \tau_{\rm adv} \lesssim \tau_{\rm setl}.$$

The chemical processes that determine the cloud particle formation occur on shorter timescales than the large scale hydrodynamical timescales. This emphasises that the cloud particle formation is a local process.

2.5. Dust opacity

Based on the results of the spatially varying cloud properties we calculate the opacity of the cloud particles. We determine the cloud particle absorption and scattering coefficients in each atmospheric layer for wavelengths 0.3 μm, 0.6 μm, 1.1 μm, 1.6 μm, 3.6 μm, 4.5 μm, 5.8 μm, 8.0 μm, 24.0 μm, corresponding to the *Hubble* and *Spitzer* average band passes. Since the cloud particles are made of mixed solids, the effective (n, k) optical constants is calculated for each particle using effective medium theory. We follow the approach of Bruggeman (1935) where

$$\sum_s \left(\frac{V_s}{V_{\rm tot}}\right)\frac{\epsilon_s - \epsilon_{\rm av}}{\epsilon_s + 2\epsilon_{\rm av}} = 0, \tag{12}$$

where $V_s/V_{\rm tot}$ is the volume fraction of solid species s, ϵ_s the dielectric function of solid species s and $\epsilon_{\rm av}$ the average dielectric function over the total cloud particle volume. The average

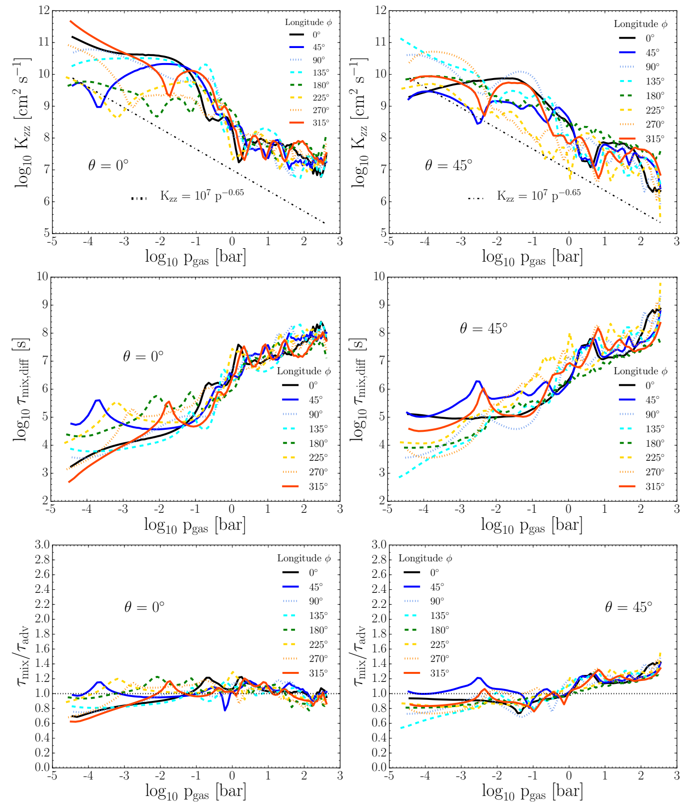

Fig. 3. *Top row*: vertical diffusion coefficient $K_{zz}(\boldsymbol{r}) = H_{\rm p} \cdot v_z(\boldsymbol{r})$ [cm^2 s^{-1}] applying the smoothed vertical velocities of the radiative-hydrodynamic HD 189733b model at latitudes θ = 0° and θ = 45°, as a function of pressure at $\Delta\phi$ = +45° longitude intervals. The $K_{zz}(\boldsymbol{r}) = 10^7 p^{-0.65}$ (p [bar]) expression from Parmentier et al. (2013) is shown as dash-dotted lines. *Middle row*: the vertical mixing timescales $\tau_{\rm mix,diff}$ [s] derived from the HD 189733b radiative-hydrodynamic model results at latitudes θ = 0°, θ = 45°, as a function of pressure at $\Delta\phi$ = +45° longitude intervals. *Bottom row*: ratio of the mixing and advective timescales at θ = 0°, 45° respectively. The ratio of the timescales stays approximately equal at all pressures. Solid, dotted and dashed lines indicate dayside, day-night terminator and nightside profiles respectively.

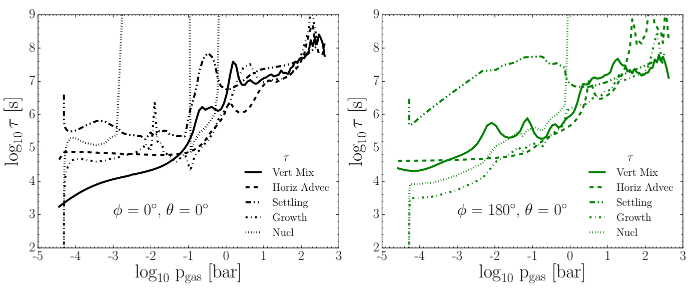

Fig. 4. Vertical mixing, horizontal advection, cloud settling, cloud growth and cloud nucleation timescales at the sub-stellar point (*Left*) and ϕ = 180°, θ = 0° (*Right*).

dielectric function is then found by Newton-Raphson minimisation of Eq. (12). The scattering and extinction cross sections are then calculated using Mie theory for spherical particles (Mie 1908). We follow the approach of Bohren & Huffman (1983) where the scattering and extinction cross sections are defined as

$$C_{\rm sca}(\lambda, a) = \frac{2\pi a^2}{x^2}\sum_{n=1}^{\infty}(2n+1)\left(|a_n|^2 + |b_n|^2\right), \tag{13}$$

$$C_{\rm ext}(\lambda, a) = \frac{2\pi a^2}{x^2}\sum_{n=1}^{\infty}(2n+1)Re\,(a_n + b_n), \tag{14}$$

respectively; where $x = 2\pi a/\lambda$ is the wavelength dependent size parameter. The scattering coefficients a_n and b_n are calculated from the material optical k constant (Bohren & Huffman 1983). The wavelength-dependent absorption and scattering efficiency of a cloud particle is then

$$Q_{\rm sca}(\lambda, a) = \frac{C_{\rm sca}(\lambda, a)}{\pi a^2}, \tag{15}$$

$$Q_{\rm abs}(\lambda, a) = \frac{C_{\rm ext}(\lambda, a)}{\pi a^2} - Q_{\rm sca}, \tag{16}$$

respectively. The total absorption and scattering efficiency κ [cm^2 g^{-1}] can then be derived by multiplying the corresponding efficiencies with the area and occurrence rate of each cloud particle.

$$\kappa_{\rm sca}(\lambda, a) = Q_{\rm sca}(\lambda, a)\pi a^2 n_{\rm d}/\rho_{\rm gas}, \tag{17}$$

$$\kappa_{\rm abs}(\lambda, a) = Q_{\rm abs}(\lambda, a)\pi a^2 n_{\rm d}/\rho_{\rm gas}. \tag{18}$$

We include all 12 solid dust species in the opacity calculations. References for their optical constants are presented in Table 2. We assume that for all Mie calculations the grain size is given by the mean grain radius $\langle a\rangle$ (Eq. (4)) with number density $n_{\rm d}$ (Eq. (3)) for each atmospheric layer.

3. Mineral clouds in the atmosphere of HD 189733b

We apply the dust formation theory developed by Woitke & Helling (2003, 2004), Helling & Woitke (2006) and Helling et al. (2008b) in its 1D stationary form to 1D output trajectories of a 3D RHD model of HD 189733b, as described in Dobbs-Dixon & Agol (2013). In the following, we present local and global cloud structures for HD 189733b and discuss detailed results on cloud properties such as grain sizes, material composition, element abundances, dust-to-gas ratio and C/O ratio. We investigate general trends of the cloud structure as it varies throughout the atmosphere and make first attempts to study the cloud properties across the planetary globe.

Table 2. References for the (n, k) optical constants of the 12 different solids.

Solid species	Source
TiO_2[s]	Ribarsky in Palik (1985)
Al_2O_3[s]	Zeidler et al. (2013)
$CaTiO_3$[s]	Posch et al. (2003)
Fe_2O_3[s]	Unpublished[a]
FeS[s]	Henning et al. (1995)
FeO[s]	Henning et al. (1995)
Fe[s]	Posch et al. (2003)
SiO[s]	Philipp in Palik (1985)
SiO_2[s]	Posch et al. (2003)
MgO[s]	Palik (1985)
$MgSiO_3$[s]	Dorschner et al. (1995)
Mg_2SiO_4[s]	Jäger et al. (2003)

Notes. [a] `http://www.astro.uni-jena.de/Laboratory/OCDB/oxsul.html`

3.1. The cloud structure of HD 189733b at the sub-stellar point

The substellar point (ϕ = 0°, θ = 0°) is the most directly irradiated point in atmospheres of hot Jupiters such as HD 189733b which is measured by observing before, during and after secondary transit (occulatation). We use this well defined location to provide a detailed description of the vertical cloud structure. We compare this atmospheric trajectory to other longitudes in Sect. 3.2 and to other latitudes in Sect. 3.3. Figure 5 shows that the cloud structure starts with the formation of seed particles

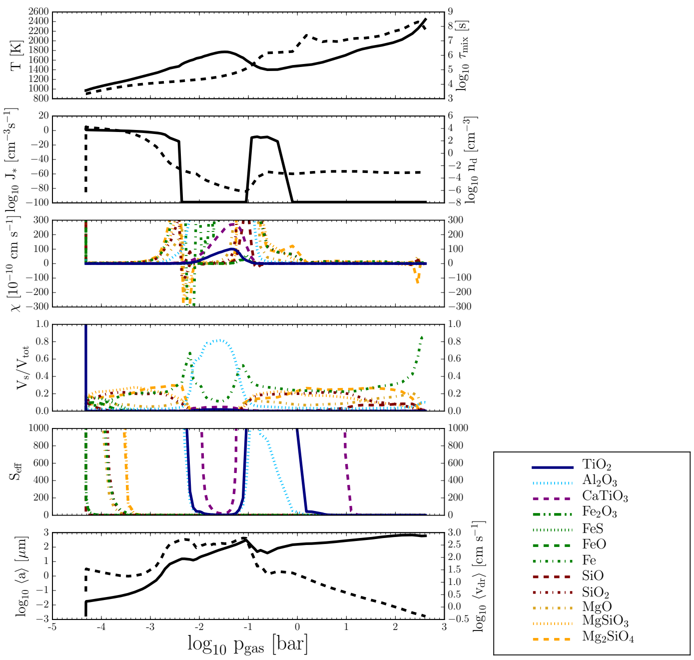

Fig. 5. HD 189733b's calculated cloud structure at the sub-stellar point (θ = 0°, ϕ = 0°). *Left: 1st panel*: local gas temperature $T_{\rm gas}$ [K] (solid, *left*) and mixing timescale $\tau_{\rm mix}$ [s] (dashed, *right*). *2nd panel*: nucleation rate J_* [cm^{-3}s^{-1}] (solid, *left*) and dust number density $n_{\rm d}$ [cm^{-3}] (dashed, *right*). *3rd panel*: growth velocity of material s χ [cm s^{-1}]. *4th panel*: volume fraction $V_s/V_{\rm tot}$ of solid s. *5th panel*: effective supersaturation ratio $S_{\rm eff}$ of individual solids. *6th panel*: cloud particle mean radius $\langle a\rangle$ [μm] (solid, *left*) and mean drift velocity $\langle v_{\rm dr}\rangle$ [cm s^{-1}] (dashed, *right*). *Right*: key showing line-style and colour of our considered dust species.

(J_* [cm^{-3} s^{-1}] - nucleation rate) occurring at the upper pressure boundary of ~10^{-4} bar. After the first surface growth processes occur on the seed particles, the cloud particles then gravitationally settle into the atmospheric regions below (towards higher density/pressure). Primary nucleation is efficient down to ~$10^{-2.5}$ bar where it drops off significantly, indicating that the local temperature is too high for further nucleation and that the seed forming species has been substantially depleted. The gas-grain surface chemical reactions that form the grain mantle (Eq. (2)) increase in rate as the cloud particles fall inward. This is due to the cloud particles encountering increasing local gas density, and therefore more condensible material is available to react with cloud particles. This surface growth becomes more efficient from ~10^{-3}...~10^{-2} bar until the local temperature is so hot that the materials become thermally unstable and evaporate. The evaporation region results in a half magnitude decrease of the cloud particle sizes (negative χ) in the center region of the cloud. The relative volume fractions of the solid "s", $V_s/V_{\rm tot}$, represents the material composition of the cloud particles. The cloud particle composition is dominated by silicates and oxides such as $MgSiO_3$[s](~27%), Mg_2SiO_4[s](~20%), SiO_2[s](~21%) at the upper regions $\lesssim 10^{-2.5}$ bar. Fe[s] contributes $\lesssim$20% to the volume of the cloud particle in this region. The other 8 growth species (TiO_2[s](~0.03%), Al_2O_3[s](~2%),

Table 3. Volume fraction $V_s/V_{tot}[\%]$ for the 12 solid species included in kinetic the cloud model.

Pressure [bar]	10^{-4}	10^{-3}	10^{-2}	10^{-1}	1	10	Cloud base
$\langle a \rangle$ [μm]	0.025	0.23	19.9	307	146	275	605
	0.018	0.035	0.15	12.3	174	338	1088
Solid species							
TiO_2[s]	0.03	0.03	1.22	0.26	0.05	0.02	0.22
	0.06	0.04	0.03	0.03	0.02	0.01	0.24
Al_2O_3[s]	2.11	2.43	60.98	13.99	3.68	2.84	10.03
	2.06	2.06	2.13	2.42	2.44	2.49	10.03
$CaTiO_3$[s]	0.13	0.16	3.56	0.87	0.24	0.22	0.64
	0.07	0.10	0.14	0.17	0.17	0.20	0.77
Fe_2O_3[s]	0.10	>0.01	>0.01	>0.01	>0.01	>0.01	>0.01
	9.69	9.68	0.07	>0.01	>0.01	>0.01	>0.01
FeS[s]	14.44	0.22	0.03	0.09	0.05	0.02	0.03
	12.12	12.12	14.45	0.10	0.05	0.02	0.03
FeO[s]	8.87	0.06	0.03	0.07	0.02	0.02	0.09
	7.63	7.63	7.93	0.03	0.02	0.02	0.09
Fe[s]	7.87	21.08	30.93	45.00	24.29	22.49	87.15
	4.52	4.52	8.50	21.14	21.29	21.75	86.80
SiO[s]	2.42	0.06	0.08	0.70	0.48	3.82	0.92
	8.84	9.03	1.12	0.11	0.44	5.20	0.99
SiO_2[s]	17.90	20.08	0.75	7.88	19.94	20.60	0.12
	9.92	10.13	19.35	21.26	22.18	20.33	0.13
MgO[s]	7.73	5.13	1.97	11.10	8.05	8.87	0.79
	7.21	7.28	7.61	5.40	6.51	9.35	0.89
$MgSiO_3$[s]	22.47	24.11	0.14	8.96	20.77	15.79	>0.01
	21.74	20.71	22.41	22.02	21.82	15.25	>0.01
Mg_2SiO_4[s]	15.93	26.64	0.30	11.09	21.41	25.31	0.02
	16.15	16.70	16.23	27.31	26.59	25.39	0.04

Notes. The *first row* of each species corresponds to the sub-stellar trajectory ($\phi = 0°$, $\theta = 0°$) cloud structure. The *second row* corresponds to the nightside trajectory $\phi = 180°$, $\theta = 0°$ cloud structure. Note: the pressure at the cloud base is different for the two profiles.

$CaTiO_3$[s](~0.15%), Fe_2O_3[s](~0.001%), FeS[s](~1.6%), FeO[s](~0.35%), SiO[s](~0.05%), MgO[s](~7%)) constitute the remaining grain volume. An evaporation region at $\sim 10^{-2.5}$ bar before the temperature maximum at $\sim 10^{-1.5}$ bar alters the grain composition dramatically. Al_2O_3[s] and Fe[s] dominate the grain composition in this region as the less stable silicates and oxides have evaporated from the grain surface. At the temperature maximum the grain is composed of Al_2O_3[s](~80%) and Fe[s](~15%). This suggests the presence of a cloud section more transparent than surrounding layers (Fig. 12). We address the issue of transparency in Sect. 5. Deeper in the atmosphere, a temperature inversion occurs (Fig. 2) starting from $\sim 10^{-1.5}$ bar. The temperature drops by ~400 K from $\sim 10^{-1.5} \ldots \sim 10^{-0.5}$ bar. This temperature decrease allows a secondary nucleation region from $\sim 10^{-1} \ldots 1$ bar. The number density of grains jumps by ~2 orders of magnitude at the secondary nucleation region, as a result of formation of many new cloud particles. This causes a dip in the mean grain size at $\sim 10^{-1}$ bar. Such secondary nucleation has not been seen in our cloud model results in brown dwarf nor non-irradiated giant gas planet atmospheres. Silicates and oxides are now thermally stable and once again form the grain mantle. The grain composition is approximately a 70-20-10% mix of silicates and oxides, iron and other material respectively in this region, similar to the composition before the temperature maximum. At the cloud base, Fe[s] dominates the composition (~35%) with MgO[s] and Mg_2SiO_4[s] making up ~16% and ~23% respectively. Table 3 shows the percentage volume fraction V_s/V_{tot} of the 12 dust species at the sub-stellar point and the $\phi = 180°$, $\theta = 0°$ trajectory at 10^{-4}, 10^{-3}, 10^{-2}, 10^{-1}, 1 and 10 bar.

Our results show that the entire vertical atmospheric range considered here ($\sim 10^{-4.5} \ldots 10^{3}$ bar) is filled with dust. The exact properties of this dust such as size, composition and number density change depending on the local thermodynamical state. The 3D RHD model does not expand to such low pressures and densities that the cloud formation processes becomes inefficient (Sect. 5). This suggests that clouds can be present at a higher and lower pressure than the present 3D RHD model boundary conditions allow.

3.2. Cloud structure changes with longitude (east-west)

One of the main features of the RHD simulation is the equatorial jet structure which transports heat over the entire 360° longitude. The presence of this jet changes the thermodynamic structure of the atmosphere which affects the resulting global cloud structure. We sampled the 3D RHD results in longitude steps of $\Delta\phi = +45°$ at the equatorial region $\theta = 0°$ to investigate if cloud properties change significantly from dayside to nightside. Figure 2 shows that the nightside (T_{gas}, p_{gas}) profiles can be ~200 K cooler than the dayside in the upper atmospheric regions ($\sim 10^{-4.5} \ldots 10^{-1}$ bar). Figure 6 shows the nucleation rate J_* [$cm^{-3}\,s^{-1}$] for dayside (solid lines), day-night terminator (dotted lines) and nightside (dashed lines) sample trajectories. The dayside nucleation rates fall off quicker with atmospheric depth compared to the terminator and nightside profiles, particularly relevant for interpreting transit spectra. At longitude $\phi = 315°$ a secondary nucleation region emerges, similar to the sub-stellar point structure (Fig. 5). The terminator and nightside nucleation regions extend further into the atmosphere to $\sim 10^{-1}$ bar. As a consequence of the different nucleation rates between dayside

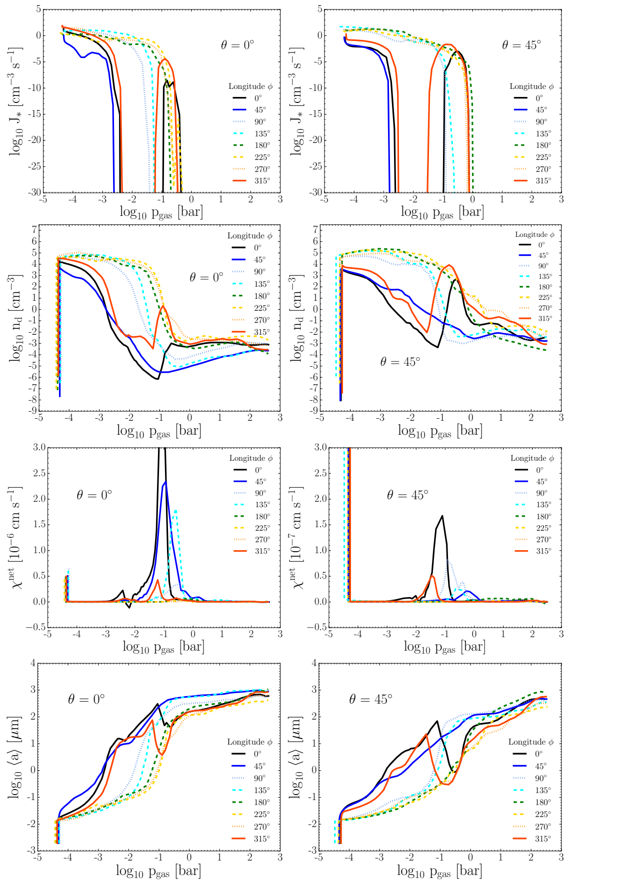

Fig. 6. Dust properties as a function of gas pressure for $\Delta\phi = +45°$ longitude intervals for latitudes $\theta = 0°$ (*left column*) and 45° (*right column*): *top row:* nucleation rate J_* [$cm^{-3}\,s^{-1}$]. *Second row*: dust number density n_d [cm^{-3}]. *Third row*: net dust growth velocity χ^{net} [$cm\,s^{-1}$]. *Bottom row*: mean grain size $\langle a \rangle$ [μm]. Solid, dotted and dashed lines indicate dayside, day-night terminator and nightside profiles respectively.

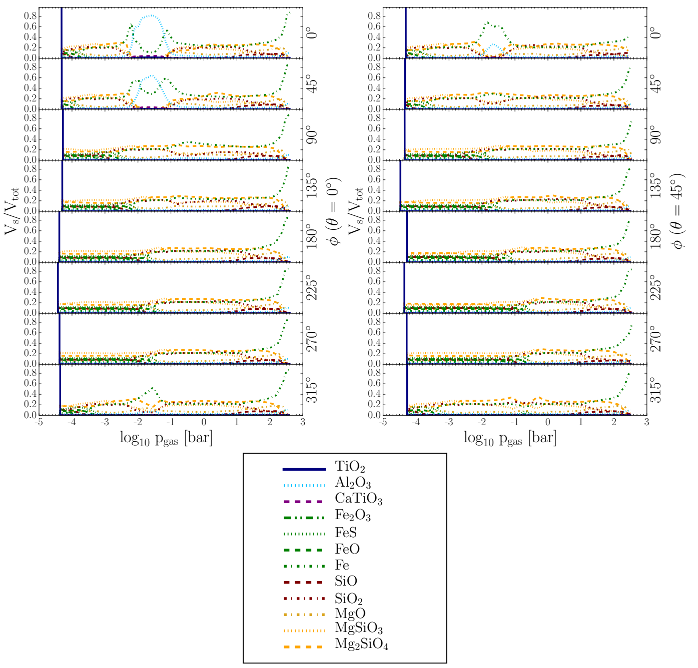

Fig. 7. *Top:* dust composition volume fraction V_s/V_{tot} as a function of pressure at $\theta = 0°$ (*Left*) and $\theta = 45°$ (*Right*) in $\Delta\phi = +45°$ longitude intervals. Grain composition is generally dominated by silicate-oxides including $MgSiO_3$[s] apart from localised regions such as $10^{-2} \ldots 10^{-1}$ bar at $\phi = 0°, 45°$, $\theta = 0°$. Fe[s] dominates at $10^{-2} \ldots 10^{-1}$ bar at $\phi = 0°$, $\theta = 45°$. Fe[s] grains remain at the cloud base as the most thermally stable element. *Bottom*: key showing line-style and colour of our considered dust species.

and nightside, the number density of cloud particles n_d [cm^{-3}] is greater on the nightside down to pressures of $\sim 10^{-1}$ bar. At this pressure, the secondary nucleation regions on the dayside, $\phi = 0°, 315°$ profiles spike up the number density comparable to values on the nightside. From Fig. 6 the net growth velocity χ^{net} [$cm\,s^{-1}$] shows that the most efficient growth regions for the grains is approximately $10^{-3} \ldots 1$ bar for the dayside and $10^{-2} \ldots 1$ bar for the nightside. Although the temperature of the local gas phase plays a role in increasing the growth rate, it is the increasing local density of material (as the particle falls thought the atmosphere) that is the dominating factor in determining growth rates (Eq. (2); Fig. 8). Consequently, the mean grain size $\langle a \rangle$ [μm] shows a stronger increase from $\sim 10^{-4} \ldots 10^{-1}$ bar on the dayside than the nightside. The mean grain size dips at $\sim 10^{-1}$ bar for longitudes $\phi = 0°$ and 315° due to the increase of grain number density as now the same number of gaseous growth species have to be distributed over a larger surface area. Figure 7 shows the volume fraction V_s/V_{tot} of the solid species "*s*". The dust composition is generally dominated by silicates and oxides (~60%) such as $MgSiO_3$[s], Mg_2SiO_4[s] and SiO_2[s] with (~20%) Fe[s] and FeO[s] content. At the cloud base the grain is primarily composed of Fe[s] (~85%) and Al_2O_3[s] (~10%). The $\phi = 45°$, $\theta = 0°$ cloud structure contains an Al_2O_3[s] (~60%) and Fe[s] (~30%) dominant region from $\sim 10^{-2} \ldots 10^{-1}$ bar similar to the sub-stellar point structure. Table 3 summarises the percentage volume fraction V_s/V_{tot} and the mean cloud particle

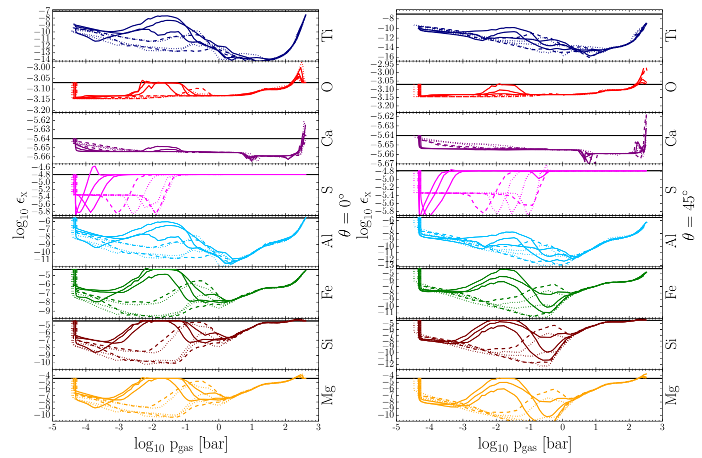

Fig. 8. Gas phase element abundances ϵ_x as a function of pressure at $\theta = 0°$ (*Left*) and $\theta = 45°$ (*Right*) in $\Delta\phi = +45°$ longitude intervals. We consider 8 elements: Mg (orange), Si (maroon), Ti (blue), O (red), Fe (green), Al (cyan), Ca (purple), S (magenta) that constitute the growth species. Horizontal black lines indicate solar abundance ϵ_x^0. A decrease in element abundance indicates condensation of growth species onto cloud particle surface. An increase indicates evaporation of molecules constituted of that element from the cloud particle surface. Dayside profiles (solid) are $\phi = 0°, 45°, 315°$, $\theta = 0°, 45°$. Day-night terminator profiles (dashed) are $\phi = 90°, 270°$, $\theta = 0°, 45°$. Nightside profiles (dotted) are $\phi = 135°, 180°, 225°$, $\theta = 0°, 45°$.

size $\langle a \rangle$ of the 12 dust species at the sub-stellar point and the $\phi = 180°$, $\theta = 0°$ trajectory at 10^{-4}, 10^{-3}, 10^{-2}, 10^{-1}, 1 and 10 bar pressures.

3.3. Cloud structure changes with latitude (north-south)

At higher latitudes $\theta \gtrsim 40°$ the 3D RHD model produces a jet structure flowing in the opposite direction to the equatorial jet at dayside longitudes (Tsai et al. 2014). This significantly alters the (T_{gas}, p_{gas}) and vertical velocity profiles (Fig. 2). These latitudes also contain the coldest regions of the nightside where vortexes easily form and dominate the atmosphere dynamics (Dobbs-Dixon & Agol 2013, Fig. 1). To investigate the cloud structure at these latitudes we repeated our trajectory sampling for latitudes of $\theta = 45°$ in longitude steps of $\Delta\phi = +45°$. Figure 6 shows the nucleation rate J_* [$cm^{-3}\,s^{-1}$] for dayside (solid lines), day-night terminator (dotted lines) and nightside (dashed lines) sample trajectories. The profiles are similar to the equatorial $\theta = 0°$ regions with double nucleation peaks at $\phi = 0°$ and 315°. Again, there is an increase in number density n_d [cm^{-3}] (Fig. 6) from $10^{-1} \ldots 1$ bar due to second nucleation regions at $\phi = 0°$ and 315°. The growth velocity χ^{net} is generally an order of magnitude lower on the dayside than the equatorial regions. This results in higher latitude clouds containing smaller grain sizes compared to their equatorial counterparts.

3.4. Element depletion, C/O ratio and dust-to-gas ratio

The cloud formation process strongly depletes the local gas phase of elements, primarily through extremely efficient solid surface growth processes. We consider the 8 elements that constitute the solid materials of the cloud particles, Mg, Si, Ti, O, Fe, Al, Ca and S assuming an initial solar element abundance (ϵ_x^0) for all layers. Figure 8 shows the elemental abundance ϵ_x (ratio to Hydrogen abundance) of each element as a function of pressure at each of the sample trajectories. Depletion occurs due to the formation of solids made of the these element onto the cloud particle surface and by nucleation of new cloud particles. Increase in element abundances correspond to regions of solid material evaporation. Ti is depleted at the upper boundary due to immediate efficient nucleation. For dayside profiles $\phi = 0°$, 45°, 315°, $\theta = 0°, 45°$, from $10^{-4.5} \ldots 10^{-3}$ bar, Mg, Ti, Si, Al and Fe are depleted by ~1 order of magnitude while O, S and Ca are depleted by ~10%. These profiles return to initial solar abundance values at $\sim 10^{-2}$ bar where the solid material from the grain surface evaporates, returning elements to the gas phase. O, Fe, Si S and Mg abundance can slightly overshoot solar abundance values at their respective maximums. Elements are most heavily depleted in these profiles at $\sim 10^{-1}$ bar where the most efficient surface growth occurs. Mg, Si, and Fe are depleted by ~3 orders of magnitude, Ti by 8 orders of magnitude and Al by 5 orders of magnitude. O, S and Ca are again depleted by ~10%. Fe, Al, S

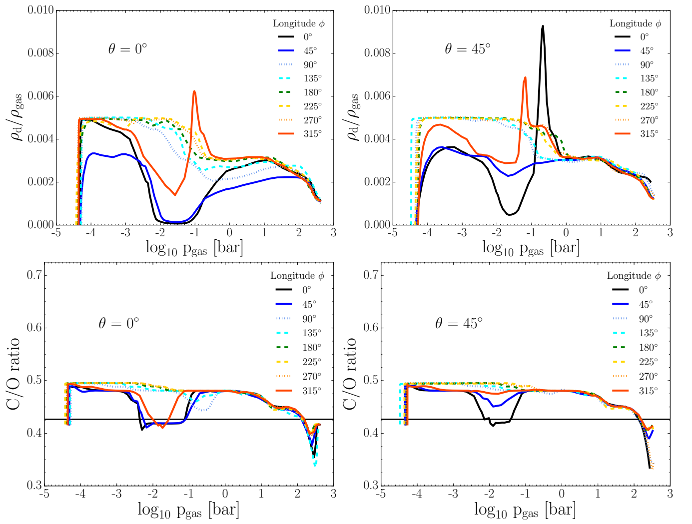

Fig. 9. Gas properties as a function of gas pressure for $\Delta\phi = +45°$ longitude intervals from the cloud formation process. *Top row*: dust-to-gas ratio ρ_d/ρ_{gas} at latitudes $\theta = 0°$ and 45°. *Bottom row*: C/O ratio at latitudes $\theta = 0°$ and 45°. Solid, dotted and dashed lines indicate dayside, day-night terminator and nightside profiles respectively. The horizontal black line indicates solar C/O ratio. Regions of decreasing ρ_d/ρ_{gas} and C/O indicate cloud particle evaporation.

and Ti return to solar abundance or slightly sub-solar abundance at the cloud base, where all materials have evaporated. The cloud base is enriched in O, Ca, Mg and Si which are ~50% above solar abundance values. For nightside and day-night terminator profiles ϕ = 90°, 135°, 180°, 225°, 270° θ = 0°, 45°, from $10^{-4.5}\ldots10^{-2}$ bar, Mg, Ti, Si, Al and Fe are depleted by 4 to 8 orders of magnitude while O and S are depleted by ~1 order of magnitude and Ca by ~10%. The ϕ = 90° and 135°, θ = 0°, 45° show a return to near initial abundance at $\sim10^{-0.5}$ bar from material evaporation. Other nightside/terminator profiles gradually return to initial abundance from ~1 bar to their respective cloud bases. Again, O, Ca, Mg and Si are slightly above solar abundance at the cloud base.

We calculate the dust-to-gas ratio and the C/O ratio of our cloud structures. Figure 9 shows the local dust-to-gas ratio of the sample trajectories at latitudes θ = 0° and 45° respectively. Dayside profiles show increases and decreases in dust-to-gas ratio corresponding to regions of nucleation/growth and evaporation. Nightside profiles show less cloud particle evaporation throughout the upper atmosphere, with only small changes in the dust-to-gas ratio which starts to drop off from $\sim10^{-2}$ bar. Figure 9 shows the local gaseous C/O ratio of our sample trajectories at latitudes θ = 0° and 45° respectively. These follow similar trends to the dust-to-gas ratio. The C/O ratio lowers where evaporation of cloud particles releases their oxygen bearing materials, replenishing the local gas phase, The abundance of C is kept constant at $\epsilon_C^0 = 10^{-3.45}$ (solar abundance) and is not affected by the formation of cloud particles in our model. Dayside equatorial profiles show C/O ratio dips by ~5% below solar values at pressures of $10^{-2.5}\ldots10^{-1}$ bar. The ϕ = 0°, θ = 45° profile also shows a dip below solar values at similar pressure levels. Apart from these localised regions of oxygen replenishment, the C/O ratio remains above solar values for the majority of the atmospheric profiles; except from the cloud base, which is enriched with oxygen by 10%–20% for all profiles.

3.5. Cloud property maps of HD 189733b

Global cloud property maps of the atmosphere of HD 189733b enable the comparison between different atmospheric regions as a whole. This has implications for interpreting cloudy observations which sample different atmospheric regions. To produce a global cloud map of the atmosphere of HD 189733b we bi-cubically interpolate our cloud structure results across

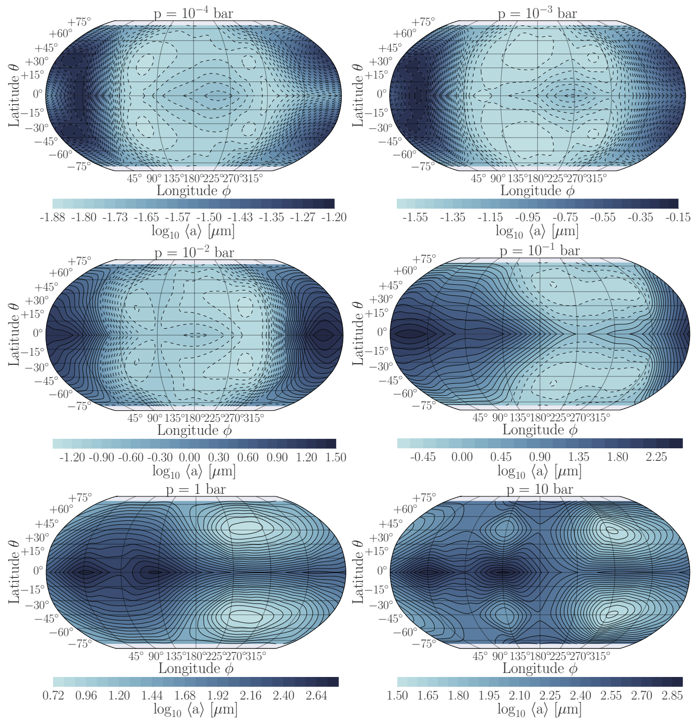

Fig. 10. Mean grain radius $\langle a\rangle$ [μm] interpolated across the globe (assuming latitudinal (north-south) symmetry) of HD 189733b. *Top row*: 10^{-4} bar, 10^{-3} bar. *Middle row*: 10^{-2} bar, 10^{-1} bar. *Bottom row*: 1 bar, 10 bar, respectively. The sub-stellar point is at $\phi = 0°$, $\theta = 0°$. The largest mean grain radii of cloud particles are generally found on the dayside at all pressure levels. Consequently, cloud particles on the dayside are larger than their pressure level counterparts on the nightside. Note: each plot contains a different colour scale.

longitudes $\phi = 0°\ldots360°$ and latitudes $\theta = 0°\ldots80°$. We include sample trajectories at latitude θ = 80° to interpolate to higher latitudes. We assume latitudinal (north-south) symmetry as thermodynamic conditions do not vary significantly from positive to negative latitudes (Dobbs-Dixon & Agol 2013). Figures 10 and 11 show maps of the mean grain radius $\langle a\rangle$ [μm] and grain number density n_d [cm^{-3}] at 10^{-4} bar, 10^{-3}, 10^{-2}, 10^{-1} bar, 1 bar and 10 bar. The mean grain radius and number density (along with material composition) are key values in calculating the wavelength dependent opacity of the clouds. At all pressures there is a contrast between the dayside and nightside mean grain radii. In the upper atmosphere (<10^{-1} bar) the globally largest cloud particles occur on the dayside face. In the deeper atmosphere (>10^{-1} bar) global maximum of the cloud particle size may also occur in nightside regions. The difference between the largest and smallest grain radii at each pressure can range from 1 to 2 orders of magnitude. The highest difference in cloud particle sizes occurs at 10^{-2} bar where grains on the

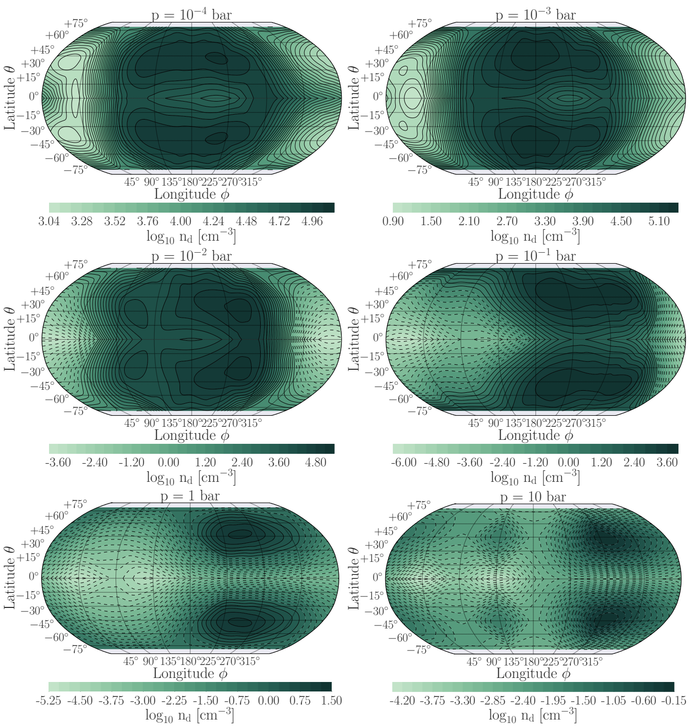

Fig. 11. Number density of cloud particles n_d [cm^{-3}] interpolated across the globe (assuming latitudinal (north-south) symmetry) of HD 189733b. *Top row*: 10^{-4} bar, 10^{-3} bar. *Middle row*: 10^{-2} bar, 10^{-1} bar. *Bottom row*: 1 bar, 10 bar, respectively. The sub-stellar point is at $\phi = 0°$, $\theta = 0°$. The maximum number of cloud particles occurs on the nightside of the planet. Note: each plot contains a different colour scale.

dayside are 2 orders of magnitude bigger than the nightside. This is due to dayside profiles undergoing very efficient cloud particle surface growth at $\sim10^{-2}$ bar, while nightside cloud particles do not grow as efficiently (Fig. 6). There are also steep gradients between the maximum and minimum mean grain radius (indicating very rapid cloud formation processes) which occur at the terminator regions (ϕ = 90°, 270°) at pressure profiles $\lesssim10^{-1}$ bar. The number density maps show similar differences between dayside and nightside profiles but with maximum values of number density generally occurring on the nightside of the planet at each pressure level. Steep gradients in number density are also present at the terminator regions. These results, taken as a whole, suggest that the wavelength dependent dust opacity significantly varies between the dayside and nightside. The mixed local composition of the cloud particles will also have an effect on the dust opacity.

4. Cloud opacities

We calculated the scattering and absorption properties of our cloud particles and produce global cloud opacity maps of the

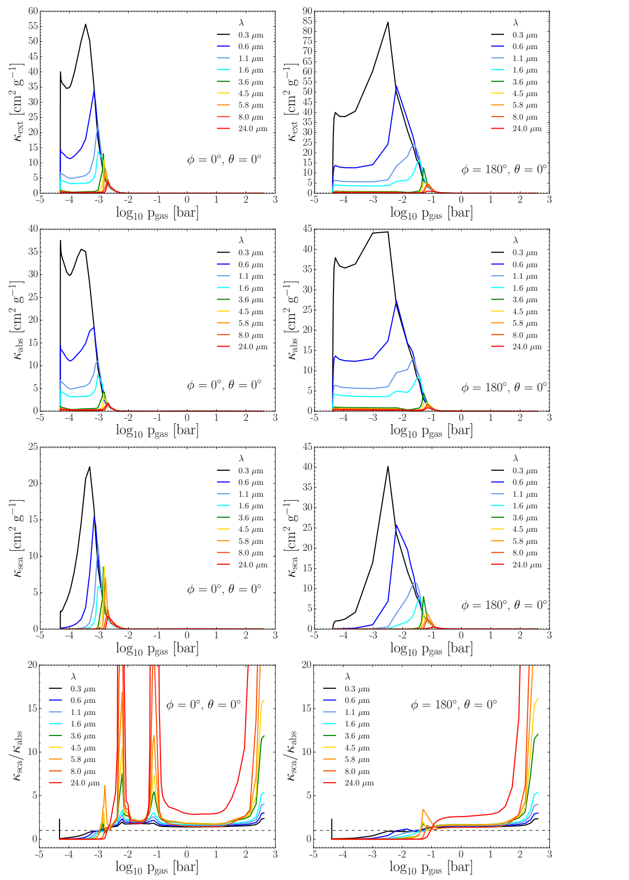

Fig. 12. Dust opacities κ [$cm^2\ g^{-1}$] for the cloud structure at $\phi = 0°, 180°$, $\theta = 0°$ as a function of pressure. *Top row*: total extinction κ_{ext}. *Second row:* absorption κ_{abs}. *Third row:* scattering κ_{sca}. *Bottom row:* scattering to absorption ratio $\kappa_{sca}/\kappa_{abs}$. Bluer wavelengths are absorbed/scattered more efficiently than redder wavelengths in the upper atmosphere. The absorption dominates the total extinction in the upper regions and scattering in the deeper atmosphere. The spikes in scattering ratio at 10^{-2} and 10^{-1} bar correspond to Fe rich grain composition.

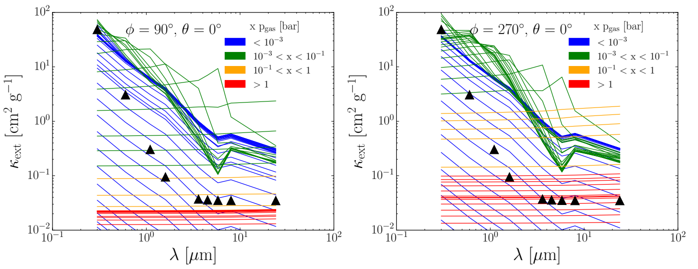

Fig. 13. Dust extinction κ_{ext} [cm^2 g^{-1}] pressure isobars at $\phi = 90°$ (*left*), 270° (*right*), $\theta = 0°$ (equatorial dayside-nightside terminator regions). Triangles denote the values from Dobbs-Dixon & Agol (2013) assumed additional Rayleigh slope opacity $\kappa_{ext} \propto \lambda^{-4}$. Isobars follow an absorption profile $\kappa_{ext} \propto \lambda^{-2}$ at the upper atmosphere $\lesssim 10^{-1}$ bar. Isobars flatten deeper than $\gtrsim 10^{-1}$ bar.

HD 189733b atmosphere. For an illustration of the results, we present cloud opacity calculations at longitude $\phi = 0°$ and 180° at the equatorial region $\theta = 0°$. Figure 12 demonstrates that the efficiency of light extinction depends on wavelength. Bluer light is more heavily scattered/absorbed in the upper atmosphere compared to the infrared. For the $\phi = 0°$ trajectory the region of highest extinction extends from $\sim 10^{-4} \ldots 10^{-2}$ bar. The $\phi = 180°$ trajectory extends from $\sim 10^{-4} \ldots 1$ bar. The fraction of scattering to absorption is shown in Fig. 12. Absorption of the stellar light is the most efficient extinction mechanism in the upper atmosphere ($\sim 10^{-3}$ bar) while scattering dominates the extinction in the deeper atmosphere $\gtrsim 10^{-2.5}$ bar. There is a large increase in the scattering component corresponding to the Fe[s] rich ($\sim$50%) grain regions at 10^{-2} and 10^{-1} bar in the $\phi = 0°$, $\theta = 0°$ trajectory. Between these Fe[s] regions a $\sim$80% Al_2O_3[s] grain composition region occurs which is more transparent in our wavelength range than the Fe[s] surrounding regions. For a discussion of these results, we refer to Sect. 5. From the upper atmosphere down to $\sim 10^{-3}$ bar the extinction profile follows an absorption profile of $\kappa_{ext} \propto \lambda^{-2}$. A transition region from $\sim 10^{-2}$ to 10^{-1} bar occurs where profiles gradually flatten from optical to infrared wavelengths. This is due to the wavelength dependent extinction efficiency of cloud particles with blue light more absorbed/scattered by small, upper atmosphere grains and red light by larger, deeper atmosphere grains. In addition, the grain composition fraction of highly opaque solid species such as Fe[s] increases from $\sim$10% to $\sim$20% deeper in the atmosphere ($> 10^{-1.5}$ bar).

A wavelength dependent "cloud opacity" global map can be produced by interpolation assuming latitudinal (north-south) symmetry of the cloud properties sample trajectories. We choose the 0.6 μm and 5.8 μm wavelengths as representative of optical and infrared wavelength extinction respectively. Figures 14 and 15 show the bi-cubic interpolated cloud particle extinction efficiency at 0.6 μm and 5.8 μm wavelengths across the globe from $10^{-4} \ldots 10$ bar. The optical 0.6 μm cloud map shows the maximum extinction regions migrate from dayside to nightside regions with increasing pressure. The 5.8 μm infrared cloud map shows the maximum extinction region also undergoes a shift, from nightside at 10^{-4} bar, to dayside at $10^{-3} \ldots 10^{-2}$ bar, to nightside for $< 10^{-1}$ bar. The most efficient extinction region deeper in the atmosphere ($10^{-1} \ldots 10$ bar) for both maps occurs at longitudes $\phi \sim 225° \ldots 315°$ which correspond to the coldest parts of the atmosphere (Fig. 2).

4.1. Reflection and sparkling of cloud particles

The visible appearance of our cloud particles can be estimated from their scattering properties. By estimating the relative fraction of scattered light in red, blue and green colour wavelengths, a rough RGB scale can be constructed to visualise a sparkling/reflection colour. We use the κ_{sca} results from Sect. 4 for cloud layers at upper regions in the atmosphere $\sim 10^{-4.5} \ldots 10^{-2}$ bar at the sub-stellar point $\phi = 0°$, $\theta = 0°$. This profile was used as being best comparable to observations from secondary transit (occultation) observations in which the albedo (or colour) of the atmosphere can be determined (Evans et al. 2013). We linearly interpolated the κ_{sca} to proxy RGB wavelengths and calculated their relative red, blue and green scattering fractions. This results in a deep midnight blue colour. Deeper in the atmosphere, $> 10^{-3}$ bar, cloud particles scatter red, blue and green light in more equal fractions which results in a redder and grayer cloud particle appearance. Helling & Rietmeijer (2009) suggest that amorphous cloud particles can re-arrange themselves into crystalline lattice structures as they gravitationally settle. This would allow light to refract and reflect inside the cloud particle volume producing a sparkle. The sparkling colour is likely to be a similar colour to the reflected light.

4.2. Reflectance of cloud particles

Cloud particles have a large effect on the observable properties by reflecting incident light on the atmosphere back into space. We estimate the reflectance of the cloud particles by calculating the pressure dependent single scattering albedo ω_0 (Bohren & Clothiaux 2006) of the cloud particles defined as

$$\omega_0 = \frac{\kappa_{sca}}{\kappa_{abs} + \kappa_{sca}}. \tag{19}$$

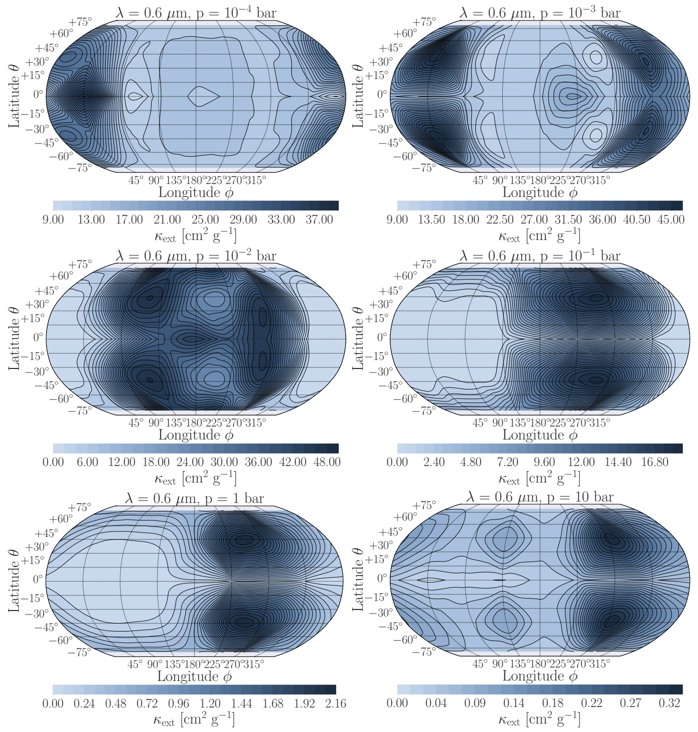

Fig. 14. Dust κ_{ext} [cm^2 g^{-1}] opacity for 0.6 μm interpolated across the globe of HD 189733b assuming latitudinal (north-south) symmetry. *Top row*: 10^{-4} bar, 10^{-3} bar. *Middle row*: 10^{-2} bar, 10^{-1} bar. *Bottom row:* 1 bar, 10 bar, respectively. We take 0.6 μm as representative of the optical wavelength extinction due to cloud. The sub-stellar point is at $\phi = 0°$, $\theta = 0°$. The maximum extinction efficiency shifts from the dayside of the planet to the nightside with increasing depth. Deep in the atmosphere the most opaque region remains at $\sim 225° \ldots 315°$longitudes. Note: the colour scale for each plot is different.

This ratio indicates where the cloud particles extinction is dominated by scattering ($\sim$1) or absorption ($\sim$0). Figure 16 shows maps of the calculated single scattering albedo for 8 μm at 10^{-1} bar and 1 bar. The maximum of the reflectance occurs in the approximate longitude range $0° \ldots 135°$ at the equatorial region. From these maps we expect the peak of the 8 μm albedo to occur from $20° \ldots 40°$ east of the sub-stellar point.

5. Discussion

Our results strongly support the idea that the *Hubble* and *Spitzer* observations of HD 189733b described in Lecavelier Des Etangs et al. (2008), Sing et al. (2011), Gibson et al. (2012) and Pont et al. (2013) can be plausibly explained by the presence of cloud particles in the atmosphere. The cloud composition is dominated

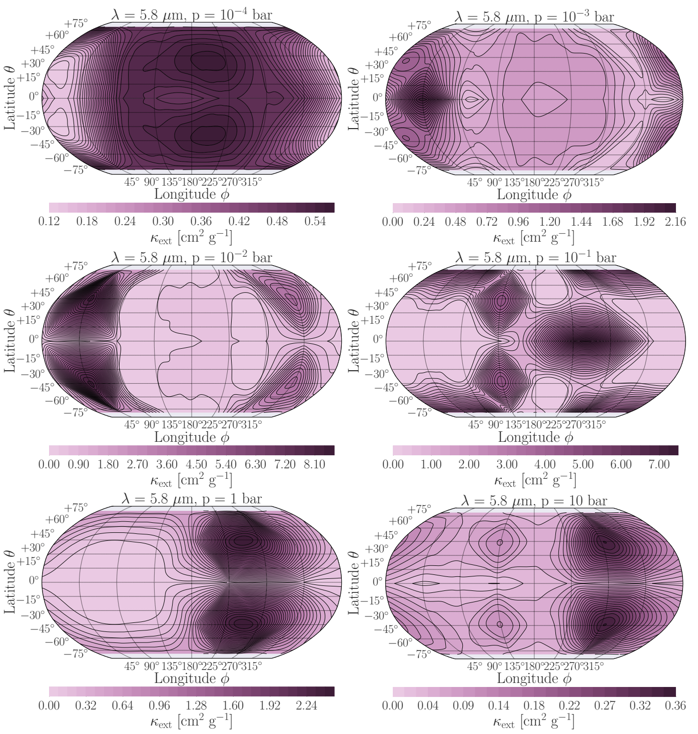

Fig. 15. Dust κ_{ext} [cm^2 g^{-1}] opacity for 5.8 μm interpolated across the globe of HD 189733b assuming latitudinal (north-south) symmetry. *Top row*: 10^{-4} bar, 10^{-3} bar. *Middle row*: 10^{-2} bar, 10^{-1} bar. *Bottom row*: 1 bar, 10 bar, respectively. We take 5.8 μm as representative of the infrared extinction due to cloud. The sub-stellar point is at $\phi = 0°$, $\theta = 0°$. The maximum extinction efficiency shifts from the dayside of the planet to the nightside with increasing depth. Deep in the atmosphere the most opaque region remains at $\sim 225° \ldots 315°$longitudes. Note: the colour scale for each plot is different.

by a silicate-oxide-iron mix (Fig. 7) which supports the suggestion of a $MgSiO_3$[s] dominated cloudy atmosphere by Lecavelier Des Etangs et al. (2008). They suggest a $MgSiO_3$[s] dominated grain composition with sizes $\sim 10^{-2} \ldots 10^{-1}$ μm at pressures of $10^{-6} \ldots 10^{-3}$ bar. Their grain size estimate is based on finding that Rayleigh scattering fits their observed feature-free slop in the optical spectral range. This analysis is consistent with our detailed model results which produce grains of $\sim$20% $MgSiO_3$[s] composition with sizes $\sim 10^{-2} \ldots 10^{-1}$ μm at $\sim 10^{-4.5} \ldots 10^{-3}$ bar, for all atmospheric profiles in this region. However, Fig. 13 shows that the isobars of the extinction κ_{ext} at the day-night terminator regions follow an absorption profile slope in the upper atmosphere which transitions into a flat profile deeper in the atmosphere. The absorption dominated profile from $10^{-4} \ldots 10^{-3}$ bar

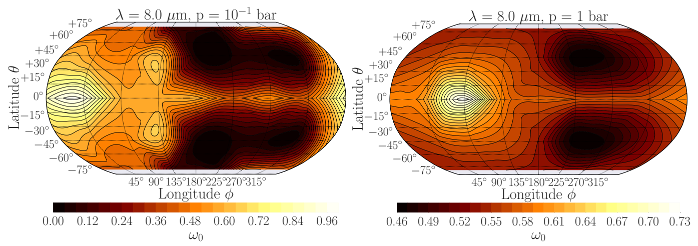

Fig. 16. Interpolated single scattering albedo ω_0 (Eq. (19)) at a wavelength of 8μm at 10^{-1} bar (*left*), 1 bar (*right*) for our cloud properties. The maximum of the reflectance occurs approximately from $\phi = 20° \ldots 135°$ longitude. These maximum reflectance regions are consistent with the 8 μm *Spitzer* flux maps of HD 189733b from Knutson et al. (2007). Note: the sub-stellar point in the diagrams is located at $\phi = 0°$, $\theta = 0°$, at the left side of the figures.

does not support the Rayleigh scattering parameterisations for the observations of HD 189733b. This does not rule out cloud particles as the source of the Rayleigh slope. A possibility is that many smaller grains form at lower pressure regions than the boundary applied. This would increase the scattering component of the cloud opacity. Furthermore, in a 3D atmosphere, small grains may be more easily lofted than larger grains in regions of upward gas flow. Our static 1D model does not include the 3D effects of a dynamic, changing atmosphere.

Section 3.4 shows the effect that cloud particles have on local element abundances. Depletion of elements occur when they are consumed by cloud particle formation and replenishment occurs when these cloud particles evaporate. In our cloud model the elements that constitute the main cloud particle composition were depleted by 3 orders of magnitude or more from $\sim 10^{-4.5} \ldots 10^{-2}$ bar. These results suggest that the presence of cloud particles would generally flatten the spectral signatures from these elements and associated molecules in the atmosphere. The evaporation of molecules from cloud particles transports elements from upper to lower atmospheric height. This suggests that elements thought to contribute to upper atmosphere thermal inversion layers such as Ti (more specifically TiO; Fortney et al. 2008; Spiegel et al. 2009; Showman et al. 2009) are transported to the deeper atmosphere by cloud particles. The depletion and movement of TiO from the upper to lower atmosphere could reduce the intensity of a stratospheric inversion and/or move it deeper into the atmosphere or destroy it completely. Figure 9 shows that regions of the atmosphere can be oxygen poor or rich depending on the cloud processes. This significantly alters the C/O ratio, where it is increased by the growth of oxygen baring solid materials onto cloud particle surfaces and decreased when these materials evaporate back into the gas phase. This could have an impact on interpreting observations of over/under abundant C/O ratios in exoplanet atmospheres as well as altering the local chemistry in oxygen depleted regions.

The opacity of the clouds will strongly influence the spectral signature from the atmosphere by absorbing or scattering various wavelengths at different efficiency. From Fig. 12 optical wavelengths are preferentially absorbed and scattered in the upper atmosphere. We therefore suggest that mineral clouds are responsible for the planets observed albedo and deep blue colour suggested by Berdyugina et al. (2011) and Evans et al. (2013). The migration of the maximum efficiency of the cloud extinction from dayside to nightside (Figs. 14, 15) at 0.6 μm and 5.8 μm shows a strong dayside-nightside opacity contrast. The terminator regions at longitude $\phi = 90°$ and 270° also show differences in dust extinction efficiency, especially deeper in the atmosphere. Different thermodynamic conditions result in mean grain sizes, compositions and opacity that is different at each terminator region. This has consequences for interpreting transmission spectroscopy measurements since observations of opposite limbs of the planet would have different extinction properties. In addition, the cloud maps also show steep gradients of cloud properties at the terminator regions. Transit spectroscopy observations that measure these regions would sample a variety of cloud particle number density, sizes and distributions dependent on wavelength. In Fig. 7 the profiles at $\phi = 0°$ and 45° show a region compositionally dominated by Al_2O_3[s] cloud particles from $\sim 10^{-2} \ldots 10^{-1}$ bar with Fe[s]-rich grains on above and below this region. The effect of this Al_2O_3[s] region is to produce a locally lower cloud opacity layer flanked by high opacity regions (Fig. 12). This would have a significant effect on radiation propagation through the atmosphere as the Fe[s] rich grains could shield photons reaching the Al_2O_3[s] layer from above or below.

Our qualitative calculation of the cloud contribution to the albedo provides yet another insight into the observational consequences of our cloud modelling. Our calculated single scattering albedo for the 8 μm band (Fig. 16) show that the maximum reflectance occurs approximately in the longitude range $0° \ldots 135°$ at the equator at 10^{-1} and 1 bar. With the peak occurring from $20° \ldots 40°$. These maximum reflectance regions reproduce the areas of maximum 8 μm flux map from Knutson et al. (2007). This suggests that cloud particles influence observed phase curves of hot Jupiters depending on the position and reflectivity of cloud particles in the atmosphere. These effects have been observed for hot Jupiter Kepler 7-b (Demory et al. 2013), where *Kepler* observations showed a westward shift in optical phase curves (GCM/RHD models predict an eastward shift). *Spitzer* phase curves showed that the shift was non-thermal in origin. This shift was attributed to non-uniform, longitude dependent optical scattering from clouds. Our 8 μm reflectance result, albeit qualitatively, show that clouds can contribute to the infrared flux

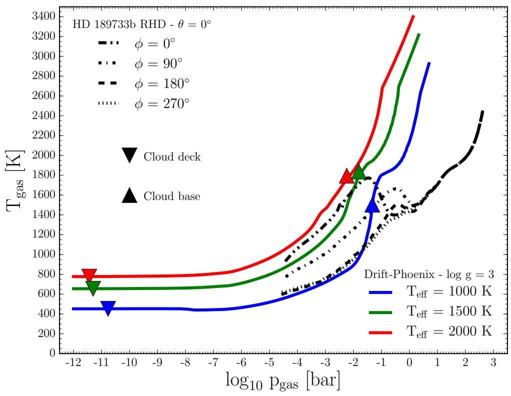

Fig. 17. (T_{gas}, p_{gas}) profiles for - atmosphere models (coloured, solid) for log g = 3, T_{eff} = 1000, 1500, 2000 K and the Dobbs-Dixon & Agol (2013) RHD model at $\phi = 0°, 90°, 180°, 270°, \theta = 0°$ (black, styled). Downward and upward facing triangles denote the cloud deck and base respectively. The - profiles show that cloud formation begins at $\sim 10^{-11}$ bar.

observed from the exoplanet atmosphere. It may not be simple to disentangle contributions by thermal emission and scattering/reflection clouds from infrared observational properties.

Figure 17 shows a (T_{gas}, p_{gas}) structure comparison between - (log g = 3, T_{eff} = 1000, 1500, 2000 K) and the Dobbs-Dixon & Agol (2013) 3D RHD model. Comparing trajectories from the 3D RHD model and the 1D Drift-Phoenix models suggests that clouds could be more extended into the lower-pressure regions than our present results show. Previous studies (e.g. - ; Witte et al. 2011; Woitke & Helling 2004) involving cloud formation, the lower pressure boundary can be up to $\sim 10^{-12}$ bar with cloud formation occurring from $\sim 10^{-11}$ bar, these studies contain a smoother non-cloud to cloudy upper atmospheric region than our present results. The cloud deck in the - models starts from $\sim 10^{-11}$ bar, 7 orders of magnitude lower that the RHD upper boundary pressure. Therefore, our results do not capture cloud formation outside the RHD model boundary conditions yet. We also suggest that cloud formation can continue further inward than the results presented here. Due to the increasing density and high pressure, cloud particle material remains thermally stable until considerably higher temperatures and survives deeper into the atmosphere.

We probed a 3D hot Jupiter atmospheric structure, irradiated by a host star, through selecting 16 1D atmospheres trajectories along the equator and latitude $\theta = 45°$. We aimed to capture the main features of a dynamic atmosphere like east-west jet streams, latitudinal differences and dayside-nightside differences. We used these thermodynamic and velocity profiles to study cloud formation in order to present consistently calculated cloud properties for HD 189733b. Our ansatz does not yet include a self-consistent feedback onto the (T_{gas}, p_{gas}, $\boldsymbol{v}_{gas}$) structure due to radiative transfer processes. We note that due to an additional wavelength dependent dust opacity term in the radiative transfer scheme of Dobbs-Dixon & Agol (2013), this feedback is already accounted for to a significant degree in the current (T_{gas}, p_{gas}) profiles. Furthermore, we do not include non-LTE kinetic gas-phase chemistry such as photochemistry. Departures from LTE have been detailed in non-equilibrium models of HD 189733b's atmosphere performed by Moses et al. (2011), Venot et al. (2012), Agúndez et al. (2014) using thermodynamic input from the Showman et al. (2009) global circulation model.

6. Conclusion and summary

We have presented the first spatially varying kinetic cloud simulation of the irradiated hot Jupiter exoplanet HD 189733b. We applied a 2-model approach with our cloud formation model using 1D thermodynamic input from a 3D RHD simulation of HD 189733b. Our results suggest that HD 189733b has a significant cloud component in the atmosphere, spanning a large pressure scale throughout the entire globe. Cloud particles remain thermally stable deep in the atmosphere up to ~10 bar pressures and reach ~mm sizes at the cloud base. We suggest that cloud particles form at a lower pressure boundary than considered here, and also survive to deeper depths. Cloud properties change significantly from dayside to nightside and from equator to mid latitudes with variations in grain size, number density and wavelength dependent opacity. The cloud property maps show that steep gradients between dayside and nightside cloud proprieties occur at dayside-nightside transition regions. These cloud property differences have implications on interpreting observations of HD 189733b, depending what region and depth of the planet

is probed. The single scattering albedo calculations showed that cloud particles could play a significant role in planetary phase curves. The reflectance of the clouds at 8 μm showed that a significant fraction of infrared flux could originate from scattering/reflecting cloud particles. Since the most reflective clouds in the infrared correspond to regions of highest temperature it may be difficult to distinguish between cloud reflections and thermal emission. The extinction properties of the cloud particles exhibit absorption signatures in the upper atmosphere ($\lesssim 10^{-2}$ bar) which flatten deeper in the atmosphere ($\gtrsim 10^{-1}$ bar). However, this does not rule out a cloud particle origin for the observations of Rayleigh scattering. The scattering properties also suggest that the cloud particles would sparkle/reflect a midnight blue colour over the optical wavelength regime.

Acknowledgements. G.L. and Ch.H. highlight the financial support of the European community under the FP7 ERC starting grant 257431. Our respective local computer support is highly acknowledged. We thank P. Woitke, C.R. Stark and P. Rimmer for helpful discussions and feedback. We thank L. Neary for insightful discussion on atmospheric mixing.

References

Agol, E., Cowan, N. B., Knutson, H. A., et al. 2010, ApJ, 721, 1861
Agúndez, M., Parmentier, V., Venot, O., Hersant, F., & Selsis, F. 2014, A&A, 564, A73
Anders, E., & Grevesse, N. 1989, Geochim. Cosmochim. Acta, 53, 197
Bailey, R. L., Helling, C., Hodosán, G., Bilger, C., & Stark, C. R. 2014, ApJ, 784, 43
Barman, T. S., Hauschildt, P. H., & Allard, F. 2001, ApJ, 556, 885
Berdyugina, S. V., Berdyugin, A. V., Fluri, D. M., & Piirola, V. 2011, ApJ, 728, L6
Bohren, C. F., & Clothiaux, E. E. 2006, Fundamentals of Atmospheric Radiation, eds. C. F. Bohren, & E. E. Clothiaux, 450
Bohren, C. F., & Huffman, D. R. 1983, Absorption and scattering of light by small particles (New York: Wiley)
Bruggeman, D. A. G. 1935, Annalen der Physik, 416, 636
Charbonneau, D., Knutson, H. A., Barman, T., et al. 2008, ApJ, 686, 1341
Danielski, C., Deroo, P., Waldmann, I. P., et al. 2014, ApJ, 785, 35
Dehn, M., Helling, C., Woitke, P., & Hauschildt, P. 2007, in IAU Symp., eds. F. Kupka, I. Roxburgh, & K. L. Chan, 239, 227
Demory, B.-O., de Wit, J., Lewis, N., et al. 2013, ApJ, 776, L25
Désert, J.-M., Sing, D., Vidal-Madjar, A., et al. 2011, A&A, 526, A12
Dobbs-Dixon, I., & Agol, E. 2013, MNRAS, 435, 3159
Dorschner, J., Begemann, B., Henning, T., Jaeger, C., & Mutschke, H. 1995, A&A, 300, 503
Evans, T. M., Pont, F., Sing, D. K., et al. 2013, ApJ, 772, L16
Fortney, J. J., Lodders, K., Marley, M. S., & Freedman, R. S. 2008, ApJ, 678, 1419
Fortney, J. J., Shabram, M., Showman, A. P., et al. 2010, ApJ, 709, 1396
Gail, H.-P., & Sedlmayr, E. 1986, A&A, 166, 225
Gibson, N. P., Aigrain, S., Pont, F., et al. 2012, MNRAS, 422, 753
Grillmair, C. J., Burrows, A., Charbonneau, D., et al. 2008, Nature, 456, 767
Hartogh, P., Medvedev, A. S., Kuroda, T., et al. 2005, J. Geophy. Res. (Planets), 110, 11008
Helling, C., & Fomins, A. 2013, Roy. Soc. London Philos. Trans. Ser. A, 371, 10581
Helling, C., & Rietmeijer, F. J. M. 2009, Inter. J. Astrobiol., 8, 3
Helling, C., & Woitke, P. 2006, A&A, 455, 325
Helling, C., Klein, R., Woitke, P., Nowak, U., & Sedlmayr, E. 2004, A&A, 423, 657
Helling, C., Dehn, M., Woitke, P., & Hauschildt, P. H. 2008a, ApJ, 677, L157
Helling, C., Woitke, P., & Thi, W.-F. 2008b, A&A, 485, 547
Helling, C., Jardine, M., & Mokler, F. 2011, ApJ, 737, 38
Henning, T., Begemann, B., Mutschke, H., & Dorschner, J. 1995, A&AS, 112, 143
Huitson, C. M., Sing, D. K., Vidal-Madjar, A., et al. 2012, MNRAS, 422, 2477
Jäger, C., Dorschner, J., Mutschke, H., Posch, T., & Henning, T. 2003, A&A, 408, 193
Jeong, K. S., Winters, J. M., Le Bertre, T., & Sedlmayr, E. 2003, A&A, 407, 191
Knutson, H. A., Charbonneau, D., Allen, L. E., et al. 2007, Nature, 447, 183
Knutson, H. A., Lewis, N., Fortney, J. J., et al. 2012, ApJ, 754, 22
Kreidberg, L., Bean, J. L., Désert, J.-M., et al. 2014, Nature, 505, 69
Lecavelier Des Etangs, A., Pont, F., Vidal-Madjar, A., & Sing, D. 2008, A&A, 481, L83
Lee, G., Helling, C., Giles, H., & Bromley, S. T. 2015, A&A, 575, A11
Ludwig, H.-G., Allard, F., & Hauschildt, P. H. 2002, A&A, 395, 99
McCullough, P. R., Crouzet, N., Deming, D., & Madhusudhan, N. 2014, ApJ, 791, 55
Mie, G. 1908, Ann. Phys., 330, 377
Moses, J. I., Visscher, C., Fortney, J. J., et al. 2011, ApJ, 737, 15
Palik, E. D. 1985, Handbook of optical constants of solids (New York: Academic Press)
Parmentier, V., Showman, A. P., & Lian, Y. 2013, A&A, 558, A91
Pont, F., Sing, D. K., Gibson, N. P., et al. 2013, MNRAS, 432, 2917
Posch, T., Kerschbaum, F., Fabian, D., et al. 2003, ApJS, 149, 437
Rimmer, P. B., & Helling, C. 2013, ApJ, 774, 108
Showman, A. P., & Polvani, L. M. 2011, ApJ, 738, 71
Showman, A. P., Fortney, J. J., Lian, Y., et al. 2009, ApJ, 699, 564
Sing, D. K., Pont, F., Aigrain, S., et al. 2011, MNRAS, 416, 1443
Spiegel, D. S., Silverio, K., & Burrows, A. 2009, ApJ, 699, 1487
Stark, C. R., Helling, C., Diver, D. A., & Rimmer, P. B. 2014, Int. J. Astrobiol., 13, 165
Swain, M. R., Vasisht, G., & Tinetti, G. 2008, Nature, 452, 329
Swain, M. R., Vasisht, G., Tinetti, G., et al. 2009, ApJ, 690, L114
Tinetti, G., Vidal-Madjar, A., Liang, M.-C., et al. 2007, Nature, 448, 169
Tsai, S.-M., Dobbs-Dixon, I., & Gu, P.-G. 2014, ApJ, 793, 141
Venot, O., Hébrard, E., Agúndez, M., et al. 2012, A&A, 546, A43
Wakeford, H. R., & Sing, D. K. 2015, A&A, 573, A122
Witte, S., Helling, C., & Hauschildt, P. H. 2009, A&A, 506, 1367
Witte, S., Helling, C., Barman, T., Heidrich, N., & Hauschildt, P. H. 2011, A&A, 529, A44
Woitke, P., & Helling, C. 2003, A&A, 399, 297
Woitke, P., & Helling, C. 2004, A&A, 414, 335
Zeidler, S., Posch, T., & Mutschke, H. 2013, A&A, 553, A81

A&A 578, A128 (2015)
DOI: 10.1051/0004-6361/201424600

Astronomy & Astrophysics

A census of variability in globular cluster M 68 (NGC 4590)*

N. Kains[1,2], A. Arellano Ferro[3], R. Figuera Jaimes[2,4], D. M. Bramich[5], J. Skottfelt[6,7], U. G. Jørgensen[6,7], Y. Tsapras[8,9]
and
R. A. Street[8], P. Browne[4], M. Dominik[4,**], K. Horne[4], M. Hundertmark[4], S. Ipatov[10], C. Snodgrass[11], I. A. Steele[12]
(The LCOGT/RoboNet consortium)
and
K. A. Alsubai[10], V. Bozza[13,14], S. Calchi Novati[13,15], S. Ciceri[16], G. D'Ago[13,14], P. Galianni[4], S.-H. Gu[17,18], K. Harpsøe[6,7], T. C. Hinse[19,6], D. Juncher[6,7], H. Korhonen[20,6,7], L. Mancini[16], A. Popovas[6,7], M. Rabus[21,16], S. Rahvar[22,23], J. Southworth[24], J. Surdej[25], C. Vilela[24], X.-B. Wang[17,18], and O. Wertz[25]
(The MiNDSTEp Consortium)

(Affiliations can be found after the references)

Received 14 July 2014 / Accepted 22 February 2015

ABSTRACT

Aims. We analyse 20 nights of CCD observations in the V and I bands of the globular cluster M 68 (NGC 4590) and use them to detect variable objects. We also obtained electron-multiplying CCD (EMCCD) observations for this cluster in order to explore its core with unprecedented spatial resolution from the ground.

Methods. We reduced our data using difference image analysis to achieve the best possible photometry in the crowded field of the cluster. In doing so, we show that when dealing with identical networked telescopes, a reference image from any telescope may be used to reduce data from any other telescope, which facilitates the analysis significantly. We then used our light curves to estimate the properties of the RR Lyrae (RRL) stars in M 68 through Fourier decomposition and empirical relations. The variable star properties then allowed us to derive the cluster's metallicity and distance.

Results. M 68 had 45 previously confirmed variables, including 42 RRL and 2 SX Phoenicis (SX Phe) stars. In this paper we determine new periods and search for new variables, especially in the core of the cluster where our method performs particularly well. We detect 4 additional SX Phe stars and confirm the variability of another star, bringing the total number of confirmed variable stars in this cluster to 50. We also used archival data stretching back to 1951 to derive period changes for some of the single-mode RRL stars, and analyse the significant number of double-mode RRL stars in M 68. Furthermore, we find evidence for double-mode pulsation in one of the SX Phe stars in this cluster. Using the different classes of variables, we derived values for the metallicity of the cluster of [Fe/H] = −2.07 ± 0.06 on the ZW scale, or −2.20 ± 0.10 on the UVES scale, and found true distance moduli μ_0 = 15.00 ± 0.11 mag (using RR0 stars), 15.00 ± 0.05 mag (using RR1 stars), 14.97 ± 0.11 mag (using SX Phe stars), and 15.00 ± 0.07 mag (using the M_V–[Fe/H] relation for RRL stars), corresponding to physical distances of 10.00 ± 0.49, 9.99 ± 0.21, 9.84 ± 0.50, and 10.00 ± 0.30 kpc, respectively. Thanks to the first use of difference image analysis on time-series observations of M 68, we are now confident that we have a complete census of the RRL stars in this cluster.

Key words. stars: variables: RR Lyrae – stars: variables: general – globular clusters: individual: M 68

1. Introduction

Globular clusters in the Milky Way are ideal environments to study the properties and evolution of old stellar populations, thanks to the relative homogeneity of the cluster contents. Over the past century, a sizeable observational effort was devoted to studying globular clusters, in particular their horizontal branch (HB) stars, including RR Lyrae (RRL) variables. Increasingly precise photometry has allowed for detailed study of pulsation properties of these stars, both from an observational point of view (e.g. Kains et al. 2012, 2013; Arellano Ferro et al. 2013a; Figuera Jaimes et al. 2013; Kunder et al. 2013a) and from a theoretical point of view using stellar evolution (e.g. Dotter et al. 2007) and pulsation models (e.g. Bono et al. 2003; Feuchtinger 1998). RRL and other types of variables can also be used to derive estimates of several properties for individual stars and for the cluster as a whole.

In this paper we analyse time-series observations of M 68 (NGC 4590, C1236-264 in the IAU nomenclature; $\alpha = 12^h39^m27.98^s, \delta = -26°44'38.6''$ at J2000.0), one of the most metal-poor globular clusters with [Fe/H] ∼ −2.2, at a distance of ∼10.3 kpc. This is a particularly interesting globular cluster, because there are hints that it might be undergoing core collapse, as well as showing signs of rotation (Lane et al. 2009). It has also been suggested that M 68 is one of a number of metal-poor clusters that were accreted into the Milky Way from a satellite galaxy, based chiefly on their co-planar alignment in the outer halo (Yoon & Lee 2002).

Metal-poor clusters are particularly important to our understanding of the origin of globular clusters in our Galaxy, since they are essential to explaining the Oosterhoff dichotomy. This phenomenon was postulated by Oosterhoff (1939), who noticed that globular clusters fell into two distinct groups, Oosterhoff types I and II, traced by the mean period of their RRL stars, and the relative numbers of RR0 to RR1 stars. Since then, many studies have confirmed the existence of the Oosterhoff dichotomy as a statistically significant phenomenon (e.g. Sollima et al. 2014, and references therein), with very few clusters falling within the "Oosterhoff gap" between the two groups.

Two metal-rich clusters are now generally thought to be part of a new Oosterhoff III type of clusters (e.g. Pritzl et al. 2001, 2002), and, interestingly, Catelan (2009) notes that globular clusters in satellite dwarf spheroidal (dSph) galaxies of the Milky Way have been observed to fall mostly within the Oosterhoff gap, which would seem to go against theories stating that the Galactic halo was formed from accretion of dwarf galaxies (e.g. Zinn 1993a,b). The strength of such arguments rests partly on our ability to obtain complete censuses of RRL stars in globular clusters. This has only really been achievable after difference image analysis (DIA) made it possible to obtain precise photometry even in the crowded cores of globular clusters (e.g. Alard 1999, 2000; Bramich 2008; Albrow et al. 2009; Bramich et al. 2013).

Here we use time-series photometry to detect known and new variable stars in M 68, which we then analyse to derive their properties and the properties of their host cluster. In particular, we were able to detect a number of SX Phoenicis (SX Phe) stars thanks to improvements in observational and reduction methods since the last comprehensive time-series studies of this cluster were published over 20 years ago (Walker 1994, hereafter W94; and Clement et al. 1993, hereafter C93). This is also the first study of this cluster making use of DIA, meaning that we can now be confident that all RRL stars in M 68 are known.

We also use electron-multiplying CCD (EMCCD) data to study the core of M 68 with unprecedented resolution from the ground. EMCCD observations, along with methods that make use of them, such as lucky imaging (LI), are becoming a powerful tool for obtaining images with a resolution close to the diffraction limit from the ground. We first demonstrated the power of EMCCD studies for globular cluster cores in a pilot study of NGC 6981 (Skottfelt et al. 2013), where we were able to detect two variables in the core of the cluster that were previously unknown owing to their proximity to a bright star.

In Sect. 2, we describe our observations and reduction of the images. In Sect. 3, we summarise previous studies of variability in this cluster and outline the methods we employed to recover known variables and to detect new ones. We also discuss period changes in several of the RRL stars in this cluster. We use Fourier decomposition in Sect. 4 to derive physical parameters for the RRL stars, using empirical relations from the literature. The double-mode pulsators in M 68 are discussed in Sect. 5, and we use individual RRL properties to estimate cluster parameters in Sect. 6. Finally, we summarise our findings in Sect. 7.

2. Observations and reductions

2.1. Observations

We obtained Bessell V- and I-band data with the LCOGT/RoboNet 1 m telescopes at the South African Astronomical Observatory (SAAO) in Sutherland, South Africa, and at Cerro Tololo, Chile. The telescopes and cameras are identical and can be treated as one instrument. The CCD cameras installed on the 1m telescopes are Kodak KAF-16803 models with 4096 × 4096 pixels and a pixel scale of 0.23″ per pixel, giving a 15.7 × 15.7 arcmin^2 field of view (FOV). The images were binned to 2048 × 2048 pixels, meaning that the effective pixel scale of our images is 0.47″ per pixel. The CCD observations spanned 74 days, with the first night on March 8 and the last night on May 20, 2013. These observations are summarised in Table 1.

Table 1. Numbers of images and exposure times for the V and I band observations of M 68.

Date	N_V	t_V(s)	N_I	t_I(s)
20130308	1	120	1	60
20130311	7	120	9	60
20130314	15	120	16	60
20130316	17	120	16	60
20130317	14	120	16	60
20130318	16	120	11	60
20130319	12	120	7	60
20130320	8	120	8	60
20130321	15	120	16	60
20130323	5	120	6	60
20130329	20	40	20	40
20130331	9	120	10	60
20130401	4	120	2	60
20130402	30	40–120	28	40–60
20130403	7	120	5	60
20130404	19	40-120	19	40-60
20130427	9	40	9	40
20130428	10	40	10	40
20130429	10	40	10	40
20130520	8	120	–	–
Total	236		219	

Notes. When varying exposure times were used, a range is given.

We also observed M 68 using the EMCCD camera mounted on the Danish 1.54m telescope at La Silla, Chile. The camera is an Andor Technology iXon+ model 897 EMCCD, with 512 × 512 16 μm pixels and a pixel scale of 0.09″ per pixel, giving a FOV of 45 × 45 arcsec^2. The small FOV means that only the core of M 68 was imaged in the EMCCD observations. The filter on the camera is approximately equivalent to the SDSS $i' + z'$ filters (Bessell 2005); more details on the filter are given in Skottfelt et al. (2013). Seventy-two good EMCCD observations were taken, spanning 2.5 months (May 1 to July 18, 2013), each observation consisting of a data cube containing 4800 0.1 s exposures; in general, one or two observations were taken on any one night.

2.2. Difference image analysis

2.2.1. CCD observations

We used the DIA software `DanDIA`[1] (Bramich et al. 2013; Bramich 2008) following the recipes devised in our previous publications of time-series globular cluster observations (Kains et al. 2012, 2013; Figuera Jaimes et al. 2013; Arellano Ferro et al. 2013b) to reduce our observations. DIA is particularly adept at dealing with crowded fields like the cores of globular clusters, as described in detail in our previous papers (e.g. Bramich et al. 2011). Here we summarise the main steps of the reduction process. We note that an interesting advantage to using data from networks of identical telescopes and setups such as the LCOGT/RoboNet network is that one can use a reference image constructed from observations from one telescope for the other telescopes in the network.

After applying bias level and flatfield corrections to our raw images, we blurred our images with a Gaussian of appropriate σ, so that all images have a full-width half-maximum (FWHM) of 3.5 pixels; images that already have a $FWHM \geq 3.5$ pixels were not blurred. This is to avoid under-sampling, which can cause difficulties in the determination of the DIA kernel solution. Images were stacked from the best-seeing photometrically stable night in order to obtain a high signal-to-noise ratio (S/N) reference image in each filter. If an image had too many saturated stars, it was excluded from the reference. The resulting images in V and I are made up of 12 and 20 stacked images, respectively, with combined exposure times of 480 s (in V) and 800s (in I), and respective point-spread function (PSF) FWHM of 3.17 pixels (1.49″) and 3.09 pixels (1.45″). The reference frames were then used to measure source positions and reference fluxes in each filter. Following this, the images were registered with the reference frame, and the convolution of the reference with the kernel solution was subtracted from each image. This resulted in a set of difference images, from which we extracted difference fluxes for each source, allowing us to build light curves for all of the objects detected in the reference images. The light curves of the variable stars we detected in M 68 are available for download at the CDS, in the format outlined in Table 2.

2.2.2. EMCCD observations

Each EMCCD data cube was first pre-processed using the algorithms of Harpsøe et al. (2012), which included bias correction, flatfielding, and alignment of all exposures (corresponding to a tip-tilt correction). This procedure also yielded the point-spread function (PSF) width of each exposure. Each data cube was then subdivided into ten groups of exposures of increasing PSF size.

We then reduced the pre-processed EMCCD cubes using a modified version of the `DanDIA` pipeline, and a different noise model was adopted to account for the difference between CCD and EMCCD observations, as detailed by Harpsøe et al. (2012). Conventional LI techniques only keep the best-quality exposures within a data cube and therefore usually discard most of them, but here we build the reference image from the best-seeing groups alone, but the photometry is measured from all exposures within the data cube. That is, once a reference image has been built, the full sets of exposures (including the ones with worse seeing) are stacked for each data cube; we do this to achieve the best possible S/N. The sharp reference image is then convolved with the kernel solution and subtracted from each of the stacked data cubes.

Our EMCCD reference image has a PSF FWHM of 4.5 pixels, or 0.40″, and has a total exposure time of 302.4 s (3024 × 0.1 s).

Table 2. Format for the time-series photometry of all confirmed variables in our V- and I-band CCD observations.

#	Filter	HJD (d, UTC)	M_{std} (mag)	m_{ins} (mag)	σ_m (mag)	f_{ref} (ADU s^{-1})	σ_{ref} (ADU s^{-1})	f_{diff} (ADU s^{-1})	σ_{diff} (ADU s^{-1})	p
V1	V	2 456 360.56581	15.994	18.128	0.008	873.400	1.095	−784.689	10.536	2.5083
V1	V	2 456 363.70715	15.999	18.133	0.008	873.400	1.095	−935.364	11.470	2.9662
⋮	⋮	⋮	⋮	⋮	⋮	⋮	⋮	⋮	⋮	⋮
V1	I	2 456 360.68185	15.057	18.303	0.009	447.298	0.950	44.675	5.617	1.4841
V1	I	2 456 363.71698	15.370	18.616	0.009	447.298	0.950	−130.860	4.495	1.4636
⋮	⋮	⋮	⋮	⋮	⋮	⋮	⋮	⋮	⋮	⋮

Notes. The standard M_{std} and instrumental m_{ins} magnitudes listed in Cols. 4 and 5 correspond to the variable star, filter, and epoch of mid-exposure listed in Cols. 1–3, respectively. The uncertainty on m_{ins} and M_{std} is listed in Col. 6. For completeness, we also list the reference flux f_{ref} and the differential flux f_{diff} (Cols. 7 and 9, respectively), along with their uncertainties (Cols. 8 and 10), as well as the photometric scale factor p. Definitions of these quantities can be found in e.g. Bramich et al. (2011), Eqs. (2), (3). This is a representative extract from the full table, which is available at the CDS.

2.3. Photometric calibration

2.3.1. Self-calibration

For the CCD data, we self-calibrated the light curves to correct for some of the systematics. Although systematic errors cannot be removed completely, substantial corrections can be made in the case of time-series photometry, as shown in our previous papers (e.g. Kains et al. 2013).

We used the method of Bramich & Freudling (2012) to derive magnitude offsets to be applied to each epoch of the photometry, which correct for any errors in the fitted values of the photometric scale factors. The method involves setting up a (linear) photometric model for all of the available photometric measurements of all stars and solving for the best-fit parameter values by minimising χ^2. In our case, the model parameters consist of the star mean magnitudes and a magnitude offset for each image. The offsets we derive are a few percentage points, and they lead to significant improvements in the light curves for this cluster. An illustration of this is shown in Fig. 1.

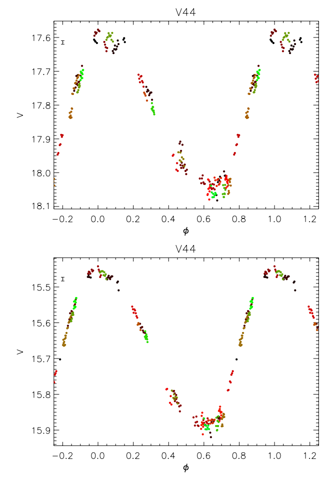

Fig. 1. V-band light curves for V44 before (*top*) and after (*bottom*) self-calibration using the method of Bramich & Freudling (2012), showing significant improvement in light curve quality.

2.3.2. Photometric standards

We used secondary photometric standards in the FOV from Stetson (2000) covering the full range of colours of our CMD to convert the instrumental magnitudes we obtained from the pipeline reduction of the CCD images to standard Johnson-Kron-Cousins magnitudes. This was done by fitting a linear relation to the difference between the standard and instrumental magnitudes, $m_{std} - m_{ins}$, and the instrumental $v - i$ colour of each photometric standard in our images. The resulting transformation relations are shown in Fig. 2. We compared our photometry with that of W94 by comparing mean magnitudes of RRL stars. This showed small differences of <1% in both V and I (see Table 3 in Sect. 3 for our mean magnitudes).

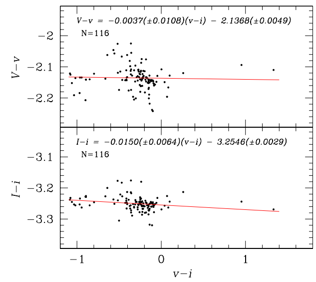

Fig. 2. Relations used to convert from instrumental to standard Johnson-Kron-Cousins magnitudes for the V (*top*) and I (*bottom*) bands.

2.4. Astrometry

We derived astrometry for our CCD reference images by using *Gaia*[2] to match ∼300 stars manually with the UCAC3 catalogue (Zacharias et al. 2010). For the EMCCD reference, we derived the transformation by matching ten stars to HST/WFC3 images (e.g. Bellini et al. 2011). The coordinates we provide for all stars in this paper (Table 4) are taken from these astrometric fits. The rms of the fit residuals are 0.27 arcsec (0.57 pixel) for the CCD reference images and 0.09 arcsec (0.96 pixel) for the EMCCD reference.

3. Variables in M 68

The first 28 (V1-V28) variables in this cluster were identified by Shapley and Ritchie (Shapley 1919, 1920), using fifteen photographs obtained with the 60-inch reflector telescope at Mt Wilson Observatory. All of these are RRL stars, except for V27, which was identified in the 1920 paper as a long-period variable. Greenstein et al. (1947) used a spectrum of V27 taken at the McDonald Observatory in 1939 to work out its radial velocity and compared this to the cluster's radial velocity to conclude that V27 is a long-period foreground variable star. Rosino & Pietra (1954) then used observations taken between 1951 and 1953 at Lojano Observatory to derive periods for 20 variables and discovered three additional RRL stars (V29–V31). They also noted some irregularities in V3, V4, V29, and V30, whereby they could not derive precise periods for those four stars. van Agt & Oosterhoff (1959) found seven more variables (V32–V38) when analysing observations taken in 1950 with the Radcliffe 74-inch reflector telescope in South Africa. They also noticed many discrepancies between their derived periods and those published a few years earlier by Rosino & Pietra (1954), as well as differences in light curve morphologies. Terzan et al. (1973) announced another four variables in M 68 (V39–V42), including the first SX Phe star in this cluster. Clement (1990) and C93 then studied 30 of the RRL stars, identifying nine double-mode pulsators and detecting period changes since the earlier studies. Brocato et al. (1994) carried out the first CCD-era study of this cluster using the 1.5 m ESO Danish Telescope, and soon after, W94 used CCD observations made in 1993 at the CTIO 0.9m telescope in Chile to discover an additional six variables (V43–V48), including another SX Phe star. Finally, Sariya et al. (2014) have recently used observations from 2011 at the Sampurnanand telescope in Nainital, northern India, to claim nine new variable detections, including five RR1 stars, bringing the total number of published variables in the cluster to 57.

3.1. Detection of variables

3.1.1. CCD observations

We searched for variables using two methods: we began by inspecting the difference images visually and checked light curves of any objects that had residuals on a significant number of images. This did not enable us to detect any new variables. We also constructed an image from the sum of the absolute values of all difference images and inspected light curves at pixel positions with significant peaks on this stacked image. As with the first method, this method recovered most known variables, but did not enable us to detect new variables. Finally, we conducted a period search for periods ranging from 0.02 to 2 days on all light curves using the "string length" method (e.g. Dworetsky 1983) and computed the ratio S_R of the string length for the best-fit period to that for the worst (i.e. the string length for phasing with a random period). For light curves without periodic variations, S_R is expected to be close to 1, although in practice, owing to

---

* The full Table 2 is only available at the CDS via anonymous ftp to `cdsarc.u-strasbg.fr` (`130.79.128.5`) or via `http://cdsarc.u-strasbg.fr/viz-bin/qcat?J/A+A/578/A128`
** Royal Society University Research Fellow.

[1] `DanDIA` is built from the `DanIDL` library of `IDL` routines available at `http://www.danidl.co.uk`

[2] `http://star-www.dur.ac.uk/~pdraper/gaia/gaia.html`

Table 3. Epochs, periods, mean magnitudes, and amplitudes A in V and I for all confirmed variable stars in M 68.

#	Epoch (HJD-2 450 000)	P (d)	β [dMyr^{-1}]	$\langle V\rangle$ [mag]	$\langle I\rangle$ [mag]	A_V [mag]	A_I [mag]	Type
RR0								
V2	6411.5879	0.5781755	−0.125	15.75	15.17	0.72	0.49	RR0
V9	6412.5455	0.579043	–	15.72	15.12	0.69	0.40	RR0*b*
V10	6363.7134	0.551920	–	15.71	–	1.08	–	RR0*b*
V12	6369.4311	0.615546	–	15.56	15.04	0.89	0.61	RR0
V14	6373.4455	0.5568499	+1.553	15.73	15.20	1.11	0.77	RR0
V17	6411.5835	0.668424	–	15.68	15.08	0.82	0.54	RR0(*b*?)
V22	6373.4162	0.5634451	–	15.67	15.13	1.15	0.75	RR0
V23	6410.5710	0.6588921	–	15.68	15.11	1.11	0.58	RR0
V25	6411.5323	0.6414842	−0.488	15.72	15.08	0.79	0.45	RR0*b*
V28	6363.7134	0.6067796	+0.102	15.75	15.14	1.18	0.70	RR0
V30	6370.5680	0.7336375	+0.044	15.64	15.00	0.37	0.25	RR0
V32	–	0.5882	–	–	–	–	–	RR0
V35	6381.6690	0.7025348	–	15.56	15.00	1.05	0.66	RR0
V46	6363.7743	0.7382510	–	15.64	15.01	0.54	0.37	RR0
RR1								
V1	6381.7111	0.3495912	+0.273	15.70	15.23	~0.45	0.40	RR1
V5	6366.6697	0.2821009	−0.497	15.72	15.36	0.45	0.28	RR1*b*
V6	6385.6186	0.3684935	−0.088	15.69	15.20	0.53	0.34	RR1
V11	6370.6253	0.3649338	+0.225	15.71	15.24	~0.55	0.37	RR1
V13	6411.5829	0.3617370	+0.116	15.74	15.26	0.58	0.36	RR1
V15	6385.6092	0.3722615	–	15.68	15.20	0.53	0.34	RR1
V16	6381.6814	0.3819671	+0.066	15.69	15.22	0.50	0.35	RR1
V18	6363.7943	0.3673459	−0.051	15.72	15.24	0.55	0.37	RR1
V20	6363.7643	0.3857892	+0.234	15.68	15.20	0.56	0.34	RR1
V24	6370.4698	0.3764448	−1.081	15.68	15.20	0.50	0.34	RR1
V33	6385.5693	0.3905647	–	15.67	15.17	0.47	0.23	RR1
V37	6363.7727	0.3846092	–	15.64	15.17	0.47	0.33	RR1
V38	6370.4420	0.3828116	–	15.63	15.17	0.53	0.33	RR1
V43	6363.7527	0.3706144	–	15.71	15.24	0.57	0.35	RR1
V44	6371.4311	0.3850912	–	15.67	15.16	0.48	0.29	RR1
V47	6385.6436	0.3729255	–	15.63	15.13	0.49	0.32	RR1
RR01								
V3	6381.6890	0.3907346	–	15.64	15.20	0.68	0.42	RR01
V4	6410.6485	0.3962175	–	15.67	15.20	0.61	0.40	RR01
V7	6381.7511	0.3879608	–	15.71	15.22	0.62	0.41	RR01
V8	6412.5861	0.3904076	–	15.65	15.18	0.53	0.34	RR01
V19	6368.6564	0.3916309	–	15.66	15.18	0.56	0.34	RR01
V21	6385.6233	0.4071121	–	15.62	15.15	0.64	0.42	RR01
V26	6369.4571	0.4070332	–	15.72	15.18	0.80	0.50	RR01
V29	6387.5498	0.3952413	–	15.71	15.14	0.56	0.30	RR01
V31	6385.6217	0.3996599	–	15.58	15.15	0.66	0.43	RR01
V34	6363.7673	0.4001371	–	15.76	15.17	~0.60	0.45	RR01
V36	6384.6470	0.415346	–	15.68	15.16	0.64	0.40	RR01
V45	6366.6760	0.3908187	–	15.72	15.17	0.52	0.30	RR01
SX Phe								
V39	6433.2863	0.0640464	–	18.04	17.66	0.85	0.64	SX
V48	6387.6218	0.043225	–	17.29	16.93	0.24	~0.11	SX
V49	6387.6120	0.048469	–	18.09	17.68	0.59	0.40	SX
V50	6370.4561	0.065820	–	17.56	17.13	0.70	0.30	SXd
V51	6383.6232	0.058925	–	17.24	16.73	0.35	0.20	SX
V52	6410.5871	0.037056	–	17.90	17.51	0.25	~0.20	SX
Others								
V27	2697.3	322.2342	–	9.8	–	4.03	–	Field Mira†
V53	–	–	–	16.98	15.26	≥0.1	–	?

Notes. V49, V50, V51, and V52 are newly discovered variables. A *b* at the end of the variable type denotes stars which exhibit Blazhko modulation in their light curve. "SX" denotes SX Phe stars, and an appended "d" denotes double-mode pulsation. $\langle V\rangle$ and $\langle I\rangle$ are intensity-weighted mean magnitudes. They are calculated from Fourier fits for all RRL stars, as the mean magnitude is stable even for unsatisfactory fits. For stars without good Fourier fits, amplitudes are calculated from the data. For V27, the data are taken from the ASAS catalogue (Pojmanski 2002). The data for V32 are taken from C93, because that star is outside of our FOV. Values of the period-change rate parameter β are also given, where relevant (see Sect. 3.2); in those cases, the value of P given corresponds to the instantaneous period at the epoch. †This star is FI Hydra.

Table 4. Equatorial celestial coordinates of all confirmed variables in M 68 at the epoch of the reference image, HJD ~ 2 456 385.6 d.

#	RA	Dec
RR0		
V2	12:39:15.29	−26:45:24.6
V9	12:39:25.57	−26:44:00.8
V10	12:39:25.96	−26:44:54.7
V12	12:39:26.918	−26:44:39.73
V14	12:39:27.54	−26:41:04.2
V17	12:39:29.02	−26:45:52.4
V22	12:39:32.30	−26:45:01.6
V23	12:39:32.41	−26:38:23.0
V25	12:39:38.15	−26:42:37.2
V28	12:40:00.31	−26:41:59.8
V30	12:39:36.07	−26:45:55.6
V32	12:39:03.29	−26:55:18.0
V35	12:39:25.19	−26:45:32.5
V46	12:39:24.84	−26:44:43.4
RR1		
V1	12:39:06.86	−26:42:53.3
V5	12:39:23.83	−26:41:52.3
V6	12:39:23.77	−26:44:23.6
V11	12:39:26.56	−26:46:32.7
V13	12:39:27.49	−26:45:35.9
V15	12:39:28.50	−26:43:40.9
V16	12:39:28.54	−26:43:22.1
V18	12:39:29.12	−26:46:15.2
V20	12:39:30.26	−26:46:33.2
V24	12:39:33.15	−26:44:46.6
V33	12:39:34.41	−26:43:40.7
V37	12:39:26.18	−26:44:20.9
V38	12:39:26.09	−26:45:08.3
V43	12:39:29.06	−26:45:43.7
V44	12:39:29.477	−26:44:38.06
V47	12:39:28.831	−26:44:19.92
RR01		
V3	12:39:17.33	−26:43:09.9
V4	12:39:19.06	−26:46:51.3
V7	12:39:24.02	−26:45:57.7
V8	12:39:25.18	−26:46:52.5
V19	12:39:30.15	−26:43:30.4
V21	12:39:31.19	−26:44:32.0
V26	12:39:39.46	−26:45:22.9
V29	12:39:48.93	−26:47:10.1
V31	12:39:19.65	−26:43:05.4
V34	12:39:47.56	−26:41:03.5
V36	12:39:24.89	−26:45:32.1
V45	12:39:29.989	−26:44:49.18
SX Phe		
V39	12:39:24.34	−26:44:51.8
V48	12:39:38.27	−26:46:12.4
V49	12:39:29.52	−26:44:09.3
V50	12:39:32.12	−26:45:10.5
V51	12:39:28.986	−26:44:48.47
V52	12:39:30.57	−26:44:30.1
Others		
V27	12:39:55.92	−26:40:17.4
V53	12:39:08.91	−26:50:33.8

Notes. More precise coordinates are given for stars within the FOV of the EMCCD reference image, with epoch ~2 456 451 d. The coordinates for V32, which is outside of our FOV, are from C93.

light curve scatter, the mean value is around 0.75; for true periodic light curves, $S_R \ll 1$. The distribution of S_R is shown in Fig. 3. We inspected all light curves that fell below an arbitrary threshold of $S_R = 0.5$, chosen by visually inspecting light curves sorted with ascending S_R.

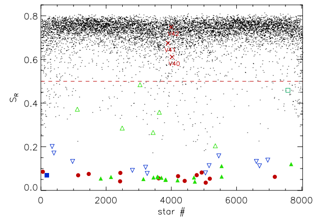

Fig. 3. Distribution of the S_R statistic as defined in the text, for our V-band light curves. A dashed line denotes the threshold below which we searched for periodic variables. RR0, RR1, and RR01 variables are shown as red filled circles, green filled triangles, and blue open inverted triangles, respectively. SX Phe is indicated as open green triangles, the field Mira variable V27 (FI Hya) as a filled blue square, and the variable of unknown type V53 as an open green square. The three marked stars above the threshold are V40-V42, which we found to be non-variable.

Table 5. Light curve mean magnitudes and rms values for V40-42, for which we do not find evidence of variability, as well as for the "new" variables published by Sariya et al. (2014).

# #	$\langle V\rangle$ [mag]	rms (V) [mag]	$\langle I\rangle$ [mag]	rms (I) [mag]
V40	18.32	0.068	17.50	0.075
V41	18.15	0.052	17.36	0.060
V42	19.05	0.083	18.36	0.156
SV49	14.72	0.008	13.67	0.007
SV50	15.15	0.010	14.14	0.008
SV51	12.68	0.013	–	–
SV52	18.17	0.225	–	–
SV53	18.60	0.077	17.94	0.14
SV54	18.48	0.361	17.00	0.14
SV55	17.04	0.023	16.21	0.03
SV56	19.81	0.192	18.97	0.31
SV57	16.81	0.016	15.91	0.02

Notes. Since Sariya et al. (2014) assigned those variables new V numbers, we add an "S" as a prefix to avoid confusion with the confirmed variables in this paper.

Using this method, we recovered all known variables except for V32, which is outside our FOV, and we were able to derive periods for all of them, except for V27, which is now known to be a foreground variable star with a period of ~322 d (Pojmanski 2002). For V27, we do not have an I-band light curve because it is saturated in our reference image. We also discovered four new variables, all of them SX Phe stars. Furthermore, we find that V40–42 are not variable within the limits of the rms in our data, given in Table 5, in agreement with the findings of W94[3]. We also find that none of the new variables recently claimed by Sariya et al. (2014) is variable within the rms scatter of our data (Table 5, see also Fig. 4), and we therefore continue the variable

[3] The mean magnitudes of V41 and V42 are significantly different from those given by W94. For V41 we suggest that this might be due to blending by V16 in their data, but no explanation is offered for the difference with V42.

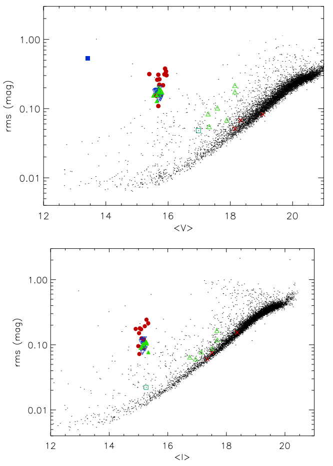

Fig. 4. Root mean square magnitude deviation versus mean magnitude for all stars for which photometry was obtained. Plots are for the V-band (*top*) and I-band (*bottom*). Classified variables are marked with red filled circles (RR0), green filled triangles (RR1) and blue open inverted triangles (RR01), green open triangles (SX Phe), a blue square (for V27, the field Mira variable FI Hya), and a green open square (variable V53, of unknown type). Non-variable objects previously catalogued as variable in the literature are denoted by red crosses.

numbering system from its standing prior to the publication of their paper.

We also confirm that many of the RRL stars are double-mode variables, as previously reported by Clement (1990) and C93, and we determine pulsation periods for both modes, when possible. Double-mode RRL stars in this cluster are discussed in Sect. 5.1.

To obtain the best possible period estimate for each star, we used archival data from previous studies of variability in this cluster by Rosino & Pietra (1953, 1954), C93, W94, and Brocato et al. (1994). This gives us a baseline of up to 62 years for stars that were observed by Rosino & Pietra (1953) and over 20 years for the stars that were observed in the 1993–1994 studies. The data of Rosino & Pietra (1953, 1954), and Brocato et al. (1994) were previously not available in electronic format, so we uploaded the light curves to the CDS for interested readers. For some of the stars, it was not possible to phase-fold the data sets without also fitting for a linear period change. For some even this did not lead to well-phased data sets, suggesting that some other effect is at work, such as a non-linear period change. Those are discussed in Sect. 3.3.

We also performed frequency analysis on all of the light curves in order to characterise the Blazhko effect (Blažko 1907), which can cause scatter in the phased light curve due to modulation of amplitude, frequency, phase, or a combination of those. We discuss the results of this search in Sect. 3.3.

Finally, we inspected the light curve of the standard star S28, which W94 found to be variable with an amplitude of ~0.1 mag. Our data show an increase in brightness of ~0.1 mag as well over the time span of our observations, confirming the variable nature of this star. We therefore assign it the variable number V53. Interestingly, however, we do not find significant variation in the I-band light curve of this star.

The V-band light curves for all of the variables objects are plotted in Figs. 5–9. I-band light curves are available for download at the CDS. A finding chart for all confirmed variables in M 68 is shown in Fig. 10 and a CMD in Fig. 11. The CMD confirms the classification of the confirmed variables, with RRL located on the instability strip and SX Phe stars in the blue straggler region. We also show stamps of variables detected on our EMCCD images ion Fig. 12.

3.1.2. EMCCD observations

We repeated the method we used for CCD observations to search for variability in the EMCCD observations we obtained. Of the known variables, only V44 has a light curve, with V12, V45, and V47 also located within our FOV, but is too close to the edge to allow for photometric measurements. Furthermore, the camera was changed in May 2013, with a slightly different filter after that, meaning that measurements from images taken before and after the change need to be treated as separate light curves.

We also detect the new variable V51, and confirm the period found with the CCD data for this object. The EMCCD light curves for V44 and V51 are shown in Fig. 13.

3.2. Period changes in RRL stars

Period changes have been observed in many RRL stars both in the Galactic field and in globular clusters. Period changes are usually classed as evolutionary or non-evolutionary. Evolutionary period changes of stars on the instability strip are understood to be due to their radius increasing and contracting. These only account for slowly increasing or decreasing changes, however, and in many RRL, abrupt period changes have been observed (e.g. Stagg & Wehlau 1980), which cannot be explained by such an evolution. As yet, there is no clear explanation for such changes.

As noted by Jurcsik et al. (2012), in spite of this, period-change rates of RRL in a globular cluster can inform us about its general evolution using theoretical models. Lee et al. (1990) suggested that in Oosterhoff type II clusters, most of the RRL pass through the instability strip from blue to red when reaching the end of helium burning in their core. Since such a blue-to-red evolution would also lead to a period increase, Lee (1991) argued that a mean positive value of the period change rate β in a cluster would support this scenario. Furthermore, Rathbun & Smith (1997) showed that the average period change should be

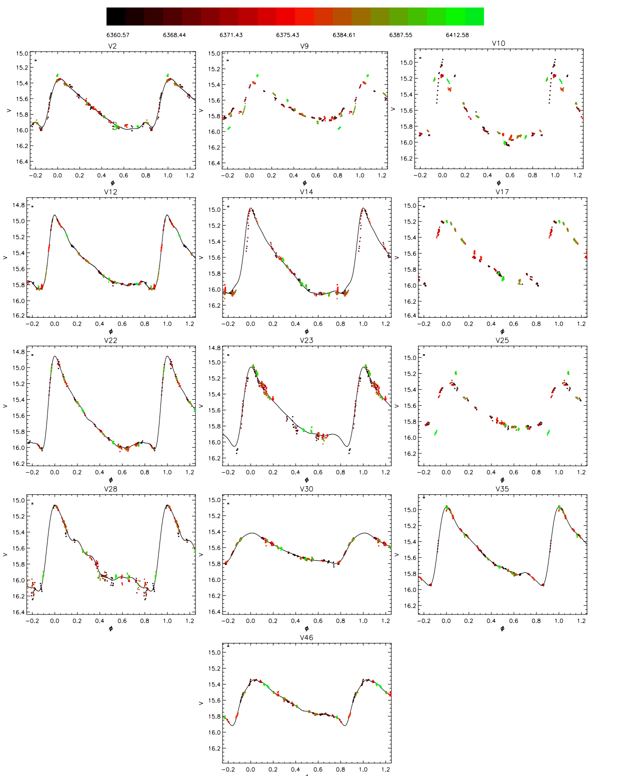

Fig. 5. Phased V-band light curves of the confirmed RR0 variables in M 68. Data from different nights are plotted in different colours (electronic version only), with a colour bar provided for reference (*top panel*). On the light curves for which a good Fourier decomposition could be obtained, the fit is overplotted. The size of typical 1σ error bars is plotted in the top left corner. The magnitude scale is the same on all plots in order to facilitate comparison of variation amplitude.

smaller for Oosterhoff I clusters than Oosterhoff II. Few comprehensive studies of period changes in cluster RRL have been published: Smith & Wesselink (1977) derived period changes for RRL in the Oosterhoff type II cluster M 15, with a mean of $\beta = 0.11 \pm 0.36\,\mathrm{d\,Myr^{-1}}$. For the Oosterhoff type I cluster M 3, Jurcsik et al. (2012) find a slightly positive mean value of $\beta \sim 0.01\,\mathrm{d\,Myr^{-1}}$, agreeing with the theoretical predictions of Lee (1991) and the findings of Rathbun & Smith (1997).

The parameter β is defined such that the period at time t is given by

$$P(t) = P_0 + \beta(t - E), \tag{1}$$

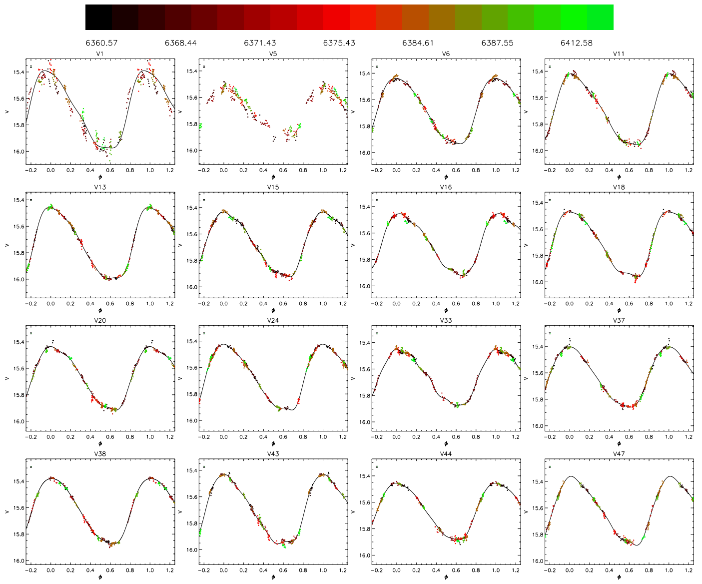

Fig. 6. Same as Fig. 5, but for RR1 stars.

where P_0 is the period at the (arbitrary) epoch E, and β as expressed in Eq. (1) is in units of d d^{-1}; however, β is usually expressed in d Myr^{-1} as a more natural unit. The number of cycles N_E elapsed at time t since the epoch E can then be calculated as

$$N_E = \int_E^t \frac{\mathrm{d}x}{P(x)} = \frac{1}{\beta}\ln\left[1+\frac{\beta}{P_0}(t-E)\right]. \tag{2}$$

The phase is then

$$\phi = N_E - \lfloor N_E \rfloor. \tag{3}$$

Here we use data stretching back to 1951 (see Sect. 3) to derive period changes for RR0 and RR1 stars for which data sets are not well phased and/or are aligned with a single constant period. To do this we performed a grid search in the (P_0, β) plane by minimising the string length of our data combined with those of W94 (both taken in V-band). We then searched manually around the best-fit solution incorporating other data sets taken in different passbands. As a consistency check, we also calculated period-change parameters using the O–C method. This consists of using an ephemeris to predict the times of maxima in the light curves and then plotting the difference between observed and predicted times of maxima against time. By fitting a quadratic function to this, a value of β can be derived; two such fits are shown in Fig. 14 for variables V14 and V28, which produced values of β consistent with the values derived using the grid method. The interested reader is referred to the papers of, for instance, Belserene (1964) and Nemec et al. (1985) for further details.

We found here that the values we found for β using the O−C method did not always produce well-phased light curves for all data sets. This is most likely due to the small number of observed maxima available for the variables in this cluster. For the cases where the two methods did not agree, we used the value found with the grid search. C93 derived period-change rates by computing periods for their light curves and for archival light curves, and by subtracting one from another. The method used here and the availability of more data mean that our period-change calculations should be more robust. The signs of our values of β agree with those of C93 except for V2 and V18, which, however, had very large associated error bars in that study.

The values of β from our analysis are listed in Table 3. Examples of phased light curves are shown in Fig. 15 for V14 and V18. The wide spread in values found for β means that we are unable to draw any firm conclusion about the general

Fig. 7. Phased V-band light curves of the RR01 stars. The light curves are phased with the first-overtone pulsation period. A typical 1σ error bar is plotted in the top left corner. The magnitude scale is the same on all plots in order to facilitate comparison of variation amplitude.

evolution of M 68. We find a mean value of $\langle\beta\rangle = 0.02 \pm 0.57$ d Myr^{-1}.

3.3. Discussion of individual RRL variables

The RR0 variables are plotted in Fig. 5, RR1 in Fig. 6, and RR01 in Fig. 7. Details of period-change calculations are given in Sect. 3.2.

- *V1*: we could only phase the different data sets by including a period-change parameter $\beta = 0.273$ d Myr^{-1}.
- *V2*: W94 noted that this star features Blazhko modulation, but our light curves do not enable us to confirm this. We found that a negative period change parameter $\beta = -0.125$ d Myr^{-1} was needed to phase-fold the various data sets.
- *V5*: this star requires a linear period change $\beta = -0.497$ d Myr^{-1} to phase the different data sets; however, the data from C93 are not phased well with our best-fit period and period change parameter β. According to W94, this star also has slow amplitude variations with a period of several days. The scatter in our data is consistent with that assessment.

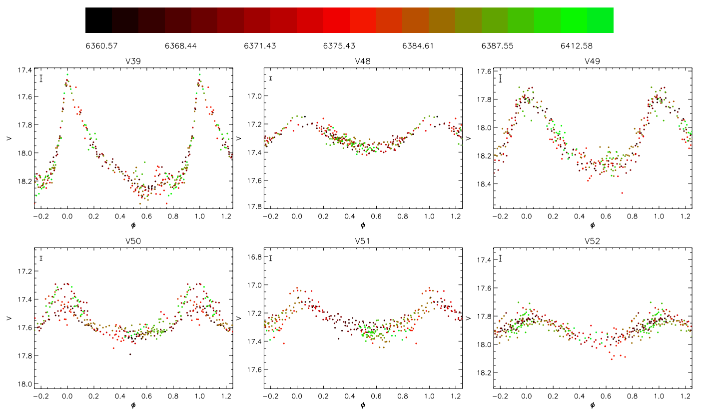

Fig. 8. Phased V-band light curves of the confirmed SX Phe stars in M 68, with a typical 1σ error bar plotted in the top left corner. The magnitude scale is the same in all plots to facilitate comparison of variation amplitude.

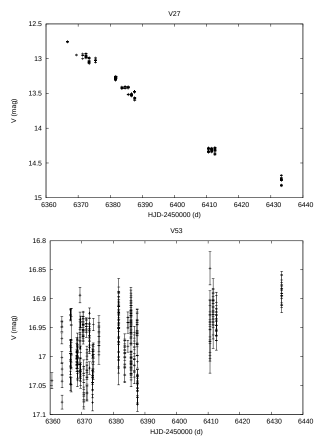

Fig. 9. Unphased V-band light curves of the variables V27 (FI Hya) and V53 (unknown type), plotted with 1σ error bars.

- *V6*: the data from Rosino & Pietra (1954) are not aligned with the other data sets with a constant period.We find a period-change parameter of $\beta = -0.088$ d Myr^{-1}. The light curve may suggest some Blazhko modulation, but our data do not allow us to make a strong claim about this.
- *V9*: our light curve shows Blazhko modulation, as proposed by W94.
- *V10*: our light curve for this object shows clear Blazhko amplitude modulation. Interestingly, W94 found a constant amplitude but a variable period.
- *V11*: we could only phase the data sets simultaneously by including a period-change parameter $\beta = 0.225$ d Myr^{-1}.
- *V12*: we find no evidence of Blazhko modulation for this star, contrary to W94, who found strong cycle-to-cycle variations, but this may be due do the baseline of W94 being longer by ~50 days.
- *V13*: we find that including period-change parameter is needed to phase all the light curves; we find $\beta = 0.116$ d Myr^{-1}.
- *V14*: W94 noted a variation in shape for the bump at minimum brightness, which we cannot confirm in our light curve. We also find that a rather large period change parameter $\beta = 1.553$ d Myr^{-1} was needed to phase-fold all the data sets (see Fig. 15).
- *V15*: our observations show some slight residual scatter, which might suggest Blazhko modulation; some evidence of similar scatter is visible in the data of W94.
- *V16*: a period-change parameter $\beta = 0.066$ d Myr^{-1} was included to improve the phase-folding of the various data sets.
- *V17*: we do not find evidence of the Blazhko effect in this star as suggested by W94 on the timescales covered by our

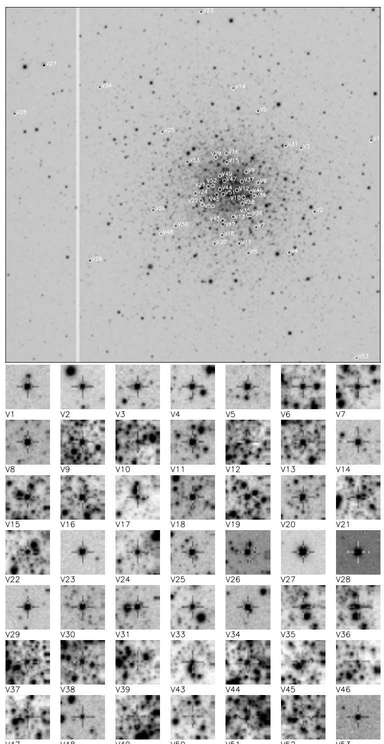

Fig. 10. Finding chart for the confirmed variable objects in M 68, using our V reference image. North is up and east to the left. The image size is 8.8×12.26 arcmin, with each stamp $27.6'' \times 27.6''$. A white circle is centred on each variable and labelled with the variable number. The display scale has been modified where necessary to make the source as clear as possible on the stamps, and the location of the variable is also marked with a cross-hair. Stamps from the EMCCD reference image for V12, V44, V45, and V51 are shown in Fig. 12.

baseline. However, comparison of our light curve with that of W94 (Fig. 16) shows clearly that the amplitude of the light curve is larger in our data set, which might indicate that modulation is present but slow.

- *V18, V20, V24*: these stars all required the inclusion of a period-change parameter for satisfactory phase-folding of available data sets.
- *V25*: we find a period-change parameter to phase all the data sets of $\beta = -0.488$ d Myr^{-1}. The light curve also shows Blazhko modulation, as already noted by W94.
- *V28*: we tentatively suggest that this star might be affected by the Blazhko effect. A period change parameter of $\beta = 0.102$ d Myr^{-1} was found to improve the phase-folding of all data sets.

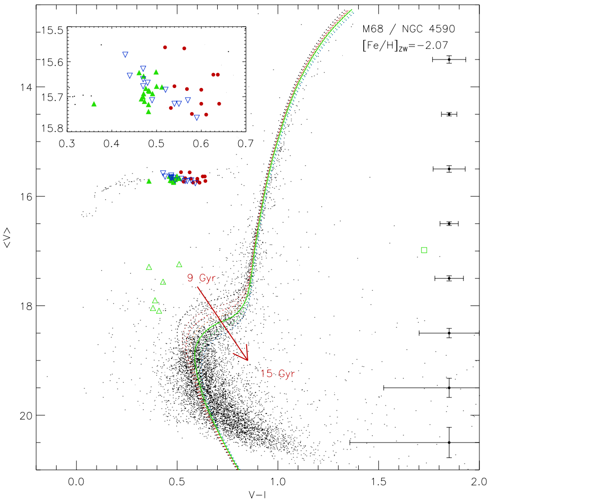

Fig. 11. $(V-I), V$ colour-magnitude diagram from our photometry. The location of RR0 (red filled circles), RR1 (green filled triangles), RR01 (blue inverted triangles), and SX Phe (open green triangles) stars are shown. The variable V53 (unknown type) is shown as an open green square. Typical error bars are shown for different magnitude levels on the right-hand side of the plot. An *inset* in the top left corner of the plot shows a zoom of the instability strip region of the HB. For added information, isochrones for 9, 10, 11, 12, 13, 14, and 15 Gyr from Dotter et al. (2008) are overplotted in different colours; the best-fit isochrone (13 Gyr) is plotted as a thick green solid line.

– *V30*: a small positive period-change parameter $\beta = 0.044\,\mathrm{d\,Myr^{-1}}$ was found to be needed to phase all data sets.
– *V33*: this star is now RR1, but used to be RR01, as first noted by C93. Like C93, we fail to detect signs of the secondary pulsations that were visible in the data of van Agt & Oosterhoff (1959).
– *V47*: we do not confirm the suggestion of W94 that this star is affected by Blazhko modulation, since it may be due to the longer baseline of the W94 data.

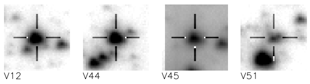

Fig. 12. Stamps from the EMCCD reference image for the stars within our EMCCD FOV, except V47, which is too close to the edge of the image. North is up and east to the left. Each stamp is 3.6″ × 3.6″ and a cross-hair marks the location of the variable star.

4. Fourier decomposition of RR Lyrae star light curves

We performed a Fourier decomposition of the V-band light curves of RRL variables in order to derive several of their properties with well-established empirical relations. We can then use individual stars' properties to estimate the parameters of the host cluster. Fourier decomposition mean fitting light curves with the Fourier series

$$m(t) = A_0 + \sum_{k=1}^{N} A_k \cos\left[\frac{2\pi k}{P}(t-E) + \phi_k\right], \tag{4}$$

where $m(t)$ is the magnitude at time t, N the number of harmonics used in the fit, P the period of the variable, E the epoch, and A_k and ϕ_k are the amplitude and phase of the k^{th} harmonic, respectively. The epoch-independent Fourier parameters are then defined as

$$R_{ij} = A_i/A_j \tag{5}$$
$$\phi_{ij} = j\phi_i - i\phi_j. \tag{6}$$

In each case we used the lowest number of harmonics that provided a good fit, to avoid over-fitting variations in the light

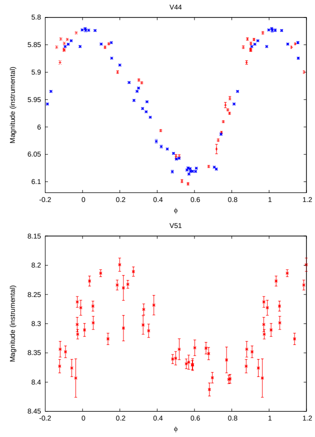

Fig. 13. EMCCD light curve for variables V44 and V51. See Table 3 for information about these variables. For V44 we show the light curves before (blue + signs) and after (red asterisks) the camera change as separate light curves, as discussed in the text. For V51, we show only the light curve after the change because the photometry before was too poor.

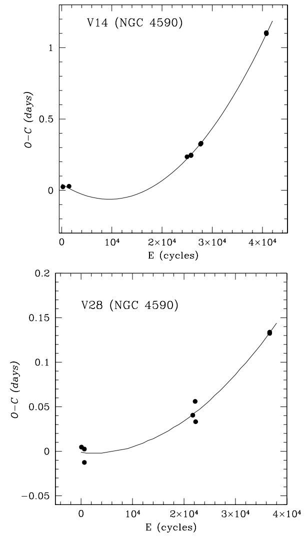

Fig. 14. O–C plots for variables V14 and V28 showing the quadratic fit to the time dependence of the difference between observed and predicted times of light curve maxima. The values found using this quadratic fit for V14 and V28 are consistent with those derived using our grid fitting method (see text), $\beta = +1.553\,\mathrm{d\,Myr^{-1}}$ (V14) and $\beta = +0.102\,\mathrm{d\,Myr^{-1}}$ (V28).

curves due to noise. We also checked the sensitivity of the parameters we derived to the number of harmonics N, and we used only light curves with stable parameters, i.e. ones that showed little variation with N, to estimate cluster parameters. Double-mode pulsators and objects exhibiting signs of Blazhko modulation are also excluded from the following analysis.

The A_k coefficients for the first four harmonics and the Fourier parameters $\phi_{21}, \phi_{31,}$ and ϕ_{41} are given in Table 6 for the light curves for which we could obtain a Fourier decomposition. We used the deviation parameter D_m, defined by Jurcsik & Kovács (1996), as an estimate of the reliability of derived parameters and use $D_m < 5$ (e.g. Cacciari et al. 2005) as a selection criterion. The value of D_m for each of the successful Fourier decompositions is given in Table 6.

We did not fit RR0 stars V9, V10, and V25 and RR1 star V5, because they all exhibit Blazhko-type modulation. Furthermore, we did not use the fits of V14, V28, V30, and V46 to derive star properties because those fits have a value of $D_m > 5$. V17 was not fitted either because the parameters varied significantly with the number of harmonics used in the fit, as well as showing signs of slow amplitude modulation (see Sect. 3.3). This leaves us with 5 RR0 and 15 RR1 stars for which we derive individual properties in the next section. We also note that for V1, V2, V14, V23, and V30, we combined our data with that of W94 in order to derive fits, owing to insufficient phase coverage of our data alone.

4.1. Metallicity

In this section we derive metallicities for each variable for which a good Fourier decomposition, according to our selection criteria discussed above, could be obtained. To do this, we use empirical relations from the literature. For RR0 stars, we used the relation of Jurcsik & Kovács (1996), which expresses [Fe/H] as a function of the period and of the Fourier parameter ϕ^s_{31}. The s superscript denotes that Jurcsik & Kovács (1996) derived their relations using *sine* series, whereas we fit cosine Fourier series (Eq. (4)). The Fourier parameters can be easily converted using the equation

$$\phi^s_{ij} = \phi_{ij} - (i-j)\,\frac{\pi}{2}. \tag{7}$$

[Fe/H] can then be expressed as

$$[\mathrm{Fe/H}]_{\mathrm{J}} = -5.038 - 5.394\,P + 1.345\,\phi^s_{31}, \tag{8}$$

where the subscript J denotes an uncalibrated metallicity, and the period P is in days. This value can be transformed to the

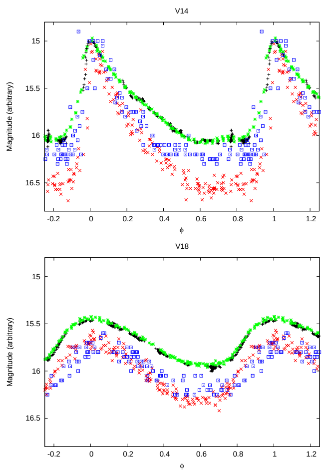

Fig. 15. Phased light curves for V14 (*top*) and V18 (*bottom*), showing the data sets of this paper (black, + symbols), W94 (green asterisks), C93 (red crosses), and Rosino & Pietra (1954, blue squares). The light curves were phased using a period change of $+1.553\,\mathrm{d\,Myr^{-1}}$ (V14) and $-0.051\,\mathrm{d\,Myr^{-1}}$ (V18).

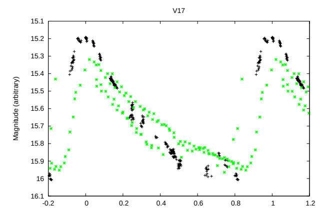

Fig. 16. Phased light curves for V17, showing the V-band data sets of this paper (black, + symbols) and W94 (green asterisks). The amplitude is larger in our data by ~0.15 mag compared to the observations of W94; we suggest that this might be due to slow amplitude modulation.

metallicity scale of Zinn & West (1984, hereafter ZW) via the simple relation from Jurcsik (1995),

$$[\mathrm{Fe/H}]_{\mathrm{ZW}} = \frac{[\mathrm{Fe/H}]_{\mathrm{J}} - 0.88}{1.431}. \tag{9}$$

Kovács (2002) investigated the validity of this relation and found that Eq. (8) yields metallicity values that are too high by ~0.2 dex for metal-poor clusters. This was supported by the findings of Gratton et al. (2004) and Di Fabrizio et al. (2005), who compared metallicity values for RRL stars in the Large Magellanic Cloud (LMC) using both spectroscopy and Fourier decomposition. We therefore include a shift of −0.20 dex (on the $[\mathrm{Fe/H}]_{\mathrm{J}}$ scale) or −0.14 dex (on the ZW scale) to the metallicity values derived for RR0 stars using Eq. (8).

More recently, Nemec et al. (2013) have derived a relation for the metallicity of RR0 stars, using observations of RRL taken with the *Kepler* space telescope,

$$[\mathrm{Fe/H}]_{\mathrm{UVES}} = b_0 + b_1 P + b_2 \phi^s_{31} + b_3 \phi^s_{31} P + b_4 \left(\phi^s_{31}\right)^2, \tag{10}$$

where $[\mathrm{Fe/H}]_{\mathrm{UVES}}$ is the metallicity on the widely used scale of Carretta et al. (2009a), and the constant coefficients were determined by Nemec et al. (2013) as $b_0 = -8.65 \pm 4.64$, $b_1 = -40.12 \pm 5.18$, $b_3 = 6.27 \pm 0.96$, and $b_4 = -0.72 \pm -0.72 \pm 0.17$. The scale of Carretta et al. (2009a) was derived using spectra of red giant branch (RGB) stars obtained using GIRAFFE and UVES. ZW metallicity values can be transformed to that scale (hereafter referred to as the UVES scale) using

$$[\mathrm{Fe/H}]_{\mathrm{UVES}} = -0.413 + 0.130\,[\mathrm{Fe/H}]_{\mathrm{ZW}} - 0.356\,[\mathrm{Fe/H}]_{\mathrm{ZW}}^2. \tag{11}$$

In the discussion that follows, we considered RR0 metallicity values obtained both with the scale of Jurcsik & Kovács (1996) and that of Nemec et al. (2013)[4]. For the RR1 variables, we used the relation of Morgan et al. (2007) to derive metallicity values.This relates [Fe/H], P, and ϕ_{31} as

$$[\mathrm{Fe/H}]_{\mathrm{ZW}} = 2.424 - 30.075\,P + 52.466\,P^2 + 0.982\,\phi_{31} + 0.131\phi_{31}^2 - 4.198\,\phi_{31} P. \tag{12}$$

Metallicity values calculated using Eqs. (8), (9), and (12) are listed in Table 7. We note that the metallicities of only two RRL stars in M 68 have previously been measured in the literature. Smith & Manduca (1983) measured the spectroscopic metallicity index ΔS for the RR0-type variables V2 and V25 as 11.0 and 10.5, respectively, which yield metallicities $[\mathrm{Fe/H}]_{\mathrm{ZW}} \approx -2.15$ and −2.07, respectively, when converted to the ZW scale via the following relation from Suntzeff et al. (1991):

$$[\mathrm{Fe/H}]_{\mathrm{ZW}} = -0.158\Delta S - 0.408. \tag{13}$$

We include these metallicity measurements as a footnote to Table 7 for the sake of completeness.

4.2. Effective temperature

Jurcsik (1998) derived empirical relations to calculate the effective temperature of fundamental-mode RRL stars, relating the $(V-K)_0$ colour to P and to several of the Fourier coefficients and parameters:

$$(V-K)_0 = 1.585 + 1.257\,P - 0.273\,A_1 - 0.234\,\phi^s_{31} + 0.062\,\phi^s_{41} \tag{14}$$
$$\log T_{\mathrm{eff}} = 3.9291 - 0.1112\,(V-K)_0 - 0.0032\,[\mathrm{Fe/H}]_{\mathrm{J}}. \tag{15}$$

[4] However, we calculated errors on metallicity values derived from the relation of Nemec et al. (2013) ignoring the errors on the coefficients b_i, since they would lead to very large errors.

Table 6. Parameters from the Fourier decomposition.

#	A_0	A_1	A_2	A_3	A_4	ϕ_{21}	ϕ_{31}	ϕ_{41}	N	D_m
RR0										
V2	15.749(2)	0.281(2)	0.086(2)	0.057(2)	0.042(2)	4.031(17)	8.039(23)	6.073(32)	9	4.34
V12	15.559(2)	0.325(2)	0.145(2)	0.113(2)	0.075(2)	3.870(10)	7.940(12)	5.774(19)	11	3.11
V14	15.732(2)	0.421(2)	0.154(3)	0.116(3)	0.068(3)	3.926(13)	7.926(18)	5.765(27)	10	5.04
V22	15.670(2)	0.424(2)	0.179(2)	0.136(2)	0.100(2)	3.836(9)	7.780(13)	5.717(18)	11	2.36
V23	15.678(3)	0.338(3)	0.159(3)	0.118(3)	0.078(3)	3.899(20)	8.157(28)	6.163(40)	8	1.83
V28	15.751(2)	0.371(2)	0.178(2)	0.146(2)	0.076(2)	3.842(8)	8.363(11)	6.064(17)	8	6.44
V30	15.637(2)	0.165(2)	0.059(2)	0.029(2)	0.011(2)	4.121(24)	8.510(43)	7.114(104)	7	17.59
V35	15.562(2)	0.338(2)	0.163(2)	0.113(2)	0.081(2)	4.041(8)	8.411(11)	6.478(14)	9	2.87
V46	15.637(2)	0.209(2)	0.091(2)	0.055(2)	0.026(3)	4.090(25)	8.684(35)	7.187(47)	10	7.94
RR1										
V1	15.700(2)	0.296(3)	0.059(3)	0.023(3)	0.016(3)	4.558(39)	2.581(93)	1.461(125)	4	–
V6	15.691(1)	0.251(1)	0.040(2)	0.021(1)	0.009(1)	4.619(15)	2.962(31)	2.102(73)	4	–
V11	15.706(1)	0.265(2)	0.052(2)	0.025(2)	0.007(2)	4.554(13)	2.521(25)	1.837(78)	4	
V13	15.742(1)	0.274(2)	0.049(2)	0.028(2)	0.013(2)	4.536(15)	2.722(23)	1.066(47)	5	–
V15	15.684(1)	0.241(1)	0.041(2)	0.019(2)	0.007(2)	4.636(15)	3.074(29)	1.883(73)	5	–
V16	15.691(1)	0.229(2)	0.039(2)	0.023(2)	0.001(2)	4.706(16)	2.865(31)	1.936(410)	6	–
V18	15.722(1)	0.249(2)	0.046(2)	0.027(2)	0.015(2)	4.566(15)	2.873(24)	1.930(48)	4	–
V20	15.676(1)	0.239(1)	0.036(1)	0.019(2)	0.004(1)	4.806(15)	3.129(27)	2.355(126)	5	–
V24	15.682(2)	0.247(2)	0.048(2)	0.022(2)	0.011(2)	4.637(17)	2.894(35)	1.978(68)	6	–
V33	15.670(1)	0.211(2)	0.030(2)	0.013(2)	0.006(2)	4.627(23)	2.983(51)	2.787(115)	6	–
V37	15.641(1)	0.227(2)	0.036(2)	0.011(2)	0.006(2)	4.392(21)	3.013(59)	2.440(98)	4	–
V38	15.631(1)	0.250(2)	0.038(2)	0.016(2)	0.006(2)	4.537(16)	3.180(37)	2.052(93)	4	–
V43	15.713(1)	0.261(2)	0.048(2)	0.021(2)	0.011(2)	4.439(17)	2.408(35)	1.378(62)	5	–
V44	15.672(2)	0.216(2)	0.032(2)	0.012(2)	0.004(2)	4.706(31)	3.205(62)	1.854(147)	5	–
V47	15.629(2)	0.248(2)	0.048(2)	0.016(2)	0.007(2)	4.645(21)	2.799(62)	2.676(123)	5	–

Notes. Numbers in parentheses are the 1σ uncertainties on the last decimal place.

Simon & Clement (1993) used theoretical model to derive a corresponding relation for RR1 stars,

$$\log\,T_{\mathrm{eff}} = 3.7746 - 0.1452\,\log\,P + 0.0056\,\phi_{31}. \tag{16}$$

We use those relations to derive $\log T_{\mathrm{eff}}$ for all of our RR0 and RR1 stars, and give the resulting values in Table 7. As mentioned in previous analyses (e.g. Arellano Ferro et al. 2008), there are some important caveats to consider when estimating temperatures with Eqs. (15) and (16). The values of $\log T_{\mathrm{eff}}$ for RR0 and RR1 stars are on different absolute scales (e.g. Cacciari et al. 2005), and temperatures derived using these relations show systematic deviations from those predicted by Castelli (1999) in their evolutionary models or on the temperature scales of Sekiguchi & Fukugita (2000). However, we use them in order to have a comparable approach to the one taken in our previous studies of clusters.

4.3. Absolute magnitude

We used the empirical relations of Kovács & Walker (2001) to derive V-band absolute magnitudes for the RR0 variables,

$$M_V = -1.876\,\log P - 1.158\,A_1 + 0.821\,A_3 + K_0, \tag{17}$$

where K_0 is the zero point of the relation. Using the absolute magnitude of the star RR Lyrae of $M_V = 0.61 \pm 0.10$ mag derived by Benedict et al. (2002) and a Fourier decomposition of its light curve, Kinman (2002) determined a zero point for Eq. (17) of $K_0 = 0.43$ mag. Here, however, we adopt a slightly different value of $K_0 = 0.41 \pm 0.02$ mag, as in several of our previous studies (e.g. Arellano Ferro et al. 2010), in order to maintain consistency with a true distance modulus of $\mu_0 = 18.5$ mag for the LMC (Freedman et al. 2001). A nominal error of 0.02 mag on K_0 was adopted in the absence of uncertainties on K_0 in the literature.

For RR1 variables, we use the relation of Kovács (1998),

$$M_V = -0.961\,P - 0.044\,\phi^s_{21} - 4.447\,A_4 + K_1, \tag{18}$$

where we adopted the zero-point value of $K_1 = 1.061 \pm 0.020$ mag (Cacciari et al. 2005), with the same justification as for our choice of K_0.

We also converted the magnitudes we obtained to luminosities using

$$\log\,(L/L_{\odot}) = -0.4\,\left[M_V + B_C(T_{\mathrm{eff}}) - M_{\mathrm{bol},\odot}\right], \tag{19}$$

where $M_{\mathrm{bol},\odot}$ is the bolometric magnitude of the Sun, $M_{\mathrm{bol},\odot} = 4.75$ mag, and $B_{\mathrm{C}}(T_{\mathrm{eff}})$ is a bolometric correction that we estimate by interpolating from the values of Montegriffo et al. (1998) for metal-poor stars, and using the value of $\log T_{\mathrm{eff}}$ we derived in the previous section. Values of M_V and $\log(L/L_{\odot})$ for the RR0 and RR1 variables are listed in Table 7. Using our average values of M_V, in conjunction with the average values of $[\mathrm{Fe/H}]_{\mathrm{ZW}}$ (Sect. 4.1), we find good agreement with the $M_V - [\mathrm{Fe/H}]_{\mathrm{ZW}}$ relation derived in the literature (e.g. Kains et al. 2012, see Fig. 9 of that paper).

Table 7. Physical parameters for the RRL variables calculated using the Fourier decomposition parameters and the relations given in the text.

#	$[Fe/H]_{ZW}$	$[Fe/H]_{UVES}$	M_V	$\log(L/L_\odot)$	$\log T_{eff}$
RR0					
V2	−1.85(2)	−2.17(6)	0.578(30)	1.679(12)	3.804(2)
V12	−2.09(1)	−2.81(3)	0.522(24)	1.704(10)	3.800(2)
V22	−2.04(1)	−2.72(4)	0.498(27)	1.709(11)	3.807(2)
V23	−2.04(3)	−2.58(8)	0.455(27)	1.733(11)	3.797(2)
V35	−1.97(1)	−2.21(3)	0.399(30)	1.758(12)	3.795(2)
RR1					
V1	−2.06(3)	–	0.521(23)	1.658(10)	3.855(2)
V6	−2.06(2)	–	0.533(21)	1.655(9)	3.854(1)
V11	−2.12(1)	–	0.548(21)	1.650(9)	3.852(1)
V13	−2.08(1)	–	0.524(21)	1.658(9)	3.854(1)
V15	−2.05(2)	–	0.538(21)	1.653(9)	3.854(1)
V16	−2.11(1)	–	0.550(21)	1.650(9)	3.851(1)
V18	−2.07(1)	–	0.511(21)	1.664(9)	3.854(1)
V20	−2.08(1)	–	0.529(21)	1.658(9)	3.852(1)
V24	−2.10(2)	–	0.517(21)	1.663(9)	3.852(1)
V33	−2.11(2)	–	0.526(21)	1.661(9)	3.851(1)
V37	−2.10(2)	–	0.540(21)	1.654(9)	3.852(1)
V38	−2.06(2)	–	0.536(21)	1.655(9)	3.853(1)
V43	−2.14(1)	–	0.531(21)	1.658(9)	3.851(1)
V44	−2.07(2)	–	0.533(21)	1.656(9)	3.853(1)
V47	−2.10(2)	–	0.536(21)	1.655(9)	3.852(1)

Notes. Numbers in parentheses are the 1σ uncertainties on the last decimal place. The values of $[Fe/H]_{UVES}$ listed in this table for RR0 stars are derived using the relation of Nemec et al. (2013). In addition, we note that Smith & Manduca (1983) found $[Fe/H]_{ZW} \approx -2.15$ for V2 and $[Fe/H]_{ZW} \approx -2.07$ for V25, using the ΔS method (see Sect. 4.1). Errors quoted for $\log T_{eff}$ are only statistical and not systematic; we could not calculate systematic errors for $\log T_{eff}$ as no errors are given on the empirical coefficients in Eqs. (15) and (16). Errors on M_V and $\log(L/L_\odot)$ for RR1 stars are dominated by the error on the zero point K_0 in Eq. (18).

4.4. Masses

Empirical relations also exist to derive masses of RRL stars from the Fourier parameters, although as noted by Simon & Clement (1993), such relations are better suited to deriving average values for RRL stars in clusters. We therefore use mean parameters to derive mean masses for our RRL stars. For RR0 stars, we use the relation of van Albada & Baker (1971),

$$\log(\mathcal{M}/\mathcal{M}_\odot) = 16.907 - 1.47\log(P) + 1.24\log(L/L_\odot) - 5.12\log T_{eff}, \quad (20)$$

where we use the symbold $\mathcal{M}$ to denote masses to avoid confusion with absolute magnitudes elsewhere in the text. Using this, we find an average mass $\langle \mathcal{M}_{RR0}/\mathcal{M}_\odot \rangle = 0.74 \pm 0.14$.

For RR1 stars, we used the relation derived by Simon & Clement (1993) from hydrodynamic pulsation models,

$$\log(\mathcal{M}/\mathcal{M}_\odot) = 0.52\log P - 0.11\phi_{31} + 0.39, \quad (21)$$

which yield a mean mass $\langle \mathcal{M}_{RR1}/\mathcal{M}_\odot \rangle = 0.70 \pm 0.05$. This is lower than the value of $\langle \mathcal{M}/\mathcal{M}_\odot \rangle = 0.79$ found by Simon & Clement (1993) for M 68, but it confirms the value of $\langle \mathcal{M}/\mathcal{M}_\odot \rangle = 0.70 \pm 0.01$ found by W94 using the same method.

5. Double-mode pulsations

5.1. RR Lyrae

M 68 contains 12 identified double-mode RRL (RR01) stars. RR01 stars are of particular interest, because given metallicity measurements, the double-mode pulsation provides us with a unique opportunity to measure the mass of these objects without assuming a stellar evolution model and to study the mass-metallicity distribution of field and cluster RRL stars (e.g. Bragaglia et al. 2001). "Canonical" RR01 have first-overtone-to-fundamental pulsation period ratios ranging from ∼0.74 to 0.75 (e.g. Soszyński et al. 2009) for radial pulsations. Other period ratios can be interpreted as evidence for non-radial pulsation or for higher-overtone secondary pulsation, with studies reporting a period ratio of ∼0.58–0.59 between the second overtone and the fundamental radial pulsation (e.g. Poretti et al. 2010).

We analysed the light curves of RR01 stars in our images using the time-series analysis software `Period04` (Lenz & Breger 2005). In Table 8, we list the periods we found for each variable, as well as the period ratio. We found ratios within the range of canonical value for all stars except for V45, for which we did not detect a second pulsation period, unlike W94.

In the past, theoretical model tracks and the "Petersen" diagram (P_1/P_0 vs. P_0, Petersen 1973) have been used to estimate the masses of RR01 pulsators. Using this approach, W94 estimated average RR01 masses of $\sim 0.77\,\mathcal{M}_\odot$ and $\sim 0.79\,\mathcal{M}_\odot$ with the models of Cox (1991) and Kovacs et al. (1991), respectively. Here we use the new relation of Marconi et al. (2015), who used new non-linear convective hydrodynamic models to derive a relation that links the stellar mass with the period ratio and the metallicity, through

$$\log(\mathcal{M}/\mathcal{M}_\odot) = (-0.85 \pm 0.05) - (2.8 \pm 0.3)\log(P_1/P_0) - (0.097 \pm 0.003)\log Z. \quad (22)$$

To convert metallicities from $[Fe/H]_{ZW}$ to Z, we used the relation of Salaris et al. (1993),

$$\log Z = [Fe/H]_{ZW} - 1.7 + \log(0.638\,f + 0.362), \quad (23)$$

where f is the α-element abundance, for which we adopt a value of 0.3 for M 68 (e.g. Carney 1996). We also adopted a value of

Table 8. Fundamental and first-overtone pulsation periods and the period ratio for the double-mode RRL detected in M 68.

#	$P_1[d]$	A_1	$P_0[d]$	A_0	P_1/P_0	$\mathcal{M}/\mathcal{M}_\odot$
V3	0.3907346	0.206	0.523746	0.101	0.7460	0.789 ± 0.119
V4	0.3962175	0.205	0.530818	0.111	0.7464	0.787 ± 0.118
V7	0.3879608	0.201	0.520186	0.107	0.7458	0.789 ± 0.119
V8	0.3904076	0.219	0.522230	0.046	0.7476	0.784 ± 0.118
V19	0.3916309	0.202	0.525259	0.061	0.7456	0.790 ± 0.119
V21	0.4071121	0.221	0.545757	0.138	0.7460	0.789 ± 0.119
V26	0.4070332	0.200	0.546782	0.147	0.7444	0.793 ± 0.120
V29	0.3952413	0.236	0.530525	0.023	0.7450	0.792 ± 0.119
V31	0.3996599	0.200	0.535115	0.121	0.7469	0.786 ± 0.118
V34	0.4001371	0.187	0.537097	0.050	0.7450	0.792 ± 0.119
V36	0.415346	0.203	0.557511	0.106	0.7450	0.792 ± 0.119
V45	0.3908187	0.224	–	–	–	–

Notes. Also listed are semi-amplitudes for each pulsation mode.

$[Fe/H]_{ZW} = -2.07 \pm 0.06$ corresponding to the mean metallicity of the RRL stars listed in Table 7. Using Eqs. (22) and (23), we find the masses given in Table 8 and a mean mass for RR01 stars of $\langle \mathcal{M}/\mathcal{M}_\odot \rangle = 0.789 \pm 0.003$ (statistical) $\pm$ 0.119 (systematic), in excellent agreement with the findings of W94.

5.2. SX Phoenicis

We also carried out a search for double-mode pulsation in the light curves of the SX Phe stars in our sample. For V50, we find a second pulsation period $P_1 = 0.051745$ d in addition to the fundamental period $P_0 = 0.065820$ d, giving a ratio $P_1/P_0 \sim 0.786$ within the range of expected values for a metal-poor double-radial-mode SX Phe star (Santolamazza et al. 2001). This is confirmed by the location of that secondary period on the $\log P - V_0$ diagram, which is discussed further in Sect. 6.4.2.

6. Cluster properties from the variable stars

6.1. Oosterhoff type

To determine the Oosterhoff type of this cluster, we calculate the mean periods of the fundamental-mode RRL, as well as the ratio of RR1 to RR0 stars. We find $\langle P_{RR0} \rangle = 0.63 \pm 0.07$ d and $\langle P_{RR1} \rangle = 0.37 \pm 0.02$ d. RR1 stars make up 54% of the single-mode RRL stars. Although $\langle P_{RR0} \rangle$ is somewhat lower than the usual canonical value of ∼0.68, these values, as well as the very low metallicity, point to M 68 being an Oosterhoff II cluster, in agreement with previous classifications (e.g. Lee & Carney 1999). As mentioned earlier, the fact that M 68 is a clear Oosterhoff II type disagrees with studies concluding that M 68 could have an extragalactic origin (e.g. Yoon & Lee 2002), since globular clusters in satellite dSph galaxies of the Milky Way fall mostly within the gap between Oosterhoff Types I and II.

Plotting the RRL stars on a "Bailey" diagram ($\log P - A$, where A denotes the amplitude of the RRL light curve; Fig. 17) also allows us to confirm the Oostheroff II classification, by comparing the location of our RRL stars to the analytical tracks derived by Zorotovic et al. (2010) by fitting the loci of normal and evolved stars of Cacciari et al. (2005). Figure 17 shows that the locations of our RRL stars are in good agreement with these tracks (for the V band) and those of Kunder et al. (2013b) (who rescaled those tracks for the I band). However, it is obvious from the I-band plot (bottom panel of Fig. 17) that the RRL loci for M 68 are different from those of Oosterhoff Type-II clusters

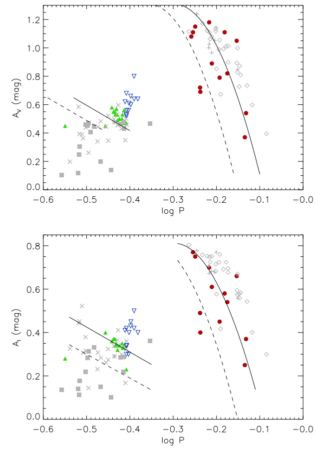

Fig. 17. Bailey diagram of the light curve amplitude A against $\log P$ for RRL stars in M 68 in the V (*top*) and I (*bottom*) bands. The locations of confirmed RRL stars are marked in red with filled circles (RR0), green filled triangles (RR1), and blue open inverted triangles (RR01). For the RR01 stars, the amplitude is that of the dominant mode, which is the first overtone in all cases here. For the V-band diagram, we also plot the tracks derived by Zorotovic et al. (2010) for evolved stars (solid lines), found by shifting the relations obtained by fitting data for the Oosterhoff type I cluster M 3 (dashed lines) by 0.06 in $\log P$. For the I-band diagram, we plot the rescaling of those relations by Kunder et al. (2013b) for Oosterhoff type I (dashed lines) and type II (solid lines) clusters. On both diagrams we also plot the RRL stars in Oosterhoff type II clusters NGC 5024 (Arellano Ferro et al. 2011) and M 9 (Arellano Ferro et al. 2013a) in light grey. For those, RR0 and RR1 stars are plotted as open diamonds and filled squares, respectively, with RRL stars exhibiting Blazhko modulation plotted as + signs (RR0) and crosses (RR1). One double-mode star is also plotted as an asterisk.

Table 9. Different metallicity estimates for M 68 in the literature.

Reference	$[Fe/H]_{ZW}$	$[Fe/H]_{UVES}$	Method
This work	−2.07 ± 0.06	−2.20 ± 0.10	Fourier decomposition of RRL light curves
This work	−2.09 ± 0.26	−2.24 ± 0.42	M_V-[Fe/H] relation
Carretta et al. (2009b)	−2.10 ± 0.04	−2.27 ± 0.07	UVES spectroscopy of red giants
Carretta et al. (2009c)	−2.08 ± 0.04	−2.23 ± 0.07	FLAMES/GIRAFFE spectra of red giants
Rutledge et al. (1997)	−2.11 ± 0.03	−2.27 ± 0.05	CaII triplet
Harris (1996)	−2.23	−2.47	Globular cluster catalogue
Suntzeff et al. (1991)	−2.09	−2.24	Spectroscopy of RR Lyrae/ ΔS index
Gratton & Ortolani (1989)	−1.92 ± 0.06	−1.97 ± 0.09	High-resolution spectroscopy
Minniti et al. (1993)	−2.17 ± 0.05	−2.37 ± 0.08	FeI and FeII spectral lines
Zinn & West (1984)	−2.09 ± 0.11	−2.24 ± 0.18	Q_{39} index
Zinn (1980)	−2.19 ± 0.06	−2.41 ± 0.10	Q_{39} index

Notes. Values were converted using Eq. (11) where necessary.

NGC 5024 (Arellano Ferro et al. 2011) and M 9 (Arellano Ferro et al. 2013a), but agree with the loci for NGC 2808 (Kunder et al. 2013b).

6.2. Cluster metallicity

Although Clement et al. (2001) found a correlation between the metallicity of a globular cluster and the mean period of its RR0 stars, $\langle P_{RR0} \rangle$, they note that this relation does not hold when $\langle P_{RR0} \rangle$ is larger than 0.6 d, i.e. for Oosterhoff Type-II clusters. Instead, we estimate the metallicity of M 68 by calculating the average of the metallicities we derived for RRL stars in this cluster. As in our previous papers (e.g. Kains et al. 2013), we assume that there is no systematic offset between the metallicities derived for RR0 and RR1 stars. Using this method, we find a mean metallicity of $[Fe/H]_{ZW} = -2.07 \pm 0.06$ (using Eq. (9) to derive RR0 metallicities) and $[Fe/H]_{ZW} = -2.13 \pm 0.11$ (using Eq. (10)), corresponding to $[Fe/H]_{UVES} = -2.20 \pm 0.10$ and $[Fe/H]_{UVES} = -2.30 \pm 0.17$, respectively. Both values are in excellent agreement with the value of Carretta et al. (2009b), who find $[Fe/H]_{UVES} = -2.27 \pm 0.01 \pm 0.07$ (statistical and systematic errors, respectively) and with most values in the literature, listed in Table 9. In the rest of this paper, we use $[Fe/H]_{ZW} = -2.07 \pm 0.06$ as the cluster metallicity, owing to the larger scatter in RR0 metallicities derived using Eq. (10) and to the problem with uncertainties in the relation of Nemec et al. (2013) already mentioned in Sect. 4.1.

6.3. Reddening

Individual RR0 light curves can be used to estimate the reddening for each star, using their colour near the point of minimum brightness. The method was first proposed by Sturch (1966) and further developed in several studies, most recently by Guldenschuh et al. (2005) and Kunder et al. (2010). Guldenschuh et al. (2005) find that the intrinsic $(V-I)_0$ colour of RR0 stars between phases 0.5 and 0.8 is $(V-I)_0^{\phi[0.5-0.8]} = 0.58 \pm 0.02$ mag. By calculating the $(V-I)$ colour for each of our light curves between those phases and comparing it to the value of Guldenschuh et al. (2005), we can therefore calculate values of $E(V-I)$, which we can then convert through $E(B-V) = E(V-I)/1.616$ (e.g. Arellano Ferro et al. 2013a). Stars showing Blazhko modulation were excluded from this calculation, as were stars with poor I−band light curves, leading to reddening estimates for V2, V12, V14, V22, V23, V35, and V46. We found a mean reddening of 0.05 ± 0.05 mag, within the range of values published (see Sect. 6.4.1).

6.4. Distance

6.4.1. Using the RRL stars

The Fourier decomposition of RRL stars can also be used to derive a distance modulus to the cluster. The Fourier fit parameter A_0 corresponds to the intensity-weighted mean V magnitude of the light curve, and since we also derived absolute magnitudes for each star with a good Fourier decomposition, this can be used to calculate the distance modulus to each star.

For RR0 stars, the mean value of A_0 is 15.64 ± 0.08 mag, while the mean absolute value is $\langle M_V \rangle = 0.49 \pm 0.07$ mag. From this, we find a distance modulus $\mu = 15.15 \pm 0.11$ mag. For RR1 stars, we find $\langle A_0 \rangle = 15.68 \pm 0.03$ mag and $\langle M_V \rangle = 0.53 \pm 0.01$ mag, yielding $\mu = 15.15 \pm 0.03$ mag.

Many values of $E(B-V)$ have been published for M 68, ranging from 0.01 mag (e.g. Racine 1973) to 0.07 mag (e.g. Bica & Pastoriza 1983). Recent studies have tended to use $E(B-V) = 0.05$ mag, which is the value listed in the catalogue of Harris (1996). Piersimoni et al. (2002) derived a value of $E(B-V) = 0.05 \pm 0.01$ from BVI photometry of RRL stars and empirical relations, and this coincides with the value we derived in Sect. 6.3, although uncertainties on our estimate are greater. We therefore adopt the value of Piersimoni et al. (2002) and a value of $R_V = 3.1$ for the Milky Way. From this we find true distance moduli of $\mu_0 = 15.00 \pm 0.11$ mag from RR0 stars and $\mu_0 = 15.00 \pm 0.05$ mag from RR1. These values correspond to physical distances of 10.00 ± 0.49 kpc and 9.99 ± 0.21 kpc, respectively, and are consistent with values reported in the literature, examples of which we list in Table 10.

6.4.2. Using SX Phoenicis stars

We can derive distances to SX Phe stars thanks to empirical period-luminosity ($P-L$) relations (e.g. Jeon et al. 2003). Here we calculate distances to the SX Phe stars in our images (see Table 3) using the $P-L$ relation of Cohen & Sarajedini (2012),

$$M_V = -(1.640 \pm 0.110) - (3.389 \pm 0.090)\log P_f, \quad (24)$$

where P_f is the fundamental-mode pulsation period. This provides us with another independent estimate of the distance to M 68. Arellano Ferro et al. (2011) derived their own $P-L$ relation, using only SX Phe stars in metal-poor globular clusters, and have shown a good match of their relation to the locus of SX Phe in other clusters (e.g. Arellano Ferro et al. 2014, 2013b).

When assuming that the values given in Table 3 are the fundamental periods and when using them with Eq. (24), as well as with the relation of Arellano Ferro et al. (2011), the distances

Table 10. Distance modulus and physical distance estimates for M 68 in the literature.

Reference	μ_0 [mag]	Distance [kpc]	Method
This work	15.00 ± 0.11	10.00 ± 0.49	Fourier decomposition of RR0 light curves
This work	15.00 ± 0.05	9.99 ± 0.21	Fourier decomposition of RR1 light curves
This work	14.97 ± 0.11	9.84 ± 0.50	SX Phe $P-L$ relation
This work	15.00 ± 0.07	10.00 ± 0.30	M_V−[Fe/H] relation for cluster RRL stars
Rosenberg et al. (1999)	15.02	10.07	CMD analysis
Caloi et al. (1997)	15.15	10.72	CMD isochrone fitting
Brocato et al. (1997)	15.16 ± 0.10	10.76 ± 0.50	CMD isochrone fitting
Gratton et al. (1997)	15.24 ± 0.08	11.17 ± 0.41	CMD analysis
Harris (1996)	15.06	10.3	Globular cluster catalogue
Straniero & Chieffi (1991)	14.99 ± 0.03	9.94 ± 0.14	CMD isochrone fitting
McClure et al. (1987)	15.03 ± 0.15	10.14 ± 0.70	CMD analysis
Alcaino (1977)	14.97	9.8	Magnitude of the HB
Harris (1975)	14.91	9.6	Mean magnitude of RRL stars

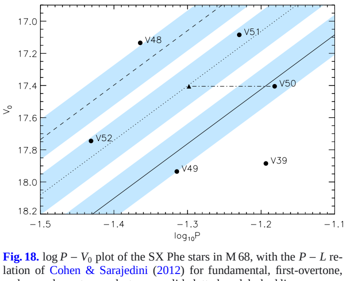

Fig. 18. $\log P - V_0$ plot of the SX Phe stars in M 68, with the $P-L$ relation of Cohen & Sarajedini (2012) for fundamental, first-overtone, and second-overtone pulsators as solid, dotted, and dashed lines, respectively. Shaded areas show $1\text{-}\sigma$ boundaries for each case. The relations have been shifted to a distance of 9.99 ± 0.21 kpc (see Sect. 6.4.1), and the SX Phe magnitudes have been dereddened using our adopted value of $E(B-V) = 0.05 \pm 0.01$ mag. The location of the black filled circles in this plot correspond to the periods listed in Table 3, and for V50 the first-overtone period is shown as a triangle with a dash-dotted line connecting the two periods.

derived for V39, V48, V51, and V52 disagree with the values we found using RRL stars and with most values in the literature (see Table 10). In Fig. 18, we plot $\log P$ against dereddened magnitudes V_0 (using our adopted value $E(B-V) = 0.05 \pm 0.01$ mag), as well as the relations of Cohen & Sarajedini (2012) for fundamental, first-, and second- overtone SX Phe pulsators, shifted to a distance of 9.99 ± 0.21 kpc, the cluster distance we derived in Sect. 6.4.1 using RR1 stars. From this, it is clear that V49 pulsates in the fundamental mode and that the periods of the double-mode pulsator V50 (see Sect. 5.2) do correspond to fundamental and first-overtone periods. Figure 18 also suggests that V51 and V52 are first-overtone pulsators and that V48 is a second-overtone pulsator. W94 suggested that V48 might be a first-overtone pulsator, noting however that it would be bright for its period. Figure 18 also suggests that V39 might not be a cluster member, with the large distance hinting that it may be a background object.

For the overtone pulsators, we can "fundamentalise" the periods to then use Eq. (24) in order to derive empirical values of

Table 11. Absolute magnitudes, true distance moduli, and physical distance for the SX Phe stars in M 68, derived using the $P-L$ relation of Cohen & Sarajedini (2012) after "fundamentalisation" of the pulsation period.

Reference	M_V[mag]	μ_0 [mag]	Distance [kpc]
V39	2.40 ± 0.11	15.48 ± 0.25	12.48 ± 1.42
V48	2.28 ± 0.11	14.86 ± 0.13	9.35 ± 0.55
V49	2.81 ± 0.11	15.12 ± 0.21	10.57 ± 1.03
V50	2.36 ± 0.11	14.04 ± 0.15	10.19 ± 0.73
V51	2.17 ± 0.11	14.92 ± 0.14	9.63 ± 0.64
V52	2.85 ± 0.11	14.89 ± 0.14	9.53 ± 0.60

M_V, μ_0, and the distance. To do this, we use the canonical first- and second-overtones to fundamental period ratios, respectively $P_1/P_f \sim 0.783$ (e.g. Jeon et al. 2004; Santolamazza et al. 2001; Gilliland et al. 1998) and $P_2/P_f \sim 0.62$ (Santolamazza et al. 2001). Using these values to calculate P_f, we found the corrected absolute magnitudes and distances listed in Table 11.

We note that the discrepant distance estimates could alternatively be due to V48 being a foreground object, while V51 clearly suffers from blending from two nearby stars of comparable brightness, meaning that its reference flux could be over-estimated by as much as a factor of 2. If this is the case, V51 would fall on the track for fundamental pulsators in Fig. 18. Higher resolution data could help determine which explanation is correct for V51, while radial velocity measurements would help address the cluster membership of V39 and V48.

Using the corrected values and excluding V39, we find an average distance modulus of $\mu_0 = 14.97 \pm 0.11$ mag, corresponding to a physical distance of 9.84 ± 0.50 kpc, in good agreement with the values we found using RRL stars in the previous section.

6.5. Distance and metallicity from the M_V–[Fe/H] relation

Many studies in the literature have compiled magnitude and metallicity measurements from globular cluster observations to fit a linear relation between the metallicity of a cluster and the mean magnitude of its RRL stars, $M_V = \alpha[Fe/H] + \beta$. Here we use the relation derived by Kains et al. (2012), with coefficients $\alpha = 0.16 \pm 0.01$ and $\beta = 0.85 \pm 0.02$, for a metallicity given on the ZW scale. Using the metallicity value of $[Fe/H]_{ZW} = -2.07 \pm 0.06$ derived in Sect. 6.2, we find a mean absolute magnitude of 0.52 ± 0.03 mag, in good agreement with the value found in Sect. 6.4.1. We can now use this to estimate the distance to M 68 in a similar way to what was done in that section. Since the M_V–[Fe/H] does not distinguish between

Table 12. Age estimates for M 68 in the literature.

Reference	Age [Gyr]	Method
VandenBerg et al. (2013)	12.00 ± 0.25	CMD isochrone fitting
Rakos & Schombert (2005)	11.2	Strömgren photometry
Salaris & Weiss (2002)	11.2 ± 0.9	CMD analysis
Caloi et al. (1997)	12 ± 2	CMD analysis
Gratton et al. (1997)	10.1 ± 1.2	CMD isochrone fitting
Gratton et al. (1997)	11.4 ± 1.4	CMD isochrone fitting
Brocato et al. (1997)	10	CMD analysis
Jimenez et al. (1996)	12.6 ± 2	CMD analysis
Chaboyer et al. (1996)	12.8 ± 0.3	CMD analysis
Sandage (1993)	12.1 ± 1.2	CMD isochrone fitting
Straniero & Chieffi (1991)	19 ± 1	CMD isochrone fitting
Alcaino et al. (1990)	13 ± 3	CMD isochrone fitting
Chieffi & Straniero (1989)	16	CMD isochrone fitting
McClure et al. (1987)	14 ± 1	CMD isochrone fitting
Peterson (1987)	15.5	CMD analysis
Vandenberg (1986)	18	CMD analysis

RR0 and RR1, we use average value over all RRL types in this calculation.

We find a mean magnitude for all RRL stars of $\langle A_0 \rangle = 15.68 \pm 0.05$ mag, yielding a distance modulus of $\mu = 15.16 \pm 0.06$ mag. With $E(B-V) = 0.05 \pm 0.01$ mag and $R_V = 3.1$ as in Sect. 6.4.1, this gives a true distance modulus of 15.00 ± 0.07 mag, corresponding to a physical distance of 10.00 ± 0.30 kpc.

Conversely, we can also estimate the mean metallicity of the cluster using the M_V–[Fe/H] relation and the values found from Eqs. (17) and (18). We find a mean value for all RRL stars with a good Fourier decomposition of $M_V = 0.52 \pm 0.04$, yielding $[\mathrm{Fe/H}]_{\mathrm{ZW}} = -2.09 \pm 0.26$, in agreement with our values in Sect. 6.2, but with a much larger error bar.

6.6. Age

Although our CMD does not allow us to derive a precise age, we used our data to check consistency of our CMD with age estimates of M 68 from the literature (Table 12) by overplotting the isochrones of Dotter et al. (2008), using our estimate of the cluster metallicity of $[\mathrm{Fe/H}]_{\mathrm{ZW}} = -2.07 \pm 0.06$. We interpolated those isochrones to match the alpha-element abundance for this cluster of $[\alpha/\mathrm{Fe}]$ of ~0.3 (e.g. Carney 1996). We found that our CMD is consistent with an age of 13.0 ± 0.50 Gyr, in agreement with the most recent values in the literature.

7. Conclusions

We carried out a detailed survey of variability in M 68 using CCD observations, as well as some EMCCD images. We have shown that data from identical telescopes in a telescope network could be reduced using a reference image from a single telescope, i.e. that the network could be considered to be a single telescope for the purposes of data handling. This significantly facilitates the analysis of time-series data taken with such networks.

With our observations we were able to recover all known variables within our field of view, as well as to detect four new SX Phe variables near the cluster core. We used the light curves of RRL stars in our data to derive estimates for their metallicity, effective temperature, luminosity, and mean mass. Those were then used to infer values for the cluster metallicity, reddening, and distance. Furthermore, the light curves of the SX Phe stars were also used to obtain an additional independent estimate of distance.

We found a metallicity $[\mathrm{Fe/H}] = -2.07 \pm 0.06$ on the ZW scale and -2.20 ± 0.10 on the UVES scale. We derived distance moduli of $\mu_0 = 15.00 \pm 0.11$ mag (using RR0 stars), $\mu_0 = 15.00 \pm 0.05$ mag (using RR1 stars), $\mu_0 = 14.97 \pm 0.11$ mag (using SX Phe stars), and $\mu_0 = 15.00 \pm 0.07$ mag (using the M_V–[Fe/H] relation for RRL stars), corresponding to physical distances of 10.00 ± 0.49, 9.99 ± 0.21, 9.84 ± 0.50, and 10.00 ± 0.30 kpc, using RR0, RR1, SX Phe stars, and the M_V–[Fe/H] relation, respectively. Finally, we used our CMD to check the consistency of age estimates in the literature for M 68. We also used archival data to refine period estimates and calculate period changes where appropriate, for the RRL stars. The grid search we used here is particularly useful for estimating period changes for stars for which not many maxima were observed; in those cases, the traditional *O–C* method struggles to yield a period-change value that phases all data sets well, while the grid search performs better. We also examined in detail the light curves of double-mode pulsators in this cluster. The ratios of the RR01 periods enabled us to estimate their masses with the new mass-period-metallicity empirical relation of Marconi et al. (2015).

Thanks to the latest DIA methods, we can now be confident that all of the RRL stars in M 68 are known. Carrying out such studies for more Milky Way globular clusters will help us strengthen observational evidence for the Oosterhoff dichotomy, which in turn can be used to shed light on the origin of the Galactic halo.

Acknowledgements. The research leading to these results has received funding from the European Community's Seventh Framework Programme (/FP7/2007-2013/) under grant agreements No. 229517 and 268421. AAF acknowledges the support of DGAPA-UNAM through project IN104612. This publication was made possible by NPRP grant # X-019-1-006 from the Qatar National Research Fund (a member of Qatar Foundation). OW and JS acknowledge support from the Communauté française de Belgique – Actions de recherche concertées – Académie universitaire Wallonie-Europe. TCH gratefully acknowledges financial support from the Korea Research Council for Fundamental Science and Technology (KRCF) through the Young Research Scientist Fellowship Program. TCH acknowledges financial support from KASI (Korea Astronomy and Space Science Institute) grant number 2012-1-410-02. KA, MD, MH, and CL are supported by NPRP grant NPRP-09-476-1-78 from the Qatar National Research Fund (a member of Qatar Foundation). The Danish 1.54m telescope is operated based on a grant from the Danish Natural Science Foundation (FNU). S.H.G. and XBW acknowledge support from National Natural Science Foundation of China (grants Nos. 10373023 and 10773027). H.K. acknowledges support from a Marie Curie Intra-European Fellowship. M.R. acknowledges support from FONDECYT postdoctoral fellowship No. 3120097. This work has made extensive use of the ADS and SIMBAD services, for which we are grateful.

References

Alard, C. 1999, A&A, 343, 10
Alard, C. 2000, A&ASS, 144, 363
Albrow, M. D., Horne, K., Bramich, D. M., et al. 2009, MNRAS, 397, 2099
Alcaino, G. 1977, A&ASS, 29, 9
Alcaino, G., Liller, W., Alvarado, F., & Wenderoth, E. 1990, AJ, 99, 1831
Arellano Ferro, A., Rojas López, V., Giridhar, S., & Bramich, D. M. 2008, MNRAS, 384, 1444
Arellano Ferro, A., Giridhar, S., & Bramich, D. M. 2010, MNRAS, 402, 226
Arellano Ferro, A., Figuera Jaimes, R., Giridhar, S., et al. 2011, MNRAS, 416, 2265
Arellano Ferro, A., Bramich, D. M., Figuera Jaimes, R., et al. 2013a, MNRAS, 434, 1220
Arellano Ferro, A., Bramich, D. M., Giridhar, S., et al. 2013b, Acta Astron., 63, 429
Arellano Ferro, A., Ahumada, J. A., Calderón, J. H., & Kains, N. 2014, Rev. Mex. Astron. Astrofis., 50, 307
Bellini, A., Anderson, J., & Bedin, L. R. 2011, PASP, 123, 622
Belserene, E. P. 1964, AJ, 69, 475
Benedict, G. F., McArthur, B. E., Fredrick, L. W., et al. 2002, AJ, 123, 473
Bessell, M. S. 2005, ARA&A, 43, 293
Bica, E. L. D., & Pastoriza, M. G. 1983, A&SS, 91, 99
Blažko, S. 1907, Astron. Nachr., 175, 325
Bono, G., Caputo, F., Castellani, V., et al. 2003, MNRAS, 344, 1097
Bragaglia, A., Gratton, R. G., Carretta, E., et al. 2001, AJ, 122, 207
Bramich, D. M. 2008, MNRAS, 386, L77
Bramich, D. M., & Freudling, W. 2012, MNRAS, 424, 1584
Bramich, D. M., Figuera Jaimes, R., Giridhar, S., & Arellano Ferro, A. 2011, MNRAS, 413, 1275
Bramich, D. M., Horne, K., Albrow, M. D., et al. 2013, MNRAS, 428, 2275
Brocato, E., Castellani, V., & Ripepi, V. 1994, AJ, 107, 622
Brocato, E., Castellani, V., & Piersimoni, A. 1997, ApJ, 491, 789
Cacciari, C., Corwin, T. M., & Carney, B. W. 2005, AJ, 129, 267
Caloi, V., D'Antona, F., & Mazzitelli, I. 1997, AS&S, 320, 823
Carney, B. W. 1996, PASP, 108, 900
Carretta, E., Bragaglia, A., Gratton, R., D'Orazi, V., & Lucatello, S. 2009a, A&A, 508, 695
Carretta, E., Bragaglia, A., Gratton, R., & Lucatello, S. 2009b, A&A, 505, 139
Carretta, E., Bragaglia, A., Gratton, R. G., et al. 2009c, A&A, 505, 117
Castelli, F. 1999, A&A, 346, 564
Catelan, M. 2009, A&SS, 320, 261
Chaboyer, B., Demarque, P., Kernan, P. J., Krauss, L. M., & Sarajedini, A. 1996, MNRAS, 283, 683
Chieffi, A., & Straniero, O. 1989, ApJS, 71, 47
Clement, C. M. 1990, AJ, 99, 240
Clement, C. M., Ferance, S., & Simon, N. R. 1993, ApJ, 412, 183
Clement, C. M., Muzzin, A., Dufton, Q., et al. 2001, AJ, 122, 2587
Cohen, R. E., & Sarajedini, A. 2012, MNRAS, 419, 342
Cox, A. N. 1991, ApJ, 381, L71
Di Fabrizio, L., Clementini, G., Maio, M., et al. 2005, A&A, 430, 603
Dotter, A., Chaboyer, B., Jevremović, D., et al. 2007, AJ, 134, 376
Dotter, A., Chaboyer, B., Jevremović, D., et al. 2008, ApJS, 178, 89
Dworetsky, M. M. 1983, MNRAS, 203, 917
Feuchtinger, M. U. 1998, A&A, 337, L29
Figuera Jaimes, R., Arellano Ferro, A., Bramich, D. M., Giridhar, S., & Kuppuswamy, K. 2013, A&A, 556, A20
Freedman, W. L., Madore, B. F., Gibson, B. K., et al. 2001, ApJ, 553, 47
Gilliland, R. L., Bono, G., Edmonds, P. D., et al. 1998, ApJ, 507, 818
Gratton, R. G., & Ortolani, S. 1989, A&A, 211, 41
Gratton, R. G., Fusi Pecci, F., Carretta, E., et al. 1997, ApJ, 491, 749
Gratton, R. G., Bragaglia, A., Clementini, G., et al. 2004, A&A, 421, 937
Greenstein, J. L., Bidelman, W. P., & Popper, D. M. 1947, PASP, 59, 143
Guldenschuh, K. A., Layden, A. C., Wan, Y., et al. 2005, PASP, 117, 721
Harpsøe, K. B. W., Jørgensen, U. G., Andersen, M. I., & Grundahl, F. 2012, A&A, 542, A23
Harris, W. E. 1975, ApJS, 29, 397
Harris, W. E. 1996, AJ, 112, 1487
Jeon, Y.-B., Lee, M. G., Kim, S.-L., & Lee, H. 2003, AJ, 125, 3165
Jeon, Y.-B., Lee, M. G., Kim, S.-L., & Lee, H. 2004, AJ, 128, 287
Jimenez, R., Thejll, P., Jorgensen, U. G., MacDonald, J., & Pagel, B. 1996, MNRAS, 282, 926
Jurcsik, J. 1995, Acta Astron., 45, 653
Jurcsik, J. 1998, A&A, 333, 571
Jurcsik, J., & Kovács, G. 1996, A&A, 312, 111
Jurcsik, J., Hajdu, G., Szeidl, B., et al. 2012, MNRAS, 419, 2173
Kains, N., Bramich, D. M., Figuera Jaimes, R., et al. 2012, A&A, 548, A92
Kains, N., Bramich, D. M., Arellano Ferro, A., et al. 2013, A&A, 555, A36
Kinman, T. D. 2002, IBVS, 5354, 1
Kovács, G. 1998, Mem. Soc. Astron. Ital., 69, 49
Kovács, G. 2002, in Omega Centauri, A Unique Window into Astrophysics, eds. F. van Leeuwen, J. D. Hughes, & G. Piotto, ASP Conf. Ser., 265, 163
Kovács, G., & Walker, A. R. 2001, A&A, 371, 579
Kovacs, G., Buchler, J. R., & Marom, A. 1991, A&A, 252, L27
Kunder, A., Chaboyer, B., & Layden, A. 2010, AJ, 139, 415
Kunder, A., Stetson, P. B., Cassisi, S., et al. 2013a, AJ, 146, 119
Kunder, A., Stetson, P. B., Catelan, M., Walker, A. R., & Amigo, P. 2013b, AJ, 145, 33
Lane, R. R., Kiss, L. L., Lewis, G. F., et al. 2009, MNRAS, 400, 917
Lee, Y.-W. 1991, ApJ, 367, 524
Lee, J.-W., & Carney, B. W. 1999, AJ, 118, 1373
Lee, Y.-W., Demarque, P., & Zinn, R. 1990, ApJ, 350, 155
Lenz, P., & Breger, M. 2005, Commun. Asteroseismol., 146, 53
Marconi, M., Coppola, G., Bono, G., et al. 2015, ApJ, submitted [arXiv:1505.02531]
McClure, R. D., Hesser, J. E., Stetson, P. B., Vandenberg, D. A., & Bell, R. A. 1987, AJ, 93, 1144
Minniti, D., Geisler, D., Peterson, R. C., & Claria, J. J. 1993, ApJ, 413, 548
Montegriffo, P., Ferraro, F. R., Origlia, L., & Fusi Pecci, F. 1998, MNRAS, 297, 872
Morgan, S. M., Wahl, J. N., & Wieckhorst, R. M. 2007, MNRAS, 374, 1421
Nemec, J. M., Hazen-Liller, M. L., & Hesser, J. E. 1985, ApJS, 57, 329
Nemec, J. M., Cohen, J. G., Ripepi, V., et al. 2013, ApJ, 773, 181
Oosterhoff, P. T. 1939, The Observatory, 62, 104
Petersen, J. O. 1973, A&A, 27, 89
Peterson, C. J. 1987, PASP, 99, 1153
Piersimoni, A. M., Bono, G., & Ripepi, V. 2002, AJ, 124, 1528
Pojmanski, G. 2002, Acta Astron., 52, 397
Poretti, E., Paparó, M., Deleuil, M., et al. 2010, A&A, 520, A108
Pritzl, B. J., Smith, H. A., Catelan, M., & Sweigart, A. V. 2001, AJ, 122, 2600
Pritzl, B. J., Smith, H. A., Catelan, M., & Sweigart, A. V. 2002, AJ, 124, 949
Racine, R. 1973, AJ, 78, 180
Rakos, K., & Schombert, J. 2005, PASP, 117, 245
Rathbun, P., & Smith, H. 1997, PASP, 109, 1128
Rosenberg, A., Saviane, I., Piotto, G., & Aparicio, A. 1999, AJ, 118, 2306
Rosino, L., & Pietra, S. 1953, Mem. Soc. Astron. Ital., 24, 331
Rosino, L., & Pietra, S. 1954, Mem. Soc. Astron. Ital., 25, 227
Rutledge, G. A., Hesser, J. E., Stetson, P. B., et al. 1997, PASP, 109, 883
Salaris, M., & Weiss, A. 2002, A&A, 388, 492
Salaris, M., Chieffi, A., & Straniero, O. 1993, ApJ, 414, 580
Sandage, A. 1993, AJ, 106, 687
Santolamazza, P., Marconi, M., Bono, G., et al. 2001, ApJ, 554, 1124
Sariya, D. P., Lata, S., & Yadav, R. K. S. 2014, New Astron., 27, 56
Sekiguchi, M., & Fukugita, M. 2000, AJ, 120, 1072
Shapley, H. 1919, PASP, 31, 226
Shapley, H. 1920, ApJ, 51, 49
Simon, N. R., & Clement, C. M. 1993, ApJ, 410, 526
Skottfelt, J., Bramich, D. M., Figuera Jaimes, R., et al. 2013, A&A, 553, A111
Smith, H. A., & Manduca, A. 1983, AJ, 88, 982
Smith, H. A., & Wesselink, A. J. 1977, A&A, 56, 135
Sollima, A., Cassisi, S., Fiorentino, G., & Gratton, R. G. 2014, MNRAS, 444, 1862
Soszyński, I., Udalski, A., Szymański, M. K., et al. 2009, Acta Astron., 59, 1
Stagg, C., & Wehlau, A. 1980, AJ, 85, 1182
Stetson, P. B. 2000, PASP, 112, 925
Straniero, O., & Chieffi, A. 1991, ApJS, 76, 525
Sturch, C. 1966, ApJ, 143, 774
Suntzeff, N. B., Kinman, T. D., & Kraft, R. P. 1991, ApJ, 367, 528
Terzan, A., Rutily, B., & Ounnas, C. 1973, in Variable Stars in Globular Clusters and in Related Systems, ed. J. D. Fernie, IAU Colloq., 21, 76
van Agt, S. L. T. J., & Oosterhoff, P. T. 1959, Annalen van de Sterrewacht te Leiden, 21, 253
van Albada, T. S., & Baker, N. 1971, ApJ, 169, 311
Vandenberg, D. A. 1986, Mem. Soc. Astron. Ital., 57, 373
VandenBerg, D. A., Brogaard, K., Leaman, R., & Casagrande, L. 2013, ApJ, 775, 134
Walker, A. R. 1994, AJ, 108, 555
Yoon, S.-J., & Lee, Y.-W. 2002, Science, 297, 578
Zacharias, N., Finch, C., Girard, T., et al. 2010, AJ, 139, 2184
Zinn, R. 1980, ApJS, 42, 19
Zinn, R. 1993a, in The Globular Cluster-Galaxy Connection, eds. G. H. Smith & J. P. Brodie, ASP Conf. Ser., 48, 302
Zinn, R. 1993b, in The Globular Cluster-Galaxy Connection, eds. G. H. Smith, & J. P. Brodie, ASP Conf. Ser., 48, 38
Zinn, R., & West, M. J. 1984, ApJS, 55, 45

Zorotovic, M., Catelan, M., Smith, H. A., et al. 2010, AJ, 139, 357

[1] Space Telescope Science Institute, 3700 San Martin Drive, Baltimore, MD 21218, USA
e-mail: nkains@stsci.edu
[2] European Southern Observatory, Karl-Schwarzschild Straße 2, 85748 Garching bei München, Germany
[3] Instituto de Astronomía, Universidad Nacional Autónoma de Mexico, 04310 Coyoácan, Mexico
[4] SUPA School of Physics & Astronomy, University of St. Andrews, North Haugh, St. Andrews, KY16 9SS, UK
[5] Qatar Environment and Energy Research Institute, Qatar Foundation, Tornado Tower, Floor 19, PO Box 5825, Doha, Qatar
[6] Niels Bohr Institute, University of Copenhagen, Juliane Maries vej 30, 2100 Copenhagen, Denmark
[7] Centre for Star and Planet Formation, Geological Museum, Øster Voldgade 5, 1350 Copenhagen, Denmark
[8] Las Cumbres Observatory Global Telescope Network, 6740 Cortona Drive, Suite 102, Goleta, CA 93117, USA
[9] School of Mathematical Sciences, Queen Mary, University of London, Mile End Road, London E1 4NS, UK
[10] Qatar Foundation, PO Box 5825, Doha, Qatar
[11] Max Planck Institute for Solar System Research, Justus-von-Liebig-Weg 3, 37077 Göttingen, Germany
[12] Astrophysics Research Institute, Liverpool John Moores University, Twelve Quays House, Egerton Wharf, Birkenhead, Wirral., CH41 1LD, UK
[13] Dipartimento di Fisica "E.R. Caianiello", Università degli Studi di Salerno, via Giovanni Paolo II 132, 84084 Fisciano, Italy
[14] Istituto Nazionale di Fisica Nucleare, Sezione di Napoli, Italy
[15] Istituto Internazionale per gli Alti Studi Scientifici (IIASS), via Giuseppe Pellegrino, 19, 84019 Vietri Sul Mare Salerno, Italy
[16] Max Planck Institute for Astronomy, Königstuhl 17, 69117 Heidelberg, Germany
[17] Yunnan Observatories, Chinese Academy of Sciences, 650011 Kunming, PR China
[18] Key Laboratory for the Structure and Evolution of Celestial Objects, Chinese Academy of Sciences, 650011 Kunming, PR China
[19] Korea Astronomy and Space Science Institute, 305–348 Daejeon, Korea
[20] Finnish Centre for Astronomy with ESO (FINCA), University of Turku, Väisäläntie 20, 21500 Piikkiö, Finland
[21] Instituto de Astrofísica, Facultad de Física, Pontificia Universidad Católica de Chile, Av. Vicuña Mackenna 4860, 7820436 Macul, Santiago, Chile
[22] Department of Physics, Sharif University of Technology, PO Box 11155–9161, Tehran, Iran
[23] Perimeter Institute for Theoretical Physics, 31 Caroline St. N., Waterloo ON, N2L 2Y5, Canada
[24] Astrophysics Group, Keele University, Staffordshire, ST5 5BG, UK
[25] Institut d'Astrophysique et de Géophysique, Université de Liège, Allée du 6 Août 17, Sart Tilman, Bât. B5c, 4000 Liège, Belgium

The Astrophysical Journal, 804:20 (25pp), 2015 May 1 doi:10.1088/0004-637X/804/1/20

PATHWAY TO THE GALACTIC DISTRIBUTION OF PLANETS: COMBINED *SPITZER* AND GROUND-BASED MICROLENS PARALLAX MEASUREMENTS OF 21 SINGLE-LENS EVENTS

S. Calchi Novati[1,2,3,53], A. Gould[4,52], A. Udalski[5,46], J. W. Menzies[6,47], I. A. Bond[7,48], Y. Shvartzvald[8,49], R. A. Street[9,50,51], M. Hundertmark[10,11,50,51], C. A. Beichman[1], J. C. Yee[12,52,54], S. Carey[13], R. Poleski[5,4], J. Skowron[5], S. Kozłowski[5], P. Mróz[5], P. Pietrukowicz[5], G. Pietrzyński[5,14], M. K. Szymański[5], I. Soszyński[5], K. Ulaczyk[5], Ł. Wyrzykowski[5,15]
(The OGLE collaboration),
M. Albrow[16], J. P. Beaulieu[17,18], J. A. R. Caldwell[19], A. Cassan[17], C. Coutures[17], C. Danielski[20], D. Dominis Prester[21], J. Donatowicz[22], K. Lončarić[21], A. McDougall[16], J. C. Morales[18], C. Ranc[17], W. Zhu[4]
(The PLANET collaboration),
F. Abe[23], R. K. Barry[24], D. P. Bennett[25], A. Bhattacharya[25], D. Fukunaga[23], K. Inayama[26], N. Koshimoto[27], S. Namba[27], T. Sumi[27], D. Suzuki[25], P. J. Tristram[28], Y. Wakiyama[23], A. Yonehara[26]
(The MOA collaboration),
D. Maoz[8], S. Kaspi[8], M. Friedmann[8]
(The Wise group),
E. Bachelet[29], R. Figuera Jaimes[11,30,51], D. M. Bramich[29,51], Y. Tsapras[9,31,51], K. Horne[11], C. Snodgrass[32,33,51], J. Wambsganss[34,51], I. A. Steele[35], N. Kains[30]
(The RoboNet collaboration),
V. Bozza[2,36], M. Dominik[11,50,55], U. G. Jørgensen[10], K. A. Alsubai[29], S. Ciceri[37], G. D'Ago[2,36,50], T. Haugbølle[10], F. V. Hessman[38], T. C. Hinse[39], D. Juncher[10], H. Korhonen[10,40], L. Mancini[37], A. Popovas[10], M. Rabus[37,41], S. Rahvar[42], G. Scarpetta[2,3,36], R. W. Schmidt[34,50], J. Skottfelt[10], J. Southworth[43], D. Starkey[11], J. Surdej[44], O. Wertz[44], M. Zarucki[3]
(The MiNDSTEp consortium),
and
B. S. Gaudi[4], R. W. Pogge[4], D. L. DePoy[45]
(The μFUN collaboration)

[1] NASA Exoplanet Science Institute, MS 100-22, California Institute of Technology, Pasadena, CA 91125, USA
[2] Dipartimento di Fisica "E. R. Caianiello," Università di Salerno, Via Giovanni Paolo II, I-84084 Fisciano (SA), Italy
[3] Istituto Internazionale per gli Alti Studi Scientifici (IIASS), Via G. Pellegrino 19, I-84019 Vietri Sul Mare (SA), Italy
[4] Department of Astronomy, Ohio State University, 140 W. 18th Ave., Columbus, OH 43210, USA
[5] Warsaw University Observatory, Al. Ujazdowskie 4, 00-478 Warszawa, Poland
[6] South African Astronomical Observatory, P.O. Box 9, Observatory 7935, South Africa
[7] Institute of Natural and Mathematical Sciences, Massey University, Private Bag 102-904, North Shore Mail Centre, Auckland, New Zealand
[8] School of Physics and Astronomy, Tel-Aviv University, Tel-Aviv 69978, Israel
[9] Las Cumbres Observatory Global Telescope Network, 6740 Cortona Drive, Suite 102, Goleta, CA 93117, USA
[10] Niels Bohr Institutet, Københavns Universitet, Juliane Maries Vej 30, DK-2100 København Ø, Denmark
[11] SUPA, School of Physics & Astronomy, North Haugh, University of St Andrews, KY16 9SS, Scotland, UK
[12] Harvard-Smithsonian Center for Astrophysics, 60 Garden St., Cambridge, MA 02138, USA
[13] Spitzer Science Center, MS 220-6, California Institute of Technology, Pasadena, CA, USA
[14] Universidad de Concepción, Departamento de Astronomia, Casilla 160-C, Concepción, Chile
[15] Institute of Astronomy, University of Cambridge, Madingley Road, Cambridge CB3 0HA, UK
[16] University of Canterbury, Dept. of Physics and Astronomy, Private Bag 4800, 8020 Christchurch, New Zealand
[17] Institut d'Astrophysique de Paris, UPMC-CNRS, UMR 7095, 98bis Boulevard Arago, F-75014 Paris, France
[18] LESIA, Observatoire de Paris, Section de Meudon 5, place Jules Janssen, F-92195 Meudon, France
[19] McDonald Observatory, 16120 St Hwy Spur 78 #2, Fort Davis, TX 79734, USA
[20] Institut d'Astrophysique Spatiale, UMR 8617, Université Paris Sud, F-91405 Orsay, France
[21] Department of Physics, University of Rijeka, Radmile Matej vcić 2, 51000 Rijeka, Croatia
[22] Technical University of Vienna, Department of Computing,Wiedner Hauptstrasse 10, A-1040 Wien, Austria
[23] Solar-Terrestrial Environment Laboratory, Nagoya University, Nagoya 464-8601, Japan
[24] Astrophysics Science Division, NASA Goddard Space Flight Center, Greenbelt, MD 20771, USA
[25] Department of Physics, University of Notre Dame, Notre Dame, IN 46556, USA
[26] Department of Physics, Faculty of Science, Kyoto Sangyo University, 603-8555 Kyoto, Japan
[27] Department of Earth and Space Science, Graduate School of Science, Osaka University, Toyonaka, Osaka 560-0043, Japan
[28] Mt. John University Observatory, P.O. Box 56, Lake Tekapo 8770, New Zealand
[29] Qatar Environment and Energy Research Institute, Qatar Foundation, P.O. Box 5825, Doha, Qatar
[30] European Southern Observatory, Karl-Schwarzschild-Str. 2, D-85748 Garching bei München, Germany
[31] School of Physics and Astronomy, Queen Mary University of London, Mile End Road, London E1 4NS, UK
[32] The Open University, Walton Hall, Milton Keynes MK7 6AA, UK
[33] Max Planck Institute for Solar System Research, Justus-von-Liebig-Weg 3, D-37077 Göttingen, Germany
[34] Astronomisches Rechen-Institut, Zentrum für Astronomie der Universität Heidelberg (ZAH), Mönchhofstraße 12-14, D-69120 Heidelberg, Germany
[35] Astrophysics Research Institute, Liverpool John Moores University, Liverpool CH41 1LD, UK
[36] Istituto Nazionale di Fisica Nucleare, Sezione di Napoli, Via Cintia, I-80126 Napoli, Italy
[37] Max Planck Institute for Astronomy, Königstuhl 17, D-69117 Heidelberg, Germany
[38] Institut für Astrophysik, Georg-August-Universität Göttingen, Friedrich-Hund-Platz 1, D-37077 Göttingen, Germany

[39] Korea Astronomy and Space Science Institute, 776 Daedeokdae-ro, Yuseong-gu, 305-348 Daejeon, Korea
[40] Finnish Centre for Astronomy with ESO (FINCA), University of Turku, Väisäläntie 20, FI-21500 Piikkiö, Finland
[41] Instituto de Astrofísica, Facultad de Física, Pontificia Universidad Católica de Chile, Av.Vicuña Mackenna 4860, 7820436 Macul, Santiago, Chile
[42] Department of Physics, Sharif University of Technology, P.O. Box 11155-9161 Tehran, Iran
[43] Astrophysics Group, Keele University, Staffordshire, ST5 5BG, UK
[44] Institut d'Astrophysique et de Géophysique, Université de Liège, 4000 Liège, Belgium
[45] Department of Physics and Astronomy, Texas A&M University, College Station, TX 77843-4242, USA
Received 2014 November 26; accepted 2015 February 23; published 2015 April 24

ABSTRACT

We present microlens parallax measurements for 21 (apparently) isolated lenses observed toward the Galactic bulge that were imaged simultaneously from Earth and *Spitzer*, which was ~1 AU west of Earth in projection. We combine these measurements with a kinematic model of the Galaxy to derive distance estimates for each lens, with error bars that are small compared to the Sun's galactocentric distance. The ensemble therefore yields a well-defined cumulative distribution of lens distances. In principle, it is possible to compare this distribution against a set of planets detected in the same experiment in order to measure the Galactic distribution of planets. Since these *Spitzer* observations yielded only one planet, this is not yet possible in practice. However, it will become possible as larger samples are accumulated.

Key words: gravitational lensing: micro – planetary systems – planets and satellites: dynamical evolution and stability

1. INTRODUCTION

It has been known for 50 yr (Liebes 1964; Refsdal 1964) that microlensing measurements are plagued by a severe degeneracy between the lens mass M, the source-lens relative parallax $\pi_{\rm rel} = {\rm AU}(D_L^{-1} - D_S^{-1})$, and the geocentric lens-source relative proper motion $\boldsymbol{\mu}_{\rm geo}$ (Gaudi 2012, Equations (1) and (17)),

$$t_{\rm E} = \frac{\theta_{\rm E}}{\mu_{\rm geo}}; \qquad \theta_{\rm E}^2 \equiv \kappa M \pi_{\rm rel}; \qquad \kappa \equiv \frac{4G}{c^2{\rm AU}} \simeq 8.14\frac{\rm mas}{M_\odot}. \tag{1}$$

Here $\theta_{\rm E}$ is the angular Einstein radius and $t_{\rm E}$ is the Einstein-radius crossing time in the ground-based reference frame. It has also been known for 50 yr (Refsdal 1966) that the best way to systematically ameliorate this degeneracy is to observe the events simultaneously from solar orbit in order to measure the microlens parallax vector $\boldsymbol{\pi}_{\rm E}$,

$$\boldsymbol{\pi}_{\rm E} \equiv \frac{\pi_{\rm rel}}{\theta_{\rm E}}\frac{\boldsymbol{\mu}}{\mu}, \tag{2}$$

where $\boldsymbol{\mu}$ can be the lens-source relative proper motion in either the geocentric or heliocentric frame, in which cases $\boldsymbol{\pi}_{\rm E}$ is the representation in the same frame. (Note that, as the ratio of two angles, $\boldsymbol{\pi}_{\rm E}$ is dimensionless.) If $\boldsymbol{\pi}_{\rm E}$ is measured, one obtains strong constraints on M and $\pi_{\rm rel}$ from

$$M = \frac{\theta_{\rm E}}{\kappa\pi_{\rm E}} = \frac{\mu_{\rm geo}t_{\rm E}}{\kappa\pi_{\rm E}}, \qquad \pi_{\rm rel} = \theta_{\rm E}\pi_{\rm E} = \mu_{\rm geo}t_{\rm E}\pi_{\rm E}. \tag{3}$$

Hence, even if $\theta_{\rm E}$ is not measured (as it almost never is for single-lens microlenses), M and $\pi_{\rm rel}$ can be estimated fairly robustly just from the fact that the great majority of the microlenses have $\mu_{\rm geo}$ within a factor 2 of $\mu_{\rm geo} \sim 4$ mas yr^{-1}. However, without the additional information from $\pi_{\rm E}$, the three physical quantities M, $\pi_{\rm rel}$, and $\mu_{\rm geo}$ cannot be disentangled from the single measured parameter $t_{\rm E}$, so that, for example, M remains uncertain by an order of magnitude (Gould 2000).

Nevertheless, before 2014, there was only one space-based parallax measurement out of more than 10,000 recorded microlensing events: Dong et al. (2007) used *Spitzer* to measure the microlens parallax of a rare (almost unique) bright event toward the Small Magellanic Cloud, OGLE-2005-SMC-001.

Spitzer (Werner et al. 2004) has several advantages but also important disadvantages as a possible "microlens parallax satellite" for observations toward the Galactic bulge. First, of course, it is in solar orbit, gradually drifting behind Earth at somewhat more than 0.1 AU yr^{-1}. Hence, by now it trails Earth by almost 90°. Second, at 3.6 μm, its IRAC camera (Fazio et al. 2004) has relatively good resolution of ~2″, not much worse than the resolutions of the ground-based surveys that discover and monitor the events. Third, it can be pointed at targets on relatively short notice. This is important because microlensing events typically peak (and then decline) within a few weeks of their discovery. Hence, either the satellite must be able to respond quickly (Refsdal 1966; Gould 1994) or it must, like ground observatories, survey an extended field in hope of detecting events from previously unidentified sources (Gould & Horne 2013).

Spitzer's most important disadvantage is that due to Sun-angle viewing restrictions, it can observe any given target that lies near the ecliptic (including the entire Galactic bulge, which hosts >99% of all recorded microlensing events) for only two ~38-day intervals per year. Moreover, during only one of these is it possible to simultaneously observe the bulge from Earth (and so measure parallaxes). Second, while *Spitzer*'s real-time

[46] The OGLE collaboration.
[47] The PLANET collaboration.
[48] The MOA collaboration.
[49] The Wise group.
[50] The RoboNet collaboration.
[51] The MiNDSTEp consortium.
[52] The μFUN collaboration.
[53] Sagan Visiting Fellow.
[54] Sagan Fellow.
[55] Royal Society University Research Fellow.

response can in principle be extremely rapid, such rapid responses are also very disruptive to its overall mission and science return. By contrast, the normal (non-disruptive) response time to unexpected requests for data is of order a month, which would be useless for the great majority of microlensing events. For completeness, we mention that the fact that *Spitzer* observes at wavelengths far redward of those used for ground-based microlensing observations was initially believed to be a problem (e.g., Gould 1999), but this now appears to be relatively minor (e.g., Yee et al. 2015).

The observations reported here derive from a 100 hr "pilot program" awarded by the Director to demonstrate the feasibility of *Spitzer* microlens parallax observations. The scientific objectives were of course driven by the overall potential of *Spitzer* to determine microlens masses, particularly for planetary events. However, these objectives were also sculpted by the challenges discussed in the previous paragraph, and in particular by the need to demonstrate concretely that these challenges could be met. For example, working with *Spitzer* operations, we developed a new observing protocol for "regular" (non-disruptive) target-of-opportunity observations with a turnaround of 3–9 days. The times of the microlensing observations were preplanned to occur in blocks approximately once per 24 hr, but the targets for a given week were not finalized until a few days before they were uploaded to the spacecraft (Section 2 and Figure 1 of Udalski et al. 2015 and also Section 2.2 of this paper). In particular, the weekly observing decisions made under this protocol were aimed primarily at maximizing the number of successful parallax measurements, while making an extra effort to measure parallaxes for as many binary and planetary events as possible.

An alternative strategy might have been to develop purely objective criteria for the weekly choices of targets and cadences. The ensemble of parallax measurements of isolated lenses made using such an objective protocol could then be forward modeled to extract the underlying mass function, as envisaged by Han & Gould (1995).

The reasons for not using purely objective criteria were threefold. First, as stated above, the overwhelming objective was to determine feasibility, which can best be done by learning from successful measurements. Second, it is very difficult to develop objective criteria without concrete experience (exactly the point of a "pilot program"). Finally, the lens mass function is not the most important scientific result that can be extracted from an ensemble of isolated-lens measurements.

Rather, the most critical application of an ensemble of isolated-lens parallaxes is to serve as the comparison sample by which the planet detections can be transformed into a measurement of the Galactic distribution of planets. That is, as long as the planetary events are not chosen for *Spitzer* observations because they are known to have planets, then the planetary events can be considered to be "drawn fairly" from the ensemble of (mainly) isolated-lens events, regardless of whether the process by which the latter are chosen can be modeled or not. This also means that if, during successive years of observations, the selection criteria change, the planet sample and the isolated-lens sample can each be concatenated, and they will still yield a fair comparison. This situation is analogous to the selection of high-magnification events for intensive follow-up that led to the first microlens-planet frequency analysis (Gould et al. 2010), the most relevant point in both cases being that events are selected for observations without regard to whether or not they have planets in them.

Now, since there was only one planet[56] in the *Spitzer* "pilot program" sample (Udalski et al. 2015), it is not yet possible to derive a Galactic distribution of planets. Nevertheless, it is important to make an initial effort to measure the distance distribution of the isolated lens sample, partly to learn practically how to do this from real data and partly to understand what type of lenses were effectively selected by the selection procedures used in the "pilot program." Even though these procedures cannot be comprehensibly quantified, they do have quantifiable elements (like delay times of 3–9 days) that by themselves select for certain types of lenses. Even a qualitative understanding of these effects may influence the choice of objective selection criteria in future years. Thus, although it is clearly too early to measure the Galactic distribution of planets, it is actually quite urgent to begin those components of the analysis that can be done.

Making a statistical estimate of the distance distribution of the ensemble of isolated lenses requires that a probability distribution be assigned to the distance of each lens. In general, this probability distribution will be much more compact if the well-known parallax degeneracy (Refsdal 1966; Gould 1994) is broken, as it was by Yee et al. (2015) for the case of OGLE-2014-BLG-0939. That is, because u (and so u_0) enters the lensing magnification equation quadratically (Equation (8) below), space-based parallax measurements generically have a fourfold degeneracy in the vector microlens parallax $\boldsymbol{\pi}_{\rm E}$,

$$\boldsymbol{\pi}_{\rm E} = \frac{\rm AU}{D_\perp}\left(\frac{\Delta t_0}{t_{\rm E}}, \Delta u_{0,\pm,\pm}\right), \tag{4}$$

where the x-axis is defined by the direction of the projected Earth-satellite separation vector $\boldsymbol{D}_\perp$, $\Delta t_0 = t_{0,\rm sat} - t_{0,\oplus}$ is the difference in times of maximum as seen at the two locations, $\Delta u_{0,-,\pm} = \pm(|u_{0,\rm sat}| - |u_{0,\oplus}|)$ is the difference in impact parameters assuming that they are on the same side of the lens, and $\Delta u_{0,+,\pm} = \pm(|u_{0,\rm sat}| + |u_{0,\oplus}|)$ is their difference assuming that they are on the opposite sides. While the two solutions $\Delta u_{0,-,\pm}$ (or two solutions $\Delta u_{0,+,\pm}$) yield very similar $\pi_{\rm E}$ (so M and $\pi_{\rm rel}$), these two *sets of solutions* can have very different $\pi_{\rm E}$ from each other. The overall sign of Δu_0, which is designated by the second "±" subscript, is positive if $u_{0,\oplus} > 0$, which by convention occurs if "the lens passes the moving source on its right as seen from Earth" (Gould 2004). See his Figure 2.

[56] In fact, OGLE-2014-BLG-0298, which showed a perturbation that was strongly suspected to be planetary in nature well before the commencement of *Spitzer* observations, was aggressively monitored during this campaign. However, exactly because these observations were triggered by the (suspected) presence of a planet, this event is not part of the "fair sample" and is therefore not considered in the present work. The value of these *Spitzer* observations, as with *Spitzer* observations of known binary microlensing events, is to measure the mass of a potentially interesting object, rather than for statistical studies. To date, planetary anomalies far out on the rising wing of the light curve (like OGLE-2014-BLG-0298) have constituted roughly 8% of all planetary events, so elimination of these events from the Galactic distribution sample is not likely to be a major loss. However, if future planet surveys have more uniform light-curve coverage than past ones (e.g., Henderson et al. 2014), then this fraction will increase somewhat.

1.1. Rich Argument

The present *ensemble* of parallax measurements provides the first opportunity to test an idea that to our knowledge was first suggested by J. Rich (ca. 1997, private communication), but never (to our knowledge) written up. Rich's original idea was that the two components of $\pi_{\rm E}D_\perp/{\rm AU}$ (namely, $\Delta\tau = \Delta t_0/t_{\rm E}$ and Δu_0) should in general be of the same order. This is true for different classes of lenses for different reasons. If the lens is in the bulge, then the direction of relative proper motion $\boldsymbol{\mu}$ (and so $\boldsymbol{\pi}_{\rm E}$) is nearly randomly distributed over a circle. Similarly, if the lens is close to the Sun (i.e., within about 1 kpc), then the direction of proper motion is primarily determined by the lens peculiar motion and is again basically random. Finally, if the lens is at intermediate distances in the Galactic disk, then its proper motion should be roughly aligned with Galactic rotation, which in ecliptic coordinates (relevant since $\boldsymbol{D}_\perp$ is closely aligned with the ecliptic) has comparable components.

According to Rich's original idea, in the case that the true solution is one of $\Delta u_{0,-,\pm}$ solutions, the two components will generally be roughly equal $|\Delta\tau| \sim |\Delta u_{0,-,\pm}|$. If these components are themselves small, $|\Delta u_{0,-,\pm}| \ll |u_{0,\oplus}|$, then the components for the other solution will be highly unequal, $|\Delta u_{0,+,\pm}| \sim 2|u_{0,\oplus}| \gg |\Delta u_{0,-,\pm}|$ and consequently $|\Delta u_{0,+,\pm}| \gg |\Delta\tau|$. Hence, seeing such roughly equal components for one solution and highly unequal components for the other, one should conclude that the first solution is probably correct.

In the course of working on the events in this paper, we realized that Rich's argument can be extended to apply constraints from two degrees of freedom, rather than just one. This increases the argument's statistical power considerably. Properly speaking, it should then be called the "Extended Rich argument," but for simplicity we continue to simply say "Rich argument." We begin by noting that the parallax amplitude basically has a twofold degeneracy, which we denote $\pi_{\rm E,\pm}$, corresponding to[57] $(|\Delta u_{0,\pm}|, \Delta\tau)$. One of these is the actual parallax $\pi_{\rm E,true}$, and the other is spurious, $\pi_{\rm E,false}$. However, it is often the case that the light curve does not distinguish between these. Nevertheless, we can define a theoretical quantity

$$\epsilon = \frac{\pi_{\rm E,false}}{\pi_{\rm E,true}} = \left(\frac{\left(|u_{0,\rm sat}| - |u_{0,\oplus}|\right)^2 + (\Delta\tau)^2}{\left(|u_{0,\rm sat}| + |u_{0,\oplus}|\right)^2 + (\Delta\tau)^2}\right)^{\pm 1/2} = \left(\frac{\left(|\Delta u_{0,-}|\right)^2 + (\Delta\tau)^2}{\left(|\Delta u_{0,+}|\right)^2 + (\Delta\tau)^2}\right)^{\pm 1/2}, \tag{5}$$

where the sign refers to the cases $\pi_{\rm E,true} = \pi_{\rm E,\pm}$. Hence, for $\pi_{\rm E,true} = \pi_{\rm E,+}$, $\epsilon < 1$, and if $\pi_{\rm E,+} \gg \pi_{\rm E,-}$, then $\epsilon \ll 1$. We can test the hypothesis that $\pi_{\rm E,true} = \pi_{\rm E,+} \gg \pi_{\rm E,-}$ by asking what is the probability of $\epsilon \leqslant \epsilon_0$ where $\epsilon_0 \ll 1$. This can be divided into two questions: first, what is the prior probability of $\epsilon < 1$ given that $\pi_{\rm E}$ has some given true value, and second, what is the conditional probability $\epsilon < \epsilon_0$ given that $\epsilon < 1$.

The first probability (namely, that $\pi_{\rm E,true} = \pi_{\rm E,+}$) is certainly less than unity, and typically of order one-half. We do not further investigate this probability because it depends on the details of event selection and because its specific value has marginal impact on the overall result.

If $\epsilon \ll 1$, then $|\Delta u_{0,-}| \lesssim \epsilon|\Delta u_{0,+}|$ and $\Delta\tau \lesssim \epsilon|\Delta u_{0,+}|$. Under this hypothesis, the latter condition gives highly unequal components for $\pi_{\rm E,true} = \pi_{\rm E,+}$, implying a very special angle α for the lens-source relative motion with respect to the direction perpendicular to the Earth-satellite axis, $|\sin\alpha| < \epsilon$, whereas a priori, α could assume any direction over the circle. This is the basis of the original Rich argument. However, the first condition also constrains $|\Delta u_{0,-}|$ to a very narrow interval relative to the full range of possibilities $-|\Delta u_{0,+}| < |\Delta u_{0,-}| < |\Delta u_{0,+}|$ over which this quantity would be expected to be uniformly distributed. Eliminating duplicate geometries, we should evaluate the probability that $[\alpha^2 + (\Delta u_{0,-}/\Delta u_{0,+})^2] < \epsilon_0^2$ under conditions where α is uniformly distributed over $[-\pi/2, \pi/2]$ and $(\Delta u_{0,-}/\Delta u_{0,+})$ is uniformly distributed over $[-1, 1]$. This probability is just

$$P\left(\epsilon < \epsilon_0\,|\,\epsilon < 1\right) = \frac{\pi\epsilon_0^2}{2\pi} = \frac{\epsilon_0^2}{2}. \tag{6}$$

That is, the probability of $\epsilon < \epsilon_0 \ll 1$ (which requires $\pi_{\rm E,true} = \pi_{\rm E,+}$) is very small.

We next note that if $\pi_{\rm E,true} \ll 1$, then the probability of $\epsilon \gg 1$ is of order unity. This is because $\pi_{\rm E,true} \ll 1$ requires that $|\Delta u_0| \ll 1$ (and $\Delta\tau \ll 1$). Hence, under typical conditions, i.e., $u_0 \sim \mathcal{O}(0.5)$, we have $\Delta u_{0,+} \sim 2|u_0| \sim \mathcal{O}(1) \gg \Delta u_{0,-}$ and similarly $\Delta u_{0,+} \gg \Delta\tau$.

Hence, if we find $\pi_{\rm E,+} \gg \pi_{\rm E,-}$, then it is highly likely that the $\pi_{\rm E,-}$ solution is correct. This is because, if $\pi_{\rm E,-}$ is correct, then we naturally expect the alternate solution $(\pi_{\rm E,+})$ to be much bigger (i.e., $|\Delta u_{0,+}| \gg |\Delta u_{0,-}|$ and $|\Delta u_{0,+}| \gg \Delta\tau$). However, if the $\pi_{\rm E,+}$ solution were correct, then we would expect the alternate solution $(\pi_{\rm E,-})$ to be of the same general order, and, in particular, the chance that the alternate solution was as small as observed or smaller would be $\epsilon^2/2$.

Such an argument cannot be considered decisive in any particular case because the proper motion can by chance be very nearly perpendicular to $\boldsymbol{D}_\perp$ and the values of Δu_0 as seen from Earth and the satellite can by chance happen to have very nearly equal magnitudes but opposite signs. Nevertheless, if the objective is to find the cumulative distribution of lens distances (rather than to securely determine the distance to a particular lens), then it is appropriate to give unequal-component solutions lower statistical weight when combining the distance estimates of the ensemble to form a cumulative distribution.

2. OBSERVATIONS

2.1. OGLE Observations

All 21 of the events analyzed in this paper were discovered by the Optical Gravitational Lens Experiment (OGLE) based on observations with the 1.4 deg^2 camera on its 1.3 m Warsaw Telescope at the Las Campanas Observatory in Chile using its Early Warning System real-time event detection software (Udalski et al. 1994; Udalski 2003). The observations reported here are entirely in I band, although some V observations were also taken with the aim of determining the source color. The specific role of such source-color measurements in the present study is discussed in Section 2.4.

[57] For simplicity of notation we will neglect the second ± in $\Delta u_{0,\pm,\pm}$ for the remainder of this section.

2.2. Spitzer Observations

The structure of our *Spitzer* observing protocol is described in detail in Section 3.1 of Udalski et al. (2015). In brief, observations were made during 38 2.63 hr windows between HJD′ ≡ HJD 2,450,000 = 6814.0 and 6850.0. Each observation consisted of six dithered 30 s exposures in a fixed pattern using the 3.6 μm channel on the IRAC camera. Observation sequences were uploaded to *Spitzer* operations on Mondays at UT 15:00, for observations to be carried out Thursday to Wednesday (with slight variations). As described in Udalski et al. (2015), J.C.Y. and A.G. balanced various criteria to determine which targets to observe and how often. In general, there were too many targets to be able to observe all viable targets during each epoch. The relation between weekly "decision dates" and subsequent observations is illustrated in Figure 1 of Udalski et al. (2015).

With three exceptions, the OGLE alerts for all 21 events occurred prior to the first "decision date" (June 2 UT 15:00, HJD′ 6811.1). The alerts for OGLE-2014-BLG-1021, OGLE-2014-BLG-1049, and OGLE-2014-BLG-1147 were announced on June 4, 6, and 18, respectively. Hence, the first two could be observed only during 4 weeks, while the third could be observed only during the final 2 weeks.

Table 1 lists the equatorial coordinates, ecliptic latitude, and number of *Spitzer* observations for each event. The ecliptic latitude is important because in the limit that both the event and the *Spitzer* spacecraft were directly on the ecliptic, the directional degeneracies $\Delta u_{0,-,\pm}$ and $\Delta u_{0,+,\pm}$ could not be broken, even in principle (Jiang et al. 2005; Skowron et al. 2011).

2.3. Additional Light-curve Data

Additional light-curve data were obtained for a total of 15 of the 21 events reported here from a total of 13 telescopes. The MOA collaboration (Bond et al. 2001; Sumi et al. 2013) obtained data on seven events as part of their normal survey operations using a broad R/I filter on their 1.8 m telescope at Mt. John, New Zealand. Similarly, the Wise Collaboration (Shvartzvald & Maoz 2012) obtained survey data on five events using an *I*-band filter on their 1.0 m telescope at Mitzpe Ramon, Israel.

Four other teams specifically targeted the *Spitzer* sample for follow-up observations, all in *I* band (or SDSS *i* band). The PLANET collaboration (Albrow et al. 1998) observed six events using the 1.0 m Elizabeth telescope at Sutherland, South Africa. The RoboNet/LCOGT (Las Cumbres Observatory Global Telescope Network) collaboration (Tsapras et al. 2009) observed a total of four events from a total of eight 1.0 m telescopes in CTIO, Chile, Sutherland, South Africa, and Siding Spring, Australia. The MiNDSTEp (Microlensing Network for the Detection of Small Terrestrial Exoplanets) consortium (Dominik et al. 2010) observed four events from their 1.54 m telescope at ESO La Silla, Chile, and four events using the 0.35 m Salerno University telescope in Salerno, Italy.

Of the 21 events, (6, 9, 1, 1, 2, 1, 1) were observed by (1, 2, 3, 4, 9, 10, 11) telescopes, respectively. We refer to Table 1 for full details on the additional data set used.

2.4. Additional Color Data

The μFUN (Microlensing Follow Up Network) collaboration obtained a very limited quantity of data on each of the 21 events using the ANDICAM (DePoy et al. 2003) dichroic camera on the SMARTS-CTIO 1.3 m telescope. These observations were made simultaneously in *I* and *H* band and were for the specific purpose of inferring the $I-[3.6]$ source color using an $(I-H)$ versus $(I-[3.6])$ instrumental color–color diagram. Yee et al. (2012) demonstrated for the case of MOA-2011-BLG-293 that this color–color method could reliably constrain the source flux even if a given data set lacked sufficient coverage for an independent flux determination from the model. The incorporation of this constraint is discussed further in Section 3.

At the time of the decision to acquire these data, it was deemed especially important to acquire *H*-band data because it was unknown whether the extrapolation from the (more routinely taken) *V*/*I* data to 3.6 μm would be feasible. In fact, in most cases, the OGLE *V*-band data did prove adequate to determine the $(I-[3.6])_S$ source color, but in five cases the source was either too red to obtain reliable *V*-band data or OGLE did not happen to observe the event in *V* band when it was sufficiently magnified to determine $V-I$. In all but one of these cases (OGLE-2014-BLG-0337), the *H*-band data could be used to determine the source color (OGLE-2014-BLG-0805, OGLE-2014-BLG-0866, OGLE-2014-BLG-0944, OGLE-2014-BLG-1021).

2.5. Reductions

With one exception the *Spitzer* data were reduced using the photometry tools available within MOPEX, a package designed to analyze IRAC data (Makovoz & Marleau 2005): the analysis has been carried out with aperture photometry for six events (OGLE-2014-BLG-0099, OGLE-2014-BLG-0337, OGLE-2014-BLG-0589, OGLE-2014-BLG-0805, OGLE-2014-BLG-0944, and OGLE-2014-BLG-1021) and, to better deal with crowding, for all the remaining ones, with a point source response function (PRF) based photometry.[58] The exception was OGLE-2014-BLG-1049, which was reduced using DoPhot (Schechter et al. 1993). All other light-curve data were reduced using image subtraction (Alard & Lupton 1998). The CTIO *H*-band data were reduced using DoPhot.

Error bars from each observatory were rescaled in order to impose $\chi^2/\mathrm{dof} \simeq 1$ based on the best-fit model.

3. LIGHT-CURVE ANALYSIS

The light curves were fitted to five-parameter models (plus two parameters for each observatory *i*, the source flux $F_{S,i}$, and the blended flux $F_{B,i}$),

$$F_i(t) = F_{S,i}A_i\left(t;\, t_0,\, u_0,\, t_{\rm E},\, \pi_{{\rm E},N},\, \pi_{{\rm E},E}\right) + F_{B,i} \qquad (7)$$

[58] For a specific discussion of PRFs fitting in IRAC data we refer to the online manual for MOPEX http://irsa.ipac.caltech.edu/data/SPITZER/docs/dataanalysistools/tools/mopex/mopexusersguide/.

where (Paczyński 1986)

$$A_i(u_i) = \frac{u_i^2+2}{\sqrt{u_i^4+4u_i^2}}; \quad u_i^2 \equiv \left(\tau_i'\right)^2 + \left(\beta_i'\right)^2;$$
$$\tau' = \frac{t-t_0}{t_{\rm E}} + \Delta\tau_i(t); \quad \beta' = u_0 + \Delta\beta_i(t) \qquad (8)$$

and where, following closely the procedure based on a geocentric point of view outlined in Gould (2004), $(\Delta\tau_i(t), \Delta\beta_i(t))$ is the apparent lens-source offset in the Einstein ring relative to a uniform trajectory, as seen by the *i*th observatory, due to the physical offset (in AU) of this observatory from a rectilinear trajectory defined by Earth's position and velocity vectors at the peak of the event, $(t_{0,\oplus})$.

The physical offset of the observatory $\Delta\boldsymbol{p}_i(t) = (\Delta p_{i,N}(t), \Delta p_{i,E}(t))$ is the sum of two terms

$$\boldsymbol{p}_i(t) = \mathbf{s}(t) + \boldsymbol{t}_i(t). \qquad (9)$$

The first term (common to all observatories) is the offset of the apparent position of the Sun (projected on the plane of the sky) relative to where it would be if Earth were in rectilinear motion (see Gould 2004, and specifically his Figure 2). The second term (called "*t*" because it usually reflects so-called "terrestrial parallax," as opposed to the "orbital parallax") is the projected separation of Earth's center from the *i*th observatory. Both terms are, by convention, scaled to 1 AU. The sign convention is due to the explicitly "geocentric" framework. For terrestrial observatories, for which we use Earth's ephemerides and the location of each observatory relative to Earth's center, $|\boldsymbol{t}_i| \ll 1$, although this term can in principle be important, particularly for high-magnification events (Gould 1997; Gould et al. 2009; Yee et al. 2009; Gould & Yee 2013). For *Spitzer* $|\boldsymbol{t}_i| \sim \mathcal{O}(1)$, with the spacecraft position relative to Earth being available as a function of time from the Horizons Ephemeris System.[59] Then, in analogy to Equation (8) of Gould (2004),

$$\Delta\tau_i = -\frac{\Delta p_{i,N}\pi_{{\rm E},N} + \Delta p_{i,E}\pi_{{\rm E},E}}{\rm AU}$$
$$\Delta\beta_i = -\frac{-\Delta p_{i,E}\pi_{{\rm E},N} + \Delta p_{i,N}\pi_{{\rm E},E}}{\rm AU}. \qquad (10)$$

As discussed in Section 2.4, for each event (except OGLE-2014-BLG-0337) we measured the instrumental source color in either $(V-I)_S$ or $(I-H)_S$. We then determined the $(I-[3.6])_S$ color using a *VI*[3.6] or *IH*[3.6] color–color relation derived from field stars. These estimates typically have errors of $\sigma_{I-[3.6]} = 0.06$–0.1 mag, although they are larger in a few cases. These color measurements were then incorporated into the fit by

$$\chi^2_{\rm color} = \frac{\left[(I-[3.6]) - 2.5\log\left(F_{S,Spitzer}/F_{S,{\rm OGLE}}\right)\right]^2}{\sigma^2_{I-[3.6]}}. \qquad (11)$$

In most cases inclusion of this term made almost no difference, generally because the fit values of $F_{S,Spitzer}$ and $F_{S,{\rm OGLE}}$ already yielded an $(I-[3.6])_S$ color that was consistent with the one derived from the color–color diagram. However, in a few cases, particularly when the *Spitzer* observations covered only a fragment of the Paczyński (1986) curve, this constraint proved to be important.

To locate the four solutions (with different parallax vectors $\boldsymbol{\pi}_{\rm E}$) that are predicted from theory (Refsdal 1966; Gould 1994), we begin by fitting the ground-based light curve to the standard Paczyński (1986) three parameters $(t_{0,\oplus}, u_{0,\oplus}, t_{\rm E})$, i.e., without parallax. We then add in *Spitzer* data and include two additional parameters $\boldsymbol{\pi}_{\rm E}$ and apply Newton's method (Simpson 1740, p. 81). This quickly locates the $\Delta u_{0,-,+}$ solution. We then reverse the signs of $(u_0, \pi_{{\rm E},N})$ (Skowron et al. 2011) and again apply Newton's method, which locates the $\Delta u_{0,-,-}$ solution. We then take the original solution, put in a large value for $\pi_{{\rm E},N}$, and apply Newton's method, which locates the $\Delta u_{0,+,+}$ solution, and finally we reverse the signs of $(u_0, \pi_{{\rm E},N})$ for this solution and again apply Newton's method to obtain the fourth solution.

The only event for which this procedure failed was OGLE-2014-BLG-1049. The reason for the failure is that the event was high magnification as seen from Earth ($u_{0,\oplus} < 0.01$) and was also high magnification as seen from *Spitzer*. However, because the first *Spitzer* point was 1 day *after* peak, $u_{0,Spitzer}$ is consistent with both zero and values that are significantly larger than $u_{0,\oplus}$. These characteristics lead to a merger of the two solutions $\Delta u_{0,\pm,+}$ and also a merger of the solutions $\Delta u_{0,\pm,-}$. Nevertheless, although the merged solutions are unstable to Newton's method, they have quite well behaved minima and constitute an interesting limiting case of the standard fourfold degeneracy.

Table 2 lists the fitted parameters for each of the four solutions for each of the 21 events. The $\Delta\chi^2$ offset between each of the other three solutions and the best one is shown in the second column.

An additional analysis we might in principle address is related to the determination of the parallax from ground-based data alone. While formally it is extremely straightforward to fit the light curves after excluding the *Spitzer* data (and indeed, within our fit procedure, the effect of parallax for ground-based data from orbital motion is automatically included), historical experience with ground-based parallax measurements shows that a more cautious approach is required. In contrast to space-based parallaxes, in which the signal derives from obvious differences in the peaks of the event as seen from well-separated observatories, ground-based parallaxes derive from subtle distortions of the light curves. These can be caused or corrupted by "xallarap" (binary motion of the source during the event), very small distortions due to unrecognized binary lenses, or just systematics in the data. These problems can be mitigated by the presence of well-understood structures in the light curve for events that contain a planet (e.g., Muraki et al. 2011), but for point-lens events, which are otherwise featureless, ground-based parallaxes are especially prone to such corruption. Indeed, in the only systematic study of point-lens ground-based parallaxes (Poindexter et al. 2005), even within a restricted sample of parallax detections with $\Delta\chi^2 > 100$, there was a strong evidence for xallarap in 23% of cases. As described in some detail by Poindexter et al. (2005), the tests for xallarap (and related systematics) are quite involved and are well beyond the scope of the present work, which relies on much more straightforward space-based parallaxes.

[59] http://ssd.jpl.nasa.gov/horizons

(a)

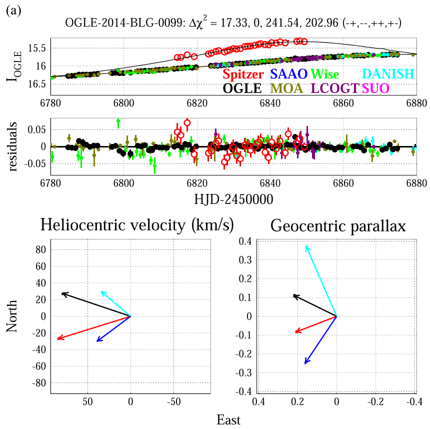

Figure 1. (a) OGLE-2014-BLG-0099. Top: light-curve data together with the *Spitzer* and the ground-based best-fit models. Second panel from top: residual light curve. In both panels the *Spitzer* and the ground-based data are shown as empty and filled circles, respectively. For purposes of display, all the data sets are binned with 1 point per epoch. The color codes are indicated in the top panel: red, black, blue, olive green, green and purple for *Spitzer*, OGLE, SAAO (PLANET), MOA, Wise, LCOGT (RoboNet; the details of the different telescopes of the network used are given in Table 1) and for the MiNDSTEp collaboration the Danish (cyan) and the Salerno University Telescope (magenta). In the two bottom panels we show the projected heliocentric velocity $\tilde{\boldsymbol{v}}_{\rm hel}$ (left) and the geocentric parallax vectors $\boldsymbol{\pi}_{\rm E,geo}$ and ellipse errors (which can, however, be too small to be seen), in the northeast equatorial frame, as given in Table 2. The values of the $\Delta\chi^2$, as reported in the title, are color-coded as black, red, cyan and blue, from the best solution to the worst. (b) OGLE-2014-BLG-0115. Panels and symbols as in (a). (c) OGLE-2014-BLG-0337. Panels and symbols as in (a). (d) OGLE-2014-BLG-0419. Panels and symbols as in (a). (e) OGLE-2014-BLG-0494. Panels and symbols as in (a). (f) OGLE-2014-BLG-0589. Panels and symbols as in (a). (g) OGLE-2014-BLG-0641. Panels and symbols as in (a). (h) OGLE-2014-BLG-0667. Panels and symbols as in (a). (i) OGLE-2014-BLG-0670. Panels and symbols as in (a). (j) OGLE-2014-BLG-0678. Panels and symbols as in (a). (k) OGLE-2014-BLG-0752. Panels and symbols as in (a). (l) OGLE-2014-BLG-0772. Panels and symbols as in (a). (m) OGLE-2014-BLG-0805. Panels and symbols as in (a). (n) OGLE-2014-BLG-0807. Panels and symbols as in (a). (o) OGLE-2014-BLG-0866. Panels and symbols as in (a). (p) OGLE-2014-BLG-0874. Panels and symbols as in (a). (q) OGLE-2014-BLG-0939. Panels and symbols as in (a). (r) OGLE-2014-BLG-0944. Panels and symbols as in (a). (s) OGLE-2014-BLG-0979. Panels and symbols as in (a). (t) OGLE-2014-BLG-1021. Panels and symbols as in (a). (u) OGLE-2014-BLG-1147. Panels and symbols as in (a).

4. VISUAL REPRESENTATIONS OF SOLUTIONS

Figure 1 gives a visual representation of all the key information for 20 of the 21 events (except OGLE-2014-BLG-1049). For each event, the upper panel shows the light-curve data from all observatories. All have been aligned to OGLE fluxes (and then converted to OGLE magnitudes) in the standard fashion. That is,

$$F_{\rm OGLE,sys} = \left(F - F_{B,i}\right)\frac{F_{S,{\rm OGLE}}}{F_{S,i}} + F_{B,{\rm OGLE}}, \qquad (12)$$

where the F_S and F_B are determined from the fit. This panel also shows the model(s), i.e., the model light curve as seen from Earth and from *Spitzer*. Note that the model is extended beyond the range of *Spitzer* observations although *Spitzer* could not actually observe the events at these times due to Sun-angle restrictions. The $\Delta\chi^2$ values for the four solutions are listed above this panel, always in the same order (−+,−−,++,+−). The next panel shows the residuals.

The lower two panels show two different representations of the four parallax solutions. In each case, the solutions are color coded in order of increasing χ^2, namely, black, red, cyan, and blue. The right panel shows the $\boldsymbol{\pi}_{\rm E,geo}$ vectors and error ellipses in the geocentric frame, i.e., those that are directly returned by the fit. As described below, the $\boldsymbol{\pi}_{\rm E,hel}$ vectors would have exactly the same lengths but slightly different directions compared to the $\boldsymbol{\pi}_{\rm E,geo}$ vectors that are shown.

In the left panel, we show the heliocentric projected velocities $\tilde{\boldsymbol{v}}_{\rm hel}$, defined as

$$\tilde{\boldsymbol{v}}_{\rm hel} = \tilde{\boldsymbol{v}}_{\rm geo} + \boldsymbol{v}_{\oplus,\perp}; \qquad \tilde{\boldsymbol{v}}_{\rm geo} = \frac{\boldsymbol{\pi}_{\rm E,geo}}{\pi_{\rm E}^2}\frac{\rm AU}{t_{\rm E,geo}}, \qquad (13)$$

where $\boldsymbol{v}_{\oplus,\perp}$ is the velocity of Earth projected on the plane of the sky and evaluated at $t_{0,\oplus}$. While this quantity varies slightly from event to event in the sample, most are quite close to

(b)

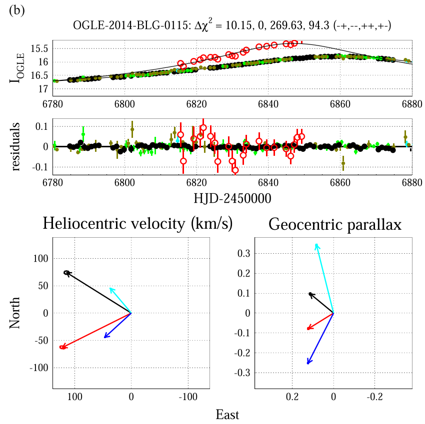

(c)

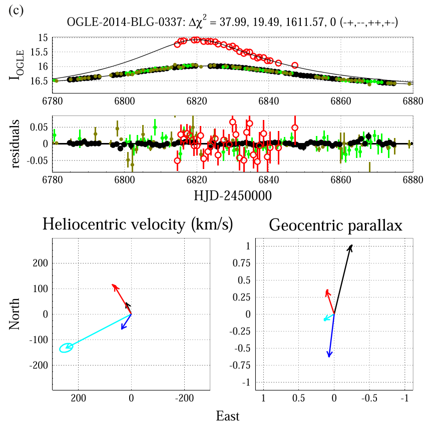

Figure 1. (Continued.)

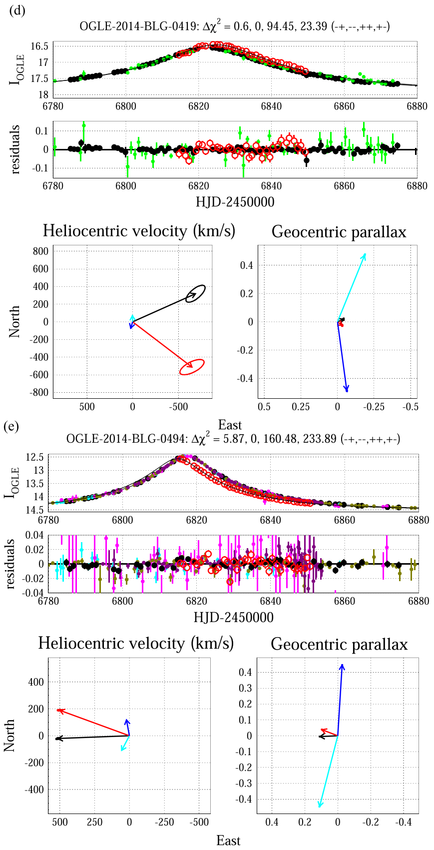

Figure 1. (Continued.)

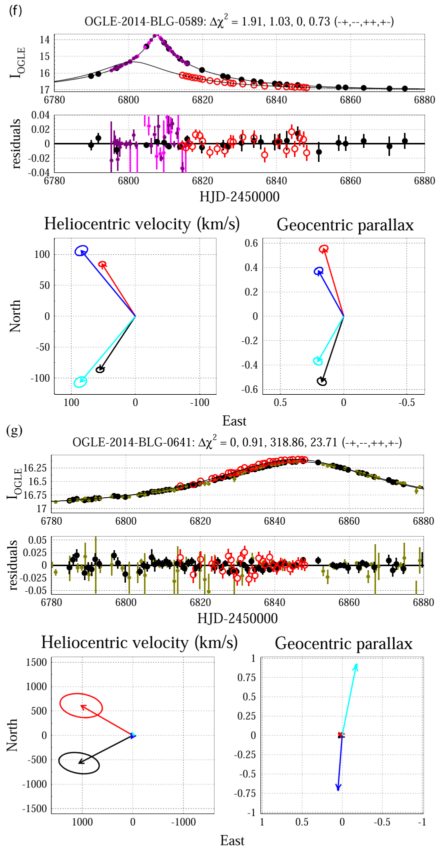

Figure 1. (Continued.)

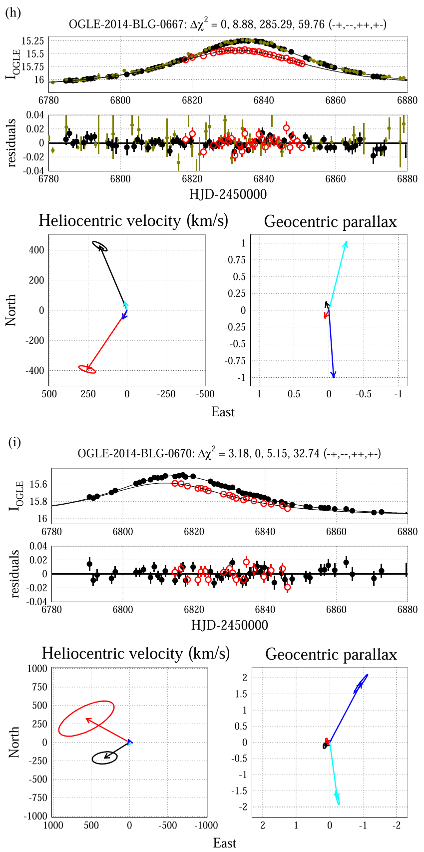

Figure 1. (Continued.)

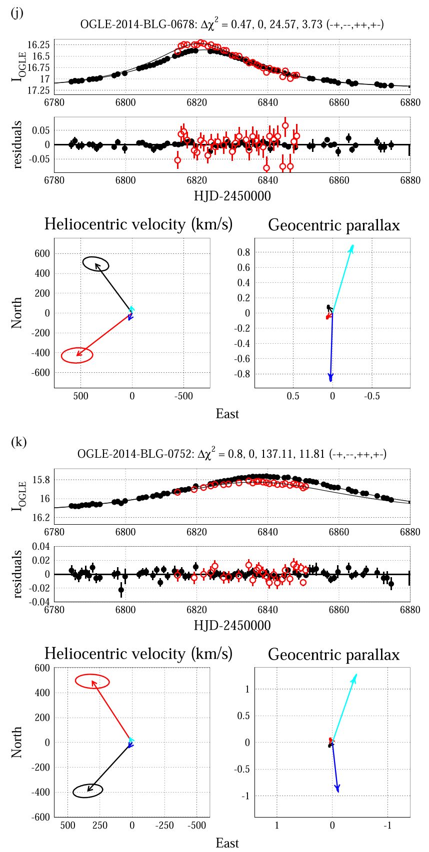

Figure 1. (Continued.)

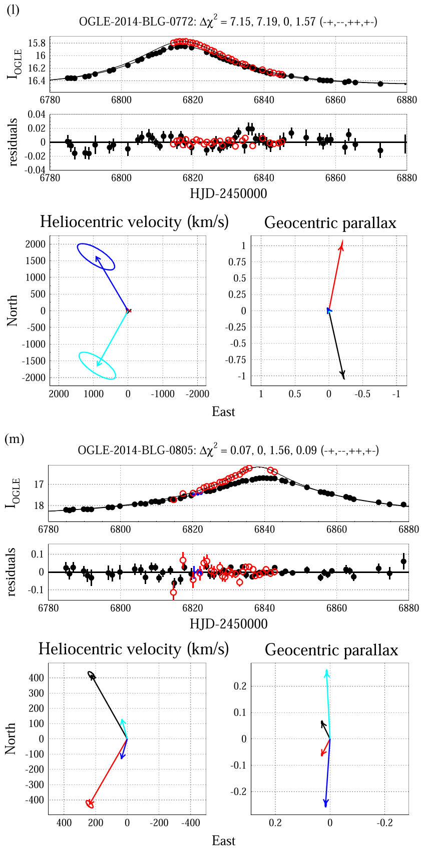

Figure 1. (Continued.)

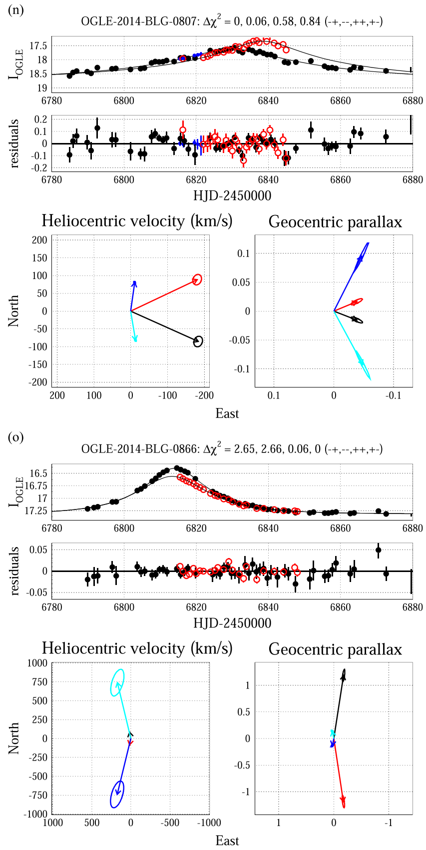

Figure 1. (Continued.)

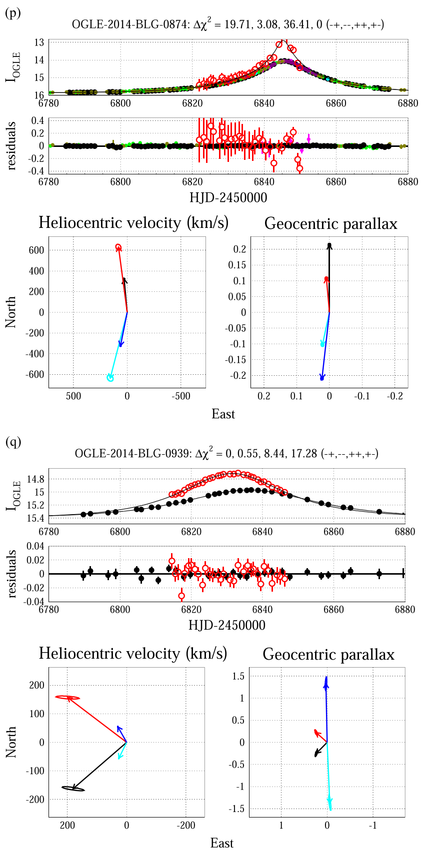

Figure 1. (Continued.)

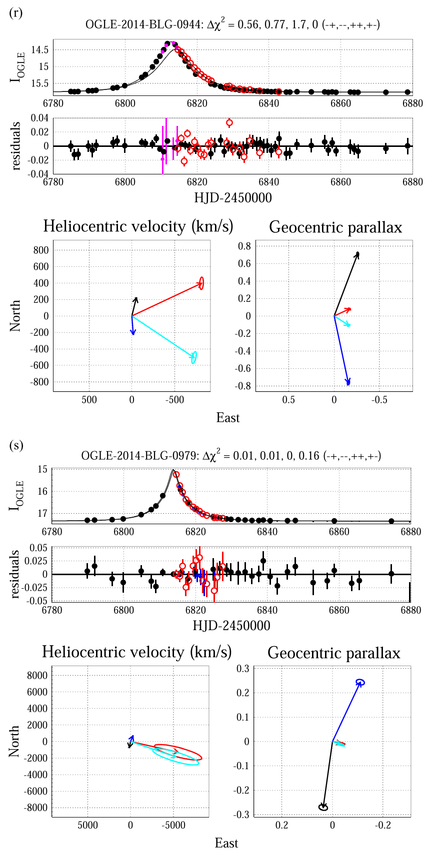

Figure 1. (Continued.)

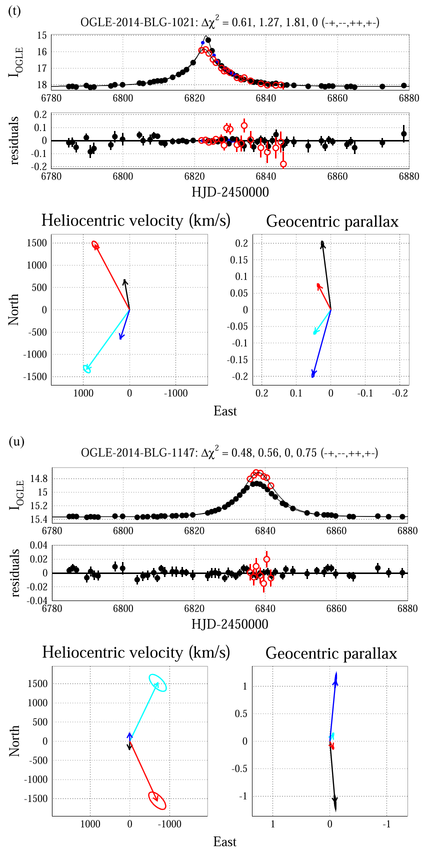

Figure 1. (Continued.)

$\boldsymbol{v}_{\oplus,\perp}(\mathrm{N, E}) \sim (0, 30)\ \mathrm{km\ s^{-1}}$. Hence, $\tilde{\boldsymbol{v}}_{\rm geo}$ can easily be estimated from these diagrams by eye simply by displacing all vectors by $30\ \mathrm{km\ s^{-1}}$ to the west. (For completeness we note that $\pi_{\rm E,hel} = (\tilde{\boldsymbol{v}}_{\rm hel}/\tilde{v}_{\rm hel})\pi_{\rm E,geo}$.)

These diagrams can be used to judge the relative plausibility of the four solutions. Consider, for example, OGLE-2014-BLG-0678. The *Spitzer* and ground-based light curves are very similar, i.e., similar t_0 and u_0. This is what would be expected if $\pi_{\rm E}$ were very small, and indeed such small $\pi_{\rm E}$ is apparent for the black $(-+)$ and red $(--)$ solutions in the lower right panel. However, this panel also shows the two $(+\pm)$ solutions, which have similarly small Δt_0 (so similar $\pi_{{\rm E},E}$) to the $(-\pm)$ solutions, but very different Δu_0 (so $\pi_{{\rm E},N}$). These correspond roughly to $\Delta u_0 \sim \pm 2u_0$. One of these solutions can clearly be ruled out by its high $\Delta\chi^2(++) = 24.6$, but the other is only slightly disfavored, $\Delta\chi^2(+-) = 3.7$.

Nevertheless, following the previously noted argument of James Rich (Section 1.1), both of the $(+\pm)$ solutions for OGLE-2014-BLG-0678 are highly disfavored. To make the general argument more concrete, we present a "worked example" for this case.

We first note the values, $|\Delta\tau| \sim 0.04$, $|\Delta u_{0,-,\pm}| \sim 0.07$, and $u_{0,\oplus} \sim 0.43$ (here $\Delta\tau \equiv \Delta t_0/t_{{\rm E},\oplus}$), with therefore $|\Delta\tau| \sim |\Delta u_{0,-,\pm}|$ and additionally $|\Delta u_{0,-,\pm}| \ll |u_{0,\oplus}|$. As expected on general grounds, we also find $|\Delta u_{0,+,\pm}| \sim 0.8 \sim 2|u_{0,\oplus}|$. We therefore fall within the situation for which the Rich argument applies, $\pi_{{\rm E},-} \ll \pi_{{\rm E},+}$, and we can conclude that the $\pi_{{\rm E},-}$ solution is correct. Indeed, according to Equations (5) and (6), if $\pi_{{\rm E},+}$ were correct, with $\epsilon_0 = 0.1$ in this case, the probability of finding such a small ratio would be about $P \sim 0.5\%$.

More generally, we evaulate the impact of the Rich argument using Equation (6), which was derived in Section 1.1. The argument applies strongly (in the sense that $\pi_{{\rm E},+\pm} \gtrsim 8\pi_{{\rm E},-,\pm}$, i.e., $P < 1/128$) to a total of 10 events. Of these 10, the argument is strongly confirmed by $\Delta\chi^2 > 16$ for three cases (OGLE-2014-BLG-0419, OGLE-2014-BLG-0641, OGLE-2014-BLG-0667), and moderately $(\Delta\chi^2 > 9)$ and marginally $(\Delta\chi^2 > 4)$ confirmed for one each, OGLE-2014-BLG-0752 and OGLE-2014-BLG-0670, respectively. For four other cases (OGLE-2014-BLG-0678, OGLE-2014-BLG-0866, OGLE-2014-BLG-0979, OGLE-2014-BLG-1147) there is no significant information from $\Delta\chi^2$. Finally, there is one case (OGLE-2014-BLG-0772) for which Rich's argument is marginally contradicted by $\Delta\chi^2 = 7.2$.

The argument applies with moderate strength $(2.5 \lesssim \pi_{{\rm E},+\pm}/\pi_{{\rm E},-,\pm} \lesssim 8)$ to five events (OGLE-2014-BLG-0337, OGLE-2014-BLG-0494, OGLE-2014-BLG-0805, OGLE-2014-BLG-0807, OGLE-2014-BLG-0944). There is strong confirmation from $\Delta\chi^2$ for the third of these, strong contradiction for the second, and no information from the remaining three.

We conclude that this argument can be reliably applied only to strong cases and should be applied to moderate cases only when significantly confirmed by $\Delta\chi^2$. In particular, we note that of the six cases for which the Rich argument was strongly tested by $\Delta\chi^2$, the only case for which it was contradicted was OGLE-2014-BLG-0337, i.e., a moderate case with $\pi_{{\rm E},+}/\pi_{{\rm E},-} \sim 2.5$.

Finally, we note that we have included OGLE-2014-BLG-0939 in Figure 1, which was previously analyzed by Yee et al. (2015), to allow easy comparison with the other isolated-lens events. At the level of analysis of the current paper this would be ranked as a case for which the Rich argument is moderately applicable and is marginally confirmed by χ^2. In fact, the source proper-motion measurement carried out by Yee et al. (2015) actually strongly confirms the $(--)$ solution.

Figure 2 illustrates the special case of OGLE-2014-BLG-1049. The Earth-based light curve (upper panel) is quite well determined by the combination of OGLE and PLANET SAAO data, which later begin just 7 hr after the high-magnification $(u_{0,\oplus} = 0.01,\ A_{{\rm max},\oplus} = 100)$ peak. By contrast, the *Spitzer* data, which begin about 13 hr later, leave the peak magnification as seen by *Spitzer* relatively unconstrained. In particular, $u_{0,Spitzer}$ is consistent with zero, implying that there are a continuum of viable solutions across this "boundary" from $u_{0,Spitzer} > 0$ to $u_{0,Spitzer} < 0$ and hence a merger of the $\Delta u_{0,\pm,+}$ solutions (also of the $\Delta u_{0,\pm,-}$ solutions). The $\pi_{\rm E,geo}$ distribution for the $\Delta u_{0,\pm,+}$ solutions is shown in the lower right panel and the corresponding $\tilde{\boldsymbol{v}}_{\rm hel}$ distribution in the lower left. The $\Delta u_{0,\pm,-}$ solutions (not shown) look extremely similar and have a nearly identical χ^2 minimum.

5. DISTRIBUTION OF LENS DISTANCES

For each of the 22 isolated-lens events (21 analyzed here plus OGLE-2014-BLG-0939), we calculate the relative likelihood of the lens being at different distances and display our results in Figure 3. As explained below, the abscissa is not the lens distance but rather

$$D \equiv \frac{\rm kpc}{\pi_{\rm rel}/{\rm mas} + 1/8.3}, \tag{14}$$

which has limiting forms

$$D \to D_L \quad (D_L \lesssim D_S/2);$$
$$(8.3\ {\rm kpc} - D) \to (D_S - D_L) \quad (D_L \gtrsim D_S/2). \tag{15}$$

The probability distribution is calculated using a restricted set of Bayesian priors, i.e., primarily *kinematic* priors, combined with the measured values of $\tilde{\boldsymbol{v}}_{\rm hel}$ and $\pi_{\rm E}$, as well as discrimination among the four solutions based on χ^2 and the Rich argument. That is, there are essentially three factors (in addition to the light-curve-based measurements): phase-space density, $\Delta\chi^2$ (displayed above the light curve for each event in Figure 1 and color coded in the bottom panels), and the Rich argument. As discussed in Section 4, the last was applied by suppressing the $(+\pm)$ solutions, but only for the 10 "strong cases" listed there.

The phase-space density combines the observed value of $\tilde{\boldsymbol{v}}_{\rm hel}$ with the kinematic priors. It is computed as an integral along the line of sight, with four factors derived from the generic rate equation "$\Gamma = n\sigma v$." The first is a volume element $D_L^2\Delta D_L$. The second is the value of the expected $\tilde{\boldsymbol{v}}$ distribution at the measured value, which we describe below. The third is the "cross section," which is $2\theta_{\rm E} = 2\pi_{\rm rel}/\pi_{\rm E}$. Since $\pi_{\rm E}$ is constant along the integral, this factor is effectively $\propto\pi_{\rm rel}$. The fourth is the "velocity" $\mu = \pi_{\rm rel}\tilde{v}/{\rm AU}$. Again, since $\tilde{v}$ is constant, this term is also $\propto\pi_{\rm rel}$. Hence, ignoring for the moment the projected-velocity distribution term, the integrand is just $(\pi_{\rm rel}D_L)^2 \to (1 - D_L/D_S)^2$, which falls off fairly slowly in the disk and then drops rapidly in the bulge.

Table 1
Event Parameters

Event OGLE-2014-BLG-	R.A. (J2000) (degree)	Decl. (J2000) (degree)	$\beta_{\rm ec}$ (J2000) (degree)	$I - [3.6]$	*Spitzer* (epochs)	Ground-based Data
0099	269.607333	−28.279833	−4.94030	-0.69 ± 0.06	32	OGLE, MOA, Wise, RoboNet[a,b,c], MiNDSTEp[d]
0115	269.156917	−28.515750	−5.17792	-0.86 ± 0.06	22	OGLE, MOA, Wise, MiNDSTEp[d]
0337	267.841125	−29.733250	−6.40733	⋯	37	OGLE, Wise
0419	269.629708	−30.100639	−6.76105	-1.01 ± 0.07	37	OGLE, Wise
0494	273.191542	−28.227139	−4.91827	-1.41 ± 0.15	43	OGLE, MOA, RoboNet[a,b,c], MiNDSTEp[d,e]
0589	268.380625	−21.014917	2.31661	0.54 ± 0.08	23	OGLE, RoboNet[a,b,c], MiNDSTEp[e]
0641	267.682667	−33.905972	−10.58165	-1.11 ± 0.06	28	OGLE, MOA
0667	272.704625	−26.418028	−3.10071	-1.20 ± 0.07	36	OGLE, MOA
0670	265.542000	−33.495472	−10.21366	1.16 ± 0.20	20	OGLE
0678	267.976667	−31.903389	−8.57554	0.03 ± 0.10	33	OGLE
0752	270.657333	−29.594694	−6.25600	-1.13 ± 0.06	29	OGLE
0772	265.581875	−23.618861	−0.34067	-0.34 ± 0.07	26	OGLE
0805	263.152708	−28.163667	−4.96693	0.34 ± 0.17	25	OGLE, PLANET
0807	265.186792	−23.863722	−0.59693	-0.86 ± 0.09	25	OGLE, PLANET
0866	268.025458	−23.409194	−0.08156	-0.47 ± 0.10	25	OGLE
0874	270.230125	−27.545861	−4.20602	-1.26 ± 0.08	34	OGLE, PLANET, MOA, Wise, RoboNet[a,b], MiNDSTEp[d,e]
0944	263.204125	−28.439028	−5.23984	0.42 ± 0.15	19	OGLE, MiNDSTEp[e]
0979	267.682500	−35.709139	−12.38457	-1.50 ± 0.12	13	OGLE, PLANET
1021	264.315042	−29.194722	−5.95271	0.02 ± 0.10	18	OGLE, PLANET
1049	274.107125	−31.012333	−7.72275	-2.31 ± 0.06	19	OGLE, PLANET
1147	261.205875	−29.600222	−6.49370	-0.35 ± 0.08	7	OGLE

Note. For the ensemble of the 21 events we report the name, according to the OGLE naming scheme, the coordinates, the instrumental color, $I - [3.6]$, evaluated as discussed in the text, the number of epochs of *Spitzer* observations, and the ground-based data used for the analysis. The reported instrumental colors are suitable for *Spitzer* data reduced by a PRF-based analysis; for data reduced by aperture photometry we use an aperture correction factor.
[a] Siding Spring LCOGT telescope (Australia).
[b] Sutherland LCOGT telescope (South Africa).
[c] Cerro Tololo LCOGT telescope (Chile).
[d] Danish telescope, La Silla (Chile).
[e] Salerno University Telescope (Italy).

All sources were assumed to be in the bulge and to have an isotropic proper-motion dispersion in the bulge frame of $\sigma_\mu = 3.0\ {\rm mas\ yr^{-1}}$ (corresponding to $\sim 120\ {\rm km\ s^{-1}}$) in each direction. Bulge lenses were assumed to have the same proper-motion distribution. Disk lenses were assumed to be moving with peculiar motions of dispersions $18\ {\rm km\ s^{-1}}$ and $33\ {\rm km\ s^{-1}}$ in the vertical and rotation directions relative to a flat rotation curve at $v_{\rm rot} = 240\ {\rm km\ s^{-1}}$. The Sun was taken to be moving at 7 and $12\ {\rm km\ s^{-1}}$ relative to the same rotation curve.

For disk lenses we simply assumed that the source was at $D_S = 8.3$ kpc. Of course, these sources are actually at a range of distances, and the mean distance varies as a function of Galactic longitude due to the tilt of the Galactic bar. However, to first order, our determinations are sensitive only to $\pi_{\rm rel}$ (rather than to D_L and D_S separately), so stepping over a discrete set of D_S would just yield extremely similar distributions in $\pi_{\rm rel}$. It is for this reason that we report the quantity "D" in Figure 3, which is a monotonic function of the quantity $(\pi_{\rm rel})$ that we are actually measuring (Equation (14)). The reasons for reporting D rather than $\pi_{\rm rel}$ itself are twofold. First, $\pi_{\rm rel}$ is not commonly used as an independent variable, and hence intuition about it is not widespread. This is particularly problematic because many lenses would be bunched up at low $\pi_{\rm rel}$. More importantly however, the figure as plotted gives direct information about D_L for essentially all lenses in the disk (just from the value of D), and it gives direct information about the distance from the lens to the source for all lenses in or near the bulge from $D_S - D_L \simeq 8.3\ {\rm kpc} - D$.

For bulge lenses we conducted an integral over lens distances for each value of "D" by first translating this quantity into $\pi_{\rm rel}$ and then holding this fixed while allowing D_L to vary. We adopted an r^{-2} profile for the bulge, flattened in the vertical direction by a factor 0.6, and we truncated it at 2 kpc. That is, in the above integrals, we weighted by the product of the densities of the lenses and sources, according to the Galactic coordinates of the source.

Since $\pi_{\rm E}$ is measured, each $\pi_{\rm rel}$ implies a mass $M = \pi_{\rm rel}/\kappa\pi_{\rm E}^2$. We truncated the bulge lenses at $M > 1.1\ M_\odot$ and the disk lenses at $M > 1.5\ M_\odot$ due to the paucity of such stars in each population. There may be additional modest constraints on lens mass from (lack of) blended light, but we did not attempt to evaluate these.

As can be seen from Figure 3, the great majority of disk lenses have distance distributions that are relatively compact and characterized by a single peak. This can be understood by inspection of Figure 1. In many cases, one solution is strongly preferred by χ^2. OGLE-2014-BLG-0678 provides a good example for which there is no strong preference in χ^2 between the two allowed solutions. However, one of the two solutions (black) is closely aligned with the direction of Galactic rotation (roughly 30° east of north) and so is strongly favored by the kinematic priors. The second (red) solution then contributes almost nothing to the total probability. OGLE-2014-BLG-0670 provides another instructive case. Here the kinematically preferred solution (red) is marginally disfavored by $\Delta\chi^2 = 3.2$. These two factors roughly cancel, but the two solutions predict very similar distance distributions, so the

Table 2
Event Fit Parameters

Event OGLE-2014-BLG-	$\Delta\chi^2$	$t_0 - 6800$ HJD −2,450,000	u_0	$t_{\rm E}$ day	$\pi_{\rm E,N}$	$\pi_{\rm E,E}$	$\tilde{v}_{\rm hel,\,N}$ (km s^{-1})	$\tilde{v}_{\rm hel,\,E}$ (km s^{-1})	$I_{\rm OGLE}$	$f_{\rm OGLE}$[a]	mag$_{Spitzer}$[b]	$f_{Spitzer}$[a]
0099	17.3	76.910	0.3828	116.2	−0.0823	0.2060	−26.7	82.9	16.831	0.147	17.849	0.230
		0.383	0.0067	1.3	0.0045	0.0033	1.0	1.5	0.026	0.028	0.078	0.161
	0.0	76.920	−0.4075	111.1	0.1092	0.2157	27.3	78.0	16.734	0.049	17.748	0.140
		−0.407	0.0057	1.0	0.0056	0.0036	1.0	1.4	0.021	0.021	0.071	0.137
	241.5	76.949	0.2033	178.2	−0.2468	0.1594	−29.6	38.4	17.728	1.618	19.042	3.534
		0.203	0.0023	1.6	0.0025	0.0022	0.2	0.2	0.015	0.035	0.047	0.385
	203.0	76.713	−0.2962	127.1	0.3698	0.1551	29.5	33.6	17.214	0.632	18.558	1.368
		−0.296	0.0029	0.9	0.0039	0.0024	0.2	0.2	0.013	0.020	0.051	0.254
0115	10.1	59.612	0.2687	105.6	−0.0777	0.1215	−62.6	121.3	17.303	0.187	18.170	0.378
		0.269	0.0036	1.0	0.0050	0.0039	2.6	4.7	0.018	0.020	0.069	0.196
	0.0	59.645	−0.2867	100.5	0.0963	0.1128	73.9	113.9	17.212	0.091	18.094	0.332
		−0.287	0.0033	0.8	0.0057	0.0040	3.1	4.6	0.016	0.016	0.063	0.179
	269.6	59.257	0.2011	129.0	−0.2519	0.1232	−44.4	46.7	17.693	0.701	18.818	1.704
		0.201	0.0022	1.1	0.0034	0.0024	0.4	0.5	0.014	0.021	0.052	0.334
	94.3	59.395	−0.2622	102.9	0.3416	0.0824	45.1	36.8	17.337	0.225	18.375	0.362
		−0.262	0.0027	0.8	0.0049	0.0033	0.4	0.5	0.014	0.015	0.056	0.227
0337	38.0	22.967	0.5315	45.0	−0.0790	0.1298	−131.9	245.7	16.759	−0.022	15.711	−0.381
		0.531	0.0077	0.4	0.0152	0.0088	17.2	24.5	0.024	0.022	0.084	0.091
	19.5	23.016	−0.5465	44.4	0.3282	0.1015	118.1	62.8	16.711	−0.063	16.670	1.242
		−0.547	0.0079	0.4	0.0294	0.0102	6.4	7.6	0.024	0.021	0.157	0.439
	1611.6	22.472	0.4691	48.8	−0.6151	0.0715	−57.1	35.8	16.959	0.187	18.399	14.687
		0.469	0.0056	0.4	0.0091	0.0039	0.5	0.4	0.019	0.021	0.078	1.295
	0.0	23.022	−0.6558	38.9	0.9844	−0.2310	42.7	19.1	16.385	−0.306	16.616	1.036
		−0.656	0.0121	0.5	0.0295	0.0208	1.1	0.4	0.034	0.022	0.161	0.427
0419	0.6	22.886	0.2401	48.6	−0.0253	−0.0334	−513.3	−648.8	18.202	0.328	19.391	0.430
		0.240	0.0048	0.7	0.0071	0.0033	86.6	132.2	0.026	0.031	0.058	0.136
	0.0	22.896	−0.2414	48.4	0.0185	−0.0417	318.3	−687.2	18.195	0.320	19.400	0.441
		−0.241	0.0049	0.7	0.0077	0.0032	96.5	104.5	0.026	0.031	0.058	0.136
	94.4	22.763	0.2345	49.4	−0.4832	−0.0630	−70.9	19.8	18.230	0.363	19.447	0.578
		0.235	0.0047	0.7	0.0114	0.0040	1.1	0.4	0.026	0.032	0.058	0.144
	23.4	22.954	−0.2549	46.5	0.4700	−0.1851	68.9	2.1	18.122	0.234	19.419	0.325
		−0.255	0.0052	0.6	0.0107	0.0058	1.0	0.4	0.027	0.030	0.059	0.141
0494	5.9	17.310	0.1540	33.2	0.0381	0.0953	189.5	499.7	14.493	−0.004	16.138	0.212
		0.154	0.0005	0.1	0.0027	0.0029	5.4	18.8	0.004	0.004	0.016	0.021
	0.0	17.306	−0.1539	33.3	−0.0048	0.1074	−20.4	511.8	14.493	−0.003	16.129	0.204
		−0.154	0.0005	0.1	0.0018	0.0037	7.3	17.0	0.004	0.004	0.017	0.021
	160.5	17.278	0.1547	33.2	−0.4448	0.1101	−109.0	55.6	14.488	−0.008	16.131	0.216
		0.155	0.0005	0.1	0.0028	0.0029	0.8	0.4	0.004	0.004	0.016	0.021
	233.9	17.340	−0.1552	33.1	0.4445	−0.0276	118.5	21.0	14.482	−0.014	16.199	0.268
		−0.155	0.0005	0.1	0.0032	0.0022	0.7	0.7	0.004	0.004	0.016	0.022
0589	1.9	7.622	0.0518	33.9	0.3727	0.1983	106.1	84.3	16.942	−0.052	16.703	0.118
		0.052	0.0006	0.3	0.0286	0.0333	8.0	9.7	0.012	0.010	0.070	0.075
	1.0	7.624	−0.0516	34.0	−0.3700	0.2040	−106.3	85.7	16.946	−0.049	16.657	0.071
		−0.052	0.0006	0.3	0.0293	0.0337	8.3	9.6	0.012	0.010	0.071	0.073
	0.0	7.624	0.0517	34.1	−0.5368	0.1728	−86.6	55.2	16.945	−0.049	16.639	0.051
		0.052	0.0006	0.3	0.0303	0.0350	4.4	5.9	0.012	0.010	0.072	0.072
	0.7	7.622	−0.0519	33.9	0.5544	0.1583	84.4	51.8	16.939	−0.054	16.701	0.115
		−0.052	0.0006	0.3	0.0277	0.0335	4.0	5.3	0.012	0.010	0.071	0.075
0641	0.0	46.959	0.5398	38.6	−0.0182	0.0333	−568.5	1062.6	16.876	−0.071	18.015	0.311
		0.540	0.0162	0.7	0.0106	0.0100	218.1	398.3	0.050	0.043	0.080	0.110
	0.9	46.974	−0.5411	38.6	0.0202	0.0327	610.3	1021.2	16.871	−0.075	17.992	0.277
		−0.541	0.0163	0.7	0.0121	0.0103	246.1	418.0	0.050	0.043	0.077	0.104
	318.9	46.465	0.4434	42.9	−0.6919	0.0509	−60.2	32.1	17.197	0.251	18.614	1.451
		0.443	0.0116	0.7	0.0194	0.0069	0.8	0.7	0.041	0.047	0.064	0.165
	23.7	46.971	−0.5893	35.1	0.8159	−0.1728	51.0	17.5	16.722	−0.193	17.882	0.028
		−0.589	0.0188	0.7	0.0286	0.0140	0.8	0.5	0.055	0.041	0.082	0.097
0667	0.0	35.115	0.4672	32.3	0.1128	0.0386	174.8	146.1	16.161	0.022	17.280	0.224
		0.467	0.0096	0.4	0.0135	0.0061	31.2	46.1	0.032	0.030	0.075	0.106
	8.9	35.093	−0.4656	32.4	−0.1021	0.0588	−392.9	255.8	16.166	0.027	17.311	0.275
		−0.466	0.0095	0.4	0.0146	0.0050	23.9	54.2	0.032	0.031	0.075	0.109
	285.3	34.818	0.4739	31.7	−0.9800	−0.0669	−54.9	25.5	16.137	0.000	17.485	0.553
		0.474	0.0102	0.4	0.0234	0.0086	0.8	0.4	0.034	0.031	0.076	0.132

Table 2
(Continued)

Event	$\Delta\chi^2$	t_{0-6800} HJD	u_0	t_E	$\pi_{E,N}$	$\pi_{E,E}$	$\tilde{v}_{hel,N}$	$\tilde{v}_{hel,E}$	I_{OGLE}	f_{OGLE}[a]	$mag_{Spitzer}$[b]	$f_{Spitzer}$[a]
OGLE-2014-BLG-		−2,450,000		day			(km s−1)	(km s−1)				
	59.8	34.999	−0.5000	30.6	1.0009	−0.2452	53.8	16.2	16.050	−0.078	17.261	0.144
		−0.500	0.0111	0.4	0.0231	0.0122	0.8	0.3	0.036	0.031	0.079	0.109
0670	3.2	15.144	0.7697	25.6	0.0557	0.0928	321.4	564.3	16.049	0.084	14.946	0.539
		0.770	0.0934	2.0	0.0697	0.0300	238.6	360.8	0.239	0.239	0.296	0.425
	0.0	15.105	−0.7478	26.2	−0.1053	0.1485	−210.1	325.2	16.106	0.142	14.777	0.310
		−0.748	0.0890	2.0	0.0809	0.0436	82.1	162.6	0.232	0.243	0.291	0.355
	5.2	14.597	0.7250	27.0	−1.7211	−0.2294	−36.5	23.9	16.162	0.203	14.978	0.579
		0.725	0.0881	2.1	0.2054	0.0596	2.1	0.7	0.233	0.258	0.289	0.428
	32.7	15.481	−0.9690	21.9	1.8265	−0.9361	34.4	11.3	15.560	−0.309	14.635	0.074
		−0.969	0.1709	2.5	0.2888	0.2070	2.5	0.6	0.391	0.248	0.437	0.453
0678	0.5	22.017	0.4260	30.3	−0.0556	0.0660	−426.8	536.0	17.467	0.267	17.381	0.309
		0.426	0.0212	1.0	0.0199	0.0105	76.4	151.7	0.076	0.088	0.107	0.156
	0.0	22.034	−0.4284	30.2	0.0810	0.0532	494.6	353.8	17.459	0.257	17.389	0.313
		−0.428	0.0214	1.0	0.0212	0.0117	71.5	125.6	0.076	0.088	0.108	0.156
	24.6	21.863	0.4149	30.8	−0.8523	0.0245	−65.7	31.0	17.506	0.312	17.413	0.383
		0.415	0.0207	1.0	0.0455	0.0111	1.9	0.9	0.075	0.091	0.107	0.162
	3.7	22.111	−0.4541	29.0	0.8474	−0.2429	65.2	10.5	17.367	0.155	17.395	0.215
		−0.454	0.0235	1.0	0.0446	0.0193	1.8	0.7	0.081	0.086	0.111	0.160
0752	0.8	39.353	0.6781	39.7	0.0669	0.0381	491.7	309.0	16.682	0.609	17.816	0.409
		0.678	0.0500	1.9	0.0165	0.0106	56.8	131.1	0.138	0.204	0.154	0.209
	0.0	39.311	−0.6611	40.5	−0.0664	0.0537	−389.6	343.6	16.730	0.681	17.857	0.474
		−0.661	0.0482	1.9	0.0189	0.0107	53.7	114.8	0.134	0.208	0.149	0.212
	137.1	38.384	0.4633	49.7	−0.8725	−0.0944	−39.7	24.8	17.340	1.949	18.565	1.878
		0.463	0.0261	1.9	0.0469	0.0132	0.8	0.4	0.090	0.244	0.107	0.307
	11.8	38.951	−0.7303	36.1	1.1933	−0.3988	35.8	16.9	16.537	0.408	17.682	0.079
		−0.730	0.0564	1.9	0.0831	0.0384	0.9	0.2	0.149	0.193	0.163	0.183
0772	7.2	17.428	0.4645	26.9	−0.0308	0.0161	−1643.0	886.4	17.066	0.727	17.353	0.417
		0.464	0.0308	1.1	0.0124	0.0046	404.1	528.5	0.104	0.166	0.089	0.112
	7.2	17.429	−0.4644	26.9	0.0304	0.0168	1618.8	923.9	17.066	0.727	17.353	0.417
		−0.464	0.0308	1.1	0.0125	0.0046	394.7	536.3	0.104	0.166	0.089	0.112
	0.0	17.403	0.4684	26.8	−0.9883	−0.2107	−63.3	15.7	17.051	0.703	17.403	0.462
		0.468	0.0308	1.1	0.0583	0.0150	1.3	0.3	0.104	0.162	0.084	0.111
	1.6	17.415	−0.4687	26.8	0.9903	−0.1883	62.1	17.0	17.050	0.701	17.412	0.472
		−0.469	0.0308	1.1	0.0583	0.0136	1.3	0.2	0.104	0.162	0.084	0.111
0805	0.1	39.907	0.1794	55.8	−0.0586	0.0289	−428.4	238.4	18.593	0.067	18.583	2.236
		0.179	0.0092	2.1	0.0054	0.0023	24.1	21.9	0.064	0.062	0.069	0.290
	0.0	39.919	−0.1808	55.4	0.0609	0.0288	417.1	226.3	18.582	0.056	18.588	2.241
		−0.181	0.0093	2.1	0.0056	0.0023	23.5	21.0	0.064	0.062	0.069	0.291
	1.6	39.865	0.1759	56.4	−0.2461	0.0157	−126.2	36.1	18.618	0.092	18.593	2.283
		0.176	0.0091	2.1	0.0120	0.0021	2.0	1.2	0.064	0.063	0.069	0.291
	0.1	39.918	−0.1823	54.8	0.2497	0.0120	124.2	34.2	18.572	0.047	18.614	2.299
		−0.182	0.0094	2.1	0.0121	0.0021	2.0	1.1	0.064	0.061	0.068	0.295
0807	0.0	30.101	0.0630	182.8	−0.0153	−0.0385	−85.4	−183.3	20.963	5.784	21.898	6.906
		0.063	0.0170	43.7	0.0051	0.0096	14.8	11.8	0.308	1.900	0.315	2.765
	0.1	30.103	−0.0632	182.2	0.0164	−0.0383	88.7	−180.5	20.958	5.755	21.894	6.859
		−0.063	0.0171	43.4	0.0053	0.0095	14.7	11.8	0.306	1.884	0.314	2.745
	0.6	30.059	0.0626	183.2	−0.0921	−0.0483	−81.5	−13.0	20.969	5.831	21.910	6.824
		0.063	0.0170	44.0	0.0248	0.0124	3.0	2.5	0.309	1.926	0.318	2.790
	0.8	30.069	−0.0636	180.5	0.0947	−0.0464	80.7	−10.8	20.951	5.717	21.890	6.612
		−0.064	0.0172	43.0	0.0253	0.0118	3.0	2.4	0.308	1.881	0.312	2.697
0866	2.7	14.116	0.4062	17.3	0.1300	0.0254	739.8	172.9	17.523	0.211	17.813	0.450
		0.406	0.0383	1.0	0.0284	0.0226	176.7	84.4	0.142	0.158	0.172	0.228
	2.7	14.115	−0.4062	17.3	−0.1298	0.0259	−740.2	175.9	17.523	0.211	17.814	0.450
		−0.406	0.0383	1.0	0.0283	0.0227	177.0	84.1	0.142	0.158	0.172	0.228
	0.1	14.119	0.4183	17.1	−1.1858	−0.1739	−84.0	16.2	17.478	0.162	17.801	0.429
		0.418	0.0405	1.0	0.1158	0.0220	3.4	1.5	0.147	0.157	0.175	0.229
	0.0	14.121	−0.4186	17.1	1.1861	−0.1788	83.2	15.9	17.477	0.161	17.799	0.427
		−0.419	0.0406	1.0	0.1159	0.0223	3.4	1.5	0.147	0.157	0.175	0.229
0874	19.7	45.665	0.1852	25.5	−0.1028	0.0212	−635.1	159.2	15.908	0.023	17.350	1.387
		0.185	0.0007	0.1	0.0052	0.0040	29.9	26.9	0.005	0.004	0.059	0.247
	3.1	45.668	−0.1855	25.4	0.1074	0.0092	629.0	82.1	15.906	0.021	17.377	1.456
		−0.186	0.0007	0.1	0.0049	0.0039	27.9	23.9	0.005	0.004	0.059	0.252

Table 2
(Continued)

Event	$\Delta\chi^2$	t_{0-6800} HJD	u_0	t_E	$\pi_{E,N}$	$\pi_{E,E}$	$\tilde{v}_{hel,N}$	$\tilde{v}_{hel,E}$	I_{OGLE}	f_{OGLE}[a]	$mag_{Spitzer}$[b]	$f_{Spitzer}$[a]
OGLE-2014-BLG-		−2,450,000		day			(km s−1)	(km s−1)				
	36.4	45.662	0.1850	25.5	−0.2097	0.0225	−321.0	62.7	15.910	0.024	17.382	1.494
		0.185	0.0007	0.1	0.0049	0.0038	7.5	5.7	0.005	0.004	0.058	0.253
	0.0	45.669	−0.1857	25.4	0.2132	−0.0002	319.3	28.0	15.905	0.020	17.374	1.434
		−0.186	0.0007	0.1	0.0051	0.0038	7.5	5.7	0.005	0.004	0.059	0.252
0944	0.6	12.751	0.2742	9.9	0.0801	−0.1700	397.2	−815.4	15.668	−0.085	15.648	0.099
		0.274	0.0077	0.2	0.0110	0.0113	75.2	21.8	0.037	0.031	0.063	0.065
	0.8	12.750	−0.2741	9.9	−0.1071	−0.1605	−505.4	−727.6	15.668	−0.084	15.638	0.089
		−0.274	0.0077	0.2	0.0103	0.0129	72.7	26.1	0.036	0.031	0.064	0.065
	1.7	12.749	0.2741	9.9	−0.7638	−0.1578	−220.9	−16.7	15.669	−0.084	15.605	0.056
		0.274	0.0077	0.2	0.0245	0.0122	2.7	4.6	0.036	0.031	0.065	0.064
	0.0	12.752	−0.2744	9.9	0.7075	−0.2602	217.6	−51.5	15.667	−0.085	15.700	0.151
		−0.274	0.0077	0.2	0.0231	0.0105	2.1	4.7	0.037	0.031	0.061	0.066
0979	0.0	13.737	0.1064	8.9	−0.0076	−0.0330	−1291.2	−5550.2	17.460	0.108	18.925	−0.162
		0.106	0.0044	0.3	0.0046	0.0166	941.7	2774.6	0.049	0.050	0.088	0.076
	0.0	13.737	−0.1064	8.9	−0.0114	−0.0326	−1849.3	−5277.8	17.460	0.108	18.925	−0.162
		−0.106	0.0044	0.3	0.0070	0.0160	988.5	2699.6	0.049	0.050	0.088	0.076
	0.0	13.737	0.1064	8.9	−0.2711	0.0365	−700.9	122.9	17.461	0.109	18.905	−0.173
		0.106	0.0044	0.3	0.0116	0.0170	10.8	45.3	0.049	0.050	0.088	0.076
	0.2	13.738	−0.1065	8.9	0.2440	−0.1105	660.7	−270.1	17.460	0.107	18.948	−0.150
		−0.106	0.0044	0.3	0.0113	0.0162	27.2	37.6	0.049	0.050	0.087	0.077
1021	0.6	23.214	0.0604	13.2	0.0729	0.0359	1451.7	744.3	18.072	−0.028	17.998	2.126
		0.060	0.0027	0.4	0.0051	0.0031	86.9	66.1	0.047	0.042	0.056	0.172
	1.3	23.214	−0.0604	13.2	−0.0680	0.0458	−1331.6	926.6	18.072	−0.028	17.992	2.111
		−0.060	0.0027	0.4	0.0049	0.0035	81.5	72.2	0.047	0.042	0.057	0.172
	1.8	23.214	0.0604	13.2	−0.1940	0.0513	−635.1	196.8	18.073	−0.028	17.987	2.098
		0.060	0.0027	0.4	0.0088	0.0035	16.9	9.0	0.047	0.042	0.057	0.172
	0.0	23.214	−0.0604	13.2	0.1973	0.0243	656.1	110.4	18.072	−0.028	18.004	2.141
		−0.060	0.0027	0.4	0.0089	0.0029	16.9	8.9	0.047	0.042	0.056	0.173
1147	0.5	37.488	0.7191	7.7	−0.1197	−0.0554	−1554.7	−689.8	15.487	0.121	15.834	0.756
		0.719	0.0854	0.6	0.0254	0.0112	225.8	213.7	0.227	0.234	0.240	0.415
	0.6	37.489	−0.7192	7.7	0.1202	−0.0576	1523.3	−703.0	15.487	0.120	15.833	0.751
		−0.719	0.0854	0.6	0.0256	0.0115	220.8	213.8	0.227	0.234	0.240	0.414
	0.0	37.484	0.7192	7.7	−1.1089	−0.0929	−204.9	11.3	15.487	0.120	15.833	0.767
		0.719	0.0854	0.6	0.1326	0.0146	9.5	2.2	0.227	0.234	0.240	0.416
	0.8	37.491	−0.7206	7.7	1.0986	−0.1023	201.6	9.2	15.483	0.116	15.829	0.726
		−0.721	0.0858	0.6	0.1314	0.0150	9.5	2.2	0.228	0.234	0.241	0.412

Note. Fit parameters for the ensemble of 20 out the 21 events discussed in the text. For the analysis of OGLE-2014-BLG-1049 we refer to the text and Figure 2. For each event we report the four solutions in the order −+, −−, ++, +−. The light curves and the ellipses for each solution for the heliocentric velocity and the parallax are show in Figure 1.

[a] f indicates the ratio of blend to source flux.

[b] Instrumental magnitude.

combined probability distribution function is only slightly broadened by the ambiguity. In fact, of all the lenses in the sample, there are only two that are double-peaked: OGLE-2014-BLG-0944 and OGLE-2014-BLG-1021. In both cases, the $(-\pm)$ solutions correspond to bulge lenses while the $(+\pm)$ solutions correspond to disk lenses. And in both cases, χ^2 does very little to discriminate between possible solutions. Hence, we treat the bulge and disk solutions as equally likely in each case. The resulting double-peaked probability distributions are shown as bold dashed curves in Figure 3. Of the six other bulge-lens events, one has somewhat double-peaked features due to slightly different $\tilde{v}$ and the fact that the direction of $\tilde{\boldsymbol{v}}$ does not differentiate between solutions for bulge lenses (because of the assumed isotropy of proper motions).

Note that the Galactic model used for the distance measurements is simplified in a number of respects. First, there is no weighting by an assumed lens mass function, which is equivalent to assuming a flat prior in log mass. Second, for the disk lenses, there is no weighting by stellar density, which is equivalent to assuming that the declining density with distance from the plane due to the vertical scale height exactly cancels the increasing density as one approaches the Galactic center due to the radial scale length. And of course, we do not attempt to model even finer details, such as varying velocity dispersion, changing scale heights, etc.

We do not develop more sophisticated models for three reasons. First, we wish to demonstrate the power of kinematic priors (combined with $\tilde{\boldsymbol{v}}$ measurements) alone to constrain the distances to individual lenses. This point has been made before theoretically (Han & Gould 1995), but has never been demonstrated practically.

Second, the distance measurements individually, and especially cumulatively, are robust against modest changes in assumptions. For example, if v_{rot} is changed from 240 to

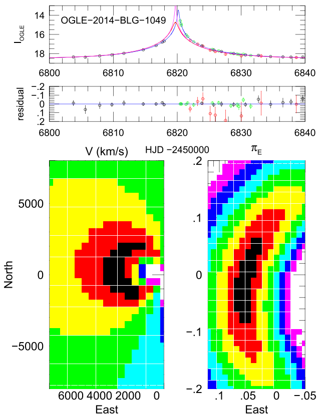

Figure 2. Top panel: OGLE-2014-BLG-1049 light curves for OGLE (black), PLANET SAAO (green), and *Spitzer* (red) data. Ground-based model (blue) is well defined, but many models are consistent with *Spitzer* data (e.g., red and magenta curves). Middle panel: residuals. Lower panel: $\Delta\chi^2$ offsets (1, 4, 9, ...) from minimum for geocentric parallax $\pi_{E,geo}$ (right) and heliocentric proper motion $\tilde{\boldsymbol{v}}_{hel}$ (left) for $u_{0,\oplus} > 0$ solution (merger of $\Delta u_{0,\pm,+}$ solutions). The $\Delta u_{0,\pm,-}$ solutions (not shown) are extremely similar. Because $u_{0,Spitzer}$ is more poorly defined than $t_{0,Spitzer}$ (top panel), Δu_0 is relatively uncertain, which translates directly into uncertainty in $\pi_{E,north}$ because the Earth-*Spitzer* axis is almost due east-west.

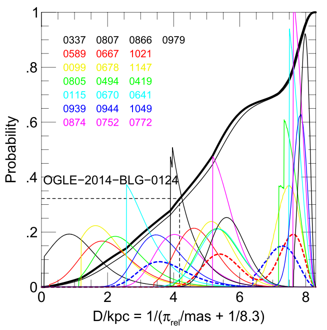

Figure 3. Distance estimates for each of the 21 lenses analyzed in the present paper plus OGLE-2014-BLG-0939 previously analyzed by Yee et al. (2015). The curves indicate the individual probability distributions. The corresponding event names are listed (upper left) in order of increasing mean estimated distance and are displayed in the same color as the distribution. The abscissa represents $D \equiv \mathrm{kpc}/(\pi_{rel}/\mathrm{mas} + 1/8.3)$ because it is the lens-source relative parallax π_{rel} that is actually measured. With this display $D_L \sim D$ for $D \lesssim D_S/2$ and $D_S - D_L \sim 8.3\ \mathrm{kpc} - D$ for $D \gtrsim D_S/2$. That is, the distance to the left boundary is very nearly the lens distance for the left half of the diagram and the distance to the right boundary is very nearly the distance between the lens and source for the right half. The value of D for the one planet detected by *Spitzer* in this campaign (orbiting the *lens* star in the event OGLE-2014-BLG-0124; Udalski et al. 2015) is shown by a dashed line. By merging the results of several such campaigns, one would measure the Galactic distribution of planets between the solar circle and the Galactic bulge. The calculation assumes a prior that is flat in log-mass with hard cutoffs at $M < 1.1\,M_\odot$ (bulge) and $M < 1.5\,M_\odot$ (disk). The cumulative distribution is shown for this calculation (bold) and also for one with a realistic mass prior (solid). The difference is extremely small because the kinematic priors completely dominate. Two events shown in bold dashed curves (OGLE-2014-BLG-0944 and OGLE-2014-BLG-1021) are the only ones with ambiguous (disk/bulge) distance determinations.

220 km s^{-1}, then the resulting version of Figure 3 is indistinguishable by eye from the current one. As another example, we have recomputed the distance distributions in Figure 3 using more realistic mass priors $dN/d\ln M \propto M^{-x}$, with $x = 0.3$ (1.3) for $M > (<)\ 0.5\,M_\odot$ for the disk and $x = 1$ (0.3) for $M > (<)\ 0.7\,M_\odot$ for the bulge. We plot the resulting cumulative distributions in Figure 3 with (solid) and without (bold) mass-function priors and note that they hardly differ. The reason for this is that over the regions of parameter space permitted by the kinematic priors, the mass priors generally do not vary very much.

Third, the proper context to study the impact of model variations is within a determination of the Galactic distribution of planets. As we discuss in Section 6 immediately below, such a measurement will require additional data.

6. PATHWAY TO GALACTIC DISTRIBUTION OF PLANETS

Figure 3 shows the cumulative distribution of D (monotonic function of π_{rel}), constructed by adding together all the lens probability distributions and normalizing to unity. The position of the one planet in the *Spitzer* sample (OGLE-2014-BLG-0124; Udalski et al. 2015) is also shown. Of course, nothing can be said about the Galactic distribution of planets based on a single planet. However, as emphasized in Section 1, events can be added from future observing campaigns by either *Spitzer* or other space observatories, with the isolated lenses forming the cumulative distribution function and the planetary events being used to measure the distance distribution of planets relative to this cumulative distribution.

Note that, in general, the individual distance measurements for the planetary events will be more accurate than for the isolated-lens events. This is because the former will mostly have measurements of θ_E (from caustic crossings and/or approaches) and thus $\pi_{rel} = \theta_E\pi_E$, while the latter will have distance estimates based on measured $\tilde{\boldsymbol{v}}_{hel}$ combined with kinematic priors. However, because there are many more isolated-lens events than planetary events and because the kinematic distance estimates for the isolated lenses are relatively accurate (see Figure 3), uncertainties in the cumulative distribution function will not contribute much to uncertainties in the overall measurement. Rather, the precision of measurement of the Galactic distribution of planets will

depend directly on how many planets are detected in space-based parallax surveys.

There are essentially two ways to increase the number of planets detected in space-based campaigns. The first is simply to observe in additional years and/or with additional satellites. Both *Spitzer* and *Kepler* (in its K2 mode) are quite well suited to this task. The second is to make more intensive use of the time available for Galactic bulge observations. In the case of *Kepler* this is an automatic feature since *Kepler* observes its targets almost continuously as a matter of course. For *Spitzer* more intensive observing can increase the number of planetary detections in two ways: first by allowing more events to be monitored and second by detecting planets from space that are not detected from the ground. Because the spacecraft probes a region of the Einstein ring that is more or less separated from the one seen from the ground, it can observe planetary caustics that are not seen from the ground (Gould & Horne 2013). However, this requires that the events be observed several to many times per day as compared to roughly once per day in the present campaign.

We note that roughly 30% of the lenses in our sample are in the bulge compared to roughly 60% expected for an unbiased sample of lensing events. Qualitatively, the reason for this is clear: the delay between recognition of the events and uploading coordinates to the spacecraft biases the sample to long events, which are preferentially in the disk. The same bias (for somewhat different reasons) affects the Gould et al. (2010) sample of high-magnification events.

This bias in the sample of underlying events does not in any way bias the measurement of the Galactic distribution of planets because the planetary events are subject to the same selection effects. However, to the extent that bulge events are underrepresented in the sample, it does mean that more planetary detections will be needed to measure the bulge-versus-disk fractions compared to what would be the case if there were more bulge events. Thus, it is important to develop more aggressive methods of identifying shorter events in time to upload coordinates, to the extent that this is possible.

Finally, we note the Galactic distribution of planets must be determined from the cumulative distribution (with distance) of *planet sensitivity* of events with parallaxes, not simply the cumulative distribution of the events themselves (as in Figure 3). Such planet-sensitivity calculations are an essential feature of all microlens planet frequency analyses. See, e.g., Figure 8 of Gaudi et al. (2002) or Figures 2–4 of Gould et al. (2010). Since microlens planet sensitivity is a function of both planet-star mass ratio q and normalized separation s, such studies of the Galactic distribution of planets can in principle also yield functions of these variables. At the first stages, however, all that will be accessible is the distribution of a planet frequency that is suitably averaged over q and s.

7. CONCLUSIONS

We have measured the microlens parallaxes of 21 events that were discovered by OGLE and observed by *Spitzer*, which was located ∼1 AU west of Earth in projection. We used kinematic priors based on a Galactic model to estimate distances to each of the lenses. In the great majority of cases, these distributions are well localized, as illustrated in Figure 3. Such localization was not guaranteed in advance because the lens distances are subject to a well-known fourfold degeneracy (Refsdal 1966; Gould 1994).

In the case of 10 of the 21 events, we were able to break the key element of this degeneracy by quantifying and testing an argument originally given by J. Rich (circa 1997, private communication). In its quantified form, this states that, provided that $\pi_{E,-} \ll \pi_{E,+}$, the $\Delta u_{0,+,\pm}$ solutions (in which the source appears on the opposite side of the lens as seen from Earth and from the satellite) are less probable than the $\Delta u_{0,-,\pm}$ solutions by a factor $\sim(\pi_{E,-}/\pi_{E,+})^2/2$. The remaining degeneracy within the $\Delta u_{0,-,\pm}$ solutions is relatively unimportant because it leads to similar distance estimates and because, at least for disk lenses, the kinematic priors usually discriminate between these two solutions. As demonstrated by Figure 3, only two of the 21 events have substantially extended probability distributions of the distance variable $D \equiv \mathrm{kpc}/(\pi_{rel}/\mathrm{mas} + 1/8.3)$.

We have shown that an accurate cumulative distribution function of lens distances can be constructed from our sample. This means that the distances of planets detected from the same program can be used to determine the Galactic distribution of planets. That is, the *Spitzer* sample is a fair parent sample for the planets detected, even though the sample itself is biased toward longer events (and so disk lenses). The reason that this sample is nevertheless fair is that planetary events and the non-planetary events suffer exactly the same bias because the planetary nature of the events is not known at the time the decision is made to observe them (e.g., Udalski et al. 2015). This means that this sample can be combined with future samples, including those observed in future years by *Spitzer* and *Kepler*, even though the selection biases of these samples are likely to differ radically.

Work by C.A.B. was carried out in part at the Jet Propulsion Laboratory (JPL), California Institute of Technology, under a contract with the National Aeronautics and Space Administration. Work by J.C.Y. A.G., and S.C. was supported by JPL grant 1500811. A.G. and B.S.G. were supported by NSF grant AST 1103471. A.G., B.S.G., and R.W.P. were supported by NASA grant NNX12AB99G. The OGLE project has received funding from the European Research Council under the European Community's Seventh Framework Programme (FP7/2007-2013)/ ERC grant agreement no. 246678 to A.U. Work by J.C.Y. was performed under contract with the California Institute of Technology (Caltech)/Jet Propulsion Laboratory (JPL) funded by NASA through the Sagan Fellowship Program executed by the NASA Exoplanet Science Institute. Work by D.D.P. and K.L. was supported by the University of Rijeka project 13.12.1.3.02. Work by T.S. is supported by grants JSPS23103002, JSPS24253004, and JSPS26247023. Work by I.A.B. was supported by the Marsden Fund of the Royal Society of New Zealand, contract no. MAU1104. The MOA project is supported by the grant JSPS25103508 and 23340064. Work by D.M. is supported by the I-CORE program of the Planning and Budgeting Committee and the Israel Science Foundation, Grant 1829/12. D.M. and A.G. acknowledge support by the US-Israel Binational Science Foundation. The operation of the Danish 1.54 m telescope at ESO's La Silla Observatory is financed by a grant to U.G.J. from the Danish Natural Science Foundation (FNU). This publication was made possible by NPRP grants 09-476-1-078 and X-019-1-006 from the Qatar National Research Fund (a member of Qatar Foundation). O.W. (FNRS research fellow) and J. Surdej acknowledge support from the Communauté française de Belgique—Actions de recherche concertées—Académie Wallonie-Europe. M.H. acknowledges support from the Villum Foundation. C.S. received funding from the European Union Seventh Framework Programme (FP7/2007-2013) under grant agreement no. 268421. This work is based in part on observations made with the Spitzer Space Telescope, which is operated by the Jet Propulsion Laboratory, California Institute of Technology under a contract with NASA. The research described in this publication was carried out in part at the Jet Propulsion Laboratory, California Institute of Technology, under a contract with the National Aeronautics and Space Administration.

REFERENCES

Alard, C., & Lupton, R. H. 1998, ApJ, 503, 325
Albrow, M., Beaulieu, J.-P., Birch, P., et al. 1998, ApJ, 509, 687
Bond, I. A., Abe, F., Dodd, R. J., et al. 2001, MNRAS, 327, 868
DePoy, D. L., Atwood, B., Belville, S. R., et al. 2003, SPIE, 4841, 827
Dominik, M., Jørgensen, U. G., Rattenbury, N. J., et al. 2010, AN, 331, 671
Dong, S., Udalski, A., Gould, A., et al. 2007, ApJ, 664, 862
Fazio, G. G., Hora, J. L., Allen, L. E., et al. 2004, ApJS, 154, 10
Gaudi, B. S. 2012, ARA&A, 50, 411
Gaudi, B. S., Albrow, M. D., & An, J. 2002, ApJ, 566, 463
Gould, A. 1994, ApJL, 421, L71
Gould, A. 1997, ApJ, 480, 188
Gould, A. 1999, ApJ, 514, 869
Gould, A. 2000, ApJ, 542, 785
Gould, A. 2004, ApJ, 606, 319
Gould, A., Dong, S., Gaudi, B. S., et al. 2010, ApJ, 720, 1073
Gould, A., & Horne, K. 2013, ApJL, 779, L28
Gould, A., Udalski, A., Monard, B., et al. 2009, ApJL, 698, L147
Gould, A., & Yee, J. C. 2013, ApJ, 764, 107
Han, C., & Gould, A. 1995, ApJ, 447, 53
Henderson, C. B., Gaudi, B. S., Han, C., et al. 2014, ApJ, 794, 52
Jiang, G., DePoy, D. L., Gal-Yan, A., et al. 2005, ApJ, 617, 1307
Liebes, S. 1964, PhRv, 133, 835
Makovoz, D., & Marleau, F. R. 2005, PASP, 117, 1113
Muraki, Y., Han, C., Bennett, D. P., et al. 2011, ApJ, 741, 22
Paczyński, B. 1986, ApJ, 304, 1
Poindexter, S., Afonso, C., Bennett, D. P., et al. 2005, ApJ, 633, 914
Refsdal, S. 1964, MNRAS, 128, 295
Refsdal, S. 1966, MNRAS, 134, 315
Schechter, P. L., Mateo, M., & Saha, A. 1993, PASP, 105, 1342
Shvartzvald, Y., & Maoz, D. 2012, MNRAS, 419, 3631
Simpson, T. 1740, Essays on Several Curious and Useful Subjects: In Speculative and Mixd Mathematicks (London: H. Woodfall Jr.)
Skowron, J., Udalski, A., Gould, A., et al. 2011, ApJ, 738, 87
Sumi, T., Bennett, D. P., Bond, I. A., et al. 2013, ApJ, 778, 150
Tsapras, Y., Street, R., Horne, K., et al. 2009, AN, 330, 4
Udalski, A. 2003, AcA, 53, 291
Udalski, A., Szymanski, M., Kaluzny, J., et al. 1994, AcA, 44, 227
Udalski, A., Yee, J. C., Gould, A., et al. 2015, ApJ, 799, 237
Werner, M. W., Roellig, T. L., Low, F. J., et al. 2004, ApJS, 154, 1
Yee, J. C., Shvartzvald, Y., Gal-Yam, A., et al. 2012, ApJ, 755, 102
Yee, J. C., Udalski, A., Calchi Novati, S., et al. 2015, ApJ, 802, 76
Yee, J. C., Udalski, A., Sumi, T., et al. 2009, ApJ, 703, 2082

Monthly Notices of the ROYAL ASTRONOMICAL SOCIETY
MNRAS **448**, 3038–3052 (2015) doi:10.1093/mnras/stu2730

Stellar activity as noise in exoplanet detection – I. Methods and application to solar-like stars and activity cycles

H. Korhonen,[1,2,3]★ J. M. Andersen,[3,4] N. Piskunov,[5] T. Hackman,[1,6] D. Juncher,[2,3] S. P. Järvinen[7] and U. G. Jørgensen[2,3]

[1]*Finnish Centre for Astronomy with ESO (FINCA), University of Turku, Väisäläntie 20, FI-21500 Piikkiö, Finland*
[2]*Niels Bohr Institute, University of Copenhagen, Juliane Maries Vej 30, DK-2100 Copenhagen, Denmark*
[3]*Centre for Star and Planet Formation, Natural History Museum of Denmark, University of Copenhagen, Øster Voldgade 5-7, DK-1350 Copenhagen, Denmark*
[4]*Department of Astronomy, Boston University, 725 Commonwealth Avenue, Boston, MA 02215, USA*
[5]*Department of Physics and Astronomy, Uppsala University, Box 515, S-75120 Uppsala, Sweden*
[6]*Department of Physics, PO Box 64, FI-00014 University of Helsinki, Finland*
[7]*Leibniz-Institut für Astrophysik Potsdam (AIP), An der Sternwarte 16, D-14482 Potsdam, Germany*

Accepted 2014 December 22. Received 2014 December 19; in original form 2014 April 15

ABSTRACT

The detection of exoplanets using any method is prone to confusion due to the intrinsic variability of the host star. We investigate the effect of cool starspots on the detectability of the exoplanets around solar-like stars using the radial velocity method. For investigating this activity-caused 'jitter' we calculate synthetic spectra using radiative transfer, known stellar atomic and molecular lines, different surface spot configurations and an added planetary signal. Here, the methods are described in detail, tested and compared to previously published studies. The methods are also applied to investigate the activity jitter in old and young solar-like stars, and over a solar-like activity cycles. We find that the mean full jitter amplitude obtained from the spot surfaces mimicking the solar activity varies during the cycle approximately between 1 and 9 m s^{-1}. With a realistic observing frequency a Neptune-mass planet on a 1-yr orbit can be reliably recovered. On the other hand, the recovery of an Earth-mass planet on a similar orbit is not feasible with high significance. The methods developed in this study have a great potential for doing statistical studies of planet detectability, and also for investigating the effect of stellar activity on recovered planetary parameters.

Key words: planets and satellites: detection – stars: activity – stars: rotation – stars: solar-type – starspots.

1 INTRODUCTION

The search for exoplanets has traditionally concentrated on stars with very little intrinsic activity. Studies have shown that the known exoplanet host stars exhibit very low levels of magnetic activity (e.g. Jenkins et al. 2006; Martínez-Arnáiz et al. 2010). Still, as the *Kepler* satellite has shown, many solar-like stars are more active than our Sun (e.g. Basri et al. 2013), and therefore show significant levels of activity, which can affect the planet detection. The spectral line profile variations caused by starspots have been confused with a radial velocity signal originating from exoplanets (e.g. Queloz et al. 2001; Huerta et al. 2008), and the sudden brightenings caused by stellar flares can mimic microlensing events from a planet-sized body (e.g. Bennett et al. 2012). Magnetic activity, and the phenomena related to it, is an integral part of stars with spectral types ranging from mid-F to M, and as these are the stars most exoplanet searches concentrate on, it is crucial to understand the effects activity sets on exoplanet detection and parameter determination.

The exoplanet detection method most prone to confusion from stellar activity is the radial velocity search. Already, Saar & Donahue (1997) showed that cool spots on the stellar surface cause spectral line profile variations that can be confused with the radial velocity variations from planets. In addition, they derived an analytical formula to represent the relation of this radial velocity jitter to the fraction of stellar surface covered by starspots (starspot filling factor). Other similar investigations have been carried out, see e.g. Desort et al. (2007), Reiners et al. (2010), Dumusque et al. (2011b), Boisse et al. (2011) and Barnes, Jeffers & Jones (2011). Also, Boisse, Bonfils & Santos (2012) provided a freely available tool, Spot Oscillation And Planet (SOAP), for the community to investigate the effects of starspots on radial velocity measurements and photometric observations. The code was expanded and improved by Oshagh et al. (2013) to include planetary transits on a spotted star, and a new modified version, SOAP 2.0, was recently published by Dumusque, Boisse & Santos (2014).

★ E-mail: heidi.h.korhonen@utu.fi

Most planet searches have concentrated on solar-like stars. Therefore, there have also been relatively many investigations on the effect of solar activity on exoplanet detection (see e.g. Lagrange, Desort & Meunier 2010; Meunier, Desort & Lagrange 2010). Meunier & Lagrange (2013) used solar activity as a template to study the effect of spots and plages on detectability of Earth-mass exoplanets in the habitable zone of their host star. They conclude that especially the contribution from the plages would prevent the detection of Earth around the Sun, even with forthcoming high-precision instruments. These investigations have concentrated on plages and spots, but these are not the only error sources. Granulation and stellar oscillations also cause noise at m s^{-1} level (see e.g. Dumusque et al. 2011a), which will hinder the detection of small-sized planets, and planets on wide orbits. Still, the time-scale for these noise sources is much shorter than the variations caused by long-period planets, therefore, they can be averaged out using long exposures and/or observing frequently. A new potential noise source, gravitational redshift, was identified recently by Cegla et al. (2012), but its magnitude is estimated to be only few cm s^{-1}.

Photometric observations have been used to estimate the activity-induced jitter in radial velocity measurements (e.g. Lanza et al. 2011; Aigrain, Pont & Zucker 2012). In a recent work based on *Galaxy Evolution Explorer* (*GALEX*) ultraviolet measurements and *Kepler* light curves, Cegla et al. (2014) investigate how well the radial velocity jitter can be estimated based on photometry alone. They conclude that for magnetically quiet stars one can use photometric measurements as a proxy for radial velocity variability.

Ma & Ge (2012) developed a technique to use the radial velocity method for detecting planets even when the host star shows significant activity. Their method relies on the wavelength dependence of the spot-caused jitter as opposed to the planetary signature which is not wavelength dependent. Moulds et al. (2013) have also shown that for active stars it is possible to remove some of the spot signature from the line profiles and still be able to recover Jupiter-sized close-in planets.

In this work we develop methods that use radiative transfer to calculate spectral line profiles from a spotted stellar surface. The stellar spot configurations are either based on spot sizes and numbers or filling factors. It is also possible to introduce active longitudes and latitudes. In addition, a planetary signal can be added to the spectra calculated from the spotted surface. This approach allows for a statistical investigation of exoplanet detection and enables obtaining information on the errors the stellar activity causes on the determined planetary parameters. In the current paper, Paper I, we describe the methods, test them and compare the results to some of the previously published studies. The methods are also applied to study jitter around solar-like stars, including a solar-like activity cycle. In the second part, Paper II, we will apply the methods to M dwarfs and investigate the reliability of recovery of planetary parameters in the presence of stellar activity (Andersen & Korhonen 2014).

2 METHODS

We create spot patterns on a simulated stellar surface using our SPOTSS code (see next section). Synthetic spectral line profiles at different rotational phases of the star are calculated based on the created surface distributions. The spectra based on the given spot configuration and local line profile grids are calculated using the code DIRECT7, which is written by NP and includes modifications introduced by TH. This code uses the same routines as INVERS7 (Piskunov, Tuominen & Vilhu 1990; Hackman, Jetsu & Tuominen 2001). Radial velocity (jitter) measurements are obtained by cross-correlation of the calculated line profiles with either one of the generated profiles or a template profile, which is obtained from a spectrum with the temperature of the unspotted stellar surface. Exoplanet radial velocity is introduced into the spectra and recovered by a new cross-correlation. These steps after the spot surface creation are all done in a code called Detection of Exoplanets under the Effect of Magnetic Activity (DEEMA). Details of all the steps are discussed in the following.

2.1 Generating spots

We developed our code, SPOTSS, to generate spot (temperature) patterns on a simulated stellar surface. The code can generate random spots across the entire surface, and has also the option to define certain 'active' regions in latitude and/or longitude. The code creates a matrix of temperatures which represents the entire stellar surface, corresponding to N points of latitude and $2 \times N$ points of longitude. Using a 60×120 grid yields a latitude resolution of 3° pixel^{-1} and a longitude resolution of 3° pixel^{-1} at the equator (note that the actual longitude resolution increases near the poles since the grid is a flat square that represents a spherical surface). The size of the matrix can be changed in order to increase or decrease the spatial resolution, but at much higher sizes the processing time is very long compared to the relatively small gains in precision.

The code takes the following (user defined) input parameters.

(i) Stellar temperature, T_p: the photospheric temperature of the unspotted stellar surface, before spots are added. Every value in the temperature matrix is originally set to this value.

(ii) Spot temperature, T_s: the temperature of the umbral regions of the spots. This is considered the spot temperature, although each spot also has a penumbral region with a temperature defined as the midpoint between the spot temperature and the photospheric temperature.

(iii) Spot radius, r_s: 'average' radius of the spots. The radius of each spot is randomly altered starting from this value to create a lognormal distribution of spot sizes around this size. Lognormal distribution is chosen because the sunspot size distribution is known to follow it (e.g. Bogdan et al. 1988; Baumann & Solanki 2005). Spots are approximately circular, and we add penumbral regions with umbral to penumbral radii ratios of 1:2, creating an umbral to penumbral area of 1:3, following Solanki (2003).

(iv) Number of spots, n_s (or filling factor, depending on which version of the code is used): spots are placed on the stellar surface randomly until the number of spots is reached or the desired filling factor is achieved. For certain purposes it was useful to investigate the effect of one large spot, so n_s was set to 1. (Note when $n_s = 1$ the exact input value of r_s is used, since it is not necessary to alter this to obtain a certain size distribution of spots. An exact latitude and longitude for the centre of the spot can also be specified.)

(v) Longitude range: defaults to the full range of longitude: 0°–360°, but active longitude ranges can be defined meaning spots will only be placed within those ranges.

(vi) Latitude range: defaults to the full range of latitude, −90°–90°, though active latitudes can also be defined. Then spots will only be placed within those ranges. This can be combined with defining an active longitude range to create a small 'active region' on the stellar surface. Active regions such as this have been observed in some Doppler images of active stars.

2.2 Calculating spectral line profiles

For calculating synthetic spectra we used two different atmospheric models: one for the solar-like stars and one for the M dwarfs. For both cases 17 limb angles (0.01, 0.025, 0.050, 0.075, 0.1, 0.125, 0.15, 0.2, 0.25, 0.3, 0.4, 0.5, 0.6, 0.7, 0.8, 0.9, 1.0) were used. For solar-like stars a grid of local line profiles was created using the SPECTRUM spectral synthesis code (Gray & Corbally 1994) and Kurucz model atmospheres (Kurucz 1993). The grid includes temperatures 4000–6000 K with a temperature step of 250 K. The line lists LUKE.LST and LUKE.NIR.LST (included in the SPECTRUM package), which include atomic lines and some molecular species, are used in the calculations. For the photometry we use the same code and models but for a sparser wavelength grid ranging from 3600 to 7350 Å and step size of 50 Å.

For the M dwarf temperatures we used the program SYNTHE (Kurucz & Avrett 1981; Sbordone et al. 2004) to compute the synthetic spectra. The spectra are based on a subset of the 2008 grid of MARCS stellar model atmospheres (Gustafsson et al. 2008) with solar metallicities. They cover a temperature range of $T = 2500$–4000 K, a surface gravity range of $\log(g) = 4.5$–5.5 and a microturbulence range of $\xi_t = 0.0$–2.0 km s^{-1}. For the atomic line opacities we used data from the on-line Vienna Atomic Line Database 2 (VALD-2; Kupka et al. 1999), and for the molecular line opacities we used the species presented in Table 1. The calculated spectra cover a wavelength range of 3000–9200 Å and have a resolution of $\Delta\lambda/\lambda = 500\,000$.

The spectra based on the given spot configuration and local line profile grids are calculated using the code DIRECT7. Before running DIRECT7 the local line profiles are convolved with a Gaussian instrumental profile and a radial-tangential macroturbulence (here set to 2 km s^{-1}). Furthermore, local fluxes for the *B*- and/or *V* magnitudes are calculated using the transmission functions for these wavelength passbands.

For each rotation phase the visible stellar hemisphere is simulated in DIRECT7 and the spectrum and *B*- and *V*-passband fluxes are calculated by integration of the line and continuum intensities over this visible stellar hemisphere. The projection effects, limb darkening and visibility of the spots are thus naturally directly taken into account. User defined $v \sin i$ and inclination values are applied to the spectral line profiles. The $v \sin i$ can be given in two ways: either the user can supply the desired value, or the DEEMA code can estimate the value based on the stellar mass, rotation period and inclination. For the estimation models by Baraffe et al. (1998) are used. From now on the term 'spectrum' refers to the synthetic spectrum that has been calculated by integration over the full visible stellar disc.

The spectra can be calculated at any given rotational phase. Here, a scheme where the length of the observing run and stellar rotation period are given in days, and the user supplied number of phases is evenly distributed over the observing run and the stellar rotational phases are calculated based on this information. The stellar rotational phases are used as an input for the line profile and *B*- and/or *V* magnitude calculations.

2.3 Cross-correlation

For obtaining the jitter values induced by spots, spectra calculated for different observational phases are cross-correlated. The cross-correlation can be carried out against different templates: spectra without spots obtained using unspotted surface temperature, spectra without spots obtained using the mean temperature of the stellar surface or using one of the spectra with spots as the template.

If one of the spectra created with surface spots is used as the template, then all the spectra are cross-correlated against each other. This means that there are $N - 1$ jitter curves, where N is the number of rotational phases. All the obtained jitter curves are normalized in such a way that the measurement at the first phase is set to zero, and the mean and the standard deviation are calculated for each phase. This provides a mean jitter curve and an estimate of the measurement error. The jitter curves are virtually identical and the error estimates small, as should be when no noise is added to the spectra. This is the method that is used in all the calculations presented in this work, and owing to this scheme the cross-correlation result is always zero for the first longitude.

In cross-correlation the accuracy is increased by improving the sampling of the cross-correlation curve using linear interpolation and fitting a polynomial to the curve. The maximum of the polynomial is calculated and the corresponding shift used as the jitter value. An example of a stellar surface and resulting jitter curve are shown in Figs 1(a) and (b), respectively. The spot is a 5° radius equatorial spot with umbral temperature of 4000 K, penumbral temperature of 4900 K and unspotted surface temperature of 5800 K. The stellar rotation period has been set to 25 d and the spectra have been calculated at 20 evenly spaced phases using the wavelength region 5952–5998 Å. The inclination is set to 90° (equator-on) and $v \sin i$ is estimated from the period and stellar radius to be 2.1 km s^{-1}. The resulting jitter curve has a full amplitude of 14.95 m s^{-1}.

Tests were also carried out using a Gaussian function instead of a second degree polynomial for determining the maximum of the cross-correlation function. Fig. 2 shows the results for three different methods: polynomial (plus signs), Gaussian function (squares) and simply taking the maximum of the cross-correlation function (diamonds). The results are shown for two different equatorial spots, one with radius of 5° (top) and one of 17° (bottom). As expected, simply taking the maximum of the cross-correlation function gives zero when the shift is small, and with larger shifts it at times gives exaggeratedly large values. On the other hand, both polynomial and Gaussian fits give very similar results. Based on calculations using 100 different spot configurations with spot filling factor of 0.02 per cent, it can be seen that the polynomial fit always gives somewhat smaller value than the Gaussian fit. The full jitter amplitude obtained from the polynomial fit is 2.85 ± 0.03 per cent smaller than the value obtained using the Gaussian fit. The tendency for smaller jitter values with the polynomial fit is also seen in Fig. 2, but for both the 5° and 17° radius spots the difference between the methods is less than 1 per cent.

There does not seem to be any correlation between the full jitter amplitude and the performance of the Gaussian and polynomial fits. Fig. 3 shows the procentual difference between the full jitter amplitude obtained using polynomial and Gaussian fits and plotted against the full jitter amplitude obtained from the Gaussian fit. The larger jitter does not result in larger (or smaller) procentual difference between the methods. On the whole, both Gaussian and polynomial fits give very similar results. In the following polynomial fits are used.

DIRECT7 uses an evenly spaced wavelength grid for calculating the spectra. Our tests show that over such a small wavelength range (50 Å) the results are not significantly affected even if a logarithmic wavelength scale is not used in the cross-correlation. Therefore, we use the DIRECT7 output directly in the cross-correlation.

Table 1. Sources of data for the molecular line opacities used in SYNTHE for the M dwarf spectral grid.

Molecule	Transitions	Wavelength range (Å)	# Lines	Source
CH	A–X, B–X, C–X	2600–17 000	71 600	R. Kurucz
CN	A–X, B–X	2000–1000 000	1645 000	R. Kurucz
CO	X–X, A–X	1100–100 000	555 000	R. Kurucz
OH	X–X, A–X	2000–1000 000	82 000	R. Kurucz
H_2O	X–X	4100–1000 000	65 900 000	R. Kurucz
SiO	X–X, A–X, E–X	1400–1000 000	1830 000	R. Kurucz
TiO	A–X, B–X, C–X, E–X, c–a, b–a, b–d, f–a	4100–1000 000	33 000 000	D. W. Schwenke

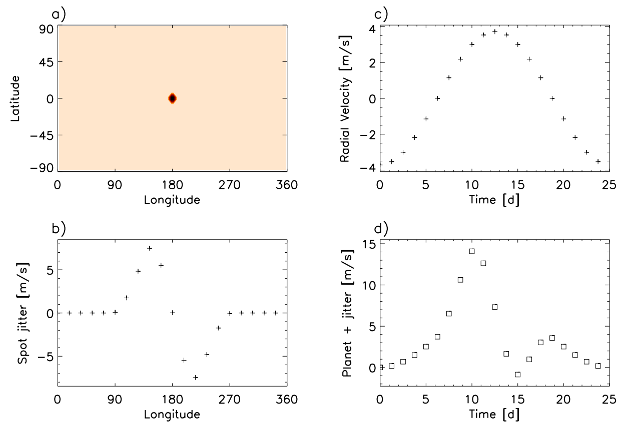

Figure 1. An example of stellar surface spot configuration and the resulting radial velocity jitter from a spot and a planet. (a) Stellar surface configuration used for calculating the spectra. The *x*-axis gives the longitude in degrees and *y*-axis the latitude, also in degrees. The unspotted surface has a temperature of 5800 K and the spot temperature is 4000 K in the umbra and 4900 K in the penumbra. The radius of the spot is ∼5°. (b) The resulting jitter curve from the 5° spot. The *x*-axis is the longitude in degrees and *y*-axis the measured radial velocity jitter in m s^{-1}. The jitter values are calculated at 20 evenly spaced rotational phases from the wavelength region 5952–5998 Å. The error of the jitter measurement is smaller than the symbol size. (c) Radial velocity curve of a Neptune-mass planet on a 25 d circular orbit around 1 M$_\odot$ star. The *x*-axis gives the time in days and *y*-axis the radial velocity in m s^{-1}. (d) The radial velocity curve from the 5° spot and Neptune-sized planet. Owing to the cross-correlation scheme used here (see Section 2.3) the first jitter measurement is always shifted to zero. This explains the different absolute values for the input and calculated radial velocities. In the plot *x*-axis has the time in days and *y*-axis the measured radial velocity in m s^{-1}.

2.4 Introducing a planet to the spectra

We generate radial velocity curves resulting from orbiting planets using Kepler's third law. The elliptical case of Kepler's equation is solved following the formalism by Mikkola (1987). The three optional variables (γ, the systemic velocity, or arbitrary instrumental offset; $\dot{\gamma}$, the systemic acceleration, due to systematics in the data or an additional body in the system with a much longer period and t_0, an arbitrary zero-point for the slope) were left out. These parameters are used when fitting radial velocity curves, but they are not necessary when simply generating a radial velocity curve. This leaves the equation

$$\mathrm{RV}(t) = K[\cos\theta(t) + \omega_* + e\cos\omega_*], \tag{1}$$

where K is the radial velocity semiamplitude and is given in m s^{-1} by

$$K = \left(\frac{2\pi G}{P(M_\mathrm{P} + M_\mathrm{S})^2}\right)^{1/3} \frac{M_\mathrm{P}\sin i}{\sqrt{1 - e^2}}. \tag{2}$$

In these equations θ is the true anomaly, ω_* is the argument of periastron, e is eccentricity of the orbit, P the orbital period of the planet in seconds, M_P the mass of the planet in kg and M_S the stellar mass in kg.

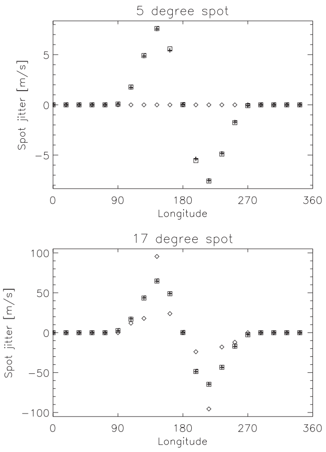

Figure 2. An example of jitter curves obtained using different methods for determining the maximum of the cross-correlation function: polynomial fit (plus signs), Gaussian function (squares) and taking the maximum of the cross-correlation function (diamonds). The results are shown for two different equatorial spots, one with radius of 5° (top) and one of 17° (bottom).

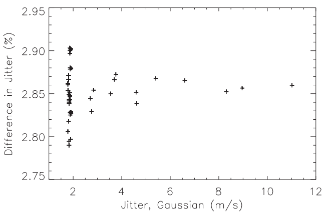

Figure 3. The procentual difference between the full jitter amplitude obtained using polynomial and Gaussian fits plotted against the full jitter amplitude from the Gaussian fit.

The radial velocity at a given orbital phase is calculated and added to the appropriate spectrum. For this process the user has to provide the stellar mass, planetary mass, eccentricity and period of the planetary orbit (or semimajor axis). As an example, Fig. 1(c) shows the calculated radial velocity curve for a Neptune-mass planet (17 $M_{\oplus}$) around a solar-mass star on a circular orbit with orbital period of 25 d. The radial velocities caused by the planet are calculated at the input rotational phases and shifts are introduced to the spectra. After this the spectra are re-analysed using the same cross-correlation method as for the case only containing the spot jitter. The resulting radial velocity curve of the spot and planet together is shown in Fig. 1(d). For this example, the full amplitude of the radial velocity variation is the same as from only the spot, 14.95 m s^{-1}, but the shape of the curve is very different.

2.5 Testing the methods

For testing the behaviour of the code a 5°radius equatorial solar-like spot was used (see Fig. 1a). The radius of the whole spot (umbra+penumbra) is 5°, the radius of the umbra alone is 3°. In some tests also a larger spot with the full radius of 17° and umbral radius of 10° is used. Both spots, which are used separately, are located at the equator and the temperature of the umbra is 4000 K, the penumbra is 4900 K and the unspotted temperature is 5800 K. All the tests were carried out using the grid size 60 × 120 (except the grid size tests). The spectra were created using spectral resolution of 100 000 (except in the resolution tests) and using 2.5 pixel sampling over one resolution element. The length of the wavelength strip used in one jitter calculation was always 46 Å. The local line profiles were calculated with ±2 Å from the ends of the wavelength strip, to allow for large $v\sin i$ values in the calculations (i.e. the length of the spectrum for which local line profiles were calculated was always 50 Å).

2.5.1 Recovering the planetary signal

The accuracy at which the planetary signal can be recovered was tested using a smooth, i.e. unspotted, stellar surface. Solar-like configuration with effective temperature of 5800 K and $v\sin i = 2.1$ were used in the calculations. An Earth-mass planet on a 25 d orbit around the 1 $M_{\odot}$ star was introduced to the spectra.

The results of the test can be seen in Fig. 4. The jitter curve calculated from the unspotted stellar surface (Fig. 4b) shows zero values for all the jitter measurements, as expected. The input curve of the Earth-mass planet (Fig. 4c) on the other hand is very well recovered from the spectra (Fig. 4d). As discussed in Section 2.3, the radial velocity curve calculated from the spectra is normalized to the first measurement, explaining the different absolute values for the input and calculated radial velocities. The full amplitude of the jitter is almost identical in the full amplitude of the input radial velocity curve (0.4373 m s^{-1}) and the calculated one (0.4299 m s^{-1}). Our tests using other planetary masses show that the calculated full amplitude tends to be underestimated by ∼1.7 per cent in comparison to the real input radial velocity curves full amplitude.

2.5.2 Effect of spectral resolution

Radial velocity measurements are typically done using high-resolution spectrographs with resolving power (λ/Δλ) 50 000–110 000. To test the effect of the spectral resolution on the jitter we calculated spectra using different resolving powers between 10 000 and 300 000 and the same spot configuration as shown in Fig. 1(a). One resolution element always spans 2.5 wavelength steps, i.e. 'pixels'.

As can be seen from Fig. 5 the full amplitude of the jitter decreases with decreasing spectrograph resolution, as has also been reported by other authors (e.g. Desort et al. 2007). The results are normalized

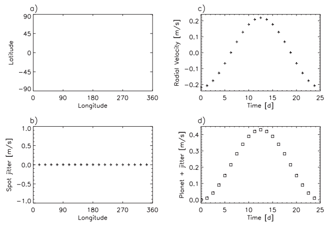

Figure 4. An example of recovering the planetary signal from the spectra. (a) Stellar surface configuration without spots and surface temperature of 5800 K. This configuration was used for calculating the spectra for the planet recovery test. The *x*-axis gives the longitude in degree and *y*-axis the latitude, also in degrees. (b) The resulting jitter curve from the unspotted surface. The *x*-axis is the longitude in degrees and *y*-axis the measured radial velocity jitter in m s^{-1}. The jitter values are calculated at 20 evenly spaced rotational phases on the wavelength region 5952–5998 Å. (c) Radial velocity curve of an Earth-mass planet on a 25 d circular orbit around 1 $M_{\odot}$ star. The *x*-axis gives the time in days and *y*-axis the radial velocity in m s^{-1}. (d) The radial velocity curve from the unspotted surface and an Earth-sized planet. The *x*-axis gives the time in days and *y*-axis the measured radial velocity in m s^{-1}.

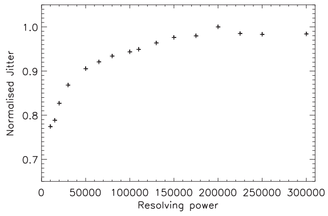

Figure 5. The spot-caused jitter with different spectrograph resolving power (λ/Δλ). The results are normalized to the maximum jitter case (i.e. resolving power of 150 000). The spot configuration used is the same as in Fig. 1(a). In the plot the *x*-axis gives the resolving power and *y*-axis the jitter in m s^{-1}. The jitter increases with increasing resolving power.

to the highest jitter, i.e. resolution 200 000 result of 15.8 m s^{-1}. Two different regimes can be seen in the jitter behaviour. Throughout the resolution range normally used for exoplanet searches, i.e. 50 000–300 000, the jitter remains at the level of about 90 per cent of the highest jitter value. The smallest jitter, about 77 per cent of the highest values, is seen at lowest spectral resolutions used in this test.

This behaviour can be explained by the spot contribution on the line profile shape being better resolved at high spectral resolution and getting more and more diluted with decreasing spectral resolution. Still, the effect of the spectrograph resolution in the jitter

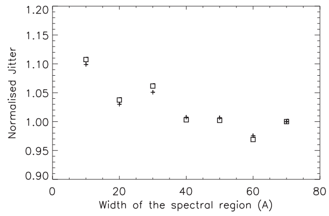

Figure 6. The spot-caused jitter with different widths of the spectral region. Two different spot configurations were used for this test: the same as in Fig. 1(a) shown by plus signs, and one with the full spot radius of 17° denoted by squares. The results for both spot configurations are normalized individually to the results from the widest spectral region (70 Å case). In the plot the *x*-axis gives the width of the spectral region in Ångström and *y*-axis the jitter in m s^{-1}.

amplitude is not very strong and the accuracy of the radial velocity measurements decreases with the decreasing spectral resolution.

2.5.3 Effect of the width of the spectral region

In real high-precision spectroscopic observations the whole optical wavelength range is typically used for determining the radial velocity. Still, as there is no noise added to the spectra the increase in the width of the spectral range should not have a major influence on the results, if wide enough wavelength region is used. To test this assumption we have calculated jitter from seven different wavelength ranges, with the width spanning from 10 to 70 Å. The test uses wavelengths between 5925 and 6000 Å, and spectral resolution of 100 000.

Fig. 6 shows the normalized jitter for two different spot configurations: 5°spot (plus signs) and 17°spot (squares). As expected, the jitter is highest for the 10 Å wide wavelength range, and decreases slightly when going to the 40 Å wide wavelength region. The wider wavelength regions, from 40 to 70 Å, all show similarly small jitter, and the results from more narrow spectral ranges have 5–10 per cent larger jitter values. Still, we cannot say based on this test, whether the jitter would decrease further if significantly wider wavelength ranges would be used, but for limiting the calculation times, 46 Å wide wavelength region is used throughout this paper.

2.5.4 Size of the spatial grid

Testing which impact the grid size, i.e. spatial resolution on the stellar surface, has on the jitter is difficult. The location and fractional size of the spots have to be kept identical throughout the test, which is of course strictly speaking impossible to do.

For the test a random spot configuration with a grid size 20 × 40 was created. The input map has a spot filling factor of 1.5 per cent and the spots were occurring at latitude range −30° to +30°. The grid resolution was increased and filling factor kept as close to the original as possible with the increasing number of grid elements. The scalings did not have a significant effect on the jitter and the filling factor. The jitter values were between 24.6 and 29.0 m s^{-1} with all the grid sizes. These tests imply that the results are not

critically dependent on the grid size, but to allow for also small spots on the surface we have used the grid size 60 × 120 throughout this paper.

2.5.5 Signal-to-noise ratio of the observations

To investigate the effect of noise on the radial velocity curves we add Gaussian noise of a specified signal-to-noise ratio (S/N) to the spectra. The level of the continuum represents signal level while the standard deviation of the noise represents the noise level. Since the continuum is normalized $\mathrm{S/N} = \frac{\text{signal level}}{\text{noise level}} = \frac{1}{\sigma}$, leading to $\sigma = \frac{1}{\mathrm{S/N}}$. A sequence of pseudo-random numbers are generated using IDL routine RANDOMN, which creates Gaussian random numbers using Box–Muller method. The noise is then applied to the spectra.

For testing the effect of noise in the jitter curves we use spectra calculated for a single equatorial spot with a full radius of 17°. Jitter curves are calculated for seven different cases, one with no noise and six with different S/N values ranging from 20 to 3000. The resulting curves are shown in Fig. 7. The symbols used in the plot also show the errors of the individual jitter values (described in Section 2.3). The shape of the jitter curve is easily recognizable until S/N less than 100. The general shape can still be recovered from the spectra with S/N = 50, but with S/N = 20 the shape becomes basically unrecognizable.

We want to still note that each spectral line represents an individual measurement of the Doppler shift of the star. If a total of *N* lines are used for the Doppler measurement, then the error will be decreased by a factor of $\sqrt{N}$ over a single line measurement. In the tests carried out here, short wavelength ranges of 50 Å are used. In the solar-like case these wavelength regions have 30–100 spectral lines, the exact number depending on the wavelength (typically more lines in the blue part and less in the red). Planet searches on the other hand use echelle spectra with a few thousand lines in them. Therefore, if our tests only have at most a 10 fold gain over single line measurements, the real planet searches usually have approximately 40 fold gain. For this reason in the following investigations we will use the calculated spectra without added noise. This will enable us also to study the ideal detection cases.

3 RESULTS

We apply the developed codes to study the starspot jitter in solar-like stars. First, general properties of jitter are studied and compared to the earlier published results by other groups. Afterwards, two different activity cases are investigated: solar-like low activity and very active young solar analogues. In these investigations solar-like temperatures (unspotted surface 5800 K, umbra 4000 K and penumbra 4900 K) are used. If not mentioned otherwise, the gird size is 60 × 120, the wavelength region is 5952–5998 Å and the spectrograph resolving power (λ/Δλ) is 100 000 with 2.5 pixel sampling. Similarly, the inclination was set to 90° and $v\sin i$ was fixed to 2.1 km s^{-1} (if not mentioned otherwise).

3.1 General properties

3.1.1 Jitter with wavelength

Several works have already shown that the spot caused jitter decreases with increasing wavelength (e.g. Desort et al. 2007; Reiners et al. 2010). In a recent paper Marchwinski et al. (2015) show that, based on solar observations, near-infrared has lower estimated radial velocity jitter throughout the entire solar cycle than the optical

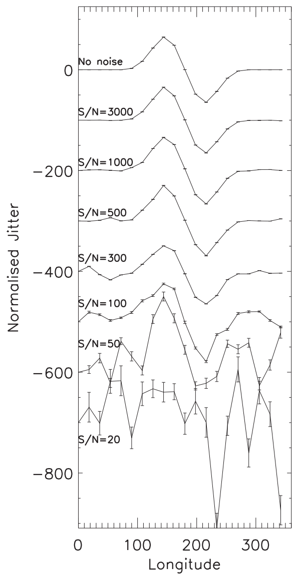

Figure 7. Jitter curves caused by a 17° radius spot with different S/N of the spectra. In the plot the *x*-axis gives the stellar longitude in degrees and *y*-axis the jitter in m s^{-1}. The topmost jitter curve is from the case without noise, and the other jitter curves are off-set from this curve to show the different behaviour better. The S/N values are written on the plot for each jitter curve. The plot also shows the error of each jitter value. The error has been calculated as described in Section 2.3.

wavelengths have. Here tests using spectra with lengths of 46 Å at different wavelength regions between 3700 and 9100 Å are carried out. The spectrograph resolving power (λ/Δλ) is kept constant at 100 000, by changing the Δλ according to the wavelength region. Two spot sizes, 5° and 17° full spot radius (umbra+penumbra), are used. The radii of the umbra are 3° and 10°, respectively.

The results of the jitter investigation over the wavelength are shown in Fig. 8. The results are normalized to the highest jitter case, that of 3700 Å. The results for the 5° spot are shown by plus signs and for the 17° spots by squares. As can be seen, the normalized values and the overall behaviour are very similar for both spot sizes. The absolute values are naturally very different: the full amplitude of the jitter for the 5° spot at 3702–3748 Å is 23.7 m s^{-1} and for the 17° spot 213.7 m s^{-1}.

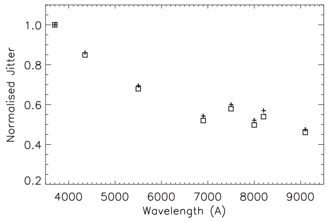

Figure 8. Full amplitude of the spot-caused jitter at different wavelengths. Two different spot configurations were used for this test: the same as in Fig. 1(a) shown by plus signs, and one with the full spot radius of 17° denoted by squares. The results are normalized to the highest jitter case of 3700 Å. In the plot the *x*-axis gives the wavelength in Ångström and *y*-axis the normalized jitter. As has been seen in other studies too, the jitter decreases towards the longer wavelengths, but also the scatter in the jitter values increases.

The jitter decreases by about 50 per cent between the wavelengths 3700 and 7000 Å. At longer wavelengths than this the reduction in jitter amplitude is not as clear as before, and the whole behaviour becomes more chaotic. The increased scatter at red wavelengths could possibly be due to varying number of spectral lines in the spectral windows used in this analysis. In general, there are less spectral lines at the red wavelengths and therefore different red regions can have very different number of spectral lines. Investigation extending to longer wavelengths would be needed to study whether or not the decrease continues to infrared. A similar plateau in the wavelength dependence of the jitter around 8000–10 000 Å is seen for solar-like stars by Reiners et al. (2010). In their work some further decrease in the jitter amplitude is seen in the infrared wavelengths, as is also detected by Marchwinski et al. (2015).

3.1.2 Jitter with $v\sin\mathrm{i}$

It has been shown before that the jitter depends strongly on the stellar rotation rate (e.g. Saar & Donahue 1997; Desort et al. 2007; Boisse et al. 2012). Also in this work the effect was studied and compared to the previously published results. Two spot cases, with the full spot radius of 5° and 17°, were used in the investigation.

Fig. 9 shows the results from the two spot cases for $v\sin i$ values ranging between 1 and 30 km s^{-1}. The results are normalized to the largest jitter case of 30 km s^{-1}. The results from the calculations using 5° spot are shown with plus signs, and the ones from 17° spot with squares. It is clear that the jitter increases with increasing $v\sin i$, as has been shown by earlier studies (e.g. Saar & Donahue 1997; Desort et al. 2007). In addition, when the results are normalized to the highest value the values calculated from the two different spot sizes show the same trends. This means that the magnitude of the jitter depends on the spot size, but the increase in $v\sin i$ affects the jitter measurement the same way regardless of the spot size.

Desort et al. (2007) published a formula for jitter–$v\sin i$ correlation. They obtained from their tests that the jitter amplitude depends on the spot coverage of the visible surface and $v\sin i$. We use their formula to compute jitter–$v\sin i$ dependence, and compare it to our results. The resulting linear trend is plotted in Fig. 9 with a dotted

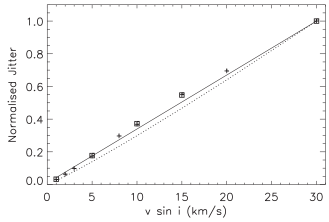

Figure 9. Full amplitude of the spot-caused jitter with different stellar rotation rates. Two different spot configurations were used for this test: 5° radius equatorial spot shown by plus signs, and 17° radius spot denoted by squares. The results are normalized to the highest jitter case of $v\sin i = 30$ km s^{-1}. In the plot the *x*-axis gives the $v\sin i$ in km s^{-1} and *y*-axis the normalized jitter. The solid curve is the fit to the jitter obtained from the 5° spot, and the dotted line is the $v\sin i$ dependence law deduced by Desort et al. (2007).

line. Our results agree well with those obtained by Desort et al. (2007). The amplitude of the jitter estimated by Desort et al. (2007) is very similar to the ones given by Saar & Donahue (1997) and Boisse et al. (2012). On the other hand, when comparing our jitter amplitudes to the ones from Desort et al. (2007), our values are larger. The jitter from the 5°spot is approximately 20 per cent lower at the low $v\sin i$ values in the results obtained using the formula by Desort et al. (2007). The situation improves towards the higher $v\sin i$ values, and for the $v\sin i = 30$ km s^{-1} the difference in only few per cent. Some of the discrepancy could be explained by different wavelength regions and spectral resolutions that were used in these investigations.

3.1.3 Effect of inclination

The effect of inclination of the stellar rotation axis was studied using a fixed $v\sin i$ of 2 km s^{-1}. When the inclination is changed, the $v\sin i$ changes too. If a star is viewed pole-on there would be no rotational broadening. As the jitter also depends on the broadening of the spectral lines, we decided to use a fixed $v\sin i$ value for this test. The full amplitude of the measured jitter at different inclination angles is shown in Fig. 10. The test reveals the expected behaviour of the jitter, where the amplitude decreases with the decreasing visibility of the equatorial spot (decreasing inclination angle). The equatorial spot has the maximum effect on the jitter when the star is viewed equator on. The visibility of the spot is reduced when viewed increasingly from the direction of the pole, and thus also the impact of the spot on the jitter amplitude decreases. When viewed from almost the pole (inclination of 1°), the spot is seen at the limb and at all the rotational phases. This test does not include the effect of decreasing line broadening with decreasing inclination, which would make the change in jitter amplitude even more pronounced.

3.2 Solar-like activity patterns

For investigating the typical jitter amplitude caused by solar activity we have created 50 random spot configurations. All the spot configurations have spot filling factors of 0.1 per cent. This value is over the whole stellar surface and represents normal solar activity level

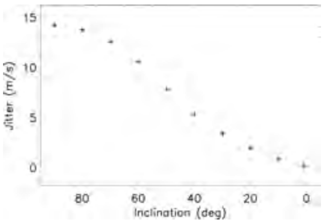

Figure 10. Full amplitude of the spot-caused jitter at different inclinations of the stellar rotation axis. The spot configuration is the same as in Fig. 1(a). In the plot the *x*-axis gives the inclination in degrees and *y*-axis the full jitter amplitude in m s^{-1}. As is expected the level of jitter lowers when the visibility of the equatorial spot decreases with decreasing inclination angle (viewing progressively more pole-on).

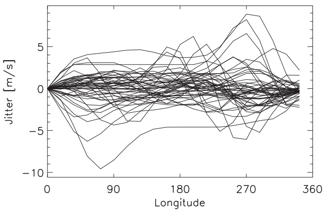

Figure 11. Jitter curves calculated from 50 different randomly created solar-like spot configurations with the spot filling factors of 0.1 per cent and spot latitudes restricted to $-30°$ and $+30°$. The *x*-axis is the longitude in degrees and *y*-axis the jitter in m s^{-1}. Note that the curves are created in such a way that the jitter at first observations (first longitude) is always zero.

(see e.g. Balmaceda et al. 2009). The spots have been restricted to occur between latitudes $-30°$ and $+30°$, which also is the typical latitude range for solar activity.

The jitter curves calculated from all the 50 different spot configurations are shown in Fig. 11. As can be seen the typical jitter with this spot configuration varies between -2 and $+2$ m s^{-1}. The mean amplitude of the full jitter is 4.5 m s^{-1} with the standard deviation being 2.8 m s^{-1}. The minimum full amplitude from these spot configurations is 1.5 m s^{-1} and the maximum 12.3 m s^{-1}.

The spot configurations and resulting jitter are plotted in Figs 12 and 13 for the minimum and maximum jitter case, respectively. The smallest jitter results from a case where several tiny spots are distributed relatively evenly over the longitude. On the other hand, the largest jitter arises from a spot configuration where there is one large spot together with one tiny one (at longitude 0, just below the equator). This is what one would expect and means that the exact jitter from a solar-like spot configuration depends largely on the exact spot distribution and how concentrated into active regions the spots are. This is in line with the studies which show that the

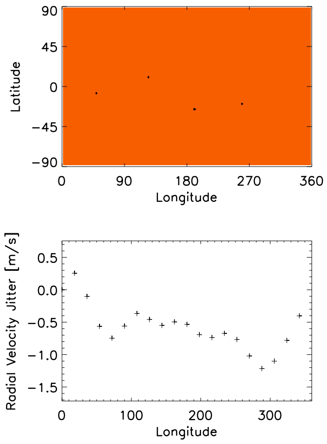

Figure 12. Spot configuration and jitter curve from the spot configuration that out of the 50 randomly created configurations results in the smallest jitter. The jitter has a full amplitude of 1.5 m s^{-1}. The upper plot gives the spot configuration. The *x*-axis is the longitude and *y*-axis the latitude, both are given in degrees. The lower plot shows the corresponding jitter curve. Here the *x*-axis is the longitude in degrees and *y*-axis jitter in m s^{-1}.

radial velocity jitter can be estimated based on the photometric variability (e.g. Aigrain et al. 2012). Concentrated spots introduce more photometric variability, and also more radial velocity jitter.

We have to note though, that due to the limited resolution of the grid on the stellar surface, the filling factor is not always exactly the same. The code for creating the spotted surface will add a spot and then check the filling factor. Another spot is added if needed. This is done until the filling factor is greater than, or equal to, the one that was specified. Therefore the generated filling factors can be slightly above the input value, and are not always exactly identical.

3.3 Active solar-like stars

For investigating what the jitter behaviour of young, very active solar-like stars would be, we use the temperature maps of V889 Her by Järvinen et al. (2008). Their observations of the photospheric and chromospheric properties of V899 Her indicate that the quiet photosphere of V889 Her is similar to the one of the present day Sun, while the chromosphere shows much stronger activity. Their temperature maps, obtained using Doppler imaging, show that the polar regions are covered by spots, which are about 1500 K cooler than the quiet photosphere. Some evidence for cyclic magnetic activity is also seen both from photometry and Doppler imaging results.

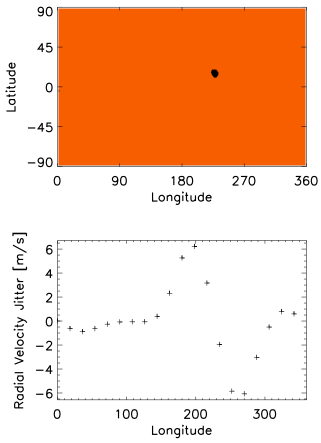

Figure 13. The same as Fig. 12, but now for the largest jitter case. The resulting jitter has full amplitude of 12.3 m s^{-1}.

Here we calculate the jitter resulting from the temperature maps of V889 Her for four different years: 1999, 2001, 2005 and 2007 (Järvinen et al. 2008). In the jitter calculations the wavelength range 5952–5998 Å is used and the inclination and $v \sin i$ are set to the ones determined from Doppler imaging, $i = 60°$ and 37.5 km s^{-1}, respectively. The spectral resolution used in the calculation was the same as the one in the original observations (77 000 and 2.5 pixels over the resolution element), and the grid size of the visible stellar surface is set to that of the original temperature map, 30 × 60.

The original V889 Her temperature maps and the calculated jitter are shown in Fig. 14. The full amplitude of jitter varies between 435 m s^{-1} calculated from the 2005 map and 774 m s^{-1} obtained from the 2001 map. These values are similar to radial velocity variations caused by a hot Jupiter around solar-mass star. Moulds et al. (2013) show that in this kind of cases some of the activity signal can be cleaned from the spectral line profiles and Jupiter-mass planets on close orbits can be recovered. In a recent paper Jeffers et al. (2014) study the detectability of planets around young active solar-like stars. They conclude that Jupiter-mass planets can be detected on close-in orbits around fast-rotating young active stars, Neptune-mass planets around moderate rotators and super-Earths only around very slowly rotating stars. The calculations carried out here based on the V889 Her spot configurations support these conclusions.

4 DISCUSSION

4.1 Starspots as a confusion factor

Not only can starspots cause noise in the radial velocity measurements, they can also mimic planetary signals and change the shape of the radial velocity curve.

For example, a large spot group close to the pole, which is viewed at low inclination, is visible on the surface all the time. The spot group causes larger jitter when it has a higher visibility, i.e. in the front, than when it is behind the pole close to the limb of the star. This behaviour can be confused with the radial velocity variation caused by an orbiting planet and Keplerian fits to the curve can be easily obtained. Several different cases of this kind of confusion have been already discussed by Desort et al. (2007).

Another confusion occurs when the location of the spot on the surface is such that together with the planetary signal it actually causes subtle changes in the shape of the measured radial velocity curve. For example spots at 'correct' location on the surface can change the shape of the radial velocity curve of a circular orbit into something that could be interpreted as a more eccentric orbit. An example of this kind of changes is given in Fig. 15. There the 5° spot from our tests (see Fig. 1a) is used together with a 0.8 Jupiter-mass planet on a circular orbit. The calculations are carried out at wavelength 5952–5998 Å and using spectral resolution of 100 000. The spot itself introduces jitter (see Fig. 15b) which is only about 10 per cent of the radial velocity variation of the planet (Fig. 15c). Still, the combination of these two changes the input radial velocity curve

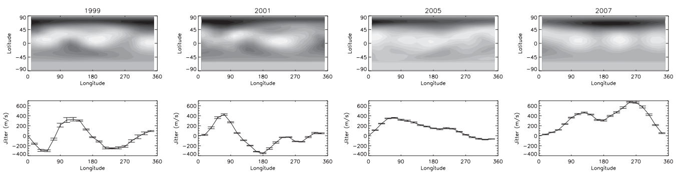

Figure 14. Temperature maps of V889 Her (Järvinen et al. 2008) and the resulting jitter. The maps shown in the upper part of the plot are from years 1999, 2001, 2005 and 2007 (from left to right). The temperature ranges in the maps are 4624–6327 K (1999), 5251–6037 K (2001), 4498–6185 K (2005) and 4561–6268 K (2007). The *x*-axis gives the longitude in degrees and *y*-axis the latitude in degrees. The lower panels in the plots show the calculated jitter from each temperature map at 20 different phases evenly distributed over the stellar rotational phase. The *x*-axes give the longitude in degrees and *y*-axes the jitter in m s^{-1}.

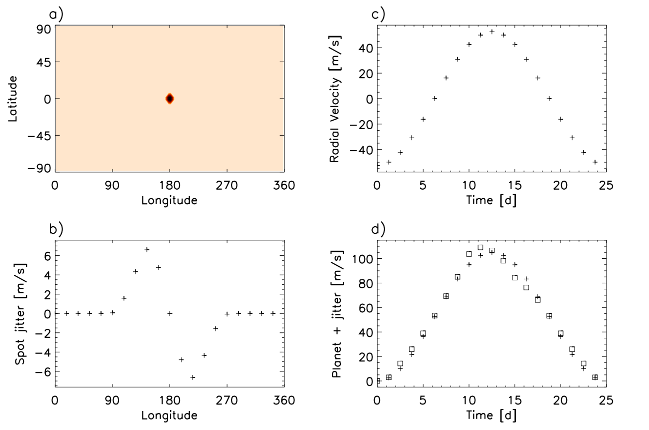

Figure 15. An example of the effect of the spot signal on the radial velocity curve of the planet. The axes in the subplots are the same as in Fig. 4 (a) Stellar surface configuration with one equatorial 5° spot of 4000 K and unspotted surface temperature of 5800 K. (b) The resulting jitter curve from the spot configuration. The jitter values are calculated at 20 evenly spaced rotational phases from the wavelength region 5952–5998 Å and spectral resolution of 100 000. (c) Radial velocity curve of a 0.8 Jupiter-mass planet on a 25 d circular orbit around 1 $M_{\odot}$ star. (d) The radial velocity curve from the spotted surface and the planet is given with squares. The plus signs give the original 'planet only' radial velocity curve (also shown in subplot c).

in subtle ways. In Fig. 15(d) the total radial velocity curve from the planet and spot jitter is plotted with squares. If that is compared to the original planet radial velocity curve, which is overplotted with plus signs, one can see that the phase of the maximum radial velocity has changed. The slope of the increase is now steeper and the declining slope more shallow. These changes would be interpreted as slightly eccentric orbit instead of a circular one. Naturally the activity could also work the other way, and make eccentric orbits appear more circular.

4.2 Solar-like activity cycle

One can question how typical the solar activity level is among solar-like stars in general. There have been early tentative suggestions that the Sun might be photometrically more quiet than similar stars (e.g. Radick et al. 1998). The high-precision photometric data from *Kepler* and *Convection, Rotation and planetary Transits* (*CoRoT*) can help to answer this question. The early results from *Kepler* implied that the Sun could indeed be more quiet than an average solar-type star (Gilliland et al. 2011; McQuillan, Aigrain & Roberts 2012). A new study by Basri, Walkowicz & Reiners (2013) has revisited the activity fraction of solar-like stars in the *Kepler* data. Their results show that 25–30 per cent of solar-type stars are more active than the Sun. The exact fraction depends on the time-scales used in the study, what is meant by 'more active than the Sun', and on the magnitude limit of the sample. In light of these investigations it seems appropriate to use the solar cycle as a proxy for cyclic activity in other stars.

4.2.1 *Jitter during activity cycle*

The number of spots on the solar surface varies with the 11-yr cycle. The spot coverage of the solar surface varies from 0 to about 0.5 per cent. Typically the minima show very small spot coverage factors of 0.01–0.02 per cent, or even zero for extended periods. The maxima on the other hand have quite varying spot coverage fractions. A small maximum has a typical spot coverage of 0.2 per cent, whereas a strong maximum has a spot coverage fraction of 0.5 per cent (see e.g. Balmaceda et al. 2009). During the cycle the latitudes of the spots also change. The new cycle starts with a small amount of spots which appear at relatively high latitudes, around ±30°. During the cycle the activity migrates slowly towards the equator, and during the next minimum the last spots of the old cycle appear at latitudes ±10°. This behaviour also affects the activity-caused jitter. For more details on the latitudinal migration of sunspots within the solar cycle see e.g. Carrington (1858), Maunder (1903) and Hathaway (2011).

We have created random spot configurations with typical sunspot coverage fractions and latitude ranges for studying the jitter over the solar-like activity cycle. In total six different activity cases were investigated: two activity minima, one average activity case and three activity maxima. The details of the cases that were studied are

Table 2. The different activity cases created to study the behaviour of the spot caused jitter over solar-like activity cycle.

Case	Spot frac. (per cent)	Latitude (°)	Jitter (m s^{-1})	σ (m s^{-1})
Minimum 1	0.02	+20 to +30	1.8	1.6
Minimum 2	0.02	−10 to +10	2.0	1.3
Average	0.1	−20 to +20	4.2	2.4
Maximum, small	0.2	−20 to +20	5.3	2.9
Maximum, medium	0.3	−20 to +20	6.6	2.4
Maximum, large	0.5	−20 to +20	7.7	2.9

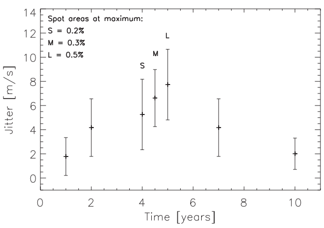

Figure 16. Results for the investigation of jitter during a solar-like activity cycle. The *x*-axis gives the time in years and *y*-axis the jitter in m s^{-1}. The mean full jitter amplitude calculated from 10 individual spot configurations with the different activity cases given in Table 2 are plotted approximately at the time they would occur during the solar 11-yr cycle. The error bar gives the standard deviation of the measurements from the 10 individual spot configurations.

given in Table 2. For all the cases 100 different spot configurations were created. The jitter was calculated at wavelengths 5952–5998 Å using a resolution of 100 000, inclination of 90° and $v \sin i$ of 2.1 km s^{-1}.

The results from the jitter calculations are shown in Fig. 16, and the mean jitter and its standard deviation are also given in Table 2. In the plot, the *x*-axis gives the time in years, and the mean jitter of the different activity cases have been plotted at a time it would typically be observed during the solar 11-yr cycle. The standard deviation of the jitter from 100 individual spot configurations has been plotted as an error bar for each activity case. The result from the average jitter case has been plotted both in the rising and declining phase of the activity.

For the maximum solar activity three different jitter cases were calculated. They are marked in Fig. 16 by letter S (small maximum, spot fraction 0.2 per cent), M (medium maximum, spot fraction 0.3 per cent) and L (large maximum, spot fraction 0.5 per cent). As expected, the large-sized maximum results in the largest jitter values, and the small-sized maximum induces the smallest jitter. Still, all the average jitter values for different solar maxima cases are the same within the standard deviation, and the variation in the jitter, as is seen from the standard deviation, is similar for all the cases.

Both of the minima cases have the smallest jitter values, and also the smallest standard deviation. This is because with such a small spot coverage (0.02 per cent) basically only one small spot is present on the surface. The exact location of the spot changes slightly, and the differences in latitude result in small changes in the full jitter amplitude. It is interesting to note that the mean jitter from the early cycle case, where the spots are around latitudes ±30° results in smaller jitter than the late cycle case with spots at latitudes ±10°. The effect of the jitter is largest when the spots are best visible, i.e. in the case of inclination 90° around equator. One should also note that the spots for the early-cycle case have been created with spot latitude 20°–30°, not taking into account that on the Sun the spots would appear both around latitude −30° and +30°. Regardless, with such small spot coverage fractions only one spot is created, and therefore this has no practical effect in the full jitter amplitude, which is what is studied here.

These calculations do not take into account the lifetime of the sunspots. On the other hand, the larger sunspot on average live longer, couple of weeks, instead of couple of days (see e.g. Gnevyshev 1938; Waldmeier 1955; Petrovay & van Driel-Gesztelyi 1997). Here we by necessity concentrate on larger spots. Therefore, not taking into account the lifetime of the spots should not significantly affect our investigation. In addition, several authors have reported that the solar activity tends to occur at active longitudes (e.g. Berdyugina & Usoskin 2003; Usoskin, Berdyugina & Poutanen 2005; Juckett 2006). This effect has not been taken into in our calculations; we have restricted the spot occurrence only in the latitude direction. The solar active longitudes would group the spots in longitudinal direction and increase the jitter. Thus, the random distribution investigated here can be considered as the lower limit for the jitter.

4.3 Detecting planets on a 1-yr orbit

An interesting question is how the jitter during a solar-like cycle would affect the detection of a planet in the habitable zone of its host star. We have studied this issue by introducing a planet on 1-yr orbit around a star showing a cycle similar to the one described in the previous section.

The cycle is thought to last 11 yr, like in the Sun, and the observing period is 5 yr, covering the cycle from minimum to maximum. Each year the target can be observed during its visibility, here called the observing season, and each season a fixed number of observing runs is carried out. The length of the observing run is always 25 d, which is also the rotation period of the target star. During one run 20 evenly spaced observations are carried out. For each observing run during the first year a spot configuration from the solar minimum case is randomly chosen. For the second and third year the spot configurations have been chosen randomly from the average activity case. During the fourth year spot configurations are from the small activity maximum case, and during the fifth year from the medium maximum maps. After this a planet on a 1-yr orbit is introduced to the jitter measurements. Fig. 17 shows an example of radial velocity measurements created this way. In the example the planet has the same mass as Neptune (17 $M_{\oplus}$) and the observing season lasts the whole year and has five individual observing runs during it. It can easily be seen that the activity caused noise in the radial velocity measurements increases with the advancing activity cycle.

For investigating the detectability of the planet we use Lomb–Scargle period search method for unevenly sampled data (Scargle 1982; Horne & Baliunas 1986; Press & Rybicki 1989). The periodogram resulting from the simulated data presented in Fig. 17 is shown in Fig. 18. The dominant frequencies in this case are the orbital period of the planet (marked by a solid vertical line) and its harmonics (marked by dashed vertical lines). The dotted

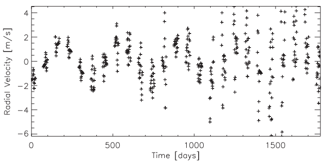

Figure 17. Simulated radial velocity measurements of Neptune-mass planet orbiting a solar-like star with a solar-like activity cycle. The observations span 5 yr, and during each year there are five separate observing runs lasting 25 nights. The *x*-axis gives time in days and *y*-axis the radial velocity in m s^{-1}.

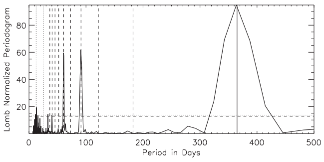

Figure 18. Lomb–Scargle periodogram obtained from the simulated radial velocity measurements presented in Fig. 17. The dotted horizontal line is the analytical 3σ detection threshold and the dashed horizontal line the numerical one. The solid vertical line gives the original period of the planet (365 d) and the dashed vertical lines give its harmonics. The dotted vertical lines are the rotation period of the star (25 d) and half of the rotation period of the star. The *x*-axis gives the period in days and *y*-axis the power spectral density.

vertical lines denote the rotation period (25 d) and half a rotation period of the star, whereas the horizontal dotted line is the analytical 3σ detection threshold following the false alarm probability (FAP) formulation of Scargle (1982) and taking into account the modifications of Horne & Baliunas (1986). The horizontal dashed line, on the other hand, is the FAP obtained from white noise simulations with 10 000 iterations. The two FAP values are similar, which is to be expected because our data are not severely unevenly distributed, the case where the analytical method would strongly underestimate the FAP. Our data are evenly distributed over the observing run, and the observing runs are evenly distributed throughout the year. In this simulation the Neptune-mass planet is easily detected even with the noise from the stellar activity. The case remains the same if we shorten the observing season to 150 d and only have three observing runs during it. This is a more realistic case because of the limited visibility of the targets and also owing to the telescope time allocation process. The Lomb–Scargle periodogram of this case is shown in Fig. 19. The orbital period of the planet is still easily detectable, but the harmonics of the orbital period have become more pronounced. Part of the effect is also due to aliasing caused by larger data gaps.

On the other hand, the possibility of detecting Earth-mass planet around a solar-like star is much more challenging. The periodogram from the optimum case where the observing season lasts the whole year and there are five individual observing runs during the season

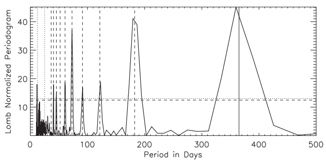

Figure 19. The same as Fig. 18, but now with observing season only lasting 150 d and with only three observing runs during this time.

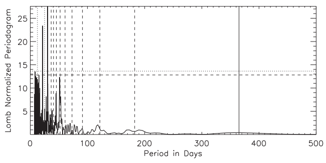

Figure 20. The same as Fig. 18, but now with an Earth-mass planet.

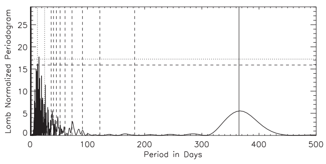

Figure 21. The same as Fig. 18, but now with an Earth-mass planet and 50 observing runs during the observing season of 1 yr.

are shown in Fig. 20. No indication of the true orbital period is seen, and the strongest periodicity is half the stellar rotation period. The situation is somewhat improved when the number of observing runs is increased. In Fig. 21 a case where there are 50 observing runs during each year is shown (this implies observing more than once a night). In this case the signature of the true orbital period starts to emerge, but still it cannot be considered significant. Our tests show that the 3σ detection limit for a planet in a habitable zone of a solar-like star with a solar-like activity cycle is around 6 $M_\oplus$ (when using five observing runs distributed over a full year, and total length of observations of 5 yr).

Lagrange et al. (2010) investigated the detectability of the Earth in the habitable zone around a solar-like star. They concluded that with the highest precision instruments one can only detect an Earth-mass planet after several years of intensive monitoring, and then preferably during the low activity phase of the star. In another investigation Dumusque et al. (2011b) investigate the detection limits with a High Accuracy Radial velocity Planet Searcher (HARPS)-like instrument, taking into account oscillation, granulation and activity effects. They study different observing strategies to minimize

the stellar noise and conclude that applying three measurements per night of 10 min every 3 d, 10 nights a month is the best strategy out of the ones they tested. Depending on the activity level this strategy would allow to detect 2.5–3.5 Earth-mass planets in the habitable zone of an early-K dwarf. Still, this means a planet larger than the Earth and in a habitable zone that is closer to the star than 1 au.

4.4 Future investigations

The codes developed here are very versatile and large variety of spot configurations and exoplanets on different orbits can easily be studied. This opens a possibility to do statistical studies of the effect of stellar activity on the detection of exoplanets. One can also use the same methods as are used to detect exoplanets in recovering the input planet from our spectra. The input parameters of the planet are know, and therefore this will also allow for determining at which accuracy different planetary parameters can be recovered. In the second part of this series of papers (Andersen & Korhonen 2014), we apply the methods developed here to M dwarfs. We will also study in detail the effect stellar activity has on the recovered planetary parameters.

5 CONCLUSIONS

We have developed methods for investigating the radial velocity jitter caused by starspots. The method allows creating many spot configurations with the same spot filling factors and also enables selecting active latitude and longitude ranges. Planetary signatures can easily be added to the spectra and analysed. From the tests and implementation to solar-like stars we can draw the following conclusions.

(i) As has been seen in the previous studies observations at longer wavelengths decrease the measured radial velocity jitter. The tests carried out in this study show that the decrease of approximately 50 per cent in the full jitter amplitude is achieved at wavelengths around 7000 Å in comparison to 3700 Å. Between wavelengths 7000 and 9000 Å no significant further decrease in the jitter amplitude is observed.

(ii) The spectral resolution does not affect the jitter amplitude significantly at the generally used resolving powers of 50 000–130 000 and higher. On the other hand, resolution of 20 000 and less decreases the jitter, but also decreases the measurement accuracy.

(iii) We verify the previous results showing that the full jitter amplitude depends on the stellar rotational velocity, $v \sin i$. The dependence is linear and even though the exact jitter amplitude depends on the spot size, the slope of the correlation does not.

(iv) The solar-like activity patterns create largely varying amounts of radial velocity jitter. From a spot coverage factor that represents average solar activity, the full jitter amplitude recovered from our simulated data varies approximately between 1 and 12 m s^{-1}. The exact value is driven by how concentrated the spots are.

(v) The mean full jitter amplitude varies during the solar-like activity cycle between approximately 1 and 9 m s^{-1}.

(vi) With realistic observing frequency and solar-like cyclic activity a Neptune-sized planet on a 1 yr orbit around a solar-mass star can be recovered with high significance. The recovery of an Earth-mass planet on a similar orbit on the other hand is very challenging.

(vii) The starspots do not only create noise in the radial velocity curves, they can also affect the shape of the radial velocity curve in such a way that the determined orbital parameters change. Eccentricity especially can be affected.

(viii) The spot surface creation and planet orbit implementation software developed in this study allow for statistical studies of effect of spot jitter in exoplanet detection. These issues are addressed in the second paper of this series.

ACKNOWLEDGEMENTS

The authors would like to thank the anonymous referee whose comments helped to improve this paper. HK acknowledges the support from the European Commission under the Marie Curie IEF Programme in FP7. JMA acknowledges support through an NSF Graduate Research Fellowship and the Nordic Research Opportunity award.

REFERENCES

Aigrain S., Pont F., Zucker S., 2012, MNRAS, 419, 3147
Andersen J. M., Korhonen H., 2014, MNRAS, preprint (arXiv:1501.01302)
Balmaceda L. A., Solanki S. K., Krivova N. A., Foster S., 2009, J. Geophys. Res., 114, 7104
Baraffe I., Chabrier G., Allard F., Hauschildt P. H., 1998, A&A, 337, 403
Barnes J. R., Jeffers S. V., Jones H. R. A., 2011, MNRAS, 412, 1599
Basri G., Walkowicz L. M., Reiners A., 2013, ApJ, 769, 37
Baumann I., Solanki S. K., 2005, A&A, 443, 1061
Bennett D. P. et al., 2012, ApJ, 757, 119
Berdyugina S. V., Usoskin I. G., 2003, A&A, 405, 1121
Bogdan T. J., Gilman P. A., Lerche I., Howard R., 1988, ApJ, 327, 451
Boisse I., Bouchy F., Hébrard G., Bonfils X., Santos N., Vauclair S., 2011, A&A, 528, A4
Boisse I., Bonfils X., Santos N. C., 2012, A&A, 545, A109
Carrington R. C., 1858, MNRAS, 19, 1
Cegla H. M. et al., 2012, MNRAS, 421, L54
Cegla H. M., Stassun K. G., Watson C. A., Bastien F. A., Pepper J., 2014, ApJ, 780, 104
Desort M., Lagrange A.-M., Galland F., Udry S., Mayor M., 2007, A&A, 473, 983
Dumusque X., Udry S., Lovis C., Santos N. C., Monteiro M. J. P. F. G., 2011a, A&A, 525, A140
Dumusque X., Santos N. C., Udry S., Lovis C., Bonfils X., 2011b, A&A, 527, A82
Dumusque X., Boisse I., Santos N. C., 2014, ApJ, 796, 132
Gilliland R. L. et al., 2011, ApJS, 197, 6
Gnevyshev M. N., 1938, Pulkovo Obser. Circ., 24, 37
Gray R. O., Corbally C. J., 1994, AJ, 107, 742
Gustafsson B., Edvardsson B., Eriksson K., Jørgensen U. G., Nordlund Å., Plez B., 2008, A&A, 486, 951
Hackman T., Jetsu L., Tuominen I., 2001, A&A, 374, 171
Hathaway D. H., 2011, Sol. Phys., 273, 221
Horne J. H., Baliunas S. L., 1986, ApJ, 302, 757
Huerta M., Johns-Krull C. M., Prato L., Hartigan P., Jaffe D. T., 2008, ApJ, 678, 472
Järvinen S. P., Korhonen H., Berdyugina S. V., Ilyin I., Strassmeier K. G., Weber M., Savanov I., Tuominen I., 2008, A&A, 488, 1047
Jeffers S. V., Barnes J. R., Jones H. R. A., Reiners A., Pinfield D. J., Marsden S. C., 2014, MNRAS, 438, 2717
Jenkins J. S. et al., 2006, MNRAS, 372, 163
Juckett D. A., 2006, Sol. Phys., 237, 351
Kupka F. G., Piskunov N. E., Ryabchikova T. A., Stempels H. C., Weiss W. W., 1999, A&AS, 138, 119
Kurucz R. L., 1993, Kurucz CD, No. 13
Kurucz R. L., Avrett E. H., 1981, SAO Special Report, No. 391
Lagrange A.-M., Desort M., Meunier N., 2010, A&A, 512, A38
Lanza A. F., Boisse I., Bouchy F., Bonomo A. S., Moutou C., 2011, A&A, 533, A44

Ma B., Ge J., 2012, ApJ, 750, 172
McQuillan A., Aigrain S., Roberts S., 2012, A&A, 539, A137
Marchwinski R. C., Mahadevan S., Robertson P., Ramsey L., Harder J., 2015, ApJ, 798, 63
Martínez-Arnáiz R., Maldonado J., Montes D., Eiroa C., Montesinos B., 2010, A&A, 520, A79
Maunder E. W., 1903, Observatory, 26, 329
Meunier N., Lagrange A.-M., 2013, A&A, 551, A101
Meunier N., Desort M., Lagrange A.-M., 2010, A&A, 512, A39
Mikkola S., 1987, Celest. Mech., 40, 329
Moulds V. E., Watson C. A., Bonfils X., Littlefair S. P., Simpson E. K., 2013, MNRAS, 430, 1709
Oshagh M., Santos N. C., Boisse I., Boué G., Montalto M., Dumusque X., Haghighipour N., 2013, A&A, 556, A19
Petrovay K., van Driel-Gesztelyi L., 1997, Sol. Phys., 176, 249
Piskunov N. E., Tuominen I., Vilhu O., 1990, A&A, 230, 363
Press W. H., Rybicki G. B., 1989, ApJ, 338, 277
Queloz D. et al., 2001, A&A, 379, 279
Radick R. R., Lockwood G. W., Skiff B. A., Baliunas S. L., 1998, ApJS, 118, 239
Reiners A., Bean J. L., Huber K. F., Dreizler S., Seifahrt A., Czesla S., 2010, ApJ, 710, 432
Saar S. H., Donahue R. A., 1997, ApJ, 485, 319
Sbordone L., Bonifacio P., Castelli F., Kurucz R. L., 2004, Mem. Soc. Astron. Ital. Suppl., 5, 93
Scargle J. D., 1982, ApJ, 263, 835
Solanki S. K., 2003, A&AR, 11, 153
Usoskin I. G., Berdyugina S. V., Poutanen J., 2005, A&A, 441, 347
Waldmeier M., 1955, Ergebnisse und Probleme der Sonnenforschung, 2. Aufl. Akad. Verlagsges., Leipzig

This paper has been typeset from a TEX/LATEX file prepared by the author.

Monthly Notices of the ROYAL ASTRONOMICAL SOCIETY
MNRAS **447,** 711–721 (2015) doi:10.1093/mnras/stu2394

High-precision photometry by telescope defocusing – VII. The ultrashort period planet WASP-103★

John Southworth,[1]† L. Mancini,[2] S. Ciceri,[2] J. Budaj,[3,4] M. Dominik,[5]‡ R. Figuera Jaimes,[5,6] T. Haugbølle,[7] U. G. Jørgensen,[8] A. Popovas,[8] M. Rabus,[2,9] S. Rahvar,[10] C. von Essen,[11] R. W. Schmidt,[12] O. Wertz,[13] K. A. Alsubai,[14] V. Bozza,[15,16] D. M. Bramich,[14] S. Calchi Novati,[17,15,18]§ G. D'Ago,[15,16] T. C. Hinse,[19] Th. Henning,[2] M. Hundertmark,[5] D. Juncher,[8] H. Korhonen,[8,20] J. Skottfelt,[8] C. Snodgrass,[21] D. Starkey[5] and J. Surdej[13]

Affiliations are listed at the end of the paper

Accepted 2014 November 11. Received 2014 October 20; in original form 2014 September 2

ABSTRACT

We present 17 transit light curves of the ultrashort period planetary system WASP-103, a strong candidate for the detection of tidally-induced orbital decay. We use these to establish a high-precision reference epoch for transit timing studies. The time of the reference transit mid-point is now measured to an accuracy of 4.8 s, versus 67.4 s in the discovery paper, aiding future searches for orbital decay. With the help of published spectroscopic measurements and theoretical stellar models, we determine the physical properties of the system to high precision and present a detailed error budget for these calculations. The planet has a Roche lobe filling factor of 0.58, leading to a significant asphericity; we correct its measured mass and mean density for this phenomenon. A high-resolution *Lucky Imaging* observation shows no evidence for faint stars close enough to contaminate the point spread function of WASP-103. Our data were obtained in the Bessell *RI* and the SDSS *griz* passbands and yield a larger planet radius at bluer optical wavelengths, to a confidence level of 7.3σ. Interpreting this as an effect of Rayleigh scattering in the planetary atmosphere leads to a measurement of the planetary mass which is too small by a factor of 5, implying that Rayleigh scattering is not the main cause of the variation of radius with wavelength.

Key words: stars: fundamental parameters – stars: individual: WASP-103 – planetary systems.

1 INTRODUCTION

An important factor governing the tidal evolution of planetary systems is the stellar tidal quality factor $Q_\star$ (e.g. Goldreich & Soter 1966), which represents the efficiency of tidal dissipation in the star. Its value is necessary for predicting the time-scales of orbital circularization, axial alignment and rotational synchronization of binary star and planet systems. Short-period giant planets suffer orbital decay due to tidal effects, and most will ultimately be devoured by their host star rather than reach an equilibrium state (Jackson, Barnes & Greenberg 2009; Levrard, Winisdoerffer & Chabrier 2009). The magnitude of $Q_\star$ therefore influences the orbital period distribution of populations of extrasolar planets.

Unfortunately, $Q_\star$ is not well constrained by current observations. Its value is often taken to be 10^6 (Ogilvie & Lin 2007) but there exist divergent results in the literature. A value of $10^{5.5}$ was found to be a good match to a sample of known extrasolar planets by Jackson, Greenberg & Barnes (2008), but theoretical work by Penev & Sasselov (2011) constrained $Q_\star$ to lie between 10^8 and $10^{9.5}$ and an observational study by Penev et al. (2012) found $Q_\star > 10^7$ to 99 per cent confidence. Inferences from the properties of binary star systems are often used but are not relevant to this issue: $Q_\star$ is not a fundamental property of a star but depends on the nature of the tidal perturbation (Goldreich 1963; Ogilvie 2014). $Q_\star$ should however be

★ Based on data collected by MiNDSTEp with the Danish 1.54 m telescope, and data collected with GROND on the MPG 2.2 m telescope, both located at ESO La Silla.

† E-mail: astro.js@keele.ac.uk

‡ Royal Society University Research Fellow.

§ Sagan visiting fellow.

Published by Oxford University Press on behalf of the Royal Astronomical Society

Table 1. Log of the observations presented in this work. N_{obs} is the number of observations, T_{exp} is the exposure time, T_{dead} is the dead time between exposures, 'Moon illum'. is the fractional illumination of the Moon at the mid-point of the transit, and N_{poly} is the order of the polynomial fitted to the out-of-transit data. The aperture radii are target aperture, inner sky and outer sky, respectively.

Instrument	Date of first obs	Start time (UT)	End time (UT)	N_{obs}	T_{exp} (s)	T_{dead} (s)	Filter	Airmass	Moon illum.	Aperture radii (pixel)	N_{poly}	Scatter (mmag)
DFOSC	2014 04 20	05:08	09:45	134	100–105	18	*R*	1.54 → 1.24 → 1.54	0.725	14 25 45	1	0.675
DFOSC	2014 05 02	05:45	10:13	113	110–130	19	*I*	1.28 → 1.24 → 2.23	0.100	14 22 50	1	0.815
DFOSC	2014 06 09	04:08	08:22	130	100	16	*R*	1.24 → 3.08	0.888	16 27 50	1	1.031
DFOSC	2014 06 23	01:44	06:19	195	50–120	16	*R*	1.35 → 1.24 → 1.86	0.168	14 22 40	1	1.329
DFOSC	2014 06 24	00:50	04:25	112	100	16	*R*	1.54 → 1.24 → 1.31	0.103	19 25 40	1	0.647
DFOSC	2014 07 06	01:28	05:20	118	100	18	*R*	1.28 → 1.24 → 1.80	0.564	16 26 50	1	0.653
DFOSC	2014 07 18	01:19	05:45	139	90–110	16	*R*	1.25 → 3.00	0.603	17 25 60	1	0.716
DFOSC	2014 07 18	23:04	04:20	181	60–110	16	*R*	1.52 → 1.24 → 1.73	0.502	16 24 55	2	0.585
GROND	2014 07 06	00:23	05:27	122	100–120	40	*g*	1.45 → 1.24 → 1.87	0.564	24 65 85	2	1.251
GROND	2014 07 06	00:23	05:27	119	100–120	40	*r*	1.45 → 1.24 → 1.87	0.564	24 65 85	2	0.707
GROND	2014 07 06	00:23	05:27	125	100–120	40	*i*	1.45 → 1.24 → 1.87	0.564	24 65 85	2	0.843
GROND	2014 07 06	00:23	05:27	121	100–120	40	*z*	1.45 → 1.24 → 1.87	0.564	24 65 85	2	1.106
GROND	2014 07 18	22:55	03:59	125	98–108	41	*g*	1.64 → 1.24 → 1.93	0.502	30 50 85	2	0.882
GROND	2014 07 18	22:55	04:43	143	98–108	41	*r*	1.64 → 1.24 → 1.93	0.502	25 45 70	2	0.915
GROND	2014 07 18	22:55	04:39	142	98–108	41	*i*	1.64 → 1.24 → 1.88	0.502	28 56 83	2	0.656
GROND	2014 07 18	22:55	04:43	144	98–108	41	*z*	1.64 → 1.24 → 1.93	0.502	30 50 80	2	0.948
CASLEO	2014 08 12	23:22	03:10	129	90–120	4	*R*	1.29 → 2.12	0.920	20 30 60	4	1.552

observationally accessible through the study of transiting extrasolar planets (TEPs).

Birkby et al. (2014) assessed the known population of TEPs for their potential for the direct determination of the strength of tidal interactions. The mechanism considered was the detection of tidally-induced orbital decay, which manifests itself as a decreasing orbital period. These authors found that WASP-18 (Hellier et al. 2009; Southworth et al. 2009b) is the most promising system, due to its short orbital period (0.94 d) and large planet mass ($10.4\,M_{Jup}$), followed by WASP-103 (Gillon et al. 2014, hereafter G14), then WASP-19 (Hebb et al. 2010; Mancini et al. 2013).

Adopting the canonical value of $Q_\star = 10^6$, Birkby et al. (2014) calculated that orbital decay would cause a shift in transit times – over a time interval of 10 yr – of 350 s for WASP-18, 100 s for WASP-103 and 60 s for WASP-19. Detection of this effect clearly requires observations over many years coupled with a precise ephemeris against which to measure deviations from strict periodicity. High-quality transit timing data are already available for WASP-18 (Maxted et al. 2013) and WASP-19 (Abe et al. 2013; Lendl et al. 2013; Mancini et al. 2013; Tregloan-Reed, Southworth & Tappert 2013), but not for WASP-103.

WASP-103 was discovered by G14 and comprises a TEP of mass $1.5\,M_{Jup}$ and radius $1.6\,R_{Jup}$ in a very short-period orbit (0.92 d) around an F8 V star of mass $1.2\,M_\odot$ and radius $1.4\,R_\odot$. G14 obtained observations of five transits, two with the Swiss Euler telescope and three with TRAPPIST, both at ESO La Silla. The Euler data each cover only half a transit, whereas the TRAPPIST data have a lower photometric precision and suffer from 180° field rotations during the transits due to the nature of the telescope mount. The properties of the system could therefore be measured to only modest precision; in particular the ephemeris zero-point is known to a precision of only 64 s. In this work, we present 17 high-quality transit light curves which we use to determine a precise orbital ephemeris for WASP-103, as well as to improve measurements of its physical properties.

2 OBSERVATIONS AND DATA REDUCTION

2.1 DFOSC observations

Eight transits were obtained using the DFOSC (Danish Faint Object Spectrograph and Camera) instrument on the 1.54 m Danish Telescope at ESO La Silla, Chile, in the context of the MiNDSTEp microlensing programme (Dominik et al. 2010). DFOSC has a field of view of 13.7 arcmin×13.7 arcmin at a plate scale of 0.39 arcsec pixel^{-1}. We windowed down the CCD to cover WASP-103 itself and seven good comparison stars, in order to shorten the dead time between exposures.

The instrument was defocused to lower the noise level of the observations, in line with our usual strategy (see Southworth et al. 2009a, 2014). The telescope was autoguided to limit pointing drifts to less than five pixels over each observing sequence. Seven of the transits were obtained through a Bessell *R* filter, but one was taken through a Bessell *I* filter by accident. An observing log is given in Table 1 and the light curves are plotted individually in Fig. 1.

2.2 GROND observations

We observed two transits of WASP-103 using the GROND instrument (Greiner et al. 2008) mounted on the MPG 2.2 m telescope at La Silla, Chile. Both transits were also observed with DFOSC. GROND was used to obtain light curves simultaneously in passbands which approximate SDSS *g*, *r*, *i* and *z*. The small field of view of this instrument (5.4 arcmin×5.4 arcmin at a plate scale of 0.158 arcsec pixel^{-1}) meant that few comparison stars were available and the best of these was several times fainter than WASP-103 itself. The scatter in the GROND light curves is therefore worse than generally achieved (e.g. Nikolov et al. 2013; Mancini et al. 2014b,c), but the data are certainly still useful. The telescope was defocused and autoguided for both sets of observations. Further details are given in the observing log (Table 1) and the light curves are plotted individually in Fig. 2.

Downloaded from http://mnras.oxfordjournals.org/ at Royal Library/Copenhagen University Library on December 20, 2015

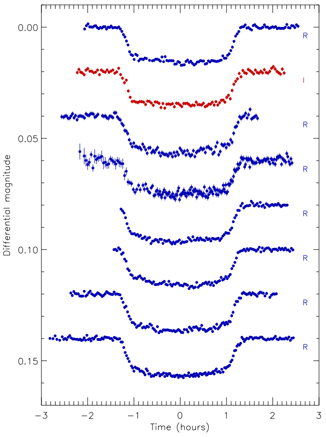

Figure 1. DFOSC light curves presented in this work, in the order they are given in Table 1. Times are given relative to the mid-point of each transit, and the filter used is indicated. Dark blue and dark red filled circles represent observations through the Bessell *R* and *I* filters, respectively.

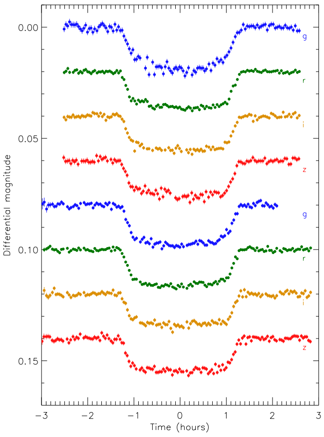

Figure 2. GROND light curves presented in this work, in the order they are given in Table 1. Times are given relative to the mid-point of each transit, and the filter used is indicated. *g*-band data are shown in light blue, *r*-band in green, *i*-band in orange and *z*-band in light red.

2.3 CASLEO observations

We observed one transit of WASP-103 (Fig. 3) using the 2.15 m Jorge Sahade telescope located at the Complejo Astronómico El Leoncito (CASLEO) in San Juan, Argentina.[1] We used the focal reducer and Roper Scientific CCD, yielding an unvignetted field of view of 9 arcmin radius at a plate scale of 0.45 arcsec pixel^{-1}. The CCD was operated without binning or windowing due to its short readout time. The observing conditions were excellent. The images were slightly defocused to a full width at half-maximum (FWHM) of 3 arcsec, and were obtained through a Johnson–Cousins Schuler *R* filter.

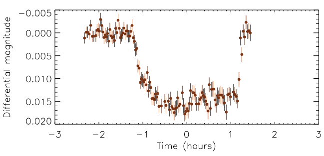

Figure 3. The CASLEO light curve of WASP-103. Times are given relative to the mid-point of the transit.

2.4 Data reduction

The DFOSC and GROND data were reduced using the DEFOT code (Southworth et al. 2009a) with the improvements discussed by Southworth et al. (2014). Master bias, dome flat-fields and sky flat-fields were constructed but not applied, as they were found not to improve the quality of the resulting light curves (see Southworth et al. 2014). Aperture photometry was performed using the IDL[2]/ASTROLIB[3] implementation of DAOPHOT (Stetson 1987). Image motion was tracked by cross-correlating individual images with a reference image.

We obtained photometry on the instrumental system using software apertures of a range of sizes, and retained those which gave light curves with the smallest scatter (Table 1). We found that the choice of aperture size does influence the scatter in the final light curve, but does not have a significant effect on the transit shape.

[1] Visiting Astronomer, Complejo Astronómico El Leoncito operated under agreement between the Consejo Nacional de Investigaciones Científicas y Técnicas de la República Argentina and the National Universities of La Plata, Córdoba and San Juan.

[2] The acronym IDL stands for Interactive Data Language and is a trademark of ITT Visual Information Solutions. For further details see: http://www.exelisvis.com/ProductsServices/IDL.aspx.

[3] The ASTROLIB subroutine library is distributed by NASA. For further details see: http://idlastro.gsfc.nasa.gov/.

Downloaded from http://mnras.oxfordjournals.org/ at Royal Library/Copenhagen University Library on December 20, 2015

Table 2. Sample of the data presented in this work (the first data point of each light curve). The full data set will be made available at the CDS.

Instrument	Filter	BJD(TDB)	Diff. mag.	Uncertainty
DFOSC	*R*	2456767.719670	0.000 8211	0.000 6953
DFOSC	*I*	2456779.746022	0.000 4141	0.000 8471
DFOSC	*R*	2456817.679055	0.000 2629	0.000 9941
DFOSC	*R*	2456831.578063	− 0.004 0473	0.003 5872
DFOSC	*R*	2456832.540736	0.001 8135	0.000 6501
DFOSC	*R*	2456844.566748	0.000 0224	0.000 6405
DFOSC	*R*	2456856.559865	− 0.000 4751	0.000 6952
DFOSC	*R*	2456857.466519	− 0.000 0459	0.000 5428
GROND	*g*	2456844.521804	0.000 8698	0.001 3610
GROND	*r*	2456844.521804	0.000 3845	0.000 7863
GROND	*i*	2456844.521804	0.000 5408	0.000 9272
GROND	*z*	2456844.521804	− 0.001 3755	0.001 2409
GROND	*g*	2456857.459724	− 0.000 5583	0.002 4887
GROND	*r*	2456857.461385	0.000 0852	0.000 9575
GROND	*i*	2456857.461385	− 0.001 6371	0.001 5169
GROND	*z*	2456857.459724	0.001 2460	0.001 5680
CASLEO	*R*	2456882.47535	0.001 14	0.001 21

The instrumental magnitudes were then transformed to differential-magnitude light curves normalized to zero magnitude outside transit. The normalization was enforced with first- or second-order polynomials (see Table 1) fitted to the out-of-transit data. The differential magnitudes are relative to a weighted ensemble of typically five (DFOSC) or two to four (GROND) comparison stars. The comparison star weights and polynomial coefficients were simultaneously optimized to minimize the scatter in the out-of-transit data.

The CASLEO data were reduced using standard aperture photometry methods, with the IRAF tasks CCDPROC and APPHOT. We found that it was necessary to flat-field the data in order to obtain a good light curve. The final light curve was obtained by dividing the flux of WASP-103 by the average flux of three comparison stars. An aperture radius of three times the FWHM was used, as it minimized the scatter in the data.

Finally, the timestamps for the data points were converted to the BJD(TDB) time-scale (Eastman, Siverd & Gaudi 2010). We performed manual time checks for several images and have verified that the FITS file timestamps are on the UTC system to within a few seconds. The reduced data are given in Table 2 and will be lodged with the CDS.[4]

2.5 High-resolution imaging

Several images were taken of WASP-103 with DFOSC in sharp focus, in order to test for the presence of faint nearby stars whose photons might bias our results (Daemgen et al. 2009). The closest star we found on any image is 42 pixels south-east of WASP-103, and 5.3 mag fainter in the *R* band. It is thus too faint and far away to contaminate the inner aperture of our target star.

We proceeded to obtain a high-resolution image of WASP-103 using the Lucky Imager (LI) mounted on the Danish telescope (see Skottfelt et al. 2013). The LI uses an Andor 512×512 pixel electron-multiplying CCD, with a pixel scale of 0.09 arcsec pixel^{-1} giving a field of view of 45 arcsec × 45 arcsec. The data were reduced using a dedicated pipeline and the 2 per cent of images with the smallest point spread function (PSF) were stacked together to yield combined images whose PSF is smaller than the seeing limit. A long-pass filter was used, resulting in a response which approximates that of SDSS $i+z$. An overall exposure time of 415 s corresponds to an effective exposure time of 8.3 s for the best 2 per cent of the images. The FWHM of the PSF is 5.9 pixels (0.53 arcsec) in both dimensions. The LI image (Fig. 4) shows no evidence for a point source closer than that found in our DFOSC images.

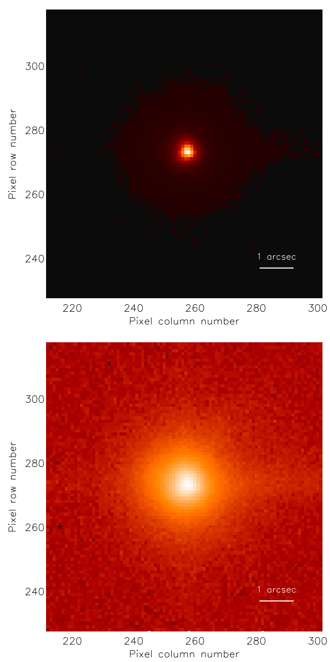

Figure 4. High-resolution Lucky Image of the field around WASP-103. The upper panel has a linear flux scale for context and the lower panel has a logarithmic flux scale to enhance the visibility of any faint stars. Each image covers 8 arcsec × 8 arcsec centred on WASP-103. A bar of length 1 arcsec is superimposed in the bottom right of each image. The image is a sum of the best 2 per cent of the original images.

[4] http://vizier.u-strasbg.fr/

Downloaded from http://mnras.oxfordjournals.org/ at Royal Library/Copenhagen University Library on December 20, 2015

Table 3. Times of minimum light and their residuals versus the ephemeris derived in this work.

Time of min. (BJD/TDB)	Error (d)	Cycle number	Residual (d)	Reference
2456459.59957	0.000 79	−407.0	0.000 19	G14
2456767.80578	0.000 17	−74.0	−0.000 29	This work (DFOSC *R*)
2456779.83870	0.000 22	−61.0	0.000 54	This work (DFOSC *I*)
2456817.78572	0.000 27	−20.0	0.000 19	This work (DFOSC *R*)
2456831.66843	0.000 39	−5.0	−0.000 29	This work (DFOSC *R*)
2456832.59401	0.000 24	−4.0	−0.000 25	This work (DFOSC *R*)
2456844.62641	0.000 19	9.0	0.000 05	This work (DFOSC *R*)
2456844.62642	0.000 34	9.0	0.000 06	This work (GROND *g*)
2456844.62633	0.000 19	9.0	−0.000 03	This work (GROND *r*)
2456844.62647	0.000 23	9.0	0.000 11	This work (GROND *i*)
2456844.62678	0.000 30	9.0	0.000 42	This work (GROND *z*)
2456856.65838	0.000 18	22.0	−0.000 07	This work (DFOSC *R*)
2456857.58383	0.000 14	23.0	−0.000 16	This work (DFOSC *R*)
2456857.58390	0.000 22	23.0	−0.000 09	This work (GROND *g*)
2456857.58398	0.000 17	23.0	0.000 01	This work (GROND *r*)
2456857.58400	0.000 25	23.0	0.000 01	This work (GROND *i*)
2456857.58421	0.000 25	23.0	0.000 22	This work (GROND *z*)
2456882.57473	0.000 50	50.0	0.001 00	This work (CASLEO *R*)

3 TRANSIT TIMING ANALYSIS

We first modelled each light curve individually using the JKTEBOP code (see below) in order to determine the times of mid-transit. In this process, the error bars for each data set were also scaled to give a reduced χ^2 of $\chi^2_\nu = 1.0$ versus the fitted model. This step is needed because the uncertainties from the APER algorithm are often moderately underestimated.

We then fitted the times of mid-transit with a straight line versus cycle number to determine a new linear orbital ephemeris. We included the ephemeris zero-point from G14, which is also on the BJD(TDB) time-scale and was obtained by them from a joint fit to all their data. Table 3 gives all transit times plus their residual versus the fitted ephemeris. We chose the reference epoch to be that which gives the lowest uncertainty in the time zero-point, as this minimizes the covariance between the reference time of minimum and the orbital period. The resulting ephemeris is

$$T_0 = \mathrm{BJD(TDB)}\ 2456836.296445(55) + 0.9255456(13) \times E,$$

where E gives the cycle count versus the reference epoch and the bracketed quantities indicate the uncertainty in the final digit of the preceding number.

The χ^2_ν of the fit is excellent at 1.055. The timestamps from DFOSC and GROND are obtained from different atomic clocks, so are unrelated to each other. The good agreement between them is therefore evidence that both are correct.

Fig. 5 shows the residuals of the times of mid-transit versus the linear ephemeris we have determined. The precision in the measurement of the mid-point of the reference transit has improved from 64.7 s (G14) to 4.8 s, meaning that we have established a high-quality set of timing data against which orbital decay could be measured in future.

4 LIGHT-CURVE ANALYSIS

We analysed our light curves using the JKTEBOP[5] code (Southworth, Maxted & Smalley 2004) and the *Homogeneous Studies* methodology (Southworth 2012, and references therein). The light curves were divided up according to their passband (Bessell *R* and *I* for DFOSC and SDSS *griz* for GROND) and each set was modelled together.

The model was parametrized by the fractional radii of the star and the planet (r_A and r_b), which are the ratios between the true radii and the semimajor axis ($r_{A,b} = \frac{R_{A,b}}{a}$). The parameters of the fit were the sum and ratio of the fractional radii ($r_A + r_b$ and $k = \frac{r_b}{r_A}$), the orbital inclination (i), limb darkening coefficients, and a reference time of mid-transit. We assumed an orbital eccentricity of zero (G14) and the orbital period found in Section 3. We also fitted for the coefficients of polynomial functions of differential magnitude versus time (Southworth et al. 2014). One polynomial was used for each transit light curve, of the order given in Table 1.

Limb darkening was incorporated using each of five laws (see Southworth 2008), with the linear coefficients either fixed at theoretically predicted values[6] or included as fitted parameters. We did not calculate fits for both limb darkening coefficients in the four two-coefficient laws as they are very strongly correlated (Southworth, Bruntt & Buzasi 2007b; Carter et al. 2008). The non-linear coefficients were instead perturbed by ±0.1 on a flat distribution during the error analysis simulations, in order to account for imperfections in the theoretical values of the coefficients.

Error estimates for the fitted parameters were obtained in three ways. Two sets were obtained using residual-permutation and Monte Carlo simulations (Southworth 2008) and the larger of the two was retained for each fitted parameter. We also ran solutions using the five different limb darkening laws, and increased the error bar for each parameter to account for any disagreement between these five solutions. Tables of results for each light curve can be found in the appendix and the best fits can be inspected in Fig. 6.

4.1 Results

For all light curves, we found that the best solutions were obtained when the linear limb darkening coefficient was fitted and the non-linear coefficient was fixed but perturbed. We found that there is a significant correlation between i and k for all light curves, which hinders the precision to which we can measure the photometric parameters. The best fit for the CASLEO and the GROND z-band data is a central transit ($i \approx 90°$), but this does not have a significant effect on the value of k measured from these data.

Table 4 holds the measured parameters from each light curve. The final value for each parameter is the weighted mean of the values from the different light curves. We find good agreement for all parameters except for k, which is in line with previous experience (see Southworth 2012 and references therein). The χ_ν^2 of the individual values of k versus the weighted mean is 3.1, and the error bar for the final value of k in Table 4 has been multiplied by $\sqrt{3.1}$ to force a χ_ν^2 of unity. Our results agree with, but are significantly more precise than, those found by G14.

5 PHYSICAL PROPERTIES

We have measured the physical properties of the WASP-103 system using the results from Section 4, five grids of predictions from theoretical models of stellar evolution (Claret 2004; Demarque et al.

[5] JKTEBOP is written in FORTRAN77 and the source code is available at http://www.astro.keele.ac.uk/jkt/codes/jktebop.html.

[6] Theoretical limb darkening coefficients were obtained by bilinear interpolation in $T_{\rm eff}$ and $\log g$ using the JKTLD code available from: http://www.astro.keele.ac.uk/jkt/codes/jktld.html.

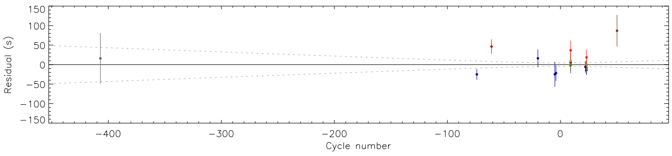

Figure 5. Plot of the residuals of the timings of mid-transit for WASP-103 versus a linear ephemeris. The leftmost point is from G14 and the remaining points are from the current work (colour-coded consistently with Figs 1–3). The dotted lines show the 1σ uncertainty in the ephemeris as a function of cycle number.

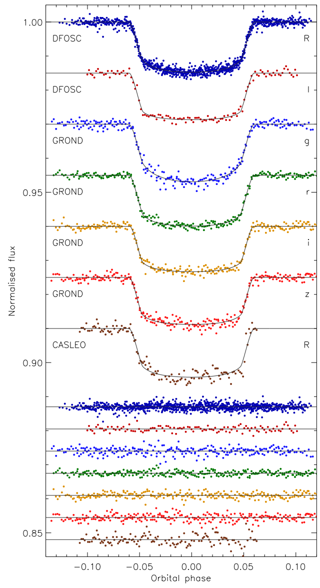

Figure 6. Phased light curves of WASP-103 compared to the JKTEBOP best fits. The residuals of the fits are plotted at the base of the figure, offset from unity. Labels give the source and passband for each data set. The polynomial baseline functions have been removed from the data before plotting.

2004; Pietrinferni et al. 2004; VandenBerg, Bergbusch & Dowler 2006; Dotter et al. 2008), and the spectroscopic properties of the host star. Theoretical models are needed to provide an additional constraint on the stellar properties as the system properties cannot be obtained from only measured quantities. The spectroscopic properties were obtained by G14 and comprise effective temperature ($T_{\rm eff} = 6110 \pm 160$ K), metallicity ([Fe/H] $= 0.06 \pm 0.13$) and velocity amplitude ($K_A = 271 \pm 15\,\mathrm{m\,s^{-1}}$). The adopted set of physical constants is given in Southworth (2011).

We first estimated the velocity amplitude of the *planet*, K_b, and used this along with the measured r_A, r_b, i and K_A to determine the physical properties of the system. K_b was then iteratively refined to find the best match between the measured r_A and the calculated $\frac{R_A}{a}$, and the observed $T_{\rm eff}$ and that predicted by a theoretical model for the obtained stellar mass, radius and [Fe/H]. This was done for a grid of ages from the zero-age main sequence to beyond the terminal-age main sequence for the star, in 0.01 Gyr increments, and the overall best K_b was adopted. The statistical errors in the input quantities were propagated to the output quantities by a perturbation approach.

We ran the above analysis for each of the five grids of theoretical stellar models, yielding five different estimates of each output quantity. These were transformed into a single final result for each parameter by taking the unweighted mean of the five estimates and their statistical errors, plus an accompanying systematic error which gives the largest difference between the mean and individual values. The final results of this process are a set of physical properties for the WASP-103 system, each with a statistical error and a systematic error. The stellar density, planetary surface gravity and planetary equilibrium temperatures can be calculated without resorting to theoretical predictions (Seager & Mallén-Ornelas 2003; Southworth, Wheatley & Sams 2007a; Southworth 2010), so do not have an associated systematic error.

5.1 Results

Our final results are given in Table 5 and have been added to TEPCat.[7] We find good agreement between the five different model sets (table A8). Some of the measured quantities, in particular the stellar and planetary mass, are still relatively uncertain. To investigate this we calculated a complete error budget for each output parameter, and show the results of this analysis in Table 6 when using the Y[2] theoretical stellar models (Demarque et al. 2004). The error budgets for the other four model sets are similar.

[7] TEPCat is The Transiting Extrasolar Planet Catalogue (Southworth 2011) at: http://www.astro.keele.ac.uk/jkt/tepcat/.

Table 4. Parameters of the fit to the light curves of WASP-103 from the JKTEBOP analysis (top). The final parameters are given in bold and the parameters found by G14 are given below this. Quantities without quoted uncertainties were not given by G14 but have been calculated from other parameters which were. The error bar for the final value of k has been inflated to account for the disagreement between different measurements.

Source	$r_A + r_b$	k	i (°)	r_A	r_b
DFOSC *R* band	0.3703 ± 0.0055	0.1129 ± 0.0009	88.1 ± 2.2	0.3328 ± 0.0048	$0.037\,55 \pm 0.000\,74$
DFOSC *I* band	0.3766 ± 0.0146	0.1118 ± 0.0013	84.8 ± 4.2	0.3387 ± 0.0128	$0.037\,88 \pm 0.001\,75$
GROND *g* band	0.3734 ± 0.0140	0.1183 ± 0.0022	86.3 ± 3.9	0.3339 ± 0.0123	$0.039\,49 \pm 0.002\,01$
GROND *r* band	0.3753 ± 0.0102	0.1150 ± 0.0011	85.2 ± 3.2	0.3366 ± 0.0087	$0.038\,70 \pm 0.001\,24$
GROND *i* band	0.3667 ± 0.0132	0.1091 ± 0.0017	87.1 ± 3.6	0.3307 ± 0.0116	$0.036\,06 \pm 0.001\,29$
GROND *z* band	0.3661 ± 0.0111	0.1106 ± 0.0016	89.9 ± 2.4	0.3297 ± 0.0099	$0.036\,45 \pm 0.001\,20$
CASLEO *R* band	0.3665 ± 0.0203	0.1117 ± 0.0055	89.6 ± 4.5	0.3296 ± 0.0167	$0.036\,83 \pm 0.003\,16$
Final results	$\mathbf{0.3712 \pm 0.0040}$	$\mathbf{0.1127 \pm 0.0009}$	$\mathbf{87.3 \pm 1.2}$	$\mathbf{0.3335 \pm 0.0035}$	$\mathbf{0.037\,54 \pm 0.000\,49}$
G14	0.3725	$0.1093^{+0.0019}_{-0.0017}$	86.3 ± 2.7	$0.3358^{+0.0111}_{-0.0055}$	0.03670

Table 5. Derived physical properties of WASP-103. Quantities marked with a ⋆ are significantly affected by the spherical approximation used to model the light curves, and revised values are given at the base of the table.

Quantity	Symbol	Unit	This work	G14
Stellar mass	M_A	$\mathrm{M_\odot}$	$1.204 \pm 0.089 \pm 0.019$	$1.220^{+0.039}_{-0.036}$
Stellar radius	R_A	$\mathrm{R_\odot}$	$1.419 \pm 0.039 \pm 0.008$	$1.436^{+0.052}_{-0.031}$
Stellar surface gravity	$\log g_A$	cgs	$4.215 \pm 0.014 \pm 0.002$	$4.22^{+0.12}_{-0.05}$
Stellar density	ρ_A	$\rho_\odot$	0.421 ± 0.013	$0.414^{+0.021}_{-0.039}$
Planet mass	M_b	$M_{\rm Jup}$	$1.47 \pm 0.11 \pm 0.02$	1.490 ± 0.088
Planet radius⋆	R_b	$R_{\rm Jup}$	$1.554 \pm 0.044 \pm 0.008$	$1.528^{+0.073}_{-0.047}$
Planet surface gravity	g_b	$\mathrm{m\,s^{-2}}$	15.12 ± 0.93	15.7 ± 1.4
Planet density⋆	ρ_b	$\rho_{\rm Jup}$	$0.367 \pm 0.027 \pm 0.002$	$0.415^{+0.046}_{-0.053}$
Equilibrium temperature	$T'_{\rm eq}$	K	2495 ± 66	2508^{+75}_{-70}
Safronov number	Θ		$0.0311 \pm 0.0019 \pm 0.0002$	
Orbital semimajor axis	a	au	$0.019\,78 \pm 0.000\,49 \pm 0.000\,10$	$0.019\,85 \pm 0.000\,21$
Age	τ	Gyr	$3.8\,^{+2.1}_{-1.6}\,^{+0.3}_{-0.4}$	3 to 5
Planetary parameters corrected for asphericity:				
Planet radius		$R_{\rm Jup}$	1.603 ± 0.052	
Planet density		$\rho_{\rm Jup}$	0.335 ± 0.025	

Table 6. Detailed error budget for the calculation of the system properties of WASP-103 from the photometric and spectroscopic parameters, and the Y[2] stellar models. Each number in the table is the fractional contribution to the final uncertainty of an output parameter from the error bar of an input parameter. The final uncertainty for each output parameter is the quadrature sum of the individual contributions from each input parameter.

Output	Input parameter					
parameter	K_A	i	r_A	r_b	$T_{\rm eff}$	[Fe/H]
Age	0.012		0.035		0.873	0.471
a	0.030		0.020		0.797	0.601
M_A	0.029		0.020		0.796	0.602
R_A	0.027		0.469		0.703	0.530
$\log g_A$	0.019		0.706		0.563	0.424
ρ_A	0.002		1.000		0.001	
M_b	0.809	0.014	0.012		0.466	0.352
R_b	0.025		0.017	0.544	0.668	0.504
g_b	0.901	0.016		0.434		
ρ_b	0.772	0.014	0.006	0.564	0.232	0.174

The uncertainties in the physical properties of the planet are dominated by that in K_A, followed by that in r_b. The uncertainties in the stellar properties are dominated by those in $T_{\rm eff}$ and [Fe/H], followed by r_A. Improvements in our understanding of the WASP-103 system would most easily be achieved by obtaining new spectra from which additional radial velocity measurements and improved $T_{\rm eff}$ and [Fe/H] measurements could be obtained.

To illustrate the progress possible from further spectroscopic analysis, we reran the analysis but with smaller errorbars of ±50 K in $T_{\rm eff}$ and ±0.05 dex in [Fe/H]. The precision in M_A changes from 0.091 to 0.041 $\mathrm{M_\odot}$. Similar improvements are seen for a, and smaller improvements for R_A, R_b and ρ_b. Augmenting this situation by adopting an error bar of $\pm 5\,\mathrm{m\,s^{-1}}$ in K_A changes the precision in M_b from 0.11 to 0.047 $M_{\rm Jup}$ and yields further improvements for R_b and ρ_b.

5.2 Comparison with G14

Table 5 also shows the parameter values found by G14, which are in good agreement with our results. Some of the error bars however

are smaller than those in the current work, despite the fact that G14 had much less observational data at their disposal. A possible reason for this discrepancy is the additional constraint used to obtain a determinate model for the system. We used each of five sets of theoretical model predictions, whilst G14 adopted a calibration of M_A as a function of ρ_A, $T_{\rm eff}$ and [Fe/H] based on semi-empirical results from the analysis of low-mass detached eclipsing binary (dEB) systems (Torres, Winn & Holman 2008; Southworth 2009, 2011; Enoch et al. 2010). The dEB calibration suffers from an astrophysical scatter of the calibrating objects which is much greater than that of the precision to which the calibration function can be fitted (see Southworth 2011). G14 accounted for the uncertainty in the calibration by perturbing the measured properties of the calibrators during their Markov chain Monte Carlo analysis (Gillon et al. 2013). They therefore accounted for the observational uncertainties in the measured properties of the calibrators, but neglected the astrophysical scatter.

There is supporting evidence for this interpretation of why our error bars for some measurements are significantly larger than those found by G14. Our own implementation of the dEB calibration (Southworth 2011) explicitly includes the astrophysical scatter and yields $M_A = 1.29 \pm 0.11\,\mathrm{M_\odot}$, where the greatest contribution to the uncertainty is the scatter of the calibrators around the calibration function. G14 themselves found a value of $M_A = 1.18 \pm 0.10\,\mathrm{M_\odot}$ from an alternative approach (comparable to our main method) of using the CLÉS theoretical models (Scuflaire et al. 2008) as their additional constraint. This is much less precise than their default value of $M_A = 1.220^{+0.039}_{-0.036}\,\mathrm{M_\odot}$ from the dEB calibration. Gillon (private communication) confirms our interpretation of the situation.

5.3 Correction for asphericity

As pointed out by Li et al. (2010) for the case of WASP-12 b, some close-in extrasolar planets may have significant departures from spherical shape. Budaj (2011) calculated the Roche shapes of all transiting planets known at that time, as well as light curves and spectra taking into account the non-spherical shape. He found that WASP-19 b and WASP-12 b had the most significant tidal distortion of all known planets. The Roche model assumes that the object is rotating synchronously with the orbital period, there is a negligible orbital eccentricity, and that masses can be treated as point masses. The Roche shape has a characteristic pronounced expansion of the object towards the substellar point, and a slightly less pronounced expansion towards the antistellar point. The radii on the side of the object are smaller, and the radii at the rotation poles are the smallest. Leconte, Lai & Chabrier (2011) developed a model of tidally distorted planets which takes into account the tidally distorted mass distribution within the object assuming an ellipsoidal shape. Burton et al. (2014) studied the consequences of the Roche shape on the measured densities of exoplanets.

The Roche shape of a planet is determined by the semimajor axis, mass ratio, and a value of the surface potential. Assuming the parameters found above ($a = 4.25 \pm 0.11\,\mathrm{R_\odot}$, $M_A/M_b = 854 \pm 4$ and $R_b = 1.554 \pm 0.044\,R_{\rm Jup}$), one can estimate the tidally distorted Roche potential, i.e. the shape of the planet which would have the same cross-section during the transit as the one inferred from the observations under the assumption of a spherical planet. The shape of WASP-103 b is described by the parameters $R_{\rm sub}$, $R_{\rm back}$, $R_{\rm side}$ and $R_{\rm pole}$ (see Budaj 2011 for more details). The descriptions and values of these are given in Table 7. The uncertainties in Table 7 are the quadrature addition of those due to each input parameter; they are dominated by the uncertainty in the radius of the planet.

Table 7. Specification of the shape of WASP-103 b obtained using Roche geometry. $R_{\rm Jup}$, the equatorial radius of Jupiter, is adopted to be 71 492 km.

Symbol	Description	Value
$R_{\rm sub}$ ($R_{\rm Jup}$)	Radius at substellar point	1.721 ± 0.075
$R_{\rm back}$ ($R_{\rm Jup}$)	Radius at antistellar point	1.710 ± 0.072
$R_{\rm side}$ ($R_{\rm Jup}$)	Radius at sides	1.571 ± 0.047
$R_{\rm pole}$ ($R_{\rm Jup}$)	Radius at poles	1.537 ± 0.043
$R_{\rm cross}$ ($R_{\rm Jup}$)	Cross-sectional radius	1.554 ± 0.045
$R_{\rm mean}$ ($R_{\rm Jup}$)	Mean radius	1.603 ± 0.052
$f_{\rm RL}$	Roche lobe filling factor	0.584 ± 0.033
$R_{\rm sub}/R_{\rm side}$		1.095 ± 0.017
$R_{\rm sub}/R_{\rm pole}$		1.120 ± 0.020
$R_{\rm side}/R_{\rm pole}$		1.022 ± 0.003
$R_{\rm back}/R_{\rm sub}$		0.994 ± 0.002
$(R_{\rm mean}/R_{\rm cross})^3$	*Density correction*	1.096 ± 0.015

The cross-sectional radius, $R_{\rm cross} = \sqrt{R_{\rm side} R_{\rm pole}}$, is the radius of the circle with the same cross-section as the Roche surface during the transit. $R_{\rm cross}$ is the quantity measured from transit light curves using spherical-approximation codes such as JKTEBOP. $R_{\rm mean}$ is the radius of a sphere with the same volume as that enclosed by the Roche surface.

Table 7 also gives ratios between $R_{\rm sub}$, $R_{\rm back}$, $R_{\rm side}$ and $R_{\rm pole}$. Moderate changes in the planetary radius lead to very small changes in the ratios. In the case that future analyses yield a revised planetary radius, these ratios can therefore be used to rescale the values of $R_{\rm sub}$, $R_{\rm back}$, $R_{\rm side}$ and $R_{\rm pole}$ appropriately. In particular, the quantity $(R_{\rm mean}/R_{\rm cross})^3$ is the correction which must be applied to the density measured in the spherical approximation to convert it to the density obtained using Roche geometry.

WASP-103 b has a Roche lobe filling factor ($f_{\rm RL}$) of 0.58, where $f_{\rm RL}$ is defined to be the radius of the planet at the substellar point relative to the radius of the L1 point. The planet is therefore well away from Roche lobe overflow but is significantly distorted. The above analysis provides corrections to the properties measured in the spherical approximation. The planetary radius increases by 2.2 per cent to $R_b = 1.603 \pm 0.052\,R_{\rm Jup}$, and its density falls by 9.6 per cent to $\rho_b = 0.335 \pm 0.025\,\rho_{\rm Jup}$. These revised values include the uncertainty in the correction for asphericity and are included in Table 5. These departures from sphericity mean WASP-103 b is one of the three most distorted planets known, alongside WASP-19 b and WASP-12 b.

6 VARIATION OF RADIUS WITH WAVELENGTH

If a planet has an extended atmosphere, then a variation of opacity with wavelength will cause a variation of the measured planetary radius with wavelength. The light-curve solutions (Table 4) show a dependence between the measured value of k and the central wavelength of the passband used, in that larger k values occur at bluer wavelengths. This implies a larger planetary radius in the blue, which might be due to Rayleigh scattering from a high-altitude atmospheric haze (e.g. Pont et al. 2008; Sing et al. 2011; Pont et al. 2013).

We followed the approach of Southworth et al. (2012) to tease out this signal from our light curves. We modelled each data set with the parameters r_A and i fixed at the final values in Table 4, but still fitting for T_0, r_b, the linear limb darkening coefficient and the polynomial coefficients. We did not consider solutions with both limb darkening

Table 8. Values of r_b for each of the light curves as plotted in Fig. 7. Note that the error bars in this table exclude all common sources of uncertainty in r_b so should only be used to compare different values of $r_b(\lambda)$.

Passband	Central wavelength (nm)	FWHM (nm)	r_b
g	477.0	137.9	$0.039\,11 \pm 0.000\,29$
r	623.1	138.2	$0.038\,06 \pm 0.000\,22$
R	658.9	164.7	$0.037\,70 \pm 0.000\,10$
i	762.5	153.5	$0.036\,43 \pm 0.000\,26$
I	820.0	140.0	$0.037\,03 \pm 0.000\,22$
z	913.4	137.0	$0.036\,98 \pm 0.000\,33$

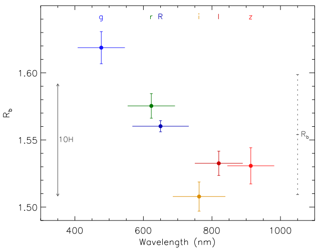

Figure 7. Measured planetary radius (R_b) as a function of the central wavelength of the passbands used for different light curves. The data points show the R_b measured from each light curve. The vertical error bars show the relative uncertainty in R_b (i.e. neglecting the common sources of error) and the horizontal error bars indicate the FWHM of the passband. The data points are colour-coded consistently with Figs 1 and 2 and the passbands are labelled at the top of the figure. The dotted grey line to the right of the figure shows the measured value of R_b from Table 5, which includes all sources of uncertainty. The solid grey line to the left of the figure shows how big 10 pressure scaleheights is.

coefficients fixed, as they had a significantly poorer fit, or with both fitted, as this resulted in unphysical values of the coefficients for most of the light curves. This process yielded a value of r_b for each light curve with all common sources of uncertainty removed from the error bars (Table 8), which we then converted to R_b using the semimajor axis from Table 5. We excluded the CASLEO data from this analysis due to the low precision of the r_b it gave.

Fig. 7 shows the R_b values found from the individual light curves as a function of wavelength. The value of R_b from Table 5 is indicated for context. We calculated the atmospheric pressure scaleheight, H, of WASP-103 b using this formula (e.g. de Pater & Lissauer 2001):

$$H = \frac{k_B T'_{eq}}{\mu g_b}, \tag{1}$$

where k_B is Botzmann's constant and μ is the mean molecular weight in the atmosphere. We adopted $\mu = 2.3$ following de Wit & Seager (2013), and the other parameters were taken from Table 5. This yielded $H = 597$ km $= 0.008\,34\,R_{Jup}$. The relative errors on our individual R_b values are therefore in the region of few pressure scaleheights, and the total variation we find between the g and i bands is $13.3H$. For comparison, Sing et al. (2011, their fig. 14) found a variation of $6H$ between 330 nm and 1 μm in transmission spectra of HD 189733 b. Similar or larger effects have been noted in transmission photometry of HAT-P-5 (Southworth et al. 2012), GJ 3470 (Nascimbeni et al. 2013) and Qatar-2 (Mancini et al. 2014a).

Is this variation with wavelength plausible? To examine this, we turned to the MassSpec concept proposed by de Wit & Seager (2013). The atmospheric scaleheight depends on surface gravity and thus the planet mass:

$$M_b = \frac{k_B T'_{eq} R_b^2}{\mu G H}, \tag{2}$$

where G is the gravitational constant. The variation of the measured radius with wavelength due to Rayleigh scattering depends on the atmospheric scaleheight under the assumption of a power-law relation between the wavelength and cross-section of the scattering species. Rayleigh scattering corresponds to a power-law coefficient of $\alpha = -4$ (Lecavelier Des Etangs et al. 2008) where

$$\alpha H = \frac{dR_b(\lambda)}{d\ln\lambda}, \tag{3}$$

which yields the equation

$$M_b = -\frac{\alpha k_B T'_{eq} [R_b(\lambda)]^2}{\mu G \frac{dR_b(\lambda)}{d\ln\lambda}}. \tag{4}$$

We applied MassSpec to our $R_b(\lambda)$ values for WASP-103 b. The slope of R_b versus $\ln\lambda$ is detected to a significance of 7.3σ and corresponds to a planet mass of $0.31 \pm 0.05\,M_{Jup}$. The slope is robustly detected, but gives a planet mass much lower than the mass of $M_b = 1.49 \pm 0.11\,M_{Jup}$ found in Section 5. The gradient of the slope is greater than it should be under the assumption outlined above. We can equalize the two mass measurements by adopting a stronger power law with a coefficient of $\alpha = 19.0 \pm 1.5$, which is extremely large. We conclude that our data are not consistent with Rayleigh scattering so are either affected by additional physical processes or are returning spurious results.

The presence of unocculted starspots on the visible disc of the star could cause a trend in the measured planetary radius similar to what we see for WASP-103. Unocculted spots cause an overestimate of the ratio of the radii (e.g. Czesla et al. 2009; Ballerini et al. 2012; Oshagh et al. 2013), and are cooler than the surrounding photosphere so have a greater effect in the blue. They therefore bias planetary radius measurements to higher values, and do so more strongly at bluer wavelengths. Occulted plage can cause an analogous effect (Oshagh et al. 2014), but we are aware of only circumstantial evidence for plage of the necessary brightness and extent in planet host stars.

The presence of starspots has not been observed on WASP-103 A, which at $T_{eff} = 6110$ K is too hot to suffer major spot activity. G14 found no evidence for spot-induced rotational modulation down to a limiting amplitude of 3 mmag, and our light curves show no features attributable to occultations of a starspot by the planet. This is therefore an unlikely explanation for the strong correlation between R_b and wavelength. Further investigation of this effect requires data with a greater spectral coverage and/or resolution.

7 SUMMARY AND CONCLUSIONS

The recently discovered planetary system WASP-103 is well suited to detailed analysis due to its short orbital period and the brightness

of the host star. These analyses include the investigation of tidal effects, the determination of high-precision physical properties, and the investigation of the atmospheric properties of the planet. We have obtained 17 new transit light curves which we use to further our understanding in all three areas.

The extremely short orbital period of the WASP-103 system makes it a strong candidate for the detection of tidally-induced orbital decay (Birkby et al. 2014). Detecting this effect could yield a measurement of the tidal quality factor for the host star, which is vital for assessing the strength of tidal effects, such as orbital circularization, and for predicting the ultimate fate of hot Jupiters. The prime limitation in attempts to observe this effect is that the strength of the signal, and therefore the length of the observational programme needed to detect it, is unknown. Our high-precision light curves improve the measurement of the time of mid-point of a transit at the reference epoch from 67.4 s (G14) to 4.8 s (this work). There are currently no indications of a change in orbital period, but these effects are expected to take of the order of a decade to become apparent. Our work establishes a high-precision transit timing at the reference epoch against which future observations can be measured.

We modelled our light curves with the JKTEBOP code following the *Homogeneous Studies* methodology in order to measure high-precision photometric parameters of the system. These were combined with published spectroscopic results and with five sets of theoretical stellar models in order to determine the physical properties of the system to high precision and with robust error estimates. We present an error budget which shows that more precise measurements of the T_{eff} and [Fe/H] of the host star would be an effective way of further improving these results. A high-resolution *Lucky Imaging* observation shows no evidence for the presence of faint stars at small (but non-zero) angular separations from WASP-103, which might have contaminated the flux from the system and thus caused us to underestimate the radius of the planet.

The short orbital period of the planet means it is extremely close to its host star: its orbital separation of 0.019 78 au corresponds to only $3.0R_A$. This distorts the planet from a spherical shape, and causes an underestimate of its radius when light curves are modelled in the spherical approximation. We determined the planetary shape using Roche geometry (Budaj 2011) and utilized these results to correct its measured radius and mean density for the effects of asphericity.

Our light curves were taken in six passbands spanning much of the optical wavelength region. There is a trend towards finding a larger planetary radius at bluer wavelengths, at a statistical significance of 7.3σ. We used the MassSpec concept (de Wit & Seager 2013) to convert this into a measurement of the planetary mass under the assumption that the slope is caused by Rayleigh scattering. The resulting mass is too small by a factor of 5, implying that Rayleigh scattering is not the main culprit for the observed variation of radius with wavelength.

We recommend that further work on the WASP-103 system includes a detailed spectral analysis for the host star, transit depth measurements in the optical and infrared with a higher spectral resolution than achieved here, and occultation depth measurements to determine the thermal emission of the planet and thus constrain its atmospheric energy budget. Long-term monitoring of its times of transit is also necessary in order to detect the predicted orbital decay due to tidal effects. Finally, the system is a good candidate for observing the Rossiter–McLaughlin effect, due to the substantial rotational velocity of the star ($v\sin i = 10.6 \pm 0.9$ km s^{-1}; G14).

ACKNOWLEDGEMENTS

The operation of the Danish 1.54 m telescope is financed by a grant to UGJ from the Danish Natural Science Research Council (FNU). This paper incorporates observations collected using the Gamma Ray Burst Optical and Near-Infrared Detector (GROND) instrument at the MPG 2.2 m telescope located at ESO La Silla, Chile, program 093.A-9007(A). GROND was built by the high-energy group of MPE in collaboration with the LSW Tautenburg and ESO, and is operated as a PI-instrument at the MPG 2.2 m telescope. We thank Mike Gillon for helpful discussions. The reduced light curves presented in this work will be made available at the CDS (http://vizier.u-strasbg.fr/) and at http://www.astro.keele.ac.uk/∼jkt/. J Southworth acknowledges financial support from STFC in the form of an Advanced Fellowship. JB acknowledges funding by the Australian Research Council Discovery Project Grant DP120101792. Funding for the Stellar Astrophysics Centre is provided by The Danish National Research Foundation (grant agreement no. DNRF106). TH is supported by a Sapere Aude Starting Grant from The Danish Council for Independent Research. This publication was supported by grant NPRP X-019-1-006 from Qatar National Research Fund (a member of Qatar Foundation). TCH is supported by the Korea Astronomy & Space Science Institute travel grant #2014-1-400-06. CS received funding from the European Union Seventh Framework Programme (FP7/2007-2013) under grant agreement no. 268421. OW (FNRS research fellow) and J Surdej acknowledge support from the Communauté française de Belgique – Actions de recherche concertées – Académie Wallonie-Europe. The following internet-based resources were used in research for this paper: the ESO Digitized Sky Survey; the NASA Astrophysics Data System; the SIMBAD data base and VizieR catalogue access tool operated at CDS, Strasbourg, France; and the arχiv scientific paper preprint service operated by Cornell University.

REFERENCES

Abe L. et al., 2013, A&A, 553, A49
Ballerini P., Micela G., Lanza A. F., Pagano I., 2012, A&A, 539, A140
Birkby J. L. et al., 2014, MNRAS, 440, 1470
Budaj J., 2011, AJ, 141, 59
Burton J. R., Watson C. A., Fitzsimmons A., Pollacco D., Moulds V., Littlefair S. P., Wheatley P. J., 2014, ApJ, 789, 113
Carter J. A., Yee J. C., Eastman J., Gaudi B. S., Winn J. N., 2008, ApJ, 689, 499
Claret A., 2004, A&A, 424, 919
Czesla S., Huber K. F., Wolter U., Schröter S., Schmitt J. H. M. M., 2009, A&A, 505, 1277
Daemgen S., Hormuth F., Brandner W., Bergfors C., Janson M., Hippler S., Henning T., 2009, A&A, 498, 567
de Pater I., Lissauer J. J., 2001, Planetary Sciences. Cambridge Univ. Press, Cambridge
de Wit J., Seager S., 2013, Science, 342, 1473
Demarque P., Woo J.-H., Kim Y.-C., Yi S. K., 2004, ApJS, 155, 667
Dominik M. et al., 2010, Astron. Nachr., 331, 671
Dotter A., Chaboyer B., Jevremović D., Kostov V., Baron E., Ferguson J. W., 2008, ApJS, 178, 89
Eastman J., Siverd R., Gaudi B. S., 2010, PASP, 122, 935
Enoch B., Collier Cameron A., Parley N. R., Hebb L., 2010, A&A, 516, A33
Gillon M. et al., 2013, A&A, 552, A82
Gillon M. et al., 2014, A&A, 562, L3 (G14)
Goldreich P., 1963, MNRAS, 126, 257
Goldreich P., Soter S., 1966, Icarus, 5, 375
Greiner J. et al., 2008, PASP, 120, 405

Hebb L. et al., 2010, ApJ, 708, 224
Hellier C. et al., 2009, Nature, 460, 1098
Jackson B., Greenberg R., Barnes R., 2008, ApJ, 678, 1396
Jackson B., Barnes R., Greenberg R., 2009, ApJ, 698, 1357
Lecavelier Des Etangs A., Pont F., Vidal-Madjar A., Sing D., 2008, A&A, 481, L83
Leconte J., Lai D., Chabrier G., 2011, A&A, 528, A41
Lendl M., Gillon M., Queloz D., Alonso R., Fumel A., Jehin E., Naef D., 2013, A&A, 552, A2
Levrard B., Winisdoerffer C., Chabrier G., 2009, ApJ, 692, L9
Li S.-L., Miller N., Lin D. N. C., Fortney J. J., 2010, Nature, 463, 1054
Mancini L. et al., 2013, MNRAS, 430, 2932
Mancini L. et al., 2014a, MNRAS, 443, 2391
Mancini L. et al., 2014b, A&A, 562, A126
Mancini L. et al., 2014c, A&A, 568, A127
Maxted P. F. L. et al., 2013, MNRAS, 428, 2645
Nascimbeni V., Piotto G., Pagano I., Scandariato G., Sani E., Fumana M., 2013, A&A, 559, A32
Nikolov N., Chen G., Fortney J., Mancini L., Southworth J., van Boekel R., Henning T., 2013, A&A, 553, A26
Ogilvie G. I., 2014, ARA&A, 52, 171
Ogilvie G. I., Lin D. N. C., 2007, ApJ, 661, 1180
Oshagh M., Santos N. C., Boisse I., Boué G., Montalto M., Dumusque X., Haghighipour N., 2013, A&A, 556, A19
Oshagh M., Santos N. C., Ehrenreich D., Haghighipour N., Figueira P., Santerne A., Montalto M., 2014, A&A, 171, A99
Penev K., Sasselov D., 2011, ApJ, 731, 67
Penev K., Jackson B., Spada F., Thom N., 2012, ApJ, 751, 96
Pietrinferni A., Cassisi S., Salaris M., Castelli F., 2004, ApJ, 612, 168
Pont F., Knutson H., Gilliland R. L., Moutou C., Charbonneau D., 2008, MNRAS, 385, 109
Pont F., Sing D. K., Gibson N. P., Aigrain S., Henry G., Husnoo N., 2013, MNRAS, 432, 2917
Scuflaire R., Théado S., Montalbán J., Miglio A., Bourge P., Godart M., Thoul A., Noels A., 2008, Ap&SS, 316, 83
Seager S., Mallén-Ornelas G., 2003, ApJ, 585, 1038
Sing D. K. et al., 2011, MNRAS, 416, 1443
Skottfelt J. et al., 2013, A&A, 553, A111
Southworth J., 2008, MNRAS, 386, 1644
Southworth J., 2009, MNRAS, 394, 272
Southworth J., 2010, MNRAS, 408, 1689
Southworth J., 2011, MNRAS, 417, 2166
Southworth J., 2012, MNRAS, 426, 1291
Southworth J., Maxted P. F. L., Smalley B., 2004, MNRAS, 349, 547
Southworth J., Wheatley P. J., Sams G., 2007a, MNRAS, 379, L11
Southworth J., Bruntt H., Buzasi D. L., 2007b, A&A, 467, 1215
Southworth J. et al., 2009a, MNRAS, 396, 1023
Southworth J. et al., 2009b, ApJ, 707, 167
Southworth J., Mancini L., Maxted P. F. L., Bruni I., Tregloan-Reed J., Barbieri M., Ruocco N., Wheatley P. J., 2012, MNRAS, 422, 3099
Southworth J. et al., 2014, MNRAS, 444, 776
Stetson P. B., 1987, PASP, 99, 191
Torres G., Winn J. N., Holman M. J., 2008, ApJ, 677, 1324
Tregloan-Reed J., Southworth J., Tappert C., 2013, MNRAS, 428, 3671
VandenBerg D. A., Bergbusch P. A., Dowler P. D., 2006, ApJS, 162, 375

SUPPORTING INFORMATION

Additional Supporting Information may be found in the online version of this article:

Table 2. Sample of the data presented in this work (the first data point of each light curve).

APPENDIX A: Full results for the light curves analysed in this work (http://mnras.oxfordjournals.org/lookup/suppl/doi:10.1093/mnras/stu2394/-/DC1).

Please note: Oxford University Press is not responsible for the content or functionality of any supporting materials supplied by the authors. Any queries (other than missing material) should be directed to the corresponding author for the paper.

[1]*Astrophysics Group, Keele University, Staffordshire ST5 5BG, UK*
[2]*Max Planck Institute for Astronomy, Königstuhl 17, D-69117 Heidelberg, Germany*
[3]*Research School of Astronomy and Astrophysics, Australian National University, Canberra, ACT 2611, Australia*
[4]*Astronomical Institute of the Slovak Academy of Sciences, 059 60 Tatranská Lomnica, Slovakia*
[5]*SUPA, University of St Andrews, School of Physics and Astronomy, North Haugh, St Andrews, Fife KY16 9SS, UK*
[6]*European Southern Observatory, Karl-Schwarzschild-Straße 2, D-85748 Garching bei München, Germany*
[7]*Centre for Star and Planet Formation, Natural History Museum, University of Copenhagen, Øster Voldgade 5-7, DK-1350 Copenhagen K, Denmark*
[8]*Niels Bohr Institute and Centre for Star and Planet Formation, University of Copenhagen, Juliane Maries vej 30, DK-2100 Copenhagen Ø, Denmark*
[9]*Instituto de Astrofısica, Facultad de Fısica, Pontificia Universidad Católica de Chile, Av. Vicuña Mackenna 4860, 7820436 Macul, Santiago, Chile*
[10]*Department of Physics, Sharif University of Technology, PO Box 11155-9161 Tehran, Iran*
[11]*Stellar Astrophysics Centre, Department of Physics and Astronomy, Aarhus University, Ny Munkegade 120, DK-8000 Aarhus C, Denmark*
[12]*Astronomisches Rechen-Institut, Zentrum für Astronomie, Universität Heidelberg, Mönchhofstraße 12-14, D-69120 Heidelberg, Germany*
[13]*Institut d'Astrophysique et de Géophysique, Université de Liège, 4000 Liège, Belgium*
[14]*Qatar Environment and Energy Research Institute, Qatar Foundation, Tornado Tower, Floor 19, PO Box 5825, Doha, Qatar*
[15]*Dipartimento di Fisica 'E.R. Caianiello', Università di Salerno, Via Giovanni Paolo II 132, I-84084 Fisciano (SA), Italy*
[16]*Istituto Nazionale di Fisica Nucleare, Sezione di Napoli, Napoli, I-80126 Napoli, Italy*
[17]*NASA Exoplanet Science Institute, MS 100-22, California Institute of Technology, Pasadena, CA 91125, USA*
[18]*Istituto Internazionale per gli Alti Studi Scientifici (IIASS), I-84019 Vietri Sul Mare (SA), Italy*
[19]*Korea Astronomy and Space Science Institute, Daejeon 305-348, Republic of Korea*
[20]*Finnish Centre for Astronomy with ESO (FINCA), University of Turku, Väisäläntie 20, FI-21500 Piikkiö, Finland*
[21]*Planetary and Space Sciences, Department of Physical Sciences, The Open University, Milton Keynes MK7 6AA, UK*

This paper has been typeset from a TEX/LATEX file prepared by the author.

A&A 573, A103 (2015)
DOI: 10.1051/0004-6361/201424967

Astronomy & Astrophysics

Searching for variable stars in the cores of five metal-rich globular clusters using EMCCD observations⋆,⋆⋆

J. Skottfelt[1,2], D. M. Bramich[3], R. Figuera Jaimes[4,5], U. G. Jørgensen[1,2], N. Kains[6,4], A. Arellano Ferro[7], K. A. Alsubai[3], V. Bozza[8,9], S. Calchi Novati[10,8,11,⋆⋆⋆], S. Ciceri[12], G. D'Ago[8,9], M. Dominik[5,⋆⋆⋆⋆], P. Galianni[5], S.-H. Gu[13,14], K. B. W Harpsøe[1,2], T. Haugbølle[2,1], T. C. Hinse[15], M. Hundertmark[1,2,5], D. Juncher[1,2], H. Korhonen[16,1,2], C. Liebig[5], L. Mancini[12], A. Popovas[1,2], M. Rabus[17,12], S. Rahvar[18], G. Scarpetta[10,8,9], R. W. Schmidt[19], C. Snodgrass[20,21], J. Southworth[22], D. Starkey[5], R. A. Street[23], J. Surdej[24], X.-B. Wang[13,14], and O. Wertz[24]
(The MiNDSTEp Consortium)

(Affiliations can be found after the references)

Received 12 September 2014 / Accepted 31 October 2014

ABSTRACT

Aims. In this paper, we present the analysis of time-series observations from 2013 and 2014 of five metal-rich ([Fe/H] > −1) globular clusters: NGC 6388, NGC 6441, NGC 6528, NGC 6638, and NGC 6652. The data have been used to perform a census of the variable stars in the central parts of these clusters.

Methods. The observations were made with the electron-multiplying charge-couple device (EMCCD) camera at the Danish 1.54 m Telescope at La Silla, Chile, and they were analysed using difference image analysis to obtain high-precision light curves of the variable stars.

Results. It was possible to identify and classify all of the previously known or suspected variable stars in the central regions of the five clusters. Furthermore, we were able to identify and, in most cases, classify 48, 49, 7, 8, and 2 previously unknown variables in NGC 6388, NGC 6441, NGC 6528, NGC 6638, and NGC 6652, respectively. Especially interesting is the case of NGC 6441, for which the variable star population of about 150 stars has been thoroughly examined by previous studies, including a *Hubble* Space Telescope study. In this paper we are able to present 49 new variable stars for this cluster, of which one (possibly two) are RR Lyrae stars, two are W Virginis stars, and the rest are long-period semi-regular or irregular variables on the red giant branch. We have also detected the first double-mode RR Lyrae in the cluster.

Key words. globular clusters: individual: – stars: variables: RR Lyrae – stars: variables: general – instrumentation: high angular resolution

1. Introduction

Galactic globular clusters represent some of the oldest stellar populations in the Galaxy and their study can provide important insight into the formation and early evolution of the Galaxy. The stars in globular clusters are believed to have formed roughly at the same time (although there is also mounting evidence that some clusters have formed via several episodes of star formation), from the same primordial material, and with the same composition. This should lead to a homogeneity in certain fundamental properties of the stars within each cluster, but with differences between the clusters. Knowledge about these properties, such as metallicity, age, and kinematics, are therefore important. One way to obtain better constraints on some of these physical parameters is to study the population of variable stars, especially RR Lyrae stars.

In Skottfelt et al. (2013) two new variable stars were discovered in the otherwise well-studied globular cluster NGC 6981. The authors made use of electron-multiplying charge-couple device (EMCCD) data, which made it possible to retrieve the photometry in an area that, in a conventional CCD, was affected by the saturation of a bright star.

Saturation of bright stars in conventional CCD observations is often hard to avoid when a reasonable signal-to-noise ratio (S/N) for the fainter objects is required. When using difference image analysis (DIA), which is currently the best method of extracting precise photometry in crowded regions, saturated pixels affect the nearby pixels during the convolution of the reference image. It is thus impossible to perform photometric measurements using DIA near a saturated star in conventional CCD observations, and this affects the completeness of variability studies in crowded regions.

An EMCCD is a conventional CCD with an extended readout register where the signal is amplified by impact ionisation before it is read out. The readout noise is thus negligible compared to the signal, even at very high readout speeds (10–100 frames/s), which makes high frame-rate imaging feasible. By shifting and adding the individual frames to counteract the blurring effects of atmospheric turbulence, it is possible to obtain very high spatial resolution, something that has been described in numerous articles (e.g. Mackay et al. 2004; Law et al. 2006).

The use of EMCCD data for precise time-series photometry, however, is a new area of investigation, and the applications are

⋆ Based on data collected by MiNDSTEp with the Danish 1.54 m telescope.

⋆⋆ The light curves presented in this paper (full Table 3) are only available at the CDS via anonymous ftp to cdsarc.u-strasbg.fr (130.79.128.5) or via http://cdsarc.u-strasbg.fr/viz-bin/qcat?J/A+A/573/A103

⋆⋆⋆ Sagan visiting fellow.

⋆⋆⋆⋆ Royal Society University Research Fellow.

Table 1. Coordinates and physical parameters of the five clusters.

Cluster	RA (J2000.0)	Dec (J2000.0)	[Fe/H]	c
NGC 6388	17:36:17.23	–44:44:07.8	−0.55 ± 0.15	1.75
NGC 6441	17:50:13.06	–37:03:05.2	−0.46 ± 0.06	1.74
NGC 6528	18:04:49.64	–30:03:22.6	−0.12 ± 0.24	1.5
NGC 6638	18:30:56.10	–25:29:50.9	−0.95 ± 0.13	1.33
NGC 6652	18:35:45.63	–32:59:26.6	−0.81 ± 0.17	1.8

Notes. The celestial coordinates are taken from Harris (1996, 2010 edition). Column 4 gives the metallicity of the cluster (from Roediger et al. 2014). Column 5 gives the central concentration $c = \log_{10}(r_t/r_c)$, where r_t and r_c are the tidal and core radii, respectively (from Harris 1996, 2010 edition).

just starting to be explored. High frame-rate imaging makes it possible to observe much brighter stars without saturating the CCD, and the required S/N for the object of interest can be achieved by combining the individual exposures into a stacked image at a later stage. Combining many exposures thus gives a very wide dynamical range, and the possibility to perform high-precision photometry for both bright and faint stars. It should be noted that EMCCD exposures need to be calibrated in a different way than conventional CCD imaging data (Harpsøe et al. 2012).

The DIA technique, first introduced by Alard & Lupton (1998), has been improved by revisions to the algorithm presented by Bramich (2008, see also Bramich et al. 2013) and is the optimal way to perform photometry with EMCCD data in crowded fields. This method uses a flexible discrete-pixel kernel model instead of modelling the kernel as a combination of Gaussian basis functions, and it has been shown to give improved photometric precision even in very crowded regions (Albrow et al. 2009). The method is also especially adept at modelling images with point spread functions (PSFs) that are not approximated well by a Gaussian or a Moffat profile.

As part of a series of papers on detecting and characterising the variable stars in globular clusters (e.g. Kains et al. 2013, 2012; Figuera Jaimes et al. 2013; Skottfelt et al. 2013; Arellano Ferro et al. 2013b; Bramich et al. 2011), we present our analysis of EMCCD observations of five metal-rich ([Fe/H] > −1) globular clusters. The clusters are listed in Table 1 along with their celestial coordinates, metallicity, and central concentration parameter.

The variable star populations of all five clusters have been examined previously, but the dates, methods, and completeness of these studies varies a lot.

NGC 6388 and NGC 6441 have been thoroughly studied. The observations made by Pritzl et al. (2001, 2002), where PSF-fitting photometric methods were used, were re-analysed by Corwin et al. (2006) using image subtraction methods, and this revealed a number of new variables, especially in the crowded central regions. NGC 6441 was furthermore included in a *Hubble* Space Telescope (HST) snapshot program where many new variables were detected (Pritzl et al. 2003).

Although NGC 6528 has been heavily studied due to its very high metal abundance, no variable stars have been found to date.

Since the central region of NGC 6638 is not heavily crowded, Rutily & Terzan (1977) were able to find several variable stars very close to the centre using only photographic plates. They were, however, not able to determine their periods.

Hazen (1989) found several variables inside the tidal radius of NGC 6652, but none in the relatively crowded centre.

Due to the relatively small field-of-view (FoV) of the instrument we used, 45″ × 45″, we only observed the central part of these clusters. These are the regions of the clusters which benefit the most from the gain in spatial resolution afforded by EMCCD observations. Therefore, this study cannot be taken as a complete census of the variable star population in each cluster, but only of their crowded central regions. Another important part of the article is to show that the techniques introduced in Skottfelt et al. (2013), i.e. using the very high spatial resolution and high-precision photometry of EMCCDs to locate variable stars in crowded fields, can be performed routinely on a much larger scale.

In Sect. 2 we describe our observations and how they were reduced. In Sect. 3 our results for each of the five clusters are presented and Sect. 4 contains a discussion of these results. Finally, in Sect. 5 a summary of our results is given.

2. Data and reductions

2.1. Observations

The observations were carried out with the EMCCD instrument at the Danish 1.54 m telescope at La Silla, Chile (Skottfelt et al. 2015). The EMCCD instrument consists of a single Andor Technology iXon+ model 897 EMCCD camera which has an imaging area of 512×512 16 μm pixels. The pixel scale is ∼0.″09, and the FoV is therefore 45″ × 45″. For these observations a frame-rate of 10 Hz and an EM gain of 1/300 photons/e⁻ was used. The small FoV means that we were limited to targeting the crowded central regions of the clusters. The camera sits behind a dichroic mirror that acts as a long-pass filter with a cut-on wavelength of 650 nm. The cut-off wavelength is determined by the sensitivity of the camera which drops to zero at 1050 nm over about 250 nm. The filter thus corresponds roughly to a combination of the SDSS $i' + z'$ filters (Bessell 2005).

The first block of observations were made over a five-month period, from the end of April 2013 to the end of September 2013. Each cluster was observed once or twice a week resulting in between 20 and 40 observations of each cluster. Due to the small FoV, it was unfortunately necessary to reject a number of the observations because of bad pointing. Because the crowded central parts of the clusters were targeted, we found that it was not possible to gain any useful information from observations that had a seeing of worse than 1.″5 in full-width at half-maximum (FWHM).

Thus only 10 to 15 observations per cluster were found to be useful, which made it nearly impossible to make reasonable period estimates of the variable stars. It was thus decided to perform a second block of observations over a 6 week period from mid-April 2014 to the start of June 2014. This increased the number of epochs to between 28 and 37, which enabled us to derive much better period estimates.

To achieve a reasonable S/N, each observation has a total exposure time of 8 min, except for NGC 6441 where they are 10 min long. With the frame-rate of 10 Hz, the 8 and 10 min observation consist of 4800 and 6000 single exposures, respectively.

2.2. EM data reduction

The algorithms described by Harpsøe et al. (2012) were used to make bias, flat and tip-tilt corrections, and to find the instantaneous image quality (PSF FWHM) for each exposure.

The tip-tilt correction and image quality are found using the Fourier cross correlation theorem. Given a set of k exposures, each containing i pixel columns and j pixel rows, a comparison

image $C(i, j)$ is constructed by taking the average of 100 randomly chosen exposures. The cross correlation $P_k(i, j)$ between C and a bias- and flat-corrected exposure $I_k(i, j)$ can be found using

$$P_k(i, j) = \left|\mathrm{FFT}^{-1}\left[\mathrm{FFT}(C) \cdot \overline{\mathrm{FFT}(I_k)}\right]\right| \tag{1}$$

where FFT is the fast Fourier transform. The appropriate shift, that will correct the tip-tilt error, can now be found by locating the (i, j) position of the global maximum in P_k.

A measure for the image quality q_k is found by scaling the maximum value of P_k with the sum of its surrounding pixels within a radius r

$$q_k = \frac{P_k(i_{\max}, j_{\max})}{\sum_{\substack{|(i-i_{\max}, j-j_{\max})|<r \\ (i,j)\neq(i_{\max}, j_{\max})}} P_k(i, j)}. \tag{2}$$

Using this factor, instead of just the maximum value of the pixel values in the frame (Smith et al. 2009), helps to mitigate the effects of fluctuations in atmospheric extinction and scintillation that can happen on longer time scales.

A cosmic ray detection and correction algorithm was used on the full set of exposures in each observation. For a conventional CCD, where the noise is normally distributed, the mean and sigma values of each (i, j) pixel in the frame over all k exposures can be found. Sigma clipping can then be used to reject cosmic rays. For an EMCCD the noise is not normally distributed, and we have therefore developed a method that takes this into account (Skottfelt et al., in prep.). Instead of finding the mean value, the rate of photons is estimated for each pixel in the frame over all the frames. Using this photon rate at each pixel position, the probability p for the observed pixel values in each exposure can be calculated and if a pixel value is too improbable, then it is rejected.

The output of the EM reduction of a single observation is a ten-layer image cube, where each layer is the sum of some percentage of the shift-and-added exposures after the exposures have been organised into ascending order by image quality. The specific percentages can be modified, but to preserve as much of the spatial information as possible, we have chosen the following (non-cumulative) percentages for the layers: (1, 2, 5, 10, 20, 50, 90, 98, 99, 100). This means that the first layer contains the sum of the best 1% of the exposures in terms of image quality, the second layer the second best 1%, the third the next 3%, and so on. If the shift needed to correct for tip-tilt error is too big (more than 20 pixels) for a given exposure, then the exposure is rejected. This is done to ensure that, except for a 20 pixel border, each layer has a uniform number of input exposures. The total number of exposures used to create the ten-layer image cube might therefore be a little lower than expected.

2.3. Photometry

To extract the photometry from the observations, the `DanDIA` pipeline[1] was used (Bramich 2008; Bramich et al. 2013).

The pipeline has been modified to stack the sharpest layers from all of the available cubes to create a high-resolution reference image, such that an optimal combination of spatial resolution and S/N is achieved. Using this method, we were able to achieve resolutions between 0.″39 and 0.″53 for the reference images for the five clusters, and still have a good S/N. Table 2 reports the combined integration time and FWHM of each of the reference images. The peculiar PSFs that can be seen in the reference images (Figs. 2, 7, 12, 15, 18) come from a triangular coma that is particular to the Danish telescope and this effect manifests itself under good seeing conditions. The telescope was commissioned in 1979 and is therefore not built for such high-resolution instruments.

Table 2. Reference image details.

Cluster	Exp. Time (s)	PSF *FWHM*	Fig. No.
NGC 6388	240.0	0.″42	2
NGC 6441	312.0	0.″39	7
NGC 6528	348.0	0.″48	12
NGC 6638	374.4	0.″53	15
NGC 6652	403.2	0.″46	18

Notes. Combined exposure time and FWHM for the reference images. The reference images are used to show the positions of the variable stars in Sect. 3 and the last column gives the Figure numbers for these.

Reference fluxes and positions of the stars are measured from the reference image. Each ten-layer cube is then stacked into a single science image. The reference image, convolved with the kernel solution, is subtracted from each of the science images to create difference images, and, in each difference image, the differential flux for each star is measured by scaling the PSF at the position of the star (for details, see Bramich et al. 2011).

The noise model for EMCCD data differs from that for conventional CCD data (Harpsøe et al. 2012). In the EMCCD noise model for a single exposure, the variance in pixel ij is found to be

$$\sigma_{ij}^2 = \frac{\sigma_0^2}{F_{ij}^2} + \frac{2 \cdot S_{ij}}{F_{ij} \cdot G_{\mathrm{EM}} \cdot G_{\mathrm{PA}}} \tag{3}$$

where σ_0 is the CCD readout noise (ADU), F_{ij} is the master flat-field image, S_{ij} is the image model (sky + object photons), G_{EM} is the EM gain (photons/e⁻) and G_{PA} is the PreAmp gain (e⁻/ADU).

When N exposures are combined by summation, the pixel variances of the combined frame are thus

$$\sigma_{ij,\mathrm{comb}}^2 = \frac{N \cdot \sigma_0^2}{F_{ij}^2} + \frac{2 \cdot S_{ij,\mathrm{comb}}}{F_{ij} \cdot G_{\mathrm{EM}} \cdot G_{\mathrm{PA}}}. \tag{4}$$

The `DanDIA` software has therefore been further modified to employ this noise model.

In Table 3, we outline the format of the data as it is provided at the CDS.

2.4. Astrometry

HST observations of all five clusters have been performed during different observing campaigns (e.g. Djorgovski 1995; Piotto 1999; Feltzing 2000). We made use of the high spatial resolution and precise astrometry of the HST images to derive an astrometric solution for each of our reference images.

The astrometric calibration was performed using the object detection and field overlay routines in the image display tool GAIA (Draper 2000). The astrometric fit was then used to calculate the J2000.0 celestial coordinates for all of the variables in our FoV.

[1] `DanDIA` is built from the DanIDL library of IDL routines available at http://www.danidl.co.uk

Table 3. Format for the time-series photometry of all confirmed variables in our field of view of the five clusters.

Cluster	#	Filter	HJD (d)	M_{std} (mag)	m_{ins} (mag)	σ_m (mag)	f_{ref} (ADU s^{-1})	σ_{ref} (ADU s^{-1})	f_{diff} (ADU s^{-1})	σ_{diff} (ADU s^{-1})	p
NGC 6388	V29	I	2 456 436.95140	14.620	5.617	0.003	44 901.760	4397.950	54 393.674	627.525	4.6389
NGC 6388	V29	I	2 456 455.86035	14.375	5.372	0.003	44 901.760	4397.950	87 182.547	578.940	3.3446
⋮	⋮	⋮	⋮	⋮	⋮	⋮	⋮	⋮	⋮	⋮	⋮
NGC 6441	V63	I	2 456 454.78961	16.770	7.889	0.007	9899.919	2247.418	–17 795.506	260.090	6.1094
NGC 6441	V63	I	2 456 509.61751	16.561	7.680	0.005	9899.919	2247.418	–8594.633	212.423	6.0163
⋮	⋮	⋮	⋮	⋮	⋮	⋮	⋮	⋮	⋮	⋮	⋮

Notes. The standard M_{std} and instrumental m_{ins} magnitudes listed in Cols. 5 and 6 respectively correspond to the cluster, variable star, filter and epoch of mid-exposure listed in Cols. 1–4, respectively. The uncertainty on m_{ins} is listed in Col. 7, which also corresponds to the uncertainty on M_{std}. For completeness, we also list the reference flux f_{ref} and the differential flux f_{diff} (Cols. 8 and 10 respectively), along with their uncertainties (Cols. 9 and 11), as well as the photometric scale factor p. Instrumental magnitudes are related to the other quantities via $m_{\mathrm{ins}} = 17.5 - 2.5 \cdot \log_{10}(f_{\mathrm{ref}} + f_{\mathrm{diff}}/p)$. This is a representative extract from the full table, which is available at the CDS.

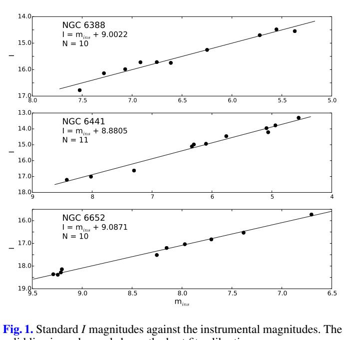

Fig. 1. Standard I magnitudes against the instrumental magnitudes. The solid line in each panel shows the best fit calibration.

2.5. Photometric calibration

Using the colour information that is available from the colour–magnitude diagram (CMD) data (see Sect. 2.6), rough photometric calibrations can be made for NGC 6388, NGC 6441 and NGC 6652.

A number of reasonably isolated stars were selected and by matching their positions with the CMD data, their standard I magnitudes were retrieved. By finding the offset between the standard I magnitudes and the mean instrumental magnitudes found by `DanDIA`, a rough photometric calibration was found. Figure 1 shows a plot of the standard I magnitudes versus the mean instrumental magnitudes along with the fit for each of the clusters where CMD data are available.

Due to the non-standard filter that is used for these observations, the photometric calibration is only approximate and there is therefore some added uncertainty in the listed I magnitudes.

For NGC 6528 and NGC 6638 where no CMD data are available, we have chosen to adopt the photometric conversion of

$$I = m_{\mathrm{ins}} + 9.0, \tag{5}$$

where m_{ins} is the instrumental magnitude, to provide approximate I magnitudes for these two clusters as well.

2.6. Colour–magnitude diagrams

As we only have observations in one filter, it is not possible to make a CMD based on our own data. Three of the clusters; NGC 6388, NGC 6441 and NGC 6652; are part of The ACS Survey of Galactic Globular Clusters (Sarajedini et al. 2007), and the data files from the survey, that include V and I magnitudes and celestial coordinates, are available online[2].

We were able to match many of the variable stars using celestial coordinates and I magnitudes, enabling us to recover colour information for these objects. Unfortunately, for some of the variables, their proximity to a bright star meant that we were unable to do this.

For NGC 6528 and NGC 6638, no suitable data to create a CMD were found. The Piotto et al. (2002) study includes NGC 6638, but the data files that are available do not contain any celestial coordinates and are therefore not useful for our purposes.

3. Results

Several methods were used to detect the variable stars in our data. Firstly an image representing the sum of the absolute-valued difference images with pixel values in units of sigma, was constructed for each cluster. These images were visually inspected for peaks indicating stars that show signs of variability. Secondly a diagram of the root-mean-square (rms) magnitude deviation versus mean magnitude for the calibrated light curves was produced, from which we selected stars with a high rms for further inspection. Finally, the difference images were blinked in sequence in order to confirm the variations of all suspected variables.

Period estimates were made using a combination of the string-length statistic S_Q (Dworetsky 1983) and the phase dispersion minimisation method (Stellingwerf 1978).

The results for each cluster are presented below. Note that the RR Lyrae (RRL) nomenclature introduced by Alcock et al. (2000) has been adopted for this paper; thus RR0 designates an RRL pulsating in the fundamental mode, RR1 designates an RRL pulsating in the first-overtone mode, and RR01 designates a double-mode (fundamental and first-overtone) RRL.

[2] http://www.astro.ufl.edu/~ata/public_hstgc/

Stars in the upper part of the instability strip are in some parts of the literature referred to as Population II Cepheids (P2C). We have adopted the "W Virginis" or "CW" nomenclature, with sub-classifications CWA for CW stars with periods between 8 and 30 days, and CWB for CW stars with periods shorter than 8 days (General Catalog of Variable Stars (GCVS), Samus et al. 2009). CW stars with periods between 0.8 and 3 days are possibly anomalous Cepheids (AC), which are believed to be too luminous for their periods. If the period is longer than 30 days, then we classify them as RV Tauri stars (RV; Clement et al. 2001).

For variable stars on the red giant branch (RGB), which in some parts of the literature are just referred to as long period variables (LPV), we have adopted the nomenclature of the GCVS. Thus stars on the RGB showing a noticeable periodicity and with periods over 20 days are classified as semi-regular (SR), and stars that show no evidence of periodicity are classified as long-period irregular (L). Note that some stars might actually be on the asymptotic giant branch (AGB) and not the RGB. However, distinguishing the two is difficult without a proper spectroscopic analysis and is therefore not possible from the CMDs in this study.

3.1. NGC 6388

3.1.1. Background information

The first 9 variable stars in NGC 6388 were reported by Lloyd Evans & Menzies (1973). These were assigned the numbers V1-V9 by Sawyer Hogg (1973) in her third catalogue of variable stars in globular clusters. Three new variables, V10-V12, were found by Lloyd Evans & Menzies (1977) using observations from V and I band photographic plates. They also confirmed the existence of the previous 9 variables, but were not able to provide periods for any of the variables. Using B-band photographic plate observations, Hazen & Hesser (1986) presented 14 new variables, V13-V26, within the tidal radius, and 4 field variables.

Silbermann et al. (1994) were the first to use CCD observations to search for variable stars in the cluster, and were able to find 3 new variables, V27-V29, and 4 suspected ones. Periods were given for the three new variables and for V17 and V20.

From observations obtained at the 0.9 m telescope at the Cerro Tololo Inter-American Observatory (CTIO), Pritzl et al. 2002, hereafter P02) were able to find 28 new variables, V30-V57, which includes 3 of the 4 suspected variables in Silbermann et al. (1994). The data for the P02 paper were obtained over 10 days, so only very few long period variables were found.

Due to the high central concentration (see Table 1) none of the variable stars found up to this point are located in the central part of the cluster, except for V29. However, when the P02 data were re-analysed by Corwin et al. (2006, hereafter C06) using the ISIS version 2.1 image-subtraction package (Alard 2000; Alard & Lupton 1998), 12 new variables, V58-V69, and 6 suspected ones, denoted SV1-SV6, were found. All of these variables are either RRL or CW stars and most of them are located in the central parts of the cluster.

3.1.2. This study

A finding chart for the cluster containing the variables detected in this study is shown in Figs. 2 and 3 shows a CMD of the stars in our FoV, with the variables overplotted.

Figure 4 shows the rms magnitude deviation for the 1824 stars with calibrated I light curves versus their mean magnitude. From this plot it is evident that stars fainter than 18th magnitude have not been detected, which can probably be explained by the very dense stellar population in the central region of the cluster. This creates a very high background intensity, which makes it hard to detect faint stars, and which increases the possibility of blending, making some stars appear brighter than they are.

3.1.3. Known variables

All of the previously known variables within our FoV are recovered in this analysis. The light curves for these variables are shown in Fig. 5 and their celestial coordinates and estimated periods are listed in Table 4, along with the periods found in C06. The table also reports the mean I magnitude, the amplitude in our filter, and the classification of the variables.

A discussion of individual variables is given below, but generally it can be noted that we find similar periods to those given in C06. Only the three CWs; V70, V72 and V73; have very different periods. In C06 these three stars are listed as suspected variables (SV) due to uncertainty in the classification.

We find some variables to be somewhat brighter than would be expected for their classification. This is most likely due to blending with very close neighbours which, as mentioned above, can lead to an overestimation of the reference flux (e.g. see Col. 9 of Table 4). An overestimated reference flux subsequently leads to an underestimation of the amplitude of the variable star. Errors in the mean magnitudes might also be caused by the rough photometric calibration, but this should only give discrepancies on a much lower level, and should not affect the amplitude.

Unless otherwise stated below, the classifications that are given in P02 or C06 are confirmed by our light curves and the CMD, and have therefore been adopted. A period-luminosity diagram for the stars in the upper part of the instability strip is shown in Fig. 22, and is discussed in more detail in Sect. 4.1.

Discussion of individual variables (square brackets gives approximate position in the CMD as $[V-I, V]$):

V29, V63: based on the relation between period and luminosity compared to the other CW stars, these two stars are classified as CWB stars and not AC stars. V29 is the only variable that is also found in the P02 paper, i.e. where difference image analysis was not used.

V59, V60: no matching stars have been found in the CMD for these two variables. However, their periods, mean magnitude, and amplitude strongly indicate that the classifications as RR0 and RR1, respectively, are correct.

V61-V62, V64-V65: CMD positions, periods, magnitudes and amplitudes all verify the classifications given in C06.

V66: this RR1 seems to have an overestimated mean magnitude, and correspondingly underestimated amplitude. This is most likely caused by blending with another star, as the position in the CMD [0.4, 16.5] verifies the classification.

V69: no CMD position for this star is found, but based on its period and mean magnitude it is classified as a CWB.

V70, V73: those are two of the suspected variables from C06 that are also in our FoV. We report reliable periods in Table 4. The periods and CMD positions ([1.0, 14.3], [1.0, 13.6]) indicate that they are CWA stars.

V71: this star is also a suspected variable from C06. The star is highly blended with a brighter star which leads to a mean magnitude that is too bright and a heavily underestimated amplitude. No CMD position is available, but its period and light curve strongly suggest that the star is an RR0.

V72: this is the last of the C06 suspected variables in our FoV, and we report a reliable period in Table 4. No CMD position is found for this variable, so it could be a SR, but CWA is a more likely classification considering the relationship between magnitude and period compared to the other CW stars (see Fig. 22).

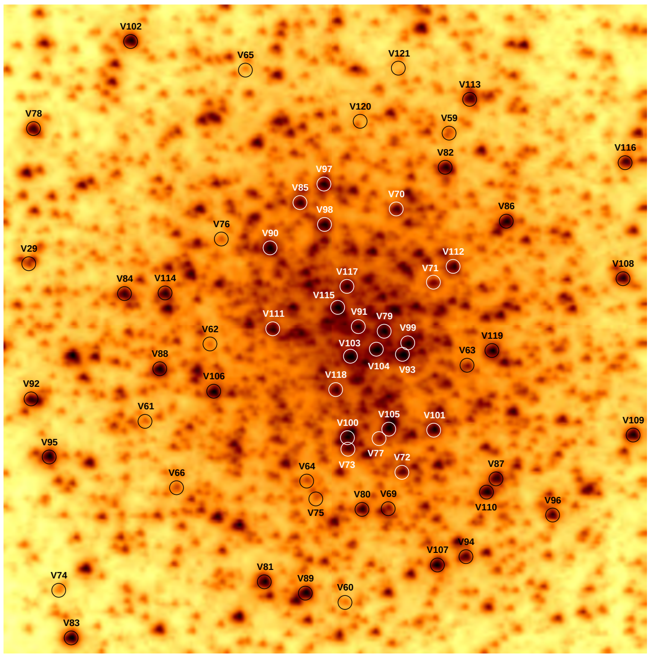

Fig. 2. NGC 6388: finding chart constructed from the reference image marking the positions of the variable stars. Labels and circles are white/black only for clarity. North is up and east is to the right. The cluster image is ~41″ by 41″.

3.1.4. New variables

In this study we were able to find 48 new variable stars for NGC 6388. Their light curves are shown in Fig. 6 and their details are listed in Table 5.

Most of the new variables are RGB stars and many of them have small amplitudes, which is probably the reason why they have not been detected until now. There are however also two (possibly three) previously undetected RRL stars and three new CW stars. For many of the new long period variables it has been hard to determine a period, which may indicate that they are irregular.

Discussion of individual variables:

V74: this star has a very noisy light curve, where a period matching an RR1 has been estimated. The mean magnitude also matches this classification, but it falls on the red-clump in the CMD [1.0, 16.9]. Our RR1 classification is therefore tentative.

V75: the light curve and the position of the star in the CMD [0.5, 16.7], strongly suggest that this is an RR1.

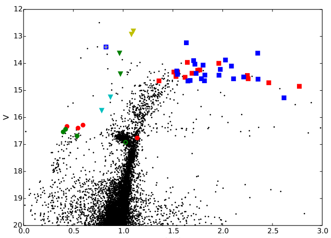

Fig. 3. NGC 6388: $(V-I), V$ colour–magnitude diagram made from HST/ACS data as explained in Sect. 2.6. The stars that show variability in our study are plotted as follows: RRL as filled circles (RR0 in red, RR1 in green, RR01 in blue), CW as filled triangles (CWA in green, CWB in cyan, AC in magenta, RV in yellow), and RGB stars as filled squares (SR in red, L in blue). An open symbol means that the classification is uncertain.

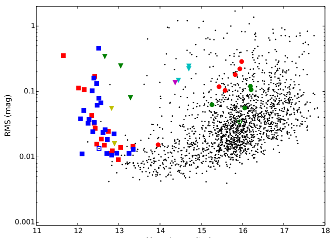

Fig. 4. NGC 6388: plot of the rms magnitude deviation versus the mean magnitude for each of the 1824 calibrated I light curves. The variables are plotted with the same symbols as in Fig. 3.

V76: this star has a very good light curve, where the light curve shape, period and mean magnitude strongly indicate an RR0. However, the CMD position [1.1, 16.8] is a little discrepant.

V77: no CMD information is available for this star, but as the luminosity seems a bit too high compared to its period, we classify it as a possible AC (see Fig. 22). The star is located very close to another and much brighter variable V105, and it would have been very difficult to resolve these stars using conventional imaging.

V78, V79, V81: these three stars have similar positions in the CMD [1.7, 14], and they are therefore most likely SR stars.

V80,V82: these two stars are most likely RV stars, based on their position in the CMD [1.1, 12.8] and their relation between period and luminosity (see Fig. 22).

V83-V92,V94,V95: all of these stars are on the RGB and combined with their long periods, these can be classified as SR stars. Most of the stars have fairly small amplitudes (0.04–0.15 mag)

V92, V93: these two stars are not in the CMD, but based on their periods and luminosity they are most likely SR stars.

V96-V118: These stars are also on the RGB, but it has not been possible to find any periods that phase their light curves satisfactorily. We have therefore classified them as L stars.

V119: the position of this star in the CMD [0.8, 13.4] puts it in the CW region. However, we have not been able to find a period that phases the light curve properly and the star has therefore been tentatively classified as an L star.

V120, V121: these two stars were not identified by the pipeline and no stars are visible at these positions on the reference image. However, when blinking the difference images some variability is clearly seen and the differential fluxes have thus been measured for these positions in the difference images. This means that there is no measurement of the reference flux and magnitudes or amplitudes are therefore not given. The fact that the stars are not visible on the reference image is probably because they are very faint at the epoch of the reference image. No good candidates for the stars have been found in the CMD, and no reasonable periods could be estimated. Without more information it is hard to classify the two stars, but one possibility could be a type of cataclysmic variable, as these are known to have prolonged low and high states, which can be quasi-periodic or have no clear periodicity.

3.2. NGC 6441

3.2.1. Background information

The first 10 variables in NGC 6441 were found by Fourcade et al. (1964). In Hesser & Hartwick (1976) the authors report that they may have found two variable stars. These two stars are, however, found to be non-variable in Layden et al. (1999), whom made use of CCD imaging. Layden et al. (1999) were able to identify, classify, and determine periods for 31 long period variables, 11 RRL stars and 4 eclipsing binaries. A further 9 suspected variables were found but not classified. From CTIO observations, Pritzl et al. (2001) were able to find 48 new variables, of which 35 are RRL stars.

Similar to NGC 6388, this cluster has a high central concentration (see Table 1), and none of the variable stars found up to this point are located in the central part of the cluster, except for V63. Pritzl et al. (2003, hereafter P03) used HST observations to reveal 41 previously undiscovered variables, V105–V145, the main part of which are located in the central parts.

The Pritzl et al. (2001) data were also re-analysed using ISIS in the C06 paper. In this analysis, five new variables, V146-V150, were found (and recovered in the HST data), but three variables (V136, V138, and V145) that were found in the HST data were not found in the ISIS analysis – all three bona-fide variables located within 10″ of the centre of the cluster.

3.2.2. This study

A finding chart for the cluster containing the variables detected in this study is shown in Figs. 7, and 8 shows a CMD of the stars within our FoV, with the variables overplotted.

Figure 9 shows the rms magnitude deviation for the 1860 stars with calibrated I magnitudes versus their mean magnitude. From this plot it is evident that stars fainter than 18th magnitude have not been detected, which can probably be

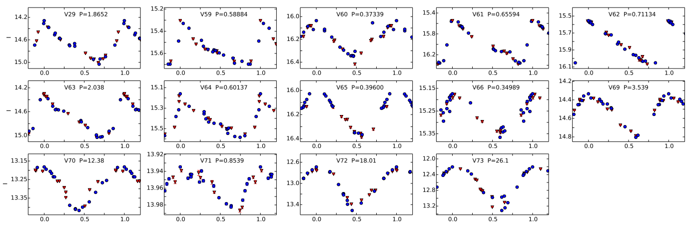

Fig. 5. NGC 6388: phased light curves for the known variables in our FoV. Red triangles are 2013 data and blue circles are 2014 data. Error bars are plotted but are smaller than the data symbols in many cases.

Table 4. NGC 6388: details of the 14 previously known variables in our FoV.

Var	RA (J2000.0)	Dec (J2000.0)	Epoch (d)	P (d)	P_{C06} (d)	$\langle I \rangle$	$A_{i'+z'}$	Blend	Classification
V29	17:36:15.321	–44:44:02.62	6772.8616	1.8652	1.88[a]	14.63	0.77	ii	CWB
V59	17:36:17.870	–44:43:54.77	6514.5622	0.58884	0.589	15.48	0.39	ii	RR0
V60	17:36:17.169	–44:44:24.41	6782.7705	0.37339	0.372	16.19	0.31	iii	RR1
V61	17:36:15.995	–44:44:12.73	6514.5622	0.65594	0.657	15.94	0.83	iii	RR0
V62	17:36:16.398	–44:44:07.89	6805.8471	0.71134	0.708	15.79	0.51	iii	RR0
V63	17:36:17.941	–44:44:09.50	6477.6692	2.038	2.045	14.64	0.73	ii	CWB
V64	17:36:16.958	–44:44:16.68	6797.8161	0.60137	0.595	15.35	0.43	ii	RR0
V65	17:36:16.655	–44:43:50.57	6809.7600	0.39600	0.395	16.19	0.36	iii	RR1
V66	17:36:16.174	–44:44:16.97	6763.9007	0.34989	0.350	15.25	0.19	ii	RR1
V69	17:36:17.444	–44:44:18.51	6808.8938	3.539	3.601	14.55	0.47	iii	CWB
V70[b]	17:36:17.540	–44:43:59.52	6783.8319	12.38	~8	13.28	0.24	iii	CWA
V71[c]	17:36:17.752	–44:44:04.20	6792.8127	0.8539	0.847	13.96	0.05	i	RR0
V72[d]	17:36:17.532	–44:44:16.22	6784.7647	18.01	~12	13.08	0.82	iii	CWA
V73[e]	17:36:17.211	–44:44:14.70	6792.8127	26.1	~4.5	12.74	1.11	iii	CWA

Notes. The celestial coordinates correspond to the epoch of the reference image, which is the HJD ~ 2 456 522.48 d. Epochs are (HJD – 2 450 000). $\langle I \rangle$ denotes mean I magnitude and $A_{i'+z'}$ are the amplitudes found in our special $i' + z'$ filter. The blend column describes whether the star is blended with (i) brighter star(s); (ii) star(s) of similar magnitude; or (iii) fainter/no star(s). P_{C06} are periods from C06, which have been included as a reference. [a] Period from Pritzl et al. (2002). [b] Denoted SV1, [c] SV2, [d] SV4, and [e] SV5 in C06.

explained by the very dense stellar population in the central region, similar to NGC 6388.

3.2.3. Known variables

All of the previously known variables within our FoV are recovered in this analysis. The light curves for these variables are shown in Fig. 10, and their details are listed in Table 6. The table includes the periods found in P03 and C06.

A discussion of individual variables is given below, but generally it can be noted that for all RRL and CW variables, the same periods are estimated as in P03 and/or C06. For the long period variables there are a few discrepancies. A number of the variables are found to be somewhat brighter than in P03. This is most likely due to blending with very close neighbours, leading to an overestimation of the reference flux.

The classification that is given in P03 and/or C06 seems to be correct in almost all cases and have thus been adopted, unless otherwise noted below. A period-luminosity diagram for the stars in the upper part of the instability strip is shown in Fig. 22, and is discussed in more detail in Sect. 4.1.

Satisfactory light curves are found for the three variables that were not detected by C06: V136, V138, and V145. Of the five new variables that C06 discovered, three (V146-V148) are within our FoV and have reasonable light curves. This highlights the power of EMCCD observations and DIA combined.

Discussion of individual variables:

V63: this RR0 is the only variable that is also found in Pritzl et al. (2001).

V105: we find a slightly shorter period for this SR than in P03.

V110, V122: no CMD positions are found for these two variables, but their periods and phased light curves clearly indicate that they are RR0 stars.

V111: this RR0 is highly blended with a brighter star, and the mean magnitude is therefore too bright. Due to the strong blending the correct position in the CMD has not been found.

V113, V121: due to blending with nearby stars of similar brightness, these RR0 stars have overestimated mean magnitudes.

V114: this RR0 star is heavily blended with a brighter star.

V117, V119: both stars are in a very crowded area and their positions and reference fluxes were not found by the pipeline. The correct positions of the stars were found in the summed difference image, and the differential fluxes have

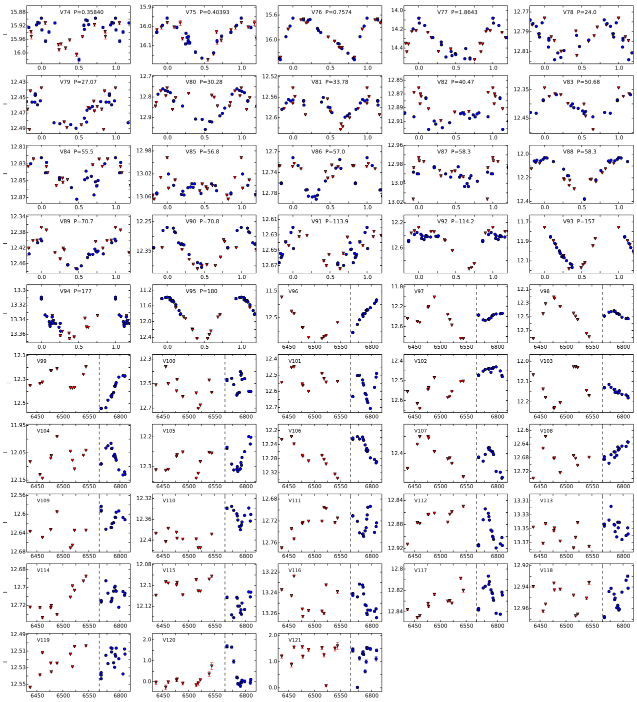

Fig. 6. NGC 6388: light curves for the new variables in our FoV. Red triangles are 2013 data and blue circles are 2014 data. Error bars are plotted but are smaller than the data symbols in many cases. Light curves with confirmed periods are phased. For those variables without periods the *x*-axis refers to (HJD – 2 450 000), and the dashed line indicates that the period from HJD 2 456 570 to 2 456 760 has been removed from the plot, as no observations were performed during this time range. Note that V120 and V121 are plotted in differential flux units, 10^3 ADU/s, and not calibrated *I* magnitudes.

been measured for these positions in the difference images. Therefore, as no reference flux could be measured, magnitudes and amplitudes are not given for either of these RR0 stars.

V118: using the period of this star, P03 and C06 can not give a certain classification, but suggest RR0 or CW. Based on the position of the star in the CMD [0.82, 16.9] we classify it as an RR0 star, although the period is unusually long for this type of star.

V120: this variable is classified as an RR1 in both P03 and C06. Due to the scatter in our light curve and the position of the star in the CMD [0.60, 17.3], we have analysed the light curve for any secondary periods, but none have been found. We therefore support the RR1 classification.

V126-V129: in P03 these stars are described as CWA candidates. The positions that these stars occupy in the CMD [(1.0–1.3), (14.0–15.5)], seem to support that they are indeed CWA stars.

Table 5. NGC 6388: Details of the 48 new variables found in the cluster.

Var	RA (J2000.0)	Dec (J2000.0)	Epoch (d)	P (d)	$\langle I \rangle$	$A_{i'+z'}$	Blend	Classification
V74	17:36:15.449	–44:44:23.35	6790.7919	0.35840	15.96	0.12	ii	RR1?
V75	17:36:17.010	–44:44:17.82	6782.7705	0.40393	16.07	0.22	ii	RR1
V76	17:36:16.483	–44:44:01.25	6792.8127	0.7574	15.98	0.67	iii	RR0
V77	17:36:17.400	–44:44:14.06	6805.8471	1.8643	14.30	0.44	iii	AC
V78	17:36:15.371	–44:43:54.06	6522.4888	24.0	12.80	0.04	iii	SR
V79	17:36:17.448	–44:44:07.26	6522.4888	27.07	12.46	0.05	ii	SR
V80	17:36:17.286	–44:44:18.53	6488.7479	30.28	12.86	0.20	iii	RV
V81	17:36:16.687	–44:44:23.02	6488.7479	33.78	12.58	0.08	iii	SR
V82	17:36:17.841	–44:43:56.93	6476.6758	40.47	12.89	0.06	ii	RV
V83	17:36:15.516	–44:44:26.38	6460.6572	50.68	12.42	0.15	iii	SR
V84	17:36:15.892	–44:44:04.61	6805.8471	55.5	12.85	0.05	iii	SR
V85	17:36:16.962	–44:43:59.02	6544.5238	56.8	13.03	0.07	iii	SR
V86	17:36:18.200	–44:44:00.41	6772.8616	57.0	12.75	0.08	ii	SR
V87	17:36:18.097	–44:44:16.73	6518.4918	58.3	12.99	0.04	ii	SR
V88	17:36:16.092	–44:44:09.41	6790.7919	58.3	12.20	0.35	iii	SR
V89	17:36:16.932	–44:44:23.78	6455.8603	70.7	12.42	0.11	iii	SR
V90	17:36:16.775	–44:44:01.86	6776.8346	70.8	12.34	0.14	ii	SR
V91	17:36:17.293	–44:44:06.94	6808.8938	113.9	12.65	0.05	iii	SR
V92	17:36:15.313	–44:44:11.19	6436.9514	114.2	12.60	0.65	ii	SR
V93	17:36:17.554	–44:44:08.74	6436.9514	157	11.97	0.43	iii	SR
V94	17:36:17.904	–44:44:21.63	6763.9007	177	13.34	0.06	iii	SR
V95	17:36:15.413	–44:44:14.89	6776.8346	180	11.91	1.06	iii	SR
V96	17:36:18.432	–44:44:19.08	–	–	12.51	1.55	iii	L
V97	17:36:17.109	–44:43:57.87	–	–	12.43	0.84	iii	L
V98	17:36:17.106	–44:44:00.43	–	–	12.52	0.60	iii	L
V99	17:36:17.588	–44:44:08.02	–	–	12.37	0.35	iii	L
V100	17:36:17.210	–44:44:13.97	–	–	12.53	0.34	ii	L
V101	17:36:17.730	–44:44:13.58	–	–	12.58	0.26	iii	L
V102	17:36:15.969	–44:43:48.64	–	–	12.54	0.21	iii	L
V103	17:36:17.241	–44:44:08.81	–	–	12.13	0.20	iii	L
V104	17:36:17.398	–44:44:08.39	–	–	12.07	0.15	iii	L
V105	17:36:17.460	–44:44:13.47	–	–	12.27	0.14	ii	L
V106	17:36:16.413	–44:44:10.89	–	–	12.28	0.12	iii	L
V107	17:36:17.731	–44:44:22.13	–	–	12.41	0.12	iii	L
V108	17:36:18.893	–44:44:04.17	–	–	12.68	0.12	iii	L
V109	17:36:18.929	–44:44:14.09	–	–	12.63	0.09	iii	L
V110	17:36:18.038	–44:44:17.56	–	–	12.38	0.08	iii	L
V111	17:36:16.778	–44:44:06.99	–	–	12.73	0.08	iii	L
V112	17:36:17.873	–44:44:03.22	–	–	12.88	0.07	iii	L
V113	17:36:17.999	–44:43:52.65	–	–	13.35	0.06	iii	L
V114	17:36:16.136	–44:44:04.61	–	–	12.71	0.05	iii	L
V115	17:36:17.172	–44:44:05.70	–	–	12.11	0.04	ii	L
V116	17:36:18.924	–44:43:56.82	–	–	13.24	0.04	iii	L
V117	17:36:17.231	–44:44:04.38	–	–	12.83	0.04	iii	L
V118	17:36:17.147	–44:44:10.91	–	–	12.95	0.04	iii	L
V119	17:36:18.093	–44:44:08.59	–	–	12.53	0.05	iii	L?
V120	17:36:17.337	–44:43:53.93	–	–	–	–	–	?
V121	17:36:17.575	–44:43:50.60	–	–	–	–	–	?

Notes. The celestial coordinates correspond to the epoch of the reference image, which is the HJD ~ 2 456 522.48 d. Epochs are (HJD – 2 450 000). $\langle I \rangle$ denotes mean *I* magnitude and $A_{i'+z'}$ are the amplitudes found in our special $i' + z'$ filter. The blend column describes whether the star is blended with (i) brighter star(s); (ii) star(s) of similar magnitude; or (iii) fainter/no star(s).

V130: the period of P03 does not phase our light curve well and our best fit period is significantly longer. Some of the data points seem to have a sort of systematic scatter and it may therefore be an L star, which is supported by its position in the CMD, [1.64, 15.0].

V132: this star is quite heavily blended, which is reflected in a rather scattered light curve and the fact that we found a mean *I* magnitude that is about a magnitude higher than what was found in P03. Based on its position in the CMD and the relation between period and luminosity, we classify this star as a CWB.

V133, V137: for these two stars it is not possible to phase the light curves properly with the periods given in P03, or any other period, and this suggests that they are L stars. No period is therefore given for these two variables.

V136, V138: these two RR0 stars were not found in the C06 analysis. Our data are properly phased by the periods of P03.

V139: this SR phases well with the period found by P03.

V144: the period from P03 does phase this SR reasonably well, but the phased light curve still looks a bit peculiar, so it might also be an L star.

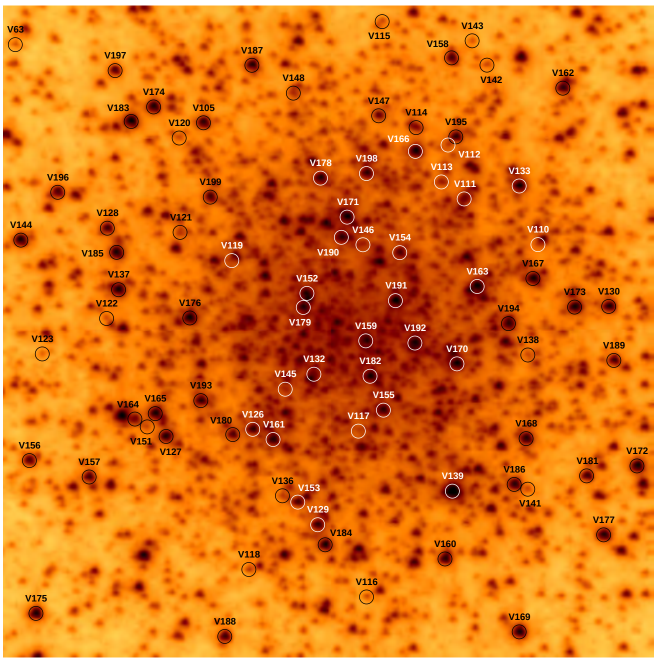

Fig. 7. NGC 6441: finding chart constructed from the reference image marking the positions of the variable stars. Labels and circles are white/black only for clarity. North is up and east is to the right. The cluster image is ~41″ by 41″.

V145: this star is highly blended with a star of similar brightness and was not found in the C06 paper. P03 classifies this as an RR1. We are able to find a fundamental and first overtone period of $P_0 = 0.72082$ and $P_1 = 0.55588$, respectively. This gives a first-overtone to fundamental period ratio of $P_1/P_0 = 0.7712$, which is only slightly higher than the "canonical" ratio of ~0.745 (Clement et al. 2001). We therefore classify this as a double-mode RRL, which also agrees well with the position of the star in the CMD [0.64, 17.3]. Studies of other clusters and dwarf galaxies have shown that the period ratio for RR01 stars generally does not exceed 0.748 (e.g. Clementini et al. 2004, figure 13), and the period ratio for this star should therefore be confirmed when more data become available for NGC 6441.

V146-V148: these RR1 stars seems to be blended with multiple stars. However, their periods and light curves, although with some scatter, are consistent with their classification.

3.2.4. New variables

In this study we were able to find 49 new variable stars for NGC 6441. These are all listed in Table 7 and their light curves are shown in Fig. 11.

Similar to NGC 6388, most of the new variables are RGB stars, many with small amplitudes, which is probably the reason why they have not been detected until now. There are, however, also one (possibly two) previously undetected

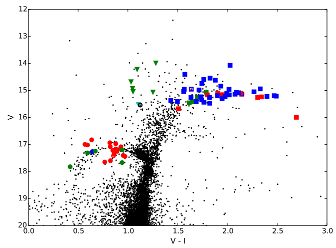

Fig. 8. NGC 6441: $(V - I), V$ colour–magnitude diagram made from HST/ACS data as explained in Sect. 2.6. The stars that show variability in our study are plotted with the same symbols as in Fig. 3.

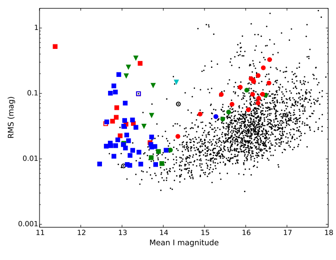

Fig. 9. NGC 6441: plot of the rms magnitude deviation versus the mean magnitude for each of the 1860 calibrated *I* light curves. The variables are plotted with the same symbols as in Fig. 3.

RRL stars and two new CW stars. For many of the new long period variables it has been hard to determine a period, which could indicate that they are irregular.

It should be noted that three of the new variables (V151, V164, and V165) are located very close to each other. Resolving these three variables would have been difficult using conventional imaging, as they are all within a radius of ~0.″9.

Discussion of individual variables:

V151: from the period and position in the CMD [0.6, 17.0] this star can be safely classified as an RRL star, and the asymmetry of the light curve suggests that it is most likely an RR0. The amplitude listed is very large compared to other RRL stars, and there seems to be some scatter in the light curve (caused by its proximity to three other brighter variables) so the actual amplitude is probably about $A_{i'+z'} \sim 0.8$ mag.

V152: this star is highly blended with a star of similar brightness and lies very close to another variable star, V179. The position and reference flux were therefore not found by the pipeline, as in the cases of V117 and V119. The positions and differential fluxes were found manually, but again the reference flux is not measured, so no magnitude or amplitude is given. Based on the period, light curve shape, and CMD position [0.85, 17.4], we classify this tentatively as an RR0 star.

V153, V154: based on their periods, light curves, and positions in the CMD [1.05, 15.0], we classify these two stars as CWA stars.

V155: both the period and magnitude suggest that this is either a CW or an SR star, but the position of this star in the CMD is [−0.5, 13.5], which means that it is far too blue to fit any of these classifications. We do not attempt to classify this variable.

V156-V162, V165-V168: the CMD puts all of these stars on the RGB. As it has been possible to estimate periods for them, we classify these as SR stars.

V163: this star has no CMD information, but based on the period, light curve, and magnitude, it is most likely an SR star.

V164: the CMD position [1.1, 15.5] and the mean magnitude of this star would normally imply that it is a CW star. However the light curve is scattered and the derived period uncertain. We refrain from classifying this variable.

V169-V199: we have classified these RGB stars for which we have been unable to derive periods as L stars.

3.3. NGC 6528

3.3.1. Background information

According to Sawyer Hogg (1973) there are a few variables from the rich Galactic field projected against the cluster, but none are considered to be cluster members. As NGC 6528 might be the most metal-rich cluster in the Galaxy, it has been studied quite extensively in a number of photometric studies (e.g. Ortolani et al. 1992; Richtler et al. 1998; Feltzing & Johnson 2002; Calamida et al. 2014). However, so far no variable stars have been reported. Ortolani et al. (1992) mention that the large spread in the RGB that is found may be due to variability, but this is not mentioned in any later article.

3.3.2. New Variables

A finding chart for the cluster containing the variables detected in this study is shown in Figs. 12, and 13 shows the rms magnitude deviation for the 1103 stars with calibrated *I* magnitudes versus their mean magnitude.

We are able to find seven new variable stars for NGC 6528. Unfortunately there is no CMD for this cluster, which complicates the classification of the variables, but we classify one (possibly two) as RRL stars and four as long period irregular stars. The light curves for these variables are shown in Fig. 14 and their details are listed in Table 8.

V1: the period of this star suggests that it is an RR1, and the magnitude indicates that it is highly blended with a brighter star. Due to the scatter in the light curve, we have analysed it for secondary periods, but none were found.

V2: the period of this star indicates that it is a RR0, even though the light curve looks somewhat noisy. Since the amplitude is somewhat smaller than what we expect for an RR0 star, we leave our classification as tentative.

V3-V6: these four stars are most likely L stars, based on their magnitudes and that it has not been possible to find any periods that phase their light curves in a reasonable way.

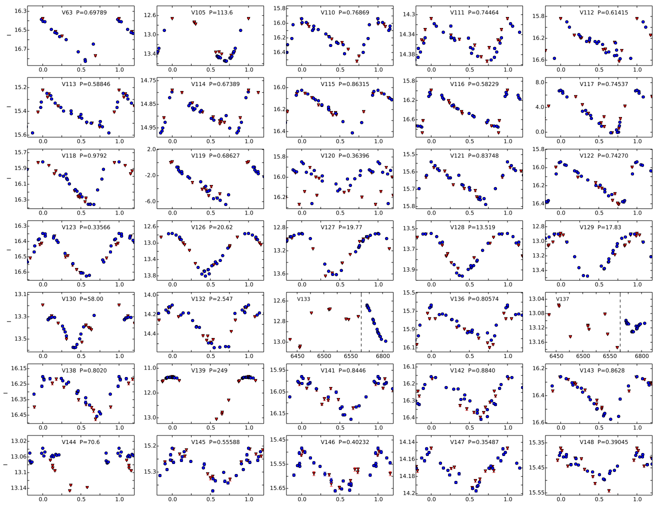

Fig. 10. NGC 6441: light curves for the known variables in our FoV. Red triangles are 2013 data and blue circles are 2014 data. Error bars are plotted but are smaller than the data symbols in many cases. Light curves with confirmed periods are phased. For those variables without periods the x-axis refers to (HJD – 2 450 000), and the dashed line indicates that the period from HJD 2 456 570 to 2 456 760 has been removed from the plot, as no observations were performed during this time range. Note that V117 and V119 are plotted in differential flux units, 10^3 ADU/s, and not calibrated I magnitudes.

V7: the mean magnitude of this star is at the limit of our detection threshold, and it disappears in ∼30% of our images. It is probably an eclipsing binary (E), but we refrain from making a firm classification.

3.4. NGC 6638

The first 19 variable stars in this cluster were found by Terzan (1968). Of these, four were classified as Mira variables with periods between 156 and 279 days, and the remaining ones were neither classified nor had their periods estimated. Sawyer Hogg et al. (1974) were able to discover the variability of a further 26 stars from a photographic collection made in 1939 and 1972. All of these 45 variable stars are distributed in a wide field of 30′ × 30′ and only a few are located close to the central parts of the cluster.

In Rutily & Terzan (1977, hereafter R77) a total of 63 variables are presented. That article contains finding charts and periods for many of the variables. As NGC 6638 does not have a very dense central region, it was possible to detect variable stars quite close to the centre, but no periods for the central stars are given.

A finding chart for the cluster containing the variables detected in this study is shown in Fig. 15. Figure 16 shows the rms magnitude deviation for the 981 stars with calibrated I magnitude versus their mean magnitude.

3.4.1. Known variables

All of the previously known variable stars within our FoV have been located and confirmed as variables, and this is the first study to present periods and classifications for these stars. The light curves are plotted in Fig. 17a and their details can be found in Table 9.

The fact that no CMD is available for this study makes it a little harder to classify the variables, but with the periods and magnitudes found, we are quite certain that they are all RRL stars.

V25-V27, V30-V32: these stars all have periods, light curve shapes, and amplitudes typical of RR0 stars.
V29: the star given as V29 in R77 is not found to be variable. A star located 3″ away *is* found to be variable and we believe that this is the actual V29. Based on the period and magnitude, this star is classified as an RR1, despite the unusual asymmetric shape of the light curve.

Table 6. NGC 6441: details of the 35 previously known variables within our FoV.

Var	RA (J2000.0)	Dec (J2000.0)	Epoch (d)	P (d)	P_{P03} (d)	P_{C06} (d)	$\langle I \rangle$	$A_{i'+z'}$	Blend	Classification
V63	17:50:11.338	–37:02:47.42	6541.5439	0.69789	0.69781	0.700[a]	16.60	0.45	iii	RR0
V105	17:50:12.320	–37:02:52.61	6476.7769	113.6	111.6	–	13.11	0.88	iii	SR
V110	17:50:14.068	–37:03:00.76	6770.9142	0.76869	0.76867	0.769	16.23	0.58	i	RR0
V111	17:50:13.685	–37:03:12.21	6509.6175	0.74464	0.74464	0.743	14.35	0.09	i	RR0
V112	17:50:13.607	–37:02:54.37	6454.7896	0.61415	0.61419	0.614	16.23	0.78	iii	RR0
V113	17:50:13.567	–37:02:56.68	6541.5439	0.58846	0.58845	0.586	15.40	0.36	iii	RR0
V114	17:50:13.441	–37:02:53.23	6541.5439	0.67389	0.67389	0.675	14.88	0.18	i	RR0
V115	17:50:13.276	–37:02:46.52	6795.7897	0.86315	0.86311	0.860	16.22	0.39	ii	RR0
V116	17:50:13.117	–37:03:22.64	6476.7769	0.58229	0.58229	0.582	16.43	0.89	iii	RR0
V117	17:50:13.096	–37:03:12.21	6781.7949	0.74537	0.74529	0.745	–	–	ii	RR0
V118	17:50:12.500	–37:03:20.74	6805.8572	0.9792	0.97923	0.979	16.09	0.54	iii	RR0
V119	17:50:12.451	–37:03:01.31	6541.5439	0.68627	0.68628	0.686	–	–	i	RR0
V120	17:50:12.190	–37:02:53.53	6789.7942	0.36396	0.36396	0.364	16.06	0.42	ii	RR1
V121	17:50:12.182	–37:02:59.46	6773.8400	0.83748	0.83748	0.848	15.66	0.25	ii	RR0
V122	17:50:11.783	–37:03:04.76	6789.7942	0.74270	0.74270	0.744	16.17	0.47	iii	RR0
V123	17:50:11.439	–37:03:06.89	6792.8040	0.33566	0.33566	0.336	16.49	0.28	iii	RR1
V126	17:50:12.539	–37:03:11.94	6782.7959	20.62	20.625	–	13.28	1.04	iii	CWA
V127	17:50:12.081	–37:03:12.26	6775.8182	19.77	19.773	–	13.27	0.74	iii	CWA
V128	17:50:11.799	–37:02:59.09	6790.8008	13.519	13.519	–	13.75	0.41	iii	CWA
V129	17:50:12.869	–37:03:18.03	6564.5424	17.83	17.832	–	13.18	0.59	iii	CWA
V130	17:50:14.433	–37:03:04.75	6476.7769	58.00	48.90	–	13.39	0.38	iii	SR?, L?
V132	17:50:12.869	–37:03:08.57	6784.7970	2.547	2.54737	–	14.32	0.44	i	CWB
V133	17:50:13.977	–37:02:57.05	–	–	122.9	–	12.85	0.41	iii	L
V136	17:50:12.687	–37:03:16.16	6791.7776	0.80574	0.80573	–	15.87	0.47	ii	RR0
V137	17:50:11.850	–37:03:02.97	–	–	51.2	–	13.12	0.12	iii	L
V138	17:50:14.000	–37:03:07.68	6797.8236	0.8020	0.80199	–	16.34	0.27	iii	RR0
V139	17:50:13.584	–37:03:16.12	6541.5439	249	249.1	–	12.20	1.72	iii	SR
V141	17:50:13.982	–37:03:16.11	6789.7942	0.8446	0.84475	0.847	16.08	0.20	iii	RR0
V142	17:50:13.823	–37:02:49.41	6784.7970	0.8840	0.88400	0.887	16.28	0.25	iii	RR0
V143	17:50:13.748	–37:02:47.86	6781.7949	0.8628	0.86279	0.863	16.42	0.32	iii	RR0
V144	17:50:11.341	–37:02:59.71	6782.7959	70.6	70.6	–	13.09	0.11	iii	SR?, L?
V145	17:50:12.716	–37:03:09.47	6770.8270	0.55588[b]	0.55581	–	15.29	0.16	ii	RR01
V146	17:50:13.145	–37:03:00.51	6797.8236	0.40232	–	0.402	15.57	0.18	ii	RR1
V147	17:50:13.245	–37:02:52.43	6455.7466	0.35487	–	0.355	14.17	0.05	i	RR1
V148	17:50:12.798	–37:02:50.88	6454.7896	0.39045	–	0.390	15.46	0.17	ii	RR1

Notes. The celestial coordinates correspond to the epoch of the reference image, which is the HJD ∼ 2 456 541.54 d. Epochs are (HJD – 2 450 000). $\langle I \rangle$ denotes mean I magnitude and $A_{i'+z'}$ are the amplitudes found in our special $i' + z'$ filter. The blend column describes whether the star is blended with (i) brighter star(s); (ii) star(s) of similar magnitude; or (iii) fainter/no star(s). P_{P03} and P_{C06}, are periods from P03 and C06, respectively, which have been included as a reference. [(a)] Period from Pritzl et al. (2001). [(b)] First-overtone period; fundamental period is found to be 0.72082 d.

V33: based on the period, light curve shape, and magnitude, we classify this star as an RR1.

3.4.2. New variables

In this study we were able to find eight new variable stars for NGC 6638. The lack of a CMD complicates the classification, but we classify five as RRL stars and three as long period variables. The light curves for these variables are shown in Fig. 17b and their details are listed in Table 10.

Especially interesting are the two variables V64 and V68, that are located very close to the same bright star (within 1.″2 and 0.″8, respectively). Using conventional imaging it would have been hard to distinguish these three stars from each other, but with the high resolution we achieve with the EMCCD camera this is possible.

V64, V65: based on the period, light curve shape, and magnitude, these stars can be safely classified as RR1.
V66-V68: three stars with periods and light curve shapes, that strongly indicate that they are RR0 stars.
V69: the period found for this SR phases the light curve reasonably well, but there are some outlier points, which might indicate that it is actually irregular.
V70: the light curve of this SR is phased well by the period.
V71: no period was found for this star, and it is therefore classified as an L star.

3.5. NGC 6652

3.5.1. Background information

Using 23 photographic plates taken with the 1m Yale telescope at CTIO in 1977, Hazen (1989) found 24 variable stars in this cluster. Nine variables (V1-9) were found within the tidal radius of the cluster, and 15 outside it. Two of the variables (V7 and V9) had already been published by Plaut (1971) as part of the Palomar-Groningen variable-star survey. None of these variable stars are close to the rather dense central part of the cluster nor do they lie within our FoV.

There are 12 known X-ray sources in NGC 6652 (Deutsch et al. 1998, 2000; Heinke et al. 2001; Coomber et al. 2011; Stacey et al. 2012; Engel et al. 2012). Sources A-C have been

Table 7. NGC 6441: details of the 49 new variables found in the cluster.

Var	RA (J2000.0)	Dec (J2000.0)	Epoch (d)	P (d)	$\langle I \rangle$	$A_{i'+z'}$	Blend	Classification
V151	17:50:11.983	–37:03:11.63	6564.5424	0.48716	16.46	0.80	iii	RR0
V152	17:50:12.843	–37:03:03.48	6564.5424	0.9432	–	–	i	RR0?
V153	17:50:12.767	–37:03:16.58	6541.5439	9.89	13.72	0.15	iii	CWA
V154	17:50:13.338	–37:03:01.06	6455.7466	10.83	13.57	0.15	iii	CWA
V155	17:50:13.231	–37:03:10.93	6564.5424	11.45	13.03	0.04	iii	?
V156	17:50:11.357	–37:03:13.57	6789.7942	11.76	13.97	0.03	iii	SR[a]
V157	17:50:11.670	–37:03:14.69	6775.8182	15.10	13.71	0.04	iii	SR[a]
V158	17:50:13.637	–37:02:48.90	6784.7970	17.50	13.89	0.05	iii	SR[a]
V159	17:50:13.147	–37:03:06.55	6782.7959	18.5	13.03	0.06	ii	SR[a]
V160	17:50:13.536	–37:03:20.37	6795.7897	20.3	13.31	0.11	iii	SR
V161	17:50:12.645	–37:03:12.61	6564.5424	24.6	12.95	0.09	iii	SR
V162	17:50:14.220	–37:02:50.97	6770.8270	29.3	13.68	0.06	iii	SR
V163	17:50:13.742	–37:03:03.30	6546.5297	41.03	12.59	0.11	iii	SR?
V164	17:50:11.919	–37:03:11.12	6564.5424	41.14	14.37	0.27	ii	?
V165	17:50:12.027	–37:03:10.81	6564.5424	51.6	12.86	0.21	iii	SR
V166	17:50:13.434	–37:02:54.72	6546.5297	52	12.83	0.17	iii	SR
V167	17:50:14.037	–37:03:02.88	6789.7942	86	12.78	0.13	iii	SR
V168	17:50:13.980	–37:03:12.93	6789.7942	128	13.13	0.11	iii	SR
V169	17:50:13.918	–37:03:25.06	–	–	12.99	0.68	iii	L
V170	17:50:13.625	–37:03:08.13	–	–	12.89	0.48	iii	L
V171	17:50:13.065	–37:02:58.75	–	–	12.71	0.29	iii	L
V172	17:50:14.561	–37:03:14.81	–	–	13.06	0.21	iii	L
V173	17:50:14.253	–37:03:04.74	–	–	13.10	0.16	iii	L
V174	17:50:12.059	–37:02:51.54	–	–	13.06	0.14	iii	L
V175	17:50:11.371	–37:03:23.18	–	–	13.27	0.14	iii	L
V176	17:50:12.222	–37:03:04.85	–	–	12.65	0.11	iii	L
V177	17:50:14.376	–37:03:19.09	–	–	13.35	0.09	iii	L
V178	17:50:12.930	–37:02:56.26	–	–	12.91	0.08	iii	L
V179	17:50:12.822	–37:03:04.36	–	–	12.72	0.07	ii	L
V180	17:50:12.433	–37:03:12.24	–	–	13.72	0.07	iii	L
V181	17:50:14.294	–37:03:15.36	–	–	13.73	0.07	iii	L
V182	17:50:13.165	–37:03:08.78	–	–	12.62	0.06	iii	L
V183	17:50:11.939	–37:02:52.42	–	–	12.72	0.06	iii	L
V184	17:50:12.906	–37:03:19.30	–	–	12.84	0.06	iii	L
V185	17:50:11.845	–37:03:00.62	–	–	13.07	0.06	iii	L
V186	17:50:13.911	–37:03:15.79	–	–	13.17	0.06	iii	L
V187	17:50:12.583	–37:02:49.07	–	–	13.25	0.06	iii	L
V188	17:50:12.364	–37:03:24.91	–	–	13.70	0.06	iii	L
V189	17:50:14.453	–37:03:08.15	–	–	13.81	0.06	iii	L
V190	17:50:13.032	–37:03:00.01	–	–	13.04	0.05	iii	L
V191	17:50:13.309	–37:03:04.07	–	–	12.46	0.04	iii	L
V192	17:50:13.406	–37:03:06.76	–	–	12.80	0.04	iii	L
V193	17:50:12.269	–37:03:10.06	–	–	13.19	0.04	iii	L
V194	17:50:13.902	–37:03:05.68	–	–	13.19	0.04	ii	L
V195	17:50:13.649	–37:02:53.87	–	–	13.41	0.04	iii	L
V196	17:50:11.542	–37:02:56.76	–	–	13.81	0.04	iii	L
V197	17:50:11.861	–37:02:49.20	–	–	14.07	0.04	iii	L
V198	17:50:13.173	–37:02:56.04	–	–	13.13	0.03	iii	L
V199	17:50:12.346	–37:02:57.29	–	–	13.46	0.03	iii	L

Notes. The celestial coordinates correspond to the epoch of the reference image, which is the HJD ∼ 2 456 541.54 d. Epochs are (HJD – 2 450 000). $\langle I \rangle$ denotes mean I magnitude and $A_{i'+z'}$ are the amplitudes found in our special $i' + z'$ filter. The blend column describes whether the star is blended with (i) brighter star(s); (ii) star(s) of similar magnitude; or (iii) fainter/no star(s). [(a)] These stars have shorter periods than expected for stars of the SR class, but it is not clear how to otherwise classify them according to the GCVS schema given their position on the RGB.

assigned variable numbers V10-V12, respectively, by Clement (priv. comm.). Seven of the X-ray sources lie within our FoV (sources B-E and G-H). Only sources B and H show signs of variability in our difference images and for the remaining sources we cannot find any clear optical counterparts in our reference image at the positions given by Coomber et al. (2011) and Stacey et al. (2012), although we note that our limiting magnitude is ∼19.5 mag (see Fig. 20).

A finding chart for the cluster containing the variables detected in this study is shown in Figs. 18 and 19 shows a CMD of the stars within our FoV with the variables overplotted. Figure 20 shows the rms magnitude deviation for the 1098 stars with calibrated I magnitudes versus their mean magnitude. The light curves of the variables are plotted in Fig. 21 and their details may be found in Table 11.

3.5.2. Known variables

V11 (source B) was found by Coomber et al. (2011) to be undergoing rapid X-ray flaring on time scales of less than 100 s.

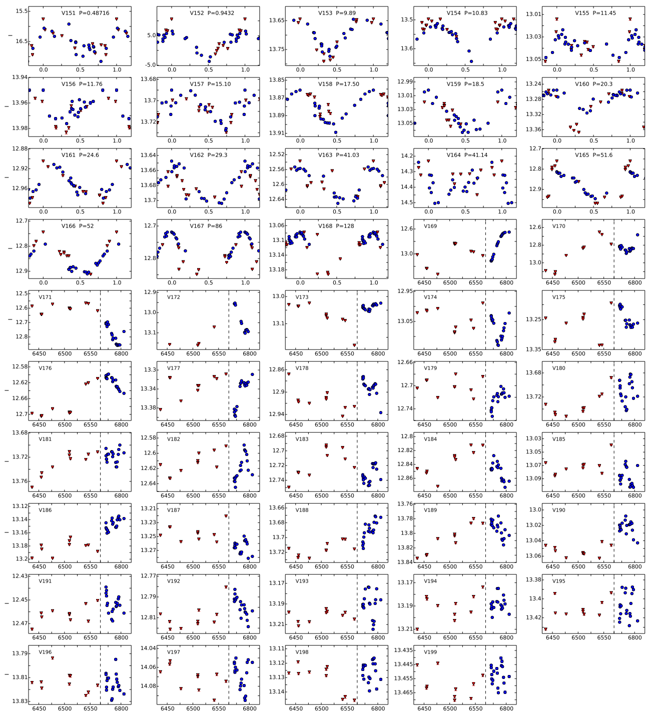

Fig. 11. NGC 6441: light curves for the new variables in our FoV. Red triangles are 2013 data and blue circles are 2014 data. Error bars are plotted but are smaller than the data symbols in many cases. Light curves with confirmed periods are phased. For those variables without periods the x-axis refers to (HJD – 2 450 000), and the dashed line indicates that the period from HJD 2 456 570 to 2 456 760 has been removed from the plot, as no observations were performed during this time range. Note that V152 is plotted in differential flux units, 10^3 ADU/s, and not calibrated I magnitudes.

Like Engel et al. (2012), we have detected clear variability in the optical counterpart with an amplitude of up to ∼1.1 mag (see Fig. 21). However, as in previous studies, we cannot find a period on which the light curve can be phased. Stacey et al. (2012) suggest that V11 might be a special type of low mass X-ray binary (LMXB) or a very faint X-ray transient (VFXT). One of the advantages of high frame-rate imaging is that it is possible to achieve a high time-resolution by combining the single exposures into short-exposure images. This technique could be applied to V11 to determine the time scale of the optical flickering, but it is too faint to be able to do this with our data.

3.5.3. New variables

We found two new variables in the cluster:

V13: this star has the same position as the X-ray source H, and we therefore assume that it is the same star. The star has a

Table 8. NGC 6528: Details of the 7 new variables found in the cluster.

Var	RA (J2000.0)	Dec (J2000.0)	Epoch (d)	P (d)	$\langle I \rangle$	$A_{i'+z'}$	Blend	Classification
V1	18:04:49.380	–30:03:27.25	6477.8478	0.25591	15.61	0.19	i	RR1
V2	18:04:49.368	–30:03:19.53	6541.5615	0.8165	16.18	0.14	iii	RR0?
V3	18:04:49.518	–30:03:26.74	–	–	12.46	0.25	iii	L
V4	18:04:49.614	–30:03:38.25	–	–	12.40	0.21	iii	L
V5	18:04:50.016	–30:03:20.90	–	–	12.70	0.10	iii	L
V6	18:04:49.099	–30:03:17.64	–	–	12.66	0.06	iii	L
V7	18:04:49.360	–30:03:28.52	–	–	19.6	–	–	E?

Notes. The celestial coordinates correspond to the epoch of the reference image, which is the HJD ~ 2456510.63 d. Epochs are (HJD – 2 450 000). $\langle I \rangle$ denotes mean I magnitude and $A_{i'+z'}$ are the amplitudes found in our special $i'+z'$ filter. The blend column describes whether the star is blended with (i) brighter star(s); (ii) star(s) of similar magnitude; or (iii) fainter/no star(s).

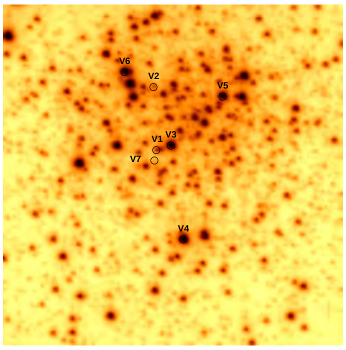

Fig. 12. NGC 6528: finding chart constructed from the reference image marking the positions of the variable stars. North is up and east is to the right. The cluster image is ~41″ by 41″.

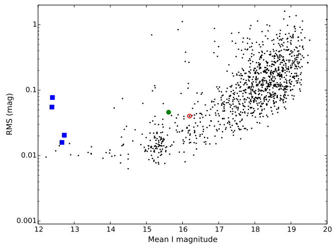

Fig. 13. NGC 6528: plot of the rms magnitude deviation versus the mean magnitude for each of the 1103 calibrated I light curves. The stars that show variability in our study are plotted with the same symbols as in Fig. 3.

light curve scatter of less than ~0.01 mag consistent with noise. However, at the epochs HJD 2 456 506 and 2 456 509 it is ~2 and 4% brighter than the base-line, suggesting that the star has undergone an outburst. However, the CMD puts the star on the RGB, where instead we might expect long period semi-regular variability, but this seems not to be the case for V13. We therefore refrain from classifying this variable.

V14: based on its position in the CMD this star could be a blue-straggler eclipsing binary. The phased light curve looks like that of a RR1 star, but the period is too short for this. Furthermore, with its position ~2.5 mag below the horizontal branch, it would be a field RR1 star lying behind the cluster.

4. Discussion

4.1. NGC 6388 and NGC 6441

Of the five clusters that we studied in this paper, NGC 6388 and NGC 6441 contain by far the largest number of variable stars. These two clusters have a very similar metallicity and central concentration (see Table 1) and very similar CMDs (see Figs. 3, 8). However, before the present study, NGC 6441 had twice as many reported variables as NGC 6388.

We were able to find ~50 new variables in each cluster, of which at least three are RRL stars and at least five are CW stars. The fact that we were able to find new short period variable stars in NGC 6441 is somewhat surprising given that a HST snapshot study has been performed on this cluster. It should be noted that the HST data were analysed using the DAOPHOT/ALLSTAR/ALLFRAME routines (see Stetson 1987, 1994), which might not perform as well as DIA in such a crowded field.

The RR0 star V151 in NGC 6441 has a very large amplitude and the reason why this star has not been detected before is most likely due to its proximity to three other variable stars, which are all several magnitudes brighter. That we are able to detect stars like this implies that there might be several other RRL stars situated close to bright stars outside our FoV that are not detected yet. Our method does, however, heighten the chances that we now have a complete census of the RRL stars in the central regions of NGC 6388 and NGC 6441.

With the newly found RRL stars there are now 23 RRL stars in NGC 6388 with robust classification (excluding V74 from our work), of which 11 are RR0 and 12 are RR1. Using these RRLs we calculate mean periods for the RR0 and RR1 stars as $\langle P_{\rm RR0} \rangle$ = 0.700 d and $\langle P_{\rm RR1} \rangle$ = 0.389 d, respectively, and the ratio of RR1s to the total number of RRLs as $\frac{n_{\rm RR1}}{n_{\rm RRL}} \approx 0.52$.

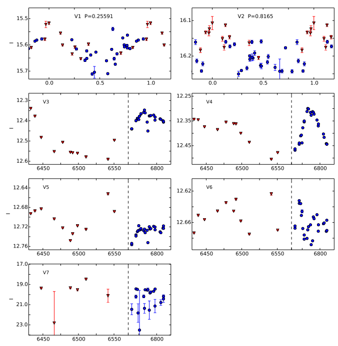

Fig. 14. NGC 6528: light curves for the variables in our FoV. Red triangles are 2013 data and blue circles are 2014 data. Error bars are plotted but are smaller than the data symbols in many cases. Light curves with confirmed periods are phased. For those variables without periods the x-axis refers to (HJD – 2 450 000), and the dashed line indicates that the period from HJD 2 456 570 to 2 456 760 has been removed from the plot, as no observations were performed during this time range.

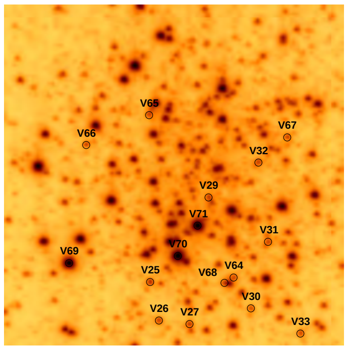

Fig. 15. NGC 6638: finding chart constructed from the reference image marking the positions of the variable stars. North is up and east is to the right. The cluster image is ~41″ by 41″.

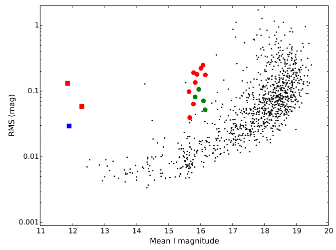

Fig. 16. NGC 6638: plot of the rms magnitude deviation versus the mean magnitude for each of the 981 calibrated I light curves. The stars that show variability in our study are plotted with the same symbols as in Fig. 3.

For NGC 6441 the total number of RRL stars with robust classification is now 69 (excluding V152 from our work), of which 45 are RR0, 23 are RR1, and 1 is RR01. From these we calculate $\langle P_{\rm RR0} \rangle = 0.745$ d, $\langle P_{\rm RR1} \rangle = 0.368$ d, and $\frac{n_{\rm RR1}}{n_{\rm RRL}} \approx 0.34$.

Oosterhoff (1939) called attention to a relation between the mean periods and relative proportions of RR0 and RR1 stars in GCs. Generally it is found that the RRLs in Oosterhoff type I (Oo I) clusters have shorter mean periods, and a lower ratio of RR1 stars, than in Oosterhoff type II (Oo II) clusters. It has also been found that Oo I clusters are usually more metal rich than Oo II clusters (Smith 1995). NGC 6388 and NGC 6441 are therefore unusual as they do not fit into either of the Oo types. Their high metallicity indicates that they are Oo I, but the long mean periods of the RRLs and the high ratio of RR1 stars, especially for NGC 6388, indicates Oo II. Based on this Pritzl et al. (2000) suggested creating a new Osterhoff type III, but Clement et al. (2001) found that the period-amplitude relation of the RR0 variables in NGC 6441 is more consistent with that of Oo II. Our new variable star discoveries have not changed the Oo classification situation for these clusters.

Period-luminosity diagrams for the CW and RV stars that are found in the two clusters are shown in Fig. 22. In P03 the relation between the absolute I magnitudes ($I_{\rm abs}$) of the CW stars and their periods is found to be $I_{\rm abs} \propto -2.03 \cdot \log_{10}(P)$. The relation is actually only based on CW stars from NGC 6441, but we have plotted it for both clusters in Fig. 22 (dashed line) using the relation $I = I_0 - 2.03 \cdot \log_{10}(P)$, where I_0 is 15.5 and 15.9 mag for NGC 6388 and NGC 6441, respectively.

For NGC 6388, there are three CWs, (V29, V63, and V77) with periods below 3 days. V29 and V63 have been classified as CWB, while V77 has been classified as an AC due to the fact that it is a little too bright for its period compared with the other two (Clement et al. 2001). The two stars with periods over 30 days are the RV stars V80, and V82. RV stars also exhibit a correlation between their luminosity and periods, but with a larger intrinsic scatter than the CW stars, which is also evident for NGC 6388. We find a relation of $I \propto 1.81 \cdot \log_{10}(P)$ for NGC 6388, which is close to the relation found in P03.

In the P03 analysis of NGC 6441 there is one CWA star that is not included in this study. The star, V6, is classified as P2C in P03 and is included in the NGC 6441 plot in Fig. 22. The CWB star V132 is heavily blended and this is probably the reason why the pipeline has measured the star to be a magnitude brighter than in P03. Using our I magnitude for V132, we

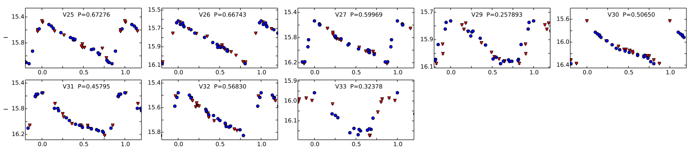

(a) Known variables

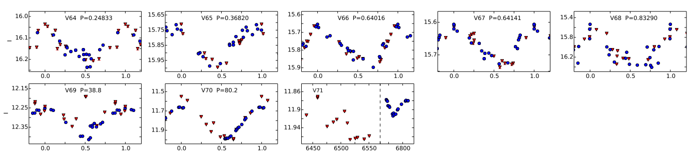

(b) New variables

Fig. 17. NGC 6638: Light curves for the variables in our FoV. Red triangles are 2013 data and blue circles are 2014 data. Error bars are plotted but are smaller than the data symbols in many cases. Light curves with confirmed periods are phased. For those variables without periods the x-axis are in (HJD – 2 450 000), and the dashed line indicates that the period from HJD 2 456 600 to 2 456 750 has been removed from the plot, as no observations were performed during this time range.

Table 9. NGC 6638: details of the 8 previously known variables in our FoV.

Var	RA (J2000.0)	Dec (J2000.0)	Epoch (d)	P (d)	$\langle I \rangle$	$A_{i'+z'}$	Blend	Classification
V25	18:30:55.564	–25:30:04.05	6511.6617	0.67276	15.79	0.66	iii	RR0
V26	18:30:55.635	–25:30:08.79	6782.8404	0.66743	15.85	0.47	iii	RR0
V27	18:30:55.912	–25:30:09.31	6773.8921	0.59969	15.87	0.68	iii	RR0
V29	18:30:56.111	–25:29:53.87	6773.8921	0.257893	15.92	0.31	iii	RR1
V30	18:30:56.471	–25:30:07.56	6458.6160	0.50650	16.00	0.75	iii	RR0
V31	18:30:56.640	–25:29:59.47	6783.8751	0.45795	15.88	0.67	iii	RR0
V32	18:30:56.570	–25:29:49.75	6773.8921	0.56830	15.65	0.35	iii	RR0
V33	18:30:56.914	–25:30:10.79	6791.7951	0.32378	16.07	0.22	iii	RR1

Notes. The celestial coordinates correspond to the epoch of the reference image, which is the HJD ~ 2 456 511.65 d. Epochs are (HJD – 2 450 000). $\langle I \rangle$ denotes mean I magnitude and $A_{i'+z'}$ are the amplitudes found in our special $i'+z'$ filter. The blend column describes whether the star is blended with (i) brighter star(s); (ii) star(s) of similar magnitude; or (iii) fainter/no star(s).

find the relation $I \propto 1.23 \cdot \log_{10}(P)$, which is quite far from the P03 relation. However, by using the I magnitude from P03 for V132 (plotted as a black cross in Fig. 22), the relation found in P03 looks much more feasible.

Most of the new variables found in the two clusters are RGB stars, which is not surprising due to a number of factors:

- The CMDs of the two clusters show a very prominent RGB, on which most stars are intrinsically variable (e.g. Percy 2007; Percy & Brekelmans 2014).
- The baseline of our data is about 14 months, which makes it possible to detect variability over a long period.
- The filter we use goes from the optical red to near-infrared wavelengths, which matches very well with the colour of the RGB stars.
- The use of high frame-rate imaging makes it possible to observe much brighter stars without saturating.

Both the SR and L classifications have several subclasses, but in order to safely assign these, one would need more information on the stars, such as spectral type and a longer baseline than is available in this study.

4.2. NGC 6638

Of the 21 variable stars in R77 where a period has been determined, one (V24) has a period consistent with that of an RR0, and 14 with RR1 periods. Two of the RR1s (V40 and V42) are located very far from the centre and might not be cluster members. We find that a further eight of the known variables (those in Table 4) have periods consistent with RRLs and we also retrieve five new RRL stars (Table 5).

The total number of RRL stars in the cluster is therefore between 26 and 28, of which 10 are RR0 and 16–18 are RR1. The mean periods have been calculated as $\langle P_{\rm RR0} \rangle = 0.625$ d and

Table 10. NGC 6638: details of the 8 new variables found in the cluster.

Var	RA (J2000.0)	Dec (J2000.0)	Epoch (d)	P (d)	$\langle I \rangle$	$A_{i'+z'}$	Blend	Classification
V64	18:30:56.321	–25:30:03.74	6541.5840	0.24833	16.14	0.20	iii	RR1
V65	18:30:55.591	–25:29:43.63	6458.8425	0.36820	15.85	0.28	iii	RR1
V66	18:30:55.015	–25:29:47.10	6783.8751	0.64016	15.78	0.24	iii	RR0
V67	18:30:56.836	–25:29:46.75	6783.8751	0.64141	15.67	0.13	iii	RR0
V68	18:30:56.237	–25:30:04.37	6797.8372	0.83290	15.97	0.87	i	RR0
V69	18:30:54.834	–25:30:01.50	6516.5499	38.8	12.30	0.22	iii	SR
V70	18:30:55.820	–25:30:00.95	6486.7350	80.2	11.77	0.45	iii	SR
V71	18:30:56.005	–25:29:57.29	–	–	11.92	0.10	iii	L

Notes. The celestial coordinates correspond to the epoch of the reference image, which is the HJD ~ 2 456 511.65 d. Epochs are (HJD – 2 450 000). $\langle I \rangle$ denotes mean I magnitude and $A_{i'+z'}$ are the amplitudes found in our special $i'+z'$ filter. The blend column describes whether the star is blended with (i) brighter star(s); (ii) star(s) of similar magnitude; or (iii) fainter/no star(s).

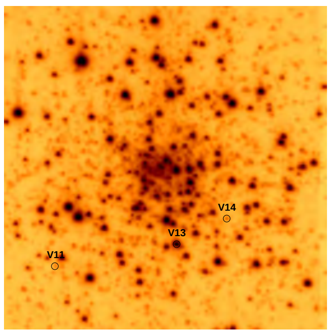

Fig. 18. NGC 6652: finding chart constructed from the reference image marking the positions of the variable stars. North is up and east is to the right. The cluster image is ~41″ by 41″.

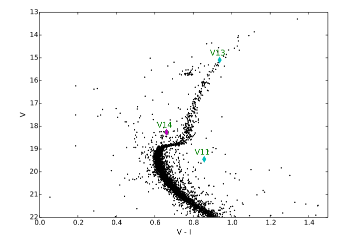

Fig. 19. NGC 6652: $(V-I), V$ colour–magnitude diagram made from HST/ACS data as explained in Sect. 2.6. The three stars that show variability in our study are plotted. The two previously known X-ray sources are marked as cyan diamonds and the new found RR1 is marked with a green circle.

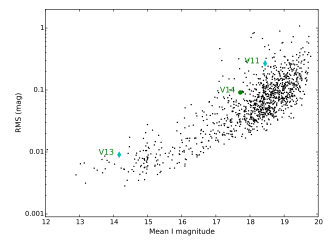

Fig. 20. NGC 6652: plot of the rms magnitude deviation versus the mean magnitude for each of the 1098 calibrated I light curves. The variables are plotted with the same symbols as in Fig. 19.

$\langle P_{\rm RR1} \rangle$ = 0.305 d excluding V40 and V42, and including them only changes this by less than 0.001 d. The ratio of RR1s to total number of RRLs is between 0.62 and 0.64, depending on the inclusion or exclusion of V40 and V42.

Figure 23 shows a Bailey diagram, i.e. a plot of the period versus the amplitude for RR Lyrae stars, for NGC 6638. The black lines in this plot are the loci calculated by Kunder et al. (2013) for the Oo I clusters for the RR0 and RR1 stars (solid lines) and for the Oo II clusters (dashed lines). The dotted blue line is the locus found by Arellano Ferro et al. (2011, 2013a) for the two Oo II clusters NGC 5024 and NGC 6333, respectively. Both sets of loci are derived from the I-band light curves and as our $i' + z'$ filter is slightly redder, our amplitudes might also be a little smaller than true I-band amplitudes. Even with slightly larger amplitudes than what is plotted in Fig. 23, the RRL stars seem to follow the loci for Oo I clusters. There are a number of RR0 stars that lie somewhat higher than the rest, and these are probably more evolved stars, following the argumentation in Clement & Shelton (1997); Cacciari et al. (2005). Based on the Bailey diagram and the metallicity of the cluster, [Fe/H] $\simeq -0.95$, we tentatively classify NGC 6638 as an Oo I cluster, despite the high $\frac{n_{\rm RR1}}{n_{\rm RRL}}$ ratio.

Table 11. NGC 6652: details of the 1 known (V11) and 2 new (V13, V14) variables in our FoV.

Var	RA (J2000.0)	Dec (J2000.0)	Epoch (d)	P (d)	$\langle I\rangle$	$A_{i'+z'}$	Blend	Classification
V11	18:35:44.551	−32:59:38.38	–	–	18.72	1.09	iii	LMXB?, VFXT?[a]
V13	18:35:45.805	−32:59:35.94	–	–	14.17	0.04	iii	?
V14	18:35:46.325	−32:59:32.79	6506.6618	0.189845	17.74	0.29	iii	RR1?, EW?

Notes. The celestial coordinates correspond to the epoch of the reference image, which is the HJD ∼ 2456458.84 d. Epochs are (HJD − 2 450 000). $\langle I\rangle$ denotes mean I magnitude and $A_{i'+z'}$ are the amplitudes found in our special $i'+z'$ filter. The blend column describes whether the star is blended with (i) brighter star(s); (ii) star(s) of similar magnitude; or (iii) fainter/no star(s). [(a)] Classification from Stacey et al. (2012) .

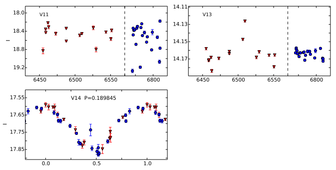

Fig. 21. NGC 6652: light curves for the variables in our FoV. Red triangles are 2013 data and blue circles are 2014 data. Error bars are plotted but are smaller than the data symbols in many cases. Light curves with confirmed periods are phased. For those variables without periods the x-axis refers to (HJD − 2 450 000), and the dashed line indicates that the period from HJD 2 456 570 to 2 456 760 has been removed from the plot, as no observations were performed during this time range.

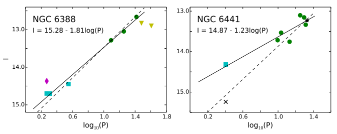

Fig. 22. Periods against I magnitudes for the CWs and RVs found in NGC 6388 and NGC 6441. Green circles are CWAs, cyan squares are CWBs, yellow triangles are RVs, and magenta diamonds are ACs. The black star and black cross in the NGC 6441 plot are the variable stars V6 and V132, respectively, for which mean I magnitudes and periods are taken from P03. The solid lines are derived based on CWAs and CWBs from this study only and have R^2-values of 0.991 and 0.848 for NGC 6388 and NGC 6441, respectively. The dashed lines are the relations found in P03 (see Sect. 4.1 for details).

Two of the newly found RRLs (V64 and V68) are found very close to the same bright star, and this is a very clear example of the advantages of the EMCCD data, as these would have been very hard to resolve using conventional imaging. It also makes it more likely that we now have a complete census of the RRLs in the central parts of this cluster, especially as this cluster does not have a very dense central region (see Table 1).

A CMD of NGC 6638 has been published by Piotto et al. (2002), and from this it is evident that the RGB of this cluster is much less prominent than the ones of NGC 6388 and NGC 6441. It is therefore not surprising that only very few variable RGB stars are found in this cluster.

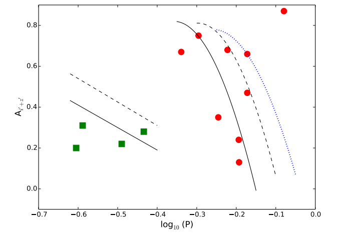

Fig. 23. Bailey diagram of NGC 6638 for I amplitudes, with RR0 and RR1 stars plotted as red circles and green squares, respectively. The black solid and dashed lines are the Oo I and Oo II loci, respectively, as calculated by Kunder et al. (2013) for I-band. The blue dotted line is the locus found by Arellano Ferro et al. (2011, 2013a) for the two Oo II clusters NGC 5024 and NGC 6333, respectively.

4.3. NGC 6528 and NGC 6652

NGC 6528 and NGC 6652 have significantly different metallicities, but they share their lack of variable stars.

Until now no variable stars had been reported for NGC 6528, but we were able to find two RRLs and four long period RGB stars, plus a very faint variable star that could not be classified.

Of the three variable stars we find in NGC 6652, two seem to be optical counterparts of X-ray sources, and the third might be a blue-straggler eclipsing binary, or a field RR1 lying behind the cluster.

The CMDs of the two clusters (a CMD of NGC 6528 can be found in Feltzing & Johnson 2002) correlate well with the number of variables found. Both clusters have very few stars in the instability strip of the horizontal branch. NGC 6652 has very few stars on the RGB, while the RGB of NGC 6528 is comparable to that of NGC 6388.

5. Conclusions

A detailed variability study of 5 metal rich ([Fe/H] > −1) globular clusters; NGC 6388, NGC 6441, NGC 6528, NGC 6638, and NGC 6652; has been performed, by using EMCCD observations with DIA. All previously known variable stars located within our field of view in each of the 5 clusters have been recovered and classified, and numerous previously unknown variables have been discovered.

For three of the clusters; NGC 6388, NGC 6441, and NGC 6652; electronically available CMD data from a HST survey have helped in the classification of the variable stars. For the two remaining clusters CMDs exist in the literature. Common for all of the clusters is that the CMDs seem to be in agreement with the number and types of variable stars we have found.

With this article we have further demonstrated the power of using EMCCDs for high-precision time-series photometry in crowded fields and it demonstrates the feasibility of large-scale observing campaigns using these methods.

Acknowledgements. The authors would like to thank Christine Clement for giving invaluable advice on variable star numbering and nomenclature, and Horace Smith for input on RR01 stars. The operation of the Danish 1.54 m telescope is financed by a grant to UGJ from the Danish Natural Science Research Council. We also acknowledge support from the Center of Excellence Centre for Star and Planet Formation (StarPlan) funded by The Danish National Research Foundation. D.M.B. and K.A.A. acknowledge support from NPRP grant # X-019-1-006 from the Qatar National Research Fund (a member of Qatar Foundation). A.A.F. acknowledges the support from DGAPA-UNAM grant through project IN104612. K.A.A., C.L., M.D., K.H. and M.H. acknowledge grant NPRP-09-476-1-78 from the Qatar National Research Fund (a member of Qatar Foundation). CS has received funding from the European Union Seventh Framework Programme (FP7/2007-2013) under grant agreement No. 268421. S.H.G. and X.B.W. would like to thank the financial support from National Natural Science Foundation of China through grants Nos. 10373023, 10773027 and 11333006. T.H. is supported by a Sapere Aude Starting Grant from The Danish Council for Independent Research. T.C.H. acknowledges support from the Korea Research Council of Fundamental Science & Technology (KRCF) via the KRCF Young Scientist Research Fellowship Programme and for financial support from KASI travel grant number 2013-9-400-00. H.K. acknowledges the support from the European Commission under the Marie Curie IEF Programme in FP7. M.R. acknowledges support from FONDECYT postdoctoral fellowship No. 3120097. O.W. (FNRS research fellow) and J. Surdej acknowledge support from the Communauté francaise de Belgique - Actions de recherche concertées – Académie Wallonie-Europe. Some of the data presented in this paper were obtained from the Mikulski Archive for Space Telescopes (MAST). STScI is operated by the Association of Universities for Research in Astronomy, Inc., under NASA contract NAS5-26555. Support for MAST for non-HST data is provided by the NASA Office of Space Science via grant NNX13AC07G and by other grants and contracts.

References

Alard, C. 2000, A&AS, 144, 363
Alard, C., & Lupton, R. H. 1998, ApJ, 503, 325
Albrow, M. D., Horne, K., Bramich, D. M., et al. 2009, MNRAS, 397, 2099
Alcock, C., Allsman, R. A., Alves, D. R., et al. 2000, ApJ, 542, 281
Arellano Ferro, A., Figuera Jaimes, R., Giridhar, S., et al. 2011, MNRAS, 416, 2265
Arellano Ferro, A., Bramich, D. M., Figuera Jaimes, R., et al. 2013a, MNRAS, 434, 1220
Arellano Ferro, A., Bramich, D. M., Giridhar, S., et al. 2013b, Acta Astron., 63, 429
Bessell, M. S. 2005, ARA&A, 43, 293
Bramich, D. M. 2008, MNRAS, 386, L77
Bramich, D. M., Figuera Jaimes, R., Giridhar, S., & Arellano Ferro, A. 2011, MNRAS, 413, 1275
Bramich, D. M., Horne, K., Albrow, M. D., et al. 2013, MNRAS, 428, 2275
Cacciari, C., Corwin, T. M., & Carney, B. W. 2005, AJ, 129, 267
Calamida, A., Bono, G., Lagioia, E. P., et al. 2014, A&A, 565, A8
Clement, C. M., & Shelton, I. 1997, AJ, 113, 1711
Clement, C. M., Muzzin, A., Dufton, Q., et al. 2001, AJ, 122, 2587
Clementini, G., Corwin, T. M., Carney, B. W., & Sumerel, A. N. 2004, AJ, 127, 938
Coomber, G., Heinke, C. O., Cohn, H. N., Lugger, P. M., & Grindlay, J. E. 2011, ApJ, 735, 95
Corwin, T. M., Sumerel, A. N., Pritzl, B. J., et al. 2006, AJ, 132, 1014
Deutsch, E. W., Margon, B., & Anderson, S. F. 1998, AJ, 116, 1301
Deutsch, E. W., Margon, B., & Anderson, S. F. 2000, ApJ, 530, L21
Djorgovski, S. 1995, in HST Proposal, 6095
Draper, P. W. 2000, in Astronomical Data Analysis Software and Systems IX, eds. N. Manset, C. Veillet, & D. Crabtree, ASP Conf. Ser., 216, 615
Dworetsky, M. M. 1983, MNRAS, 203, 917
Engel, M. C., Heinke, C. O., Sivakoff, G. R., Elshamouty, K. G., & Edmonds, P. D. 2012, ApJ, 747, 119
Feltzing, S. 2000, in HST Proposal, 8696
Feltzing, S., & Johnson, R. A. 2002, A&A, 385, 67
Figuera Jaimes, R., Arellano Ferro, A., Bramich, D. M., Giridhar, S., & Kuppuswamy, K. 2013, A&A, 556, A20
Fourcade, C. R., Laborde, J. R., & Albarraciin, J. D. 1964, Boletin de la Asociacion Argentina de Astronomia La Plata Argentina, 8, 23
Harpsøe, K. B. W., Jørgensen, U. G., Andersen, M. I., & Grundahl, F. 2012, A&A, 542, A23
Harris, W. E. 1996, AJ, 112, 1487
Hazen, M. L. 1989, AJ, 97, 771
Hazen, M. L., & Hesser, B. H. 1986, AJ, 92, 1094
Heinke, C. O., Edmonds, P. D., & Grindlay, J. E. 2001, ApJ, 562, 363
Hesser, J. E., & Hartwick, F. D. A. 1976, ApJ, 203, 97
Kains, N., Bramich, D. M., Figuera Jaimes, R., et al. 2012, A&A, 548, A92
Kains, N., Bramich, D. M., Arellano Ferro, A., et al. 2013, A&A, 555, A36
Kunder, A., Stetson, P. B., Catelan, M., Walker, A. R., & Amigo, P. 2013, AJ, 145, 33
Law, N. M., Mackay, C. D., & Baldwin, J. E. 2006, A&A, 446, 739
Layden, A. C., Ritter, L. A., Welch, D. L., & Webb, T. M. A. 1999, AJ, 117, 1313
Lloyd Evans, T., & Menzies, J. W. 1973, in Variable Stars in Globular Clusters and in Related Systems, ed. J. D. Fernie, Astrophys. Space Sci. Lib., 36, IAU Colloq. 21, 151
Lloyd Evans, T., & Menzies, J. W. 1977, MNRAS, 178, 163
Mackay, C. D., Baldwin, J., Law, N., & Warner, P. 2004, in SPIE Conf. Ser. 5492, eds. A. F. M. Moorwood, & M. Iye, 128
Oosterhoff, P. T. 1939, The Observatory, 62, 104
Ortolani, S., Bica, E., & Barbuy, B. 1992, A&AS, 92, 441
Percy, J. R. 2007, Understanding Variable Stars (Cambridge University Press)
Percy, J. R., & Brekelmans, T. 2014 [arXiv:1407.4429]
Piotto, G. 1999, in HST Proposal, 8118
Piotto, G., King, I. R., Djorgovski, S. G., et al. 2002, A&A, 391, 945
Plaut, L. 1971, A&AS, 4, 75
Pritzl, B., Smith, H. A., Catelan, M., & Sweigart, A. V. 2000, ApJ, 530, L41
Pritzl, B. J., Smith, H. A., Catelan, M., & Sweigart, A. V. 2001, AJ, 122, 2600
Pritzl, B. J., Smith, H. A., Catelan, M., & Sweigart, A. V. 2002, AJ, 124, 949
Pritzl, B. J., Smith, H. A., Stetson, P. B., et al. 2003, AJ, 126, 1381
Richtler, T., Grebel, E. K., Subramaniam, A., & Sagar, R. 1998, A&AS, 127, 167
Roediger, J. C., Courteau, S., Graves, G., & Schiavon, R. P. 2014, ApJS, 210, 10
Rutily, B., & Terzan, A. 1977, A&AS, 30, 315
Samus, N. N., Durlevich, O. V., & et al. 2009, VizieR Online Data Catalog: I/2025
Sarajedini, A., Bedin, L. R., Chaboyer, B., et al. 2007, AJ, 133, 1658
Sawyer Hogg, H. 1973, Publications of the David Dunlap Observatory, 3, 6
Sawyer Hogg, H., Rutily, B., & Terzan, A. 1974, Académie des Sciences Paris Comptes Rendus Serie B Sciences Physiques, 279, 333
Silbermann, N. A., Smith, H. A., Bolte, M., & Hazen, M. L. 1994, AJ, 107, 1764
Skottfelt, J., Bramich, D. M., Figuera Jaimes, R., et al. 2013, A&A, 553, A111
Skottfelt, J., Bramich, D. M., Hundertmark, M., et al. 2015, A&A, in press, DOI: 10.1051/0004-6361/201425260
Smith, H. A. 1995, RR Lyrae Stars Cambridge Astrophysics Series (Cambridge University Press), 27
Smith, A., Bailey, J., Hough, J. H., & Lee, S. 2009, MNRAS, 398, 2069
Stacey, W. S., Heinke, C. O., Cohn, H. N., Lugger, P. M., & Bahramian, A. 2012, ApJ, 751, 62
Stellingwerf, R. F. 1978, ApJ, 224, 953
Stetson, P. B. 1987, PASP, 99, 191
Stetson, P. B. 1994, PASP, 106, 250
Terzan, A. 1968, Publications of the Observatoire Haute-Provence, 9, 24

[1] Niels Bohr Institute, University of Copenhagen, Juliane Maries Vej 30, 2100 København Ø, Denmark
e-mail: skottfelt@nbi.dk
[2] Centre for Star and Planet Formation, Natural History Museum, University of Copenhagen, Østervoldgade 5–7, 1350 København K, Denmark
[3] Qatar Environment and Energy Research Institute, Qatar Foundation, Tornado Tower, Floor 19, PO Box 5825, Doha, Qatar
[4] European Southern Observatory, Karl-Schwarzschild-Straße 2, 85748 Garching bei München, Germany

[5] SUPA, School of Physics and Astronomy, University of St. Andrews, North Haugh, St Andrews, KY16 9SS, UK
[6] Space Telescope Science Institute, 3700 San Martin Drive, Baltimore, MD 21218, USA
[7] Instituto de Astronomía Universidad Nacional Autónomade Mexico, 04510 Mexico, Mexico
[8] Dipartimento di Fisica "E. R. Caianiello", Università di Salerno, via Giovanni Paolo II 132, 84084-Fisciano (SA), Italy
[9] Istituto Nazionale di Fisica Nucleare, Sezione di Napoli, 680126 Napoli, Italy
[10] NASA Exoplanet Science Institute, MS 100-22, California Institute of Technology, Pasadena CA 91125, USA
[11] Istituto Internazionale per gli Alti Studi Scientifici (IIASS), 84019 Vietri Sul Mare (SA), Italy
[12] Max Planck Institute for Astronomy, Königstuhl 17, 69117 Heidelberg, Germany
[13] Yunnan Observatories, Chinese Academy of Sciences, 650011 Kunming, PR China
[14] Key Laboratory for the Structure and Evolution of Celestial Objects, Chinese Academy of Sciences, Kunming 650011, PR China
[15] Korea Astronomy and Space Science Institute, 305-348 Daejeon, Republic of Korea
[16] Finnish Centre for Astronomy with ESO (FINCA), University of Turku, Väisäläntie 20, 21500 Piikkiö, Finland
[17] Instituto de Astrofísica, Facultad de Física, Pontificia Universidad Católica de Chile, Av. Vicuña Mackenna 4860, 7820436 Macul, Santiago, Chile
[18] Department of Physics, Sharif University of Technology, PO Box 11155-9161, Tehran, Iran
[19] Astronomisches Rechen-Institut, Zentrum für Astronomie der Universität Heidelberg, Mönchhofstr. 12-14, 69120 Heidelberg, Germany
[20] Planetary and Space Sciences, Department of Physical Sciences, The Open University, Milton Keynes, MK7 6AA, UK
[21] Max-Planck-Institute for Solar System Research, Justus-von-Liebig-Weg 3, 37077 Göttingen, Germany
[22] Astrophysics Group, Keele University, Staffordshire, ST5 5BG, UK
[23] Las Cumbres Observatory Global Telescope Network, 6740 Cortona Drive, Suite 102, Goleta, CA 93117, USA
[24] Institut d'Astrophysique et de Géophysique, Université de Liège, Allée du 6 Août, Bât. B5c, 4000 Liège, Belgium

Monthly Notices of the ROYAL ASTRONOMICAL SOCIETY

MNRAS 444, 776–789 (2014) doi:10.1093/mnras/stu1492

High-precision photometry by telescope defocussing – VI. WASP-24, WASP-25 and WASP-26★

John Southworth,[1†] T. C. Hinse,[2] M. Burgdorf,[3] S. Calchi Novati,[4,5] M. Dominik,[6‡] P. Galianni,[6] T. Gerner,[7] E. Giannini,[7] S.-H. Gu,[8,9] M. Hundertmark,[6] U. G. Jørgensen,[10] D. Juncher,[10] E. Kerins,[11] L. Mancini,[12] M. Rabus,[13,12] D. Ricci,[14] S. Schäfer,[15] J. Skottfelt,[10] J. Tregloan-Reed,[1,16] X.-B. Wang,[8,9] O. Wertz,[17] K. A. Alsubai,[18] J. M. Andersen,[10,19] V. Bozza,[4,20] D. M. Bramich,[18] P. Browne,[6] S. Ciceri,[12] G. D'Ago,[4,20] Y. Damerdji,[17] C. Diehl,[7,21] P. Dodds,[6] A. Elyiv,[22,17,23] X.-S. Fang,[8,9] F. Finet,[17,24] R. Figuera Jaimes,[6,25] S. Hardis,[10] K. Harpsøe,[10] J. Jessen-Hansen,[26] N. Kains,[27] H. Kjeldsen,[26] H. Korhonen,[28,10] C. Liebig,[6] M. N. Lund,[26] M. Lundkvist,[26] M. Mathiasen,[10] M. T. Penny,[29] A. Popovas,[10] S. Prof.,[7] S. Rahvar,[30] K. Sahu,[27] G. Scarpetta,[5,4,20] R. W. Schmidt,[7] F. Schönebeck,[7] C. Snodgrass,[31] R. A. Street,[32] J. Surdej,[17] Y. Tsapras[32,33] and C. Vilela[1]

Affiliations are listed at the end of the paper

Accepted 2014 July 23. Received 2014 July 22; in original form 2014 May 28

ABSTRACT

We present time series photometric observations of 13 transits in the planetary systems WASP-24, WASP-25 and WASP-26. All three systems have orbital obliquity measurements, WASP-24 and WASP-26 have been observed with *Spitzer*, and WASP-25 was previously comparatively neglected. Our light curves were obtained using the telescope-defocussing method and have scatters of 0.5–1.2 mmag relative to their best-fitting geometric models. We use these data to measure the physical properties and orbital ephemerides of the systems to high precision, finding that our improved measurements are in good agreement with previous studies. High-resolution *Lucky Imaging* observations of all three targets show no evidence for faint stars close enough to contaminate our photometry. We confirm the eclipsing nature of the star closest to WASP-24 and present the detection of a detached eclipsing binary within 4.25 arcmin of WASP-26.

Key words: stars: fundamental parameters – planetary systems – stars: individual: WASP-24 – stars: individual: WASP-25 – stars: individual: WASP-26.

1 INTRODUCTION

Whilst there are over 1000 extrasolar planets now known, much of our understanding of these objects rests on those which transit their parent star. For these exoplanets only is it possible to measure their radius and true mass, allowing the determination of their surface gravity and density, and thus inference of their internal structure and formation processes.

A total of 1137[1] transiting extrasolar planets (TEPs) are now known, but only a small fraction of these have high-precision measurements of their physical properties. Of these 1150 planets, 58 have mass and radius measurements to 5 per cent precision, and only eight to 3 per cent precision.

The two main limitations to the high-fidelity measurements of the masses and radii of TEPs are the precision of spectroscopic radial velocity (RV) measurements (mainly affecting objects discovered using the *CoRoT* and *Kepler* satellites) and the quality of the transit light curves (for objects discovered via ground-based facilities). Whilst the former problem is intractable with current instrumentation, the latter problem can be solved by obtaining high-precision transit light curves of TEP systems which are bright enough for high-precision spectroscopic observations to be available.

We are therefore undertaking a project to characterize bright TEPs visible from the Southern hemisphere, using the 1.54 m Danish Telescope in defocussed mode. In this work, we present transit light curves of three targets discovered by the SuperWASP project (Pollacco et al. 2006). From these, and published spectroscopic analyses, we measure their physical properties and orbital ephemerides to high precision.

★Based on data collected by MiNDSTEp with the Danish 1.54 m telescope at the ESO La Silla Observatory.

†E-mail: astro.js@keele.ac.uk

‡Royal Society University Research Fellow.

[1] Data taken from the Transiting Extrasolar Planet Catalogue (TEPCat) available at http://www.astro.keele.ac.uk/jkt/tepcat/ on 2014/07/16.

1.1 WASP-24

This planetary system was discovered by Street et al. (2010) and consists of a Jupiter-like planet (mass $1.2M_{\rm Jup}$ and radius $1.3R_{\rm Jup}$) on a circular orbit around a late-F star (mass $1.2\,{\rm M}_{\odot}$ and radius $1.3\,{\rm R}_{\odot}$) every 2.34 d. The comparatively short orbital period and hot host star means that WASP-24 b has a high equilibrium temperature of 1800 K. Street et al. (2010) obtained photometry of eight transits, of which three were fully observed, from the Liverpool, Faulkes North and Faulkes South telescopes (LT, FTN and FTS). The nearest star to WASP-24 (21.2 arcsec) was found to be an eclipsing binary system with 0.8 mag deep eclipses on a possible period of 1.156 d.

Simpson et al. (2011) obtained high-precision RVs of one transit using the HARPS spectrograph. From modelling of the Rossiter–McLauglin (RM) effect (McLaughlin 1924; Rossiter 1924), they found a projected spin–orbit alignment angle $\lambda = -4\overset{\circ}{.}7 \pm 4\overset{\circ}{.}0$. This is consistent with WASP-24 b having zero orbital obliquity.

Smith et al. (2012) presented observations of two occultations (at 3.6 and 4.5 μm) with the *Spitzer* space telescope. These data were used to constrain the orbital eccentricity to be $e < 0.039$ (3σ), but were not sufficient to determine whether WASP-24 b possesses an atmospheric inversion layer. Smith et al. (2012) also observed one transit in the Strömgren u and y passbands with the BUSCA multiband imager (see Southworth et al. 2012) and provided new measurements of the physical properties of the system.

Knutson et al. (2014) studied the orbital motion of WASP-24 over 3.5 yr using high-precision RVs from multiple telescopes. They found no evidence for orbital eccentricity or for a long-term drift attributable to a third body in the system. Finally, Sada et al. (2012) obtained one transit light curve of WASP-24, and spectral analyses of the host star have been performed by Torres et al. (2012) and Mortier et al. (2013).

1.2 WASP-25

WASP-25 (Enoch et al. 2011) is a comparatively unstudied system containing a low-density transiting planet (mass $0.6M_{\rm Jup}$, radius $1.2R_{\rm Jup}$) orbiting a solar-like star (mass $1.1\,{\rm M}_{\odot}$, radius $0.9\,{\rm R}_{\odot}$) every 3.76 d. Their follow-up observations included two transits, one observed with FTS and one with the Euler telescope. Brown et al. (2012) observed one transit with HARPS, detecting the RM effect and finding $\lambda = 14\overset{\circ}{.}6 \pm 6\overset{\circ}{.}7$. They deduced that this is consistent with an aligned orbit, using the Bayesian Information Criterion.

Maxted, Koen & Smalley (2011) measured the effective temperature ($T_{\rm eff}$) of WASP-25 A using the infrared flux method. Mortier et al. (2013) obtained the spectral parameters of the star from high-resolution spectroscopy.

1.3 WASP-26

WASP-26 was discovered by Smalley et al. (2010) and contains a typical hot Jupiter (mass $1.0M_{\rm Jup}$, radius $1.2R_{\rm Jup}$) orbiting a G0 V star (mass $1.1\,{\rm M}_{\odot}$, radius $1.3\,{\rm R}_{\odot}$) in a circular 2.75 d orbit. WASP-26 has a common-proper-motion companion at 15 arcsec which is roughly 2.5 mag fainter than the planet host star. Smalley et al. (2010) observed one transit of WASP-26 with FTS and one with a large scatter with FTN.

Anderson et al. (2011) obtained high-precision RVs using HARPS through one transit of WASP-26, but their data were insufficient to allow detection of the RM effect. They also observed a transit with a 35 cm telescope; the data are too scattered to be useful for the current work. Albrecht et al. (2012) observed a spectroscopic transit using Keck/HIRES and made a low-confidence detection of the RM effect resulting in $\lambda = -34^{\circ}{}^{+36^{\circ}}_{-26^{\circ}}$.

Mahtani et al. (2013) observed two occultations, at 3.6 and 4.5 μm, using *Spitzer*. They were unable to distinguish whether the planet has an atmosphere with or without a thermal inversion, but could conclude that the orbit was likely circular with $e < 0.04$ at 3σ confidence. Mahtani et al. (2013) also presented light curves of a transit taken in the g, r and i filters, using BUSCA.

Maxted et al. (2011) measured the $T_{\rm eff}$ of WASP-26 A using the infrared flux method. Mortier et al. (2013) determined the atmospheric parameters of the star from high-resolution spectroscopy.

2 OBSERVATIONS AND DATA REDUCTION

2.1 Observations

All observations were taken with the DFOSC (Danish Faint Object Spectrograph and Camera) instrument mounted on the 1.54 m Danish Telescope at ESO La Silla, Chile. This setup yields a field of view of 13.7 arcmin ×13.7 arcmin at a plate scale of 0.39 arcsec pixel^{-1}. We defocussed the telescope in order to improve the precision and efficiency of our observations (see Southworth et al. 2009a for detailed signal-to-noise calculations). We windowed the CCD in order to lower the amount of observing time lost to readout. The autoguider was used to maintain pointing, resulting in a drift of no more than five pixels through individual observing sequences. Most nights were photometric. An observing log is given in Table 1 and the final light curves are plotted in Fig. 1. The data were taken through either a Bessell R or Bessell I filter.

Two of our light curves do not have full coverage of a transit. We missed the start of the transit of WASP-24 on 2013/05/22 due to telescope pointing restrictions. Parts of the transit of WASP-25 on 2010/06/13 were lost to technical problems and then cloud. Finally, data for one transit of WASP-24 and one of WASP-26 extend only slightly beyond egress as high winds demanded closure of the telescope dome.

2.2 Telescope and instrument upgrades

Up to and including the 2011 observing season, the CCD in DFOSC was operated with a gain of ∼1.4 ADU per e$^-$, a readout noise of ∼4.3 e$^-$ and 16-bit digitization. As part of a major overhaul of the Danish telescope, a new CCD controller was installed for the 2012 season. The CCD is now operated with a much higher gain (∼4.2 ADU per e$^-$) and 32-bit digitization, so the readout noise (∼5.0 e$^-$) is much smaller relative to the number of ADU recorded for a particular star. The onset of saturation with the new CCD controller is at roughly 680 000 ADU (Andersen, private communication).

Downloaded from http://mnras.oxfordjournals.org/ at Royal Library/Copenhagen University Library on December 20, 2015

Table 1. Log of the observations presented in this work. $N_{\rm obs}$ is the number of observations, $T_{\rm exp}$ is the exposure time, $T_{\rm dead}$ is the dead time between exposures, 'Moon illum.' is the fractional illumination of the Moon at the mid-point of the transit and $N_{\rm poly}$ is the order of the polynomial fitted to the out-of-transit data. The aperture radii are target aperture, inner sky and outer sky, respectively.

Target	Date of first obs	Start time (UT)	End time (UT)	$N_{\rm obs}$	$T_{\rm exp}$ (s)	$T_{\rm dead}$ (s)	Filter	Airmass	Moon illum.	Aperture radii (pixels)	$N_{\rm poly}$	Scatter (mmag)
WASP-24	2010 06 16	00:29	06:08	129	120	39	R	1.36 → 1.17 → 2.38	0.275	29 45 80	2	0.454
WASP-24	2011 05 06	02:29	08:07	125	120	42	R	1.47 → 1.17 → 1.77	0.085	30 40 70	2	0.745
WASP-24	2011 06 29	00:03	05:03	113	120	40	R	1.25 → 1.17 → 2.08	0.056	29 40 70	2	0.959
WASP-24	2013 05 22	01:47	05:14	123	80–100	9	I	1.37 → 1.17 → 1.26	0.871	16 28 60	1	0.825
WASP-24	2013 05 29	00:58	05:15	151	80–100	16	I	1.46 → 1.17 → 1.33	0.785	17 26 50	1	1.061
WASP-24	2013 06 05	00:51	05:48	149	100	20	I	1.37 → 1.17 → 1.63	0.111	22 30 50	1	1.185
WASP-25	2010 06 13	23:02	02:42	72	100–120	41	R	1.04 → 1.00 → 1.63	0.035	28 40 65	1	0.494
WASP-25	2013 05 03	02:12	08:00	139	112–122	25	R	1.01 → 1.00 → 2.41	0.417	20 32 70	2	1.040
WASP-25	2013 06 05	23:58	05:17	173	100	9	R	1.02 → 1.00 → 2.07	0.058	22 35 70	1	0.663
WASP-26	2012 09 17	02:26	05:42	222	31–60	46	I	1.33 → 1.03 → 1.04	0.017	20 50 80	1	1.201
WASP-26	2013 08 22	03:39	08:17	124	120	14	I	1.43 → 1.03 → 1.45	0.980	18 50 80	1	0.689
WASP-26	2013 09 02	04:11	09:29	153	100	25	I	1.17 → 1.03 → 1.47	0.101	20 55 80	2	0.621
WASP-26	2013 09 12	03:36	09:16	393	30	25	I	1.15 → 1.03 → 1.69	0.567	14 50 80	1	1.029

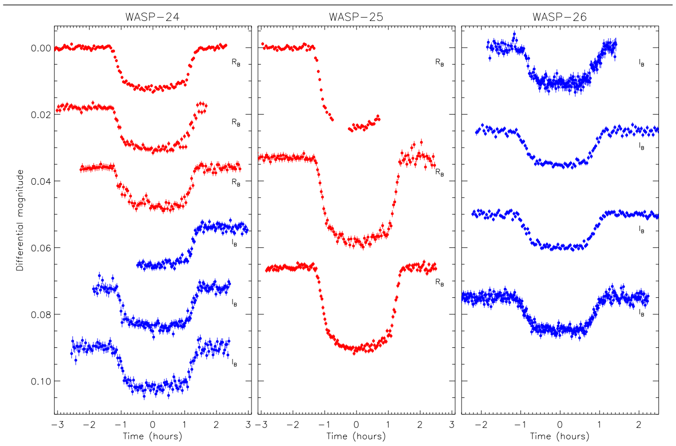

Figure 1. Light curves presented in this work, in the order they are given in Table 1. Times are given relative to the mid-point of each transit, and the filter used is indicated. Blue and red filled circles represent observations through the Bessell R and I filters, respectively.

For the current project, we aimed for a maximum pixel count rate of between 250 000 and 350 000 ADU, in order to ensure that we stayed well below the threshold for saturation. The effect of this is that less defocussing was required due to the greater dynamic range of the CCD controller, so the object apertures for the 2012 and 2013 season are smaller than those for the 2010 and 2011 seasons. The lesser importance of readout noise also means that the CCD could be read out more quickly, so the newer data have a higher observational cadence. These effects are visible in Table 1.

2.3 Aperture photometry

The data were reduced using the DEFOT pipeline, which is written in IDL[2] and uses routines from the ASTROLIB library.[3] DEFOT has undergone several modifications since its first use (Southworth et al. 2009a) and we review these below.

The first modification is that pointing changes due to telescope guiding errors are measured by cross-correlating each image against a reference image, using the following procedure. First, the image in question and the reference image are each collapsed in the x and y directions, whilst avoiding areas affected by a significant number of bad pixels. The resulting one-dimensional arrays are each divided by a robust polynomial fit, where the quantity minimized is the mean-absolute-deviation rather than the usual least squares. The x and y arrays are then cross-correlated, and Gaussian functions are fitted to the peaks of the cross-correlation functions in order to measure the spatial offset. The photometric apertures are then shifted by the measured amounts in order to track the motion of the stellar images across the CCD.

This modification has been in routine use since our analysis of WASP-2 (Southworth et al. 2010). It performs extremely well as long as there is no field rotation during observations. It is much easier to track offsets between entire images rather than the alternative of following the positions of individual stars in the images, as the point spread functions (PSFs) are highly non-Gaussian so their centroids are difficult to measure.[4]

Aperture photometry was performed by the DEFOT pipeline using the APER algorithm from the ASTROLIB implementation of the DAOPHOT package (Stetson 1987). We placed the apertures by hand on the target and comparison stars, and tried a wide range of sizes for all three apertures. For our final light curves, we used the aperture sizes which yielded the most precise photometry, measured versus a fitted transit model (see below). We find that different choices of aperture size do affect the photometric precision but do not yield differing transit shapes. The aperture sizes are reported in Table 1.

2.4 Bias and flat-field calibrations

Master bias and flat-field calibration frames were constructed for each observing season, by median-combining large numbers of individual bias and twilight-sky images. For each observing sequence, we tested whether their inclusion in the analysis produces photometry with a lower scatter. Inclusion of the master bias image was found to have a negligible effect in all cases, whereas using a master flat-field can either aid or hinder the quality of the resulting photometry. It only led to a significant improvement in the scatter of the light curve for the observation of WASP-24 on 2010/06/16. It is probably not a coincidence that this data set yielded the least scattered light curve either with or without flat-fielding.

We attribute the divergent effects of flat-fielding to the varying relative importance of the advantages and disadvantages of the calibration process. The main advantage is that variations in pixel efficiency, which occur on several spatial scales, can be compensated for. Small-scale variations (i.e. variations between adjacent pixels) average down to a low level as our defocussed PSFs cover of the order of 1000 pixels, so this effect is unimportant. Large-scale variations (e.g. differing illumination levels over the CCD) are usually dealt with by autoguiding the telescope – flat-fielding is in general more important for cases when the telescope tracking is poor. The disadvantages of the standard approach to flat-fielding are (1) the master flat-field image has Poisson noise which is propagated into the science images; (2) pixel efficiency depends on wavelength, so observations of red stars are not properly calibrated using observations of a blue twilight sky; (3) pixel efficiency depends on the number of counts, which is in general different for the science and the calibration observations.

[2] The acronym IDL stands for Interactive Data Language and is a trademark of ITT Visual Information Solutions. For further details see http://www.ittvis.com/ProductsServices/IDL.aspx.

[3] The ASTROLIB subroutine library is distributed by NASA. For further details see http://idlastro.gsfc.nasa.gov/.

[4] See Nikolov et al. (2013) for one way of determining the centroid of a highly defocussed PSF.

Downloaded from http://mnras.oxfordjournals.org/ at Royal Library/Copenhagen University Library on December 20, 2015

Table 2. Excerpts of the light curves presented in this work. The full data set will be made available at the CDS.

Target	Filter	BJD(TDB)	Diff. mag.	Uncertainty
WASP-24	R	2455364.525808	− 0.00079	0.00054
WASP-24	R	2455364.527590	− 0.00018	0.00053
WASP-24	R	2455364.529430	− 0.00001	0.00055
WASP-25	R	2455361.464729	− 0.00113	0.00052
WASP-25	R	2455361.466882	0.00019	0.00051
WASP-25	R	2455361.469289	− 0.00049	0.00051
WASP-26	I	2456187.608599	− 0.00016	0.00101
WASP-26	I	2456187.609444	− 0.00161	0.00103
WASP-26	I	2456187.611111	0.00316	0.00103

2.5 Light-curve generation

The instrumental magnitudes of the target and comparison stars were converted into differential-magnitude light curves normalized to zero magnitude outside transit, using the following procedure. For each observing sequence, an ensemble comparison star was constructed by adding the fluxes of all good comparison stars with weights adjusted to give the lowest possible scatter for the data taken outside transit. The normalization was performed by fitting a polynomial to the out-of-transit data points. We used a first-order polynomial when possible, as this cannot modify the shape of the transit, but switched to a second-order polynomial when the observations demanded. The weights of the comparison stars and the coefficients were optimized simultaneously to yield the final differential-magnitude light curve. The order of the polynomial used for each data set is given in Table 1.

In the original version of the DEFOT pipeline, the optimization of the weights and coefficients was performed using the IDL AMOEBA routine, which is an implementation of the downhill simplex algorithm of Nelder & Mead (1965). We have found that this routine can suffer from irreproducibility of results, primarily as it is prone to getting trapped in local minima. We have therefore modified DEFOT to use the MPFIT implementation of the Levenberg–Marquardt algorithm (Markwardt 2009). We find the fitting process to be much faster and more reliable when using MPFIT compared to using AMOEBA.

The timestamps for the data points have been converted to the BJD(TDB) time-scale (Eastman, Siverd & Gaudi 2010). Manual time checks were obtained for several frames and the FITS file timestamps were confirmed to be on the UTC system to within a few seconds. The timings therefore appear not to suffer from the same problems as previously found for WASP-18 and suspected for WASP-16 (Southworth et al. 2009b, 2013). The light curves are shown in Fig. 1. The reduced data are enumerated in Table 2 and will be made available at the CDS.[5]

3 HIGH-RESOLUTION IMAGING

For each object, we obtained well-focused images with DFOSC in order to check for faint nearby stars whose light might have

[5] http://vizier.u-strasbg.fr/

Downloaded from http://mnras.oxfordjournals.org/ at Royal Library/Copenhagen University Library on December 20, 2015

contaminated that from our target star. Such objects would dilute the transit and cause us to underestimate the radius of the planet (Daemgen et al. 2009). The worst-case scenario is a contaminant which is an eclipsing binary, as this would render the planetary nature of the system questionable.

For WASP-24, we find nearby stars at 43 and 55 pixels (16.8 and 21.5 arcsec), which are more than 7.6 and 4.5 mag fainter than the target star in the *R* filter. Precise photometry is not available for the focused images as WASP-24 itself is saturated to varying degrees. We estimate that the star at 43 pixels contributes less than 0.01 per cent of the flux in the inner aperture of WASP-24, which is much too small to affect our results. The star at 55 pixels is an eclipsing binary (see Section 7) but its PSF was always clearly separated from that of WASP-24 so it also contributes an unmeasurably small amount of flux to the inner aperture of WASP-24.

For WASP-25, the nearest star is at 94 pixels and is 5.36 mag fainter than our target. The inner aperture for WASP-25 is significantly smaller than this distance, so the presence of the nearby star has a negligible effect on our photometry. For WASP-26, there is a known star which is 39 pixels (15.2 arcsec) away from the target and 2.55 mag fainter in our images. The object and sky apertures in Section 2 were selected such that this star was in no-man's land between them, and thus had an insignificant effect on our photometry.

In order to search for stars which are very close to our target systems, we obtained high-resolution images of all three targets using the Lucky Imager (LI) mounted on the Danish telescope. The LI uses an Andor 512 × 512 pixel electron-multiplying CCD, with a pixel scale of 0.09 arcsec pixel^{-1} and a field of view of 45 arcsec × 45 arcsec. The data were reduced using a dedicated pipeline and the best 2 per cent of images were stacked together to yield combined images whose PSF is smaller than the seeing limit. A long-pass filter was used, resulting in a response which approximates that of SDSS $i + z$ (Skottfelt et al. 2013). Exposure times of 120, 220 and 109 s were used for WASP-24, WASP-25 and WASP-26, respectively. The LI observations are thus shallower than the focused DFOSC images, but have a better resolution. A detailed examination of different high-resolution imaging approaches was recently given by Lillo-Box, Barrado & Bouy (2014).

The central parts of the images are shown in Figs 2 and 3. The image for WASP-24 has a PSF full width at half-maximum of 4.1 pixels in *x* (pixel column) and 4.8 pixels in *y* (pixel row), corresponding to 0.37 arcsec× 0.43 arcsec. The image of WASP-25 is nearly as good (4.2 × 5.3 pixels), and that for WASP-26 is better (3.8 × 4.4 pixels). None of the images show any stars which were undetected on our focused DFOSC observations, so we find no evidence for contaminating light in the PSFs of the targets. There is a suggestion of a very faint star north-east of WASP-24, but this was not confirmed

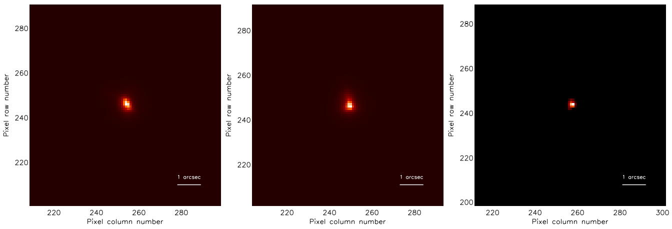

Figure 2. High-resolution Lucky Imaging observations of WASP-24 (left), WASP-25 (middle) and WASP-26 (right). In each case, an image covering 8 arcsec × 8 arcsec and centred on our target star is shown. A bar of length 1 arcsec is superimposed in the bottom right of each image. The flux scale is linear. Each image is a sum of the best 2 per cent of the original images, so the effective exposure times are 2.4, 4.4 and 2.1 s, respectively.

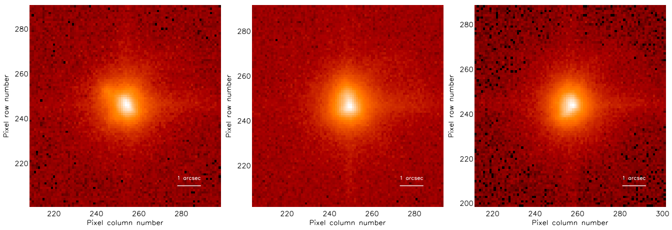

Figure 3. Same as Fig. 2, except that the flux scale is logarithmic so faint stars are more easily identified.

Table 3. Times of minimum light and their residuals versus the ephemeris derived in this work.

Target	Time of minimum (BJD/TDB)	Uncertainty (d)	Cycle number	Residual (d)	Reference
WASP-24	2455081.38018	0.000 17	−259.0	0.000 44	Street et al. (2010)
WASP-24	2455308.47842	0.001 51	−162.0	0.000 17	Ayiomamitis (TRESCA)
WASP-24	2455308.48020	0.001 63	−162.0	0.001 95	Brát (TRESCA)
WASP-24	2455322.52496	0.000 74	−156.0	−0.000 61	This work (BUSCA *u* band)
WASP-24	2455322.52498	0.000 49	−156.0	−0.000 59	This work (BUSCA *y* band)
WASP-24	2455364.66718	0.000 24	−138.0	−0.000 38	This work (Danish Telescope)
WASP-24	2455687.75622	0.000 38	0.0	0.000 06	This work (Danish Telescope)
WASP-24	2455701.80338	0.000 49	6.0	−0.000 11	Sada et al. (2012)
WASP-24	2455741.60468	0.000 52	23.0	0.000 42	This work (Danish Telescope)
WASP-24	2456010.84351	0.000 52	138.0	−0.001 25	Wallace et al. (TRESCA)
WASP-24	2456010.84412	0.000 62	138.0	−0.000 64	Wallace et al. (TRESCA)
WASP-24	2456408.85005	0.002 57	308.0	−0.002 40	Garlitz (TRESCA)
WASP-24	2456441.63058	0.000 42	322.0	0.001 02	This work (Danish Telescope)
WASP-24	2456448.65324	0.000 49	325.0	0.000 02	This work (Danish Telescope)
WASP-25	2455274.99726	0.000 21	−163.0	0.000 15	Enoch et al. (2011)
WASP-25	2455338.99804	0.000 75	−146.0	−0.001 23	Curtis (TRESCA)
WASP-25	2455659.01066	0.001 18	−61.0	0.000 61	Curtis (TRESCA)
WASP-25	2455677.83276	0.000 78	−56.0	−0.001 45	Evans (TRESCA)
WASP-25	2456415.74114	0.000 21	140.0	−0.000 28	This work
WASP-25	2456430.80140	0.000 63	144.0	0.000 65	Evans (TRESCA)
WASP-25	2456449.62499	0.000 12	149.0	0.000 08	This work
WASP-26	2455123.63867	0.000 70	−259.0	−0.000 86	Smalley et al. (2010)
WASP-26	2455493.02404	0.001 83	−125.0	0.000 48	Curtis (TRESCA)
WASP-26	2456187.68731	0.000 43	127.0	0.001 25	This work
WASP-26	2456526.74716	0.000 41	250.0	−0.000 36	This work
WASP-26	2456537.77389	0.000 36	254.0	−0.000 02	This work
WASP-26	2456548.79992	0.000 38	258.0	−0.000 38	This work

by a repeat image. If present, its brightness is insufficient to have a significant effect on our analysis.

4 ORBITAL PERIOD DETERMINATION

Our first step was to improve the measured orbital ephemerides of the three TEPs using our new data. Each of our light curves was fitted using the JKTEBOP code (see below) and their error bars were rescaled to give a reduced χ^2 of $\chi^2_\nu = 1.0$ versus the fitted model. This step is necessary as the uncertainties from the APER algorithm tend to be underestimated. We then fitted each revised data set to measure the transit mid-points and ran Monte Carlo simulations to estimate the uncertainties in the mid-points. The two transits with only partial coverage were not included in this analysis, as they yield less reliable timings (e.g. Gibson et al. 2009).

We have collected additional times of transit mid-point from literature sources. Those from the discovery papers (Smalley et al. 2010; Street et al. 2010; Enoch et al. 2011) are on the UTC time-scale (Anderson, private communication) so we converted them to TDB to match our own results. We used the timings from our own fits to the BUSCA light curves presented by Smith et al. (2012) for WASP-24.

We also collated minimum timings from the Exoplanet Transit Database[6] (Poddaný, Brát & Pejcha 2010), which provides data and times of minimum from amateur observers affiliated with TRESCA.[7] We retained only those timing measurements based on light curves where all four contact points of the transit are easily identifiable by eye. We assumed that the times were all on the UTC time-scale and converted them to TDB.

For each object, we fitted the times of mid-transit with straight lines to determine new linear orbital ephemerides. Table 3 gives all transit times plus their residual versus the fitted ephemeris. The uncertainties have been increased to force $\chi^2_\nu = 1.0$, E gives the cycle count versus the reference epoch and the bracketed numbers show the uncertainty in the final digit of the preceding number.

The revised ephemeris for WASP-24 is

$$T_0 = \mathrm{BJD(TDB)}\ 2\,455\,687.75616(16) + 2.3412217(8) \times E,$$

where the error bars have been inflated to account for $\chi^2_\nu = 1.75$. We have adopted one of our timings from the 2011 season as the reference epoch. This is close to the mid-point of the available data so the covariance between the orbital period and the time of reference epoch is small.

Our orbital ephemeris for WASP-25 is

$$T_0 = \mathrm{BJD(TDB)}\ 2\,455\,888.66484(13) + 3.7648327(9) \times E,$$

accounting for $\chi^2_\nu = 1.21$. We have adopted a reference epoch midway between our 2013 data and the timing from the discovery paper.

The new orbital ephemeris for WASP-26 is

$$T_0 = \mathrm{BJD(TDB)}\ 2\,455\,837.59821(44) + 2.7565972(19) \times E,$$

accounting for $\chi^2_\nu = 1.40$ and using a reference epoch in mid-2011. The main contributor to the χ^2_ν is our transit from 2012, which was observed under conditions of poor sky transparency. Whilst a parabolic ephemeris provides a formally better fit to the transit times, this improvement is due almost entirely to our 2012 transit so is not reliable.

[6] The Exoplanet Transit Database (ETD) can be found at http://var2.astro.cz/ETD/credit.php
[7] The TRansiting ExoplanetS and CAndidates (TRESCA) website can be found at http://var2.astro.cz/EN/tresca/index.php

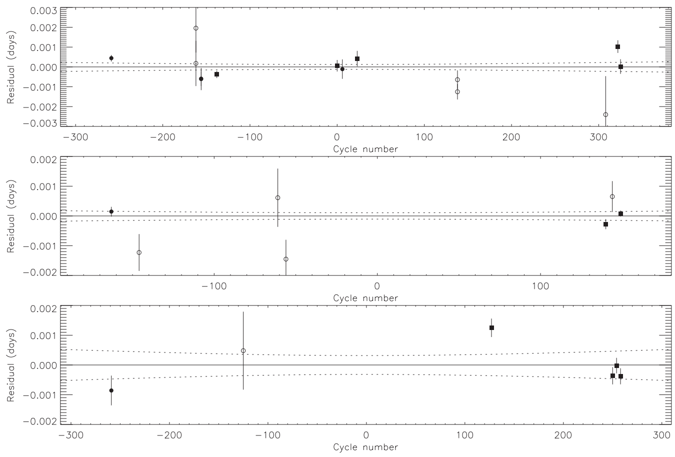

Figure 4. Plot of the residuals of the timings of mid-transit versus a linear ephemeris, for WASP-24 (top), WASP-25 (middle) and WASP-26 (bottom). The results from this work are shown using filled squares, and from amateur observers with open circles. All other timings are shown by filled circles. The dotted lines show the 1σ uncertainty in the ephemeris as a function of cycle number. The error bars have been scaled up to force $\chi^2_\nu = 1.0$.

Fig. 4 shows the residuals versus the linear ephemeris for each of our three targets. No transit timing variations are discernable by eye, and there are insufficient timing measurements to perform a quantitative search for such variations. Our period values for all three systems are consistent with previous measurements but are significantly more precise due to the longer temporal baseline of the available transit timings.

5 LIGHT-CURVE ANALYSIS

We have analysed the light curves using the *Homogeneous Studies* methodology (see Southworth 2012 and references therein), which utilizes the JKTEBOP[8] code (Southworth, Maxted & Smalley 2004) and the NDE model (Nelson & Davis 1972; Popper & Etzel 1981). This represents the star and planet as spheres for the calculation of eclipse shapes and as biaxial spheroids for proximity effects.

The fitted parameters of the model for each system were the fractional radii of the star and planet ($r_{\rm A}$ and $r_{\rm b}$), the orbital inclination (i), limb darkening (LD) coefficients and the reference time of mid-transit. The fractional radii are the ratio between the true radii and the semimajor axis: $r_{\rm A,b} = \frac{R_{\rm A,b}}{a}$. They were expressed as their sum and ratio, $r_{\rm A} + r_{\rm b}$ and $k = \frac{r_{\rm b}}{r_{\rm A}}$, because these two quantities are more weakly correlated. The orbital period was held fixed at the value found in Section 4. We assumed a circular orbit for each system based on the case histories given in Section 1.

Whilst the light curves had already been rectified to zero differential magnitude outside transit, the uncertainties in this process need to be propagated through subsequent analyses. This effect is relatively unimportant for transits with plenty of data before ingress and after egress, as the rectification polynomial is well defined and needs only to be interpolated to the data within transit. It is, however, crucial for partial transits as the rectification polynomial is defined on only a short stretch of data on one side of the transit, which then needs to be extrapolated to all in-transit data. JKTEBOP was therefore modified to allow multiple polynomials to be specified, each operating on only a subset of data within a specific time interval. This allowed multiple light curves to be modelled simultaneously but subject to independent polynomial fits to the out-of-transit data. For each transit, we included as fitted parameters the coefficients of a polynomial of order given in Table 1. We found that the coefficients of the polynomials did not exhibit strong correlations against the other model parameters: the correlation coefficients are normally less than 0.4.

LD was accounted for by each of five LD laws (see Southworth 2008), with the linear coefficients either fixed at

[8] JKTEBOP is written in FORTRAN77 and the source code is available at http://www.astro.keele.ac.uk/jkt/codes/jktebop.html.

theoretically predicted values[9] or included as fitted parameters. We did not calculate fits for both LD coefficients in the four bi-parametric laws as they are very strongly correlated (Carter et al. 2008; Southworth 2008). The non-linear coefficients were instead perturbed by ±0.1 on a flat distribution during the error analysis simulations, in order to account for imperfections in the theoretically predicted coefficients.

Error estimates for the fitted parameters were obtained in several ways. We ran solutions using different LD laws, and also calculated error bars using residual-permutation and Monte Carlo algorithms (Southworth 2008). The final value for each parameter is the unweighted mean of the four values from the solutions using the two-parameter LD laws. Its error bar was taken to be the larger of the Monte Carlo or residual-permutation alternatives, with an extra contribution to account for variations between solutions with the different LD laws. Tables of results for each light curve, including our reanalysis of published data, can be found in the Supplementary Information.

5.1 Results for WASP-24

For WASP-24, we divided our data into two data sets, one for the *R* and one for the *I* filters. For each we calculated solutions for all five LD laws under two scenarios: both LD coefficients fixed ('LD-fixed'), and the linear coefficient fitted whilst the non-linear coefficient was fixed but then perturbed in the error analysis simulations ('LD-fit/fix'). The two data sets give consistent results and show no signs of red noise (the Monte Carlo error bars were similar to or larger than the residual-permutation error bars).

We also modelled published transit light curves of WASP-24. The discovery paper (Street et al. 2010) presented two light curves which covered complete transits, one from the RISE instrument on the LT and one using Merope on the FTN. The RISE data were first binned by a factor of 10 from 3454 to 346 data points to lower the required CPU time. Sada et al. (2012) observed one transit in the *J* band with the KPNO 2.1 m telescope. Smith et al. (2012) obtained photometry of one transit simultaneously in the Strömgren *u* and *y* bands.

We found that red noise was strong in the RISE and KPNO data (see Fig. 5) so the results from these data sets were not included in our final values. The *u*-band data gave exceptionally uncertain results so we also discounted this data set. The photometric results from the LD-fit/fix cases for the remaining four data sets were combined according to weighted means, to obtain the final photometric parameters of WASP-24 (Table 4). We also checked what the values would be had we not rejected any combination of the three least reliable data sets, and found changes of less than half the error bars in all cases.

Table 4 also shows a comparison between our values and literature results. We note that the two previous publications gave inconsistent results (see in particular the respective values for *k*) despite being based on much of the same data. This implies that their error estimates were optimistic. To obtain final values for the photometric parameters of WASP-24, we have calculated the weighted mean of those from individual data sets. The results found in the current work are based on more extensive data and analysis, and should be preferred over previous values.

[9] Theoretical LD coefficients were obtained by bilinear interpolation to the host star's $T_{\rm eff}$ and $\log g$ using the JKTLD code available from http://www.astro.keele.ac.uk/jkt/codes/jktld.html

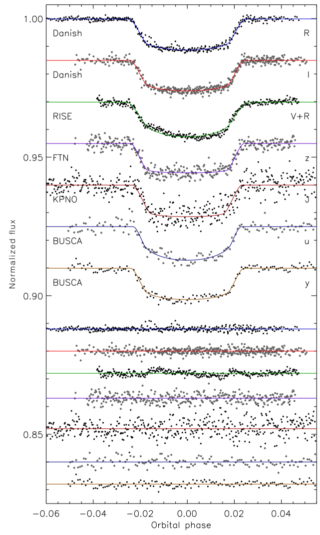

Figure 5. The phased light curves of WASP-24 analysed in this work, compared to the JKTEBOP best fits. The residuals of the fits are plotted at the base of the figure, offset from unity. Labels give the source and passband for each data set. The polynomial baseline functions have been removed from the data before plotting.

5.2 Results for WASP-25

Our three transits were all taken in the Bessell *R* band so were modelled together. We found that red noise was not important and that the data contained sufficient information to fit for the linear LD coefficient. The best fits are plotted in Fig. 6.

Enoch et al. (2011) obtained two transit light curves of WASP-25 in their initial characterization of this object, one from FTS with the Spectral camera and one from the Swiss Euler telescope with EulerCam. For both data sets, we have adopted the LD-fit/fix values. The FTS data have significant curvature outside transit, implying that a quadratic baseline should be included. If this is done, then $r_{\rm A} + r_{\rm b}$ and k become smaller by approximately 1σ and i greater by 1.5σ, yielding the values in Table 5. This change is significantly larger than the error bars quoted by Enoch et al. (2011), which are based primarily on the FTS and the less precise Euler data.

Table 4. Parameters of the fit to the light curves of WASP-24 from the JKTEBOP analysis (top). The final parameters are given in bold and the parameters found by other studies are shown (below). Quantities without quoted uncertainties were not given by those authors but have been calculated from other parameters which were.

Source	$r_A + r_b$	k	$i(°)$	r_A	r_b
Danish Telescope R band	0.1900 ± 0.0057	0.1029 ± 0.0013	83.60 ± 0.50	0.1723 ± 0.0050	0.017 73 ± 0.000 70
Danish Telescope I band	0.1805 ± 0.0077	0.1012 ± 0.0013	84.23 ± 0.72	0.1639 ± 0.0068	0.016 59 ± 0.000 86
Street LT/RISE	0.2028 ± 0.0157	0.1080 ± 0.0044	82.85 ± 1.31	0.1830 ± 0.0135	0.019 76 ± 0.002 13
Street FTN	0.1807 ± 0.0138	0.1011 ± 0.0014	84.12 ± 1.21	0.1642 ± 0.0123	0.016 59 ± 0.001 38
Sada KPNO J band	0.2146 ± 0.0370	0.1090 ± 0.0063	81.34 ± 2.53	0.1935 ± 0.0327	0.021 08 ± 0.004 33
Smith BUSCA u band	0.1556 ± 0.1203	0.0990 ± 0.0061	86.57 ± 3.43	0.1416 ± 0.0212	0.014 01 ± 0.003 12
Smith BUSCA y band	0.1766 ± 0.0173	0.1016 ± 0.0032	84.59 ± 1.90	0.1603 ± 0.0156	0.016 30 ± 0.001 89
Final results	**0.1855 ± 0.0042**	**0.1018 ± 0.0007**	**83.87 ± 0.38**	**0.1684 ± 0.0037**	**0.017 13± 0.000 49**
Street et al. (2010)	0.1866	0.1004 ± 0.0006	83.64 ± 0.31	0.1696	0.017 02
Smith et al. (2012)	0.1922	0.1050 ± 0.0006	83.30 ± 0.30	0.1739 ± 0.0033	0.018 26

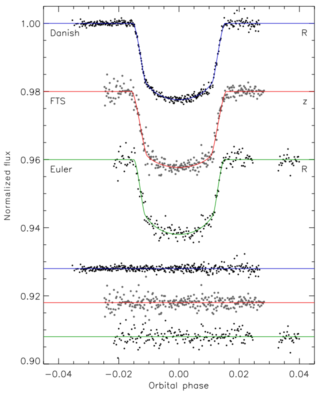

Figure 6. The phased light curves of WASP-25 analysed in this work, compared to the JKTEBOP best fits. The residuals of the fits are plotted at the base of the figure, offset from unity. Labels give the source and passband for each data set. The polynomial baseline functions have been removed from the data before plotting.

5.3 Results for WASP-26

The four transits presented in this work were all taken in the Bessell I band, so were modelled together. We found once again that red noise was not important and that the data contained sufficient information to fit for the linear LD coefficient. The best fit is shown in Fig. 7 and the parameter values are given in Table 6.

Smalley et al. (2010) obtained two transit light curves, one each from FTS/Spectral and FTN/Merope. The former has almost no out-of-transit data, and the latter is very scattered. We modelled the FTS light curve here but did not attempt to extract information from the FTN data. We found that the scatter was dominated by white noise and it was not possible to fit for any LD coefficients.

Mahtani et al. (2013) presented photometry of one transit of WASP-26 obtained simultaneously in the g, r and i bands using BUSCA. We modelled these data sets individually. The g- and r-band data could only support an LD-fixed solution. Red noise was unimportant for g and r but the residual-permutation error bars were a factor of 2.5 greater than the Monte Carlo error bars for i.

Table 6 collects the parameter values found from each light curve. The data from the Danish Telescope are of much higher precision than previous data sets, and yield a solution with larger orbital inclination and smaller fractional radii than obtained in previous studies. Whilst $r_A + r_b$ and i are in overall agreement ($\chi^2_\nu = 1.0$ and 0.8 versus the weighted mean value), k and r_B are not ($\chi^2_\nu = 3.4$ and 1.8). These moderate discrepancies were accounted for by increasing the error bars on the final weighted-mean parameter values, by an amount sufficient to force $\chi^2_\nu = 1.0$.

6 PHYSICAL PROPERTIES

We have measured the physical properties of the three planetary systems using the photometric quantities found in Section 5, published spectroscopic results and five sets of theoretical stellar evolutionary

Table 5. Parameters of the fit to the light curves of WASP-25 from the JKTEBOP analysis (top). The final parameters are given in bold and the parameters found by other studies are shown (below). Quantities without quoted uncertainties were not given by Enoch et al. (2011) but have been calculated from other parameters which were.

Source	$r_A + r_b$	k	$i(°)$	r_A	r_b
Danish Telescope	0.1004 ± 0.0019	0.1384 ± 0.0011	88.33 ± 0.32	0.0882 ± 0.0016	0.012 21 ± 0.000 30
Enoch FTS	0.1072 ± 0.0043	0.1416 ± 0.0026	87.54 ± 0.52	0.0939 ± 0.0036	0.013 28 ± 0.000 67
Enoch Euler	0.1004 ± 0.0067	0.1374 ± 0.0029	88.13 ± 1.37	0.0883 ± 0.0056	0.012 14 ± 0.000 98
Final results	**0.1015 ± 0.0017**	**0.1387 ± 0.0010**	**88.12 ± 0.27**	**0.0891 ± 0.0014**	**0.012 37± 0.000 28**
Enoch et al. (2011)	0.1029	0.1367 ± 0.0007	88.0 ± 0.5	0.09049	0.012 37

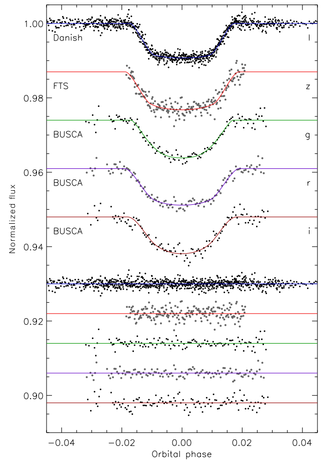

Figure 7. The phased light curves of WASP-26 analysed in this work, compared to the JKTEBOP best fits. The residuals of the fits are plotted at the base of the figure, offset from unity. Labels give the source and passband for each data set. The polynomial baseline functions have been removed from the data before plotting.

models (Claret 2004; Demarque et al. 2004; Pietrinferni et al. 2004; VandenBerg, Bergbusch & Dowler 2006; Dotter et al. 2008). Table 7 gives the spectroscopic quantities adopted from the literature, where K_A denotes the velocity amplitude of the star.

In the case of WASP-24, there are two recent conflicting spectroscopic analyses: Torres et al. (2012) measured $T_{eff} = 6107 \pm 77$ K and $\log g = 4.26 \pm 0.01$ (c.g.s.), whereas Mortier et al. (2013) obtained $T_{eff} = 6297 \pm 58$ K and $\log g = 4.76 \pm 0.17$. We have adopted the former T_{eff} as it agrees with an independent value from

Table 7. Spectroscopic properties of the planet host stars used in the determination of the physical properties of the systems.

Target	T_{eff} (K)	$\left[\frac{Fe}{H}\right]$ (dex)	K_A (m s^{-1})	Ref
WASP-24	6107 ± 77	−0.02 ± 0.10	152.1 ± 3.2	1,1,2
WASP-25	5736 ± 50	0.06 ± 0.05	75.5 ± 5.3	3,3,4
WASP-26	6015 ± 55	−0.02 ± 0.09	138 ± 2	5,6,7

References: (1) Torres et al. (2012); (2) Knutson et al. (2014); (3) Mortier et al. (2013); (4) Enoch et al. (2010); (5) Maxted et al. (2011); (6) Smalley et al. (2010); (7) Mahtani et al. (2013).

Street et al. (2010) and the corresponding $\log g$ is in good agreement with that derived from our own analysis.

For each object, we used the measured values of r_A, r_b, i and K_A, and an estimated value of the velocity amplitude of the planet, K_b, to calculate the physical properties of the system. K_b was then iteratively refined to obtain the best agreement between the calculated $\frac{R_A}{a}$ and the measured r_A, and between the spectroscopic T_{eff} and that predicted by the stellar models for the observed $\left[\frac{Fe}{H}\right]$ and the calculated stellar mass (M_A). This was done for a range of ages in order to determine the overall best fit and age of the system. Further details on the method can be found in Southworth (2009). This process was performed for each of the five sets of theoretical stellar models, in order to estimate the systematic error incurred by the use of stellar theory.

The final physical properties of the three planetary systems are given in Table 8. The equilibrium temperatures of the planets were calculated ignoring the effects of albedo and heat redistribution: $T'_{eq} = T_{eff}\sqrt{\frac{r_A}{2}}$. For each parameter which depends on theoretical models, there are five different values, one from using each of the five model sets. In these cases, we give two error bars: the statistical uncertainty (calculated by propagating the random errors via a perturbation analysis) and the systematic uncertainty (the maximum deviation between the final value and the five values from using the different stellar models).

The intermediate results for each set of stellar models are given in Tables A16– A18, along with a comparison to published values. We find that literature values are in generally good agreement with our own, despite being based on much less extensive follow-up photometry (see Figs 5–7) and less precise spectroscopic properties for the host stars. The uncertainties in the radii of WASP-25 b and WASP-26 b are significantly improved by our new results. The uncertainties in the host star mass and semimajor axis measurements for WASP-24 b and WASP-25 b have a significant contribution from the differences in the theoretical model predictions we used, an issue which was not considered in previous studies of these objects.

Table 6. Parameters of the fit to the light curves of WASP-26 from the JKTEBOP analysis (top). The final parameters are given in bold and the parameters found by other studies are shown (below). Quantities without quoted uncertainties were not given by those authors but have been calculated from other parameters which were.

Source	$r_A + r_b$	k	$i(°)$	r_A	r_b
Danish Telescope	0.1584 ± 0.0044	0.0973 ± 0.0008	83.29 ± 0.32	0.1444 ± 0.0040	0.014 05 ± 0.000 38
Smalley FTS	0.176 ± 0.011	0.1027 ± 0.0044	82.47 ± 0.63	0.160 ± 0.010	0.0164 ± 0.0016
Mahtani g band	0.1733 ± 0.0089	0.1081 ± 0.0029	82.31 ± 0.53	0.1564 ± 0.0077	0.0169 ± 0.0012
Mahtani r band	0.174 ± 0.017	0.1026 ± 0.0042	82.6 ± 1.2	0.158 ± 0.015	0.0162 ± 0.0016
Mahtani i band	0.184 ± 0.035	0.103 ± 0.032	81.5 ± 2.2	0.166 ± 0.020	0.0172 ± 0.0091
Final results	**0.1649 ± 0.0040**	**0.0991 ± 0.0018**	**82.83 ± 0.27**	**0.1505 ± 0.0036**	**0.014 65 ± 0.000 54**
Smalley et al. (2010)	0.1716	0.101 ± 0.002	82.5 ± 0.5	0.1559	0.015 74
Anderson et al. (2011)	0.1675	0.1011 ± 0.0017	82.5 ± 0.5	0.1521	0.015 38
Mahtani et al. (2013)	0.1661	0.1015 ± 0.0015	82.5 ± 0.5	0.1508	0.015 36

Table 8. Derived physical properties of the three systems. Where two sets of error bars are given, the first is the statistical uncertainty and the second is the systematic uncertainty.

Quantity	Symbol	Unit	WASP-24	WASP-25	WASP-26
Stellar mass	M_A	$M_\odot$	1.168 ± 0.056 ± 0.050	1.053 ± 0.023 ± 0.030	1.095 ± 0.043 ± 0.017
Stellar radius	R_A	$R_\odot$	1.317 ± 0.036 ± 0.019	0.924 ± 0.016 ± 0.009	1.284 ± 0.035 ± 0.007
Stellar surface gravity	$\log g_A$	c.g.s.	4.267 ± 0.021 ± 0.006	4.530 ± 0.014 ± 0.004	4.260 ± 0.022 ± 0.002
Stellar density	ρ_A	$\rho_\odot$	0.512 ± 0.034	1.336 ± 0.063	0.517 ± 0.037
Planet mass	M_b	M_{Jup}	1.109 ± 0.043 ± 0.032	0.598 ± 0.044 ± 0.012	1.020 ± 0.031 ± 0.011
Planet radius	R_b	R_{Jup}	1.303 ± 0.043 ± 0.019	1.247 ± 0.030 ± 0.012	1.216 ± 0.047 ± 0.006
Planet surface gravity	g_b	m s^{-2}	16.19 ± 0.99	9.54 ± 0.80	17.1 ± 1.3
Planet density	ρ_b	ρ_{Jup}	0.469 ± 0.042 ± 0.007	0.288 ± 0.028 ± 0.003	0.530 ± 0.060 ± 0.003
Equilibrium temperature	T'_{eq}	K	1772 ± 29	1210 ± 14	1650 ± 24
Safronov number	Θ		0.0529 ± 0.0021 ± 0.0007	0.0439 ± 0.0033 ± 0.0004	0.0607 ± 0.0026 ± 0.0003
Orbital semimajor axis	a	au	0.036 35 ± 0.000 59 ± 0.000 52	0.048 19 ± 0.000 35 ± 0.000 46	0.039 66 ± 0.000 52 ± 0.000 21
Age	τ	Gyr	$2.5\,^{+9.6}_{-1.5}\,^{+1.8}_{-2.5}$	$0.1\,^{+5.7}_{-0.1}\,^{+0.2}_{-0.0}$	$4.0\,^{+5.7}_{-4.5}\,^{+1.4}_{-4.0}$

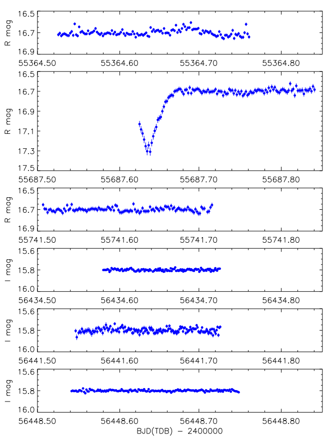

Figure 8. The light curves of the eclipsing binary system near WASP-24 from our observations. Each light curve has been shifted to an out-of-eclipse magnitude of $R = 16.7$ (Zacharias et al. 2004) or $I = 15.8$.

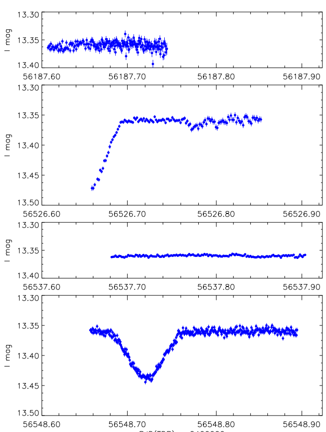

Figure 9. The light curves of the eclipsing binary system near WASP-26 from our observations. Each light curve has been shifted to an out-of-eclipse magnitude of $I = 13.36$, calculated from its spectral type and observed V magnitude.

7 ECLIPSING BINARY STAR SYSTEMS NEAR WASP-24 AND WASP-26

Street et al. (2010) found the closest detected star to WASP-24 (21.2 arcsec) to be a detached eclipsing binary system. It showed eclipses of depth 0.8 mag in four of their follow-up photometric data sets, suggesting an orbital period of 1.156 d. Its faintness ($V = 17.97$) means that it was not measurable in the SuperWASP images. We observed one eclipse, on the night of 2011/05/05 (Fig. 8). This confirms the eclipsing nature of the object, but is not helpful in deducing its orbital period. Further observations of this eclipsing binary would be useful in pinning down the mass–radius relation for low-mass main-sequence stars (e.g. López-Morales 2007; Torres, Andersen & Giménez 2010).

In two of our data sets for WASP-26, we detected eclipses on one object which appears to be a previously unknown detached eclipsing binary system. Its sky position is approximately RA = 00:18:26.5, Dec. = −15:11:49 (J2000). The AAVSO Photometric All-Sky Survey gives apparent magnitudes of $B = 16.02 \pm 0.07$ and $V = 14.98 \pm 0.02$ (Henden et al. 2012). The Two Micron All-Sky Survey lists it under the designation 2MASS J00182645−1511492

(Skrutskie et al. 2006), and its colour of $J - K = 0.72$ implies a spectral type of approximately K4 V (Currie et al. 2010). The object is not listed in the General Catalogue of Variable Stars (GCVS)[10] or the AAVSO Variable Star Index (VSX).[11]

Two eclipses were seen in the 2MASS J00182645−1511492 system, separated by approximately 22.1 d Fig. 9. The first was only partially observed and has a depth of at least 0.11 mag, whereas the full duration of the second eclipse was seen, with a depth of 0.08 mag. The different depths mean that the former is a primary and the latter a secondary eclipse. The orbital period cannot be determined from these data, but is likely quite short as the eclipses do not last long. The SuperWASP survey (Pollacco et al. 2006) has obtained 5800 observations of this object, but these show no obvious variability due to the faintness of the object and the shallowness of the eclipses. Whilst it would be a useful probe of the properties of stars on the lower main sequence, 2MASS J00182645−1511492 is not a particularly promising object for further study due to its shallow eclipses, which makes the measurement of precise photometric parameters difficult, and unknown orbital period.

8 SUMMARY AND CONCLUSIONS

We have presented extensive photometric observations of three Southern hemisphere transiting planetary systems discovered by SuperWASP. All three systems have spectroscopic measurements of the RM effect which are consistent with orbital alignment; two have also been observed with *Spitzer*. Our observations of the third, WASP-25, comprise the first follow-up photometry of this object since its discovery paper.

Our data cover 13 transits of the gas giant planets in front of their host stars, plus single-epoch high-resolution images taken with a Lucky Imaging camera. From these observations, and published spectroscopic measurements, we have measured the orbital ephemerides and physical properties of the systems to high precision. Care was taken to propagate random errors for all quantities and assess separate statistical errors for those quantities whose evaluation depends on the use of theoretical stellar models. Previously published studies of all three objects are in good agreement with our refined values, although we find evidence that their error estimates are unrealistically small.

We have observed one eclipse for the known eclipsing binary very close to WASP-24, and discovered a new K4 V detached eclipsing binary 4.25 arcmin north of WASP-26. We have observed part of one primary eclipse and a full secondary eclipse for the latter object, but are not able to measure its orbital period from these observations.

Fig. 10 shows a plot of planet radius versus mass for all known TEPs (data taken from the TEPCat[12] catalogue on 2014/02/15). WASP-24 b and WASP-26 b are representative of the dominant population of Hot Jupiters, with masses near $1.0M_{Jup}$. WASP-25 b appears near the mid-point of a second cluster of planets with masses of approximately 0.5–0.7M_{Jup}; such objects are sometimes termed 'Hot Saturns' although they are more massive than Saturn itself ($0.3M_{Jup}$).

All three planets have radii greater than predicted by theoretical models for gaseous bodies without a heavy-element core (Bodenheimer, Laughlin & Lin 2003; Fortney, Marley & Barnes 2007; Baraffe, Chabrier & Barman 2008) so exhibit the

[10] http://www.sai.msu.su/gcvs/gcvs/
[11] http://www.aavso.org/vsx
[12] The TEPCat is available at `http://www.astro.keele.ac.uk/jkt/tepcat/`.

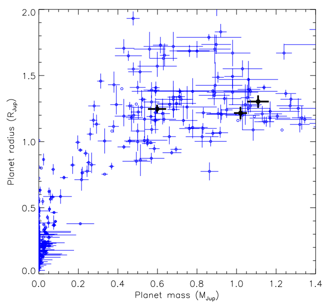

Figure 10. Plot of planet radii versus their masses. WASP-24 b, WASP-25b and WASP-26b are indicated using black filled circles. The overall population of planets is shown using blue open circles, using data taken from TEPCat on 2014/02/15. Error bars are suppressed for clarity if they are larger than $0.2M_{Jup}$ or $0.2R_{Jup}$. The outlier with a mass of $0.86M_{Jup}$ but a radius of only $0.78R_{Jup}$ is the recently discovered system WASP-59 (Hébrard et al. 2013).

inflated radii commonly observed for Hot Jupiters (e.g. Enoch, Collier Cameron & Horne 2012, and references therein). Its deep transit and low surface gravity make WASP-25 b a good candidate for transmission photometry and spectroscopy to probe the atmospheric properties of a transiting gas giant planet (see Bento et al. 2014).

ACKNOWLEDGEMENTS

The operation of the Danish 1.54 m telescope is financed by a grant to UGJ from the Danish Natural Science Research Council. The reduced light curves presented in this work will be made available at the CDS (http://vizier.u-strasbg.fr/) and at http://www.astro.keele.ac.uk/∼jkt/. J Southworth acknowledges financial support from STFC in the form of an Advanced Fellowship. The research leading to these results has received funding from the European Community's Seventh Framework Programme (FP7/2007-2013/) under grant agreement nos. 229517 and 268421. Funding for the Stellar Astrophysics Centre (SAC) is provided by The Danish National Research Foundation. This publication was supported by grants NPRP 09-476-1-078 and NPRP X-019-1-006 from Qatar National Research Fund (a member of Qatar Foundation). TCH acknowledges financial support from the Korea Research Council for Fundamental Science and Technology (KRCF) through the Young Research Scientist Fellowship Programme and is supported by the KASI (Korea Astronomy and Space Science Institute) grant 2012-1-410-02/2013-9-400-00. SG, XW and XF acknowledge the support from NSFC under the grant no. 10873031. The research is supported by the ASTERISK project (ASTERoseismic Investigations with SONG and Kepler) funded by the European Research Council (grant agreement no. 267864). DR, YD, AE, FF (ARC), OW (FNRS research fellow) and J Surdej acknowledge support from the Communauté française de Belgique – Actions de recherche concertées – Académie Wallonie-Europe. The following internet-based resources were used in research for this paper: the ESO Digitized Sky Survey; the NASA Astrophysics Data System; the SIMBAD data base and VizieR catalogue access tool operated at CDS, Strasbourg, France; and the arXiv scientific paper preprint service operated by Cornell University. We thank the anonymous referee for a helpful report.

REFERENCES

Albrecht S. et al., 2012, ApJ, 757, 18
Anderson D. R. et al., 2011, A&A, 534, A16
Baraffe I., Chabrier G., Barman T., 2008, A&A, 482, 315
Bento J. et al., 2014, MNRAS, 437, 1511
Bodenheimer P., Laughlin G., Lin D. N. C., 2003, ApJ, 592, 555
Brown D. J. A. et al., 2012, MNRAS, 423, 1503
Carter J. A., Yee J. C., Eastman J., Gaudi B. S., Winn J. N., 2008, ApJ, 689, 499
Claret A., 2004, A&A, 424, 919
Currie T. et al., 2010, ApJS, 186, 191
Daemgen S., Hormuth F., Brandner W., Bergfors C., Janson M., Hippler S., Henning T., 2009, A&A, 498, 567
Demarque P., Woo J.-H., Kim Y.-C., Yi S. K., 2004, ApJS, 155, 667
Dotter A., Chaboyer B., Jevremović D., Kostov V., Baron E., Ferguson J. W., 2008, ApJS, 178, 89
Eastman J., Siverd R., Gaudi B. S., 2010, PASP, 122, 935
Enoch B., Collier Cameron A., Parley N. R., Hebb L., 2010, A&A, 516, A33
Enoch B. et al., 2011, MNRAS, 410, 1631
Enoch B., Collier Cameron A., Horne K., 2012, A&A, 540, A99
Fortney J. J., Marley M. S., Barnes J. W., 2007, ApJ, 659, 1661
Gibson N. P. et al., 2009, ApJ, 700, 1078
Hébrard G. et al., 2013, A&A, 549, A134
Henden A. A., Levine S. E., Terrell D., Smith T. C., Welch D., 2012, J. Am. Assoc. Var. Star Obs., 40, 430
Knutson H. A. et al., 2014, ApJ, 785, 126
Lillo-Box J., Barrado D., Bouy H., 2014, A&A, 566, A103
López-Morales M., 2007, ApJ, 660, 732
McLaughlin D. B., 1924, ApJ, 60, 22
Mahtani D. P. et al., 2013, MNRAS, 432, 693
Markwardt C. B., 2009, in Bohlender D. A., Durand D., Dowler P., ASP Conf. Ser. Vol. 411 Astronomical Data Analysis Software and Systems XVIII. Astron. Soc. Pac., San Francisco, p. 251
Maxted P. F. L., Koen C., Smalley B., 2011, MNRAS, 418, 1039
Mortier A., Santos N. C., Sousa S. G., Fernandes J. M., Adibekyan V. Z., Delgado Mena E., Montalto M., Israelian G., 2013, A&A, 558, A106
Nelder J. A., Mead R., 1965, Comp. J., 7, 308
Nelson B., Davis W. D., 1972, ApJ, 174, 617
Nikolov N., Chen G., Fortney J., Mancini L., Southworth J., van Boekel R., Henning T., 2013, A&A, 553, A26
Pietrinferni A., Cassisi S., Salaris M., Castelli F., 2004, ApJ, 612, 168
Poddaný S., Brát L., Pejcha O., 2010, New Astron., 15, 297
Pollacco D. L. et al., 2006, PASP, 118, 1407
Popper D. M., Etzel P. B., 1981, AJ, 86, 102
Rossiter R. A., 1924, ApJ, 60, 15
Sada P. V. et al., 2012, PASP, 124, 212
Simpson E. K. et al., 2011, MNRAS, 414, 3023
Skottfelt J. et al., 2013, A&A, 553, A111
Skrutskie M. F. et al., 2006, AJ, 131, 1163
Smalley B. et al., 2010, A&A, 520, A56
Smith A. M. S. et al., 2012, A&A, 545, A93
Southworth J., 2008, MNRAS, 386, 1644
Southworth J., 2009, MNRAS, 394, 272
Southworth J., 2012, MNRAS, 426, 1291
Southworth J., Maxted P. F. L., Smalley B., 2004, MNRAS, 349, 547
Southworth J. et al., 2009a, MNRAS, 396, 1023
Southworth J. et al., 2009b, ApJ, 707, 167
Southworth J. et al., 2010, MNRAS, 408, 1680
Southworth J., Mancini L., Maxted P. F. L., Bruni I., Tregloan-Reed J., Barbieri M., Ruocco N., Wheatley P. J., 2012, MNRAS, 422, 3099
Southworth J. et al., 2013, MNRAS, 434, 1300
Stetson P. B., 1987, PASP, 99, 191
Street R. A. et al., 2010, ApJ, 720, 337
Torres G., Andersen J., Giménez A., 2010, A&AR, 18, 67
Torres G., Fischer D. A., Sozzetti A., Buchhave L. A., Winn J. N., Holman M. J., Carter J. A., 2012, ApJ, 757, 161
VandenBerg D. A., Bergbusch P. A., Dowler P. D., 2006, ApJS, 162, 375
Zacharias N., Monet D. G., Levine S. E., Urban S. E., Gaume R., Wycoff G. L., 2004, Am. Astron. Soc. Meeting Abstr. 36, 1418

SUPPORTING INFORMATION

Additional Supporting Information may be found in the online version of this article:

Appendix.
(http://mnras.oxfordjournals.org/lookup/suppl/doi:10.1093/mnras/stu1492/-/DC1).

Please note: Oxford University Press are not responsible for the content or functionality of any supporting materials supplied by the authors. Any queries (other than missing material) should be directed to the corresponding author for the article.

[1]*Astrophysics Group, Keele University, Staffordshire ST5 5BG, UK*
[2]*Korea Astronomy and Space Science Institute, Daejeon 305-348, Republic of Korea*
[3]*HE Space Operations GmbH, Flughafenallee 24, D-28199 Bremen, Germany*
[4]*Dipartimento di Fisica 'E.R. Caianiello', Università di Salerno, Via Giovanni Paolo II 132, I-84084 Fisciano (SA), Italy*
[5]*Istituto Internazionale per gli Alti Studi Scientifici (IIASS), I-84019 Vietri Sul Mare (SA), Italy*
[6]*SUPA, University of St Andrews, School of Physics and Astronomy, North Haugh, St Andrews KY16 9SS, UK*
[7]*Astronomisches Rechen-Institut, Zentrum für Astronomie, Universität Heidelberg, Mönchhofstraße 12-14, D-69120 Heidelberg, Germany*
[8]*Yunnan Observatories, Chinese Academy of Sciences, Kunming 650011, China*
[9]*Key Laboratory for the Structure and Evolution of Celestial Objects, Chinese Academy of Sciences, Kunming 650011, China*
[10]*Niels Bohr Institute & Centre for Star and Planet Formation, University of Copenhagen, Juliane Maries vej 30, DK-2100 Copenhagen Ø, Denmark*
[11]*Jodrell Bank Centre for Astrophysics, University of Manchester, Oxford Road, Manchester M13 9PL, UK*
[12]*Max Planck Institute for Astronomy, Königstuhl 17, D-69117 Heidelberg, Germany*
[13]*Instituto de Astrofísica, Facultad de Física, Pontificia Universidad Católica de Chile, Av. Vicuña Mackenna 4860, 7820436 Macul, Santiago, Chile*
[14]*Instituto de Astronomía – UNAM, Km 103 Carretera Tijuana Ensenada, 422860 Ensenada (Baja Cfa), Mexico*
[15]*Institut für Astrophysik, Georg-August-Universität Göttingen, Friedrich-Hund-Platz 1, D-37077 Göttingen, Germany*
[16]*NASA Ames Research Center, Moffett Field, CA 94035, USA*
[17]*Institut d'Astrophysique et de Géophysique, Université de Liège, B-4000 Liège, Belgium*
[18]*Qatar Environment and Energy Research Institute, Qatar Foundation, Tornado Tower, Floor 19, PO Box 5825 Doha, Qatar*
[19]*Department of Astronomy, Boston University, 725 Commonwealth Avenue, Boston, MA 02215, USA*
[20]*Istituto Nazionale di Fisica Nucleare, Sezione di Napoli, I-80126 Napoli, Italy*
[21]*Hamburger Sternwarte, Universität Hamburg, Gojenbergsweg 112, D-21029 Hamburg, Germany*

[22]*Dipartimento di Fisica e Astronomia, Università di Bologna, Viale Berti Pichat 6/2, I-40127 Bologna, Italy*
[23]*Main Astronomical Observatory, Academy of Sciences of Ukraine, vul. Akademika Zabolotnoho 27, UA-03680 Kyiv, Ukraine*
[24]*Aryabhatta Research Institute of Observational Sciences (ARIES), Manora Peak, Nainital 263 129, Uttarakhand, India*
[25]*European Southern Observatory, Karl-Schwarzschild-Straße 2, D-85748 Garching bei München, Germany*
[26]*Stellar Astrophysics Centre (SAC), Department of Physics and Astronomy, Aarhus University, Ny Munkegade 120, DK-8000 Aarhus C, Denmark*
[27]*Space Telescope Science Institute, 3700 San Martin Drive, Baltimore, MD 21218, USA*
[28]*Finnish Centre for Astronomy with ESO (FINCA), University of Turku, Väisäläntie 20, FI-21500 Piikkiö, Finland*
[29]*Department of Astronomy, Ohio State University, 140 W. 18th Ave, Columbus, OH 43210, USA*
[30]*Department of Physics, Sharif University of Technology, P. O. Box 11155-9161 Tehran, Iran*
[31]*Max Planck Institute for Solar System Research, Justus-von-Liebig-Weg 3, D-37077 Göttingen, Germany*
[32]*LCOGT, 6740 Cortona Drive, Suite 102, Goleta, CA 93117, USA*
[33]*School of Mathematical Sciences, Queen Mary, University of London, Mile End Road, London E1 4NS, UK*

This paper has been typeset from a TEX/LATEX file prepared by the author.

A&A 568, A127 (2014)
DOI: 10.1051/0004-6361/201424106

Astronomy & Astrophysics

Physical properties of the WASP-67 planetary system from multi-colour photometry[⋆,⋆⋆]

L. Mancini[1], J. Southworth[2], S. Ciceri[1], S. Calchi Novati[3,4], M. Dominik[5], Th. Henning[1], U. G. Jørgensen[6,7], H. Korhonen[8,6,7], N. Nikolov[9], K. A. Alsubai[10], V. Bozza[4,11], D. M. Bramich[12], G. D'Ago[4,11], R. Figuera Jaimes[5,13], P. Galianni[5], S.-H. Gu[14,15], K. Harpsøe[6,7], T. C. Hinse[16], M. Hundertmark[5], D. Juncher[6,7], N. Kains[17], A. Popovas[6,7], M. Rabus[18,1], S. Rahvar[19], J. Skottfelt[6,7], C. Snodgrass[20], R. Street[21], J. Surdej[22], Y. Tsapras[21,23], C. Vilela[2], X.-B. Wang[14,15], and O. Wertz[22]

1 Max-Planck Institute for Astronomy, Königstuhl 17, 69117 Heidelberg, Germany
e-mail: mancini@mpia.de
2 Astrophysics Group, Keele University, Staffordshire, ST5 5BG, UK
3 International Institute for Advanced Scientific Studies (IIASS), 84019 Vietri Sul Mare (SA), Italy
4 Department of Physics, University of Salerno, Via Giovanni Paolo II, 84084 Fisciano, Italy
5 SUPA, University of St Andrews, School of Physics & Astronomy, North Haugh, St Andrews, KY16 9SS, UK
6 Niels Bohr Institute, University of Copenhagen, Juliane Maries vej 30, 2100 Copenhagen Ø, Denmark
7 Centre for Star and Planet Formation, Geological Museum, Øster Voldgade 5-7, 1350 Copenhagen, Denmark
8 Finnish Centre for Astronomy with ESO (FINCA), University of Turku, Väisäläntie 20, 21500 Piikkiö, Finland
9 Astrophysics Group, University of Exeter, Stocker Road, EX4 4QL, Exeter, UK
10 Qatar Foundation, PO Box 5825, Doha, Qatar
11 Istituto Nazionale di Fisica Nucleare (INFN), Sezione di Napoli, 80126 Napoli, Italy
12 Qatar Environment and Energy Research Institute, Qatar Foundation, Tornado Tower, Floor 19, PO Box 5825, Doha, Qatar
13 European Southern Observatory, Karl-Schwarzschild-Straße 2, 85748 Garching bei München, Germany
14 Yunnan Observatories, Chinese Academy of Sciences, 650011 Kunming, PR China
15 Key Laboratory for the Structure and Evolution of Celestial Objects, Chinese Academy of Sciences, 650011 Kunming, PR China
16 Korea Astronomy and Space Science Institute, Daejeon 305-348, Republic of Korea
17 Space Telescope Science Institute, 3700 San Martin Drive, Baltimore, MD 21218, USA
18 Instituto de Astrofísica, Facultad de Física, Pontificia Universidad Católica de Chile, Av. Vicuña Mackenna 4860, 7820436 Macul, Santiago, Chile
19 Department of Physics, Sharif University of Technology, PO Box 11155-9161 Tehran, Iran
20 Max Planck Institute for Solar System Research, Justus-von-Liebig-Weg 3, 37077 Göttingen, Germany
21 Las Cumbres Observatory Global Telescope Network, 6740B Cortona Drive, Goleta, CA 93117, USA
22 Institut d'Astrophysique et de Géophysique, Université de Liège, 4000 Liège, Belgium
23 School of Physics and Astronomy, Queen Mary University of London, Mile End Road, London, E1 4NS, UK

Received 30 April 2014 / Accepted 28 June 2014

ABSTRACT

Context. The extrasolar planet WASP-67 b is the first hot Jupiter definitively known to undergo only partial eclipses. The lack of the second and third contact points in this planetary system makes it difficult to obtain accurate measurements of its physical parameters.
Aims. By using new high-precision photometric data, we confirm that WASP-67 b shows grazing eclipses and compute accurate estimates of the physical properties of the planet and its parent star.
Methods. We present high-quality, multi-colour, broad-band photometric observations comprising five light curves covering two transit events, obtained using two medium-class telescopes and the telescope-defocusing technique. One transit was observed through a Bessel-R filter and the other simultaneously through filters similar to Sloan $g'r'i'z'$. We modelled these data using . The physical parameters of the system were obtained from the analysis of these light curves and from published spectroscopic measurements.
Results. All five of our light curves satisfy the criterion for being grazing eclipses. We revise the physical parameters of the whole WASP-67 system and, in particular, significantly improve the measurements of the planet's radius ($R_\mathrm{b} = 1.091 \pm 0.046\,R_\mathrm{Jup}$) and density ($\rho_\mathrm{b} = 0.292 \pm 0.036\,\rho_\mathrm{Jup}$), as compared to the values in the discovery paper ($R_\mathrm{b} = 1.4^{+0.3}_{-0.2}\,R_\mathrm{Jup}$ and $\rho_\mathrm{b} = 0.16 \pm 0.08\,\rho_\mathrm{Jup}$). The transit ephemeris was also substantially refined. We investigated the variation of the planet's radius as a function of the wavelength, using the simultaneous multi-band data, finding that our measurements are consistent with a flat spectrum to within the experimental uncertainties.

Key words. planetary systems – stars: fundamental parameters – techniques: photometric

1. Introduction

WASP-67 b (Hellier et al. 2012) is a transiting extrasolar planet (TEP), discovered by the SuperWASP group (Pollacco et al. 2006), orbiting a K0 V star ($V = 12.5$ mag) every 4.61 d. It is

⋆ Based on data collected with GROND at the MPG 2.2 m telescope and DFOSC at the Danish 1.54 m telescope.
⋆⋆ Full Table 2 is only available at the CDS via anonymous ftp to cdsarc.u-strasbg.fr (130.79.128.5) or via http://cdsarc.u-strasbg.fr/viz-bin/qcat?J/A+A/568/A127

Table 1. Details of the transit observations presented in this work.

Instrument	Date of first obs.	Start time (UT)	End time (UT)	N_obs	T_exp (s)	T_obs (s)	Filter	Airmass	Moon illum.	Aperture radii (px)	Scatter (mmag)
GROND	2012 06 04	03:00	10:50	162	70/90	110/120	Sloan g'	2.14 → 1.01 → 1.22	98%	34, 50, 80	1.08
GROND	2012 06 04	03:00	10:50	162	70/90	110/120	Sloan r'	2.14 → 1.01 → 1.22	98%	38, 60, 85	0.56
GROND	2012 06 04	03:00	10:50	162	70/90	110/120	Sloan i'	2.14 → 1.01 → 1.22	98%	40, 60, 85	0.72
GROND	2012 06 04	03:00	10:50	162	70/90	110/120	Sloan z'	2.14 → 1.01 → 1.22	98%	40, 60, 85	0.64
DFOSC	2013 06 22	04:30	08:33	136	100	110	Bessel R	1.12 → 1.01 → 1.17	97%	20, 35, 55	0.48

Notes. N_obs is the number of observations, T_exp is the exposure time, T_obs is the observational cadence, and "Moon illum." is the fractional illumination of the Moon at the midpoint of the transit. The aperture sizes are the radii of the software apertures for the star, inner sky and outer sky, respectively. Scatter is the rms scatter of the data versus a fitted model.

an inflated ($\rho_\mathrm{b} \ll \rho_\mathrm{Jup}$) hot Jupiter ($a \sim 0.05$ AU) on a grazing orbit (impact parameter $b > 0.9$), causing the transit light curve to have an atypical V shape. Hellier et al. (2012) found that WASP-67 b satisfies the grazing criterion ($X = b + R_\mathrm{b}/R_\star > 1$) by 3σ, which makes it the first TEP definitively known to have a grazing eclipse[1]. In this particular configuration, the second and third contact points (e.g. Winn 2010) are missing and the light curve solution becomes degenerate. This hampers accurate measurements of the photometric parameters of the system. Consequently, Hellier et al. (2012) measured the radius of the planet with a large uncertainty of ∼20%. In such cases, high-quality light curves are mandatory to reduce the error bars to levels similar to those of other known TEPs.

Here, we present the first photometric follow-up study of WASP-67 since its discovery paper. The main aim of this study is to refine the physical parameters of the system and ephemeris, setting the stage for a more detailed study in the near future. WASP-67 is located in field #7 of the K2 phase of the NASA's *Kepler* mission[2] and will be observed continuously for approximately 80 d in late 2015.

2. Observations and data reduction

A complete transit of WASP-67 b was observed on 2012 June 4 (Table 1) using the Gamma Ray burst Optical and Near-infrared Detector (GROND) instrument mounted on the MPG[3] 2.2 m telescope, which is located at the ESO observatory in La Silla (Chile). GROND is an imaging system capable of simultaneous photometric observations in four optical (similar to Sloan g', r', i', z') and three NIR (J, H, K) passbands (Greiner et al. 2008). Each of the four optical channels is equipped with a back-illuminated 2048 × 2048 E2V CCD with a field of view of 5.4′ × 5.4′ at 0.158″ pixel^{-1}. The three NIR channels use 1024 × 1024 Rockwell HAWAII-1 arrays with a field of view of 10′ × 10′ at 0.6″ pixel^{-1}. The telescope was autoguided during the observations, which were performed with the defocusing technique (Southworth et al. 2009).

Another complete transit of WASP-67 b was observed on 2013 June 22 by using the DFOSC imager mounted on the 1.54 m Danish Telescope, which is also at the ESO observatory in La Silla, during the 2013 observing campaign by the MiNDSTEp consortium (Dominik et al. 2010). The instrument has a E2V44-82 CCD camera with a field of view of 13.7′ × 13.7′ and a plate scale of 0.39″ pixel^{-1}. The observations were performed through a Bessel R filter; the telescope was defocused and autoguided, and the CCD was windowed to reduce the readout time. With the applied defocus, the diameter of the PSF of the target and reference stars was ∼12″, which is similar to that for the GROND images.

The optical data collected from both telescopes were reduced using , an [4] pipeline for time-series photometry (Southworth et al. 2009). The images were debiased and flat-fielded using standard methods and then subjected to aperture photometry using the [5] task and an optimal ensemble of comparison stars. Pointing variations were followed by cross-correlating each image against a reference image. The shape of the light curve is very insensitive to the aperture sizes, so we chose those that yielded the lowest scatter. The relative weights of the comparison stars were optimised simultaneously with a de-trending of the light curve to remove slow instrumental and astrophysical trends. This was achieved by fitting a straight line to the out-of-transit data for the DFOSC data and with a fourth-order polynomial for the GROND data (to compensate for the lack of reference stars caused by the smaller field of view).

The final differential-flux light curves are plotted in Fig. 1 and tabulated in Table 2. In particular, the GROND light curves in the top panel of Fig. 1 are reported superimposed to highlight the differences of the light-curve shape and the transit depth along the four passbands. Contrary to what is expected for higher-inclination systems (e.g. Knutson et al. 2007), the transit depth gradually increases moving from blue to red bands. This phenomenon happens because the planet only covers the limb of

Table 2. Excerpts of the light curves of WASP-67.

Telescope	Filter	BJD (TDB)	Diff. mag.	Uncertainty
ESO 2.2 m	g'	2 456 082.655745	0.00061	0.00043
ESO 2.2 m	g'	2 456 082.657102	0.00142	0.00043
ESO 2.2 m	r'	2 456 082.655745	0.00083	0.00038
ESO 2.2 m	r'	2 456 082.657102	0.00101	0.00033
ESO 2.2 m	i'	2 456 082.655745	0.00069	0.00041
ESO 2.2 m	i'	2 456 082.657102	0.00117	0.00043
ESO 2.2 m	z'	2 456 082.653032	−0.00041	0.00048
ESO 2.2 m	z'	2 456 082.654390	−0.00117	0.00048
DK 1.54 m	R	2 456 465.694278	0.00066	0.00141
DK 1.54 m	R	2 456 465.695528	0.00033	0.00141

Notes. This table is available at the CDS. A portion is shown here for guidance regarding its form and content.

[1] Other TEPs which might undergo grazing eclipses are WASP-34 (Smalley et al. 2011) and HAT-P-27/WASP-40 (Béky et al. 2011; Anderson et al. 2011).
[2] http://keplerscience.arc.nasa.gov/K2/
[3] Max Planck Gesellschaft.
[4] is a trademark of the ITT Visual Information Solutions: http://www.ittvis.com/ProductServices/IDL.aspx
[5] is part of the subroutine library distributed by NASA on http://idlastro.gsfc.nasa.gov

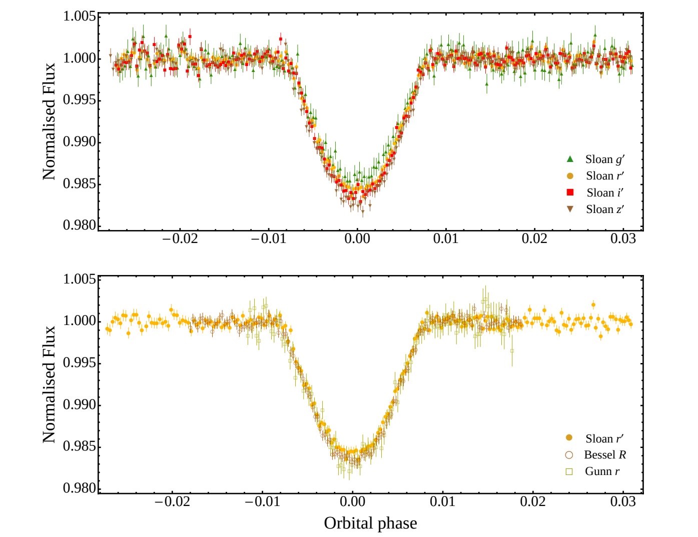

Fig. 1. Light curves of WASP-67 b eclipses. *Top panel*: light curves obtained with GROND in $g'r'i'z'$, showing how the transit light curve shape changes with wavelength. The transit in the g' band is shallower than the other bands, as expected for a grazing eclipse, as limb darkening is stronger at bluer wavelengths. *Bottom panel*: light curves obtained with DFOSC in the R-band (June 2013, brown open circles), with GROND in the r'-band (June 2012, yellow points) and with the *Euler* 1.2 m telescope in the r-band (July 2011, green open squares, Hellier et al. 2012). The light curves are superimposed to highlight variations in transit shape between the three measurements.

the star (as this is a grazing eclipse), which is fainter in the blue part of the optical spectrum than the red one due to the stronger limb darkening. Thus, we expect to see shallower eclipses in the bluest bands for this system.

The DFOSC Bessel-R light curve is shown in the bottom panel of Fig. 1 and is superimposed with the GROND Sloan-r' light curve and that from Hellier et al. (2012), which was obtained with the *Euler* 1.2 m telescope through a Gunn-r filter. This panel highlights the slight variation of the transit depth between the DFOSC and GROND light curves; the *Euler* data are more scattered and agree with both. Slight differences can be caused by the different filters used or by unocculted starspots. The latter hypothesis suggests a variation of the starspot activity of the WASP-67 A during a period of two years, which is reasonable for a 5200 K star.

Similar to some previous cases (Nikolov et al. 2012; Mancini et al. 2013b, 2014), the quality of the GROND NIR data were not good enough to extract usable photometry. We were only able to obtain a noisy light curve in the J band that, which if we consider the particular transit geometry of the WASP-67 system, returned very inaccurate estimates of the photometric parameters in the light-curve fitting process (see next section) in comparison with the optical ones.

3. Light-curve analysis

Our light curves were modelled using the [6] code (see Southworth 2012, and references therein), which represents the star and planet as biaxial spheroids for the calculation of the reflection and ellipsoidal effects and as spheres for calculation of the eclipse shapes. The main parameters fitted by are the orbital inclination, i, the transit midpoint, T_0, and the sum and ratio of the fractional radii of the star and planet, $r_\mathrm{A} + r_\mathrm{b}$ and $k = r_\mathrm{b}/r_\mathrm{A}$. The fractional radii are defined as $r_\mathrm{A} = R_\mathrm{A}/a$ and $r_\mathrm{b} = R_\mathrm{b}/a$, where a is the orbital semimajor axis, and R_A and R_b are the absolute radii of the star and the planet, respectively.

Each light curve was analysed separately, using a quadratic law to model the limb darkening (LD) effect. Due to the difficulty of measuring accurate LD coefficients in TEP systems with impact parameters $b \geq 0.8$ (Müller et al. 2013), the WASP-67 A LD

[6] The source code of is available at http://www.astro.keele.ac.uk/jkt/codes/jktebop.html

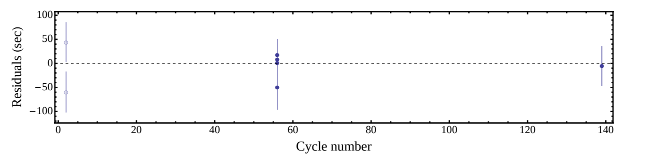

Fig. 2. Residuals for the timings of WASP-67 b at mid-transit versus a linear ephemeris. The two timings, based on the observations reported by Hellier et al. (2012), are plotted using open circles, while the other timings (this work) are plotted with filled circles.

Table 3. Times of WASP-67 b at mid-transit and their residuals versus a linear orbital ephemeris.

Time of minimum BJD(TDB)−2 400 000	Cycle No.	Residual (d)	Reference
55 833.60357 ± 0.00032	2	0.000510	1
55 833.60237 ± 0.00033	2	−0.000690	2
56 082.78067 ± 0.00034	56	−0.000578	3
56 082.78126 ± 0.00016	56	0.000012	4
56 082.78135 ± 0.00019	56	0.000102	5
56 082.78145 ± 0.00019	56	0.000202	6
56 465.77729 ± 0.00016	139	−0.000064	7

Notes. References: (1) *Euler* 1.2 m telescope (Hellier et al. 2012); (2) Trappist 0.6-m telescope (Hellier et al. 2012); (3) GROND g'-band (this work); (4) GROND r'-band (this work); (5) GROND i'-band (this work); (6) GROND z'-band (this work); (7) Danish 1.52-m telescope (this work)

coefficients were fixed to their theoretical values (Claret 2004b). We also assumed that the planetary orbit is circular (Hellier et al. 2012). We included the coefficients of a linear (DFOSC) or fourth (GROND) polynomial versus time in the fits to fully account for the uncertainty in the de-trending of the light curves.

We also considered the two light curves obtained with the *Euler* 1.2 m and Trappist 0.6 m telescopes, which were reported in Hellier et al. (2012). To present a homogeneous analysis, we re-fitted these two light curves using in the same manner as for our own data.

As in previous works (Mancini et al. 2013a,b,c, 2014), we enlarged the error bars of the light curve points generated by our reduction pipeline. Such a process is necessary because the algorithm, which is used to perform aperture photometry, tends to underestimate the true uncertainties in the relative magnitude measurements. This is a typical situation in time-series photometry, where additional noise sources, such as red noise, are not accounted for by standard error-estimation algorithms (e.g. Carter & Winn 2009). We, therefore, rescaled the error bars for each eclipse to give a reduced χ^2 of $\chi^2_\nu = 1$ and then again by using the β approach (e.g. Gillon et al. 2006; Winn et al. 2008; Gibson et al. 2008).

3.1. Orbital period determination

We used our photometric data and those coming from the discovery paper (Hellier et al. 2012) to refine the orbital period of WASP-67 b. The transit time for each of the datasets was obtained by fitting with , and uncertainties were estimated using Monte Carlo simulations. All timings were placed on the BJD(TDB) time system and are summarised in Table 3. The plot of the residuals is shown in Fig. 2. The resulting measurements of transit midpoints were fitted with a straight line to obtain a final orbital ephemeris:

$$T_0 = \mathrm{BJD(TDB)}\,2\,455\,824.37424(22) + 4.6144109(27)\,E,$$

where E is the number of orbital cycles after the reference epoch, which we take to be that estimated by Hellier et al. (2012), and quantities in brackets denote the uncertainty in the final digit of the preceding number. The quality of fit, $\chi^2_\nu = 1.90$, indicates that a linear ephemeris is not a perfect match to the observations. However, considering that our timings cover only three epochs, it is difficult to claim systematic deviations from the predicted transit times. Future *Kepler* data will enlarge the number of observed transit events of WASP-67 b and may rule in or out possible transit timing variations.

3.2. Photometric parameters

The GROND light curves and the best-fitting models are shown in Fig. 3. A similar plot is reported in Fig. 4 for the light curves from the Danish Telescope and Hellier et al. (2012). The parameters of the fits are given in Table 4. Uncertainties in the fitted parameters from each solution were calculated from 5500 Monte Carlo simulations and by a residual-permutation algorithm (Southworth 2008). The larger of the two possible error bars was adopted for each case. The error bars for the fits to individual light curves are often strongly asymmetric due to the morphology of the light curve. The final photometric parameters were therefore calculated by multiplying the probability density functions of the different values. This procedure yielded error bars, which are close to symmetric for all photometric parameters, and are given in Table 4. The values obtained by Hellier et al. (2012) are also reported for comparison. Due to their lower quality, we did not use any of the GROND-NIR light curves to estimate the final photometric parameters of WASP-67.

4. Physical properties

Similarly to the *Homogeneous Studies* approach (Southworth 2012, and references therein), we used the photometric parameters estimated in the previous section and the spectroscopic properties of the parent star (velocity amplitude $K_\mathrm{A} = 0.056 \pm 0.004$ km s^{-1}, effective temperature $T_\mathrm{eff} = 5200 \pm 100$ K, and metallicity $\left[\frac{\mathrm{Fe}}{\mathrm{H}}\right] = -0.07 \pm 0.09$; Hellier et al. 2012), to revise the physical properties of the WASP-67 system using the code.

We iteratively determined the velocity amplitude of the planet (K_b), which yielded the best agreement between the measured r_A and T_eff, and the values of R_A/a and T_eff predicted by a

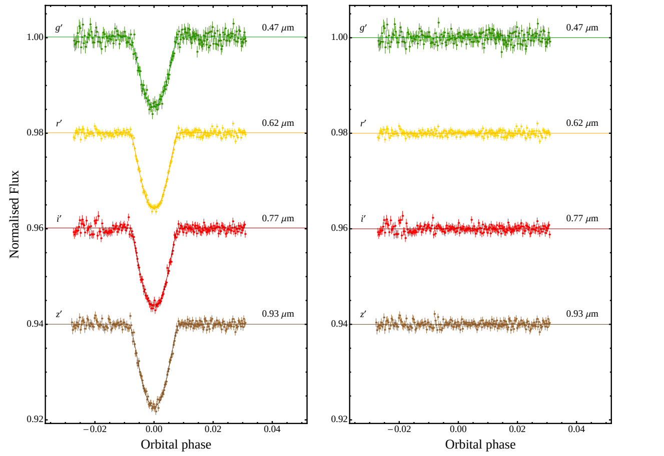

Fig. 3. *Left-hand panel*: simultaneous optical light curves of the WASP-67 eclipse observed with GROND. The best fits are shown as solid lines for each optical data set. The passbands are labelled on the left of the figure, and their central wavelengths are given on the right. *Right-hand panel*: residuals of each fit.

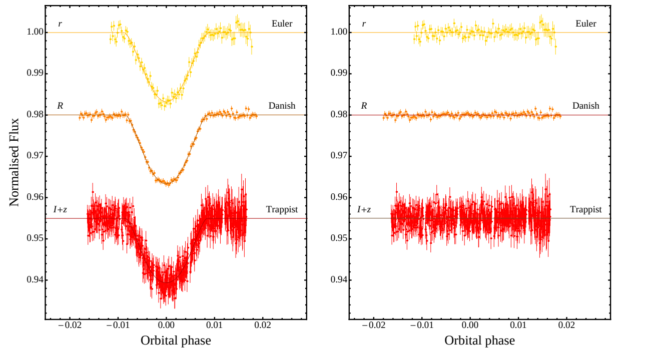

Fig. 4. *Left-hand panel*: light curves of the WASP-67 eclipses observed in Gunn-*r* with the *Euler* telescope (Hellier et al. 2012), in Bessell-*R* with the Danish telescope (this work) and with an $I + z$ filter with the TRAPPIST telescope (Hellier et al. 2012). The filters and the name of each telescope are labelled on the figure. The best fits are shown as solid lines for each optical dataset. *Right-hand panel*: residuals of each fit.

Table 4. Parameters of the fits to the light curves of WASP-67.

Telescope	Filter	$r_A + r_b$	k	i°	r_A	r_b
MPG 2.2 m	Sloan g'	$0.0831^{+0.0061}_{-0.0036}$	$0.1323^{+0.0192}_{-0.0058}$	$86.30^{+0.20}_{-0.39}$	$0.0734^{+0.0040}_{-0.0029}$	$0.00972^{+0.00200}_{-0.00074}$
MPG 2.2 m	Sloan r'	$0.0827^{+0.0023}_{-0.0019}$	$0.1345^{+0.0061}_{-0.0035}$	$86.31^{+0.11}_{-0.14}$	$0.0729^{+0.0016}_{-0.0015}$	$0.00980^{+0.00065}_{-0.00043}$
MPG 2.2 m	Sloan i'	$0.0823^{+0.0027}_{-0.0020}$	$0.1337^{+0.0061}_{-0.0034}$	$85.34^{+0.12}_{-0.17}$	$0.0726^{+0.0020}_{-0.0016}$	$0.00970^{+0.00069}_{-0.00044}$
MPG 2.2 m	Sloan z'	$0.0865^{+0.0040}_{-0.0027}$	$0.1424^{+0.0139}_{-0.0065}$	$86.09^{+0.17}_{-0.25}$	$0.0757^{+0.0025}_{-0.0019}$	$0.01078^{+0.00143}_{-0.00075}$
Danish 1.54 m	Bessel R	$0.0868^{+0.0038}_{-0.0026}$	$0.1445^{+0.0151}_{-0.0070}$	$86.08^{+0.16}_{-0.25}$	$0.0758^{+0.0023}_{-0.0018}$	$0.01095^{+0.00148}_{-0.00077}$
Euler 1.2 m	Gunn r	$0.102^{+0.013}_{-0.013}$	$0.229^{+0.150}_{-0.080}$	$85.09^{+0.86}_{-0.87}$	$0.0828^{+0.0021}_{-0.0047}$	$0.0189^{+0.0127}_{-0.0074}$
Trappist 0.6 m	$I + z$ filter	$0.0854^{+0.0054}_{-0.0035}$	$0.1310^{+0.0149}_{-0.0047}$	$86.16^{+0.20}_{-0.35}$	$0.0755^{+0.0038}_{-0.0028}$	$0.00989^{+0.00164}_{-0.00065}$
Final results		0.0846 ± 0.0012	0.1379 ± 0.0030	86.20 ± 0.07	0.07455 ± 0.00083	0.01023 ± 0.00034
Hellier et al. (2012)			$0.1345^{+0.0048}_{-0.0019}$	$85.8^{+0.3}_{-0.4}$		

Notes. The final parameters, given in bold, are the weighted means of the results for the datasets. Results from the discovery paper are included at the base of the table for comparison. The *Euler* and TRAPPIST data sets are from Hellier et al. (2012), while the others are from this work.

Table 5. Final physical properties of the WASP-67 planetary system compared with results from Hellier et al. (2012).

		This work (final)	Hellier et al. (2012)
Stellar mass	M_A ($M_\odot$)	0.829 ± 0.050 ± 0.037	0.87 ± 0.04
Stellar radius	R_A ($R_\odot$)	0.817 ± 0.019 ± 0.012	0.87 ± 0.04
Stellar surface gravity	$\log g_A$ (cgs)	4.533 ± 0.014 ± 0.007	4.50 ± 0.03
Stellar density	ρ_A ($\rho_\odot$)	1.522 ± 0.049	1.32 ± 0.15
Planetary mass	M_b (M_{Jup})	0.406 ± 0.033 ± 0.012	0.42 ± 0.04
Planetary radius	R_b (R_{Jup})	1.091 ± 0.043 ± 0.016	$1.4^{+0.3}_{-0.2}$
Planetary surface gravity	g_b (m s^{-2})	8.45 ± 0.83	$5.0^{+1.2}_{-2.3}$
Planetary density	ρ_b (ρ_{Jup})	0.292 ± 0.036 ± 0.004	0.16 ± 0.08
Planetary equilibrium temperature	T'_{eq} (K)	1003 ± 20	1040 ± 30
Safronov number	Θ	0.0457 ± 0.0037 ± 0.0007	
Orbital semimajor axis	a (au)	0.0510 ± 0.0010 ± 0.0008	0.0517 ± 0.0008
Age	Gyr	$8.7^{+12.7}_{-7.3}{}^{+5.5}_{-8.6}$	$2.0^{+1.6}_{-1.0}$

Notes. Two sets of errorbars are given for the results from the current work, the former being statistical and the latter systematic.

set of theoretical stellar models for the calculated stellar mass and $\left[\frac{Fe}{H}\right]$. Statistical errors were propagated by a perturbation analysis, and the overall best fit was found by evaluating results for a grid of ages. We assessed the contribution of systematic errors from theoretical stellar models by running solutions for five different grids of models (Claret 2004a; Demarque et al. 2004; Pietrinferni et al. 2004; VandenBerg et al. 2006; Dotter et al. 2008). The final set of physical properties was calculated by taking the unweighted mean of the five sets of values found from the different stellar models, and the systematic errors were taken to be the maximum deviation of a single value from the mean. The physical parameters of the WASP-67 planetary system are given in Table 5.

Table 5 also shows the values obtained by Hellier et al. (2012) for comparison. We find a smaller radius for the star, which is attributable to the better constraint on the stellar density from our high-precision light curves. We also obtain a significantly smaller planetary radius and, hence, a larger surface gravity and density. This is due partly to the smaller stellar radius combined with a comparable measurement of k (Table 4) and partly to an inconsistency among the R_A, R_b, and k values found by Hellier et al. (2012). The latter issue arises because Hellier et al. (2012) quote the median value of each fitted parameter from Markov Chain Monte Carlo simulations rather than giving the set of parameters corresponding to the single best-fitting link in the Markov chain (D. R. Anderson, priv. comm.).

5. Variation of the planetary radius with wavelength

If it were not for the difficulty of measuring its radius, WASP-67 b would be a good target for studies of the planetary atmosphere due to its low surface gravity. However, its moderate equilibrium temperature (T'_{eq} = 1003 ± 20 K) indicates that the planet should belong to the pL class (Fortney et al. 2008), implying that we do not expect to measure large variations of the planet radius with wavelength. As the GROND instrument is able to cover different optical passbands, we used our data to probe the terminator region of the planetary atmosphere.

Following our method in previous works (Southworth et al. 2012; Mancini et al. 2013b), we re-fitted the GROND light curves with all parameters, except k, fixed to the final values given in Table 4. This approach maximizes the precision of estimations of the planet/star radius ratio by removing common sources of uncertainty. We find the following values: k = 0.1369 ± 0.0063 for g', k = 0.1384 ± 0.0026 for r', k = 0.1381 ± 0.0024 for i', and k = 0.1387 ± 0.0023 for z'. These results are shown in Fig. 5, where the vertical errorbars represent the relative errors in the measurements and the horizontal errorbars show the FWHM transmission of the passbands used. For illustration, we also show the predictions from a model atmosphere calculated by Fortney et al. (2010) for a Jupiter-mass planet with a surface gravity of g_b = 10 m s^{-2}, a base radius of 1.25 R_{Jup} at 10 bar, and T'_{eq} = 1000 K. The opacity of

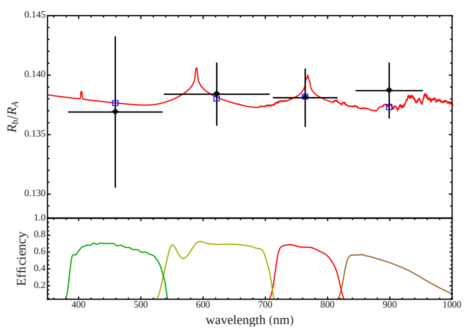

Fig. 5. Variation of the planetary radius, in terms of planet/star radius ratio, with wavelength. The black diamonds are from the transit observations performed with GROND. The vertical bars represent the errors in the measurements and the horizontal bars show the FWHM transmission of the passbands used. The observational points are compared with a synthetic spectrum (see text for details). Total efficiencies of the GROND filters are shown in the bottom panel. The blue boxes indicate the predicted values for the model integrated over the passbands of the observations.

strong-absorber molecules, such as gaseous titanium oxide (TiO) and vanadium oxide (VO), was removed from the model. Our experimental points agree with the prominent absorption features of the model (sodium at ~590 nm and potassium at ~770 nm) and, being compatible with a flat transmission spectrum, do not indicate any large variation of the WASP-67 b's radius.

6. High-resolution image

Eclipsing binary star systems are a common source of false positives for transiting planets detected by wide-field photometry. The host star can have a gravitationally bound companion, or its light can be contaminated by a background eclipsing binary, which is coincidentally at the same sky position. Both cases can mimic a planetary-transit signal. Faint, close stars may also contaminate the PSF of the target star, thus slightly lowering the depth of the transit and causing us to underestimate the radius of both the TEP and its host star. Finally, these faint nearby stars could also affect the radial velocity measurements of the star and, thus, the measured mass of the planet (e.g. Buchhave et al. 2011).

To check if WASP-67 A is contaminated by any faint companion or background stars, we observed it on 2014/04/21 with the Andor Technology iXon+ model 897 EMCCD Lucky Camera mounted at the Danish 1.54 m telescope. The imaging area of this camera is 512 × 512 pixels, and each 16 μm pixel projects to 0.″09 on the sky, which gives a 45 × 45 arcsec^2 field of view. The camera has a special long-pass filter with a cut-on wavelength of 650 nm, which corresponds roughly to a combination of the SDSS $i' + z'$ filters (Skottfelt et al. 2013).

Figure 6 shows the resulting image. WASP-67 A is the bright star in the centre of the image. Figure 7 shows the central region of the image, and it can be seen that two stars (A and B) occur approximately 4.5″ and 6.0″ northeast of WASP-67 A. The plate scales and inner apertures of DFOSC and GROND (Table 1) are such that both stars are inside the defocused PSFs of WASP-67. However, they are much fainter than WASP-67 A with $\Delta(i' + z')$ = 7.6 mag and 7.9 mag, respectively. They, therefore, contribute only 0.1% and 0.07% of the total flux in each image, so have a negligible effect on our results.

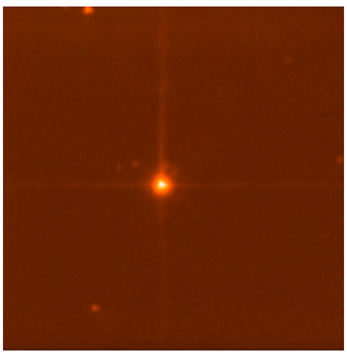

Fig. 6. Lucky Camera image of WASP-67. The image size is 45 × 45 arcsec^2 and is shown in a logarithmic flux scale with north up and east to the left. The FWHM of the image is 0.″54. The triangular PSF comes from the telescope in very good seeing. The extra flux north-west of WASP-67 A is not a real contaminating flux source but an optical ghost from the star caused by internal reflections within the beamsplitters.

In the eventuality that the two faint nearby stars are intrinsically very blue objects, they could have affected our g'-band observations by more than the amount given above. Measurement of a colour index from multiple high-resolution images would allow this possibility to be investigated. As a worst-case scenario, if both contaminants have T_{eff} = 30 000 K and are located at such as distance as to contribute 0.1% of the flux in the Lucky Camera

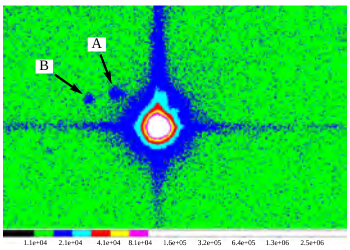

Fig. 7. Central part of the Lucky Camera image in Fig. 6. The image is shown in with a logarithmic flux scale with north up and east to the left. Two faint stars, A at ~4.4″ and B at ~6.0″ north-east of WASP-67 A, are evident. Values in the colour bar refer to the number of counts in ADU.

passband, the contamination in the g'-band would be 1.1%. This figure remains too small to be important to the current analysis.

7. Kepler-K2 observations

A more extensive study of the WASP-67 planetary system is anticipated, as this object will be observed by the *Kepler* satellite during its K2 phase. To explore the impact of these forthcoming observations, we have generated a synthetic light curve matching the K2 data characteristics and subjected it to the same modelling process as for the real data presented in the current work.

We calculated a model light curve for the best-fitting photometric parameters (Table 4) using and for quadratic LD coefficients appropriate for the K_p passband (Claret 2004b). This was extended over the full duration of the observations for field #2 (as the schedule for field #7 is not yet set) and numerically integrated to the duration of the short-cadence (58.8 s) and long-cadence (29.4 min) data types obtained by *Kepler*. Gaussian random noise was added to each data point equivalent to a scatter of 100 parts per million per six-hour time interval (Howell et al. 2014, their Fig. 10). Data points outside orbital phases −0.02 to 0.02 were discarded for computational convenience.

The synthetic light curves were fitted with using the same treatment as our real data sets for WASP-67, with the exception that we numerically integrated the model for the long-cadence simulated data to match its sampling rate (Southworth 2011). We find that the uncertainties in the resulting photometric parameters are quite similar between the two cadences, which is due to the relatively smooth brightness variation through the partial eclipse of WASP-67. They are also similar to those of our final parameters in Table 4, suggesting that the *Kepler* data will not allow a substantial improvement in the measured physical properties of WASP-67. This result was unexpected but can be explained by the larger scatter of the *Kepler* data (0.83 mmag for short-cadence) versus our best light curves (see Table 1).

One possibility, which is much better suited to K2 observations, is the detection of the rotational period of WASP-67 A due to spot-induced brightness modulations. WASP-67 A is a cool star (5200 K), but no spot modulation was detected in the SuperWASP light curve to a level of roughly 1 mmag. The data acquired by K2 may allow the rotational period to be estimated, which is useful for dynamical and tidal studies.

8. Summary and conclusions

We have presented the first follow-up study of the planetary system WASP-67, which is based on the analysis of five new light curves of two transit events of WASP-67 b. The first transit was observed simultaneously with GROND through Sloan g', r', i', z' filters; the second was observed in Bessell-*R* with DFOSC. The transits were monitored roughly one and two years, respectively, after the reference epoch used by Hellier et al. (2012). Both transit events were observed in telescope-defocusing mode, resulting in a photometric precision of 0.48–1.08 mmag per observation. We modelled our new and two published datasets using the code. By estimating the impact parameter b and the ratio of the planet/star radii, we found that the criterion for a grazing eclipse, $b + k > 1$, is satisfied for all the light curves, confirming that the eclipse is grazing.

We used the results of the light-curve analysis to substantially improve the measurements of the physical properties of the planet and its host star (Table 5). Compared to the discovery paper (Hellier et al. 2012), we find a significantly smaller radius and a greater density for WASP-67 b. We obtain R_b = 1.091 ± 0.046 R_{Jup} versus $1.4^{+0.3}_{-0.2}$ R_{Jup}, and ρ_b = 0.292 ± 0.036 ρ_{Jup} versus 0.16 ± 0.08 ρ_{Jup}. Our revised physical properties move WASP-67 b into a quite different region of parameter space. Figure 8 shows the change in position in the planet mass-radius plot (top panel) and in the planet mass-density plot (bottom panel). The revised positions are marked with a green circle, while the red circle indicates the old values from Hellier et al. (2012). The values of the other TEPs were taken from the TEPCat catalogue[7]. For illustration, the bottom panel of Fig. 8 also shows 10 Gyr isochrones of exoplanets at 0.045 AU orbital separation from a solar analogue (Fortney et al. 2007). The plot suggests that WASP-67 b should have a more massive core than previously thought.

As an additional possibility offered by the GROND data, we made an attempt to investigate possible variations of the radius of WASP-67 b in different optical passbands. Our experimental points are compatible with a flat transmission spectrum and do not indicate any large variation of the planet's radius. The gradual increase of the transit depth moving from the GROND g' to z' band, which is opposite to the case for higher-inclination systems, is explicable in that WASP-67 b only produces grazing eclipses. Due to stronger limb darkening, these are shallower in the blue bands than in the red ones.

Acknowledgements. This paper is based on observations collected with the MPG 2.2 m and the Danish 1.54 m telescopes, both located at ESO Observatory in La Silla, Chile. Operation of the Danish telescope is based on a grant to U.G.J. by the Danish Natural Science Research Council (FNU). GROND was built by the high-energy group of MPE in collaboration with the LSW Tautenburg and ESO, and is operated as a PI-instrument at the MPG 2.2 m telescope. We thank David Anderson and Coel Hellier for useful discussions, and the referee for a helpful report. J.S. (Keele) acknowledges financial support from STFC in the form of an Advanced Fellowship. C.S. received funding from the European Union Seventh Framework Programme (FP7/2007-2013) under grant agreement No. 268421. M.R. acknowledges support from FONDECYT postdoctoral fellowship N°3120097. T.C.H. would like to acknowledge KASI grant #2014-1-400-06. H.K. acknowledges support by the European Commission under the Marie Curie Intra-European Fellowship Programme in FP7. S.-H.G. and X.-B.W. would like to thank the financial support from National Natural Science Foundation of China (No. 10873031) and Chinese Academy of Sciences (project KJCX2-YW-T24). O.W. thanks the Belgian National Fund for Scientific

[7] http://www.astro.keele.ac.uk/jkt/tepcat/

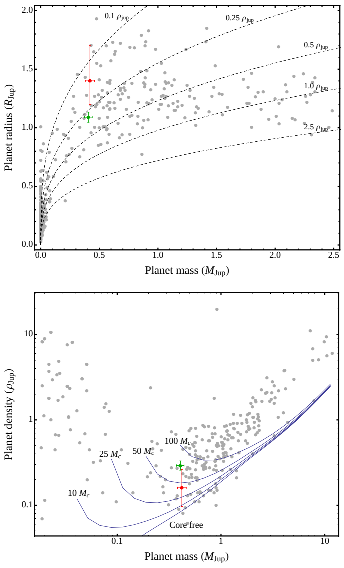

Fig. 8. *Top panel*: masses and radii of the known TEPs. The grey points denote values taken from TEPCat. Their error bars have been suppressed for clarity. WASP-67 b is shown with red (Hellier et al. 2012) and green (this work) points with error bars. Dotted lines show where density is 2.5, 1.0, 0.5, 0.25 and 0.1 ρ_{Jup}. *Bottom panel*: the mass-density diagram of the currently known transiting exoplanets (taken from TEPCat). Four planetary models with various core masses and another without a core (Fortney et al. 2007) are plotted for comparison.

Research (FNRS). J.S. and O.W. acknowledge support from the Communauté française de Belgique – Actions de recherche concertées – Académie universitaire Wallonie-Europe. K.A., M.D. and M.H. acknowledge grant NPRP-09-476-1-78 from the Qatar National Research Fund (a member of Qatar Foundation). This publication was aided by NPRP grant # X-019-1-006 from the Qatar National Research Fund (a member of Qatar Foundation). The reduced light curves presented in this work will be made available at the CDS (http://cdsweb.u-strasbg.fr/). The following internet-based resources were used in research for this paper: the ESO Digitized Sky Survey; the NASA Astrophysics Data System; the SIMBAD data base operated at CDS, Strasbourg, France; and the arXiv scientific paper preprint service operated by Cornell University.

References

Anderson, D. R., Barros, S. C. C., Boisse, I., et al. 2011, PASP, 123, 555
Béky, B., Bakos, G. Á., Hartman, J., et al. 2011, ApJ, 734, 109
Buchhave, L. A. , Latham, D. W., Carter, J. A., et al. 2011, ApJS, 197, 3
Carter, J. A., & Winn, J. N. 2009, ApJ, 704, 51
Claret, A. 2004a, A&A, 424, 919
Claret, A. 2004b, A&A, 428, 1001
Demarque, P., Woo, J.-H., Kim, Y.-C., Yi, S. K. 2004, ApJS, 155, 667
Dotter, A., Chaboyer, B., Jevremović, D., et al. 2008, ApJS, 178, 89
Dominik, M., Jørgensen, U. G. , Rattenbury, N. J., et al. 2010, Astron. Nachr., 331, 671
Fortney, J. J., Marley, M. S., & Barnes J. W. 2007, ApJ, 659, 1661
Fortney, J. J., Lodders, K., Marley, M. S., & Freedman R. S. 2008, ApJ, 678, 1419
Fortney, J. J., Shabram, M., Showman, A. P., et al. 2010, ApJ, 709, 1396
Gillon, M., Pont, F., Moutou, C., et al. 2006, A&A, 459, 249
Gibson, N. P., Pollacco D., Simpson E. K., et al. 2008, A&A, 492, 603
Greiner, J., Bornemann, W., Clemens, C., et al. 2008, PASP, 120, 405
Hellier, C., Anderson, D. R., Collier Cameron, A., et al. 2012, MNRAS, 426, 739
Howell, S. B., Sobeck, C., Haas, M., et al. 2014, PASP, 126, 398
Knutson, H. A., Charbonneau, D., & Noyes, R. W. 2007, ApJ, 655, 564
Mancini, L., Southworth, J., Ciceri, S., et al. 2013a, A&A, 551, A11
Mancini, L., Nikolov, N., Southworth, J., et al. 2013b, MNRAS, 430, 2932
Mancini, L., Ciceri, S., Chen, G., et al. 2013c, MNRAS, 436, 2
Mancini, L., Southworth, J., Ciceri, S., et al. 2014, A&A, 562, A126
Nikolov, N., Henning, Th., Koppenhoefer, J., et al. 2012, A&A, 539, 159
Müller, H. M., Huber, K. F., Czesla, S., et al. 2013, A&A, 560, A112
Pietrinferni, A., Cassisi, S., Salaris, M., & Castelli, F. 2004, ApJ, 612, 168
Pollacco, D. L., Skillen, I., Collier Cameron, A., et al. 2006, PASP, 118, 1407
Skottfelt, J., Bramich, D. M., Figuera Jaimes, R., et al. 2013, A&A, 553, A111
Smalley, B., Anderson, D. R., Collier Cameron, A., et al. 2011, A&A, 526, A130
Southworth, J. 2008, MNRAS, 386, 1644
Southworth, J. 2011, MNRAS, 417, 2166
Southworth, J. 2012, MNRAS, 426, 1291
Southworth, J., Hinse, T. C., Jørgensen, U. G., et al. 2009, MNRAS, 396, 1023
Southworth, J., Mancini, L., Maxted, P. F. L., et al. 2012, MNRAS, 422, 3099
VandenBerg, D. A., Bergbusch, P. A., & Dowler, P. D. 2006, ApJS, 162, 375
Winn J. N. 2010, in Exoplanet, ed. S. Seager (The University of Arizona Press), 56
Winn, J. N., Holman, M. J., Torres, G., et al. 2008, ApJ, 683, 1076

LETTER

doi:10.1038/nature13254

Three regimes of extrasolar planet radius inferred from host star metallicities

Lars A. Buchhave[1,2], Martin Bizzarro[2], David W. Latham[1], Dimitar Sasselov[1], William D. Cochran[3], Michael Endl[3], Howard Isaacson[4], Diana Juncher[2,5] & Geoffrey W. Marcy[4]

Approximately half of the extrasolar planets (exoplanets) with radii less than four Earth radii are in orbits with short periods[1]. Despite their sheer abundance, the compositions of such planets are largely unknown. The available evidence suggests that they range in composition from small, high-density rocky planets to low-density planets consisting of rocky cores surrounded by thick hydrogen and helium gas envelopes. Here we report the metallicities (that is, the abundances of elements heavier than hydrogen and helium) of more than 400 stars hosting 600 exoplanet candidates, and find that the exoplanets can be categorized into three populations defined by statistically distinct (∼4.5σ) metallicity regions. We interpret these regions as reflecting the formation regimes of terrestrial-like planets (radii less than 1.7 Earth radii), gas dwarf planets with rocky cores and hydrogen–helium envelopes (radii between 1.7 and 3.9 Earth radii) and ice or gas giant planets (radii greater than 3.9 Earth radii). These transitions correspond well with those inferred from dynamical mass estimates[2,3], implying that host star metallicity, which is a proxy for the initial solids inventory of the protoplanetary disk, is a key ingredient regulating the structure of planetary systems.

Shortly after the discovery of the first exoplanets, host star metallicity was suggested to have a role in the formation of planetary systems[4]. Indeed, the well-established tendency for hot Jupiters to be more frequently found orbiting metal-rich stars has been confirmed by a number of studies[5,6]. Although it has recently been shown that small planets form for a wide range of host star metallicities[7–11], it is clear that the metallicities of stars with small planets are on average lower than those of gas giants. This suggests that subtle differences may exist in the metallicities of the host stars of small exoplanets, and this, in turn, may be linked to distinct physical properties of the underlying planet populations. However, effectively probing this regime requires a large sample of homogeneously derived metallicities for stars with small planets. Therefore, using our stellar parameters classification (SPC) tool[7] (Methods Summary), we analyse more than 2,000 high-resolution spectra of Kepler Objects of Interest[12] (KOIs) gathered by the Kepler Follow-up Program, yielding precise stellar parameters (provided as a table in machine-readable form), including metallicities, of 405 stars orbited by 600 exoplanet candidates.

Our sample of spectroscopic metallicities of stars hosting small planets is a factor of two larger than any previous sample[7], allowing us to probe in greater detail for significant differences in the metallicities of stars hosting planets of different sizes. At various radii, we divide the sample into two bins of stars hosting small and large planets, and perform a two-sample Kolmogorov–Smirnov test to determine whether the metallicities of the two distributions of host stars are not drawn randomly from the same parent population. We find two significant features in the Kolmogorov–Smirnov test diagram, one at $1.7R_\oplus$ (Earth radii) with a significance of 4.5σ and one at $3.9R_\oplus$ with a significance of 4.6σ, suggesting transitions between three exoplanet size regimes (Fig. 1). The average metallicity of the host stars increases with planet size, yielding average metallicities of -0.02 ± 0.02, 0.05 ± 0.01 and 0.18 ± 0.02 dex in the respective regimes. To assess the uncertainty in radius at which these transitions occur, we perform a Monte Carlo simulation by drawing 10^6 sets of data, where the host star metallicities and planetary radii are randomly perturbed within the uncertainties (the uncertainty in the planetary radius is assumed to be dominated by the uncertainty in the radius of the host star). We find the two features to be at $1.55^{+0.88}_{-0.04}R_\oplus$ ($4.2^{+0.5}_{-0.4}\sigma$) and $3.52^{+0.74}_{-0.28}R_\oplus$ ($4.7^{+0.6}_{-0.4}\sigma$), consistent with the original data.

Small planets with short periods could undergo significant evaporation of their atmospheres[13]. These planets will therefore not obey the radius–metallicity relation we are studying, because any accumulated gas would have evaporated. Therefore, we remove small ($R_P < 3R_\oplus$, where R_P is the exoplanet radius), highly irradiated planets (stellar flux, $F_\nu > 5 \times 10^5\,\mathrm{J\,s^{-1}\,m^{-2}}$) from the sample, leaving 463 planets orbiting 324 stars, which increases the significance of the feature at $1.7R_\oplus$ from 3.5σ to the reported 4.5σ. For comparison, the rocky planet Kepler-10b, with an 0.8-d period[14], receives a flux of $F_\nu \approx 48 \times 10^5\,\mathrm{J\,s^{-1}\,m^{-2}}$, whereas Kepler-11c[15], whose density suggests it is gaseous, receives $F_\nu \approx 1.3 \times 10^5\,\mathrm{J\,s^{-1}\,m^{-2}}$.

Recent studies suggest that the masses and radii of small planets ($1.5R_\oplus$–$4R_\oplus$) follow a linear relationship, implying that planet density decreases with increasing planet radius[2]. However, this relationship must change significantly for larger planets ($>4R_\oplus$) to explain the large mass of gas giant planets such as Jupiter[2]. Our data indicate a statistically significant increase in metallicity at a comparable planetary radius, $R_P = 3.9R_\oplus$. This observation is in agreement with the well-established correlation between a star's metallicity and its likelihood to host hot Jupiters[5,6], confirming that the formation regime for larger planets ($>3.9R_\oplus$) requires exceptionally high metallicity environments[7]. We therefore interpret the regime of larger planets ($R_P > 3.9R_\oplus$) to consist of ice and gas giant planets formed beyond the 'snow line' at around ∼3 AU (1 AU is the average Sun–Earth distance), where the availability of solids is a factor of four higher because volatile elements are able to condense and form solids at cooler temperatures[16]. The high concentration of heavy elements in the protoplanetary disk, resulting from the higher metallicity and the condensation of volatiles, and the planet's large distance to the host star allow these planets to grow rapidly and amass a gaseous atmosphere before the gas in the protoplanetary disk dissipates. These planets then migrate to their present positions much closer to their host stars[17], yielding the hot Jupiters seen orbiting stars with high metallicities.

To explore the implications of the feature at $1.7R_\oplus$ in the metallicity–radius plane (Fig. 1), we compare our results with recent work attempting to determine the radius at which the transition from gaseous to rocky planets occurs. Dynamical masses derived from precise radial velocities of transiting exoplanets indicate that planets with $R_P > 2R_\oplus$ have densities that imply increasing amounts by volume of light material, whereas planets with $R_P < 1.5R_\oplus$ have densities systematically greater than that of Earth[2]. Moreover, an analysis of data for a larger sample of planets (including masses derived from transit timing variations), has shown that planets with $R_P < 1.5R_\oplus$ probably are of rocky composition[3]. Finally, it has been suggested that $R_P \approx 1.75R_\oplus$ is a physically motivated transition point between rocky and gaseous planets, based on reported masses and radii combined with thermal evolutionary atmosphere models[18]. The statistically significant peak in the metallicity–radius plane at $1.7R_\oplus$ agrees with these findings, suggesting that the compositions of small exoplanets ($R_P < 3.9R_\oplus$) in close proximity to their host stars are also regulated by the number density of solids in the protoplanetary disk. Thus, we interpret the two regimes of smaller planets identified by the host star metallicities as reflecting the transition between rocky terrestrial exoplanets that have not amassed a gaseous atmosphere ($R_P < 1.7R_\oplus$) and planets with rocky cores that have accumulated an envelope of hydrogen, helium and other volatiles, which we denote gas dwarfs ($1.7R_\oplus < R_P < 3.9R_\oplus$).

The formation mechanism of the terrestrial and gas dwarf exoplanet regimes in short orbital periods is not fully understood. In one model, these small exoplanets are believed to form *in situ* with little post-assembly migration[19,20]. Although the *in situ* accretion model seems to be successful in reproducing the observed distribution of the 'hot Neptune' and super-Earth systems, including their orbital spacing[21], it requires unusually large amounts of solids in the innermost protoplanetary disk. A competing model invokes accretion during the inward migration of a population of planetary embryos formed at a range of orbital distances beyond the snow line[22,23]. On this view, Mars- and Earth-size embryos migrate inwards owing to tidal interaction with the disk[24], and accumulate at the inner edge of the protoplanetary disk, where they complete their assembly[25]. Irrespective of the formation mechanism, however, the observed peak in the metallicity–radius plane at $1.7R_\oplus$ suggests that the final mass and composition of a small exoplanet is controlled by the amount of solid material available in the protoplanetary disk. A higher-metallicity environment promotes a more rapid and effective accretion process, thereby allowing the cores to amass a gaseous envelope before dissipation of the gas. In contrast, lower-metallicity environments may result in the assembly of rocky cores of several Earth masses on timescales greater than that inferred for gas dispersal in protoplanetary disks[19] (<10 Myr), yielding cores without gaseous hydrogen–helium atmospheres.

A prediction from gas accretion on short orbital periods is that the critical mass at which a core can accrete an atmosphere is $M_{cr} \approx 2.6M_\oplus(\eta/0.3)^{1/2}(P_{orb}/1\ \mathrm{d})^{5/12}$, where $\eta = M_{atm}/M_{cr}$ is the fractional mass comprised by the atmosphere[26]. In this model, the planetary mass and, thus, radius indicating the transition from rocky to gaseous planets should increase with orbital period. However, the exact opposite dependence, namely a decrease in core mass with increased orbital period, has also been suggested[27]. To investigate whether the radius of transition from rocky to gaseous planets found in our data shows a dependence on orbital period, we segregate the sample by period into four bins with approximately equal numbers of planets. We repeat the previously described Kolmogorov–Smirnov test for the planets in each of the period bins: we remove the larger planets ($R_P > 3.9R_\oplus$) and perform a Monte Carlo simulation by drawing 10^6 sets of data, where the host star metallicities and planetary radii are randomly perturbed within the uncertainties. The red line in Fig. 2 is a power-law fit to the transition radius, R_{cr}, inferred from our data ($R_{cr} = 1.06R_\oplus(P_{orb}/1\ \mathrm{day})^{0.17}$). Although additional data are required to confirm this relationship, the fit is apparently consistent with a critical core mass that increases with orbital period and an atmospheric fraction of 5% (ref. 26; blue dashed line in Fig. 2). If correct, this predicts the existence of more massive rocky exoplanets at longer orbital periods.

Although our analysis of a statistically significant number of planets and their host star metallicities allows us to distinguish between three distinct exoplanet regimes, we emphasize that a multitude of factors can affect the outcome of planet formation. Therefore, the transition radii inferred from our analysis probably represent gradual transitions between the different planet regimes and so may not apply to all planetary systems. However, the agreement between the transition radii inferred here and those deduced from dynamical mass measurements of transiting planets[2,3] implies that host star metallicity—and, by extension, the solids inventory of a protoplanetary disk—is one of the driving factors determining the outcome of planet formation.

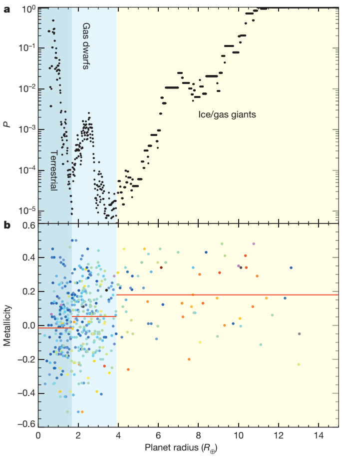

Figure 1 | Host star metallicities and three types of exoplanets with different composition. a, *P* value of the two-sample Kolmogorov–Smirnov test. **b**, Radii of the individual planets and their host star metallicities. Point colour represents the logarithm of the period of the planets (blue, shortest period; red, longest period). The solid red lines are the average metallicities in the three regions (-0.02 ± 0.02, 0.05 ± 0.01 and 0.18 ± 0.02 dex, where each uncertainty is 1 s.e.m. of the host star metallicities in the corresponding bin).

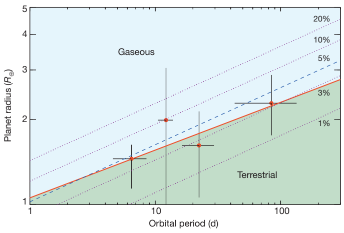

Figure 2 | The radius of transition from rocky to gaseous exoplanets. The transition radii (red points) are the means of the posterior distributions resulting from the Monte Carlo analysis (main text), and the error bars indicate the 1σ uncertainties. Using the mass–radius approximation[29] $M/M_\oplus = (R/R_\oplus)^{2.06}$, we plot the radius corresponding to M_{cr} with an atmosphere fraction of 5% as the blue dashed line and those for respective atmosphere fractions of 1%, 3%, 10% and 20% as the dotted purple lines. The solid red line is a power-law fit to the Monte Carlo data: $R_{cr} = 1.06R_\oplus(P_{orb}/1\ \mathrm{day})^{0.17}$.

[1]Harvard-Smithsonian Center for Astrophysics, Cambridge, Massachusetts 02138, USA. [2]Centre for Star and Planet Formation, Natural History Museum of Denmark, University of Copenhagen, DK-1350 Copenhagen, Denmark. [3]McDonald Observatory, The University of Texas, Austin, Texas 78712, USA. [4]University of California, Berkeley, California 94720, USA. [5]Niels Bohr Institute, University of Copenhagen, DK-2100 Copenhagen, Denmark.

METHODS SUMMARY

We use SPC[7] for the spectroscopic analysis yielding the stellar parameters in this work. SPC uses a grid of synthetic library spectra to derive the effective temperature, surface gravity, metallicity and rotational velocity simultaneously by matching the models with the observed spectra originating from a number of different instruments (Methods). The stellar parameters from SPC and Yonsei–Yale stellar evolutionary models[28] are used to estimate the radii of the host stars, which we couple with the photometric data from the Kepler mission to infer the planet radii. The majority of planets in the sample have short orbital periods, owing to the observational bias of Kepler towards shorter period planets. The mean and median periods are 38.0 and 12.4 d, respectively.

To investigate whether the radius of transition from rocky to gaseous planets found in our data shows a dependence on orbital period (Fig. 2), we remove the larger planets ($R_P > 3.9R_\oplus$) and segregate the remainder of the sample by period into four bins with approximately equal numbers of planets. The previously described Kolmogorov–Smirnov test (Fig. 1) is repeated for each bin by performing a Monte Carlo simulation in which the host star metallicities and planetary radii are randomly perturbed within the uncertainties. The data points plotted in Fig. 2 are the means of the resulting posterior distributions, and the error bars indicate the 1σ uncertainties.

To ensure that the statistical analyses are sound, we perform further tests evaluating the effects of uneven sampling and contamination (Methods). We find results consistent with those presented in the paper within the uncertainties, and conclude that our statistical analyses are robust.

Online Content Any additional Methods, Extended Data display items and Source Data are available in the online version of the paper; references unique to these sections appear only in the online paper.

Received 21 November 2013; accepted 12 March 2014.

1. Fressin, F. *et al.* The false positive rate of Kepler and the occurrence of planets. *Astrophys. J.* **766,** 81 (2013).
2. Marcy, G. W. *et al.* Masses, radii, and orbits of small Kepler planets: the transition from gaseous to rocky planets. *Astrophys. J. Suppl. Ser.* **210,** 20 (2014).
3. Weiss, L. M. & Marcy, G. W. The mass-radius relation for 65 exoplanets smaller than 4 Earth radii. *Astrophys. J.* **783,** L6 (2014).
4. Gonzalez, G. The stellar metallicity-giant planet connection. *Mon. Not. R. Astron. Soc.* **285,** 403–412 (1997).
5. Santos, N. C., Israelian, G. & Mayor, M. Chemical analysis of 8 recently discovered extra-solar planet host stars. *Astron. Astrophys.* **363,** 228–238 (2000).
6. Fischer, D. A. & Valenti, J. The planet-metallicity correlation. *Astrophys. J.* **622,** 1102–1117 (2005).
7. Buchhave, L. A. *et al.* An abundance of small exoplanets around stars with a wide range of metallicities. *Nature* **486,** 375–377 (2012).
8. Sousa, S. G., Santos, N. C., Israelian, G., Mayor, M. & Udry, S. Spectroscopic stellar parameters for 582 FGK stars in the HARPS volume-limited sample. Revising the metallicity-planet correlation. *Astron. Astrophys.* **533,** A141 (2011).
9. Sousa, S. G. *et al.* Spectroscopic parameters for 451 stars in the HARPS GTO planet search program. Stellar [Fe/H] and the frequency of exo-Neptunes. *Astron. Astrophys.* **487,** 373–381 (2008).
10. Ghezzi, L. *et al.* Stellar parameters and metallicities of stars hosting Jovian and Neptunian mass planets: a possible dependence of planetary mass on metallicity. *Astrophys. J.* **720,** 1290–1302 (2010).
11. Everett, M. E., Howell, S. B., Silva, D. R. & Szkody, P. Spectroscopy of faint Kepler mission exoplanet candidate host stars. *Astrophys. J.* **771,** 107 (2013).
12. Batalha, N. M. *et al.* Planetary candidates observed by Kepler. III. Analysis of the first 16 months of data. *Astrophys. J. Suppl. Ser.* **204,** 24 (2013).
13. Owen, J. E. & Wu, Y. Kepler planets: a tale of evaporation. *Astrophys. J.* **775,** 105 (2013).
14. Batalha, N. M. *et al.* Kepler's first rocky planet: Kepler-10b. *Astrophys. J.* **729,** 27 (2011).
15. Lissauer, J. J. *et al.* All six planets known to orbit Kepler-11 have low densities. *Astrophys. J.* **770,** 131 (2013).
16. Ida, S. & Lin, D. N. C. Toward a deterministic model of planetary formation. II. The formation and retention of gas giant planets around stars with a range of metallicities. *Astrophys. J.* **616,** 567–572 (2004).
17. Lin, D. N. C., Bodenheimer, P. & Richardson, D. C. Orbital migration of the planetary companion of 51 Pegasi to its present location. *Nature* **380,** 606–607 (1996).
18. Lopez, E. D. & Fortney, J. J. Understanding the mass-radius relation for sub-Neptunes: radius as a proxy for composition. Preprint at http://arxiv.org/abs/1311.0329 (2013).
19. Hansen, B. M. S. & Murray, N. Migration then assembly: formation of Neptune-mass planets inside 1 AU. *Astrophys. J.* **751,** 158 (2012).
20. Chiang, E. & Laughlin, G. The minimum-mass extrasolar nebula: in situ formation of close-in super-Earths. *Mon. Not. R. Astron. Soc.* **431,** 3444–3455 (2013).
21. Hansen, B. M. S. & Murray, N. Testing in situ assembly with the Kepler planet candidate sample. *Astrophys. J.* **775,** 53 (2013).
22. Terquem, C. & Papaloizou, J. C. B. Migration and the formation of systems of hot super-Earths and Neptunes. *Astrophys. J.* **654,** 1110–1120 (2007).
23. McNeil, D. S. & Nelson, R. P. On the formation of hot Neptunes and super-Earths. *Mon. Not. R. Astron. Soc.* **401,** 1691–1708 (2010).
24. Goldreich, P. & Tremaine, S. The excitation of density waves at the Lindblad and corotation resonances by an external potential. *Astrophys. J.* **233,** 857–871 (1979).
25. Raymond, S. N. & Cossou, C. No universal minimum-mass extrasolar nebula: Evidence against in-situ accretion of systems of hot super-Earths. Preprint at http://arxiv.org/abs/1401.3743 (2014).
26. Rafikov, R. R. Atmospheres of protoplanetary cores: critical mass for nucleated instability. *Astrophys. J.* **648,** 666–682 (2006).
27. Papaloizou, J. C. B. & Terquem, C. Critical protoplanetary core masses in protoplanetary disks and the formation of short-period giant planets. *Astrophys. J.* **521,** 823–838 (1999).
28. Yi, S. *et al.* Toward better age estimates for stellar populations: the Y^2 isochrones for solar mixture. *Astrophys. J. Suppl. Ser.* **136,** 417–437 (2001).
29. Lissauer, J. J. *et al.* Architecture and dynamics of Kepler's candidate multiple transiting planet systems. *Astrophys. J. Suppl. Ser.* **197,** 8 (2011).

Supplementary Information is available in the online version of the paper.

Acknowledgements L.A.B. acknowledges support from the Harvard Origins of Life Initiative. M.B. acknowledges funding from the Danish National Research Foundation (grant number DNRF97) and from the European Research Council under ERC Consolidator grant agreement 616027- STARDUST2ASTEROIDS. D.W.L. acknowledges support from the Kepler Mission under NASA Cooperative Agreements NCC2-1390, NNX11AB99A and NNX13AB58A with the Smithsonian Astrophysical Observatory, and thanks the observers who helped obtain the TRES observations reported here, especially R. Stefanik, G. Esquerdo, P. Berlind and M. Calkins.

Author Contributions L.A.B. led the project and developed the classification tools for the metallicity analysis. M.B., D.W.L. and D.S. contributed to the discussion of the theoretical implications of the data. L.A.B., D.W.L., W.D.C., M.E., H.I., D.J. and G.W.M. worked on gathering the spectroscopic observations. All authors discussed the results and commented on the manuscript. L.A.B. and M.B. wrote the paper with input from D.W.L. and D.S.

Author Information Reprints and permissions information is available at www.nature.com/reprints. The authors declare no competing financial interests. Readers are welcome to comment on the online version of the paper. Correspondence and requests for materials should be addressed to L.A.B. (lbuchhave@cfa.harvard.edu).

METHODS

Observations and stellar parameters. This study is based on stellar classifications by SPC[7] of 2,297 spectra observed using the Fibre-fed Echelle Spectrograph on the 2.6-m Nordic Optical Telescope on La Palma, Spain (488 spectra), the fibre-fed Tillinghast Reflector Echelle Spectrograph on the 1.5-m Tillinghast Reflector at the Fred Lawrence Whipple Observatory on Mt Hopkins, Arizona (985 spectra), the Tull Coudé Spectrograph on the 2.7-m Harlan J. Smith Telescope at the McDonald Observatory Texas (653 spectra) and the HIRES spectrograph on the 10-m Keck I telescope at Mauna Kea, Hawaii (171 spectra). We included only the most secure stellar classifications by limiting our sample to stars with effective temperatures of $4{,}800\,\mathrm{K} < T_{eff} < 6{,}500\,\mathrm{K}$, projected rotational velocities of $v\sin(i) < 20\,\mathrm{km\,s^{-1}}$, spectra with signal-to-noise ratios per resolution element of more than 25, and normalized cross-correlation function peak heights of more than 0.9 (indicating the quality of the stellar classification).

We improve on the determination of the surface gravity, known to be prone to degeneracies with effective temperature and metallicity[30], by imposing a prior on the surface gravity from stellar evolutionary models and an initial estimate of the star's effective temperature and metallicity. This is particularly useful for cooler stars, where the evolutionary models put tight constraints on the surface gravity. We use the stellar parameters from SPC and the Yonsei–Yale stellar evolutionary models[28] to estimate the radii of the host stars, and, using the photometrically derived planet radii from Kepler, we correct the planetary radii based on the Kepler Input Catalogue photometry, which are known to be prone to systematic biases and large uncertainties. The improved stellar radii reduce the uncertainties in the planetary radii from an average error of 34% to one of 11%, assuming that the major contribution to the uncertainty in the planetary radii originates from the stellar radii.

Uneven sampling. To investigate the effect of uneven sample size, we performed a Monte Carlo test with 10^6 realizations where we randomly drew observations from the smaller of the two samples, making each of the two samples equal in size at all times. We find the ice or gas giant transition to be at $3.58^{+0.75}_{-0.38}R_\oplus$ with a significance of $4.9^{+0.5}_{-0.4}\sigma$ and the rocky transition to be at $1.60^{+0.83}_{-0.10}R_\oplus$ with a significance of $4.4^{+0.5}_{-0.4}\sigma$. Both values are consistent with the Monte Carlo analysis reported in the paper. We conclude that the uneven sample size does not affect the significance of our statistical analysis.

Contamination. We are using the two-sample Kolmogorov–Smirnov test for the statistical analysis, but we find three distinct populations of exoplanets. To establish whether contamination from the third sample affects our results, we remove the planets from the third sample (removing $R_P > 3.9R_\oplus$ when searching for the peak at $1.7R_\oplus$ and removing $R_P < 1.7R_\oplus$ for the peak at $3.9R_\oplus$) and subsequently carry out the Kolmogorov–Smirnov test in an attempt to recover each of the peaks in Fig. 1. We find the first transition to be at the same radius ($1.7R_\oplus$), albeit with a lower significance (3.1σ). We find the ice/gas giant transition close to the one reported in the paper, again with a slightly lower significance ($4.2R_\oplus$ at 3.9σ). Again, evaluation of our data using a different approach supports our results and conclusions.

30. Torres, G. *et al.* Improved spectroscopic parameters for transiting planet hosts. *Astrophys. J.* **757,** 161 (2012).

The Astrophysical Journal, 782:48 (9pp), 2014 February 10 doi:10.1088/0004-637X/782/1/48

A SUPER-JUPITER ORBITING A LATE-TYPE STAR: A REFINED ANALYSIS OF MICROLENSING EVENT OGLE-2012-BLG-0406

Y. Tsapras[1,2,64], J.-Y. Choi[3], R. A. Street[1,64], C. Han[3,65,66], V. Bozza[4,67], A. Gould[5,66], M. Dominik[6,64,67,68,69], J.-P. Beaulieu[7,69], A. Udalski[8,70], U. G. Jørgensen[9,67], T. Sumi[10,71],
and
D. M. Bramich[11,12], P. Browne[6,67], K. Horne[6,69], M. Hundertmark[6,67], S. Ipatov[13,67], N. Kains[11,67], C. Snodgrass[14,67], I. A. Steele[15]
(The RoboNet Collaboration)
K. A. Alsubai[13], J. M. Andersen[16], S. Calchi Novati[4,17], Y. Damerdji[18], C. Diehl[19,20], A. Elyiv[18,21], E. Giannini[19], S. Hardis[9], K. Harpsøe[22], T. C. Hinse[9,23,24], D. Juncher[9], E. Kerins[25], H. Korhonen[9], C. Liebig[6], L. Mancini[26], M. Mathiasen[9], M. T. Penny[5,66], M. Rabus[27], S. Rahvar[28], G. Scarpetta[4,29,30], J. Skottfelt[9,22], J. Southworth[31], J. Surdej[18], J. Tregloan-Reed[31], C. Vilela[31], J. Wambsganss[19]
(The MiNDSTEp Collaboration)
J. Skowron[8], R. Poleski[5,8,66], S. Kozłowski[8], Ł. Wyrzykowski[8,32], M. K. Szymański[8], M. Kubiak[8], P. Pietrukowicz[8], G. Pietrzyński[8,33], I. Soszyński[8], K. Ulaczyk[8]
(The OGLE Collaboration)
M. D. Albrow[34], E. Bachelet[35,36], R. Barry[37], V. Batista[7], A. Bhattacharya[38,71], S. Brillant[39], J. A. R. Caldwell[40], A. Cassan[7], A. Cole[41], E. Corrales[7], Ch. Coutures[7], S. Dieters[35], D. Dominis Prester[42], J. Donatowicz[43], P. Fouqué[35,36], J. Greenhill[41], S. R. Kane[44], D. Kubas[7,39], J.-B. Marquette[7], J. Menzies[45], C. Père[7], K. R. Pollard[34], M. Zub[19,67]
(The PLANET Collaboration)
G. Christie[46], D. L. DePoy[47], S. Dong[48], J. Drummond[49], B. S. Gaudi[5], C. B. Henderson[5], K. H. Hwang[3], Y. K. Jung[3], A. Kavka[5], J.-R. Koo[50], C.-U. Lee[50], D. Maoz[51], L. A. G. Monard[52], T. Natusch[46], H. Ngan[46], H. Park[3], R. W. Pogge[5], I. Porritt[53], I.-G. Shin[3], Y. Shvartzvald[51], T. G. Tan[54], J. C. Yee[5]
(The μFUN Collaboration)
F. Abe[55], D. P. Bennett[38], I. A. Bond[56], C. S. Botzler[57], M. Freeman[57], A. Fukui[58], D. Fukunaga[55], Y. Itow[55], N. Koshimoto[10], C. H. Ling[56], K. Masuda[55], Y. Matsubara[55], Y. Muraki[55], S. Namba[10], K. Ohnishi[59], N. J. Rattenbury[57], To. Saito[60], D. J. Sullivan[61], W. L. Sweatman[56], D. Suzuki[10], P. J. Tristram[62], N. Tsurumi[55], K. Wada[10], N. Yamai[63], P. C. M. Yock[57], and A. Yonehara[63]
(The MOA Collaboration)
[1] Las Cumbres Observatory Global Telescope Network, 6740 Cortona Drive, Suite 102, Goleta, CA 93117, USA
[2] School of Physics and Astronomy, Queen Mary University of London, Mile End Road, London E1 4NS, UK
[3] Department of Physics, Chungbuk National University, Cheongju 361-763, Korea
[4] Dipartimento di Fisica "E. R. Caianiello," Università di Salerno, Via Giovanni Paolo II n. 132, I-84084 Fisciano (SA), Italy
[5] Department of Astronomy, Ohio State University, 140 West 18th Avenue, Columbus, OH 43210, USA
[6] SUPA, School of Physics & Astronomy, University of St Andrews, North Haugh, St Andrews KY16 9SS, UK
[7] UPMC-CNRS, UMR7095, Institut d'Astrophysique de Paris, 98bis boulevard Arago, F-75014 Paris, France
[8] Warsaw University Observatory, Al. Ujazdowskie 4, 00-478 Warszawa, Poland
[9] Niels Bohr Institute, Astronomical Observatory, Juliane Maries vej 30, DK-2100 Copenhagen, Denmark
[10] Department of Earth and Space Science, Osaka University, Osaka 560-0043, Japan
[11] European Southern Observatory, Karl-Schwarzschild-Str. 2, D-85748 Garching bei München, Germany
[12] Qatar Environment and Energy Research Institute, Qatar Foundation, Tornado Tower, Floor 19, P.O. Box 5825, Doha, Qatar
[13] Qatar Foundation, P.O. Box 5825, Doha, Qatar
[14] Max Planck Institute for Solar System Research, Max-Planck-Str. 2, D-37191 Katlenburg-Lindau, Germany
[15] Astrophysics Research Institute, Liverpool John Moores University, Liverpool CH41 1LD, UK
[16] Astronomy Department, Boston University, 725 Commonwealth Avenue, Boston, MA 02215, USA
[17] Istituto Internazionale per gli Alti Studi Scientifici (IIASS), I-84019 Vietri Sul Mare (SA), Italy
[18] Institut d'Astrophysique et de Géophysique, Allée du 6 Août 17, Sart Tilman, Bât. B5c, B-4000 Liège, Belgium
[19] Astronomisches Rechen-Institut, Zentrum für Astronomie der Universität Heidelberg (ZAH), Mönchhofstr. 12-14, D-69120 Heidelberg, Germany
[20] Hamburger Sternwarte, Universität Hamburg, Gojenbergsweg 112, D-21029 Hamburg, Germany
[21] Main Astronomical Observatory, Academy of Sciences of Ukraine, vul. Akademika Zabolotnoho 27, 03680 Kyiv, Ukraine
[22] Centre for Star and Planet formation, Geological Museum, Øster Voldgade 5, DK-1350, Copenhagen, Denmark
[23] Armagh Observatory, College Hill, Armagh, BT61 9DG, UK
[24] Korea Astronomy and Space Science Institute, 776 Daedukdae-ro, Yuseong-gu, Daejeon 305-348, Korea
[25] Jodrell Bank Centre for Astrophysics, University of Manchester, Oxford Road, Manchester, M13 9PL, UK
[26] Max Planck Institute for Astronomy, Königstuhl 17, D-69117 Heidelberg, Germany
[27] Instituto de Astrofísica, Facultad de Física, Pontificia Universidad Católica de Chile, Av. Vicuña Mackenna 4860, 7820436 Macul, Santiago, Chile
[28] Department of Physics, Sharif University of Technology, P.O. Box 11155-9161, Tehran, Iran
[29] International Institute for Advanced Scientific Studies (IIASS), I-84019 Vietri Sul Mare (SA), Italy
[30] INFN, Gruppo Collegato di Salerno, Sezione di Napoli, Italy
[31] Astrophysics Group, Keele University, Staffordshire, ST5 5BG, UK
[32] Institute of Astronomy, University of Cambridge, Madingley Road, Cambridge CB3 0HA, UK
[33] Departamento de Astronomia, Universidad de Concepción, Casilla 160-C, Concepción, Chile
[34] Department of Physics and Astronomy, University of Canterbury, Private Bag 4800, 8020 Christchurch, New Zealand
[35] Université de Toulouse, UPS-OMP, IRAP, F-31400 Toulouse, France

[36] CNRS, IRAP, 14 avenue Edouard Belin, F-31400 Toulouse, France
[37] Laboratory for Exoplanets and Stellar Astrophysics, Mail Code 667, NASA/GSFC, Bldg 34, Room E317, Greenbelt, MD 20771, USA
[38] Department of Physics, University of Notre Dame, 225 Nieuwland Science Hall, Notre Dame, IN 46556-5670, USA
[39] European Southern Observatory (ESO), Alonso de Cordova 3107, Casilla 19001, Santiago 19, Chile
[40] McDonald Observatory, 16120 Street Highway Spur 78 #2, Fort Davis, TX 79734, USA
[41] School of Math and Physics, University of Tasmania, Private Bag 37, GPO Hobart, 7001 Tasmania, Australia
[42] Physics Department, Faculty of Arts and Sciences, University of Rijeka, Omladinska 14, 51000 Rijeka, Croatia
[43] Department of Computing, Technical University of Vienna, Wiedner Hauptstrasse 10, Vienna, Austria
[44] Department of Physics & Astronomy, San Francisco State University, 1600 Holloway Avenue, San Francisco, CA 94132, USA
[45] South African Astronomical Observatory, P.O. Box 9, Observatory 7935, South Africa
[46] Auckland Observatory, Auckland, New Zealand
[47] Department of Physics and Astronomy, Texas A&M University, College Station, TX 77843, USA
[48] Kavli Institute for Astronomy and Astrophysics, Peking University, Yi He Yuan Road 5, Hai Dian District, Beijing 100871, China
[49] Possum Observatory, Patutahi, Gisbourne, New Zealand
[50] Korea Astronomy and Space Science Institute, Daejeon 305-348, Korea
[51] School of Physics and Astronomy, Tel-Aviv University, Tel-Aviv 69978, Israel
[52] Klein Karoo Observatory, Calitzdorp, and Bronberg Observatory, Pretoria, South Africa
[53] Turitea Observatory, Palmerston North, New Zealand
[54] Perth Exoplanet Survey Telescope, Perth, Australia
[55] Solar-Terrestrial Environment Laboratory, Nagoya University, Nagoya 464-8601, Japan
[56] Institute of Information and Mathematical Sciences, Massey University, Private Bag 102-904, North Shore Mail Centre, Auckland, New Zealand
[57] Department of Physics, University of Auckland, Private Bag 92-019, Auckland 1001, New Zealand
[58] Okayama Astrophysical Observatory, National Astronomical Observatory of Japan, Asakuchi, Okayama 719-0232, Japan
[59] Nagano National College of Technology, Nagano 381-8550, Japan
[60] Tokyo Metropolitan College of Aeronautics, Tokyo 116-8523, Japan
[61] School of Chemical and Physical Sciences, Victoria University, Wellington, New Zealand
[62] Mt. John University Observatory, P.O. Box 56, Lake Tekapo 8770, New Zealand
[63] Department of Physics, Faculty of Science, Kyoto Sangyo University, 603-8555 Kyoto, Japan
Received 2013 October 9; accepted 2013 December 4; published 2014 January 27

ABSTRACT

We present a detailed analysis of survey and follow-up observations of microlensing event OGLE-2012-BLG-0406 based on data obtained from 10 different observatories. Intensive coverage of the light curve, especially the perturbation part, allowed us to accurately measure the parallax effect and lens orbital motion. Combining our measurement of the lens parallax with the angular Einstein radius determined from finite-source effects, we estimate the physical parameters of the lens system. We find that the event was caused by a $2.73 \pm 0.43\ M_J$ planet orbiting a $0.44 \pm 0.07\ M_\odot$ early M-type star. The distance to the lens is 4.97 ± 0.29 kpc and the projected separation between the host star and its planet at the time of the event is 3.45 ± 0.26 AU. We find that the additional coverage provided by follow-up observations, especially during the planetary perturbation, leads to a more accurate determination of the physical parameters of the lens.

Key words: binaries: general – gravitational lensing: micro – planetary systems

Online-only material: color figures

1. INTRODUCTION

Radial velocity and transit surveys, which primarily target main-sequence stars, have already discovered hundreds of giant planets and are now beginning to explore the reservoir of lower mass planets with orbit sizes extending to a few astronomical units (AUs). These planets mostly lie well inside the snow line[72] of their host stars. Meanwhile, direct imaging with large aperture telescopes has been discovering giant planets tens to hundreds of AUs away from their stars (Kalas et al. 2005). The region of sensitivity of microlensing lies somewhere in between and extends to low-mass exoplanets lying beyond the snow line of their low-mass host stars, between ∼1 and 10 AU (Tsapras et al. 2003; Gaudi 2012). Although there is already strong evidence that cold sub-Jovian planets are more common than originally thought around low-mass stars (Gould et al. 2006; Sumi et al. 2010; Kains et al. 2013; Batalha et al. 2013), cold super-Jupiters orbiting K or M dwarfs were believed to be a rarer class of objects[73] (Laughlin et al. 2004; Miguel et al. 2011; Cassan et al. 2012).

Both gravitational instability and core accretion models of planetary formation have a hard time generating these planets, although it is possible to produce them given appropriate initial conditions. The main argument against core accretion is that it takes too long to produce a massive planet but this crucially depends on the core mass and the opacity of the planet envelope during gas accretion. In the case of gravitational instability, a massive protoplanetary disc would probably have too high an opacity to fragment locally at distances of a few AU.

The radial velocity method has been remarkably successful in tabulating the part of the distribution that lies within the snow line, but discoveries of super-Jupiters beyond the snow line of M dwarfs have been comparatively few (Johnson et al. 2010; Montet et al. 2013). Since microlensing is most sensitive to planets that are further away from their host stars, typically M and K dwarfs, the two techniques are complementary (Gaudi 2012).

Three brown dwarf and 19 planet microlensing discoveries have been published to date, including the discoveries of two multiple-planet systems (Gaudi et al. 2008; Han et al. 2013).[74] It is also worth noting that unbound objects of planetary mass have also been reported (Sumi et al. 2011).

Microlensing involves the chance alignment along an observer's line of sight of a foreground object (lens) and a background star (source). This results in a characteristic variation of the brightness of the background source as it is being gravitationally lensed. As seen from the Earth, the brightness of the source increases as it approaches the lens, reaching a maximum value at the time of closest approach. The brightness then decreases again as the source moves away from the lens.

In microlensing events, planets orbiting the lens star can reveal their presence through distortions in the otherwise smoothly varying standard single lens light curve. Together, the host star and planet constitute a binary lens. Binary lenses have a magnification pattern that is more complex than the single lens case due to the presence of extended caustics that represent the positions on the source plane at which the lensing magnification diverges. Distortions in the light curve arise when the trajectory of the source star approaches (or crosses) the caustics (Mao & Paczyński 1991). Recent reviews of the method can be found in Dominik (2010) and Gaudi (2011).

Upgrades to the OGLE[75] (Udalski 2003) survey observing setup and MOA[76] (Sumi et al. 2003) microlensing survey telescope in the past couple of years brought greater precision and enhanced observing cadence, resulting in an increased rate of exoplanet discoveries. For example, the Optical Gravitational Lensing Experiment (OGLE) has regularly been monitoring the field of the OGLE-2012-BLG-0406 event since 2010 March with a cadence of 55 minutes. When a microlensing alert was issued notifying the astronomical community that event OGLE-2012-BLG-0406 was exhibiting anomalous behavior, intense follow-up observations from multiple observatories around the world were initiated in order to better characterize the deviation. This event was first analyzed by Poleski et al. (2013) using the OGLE-IV survey photometry exclusively. That study concluded that the event was caused by a planetary system consisting of a 3.9 ± 1.2 M_J planet orbiting a low-mass late K/early M dwarf.

In this paper, we present the analysis of the event based on the combined data obtained from 10 different telescopes, spread out in longitude, providing dense and continuous coverage of the light curve.

The paper is structured as follows. Details of the discovery of this event, follow-up observations and image analysis procedures are described in Section 2. Section 3 presents the methodology of modeling the features of the light curve. We provide a summary and conclude in Section 4.

2. OBSERVATIONS AND DATA

Microlensing event OGLE-2012-BLG-0406 was discovered at equatorial coordinates $\alpha = 17^{h}53^{m}18^{s}.17$, $\delta = -30°28'16''.2$ (J2000.0)[77] by the OGLE-IV survey and announced by their Early Warning System (EWS)[78] on 2012 April 6. The event had a baseline *I*-band magnitude of 16.35 and was gradually increasing in brightness. The predicted maximum magnification at the time of announcement was low, therefore the event was considered a low-priority target for most follow-up teams who preferentially observe high-magnification events as they are associated with a higher probability of detecting planets (Griest & Safizadeh 1998).

OGLE observations of the event were carried out with the 1.3-m Warsaw telescope at the Las Campanas Observatory, Chile, equipped with the 32 chip mosaic camera. The event's field was visited every 55 minutes, providing very dense and precise coverage of the entire light curve from the baseline back to the baseline. For more details on the OGLE data and coverage, see Poleski et al. (2013).

An assessment of data acquired by the OGLE team until 1 July (08:47 UT, HJD ∼ 2456109.87), which was carried out by the SIGNALMEN anomaly detector (Dominik et al. 2007) on 2 July (02:19 UT) concluded that a microlensing anomaly, i.e., a deviation from the standard bell-shaped Paczyński curve (Paczyński 1986), was in progress. This was electronically communicated via the ARTEMiS (Automated Robotic Terrestrial Exoplanet Microlensing Search) system (Dominik et al. 2008) to trigger prompt observations by both the RoboNet-II[79] collaboration (Tsapras et al. 2009) and the MiNDSTEp[80] consortium (Dominik et al. 2010). RoboNet's web-PLOP system (Horne et al. 2009) reacted to the trigger by scheduling observations already from 2 July (02:30 UT), just 11 minutes after the SIGNALMEN assessment started. However, the first RoboNet observations did not occur before 4 July (15:26 UT), when the event was observed with the Faulkes Telescope South (FTS). This delayed response was due to the telescopes being offline for engineering work and bad weather at the observing sites. It fell to the Danish 1.54m at ESO La Silla to provide the first data point following the anomaly alert (2 July, 03:42 UT) as part of the MiNDSTEp efforts. The alert also triggered automated anomaly modeling by RTModel (Bozza 2010), which by 2 July (04:22 UT) delivered a rather broad variety of solutions in the stellar binary or planetary range, reflecting the fact that the true nature was not well-constrained by the data available at that time. This process chain did not involve any human interaction at all.

The first human involvement was an e-mail circulated to all microlensing teams by V. Bozza on 2 July (07:26 UT) informing the community about the ongoing anomaly and modeling results. Including OGLE data from a subsequent night, the apparent anomaly was also independently spotted by E. Bachelet (e-mail by D. P. Bennett 3 July, 13:42 UT), and subsequently PLANET[81] team (Beaulieu et al. 2006) SAAO data as well as μFUN[82] (Gould et al. 2006) SMARTS (CTIO) data were acquired the coming night, which, along with the RoboNet FTS data, cover the main peak of the anomaly. It should be noted that the observers at CTIO decided to follow the event even while the moon was full in order to obtain crucial data. A model circulated by T. Sumi on 5 July (00:38 UT) did not distinguish between the various solutions.

However, when the rapidly changing features of the anomaly were independently assessed by the Chungbuk National University group (CBNU, C. Han), the community was informed on 5 July (10:43 UT) that the anomaly is very likely due to the presence of a planetary companion. An independent modeling run by V. Bozza's automatic software (5 July, 10:55 UT) confirmed the result. While the OGLE collaboration (A. Udalski) notified observers on 5 July that a caustic exit was occurring, a geometry leading to a further small peak successively emerged from the models. D.P. Bennett circulated a model using updated data on 6 July (00:14 UT) which highlighted the presence of a second prominent feature expected to occur ∼10 July. Another modeling run performed at CBNU on 7 July (02:39 UT) also identified this feature and estimated that the secondary peak would occur on 11 July.

Follow-up teams continued to monitor the progress of the event intensively until the beginning of September, well after the planetary deviation had ceased, and provided dense coverage of the main peak of the event. A preliminary model using available OGLE and follow-up data at the time circulated on 31 October (C. Han, J.-Y. Choi), classified the companion to the lens as a super-Jupiter. Poleski et al. (2013) presented an analysis of this event using reprocessed survey data exclusively. In this paper, we present a refined analysis using survey and follow-up data together.

The groups that contributed to the observations of this event, along with the telescopes used, are listed in Table 1. Most observations were obtained in the *I* band and some images were also taken in other bands in order to create a color–magnitude diagram and classify the source star. We note that there are also observations obtained from the MOA 1.8m survey telescope, which we did not include in our modeling because the target was very close to the edge of the CCD. We also do not include data from the μFUN Auckland 0.4m, PEST 0.3m, Possum 0.36m, and Turitea 0.36m telescopes due to poor observing conditions at the sites.

Extracting accurate photometry from observations of crowded fields, such as the Galactic Bulge, is a challenging process. Each image contains thousands of stars whose stellar point spread functions (PSFs) often overlap so aperture and PSF-fitting photometry can at best offer limited precision. In order to optimize the photometry, it is necessary to use difference imaging (DI) techniques (Alard & Lupton 1998). For any particular telescope/camera combination, DI uses a reference image of the event taken under optimal seeing conditions which is then degraded to match the seeing conditions of every other image of the event taken from that telescope. The degraded reference image is then subtracted from the matching image to produce a residual (or difference) image. Stars that have not varied in brightness in the time interval between the two images will cancel, leaving no systematic residuals on the difference image but variable stars will leave either a positive or negative residual.

DI is the preferred method of photometric analysis among microlensing groups and each group has developed custom pipelines to reduce their observations. OGLE and MOA images were reduced using the pipelines described in Udalski (2003) and Bond et al. (2001), respectively. PLANET, μFUN, and *WISE* images were processed using variants of the PySIS (Albrow et al. 2009) pipeline, whereas RoboNet and MiNDSTEp observations were analyzed using customized versions of the DanDIA package (Bramich 2008). Once the source star returned to its baseline magnitude, each data set was reprocessed to optimize photometric precision. These photometrically optimized data sets were used as input for our modeling run.

3. MODELING

Figure 1 shows the light curve of OGLE-2012-BLG-406. The light curve displays two main features that deviate significantly

[64] The RoboNet Collaboration.
[65] Corresponding author.
[66] The μFUN Collaboration.
[67] The MiNDSTEp Collaboration.
[68] Royal Society University Research Fellow.
[69] The PLANET Collaboration.
[70] The OGLE Collaboration.
[71] The MOA Collaboration.
[72] The snow line is defined as the distance from the star in a protoplanetary disk where ice grains can form (Lecar et al. 2006).
[73] However, a metal-rich protoplanetary disk might allow the formation of sufficiently massive solid cores.

[74] For a complete list, consult http://exoplanet.eu/catalog/ and references therein.
[75] http://ogle.astrouw.edu.pl
[76] http://www.phys.canterbury.ac.nz/moa
[77] $(l, b) = -0°.46, -2°.22$
[78] http://ogle.astrouw.edu.pl/ogle4/ews/ews.html
[79] http://robonet.lcogt.net
[80] http://www.mindstep-science.org
[81] http://planet.iap.fr
[82] http://www.astronomy.ohio-state.edu/∼microfun

Table 1
Observations

Group	Telescope	Passband	Data Points
OGLE	1.3m Warsaw Telescope, Las Campanas Observatory (LCO), Chile	*I*	3013
RoboNet	2.0m Faulkes Telescope North (FTN), Haleakala, Hawaii, USA	*I*	83
RoboNet	2.0m Faulkes Telescope South (FTS), Siding Spring Observatory (SSO), Australia	*I*	121
RoboNet	2.0m Liverpool Telescope (LT), La Palma, Spain	*I*	131
MiNDSTEp	1.5m Danish Telescope, La Silla, Chile	*I*	473
MOA	0.6m Boller & Chivens (B&C), Mt. John, New Zealand	*I*	1856
μFUN	1.3m SMARTS, Cerro Tololo Inter-American Observatory (CTIO), Chile	*V*, *I*	16, 81
PLANET	1.0m Elizabeth Telescope, South African Astronomical Observatory (SAAO), South Africa	*I*	226
PLANET	1.0m Canopus Telescope, Mt. Canopus Observatory, Tasmania, Australia	*I*	210
WISE	1.0m Wise Telescope, Wise Observatory, Israel	*I*	180

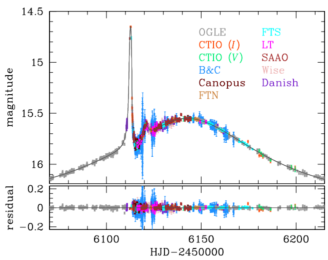

Figure 1. Light curve of OGLE-2012-BLG-0406 showing our best-fit binary-lens model including parallax and orbital motion. The legend on the right of the figure lists the contributing telescopes. All data were taken in the *I* band, except where otherwise indicated.

(A color version of this figure is available in the online journal.)

from the standard Paczyński curve. The first feature, which peaked at HJD $\sim$ 2456112 (3 July), is produced by the source trajectory grazing the cusp of a caustic. The brightness then quickly drops as the source moves away from the cusp (Schneider & Weiss 1992; Zakharov 1995), increases again for a brief period as it passes close to another cusp at HJD $\sim$ 2456121 (12 July), and eventually returns to the standard shape as the source moves further away from the caustic structure. The anomalous behavior, when both features are considered, lasts for a total of $\sim$15 days, while the full duration of the event is $\gtrsim$120 days. These are typical light curve features expected from lensing phenomena involving planetary lenses.

We begin our analysis by exploring a standard set of solutions that involve modeling the event as a static binary lens. The Paczyński curve representing the evolution of the event for most of its duration is described by three parameters: the time of closest approach between the projected position of the source on the lens plane and the position of the lens photocenter,[83] t_0, the minimum impact parameter of the source, u_0, expressed in units of the angular Einstein radius of the lens (θ_E), and the duration of time, t_E (the Einstein timescale), required for the source to cross θ_E. The binary nature of the lens requires the introduction of three extra parameters: The mass ratio q between the two components of the lens; their projected separation s, expressed in units of θ_E; and the source trajectory angle α with respect to the axis defined by the two components of the lens. A seventh parameter, ρ_*, representing the source radius normalized by the angular Einstein radius is also required to account for finite-source effects that are important when the source trajectory approaches or crosses a caustic (Ingrosso et al. 2009).

The magnification pattern produced by binary lenses is very sensitive to variations in s, q, which are the parameters that affect the shape and orientation of the caustics, and α, the source trajectory angle. Even small changes in these parameters can produce extreme changes in magnification as they may result in the trajectory of the source approaching or crossing a caustic (Dong et al. 2006, 2009a). On the other hand, changes in the other parameters cause the overall magnification pattern to vary smoothly.

To assess how the magnification pattern depends on the parameters, we start the modeling run by performing a hybrid search in parameter space whereby we explore a grid of s, q, and α values and optimize t_0, u_0, t_E, and ρ_* at each grid point by χ^2 minimization using Markov Chain Monte Carlo (MCMC). Our grid limits are set at $-1 \leqslant \log s \leqslant 1$, $-5 \leqslant \log q \leqslant 1$, and $0 \leqslant \alpha < 2\pi$, which are wide enough to guarantee that all local minima in parameter space have been identified. An initial MCMC run provides a map of the topology of the χ^2 surface, which is subsequently further refined by gradually narrowing down the grid parameter search space (Shin et al. 2012a; Street et al. 2013). Once we know the approximate locations of the local minima, we perform a χ^2 optimization using all seven parameters at each of those locations in order to determine the refined position of the minimum. From this set of local minima, we identify the location of the global minimum

[83] The "photocenter" refers to the center of the lensing magnification pattern. For a binary lens with a projected separation between the lens components less than the Einstein radius of the lens, the photocenter corresponds to the center of mass. For a lens with a separation greater than the Einstein radius, there exist two photocenters, each of which is located close to each lens component with an offset $q/[s(1+q)]$ toward the other lens component (Kim et al. 2009). In this case, the reference t_0, u_0 measurement is obtained from the photocenter to which the source trajectory approaches closest.

and check for the possible existence of degenerate solutions. We find no other solutions.

Since our analysis relies on data sets obtained from different telescopes and instruments that use different estimates for the reported photometric precision, we normalize the flux uncertainties of each data set by adjusting them as $e_i = f_i(\sigma_0^2 + \sigma_i^2)^{1/2}$, where f_i is a scale factor, σ_0 are the originally reported uncertainties, and σ_i is an additive uncertainty term for each data set i. The rescaling ensures that χ^2 per degree of freedom (χ^2/dof) for each data set relative to the model becomes unity. Data points with very large uncertainties and obvious outliers are also removed in the process.

In computing finite-source magnifications, we take into account the limb darkening of the source by modeling the surface brightness as $S_\lambda(\vartheta) \propto 1 - \Gamma_\lambda(1 - 1.5\cos\vartheta)$ (Albrow et al. 2001), where ϑ is the angle between the line of sight toward the source star and the normal to the source surface, and Γ_λ is the limb-darkening coefficient in passband λ. We adopt $\Gamma_V = 0.74$ and $\Gamma_I = 0.53$ from the Claret (2000) tables. These values are based on our classification of the stellar type of the source, as subsequently described.

The residuals contained additional smooth structure that the static binary model did not account for. This indicated the need to consider additional second-order effects. The event lasted for $\gtrsim$120 days, so the positional change of the observer caused by the orbital motion of the Earth around the Sun may have affected the lensing magnification. This introduces subtle long-term perturbations in the event light curve by causing the apparent lens-source motion to deviate from a rectilinear trajectory (Gould 1992; Alcock et al. 1995). Modeling this parallax effect requires the introduction of two extra parameters, $\pi_{E,N}$ and $\pi_{E,E}$, representing the components of the parallax vector $\boldsymbol{\pi}_E$ projected on the sky along the north and east equatorial axes, respectively. When parallax effects are included in the model, we use the geocentric formalism of Gould et al. (2004), which ensures that the parameters t_0, u_0, and t_E will be almost the same as when the event is fitted without parallax.

An additional effect that needs to be considered is the orbital motion of the lens system. The lens orbital motion causes the shape of the caustics to vary with time. To a first-order approximation, the orbital effect can be modeled by introducing two extra parameters that represent the rate of change of the normalized separation between the two lensing components ds/dt and the rate of change of the source trajectory angle relative to the caustics $d\alpha/dt$ (Albrow et al. 2000).

We conduct further modeling considering each of the higher-order effects separately and also model their combined effect. Furthermore, for each run considering a higher-order effect, we test models with $u_0 > 0$ and $u_0 < 0$ that form a pair of degenerate solutions resulting from the mirror-image symmetry of the source trajectory with respect to the binary lens axis. For each model, we repeat our calculations starting from different initial positions in parameter space to verify that the fits converge to our previous solution and that there are no other possible minima.

Table 2 lists the optimized parameters for the models we considered. We find that higher-order effects contribute strongly to the shape of the light curve. The model including the parallax effect provides a better fit than the standard model by $\Delta\chi^2 = 243.3$. The orbital effect also improves the fit by $\Delta\chi^2 = 512.8$. The combination of both parallax and orbital effects improves the fit by $\Delta\chi^2 = 563.3$. Due to the $u_0 > 0$ and $u_0 < 0$ degeneracy, there are two solutions for the orbital

Table 2
Lensing Parameters

Parameters	Standard	Parallax		Orbit		Orbit+Parallax	
		$u_0 > 0$	$u_0 < 0$	$u_0 > 0$	$u_0 < 0$	$u_0 > 0$	$u_0 < 0$
χ^2/dof	6921.019/6383	6850.358/6381	6677.685/6381	6408.371/6381	6408.255/6381	6357.680/6379	6381.358/6379
t_0 (HJD')	6141.63 ± 0.04	6141.70 ± 0.05	6141.66 ± 0.05	6141.24 ± 0.05	6141.28 ± 0.04	6141.33 ± 0.05	6141.19 ± 0.06
u_0	0.532 ± 0.001	0.527 ± 0.001	−0.520 ± 0.001	0.500 ± 0.002	−0.499 ± 0.002	0.496 ± 0.002	−0.497 ± 0.002
t_E (days)	62.37 ± 0.06	63.75 ± 0.18	69.39 ± 0.32	65.33 ± 0.20	65.53 ± 0.15	64.77 ± 0.19	61.91 ± 0.42
s	1.346 ± 0.001	1.345 ± 0.001	1.341 ± 0.001	1.300 ± 0.002	1.301 ± 0.001	1.301 ± 0.002	1.296 ± 0.002
q (10^{-3})	5.33 ± 0.04	5.07 ± 0.03	4.45 ± 0.04	6.97 ± 0.27	6.63 ± 0.05	5.92 ± 0.11	6.82 ± 0.19
α	0.852 ± 0.001	0.864 ± 0.002	−0.906 ± 0.002	0.861 ± 0.002	−0.859 ± 0.001	0.837 ± 0.002	−0.810 ± 0.005
ρ_* (10^{-2})	1.103 ± 0.008	1.053 ± 0.007	0.968 ± 0.009	1.233 ± 0.031	1.194 ± 0.011	1.111 ± 0.014	1.207 ± 0.023
$\pi_{E,N}$	...	0.118 ± 0.011	−0.414 ± 0.016	...	...	−0.143 ± 0.018	0.358 ± 0.042
$\pi_{E,E}$	...	−0.033 ± 0.007	−0.069 ± 0.009	...	...	0.047 ± 0.007	0.008 ± 0.006
ds/dt (yr^{-1})	...	...	...	0.765 ± 0.046	0.727 ± 0.017	0.669 ± 0.028	0.802 ± 0.033
$d\alpha/dt$ (yr^{-1})	...	...	...	1.284 ± 0.159	−1.108 ± 0.019	0.497 ± 0.059	−0.732 ± 0.085

Note. HJD' = HJD-2450000.

motion + parallax model, which have similar χ^2 values. Models involving the xallarap effect (source orbital motion) were also considered, but they did not outperform equivalent models involving only parallax.

In Figure 1, we present the best-fit model light curve superposed on the observed data. Figure 2 displays an enlarged view of the perturbation region of the light curve along with the source trajectory with respect to the caustic. The follow-up observations cover critical features of the perturbation regions that were not covered by the survey data. We note that the caustic varies with time and thus we present the shape of the caustic at the times of the first (t_1 = HJD $\sim$ 2456112) and second perturbations (t_2 = HJD $\sim$ 2456121). The source trajectory grazes the caustic structure at t_1 causing a substantial increase in magnification. As the caustic structure and trajectory evolve with time, the trajectory approaches another cusp at t_2, but does not cross it. This second approach causes an increase in magnification that is appreciably lower than that of the first encounter at t_1. The source trajectory is curved due to the combination of the parallax and orbital effects.

The mass and distance to the lens are determined by

$$M_{\rm tot} = \frac{\theta_E}{\kappa \pi_E}; \qquad D_L = \frac{\rm AU}{\pi_E \theta_E + \pi_S}, \tag{1}$$

where $\kappa = 4G/(c^2{\rm AU})$ and π_S is the parallax of the source star (Gould 1992). To determine these physical quantities, we require the values of π_E and θ_E. Modeling the event returns the value of π_E, whereas $\theta_E = \theta_*/\rho_*$ depends on the angular radius of the source star, θ_*, and the normalized source radius, ρ_*, which is also returned from modeling (see Table 2). Therefore, determining θ_E requires an estimate of θ_*.

To estimate the angular source radius, we use the standard method described in Yoo et al. (2004). In this procedure, we first measure the de-reddened color and brightness of the source star by using the centroid of the giant clump as a reference because its de-reddened magnitude $I_{0,c} = 14.45$ (Nataf et al. 2013) and color $(V-I)_{0,c} = 1.06$ (Bensby et al. 2011) are already known. For this calibration, we use a color–magnitude diagram obtained from CTIO observations in the I and V bands. We then convert the $V-I$ source color to $V-K$ using the color–color relations from Bessell & Brett (1988) and the source radius is obtained from the $\theta_* - (V-K)$ relations of Kervella et al. (2004). We

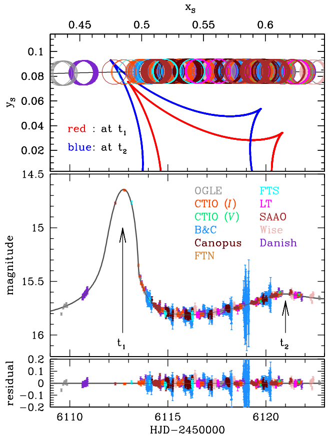

Figure 2. Bottom panel zooms in on the anomalous region of the light curve presented in Figure 1. Top panel displays the source trajectory, color coded for the individual contributions of each observatory and caustic structure at two different times corresponding to the first and second peaks of the anomaly. All scales are normalized by θ_E, and the size of the circles corresponds to the size of the source. The first peak deviates the strongest. This is a result of the trajectory of the source grazing the cusp of the caustic at t_1 (HJD $\sim$ 2456112), shown in red. The second deviation at t_2 (HJD $\sim$ 2456121) is significantly weaker and is due to the source trajectory passing close to another cusp of the caustic, shown in blue. The differences in the shape of the caustic shown at t_1 and t_2 are due to the orbital motion of the lens planet system.

(A color version of this figure is available in the online journal.)

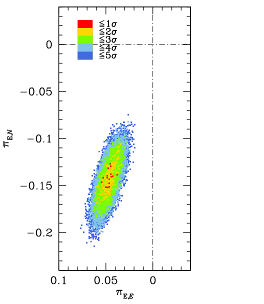

Figure 3. $\Delta\chi^2$ contours for the parallax parameters derived from our MCMC fits for the best binary lens model including orbital motion and the parallax effect.

(A color version of this figure is available in the online journal.)

derive the de-reddened magnitude and color of the source star as $I_0 = 14.62$ and $(V-I)_0 = 1.12$, respectively. This confirms that the source star is an early K-type giant. The estimated angular source radius is $\theta_* = 5.94 \pm 0.51$ μas. Combining this with our evaluation of ρ_*, we obtain $\theta_E = 0.53 \pm 0.05$ mas for the angular Einstein radius of the lens.

Our analysis is consistent with the results of Poleski et al. (2013). We confirm that the lens is a planetary system composed of a giant planet orbiting a low-mass star and we report the refined parameters of the system. Poleski et al. (2013) reported that there existed a pair of degenerate solutions with $u_0 > 0$ and $u_0 < 0$, although the positive u_0 solution is slightly preferred with $\Delta\chi^2 = 13.6$. We find a consistent result that the positive u_0 solution is preferred but the degeneracy is better discriminated by $\Delta\chi^2 = 23.7$.

The error contours of the parallax parameters for the best-fit model are presented in Figure 3. The uncertainty of each parameter is determined from the distribution of MCMC chain, and the reported uncertainty corresponds to the standard deviation of the distribution. We list the physical parameters of the system in Table 3 and their posterior probability distributions are shown in Figure 4.

The lens lies $D_L = 4.97 \pm 0.29$ kpc away in the direction of the Galactic Bulge. The more massive component of the lens has mass $M_\star = 0.44 \pm 0.07\,M_\odot$, so it is an early M-type dwarf star and its companion is a super-Jupiter planet with a mass $M_p = 2.73 \pm 0.43\,M_J$. The projected separation between the two components of the lens is $d_\perp = 3.45 \pm 0.26$ AU. The geocentric relative proper motion between the lens and the source is $\mu_{\rm Geo} = \theta_E/t_E = 3.02 \pm 0.26$ mas yr^{-1}. In the heliocentric frame, the proper motion is $\boldsymbol{\mu}_{\rm Helio} = (\mu_N, \mu_E) = (-2.91 \pm 0.26, 1.31 \pm 0.16)$ mas yr^{-1}.

We note that the derived physical lens parameters are somewhat different from those of Poleski et al. (2013). Specifically, the mass of the host star derived in Poleski et al. (2013) is 0.59 $M_\odot$, which is $\sim$34% greater than our estimate. Half of this difference comes from the slightly larger Einstein radius ob-

Table 3
Physical Parameters

Parameters	Quantity
Mass of the host star ($M_\star$)	$0.44 \pm 0.07\,M_\odot$
Mass of the planet (M_p)	$2.73 \pm 0.43\,M_J$
Distance to the lens (D_L)	4.97 ± 0.29 kpc
Projected star-planet separation ($d_\perp$)	3.45 ± 0.26 AU
Einstein radius (θ_E)	0.53 ± 0.05 mas
Geocentric proper motion ($\mu_{\rm Geo}$)	3.02 ± 0.26 mas yr^{-1}

tained by Poleski et al. (2013) from the OGLE-IV photometry and the remaining part from the slightly larger $\pi_{E,N}$ component of the parallax obtained from modeling the survey and follow-up photometry as presented in this paper. It should be noted that the parameters derived by both our and the Poleski et al. (2013) models are consistent within the 1σ level.

To further check the consistency between our model and that of Poleski et al. (2013), we conducted additional modeling based on different combinations of data sets. We first test a model based on OGLE data exclusively in order to see whether we can retrieve the physical parameters reported in Poleski et al. (2013). From this modeling, we derive physical parameters consistent with those of Poleski et al. (2013), indicating that the differences are due to the additional coverage provided by the follow-up observations. We conducted another modeling run using OGLE observations, but also included CTIO, FTS, and SAAO data, i.e., those data sets covering the anomalous peak. This modeling run resulted in physical parameters that are consistent with the values extracted from fitting all combined data together, as reported in this paper. This indicates that the differences between Poleski et al. (2013) and this analysis, although consistent within the 1σ level, come mainly from follow-up data that provide better coverage of the perturbation. Therefore, using survey and follow-up data together, we arrive at a more accurate determination of the ρ and $\pi_{E,N}$ parameters, which leads to a refinement of the physical parameters of the planetary system.

4. CONCLUSIONS

Microlensing event OGLE-2012-BLG-0406 was intensively observed by survey and follow-up groups using 10 different telescopes around the world. Anomalous deviations observed in the light curve were recognized to be due to the presence of a planetary companion even before the event reached its central peak. The anomalous behavior was first identified and assessed automatically via software agents. Most follow-up teams responded to these alerts by adjusting their observing strategies accordingly. This highlights the importance of circulating early models to the astronomical community that help to identify important targets for follow-up observations (Shin et al. 2012b). There are $\sim$100 follow-up alerts circulated annually, $\sim$10% of which turn out to be planet candidates.

Our analysis of the combined data is consistent with the results of Poleski et al. (2013) and we report the refined parameters of the system. We find that this refinement is mainly due to follow-up observations over the anomaly. The primary lens with mass $M_\star = 0.44 \pm 0.07\,M_\odot$ is orbited by a planetary companion with mass $M_p = 2.73 \pm 0.43\,M_J$ at a projected separation of $d_\perp = 3.45 \pm 0.26$ AU. The distance to the system is $D_L = 4.97 \pm 0.29$ kpc in the direction of the Galactic Bulge.

This is the fourth cold super-Jupiter planet around a low-mass star discovered by microlensing (Dong et al. 2009b;

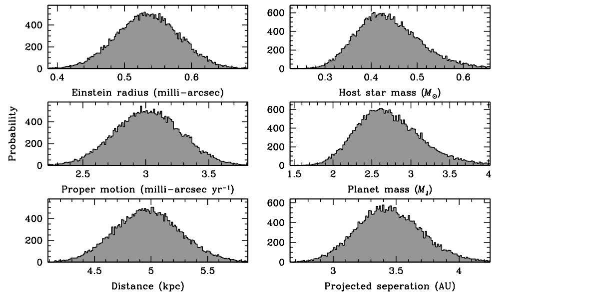

Figure 4. Physical parameter uncertainties pertaining to the lens as derived from the MCMC runs optimizing our binary lens model including parallax and orbital motion for the $u_0 > 0$ trajectory.

Batista et al. 2011; Yee et al. 2012) and the first such system whose characteristics were derived solely from microlensing data, without considering any external information.

Microlensing is currently the only way to obtain high precision mass measurements for this type of system. Radial velocity, in addition to the $m \sin i$ degeneracy, at present does not have long enough data streams to measure the parameters of such systems. However, recently Montet et al. (2013) have developed a promising new method to discover them using a combination of radial velocity and direct imaging. They identify long term trends in radial velocity data and use adaptive optics imaging to rule out the possibility that these are due to stars. This means that the trends are either due to large planets or brown dwarfs. This approach does not yield precise characterization but provides important statistical information. Their results are consistent with gravitational microlensing estimates of planet abundance in that region of parameter space.

The precise mechanism of how such large planets form and evolve around low mass stars is still an open question. Radial velocity and transit surveys have been finding massive gas-giant planets around FGK stars for years (Batalha et al. 2013) but these stars have protoplanetary disks that are sufficiently massive to allow the formation of super-Jupiter planets. On the other hand, protoplanetary disks around M dwarfs have masses of only a few Jupiter mass, so massive gas giants should be relatively hard to produce (Apai 2013).

Recent observational studies have revealed that protoplanetary disks are as common around low-mass stars as higher-mass stars (Williams & Cieza 2011), arguing for the same formation processes. In addition, there is mounting evidence, but not yet conclusive, that disks last much longer around low-mass stars (Apai 2013). Longer disk lifetimes may be conducive to the formation of super-Jupiters. The microlensing discoveries suggest that giant planets around low-mass stars may be as common as around higher-mass stars but may not undergo significant migration (Gould et al. 2010).

Simulations using the core accretion formalism can produce such planets within reasonable disk lifetimes of a few Myr (Mordasini et al. 2012) provided the core mass is sufficiently large or the opacity of the planet envelope during gas accretion is decreased by assuming that the dust grains have grown to larger sizes than the typical interstellar values (R. Nelson, 2013, private communication). Furthermore, gravitational instability models of planet formation can also potentially produce such objects when the opacity of the protoplanetary disk is low enough to allow local fragmentation at greater distances from the host star, and subsequently migrating the planet to distances of a few AU.

It is worth noting that highly magnified microlensing events involving extended stellar sources may produce appreciable polarization signals (Ingrosso et al. 2012). If such signals are observed during a microlensing event, they can be combined with photometric observations to place further constraints on the lensing geometry and physical properties of the lens.

Y.T. thanks the CBNU group for their advice and hospitality while in Korea. D.M.B., M.D., K.H., C.S., R.A.S., K.A.A., M.H., and Y.T. are supported by NPRP grant NPRP-09-476-1-78 from the Qatar National Research Fund (a member of Qatar Foundation). C.S. received funding from the European Union Seventh Framework Programme (FP7/2007-2013) under grant agreement No. 268421. K.H. is supported by a Royal Society Leverhulme Trust Senior Research Fellowship. J.P.B. and P.F. acknowledge the financial support of Programme National de Plantologie and of IAP. The OGLE project has received funding from the European Research Council under the European Community's Seventh Framework Programme (FP7/2007-2013)/ERC grant agreement No. 246678 to AU. Work by C.H. was supported by Creative Research Initiative Program (2009-0081561) of National Research Foundation of Korea. The MOA experiment was supported by grants JSPS22403003 and JSPS23340064. T.S. acknowledges the support JSPS24253004. T.S. is supported by the grant JSPS23340044. T.C.H. acknowledges support from KRCF via the KRCF Young Scientist Fellowship program and financial support from KASI grant number 2013-9-400-00. Y.M. acknowledges support from JSPS grants JSPS23540339 and JSPS19340058. A.G. and B.S.G. acknowledge support from NSF AST-1103471. M.R. acknowledges support from

FONDECYT postdoctoral fellowship No3120097. B.S.G., A.G., and R.W.P. acknowledge support from NASA grant NNX12AB99G. Y.D., A.E., and J.S. acknowledge support from the Communaute francaise de Belgique—Actions de recherche concertees—Academie Wallonie-Europe. This work is based in part on data collected by MiNDSTEp with the Danish 1.54m telescope at the ESO La Silla Observatory. The Danish 1.54m telescope is operated based on a grant from the Danish Natural Science Foundation (FNU).

REFERENCES

Alard, C., & Lupton, R. H. 1998, ApJ, 503, 325
Albrow, M. D., An, J., Beaulieu, J.-P., et al. 2001, ApJ, 549, 759
Albrow, M. D., Beaulieu, J.-P., Caldwell, J. A. R., et al. 2000, ApJ, 534, 894
Albrow, M. D., Horne, K., Bramich, D. M., et al. 2009, MNRAS, 397, 2099
Alcock, C., Allsman, R. A., Alves, D., et al. 1995, ApJ, 454, 125
Apai, D. 2013, AN, 334, 57
Batalha, N. M., Rowe, J. F., Bryson, S. T., et al. 2013, ApJS, 204, 24
Batista, V., Gould, A., Dieters, S., et al. 2011, A&A, 529, 102
Beaulieu, J.-P., Bennett, D. P., Fouqué, P., et al. 2006, Natur, 439, 437
Bensby, T., Adén, D., Meléndez, J., et al. 2011, A&A, 533, A134
Bessell, M. S., & Brett, J. M. 1988, PASP, 100, 1134
Bond, I. A., Abe, F., Dodd, R. J., et al. 2001, MNRAS, 327, 868
Bozza, V. 2010, MNRAS, 408, 2188
Bramich, D. M. 2008, MNRAS, 386, L77
Cassan, A., Kubas, D., Beaulieu, J.-P., et al. 2012, Natur, 481, 167
Claret, A. 2000, A&A, 363, 1081
Dominik, M. 2010, GReGr, 42, 2075
Dominik, M., Horne, K., Allan, A., et al. 2008, AN, 329, 248
Dominik, M., Jørgensen, U. G., Rattenbury, N. J., et al. 2010, AN, 331, 671
Dominik, M., Rattenbury, N. J., Allan, A., et al. 2007, MNRAS, 380, 792
Dong, S., Bond, I. A., Gould, A., et al. 2009a, ApJ, 698, 1826
Dong, S., DePoy, D. L., Gaudi, B. S., et al. 2006, ApJ, 642, 842
Dong, S., Gould, A., Udalski, A., et al. 2009b, ApJ, 695, 970
Gaudi, B. S. 2011, in Exoplanets, ed. S. Seager (Tucson, AZ: Univ. Arizona Press), 79
Gaudi, B. S. 2012, ARA&A, 50, 411
Gaudi, B. S., Bennett, D. P., Udalski, A., et al. 2008, Sci, 319, 927
Gould, A. 1992, ApJ, 392, 442
Gould, A. 2004, ApJ, 606, 319
Gould, A., Dong, S., Gaudi, B. S., et al. 2010, ApJ, 720, 1073
Gould, A., Udalski, A., An, D., et al. 2006, ApJL, 644, L37
Griest, K., & Safizadeh, N. 1998, ApJ, 500, 37
Han, C., Udalski, A., Choi, J.-Y., et al. 2013, ApJ, 762, 28
Horne, K., Snodgrass, C., & Tsapras, Y. 2009, MNRAS, 396, 2087
Ingrosso, G., Novati, S. C., de Paolis, F., et al. 2009, MNRAS, 399, 219
Ingrosso, G., Novati, S. C., de Paolis, F., et al. 2012, MNRAS, 426, 1496
Johnson, J. A., Howard, A. W., Marcy, G. W., et al. 2010, PASP, 122, 149
Kains, N., Street, R. A., Choi, J.-Y., et al. 2013, A&A, 552, 70
Kalas, P., Graham, J. R., & Clampin, M. 2005, Natur, 435, 1067
Kervella, P., Bersier, D., Mourard, D., et al. 2004, A&A, 428, 587
Kim, D., Han, C., & Park, B.-J. 2009, JKAS, 42, 39
Laughlin, G., Bodenheimer, P., & Adams, F. C. 2004, ApJ, 612, 73
Lecar, M., Podolak, M., Sasselov, D., & Chiang, E. 2006, ApJ, 640, 1115
Mao, S., & Paczyński, B. 1991, ApJL, 374, L37
Miguel, Y., Guilera, O. M., & Brunini, A. 2011, MNRAS, 417, 314
Montet, B. T., Crepp, J. R., Johnson, J. A., et al. 2013, ApJ, arXiv:1307.5849M, submitted
Mordasini, C., Alibert, Y., Benz, W., et al. 2012, A&A, 547, 112
Nataf, D. M., Gould, A., Fouqué, P., et al. 2013, ApJ, 769, 88
Paczyński, B. 1986, ApJ, 304, 1
Poleski, R., Udalski, A., Dong, S., et al. 2013, ApJ, arXiv:1307.4084P, in press
Schneider, P., & Weiss, A. 1992, A&A, 260, 1
Shin, I.-G., Choi, J.-Y., Park, S.-Y., et al. 2012a, ApJ, 746, 127
Shin, I.-G., Han, C., Gould, A., et al. 2012b, ApJ, 760, 116
Street, R., Choi, J.-Y., Tsapras, Y., et al. 2013, ApJ, 763, 67
Sumi, T., Abe, F., Bond, I. A., et al. 2003, ApJ, 591, 204
Sumi, T., Bennett, D. P., Bond, I. A., et al. 2010, ApJ, 710, 1641
Sumi, T., Kamiya, K., Bennett, D. P., et al. 2011, Natur, 473, 349
Tsapras, Y., Horne, K., Kane, S., et al. 2003, MNRAS, 343, 1131
Tsapras, Y., Street, R., Horne, K., et al. 2009, AN, 330, 4
Udalski, A. 2003, AcA, 53, 291
Williams, P. W., & Cieza, A. L. 2011, ARA&A, 49, 67
Yee, J., Shvartzvald, Y., Gal-Yam, A., et al. 2012, ApJ, 775, 102
Yoo, J., DePoy, D. L., Gal-Yam, A., et al. 2004, ApJ, 603, 139
Zakharov, A. F. 1995, A&A, 293, 1

A&A 562, A126 (2014)
DOI: 10.1051/0004-6361/201323265

Astronomy & Astrophysics

Physical properties and transmission spectrum of the WASP-80 planetary system from multi-colour photometry★

L. Mancini[1], J. Southworth[2], S. Ciceri[1], M. Dominik[3], Th. Henning[1], U. G. Jørgensen[4,5], A. F. Lanza[6], M. Rabus[7,1], C. Snodgrass[8], C. Vilela[2], K. A. Alsubai[9], V. Bozza[10,11], D. M. Bramich[12], S. Calchi Novati[13,10], G. D'Ago[10,11], R. Figuera Jaimes[14,3], P. Galianni[3], S.-H. Gu[15,16], K. Harpsøe[4,5], T. Hinse[17], M. Hundertmark[3], D. Juncher[4,5], N. Kains[14], H. Korhonen[18,4,5], A. Popovas[4,5], S. Rahvar[19,20], J. Skottfelt[4,5], R. Street[21], J. Surdej[22], Y. Tsapras[21,23], X.-B. Wang[15,16], and O. Wertz[22]

[1] Max Planck Institute for Astronomy, Königstuhl 17, 69117 Heidelberg, Germany
e-mail: mancini@mpia.de
[2] Astrophysics Group, Keele University, Keele, ST5 5BG, UK
[3] SUPA, University of St Andrews, School of Physics & Astronomy, North Haugh, St Andrews KY16 9SS, UK
[4] Niels Bohr Institute, University of Copenhagen, Juliane Maries vej 30, 2100 Copenhagen Ø, Denmark
[5] Centre for Star and Planet Formation, Geological Museum, Øster Voldgade 5–7, 1350 Copenhagen, Denmark
[6] INAF–Osservatorio Astrofisico di Catania, via S.Sofia 78, 95123 Catania, Italy
[7] Instituto de Astrofísica, Facultad de Física, Pontificia Universidad Católica de Chile, Av. Vicuña Mackenna 4860, 7820436 Macul, Santiago, Chile
[8] Max-Planck-Institute for Solar System Research, Max-Planck Str. 2, 37191 Katlenburg-Lindau, Germany
[9] Qatar Foundation, PO Box 5825, Doha, Qatar
[10] Dipartimento di Fisica "E.R. Caianiello", University of Salerno, via Giovanni Paolo II, 84084 Fisciano, Italy
[11] Istituto Nazionale di Fisica Nucleare, Sezione di Napoli, Napoli, Italy
[12] Qatar Environment and Energy Research Institute, Qatar Foundation, Tornado Tower, Floor 19, PO Box 5825, Doha, Qatar
[13] Istituto Internazionale per gli Alti Studi Scientifici (IIASS), 84019 Vietri Sul Mare, Italy
[14] European Southern Observatory, Karl-Schwarzschild-Straße 2, 85748 Garching bei München, Germany
[15] Yunnan Observatory, Chinese Academy of Sciences, 650011 Kunming, PR China
[16] Key Laboratory for the Structure and Evolution of Celestial Objects, Chinese Academy of Sciences, 650011 Kunming, PR China
[17] Korea Astronomy and Space Science Institute, 305–348 Daejeon, Republic of Korea
[18] Finnish Centre for Astronomy with ESO (FINCA), University of Turku, Väisäläntie 20, 21500 Piikkiö, Finland
[19] Department of Physics, Sharif University of Technology, PO Box 11155-9161 Tehran, Iran
[20] Perimeter Institute for Theoretical Physics, 31 Caroline St. N., Waterloo N2L 2Y5,Canada
[21] Las Cumbres Observatory Global Telescope Network, 6740B Cortona Drive, Goleta CA 93117, USA
[22] Institut d'Astrophysique et de Géophysique, Université de Liège, 4000 Liège, Belgium
[23] School of Physics and Astronomy, Queen Mary University of London, Mile End Road, London E1 4NS, UK

Received 17 December 2013 / Accepted 18 January 2014

ABSTRACT

WASP-80 is one of only two systems known to contain a hot Jupiter which transits its M-dwarf host star. We present eight light curves of one transit event, obtained simultaneously using two defocussed telescopes. These data were taken through the Bessell *I*, Sloan $g'r'i'z'$ and near-infrared *JHK* passbands. We use our data to search for opacity-induced changes in the planetary radius, but find that all values agree with each other. Our data are therefore consistent with a flat transmission spectrum to within the observational uncertainties. We also measure an activity index of the host star of $\log R'_{\rm HK} = -4.495$, meaning that WASP-80 A shows strong chromospheric activity. The non-detection of starspots implies that, if they exist, they must be small and symmetrically distributed on the stellar surface. We model all available optical transit light curves and obtain improved physical properties and orbital ephemerides for the system.

Key words. planetary systems – stars: fundamental parameters – stars: individual: WASP-80 – techniques: photometric

1. Introduction

Planetary systems in which the host star is a late-type dwarf are of particular interest because they have favourable ratios of planetary mass and radius to those of the star. This makes the detections of small and low-mass planets easier for the transit and Doppler methods, respectively. If the planet is transiting and the parent star is bright, then the planetary atmosphere can be probed by transmission spectroscopy (e.g. GJ 1214 b: Croll et al. 2011; Crossfield et al. 2011; Bean et al. 2011; Berta et al. 2012; Colòn & Gaidos 2013; GJ 3470 b: Crossfield et al. 2013; GJ 436 b: Pont et al. 2009; Gibson et al. 2011), transmission photometry (e.g. GJ 1214 b: de Mooij et al. 2012; Murgas et al. 2012; de Mooij et al. 2013; Narita et al. 2013; GJ 3470 b: Nascimbeni et al. 2013) and observations of secondary eclipses

★ Full Table 2 is only available at the CDS via anonymous ftp to cdsarc.u-strasbg.fr (130.79.128.5) or via http://cdsarc.u-strasbg.fr/viz-bin/qcat?J/A+A/562/A126

Table 1. Details of the transit observations presented in this work.

Telescope	Date of first obs.	Start time (UT)	End time (UT)	$N_{\rm obs}$	$T_{\rm exp}$ (s)	$T_{\rm obs}$ (s)	Filter	Airmass	Moon illum.	Aperture radii (px)	Scatter (mmag)
DFOSC	2013 06 16	05:35	09:44	200	60	75	Bessel *I*	$1.33 \rightarrow 1.12 \rightarrow 1.37$	46%	16, 38, 60	0.49
GROND	2013 06 16	05:00	10:50	162	60	120	Sloan g'	$1.38 \rightarrow 1.12 \rightarrow 1.79$	46%	30, 90, 120	0.80
GROND	2013 06 16	05:00	10:50	162	60	120	Sloan r'	$1.38 \rightarrow 1.12 \rightarrow 1.79$	46%	35, 100,120	0.49
GROND	2013 06 16	05:00	10:50	162	60	120	Sloan i'	$1.38 \rightarrow 1.12 \rightarrow 1.79$	46%	35, 80, 100	0.82
GROND	2013 06 16	05:00	10:50	162	60	120	Sloan z'	$1.38 \rightarrow 1.12 \rightarrow 1.79$	46%	30, 80, 100	1.06
GROND	2013 06 16	05:00	10:50	523	4	38	*J*	$1.38 \rightarrow 1.12 \rightarrow 1.79$	46%	6, 11, 21	4.15
GROND	2013 06 16	05:00	10:50	523	4	38	*H*	$1.38 \rightarrow 1.12 \rightarrow 1.79$	46%	5, 12, 22	3.28
GROND	2013 06 16	05:00	10:50	523	4	38	*K*	$1.38 \rightarrow 1.12 \rightarrow 1.79$	46%	7, 11, 20	5.14

Notes. $N_{\rm obs}$ is the number of observations, $T_{\rm exp}$ is the exposure time, $T_{\rm obs}$ is the observational cadence, and "Moon illum." is the fractional illumination of the Moon at the midpoint of the transit. The aperture sizes are the radii of the software apertures for the star, inner sky and outer sky, respectively. Scatter is the rms scatter of the data versus a fitted model.

(e.g. GJ 1214 b: Fraine et al. 2013; GJ 436 b: Stevenson et al. 2010; Knutson et al. 2011).

Recent analyses of HARPS and *Kepler* data suggest that Neptunes and super-Earths with orbital periods shorter than 50 days are very abundant around M stars (Bonfils et al. 2013; Dressing & Charbonneau 2013). Bonfils et al. (2013) also established that giant planets have a much lower occurrence rate for orbital periods in the range 10–100 d, supporting the idea that the frequency of giant planets decreases toward less massive parent stars, irrespective of period (Johnson et al. 2010).

Accordingly, only two transiting hot Jupiters have so far been found orbiting M dwarfs[1]. These are Kepler-45 b (KOI-254; $R_{\rm p} = 0.999\,R_{\rm Jup}$, $M_{\rm p} = 0.500\,M_{\rm Jup}$, Johnson et al. 2012; Southworth 2012) and WASP-80 b ($R_{\rm p} = 0.95\,R_{\rm Jup}$, $M_{\rm p} = 0.55\,M_{\rm Jup}$, Triaud et al. 2013). Whilst Kepler-45 is a distant (333 pc) and faint ($V = 16.9$) star, WASP-80 is much closer (60 pc) and brighter ($V = 11.9$), enabling a detailed study of its characteristics with ground-based facilities. Moreover, due to its low density and large transit depth (∼3%), WASP-80 b is a very suitable target for transmission spectroscopy and photometry.

Here we present photometric observations of a transit of WASP-80 b, observed simultaneously with two telescopes and in eight different passbands. We use these data to refine the physical parameters of the planetary system and provide the first probe of the day-night terminator region of this giant planet by transmission photometry.

2. Observations and data reduction

A complete transit of WASP-80 b was observed on 2013 June 16 (see Table 1), using the DFOSC imager mounted on the 1.54-m Danish Telescope at ESO La Silla during the 2013 observing campaign by the MiNDSTEp consortium (Dominik et al. 2010). The instrument has a field of view of $13.7' \times 13.7'$ and a plate scale of $0.39''$ pixel^{-1}. The observations were performed through a Bessel *I* filter and using the *defocussing* method. The telescope was autoguided and the CCD was windowed to reduce the readout time. The night was photometric.

The data were reduced using , an IDL[2] pipeline for time-series photometry (Southworth et al. 2009). The images were debiased and flat-fielded using standard methods, then subjected to aperture photometry using the [3] task and an optimal ensemble of comparison stars. Pointing variations were followed by cross-correlating each image against a reference image. The shape of the light curve is very insensitive to the aperture sizes, so we chose those which yielded the lowest scatter. The final light curve was detrended to remove slow instrumental and astrophysical trends by fitting a straight line to the out-of-transit data. This process was simultaneous with the optimisation of the weights of an ensemble of comparison stars. The final differential-flux light curve is plotted in Fig. 1.

The same transit was also observed using the Gamma Ray burst Optical and Near-infrared Detector (GROND) instrument mounted on the MPG[4]/ESO 2.2-m telescope, also located at ESO La Silla. GROND is an imaging system capable of simultaneous photometric observations in four optical (similar to Sloan g', r', i', z') and three near-infrared (NIR; *J*, *H*, *K*) passbands (Greiner et al. 2008). Each of the four optical channels is equipped with a back-illuminated 2048×2048 E2V CCD, with a field of view of $5.4' \times 5.4'$ at $0.158''$pixel^{-1}. The three NIR channels use 1024×1024 Rockwell HAWAII-1 arrays with a field of view of $10' \times 10'$ at $0.6''$ pixel^{-1}. The observations were also performed with the telescope defocussed.

The optical data were reduced as for the Danish Telescope, except that a quadratic function was used to detrend the light curves. The NIR data were reduced following the procedure described in Mancini et al. (2013c). The optical light curves are plotted superimposed in the bottom panel of Fig. 1 in order to highlight the differences among the transit depths and light curve shapes of the simultaneous multi-band observations. The GROND i' and Danish Telescope *I* light curves are in excellent agreement. The differential-magnitude light curves are given in Table 2.

2.1. Stellar activity measurement

We obtained a spectrum of the Ca II H and K lines on the night of 2012 October 1, using the *William Herschel* Telescope with the ISIS grating spectrograph, in order to measure the $\log R'_{\rm HK}$ stellar activity index. With the H2400B grating we obtained a spectrum covering 375–415 nm at a reciprocal dispersion of 0.011 nm pixel^{-1}. An exposure time of 600 s yielded a continuum signal to noise ratio of approximately 20 in the region of the H and K lines. The data were reduced using optimal

[1] Two brown dwarfs are also known to transit M stars: NLTT 41135 (Irwin et al. 2010) and LHS 6343 (Johnson et al. 2011).
[2] IDL is a trademark of the ITT Visual Information Solutions: http://www.ittvis.com/ProductServices/IDL.aspx
[3] is part of the subroutine library distributed by NASA on http://idlastro.gsfc.nasa.gov
[4] Max Planck Gesellschaft.

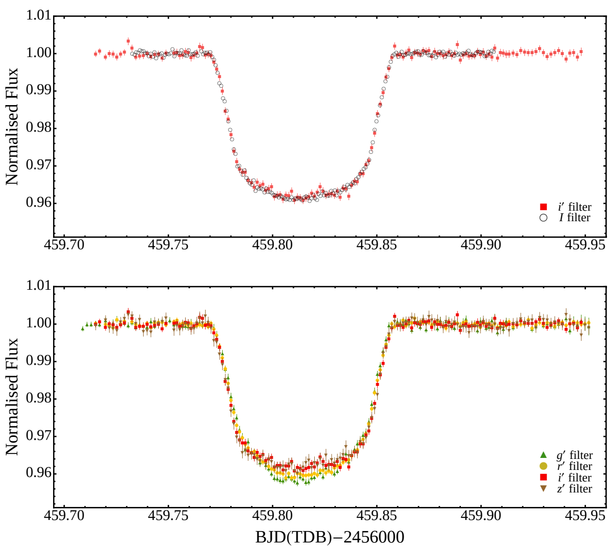

Fig. 1. Light curves of a transit of WASP-80 b. *Top panel*: light curves obtained with the Danish Telescope (Bessel-*I* filter) and with GROND (Sloan-i'), highlighting the good match between the transit shapes in the two independent observations. The circles denoting the DK points have the same size as the corresponding error bars, which have been suppressed for clarity. *Bottom panel*: light curves obtained with GROND through four optical filters simultaneously, showing how the transit shape changes with wavelength.

Table 2. Excerpts of the light curves of WASP-80.

Telescope	Filter	BJD (TDB)	Diff. mag.	Uncertainty
DK 1.54-m	*I*	2456459.732729	0.00002	0.00055
DK 1.54-m	*I*	2456459.733794	0.00029	0.00055
ESO 2.2-m	g'	2456459.708924	0.00122	0.00087
ESO 2.2-m	g'	2456459.710953	0.00079	0.00087
ESO 2.2-m	r'	2456459.715126	−0.00021	0.00033
ESO 2.2-m	r'	2456459.719854	0.00084	0.00033
ESO 2.2-m	i'	2456459.715126	0.00009	0.00064
ESO 2.2-m	i'	2456459.716988	−0.00059	0.00064
ESO 2.2-m	z'	2456459.715126	0.00041	0.00064
ESO 2.2-m	z'	2456459.719854	−0.00109	0.00064

Notes. Full Table 2 is available at the CDS. A portion is shown here for guidance regarding its form and content.

extraction as implemented in the and packages (Marsh 1989) and calibrated onto the Mt. Wilson system using 20 standard stars from Vaughan et al. (1978); further details can be found in Vilela et al. (in prep.).

The very strong H and K emission lines for WASP-80 A (Fig. 2) yield the emission measure $\log R'_{\rm HK} = -4.495$, which is indicative of high activity (e.g. Noyes et al. 1984). Given this strong chromospheric emission one might expect to see evidence of spot activity, but Triaud et al. (2013) found no rotational modulation in the SuperWASP light curves to a limit of ∼1 mmag, and we see no evidence of spot anomalies (e.g. Tregloan-Reed et al. 2013) in our light curves. A plausible explanation is that the stellar surface contains many spots which are too small to noticeably affect transit light curves, and which are approximately symmetrically distributed so cause no measurable rotation signal in the SuperWASP light curves.

This suggestion is in agreement with the conclusions of Jackson & Jeffries (2012) (see also Jackson & Jeffries 2013), who analysed two large samples of low-mass stars ($0.2 < M_\star/M_\odot < 0.7$) in the open cluster NGC 2516: one sample with measurable rotational modulation and one without. The two samples coincide on the colour–magnitude diagram for the cluster, and have the same rotational velocities and levels of chromospheric activity. This difference can be explained by the photometrically constant stars having many small starspots rather than few large ones.

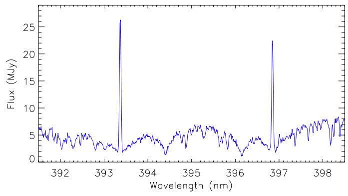

Fig. 2. Spectrum of WASP-80 in the region of the Ca II H and K lines showing the strong chromospheric emission in the line cores.

In the case of WASP-80, assuming that the photometric modulation due to starspots is smaller than 1 mmag, we can estimate the maximum deviation of the covering factor from uniformity of a few 10^{-3} of the disc area, by considering that the spot temperature contrast is probably smaller in cooler stars with respect to the Sun (see Berdyugina 2005).

3. Light-curve analysis

The light curves were modelled using the [5] code (see Southworth 2012, and references therein), which represents the star and planet as biaxial spheroids for calculation of the reflection and ellipsoidal effects and as spheres for calculation of the eclipse shapes. The main parameters fitted by are the orbital inclination, *i*, the transit midpoint, T_0, and the sum and ratio of the fractional radii of the star and planet, $r_{\rm A} + r_{\rm b}$ and $k = r_{\rm b}/r_{\rm A}$. The fractional radii are defined as $r_{\rm A} = R_{\rm A}/a$ and $r_{\rm b} = R_{\rm b}/a$, where *a* is the orbital semimajor axis, and $R_{\rm A}$ and $R_{\rm b}$ are the absolute radii of the star and the planet, respectively. Each light curve was modelled separately using the quadratic limb darkening (LD) law. The linear LD coefficients were fitted to the data whereas the quadratic LD coefficients were fixed at theoretical values (Claret 2004b) but perturbed by ±0.1 during the process of error estimation. We assumed that the orbit was circular (Triaud et al. 2013). We included in the fits the coefficients of a linear (DFOSC) or quadratic (GROND) polynomial versus time in order to fully account for the uncertainty in the detrending of the light curves.

Time-series photometry is unavoidably afflicted by correlated (red) noise which is not accounted for by standard error estimation algorithms (e.g. Carter & Winn 2009). The algorithm we use to perform aperture photometry also tends to underestimate the true uncertainties in the relative magnitude measurements. We therefore rescaled the error bars as in our previous works (Mancini et al. 2013a,b,c), first to give a reduced χ^2 of $\chi^2_\nu = 1$ and then using the β approach (e.g. Gillon et al. 2006; Winn et al. 2008; Gibson et al. 2008).

3.1. Orbital period determination

We used our photometric data to refine the orbital period of WASP-80 b. The transit time for each of our datasets was obtained by fitting with , and uncertainties were estimated using Monte Carlo simulations. We also modelled the follow-up light curves reported in Triaud et al. (2013) in order to obtain a timing for each dataset. All timings were placed on the BJD(TDB) time system and are summarised in Table 3. The resulting measurements of transit midpoints were fitted with a straight line to obtain a final orbital ephemeris:

$$T_0 = {\rm BJD(TDB)}\,2\,456\,125.417405(99) + 3.06786144(87)\,E,$$

where *E* is the number of orbital cycles after the reference epoch, which we take to be that estimated by Triaud et al. (2013), and quantities in brackets denote the uncertainty in the final digit of the preceding number. The quality of fit, $\chi^2_\nu = 0.99$, indicates that a linear ephemeris is a good match to the observations. A plot of the residuals (Fig. 3) shows no evidence for systematic deviations from the predicted transit times. However, the number of observed transits of this planet is still very low so transit timing variations cannot be ruled out.

Table 3. Times of mid-transit of WASP-80 b and their residuals versus a linear orbital ephemeris.

Time of minimum BJD(TDB)−2400000	Cycle No.	Residual (d)	Reference
56054.856812 ± 0.000135	−23	0.000220	1
56134.620911 ± 0.000222	3	−0.000078	1
56180.638678 ± 0.000165	18	−0.000233	1
56459.814384 ± 0.000044	109	0.000081	2
56459.814284 ± 0.000096	109	−0.000019	3
56459.814414 ± 0.000082	109	0.000111	4
56459.814350 ± 0.000103	109	0.000047	5
56459.814233 ± 0.000161	109	−0.000070	6

Notes. References: (1) Triaud et al. (2013); (2) Danish telescope (this work); (3) GROND g' (this work); (4) GROND r' (this work); (5) GROND i' (this work); (6) GROND z' (this work).

3.2. Photometric parameters

The GROND light curves and the best-fitting models are shown in Fig. 4. A similar plot is reported in Fig. 5 for the light curves from the Danish Telescope and from Triaud et al. (2013). The parameters of the fits are given in Table 4. Uncertainties in the fitted parameters from each solution were calculated from 3500 Monte Carlo simulations and by a residual-permutation algorithm (Southworth 2008). The larger of the two possible error bars was retained in each case. The final photometric parameters are the weighted mean of the results presented in Table 4. Values obtained by Triaud et al. (2013) are also reported for comparison. Due to their lower quality (see Fig. 4), we did not use the GROND-NIR light curves to estimate the final photometric parameters of WASP-80.

4. Physical properties

Following the *Homogeneous Studies* approach (Southworth 2012, and references therein), we used the photometric parameters estimated in the previous section and the spectroscopic properties of the parent star (velocity amplitude $K_{\rm A} = 110.9^{+3.0}_{-3.3}\,{\rm m\,s^{-1}}$, effective temperature $T_{\rm eff} = 4145 \pm 100$ K and metallicity $\left[\frac{\rm Fe}{\rm H}\right] = -0.14 \pm 0.16$) taken from Triaud et al. (2013), to revise the physical properties of the WASP-80 system using the code.

We iteratively determined the velocity amplitude of the planet ($K_{\rm b}$) which yielded the best agreement between the

[5] The source code of is available at: http://www.astro.keele.ac.uk/jkt/codes/jktebop.html

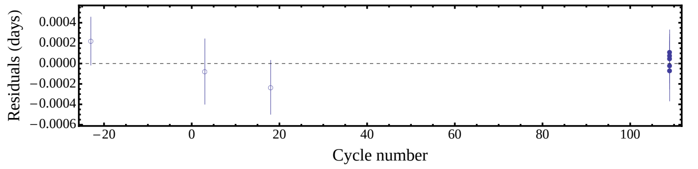

Fig. 3. Residuals of the timings of mid-transit of WASP-80 b versus a linear ephemeris. Timings based on the observations obtained by Triaud et al. (2013) are plotted using open circles, while the other timings (this work) are plotted with filled circles.

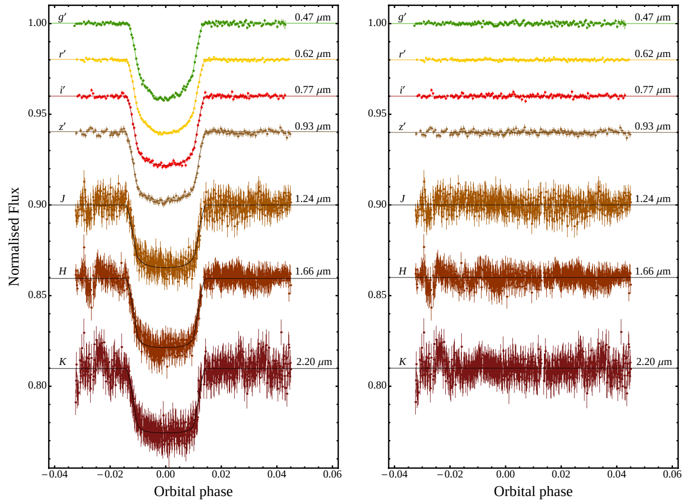

Fig. 4. *Left-hand panel*: simultaneous optical and NIR light curves of the transit event of WASP-80 b observed with GROND. The best fits are shown as solid lines for each data set. The passbands are labelled on the left of the figure, and their central wavelengths are given on the right. *Right-hand panel*: residuals of each fit.

measured R_A/a and T_{eff}, and those predicted by a set of theoretical stellar models for the calculated stellar mass and $\left[\frac{\mathrm{Fe}}{\mathrm{H}}\right]$. The overall best fit was found over a grid of ages extending from the zero-age main sequence to a maximum of 5 Gyr, imposed because WASP-80 A shows strong activity indicative of youth (e.g. West et al. 2008). Statistical errors were propagated by a perturbation analysis. Systematic errors were estimated by calculating sets of results using five different sets of theoretical models (Claret 2004a; Demarque et al. 2004; Pietrinferni et al. 2004; VandenBerg et al. 2006; Dotter et al. 2008). The five models were given equal relative weighting. The resulting estimates of the physical properties are given in Table 5. For completeness we also estimated the physical properties of the WASP-80 system using empirical calibrations based on detached eclipsing binary systems, instead of theoretical stellar models, using the method proposed by Enoch et al. (2010) and the calibration equations by Southworth (2010). Table 5 shows that the system properties obtained using the empirical calibration and the theoretical model sets agree well, except for the models by Claret (2004a). This discrepancy can be attributed to the differences in the T_{eff} scale

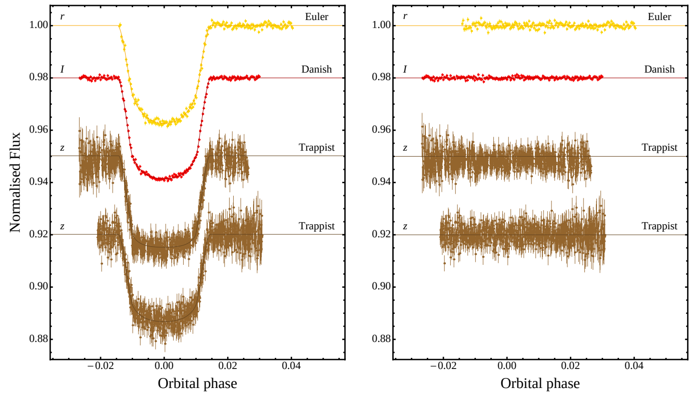

Fig. 5. *Left-hand panel*: light curves of transit events of WASP-80 b observed in Gunn r with the *Euler* telescope (Triaud et al. 2013), in Bessell I with the Danish telescope (this work) and in z with TRAPPIST (Triaud et al. 2013). The light curves are ordered according to central wavelength of the filter used. The best fits are shown as solid lines for each optical data set. *Right-hand panel*: residuals of each fit.

Table 4. Parameters of the fits to the light curves of WASP-80.

Telescope	Filter	$r_A + r_b$	k	i°	r_A	r_b
Danish 1.54-m	Bessel I	0.09324 ± 0.00095	0.17135 ± 0.00099	88.99 ± 0.23	0.07960 ± 0.00074	0.01364 ± 0.00018
MPG/ESO 2.2-m	Sloan g'	0.09131 ± 0.00161	0.17033 ± 0.00217	89.20 ± 0.59	0.07802 ± 0.00128	0.01329 ± 0.00035
MPG/ESO 2.2-m	Sloan r'	0.09001 ± 0.00290	0.17041 ± 0.00175	89.16 ± 0.50	0.07691 ± 0.00245	0.01311 ± 0.00047
MPG/ESO 2.2-m	Sloan i'	0.09239 ± 0.00167	0.17183 ± 0.00161	89.10 ± 0.58	0.07885 ± 0.00134	0.01355 ± 0.00033
MPG/ESO 2.2-m	Sloan z'	0.09391 ± 0.00575	0.17274 ± 0.00226	89.11 ± 0.72	0.08007 ± 0.00091	0.01383 ± 0.00090
MPG/ESO 2.2-m	J	0.08937 ± 0.00567	0.16813 ± 0.00424	90.00 ± 1.16	0.07651 ± 0.00476	0.01286 ± 0.00094
MPG/ESO 2.2-m	H	0.09393 ± 0.00365	0.17525 ± 0.00472	89.34 ± 0.91	0.07993 ± 0.00296	0.01401 ± 0.00076
MPG/ESO 2.2-m	K	0.09067 ± 0.00773	0.16383 ± 0.00809	89.99 ± 1.29	0.07791 ± 0.00673	0.01276 ± 0.00128
Euler 1.2-m	Gunn r	0.09694 ± 0.00277	0.16726 ± 0.00270	88.43 ± 0.45	0.08305 ± 0.00223	0.01389 ± 0.00059
Trappist 0.60-m	Gunn z	0.09261 ± 0.00251	0.17079 ± 0.00201	88.64 ± 0.49	0.07910 ± 0.00204	0.01351 ± 0.00047
Trappist 0.60-m	Gunn z	0.09464 ± 0.00550	0.16285 ± 0.00230	88.63 ± 0.87	0.08139 ± 0.00467	0.01325 ± 0.00087
Final results		**0.09283 ± 0.00058**	**0.17058 ± 0.00057**	**88.91 ± 0.16**	**0.07929 ± 0.00046**	**0.01354 ± 0.00012**
Triaud et al. (2013)		–	$0.17126^{+0.00031}_{-0.00026}$	$89.92^{+0.07}_{-0.12}$	–	–

Notes. The final parameters, given in bold, are the weighted means of the results for the datasets. Results from the discovery paper are included at the base of the table for comparison.

Table 5. Derived physical properties of the WASP-80 planetary system using empirical calibrations and each of five sets of theoretical models.

	This work (dEB constraint)	This work (Claret models)	This work (Y^2 models)	This work (Teramo models)	This work (VRSS models)	This work (DSEP models)
K_b (km s^{-1})	122.7 ± 2.8	126.9 ± 1.3	122.7 ± 2.3	122.5 ± 2.2	124.2 ± 1.7	123.6 ± 1.8
M_A ($M_{\odot}$)	0.589 ± 0.040	0.652 ± 0.020	0.588 ± 0.034	0.585 ± 0.032	0.610 ± 0.024	0.602 ± 0.026
R_A ($R_{\odot}$)	0.590 ± 0.014	0.611 ± 0.007	0.590 ± 0.014	0.589 ± 0.011	0.597 ± 0.009	0.595 ± 0.010
$\log g_A$ (cgs)	4.666 ± 0.011	4.681 ± 0.007	4.666 ± 0.006	4.665 ± 0.009	4.671 ± 0.008	4.669 ± 0.008
M_b (M_{Jup})	0.557 ± 0.030	0.596 ± 0.020	0.557 ± 0.030	0.555 ± 0.025	0.571 ± 0.022	0.566 ± 0.023
R_b (R_{Jup})	0.981 ± 0.024	1.015 ± 0.014	0.981 ± 0.023	0.979 ± 0.020	0.993 ± 0.016	0.989 ± 0.017
ρ_b (ρ_{Jup})	0.551 ± 0.024	0.533 ± 0.021	0.551 ± 0.025	0.552 ± 0.023	0.545 ± 0.022	0.547 ± 0.022
Θ	0.0668 ± 0.0024	0.0645 ± 0.0020	0.0668 ± 0.0025	0.0669 ± 0.0023	0.0660 ± 0.0021	0.0663 ± 0.0021
a (AU)	0.03464 ± 0.00079	0.03583 ± 0.00037	0.03463 ± 0.00064	0.03457 ± 0.00062	0.03506 ± 0.00047	0.03490 ± 0.00050

Table 6. Final physical properties of the WASP-80 planetary system, compared with results from Triaud et al. (2013).

		This work (final)	Triaud et al. (2013)
Stellar mass	M_A ($M_{\odot}$)	0.596 ± 0.032 ± 0.014	$0.57^{+0.05}_{-0.05}$
Stellar radius	R_A ($R_{\odot}$)	0.593 ± 0.011 ± 0.005	$0.571^{+0.016}_{-0.016}$
Stellar surface gravity	$\log g_A$ (cgs)	4.6678 ± 0.0077 ± 0.0034	$4.689^{+0.012}_{-0.013}$
Stellar density	ρ_A ($\rho_{\odot}$)	2.862 ± 0.050	$3.117^{+0.021}_{-0.020}$
Planetary mass	M_b (M_{Jup})	0.562 ± 0.025 ± 0.009	$0.554^{+0.030}_{-0.039}$
Planetary radius	R_b (R_{Jup})	0.986 ± 0.020 ± 0.008	$0.952^{+0.026}_{-0.027}$
Planetary surface gravity	g_b (m s^{-2})	14.34 ± 0.46	$15.07^{+0.45}_{-0.42}$
Planetary density	ρ_b (ρ_{Jup})	0.549 ± 0.023 ± 0.004	$0.554^{+0.030}_{-0.039}$
Planetary equilibrium temperature	T'_{eq} (K)	825 ± 20	∼800
Safronov number	Θ	0.0665 ± 0.0023 ± 0.0005	–
Orbital semimajor axis	a (au)	0.03479 ± 0.00062 ± 0.00027	$0.0346^{+0.008}_{-0.011}$

Notes. Separate statistical and systematic error bars are given for the results from the current work.

predicted by the various model sets (see Fig. 4 in Southworth 2010).

Theoretical models prefer a larger age for the system than is reasonable based on the activity level of the host star. There are several cases (e.g. CoRoT-2 and HD 189733), where a planet-hosting star displays a much higher magnetic activity level than expected for their age (Poppenhaeger & Wolk 2013). A similar behaviour has also been suggested in the case of Qatar-1 (Covino et al. 2013). Several studies pointed out that a close-in hot-Jupiter can produce different effects on its parent star. Tidal forces can increase the rotational velocity of the star (Pont 2009). The effect of the magnetized stellar wind, which causes loss of angular momentum, is inhibited by the planet (Lanza et al. 2010; Cohen et al. 2010). Both processes make the star appear younger than it is. This situation can be investigated through a detailed spectroscopic analysis of the host star to refine its measured atmospheric parameters, and a study of its X-ray luminosity, which is known to decline with stellar age (e.g. Wright et al. 2011). In the meantime we do not report an age measurement for the system.

For the final system properties we took the unweighted means of the four concordant model sets and calculated systematic error bars based on the interagreement between them. A comparison between our final values and those found by Triaud et al. (2013) is given in Table 6.

5. Variation of the planetary radius with wavelength

WASP-80 b is a good target for studies of the planetary atmosphere due to the low surface gravity, deep transit, and bright host star. However, its moderate equilibrium temperature (T'_{eq} = 825 ± 20 K) indicates that the planet should belong to the pL class, as suggested by Fortney et al. (2008). We therefore do not expect a big variation of the measured planet radius with wavelength. Our GROND data, however, are very well suited to investigating this possibility as they cover many passbands.

We have measured the ratio of the planetary and stellar radius, k, in the GROND light curves. Figure 6 shows the result as a function of wavelength. The vertical error bars represent the relative errors in the measurements (i.e. neglecting sources of error which affect all light curves equally), and the horizontal error bars show the FWHM transmission of the passbands used. Due to the very large uncertainty, the values of k measured in the H and K bands were ignored. For the J band, following Southworth et al. (2012) and Mancini et al. (2013b), we refitted the data with all parameters fixed to the final values given in Table 4, with the exception of k. This approach maximizes the precision of estimations of the planet/star radius ratio. As our final value for k in the J band, we got k = 0.1695 ± 0.0028.

The k found for the data from the Danish Telescope is also shown in green, and is a good match with the results for the GROND i' data. For illustration, Fig. 6 also shows the predictions from a model atmosphere calculated by Fortney et al. (2010) for a Jupiter-mass planet with gravity g_b = 10 m s^{-2}, a base radius of 1.25 R_{Jup} at 10 bar, and T'_{eq} = 750 K. The opacity of strong-absorber molecules, such as gaseous titanium oxide (TiO) and vanadium oxide (VO), was removed from the model. Our experimental points are in agreement with the prominent absorption features of the model and, being compatible with a flat transmission spectrum, do not indicate any large variation of the WASP-80 b's radius.

6. Summary and conclusions

The WASP-80 system contains a low-mass star which is at the border of the M spectral class, and a transiting hot Jupiter. It is one of only two systems containing an M-dwarf and a Jupiter-size object, the other being the much fainter Kepler-45. The brightness and small radius of the host star, which means the planetary transits are deep, and the low surface gravity of the planet make it a very important object for studying the atmospheric characteristics of irradiated gas giant planets.

We present eight light curves of one transit event, taken simultaneously using two telescopes, in the Bessell I, Sloan g', r', i', z', and the NIR JHK passbands. We find a good agreement for the ratio of the planetary to stellar radius determined from our optical light curves, which means that we do not detect any opacity-induced changes in planetary radius. We model all available optical transit light curves and use these results to determine the physical properties of the system. Our values are consistent with previous measurements, although our value for the planetary radius is 1σ larger than that in the discovery paper.

We also present a spectrum of WASP-80 covering the Ca H and K lines, which shows strong emission in the line cores. We measure a chromospheric activity indicator of $\log R'_{HK}$ = −4.495, which makes WASP-80 one of the most

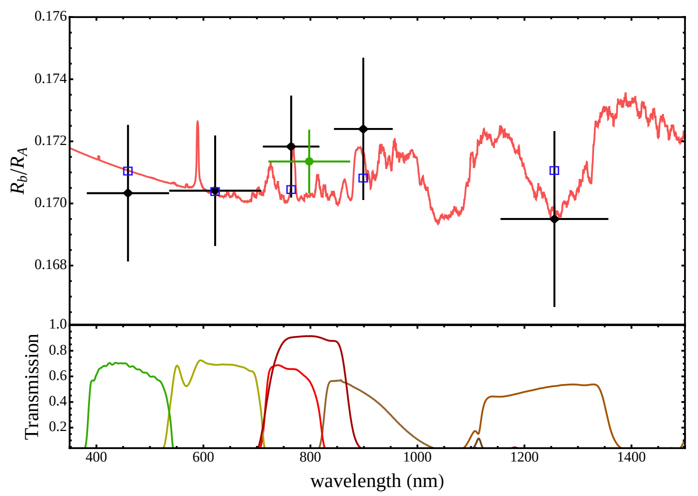

Fig. 6. Variation of the planetary radius, in terms of planet/star radius ratio, with wavelength. The black diamonds are from the transit observations performed with GROND while the green point is from the same transit observed using the Danish Telescope. The vertical bars represent the errors in the measurements and the horizontal bars show the FWHM transmission of the passbands used. The observational points are compared with a synthetic spectrum (see text for details). Transmission curves for the Bessel I filter and the total efficiencies of the GROND filters are shown in the *bottom panel*. The blue boxes indicate the predicted values for the model integrated over the passbands of the observations.

active planet hosts known. This implies strong magnetic activity and the presence of starspots, although we see no evidence in our high-precision photometry for starspot crossing events. If starspots exist on the surface of WASP-80 A, they are likely small, numerous and evenly distributed on the stellar photosphere.

Triaud et al. (2013) do not report a conclusive measurement of $\upsilon \sin i_{\star}$. This is because the one obtained by the broadening of the spectral lines is incompatible with the one derived from fitting the Rossiter-McLaughlin effect, suggesting that the planet's orbital spin could be very inclined. Since the stellar rotation period is highly uncertain, an estimate of the stellar age based on gyrochronology is not possible. The age constraints implied by the stellar models in Sect. 4 are older than the strong activity of WASP-80 A suggests (see Pace 2013, Fig. 1). A possible explanation is that the stellar activity is enhanced by its planet. However, an estimation of the stellar age based on theoretical models is very uncertain because M stars evolve very slowly during their main-sequence lifetime. X-ray observations may help explain this discrepancy.

A detailed characterisation of the atmosphere of WASP-80 b could be performed using transmission spectroscopy. We caution that such investigations should be based on simultaneous observations in order to avoid complications due to starspot activity.

Acknowledgements. This paper is based on observations collected with the MPG/ESO 2.2-m and the Danish 1.54-m telescopes, both located at ESO La Silla, Chile. Operation of the MPG/ESO 2.2-m telescope is jointly performed by the Max Planck Gesellschaft and the European Southern Observatory. Operation of the Danish telescope is based on a grant to U.G.J. by the Danish Natural Science Research Council (FNU). GROND was built by the high-energy group of MPE in collaboration with the LSW Tautenburg and ESO, and is operated as a PI-instrument at the MPG/ESO 2.2-m telescope. J.S. (Keele) acknowledges financial support from STFC in the form of an Advanced Fellowship. C.S. received funding from the European Union Seventh Framework Programme (FP7/2007-2013) under grant agreement No. 268421. M.R. acknowledges support from FONDECYT postdoctoral fellowship N°3120097. S.-H.G. and X.-B.W. would like to thank the financial support from National Natural Science Foundation of China (No.10873031) and Chinese Academy of Sciences (project KJCX2-YW-T24). O.W. thanks the Belgian National Fund for Scientific Research (FNRS). J.S. and O.W. acknowledge support from the Communauté française de Belgique – Actions de recherche concertées – Académie universitaire Wallonie-Europe. K.A., M.D. and M.H. acknowledge grant NPRP-09-476-1-78 from the Qatar National Research Fund (a member of Qatar Foundation). The following internet-based resources were used in research for this paper: the ESO Digitized Sky Survey; the NASA Astrophysics Data System; the SIMBAD data base operated at the CDS, Strasbourg, France; and the arXiv scientific paper preprint service operated by Cornell University.

References

Bean, J. L., Désert, J.-M., Kabath, P., et al. 2011, ApJ, 743, 92
Berdyugina, S. V. 2005, LRSP, 2, 8

Berta, Z. K., Charbonneau, D., Désert, J.-M., et al. 2012, ApJ, 747, 35
Bonfils, X., Delfosse, X., Udry, S., et al. 2013, 549, A109
Carter, J. A., & Winn, J. N. 2009, ApJ, 704, 51
Claret, A. 2004a, A&A, 424, 919
Claret, A. 2004b, A&A, 428, 1001
Cohen, O., Drake, J. J., Kashyap, V. L., et al. 2010, ApJ, 723, L64
Colòn, K. D., & Gaidos, E. 2013, ApJ, 776, 49
Covino, E., Esposito, M., Barbieri, M., et al. 2013, A&A, 554, A28
Croll, B., Albert, L., Jayawardhana, R., et al. 2011, ApJ, 736, 78
Crossfield, I. J. M., Barman, T., & Hansen, B. M. S. 2011, ApJ, 736, 132
Crossfield, I. J. M., Barman, T., Hansen, B. M. S., & Howard, A. 2013, A&A, 559, A33
de Mooij, E. J. W., Brogi, M., de Kok, R. J., et al. 2012, A&A, 538, A46
de Mooij, E. J. W., Brogi, M., de Kok, R. J., et al. 2013, ApJ, 771, 109
Demarque, P., Woo, J.-H., Kim, Y.-C., & Yi, S. K. 2004, ApJS, 155, 667
Dominik, M., Jørgensen, U. G. , Rattenbury, N. J., et al. 2010, AN, 331, 671
Dotter, A., Chaboyer, B., Jevremović, D., et al. 2008, ApJS, 178, 89
Dressing, C. D., & Charbonneau, D. 2013, ApJ, 767, 95
Enoch, B., Collier Cameron, A., Parley, N. R., & Hebb, L. 2010, A&A, 516, A33
Fortney, J. J., Lodders, K., Marley, M. S., & Freedman R. S. 2008, ApJ, 678, 1419
Fortney, J. J., Shabram, M., & Showman, A. P. 2010, ApJ, 709, 1396
Fraine, J. D., Deming, D., Gillon, M., et al. 2013, ApJ, 765, 127
Gibson, N. P., Pollacco, D., Simpson, E. K., et al. 2008, A&A, 492, 603
Gibson, N. P., Pont, F., & Aigrain, S. 2011, MNRAS, 411, 2199
Gillon, M., Pont, F., Moutou, C., et al. 2006, A&A, 459, 249
Greiner, J., Bornemann, W., Clemens, C., et al. 2008, PASP, 120, 405
Irwin, J., Buchhave, L., Berta, Z. K., et al. 2010, ApJ, 718, 1353
Jackson, R. J., & Jeffries, R. D. 2012, MNRAS, 423, 2966
Jackson, R. J., & Jeffries, R. D. 2013, MNRAS, 431, 1883
Johnson, J. A., Aller, K. M., Howard, A. W., & Crepp, J. R. 2010, PASP, 122, 905
Johnson, J. A., Apps, K., Gazak, J. Z., et al. 2011, ApJ, 730, 79
Johnson, J. A., Gazak, J. Z., Apps, K., et al. 2012, AJ, 143, 111
Knutson, H. A., Madhusudhan, N., Cowan, N. B., et al. 2011, ApJ, 735, 27
Lanza, A. F. 2010, A&A, 512, A77
Mancini, L., Southworth, J., Ciceri, S., et al. 2013a, A&A, 551, A11
Mancini, L., Nikolov, N., Southworth, J., et al. 2013b, MNRAS, 430, 2932
Mancini, L., Ciceri, S., Chen, G., et al. 2013c, MNRAS, 436, 2
Marsh, T. R. 1989, PASP, 101, 1032
Murgas, F., Pallé, E., Cabrera-Lavers, A., et al. 2012, A&A, 544, A41
Narita, N., Fukui, A, Ikoma, M., et al. 2013, ApJ, 773, 144
Nascimbeni, V., Cunial, A., Murabito, S., et al. 2013, A&A, 549, A30
Noyes, R. W., Hartmann, L. W., Baliunas, S. L., et al. 1984, ApJ, 279, 763
Pace, G. 2013, A&A, 551, L8
Pietrinferni, A., Cassisi, S., Salaris, M., & Castelli, F. 2004, ApJ, 612, 168
Pont, F. 2009, MNRAS, 396, 1789
Pont, F., Gilliland, R. L., Knutson, H., et al. 2009, MNRAS, 393, L6
Poppenhaeger, K., & Wolk, S. J. 2013, Proc. IAUS 302: Magnetic Fields Throughout Stellar Evolution, in press [arXiv:1309.6356]
Southworth, J. 2008, MNRAS, 386, 1644
Southworth, J. 2009, MNRAS, 394, 272
Southworth, J. 2010, MNRAS, 408, 1689
Southworth, J. 2012, MNRAS, 426, 1291
Southworth, J., Hinse, T. C., Jørgensen, U. G., et al. 2009, MNRAS, 396, 1023
Southworth, J., Mancini, L., Maxted, P. F. L., et al. 2012, MNRAS, 422, 3099
Stevenson, K. B., Harrington, J., Nymeyer, S., et al. 2010, Nature, 464, 161
Tregloan-Reed, J., Southworth, J., & Tappert, C. 2013, MNRAS, 428, 3671
Triaud, A. H. M. J., Anderson, D. R., Collier Cameron, A., et al. 2013, A&A, 551, A80
VandenBerg, D. A., Bergbusch, P. A., & Dowler, P. D. 2006, ApJS, 162, 375
Vaughan, A. H., Preston, G. W., & Wilson, O. C. 1978, PASP, 90, 267
West, A. A., Hawley, S. L., & Bochanski, J. J. 2008, ApJ, 135, 785
Winn, J. N., Holman, M. J., Torres, G., et al. 2008, ApJ, 683, 1076
Wright, N. J., Drake, J. J., Mamajek, E. E., & Henry, G. W. 2011, ApJ, 743, 48

Monthly Notices of the Royal Astronomical Society
MNRAS 434, 1220–1238 (2013)
Advance Access publication 2013 July 15
doi:10.1093/mnras/stt1080

A detailed census of variable stars in the globular cluster NGC 6333 (M9) from CCD differential photometry*

A. Arellano Ferro,[1]† D. M. Bramich,[2] R. Figuera Jaimes,[2,3] Sunetra Giridhar,[4] N. Kains,[2] K. Kuppuswamy,[4] U. G. Jørgensen,[5,6] K. A. Alsubai,[7] J. M. Andersen,[8,6] V. Bozza,[9,10] P. Browne,[3] S. Calchi Novati,[9,11] Y. Damerdji,[12] C. Diehl,[13,14] M. Dominik,[3] S. Dreizler,[15] A. Elyiv,[12,16] E. Giannini,[13] K. Harpsøe,[5,6] F. V. Hessman,[15] T. C. Hinse,[17,5] M. Hundertmark,[3] D. Juncher,[5,6] E. Kerins,[18] H. Korhonen,[5,6] C. Liebig,[3] L. Mancini,[19] M. Mathiasen,[5] M. T. Penny,[20] M. Rabus,[21] S. Rahvar,[22,23] D. Ricci,[12,24] G. Scarpetta,[9,25] J. Skottfelt,[5,6] C. Snodgrass,[26] J. Southworth,[27] J. Surdej,[12] J. Tregloan-Reed,[27] C. Vilela[27] and O. Wertz[12] (The MiNDSTEp consortium)

[1] *Instituto de Astronomía, Universidad Nacional Autónoma de México, Ciudad Universitaria CP 04510, Mexico*
[2] *European Southern Observatory, Karl-Schwarzschild-Straβe 2, D-85748 Garching bei München, Germany*
[3] *SUPA, School of Physics and Astronomy, University of St. Andrews, North Haugh, St Andrews KY16 9SS, UK*
[4] *Indian Institute of Astrophysics, Koramangala 560034, Bangalore, India*
[5] *Niels Bohr Institute, University of Copenhagen, Juliane Maries vej 30, DK-2100 Copenhagen, Denmark*
[6] *Centre for Star and Planet Formation, Geological Museum, Øster Voldgade 5, DK-1350 Copenhagen, Denmark*
[7] *Qatar Foundation, PO Box 5825, Doha, Qatar*
[8] *Department of Astronomy, Boston University, 725 Commonwealth Ave, Boston, MA 02215, USA*
[9] *Dipartimento di Fisica 'E.R Caianiello', Universit di Salerno, Via Ponte Don Melillo, I-84084 Fisciano, Italy*
[10] *Istituto Nazionale di Fisica Nucleare, Sezione di Napoli, Italy*
[11] *Istituto Internazionale per gli Alti Studi Scientifici (IIASS), Vietri Sul Mare (SA), Italy*
[12] *Institut d'Astrophysique et de Géophysique, Université de Liège, Allée du 6 Août 17, Sart Tilman, Bât. B5c, B-4000 Liège, Belgium*
[13] *Astronomisches Rechen-Institut, Zentrum für Astronomie der Universität Heidelberg (ZAH), Mönchhofstr. 12-14, D-69120 Heidelberg, Germany*
[14] *Hamburger Sternwarte, Universität Hamburg, Gojenbergsweg 112, D-21029 Hamburg, Germany*
[15] *Institut für Astrophysik, Georg-August-Universität, Friedrich-Hund-Platz 1, D-37077 Göttingen, Germany*
[16] *Main Astronomical Observatory, Academy of Sciences of Ukraine, vul. Akademika Zabolotnoho 27, 03680 Kyiv, Ukraine*
[17] *Korea Astronomy and Space Science Institute, Daejeon 305-348, Korea*
[18] *Jodrell Bank Centre for Astrophysics, University of Manchester, Oxford Road, Manchester M13 9PL, UK*
[19] *Max Planck Institute for Astronomy, Königstuhl 17, D-69117 Heidelberg, Germany*
[20] *Department of Astronomy, Ohio State University, 140 West 18th Avenue, Columbus, OH 43210, USA*
[21] *Instituto de Astrofísica, Facultad de Física, Pontificia Universidad Católica de Chile, Av. Vicuña Mackenna 4860, 7820436 Macul, Santiago, Chile*
[22] *Department of Physics, Sharif University of Technology, PO Box 11155–9161, Tehran, Iran*
[23] *Perimeter Institute for Theoretical Physics, 31 Caroline St. N., Waterloo ON N2L 2Y5, Canada*
[24] *Instituto de Astronomía - UNAM, Km 103 Carretera Tijuana Ensenada, 422860 Ensenada (Baja Cfa), Mexico*
[25] *INFN, Gruppo Collegato di Salerno, Sezione di Napoli, Italy*
[26] *Max Planck Institute for Solar System Research, Max-Planck-Str. 2, D-37191 Katlenburg-Lindau, Germany*
[27] *Astrophysics Group, Keele University, Staffordshire ST5 5BG, UK*

Accepted 2013 June 13. Received 2013 June 9; in original form 2013 May 19

ABSTRACT

We report CCD *V* and *I* time series photometry of the globular cluster NGC 6333 (M9). The technique of difference image analysis has been used, which enables photometric precision better than 0.05 mag for stars brighter than $V \sim 19.0$ mag, even in the crowded central regions of the cluster. The high photometric precision has resulted in the discovery of two new RRc stars, three eclipsing binaries, seven long-term variables and one field RRab star behind the cluster. A detailed identification chart and equatorial coordinates are given for all the variable stars in the field of our images of the cluster. Our data together with the literature *V*-data obtained in 1994 and 1995 allowed us to refine considerably the periods for all RR Lyrae stars. The nature of the new variables is discussed. We argue that variable V12 is a cluster member and an Anomalous Cepheid. Secular period variations, double-mode pulsations and/or the Blazhko-like modulations in some RRc variables are addressed. Through the light-curve Fourier decomposition of 12 RR Lyrae stars we have calculated a mean metallicity of $[\mathrm{Fe/H}]_{\mathrm{ZW}} = -1.70 \pm 0.01$(statistical) $\pm$ 0.14(systematic) or $[\mathrm{Fe/H}]_{\mathrm{UVES}} = -1.67 \pm 0.01$(statistical) $\pm$ 0.19(systematic). Absolute magnitudes, radii and masses are also estimated for the RR Lyrae stars. A detailed search for SX Phe stars in the Blue Straggler region was conducted but none were discovered. If SX Phe exist in the cluster then their amplitudes must be smaller than the detection limit of our photometry. The colour–magnitude diagram has been corrected for heavy differential reddening using the detailed extinction map of the cluster of Alonso-García et al. This has allowed us to set the mean cluster distance from two independent estimates; from the RRab and RRc absolute magnitudes, we find 8.04 ± 0.19 and 7.88 ± 0.30 kpc, respectively.

Key words: stars: fundamental parameters – globular clusters: individual: NGC 6333 – stars: variables: general – stars: variables: RR Lyrae.

* Based on observations collected with the 2.0 m telescope at the Indian Astrophysical Observatory, Hanle, India, and with the Danish 1.54 m telescope at the ESO La Silla Observatory in Chile.

† E-mail: armando@astro.unam.mx

Published by Oxford University Press on behalf of the Royal Astronomical Society

1 INTRODUCTION

In the last thirty years, the variable stars in the globular cluster NGC 6333 (M9 or C1716−184 in the IAU nomenclature) ($\alpha = 17^{\mathrm{h}}19^{\mathrm{m}}11\overset{\mathrm{s}}{.}8$, $\delta = -18^{\circ}30'58\overset{''}{.}5$, J2000; $l = 5\overset{\circ}{.}54$, $b = +10\overset{\circ}{.}71$) have been the subject of some analyses based on photographic and CCD time series photometry (Clement, Ip & Robert 1984; Clement & Walker 1991; Clement & Shelton 1996, 1999). The 2012 update for NGC 6333 in the Clement et al. (2001) Catalogue of Variable Stars in Globular Clusters (CVSGC) lists 21 known variable stars; nine RRab, nine RRc, one long period variable (V8), one Pop II Cepheid (V12) and one eclipsing binary (V21). This makes the cluster attractive for a Fourier decomposition analysis of the RR Lyrae star light curves with the aim of calculating their physical parameters from semi-empirical calibrations. Furthermore, this cluster has a crowded central region where it is difficult to perform conventional point spread function (PSF) fitting photometry. The application of difference image analysis (DIA) to image data for this cluster for the first time therefore opens up the possibility of new variable star discoveries.

Recently our team has performed CCD photometry of several globular clusters by employing the DIA technique to produce precise time series photometry of individual stars down to $V \sim 19.5$ mag. The DIA photometry has proven to be a very useful tool in obtaining high-quality light curves of known variables, and for discovering and classifying new variables (e.g. Arellano Ferro et al. 2011; Bramich et al. 2011; Kains et al. 2012; Figuera Jaimes et al. 2013; and references therein), where previous CCD photometric studies have not detected stellar variability, particularly in the crowded central regions of the clusters. Thus, in this paper we report the analysis of new time series photometry of NGC 6333 in the *V* and *I* filters. In Section 2, we describe the observations and data reductions. In Section 3, the problem of the differential reddening in the cluster field of view (FOV) is addressed and the approach we used to correct it is described. Section 4 contains a detailed discussion on the approach to the identification of new variables and their classification. In Section 5, we apply Fourier light-curve decomposition to some of the RR Lyrae stars and calculate their metallicity and absolute magnitude. Given the differential reddening correction, the accuracy in the cluster distance determination is highlighted. In Section 6, we discuss the A_V - log *P* relation for the RR Lyrae stars and the Oosterhoff type of the cluster. In Section 7, we summarize our results.

2 OBSERVATIONS AND REDUCTIONS

2.1 Observations

The observations employed in this work were performed using the Johnson *V* and *I* filters on 15 nights during 2010–2012 at two different observatories. The 2.0 m telescope of the Indian Astronomical Observatory (IAO), Hanle, India, located at 4500 m above sea level, was used to obtain 212 and 171 epochs in the *V* and *I* filters, respectively. The detector was a Thompson CCD of 2048 × 2048 pixels with a pixel scale of 0.296 arcsec pixel^{-1} translating to an FOV of approximately 10.1 × 10.1 arcmin^2. Also, the Danish Faint Object Spectrograph and Camera (DFOSC) at the Danish 1.54 m telescope at La Silla, Chile, was used to collect 118 epochs in the *V* filter. DFOSC has a 2147 × 2101 pixel Loral CCD with a pixel scale of 0.396 arcsec pixel^{-1} and an FOV of ∼14.2 × 13.9 arcmin^2.

The log of observations is shown in Table 1 where the dates, site, number of frames, exposure times and average nightly seeing are recorded. A total of 330 epochs in the *V* filter and 171 in the *I* filter spanning just over two years are included in this study.

2.2 Difference image analysis

We employed the technique of DIA to extract high-precision photometry for all of the point sources in the images of NGC 6333 and we used the DANDIA[1] pipeline for the data reduction process

[1] DANDIA is built from the DanIDL library of IDL routines available at http://www.danidl.co.uk.

Downloaded from http://mnras.oxfordjournals.org/ at Royal Library/Copenhagen University Library on December 20, 2015

Table 1. The distribution of observations of NGC 6333 for each filter, where the columns N_V and N_I represent the number of images taken with the *V* and *I* filters, respectively. We also provide the exposure time, or range of exposure times, employed during each night for each filter in the columns t_V and t_I and the average seeing in the last column.

Date	Telescope	N_V	t_V (s)	N_I	t_I (s)	Avg seeing (arcsec)
20100506	2.0 m IAO, Hanle, India	29	180–250	26	40–60	2.2
20110412	2.0 m IAO, Hanle, India	4	75–125	5	10–60	1.5
20110413	2.0 m IAO, Hanle, India	11	70	11	8–10	1.4
20110414	2.0 m IAO, Hanle, India	14	70	14	10	1.4
20110610	2.0 m IAO, Hanle, India	13	70–100	13	10–15	1.7
20110611	2.0 m IAO, Hanle, India	3	200–250	3	10–40	2.8
20110805	2.0 m IAO, Hanle, India	13	100–200	13	15–50	1.8
20110806	2.0 m IAO, Hanle, India	6	90–100	6	12–15	1.9
20120515	2.0 m IAO, Hanle, India	3	20–40	3	7–20	1.9
20120516	2.0 m IAO, Hanle, India	23	10–35	24	4–35	1.8
20120628	2.0 m IAO, Hanle, India	52	20–60	53	3–15	2.2
20120629	2.0 m IAO, Hanle, India	41	40–100	–	–	2.7
20120822	1.54 m Danish, La Silla, Chile	28	100–180	–	–	3.1
20120824	1.54m Danish, La Silla, Chile	39	50–100	–	–	1.8
20120826	1.54m Danish, La Silla, Chile	51	50	–	–	1.0
Total:		330		171		

(Bramich et al. 2013) which includes an algorithm that models the convolution kernel matching the PSF of a pair of images of the same field as a discrete pixel array (Bramich 2008).

The DANDIA pipeline performs standard overscan bias level and flat-field corrections of the raw images, and creates a reference image for each filter by stacking a set of registered best seeing calibrated images. For the La Silla image data, which are slightly undersampled in the best seeing images, it was necessary to preblur any images with a seeing of less than 3 pixel to force a full width at half-maximum (FWHM) of the PSF of at least 3 pixel. This is because undersampling can cause problems in determining the kernel solution matching the PSFs between images.

We constructed three reference images, one in the *V* filter for each telescope and one in *I* for the Hanle data. For each of these reference images, 5, 10 and 6 calibrated images were stacked with total exposure times of 350, 500 and 50 s in the *V* (Hanle), *V* (La Silla) and *I* (Hanle) filters, respectively, with PSF FWHMs of ∼4.3, ∼3.2 and ∼3.5 pixel, respectively. In each reference image, we measured the fluxes (referred to as reference fluxes) and positions of all PSF-like objects (stars) by extracting a spatially variable (with a third-degree polynomial) empirical PSF from the image and fitting this PSF to each detected object. The detected stars in each image in the time series were matched with those detected in the corresponding reference image, and a linear transformation was derived which was used to register each image with the reference image.

For each filter, a sequence of difference images was created by subtracting the relevant reference image, convolved with an appropriate spatially variable kernel, from each registered image. The spatially variable convolution kernel for each registered image was determined using bilinear interpolation of a set of kernels that were derived for a uniform 6 × 6 grid of subregions across the image.

The differential fluxes for each star detected in the reference image were measured on each difference image. Light curves for each star were constructed by calculating the total flux $f_{\mathrm{tot}}(t)$ in ADU/s at each epoch *t* from:

$$f_{\mathrm{tot}}(t) = f_{\mathrm{ref}} + \frac{f_{\mathrm{diff}}(t)}{p(t)}, \tag{1}$$

where f_{ref} is the reference flux (ADU/s), $f_{\mathrm{diff}}(t)$ is the differential flux (ADU/s) and $p(t)$ is the photometric scale factor (the integral of the kernel solution). Conversion to instrumental magnitudes was achieved using

$$m_{\mathrm{ins}}(t) = 25.0 - 2.5 \log\left[f_{\mathrm{tot}}(t)\right], \tag{2}$$

where $m_{\mathrm{ins}}(t)$ is the instrumental magnitude of the star at time *t*. Uncertainties were propagated in the correct analytical fashion.

The above procedure and its caveats have been described in detail in Bramich et al. (2011) and the interested reader is referred there for the relevant details.

2.3 Photometric calibrations

2.3.1 *Relative*

All photometric data suffer from systematic errors to some level. Sometimes they may be severe enough to be mistaken for bona fide variability in light curves (e.g. Safonova & Stalin 2011). However, multiple observations of a set of objects at different epochs, such as time series photometry, may be used to investigate, and possibly correct, these systematic errors (see for example Honeycutt 1992). This process is a relative self-calibration of the photometry, which is being performed as a standard post-processing step for large-scale surveys (e.g. Padmanabhan et al. 2008; Regnault et al. 2009; etc.).

We apply the methodology developed in Bramich & Freudling (2012) to solve for the magnitude offsets Z_k that should be applied to each photometric measurement from the image *k*. In terms of DIA, this translates into a correction (to first order) for the systematic error introduced into the photometry from an image due to an error in the fitted value of the photometric scale factor *p*. We found that for Hanle images in either filter the magnitude offsets that we derive are of the order of ∼10 mmag with a handful of worse cases reaching ∼30 mmag. For the La Silla data, the magnitude offsets that we derive are of the order of ∼1–5 mmag. Applying these magnitude offsets to our DIA photometry notably improves the light-curve quality, especially for the brighter stars.

Downloaded from http://mnras.oxfordjournals.org/ at Royal Library/Copenhagen University Library on December 20, 2015

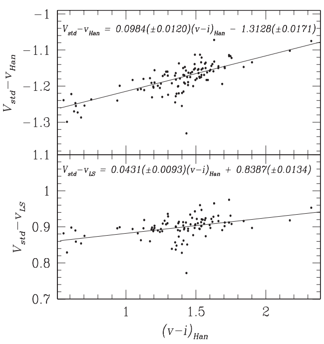

Figure 1. Transformation relations between the instrumental and the standard photometric systems using a set of standard stars in the field of NGC 6333 provided by Peter Stetson. Top and bottom panels correspond to the observations from Hanle and La Silla, respectively. The lack of *I*-band standards forced us to leave the Hanle *I* data in the instrumental system. The *V* observations from La Silla have been fitted with the Hanle colour $(v-i)_{\mathrm{Han}}$ to reveal the colour dependence. See Section 2.3.2 for a discussion.

2.3.2 *Absolute*

Standard stars in the field of NGC 6333 are not included in the online collection of Peter Stetson.[2] However, Professor Stetson has kindly provided us with a set of preliminary standard stars which we have used to transform instrumental *v* magnitudes into the standard *V* system. The lack of equivalent values in the *I* filter forced us to leave our observations for this filter in the instrumental system.

The standard minus the instrumental magnitudes show mild dependences on the colour, as can be seen in Fig. 1. The transformations are of the form

$$V_{\mathrm{std}} = v_{\mathrm{Han}} + 0.0984(\pm 0.0120)(v-i)_{\mathrm{Han}} - 1.3128(\pm 0.0171), \tag{3}$$

$$V_{\mathrm{std}} = v_{\mathrm{LS}} + 0.0431(\pm 0.0093)(v-i)_{\mathrm{Han}} + 0.8387(\pm 0.0134). \tag{4}$$

Due to the lack of observations in the *I* band for La Silla, equation (4) was fit using the Hanle colour $(v-i)_{\mathrm{Han}}$. For the La Silla data, we have adopted $(v-i)_{\mathrm{Han}} = 0.8$ mag which corresponds approximately to the centre of RR Lyrae horizontal branch (HB), hence

$$V_{\mathrm{std}} = v_{\mathrm{LS}} + 0.8731(\pm 0.0163), \tag{5}$$

which we have used to transform the instrumental into the standard magnitudes for La Silla. Given the instrumental colour range of RR Lyrae stars, 0.60–1.0, this practice produces standard *V* magnitudes consistent with the zero-point uncertainties of the above equations. For much redder variables, like those at the tip of the red giant branch (RGB), the standard *V* magnitudes for the La Silla data may be off by as much as 0.025 mag. Due to saturation in the *I*-band images, variable V29 has no $v-i$ value and we have also adopted $(v-i)_{\mathrm{Han}} = 0.8$ to calculate its standard *V* magnitudes.

All of our *Vi* photometry for the variable stars in the field of the La Silla images of NGC 6333 is provided in Table 2. Only a small portion of this table is given in the printed version of this paper while the full table is available in electronic form.

Fig. 2 shows the rms magnitude deviation in our *V* and *i* light curves, after the relative photometric calibration of Section 2.3.1, as a function of mean magnitude. We achieve rms scatter at the bright end of ∼10–20 mmag in both the *V* and *I* filters for the Hanle data, while we achieve an even better rms for all magnitudes for the La Silla data with an rms at the bright end of ∼3–5 mmag. We believe that the La Silla data, which come from the smaller of the two telescopes, performed significantly better in terms of S/N due to a combination of better seeing for the majority of images and more stable flat-fielding.

2.4 Astrometry

A linear astrometric solution was derived for the *V*-filter reference image from La Silla (which has the larger FOV) by matching ∼600 hand-picked stars with the Third US Naval Observatory CCD Astrograph Catalog (UCAC3; Zacharias et al. 2010) using a field overlay in the image display tool GAIA (Draper 2000). We achieved a radial rms scatter in the residuals of ∼0.3 arcsec. The astrometric fit was then used to calculate the J2000.0 celestial coordinates for all of the confirmed variables in our FOV (see Table 3). The coordinates correspond to the epoch of the *V* reference image from La Silla, which pertains to the heliocentric Julian day 245 6166.51 d.

3 REDDENING

NGC 6333 is known to have differential reddening (Clement et al. 1984) with a heavily obscuring cloud to the SW of the cluster which is evident in the cluster images. Hence, without a proper correction for the differential reddening effects it would be difficult to tell how much of the dispersion in the position of the RR Lyrae stars in the colour–magnitude diagram (CMD) is due to reddening and how much is due to physical and evolutionary effects. The large dispersion in the HB and RGB in the uncorrected CMD shown in the left-hand panel of Fig. 3 is evident, and it is particularly visible in the distribution of the RR Lyrae stars.

Foreground reddening estimates for NGC 6333 can be found in the literature, e.g. $E(B-V) = 0.34$ mag (Zinn 1985); 0.32–0.37 mag (Reed, Hesser & Shawl 1988); 0.38 mag (Harris 1996, 2010 edition).

To correct for the differential reddening, we have taken advantage of the detailed reddening maps calculated by Alonso-García et al. (2012) for a group of globular clusters in the inner Galaxy including NGC 6333. In the map for this cluster, differential reddenings are presented for a grid of 27 668 coordinates within ∼11 arcmin centred in the field of the cluster and with a spatial resolution of ∼3.6 arcsec. For each star in our Hanle reference images, we averaged the differential reddenings for the four neighbouring values in the grid and follow Alonso-García et al. in using the absolute extinction zero-point of $E(B-V) = 0.43$ mag, estimated by comparing with the map of Schlegel, Finkbeiner & Davis (1998) to obtain a reddening. Then, we corrected our *V* and *i* magnitudes for each star by adopting a normal extinction $A_V = 3.1E(B-V)$ and the ratio $A_I/A_V = 0.479$ (Cardelli, Clayton & Mathis 1989) from which

[2] http://www3.cadc-ccda.hia-iha.nrc-cnrc.gc.ca/community/STETSON/standards

Downloaded from http://mnras.oxfordjournals.org/ at Royal Library/Copenhagen University Library on December 20, 2015

Table 2. Time series V and i photometry for all the confirmed variables in our FOV. The telescope employed is coded in column 2 (2.0H = 2 m telescope in Hanle; 1.5LS = 1.54 m telescope in La Silla). The standard $M_{\rm std}$ and instrumental $m_{\rm ins}$ magnitudes are listed in columns 5 and 6, respectively, corresponding to the variable star in column 1. Filter and epoch of mid-exposure are listed in columns 3 and 4, respectively. The uncertainty on $m_{\rm ins}$ is listed in column 7, which also corresponds to the uncertainty on $M_{\rm std}$. For completeness, we also list the quantities $f_{\rm ref}$, $f_{\rm diff}$ and p from equation (1) in columns 8, 10 and 12, along with the uncertainties $\sigma_{\rm ref}$ and $\sigma_{\rm diff}$ in columns 9 and 11. This is an extract from the full table, which is available with the electronic version of the article (see the supporting information).

Variable star ID	Telescope	Filter	HJD (d)	$M_{\rm std}$ (mag)	$m_{\rm ins}$ (mag)	σ_m (mag)	$f_{\rm ref}$ (ADU s^{-1})	$\sigma_{\rm ref}$ (ADU s^{-1})	$f_{\rm diff}$ (ADU s^{-1})	$\sigma_{\rm diff}$ (ADU s^{-1})	p
V1	2.0H	V	245 5323.252 94	16.512	17.735	0.004	843.914	3.864	−28.802	2.353	0.7536
V1	2.0H	V	245 5323.266 83	16.520	17.742	0.004	843.914	3.864	−34.345	2.301	0.7816
⋮	⋮	⋮	⋮	⋮	⋮	⋮	⋮	⋮	⋮	⋮	
V1	2.0H	I	245 5323.271 16	0.000	16.632	0.007	2073.761	12.792	+115.682	10.584	0.7681
V1	2.0H	I	245 5323.297 22	0.000	16.636	0.006	2073.761	12.792	+110.797	10.198	0.7825
⋮	⋮	⋮	⋮	⋮	⋮	⋮	⋮	⋮	⋮	⋮	
V1	1.5LS	V	245 6162.621 83	16.488	15.615	0.004	9079.038	11.294	−3191.886	21.994	0.9373
V1	1.5LS	V	245 6162.623 29	16.486	15.613	0.004	9079.038	11.294	−3193.007	21.104	0.9406

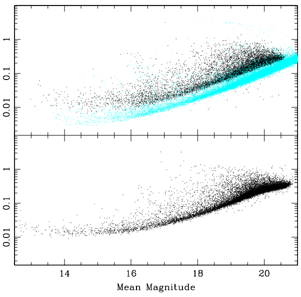

Figure 2. The rms magnitude deviations as a function of magnitude. The upper panel corresponds to the V light curves from Hanle (black dots, 12 519 stars) and La Silla (cyan dots, 21 143 stars). The lower panel corresponds to the i light curves from Hanle (15 524 stars).

$E(V-I)/E(B-V) = 1.616$ follows. The resulting corrected CMD is shown in the right-hand panel of Fig. 3. The RR Lyrae stars have been plotted using their intensity-weighted magnitudes calculated by fitting equation (9) (A_o) to their light curves.

Individual reddenings for the RRab stars may also be calculated from their colour near minimum light. The method, originally proposed by Sturch (1966), has been further investigated by Blanco (1992), Mateo et al. (1995), Guldenschuh et al. (2005) and Kunder, Chaboyer & Layden (2010). Guldenschuh et al. (2005) concluded that for RRab stars the intrinsic colour between phases 0.5 and 0.8 is $(V-I)_o^{\phi(0.5-0.8)} = 0.58 \pm 0.02$ mag. For the RRab stars in NGC 6333 we have calculated the mean $V-i$ colour curves as the difference between the Fourier fits from equation (9) for the standard V and instrumental i light curves. A plot of the colour curves in the 0.5–0.8 phase interval is shown for each star in the top panel of Fig. 4. The different mean levels of the $(V-i)^{\phi(0.5-0.8)}$ curves are due to the differential reddening affecting the cluster. Then, relative to V1, $\Delta E(V-I)^{\phi(0.5-0.8)} = (V-i)_{var}^{\phi(0.5-0.8)} - (V-i)_{V1}^{\phi(0.5-0.8)}$ which in turn is used to calculate $\Delta E(B-V)^{\phi(0.5-0.8)} = \Delta E(V-I)^{\phi(0.5-0.8)}/1.616$ for each RRab star. These colour excesses can be compared with the independent values obtained from the reddening map $E(B-V)^{\rm map}$. In the bottom panel of Fig. 4, we show the comparison of $\Delta E(B-V)^{\phi(0.5-0.8)}$ versus $\Delta E(B-V)^{\rm map} = E(B-V)^{\rm map}_{\rm var} - E(B-V)^{\rm map}_{V1}$. The result should be a linear relation with unit gradient. Clearly the differential reddening in the Alonso-Garcia et al. maps and the estimated ones from the RR Lyrae stars $V-i$ curves in the 0.5–0.8 phase range are, within the uncertainties, consistent.

The final adopted values of $E(B-V)$ for all of the RR Lyrae stars are those from the Alonso-García et al. (2012) reddening map and they are listed in column 12 of Table 4.

4 VARIABLE STARS IN NGC 6333

The globular cluster NGC 6333 has not been explored by many investigators in search of variable stars. The first variable star was discovered by Shapley (1916). 35 years passed until 12 more variable stars were discovered by Sawyer (1951) as part of a photographic survey. Sawyer (1951) also measured the periods of the 13 known variables and labelled them V1–V13. The variable stars in NGC 6333 were not studied again until Christine Clement and collaborators started to work on the cluster another 35 years later publishing four papers of interest. One of the papers (Clement & Shelton 1996) reports on a search for new variables using CCD data which was successful in yielding eight new detections (V14–V21) and extracting a light curve for V11 for the first time. The other papers in the Clement series (Clement et al. 1984; Clement & Walker 1991; Clement & Shelton 1999) present various analyses of the known variables at their times of writing.

In the following sections, we describe the use of our time series Vi photometry to search for new variables and to revisit the identifications, periodicities and light curves of the known variables.

4.1 Search for variable stars

We have been guided in the identification of the known variables by the finding charts of Clement et al. (1984) and Clement & Shelton (1996) and by the equatorial coordinates of the variables in NGC 6333 given by Samus et al. (2009). We had no problems identifying

Table 3. General data for all of the confirmed variables in NGC 6333 in the FOV of our images. Stars V22–V34 are new discoveries in this work. Labels 'Bl' and 'd' are for Blazhko variables and double-mode RRd, respectively. The best previous period estimates for each variable from the Clement series of papers (Clement et al. 1984; Clement & Walker 1991; Clement & Shelton 1996, 1999) are reported in column 10 for comparison with our refined periods in column 7.

Variable star ID	Variable type	⟨V⟩ (mag)	⟨i⟩ (mag)	A_V (mag)	A_i (mag)	P (d) This work	β d Myr^{-1}	HJD$_{\rm max}$ (+245 0000)	P (d) Clement papers	RA (J2000.0)	Dec. (J2000.0)
V1	RRab	16.276	16.520	1.155	0.758	0.585 7309		5779.2366	0.585 728	17:19:18.32	−18:32:21.6
V2	RRab	16.209	16.391	1.110	0.683	0.628 1843		5665.4329	0.628 186	17:19:14.77	−18:31:36.2
V3	RRab-Bl	16.364	16.586	>1.00	>0.70	0.605 206		5664.4684	0.605 353	17:19:26.41	−18:34:34.8
V4	RRab	16.168	16.456	1.017	0.677	0.671 3000		5723.4130	0.671 3021	17:19:13.62	−18:31:39.6
V5	RRc	16.256	16.548	0.449	0.285	0.378 8136		5666.4490	0.378 812	17:19:14.36	−18:31:12.5
V6	RRab	16.351	16.478	1.000	0.672	0.606 7809		5666.4452	0.607 795	17:19:07.02	−18:31:20.9
V7	RRab	16.566	16.655	1.120	0.715	0.628 4626		5723.3838	0.628 4615	17:19:04.18	−18:32:24.4
V8	LPV	14.871	12.684	>0.69	>0.18	–		–	407	17:19:06.84	−18:32:42.8
V9	RRc	16.261	–	>0.38	–	0.322 9883		6166.5212	0.322 989	17:19:35.41	−18:34:17.1
V10	RRc-Bl	16.285	16.674	0.449	0.313	0.319 8454		6107.2557	0.319 820	17:19:14.53	−18:30:39.7
V11	RRab	16.065	16.300	0.704	0.543	0.742 4499		5723.4130	0.736 30	17:19:11.73	−18:31:14.8
V12	An.Cep	15.671	15.765	0.92	>0.51	1.340 255		5323.3075	1.340 204	17:18:52.69	−18:33:20.3
V13	RRab	17.681	17.963	1.183	0.780	0.479 8682		5323.3927	0.479 874	17:19:30.29	−18:30:54.6
V14	RRc	16.253	16.580	0.443	0.250	0.327 0530	4.67	5323.3708	0.326 91	17:19:14.14	−18:31:20.3
V15	RRab	16.239	16.343	0.971	0.760	0.641 7673		5723.4130	0.641 77	17:19:10.52	−18:29:59.2
V16	RRc-Bl?	16.073	16.569	0.336	0.218	0.384 6714		5724.3724	0.385 51	17:19:13.52	−18:30:43.0
V17	RRc	16.243	16.593	0.375	0.283	0.317 5888		5666.4294	0.317 59	17:19:10.48	−18:31:20.4
V18	RRc-Bl?	16.187	16.635	0.39	0.28	0.341 3440	11.50	5323.2745	0.342 28	17:19:10.61	−18:30:41.9
V19	RRd:	16.264	16.580	0.47	0.29	0.366 7937		5723.4130	0.366 48	17:19:12.76	−18:30:38.2
V20	RRc	16.340	16.591	0.423	0.219	0.314 1782		5323.2668	0.314 73	17:19:11.09	−18:31:02.7
V21	EW	16.818	16.884	0.30[b]	0.23[b]	0.720 4518		5724.3785	0.360 225	17:19:09.85	−18:32:34.5
V22	RRc-Bl	16.483	16.740	0.510	0.261	0.350 7561		5779.1641	–	17:19:03.12	−18:35:31.1
V23	RRc-Bl	16.513	16.827	0.311	0.178	0.304 6535		6108.1256	–	17:19:21.15	−18:30:10.2
V24	EW	17.381	17.520	0.45[b]	0.380[b]	0.366 784		6107.2525	–	17:19:13.04	−18:27:39.4
V25	E[c]	17.111	17.333	1.642[b]	1.330[b]	–		6107.2384[a]	–	17:19:25.94	−18:27:43.9
V26	LPV	17.380	17.066	>0.3	>0.18	–		–	–	17:19:13.84	−18:29:37.4
V27	LPV	17.069	16.625	>0.15	>0.2	–		–	–	17:18:56.40	−18:32:47.4
V28	LPV	13.216	12.413	>0.2	>0.15	–		–	–	17:19:11.68	−18:31:04.5
V29	LPV	13.591	–	>0.2	–	–		–	–	17:19:02.68	−18:32:53.6
V30	LPV	13.342	12.670	>0.1	>0.1	–		–	–	17:19:11.83	−18:31:27.9
V31	LPV	13.190	12.413	>0.15	>0.1	–		–	–	17:19:12.65	−18:31:01.7
V32	EW	15.961	–	0.19	–	0.172 30[d]		6162.6608	–	17:19:37.10	−18:35:40.1
V33	RRab	17.920	–	0.517	–	0.575 97		6164.5019	–	17:18:46.97	−18:25:29.5
V34	LPV	15.045	–	>0.1	–	–		–	–	17:18:45.62	−18:28:52.0

[a] Time of minimum light. [b] Depth of eclipse. [c] Possibly EA. [d] Real period may be twice this value.

all 21 known variables in our own time series data. Then, we applied a few approaches in the search for new variable star discoveries as we describe below.

First, we have defined a variability statistic $\mathcal{S}_\mathcal{B}$ as

$$\mathcal{S}_\mathcal{B} = \frac{1}{NM}\sum_{i=1}^{M}\left(\frac{r_{i,1}}{\sigma_{i,1}} + \frac{r_{i,2}}{\sigma_{i,2}} + \ldots + \frac{r_{i,k_i}}{\sigma_{i,k_i}}\right)^2, \tag{6}$$

where N is the total number of data points in the light curve and M is the number of groups of time-consecutive residuals of the same sign from the inverse-variance-weighted mean magnitude. The residuals $r_{i,1}$ to r_{i,k_i} form the ith group of k_i time-consecutive residuals of the same sign with corresponding uncertainties $\sigma_{i,1}$ to σ_{i,k_i}. Fig. 5 shows the distribution of the $\mathcal{S}_\mathcal{B}$ statistic as a function of mean magnitude for the 12 519 light curves for the stars in the Hanle V images.

This statistic, based on the original 'alarm' statistic $\mathcal{A}$ defined by Tamuz, Mazeh & North (2006), has been used by Arellano Ferro et al. (2012) to detect amplitude and period modulations in Blazhko variables. Its application to detecting light-curve variability was first introduced into our work by Figuera Jaimes et al. (2013), where we discuss in detail its application and how to set theoretical detection thresholds using simulated light curves.

As in Figuera Jaimes et al. (2013), we generated 10^5 simulated light curves for each star by randomly modifying the mean $\overline{V}$ magnitude within the uncertainty σ_i of each data point, i.e. $m_i = \overline{V} + \lambda_i\sigma_i$, where λ_i is a random deviate drawn from a normal distribution with zero mean and unit σ. Then, we used the resulting distribution of $\mathcal{S}_\mathcal{B}$ values to determine the 50 per cent and 99.9 per cent percentiles which we plot in Fig. 5 as the horizontal blue and red lines, respectively. Clearly the noise in the real Hanle V light curves is not Gaussian since many more than the expected ∼13 stars lie above the 99.9 per cent percentile for pure Gaussian noise. Furthermore, for stars brighter than ∼17.5 mag, the $\mathcal{S}_\mathcal{B}$ statistic increases with brightness in an exponential manner (linear in a logarithmic plot). All of these effects are due to residual systematic errors in the light curves that can mimic real variability. It is clear that our method of using simulated light curves to define the variability detection threshold has not worked very well for our Hanle V light curves of NGC 6333, contrary to what we found for the NGC 7492 light curves from Figuera Jaimes et al. (2013). This is because the $\mathcal{S}_\mathcal{B}$ statistic is especially sensitive to the systematic trends in the light

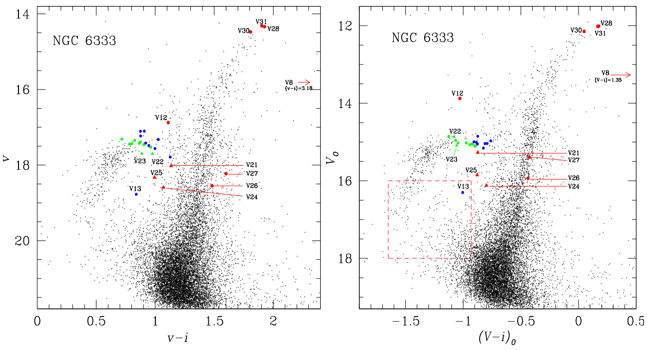

Figure 3. Colour–magnitude diagram of NGC 6333 for the Hanle data in the instrumental system (left) and after transforming v into the standard system and correcting for differential reddening (right) as described in the text. The coloured symbols correspond to the known variables and the new variables discovered in this paper. The colour coding is as follows: RRab stars – blue circles, known RRc stars – green circles, new RRc stars (V22, V23) – green triangles, long period variables (V8, V26, V27, V28, V30, V31) and AC (V12) – red circles, eclipsing binaries – red triangles. The region bounded by red dashed lines is an arbitrarily defined Blue Straggler region. New variables or interesting stars are discussed in Section 4.3 are labelled. The variables V29, V32, V33 and V34 are not plotted because they are either saturated in the I images, or outside the FOV of the Hanle data.

curves, and these trends are simply stronger and more coherent in the NGC 6333 light curves compared to the NGC 7492 light curves.

We therefore opted to define our variability detection threshold by eye as the dashed blue line in Fig. 5. All known variable stars in the FOV of our Hanle images lie above our chosen detection threshold by design. It is clear that the RR Lyrae stars have substantially larger values of $\mathcal{S}_\mathcal{B}$ among stars of their magnitude range. Long-term variables also stand clearly above the line. We explored the light curves of all of the other stars above the threshold and could identify seven clear new variables to which we assigned variable numbers; two RRc stars (V22 and V23), two eclipsing binaries (V24 and V25) and three long-period variables (V26, V27 and V28). Their classifications and interesting properties will be discussed in Section 4.3. Candidate variables in the Blue Straggler (BS) region (see caption of Fig. 5) were investigated individually but none showed convincing indications of variability. A similar plot as in Fig. 5 was constructed for our V data from La Silla with very similar results.

As a second strategy, we also applied the string-length method (Burke, Rolland & Boy 1970; Dworetsky 1983) to each light curve to determine the period and a normalized string-length statistic S_Q. In Fig. 6, we plot the minimum S_Q value for each light curve as a function of their corresponding CCD x-coordinate. The known variables are plotted with the coloured symbols as described in the caption. The horizontal blue line is not a statistically defined threshold but rather an upper limit, set by eye, that contains the majority of the known variables. Below this line we might expect to find previously undetected variables. In addition to the known variables, there are 10 other stars with S_Q values below the blue line and their light curves were thoroughly examined for variability. We found long-term variability for three of them, which we assign variable star names as V29, V30 and V31. We note that this method did not work for V27 but its variability was confirmed by the analysis described below.

Finally, a third approach we have followed to identify variables in the field of our images is by detecting PSF-like peaks in a stacked image built from the sum of the absolute valued difference images normalized by the standard deviation in each pixel as described by Bramich et al. (2011). This method allowed us to confirm the variability of all of the new variables discovered so far and to find the new variables V32, V33 and V34.

The previously known variables, along with all of the new discoveries, are listed in Table 3.

The combination of the three approaches described above lead us to believe that our search for variable stars with continuous variations (i.e. *not* eclipsing binaries etc.) is fairly complete down to $V \sim 19$ for amplitudes larger than 0.05 mag and periods between about 0.02 d and a few hundred days.

4.2 Period determination and refinement

To aid in the refinement of the periods of the known and newly discovered variables, we have combined our data with the V light-curve data from Clement & Shelton (1999). We have noticed small zero-point differences, of the order of a few hundreds of a magnitude, between the three sets of data which may be different from star to star. This is to be expected since, at least for DIA, the reference flux affects all photometric measurements for a single star from the same data set in the same way, and the data for Hanle and La Silla each have a separate reference image with independently measured reference fluxes. Thus, for the period calculation we have

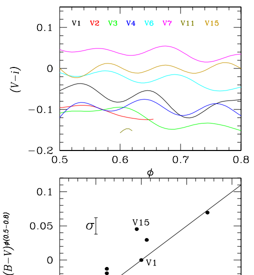

Figure 4. The top panel shows the difference between the Fourier fits to the standard V and instrumental i magnitudes for the light curves of the RRab stars in the phase interval 0.5–0.8. The different mean levels of these curves are due to the differential reddening affecting the cluster. V13 is not included in this analysis since it is not a cluster member (see Section 4.3). The Fourier fits of V2 and V11 are shown only in part since their light curves are not fully covered by data in the 0.5–0.8 phase range. In the bottom panel, we compare the differential values $\Delta E(B-V)^{\phi(0.5-0.8)}$ of a given variable relative to V1 with $\Delta E(B-V)^{\rm map}$ also relative to V1. The error bar represents the typical uncertainty in the colour differences.

proceeded as follows. First, the string-length method (Burke et al. 1970; Dworetsky 1983) was used to get a first estimate of the period. Then small magnitude shifts were applied as necessary to the light-curve data for each star so as to better align the data and a second string length was run on the levelled up light curve. The new period was used to phase the light curve and we explored for further magnitude shifts if any. Generally two to three iterations were sufficient to find an accurate period that phases the data precisely.

The new periods and those from the Clement series of papers are given in columns 7 and 10, respectively of Table 3. We note that in general the agreement is good but the new periods are considerably more precise. The light curves phased with the new periods are displayed in Figs. 7 and 8.

4.3 Individual stars

In this section, we discuss the nature of some interesting known variables and the newly discovered variable stars. To discuss their nature and cluster membership we have built the CMD of Fig. 3 by calculating the inverse-variance-weighted mean magnitudes of ∼11 800 stars that have both standard V and instrumental i magnitudes.

V3. This is an RRab star for which a strong evidence of exhibiting the Blazhko effect has been detected for the first time. Unfortunately our data do not fully cover the phased light curve at different amplitudes (see Fig. 7).

V5. Clement & Walker 1991 report this star as undergoing a period change. However, we do not detect this in our light curves combined with that from Clement & Shelton (1999), which have a combined baseline of ∼18 yr (see Fig. 8).

V8. This variable was announced by Sawyer (1951) as a long-period variable. A period of 407 d was suggested by Clement et al. (1984) and they commented on its small B amplitude of less than one magnitude. We show our light curves in V and i for this variable in Fig. 9. We are unable to estimate a period although the two observed minima are indeed separated by about 400 d. More data are required to complete the period analysis. The position of the star in the CMD is much to the red of the RGB, even in the CMD corrected for differential reddening, which implies that this star is not a cluster member. We note that the reddening required to bring this star back to the RGB if it is a cluster member is too large to be feasible for this field ($E(B-V) \approx 1.5$ mag).

V10. Clement & Walker 1991 also report this star as undergoing a period change as a period increase. Our light-curve data show small phase and amplitude variations reminiscent of the Blazhko effect in RRc stars (Arellano Ferro et al. 2012). Therefore, we believe that it is the Blazhko effect that has been detected previously and for which we present the first conclusive evidence of its presence in this star.

V12. The variability of this star was discovered by Sawyer (1951) who finds it of similar brightness to the RR Lyrae stars. Clement et al. (1984) classified it as a Population II (Pop II) Cepheid with a period of 1.340 204 d. They also find the star to be of similar B mag as the RR Lyrae stars which they use to argue that the star is either much obscured by the presence of a prominent cloud to the SW of the cluster or that it is not a cluster member. We confirm its periodicity as 1.340 255 d and we note that its position in the corrected CMD is about 1.05 mag brighter than the mean HB, suggesting that indeed it is likely to be a cluster member that suffers higher than usual extinction due to the obscuring cloud to the SW of the cluster (see Fig. 10). Clement et al. (2001) have pointed out that Cepheids tend to occur in globular clusters with blue HBs. Assuming that V12 is indeed a cluster member, and given the distance to the cluster (see Section 5.4), its absolute magnitude M_V is ~ -0.63 mag which along with its period, $\log P = 0.127$, places the star on the P–L relation for anomalous Cepheids (ACs) pulsating in the fundamental mode (Pritzl et al. 2002, see their fig. 6). ACs are more luminous than Pop II Cepheids for a given period, they have a similar colour to RRc stars but are 0.5–1.5 mag brighter, and their period can be between 0.5 and 3 d (Wallerstein & Cox 1984). V12 fulfils all of these characteristics, hence in the remainder of this paper we shall refer to V12 as an AC.

V13. This star was noted by Clement et al. (1984) to be much fainter than the other RR Lyrae stars in the cluster and they consider it to be a field star. This is a clear RRab star (see Fig. 7) and indeed it is ∼1.4 mag fainter than the other RRab stars. While NGC 6333 is known for having heavy differential reddening, we discard interstellar extinction as the cause of its faintness because its colour is similar to that of other RR Lyrae stars (Fig. 3). Hence, we agree with Clement et al. (1984) in arguing that V13 is not a member of the cluster but that instead it is a background object.

V14. The two periods 0.326 91 d from Clement & Shelton (1999) and 0.327 0659 d from the string-length method in this work fail to phase properly the combined light-curve data from Clement & Shelton (1999) and our light curves (Fig. 8). However, the period 0.327 0530 d accompanied with a secular period change rate of 4.67 d Myr^{-1} phases the light curve much better as it will be shown in Section 4.5.

Table 4. Fourier coefficients A_k for $k = 0, 1, 2, 3, 4$, and phases ϕ_{21}, ϕ_{31} and ϕ_{41}, for the nine RRab and seven RRc type variables for which the Fourier decomposition fit was successful. The numbers in parentheses indicate the uncertainty on the last decimal place. Also listed are the number of harmonics N used to fit the light curve of each variable, the deviation parameter D_m (see Section 5.1) and the colour excess $E(B-V)$.

Variable ID	A_0 (V mag)	A_1 (V mag)	A_2 (V mag)	A_3 (V mag)	A_4 (V mag)	ϕ_{21}	ϕ_{31}	ϕ_{41}	N	D_m	$E(B-V)$ (mag)
					RRab stars						
V1	16.276(1)	0.401(1)	0.198(1)	0.141(1)	0.095(1)	3.910(8)	8.118(12)	6.109(16)	9	1.9	0.416
V2	16.209(1)	0.372(2)	0.187(2)	0.129(2)	0.093(2)	3.863(14)	8.167(22)	6.147(31)	9	2.4	0.378
V4	16.168(1)	0.341(1)	0.184(1)	0.119(1)	0.071(1)	4.124(11)	8.495(19)	6.664(27)	9	0.8	0.378
V6	16.351(1)	0.341(2)	0.175(2)	0.119(2)	0.079(2)	3.965(14)	8.194(21)	6.121(30)	9	2.7	0.422
V7	16.566(1)	0.379(1)	0.187(1)	0.130(1)	0.089(1)	3.941(9)	8.209(12)	6.226(17)	9	0.7	0.489
V11	16.065(1)	0.252(4)	0.129(4)	0.074(4)	0.031(4)	4.410(43)	8.903(67)	7.210(137)	7	4.9	0.387
V13	17.681(3)	0.403(4)	0.186(4)	0.139(4)	0.097(3)	3.804(31)	7.961(42)	5.870(64)	8	3.3	0.443
V15	16.239(3)	0.350(4)	0.186(4)	0.139(4)	0.074(4)	3.810(32)	8.060(49)	6.100(68)	8	3.7	0.411
V33	17.904(3)	0.212(5)	0.090(4)	0.025(4)	0.016(5)	4.407(75)	8.674(191)	7.929(271)	4	3.1	0.507
					RRc stars						
V5	16.256(1)	0.225(1)	0.028(1)	0.012(1)	0.008(1)	4.828(47)	3.932(105)	2.206(150)	4	–	0.388
V10	16.285(2)	0.232(3)	0.033(3)	0.013(3)	0.017(3)	5.013(87)	2.746(241)	1.390(164)	4	–	0.407
V14	16.253(2)	0.221(3)	0.048(3)	0.024(3)	0.021(3)	5.073(70)	3.241(126)	1.523(157)	4	–	0.382
V16	16.073(2)	0.188(2)	0.015(2)	0.025(2)	0.013(2)	3.919(137)	4.353(103)	1.580(157)	4	–	0.395
V17	16.243(2)	0.187(2)	0.044(2)	0.007(3)	0.016(2)	4.921(74)	3.894(400)	1.747(166)	4	–	0.403
V20	16.340 (1)	0.211(1)	0.036(2)	0.012(2)	0.001(1)	4.886(46)	2.967(123)	1.821(550)	4	–	0.396
V23	16.513(1)	0.149(2)	0.024(2)	0.007(2)	0.004(2)	4.891(73)	4.619(249)	2.684(294)	4	–	0.457

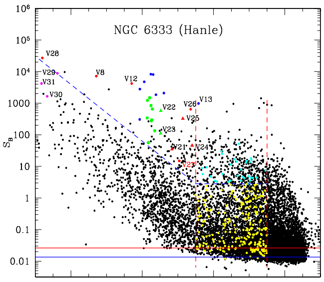

Figure 5. Distribution of the $\mathcal{S}_{\mathcal{B}}$ statistic as a function of mean V magnitude for 12 519 stars measured in the V Hanle images of NGC 6333. The coloured symbols for variable stars are as described in the caption of Fig. 3. Stars in the Blue Straggler region with $\mathcal{S}_{\mathcal{B}}$ below the variability detection threshold are plotted as yellow circles while cyan circles represent Blue Straggler stars with $\mathcal{S}_{\mathcal{B}}$ above the detection threshold and hence potential variable candidates of the SX Phe type. However, none of the Blue Stragglers was found to display convincing variability. The two vertical dashed red lines correspond to the magnitude limits set for the Blue Straggler region in the CMD.

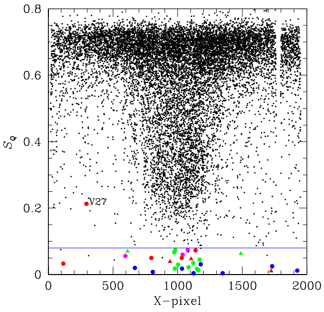

Figure 6. Minimum value of the string-length parameter S_Q calculated for the 12 519 stars with a light curve in our V reference image for the Hanle data, versus the CCD x-coordinate. The coloured symbols are as described in the caption of Fig. 3.

V16. Clement & Shelton (1996) speculate that this star is a double-mode RR Lyrae (RRd). However, we have been able to phase the three available sets of V data with one single period 0.384 6714 d, and we do not find any signs of secondary frequencies in the frequency spectrum. Thus, we do not confirm the double-mode nature of this RRc star (see discussion in Section 4.4) but the star may be a Blazhko variable (see Fig. 8).

V17. The light curve of this star can be seen in Fig. 8. We note that the celestial coordinates given by Samus et al. (2009) seem to point to the bright star near V17 while the authentic V17 is the more northern fainter star of the pair. The correct coordinates are given in Table 3 and a proper identification is in Fig. 10.

V18. The light curve of this RRc star displays nightly phase modulations which can be partially explained by a secular period change

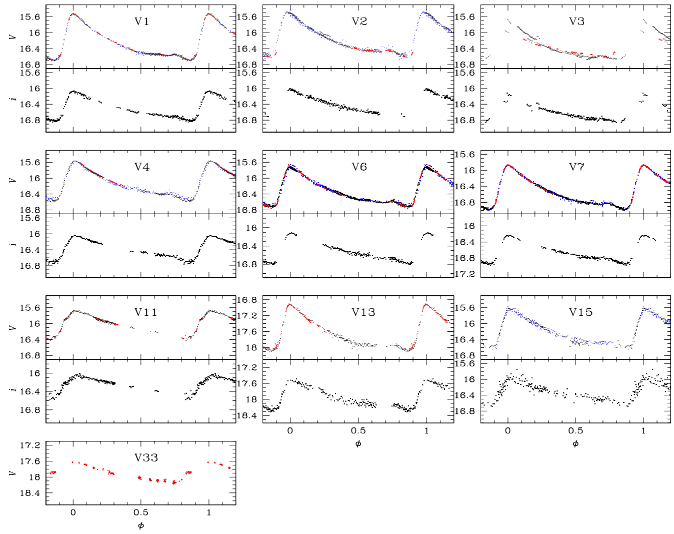

Figure 7. Standard V and instrumental i light curves of the RRab stars in NGC 6333 phased with the periods listed in Table 3. The blue points represent V data from Clement & Shelton (1999). The black and red points represent Hanle and La Silla data, respectively.

(see Section 4.5). However, some modulations remain suggesting the presence of the Blazhko effect. Unfortunately, its light curve is noisy due to the position of the star in a heavily crowded region.

V19. The light curve of this RR Lyrae star displays nightly phase modulations since its light curve is not cleanly phased with the period found by the string-length method (see Table 3). It also seems to show some very mild amplitude variations (Fig. 8). The light curve is also reminiscent of the RRc stars with Blazhko effect found in M53 by Arellano Ferro et al. (2012). In Section 4.4, we shall discuss the possible double-mode nature of V19.

V21. The variability of this star was discovered by Clement & Shelton (1996). These authors noticed that the star is fainter than the other RR Lyrae stars in the cluster and that it has a substantially different Fourier ϕ_{21} parameter. Hence, they concluded that it is either not an RR Lyrae star or that it is not a cluster member. Later, Clement in the CVSGC classify it as an EW variable. In the corrected CMD, the star falls just below the HB by ∼0.3 mag. Our best period is 0.720 4518 d and it produces the light curve of Fig. 11, where we notice two minima of different depths, typical of semi-contact binaries. Thus, we agree that the star is an EW star but with a period approximately double the one reported in Clement & Shelton (1996, 1999). The finding chart in Clement & Shelton (1996) is a bit misleading since the star is hardly visible in their map. This has probably led Samus (2009) to providing the wrong RA and Dec. which correspond to a neighbouring star. The correct coordinates are given in Table 3. The star is properly identified in our finding chart of Fig. 10.

V22 and V23. We have discovered these two new variables. Their period, light curves (see Fig. 8) and position in the CMD lead us to classify them as RRc stars. The light curve of V22 shows strong phase and amplitude modulations, while the light curve of V23 also shows phase and amplitude modulations to a lower level. We therefore conclude that both stars may exhibit the Blazhko effect. However, in Section 4.4 we shall explore the double-mode possibility by searching for a secondary frequency in the spectrum.

V24. This is a new eclipsing binary with a period of 0.366 784 d with two different eclipse depths (see Fig. 11). Its period along with its position in the corrected CMD ∼1.2 mag below the HB support its classification as a W Ursae Majoris-type binary (or EW).

V25. The light curve of this new eclipsing binary is shown in Fig. 12. One eclipse has been detected at HJD 245 6107.24 in both

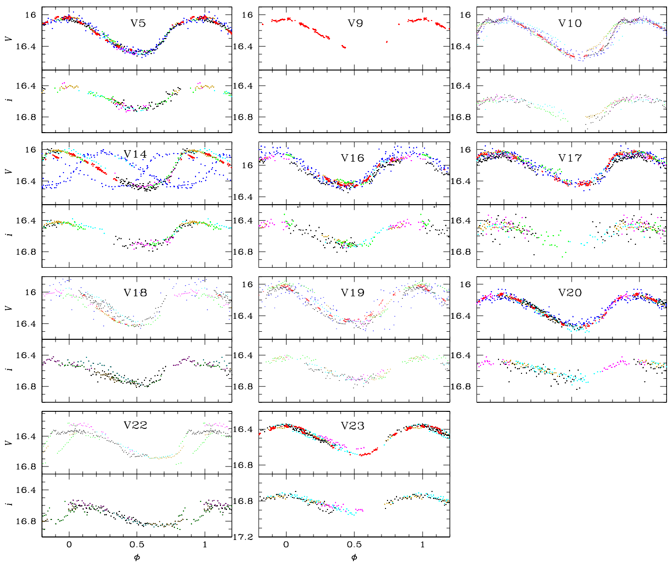

Figure 8. Standard V and instrumental i light curves of the RRc stars in NGC 6333 phased with the periods listed in Table 3. To highlight any phase and amplitude modulations, colours have been assigned for different observing runs: 1994 and 1995 May – blue (Clement & Shelton 1999), 2010 May – cyan, 2011 April – olive, 2011 June–August – green, 2012 May – purple, 2012 June – black, 2012 August – red. The variable V9 is outside of the FOV of the Hanle images and thus only its V light curve from the La Silla data is displayed. Note that the light curves for V14 and V18 have been phased with the best period determined without modelling a secular period change.

the V and I filters. With only one eclipse we are unable to estimate the orbital period. We note that there is also the hint of ellipsoidal variations in the out-of-eclipse light curve.

V26, V27, V28, V29, V30, V31 and V34. The light curves of these new variable stars show long-term variations (Fig 9). For V29 and V34, we have no I-band data. However, the rest of these variables are located well within the RGB in the CMD (Fig. 3). Our data are not sufficient to calculate their periods.

V32. The light curve of this new variable is shown in Fig. 13 phased with our best period found by the string-length method of 0.172 30 d. Twice this period would produce a clean double-wave light curve with some suggestion of different depth minima. The star is outside the FOV of our Hanle images and therefore we only have V-band data from La Silla. Although its mean magnitude $V\sim$ 16 mag is similar to the brightness of the RRc stars in the cluster, we believe the star is rather an eclipsing binary of the W Ursae Majoris-type (or EW), whose period and nature can be better defined upon obtaining further accurate data.

V33. The light curve phased with our best period 0.575 40 d is shown in Fig. 7. This new variable star is obviously an RRab star but given its mean magnitude $V\sim$17.94 mag it must be a field star further away than NGC 6333. The star is outside the FOV of our Hanle images.

V34. This new variable is a long-term pulsator whose variability is clear in the three nights of data as shown in Fig. 9. The star is outside the FOV of our Hanle images.

4.4 Double-mode pulsators

Clear phase and/or amplitude modulations are seen in several of the RRc light curves in Fig. 8. Phase and amplitude modulations can be the result of a Blazhko effect or a double-mode pulsation. To distinguish between these possibilities one requires a convincing identification of secondary periods in the light curve and a long time series of accurate photometry is generally needed. Despite the limitations of our data set we have attempted the identification of such secondary periods for the RRc stars showing, to some extent, phase modulations, i.e. V10, V16, V18, V19, V22 and V23.

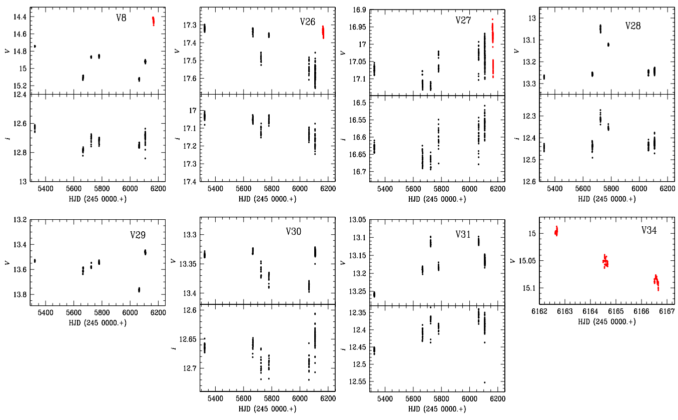

Figure 9. V and i magnitude variations of the LPVs in NGC 6333. The black and red symbols are data from Hanle and La Silla, respectively. V29 is saturated in our Hanle I-band images. V28, V29, V30 and V31 are saturated in our La Silla V-band images. V34 is outside the FOV of our Hanle images.

We used the program PERIOD04 (Lenz & Breger 2005) to identify the primary or first overtone period P_1 previously found by the string-length method described in Section 4.2 and given in column 7 of Table 3. Then, we pre-whitened the data from the primary period and searched the residuals for a secondary period. The frequency spectra of the original light curves and the residuals are shown in Fig. 14. No significant secondary frequencies were detected in the residual spectra of V10, V16, V18, V22 and V23 other than small residuals at the 1 d aliases of the main frequency f1. For V22 however, the amplitude modulations are so prominent that they could not be explained by period variations and rather they must be the result of the Blazhko effect whose periodicity we are not in position to estimate given our data set.

For V19, a rather prominent frequency was found in the residual spectrum at 2.029 49 d^{-1}, or a period of 0.492 734d. If this period is interpreted as the fundamental P_0 and with $P_1 = 0.366\ 7937$d we find a ratio $P_1/P_0 = 0.744$ which corresponds to the canonical 0.746 ± 0.001 ratio in RRd stars (Cox, Hudson & Clancy 1983; Catelan 2009) and with the period ratio found in a large sample of double-mode RRd stars in the Large Magellanic Cloud (LMC) (Alcock et al. 2000). P_0 produces a residuals light curve shown in Fig. 15. The above two facts strongly suggest that V19 is indeed a double-mode RR Lyrae or RRd star. An inspection of the light curve of V19 in fig. 4 b of Clement & Shelton (1996) reveals clear nightly phase drifts like those noted by these authors for V16; however, this case was not pursued further by them.

Thus, V10, V16, V18, V22 and V23 are rather reminiscent of the Blazhko RRc variables in NGC 5024 (Arellano Ferro et al. 2012). Given the nature of our time series we cannot estimate their Blazhko period or the possible presence of non-radial modes for which dense, accurate and prolonged observations are required as recent experience has shown in targets of space missions (e.g. Guggenberger et al. 2012, and references there in).

4.5 RRc stars with secular period variation

The RRc stars V14 and V18 show the largest phase variations not obviously accompanied with amplitude modulations. This is suggestive of a secular period change. To investigate this possibility, we have used a variation of the string-length method previously described in Bramich et al. (2011). We define

$$\phi(t) = \frac{t-E}{P(t)} - \left\lfloor \frac{t-E}{P(t)} \right\rfloor \qquad (7)$$

$$P(t) = P_0 + \beta(t-E), \qquad (8)$$

where $\phi(t)$ is the phase at time t, $P(t)$ is the period at time t, P_0 is the period at the epoch E and β is the rate of period change. We fix the value of E and calculate the best-fitting values of P_0 and β (in units d d^{-1}) within a small range of possible periods around the previously found best-fitting period as described in Section 4.2. We have applied this approach to the light curves of V14 and V18, both of which show clear phase displacements over time (see Section 4.3).

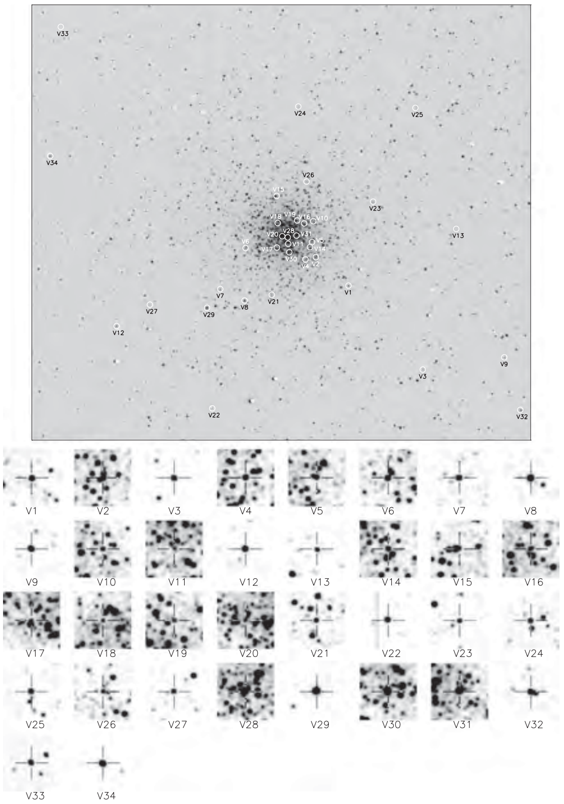

Figure 10. Finding charts constructed from our La Silla *V* reference image; north is up and east is to the right. The cluster image is 13.04 × 11.39 arcmin^2, and the image stamps are of size 20.6 × 20.6 arcsec^2. Each confirmed variable lies at the centre of its corresponding image stamp and is marked by a cross-hair.

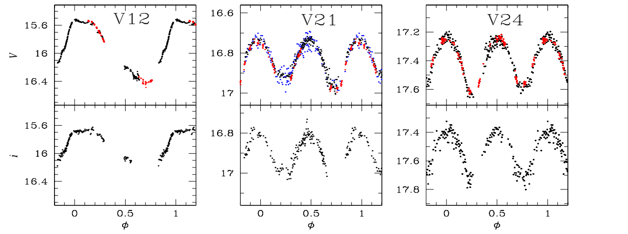

Figure 11. *V* and *i* light curves of the AC V12, and the eclipsing binaries V21 and V24, phased with the periods given in Table 3. The black and red points are data from Hanle and La Silla, respectively. The blue points correspond to the *V* observations of Clement & Shelton (1999).

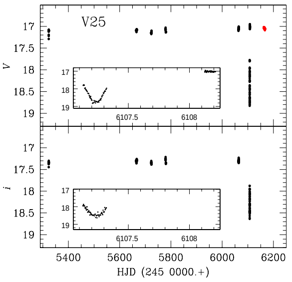

Figure 12. Light curve of V25 where one eclipse has been detected at HJD 245 6107.24d. The inset panel is a zoom-in on the eclipse. The black and red points represent Hanle and La Silla data, respectively.

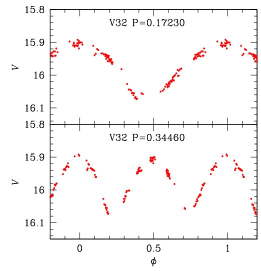

Figure 13. Light curve of the binary star V32 phased with two possible periods. The star is out the FOV of Hanle, hence we can only plot data from La Silla.

In Fig. 16, we show the light curves of these two stars phased with a constant period (top panels), and with the new period and period change rate calculated with the above equations (bottom panels). It is clear that the new periods and period change rates produce much cleaner and more coherent light curves. We conclude that V14 and V18 have secular period changes at the rates of 4.67 and 11.5 d Myr^{-1}, respectively. In the case of V18, the light curve phasing is still not fully satisfactory and therefore we do not discard the possibility of additional amplitude modulations that could be associated with a Blazhko effect similar to many of the RRc stars in NGC 5024 (Arellano Ferro et al. 2012).

4.6 Search for variable stars among the blue stragglers

The BS region in NGC 6333 is arbitrarily defined in Fig. 3 by the dashed red lines. In Fig. 5, this translates to the magnitude limits indicated by the two vertical red dashed lines. In this figure, all of the stars in the BS region are plotted with coloured points; yellow or cyan depending on whether they lie below or above the chosen variability detection threshold for $\mathcal{S}_{\mathcal{B}}$. We found that 40 of the BS stars have the $\mathcal{S}_{\mathcal{B}}$ statistic for the Hanle data above this threshold and their light curves were explored in detail. However, no clear and convincing variability was found in any of these stars and the relatively high value of $\mathcal{S}_{\mathcal{B}}$ could always be explained by groups of spurious photometric measurements or by the effect on the photometry of a nearby known variable. We conclude that if SX Phe stars exist in this cluster, then they must be of an amplitude similar to or smaller than the rms achieved by our photometry (see Fig. 2). To highlight this point, if we consider that the known SX Phe stars in NGC 5024 (another OoII cluster, with a blue HB and similar metallicity to NGC 6333) (Arellano Ferro et al. 2011) actually existed instead in NGC 6333, then we would have been able to detect about 19 out of 25(76 per cent) of them in our data, given the completeness of our variable star search reported at the end of Section 4.1.

Downloaded from http://mnras.oxfordjournals.org/ at Royal Library/Copenhagen University Library on December 20, 2015

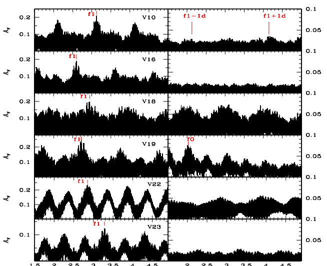

Figure 14. Frequency spectra of selected RRc stars. The left-hand panels show the spectrum produced by the original data. The major peaks correspond to the periods listed in Table 3 and used to produce the light curves in Figs 7 and 8. The right-hand panels show the spectra of the residuals after pre-whitening the main frequency. Note that the vertical scale in the right-hand panels has been increased to highlight possible secondary frequencies. See the text for a discussion.

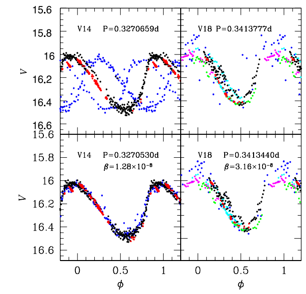

Figure 16. Two RRc stars with secular period change. The top panels show the light curves phased with a constant period found as described in Section 4.2. The bottom panels show the light curves phased with the new period and period change rate β given in the legend. The colours are coded as in the caption of Fig. 8.

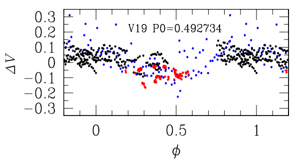

Figure 15. Residuals of V19 phased with the fundamental period given in the legend. The blue points are the *V* data from Clement & Shelton (1999). The black and red points are the *V* data from Hanle and La Silla, respectively. See Section 4.4 for a discussion.

5 RR Lyrae STARS

5.1 [Fe/H] and M_V from light-curve Fourier decomposition

Estimates of physical parameters, such as metallicity, luminosity and effective temperatures can be made from the Fourier decomposition of the light curves of RR Lyrae stars into their harmonics and from semi-empirical relationships (e.g. Jurcsik & Kovács 1996; Morgan, Wahl & Wieckhorts 2007). Traditionally the light curves are represented by the equation:

$$m(t) = A_o + \sum_{k=1}^{N} A_k \cos\left(\frac{2\pi}{P}k(t-E) + \phi_k\right), \qquad (9)$$

where $m(t)$ are magnitudes at time t, P the period and E the epoch. A linear minimization routine is used to fit the data with the Fourier series model, deriving the best-fitting values of the amplitudes A_k and phases ϕ_k of the sinusoidal components. From the amplitudes and phases of the harmonics in equation (9), the Fourier parameters $\phi_{ij} = j\phi_i - i\phi_j$ and $R_{ij} = A_i/A_j$ are defined. Although the *V* data from Clement & Shelton (1999) have been very useful in refining the periods of the RR Lyrae stars, in fitting the light curves we have opted not to include the data since they have a considerably larger scatter. The mean magnitudes A_0, and the Fourier light-curve fitting parameters of the individual RRab- and RRc-type stars in *V* are listed in Table 4.

The Fourier decomposition parameters can be used to calculate [Fe/H] and M_V for both RRab and RRc stars by means of the semi-empirical calibrations given in equations (10), (11), (12) and (13).

The calibrations for [Fe/H] and M_V used for RRab stars are

$$[\mathrm{Fe/H}]_J = -5.038 - 5.394P + 1.345\phi_{31}^{(s)}, \qquad (10)$$

$$M_V = -1.876 \log P - 1.158A_1 + 0.821A_3 + K, \qquad (11)$$

given by Jurcsik & Kovács (1996) and Kovács & Walker (2001), respectively. The standard deviations of the above calibrations are 0.14 dex (Jurcsik 1998) and 0.04 mag, respectively. In equation (11), we have used $K = 0.41$ to scale the luminosities of the RRab with the distance modulus of 18.5 mag for the LMC (see the discussion in section 4.2 of Arellano Ferro, Giridhar & Bramich 2010). Equation (10) is applicable to RRab stars with a *deviation parameter* D_m, defined by Jurcsik & Kovács (1996) and Kovács & Kanbur (1998), not exceeding an upper limit. These authors suggest $D_m \leq 3.0$. The D_m is listed in column 11 of Table 4. A few stars have D_m marginally larger than this limit but given the quality of their light curve and the good coverage of the cycle we opted for reporting their iron abundance. The metallicity scale of equation (10) was transformed into the widely used scale of Zinn & West (1984) using the relation $[\mathrm{Fe/H}]_J = 1.431[\mathrm{Fe/H}]_{\mathrm{ZW}} + 0.88$ (Jurcsik 1995). These two metallicity scales closely coincide for $[\mathrm{Fe/H}] \sim -2.0$ while for $[\mathrm{Fe/H}] \sim -1.5$, the $[\mathrm{Fe/H}]_J$ is about 0.24 dex less metal poor than $[\mathrm{Fe/H}]_{\mathrm{ZW}}$ (see also Fig. 2 of Jurcsik 1995). Therefore, for a metal poor cluster such as NGC 6333, the two scales are not significantly different.

Downloaded from http://mnras.oxfordjournals.org/ at Royal Library/Copenhagen University Library on December 20, 2015

Table 5. Physical parameters for the RRab and RRc stars. The numbers in parentheses indicate the uncertainty on the last decimal place and have been calculated as described in the text.

Star	$[\mathrm{Fe/H}]_{\mathrm{ZW}}$	M_V	$\log(L/\mathrm{L}_\odot)$	$\log T_{\mathrm{eff}}$	$M/\mathrm{M}_\odot$	$R/\mathrm{R}_\odot$
			RRab stars			
V1	−1.666(11)	0.497(1)	1.701(1)	3.808(7)	0.73(6)	5.77(1)
V2	−1.780(21)	0.464(3)	1.714(1)	3.803(8)	0.73(7)	6.00(1)
V4	−1.634(18)	0.438(1)	1.725(1)	3.800(8)	0.70(6)	6.15(1)
V6	−1.674(20)	0.520(3)	1.692(1)	3.805(8)	0.70(6)	5.78(1)
V7	−1.742(11)	0.456(1)	1.717(1)	3.803(7)	0.73(6)	6.01(1)
V11	−1.519(63)	0.422(6)	1.731(2)	3.794(17)	0.66(13)	6.38(4)
V13[a]	−1.415(43)	0.656(6)	1.638(2)	3.819(10)	0.71(8)	5.09(2)
V15	−1.932(46)	0.456(6)	1.717(2)	3.798(10)	0.75(9)	6.14(2)
V33[a]	−1.107(181)	0.635(7)	1.646(3)	3.803(31)	0.68(25)	5.54(7)
Weighted mean	−1.702(6)	0.467(1)	1.713(1)	3.803(3)	0.72(3)	5.73(1)
			RRc stars			
V5	−1.81(22)	0.518(2)	1.693(1)	3.885(1)	0.49(1)	4.54(7)
V10	−1.83(44)	0.527(4)	1.689(2)	3.862(1)	0.59(1)	4.44(13)
V14	−1.69(24)	0.499(3)	1.700(1)	3.863(1)	0.58(1)	4.46(7)
V16	−1.65(23)	0.530(6)	1.688(3)	3.859(1)	0.46(1)	4.48(7)
V17	−1.22(78)	0.537(3)	1.685(1)	3.869(2)	0.54(2)	4.28(20)
V20	−1.69(22)	0.609(2)	1.656(1)	3.864(1)	0.54(1)	4.23(7)
V23	−0.45(50)[a]	0.604(3)	1.658(1)	3.875(1)	0.49(1)	4.02(11)
Weighted mean	−1.71(11)	0.554(1)	1.638(1)	3.862(1)	0.51(1)	4.79(4)

[a] Values not included in the average. V13 and V33 are not cluster members.

For the RRc stars we employ the calibrations:

$$[\mathrm{Fe/H}]_{\mathrm{ZW}} = 52.466P^2 - 30.075P + 0.131\phi_{31}^{(c)2} \\ -0.982\phi_{31}^{(c)} - 4.198\phi_{31}^{(c)}P + 2.424, \qquad (12)$$

$$M_V = 1.061 - 0.961P - 0.044\phi_{21}^{(s)} - 4.447A_4, \qquad (13)$$

given by Morgan et al. (2007) and Kovács (1998), respectively. The standard deviations of the above calibrations are 0.14 dex and 0.042 mag, respectively. For equation (13) the zero-point was reduced to 1.061 mag to make the luminosities of the RRc consistent with the distance modulus of 18.5 mag for the LMC (see discussions by Cacciari, Corwin & Carney 2005; Arellano Ferro et al. 2010). The original zero-point given by Kovács (1998) is 1.261.

In the above calibrations the phases are calculated either from series of sines or of cosines as indicated by the superscript. We transformed our cosine series phases into the sine ones where necessary via the relation $\phi_{jk}^{(s)} = \phi_{jk}^{(c)} - (j-k)\frac{\pi}{2}$.

The physical parameters for the RR Lyrae stars are reported in Table 5. We have not included the star V3 since it has prominent Blazhko modulations and V9 because our observations are not sufficient to cover the complete light curve. Despite the fact that most RRc stars show to some extent amplitude and/or phase modulations, in calculating mean parameters, we only excluded stars with extreme modulations; namely V18 and V22. V19 was also not considered given its double-mode nature. We also excluded V13 and V33 which are not cluster members. V14 was considered only after the light curve was phased with the period change rate included, i.e. the light curve in the bottom panel of Fig. 16. The inverse-variance-square-weighted means are also given in Table 5. The systematic error in the metallicity estimates is of the order of the scatter in the calibrations of equations (10) and (12), i.e. 0.14 dex. Thus, the metallicity obtained from the RRab and RRc stars is $[\mathrm{Fe/H}]_{\mathrm{ZW}} = -1.70 \pm 0.01$ which can be converted to the new scale defined by Carretta et al. (2009) using UVES spectra of RGB stars in globular clusters by $[\mathrm{Fe/H}]_{\mathrm{UVES}} = -0.413 + 0.130[\mathrm{Fe/H}]_{\mathrm{ZW}} - 0.356[\mathrm{Fe/H}]_{\mathrm{ZW}}^2$. We find $[\mathrm{Fe/H}]_{\mathrm{UVES}} = -1.67 \pm 0.01$. Clement & Shelton (1999) found, from the light-curve Fourier decomposition of V2, V4, V6 and V7, the average $[\mathrm{Fe/H}]_{\mathrm{ZW}} = -1.77 \pm 0.08$ in good agreement with our result.

To the best of our knowledge no iron abundance of NGC 6333 has been calculated from high resolution spectroscopy. The first calculation of $[\mathrm{Fe/H}]_{\mathrm{ZW}} = -1.81 \pm 0.15$ was made from integrated photometry in the Q_{39} index calibration by Zinn (1980) and reported by Harris (1996) (2010 edition) on the modern ZW scale, $[\mathrm{Fe/H}]_{\mathrm{ZW}} = -1.77$. The iron abundance of NGC 6333 has also been estimated by Costar & Smith (1988) from the Preston (1959) ΔS parameter estimated on V1 and V3. These authors calculated a [Fe/H] value of −1.93 and −1.45 for these two variables, respectively, for an average of −1.71. They used the ΔS–[Fe/H] calibration of Butler (1975). Had they used the calibration of Suntzeff, Kraft & Kinman (1994) for RRab stars or Jurcsik's (1995) or Fernley's et al. (1998) their average [Fe/H] would have been −1.72, −1.73 and −1.92, respectively. The value [Fe/H] = −1.72 is commonly cited in the literature on NGC 6333, most likely from the ΔS result. We have to note however that the ΔS values were obtained only on two RR Lyrae stars (V1 and V3) at a single phase and that the method is strongly phase dependent. We should also keep in mind that V3 is a clear Blazhko variable. Thus, despite the good numerical

Downloaded from http://mnras.oxfordjournals.org/ at Royal Library/Copenhagen University Library on December 20, 2015

agreement with our results we do not find the comparison of particular relevance, and believe that our result $[\mathrm{Fe/H}]_{\rm ZW} = -1.70 \pm 0.01$ is more solidly sustained.

The weighted mean M_V values for the RRab and RRc stars are 0.467 ± 0.001 and 0.554 ± 0.001 mag, respectively (see Table 5) and will be used in Section 5.4 to estimate the mean distance to the cluster after differential reddening is considered.

5.2 RR Lyrae luminosities and effective temperatures

The values of M_V in Table 5 were transformed into $\log L/{\rm L}_{\odot} = -0.4(M_V - {\rm M}^{\odot}_{\rm bol} + BC)$. The bolometric correction was calculated using the formula $BC = 0.06\,[\mathrm{Fe/H}]_{\rm ZW} + 0.06$ given by Sandage & Cacciari (1990). We adopted the value ${\rm M}^{\odot}_{\rm bol} = 4.75$ mag.

The effective temperature $T_{\rm eff}$ can be estimated for RRab stars from the calibrations of Jurcsik (1998):

$$\log(T_{\rm eff}) = 3.9291 - 0.1112(V-K)_o - 0.0032[\mathrm{Fe/H}], \qquad (14)$$

with

$$(V-K)_o = 1.585 + 1.257P - 0.273A_1 - 0.234\phi_{31}^{(s)} + 0.062\phi_{41}^{(s)}. \qquad (15)$$

For the RRc stars the calibration of Simon & Clement (1993) can be used:

$$\log(T_{\rm eff}) = 3.7746 - 0.1452\log(P) + 0.0056\phi_{31}^{(c)}. \qquad (16)$$

The validity and caveats of the above calibrations have been discussed in several recent papers (Cacciari et al. 2005; Arellano Ferro et al. 2008, 2010; Bramich et al. 2011) and the reader is referred to them for the details. We list the obtained $T_{\rm eff}$ values for the RR Lyrae stars in NGC 6333 for comparison with similar work in other clusters.

5.3 RR Lyrae masses and radii

Once the period, luminosity and temperature are known for each RR Lyrae star, its mass and radius can be estimated from the equations: $\log {\rm M/M}_{\odot} = 16.907 - 1.47\log P_F + 1.24\log({\rm L/L}_{\odot}) - 5.12\log T_{\rm eff}$ (van Albada & Baker 1971) and $L = 4\pi R^2\sigma T^4$, respectively. The masses and radii are given in Table 5 in solar units.

5.4 Distance to NGC 6333 from the RR Lyrae stars

The weighted mean M_V, calculated for the RRab and RRc in Table 5 can be used to estimate the true distance modulus; $V - M_V = 5\log d - 5 + 3.1E(B-V)$. The individual colour excesses are listed in Table 4 which were calculated after differential reddening was considered (Section 3). Although the internal errors in M_V are small, given the mean magnitude dispersion in the HB, a better estimate of the uncertainty in the distance is the standard deviation of the mean and so we find the distance modulus of 14.527 ± 0.052 mag and 14.482 ± 0.081 mag using the RRab and RRc stars, respectively, which correspond to the distances 8.04 ± 0.19 and 7.88 ± 0.30 kpc.

The above distances for the RRab and RRc stars are calculated from independent empirical calibrations, with their own systematic uncertainties, hence they should be considered as two independent estimates. The correction for differential reddening has contributed to the good agreement between these two estimates of the distance and to reduce the uncertainties.

The distance to NGC 6333 listed in the catalogue of Harris (1996) (2010 edition) is 7.9 kpc, estimated from the mean M_V magnitudes calculated by Clement & Shelton (1999). The calibrations of M_V used by Clement & Shelton for the RRab and RRc stars are the same as our equations (11) and (13) but before correcting the zero-points as discussed in Section 5.1. Also, in their calculation of the distance the differential reddening was not taken into account. These facts may account for the small difference in the distance we derive for the cluster.

The most recent discussion on the distance of the cluster is perhaps the one given by Casetti-Dinescu et al. (2010) in which they adopt the distance 7.9 kpc from Harris (1996) (2010 edition) but argue that due to reasonable uncertainties in the distance(10 per cent) the alternative distance of 8.6 kpc is selected such that it places the cluster on the opposite side of the Galactic centre. In our opinion and given our results, 10 per cent is large for a distance error and note that if our distance is adopted then the cluster would be located on the near side of the Galactic centre.

6 BAILEY DIAGRAM AND OOSTERHOFF TYPE

Using the periods listed in Table 3, we calculate mean periods of 0.639 and 0.336 d for the 8 RRab and 10 RRc stars, respectively, that are cluster members (i.e. excluding V13 and V33), and excluding the RRd star V19. These values clearly identify NGC 6333 as an Oosterhoff-type II (OoII) cluster.

The Bailey diagram ($\log P$ versus A_V and $\log P$ versus A_i) for the RR Lyrae variables is shown in Fig. 17. The RRab stars have longer periods for a given amplitude than their counterparts in the OoI cluster M3. This is also seen in the OoII clusters M53 (Arellano Ferro et al. 2011), M15 and M68 (Cacciari et al. 2005). This fact confirms the OoII type of NGC 6333. V13 and V33 are discordant stars and this supports the idea that they are not cluster members (Clement et al. 1984, Section 4.3). Other than V13 and V33 there are no RRab stars with peculiar amplitude, which gives support to the physical parameters obtained in Section 5 from the light-curve Fourier decomposition. The RRc stars show some scatter which is likely due to the amplitude modulations observed in the population of RRc stars in NGC 6333, the majority of the RRc stars seem to show some amplitude and/or phase modulations that can be attributed to the Blazhko effect (see Section 4.3 and Fig. 8). A similar case was found in NGC 5024 which probably contains the largest sample of RRc Blazhko variables (Arellano Ferro et al. 2011, 2012).

As in Arellano Ferro et al. (2011) for NGC 5024, in the bottom panel of Fig. 17 we show the Bailey diagram using the amplitudes in the I band, or A_i in Table 3, for NGC 6333. The solid curve is the fit calculated by Arellano Ferro et al. for the RRab stars in NGC 5024 (their equation 3). Being the two clusters of the OoII type and of similar metallicity, the match is rewarding.

7 CONCLUSIONS

In their analysis on the completeness of the variable stars sample in NGC 6333, Clement & Shelton (1996) concluded that the discovery of new RRc stars was unlikely but that some RRab stars might have escaped their attention. In fact, we have not found any new RR Lyrae, neither RRab nor RRc, in the corresponding field of Clement & Shelton's images. However, we found in this work two RRc stars, V22 and V23, and one RRab, V33; the three of them are relatively isolated in the outskirts of the cluster. While V22 and V23 are clear members of NGC 6333, V33 is a field RRab further away than the cluster. Likewise we corroborate that the RRab star V13 is not a cluster member. We have also been able to find three new eclipsing binaries and seven long-period variables. Pulsation period refinements have been calculated for nearly all variables. Accurate celestial coordinates and a finding chart for all previously known and new variables are provided.

Although a cluster membership confirmation from radial velocity data would be necessary, we argue that V12 is a cluster member since the correction from interstellar reddening places this star in the Cepheid instability strip at about 1 mag above the HB. Although V12 is about 5 arcmin away from the cluster centre, it has been noted by Clement et al. (2001) in the CVSGC (2012 update) that the star is within the tidal radius of NGC 6333 of ~8 arcmin. V12 also follows the *P–L* relation of ACs pulsating in the fundamental mode of Pritzl et al. (2002). While ACs are common in dwarf spheroidal galaxies (e.g. Nemec, Nemec & Lutz 1994; Pritzl et al. 2002, 2005), they are rare in globular clusters; only four are presently known, V19 in NGC 5466 (Zinn & Dahn 1976) and three in ω Cen (Kaluzny et al. 1997). We argue that V12 in NGC 6333 is an AC.

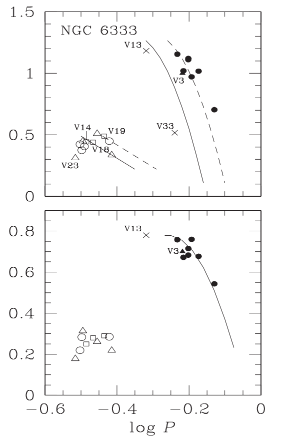

Figure 17. The RR Lyrae stars in NGC 6333 on the amplitude–period plane or Bailey diagram for the V and I bands. In the top panel, the solid lines represent the average distributions of fundamental and first overtone RRL's in M3. The segmented lines are the loci for the evolved stars according to Cacciari et al. (2005). The filled symbols are used for RRab stars and open symbols for RRc stars. Circles represent stars with no apparent signs of amplitude modulations and triangles indicate stars with clear and prominent amplitude modulations or Blazhko variables. Variables with secular period change, V14 and V18 and the double-mode star V19 are shown as squares. V13 and V33 are not cluster members. The bottom panel shows the case for the I amplitudes. The solid curve is the locus defined by Arellano Ferro et al. (2011) for the RRab stars in the OoII cluster NGC 5024.

Among the RR Lyrae stars, we have identified the double-mode or RRd nature of V19 and the secular period changes in V14 and V18 at the rates of 4.67 and 11.5 d Myr^{-1}, respectively. We stress that similar to NGC 5024 (Arellano Ferro et al. 2012), NGC 6333 has a rather large number of Blazhko stars among the RRc population.

A deep search for variability among the BSs in the cluster was conducted but none was found. If SX Phe stars do exist in the cluster they must be of amplitudes smaller than the detection limit of our data.

The Fourier decomposition of the light curves of nine RRab and seven RRc stars was performed and individual values of [Fe/H], M_V, $\log {\rm L/L}_{\odot}$, $T_{\rm eff}$ and stellar mass and radius were calculated using ad hoc semi-empirical calibrations. The weighted mean values of the iron abundance of selected stars gives a cluster mean metallicity of $[\mathrm{Fe/H}]_{\rm ZW} = -1.70 \pm 0.01$ in the Zinn & West (1984) scale or $[\mathrm{Fe/H}]_{\rm UVES} = -1.67 \pm 0.01$ in the scale defined more recently by Carretta et al. (2009). The weighted mean values of the absolute magnitude of the RRab and the RRc stars lead to a distance of 8.04 ± 0.19 and 7.88 ± 0.30 kpc, respectively. In calculating these distances the heavy differential reddening affecting the cluster was taken into account by using the detailed reddening map of Alonso-García et al. (2012).

ACKNOWLEDGEMENTS

We acknowledge an anonymous referee for very relevant input and comments. We are grateful to the TAC's of the Hanle and La Silla observatories for generous telescope time allocation to this project and to the support astronomers of IAO, at Hanle and CREST (Hosakote) for their very efficient help while acquiring the data. This project was supported by DGAPA-UNAM grant through project IN104612 and by the INDO-MEXICAN collaborative programme by DST-CONACyT. NK acknowledges an ESO Fellowship. The research leading to these results has received funding from the European Community's Seventh Framework Programme (/FP7/2007-2013/) under grant agreement No 229517. OW (aspirant FRS - FNRS), AE, YD, DR (FRIA PhD student), and J. Surdej acknowledge support from the Communauté française de Belgique – Actions de recherche concertées – Académie universitaire Wallonie-Europe. TCH gratefully acknowledges financial support from the Korea Research Council for Fundamental Science and Technology (KRCF) through the Young Research Scientist Fellowship Program. TCH acknowledges financial support from Korea Astronomy and Space Science Institute (KASI) grant number 2012-1-410-02. KA, DB, MD, MH and CL are supported by NPRP grant NPRP-09-476-1-78 from the Qatar National Research Fund (a member of Qatar Foundation). MR acknowledges support from FONDECYT postdoctoral fellowship N3120097. The Danish 1.54 m telescope is operated based on a grant from the Danish Natural Science Foundation (FNU). Funding for the Centre for Star and Planet Formation is provided by the Danish National Research Foundation. CS received funding from the European Union's Seventh Framework Programme (FP7/2007-2013) under grant agreement no. 268421. HK acknowledges support from a Marie-Curie Intra-European Fellowship.

This work has made a large use of the SIMBAD and ADS services.

REFERENCES

Alcock C. et al., 2000, ApJ, 542, 257
Alonso-García J., Mateo M., Sen B., Banerjee M., Catelan M., Minniti D., von Braun K., 2012, AJ, 143, 70

Arellano Ferro A., Rojas López V., Giridhar S., Bramich D. M., 2008, MNRAS, 384, 1444
Arellano Ferro A., Giridhar S., Bramich D. M., 2010, MNRAS, 402, 226
Arellano Ferro A., Figuera Jaimes R., Giridhar S., Bramich D. M., Hernández Santisteban J. V., Kuppuswamy K., 2011, MNRAS, 416, 2265
Arellano Ferro A., Bramich D. M., Figuera Jaimes R., Giridhar S., Kuppuswamy K., 2012, MNRAS, 420, 1333
Blanco V. M., 1992, AJ, 104, 734
Bramich D. M., 2008, MNRAS, 386, L77
Bramich D. M., Freudling W., 2012, MNRAS, 424, 1584
Bramich D. M., Figuera Jaimes R., Giridhar S., Arellano Ferro A., 2011, MNRAS, 413, 1275
Bramich D. M. et al., 2013, MNRAS, 428, 2275
Burke E. W., Rolland W. W., Boy W. R., 1970, J. R. Astron. Soc. Can., 64, 353
Butler D., 1975, ApJ, 200, 68
Cacciari C., Corwin T. M., Carney B. W., 2005, AJ, 129, 267
Cardelli J. A., Clayton G. C., Mathis J. S., 1989, ApJ, 345, 245
Carretta E., Bragaglia A., Gratton R., DOrazi V., Lucatello S., 2009, A&A, 508, 695
Casetti-Dinescu D. I., Girard T. M., Korchagin V. I., van Altena W. F., López C. E., 2010, AJ, 140, 1282
Catelan M., 2009, Ap&SS, 320, 261
Clement C. M., Shelton I., 1996, AJ, 112, 618
Clement C. M., Shelton I., 1999, AJ, 118, 453
Clement C. M., Walker I. R., 1991, AJ, 101, 1352
Clement C. M., Ip P., Robert N., 1984, AJ, 89, 1707
Clement C. M. et al., 2001, AJ, 122, 2587
Costar D., Smith H. A., 1988, AJ, 96, 1925
Cox A. N., Hudson S. W., Clancy S. P., 1983, ApJ, 266, 94
Draper P. W., 2000, in Manset N., Veillet C., Crabtree D., eds. ASP Conf. Ser. Vol. 216, Astronomical Data Analysis Software and Systems IX. Astron. Soc. Pac., San Francisco, p. 615
Dworetsky M. M., 1983, MNRAS, 203, 917
Fernley J., Skillen I., Carney B. W., Cacciari C., Janes K., 1998, A&A, 330, 515
Figuera Jaimes R., Arellano Ferro A., Bramich D. M., Giridhar S., 2013, A&A, in press (arXiv1305.4837)
Guggenberger E. et al., 2012, MNRAS, 424, 649
Guldenschuh K. A. et al., 2005, PASP, 117, 721
Harris W. E., 1996, AJ, 112, 1487
Honeycutt R. K., 1992, PASP, 104, 435
Jurcsik J., 1995, Acta Astron, 45, 653
Jurcsik J., 1998, A&A, 333, 571
Jurcsik J., Kovács G., 1996, A&A, 312, 111
Kains N., Bramich D. M., Figuera Jaimes R., Arellano Ferro A., Giridhar S., Kuppuswamy K., 2012, A&A, 548, 92
Kaluzny J., Kubiak M., Szymański, Udalski A., Krzemiński W., Mateo M., 1997, A&AS, 125, 343
Kovács G., 1998, Mem. Soc. Astron. Ital. 69, 49
Kovács G., Kanbur S. M., 1998, MNRAS, 295, 834
Kovács G., Walker A. R., 2001, A&A, 371, 579
Kunder A., Chaboyer B., Layden A., 2010, AJ, 139, 415
Lenz P., Breger M., 2005, Commun. Asteroseismol., 146, 53
Mateo M., Udalski A., Szymanski M., Kaluzny J., Kubiak M., Krzeminski W., 1995, AJ, 109, 588
Morgan S., Wahl J. N., Wieckhorts R. M., 2007, MNRAS, 374, 1421
Nemec J. M., Nemec A. F. L., Lutz T. E., 1994, AJ, 108, 222
Padmanabhan N. et al., 2008, ApJ, 674, 1217
Preston G. W., 1959, ApJ, 130, 507
Pritzl B. J., Armandroff T. E., Jacoby G. H., Da Costa G. S., 2002, AJ, 124, 1464
Pritzl B. J., Armandroff T. E., Jacoby G. H., Da Costa G. S., 2005, AJ, 129, 2232
Reed B. C., Hesser J. E., Shawl S. J., 1988, PASP, 100, 545
Regnault N. et al., 2009, A&A, 506, 999
Safonova M., Stalin C. S., 2011, AJ, 142, 179
Samus N. N., Kazarovets E. V., Pastukhova E. N., Tsvetkova T. M., Durlevich O. V., 2009, PASP, 121, 1378
Sandage A., Cacciari C., 1990, ApJ, 350, 645
Sawyer H. B., 1951, Pub. DDO, 1, 511
Schlegel D. J., Finkbeiner D. P., Davis M., 1998, ApJ, 500, 525
Shapley H., 1916, PASP, 28, 282
Simon N. R., Clement C. M., 1993, ApJ, 410, 526
Sturch C., 1966, ApJ, 143, 774
Suntzeff N. B., Kraft R. P., Kinman T. D., 1994, ApJS, 93, 271
Tamuz O., Mazeh T., North P., 2006, MNRAS, 367, 1521
van Albada T. S., Baker N., 1971, ApJ, 169, 311
Wallerstein G., Cox A. N., 1984, PASP, 96, 677
Zacharias N. et al., 2010, AJ, 139, 2184
Zinn R., 1980, ApJS, 42, 19
Zinn R., 1985, ApJ, 293, 424
Zinn R., Dahn C. C., 1976, AJ, 81, 527
Zinn R., West M. J., 1984, ApJS, 55, 45

SUPPORTING INFORMATION

Additional Supporting Information may be found in the online version of this article:

Table 2. Time-series V and i photometry for all the confirmed variables in our FOV (http://mnras.oxfordjournals.org/lookup/suppl/doi:10.1093/mnras/stt1080/-/DC1).

Please note: Oxford University Press is not responsible for the content or functionality of any supporting materials supplied by the authors. Any queries (other than missing material) should be directed to the corresponding author for the Paper.

This paper has been typeset from a TEX/LATEX file prepared by the author.

A&A 555, A36 (2013)
DOI: 10.1051/0004-6361/201321819

Astronomy & Astrophysics

Estimating the parameters of globular cluster M 30 (NGC 7099) from time-series photometry★,★★,★★★

N. Kains[1], D. M. Bramich[1], A. Arellano Ferro[2], R. Figuera Jaimes[1,3], U. G. Jørgensen[4,5], S. Giridhar[6], M. T. Penny[7], K. A. Alsubai[8], J. M. Andersen[9,5], V. Bozza[10,11], P. Browne[3], M. Burgdorf[12], S. Calchi Novati[10,13], Y. Damerdji[14], C. Diehl[15,16], P. Dodds[3], M. Dominik[3,★★★★], A. Elyiv[14,17], X.-S. Fang[18,19], E. Giannini[15], S.-H. Gu[18,19], S. Hardis[4], K. Harpsøe[4,5], T. C. Hinse[20,4], A. Hornstrup[21], M. Hundertmark[3], J. Jessen-Hansen[22], D. Juncher[4,5], E. Kerins[23], H. Kjeldsen[22], H. Korhonen[4,5], C. Liebig[3], M. N. Lund[22], M. Lundkvist[22], L. Mancini[24], R. Martin[25], M. Mathiasen[4], M. Rabus[26], S. Rahvar[27,28], D. Ricci[29,14], K. Sahu[30], G. Scarpetta[10,31], J. Skottfelt[4,5], C. Snodgrass[32], J. Southworth[33], J. Surdej[14], J. Tregloan-Reed[33], C. Vilela[33], O. Wertz[14], and A. Williams[25]
(The MiNDSTEp consortium)

(Affiliations can be found after the references)

Received 2 May 2013 / Accepted 15 May 2013

ABSTRACT

Aims. We present the analysis of 26 nights of *V* and *I* time-series observations from 2011 and 2012 of the globular cluster M 30 (NGC 7099). We used our data to search for variable stars in this cluster and refine the periods of known variables; we then used our variable star light curves to derive values for the cluster's parameters.

Methods. We used difference image analysis to reduce our data to obtain high-precision light curves of variable stars. We then estimated the cluster parameters by performing a Fourier decomposition of the light curves of RR Lyrae stars for which a good period estimate was possible. We also derived an estimate for the age of the cluster by fitting theoretical isochrones to our colour-magnitude diagram (CMD).

Results. Out of 13 stars previously catalogued as variables, we find that only 4 are bona fide variables. We detect two new RR Lyrae variables, and confirm two additional RR Lyrae candidates from the literature. We also detect four other new variables, including an eclipsing blue straggler system, and an SX Phoenicis star. This amounts to a total number of confirmed variable stars in M 30 of 12. We perform Fourier decomposition of the light curves of the RR Lyrae stars to derive cluster parameters using empirical relations. We find a cluster metallicity $[Fe/H]_{ZW} = -2.01 \pm 0.04$, or $[Fe/H]_{UVES} = -2.11 \pm 0.06$, and a distance of 8.32 ± 0.20 kpc (using RR0 variables), 8.10 kpc (using one RR1 variable), and 8.35 ± 0.42 kpc (using our SX Phoenicis star detection in M 30). Fitting isochrones to the CMD, we estimate an age of 13.0 ± 1.0 Gyr for M 30.

Key words. stars: variables: general – stars: variables: RR Lyrae – globular clusters: individual: M 30 (NGC 7099)

1. Introduction

In this paper we analyse time-series observations of M 30 (NGC 7099, or C2137-234 in the IAU nomenclature; $\alpha = 21^h40^m22^s, \delta = -23°10'47.5''$ at J2000.0), one of the most metal-poor globular clusters known, with $[Fe/H] \sim -2.1$, located at a distance of ~8 kpc. This cluster is thought to be of extra-Galactic origin, due to its retrograde orbit (Allen et al. 2006), pointing to its possible accretion by the Milky Way following an encounter with a satellite, as well as its position on the age-metallicity diagram (Forbes & Bridges 2010). M 30 is also thought to have undergone core collapse (e.g. Djorgovski & King 1986). Here we detect and classify already reported, as well as new variables, and use Fourier decomposition to derive properties of the RR Lyrae stars in this cluster. We then estimate the cluster parameters of M 30, providing us with an independent estimate of the metallicity, distance and age of this cluster, and the first using this method.

Our observations are detailed in Sect. 2; we discuss the variables in M 30 in Sect. 3, and in Sect. 4 we derive properties of the RR Lyrae stars in this cluster using Fourier decomposition and empirical relations. We use this to derive properties of the cluster in Sect. 5 and summarise our findings.

2. Observations and reductions

2.1. Observations

We obtained Johnson *V*- and *I*-band data with the Danish Faint Object Spectrograph and Camera (DFOSC) imaging camera at the Danish 1.54 m telescope at La Silla in Chile, as part of a programme with the MiNDSTEp consortium. In this programme we are making use of parts of the night when the MiNDSTEp primary-science microlensing observations towards the Galactic Bulge are not possible. The data were obtained in 2011 and 2012, with the 2011 data consisting mostly of *I*-band observations, while the 2012 observations are evenly split between *V* and *I*-band images. The observations are summarised in Table 1.

★ This work is based on data collected by MiNDSTEp with the Danish 1.54 m telescope at the ESO La Silla Observatory.
★★ The full light curves, an extract of which is shown in Table 2 are only available at the CDS via anonymous ftp to cdsarc.u-strasbg.fr (130.79.128.5) or via http://cdsarc.u-strasbg.fr/viz-bin/qcat?J/A+A/555/A36
★★★ Tables 8–10, and Figs. 6 and 9 are available in electronic form at http://www.aanda.org
★★★★ Royal Society University Research Fellow.

Table 1. Numbers of images and exposure times for the *V* and *I* band observations of M 30.

Date	N_V	t_V (s)	N_I	t_I (s)
20110728	–	–	48	10
20110730	–	–	27	15–20
20110803	–	–	12	30
20110804	–	–	4	30
20110806	6	30	14	30
20110809	–	–	16	30–40
20110810	1	30	12	30
20110811	–	–	12	30
20110813	6	40	6	30
20110814	–	–	10	27
20110815	–	–	6	27
20110817	–	–	6	30
20110820	–	–	16	30
20110821	–	–	16	30
20110822	–	–	7	30
20110828	–	–	8	30
20110830	6	20	11	30
20110831	–	–	16	30
20120807	37	10–20	36	10–20
20120810	38	20	38	20
20120811	34	20	41	20
20120819	6	100	4	100
20120820	24	100	22	100
20120821	38	70–100	38	70–100
20120828	65	50–100	65	40–50
20120919	40	50	39	40
Total	301		530	

Notes. When varying exposure times were used, a range is given.

The imaging CCD is 2147×2101 pixel, with a scale of 0.396 arcsec per pixel, giving a field of view of 14.2×13.9 arcmin^2.

2.2. Difference image analysis

As in our previous studies of variables in globular clusters (Figuera Jaimes et al. 2013; Kains et al. 2012; Arellano Ferro et al. 2011), we used the DanDIA[1] pipeline (Bramich et al. 2013; Bramich 2008) to reduce our observations. Using difference image analysis (DIA) enabled us to obtain high-precision photometry for sources within our field of view. The reader is referred to our previous papers (e.g. Bramich et al. 2011) for a detailed description of the software used; we provide a short summary of the main steps here.

After preprocessing (bias level correction and flat-fielding), our images were blurred with a Gaussian of full-width half-maximum (FWHM) of 3 pixels to avoid undersampling, which is detrimental for determining the kernel in DIA. We then produce a reference image for each filter, stacking images within 10% of the best seeing (~1.2″), also taking care to avoid including images with many saturated stars. Our reference image consists of 5 stacked images, with a combined exposure time of 100 s, and a FWHM of the point-spread function (PSF) of 3.88 pixels (~1.5″) in *V*, while in *I* the combined exposure time is 80 s from 4 images, and the PSF FWHM is 3.31 pixels (~1.3″). For each filter, the source positions and reference fluxes were then extracted from the reference image. Images were then registered with the reference, and the reference was convolved with the kernel solution and subtracted from each image, producing a set of difference images. Finally, difference fluxes were measured from each difference image for each source, which was used to construct a set of light curves. In Table 2, we outline the format of the data as it is provided at the CDS.

As was noted in previous papers, blending due to the presence of other objects near a source may lead to the reference flux being overestimated. However, non-variable sources are still fully subtracted in the difference images, while variable sources have the amplitude of their variability underestimated if their reference flux is affected by blending, although the shape of their light curve, crucially, will remain unaffected.

[1] DanDIA is built from the DanIDL library of IDL routines available at http://www.danidl.co.uk

2.3. Photometric calibration

2.3.1. Self-calibration

Although all photometry is affected by systematic errors, steps can be taken to correct for this, in particular with time-series photometry, for which we can carry out a *self-calibration* of the data (e.g. Padmanabhan et al. 2008). To do this, we use the method of Bramich & Freudling (2012) to derive magnitude offsets to be applied to each photometric measurement. In practice, this equates to correcting for errors in the fitted value of the photometric scale factor *p*. We find magnitude offsets of the order of 2–3 mmag for most data points, which leads to small difference in the resulting light curves.

2.3.2. Photometric standards

We converted the instrumental magnitudes from our data reduction pipeline to standard Johnson-Kron-Cousins magnitudes by carrying out a linear fit to the relation between our light curve magnitudes and those of the photometric standards of Stetson (2000) in the field of this cluster. The relations, shown in Fig. 1, were used to obtain light curves in standard magnitudes. The standard stars we used cover the full range of colour and magnitude spanned by our CMD. No significant colour term was found and the correlation coefficients are ~1 for both filters.

2.4. Astrometry

We used *Gaia* to perform the astrometry by matching ~400 manually picked stars from our reference images with the USNO-B1.0 catalogue of stars (Monet et al. 2003) to derive a linear transformation between our image positions and equatorial coordinates. This means that the coordinates in Table 3 are given at the effective epoch of our reference image, HJD ~ 2 456 151.84. The root mean square (rms) of the residuals from our astrometric fit is 0.23 arcsec, or 0.59 pixels.

3. Variables in M 30

The first three variables (V1-3) in this cluster were detected by Bailey (1902) using photographic observations made at the Harvard College Station in Arequipa, Peru. V4 was then reported by Rosino (1949), who discovered it using observations of M 30 at 175 epochs, taken between 1946 and 1948 with the 60 cm reflecting telescope at the Lojano Astronomical Station, near Bologna in Italy. Rosino also derived periods for V1-3, and refined his period for V1 in a later paper (Rosino 1961). He also noted that V4 did not present the characteristics of an RR Lyrae type variable. He described it as an unusual object, reaching a magnitude of 16.4, remaining at that level for

Table 2. Format for the time-series photometry of all confirmed variables in our field of view.

#	Filter	HJD (*d*)	M_{std} (mag)	m_{ins} (mag)	σ_m (mag)	f_{ref} (ADU s^{-1})	σ_{ref} (ADU s^{-1})	f_{diff} (ADU s^{-1})	σ_{diff} (ADU s^{-1})	*p*
V1	*V*	2 455 779.84508	15.360	14.475	0.004	4619.581	1.991	–500.380	4.612	0.3633
V1	*V*	2 455 779.84637	15.378	14.493	0.005	4619.581	1.991	–455.515	4.326	0.3185
⋮	⋮	⋮	⋮	⋮	⋮	⋮	⋮	⋮	⋮	⋮
V1	*I*	2 455 770.83621	14.628	14.797	0.007	2843.148	3.237	–68.927	2.472	0.1593
V1	*I*	2 455 770.83726	14.639	14.809	0.007	2843.148	3.237	–72.977	2.461	0.1593
⋮	⋮	⋮	⋮	⋮	⋮	⋮	⋮	⋮	⋮	⋮

Notes. The standard M_{std} and instrumental m_{ins} magnitudes listed in Cols. 4 and 5 respectively correspond to the variable star, filter and epoch of mid-exposure listed in Cols. 1–3, respectively. The uncertainty on m_{ins} is listed in Col. 6, which also corresponds to the uncertainty on M_{std}. For completeness, we also list the reference flux f_{ref} and the differential flux f_{diff} (Cols. 7 and 9 respectively), along with their uncertainties (Cols. 8 and 10), as well as the photometric scale factor *p*. Definitions of these quantities can be found in e.g. Bramich et al. (2011), Eqs. (2), (3). This is a representative extract from the full table, which is available at the CDS.

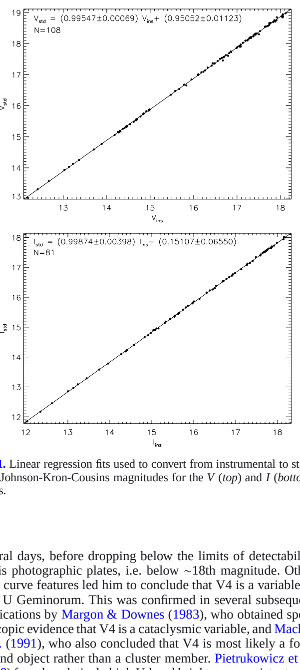

Fig. 1. Linear regression fits used to convert from instrumental to standard Johnson-Kron-Cousins magnitudes for the *V* (*top*) and *I* (*bottom*) bands.

several days, before dropping below the limits of detectability of his photographic plates, i.e. below ~18th magnitude. Other light curve features led him to conclude that V4 is a variable of type U Geminorum. This was confirmed in several subsequent publications by Margon & Downes (1983), who obtained spectroscopic evidence that V4 is a cataclysmic variable, and Machin et al. (1991), who also concluded that V4 is most likely a foreground object rather than a cluster member. Pietrukowicz et al. (2008) found a relatively high *V*-band brightness consistent with that assessment, and also noted that V4 has a likely X-ray counterpart detected by the *ROSAT* satellite.

Table 3. Equatorial celestial coordinates of confirmed variables in M 30 at the epoch of the reference image, HJD ~ 2 456 151.84.

#	RA	Dec
V1	21:40:24.25	–23:11:46.4
V2	21:40:26.44	–23:12:51.2
V3	21:40:15.04	–23:11:27.9
V4	21:39:58.46	–23:11:43.3
V14	21:40:21.10	–23:11:30.8
V15	21:40:21.79	–23:10:50.1
V16	21:40:24.81	–23:11:48.8
V17	21:40:23.66	–23:11:01.1
V18	21:40:21.88	–23:09:32.4
V19	21:40:22.09	–23:10:43.3
V20	21:40:29.83	–23:11:05.9
V21	21:40:47.80	–23:10:23.9

Finally, V5-12 were all reported as variable by Terzan (1968), and V13 was reported by Terzan & Rutily (1975), based on photographic observations taken at the 1.52 m telescope at ESO between 1972 and 1974; however they did not publish light curves or periods for any of those variables.

Pietrukowicz & Kaluzny (2004) analysed HST archival data of M 30 and identified two previously unknown RR Lyrae variables, as well as four W UMa-type contact binaries, and an eclipsing close-binary variable with ellipsoidal variations. However, they did not assign those variables catalogue V numbers. Finally, although Smitka & Layden (2010) also studied this cluster, their photometric accuracy is poor due to the cluster's low altitude for northern hemisphere observations. They reported three new RR Lyrae star candidates, but did not provide coordinates or a finding chart, so we are not able to cross-correlate our findings with theirs; they also did not assign their variables V numbers.

This amounts to a total of 13 catalogued variables in the cluster, although V4 is now thought to be a foreground object. There are also 7 additional variables reported by Pietrukowicz & Kaluzny (2004), including 2 new RR Lyrae. The present study of M 30 is the first from the southern hemisphere using CCD photometry, allowing us to carry out a significant update of the variable star population in this cluster.

Table 4. Mean magnitudes and rms limits for the stars previously catalogued as variable, but for which we do not find variability.

#	⟨*V*⟩	rms (*V*)	⟨*I*⟩	rms (*I*)
V5	17.42	0.035	16.75	0.047
V6	15.34	0.013	15.13	0.037
V7	16.63	0.021	15.84	0.018
V8	15.00	0.010	14.31	0.011
V9	15.40	0.012	15.08	0.021
V10	15.44	0.010	15.22	0.017
V11	16.11	0.013	15.25	0.012
V12	15.49	0.011	15.38	0.015
V13	15.69	0.040	14.78	0.030

3.1. Stars that do not show variability

We find that all of the stars V5-V13, reported by Terzan (1968) and Terzan & Rutily (1975) as variables, do not show signs of variability in our data, to within the limits of the rms scatter in our light curves; those limits are given in Table 4. We are also unable to detect variability of the five contact binaries listed by Pietrukowicz & Kaluzny (2004); for most of these, we attribute this to the fact that the variations have amplitudes of ~0.3 mag, for objects with $V \sim 20$ mag, which is very challenging to detect within the rms of our data (Fig. 2). This is especially difficult in the crowded central core, where blending leads to photon noise dominating any intrinsic variability signal. This is also true for the two brightest eclipsing variables, which have *V* magnitudes of ~17.3 and ~17.9 and variation amplitudes of ~0.3 mag. The advent of electron-multiplying CCD (EMCCD) cameras, coupled with DIA, will allow us in the future to obtain high-quality photometry even for stars in the crowded cores of clusters (Skottfelt et al. 2013), and to verify the variability status of these objects using ground-based photometry.

3.2. Detection of known variables

We recover the first three known RR Lyrae in this cluster (V1-V3) in our data, and calculate periods for each of them, using phase dispersion minimisation (PDM; Stellingwerf 1978) and the "string length" method (Lafler & Kinman 1965). In order to use the longest possible baseline to derive precise periods for these three variables, we used the data from Rosino (1949); these data are published in a table in that paper, and we provide them as an additional resource with the electronic version of this paper[2]. We also used these data to refine our periods by optimising the alignment in phase of that data set with ours; this is highly sensitive to the period, thanks to the baseline of ~63 years. We also recovered the two additional RR Lyrae stars reported by Pietrukowicz & Kaluzny (2004) and assign them catalogue numbers V15 and V19, and calculated refined periods for these two stars. We note that V19 is highly blended due to its location in the very centre of the cluster, which explains its peculiar position on the CMD.

We also detect the U Gem variable V4, including some data taken during an outburst period. This star is discussed in more detail in Sect. 3.4.

[2] The light curves for V1–V3 from Rosino (1949), as well as the additional data for V1 from Rosino (1961), are available at the CDS.

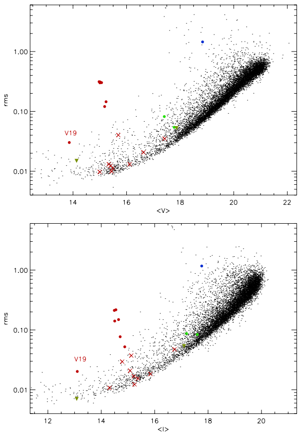

Fig. 2. Root mean square magnitude deviation versus mean magnitude for all stars for which photometry was obtained. Plots are for the *V*-band (*top*) and *I*-band (*bottom*). Classified variables are marked as filled circles, with RR Lyrae in red, SX Phoenicis and blue stragglers in light green, U Geminorum in blue, and variables of unknown type as dark green triangles. Non-variable objects previously catalogued as variable in the literature are marked with red crosses.

3.3. Detection of new variables

As in our previous studies, we searched for new variables using three methods. Firstly, we constructed a stacked image *S* consisting of the sum of the absolute values of the deviations *D* of each image from the convolved reference image, divided by the pixel uncertainty σ, so that

$$S_{ij} = \sum_k \frac{|D_{kij}|}{\sigma_{kij}}. \quad (1)$$

Stars that deviate consistently from the reference image then stand out in this stacked image. Using this method, we discovered 2 new RR Lyrae stars, V14 and V16, both of RR1 type, with V16 also showing signs of amplitude and period modulation due to Blazhko effects or non-radial pulsation (see Sect. 3.4). Secondly, we inspected the light curves of objects which stand out on a plot of root mean square magnitude deviation versus mean magnitude, shown in Fig. 2.

Finally, we also searched for variables by conducting a period search for all our light curves using the string length method, and computing the ratio S_R of the string length for the best- to that of the worst-fit periods, with the smallest ratios expected for true periodic variations. We inspected visually all of the light curves of stars with $S_R < 0.55$, where the threshold value of 0.55 was chosen by inspecting the distribution of S_R

Table 5. Epochs, periods, mean magnitudes and amplitudes A in V and I for all confirmed variable stars in M 30.

#	Epoch (HJD-2 450 000)	P (d)	P (Rosino 1949) (d)	P (Pietrukowicz et al. 2004) (d)	$\langle V \rangle$ (mag)	$\langle I \rangle$ (mag)	A_V (mag)	A_I (mag)	Type
V1	6160.8234	0.7436296	0.74365[a]	0.751	15.12	14.52	0.93	0.74	RR0
V2	6150.8616	0.6535119	0.6535049	–	15.20	14.62	0.92	0.65	RR0
V3	6147.8307	0.6963265	0.69632	–	15.12	14.54	0.94	0.67	RR0
V4[b]	6147.8569	0.092318	–	–	20.19	19.14	2.74	1.91	U Gem
V14	6150.8758	0.347953	–	–	15.18	14.77	0.48	0.32	RR1
V15	6160.7960	0.679015	–	0.689	15.07	14.52	1.08	0.68	RR0
V16	6190.7559	0.325366	–	–	15.22	14.81	0.33	0.27	RR1
V17	6150.8805	0.059954	–	–	14.14	13.08	0.07	0.04	SX Phoenicis + blend?
V18	6161.8536	0.307099	–	–	17.43	17.19	0.41	0.49	Eclipsing blue straggler
V19[c]	5779.8451	0.343379	–	0.341	13.85	13.10	0.15	0.11	RR1
V20	6147.8377	0.040199	–	–	17.79	17.57	0.15	0.13	SX Phoenicis
V21	6147.8589	0.113151	–	–	17.87	17.11	~0.2	–	?

Notes. For RR Lyrae stars, $\langle V \rangle$ and $\langle I \rangle$ are intensity-weighted mean magnitudes, while for the other variables, they are inverse-variance-weighted mean magnitudes. [(a)] Rosino (1961) revised the period of V1 to 0.743608 d. [(b)] The period given for V4 is that of the sinusoidal variations seen during the quiescent part of the light curve, and the mean magnitudes are also those during quiescent phase; outburst mean magnitudes are given in the text (see Sect. 3.4). [(c)] For V19, the mean magnitudes are overestimated and amplitudes are underestimated due to blending, as discussed in the text.

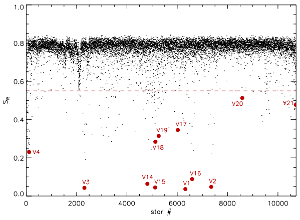

Fig. 3. Distribution of the S_R statistic as defined in the text, for our V-band light curves.

(see Fig. 3). Using this method, we discovered V17, V18, V20 and V21.

All confirmed variables are listed in Table 5, in which we also give epochs, periods and amplitudes. The corresponding light curves are shown in Figs. 4 and 5. A finding chart of the cluster with the location of the confirmed variables is shown in Fig. 6, and a CMD showing the locations of all confirmed variables is shown in Fig. 7.

3.4. Discussion of individual variables

We are unable to determine the nature of V17 with certainty. The combination of its position on the red giant branch and a short period of ~0.06d makes it difficult to classify, although the shape of the light curve and the period would both be consistent with an SX Phoenicis variable blended with a red giant star (e.g. Darragh & Murphy 2012). This is difficult to quantify, and higher-resolution data would be needed to investigate that possibility. From the position of V18 on the CMD and its light curve showing minima of different depths, we suggest that it is an eclipsing blue straggler binary system, of which only 6 examples are known in globular clusters (Kai & Sheng-Giant 2012). We classify V20 as an SX Phoenicis variable, from its light curve, period, and position on the CMD; we only identify one pulsation period for this variable. We could not reach any conclusion as to the nature of V21, because of the quality of its light curve; however variability is clear from both the $V-$ and I-band light curves, when discarding the poor-quality 2011 data, and data with large error bars, from the I light curve. We verify that the variability of V21 is genuine in the difference images, and it is isolated, so there is no reason to believe that the variability is due to contamination from other variables. Below we discuss some of the variables in more detail.

3.4.1. V2

Figures 4 and 5 show that our best period for V2 leads to an unsatisfactory phased light curve in both V and I. We suggest that the disjointed light curve may be due to a Blazhko effect (Blažko 1907) in this object; more observations are needed to confirm this.

3.4.2. V3

Like V2, but to a lesser extent, the light curves V3 seem disjointed, which we suggest may be due to a Blazhko effect. However, and more observations are needed to investigate this further.

3.4.3. V4

For the U Geminorum variable V4, we measured a quiet V-band median magnitude of 20.21 ± 0.48 mag, while during outburst, we find a median magnitude of 17.44 ± 0.04 mag, giving an amplitude of 2.74 mag; in the I band we find median values of 19.05 ± 0.40 (quiet) and 16.84 ± 0.48 (outburst), and an amplitude of 1.91 mag. Machin et al. (1991) found V4 to be significantly brighter, with $\langle V \rangle_{\rm quiet} \sim 18.7$ mag, and Pietrukowicz et al. (2008) also found $\langle V \rangle_{\rm quiet} < 19$ mag. It is interesting to note that, while our V data only covers one outburst, the I data covers three outburst, which show large variations in magnitude, by as much as ~1 mag between different outbursts.

We also conducted a period search for the quiet part of the light curve; Machin et al. (1991) used the quiescent $B-V$ colour

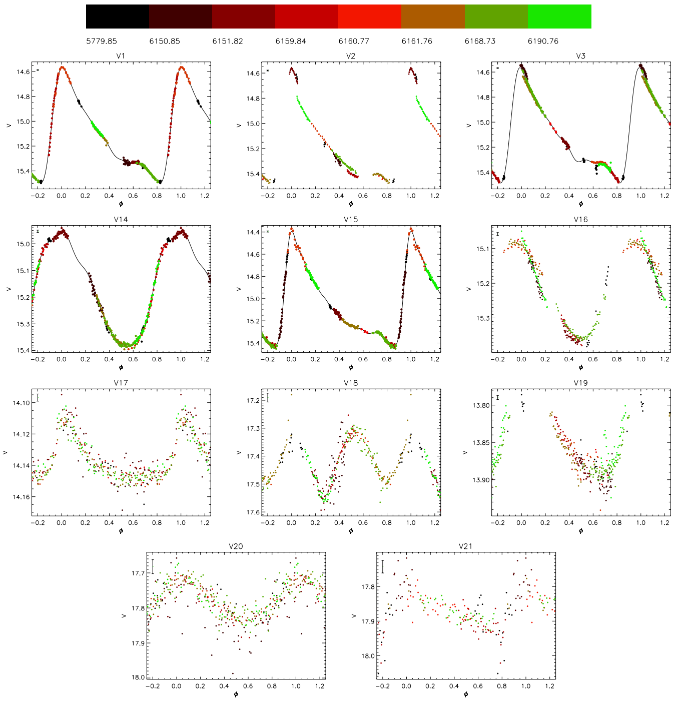

Fig. 4. Phased V-band light curves of the variables with a period estimate. Different colours are used for different nights, with the colour coding given in the form of a colour bar spanning the whole time range of the observations (*top panel*). Fourier decomposition fits are overplotted for the objects for which those were successful.

they find from their spectra of this object, and the relations of Echevarria & Jones (1984) between $B-V$ and P for dwarf novae, to conclude that the orbital period of V4 must be <5 h. We find a period during quiescence of P = 0.0923 days, or $P \sim 2.22$ h, in agreement with that conclusion. In Fig. 8, we show the phased quiescent light curves with this period, while the unphased light curve is shown in Fig. 9.

3.4.4. V16

The light curves in both V and I suggest that our single best period does not lead to a satisfactory phased light curve; we discuss possible explanations for this here. First we considered the possibility that V16 might be a double-mode RR Lyrae (RR01) star, which have only been detected in a few Galactic globular clusters (e.g. Nemec 1985; Clement et al. 1993; Clementini et al. 2004, and references therein). To investigate this, a search for the fundamental and first-overtone pulsation periods was conducted using the string-length method. We start by conducting a period search to identify a first period; for this we find P = 0.3254. Assuming this to be the first-overtone period, and assuming an overtone-to-fundamental period ratio similar to what was found for double-mode RR Lyrae stars in M15, $P_1/P_0 \sim 0.748$ (Cox et al. 1983), we expect a fundamental period around $P_0 \sim 0.435$.

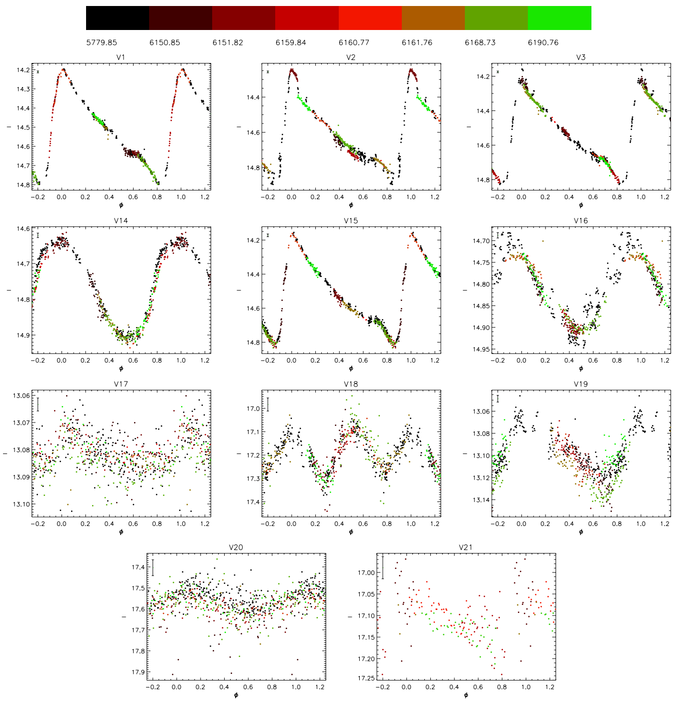

Fig. 5. Same as Fig. 4 but for the I band. For V21, we only plot data points with error $\sigma < 0.3$ mag and do not plot 2011 data due to poor photometry.

We pre-whiten our data for the first-overtone period to check whether we can recover this period. In the V data, we find no evidence for such a period or any other pulsation period in our resulting power spectrum. We find similar results using the I data, leading us to conclude that the unsatisfactory phasing of the V16 light curves is not due to double-mode pulsation.

Secondly, we also tried to fit the light curve by including a secular period change. To do this, we minimise the string length, but with a time-dependent period $P(t)$ and phase $\phi(t)$,

$$P(t) = P_0 + \beta(t - E) \tag{2}$$

$$\phi(t) = (t - E)/P(t) - \lfloor (t - E)/P(t) \rfloor, \tag{3}$$

where β is the rate of change of the period and P_0 is the period at epoch E. We varied P_0 within a small range near the value we found using the string-length method, and for each value of P_0 we explored a grid of values for β ranging between -10^{-7} and 10^{-7} dd^{-1}. From this we found that no such secular period change can explain the scatter in our phased light curve of V16.

This leads us to conclude that V16 either exhibits the Blazhko effect, or shows signs of non-radial pulsation. Amplitude variations are clear when comparing the 2011 (black filled circles in Figs. 4 and 5) and 2012 data, and Blazhko-like effects cause period modulations as well, which would explain

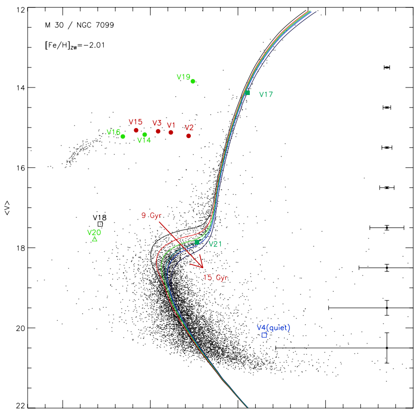

Fig. 7. $(V-I)$, V colour-magnitude diagram from our photometry. The location of RR Lyrae (filled circles, RR0 in red, RR1 in green), SX Phoenicis (green triangles), U Geminorum (blue square), eclipsing blue straggler (black open square) and other variables of uncertain type (green filled squares) are shown. On the right of the plot, typical error bars are plotted for different magnitude levels. Also plotted are isochrones from VandenBerg & Clem (2003) for ages of 9, 10.5, 12, 13.0 (our best-fit isochrone), 13.5 and 15 Gyr.

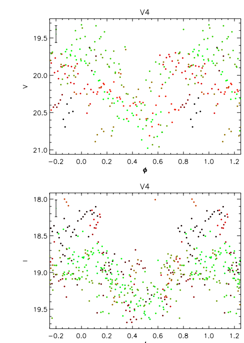

Fig. 8. Phased quiescent light curves of V4 in the V- (*top*) and I-band (*bottom*). Colour coding is the same as for Fig. 4. For clarity we only plot data points with errors $\sigma < 0.3$ mag.

that the light curve is not phased properly when using a single best-fit period. On the other hand, the scatter in the light curves, particularly in the I-band, is very similar to that observed in light curves of some of the variables in M 55 detected by Olech et al. (1999). They concluded that the scatter in the variations were caused by non-radial oscillations, and we suggest here that non-radial pulsation could also be the source of the scatter in the light curves of V16.

4. Fourier decomposition of RR Lyrae star light curves

Applying Fourier decomposition to the V-band light curves of RR Lyrae variables with sufficient phase coverage allows us to derive several of their properties, which we then use as a proxy for the parameters of their host cluster. Fourier decomposition consists in fitting light curves with the Fourier series

$$m(t) = A_0 + \sum_{k=1}^{N} A_k \cos\left[\frac{2\pi k}{P}(t - E) + \phi_k\right], \tag{4}$$

where $m(t)$ is the magnitude at time t, N is the number of harmonics used in the fit, P is the period of the variable, E is the epoch, and A_k and ϕ_k are the amplitude and phase of the kth harmonic. The Fourier parameters, which are epoch-independent, are then defined as

$$R_{ij} = A_i/A_j \tag{5}$$

$$\phi_{ij} = j\phi_i - i\phi_j. \tag{6}$$

To avoid over-fitting light curve features, we used the minimum number of harmonics that provided a good fit. Furthermore, for each variable, we checked the dependence on N of the parameters we derive in the next sections. We found very little variation with N, with any changes smaller than the error bars associated with the relevant quantities. In the following analysis, we excluded V16 because we suspect from its light curve that it may be affected by Blazhko effects or by non-radial pulsation (see Sect. 3.4).

Table 6. Parameters from the Fourier decomposition.

#	A_0	A_1	A_2	A_3	A_4	ϕ_{21}	ϕ_{31}	ϕ_{41}	N	D_m
RR0										
V1	15.121(2)	0.337(2)	0.160(2)	0.110(2)	0.050(2)	4.045(12)	8.498(16)	6.581(22)	7	2.6
V2^a	15.196(2)	0.320(2)	0.134(2)	0.107(2)	0.081(2)	4.005(11)	8.511(15)	6.668(16)	7	3.0
V3	15.118(2)	0.319(2)	0.152(2)	0.112(2)	0.059(2)	3.973(11)	8.413(13)	6.468(19)	7	4.9
V15	15.067(2)	0.344(2)	0.181(2)	0.122(1)	0.081(2)	3.987(7)	8.274(12)	6.431(14)	10	2.5
RR1										
V14	15.176(2)	0.214(3)	0.030(3)	0.012(2)	0.010(2)	4.773(26)	2.673(137)	2.338(104)	6	–

Notes. A good decomposition could not be obtained for V19, due to poor phase coverage; the Fourier fit to V2 was also poor, and V16 is excluded because it shows signs of amplitude and period modulation due to Blazhko effects or non-radial pulsation. Numbers in parentheses are the 1-σ uncertainties on the last decimal place. [(a)] We provide our best-fit Fourier parameters but do not use the decomposition of V2 in the derivation of the cluster parameters, due to the sensitivity of the V2 parameters to the number of harmonics used.

We list the coefficients A_k we obtained for the first four harmonics in Table 6, as well as the Fourier parameters ϕ_{21}, ϕ_{31} and ϕ_{41} for the variables for which we could obtain a Fourier decomposition. We also list the deviation parameter D_m, defined by Jurcsik & Kovács (1996) in order to assess whether fit parameters are reliable to derive properties of the RR Lyrae variables. Although Jurcsik & Kovács (1996) used a criterion whereby fits should have $D_m < 3$ for their empirical relations to yield reliable estimates of stellar properties, a less stringent criterion of $D_m < 5$ has been used by other authors (e.g. Cacciari et al. 2005). Here we also adopt $D_m < 5$ as a selection criterion to estimate stellar properties.

Although some acceptable fits could be obtained for V2, with $D_m < 5$, we exclude it from the analysis as well because we suspect its light curve might be affected by Blazhko effects. Furthermore, the value of the physical parameters is very sensitive to the number of harmonics used in the fit. Although we suggested in Sect. 3.4 that V3 might also be affected by Blazhko effects, we find that the Fourier fits and resulting physical parameters are stable for V3, and therefore include it in the following analysis. We note, however, that this may account for the higher value of D_m we find for V3. We also exclude V19 because our phase coverage does not enable us to find a good Fourier fit. This leaves us with 4 RR Lyrae stars with good Fourier decompositions, three RR0 (V1, V3 and V15) and one RR1 (V14).

4.1. Metallicity

We use the empirical relations of Jurcsik & Kovács (1996) to derive the metallicity [Fe/H] for each of the variables for which we could obtain a successful Fourier decomposition. The relation is derived from the spectroscopic metallicity measurement of field RR0 variables, and it relates [Fe/H] to the period P and the Fourier parameter ϕ^s_{31}, where s denotes a parameter obtained by fitting a *sine* series rather than the cosine series we fit with Eq. (4). [Fe/H] is then expressed as

$$[\mathrm{Fe/H}]_{\mathrm{J}} = -5.038 - 5.394\,P + 1.345\,\phi^s_{31} \tag{7}$$

where the subscript J denotes a non-calibrated metallicity, the period P is in days, and ϕ^s_{ij} can be calculated via

$$\phi^s_{ij} = \phi_{ij} - (i-j)\,\frac{\pi}{2}. \tag{8}$$

We transform these to the metallicity scale of Zinn & West (1984; hereafter ZW) using the relation from Jurcsik (1995):

$$[\mathrm{Fe/H}]_{\mathrm{ZW}} = \frac{[\mathrm{Fe/H}]_{\mathrm{J}} - 0.88}{1.431}. \tag{9}$$

Table 7. Physical parameters for the RR Lyrae variables calculated using the Fourier decomposition parameters and the relations given in the text.

#	$[\mathrm{Fe/H}]_{\mathrm{ZW}}$	M_V	$\log(L/L_\odot)$	T_{eff}
RR0				
V1	−2.04(2)	0.351(2)	1.780(1)	6187(7)
V3	−1.95(2)	0.428(2)	1.746(1)	6247(6)
V15	−2.01(2)	0.428(2)	1.746(1)	6249(5)
RR1				
V14	−2.03(4)	0.540(6)	1.650(3)	7180(13)

Notes. Numbers in parentheses are the 1-σ uncertainties on the last decimal place.

However, Kovács (2002) noted that for metal-poor clusters, Eq. (7) yields metallicity values that are too high by ~0.2 dex. This was also confirmed by Gratton et al. (2004) and Di Fabrizio et al. (2005) by comparing spectroscopic and Fourier-decomposition metallicity values for RR Lyrae in the Large Magellanic Cloud (LMC). Therefore here we include a shift of −0.20 dex (on the $[\mathrm{Fe/H}]_{\mathrm{J}}$ scale) to metallicity values we derive for RR0 stars using Eq. (7), which corresponds to a shift on the ZW scale of −0.14 dex.

For the RR1 variables, we calculated the metallicity using the empirical relation of Morgan et al. (2007), linking [Fe/H], P and ϕ_{31}:

$$[\mathrm{Fe/H}]_{\mathrm{ZW}} = 2.424 - 30.075\,P + 52.466\,P^2 + 0.982\,\phi_{31} + 0.131\phi^2_{31} - 4.198\,\phi_{31}P. \tag{10}$$

Metallicity values calculated using Eqs. (7), (9) and (10) are given in Table 7.

4.2. Effective temperature

The Fourier parameters can also be used to calculate the effective temperature, using empirical relations derived by Jurcsik (1998). Those relations link the $(V-K)_0$ colour to P as well as several of the Fourier coefficients and parameters:

$$(V-K)_0 = 1.585 + 1.257\,P - 0.273\,A_1 - 0.234\,\phi^s_{31} + 0.062\,\phi^s_{41} \tag{11}$$

$$\log T_{\mathrm{eff}} = 3.9291 - 0.1112\,(V-K)_0 - 0.0032\,[\mathrm{Fe/H}]_{\mathrm{J}}. \tag{12}$$

For RR1 variables, Simon & Clement (1993) used theoretical models to derive an empirical relation,

$$\log\,T_{\mathrm{eff}} = 3.7746 - 0.1452\log\,P + 0.0056\,\phi_{31}. \tag{13}$$

We list the temperatures we derived for each RR Lyrae star in Table 7. As noted in our previous analyses, there are several caveats to deriving temperatures with Eqs. (12) and (13). These relations yield values of T_{eff} for RR0 and RR1 stars on different absolute scales. Furthermore, the effective temperatures we derive here show systematic deviations from the relations predicted by evolutionary models of Castelli (1999) or the temperature scales of Sekiguchi & Fukugita (2000). Bearing these caveats in mind, we use these relations to derive temperature estimates in order to be consistent with our previous studies.

4.3. Absolute magnitude

Kovács & Walker (2001) derived empirical relations to calculate V-band absolute magnitudes for the RR0 variables, linking the magnitude to Fourier coefficients through

$$M_V = -1.876\log P - 1.158\,A_1 + 0.821\,A_3 + K_0, \tag{14}$$

where K_0 is a constant. As in our previous studies, we adopt a value of $K_0 = 0.41$ mag to be consistent with a true LMC distance modulus of $\mu_0 = 18.5$ mag (Freedman et al. 2001). For RR1 variables, we use the relation of Kovács (1998),

$$M_V = -0.961\,P - 0.044\,\phi^s_{21} - 4.447\,A_4 + K_1, \tag{15}$$

where K_1 is a constant, for which we choose a value of 1.061 mag with the same justification as for our choice of K_0.

We also converted the magnitudes we obtained to luminosities using

$$\log(L/L_\odot) = -0.4\,[M_V + B_C(T_{\mathrm{eff}}) - M_{\mathrm{bol},\odot}], \tag{16}$$

where $M_{\mathrm{bol},\odot}$ is the bolometric magnitude of the Sun, $M_{\mathrm{bol},\odot} = 4.75$, and $B_C(T_{\mathrm{eff}})$ is a bolometric correction which we determine by interpolating from the values of Montegriffo et al. (1998) for metal-poor stars, and using the value of T_{eff} we derived in the previous section. Values of M_V and $\log(L/L_\odot)$ for the RR0 and RR1 variables are listed in Table 7. Using our average values of M_V, in conjunction with the average values of $[\mathrm{Fe/H}]_{\mathrm{ZW}}$ (Sect. 4.1), we find a good agreement with the $M_V - [\mathrm{Fe/H}]_{\mathrm{ZW}}$ relation derived in the literature (e.g. Kains et al. 2012, see Fig. 9 of that paper).

5. Cluster properties

5.1. Oosterhoff type

We find mean periods $\langle P_{\mathrm{RR0}}\rangle = 0.693 \pm 0.038$ d and $\langle P_{\mathrm{RR1}}\rangle = 0.346 \pm 0.003$ d, with a proportion of 43% of the RR Lyrae in this cluster being of RR1 type.

From these values of $\langle P_{\mathrm{RR0}}\rangle$ and the fraction of RR1 stars in M 30, as well as its low metallicity, we confirm previous classification of this cluster in the literature as Oosterhoff type II (e.g. Lee & Carney 1999). This is also confirmed by comparing the locations of our variables on a Bailey diagram (Fig. 10) to the tracks derived by Cacciari et al. (2005) for evolved stars.

5.2. Distance

5.2.1. Using the RR Lyrae stars

We can use the A_0 parameter from our Fourier decompositions, which corresponds to the mean apparent V magnitude of the RR Lyrae, as well as the absolute magnitudes of the RR Lyrae we derived in Sect. 4.3 to derive the distance modulus to M 30. The mean value of the A_0 for our RR0 variables is 15.09 ± 0.03 mag, while the mean of the absolute magnitudes is 0.40 ± 0.04 mag. This yields a distance modulus of $\mu = 14.69 \pm 0.05$ mag. Using the parameters for our RR1 variable (V14, see Tables 6 and 7), we find $\mu = 14.64$ mag.

The reddening towards this cluster has been estimated in the literature by several authors, with values of $E(B-V)$ ranging from 0.01 to 0.12 mag. Zinn (1980) derived a value of $E(B-V) = 0.01$ mag from integrated light measurements, Bolte (1987) adopted a value of $E(B-V) = 0.02$ mag, while Richer et al. (1988) found a value of $E(B-V) = 0.068 \pm 0.035$ mag; Piotto et al. (1990) derived $E(B-V) = 0.05$ mag from their CMD analysis, and Samus et al. (1995) found values of $E(B-V) = 0.09$ or 0.12 mag, depending on the metallicity of the isochrone they fitted to their CMD. Ferraro et al. (1999) report a value for this cluster $E(B-V) = 0.03$ mag.

Here we adopt a value of $E(B-V) = 0.03 \pm 0.01$ mag, as well as a value of $R_V = 3.1$ for our Galaxy. We use these to derive mean true distance moduli of $\mu_0 = 14.60 \pm 0.05$ mag and $\mu_0 = 14.54$ mag, from our RR0 and RR1 variables respectively. These

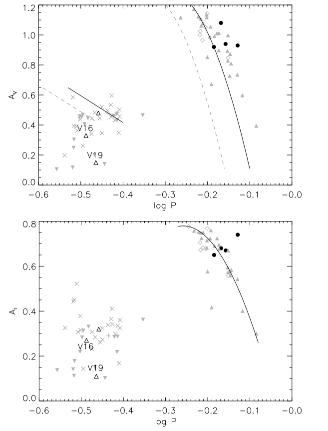

Fig. 10. Bailey diagram of the light curve amplitude versus the logarithm of the period for RR Lyrae stars in M 30, in V (*top*) and I (*bottom*). RR0 variables are plotted as filled circles, and RR1 variables as open triangles; we mark the locations of V16 which we suggest is affected by Blazhko effects or non-radial pulsation, and of V19, which has an underestimated amplitude due to blending. Also plotted on the V-band diagram as solid lines are the relations of Cacciari et al. (2005) for evolved stars, obtained by applying a shift of +0.06 to log P in the relations derived for the Oosterhoff type I cluster M 3; the original relations (without the shift of 0.06 in log P) are also plotted in light grey dashed lines. For the I-band we plot the relation derived by Arellano Ferro et al. (2011) for RR0 stars. For comparison we also plot the populations of RR Lyrae detected in the Oosterhoff type II clusters M 9 (Arellano Ferro et al., in prep.) and NGC 5024 (Arellano Ferro et al. 2011) in light grey, with filled triangles and inverted triangles for RR0 and RR1 stars respectively. For stars with Blazhko effects, we use open diamonds for RR0 stars and crosses for RR1 stars; the star marked with a + sign is a double-mode RR1 star.

values correspond to mean physical distances of 8.32 ± 0.20 kpc and 8.10 kpc. Since the distance values are sensitive to our chosen value of $E(B-V)$, we also derive distances using the highest value of reddening in the literature $E(B-V) = 0.12$ mag, to find a lower limit for the distances of 7.32 ± 0.17 and 7.13 kpc. Our values for the distance to the cluster are consistent with previous estimates in the literature, reported in Table 8.

5.2.2. Using SX Phoenicis stars

SX Phoenicis stars can be used as standard candles thanks to their period-luminosity $(P-L)$ relation (e.g. Jeon et al. 2003), allowing us to estimate the distance to M 30 using the detected SX Phoenicis star in our sample, V20. We use the $P-L$ relation of Cohen & Sarajedini (2012),

$$M_V = -(1.640 \pm 0.110) - (3.389 \pm 0.090)\log P_{\mathrm{f}}, \tag{17}$$

where P_{f} denotes the fundamental-mode pulsation period. Using $P_{\mathrm{f}} = 0.040199$ d for V20, we find $M_V = 3.09 \pm 0.11$ mag. Using a mean magnitude of $\langle V\rangle = 17.79$ mag, $E(B-V) = 0.03$ mag, this yields a distance modulus of 14.61 ± 0.11 mag, which corresponds to a physical distance of 8.35 ± 0.42 kpc, in excellent agreement with the distance calculated using the RR Lyrae stars, and consistent with estimates in the literature.

5.3. Metallicity

Although the relation of Sandage (2006) relating the mean period of RR0 stars to the cluster metallicity is not applicable for Oosterhoff type II clusters (Clement et al. 2001), we can use the metallicities we calculated in Sect. 4.1 for the RR Lyrae stars in the cluster to derive an estimate for the metallicity of M 30. To do this, we simply compute an average of the RR Lyrae metallicities given in Table 7, excluding the variables for which the metallicity estimate is unreliable. Assuming that there is no systematic offset between the different types of variables, as in previous studies (Kains et al. 2012; Bramich et al. 2011), we find a mean metallicity $[\mathrm{Fe/H}]_{\mathrm{ZW}} = -2.01 \pm 0.04$, in good agreement with values found in the literature (see Table 9).

Carretta et al. (2009a) derived a new metallicity scale based on GIRAFFE and UVES spectra of red giant branch (RGB) stars in 19 globular clusters, which is now widely used to quote metallicity values for globular clusters. The transformation from the ZW to the UVES (Carretta et al. 2009a) scale is given as

$$[\mathrm{Fe/H}]_{\mathrm{UVES}} = -0.413 + 0.130\,[\mathrm{Fe/H}]_{\mathrm{ZW}} - 0.356\,[\mathrm{Fe/H}]^2_{\mathrm{ZW}}. \tag{18}$$

Using this we find a metallicity for M 30 of $[\mathrm{Fe/H}]_{\mathrm{UVES}} = -2.11 \pm 0.06$, significantly higher than the value found for this cluster by Carretta et al. (2009b) of $[\mathrm{Fe/H}]_{\mathrm{UVES}} = -2.34 \pm 0.05$.

5.4. Age

We use our CMD to derive an estimate for the age of M 30, by fitting to it the isochrones of VandenBerg & Clem (2003), using our estimate of the cluster metallicity, $[\mathrm{Fe/H}]_{\mathrm{ZW}} = -2.01 \pm 0.04$. We also used a value for the α-enhancement of $[\alpha/\mathrm{Fe}] = +0.2$ (Dotter et al. 2010). From the best-fitting isochrones, we estimate the age of the cluster to be 13.0 ± 1.0 Gyr, in good agreement with recent estimates in the literature (see Table 10). A set of isochrones is overplotted on the CMD in Fig. 7.

6. Conclusions

We have used V- and I-band observations spanning a baseline of ~14 months to survey stellar photometric variability in M 30. This allows us to update the catalogue of variables in this cluster significantly, with detections and refined analysis of three previously known RR Lyrae stars, one known U Gem star, as well as of two candidate RR Lyrae stars, to which we assigned catalogue numbers. Furthermore, we detect previously unknown variables, including two RR1 stars, an SX Phoenicis star, an eclipsing blue straggler system, and two variables that we are unable to classify with certainty. We provide refined period estimates for all variables, and then carry out Fourier decomposition of RR Lyrae stars. Using the Fourier parameters of stars for which this was successful, we derive properties for the RR Lyrae, and use these as proxies for the cluster's properties.

We find a cluster metallicity of $[\mathrm{Fe/H}]_{\mathrm{ZW}} = -2.01 \pm 0.04$, or $[\mathrm{Fe/H}]_{\mathrm{UVES}} = -2.11 \pm 0.06$, and distances of 8.32 ± 0.20 or 8.10 kpc, using RR0 and RR1 stars respectively. Our light curve of the SX Phoenicis variable V20 also affords another way to estimate the cluster distance; using this, we find a distance of 8.35 ± 0.42 kpc. Our CMD also allows us to estimate the age of the cluster by fitting isochrones to it. We find an age of 13 ± 1 Gyr. All of these values agree well with estimates in the literature, and are independent estimates calculated for the first time using Fourier decomposition of RR Lyrae in this cluster.

Acknowledgements. We thank the referee Christine Clement for constructive comments. We also thank the ESO librarians for tracking down historical papers. N.K. acknowledges an ESO Fellowship. The research leading to these results has received funding from the European Community's Seventh Framework Programme (/FP7/2007-2013/) under grant agreement No. 229517. A.A.F. acknowledges the support of DGAPA-UNAM through project IN104612. A.A.F. and S.G. are thankful to the CONACyT (México) and the Department of Science and Technology (India) for financial support under the Indo-Mexican collaborative project DST/INT/MEXICO/RP001/2008. O.W. (aspirant FRS – FNRS), A.E. (post-doc PRODEX), Y.D. (post-doc PRODEX) and J. Surdej acknowledge support from the Communauté française de Belgique – Actions de recherche concertées – Académie universitaire Wallonie-Europe. T.C.H. gratefully acknowledges financial support from the Korea Research Council for Fundamental Science and Technology (KRCF) through the Young Research Scientist Fellowship Program. T.C.H. acknowledges financial support from KASI (Korea Astronomy and Space Science Institute) grant number 2012-1-410-02. K.A., D.B., M.D., M.H., and C.L. are supported by NPRP grant NPRP-09-476-1-78 from the Qatar National Research Fund (a member of Qatar Foundation). The Danish 1.54 m telescope is operated based on a grant from the Danish Natural Science Foundation (FNU). Funding for the Stellar Astrophysics Centre at Aarhus University is provided by The Danish National Research Foundation. This research was supported in part by the project ASTERoseismic Investigations with SONG and *Kepler* (ASTERISK), funded by the European Research Council (grant agreement No.: 267864). C.S. received funding from the European Union Seventh Framework Programme (FP7/2007-2013) under grant agreement No. 268421. C.H.G. and X.S.F. acknowledge support from National Natural Science Foundation of China (grants Nos. 10373023 and 10773027). H.K. acknowledges support from a Marie-Curie Intra-European Fellowship.

References

Allen, C., Moreno, E., & Pichardo, B. 2006, ApJ, 652, 1150
Arellano Ferro, A., Figuera Jaimes, R., Giridhar, S., et al. 2011, MNRAS, 416, 2265
Bailey, S. I. 1902, Annals of Harvard College Observatory, 38, 1
Bergbusch, P. A. 1996, AJ, 112, 1061
Blažko, S. 1907, Astron. Nachr., 175, 325
Bolte, M. 1987, ApJ, 319, 760
Bramich, D. M. 2008, MNRAS, 386, L77
Bramich, D. M., & Freudling, W. 2012, MNRAS, 424, 1584
Bramich, D. M., Figuera Jaimes, R., Giridhar, S., & Arellano Ferro, A. 2011, MNRAS, 413, 1275
Bramich, D. M., Horne, K., Albrow, M. D., et al. 2013, MNRAS, 428, 2275
Cacciari, C., Corwin, T. M., & Carney, B. W. 2005, AJ, 129, 267
Carretta, E., Gratton, R. G., Clementini, G., & Fusi Pecci, F. 2000, ApJ, 533, 215
Carretta, E., Bragaglia, A., Gratton, R., D'Orazi, V., & Lucatello, S. 2009a, A&A, 508, 695
Carretta, E., Bragaglia, A., Gratton, R., & Lucatello, S. 2009b, A&A, 505, 139

Carretta, E., Bragaglia, A., Gratton, R. G., et al. 2009c, A&A, 505, 117
Castelli, F. 1999, A&A, 346, 564
Claria, J. J., Minniti, D., & Gomez, M. N. 1988, A&A, 199, L1
Clement, C. M., Ferance, S., & Simon, N. R. 1993, ApJ, 412, 183
Clement, C. M., Muzzin, A., Dufton, Q., et al. 2001, AJ, 122, 2587
Clementini, G., Corwin, T. M., Carney, B. W., & Sumerel, A. N. 2004, AJ, 127, 938
Cohen, R. E., & Sarajedini, A. 2012, MNRAS, 419, 342
Cox, A. N., Hodson, S. W., & Clancy, S. P. 1983, ApJ, 266, 94
Darragh, A. N., & Murphy, B. W. 2012, J. South. Assoc. Res. Astron., 6, 72
Di Fabrizio, L., Clementini, G., Maio, M., et al. 2005, A&A, 430, 603
Djorgovski, S., & King, I. R. 1986, ApJ, 305, L61
Dotter, A., Sarajedini, A., Anderson, J., et al. 2010, ApJ, 708, 698
Echevarria, J., & Jones, D. H. P. 1984, MNRAS, 206, 919
Ferraro, F. R., Messineo, M., Fusi Pecci, F., et al. 1999, AJ, 118, 1738
Figuera Jaimes, R., Arellano Ferro, A., Bramich, D. M., Giridhar, S., & Kuppuswamy, K. 2013, A&A, in press, DOI: 10.1051/0004-6361/201220824
Forbes, D. A., & Bridges, T. 2010, MNRAS, 404, 1203
Freedman, W. L., Madore, B. F., Gibson, B. K., et al. 2001, ApJ, 553, 47
Gratton, R. G., Fusi Pecci, F., Carretta, E., et al. 1997, ApJ, 491, 749
Gratton, R. G., Bragaglia, A., Clementini, G., et al. 2004, A&A, 421, 937
Jeon, Y.-B., Lee, M. G., Kim, S.-L., & Lee, H. 2003, AJ, 125, 3165
Jurcsik, J. 1995, Act. Astron., 45, 653
Jurcsik, J. 1998, A&A, 333, 571
Jurcsik, J., & Kovács, G. 1996, A&A, 312, 111
Kai, L., & Sheng-Bang, Q. 2012, AJ, 144, 161
Kains, N., Bramich, D. M., Figuera Jaimes, R., et al. 2012, A&A, 548, A92
Kovács, G. 1998, Mem. Soc. Astron. It., 69, 49
Kovács, G. 2002, in Omega Centauri, A Unique Window into Astrophysics, eds. F. van Leeuwen, J. D. Hughes, & G. Piotto, ASP Conf. Ser., 265, 163
Kovács, G., & Walker, A. R. 2001, A&A, 371, 579
Lafler, J., & Kinman, T. D. 1965, ApJS, 11, 216
Lee, J.-W., & Carney, B. W. 1999, AJ, 118, 1373
Machin, G., Callanan, P. J., Allington-Smith, J., Charles, P. A., & Hassall, B. J. M. 1991, MNRAS, 250, 602
Margon, B., & Downes, R. A. 1983, ApJ, 274, L31
Minniti, D., Geisler, D., Peterson, R. C., & Claria, J. J. 1993, ApJ, 413, 548
Monet, D. G., Levine, S. E., Canzian, B., et al. 2003, AJ, 125, 984
Montegriffo, P., Ferraro, F. R., Origlia, L., & Fusi Pecci, F. 1998, MNRAS, 297, 872
Morgan, S. M., Wahl, J. N., & Wieckhorst, R. M. 2007, MNRAS, 374, 1421
Nemec, J. M. 1985, AJ, 90, 240
Olech, A., Kaluzny, J., Thompson, I. B., et al. 1999, AJ, 118, 442
Padmanabhan, N., Schlegel, D. J., Finkbeiner, D. P., et al. 2008, ApJ, 674, 1217
Pietrukowicz, P., & Kaluzny, J. 2004, Act. Astron., 54, 19
Pietrukowicz, P., Kaluzny, J., Schwarzenberg-Czerny, A., et al. 2008, MNRAS, 388, 1111
Piotto, G., Capaccioli, M., Ortolani, S., et al. 1987, AJ, 94, 360
Piotto, G., King, I. R., Capaccioli, M., Ortolani, S., & Djorgovski, S. 1990, ApJ, 350, 662
Richer, H. B., Fahlman, G. G., & Vandenberg, D. A. 1988, ApJ, 329, 187
Rosino, L. 1949, Mem. Soc. Astron. It., 20, 63
Rosino, L. 1961, Asiago-Padova Cont., 117
Samus, N. N., Ipatov, A. P., Smirnov, O. M., et al. 1995, Astron. Lett., 21, 810
Sandage, A. 2006, AJ, 131, 1750
Sandquist, E. L., Bolte, M., Langer, G. E., Hesser, J. E., & Mendes de Oliveira, C. 1999, ApJ, 518, 262
Sekiguchi, M., & Fukugita, M. 2000, AJ, 120, 1072
Simon, N. R., & Clement, C. M. 1993, ApJ, 410, 526
Skottfelt, J., Bramich, D. M., Figuera Jaimes, R., et al. 2013, A&A, 553, A111
Smith, H. A. 1984, ApJ, 281, 148
Smitka, M. T., & Layden, A. C. 2010, in BAAS 36, Amer. Astron. Soc. Meet. Abstracts 215, 606.18
Stellingwerf, R. F. 1978, ApJ, 224, 953
Stetson, P. B. 2000, PASP, 112, 925
Terzan, A. 1968, Publications of the Observatoire Haute-Provence, 9, 24
Terzan, A., & Rutily, B. 1975, A&A, 38, 307
VandenBerg, D. A., & Clem, J. L. 2003, AJ, 126, 778
Zinn, R. 1980, ApJS, 42, 19
Zinn, R., & West, M. J. 1984, ApJS, 55, 45

[1] European Southern Observatory, Karl-Schwarzschild Straße 2, 85748 Garching bei München, Germany
e-mail: nkains@eso.org
[2] Instituto de Astronomía, Universidad Nacional Autónoma de Mexico, 04510 Ciudad de Mexico, Mexico
[3] SUPA School of Physics & Astronomy, University of St Andrews, North Haugh, St. Andrews, KY16 9SS, UK
[4] Niels Bohr Institute, University of Copenhagen, Juliane Maries vej 30, 2100 Copenhagen, Denmark
[5] Centre for Star and Planet Formation, Geological Museum, Øster Voldgade 5, 1350 Copenhagen, Denmark
[6] Indian Institute of Astrophysics, Koramangala, 560034 Bangalore, India
[7] Department of Astronomy, Ohio State University, 140 West 18th Avenue, Columbus, OH 43210, USA
[8] Qatar Foundation, PO Box, 5825 Doha, Qatar
[9] Department of Astronomy, Boston University, 725 Commonwealth Ave, Boston, MA 02215, USA
[10] Dipartimento di Fisica "E.R Caianiello", Universit di Salerno, via Ponte Don Melillo, 84084 Fisciano, Italy
[11] Istituto Nazionale di Fisica Nucleare, Sezione di Napoli, Italy
[12] HE Space Operations GmbH, Flughafenallee 24, 28199 Bremen, Germany
[13] Istituto Internazionale per gli Alti Studi Scientifici (IIASS), 84019 Vietri Sul Mare (SA), Italy
[14] Institut d'Astrophysique et de Géophysique, Université de Liège, Allée du 6 Août 17, Sart Tilman, Bât. B5c, 4000 Liège, Belgium
[15] Astronomisches Rechen – Institut, Zentrum für Astronomie der Universität Heidelberg (ZAH), Mönchhofstr. 12–14, 69120 Heidelberg, Germany
[16] Hamburger Sternwarte, Universität Hamburg, Gojenbergsweg 112, 21029 Hamburg, Germany
[17] Main Astronomical Observatory, Academy of Sciences of Ukraine, vul. Akademika Zabolotnoho 27, 03680 Kyiv, Ukraine
[18] National Astronomical Observatories/Yunnan Observatory, Chinese Academy of Sciences, 650011 Kunming, PR China
[19] Key Laboratory for the Structure and Evolution of Celestial Objects, Chinese Academy of Sciences, 650011 Kunming, PR China
[20] Korea Astronomy and Space Science Institute, 305-348 Daejeon, Korea
[21] Institut for Rumforskning og -teknologi, Danmarks Tekniske Universitet, Juliane Maries 30, 2100 København Ø, Denmark
[22] Stellar Astrophysics Centre, Department of Physics and Astronomy, Aarhus University, Ny Munkegade 120, 8000 Aarhus C, Denmark
[23] Jodrell Bank Centre for Astrophysics, University of Manchester, Oxford Road, Manchester, M13 9PL, UK
[24] Max Planck Institute for Astronomy, Königstuhl 17, 69117 Heidelberg, Germany
[25] Perth Observatory, Walnut Road, Bickley, 6076 Perth, Australia
[26] Departamento de Astronomía y Astrofísica, Pontificia Universidad Católica de Chile, Av. Vicuña Mackenna 4860, 7820436 Macul, Santiago, Chile
[27] Department of Physics, Sharif University of Technology, PO Box, 11155–9161 Tehran, Iran
[28] Perimeter Institute for Theoretical Physics, 31 Caroline St. N., Waterloo ON, N2L 2Y5, Canada
[29] Instituto de Astronomía – UNAM, Km 103 Carretera Tijuana Ensenada, 422860 Ensenada (Baja Cfa), Mexico
[30] Space Telescope Science Institute, 3700 San Martin Drive, Baltimore, MD 21218, USA
[31] INFN, Gruppo Collegato di Salerno, Sezione di Napoli, Italy
[32] Max Planck Institute for Solar System Research, Max-Planck-Str. 2, 37191 Katlenburg-Lindau, Germany
[33] Astrophysics Group, Keele University, Staffordshire, ST5 5BG, UK

Pages 13 to 15 are available in the electronic edition of the journal at http://www.aanda.org

Table 8. Modulus and distance estimates for M 30 in the literature.

Reference	μ_0 [mag]	Distance [kpc]	Method
This work	14.60 ± 0.05	8.32 ± 0.20	Fourier decomposition of RR0 light curves
This work	14.54	8.10	Fourier decomposition of RR1 light curves
This work	14.61 ± 0.11	8.35 ± 0.42	SX Phoenicis $P-L$ relation
Carretta et al. (2000)	14.88 ± 0.05	9.46 ± 0.22	Parallax of local subdwarfs
Ferraro et al. (1999)	14.71	8.75	Magnitude of the horizontal branch
Sandquist et al. (1999)	14.65 ± 0.12	8.51 ± 0.47	Parallax of local subdwarfs
Sandquist et al. (1999)	14.87 ± 0.12	9.42 ± 0.52	Parallax of local subdwarfs
Gratton et al. (1997)	14.94 ± 0.08	9.72 ± 0.36	Parallax of local subdwarfs
Bergbusch (1996)	14.83	9.25	CMD analysis
Samus et al. (1995)	14.70 ± 0.10	8.71 ± 0.40	CMD analysis
Piotto et al. (1990)	14.65 ± 0.15	8.51 ± 0.59	CMD analysis
Piotto et al. (1987)	14.50 ± 0.50	7.94 ± 1.83	CMD analysis
Bolte (1987)	14.65	8.51	Parallax of local subdwarfs

Table 9. Different metallicity estimates for M 30 in the literature.

Reference	$[Fe/H]_{ZW}$	$[Fe/H]_{UVES}$	Method
This work	−2.01 ± 0.04	−2.11 ± 0.06	Fourier decomposition of RR Lyrae light curves
Carretta et al. (2009b)	−2.04 ± 0.16	−2.34 ± 0.05	UVES spectroscopy of red giants
Carretta et al. (2009c)	−2.05 ± 0.16	−2.36 ± 0.05	FLAMES/GIRAFFE specta of red giants
Sandquist et al. (1999)	−2.01 ± 0.09	−2.11 ± 0.14	Simultaneous reddening-metallicity method
Bergbusch (1996)	−2.03	−2.14	CMD isochrone fitting
Minniti et al. (1993)	−2.11 ± 0.08	−2.27 ± 0.13	Spectroscopy of red giants
Claria et al. (1988)	−2.4	−2.78 ± 0.20	Spectroscopy of red giants
Bolte (1987)	−2.03 ± 0.13	−2.14 ± 0.20	CMD isochrone fitting
Smith (1984)	−2.02 ± 0.14	−2.13 ± 0.22	Q'_{39} spectral index
Zinn & West (1984)	−2.13 ± 0.13	−2.31 ± 0.21	Q_{39} spectral index
Zinn (1980)	−1.96 ± 0.12	−2.04 ± 0.18	Q_{39} spectral index

Notes. Values were converted using Eq. (18) where necessary.

Table 10. Age estimates for M 30 in the literature.

Reference	Age [Gyr]	Method
This work	13 ± 1	CMD isochrone fitting
Dotter et al. (2010)	13.25 ± 1.00	CMD isochrone fitting
Carretta et al. (2000)	12.3	Parallax of local subdwarfs
Bergbusch (1996)	14	CMD isochrone fitting
Samus et al. (1995)	17	CMD isochrone fitting
Samus et al. (1995)	15	CMD isochrone fitting
Piotto et al. (1990)	16 ± 2	CMD isochrone fitting
Bolte (1987)	17	CMD isochrone fitting

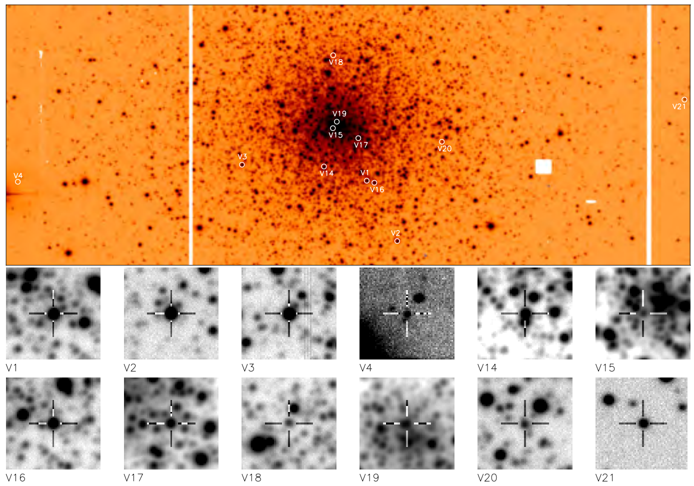

Fig. 6. Finding chart for the confirmed variable objects in M 30, using our V reference image. North is up and east is to the right. The image size is 11.57×4.55 arcmin^2, while each stamp size is 23.4×23.4 arcsec^2. White circles and labels indicate the locations of the variables, and each of the variables we detect in our data is shown with a crosshair at the centre of an individual stamp. Note that the display scale of each stamp is different in order to make the source visible.

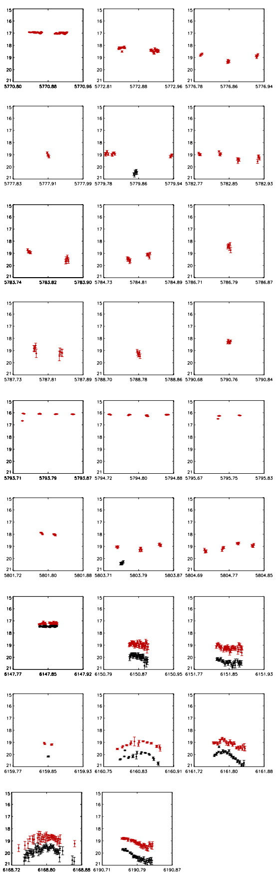

Fig. 9. 2012 V- and I-band light curves of V4. V data is plotted in black, and I data in red. For clarity we plot only data points with errors $\sigma <$ 0.3 mag. The x-axes are given in HJD-2 450 000.

A&A 553, A111 (2013)
DOI: 10.1051/0004-6361/201321430

Astronomy & Astrophysics

EMCCD photometry reveals two new variable stars in the crowded central region of the globular cluster NGC 6981★ *(Research Note)*

J. Skottfelt[1,2], D. M. Bramich[3], R. Figuera Jaimes[3,4], U. G. Jørgensen[1,2], N. Kains[3], K. B. W Harpsøe[1,2], C. Liebig[4], M. T. Penny[5], K. A. Alsubai[6], J. M. Andersen[7,2], V. Bozza[8,9], P. Browne[4], S. Calchi Novati[10], Y. Damerdji[11], C. Diehl[12,13], M. Dominik[4,★★], A. Elyiv[11,14], E. Giannini[12], F. Hessman[15], T. C. Hinse[16], M. Hundertmark[4], D. Juncher[1,2], E. Kerins[17], H. Korhonen[1,2], L. Mancini[18], R. Martin[19], M. Rabus[20], S. Rahvar[21], G. Scarpetta[10,8,9], J. Southworth[22], C. Snodgrass[23], R. A. Street[24], J. Surdej[11], J. Tregloan-Reed[22], C. Vilela[22], and A. Williams[19]

1 Niels Bohr Institute, University of Copenhagen, Juliane Maries Vej 30, 2100 København Ø, Denmark
e-mail: skottfelt@astro.ku.dk; uffegj@nbi.dk
2 Centre for Star and Planet Formation, Natural History Museum, University of Copenhagen, Østervoldgade 5-7, 1350 København K, Denmark
3 European Southern Observatory, Karl-Schwarzschild-Straße 2, 85748 Garching bei München, Germany
e-mail: dbramich@eso.org
4 SUPA, University of St Andrews, School of Physics & Astronomy, North Haugh, St Andrews, KY16 9SS, UK
e-mail: rfiguera@eso.org; robertofiguera@gmail.com
5 Department of Astronomy, Ohio State University, 140 W. 18th Ave., Columbus, OH 43210, USA
6 Qatar Foundation, PO Box 5825 Doha, Qatar
7 Department of Astronomy, Boston University, 725 Commonwealth Avenue, Boston, MA 02215, USA
8 Dipartimento di Fisica "E. R. Caianiello", Università di Salerno, via Ponte Don Melillo, 84084 Fisciano (SA), Italy
9 Istituto Nazionale di Fisica Nucleare, Sezione di Napoli, Napoli, Italy
10 Istituto Internazionale per gli Alti Studi Scientifici (IIASS), 84019 Vietri Sul Mare (SA), Italy
11 Institut d'Astrophysique et de Géophysique, Université de Liège, Allée du 6 Août, Bât. B5c, 4000 Liège, Belgium
12 Astronomisches Rechen-Institut, Zentrum für Astronomie der Universität Heidelberg, Mönchhofstr. 12-14, 69120 Heidelberg, Germany
13 Hamburger Sternwarte, Universität Hamburg, Gojenbergsweg 112, 21029 Hamburg, Germany
14 Main Astronomical Observatory, Academy of Sciences of Ukraine, vul. Akademika Zabolotnoho 27, 03680 Kyiv, Ukraine
15 Institut für Astrophysik, Georg-August-Universität Göttingen, Friedrich-Hund-Platz 1, 37077 Göttingen, Germany
16 Korea Astronomy and Space Science Institute, 305-348 Daejeon, Republic of Korea
17 Jodrell Bank Centre for Astrophysics, University of Manchester, Oxford Road, Manchester M13 9PL, UK
18 Max Planck Institute for Astronomy, Königstuhl 17, 69117 Heidelberg, Germany
19 Perth Observatory, Walnut Road, Bickley, Perth 6076, WA, Australia
20 Departamento de Astronomía y Astrofísica, Pontificia Universidad Católica de Chile, Av. Vicuña Mackenna 4860, 7820436 Macul, Santiago, Chile
21 Department of Physics, Sharif University of Technology, PO Box 11155-9161 Tehran, Iran
22 Astrophysics Group, Keele University, Staffordshire, ST5 5BG, UK
23 Max-Planck-Institute for Solar System Research, Max-Planck Str. 2, 37191 Katlenburg-Lindau, Germany
24 Las Cumbres Observatory Global Telescope Network, 6740 Cortona Drive, Suite 102, Goleta, CA 93117, USA

Received 7 March 2013 / Accepted 12 April 2013

ABSTRACT

Two previously unknown variable stars in the crowded central region of the globular cluster NGC 6981 are presented. The observations were made using the electron multiplying CCD (EMCCD) camera at the Danish 1.54 m Telescope at La Silla, Chile. The two variables were not previously detected by conventional CCD imaging because of their proximity to a bright star. This discovery demonstrates that EMCCDs are a powerful tool for performing high-precision time-series photometry in crowded fields and near bright stars, especially when combined with difference image analysis.

Key words. globular clusters: individual: NGC 6981 – stars: variables: RR Lyrae – instrumentation: high angular resolution – stars: variables: general

1. Introduction

A census of the variable stars in the globular cluster NGC 6981 was performed by Bramich et al. (2011, hereafter B11). Using data from 10 nights of observations with a conventional CCD they were able to confirm the variability of 29 stars and refute the suspected variability of 20 others. Furthermore, 11 new RR Lyrae stars and 3 new SX Phoenicis stars were found in the study, bringing the total number of confirmed variable stars in NGC 6981 to 43.

A problem with using a conventional CCD is that to obtain a reasonable signal-to-noise ratio (S/N) for the fainter objects in an image, the pixels in the brightest stars may well be saturated. For difference image analysis (DIA), which is currently the best way to extract precise photometry in crowded star fields (e.g. towards the Galactic bulge, in the central regions of globular clusters, etc.), the saturation of the brightest stars is even more problematic because the saturated pixels affect nearby pixels during the convolution of the reference image. Hence we cannot perform photometric measurements using DIA near saturated stars in conventional CCD images, which has a negative impact on the completeness of variability studies in crowded fields. In B11, there are 4 saturated stars in the central region of their V reference image for NGC 6981, and it is therefore conceivable that their variable star census could have missed relatively bright variable stars (e.g. RR Lyraes). An improved completeness in variability studies makes it possible to draw firmer conclusions about Oosterhoff classification (Smith 1995) and to examine whether there is a gradient in the physical properties between the central and outer parts of the cluster.

Electron multiplying CCDs (EMCCDs) are conventional CCDs with an extended serial register where the signal is amplified by impact ionisation before it is read out. This means that the readout noise is negligible when compared to the signal, even at very high readout speeds (10−100 frames/s), enabling the possibility of high frame-rate imaging. Numerous articles have described the possibility of using EMCCDs to obtain very high spatial resolution; see for instance Mackay et al. (2004); Law et al. (2006). However, using EMCCDs to perform precise time-series photometry without throwing away photons (i.e. *not* Lucky Imaging) is a new area of investigation and the applications are just starting to be explored.

With high frame-rate imaging much brighter stars can be observed without saturating the CCD and the individual exposures can be combined into stacked images at a later stage in order to achieve the required S/N for the objects of interest. We note that EMCCD exposures need to be calibrated in a different way to conventional CCD imaging data. The algorithms required to do this have already been developed and described by Harpsøe et al. (2012).

A previous attempt to study variability in the central region of a globular cluster using EMCCD data has been made by Díaz-Sánchez et al. (2012). They used FastCam at the 2.5 m Nordic Optical Telescope to obtain 200 000 exposures of the globular cluster M15 with an exposure time of 30 ms. To study the variable stars, they made a Lucky Imaging selection of the 7% sharpest images in each time interval of 8.1 min. This resulted in 20 combined images each of exposure time 21 s, where each image comes from the combination of 700 short exposures. To extract the photometry they used standard DAOPHOT PSF fitting routines. They did not find any new variable stars and no analysis of the photometric precision achieved is offered.

The DIA technique, first introduced by Alard & Lupton (1998), has been improved by revisions to the algorithm presented by Bramich (2008); Bramich et al. (2013) and is the optimal way to perform photometry with EMCCD data in crowded fields. This method uses a numerical kernel model instead of modelling the kernel as a combination of Gaussian basis functions and can thus give better photometric precision even in very crowded regions (Albrow et al. 2009). The method is also especially adept at modelling images with PSFs that are not well approximated by a Gaussian.

Using the superior resolution provided by high frame-rate imaging EMCCDs in tandem with DIA we can probe the surroundings of bright stars for variable stars which are inaccessible with conventional CCD imaging. Using this technique we are able to present EMCCD photometry of two new RR Lyrae stars in the central region of NGC 6981.

2. Data and reductions

The data were obtained over two half nights (26th and 27th August 2012) at the Danish 1.54 m Telescope at La Silla Observatory, Chile, using the Andor Technology iXon+ model 897 EMCCD camera. The imaging area of the camera is 512×512 16 μm pixels with a pixel scale of 0.″09 which gives a 45×45 arcsec^2 field-of-view (FOV). With such a small FOV, we chose to target the crowded central region of NGC 6981 including the saturated stars from B11. The camera is equipped with a special long-pass filter with a cut-on wavelength of 650nm. The cut-off wavelength is determined by the sensitivity of the camera which drops to zero% at 1050 nm over about 250 nm. The filter thus corresponds roughly to a combination of the SDSS $i'+z'$ filters (Bessell 2005). A total of 44 observations with a frame-rate of 10 Hz were obtained. Each observation contains between 3000 to 3500 exposures.

Using the algorithms described in Harpsøe et al. (2012), each exposure is bias, flat, and tip-tilt corrected, and the instantaneous image quality (PSF width) is found. Then, for each observation, the exposures are combined into images in two distinct ways:

- Quality-binned: exposures are grouped according to a binning in image quality and combined to produce images that cover a range in point-spread-function (PSF) width.
- Time-binned: exposures are grouped into time bins of width 2 min to achieve a reasonable S/N at the brightness of the RR Lyrae stars. As opposed to Lucky Imaging, all frames are used. This gives a total of 125 data points in each light curve.

To extract the photometry from the time-binned images we used the DanDIA pipeline[1] (Bramich 2008; Bramich et al. 2013). The pipeline has been modified to stack the sharpest of the quality-binned images to create a high-resolution reference image from which the reference fluxes and positions of the stars are measured. The reference image, convolved with the kernel solution, is subtracted from each of the time-binned images to create difference images, and, in each difference image, the differential flux for each star is measured by scaling the PSF at the position of the star (see B11 for details). Note that we have further modified the DanDIA software to employ the appropriate noise model for EMCCD data (Harpsøe et al. 2012).

3. Results

In order to detect new variable stars in our data, we constructed and visually inspected an image representing the sum of the absolute-valued difference images with pixel values in units of sigma. We found two new variable stars which we assign names V57 and V58, and the details of which are given in Table 1. Both stars are located close to a bright star as can be seen in Fig. 1. In the B11 data, both of these variables are within the area that cannot be measured because of the saturated pixels from the bright star. Using the saturation limits from B11 it can be concluded that the bright star is brighter than 14th magnitude in V. In our data we find that the bright star is about 4 mag brighter than the RR Lyrae stars, which suggest that it is $V \sim 13$ mag.

The light curves for the two variables are shown in Fig. 2. There is increased scatter towards the end of each night which is due to a combination of high airmass and deteriorating seeing. The variable star periods were estimated using the string-length statistic S_Q (Dworetsky 1983) and the phased light curves are shown in Fig. 3.

V57: with a period of 0.334 days, a sinusoidal-like light curve, and a brightness on the reference image similar to that of the other RR Lyrae stars, we can safely classify this variable as a first-overtone RR Lyrae star (RR1).

V58: this object has no detectable PSF-like peak in the reference image even though it shows clear PSF-like variations in the difference images. Hence the associated object is fainter than the cluster RR Lyrae stars. The period of 0.285 days is typical of an RR1 star, although the light curve clearly deviates somewhat from being sinusoidal with relatively flat peaks and sharp drops in intensity. This star could be an eclipsing binary or an RR1 star behind the cluster. However, due to the lack of decisive evidence for either classification, we prefer to leave the variable as unclassified.

The discovery of a new RR1 variable in NGC 6981 changes the mean period of the RR1 stars from 0.308 d (B11) to 0.312 d. The updated ratio of the number of RR1 to RR Lyrae stars is found to be ~0.17 (compared to ~0.14 in B11). Both of these quantities still agree very well with the classification of NGC 6981 as an Oosterhoff type I cluster (Smith 1995).

Table 1. Details of the two new variable stars found in NGC 6981.

Variable Star ID	Var. Type	RA (J2000.0)	Dec (J2000.0)	T_{max} (d)	P (d)
V57	RR1	20 53 27.12	−12 32 13.9	6166.779	0.334
V58	?[a]	20 53 27.38	−12 32 13.3	6166.76	0.285

Notes. The celestial coordinates correspond to the epoch of the reference image, which is the heliocentric Julian date ~2 456 167 d. The epoch of maximum light is given as a heliocentric Julian date (2 450 000 +) in Col. 5 and the period is given in Col. 6. [(a)] We are unable to classify this variable (see Sect. 3).

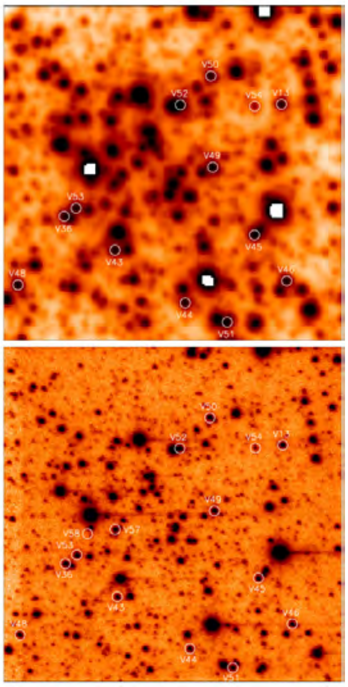

Fig. 1. *Top*: a cut-out of the B11 V reference image corresponding to the field of view of the EMCCD camera. *Bottom*: finding chart (constructed using our reference image) for the variables confirmed by B11 and the two new variables V57 and V58 (note that V58 is not the star that is located at the *upper right* edge of the circle). North is up and east is to the right. The image size is 45×45 arcsec^2. Notice the greatly improved resolution compared to the B11 finding chart.

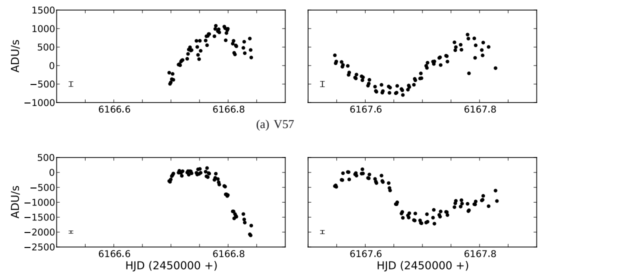

Fig. 2. Light curves, plotted in differential flux units, for the two new variable stars. *Left and right panels* show the first and second nights, respectively. The typical photometric uncertainty is plotted as an error bar in *each panel*.

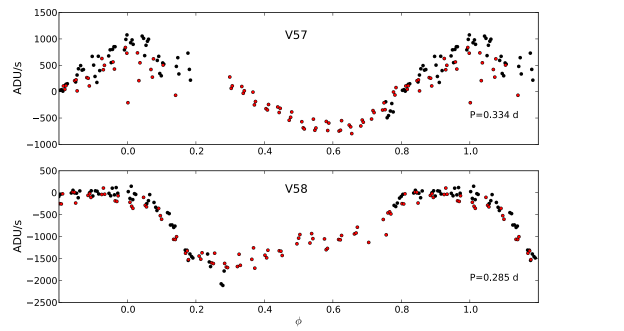

Fig. 3. Phased light curves for the two new variable stars, plotted in differential flux units and using the periods from Table 1. Black and red dots represent the data from the first and second nights of observation, respectively. The typical uncertainty in the period is about 0.01 d for both variables.

4. Conclusions

Using EMCCD data with DIA we found two previously unknown variable stars in the crowded central region of the globular cluster NGC 6981. We have classified one variable as a first-overtone RR Lyrae and we have been unable to classify the other. The discovery of the new RR1 star consolidates the classification of NGC 6981 as an Oosterhoff type I cluster.

Both variables are located in a crowded field and close to a much brighter star. The previous study by B11 employing conventional CCD data with DIA failed to find these variables. Our discovery of these new variables in a carefully studied globular cluster is thus one of the first results to demonstrate the power of EMCCDs for high-precision time-series photometry in crowded fields. This means that EMCCDs can improve the results in a number of areas in astrophysical research, for instance the search for Earth-mass exoplanets in gravitational microlensing events, or, as mentioned here, a better constraint on the physical parameters of globular clusters.

Acknowledgements. J.S. acknowledges support from the ESO 2012 DGDF for a two month visit to ESO Garching. The operation of the Danish 1.54 m telescope is financed by a grant to UGJ from the Danish Natural Science Research Council. We also acknowledge support from the European Community's Seventh Framework Programme (FP7/2007−2013/) under grant agreement Nos. 229517, 268421 and 274889 and from the Center of Excellence Centre for Star and Planet Formation (StarPlan) funded by The Danish National Research Foundation. K.A.A., M.D., D.M.B., C.L., M.H., R.A.S. and C.S. are thankful to Qatar National Research Fund (QNRF), member of Qatar Foundation, for support by grant NPRP 09-476-1-078. Y.D., A.E. under J.S. acknowledge support from the Communauté française de Belgique – Actions de recherche concertées – Académie universitaire to Wallonie-Europe. TCH acknowledges support from the Korea Research Council of Fundamental Science & Technology (KRCF) via the KRCF Young Scientist Research Fellowship Programme and for financial support from KASI travel grant number 2013-9-400-00. M.R. acknowledges support from FONDECYT postdoctoral fellowship No. 3120097.

References

Alard, C., & Lupton, R. H. 1998, ApJ, 503, 325
Albrow, M. D., Horne, K., Bramich, D. M., et al. 2009, MNRAS, 397, 2099
Bessell, M. S. 2005, ARA&A, 43, 293
Bramich, D. M. 2008, MNRAS, 386, L77
Bramich, D. M., Figuera Jaimes, R., Giridhar, S., & Arellano Ferro, A. 2011, MNRAS, 413, 1275
Bramich, D. M., Horne, K., Albrow, M. D., et al. 2013, MNRAS, 428, 2275
Díaz-Sánchez, A., Pérez-Garrido, A., Villó, I., et al. 2012, MNRAS, 423, 2260
Dworetsky, M. M. 1983, MNRAS, 203, 917
Harpsøe, K. B. W., Jørgensen, U. G., Andersen, M. I., & Grundahl, F. 2012, A&A, 542, A23
Law, N. M., Mackay, C. D., & Baldwin, J. E. 2006, A&A, 446, 739
Mackay, C. D., Baldwin, J., Law, N., & Warner, P. 2004, in SPIE Conf. Ser. 5492, eds. A. F. M. Moorwood, & M. Iye, 128
Smith, H. A. 1995, Cambridge Astrophys. Ser., 27

★ Based on data collected by MiNDSTEp with the Danish 1.54 m telescope.
★★ Royal Society University Research Fellow.

[1] DanDIA is built from the DanIDL library of IDL routines available at http://www.danidl.co.uk

Modelling cloudy atmospheres with MARCS

Diana Juncher[1,2], Christiane Helling[1], Uffe Gråe Jørgensen[2]
[1]University of St Andrews, UK; [2]University of Copenhagen, DK
astro.ku.dk/~diana

At a first glance M-dwarfs appear to be perfect planet-hunting candidates; they are very common, their small dimensions make exoplanet detection easier, and their lower temperatures provide for relatively large habitable zones. Unfortunately, M-dwarfs can be very difficult to model, and for exoplanet hunters good stellar models are a crucial tool for classifying observed stars and determining the physical properties of them and their planets.

M-dwarfs were originally thought to be dust free, but observations have revealed weaker molecular line absorptions than predicted by stellar atmosphere models (T. Tsuji et al., 1996). This is consistent with the formation of dust that strongly influences the local element abundances and thereby the spectra. In agreement with this, recent modelling of cool stellar atmospheres with dust demonstrate that it is necessary to include dust formation when modelling the atmospheres of objects that have effective temperatures below ~2700 K (Witte et al., 2009).

MARCS: Modelling stellar atmospheres since the 70's

MARCS is the Scandinavian code for modelling stellar atmospheres (B. Gustafsson et al.). It was introduced in 1975 and today it provides consistent solutions of the radiative transfer and the atmosphere structure and chemistry for stellar atmospheres of late A-type to early M-type stars. To model late M-type stars and sub-stellar objects, dust formation needs to be included.

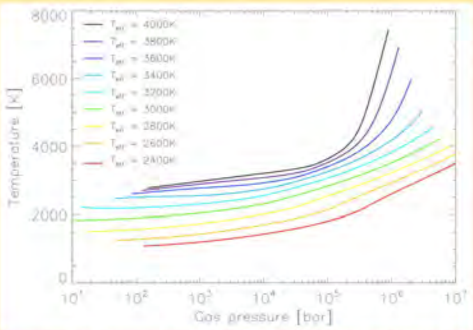

Temperature versus gas pressure for a range of M-dwarf stellar atmospheres modeled by MARCS.

Introducing dust into MARCS

As a first tentative step of introducing dust formation to the MARCS code we take a cloud model produced by DRIFT and use it in MARCS as a constant opacity source, i.e. there is no feedback between the two yet. The resulting dusty atmosphere is significantly different, once again proving how important it is to include dust formation for low effective temperatures.

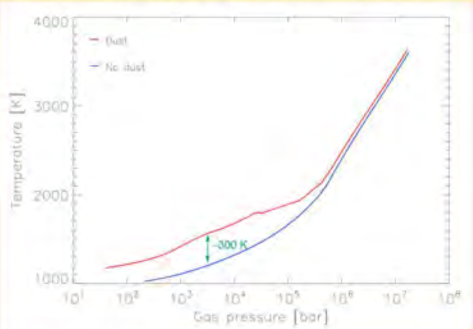

M-dwarfs with T_{eff} = 2300 K with and without dust formation.

DRIFT: A quasi-static cloud model

The DRIFT code models clouds in cool atmospheres using non-equilibrium dust formation and drift (C. Helling et al., 2008). The illustration below describes the life cycle of the dust from atom to molecule to seed particle to mixed grain and back to atom again. Convection makes sure that the elements of the upper layers are replenished.

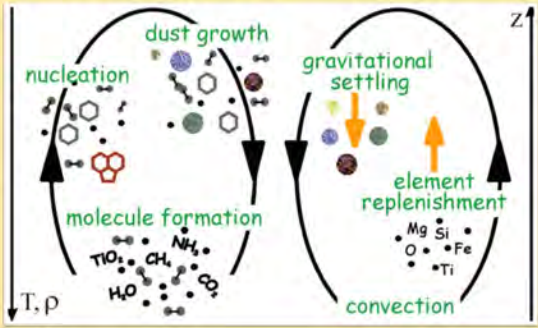

Dust grain types

The dust particles in DRIFT are compact, mixed grains composed of many small islands of different solid condensates such as TiO_2, Fe, Mg_2SiO_4 and Al_2O_3. Different alternatives exist, for example pure grains or porous, mixed grains (A. Kataoka et al., 2013).

The choice of dust grain type can have a great effect on the opacity as demonstrated below. Here the size of the dust particles and the relative solid abundances are the same in each layer height, only the type of the grains have been changed.

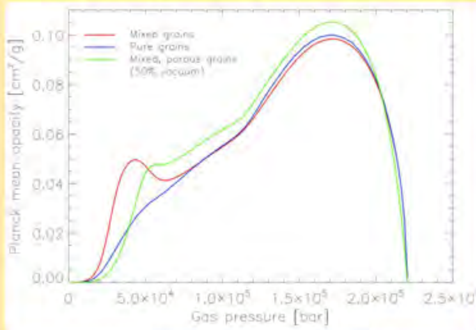

The Planck mean opacity for mixed, pure and porous dust grains for an M-dwarf with T_{eff} = 2000 K.

Modelling the Cloudy Atmospheres of Cool Stars

Diana Juncher[1,2], Andrius Popovas[1], Christiane Helling[2] and Uffe Gråe Jørgensen[1]
[1]University of Copenhagen, DK; [2]University of St Andrews, UK

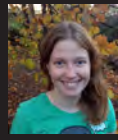

diana@nbi.dk

Introduction

M-dwarfs, small and cool stars on the main sequence, are particularly interesting when it comes to searching for new exoplanets as they are very common and their smaller sizes makes detection easier. Unfortunately, their low temperatures cause clouds to form in the upper layers of their atmospheres which makes them difficult to model. And since the biggest uncertainties of the properties of an exoplanet come from the uncertainties in the fundamental parameters of its host star, it is therefore crucial that the stellar models linking the observations of a star to its fundamental properties are determined as precisely as possible.

M-dwarfs were originally thought to be cloud free, but observations have revealed weaker molecular line absorptions than predicted by cloud free stellar atmospheres models (T. Tsuji et al., 1996). This is consistent with the formation of dust that strongly influences the local element abundances and thereby the spectra. In agreement with this, recent modelling of cool stellar atmospheres with clouds demonstrates that it is necessary to include dust formation when modelling the atmospheres of objects that have effective temperatures below 2700K (S. Witte et al., 2009).

MARCS: Modelling stellar atmospheres since the 70's

MARCS is the Scandinavian code for modelling stellar atmospheres (B. Gustafsson et al., 1975, 2008). It was introduced in 1975 and today it provides consistent solutions of the radiative transfer and the atmosphere structure and chemistry for stellar atmospheres of late A-type to early M-type stars. For MARCS to model late type M-dwarfs properly cloud formation needs to be included.

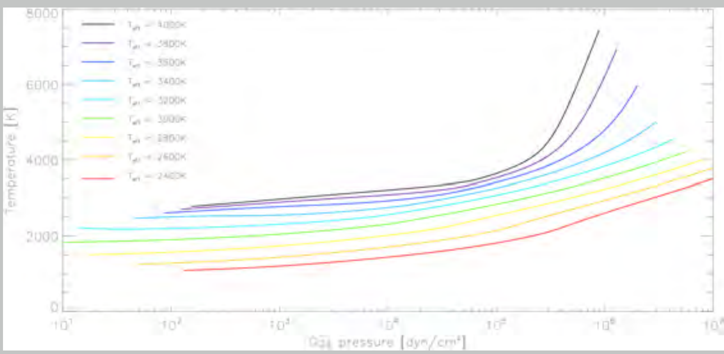

Temperature versus gas pressure for a range of stellar atmospheres modelled by MARCS.

The past few years have seen an explosion in the available line list data for both atoms and molecules. We have updated the atomic line database from VALD-2 to VALD-3 (F. Kupka et al., 2011) and updated or included new line data for the molecules CaH, CH_4, CN, CO, CO_2, CS, FeH, H_2O, HCN, MgH, OH, SiO, TiH and TiO.

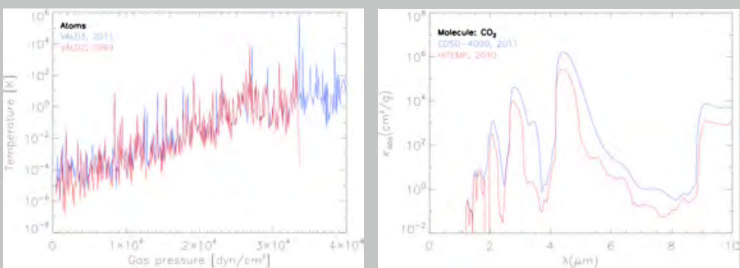

Comparison of old and new data for the atomic lines and the lines for the molecule CO_2.

DRIFT: A quasi-static cloud model

The DRIFT code models clouds in cool atmospheres using non-equilibrium dust formation and drift (C. Helling et al., 2008). The illustration on the right describes the life cycle of the dust from atoms to molecules to seed particles to mixed grains and back to atoms again. Convection makes sure that the elements of the upper layers are replenished.

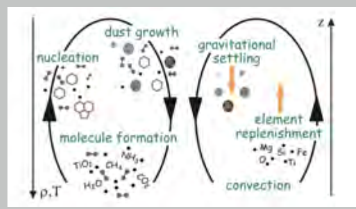

Given a stellar atmosphere with height-dependent temperature, pressure, convection velocity etc., DRIFT calculates the clouds that will form. Because of the high temperatures these clouds consist, not of water as we are used to here on Earth, but of mixed metallic dust grains composed of many small islands of different solid condensates such as TiO_2, Fe, Mg_2SiO_4 and Al_2O_3.

DRIFT provides information about the average sizes, composition and distribution of the dust grains in the clouds. From this the absorption and extinction as a function of wavelength can be calculated for each layer, and this is exactly what MARCS needs to know in order to calculate how the stellar atmosphere reacts to the increased opacity of the cloud layers.

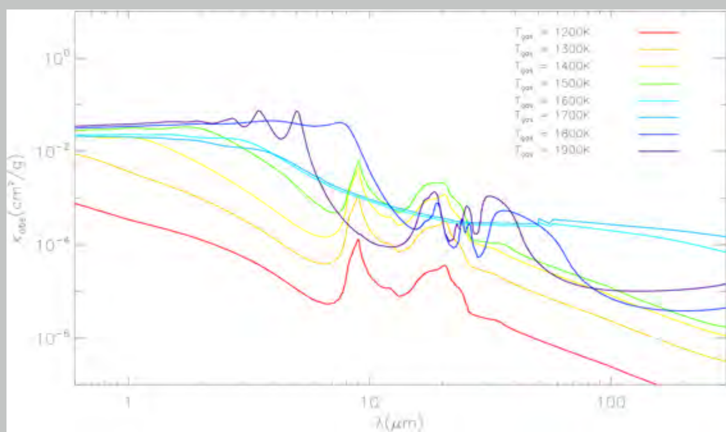

Absorption as a function of wavelength for different layers of an M-dwarf with $T_{eff} = 2000K$.

MARCS and DRIFT: Modelling cloudy stellar atmospheres

To create a stellar model atmosphere with clouds we start with a dust free model atmosphere. We use DRIFT to calculate its cloud layer and then MARCS to calculate the corresponding opacities and adjust the model atmosphere. An increase in opacity may typically cause the temperature to rise, so when we again use DRIFT to calculate the new cloud layer of the adjusted model, fewer clouds will form. The result is typically a decrease in opacity and temperature. We continue to run MARCS and DRIFT in turn until the model has converged.

The figure on the right shows dust free and dusty models at two effective temperatures. At $T_{eff} = 2700K$ the stellar atmosphere is so warm that cloud formation can barely take place. Interestingly enough, the dusty model is slightly cooler than the dust free model. This is because the decrease in the molecular opacity (caused by the depleted element abundances) has a larger effect than the increase in the dust opacity. At $T_{eff} = 2400K$ we see a large heating of the outer layers due to the increased opacity from the clouds. Note that the temperature of some of the layers increases by several hundred Kelvin - dust formation can have a big effect on a stellar atmosphere!

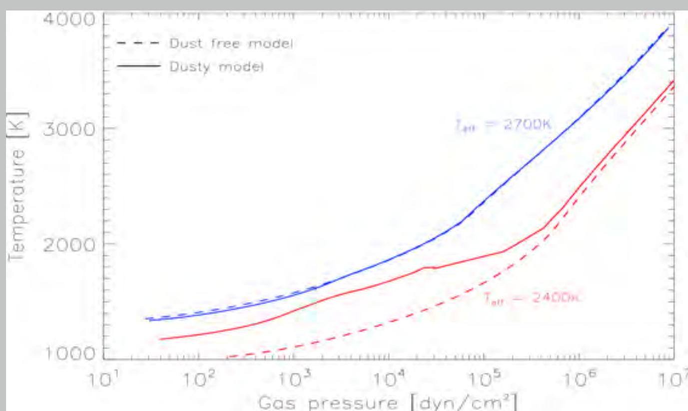

Comparison of dust free and dusty stellar atmosphere models.

Modelling the Cloudy Atmospheres of Cool Stars

Diana Juncher[1,2], Andrius Popovas[1], Uffe Gråe Jørgensen[1] and Christiane Helling[2]
[1]University of Copenhagen, DK; [2]University of St Andrews, UK

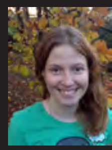
diana@nbi.dk

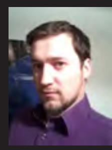
popovas@nbi.dk

Introduction

M-dwarfs, the coolest and most abundant stars in our galaxy, are particularly interesting when it comes to searching for new exoplanets, since their relatively small sizes and masses makes them the easiest targets for the detection of low-mass planets. Indeed, recent studies show that M-dwarfs are hosts to an abundance of low-mass planets and that the occurrence rate of planets less massive than $10M_\oplus$ is of the order of one planet per star, possibly even greater (M. Tuomi et al., 2014). Unfortunately, the physical and chemical properties of the atmosphere of an M-dwarf can be very difficult to model, mainly because the temperatures are so low that elements present in the atmosphere condense out and form dust clouds. And since the biggest uncertainties of the properties of an exoplanet come from the uncertainties in the fundamental parameters of its host star, it is crucial that the stellar models linking the observations of a star to its fundamental properties are determined as precisely as possible.

M-dwarfs were originally thought to be cloud free, but observations have revealed weaker molecular line absorptions than predicted by cloud free stellar atmospheres models (T. Tsuji et al., 1996). This is consistent with the formation of dust that strongly influences the local element abundances and thereby the spectra. In agreement with this, recent modelling of cool stellar atmospheres with clouds demonstrates that it is necessary to include dust formation when modelling the atmospheres of objects that have effective temperatures below $T_{eff} < 2700$K (S. Witte et al., 2009).

MARCS: Modelling stellar atmospheres since the 70's

MARCS is the Scandinavian code for modelling stellar atmospheres (B. Gustafsson et al., 1975, 2008). It was introduced in 1975 and today it provides consistent solutions of the radiative transfer and the atmosphere structure and chemistry for stellar atmospheres of late A-type to early M-type stars. For MARCS to model late type M-dwarfs properly cloud formation needs to be included.

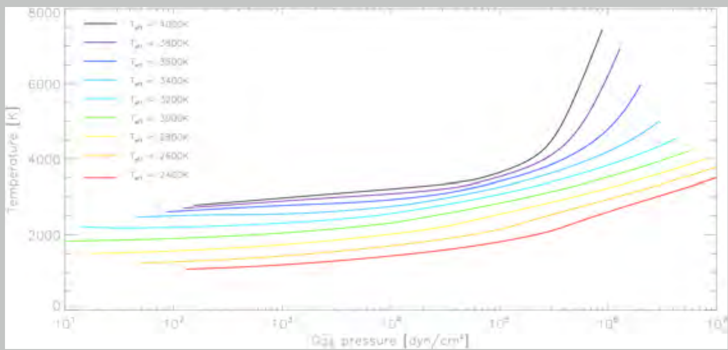

Temperature versus gas pressure for a range of stellar atmospheres modelled by MARCS.

Updating MARCS: New line data for atoms and molecules

The past few years have seen an explosion in the available line list data for both atoms and molecules. We have updated the atomic line database from VALD-2 to VALD-3 (F. Kupka et al., 2011) and updated or included new line data for the molecules *CaH*, CH_4, *CN*, *CO*, CO_2, *CS*, *FeH*, H_2O, *HCN*, *MgH*, *OH*, *SiO*, *TiH* and *TiO*.

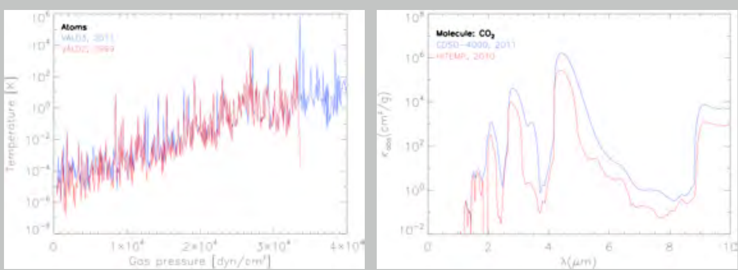

Comparison of old and new data for the atomic lines (left) and the lines for the molecule CO_2 (right).

To model a stellar atmosphere perfectly, we would have to include every absorption line of every element. This would result in too long computation times and we therefore have to simplify the treatment of line opacities. We have implemented a new method called Active Opacity Sampling that works by evaluating the radiative transfer in a limited number of wavelengths focusing on the interesting part of the spectrum. It is both faster and more precise than the old opacity sampling methods of MARCS.

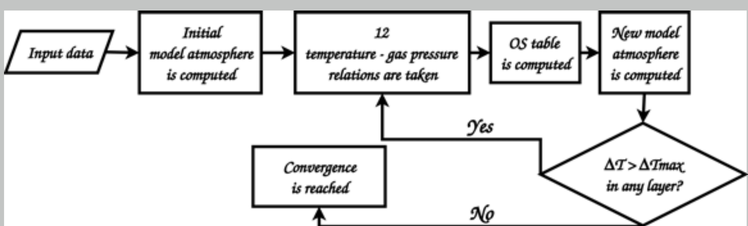

Flowchart showing how active opacity sampling works.

Total internal partition functions are used to calculate the intensity of an atomic or molecular line at the standard temperature as well as quickly estimate the line intensity at other temperatures. Furthermore, its derivatives are fundamental thermodynamic quantities that can be used to compute the physical structure and chemical equilibrium of stellar atmosphere models.

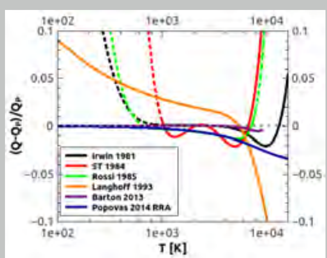

Comparison of commonly used studies of partition functions for SiO.

Due to the importance of total internal partition functions, numerous studies have been carried out during the past several decades in order to get more accurate values and to present them in a convenient way. In order to make any meaningful astrophysical conclusions about comparisons between different stellar atmosphere models and observations, it is essential that a single, coherent set of partition functions are used. We are constructing such a set of total internal partition functions and compare them to the partition functions of commonly used studies.

Cool stars: The influence of atomic opacities

In the atmospheres of the hottest stars, the temperatures are so high that all the elements, even hydrogen and helium, are strongly ionised. As we move towards lower temperatures, the amount of ionisation becomes smaller and smaller and eventually the neutral atoms will start to group into molecules. It makes sense, then, to suggest that the absorption lines in spectrum of a star will be dominated by ions or neutral atoms, if the star's temperature is above a certain value, and by molecules if the star's temperature is below that value. We have shown numerically that the absorption from atomic lines can be neglected when modelling the physical structure of stellar atmospheres with effective temperature $T_{eff} < 3100$K.

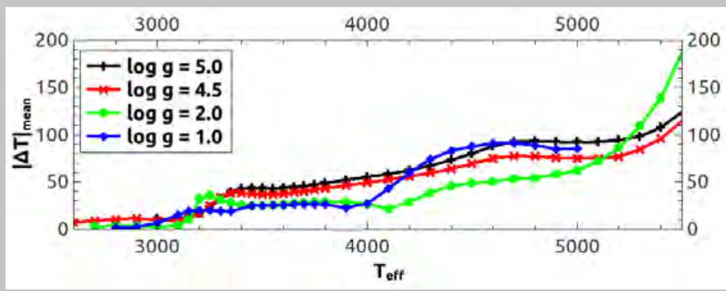

Mean temperature difference between models with and without atomic opacities.

DRIFT: A quasi-static cloud model

The DRIFT code models clouds in cool atmospheres using non-equilibrium dust formation and drift (C. Helling et al., 2008). The illustration on the right describes the life cycle of the dust from atoms to molecules to seed particles to mixed grains and back to atoms again. Convection makes sure that the elements of the upper layers are replenished.

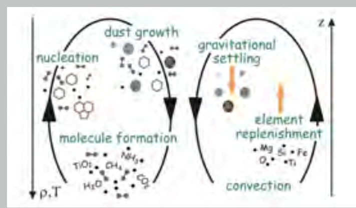

The life circle of dust in the DRIFT model.

Given a stellar atmosphere with height-dependent temperature, pressure, convection velocity etc., DRIFT calculates the clouds that will form. Because of the high temperatures these clouds consist, not of water as we are used to here on Earth, but of mixed metallic dust grains composed of many small islands of different solid condensates such as TiO_2, *Fe*, Mg_2SiO_4 and Al_2O_3.

DRIFT provides information about the average sizes, composition and distribution of the dust grains in the clouds. From this the absorption and extinction as a function of wavelength can be calculated for each layer, and this is exactly what MARCS needs to know in order to calculate how the stellar atmosphere reacts to the increased opacity of the cloud layers.

Combining MARCS and DRIFT: Modelling cloudy stellar atmospheres

To create a stellar model atmosphere with clouds we start with a dust free model atmosphere. We use DRIFT to calculate its cloud layer and then MARCS to calculate the corresponding opacities and adjust the model atmosphere. An increase in opacity may typically cause the temperature to rise, so when we again use DRIFT to calculate the new cloud layer of the adjusted model, fewer clouds will form. The result is typically a decrease in opacity and temperature. We continue to run MARCS and DRIFT in turn until the model has converged.

The figure on the right shows dust free and dusty models at two effective temperatures. At $T_{eff} = 2700$K the stellar atmosphere is so warm that cloud formation can barely take place. Interestingly enough, the dusty model is slightly cooler than the dust free model. This is because the decrease in the molecular opacity (caused by the depleted element abundances) has a larger effect than the increase in the dust opacity. At $T_{eff} = 2400$K we see a large heating of the outer layers due to the increased opacity from the clouds. Note that the temperature of some of the layers increases by several hundred Kelvin - dust formation can have a big effect on a stellar atmosphere!

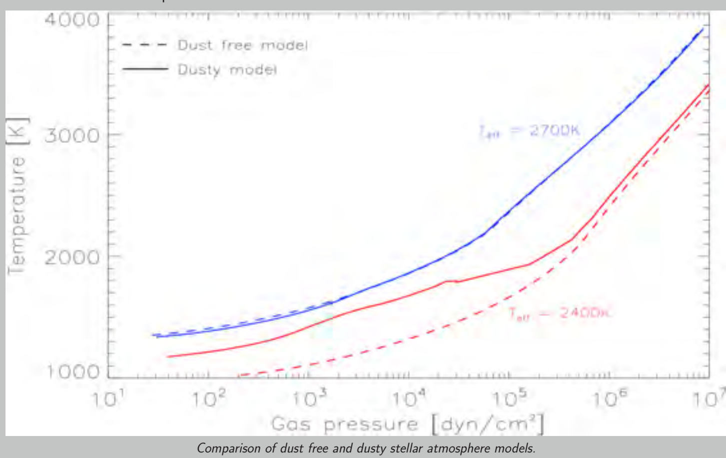

Comparison of dust free and dusty stellar atmosphere models.

Literature

Ackerman, A. S. and Marley, M. S. (2001). Precipitating Condensation Clouds in Substellar Atmospheres. *Astrophysical Journal*, 556:872–884.

Alcock, C., Allsman, R. A., Alves, D. R., Axelrod, T. S., Becker, A. C., et al. (2000). The MACHO Project: Microlensing Optical Depth toward the Galactic Bulge from Difference Image Analysis. *Astrophysical Journal*, 541:734–766.

Allard, F. (2014). The BT-Settl Model Atmospheres for Stars, Brown Dwarfs and Planets. In Booth, M., Matthews, B. C., and Graham, J. R., editors, *IAU Symposium*, volume 299 of *IAU Symposium*, pages 271–272.

Allard, F., Guillot, T., Ludwig, H.-G., Hauschildt, P. H., Schweitzer, A., et al. (2003). Model Atmospheres and Spectra: The Role of Dust. In Martín, E., editor, *Brown Dwarfs*, volume 211 of *IAU Symposium*, page 325.

Allard, F., Hauschildt, P. H., Alexander, D. R., Tamanai, A., and Schweitzer, A. (2001). The Limiting Effects of Dust in Brown Dwarf Model Atmospheres. *Astrophysical Journal*, 556:357–372.

Allard, F., Homeier, D., and Freytag, B. (2012). Models of very-low-mass stars, brown dwarfs and exoplanets. *Philosophical Transactions of the Royal Society of London Series A*, 370:2765–2777.

Allard, F., Homeier, D., and Freytag, B. (2014). Synthetic spectral libraries. In *Astronomical Society of India Conference Series*, volume 11, pages 33–45.

Anderson, D. R., Gillon, M., Maxted, P. F. L., Barman, T. S., Collier Cameron, A., et al. (2010). H-band thermal emission from the 19-h period planet WASP-19b. *Astronomy & Astrophysics*, 513:L3.

Anderson, D. R., Smith, A. M. S., Madhusudhan, N., Wheatley, P. J., Collier Cameron, A., et al. (2013). Thermal emission at 3.6-8 μm from WASP-19b: a hot Jupiter without a stratosphere orbiting an active star. *Monthly Notices of the RAS*, 430:3422–3431.

Apai, D., Radigan, J., Buenzli, E., Burrows, A., Reid, I. N., et al. (2013). HST Spectral Mapping of L/T Transition Brown Dwarfs Reveals Cloud Thickness Variations. *Astrophysical Journal*, 768:121.

Arellano Ferro, A., Bramich, D. M., Figuera Jaimes, R., Giridhar, S., Kains, N., et al. (2013). A detailed census of variable stars in the globular cluster NGC 6333 (M9) from CCD differential photometry. *Monthly Notices of the RAS*, 434:1220–1238.

Asplund, M., Gustafsson, B., Kiselman, D., and Eriksson, K. (1997). Line-blanketed model atmospheres for R Coronae Borealis stars and hydrogen-deficient carbon stars. *Astronomy & Astrophysics*, 318:521–534.

Bachelet, E., Bramich, D. M., Han, C., Greenhill, J., Street, R. A., et al. (2015). Red Noise Versus Planetary Interpretations in the Microlensing Event Ogle-2013-BLG-446. *Astrophysical Journal*, 812:136.

Bahcall, J. N., Pinsonneault, M. H., and Basu, S. (2001). Solar Models: Current Epoch and Time Dependences, Neutrinos, and Helioseismological Properties. *Astrophysical Journal*, 555:990–1012.

Bakos, G., Noyes, R. W., Kovács, G., Stanek, K. Z., Sasselov, D. D., et al. (2004). Wide-Field Millimagnitude Photometry with the HAT: A Tool for Extrasolar Planet Detection. *The Publications of the Astronomical Society of the Pacific*, 116:266–277.

Baraffe, I., Chabrier, G., Barman, T. S., Allard, F., and Hauschildt, P. H. (2003). Evolutionary models for cool brown dwarfs and extrasolar giant planets. The case of HD 209458. *Astronomy & Astrophysics*, 402:701–712.

Barclay, T., Rowe, J. F., Lissauer, J. J., Huber, D., Fressin, F., et al. (2013). A sub-Mercury-sized exoplanet. *Nature*, 494:452–454.

Barman, T. S., Macintosh, B., Konopacky, Q. M., and Marois, C. (2011). Clouds and Chemistry in the Atmosphere of Extrasolar Planet HR8799b. *Astrophysical Journal*, 733:65.

Barton, E. J., Yurchenko, S. N., and Jonathan, T. (2013). ExoMol line lists - II. The ro-vibrational spectrum of SiO. *Monthly Notices of the RAS*, 434:1469–1475.

Basri, G. (2000). Observations of Brown Dwarfs. *Annual Review of Astronomy & Astrophysics*, 38:485–519.

Beaulieu, J.-P., Bennett, D. P., Fouqué, P., Williams, A., Dominik, M., et al. (2006). Discovery of a cool planet of 5.5 Earth masses through gravitational microlensing. *Nature*, 439:437–440.

Béjar, V. J. S., Martín, E. L., Zapatero Osorio, M. R., Rebolo, R., Barrado y Navascués, D., et al. (2001). The Substellar Mass Function in σ Orionis. *Astrophysical Journal*, 556:830–836.

Bell, R. A., Eriksson, K., Gustafsson, B., and Nordlund, A. (1976). A grid of model atmospheres for metal-deficient giant stars. II. *Astronomy & Astrophysics Supplement Series*, 23:37–95.

Bennett, D. P. and Rhie, S. H. (1996). Detecting Earth-Mass Planets with Gravitational Microlensing. *Astrophysical Journal*, 472:660.

Bennett, D. P. and Rhie, S. H. (2002). Simulation of a Space-based Microlensing Survey for Terrestrial Extrasolar Planets. *Astrophysical Journal*, 574:985–1003.

Bohren, C. F. and Huffman, D. R. (1983). *Absorption and Scattering of Light by Small Particles.* John Wiley & Sons Ltd.

Bonfils, X., Delfosse, X., Udry, S., Forveille, T., Mayor, M., et al. (2013). The HARPS search for southern extra-solar planets. XXXI. The M-dwarf sample. *Astronomy & Astrophysics*, 549:A109.

Bosch, S., Ferré-Borrull, J., Leinfellner, N., and Canillas, A. (2000). Effective dielectric function of mixtures of three or more materials: a numerical procedure for computations. *Surface Science*, 453:9–17.

Brett, J. M. and Plez, B. (1993). Model Atmospheres and the T/eff Scale for M Dwarfs. *Proceedings of the Astronomical Society of Australia*, 10:250.

Brooke, J. S. A., Bernath, P. F., Schmidt, T. W., and Bacskay, G. B. (2013). Line strengths and updated molecular constants for the C_2 Swan system. *Journal of Quantitative Spectroscopy & Radiative Transfer*, 124:11–20.

Brooke, J. S. A., Bernath, P. F., Western, C. M., Hemert, C. v., and Groenenboom, G. C. (2014a). Line strengths of rovibrational and rotational transitions within the $X^3\Sigma^-$ ground state of NH. *The Journal of Chemical Physics*, 141.

Brooke, J. S. A., Ram, R., Western, C. M., Li, G., Schwenke, D. W., et al. (2014b). Einstein A coefficients and oscillator strengths for the $A^2\Pi - X^2\Sigma^+$ (red) and $B^2\Sigma^+ - X^2\Sigma?^+$ (violet) systems and rovibrational transitions in the $X^2\Sigma^+$ state of CN. *Astrophysical Journal Supplement Series*, 210:23–38.

Brown, T. M. and Charbonneau, D. (2000). The STARE Project: a Transit Search for Hot Jupiters. In *Disks, Planetesimals, and Planets*, volume 219 of *Astronomical Society of the Pacific Conference Series*, page 584.

Brown, T. M., Charbonneau, D., Gilliland, R. L., Noyes, R. W., and Burrows, A. (2001). Hubble Space Telescope Time-Series Photometry of the Transiting Planet of HD 209458. *Astrophysical Journal*, 552:699–709.

Bruggeman, D. A. G. (1935). Berechnung verschiedener physikalischer Konstanten von heterogenen Substanzen. I. Dielektrizitätskonstanten und Leitfähigkeiten der Mischkörper aus isotropen Substanzen. *Annalen der Physik*, 416:636–664.

Buchhave, L. A., Bizzarro, M., Latham, D. W., Sasselov, D., Cochran, W. D., et al. (2014). Three regimes of extrasolar planet radius inferred from host star metallicities. *Nature*, 509:593–595.

Burgasser, A. (2008). The SpeX Prism Spectral Libraries. http://www.browndwarfs.org/spexprism.

Burgasser, A. J. (2014). The SpeX Prism Library: 1000+ low-resolution, near-infrared spectra of ultracool M, L, T and Y dwarfs. In *Astronomical Society of India Conference Series*, volume 11, pages 7–16.

Burgasser, A. J., Dhital, S., and West, A. A. (2009). Resolved Spectroscopy of M Dwarf/L Dwarf Binaries. III. The "Wide" L3.5/L4 Dwarf Binary 2Mass J15500845+1455180AB. *Astronomical Journal*, 138:1563–1569.

Burgasser, A. J., Kirkpatrick, J. D., Liebert, J., and Burrows, A. (2003). The Spectra of T Dwarfs. II. Red Optical Data. *Astrophysical Journal*, 594:510–524.

Burgasser, A. J., Liu, M. C., Ireland, M. J., Cruz, K. L., and Dupuy, T. J. (2008). Subtle Signatures of Multiplicity in Late-type Dwarf Spectra: The Unresolved M8.5 + T5 Binary 2MASS J03202839-0446358. *Astrophysical Journal*, 681:579–593.

Burgasser, A. J., McElwain, M. W., Kirkpatrick, J. D., Cruz, K. L., Tinney, C. G., et al. (2004). The 2MASS Wide-Field T Dwarf Search. III. Seven New T Dwarfs and Other Cool Dwarf Discoveries. *Astronomical Journal*, 127:2856–2870.

Burrows, A., Dulick, M., Bauschlicher, C. W., Bernath, P. F., Ram, R. S., et al. (2005). Spectroscopic constants, abundances, and opacities of the TiH molecule. *Astrophysical Journal*, 624:988–1002.

Burrows, A., Heng, K., and Nampaisarn, T. (2011). The Dependence of Brown Dwarf Radii on Atmospheric Metallicity and Clouds: Theory and Comparison with Observations. *Astrophysical Journal*, 736:47.

Burrows, A., Hubbard, W. B., and Lunine, J. I. (1989). Theoretical models of very low mass stars and brown dwarfs. *Astrophysical Journal*, 345:939–958.

Burrows, A., Ram, R. S., Bernath, P., Sharp, C. M., and Milsom, J. A. (2002). New CrH opacities for the study of L and brown dwarf atmospheres. *Astrophysical Journal*, 577:986–992.

Burrows, A. and Sharp, C. M. (1999). Chemical Equilibrium Abundances in Brown Dwarf and Extrasolar Giant Planet Atmospheres. *Astrophysical Journal*, 512:843–863.

Burrows, A., Sudarsky, D., and Hubeny, I. (2006). L and T Dwarf Models and the L to T Transition. *Astrophysical Journal*, 640:1063–1077.

Calchi Novati, S., Gould, A., Udalski, A., Menzies, J. W., Bond, I. A., et al. (2015). Pathway to the Galactic Distribution of Planets: Combined Spitzer and Ground-Based Microlens Parallax Measurements of 21 Single-Lens Events. *Astrophysical Journal*, 804:20.

Carlson, B. E., Rossow, W. B., and Orton, G. S. (1988). Cloud microphysics of the giant planets. *Journal of Atmospheric Sciences*, 45:2066–2081.

Cassan, A., Kubas, D., Beaulieu, J.-P., Dominik, M., Horne, K., et al. (2012). One or more bound planets per Milky Way star from microlensing observations. *Nature*, 481:167–169.

Chabrier, G. and Baraffe, I. (1997). Structure and evolution of low-mass stars. *Astronomy & Astrophysics*, 327:1039–1053.

Chabrier, G., Baraffe, I., Allard, F., and Hauschildt, P. (2000). Evolutionary Models for Very Low-Mass Stars and Brown Dwarfs with Dusty Atmospheres. *Astrophysical Journal*, 542:464–472.

Chabrier, G., Baraffe, I., Allard, F., and Hauschildt, P. H. (2005). Review on low-mass stars and brown dwarfs. *ArXiv Astrophysics e-prints*.

Charbonneau, D., Brown, T. M., Latham, D. W., and Mayor, M. (2000). Detection of Planetary Transits Across a Sun-like Star. *Astrophysical Journal*, 529:L45–L48.

Chase, M. W., Davies, C. A., Downey Jr., J. R., Frurip, D. J., McDonald, R. A., et al. (1985). NIST-JANAF Thermochemical Tables. http://kinetics.nist.gov/janaf.

Chiu, K., Fan, X., Leggett, S. K., Golimowski, D. A., Zheng, W., et al. (2006). Seventy-One New L and T Dwarfs from the Sloan Digital Sky Survey. *Astronomical Journal*, 131:2722–2736.

Ciceri, S., Mancini, L., Southworth, J., Lendl, M., Tregloan-Reed, J., et al. (2015). Physical properties of the planetary systems WASP-45 and WASP-46 from simultaneous multi-band photometry. *Monthly Notices of the RAS*, in press.

Cochran, W. D., Hatzes, A. P., and Hancock, T. J. (1991). Constraints on the companion object to HD 114762. *Astrophysical Journal Letters*, 380:L35–L38.

Cooper, C. S., Sudarsky, D., Milsom, J. A., Lunine, J. I., and Burrows, A. (2003). Modeling the Formation of Clouds in Brown Dwarf Atmospheres. *Astrophysical Journal*, 586:1320–1337.

Coppola, C. M., Lodi, L., and Tennyson, J. (2011). Radiative cooling functions for primordial molecules. *Monthly Notices of the RAS*, 415:487–493.

Crossfield, I. J. M., Biller, B., Schlieder, J. E., Deacon, N. R., Bonnefoy, M., et al. (2014). A global cloud map of the nearest known brown dwarf. *Nature*, 505:654–656.

Cushing, M. C., Rayner, J. T., and Vacca, W. D. (2005). An Infrared Spectroscopic Sequence of M, L, and T Dwarfs. *Astrophysical Journal*, 623:1115–1140.

Cushing, M. C., Roellig, T. L., Marley, M. S., Saumon, D., Leggett, S. K., et al. (2006). A Spitzer Infrared Spectrograph Spectral Sequence of M, L, and T Dwarfs. *Astrophysical Journal*, 648:614–628.

Dehn, M. (2007). PhD thesis, University of Hamburg.

Dickens, R. J., Bell, R. A., and Gustafsson, B. (1979). Carbon and nitrogen abundances in red giant stars in the globular cluster 47 Tucanae. *Astrophysical Journal*, 232:428–450.

Djupvik, A. A. and Andersen, J. (2010). The Nordic Optical Telescope. In J. M. Diego, L. J. Goicoechea, J. I. González-Serrano, & J. Gorgas, editor, *Highlights of Spanish Astrophysics V*, page 211.

Dominik, C., Sedlmayr, E., and Gail, H.-P. (1993). Dust formation in stellar winds. VI. Moment equations for the formation of heterogeneous and core-mantle grains. *Astronomy & Astrophysics*, 277:578.

Dominik, M., Jorgensen, U. G., Horne, K., Tsapras, Y., Street, R. A., et al. (2008). Inferring statistics of planet populations by means of automated microlensing searches. *ArXiv e-prints*.

Dominik, M., Jørgensen, U. G., Rattenbury, N. J., Mathiasen, M., Hinse, T. C., et al. (2010). Realisation of a fully-deterministic microlensing observing strategy for inferring planet populations. *Astronomische Nachrichten*, 331:671.

Dorschner, J., Begemann, B., Henning, T., Jäger, C., and Mutschke, H. (1995). Steps toward interstellar silicate mineralogy II. *Astronomy & Astrophysics*, 300:503–520.

Doughty, N. A. and Fraser, P. A. (1966). The free-free absorption coefficient of the negative hydrogen ion. *Monthly Notices of the RAS*, 132:267.

Doughty, N. A., Fraser, P. A., and McEachran, R. P. (1966). The bound-free absorption coefficient of the negative hydrogen ion. *Monthly Notices of the RAS*, 132:255.

Doyle, R. O. (1968). The Astrophysical Significance of the Continuous Spectrum of the Hydrogen Quasi-Molecule. *Astrophysical Journal*, 153:987.

Einstein, A. (1905). Zur Elektrodynamik bewegter Körper. *Annalen der Physik*, 322:891–921.

Emerson, D. (1996). *Interpreting Astronomical Spectra*. John Wiley & Sons Ltd.

Fegley, B. (2012). *Practical Chemical Thermodynamics for Geoscientists*. Academic Press.

Fegley, Jr., B. and Lodders, K. (1994). Chemical models of the deep atmospheres of Jupiter and Saturn. *Icarus*, 110:117–154.

Fegley, Jr., B. and Lodders, K. (1996). Atmospheric Chemistry of the Brown Dwarf Gliese 229B: Thermochemical Equilibrium Predictions. *Astrophysical Journal Letters*, 472:L37.

Ferguson, J. W., Alexander, D. R., Allard, F., Barman, T., Bodnarik, J. G., et al. (2005). Low-Temperature Opacities. *Astrophysical Journal*, 623:585–596.

Fortney, J. J., Lodders, K., Marley, M. S., and Freedman, R. S. (2008). A Unified Theory for the Atmospheres of the Hot and Very Hot Jupiters: Two Classes of Irradiated Atmospheres. *Astrophysical Journal*, 678:1419–1435.

Freytag, B., Steffen, M., Ludwig, H.-G., Wedemeyer-Böhm, S., Schaffenberger, W., et al. (2012). Simulations of stellar convection with CO5BOLD. *Journal of Computational Physics*, 231:919–959.

Gail, H.-P., Keller, R., and Sedlmayr, E. (1984). Dust formation in stellar winds. I - A rapid computational method and application to graphite condensation. *Astronomy & Astrophysics*, 133:320–332.

Gail, H.-P. and Sedlmayr, E. (1988). Dust formation in stellar winds. IV - Heteromolecular carbon grain formation and growth. *Astronomy & Astrophysics*, 206:153–168.

Gaudi, B. S. (2010). *Exoplanetary Microlensing*, pages 79–110. University of Arizona Press.

GharibNezhad, E., Shayesteh, A., and Bernath, P. (2013). Einstein A coefficients for rovibronic lines of the $A^2\Pi \rightarrow X^2\Sigma^+$ and $B'^2\Sigma^+ \rightarrow X^2\Sigma^+$ transitions of MgH. *Monthly Notices of the RAS*, 432:2043–2047.

Gibson, N. P., Aigrain, S., Pollacco, D. L., Barros, S. C. C., Hebb, L., et al. (2010). Ground-based detection of thermal emission from the exoplanet WASP-19b. *Monthly Notices of the RAS*, 404:L114–L118.

Gray, D. F. (2005). *Stellar Photospheres*. Cambridge University Press.

Grevesse, N., Asplund, M., and Sauval, A. J. (2007). The Solar Chemical Composition. *Space Science Reviews*, 130:105–114.

Gustafsson, B., Bell, R. A., Eriksson, K., and Nordlund, A. (1975). A grid of model atmospheres for metal-deficient giant stars. I. *Astronomy & Astrophysics*, 42:407–432.

Gustafsson, B., Edvardsson, B., Eriksson, K., Jørgensen, U. G., Nordlund, A., et al. (2008). A grid of model atmospheres for late-type stars. *Astronomy & Astrophysics*, 486:951–970.

Harris, G. J., Larner, F. C., Tennyson, J., Kaminsky, B. M., Pavlenko, Y. C., et al. (2008). A $H^{13}CN/HN^{13}C$ linelist, model atmospheres and synthetic spectra for carbon stars. *Monthly Notices of the RAS*, 390:143–148.

Harris, G. J., Tennyson, J., Kaminsky, B. M., Pavlenko, Y. C., and Jones, H. R. A. (2006). Improved HCN/HNC linelist, model atmospheres and synthetic spectra for WZ Cas. *Monthly Notices of the RAS*, 367:400–406.

Hauschildt, P. H. (1992). A fast operator perturbation method for the solution of the special relativistic equation of radiative transfer in spherical symmetry. *Journal of Quantitative Spectroscopy & Radiative Transfer*, 47:433–453.

Haynes, W. M., editor (2015). *CRC Handbook of Chemistry and Physics*. Boca Raton: CRC Press, 96 edition.

Helling, C., Ackerman, A., Allard, F., Dehn, M., Hauschildt, P., et al. (2008a). A comparison of chemistry and dust cloud formation in ultracool dwarf model atmospheres. *Monthly Notices of the RAS*, 391:1854–1873.

Helling, C., Dehn, M., Woitke, P., and Hauschildt, P. H. (2008b). Consistent Simulations of Substellar Atmospheres and Nonequilibrium Dust Cloud Formation. *Astrophysical Journal*, 675:L105–L108.

Helling, C. and Fomins, A. (2013). Modelling the formation of atmospheric dust in brown dwarfs and planetary atmospheres. *Philosophical Transactions of the Royal Society of London Series A*, 371:20110581–20110581.

Helling, C., Jardine, M., and Mokler, F. (2011a). Ionization in Atmospheres of Brown Dwarfs and Extrasolar Planets. II. Dust-induced Collisional Ionization. *Astrophysical Journal*, 737:38.

Helling, C., Jardine, M., Stark, C., and Diver, D. (2013). Ionization in Atmospheres of Brown Dwarfs and Extrasolar Planets. III. Breakdown Conditions for Mineral Clouds. *Astrophysical Journal*, 767:136.

Helling, C., Jardine, M., Witte, S., and Diver, D. A. (2011b). Ionization in Atmospheres of Brown Dwarfs and Extrasolar Planets. I. The Role of Electron Avalanche. *Astrophysical Journal*, 727:4.

Helling, C., Jorgensen, U. G., Plez, B., and Johnson, H. R. (1996). Formation of PAHs, polyynes, and other macromolecules in the photosphere of carbon stars. *Astronomy & Astrophysics*, 315:194–203.

Helling, C., Oevermann, M., Lüttke, M. J. H., Klein, R., and Sedlmayr, E. (2001). Dust in brown dwarfs. I. Dust formation under turbulent conditions on microscopic scales. *Astronomy & Astrophysics*, 376:194–212.

Helling, C. and Woitke, P. (2006). Dust in brown dwarfs V. *Astronomy & Astrophysics*, 455:325–338.

Helling, C., Woitke, P., and Thi, W.-F. (2008c). Dust in brown dwarfs and extra-solar planets. I. Chemical composition and spectral appearance of quasi-static cloud layers. *Astronomy & Astrophysics*, 485:547–560.

Howard, A. W., Marcy, G. W., Bryson, S. T., Jenkins, J. M., Rowe, J. F., et al. (2012). Planet Occurrence within 0.25 AU of Solar-type Stars from Kepler. *Astrophysical Journal Supplement*, 201:15–34.

Hui-Bon-Hoa, A., LeBlanc, F., and Hauschildt, P. H. (2000). Diffusion in the Atmospheres of Blue Horizontal-Branch Stars. *Astrophysical Journal*, 535:L43–L45.

Irwin, A. W. (1981). Polynomial partition function approximations of 344 atomic and molecular species. *Astrophysical Journal Supplement Series*, 45:621–633.

Jäger, C., Dorschner, J., Mutschke, H., Posch, T., and Henning, T. (2003). Steps toward interstellar silicate mineralogy VII. *Astronomy & Astrophysics*, 408:193–204.

Jeans, J. H. (1902). The Stability of a Spherical Nebula. *Philosophical Transactions of the Royal Society of London Series A*, 199:1–53.

Jeong, K. (2000). *Dust shells around oxygen-rich Miras and long-period variables.* PhD thesis, Technische Universität, Berlin.

Jeong, K. S., Winters, J. M., Le Bertre, T., and Sedlmayr, E. (2003). Self-consistent modeling of the outflow from the O-rich Mira IRC -20197. *Astronomy and Astrophysics*, 407:191–206.

John, M. (1995). Master's thesis, Technische Universität, Berlin.

John, T. L. (1967). The Free-Free Transitions of Heˆ- at Threshold. *Astrophysical Journal*, 149:449.

Jørgensen, U. G. (1996). Cool star models. In van Dishoeck, E. F., editor, *Molecules in astrophysics: Probes & processes*, volume 178 of *IAU Sympostium*.

Jørgensen, U. G. (2001). SCAN database. http://www.astro.ku.dk/~uffegj.

Jørgensen, U. G. (2015). Exoplanets - planets around other stars than the Sun. Lecture notes.

Jørgensen, U. G., Jensen, P., Sørensen, G. O., and Aringer, B. (2001). H_2O in stellar atmospheres. *Astronomy & Astrophysics*, 372:249–259.

Juncher, D., Buchhave, L. A., Hartman, J. D., Bakos, G. Á., Bieryla, A., et al. (2015). HAT-P-55b: A Hot Jupiter Transiting a Sun-Like Star. *Publications of the Astronomical Society of the Pacific*, 127:851–856.

Juncher, D., Jørgensen, U. G., and Helling, C. (2016a). Modeling the Cloudy Atmospheres of Ultra Cool Dwarfs I: Creating a cloudy model atmosphere. Manuscript in preparation.

Juncher, D., Jørgensen, U. G., and Helling, C. (2016b). Modeling the Cloudy Atmospheres of Ultra Cool Dwarfs II: Comparison of synthetic and observed spectra. Manuscript in preparation.

Kains, N., Arellano Ferro, A., Figuera Jaimes, R., Bramich, D. M., Skottfelt, J., et al. (2015). A census of variability in globular cluster M 68 (NGC 4590). *Astronomy & Astrophysics*, 578:A128.

Kains, N., Bramich, D. M., Arellano Ferro, A., Figuera Jaimes, R., Jørgensen, U. G., et al. (2013). Estimating the parameters of globular cluster M 30 (NGC 7099) from time-series photometry. *Astronomy & Astrophysics*, 555:A36.

Kaltenegger, L. and Traub, W. A. (2009). Transits of Earth-like Planets. *Astrophysical Journal*, 698:519–527.

Karzas, W. J. and Latter, R. (1961). Electron Radiative Transitions in a Coulomb Field. *Astrophysical Journal Supplement Series*, 6:167.

Kirkpatrick, J. D. (2005). New Spectral Types L and T. *Annual Review of Astronomy & Astrophysics*, 43:195–245.

Kirkpatrick, J. D., Henry, T. J., and McCarthy, Jr., D. W. (1991). A standard stellar spectral sequence in the red/near-infrared - Classes K5 to M9. *Astrophysical Journal Supplement Series*, 77:417–440.

Kirkpatrick, J. D., Looper, D. L., Burgasser, A. J., Schurr, S. D., Cutri, R. M., et al. (2010). Discoveries from a Near-infrared Proper Motion Survey Using Multi-epoch Two Micron All-Sky Survey Data. *Astrophysical Journal Supplement*, 190:100–146.

Knutson, H. A., Howard, A. W., and Isaacson, H. (2010). A Correlation Between Stellar Activity and Hot Jupiter Emission Spectra. *Astrophysical Journal*, 720:1569–1576.

Korhonen, H., Andersen, J. M., Piskunov, N., Hackman, T., Juncher, D., et al. (2015). Stellar activity as noise in exoplanet detection - I. Methods and application to solar-like stars and activity cycles. *Monthly Notices of the Royal Astronomical Society*, 448:3038–3052.

Kreidberg, L., Bean, J. L., Désert, J.-M., Benneke, B., Deming, D., et al. (2014). Clouds in the atmosphere of the super-Earth exoplanet GJ1214b. *Nature*, 505:69–72.

Kupka, F., Dubernet, M.-L., and Collaboration, V. (2011). Vamdc as a Resource for Atomic and Molecular Data and the New Release of VALD. *Baltic Astronomy*, 20:503–510.

Kurucz, R. L. (1970). Atlas: A Computer Program for Calculating Model Stellar Atmospheres. *SAO Special Report*, 309.

Kurucz, R. L. (2001). Molecular line lists. http://kurucz.harvard.edu.

Kurucz, R. L. (2005). ATLAS12, SYNTHE, ATLAS9, WIDTH9, et cetera. *Memorie della Societa Astronomica Italiana Supplementi*, 8:14.

Kurucz, R. L. (2011). Including all the lines. *Canadian Journal of Physics*, 89:417–428.

Lambert, D. L., Gustafsson, B., Eriksson, K., and Hinkle, K. H. (1986). The chemical composition of carbon stars. I - Carbon, nitrogen, and oxygen in 30 cool carbon stars in the Galactic disk. *Astrophysical Journal Supplement Series*, 62:373–425.

Latham, D. W. and HARPS-N Collaboration (2013). HARPS-N: A New Tool for Characterizing Kepler Planets. In *American Astronomical Society Meeting Abstracts #221*, volume 221 of *American Astronomical Society Meeting Abstracts*, page #231.02.

Latham, D. W., Stefanik, R. P., Mazeh, T., Mayor, M., and Burki, G. (1989). The unseen companion of HD114762 - A probable brown dwarf. *Nature*, 339:38–40.

Lee, G., Helling, C., Dobbs-Dixon, I., and Juncher, D. (2015). Modelling the local and global cloud formation on HD 189733b. *Astronomy & Astrophysics*, 580:A12.

Lewis, J. S. (1969). The clouds of Jupiter and the NH $_3$#58872H $_2$O and NH $_3$#58872H $_2$S systems. *Icarus*, 10:365–378.

Lodders, K. (2002). Titanium and Vanadium Chemistry in Low-Mass Dwarf Stars. *Astrophysical Journal*, 577:974–985.

Lodders, K. (2004). Jupiter Formed with More Tar than Ice. *Astrophysical Journal*, 611:587–597.

Lodders, K. and Fegley, Jr., B. (1993). Chemistry in Circumstellar Envelopes of Carbon Stars: The Influence of P, T, and Elemental Abundances. *Meteoritics*, 28:387.

Lodders, K. and Fegley, Jr., B. (2006). *Chemistry of Low Mass Substellar Objects*, pages 1–28. Springer Berlin Heidelberg.

Lovis, C. and Fischer, D. (2010). *Radial Velocity Techniques for Exoplanets*, pages 27–53. University of Arizona Press.

Ludwig, H.-G., Allard, F., and Hauschildt, P. H. (2002). Numerical simulations of surface convection in a late M-dwarf. *Astronomy & Astrophysics*, 395:99–115.

Luhman, K. L. (2013). Discovery of a Binary Brown Dwarf at 2 pc from the Sun. *Astrophysical Journal Letters*, 767:L1.

Lunine, J. I., Hubbard, W. B., and Marley, M. S. (1986). Evolution and infrared spectra of brown dwarfs. *Astrophysical Journal*, 310:238–260.

Madhusudhan, N. and Seager, S. (2009). A Temperature and Abundance Retrieval Method for Exoplanet Atmospheres. *Astrophysical Journal*, 707:24–39.

Madhusudhan, N. and Seager, S. (2010). On the Inference of Thermal Inversions in Hot Jupiter Atmospheres. *Astrophysical Journal*, 725:261–274.

Madhusudhan, N. and Seager, S. (2011). High Metallicity and Non-equilibrium Chemistry in the Dayside Atmosphere of hot-Neptune GJ 436b. *Astrophysical Journal*, 729:41.

Magic, Z., Collet, R., Asplund, M., Trampedach, R., Hayek, W., et al. (2013). The Stagger-grid: A grid of 3D stellar atmosphere models. I. Methods and general properties. *Astronomy & Astrophysics*, 557:A26.

Mancini, L., Giacobbe, P., Littlefair, S. P., Southworth, J., Bozza, V., et al. (2015). Rotation periods and astrometric motions of the Luhman 16AB brown dwarfs by high-resolution lucky-imaging monitoring. *Astronomy & Astrophysics*, 584:A104.

Mancini, L., Southworth, J., Ciceri, S., Calchi Novati, S., Dominik, M., et al. (2014a). Physical properties of the WASP-67 planetary system from multi-colour photometry. *Astronomy & Astrophysics*, 568:A127.

Mancini, L., Southworth, J., Ciceri, S., Dominik, M., Henning, T., et al. (2014b). Physical properties and transmission spectrum of the WASP-80 planetary system from multi-colour photometry. *Astronomy & Astrophysics*, 562:A126.

Mandel, K. and Agol, E. (2002). Analytic Light Curves for Planetary Transit Searches. *Astrophysical Journal*, 580:L171–L175.

Marley, M. S., Seager, S., Saumon, D., Lodders, K., Ackerman, A. S., et al. (2002). Clouds and Chemistry: Ultracool Dwarf Atmospheric Properties from Optical and Infrared Colors. *Astrophysical Journal*, 568:335–342.

Masseron, T., Plez, B., Eck, S. V., Colin, R., Daoutidis, I., et al. (2014). CH in stellar atmospheres: an extensive linelist. *Astronomy & Astrophysics*, 571:A47.

Maxwell Garnett, J. C. (1904). Colours in Metal Glasses and in Metallic Films. *Royal Society of London Philosophical Transactions Series A*, 203:385–420.

Mayor, M., Pepe, F., Queloz, D., Bouchy, F., Rupprecht, G., et al. (2003). Setting New Standards with HARPS. *The Messenger*, 114:20–24.

Mayor, M. and Queloz, D. (1995). A Jupiter-mass companion to a solar-type star. *Nature*, 378:355–359.

Mayor, M., Udry, S., Naef, D., Pepe, F., Queloz, D., et al. (2004). The CORALIE survey for southern extra-solar planets. XII. Orbital solutions for 16 extra-solar planets discovered with CORALIE. *Astronomy & Astrophysics*, 415:391–402.

Mie, G. (1908). Beiträge zur Optik trüber Medien, speziell kolloidaler Metallösungen. *Annalen der Physik*, 330:377–445.

Mihalas, D. (1965). Model Atmospheres and Line Profiles for Early-Type Stars. *Astrophysical Journal Supplement,*, 9:321.

Mihalas, D. (1978). *Stellar atmospheres*. W. H. Freeman and Co.

Mitalas, R. and Sills, K. R. (1992). On the photon diffusion time scale for the sun. *Astrophysical Journal*, 401:759.

Morley, C. V., Fortney, J. J., Marley, M. S., Visscher, C., Saumon, D., et al. (2012). Neglected Clouds in T and Y Dwarf Atmospheres. *Astrophysical Journal*, 756:172.

Murray, C. D. and Correia, A. C. M. (2010). *Keplerian Orbits and Dynamics of Exoplanets*, pages 15–23. University of Arizona Press.

Muthsam, H. J., Kupka, F., Löw-Baselli, B., Obertscheider, C., Langer, M., et al. (2010). ANTARES - A Numerical Tool for Astrophysical RESearch with applications to solar granulation. *New Astronomy*, 15:460–475.

NASA Exoplanet Archive. http://exoplanetarchive.ipac.caltech.edu.

Nordlund, A. and Stein, R. F. (1995). Convection; Significance for Stellar Structure and Evolution. In *Liege International Astrophysical Colloquia*, volume 32, page 75.

Nuth, III, J. A. and Ferguson, F. T. (2006). Silicates Do Nucleate in Oxygen-rich Circumstellar Outflows: New Vapor Pressure Data for SiO. *Astrophysical Journal*, 649:1178–1183.

Olander, N. (1981). PhD thesis, Uppsala University.

Palik, E. D. (1985). *Handbook of Optical Constants of Solids*. Academic Press.

Partridge, H. and Schwenke, D. W. (1997). The determination of an accurate isotope dependent potential energy surface for water from extensive ab initio calculations and experimental data. *The Journal of Chemical Physics*, 106:4618–4639.

Patzer, A. B. C., Chang, C., Sedlmayr, E., and Sülzle, D. (1999). Ab initio thermodynamic properties for different isomers of the Al O molecule. *European Physical Journal D*, 6:57–62.

Peach, G. (1970). Continuous absorption coefficients for non-hydrogenic atoms. *Memoirs of the RAS*, 73:1.

Pepe, F. A., Cristiani, S., Rebolo Lopez, R., Santos, N. C., Amorim, A., et al. (2010). ESPRESSO: the Echelle spectrograph for rocky exoplanets and stable spectroscopic observations. In *Society of Photo-Optical Instrumentation Engineers (SPIE) Conference Series*, volume 7735 of *Society of Photo-Optical Instrumentation Engineers (SPIE) Conference Series*, page 0.

Petigura, E. A., Howard, A. W., and Marcy, G. W. (2013). Prevalence of Earth-size planets orbiting Sun-like stars. *Proceedings of the National Academy of Science*, 110:19273–19278.

Plane, J. M. C. (2013). On the nucleation of dust in oxygen-rich stellar outflows. *Philosophical Transactions of the Royal Society of London Series A*, 371:20120335–20120335.

Plez, B. (1992). Spherical opacity sampling model atmospheres for M-giants and supergiants. II - A grid. *Astrophysical Journal Supplement Series*, 94:527–552.

Plez, B., van Eck, S., Jorissen, A., Edvardsson, B., Eriksson, K., et al. (2003). A MARCS Grid of S-Type Star Atmospheres. In Piskunov, N., Weiss, W. W., and Gray, D. F., editors, *Modelling of Stellar Atmospheres*, volume 210 of *IAU Symposium*, page 2P.

Popovas, A. (2014). Stellar model atmospheres of late spectra type stars. Master's thesis, University of Copenhagen.

Posch, T., Kerschbaum, F., Fabian, D., Mutschke, H., Dorschner, J., et al. (2003). Infrared properties of solid titanium oxides: Exploring potential primary dust condensates. *Astrophysical Journal Supplement Series*, 149:437–445.

Prandtl, L. (1925). Untersuchungen zur ausgebildeten Turbulenz. *Zeitschrift für angewandte Mathematik und Mechanik*, 5:136–139.

Press, W. H., Flannery, B. P., Teukolsky, S. A., and Vetterling, W. T. (1992). *Numerical Recipes in Fortran 77: The Art of Scientific Computing*. Cambridge University Press.

Rayner, J. T., Toomey, D. W., Onaka, P. M., Denault, A. J., Stahlberger, W. E., et al. (2003). SpeX: A Medium-Resolution 0.8-5.5 Micron Spectrograph and Imager for the NASA Infrared Telescope Facility. *The Publications of the Astronomical Society of the Pacific*, 115:362–382.

Reid, I. N., Kirkpatrick, J. D., Gizis, J. E., Dahn, C. C., Monet, D. G., et al. (2000). Four Nearby L Dwarfs. *Astronomical Journal*, 119:369–377.

Rimmer, P. B. and Helling, C. (2013). Ionization in Atmospheres of Brown Dwarfs and Extrasolar Planets. IV. The Effect of Cosmic Rays. *Astrophysical Journal*, 774:108.

Rossow, W. B. (1978). Cloud microphysics - Analysis of the clouds of Earth, Venus, Mars, and Jupiter. *Icarus*, 36:1–50.

Rothman, L. S., Gordon, I. E., Barber, R. J., Dothe, H., Gamache, R. R., et al. (2005). HITEMP database. https://www.cfa.harvard.edu/hitran.

Rothman, L. S., Gordon, I. E., Barber, R. J., Dothe, H., Gamache, R. R., et al. (2010). HITEMP, the high-temperature molecular spectroscopic database. *Journal of Quantitative Spectroscopy & Radiative Trasnfer*, 111:2139–2150.

Sako, T., Sekiguchi, T., Sasaki, M., Okajima, K., Abe, F., et al. (2008). MOA-cam3: a wide-field mosaic CCD camera for a gravitational microlensing survey in New Zealand. *Experimental Astronomy*, 22:51–66.

Saumon, D., Hubbard, W. B., Burrows, A., Guillot, T., Lunine, J. I., et al. (1996). A Theory of Extrasolar Giant Planets. *Astrophysical Journal*, 460:993.

Schmidt, S. J., West, A. A., Burgasser, A. J., Bochanski, J. J., and Hawley, S. L. (2010). Discovery of an Unusually Blue L Dwarf Within 10 pc of the Sun. *Astronomical Journal*, 139:1045–1050.

Schwenke, D. W. (1998). Opacity of TiO from a coupled electronic state calculation parametrized by AB initio and experimental data. *Faraday Discussions*, 109:321–334.

Seinfeld, J. H. and Pandis, S. N., editors (1998). *Atmospheric chemistry and physics : from air pollution to climate change*.

Sharp, C. M. and Huebner, W. F. (1990). Molecular equilibrium with condensation. *Astrophysical Journal Supplement Series*, 72:417–431.

Skottfelt, J., Bramich, D. M., Figuera Jaimes, R., Jørgensen, U. G., Kains, N., et al. (2015). Searching for variable stars in the cores of five metal-rich globular clusters using EMCCD observations. *Astronomy & Astrophysics*, 573:A103.

Skottfelt, J., Bramich, D. M., Figuera Jaimes, R., Jørgensen, U. G., Kains, N., et al. (2013). EMCCD photometry reveals two new variable stars in the crowded central region of the globular cluster NGC 6981. *Astronomy & Astrophysics*, 553:A111.

Smith, G. H., Bell, R. A., and Hesser, J. E. (1989). CN and CH variations among subgiants in the globular cluster 47 Tucanae. *Astrophysical Journal*, 341:190–200.

Somerville, W. B. (1964). The Continuous Absoprtion Coefficient of the Negative Hydrogen Molecular Ion. *Astrophysical Journal*, 139:192.

Somerville, W. B. (1965). The Continuous Absorption Coefficient of HEˆ-. *Astrophysical Journal*, 141:811.

Sorahana, S., Suzuki, T. K., and Yamamura, I. (2014). A signature of chromospheric activity in brown dwarfs revealed by 2.5-5.0 μm AKARI spectra. *Monthly Notices of the RAS*, 440:3675–3684.

Sorahana, S. and Yamamura, I. (2012). AKARI Observations of Brown Dwarfs. III. CO, CO_2, and CH_4 Fundamental Bands and Physical Parameters. *Astrophysical Journal*, 760:151.

Sorahana, S. and Yamamura, I. (2014). AKARI Observations of Brown Dwarfs. IV. Effect of Elemental Abundances on Near-infrared Spectra between 1.0 and 5.0 μm. *Astrophysical Journal*, 793:47.

Southworth, J., Hinse, T. C., Burgdorf, M., Calchi Novati, S., Dominik, M., et al. (2014). High-precision photometry by telescope defocussing - VI. WASP-24, WASP-25 and WASP-26. *Monthly Notices of the Royal Astronomical Society*, 444:776–789.

Southworth, J., Hinse, T. C., Jørgensen, U. G., Dominik, M., Ricci, D., et al. (2009). High-precision photometry by telescope defocusing - I. The transiting planetary system WASP-5. *Monthly Notices of the Royal Astronomical Society*, 396:1023–1031.

Southworth, J., Mancini, L., Ciceri, S., Budaj, J., Dominik, M., et al. (2015a). High-precision photometry by telescope defocusing - VII. The ultrashort period planet WASP-103. *Monthly Notices of the Royal Astronomical Society*, 447:711–721.

Southworth, J., Mancini, L., Tregloan-Reed, J., Calchi Novati, S., Ciceri, S., et al. (2015b). Larger and faster: revised properties and a shorter orbital period for the WASP-57 planetary system from a pro-am collaboration. *Monthly Notices of the RAS*, 454:3094–3107.

Southworth, J., Tregloan-Reed, J., Andersen, M. I., Calchi Novati, S., Ciceri, S., et al. (2015c). High-precision photometry by telescope defocussing. VIII. WASP-22, WASP-41, WASP-42 and WASP-55. *ArXiv e-prints*.

Stancil, P. C., Zhao, L., Benhui, Y., and Osborn, A. (2002). Molecular Opacity Project Database of the University of Georgia. http://www.physast.uga.edu/ugamop.

Stark, C. R., Helling, C., Diver, D. A., and Rimmer, P. B. (2013). Ionization in Atmospheres of Brown Dwarfs and Extrasolar Planets. V. Alfvén Ionization. *Astrophysical Journal*, 776:11.

Street, R. A., Fulton, B. J., Scholz, A., Horne, K., Helling, C., et al. (2015). Extended Baseline Photometry of Rapidly Changing Weather Patterns on the Brown Dwarf Binary Luhman-16. *Astrophysical Journal*, 812:161.

Struve, O. (1952). Proposal for a project of high-precision stellar radial velocity work. *The Observatory*, 72:199–200.

Sudarsky, D., Burrows, A., and Pinto, P. (2000). Albedo and Reflection Spectra of Extrasolar Giant Planets. *Astrophysical Journal*, 538:885–903.

Tamuz, O., Ségransan, D., Udry, S., Mayor, M., Eggenberger, A., et al. (2008). The CORALIE survey for southern extra-solar planets. XV. Discovery of two eccentric planets orbiting <ASTROBJ>HD 4113</ASTROBJ> and <ASTROBJ>HD 156846</ASTROBJ>. *Astronomy & Astrophysics*, 480:L33–L36.

Tatum, J. B. (1966). Accurate Partition Functions and Dissociation Equilibrium Constants of Diatomic Molecules of Astrophysical Interest. *Publications of the Dominion Astrophysical Observatory Victoria*, 13:1.

Tennyson, J. (2012). Accurate variational calculations for line lists to model the vibration rotation spectra of hot astrophysical atmospheres. *WIREs Computational Molecular Science*, 2:698–715.

Tennyson, J., Yurchenko, S., Hill, C., Polyansky, O., Lodi, L., et al. (2011). ExoMol database. http://www.exomol.com.

Tsapras, Y., Choi, J.-Y., Street, R. A., Han, C., Bozza, V., et al. (2014). A Super-Jupiter Orbiting a Late-type Star: A Refined Analysis of Microlensing Event OGLE-2012-BLG-0406. *Astrophysical Journal*, 782:48.

Tsapras, Y., Street, R., Horne, K., Snodgrass, C., Dominik, M., et al. (2009). RoboNet-II: Follow-up observations of microlensing events with a robotic network of telescopes. *Astronomische Nachrichten*, 330:4.

Tsuji, T. (1964). Molecular abundance in stellar atmospheres. *Annals of the Tokyo Astronomical Observatory*, 9:1–110.

Tsuji, T. (1973). Molecular Abundances in Stellar Atmospheres. II. *Astronomy & Astrophysics*, 23:411–431.

Tsuji, T. (1986). Molecules in stars. *Annual Review of Astronomy & Astrophysics*, 24:89–125.

Tsuji, T. (2001). Unified Model Photospheres for Ultracool Dwarfs of Types L and T. In Jones, H. R. A. and Steele, I. A., editors, *Ultracool Dwarfs: New Spectral Types L and T*, page 9.

Tsuji, T. (2002). Dust in the Photospheric Environment: Unified Cloudy Models of M, L, and T Dwarfs. *Astrophysical Journal*, 575:264–290.

Tsuji, T. (2005). Dust in the Photospheric Environment. III. A Fundamental Element in the Characterization of Ultracool Dwarfs. *Astrophysical Journal*, 621:1033–1048.

Tsuji, T., Nakajima, T., and Yanagisawa, K. (2004). Dust in the Photospheric Environment. II. Effect on the Near-Infrared Spectra of L and T Dwarfs. *Astrophysical Journal*, 607:511–529.

Tsuji, T., Ohnaka, K., and Aoki, W. (1996). Dust formation in stellar photospheres: a case of very low mass stars and a possible resolution on the effective temperature scale of M dwarfs. *Astronomy & Astrophysics*, 305:L1.

Tsuji, T., Yamamura, I., and Sorahana, S. (2011). AKARI Observations of Brown Dwarfs. II. CO_2 as Probe of Carbon and Oxygen Abundances in Brown Dwarfs. *Astrophysical Journal*, 734:73.

Udalski, A. (2003). The Optical Gravitational Lensing Experiment. Real Time Data Analysis Systems in the OGLE-III Survey. *Acta Astronomica*, 53:291–305.

Vögler, A., Shelyag, S., Schüssler, M., Cattaneo, F., Emonet, T., et al. (2005). Simulations of magneto-convection in the solar photosphere. Equations, methods, and results of the MURaM code. *Astronomy & Astrophysics*, 429:335–351.

Walker, R. (2014). Spectroscopic Atlas for Amateur Astronomers. http://www.ursusmajor.ch/downloads/spectroscopic-atlas-5_0-english.pdf.

Weck, P. F., Stancil, P. C., and Kirby, K. (2003). Theoretical study of the rovibrationally resolved transitions of CaH. *The Journal of Chemical Physics*, 118:9997–10005.

Wende, S., Reiners, A., Seifahrt, A., and Bernath, P. F. (2010). CRIRES spectroscopy and empirical line-by-line identification of FeH molecular absorption in an M dwarf. *Astronomy & Astrophysics*, 523:A58.

Winn, J. N. (2010). *Exoplanet Transits and Occultations*, pages 55–77. University of Arizona Press.

Witte, S. (2011). *Simulation of atmospheric dust clouds*. PhD thesis, University of Hamburg.

Witte, S., Helling, C., and Hauschildt, P. H. (2009). Dust in brown dwarfs and extra-solar planets. II. Cloud formation for cosmologically evolving abundances. *Astronomy & Astrophysics*, 506:1367–1380.

Woitke, P. and Helling, C. (2003). Dust in brown dwarfs II. *Astronomy & Astrophysics*, 399:297–313.

Woitke, P. and Helling, C. (2004). Dust in brown dwarfs III. *Astronomy & Astrophysics*, 414:335–350.

Woitke, P., Riaz, B., Duchêne, G., Pascucci, I., Lyo, A.-R., et al. (2011). The unusual protoplanetary disk around the T Tauri star ET Chamaeleontis. *Astronomy & Astrophysics*, 534:A44.

Wolszczan, A. and Frail, D. A. (1992). A planetary system around the millisecond pulsar PSR1257 + 12. *Nature*, 355:145–147.

Wright, E. L., Mainzer, A., Kirkpatrick, J. D., Masci, F., Cushing, M. C., et al. (2014). NEOWISE-R Observation of the Coolest Known Brown Dwarf. *Astronomical Journal*, 148:82.

Yadin, B., Veness, T., Conti, P., Hill, C., Yurchnko, S. N., et al. (2012). ExoMol line lists - I. The rovibrational spectrum of BeH, MgH and CaH in the $X^2\sum^+$state. *Monthly Notices of the RAS*, 425:34–43.

Yamamura, I., Tsuji, T., and Tanabé, T. (2010). AKARI Observations of Brown Dwarfs. I. CO and CO_2 Bands in the Near-infrared Spectra. *Astrophysical Journal*, 722:682–698.

Zeidler, S., Posch, T., and Mutschke, H. (2013). Optical constants of refractory oxides at high temperatures. *Astronomy & Astrophysics*, 553:A81.